frontiers | Research Topics

Frontiers in chemistry: Rising stars 2020

Edited by
Chun Xu, Jie He, Jianping Yang and Ping Yu

Published in
Frontiers in Chemistry

FRONTIERS EBOOK COPYRIGHT STATEMENT

The copyright in the text of individual articles in this ebook is the property of their respective authors or their respective institutions or funders. The copyright in graphics and images within each article may be subject to copyright of other parties. In both cases this is subject to a license granted to Frontiers.

The compilation of articles constituting this ebook is the property of Frontiers.

Each article within this ebook, and the ebook itself, are published under the most recent version of the Creative Commons CC-BY licence. The version current at the date of publication of this ebook is CC-BY 4.0. If the CC-BY licence is updated, the licence granted by Frontiers is automatically updated to the new version.

When exercising any right under the CC-BY licence, Frontiers must be attributed as the original publisher of the article or ebook, as applicable.

Authors have the responsibility of ensuring that any graphics or other materials which are the property of others may be included in the CC-BY licence, but this should be checked before relying on the CC-BY licence to reproduce those materials. Any copyright notices relating to those materials must be complied with.

Copyright and source acknowledgement notices may not be removed and must be displayed in any copy, derivative work or partial copy which includes the elements in question.

All copyright, and all rights therein, are protected by national and international copyright laws. The above represents a summary only. For further information please read Frontiers' Conditions for Website Use and Copyright Statement, and the applicable CC-BY licence.

ISSN 1664-8714
ISBN 978-2-8325-4142-5
DOI 10.3389/978-2-8325-4142-5

About Frontiers

Frontiers is more than just an open access publisher of scholarly articles: it is a pioneering approach to the world of academia, radically improving the way scholarly research is managed. The grand vision of Frontiers is a world where all people have an equal opportunity to seek, share and generate knowledge. Frontiers provides immediate and permanent online open access to all its publications, but this alone is not enough to realize our grand goals.

Frontiers journal series

The Frontiers journal series is a multi-tier and interdisciplinary set of open-access, online journals, promising a paradigm shift from the current review, selection and dissemination processes in academic publishing. All Frontiers journals are driven by researchers for researchers; therefore, they constitute a service to the scholarly community. At the same time, the *Frontiers journal series* operates on a revolutionary invention, the tiered publishing system, initially addressing specific communities of scholars, and gradually climbing up to broader public understanding, thus serving the interests of the lay society, too.

Dedication to quality

Each Frontiers article is a landmark of the highest quality, thanks to genuinely collaborative interactions between authors and review editors, who include some of the world's best academicians. Research must be certified by peers before entering a stream of knowledge that may eventually reach the public - and shape society; therefore, Frontiers only applies the most rigorous and unbiased reviews. Frontiers revolutionizes research publishing by freely delivering the most outstanding research, evaluated with no bias from both the academic and social point of view. By applying the most advanced information technologies, Frontiers is catapulting scholarly publishing into a new generation.

What are Frontiers Research Topics?

Frontiers Research Topics are very popular trademarks of the *Frontiers journals series*: they are collections of at least ten articles, all centered on a particular subject. With their unique mix of varied contributions from Original Research to Review Articles, Frontiers Research Topics unify the most influential researchers, the latest key findings and historical advances in a hot research area.

Find out more on how to host your own Frontiers Research Topic or contribute to one as an author by contacting the Frontiers editorial office: frontiersin.org/about/contact

Frontiers in chemistry: Rising stars 2020

Topic editors
Chun Xu — The University of Queensland, Australia
Jie He — University of Connecticut, United States
Jianping Yang — Donghua University, China
Ping Yu — Institute of Chemistry, Chinese Academy of Sciences (CAS), China

Citation
Xu, C., He, J., Yang, J., Yu, P., eds. (2023). *Frontiers in chemistry: Rising stars 2020*. Lausanne: Frontiers Media SA. doi: 10.3389/978-2-8325-4142-5

Table of contents

06 Recent Progress in Enhancing Poly(Lactic Acid) Stereocomplex Formation for Material Property Improvement
Fuhong Luo, Alexander Fortenberry, Jie Ren and Zhe Qiang

14 Reconfigurable and Recyclable Photoactuators Based on Azobenzene-Containing Polymers
Mingsen Chen, Shuofeng Liang, Chengwei Liu, Yuanli Liu and Si Wu

20 A Degradable and Self-Healable Vitrimer Based on Non-isocyanate Polyurethane
Haitao Wu, Biqiang Jin, Hao Wang, Wenqiang Wu, Zhenxing Cao, Jinrong Wu and Guangsu Huang

30 Advances of Carbon-Based Materials for Lithium Metal Anodes
Kaikai Tang, Jun Xiao, Xiao Li, Dandan Wang, Mengqi Long, Jun Chen, Hong Gao, Weihua Chen, Chuntai Liu and Hao Liu

38 Two-Dimensional Metal Organic Framework Nanosheets as Bifunctional Catalyst for Electrochemical and Photoelectrochemical Water Oxidation
Chang Liu, Xiaochen Shen, Grayson Johnson, Yulu Zhang, Changlin Zhang, Jiafu Chen, Lingyan Li, Colton Sheehan, Zhenmeng Peng and Sen Zhang

45 Nature's Chemists: The Discovery and Engineering of Phytochemical Biosynthesis
Kaouthar Eljounaidi and Benjamin R. Lichman

55 Nitrogen-Doped Mesoporous Carbon Microspheres by Spray Drying-Vapor Deposition for High-Performance Supercapacitor
Xiaoran Sun, Yueqi Kong, Yang Liu, Liang Zhou, Ashok Kumar Nanjundan, Xiaodan Huang and Chengzhong Yu

65 Applications of Thiol-Ene Chemistry for Peptide Science
Mark D. Nolan and Eoin M. Scanlan

86 Supported Pt Nanoparticles on Mesoporous Titania for Selective Hydrogenation of Phenylacetylene
Mingzhen Hu, Lei Jin, Yanliu Dang, Steven L. Suib, Jie He and Ben Liu

95 Cobalt-Based Metal-Organic Frameworks and Their Derivatives for Hydrogen Evolution Reaction
Wenjuan Han, Minhan Li, Yuanyuan Ma and Jianping Yang

113 Leverage Surface Chemistry for High-Performance Triboelectric Nanogenerators
Jing Xu, Yongjiu Zou, Ardo Nashalian and Jun Chen

136 Influence of Solvents' Polarity on the Physicochemical Properties and Photocatalytic Activity of Titania Synthesized Using *Deinbollia pinnata* Leaves
Yakubu Rufai, Sheela Chandren and Norazah Basar

147 Current Methods for Detecting Cell Membrane Transient Interactions
Yousef Bagheri, Ahsan Ausaf Ali and Mingxu You

161 Functional Nucleic Acid-Based Live-Cell Fluorescence Imaging
Yutong Zhang, Yulin Du, Yuting Zhuo and Liping Qiu

168 Controlling Experimental Parameters to Improve Characterization of Biomaterial Fouling
Alexander H. Jesmer and Ryan G. Wylie

183 Trends of Bead Counting-Based Technologies Toward the Detection of Disease-Related Biomarkers
Wenjiao Fan, Dou Liu, Wei Ren and Chenghui Liu

190 Recent Progress in Quantitatively Monitoring Vesicular Neurotransmitter Release and Storage With Micro/Nanoelectrodes
Yuying Liu, Jinchang Du, Mengying Wang, Jing Zhang, Chunlan Liu and Xianchan Li

208 Co-delivery of Salinomycin and Curcumin for Cancer Stem Cell Treatment by Inhibition of Cell Proliferation, Cell Cycle Arrest, and Epithelial–Mesenchymal Transition
Yongmei Zhao, Kaikai Wang, Yuanlin Zheng, Xiaobao Zeng, Yi Chieh Lim and Tianqing Liu

216 Viral Mimicry as a Design Template for Nucleic Acid Nanocarriers
Ina F. de la Fuente, Shraddha S. Sawant, Mark Q. Tolentino, Patrick M. Corrigan and Jessica L. Rouge

247 Optical Devices Constructed From Responsive Microgels for Polyphenols Detection
Jingying Wang, Xieli Zhang, Kaiyao Shi and Qiang Zhang

254 Structural Proteomics Methods to Interrogate the Conformations and Dynamics of Intrinsically Disordered Proteins
Rebecca Beveridge and Antonio N. Calabrese

274 Wide-Bandgap Halide Perovskites for Indoor Photovoltaics
Lethy Krishnan Jagadamma and Shaoyang Wang

282 Recent Advances in TiO_2-Based Heterojunctions for Photocatalytic CO_2 Reduction With Water Oxidation: A Review
Kai Li, Chao Teng, Shuang Wang and Qianhao Min

307 Iterative Exponential Growth of Oxygen-Linked Aromatic Polymers Driven by Nucleophilic Aromatic Substitution Reactions
Tyler J. Jaynes, Mona Sharafi, Joseph P. Campbell, Jessica Bocanegra, Kyle T. McKay, Kassondra Little, Reilly Osadchey Brown, Danielle L. Gray, Toby J. Woods, Jianing Li and Severin T. Schneebeli

315 Investigation of Nucleation and Growth at a Liquid–Liquid Interface by Solvent Exchange and Synchrotron Small-Angle X-Ray Scattering
Elyse A. Schriber, Daniel J. Rosenberg, Ryan P. Kelly, Anita Ghodsi and J. Nathan Hohman

frontiers in Chemistry

MINI REVIEW
published: 20 August 2020
doi: 10.3389/fchem.2020.00688

Recent Progress in Enhancing Poly(Lactic Acid) Stereocomplex Formation for Material Property Improvement

Fuhong Luo[1], Alexander Fortenberry[2], Jie Ren[1] and Zhe Qiang[2]**

[1] Department of Polymeric Materials, School of Materials Science and Engineering, Institute of Nano and Biopolymeric Materials, Tongji University, Shanghai, China, [2] School of Polymer Science and Engineering, The University of Southern Mississippi, Hattiesburg, MS, United States

The production and utilization of polymers have been widely implemented into diverse applications that benefit modern human society, but one of the most valuable properties of polymers, durability, has posed a long-standing environmental challenge from its inception since plastic waste can lead to significant contamination and remains in landfills and oceans for at least hundreds of years. Poly(lactic acid) (PLA) derived from renewable resources provides a sustainable alternative to traditional polymers due to its advantages of comparable mechanical properties with common plastics and biodegradability. However, the poor thermal and hydrolytic stability of PLA-based materials limit their potential for durable applications. Stereocomplex crystallization of enantiomeric poly (l-lactide) (PLLA) and poly (d-lactide) (PDLA) provides a robust approach to significantly enhance material properties such as stability and biocompatibility through strong intermolecular interactions between L-lactyl and D-lactyl units, which has been the key strategy to further PLA applications. This review focuses on discussing recent progress in the development of processing strategies for enhancing the formation of stereocomplexes within PLA materials, including thermal processing, additive manufacturing, and solution casting. The mechanism for enhancing SC formation and resulting material property improvement enabled by each method are also discussed. Finally, we also provide the perspectives on current challenges and opportunities for improving the understanding of processing-structure-property relationship in PLA materials that could be beneficial to their wide practical applications for a sustainable society.

Keywords: sustainable, biodegradability, structure-property relationship, crystallization, advanced manufacturing

OPEN ACCESS

Edited by:
Jianping Yang,
Donghua University, China

Reviewed by:
Yanping Wang,
Donghua University, China
Mattia Bartoli,
Politecnico di Torino, Italy

****Correspondence:***
Jie Ren
renjie6598@163.com
Zhe Qiang
zhe.qiang@usm.edu

Specialty section:
This article was submitted to Green and Sustainable Chemistry, a section of the journal Frontiers in Chemistry

Received: *31 May 2020*
Accepted: *01 July 2020*
Published: *20 August 2020*

Citation:
Luo F, Fortenberry A, Ren J and Qiang Z (2020) Recent Progress in Enhancing Poly(Lactic Acid) Stereocomplex Formation for Material Property Improvement. Front. Chem. 8:688. doi: 10.3389/fchem.2020.00688

INTRODUCTION

Traditional petroleum-derived plastics have been "ideal" materials and widely used in a variety of industrial and consumer products over past decades due to their high strength, flexibility, and durability and low manufacturing cost (Andrady and Neal, 2009). However, the accumulation of these non-degradable plastic wastes brings harmful impact on the environment for developing a sustainable society since a substantial amount of them has been disposed into ocean and landfills (Al-Salem et al., 2009). In order to address this grand challenge, tremendous efforts

have been focused on the development of sustainable polymers toward an environmentally friendly future (Schneiderman and Hillmyer, 2017). Among various materials that have been proposed as promising candidates, polylactic acid (PLA) currently holds the leading position with the largest industrial production scale and explosive market growth (Murariu and Dubois, 2016), which has received significant attention for various applications such as biodegradable thermosets (Li et al., 2019), drug delivery (Casalini et al., 2019), shape memory materials (Cai et al., 2019), and food packaging (Bai et al., 2014; Tawakkal et al., 2014). However, key bottlenecks still remain for fully utilizing its potential for implementation into wide practical applications, which are associated with their inherently unsatisfactory material performances including low heating distortion temperature, brittleness, and poor thermal and hydrolytic stability (Rasal et al., 2010; Ren, 2010). The most common and robust solution to produce reinforced PLA materials is *via* stereocomplex crystallization using enantiomeric pairs of poly (L-lactide) (PLLA) and poly (D-lactide) (PDLA), which can occur from both melt and solution state (Ikada et al., 1987). For a well-mixed PLLA and PDLA blend, multicenter hydrogen bonding interactions lead to a possible alternative arrangement of helical chains between L-lactyl and D-lactyl units with opposite chiral conformation for PLA stereocomplexation (SC) (Okihara et al., 2006; Wan et al., 2019). As opposed to homocrystallites (HCs) from enantiopure PLLA or PDLA, the blend of enantiomeric PLLA and PDLA provides enhanced intermolecular interactions through dipole–dipole interaction and hydrogen bonding, leading to more tightly packed chain conformations in a side-by-side manner within the SC crystal lattice (Tsuji, 2005), thus improving mechanical property, thermal stability, and hydrolytic resistance (Tsuji and Ikada, 1999). PLA-SC exhibits a melting temperature of ∼230°C, which is at least 50°C higher than the HC from neat PLLA or PDLA (Tsuji and Fukui, 2003). The hydrolytic degradation of PLA-SC is more retarded (more than three times slower) than PLA-HC when immersed in a water and phosphate buffer solution (Tsuji, 2000; Karst and Yang, 2006). Tensile strength, Young's modulus, and elongation-at-break of PLA-SC film all exhibit almost two times higher than those of homopolymer film since 3D micro crystal networks from SCs serve as intermolecular crosslinks for mechanical property enhancement (Shirahama et al., 2005). These results all indicate the significance of forming SC within PLA matrix for material property improvement and in general, a higher degree of crystallinity can provide better material physicochemical properties. Such improvement of chemical and thermal stability enables several practical applications of PLA-based materials in different fields including medicine, adhesives, and agricultural materials. As an example, the dimensional stability of PLA-SC bioplastics to heat (80°C for 30 s under 200 g load) increases nearly 4-fold (from 22 to 80%) compared with PLA-HC films (Lim et al., 2008). Water vapor permeability of PLA-SC film is also found to be 14–23% lower than that of homopolymer film (pure PLLA or PDLA), suggesting its potential applications in coating and packaging materials (Hortos et al., 2019).

However, achieving the ideal scenario of exclusively forming highly crystalline SC in PLA is not a straightforward pathway. Difficulties date back to the first report of PLA-SC formation by Ikada et al. in the 1980s (Ikada et al., 1987). Conventional methods for polymer processing such as melt blowing and injection molding require a high processing temperature (220–260°C) and often yield a relatively low SC content for commercial high molecular weight (MW) PLA (Katti and Schultz, 1982; Tsuji and Tezuka, 2004; Tsuji, 2016). The challenge arises from the relatively poor thermal stability of PLA, leading to potential material decomposition when the temperature is above 230°C and the competition between simultaneous formation of SC and HC. From a kinetic perspective, HC is usually more dominant during PLA crystallization due to its lower energy barrier and has a less prolonged and restricted chain diffusion than forming SC. While a wide variety of approaches have been demonstrated to enhance the SC formation within PLLA/PDLA blend (Bai H. et al., 2017), advanced processing techniques that can offer distinct advantages of scalability and low cost for raw materials are more relevant for industrial applications compared with molecular-level engineering of PLA that involves sophisticated chemistry for controlling MW and chain architecture. Herein, this review focuses on discussing recent progress in the development of methodologies for preparing PLA-SC (**Figure 1**), which not only includes scientific mechanisms for the origin of PLA-SC formation enhancement from each method but also highlights their processing-structure-property relationship for different applications including engineering plastics, biomedicine, and bioelectronics. We want to note, as a mini-review, there is no attempt to be comprehensive, and interested readers can find many excellent reviews on relevant topics of PLA-based materials including material synthesis, processing, macroscopic property, and applications that provide a more in-depth discussion (Pan et al., 2017, 2018; Li et al., 2018). Our goal is rather to provide a succinct summary about progress to date on technology development for enhancing PLA-SC formation in order to compel new or interdisciplinary researchers to enter the fray and inspire more progress in the field. Therefore, we also briefly discuss the challenges that need to be addressed in this field in order to allow further advancement of PLA-based materials that warrants a green and sustainable future.

MELT PROCESSING AT SPECIFIC TEMPERATURE WINDOW

Temperature is one of the most important processing parameters to control the crystallization behavior of semicrystalline polymers (Zhang et al., 2017). PLA-SC formation can occur from either melt state by melt crystallization or glassy state by cold crystallization from PLLA/PDLA blend (Cui et al., 2018). During PLA crystallization, a higher temperature may favor to produce SCs and suppress the formation of HCs, and therefore the difference in melting temperature between SC and HC, enabling a unique processing window (190–230°C) for predominant SC formation in PLA blend. Thermal annealing of PLLA/PDLA blend at this temperature range can also induce HC to SC

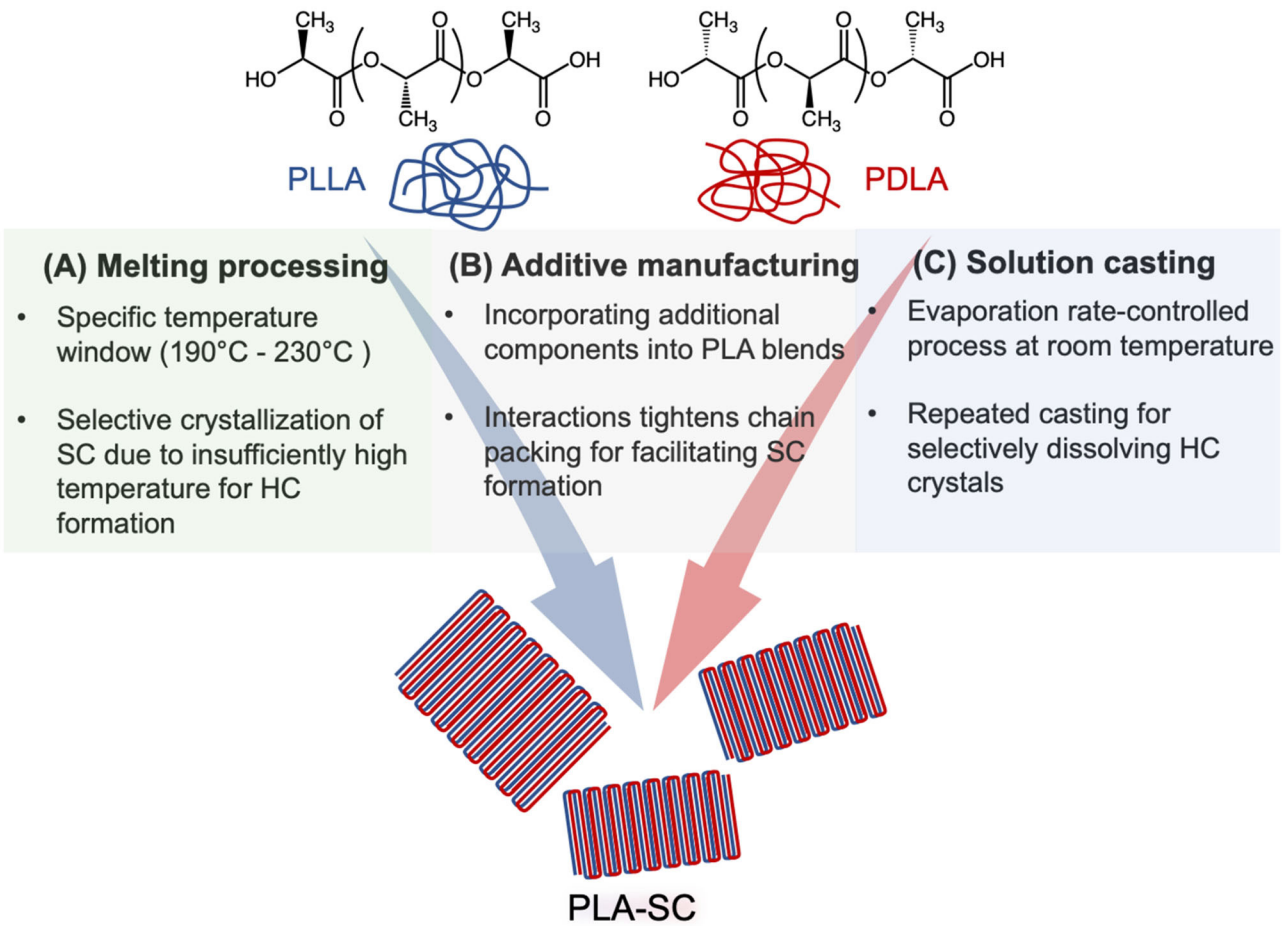

FIGURE 1 | Schematic illustration of different processing methods that have been developed for enhancing the stereocomplex (SC) formation from PLLA and PDLA, which are primarily composed of either one or multiple of following strategies: **(A)** melt processing; **(B)** additive manufacturing, and **(C)** solution casting.

transition for obtaining complete SCs (**Figure 2A**) because HC in the PLA matrix is melted at the specific temperature while SC can still be retained, which renders partial PLA melt with improved chain mobilty to form new SCs *via* molecular rearrangements (Bai et al., 2018; Gao et al., 2019). During this process, the content of SC gradually increases with extending annealing time until a complete SC formation achieved in the matrix. This method is also effective when a mismatch in molecular weight of PLLA and PDLA exists for stereocomplexation. Complete SC formation can be achieved from a high MW PLLA/low MW PDLA blend by thermal annealing, leading to improved hydrolytic resistance and mechanical properties from enhanced molecular packing between polymer chains in the exclusive presence of SC (Liu et al., 2019). Imposing external forces on PLLA/PDLA samples such as using oscillation shear injection molding (OSIM) for intense shear also induces higher crystallinity of SCs in comparison with conventional injection molding (Bai D. et al., 2016; Bai D.-Y. et al., 2016). The kinetics of SC formation can be improved by decreasing the viscoity of polymer melt during processing such as inclusion of a low T_g, biodegradable polymer, for reducing the activation energy of PLA melt flow for shear-thinning in order to facilitate the exclusive SC formation with high degree of crystallinity (Fu et al., 2018). Furthermore, a low-temperature sintering method for high MW PLLA/PDLA blend, involving densification, welding, and co-crystallization of powder particles, is developed to improve the degree of SC formation at a relatively low melt processing temperature of ∼180°C (Bai D. et al., 2017; Ji et al., 2019). This compounding technology, inspired by powder metallurgy to produce near net metallic particles, enables improved interdiffusion of PLA chains between adjacent particles in order to co-crystallize into SCs for tightly welding the interfaces (Pan et al., 2016; Zhang et al., 2018). The formed crystalline network, which is primarily located at particle-particle interfaces, imparts the sintered PLA-SC with enhanced mechanical strength and hydrolytic stability, excellent heat resistance, and high optical transparency. Fu et al. further broaden the application of low-temperature sintering by injection molding of partially melted nascent SC-PLA powder with small amounts of glyceryl monostearate incorporated as a lubricant (Ma et al., 2015a; Zhang et al.,

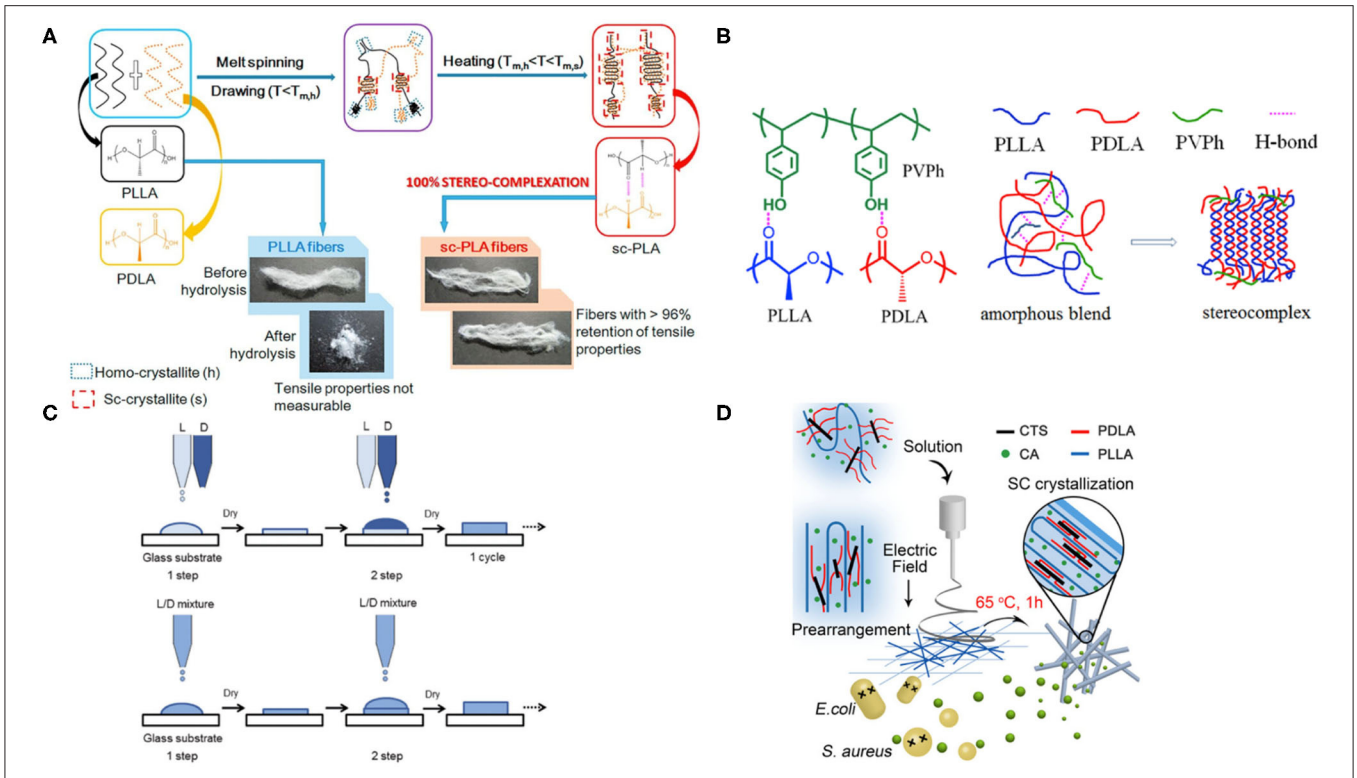

FIGURE 2 | Schematic illustration of some representative processing techniques for preparing PLA materials with high degree of SC formation. **(A)** melt processing at a specific temperature window (Gao et al., 2019) (Reproduced with permission. Copyright 2017, Elsevier); **(B)** using homopolymer (He et al., 2019) (Reproduced with permission. Copyright 2016, Elsevier); **(C)** layer-by-layer inkjet printing (Mei et al., 2018) (Reproduced with permission. Copyright 2012, Wiley); and **(D)** electrospinning (Yu et al., 2018) (Reproduced with permission. Copyright 2018, ACS).

2020). The non-melted SC crystallites act as nucleating agents to induce exclusive SC crystallization across the interface of the particles and accelerated the crystallization kinetics. Utilizing this method, a significantly reduced sintering time of 2 min and the ability to fabricate complex shapes like gears are achieved.

ADDITIVE MANUFACTURING

Many types of additives such as compatibilizers and nucleating agents have been utilized for improving the degree of PLA-SC formation *via* providing heterogeneous nucleation surfaces and promoting chain diffusion kinetics (Wu et al., 2019). Introducing physical interactions between PLA and additives is also effective for enhancing the intermolecular packing of PLLA and PDLA chains. For example, in a miscible ternary polymer blend (PLLA/PDLA/polyvinyl phenol, or PVPh, **Figure 2B**), an exclusive SC formation can be achieved by employing ∼30 wt% of PVPh in the system (He et al., 2019). This significant improvement is attributed to the enhanced intermolecular interactions at the initial stage of SC crystallization due to hydrogen bonding interactions between PVPh and PLLA, which not only act as precursors for facilitating SC formation but also shorten the diffusion pathway of enantiomeric chains for crystal growth. Zhang et al. demonstrate a pressure-controlled process for manipulating the morphology of SC crystals within PLLA/PDLA/PDLLA ternary blend in order to achieve combinatorial properties of improved heat resistance and faster hydrolytic degradation, providing a promising solution to on-demand tailor PLA-SC properties for a specific application (Liu et al., 2020). Confined SC formation within a cellulose template also leads to improved distortion temperature of PLA blends at 5% strain from 90 to 221°C and high specific moduli of 288.9. MPa/g from enhanced stereocomplexation due to synergesitc effects of promoted racemic helical pair formation and facilitated SC nucleation, which are both induced from the interfacial hydrogen bonding interations between cellulose and PLA chains (Brzezinski and Biela, 2014). The SC formation is further improved when polymer chains are chemically grafted onto nanoparticles or other components. In a PLLA-grafted nanocrystal cellulose (PLLA-NCC) /PDLA composite, a much higher degree of SC crystallinity (∼0.5), is obtained compared with PLLA/NCC/PDLA physical blend (∼0.06) after a rapid cooling from 250°C at 50°C/min. A leading explanation for this phenomenon is that PDLA molecules could assemble more easily with the bonded PLLA chains, resulting in SC with preferred closely packed geometry (Wang et al., 2020). Supertough and highly heat-resistant PLA composites are prepared by stereocomplexation

between PLLA and ethylene–vinyl acetate–glycidyl methacrylate grafted PDLA (PLLA/EVMG-g-PDLA), in which EVMG elastomer is used to improve interfacial adhesion, control melt matrix viscosity for obtaining co-continuous morphology, as well as facilitate SC formation (Tsuji et al., 1991). Similarly, melt blending of the equimolar PLLA/PDLA with reactive poly (ethylene–methyl acrylate–glycidyl methacrylate) (E-MA-GMA) results in a significant increase in softening temperature (from 151 to 201°C) and heat deflection temperature (from 121 to 174°C), which can be attributed to the exclusive SC crystallite formation from *in-situ* grafting of PLA chains onto epoxy units from E-MA-GMA backbone (Tsuji and Yamamoto, 2011). Additive manufacturing stratgey can be combined with low-temperature sintering method to further enhance the formation of SC crystallites at a relatively low melt processing temperature. He et al. introduced a trace amount of untwisted carbon nanotubes (CNTs) onto PLA-SC particle surfaces, and these unentangled CNTs act as nucleating agents for promoting SC formation of PLLA/PDLA homopolymer blend on the surfaces, as well as favor SC crystals to strongly weld the interfaces during low pressure sintering process (Akagi et al., 2012). As a result, the tensile strength of PLA-SC film significantly increases from 45.8 MPa (no CNT additive) to 67.2 MPa with using only 0.001 wt% CNT additives and a linear relationship was reported between its mechanical strength and SC crystallite content. The inclusion of nanoparticles into PLA-SC matrix also enables additional functionality for more diverse applications (Becker et al., 2010). For example, an optimized electrical conductivity of PLA-SC composites can be achieved from the introduction of multiwall carbon nanotubes (MWCNTs) with a continuous domain morphology to facilitate electron transportation (Hang Thi et al., 2017). Alternatively, embedding silver nanowires (AgNW) into PLLA/PDLA blend significantly improves the electric conductivity for optoelectronic devices that are stable over 10,000 bending cycles while enhancing tensile strength, modulus, and heat resistance from SC formation. The organic light-emitting diode (OLED) prepared from the optimal AgNW/PLA-SC composite exhibits high flexibility and luminosity, suggesting the great potential of PLA-SC based materials in bioelectronic applications (Koide et al., 2017).

SOLUTION CASTING

Since melt processing of PLA imposes potential concerns about thermal degradation and property deterioration, solution-casting is often used as an alternative to prepare PLA-SC from PLLA/PDLA homopolymer blend solution, followed by solvent evaporation at room temperature. During this dynamic process, an exclusive SC formation can occur at a specific concentration range between critical solution concentrations for SC and HC formation ($c_{SC}^* < c < c_{HC}*$) (Gardella et al., 2015). A sufficiently slow solvent evaporation rate likely yields a high content of SC in the blend, but it is not desired for industrial production rate/volume due to its inevitably long processing time. To address this challenge, a method involving repeated castings of PLLA/PDLA blend is developed to enhance the degree of SC crystallization by utilizing the solubility difference between HC and SC in the solvent so that only HCs are dissolved during sequential casting while preserving previously formed SCs (Ma et al., 2015b). A multiple casting strategy significantly increases the content of SCs and eventually leads to almost no presence of HC in the films. The concept of simultaneous casting and selective dissolution of HCs can be extended to a layer-by-layer casting approach (**Figure 2C**) through alternative deposition of PLLA and PDLA homopolymers onto the substrate using inkjet printing technique for achieving a predominant SC formation (Mei et al., 2018; Xie et al., 2018). Hang et al. deomonstrate that the thermal decomposition temperature of PLA-SC formed *via* this inkjet printing approach shows an increase of more than 90°C compared with original PLA without inclusion of SCs (Im et al., 2018). The layer-by-layer deposition process is suitable for manufacturing three-dimensional polymer composites with a customizable material shape. Strategies including adding small amounts of non-solvent and using ionic liquids also facilitate the formation of SCs in the polymer blends (Ishii et al., 2009; Jing et al., 2016). Furthermore, an additional thermal annealing step for cold crystallization of these as-cast films would be useful for further improving their thermal stability and mechanical properties from the nucleating effect of SC crystallines in PLA matrix (Boi et al., 2019b). The enantiomeric polymer blend solution can be used for other processing techniques such as electrospining and templated-drying in order to produce SC crystal embedded PLA with complex macroscopic shapes and enhanced final material properties. Electrospinning of PLA blend solution is able to produce a high degree of SC content due to the improved intermolecular ordering between PLLA and PDLA chains from high shear force induced by electric field (**Figure 2D**) (Yu et al., 2018). Strengthened PLA-based materials with improved thermal (melting temprature over 200°C) and mechanical properteis (Young's modulus up to 270 MPa) are prepared by the electrospinning of a PDLA-grafted chitosan (PDLA-CTC) /PLLA mixture, in which SC formation is assisted by intermolecular hydrogen bonding interactions between stereoisomers. Additionally, Xie et al. demonstrate a simple method for fabricating biodegradable PLA-SC porous scaffolds by solution casting of salt-embedding PLLA/PDLA blend, in which the salt particles (sodium chloride) are served as pore-forming agents by leaching. The obtained foam shows an improved thermal stability with a high structural intergrity even at elevated temperatures (∼120°C) due to the presence of PLA-SCs (Boi et al., 2019a). It is also very important to point out that these solution-based processing methods lead to additional environmental and safety concerns due to the requirement of using large amounts of volatile and toxic organics solvents, so more environmentally friendly solvents such as supercritical fluid should be considered in the future (Cui et al., 2013).

PROPERTY IMPROVEMENT FOR BIOMEDICAL APPLICATIONS

Besides being an alternative for conventional plastics, PLA-SC holds great promise for use in medical applications such as tissue scaffold and membrane for cell growth or proliferation due to its improved biocompatibility and bioresorbability compared with HC from analogous PLLA and PDLA (Tobió et al., 1998). An *in vivo* study from Ishii et al. demonstrates a slower degradation rate and a much milder inflammation of PLA-SC fibers than PLLA homopolymer fibers after 12 weeks of subcutaneous implantation in rats (Campana et al., 2014). PLA-SC can also serve as universal carriers for drugs (Ouchi and Ohya, 2004), proteins, and vaccines with the programmable release kinetics controlled by its microstructure (Oh, 2011; Dong et al., 2020). Furthermore, micellar particles self-assembled from stereocomplexation of PLA-based block copolymers have been commonly used in biomaterial research for injectable hydrogel (Nguyen and Lee, 2010), drug delivery (Feng et al., 2016), advanced diagnosis and treatment (Kersey et al., 2010), imaging agents, and antibacterial coating (Spasova et al., 2010; Qi et al., 2019).

CONCLUSIONS AND PERSPECTIVES

In conclusion, the stereocomplexation (SC) of PLLA and PDLA homopolymers is a very effective strategy for enhancing the properties of PLA-based materials in order to overcome their inherent limitations, which include poor thermal and hydrolytic stability, brittleness, and insufficient toughness. This review highlights recent advances in material preparation and processing technologies for enhancing SC crystallization, which is a key parameter for material property improvement. It is notable that even with these remarkable developments, there are still some challenges that remain unresolved for enabling wide applications of PLA-SC in biomedicine, commodity, and engineering plastics. For example, (1) the high cost of PDLA has been a major obstacle for large-scale industrial manufacturing, so the development of high-performance PLA-SC with a low PDLA content is beneficial for reducing production costs; (2) research has been intensively focused on controlling the structure and property of PLA-SC blends, but studies about quantitatively understanding their biodegradability and associated degradation kinetics upon local environment are still limited. A whole life cycle analysis of PLA products would be useful for promoting the development of relevant industrial chains; (3) the development of engineering solutions for on-demand manipulating crystal morphology of PLA-SCs would be essential for controlling ultimate material performance; (4) finally, exciting new opportunities have recently emerged for degradable bioelectronic applications for health monitoring and advanced therapeutic technologies (Tan et al., 2016), by which PLA has much to offer in this context. The continuous research progress in these areas is anticipated for enabling a more significant role of PLA-based materials toward a sustainable development of life and technology in the future.

AUTHOR CONTRIBUTIONS

All authors listed have made a substantial, direct and intellectual contribution to the work, and approved it for publication.

FUNDING

AF and ZQ acknowledge the University of Southern Mississippi for providing generous financial support.

REFERENCES

Akagi, T., Fujiwara, T., and Akashi, M. (2012). Rapid fabrication of polylactide stereocomplex using layer-by-layer deposition by inkjet printing. *Angew. Chem. Int. Ed.* 51, 5493–5496. doi: 10.1002/anie.201201586

Al-Salem, S. M., Lettieri, P., and Baeyens, J. (2009). Recycling and recovery routes of plastic solid waste (PSW): a review. *J. Waste Mana* 29, 2625–2643. doi: 10.1016/j.wasman.2009.06.004

Andrady, A. L., and Neal, M. A. (2009). Applications and societal benefits of plastics. *Phil. Trans. R. Soc. B* 364, 1977–1984. doi: 10.1098/rstb.2008.0304

Bai, D., Diao, X., Ju, Y., Liu, H., Bai, H., Zhang, Q., et al. (2018). Low-temperature sintering of stereocomplex-type polylactide nascent powder: the role of optical purity in directing the chain interdiffusion and cocrystallization across the particle interfaces. *Polymer* 150, 169–176. doi: 10.1016/j.polymer.2018.07.028

Bai, D., Liu, H., Bai, H., Zhang, Q., and Fu, Q. (2016). Powder metallurgy inspired low-temperature fabrication of high-performance stereocomplexed polylactide products with good optical transparency. *Sci. Rep.* 6:20260. doi: 10.1038/srep20260

Bai, D., Liu, H., Bai, H., Zhang, Q., and Fu, Q. (2017). Low-temperature sintering of stereocomplex-type polylactide nascent powder: effect of crystallinity. *Macromolecules* 50, 7611–7619. doi: 10.1021/acs.macromol.7b01794

Bai, D.-Y., Wang, K., Bai, H.-W., Zhang, Q., and Fu, Q. (2016). Polymer processing via, earning from nature and metal metallurgy. *Acta Polym. Sin.* 7, 843–849.

Bai, H., Deng, S., Bai, D., Zhang, Q., and Fu, Q. (2017). Recent advances in processing of stereocomplex-type polylactide. *Macromol. Rapid Commun.* 38:1700454. doi: 10.1002/marc.201700454

Bai, H., Huang, C., Xiu, H., Zhang, Q., Deng, H., Wang, K., et al. (2014). Significantly improving oxygen barrier properties of polylactide via constructing parallel-aligned Shish-Kebab-like crystals with well-interlocked boundaries. *Biomacromolecules* 15, 1507–1514. doi: 10.1021/bm500167u

Becker, A. L., Johnston, A. P., and Caruso, F. (2010). Layer-by-layer-assembled capsules and films for therapeutic delivery. *Small* 6, 1836–1852. doi: 10.1002/smll.201000379

Boi, S., Dellacasa, E., Bianchini, P., Pasotrino, L., and Monticelli, O. (2019a). *Colloids Sur. B Biointerfaces* 179, 190–198. doi: 10.1016/j.colsurfb.2019.03.071

Boi, S., Pastorino, L., and Monticelli, O. (2019b). Multi-applicable stereocomplex PLA particles decorated with cyclodextrins. *Mater. Lett.* 250, 135–138. doi: 10.1016/j.matlet.2019.05.007

Brzezinski, M., and Biela, T. (2014). Polylactide nanocomposites with functionalized carbon nanotubes and their stereocomplexes: a focused review. *Mater. Lett.* 121, 244–250. doi: 10.1016/j.matlet.2014.01.159

Cai, S., Qiang, Z., Zeng, C., and Ren, J. (2019). Multifunctional poly(lactic acid) copolymers with room temperature self-healing and rewritable shape memory properties via Diels-Alder reaction. *Mater. Res. Express* 6:045701. doi: 10.1088/2053-1591/aafba3

Campana, A., Cramer, T., Simon, D. T., Berggren, M., and Biscarini, F. (2014). Electrocardiographic recording with conformable organic electrochemical

transistor fabricated on resorbable bioscaffold. *Adv. Mater.* 26, 3874–3878. doi: 10.1002/adma.201400263

Casalini, T., Rossi, F., Castrovinci, A., and Perale, G. (2019). Perspective on polylactic acid-based polymers use for naoparticle synthesis and applications. *Front. Bioeng. Biotech.* 7:259. doi: 10.3389/fbioe.2019.00259

Cui, H., Shao, J., Wang, Y., Zhang, P., Chen, X., and Wei, Y. (2013). PLA-PEG-PLA and its electroactive tetraaniline copolymer as multi-interactive injectable hydrogels for tissue engineering. *Biomacromolecules* 14, 1904–1912. doi: 10.1021/bm4002766

Cui, L., Wang, Y., Guo, Y., Liu, Y., Zhao, J., Zhang, C., et al. (2018). Effects of temperature and external force on the stereocomplex crystallization in poly(lactic acid) blends. *Adv. Polym. Tech.* 37, 962–967. doi: 10.1002/adv.21743

Dong, R., Ma, P., and Guo, B. (2020). Conductive biomaterials for muscle tissue engineering. *Biomaterials*. 229:119584. doi: 10.1016/j.biomaterials.2019.119584

Feng, C., Piao, M., and Li, D. (2016). Stereocomplex-reinforced PEGylated polylactide micelle for optimized drug delivery. *Polymers*. 8:165. doi: 10.3390/polym8040165

Fu, M., Liu, Z., Bai, D., Ling, F., Bai, H., Zhang, Q., et al. (2018). Low-temperature sintering of stereocomplex-type polylactide nascent powder: from compression molding to injection molding. *Macromol. Mater. Eng.* 303:1800178. doi: 10.1002/mame.201800178

Gao, X.-R., Niu, B., Hua, W.-Q., Li, Y., Xu, L., Wang, Y., et al. (2019). Rapid preparation and continuous processing of polylactide stereocomplex crystallite below its melting point. *Polym. Bull.* 76, 3371–3385. doi: 10.1007/s00289-018-2544-2

Gardella, L., Furfaro, D., Galimberti, M., and Monticelli, O. (2015). On the development of a facile approach based on the use of ionic liquids: preparation of PLLA (sc-PLA) /high surface area nano-graphite systems. *Green Chem.* 17, 4082–4088. doi: 10.1039/C5GC00964B

Hang Thi, T., Ajiro, H., Hsiao, Y.-J., and Akashi, M. (2017). Thermally resistant polylactide layer-by-layer film prepared using an inkjet approach. *Polym. J.* 49, 327–334. doi: 10.1038/pj.2016.119

He, S., Bai, H., Bai, D., Ju, Y., Zhang, Q., and Fu, Q. (2019). A promising strategy for fabricating high-performance stereocomplex-type polylactide products via carbon nanotubes-assisted low-temperature sintering. *Polymer* 162, 50–57. doi: 10.1016/j.polymer.2018.12.032

Hortos, M., Vinas, M., Espino, S., and Bou, J. J. (2019). Influence of temperature on high molecular weight poly(lactic acid) stereocomplex formation. *Express Polym. Lett.* 13, 123–134. doi: 10.3144/expresspolymlett.2019.12

Ikada, Y., Jamshidi, K., Tsuji, H., and Hyon, S. H. (1987). Stereocomplex formation between enantiomeric poly (lactides). *Macromolecules* 20, 904–906. doi: 10.1021/ma00170a034

Im, S. H., Lee, C. W., Bibi, G., Jung, Y., and Kim, S. H. (2018). Supercritical fluid technology parameters affecting size and behavior of stereocomplex polylactide particles and their composites. *Polym. Eng. Sci.* 58, 1193–1200. doi: 10.1002/pen.24681

Ishii, D., Ying, T. H., Mahara, A., Murakami, S., Yamaoka, T., Lee, W.-K., et al. (2009). *In vivo* tissue response and degradation behavior of PLLA and stereocomplexed PLA nanofibers. *Biomacromolecules* 10, 237–242. doi: 10.1021/bm8009363

Ji, N., Hu, G., Li, J., and Ren, J. (2019). Influence of poly (lactide) stereocomplexes as nucleating agents on the crystallization behavior of poly (lactide) s. *RSC Adv.* 9, 6221–6227. doi: 10.1039/C8RA09856E

Jing, Y., Quan, C., Liu, B., Jiang, Q., and Zhang, C. (2016). A mini review on the functional biomaterials based on poly(lactic acid) stereocomplex. *Polym. Rev.* 56, 262–286. doi: 10.1080/15583724.2015.1111380

Karst, D., and Yang, Y. (2006). Molecular modeling study of the resistance of PLA to hydrolysis based on the blending of PLLA and PDLA. *Polymer* 47, 4845–4850. doi: 10.1016/j.polymer.2006.05.002

Katti, S. S., and Schultz, M. (1982). The microstructure of injection-molded semicrystalline polymers: a review. *Polym. Eng. Sci.* 22, 1001–1017. doi: 10.1002/pen.760221602

Kersey, F. R., Zhang, G., Palmer, G. M., Dewhirst, M. W., and Fraser, C. L. (2010). Stereocomplexed poly(lactic acid)-poly(ethlyene glycol) nanoparticles with dual-emissive boron dyes for tumor accumulation. *ACS Nano*. 4, 4989–4996. doi: 10.1021/nn901873t

Koide, Y., Ikake, H., Muroga, Y., and Shimizu, S. (2017). Effect of the cast-solvent on the morphology of cast films formed with a mixture of steroisomeric poly(lactic acids). *Polym. J.* 45, 645–650. doi: 10.1038/pj.2012.192

Li, Y., Li, Q., Yang, G., Ming, R., Yu, M., Zhang, H., et al. (2018). Evaluation of thermal resistance and mechanical properties of injected molded stereocomplex of poly(L-lactic acid) and poly(D-lactic acid) with various molecular weights. *Adv. Polym. Tech.* 37, 1674–1681. doi: 10.1002/adv.21824

Li, Y., Qiang, Z., Chen, X., and Ren, J. (2019). Understanding thermal decomposition kinetics of flame-retardant thermoset polylactic acid. *RSC Adv.* 9, 3128–3139. doi: 10.1039/C8RA08770A

Lim, L. T., Auras, R., and Rubino, M. (2008). Processing technologies for poly(lactic acid). *Prog. Polym. Sci.* 33, 820–852. doi: 10.1016/j.progpolymsci.2008.05.004

Liu, Z., Fu, M., Ling, F., Sui, G., Bai, H., Zhang, Q., et al. (2019). Stereocomplex-type polylactide with bimodal melting temperature distribution: toward desirable melt-processability and thermomechanical performance. *Polymer* 169, 21–28. doi: 10.1016/j.polymer.2019.02.029

Liu, Z., Ling, F., Diao, X., Fu, M., Bai, H., Zhang, Q., et al. (2020). Stereocomplex-type polylactide with remarkably enhanced melt-processability and electrical performance via incorporating multifunctional carbon black. *Polymer* 188:122136. doi: 10.1016/j.polymer.2019.122136

Ma, P., Jiang, L., Xu, P., Dong, W., Chen, M., and Lemstra, P. J. (2015a). Rapid stereocomplexation between enantiomeric comb-shaped cellulose-g-poly (L-lactide) nanohybrids and poly (D-lactide) from the melt. *Biomacromolecules* 16, 3723–3729. doi: 10.1021/acs.biomac.5b01135

Ma, P., Shen, T., Xu, P., Dong, W., Lemstra, P. J., and Chen, M. (2015b). Superior performance of fully biobased poly (lactide) via stereocomplexation-induced phase separation: structure versus property. *ACS Sustain. Chem. Eng.* 3, 1470–1478. doi: 10.1021/acssuschemeng.5b00208

Mei, L., Ren, Y., Gu, Y., Li, X., Wang, C., Du, Y., et al. (2018). Strengthened and thermally resistant poly(lactic acid)-based composite nanofibers prepared via easy stereocomplexation with antibacterial effects. *ACS Appl. Mater. Interfaces* 10, 42992–43002. doi: 10.1021/acsami.8b14841

Murariu, M., and Dubois, P. (2016). PLA composites: from production to properties. *Adv. Drug Deliv. Rev.* 107, 17–46. doi: 10.1016/j.addr.2016.04.003

Nguyen, M. K., and Lee, D. S. (2010). Injectable biodegradable hydrogels. *Macromol. Biosci.* 10, 563–579. doi: 10.1002/mabi.200900402

Oh, J. K. (2011). Polylactide (PLA)-based amphiphilic block copolymers: synthesis, self-assembly, and biomedical applications. *Soft matt.* 7, 5096–5108. doi: 10.1039/c0sm01539c

Okihara, T., Tsuji, M., Kawaguchi, A., Katayama, K.-I., Tsuji, H., Hyon, S.-H., et al. (2006). Crystal structure of stereocomplex of poly (L-lactide) and poly (D-lactide). *J. Macromol. Sci. B* 30, 119–140. doi: 10.1080/00222349108245788

Ouchi, T., and Ohya, Y. (2004). Design of lactide copolymers as biomaterials. *J. Polym. Sci. Poly. Chem.* 42, 453–462. doi: 10.1002/pola.10848

Pan, G., Xu, H., Ma, B., Wizi, J., and Yang, Y. (2018). Polylactide fibers with enhanced hydrolytic and thermal stability via complete stereo-complexation of poly (l-lactide) with high molecular weight of 600000 and lower-molecular-weight poly (d-lactide). *J. Mater. Sci.* 53, 5490–5500. doi: 10.1007/s10853-017-1944-2

Pan, G., Xu, H., Mu, B., Ma, B., Yang, J., and Yang, Y. (2017). Complete stereo-complexation of enantiomeric polylactides for scalable continuous production. *Chem. Eng. J.* 328, 759–767. doi: 10.1016/j.cej.2017.07.068

Pan, P., Bao, J., Han, L., Xie, Q., Shan, G., and Bao, Y. (2016). Stereocomplexation of high-molecular-weight enantiomeric poly(lactic acid)s enhanced by miscible polymer blending with hydrogen bond interactions. *Polymer* 98, 80–87. doi: 10.1016/j.polymer.2016.06.014

Qi, Y., Ma, H.-L., Du, Z.-H., Yang, B., Wu, J., Wang, R. et al. (2019). Hydrophilic and antibacterial modifications of poly(lactic acid) films by gamma-ray irradiation, *ACS Omega* 4, 21439–21445. doi: 10.1021/acsomega.9b03132

Rasal, R. M., Janorkar, A. V., and Hirt, D. E. (2010). Poly(lactic acid) modifications. *Prog. Polym. Sci.* 35, 338–356. doi: 10.1016/j.progpolymsci.2009.12.003

Ren, J. (2010). *Biodegradable Poly(Lactic Acid): Synthesis, Modification, Processing and Applications*. Berlin: Springer-Verlag.

Schneiderman, D. K., and Hillmyer, M. A. (2017). 50th Anniversary perspective: there is a great future in sustainable polymers. *Macromolecules* 50, 3733–3749. doi: 10.1021/acs.macromol.7b00293

Shirahama, H., Ichimaru, A., Tsutsumi, C., Nakayama, Y., and Yasuda, H. (2005). Characteristics of the biodegradability and physical properties of stereocomplexes between poly (L-lactide) and poly (D-lactide) copolymers. *J. Polym. Sci. Poly. Chem.* 43, 438–454. doi: 10.1002/pola.20516

Spasova, M., Manolova, N., Paneva, D., Mincheva, R., Dubois, P., and Rashkov, I. (2010). Polylactide stereocomplex-based electrospun materials possessing surface with antibacterial and hemostatic properties. *Biomacromolecules* 11, 151–159. doi: 10.1021/bm901016y

Tan, M. J., Owh, C., Chee, P. L., Kyaw, A. K. K., Kai, D., and Loh, X. J. (2016). Biodegradable electronics: cornerstone for sustainable electronics and transiet applications. *J. Mater. Chem. C* 4, 5531–5558. doi: 10.1039/C6TC00678G

Tawakkal, I. S., Cran, M. J., Miltz, J., and Bigger, S. W. (2014). A review of poly(lactic acid)-based materials for antimicrobial packaging. *J. Food Sci.* 79, R1477–R1490. doi: 10.1111/1750-3841.12534

Tobió, M., Gref, R., Sánchez, A., Langer, R., and Alanso, M. J. (1998). Stealth PLA-PEG nanoparticles as protein carriers for nasal administration. *Pharm. Res.* 15, 270–275. doi: 10.1023/A:1011922819926

Tsuji, H. (2000). *In vitro* hydrolysis of blends from enantiomeric poly (lactide) s Part 1. Well-stereo-complexed blend and non-blended films. *Polymer* 41, 3621–3630. doi: 10.1016/S0032-3861(99)00545-5

Tsuji, H. (2005). Poly (lactide) stereocomplexes: formation, structure, properties, degradation, and applications. *Macromol. Biosci.* 5, 569–597. doi: 10.1002/mabi.200500062

Tsuji, H. (2016). Poly(lactic acid) stereocomplexes: a decade of progess. *Adv. Drug Deliv. Rev.* 107, 97–135. doi: 10.1016/j.addr.2016.04.017

Tsuji, H., and Fukui, I. (2003). Enhanced thermal stability of poly (lactide) s in the melt by enantiomeric polymer blending. *Polymer* 44, 2891–2896. doi: 10.1016/S0032-3861(03)00175-7

Tsuji, H., Horii, F., Hyon,. S. H., and Ikada, Y. (1991). Stereocomple formation between enantiomeric poly(lactic acid)s. 2. Stereocomplex formation in concentrated solutions. *Macromoleculs* 24, 2719–2724. doi: 10.1021/ma00010a013

Tsuji, H., and Ikada, Y. (1999). Stereocomplex formation between enantiomeric poly(lactic acid)s. XI. Mechanical properties and morphology of solution-cast films. *Polymer* 40, 6699–6708. doi: 10.1016/S0032-3861(99)00004-X

Tsuji, H., and Tezuka, Y. (2004). Stereocomplex formation between enantiomeric poly(lactic acid)s. 12. Spherulite growth of low-molecular-weight poly(lactic acid)s from the melt. *Biomacromolecules* 5, 1181–1186. doi: 10.1021/bm049835i

Tsuji, H., and Yamamoto, S. (2011). Enhanced stereocomplex crystallization of biodegradable enantiomeric poly(lactic acid)s by repeated casting. *Macromol. Mater. Eng.* 296, 583–589. doi: 10.1002/mame.201000397

Wan, Z. Q., Longo, J. M., Liang, L. X., Chen, H. Y., Hou, G. J., Yang, S., et al. (2019). Comprehensive understanding of polyester stereocomplexation. *J. Am. Chem. Soc.* 141, 14780–14787. doi: 10.1021/jacs.9b07058

Wang, J., Yu, J., Bai, D., Li, Z., Liu, H., Li, Y., et al. (2020). Biodegradable, flexible, and transparent conducting silver nanowires/polylactide film with high performance for optoelectronic devices. *Polymers* 12:604. doi: 10.3390/polym12030604

Wu, B., Zeng, Q., Niu, D., Yang, W., Dong, W., Chen, M., et al. (2019). Design of supertoughened and heat-resistant PLLA/elastomer blends by controlling the distribution of stereocomplex crystallites and the morphology. *Macromolecules* 52, 1092–1103. doi: 10.1021/acs.macromol.8b02262

Xie, Y., Lan, X. R., Bao, R. Y., Lei, Y., Cao, Z. Q., Yang, M. B., et al. (2018). High-performance porous polylactide stereocomplex crystallite scaffolds prepared by solution blending and salt leaching. *Mater. Sci. Eng. C Mater. Biol. Appl.* 90, 602–609. doi: 10.1016/j.msec.2018.05.023

Yu, B., Meng, L., Fu, S., Zhao, Z., Liu, Y., Wang, K., et al. (2018). Morphology and internal structure control over PLA microspheres by compounding PLLA and PDLA and effects on drug release behavior. *Colloids Sur. B Biointerfaces* 172, 105–112. doi: 10.1016/j.colsurfb.2018.08.037

Zhang, H., Wang, C., Xu, Y., Huang, X., He, X., Zhang, C., et al. (2018). Pressure-controlled crystallization of stereocomplex crystals in enantiomeric polylactides with remarkably enhanced hydrolytic degradation. *CrystEngComm* 20, 7337–7347. doi: 10.1039/C8CE01199K

Zhang, L.-Q., Yang, S.-G., Li, Y., Huang, H.-D., Xu, L., Xu, J.-Z., et al. (2020). Polylactide porous biocomposites with high heat resistance by utilizing cellulose template-directed construction. *Cellulose* 27, 3805–3819. doi: 10.1007/s10570-020-03056-2

Zhang, Z.-C., Sang, Z.-H., Huang, Y.-F., Ru, J.-F., Zhong, G.-J., Ji, X., et al. (2017). Enhanced heat deflection resistance via shear flow-induced stereocomplex crystallization of polylactide systems. *ACS Sustain. Chem. Eng.* 5, 1692–1703. doi: 10.1021/acssuschemeng.6b02438

Conflict of Interest: The authors declare that the research was conducted in the absence of any commercial or financial relationships that could be construed as a potential conflict of interest.

Copyright © 2020 Luo, Fortenberry, Ren and Qiang. This is an open-access article distributed under the terms of the Creative Commons Attribution License (CC BY). The use, distribution or reproduction in other forums is permitted, provided the original author(s) and the copyright owner(s) are credited and that the original publication in this journal is cited, in accordance with accepted academic practice. No use, distribution or reproduction is permitted which does not comply with these terms.

frontiers in Chemistry

MINI REVIEW
published: 21 August 2020
doi: 10.3389/fchem.2020.00706

Reconfigurable and Recyclable Photoactuators Based on Azobenzene-Containing Polymers

Mingsen Chen[1,2,3], *Shuofeng Liang*[1], *Chengwei Liu*[1], *Yuanli Liu*[2]* and *Si Wu*[1,4]*

[1] CAS Key Laboratory of Soft Matter Chemistry, Hefei National Laboratory for Physical Sciences at the Microscale, Department of Polymer Science and Engineering, University of Science and Technology of China, Hefei, China, [2] College of Materials Science and Engineering, Guilin University of Technology, Guilin, China, [3] Department of Chemical Engineering, Tsinghua University, Beijing, China, [4] Max Planck Institute for Polymer Research, Mainz, Germany

Photoactuators are promising smart materials that can adapt their shapes upon light illumination. Smart materials with recycling, reusable, and reconfigurable properties are crucial for a sustainable society, and it is important to expand their function. Recently, much effort was made to address the issue of reprocessability and recyclability of photoactuators. Based on the development of polymer chemistry, supramolecular chemistry, and dynamic covalent chemistry, it is now possible to prepare reconfigurable and recyclable photoactuators using azobenzene-containing polymers (azopolymers). Herein, the recent advances on reconfigurable and reprocessable photoactuators, including dynamic crosslinked networks systems and non-covalently crosslinked azobenzene-containing polymers, were reviewed. We discuss the challenges in the field as well as the directions for the development of such photoactuators.

Keywords: photoresponsive, reprocessable, actuators, polymers, azobenzene

OPEN ACCESS

Edited by:
Jie He,
University of Connecticut,
United States

Reviewed by:
Yue Zhao,
Université de Sherbrooke, Canada
Arri Priimagi,
Tampere University, Finland

Correspondence:
Yuanli Liu
lyuanli@glut.edu.cn
Si Wu
siwu@ustc.edu.cn;
wusi@mpip-mainz.mpg.de

Specialty section:
This article was submitted to Polymer Chemistry, a section of the journal Frontiers in Chemistry

Received: *04 June 2020*
Accepted: *09 July 2020*
Published: *21 August 2020*

Citation:
Chen M, Liang S, Liu C, Liu Y and Wu S (2020) Reconfigurable and Recyclable Photoactuators Based on Azobenzene-Containing Polymers. Front. Chem. 8:706. doi: 10.3389/fchem.2020.00706

INTRODUCTION

Over the past decades, significant progress has been achieved in the development of stimuli-responsive soft materials. They are used for designing soft actuators that show complex, rapid, and reversible macroscopic movements via external or internal stimuli (Hines et al., 2017). Azobenzene-containing polymers (azopolymers) are commonly used to design and fabricate photo-controlled soft actuators (Gelebart et al., 2017b; Lu et al., 2017; Pang et al., 2019). Azopolymers can be switched reversibly between the thermally stable *trans* form and the metastable *cis* form because of the reversible photoisomerization of azo bond (Merino, 2011). Ultraviolet (UV) light induces the *trans* azo-form into the *cis* azo-form, and the *cis* azo-form can be converted back to the *trans* azo-form photochemically upon irradiation of visible light or thermally by heating.

Azobenzene mesogens incorporating into liquid crystalline networks (LCN) or liquid crystalline elastomers (LCE) can directly convert light energy into mechanical work (White, 2018). Through rational design of molecular structures and orientations, the soft actuators containing azobenzene moieties can generate sophisticated movements including contraction/expansion (Finkelmann et al., 2001), bending (Yu et al., 2003), oscillation (Kumar et al., 2016), and twisting (Iamsaard et al., 2014), which brings broad applications in artificial muscles, microrobots, microfluidics, and so on. However, the existence of covalently crosslinked networks makes them insoluble and unmeltable. Therefore, they cannot be processed by traditional melt-processing and solution-processing methods.

Crosslinking provides materials with mechanical robustness but sacrifices the reprocessing and recycling performance. With the development of the introduction of post-crosslinkable moieties (Yoshino et al., 2010), dynamic/reversible covalent bonds (Chakma and Konkolewicz, 2019), reconfigurable and reprocessable LCEs and LCNs under high temperatures have been prepared (Han et al., 2016; Ube et al., 2016; Yang et al., 2016; Lu et al., 2017; Lahikainen et al., 2018). Furthermore, photoactuators without chemical crosslinking networks achieved a breakthrough in processing performance compared with the traditional crosslinked systems (Choi et al., 2009; Lv et al., 2016; Chen et al., 2020).

Here, we provide a brief overview of recent advances on reconfigurable and recyclable photoactuators based on azopolymers. New types of photoactuators including covalently crosslinked networks and non-covalently crosslinked networks were reviewed. Some challenges in this field were proposed.

RECENT ADVANCES IN PHOTOACTUATORS BASED ON AZOBENZENE-CONTAINING POLYMERS

Reconfigurable or Recyclable Photoactuators With Covalently Crosslinked Networks

Dynamic/reversible covalent bonds can fast break and reform between several molecules under appropriate conditions (Chakma and Konkolewicz, 2019). The introduction of dynamic bonds into photoactuators affords them reprocessability and reshaping ability. Lu et al. (2017) demonstrated that large-size polymer photoactuators can be reconfigured into wheels or spring-like "motors" using a reprocessable azobenzene-containing liquid crystalline network (**Figure 1A**). The dynamic reaction occurs between an ester bond and a hydroxyl group within the polymer backbone, while it has to react at elevated temperature and catalysts (**Figure 1B**). At elevated temperature, the catalytic transesterification reaction occurs and allows the epoxy-acid-derived network rearranged without changing the numbers of links and average functionality, and thus affording malleable and easy processing properties (Lu et al., 2017).

Some reconfigurable actuators based on conventional crosslinked networks were developed by synergistic use of photochemical and photothermal effects or interplay between light and humidity or pH (Gelebart et al., 2017a; Lahikainen et al., 2018; Wani et al., 2019). Lahikainen et al. (2018) prepared a reconfigurable actuator that can be programmed to adapt different shapes under an identical stimulus through synergistic use of photochemical and photothermal effects. The basic idea is to use azobenzene photoisomerization to locally control the *cis*-isomer content and to program the actuator response. Afterward, photothermal stimulus was used to actuate the shape deformation of the actuators. Six different shapes reconfigured from one single actuator were demonstrated under identical irradiation conditions (**Figure 1C**). An initial actuator was irradiated through masked UV exposure from either one side or both sides of the sample to achieve spatially patterning areas with high *cis*-isomer content. The UV pre-irradiation altered the *cis*-content within the actuator. Upon red-light illumination, the actuator quickly deformed into different geometries determined by the UV pre-irradiation (Lahikainen et al., 2018).

Besides, many other reactions promoting exchangeable covalent bonds have also been applied to prepare reprocessable actuators, including transcarbamoylation (Wen et al., 2018), boronic-ester exchange reaction (Saed et al., 2020), and photo-exchange reaction of disulfide (McBride et al., 2018) and allyl sulfide (McBride et al., 2017). All these examples require an external force at high temperatures or under illumination. Developing actuators capable of reprocessing at room temperature can open up large-scale applications. Recently, Jiang et al. (2020) demonstrated a "self-lockable" liquid crystalline Diels-Alder dynamic network actuator that exhibited room temperature programmability and solution-reprocessability. The liquid crystalline dynamic networks can be reprogrammed and self-locked into 3D objects at ambient temperature simultaneously stabilized by slowly formed Diels-Alder bonded crosslinks (**Figure 1D**). The actuator showed a reversible shape change upon heating above and cooling below the ordered-disordered phase transition temperature. Moreover, such polymers can fabricate a light-fueled walker or wheel (Jiang et al., 2020). This new actuator displayed unmatched recycling and reprocessing performance. It can be dissolved in organic solvents and reprocessed from solution, which cannot be achieved with liquid crystalline networks using exchangeable covalent bonds.

Reconfigurable and Recyclable Photoactuators Using Non-covalently Crosslinked Networks

Another strategy to produce the recyclable photoactuators is directly using linear photoresponsive materials or supramolecular non-covalent interactions (e.g., hydrogen bonding or other weak interactions) without chemical crosslinking networks. The hydrogen bonding-induced physically crosslinked networks in photoactuators based on azopolymers or hydrogels were reprogrammable or recyclable (Mamiya et al., 2008; He et al., 2009; Ni et al., 2016; Jeon et al., 2017; Nie et al., 2017; Si et al., 2018; Mauro, 2019). Lee et al. synthesized the azobenzene-containing linear polymers via acyclic diene metathesis polymerization (Choi et al., 2009; Kim et al., 2013). Fibers or films were prepared by melt-spinning and solution-casting. However, the mechanical properties of the actuators were insufficient due to the low-molecular-weight ($M_n \approx 10\,\text{kg mol}^{-1}$) of the azopolymer. Design and synthesis of linear liquid crystal polymers with robust mechanical properties can address the abovementioned problem.

By imitating the structure of artery walls, Yu and co-workers designed a novel tubular microactuator used for the manipulation of fluid slugs by light (Lv et al., 2016). To improve the mechanical robustness, a high-molecular-weight ($M_n = 360\,\text{kg mol}^{-1}$) linear azopolymer was synthesized by ring-opening metathesis polymerization (ROMP) and acted as "photonic muscles" of the microactuator. Subsequently, they

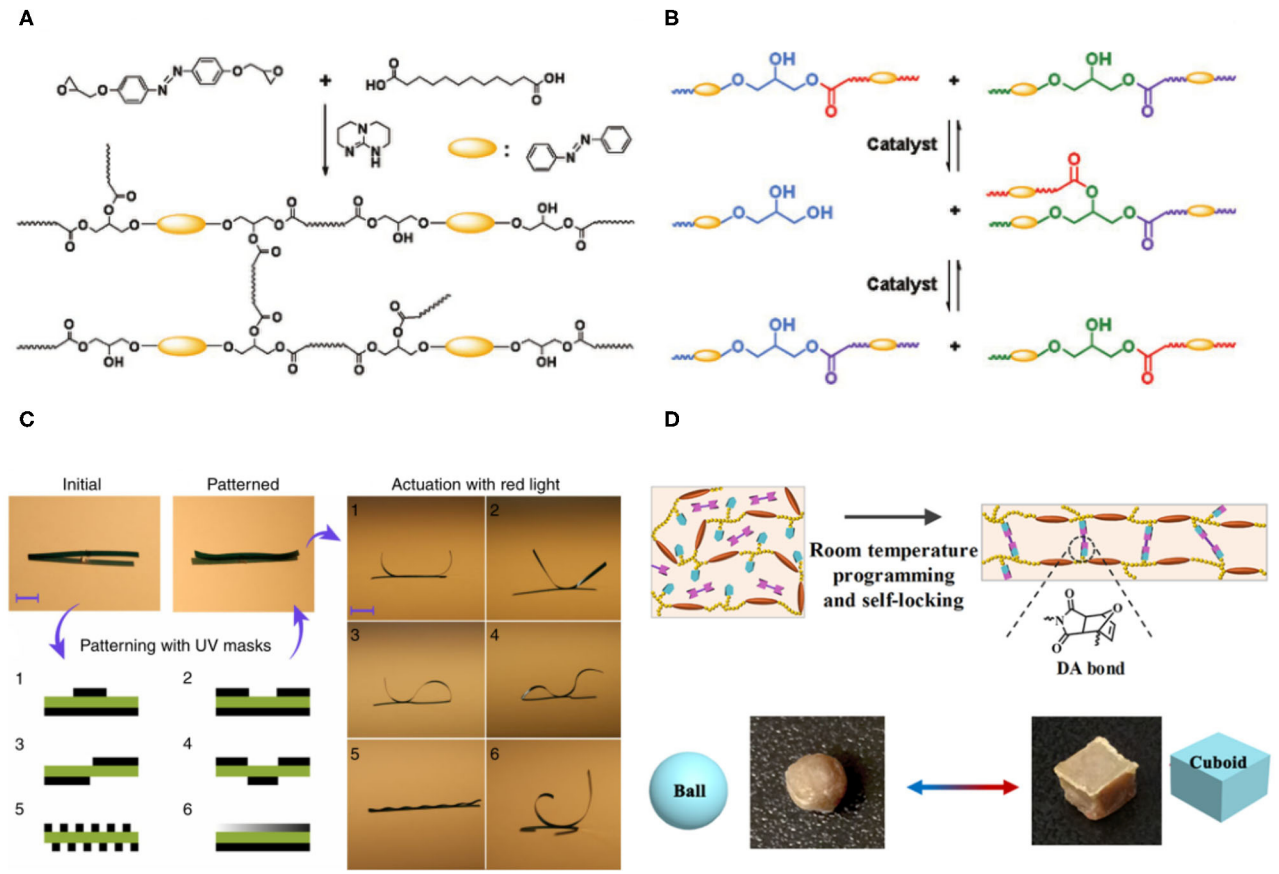

FIGURE 1 | (A) Synthesis route of the azobenzene liquid crystalline elastomers. **(B)** Schematic illustration of the reversible transesterification reaction. **(A,B)** Reprinted with permission from Lu et al. (2017) Copyright Wiley-VCH. **(C)** Reconfigurable shape morphing of a single actuator through synergistic use of photochemical and photothermal effects. Reprinted with permission from Lahikainen et al. (2018) Copyright Springer Nature. **(D)** Schematic showing the "self-lockable" liquid crystalline Diels-Alder dynamic network (LCDAN) actuators that can be (re) shaped into 3D objects at room temperature. Reprinted with permission from Jiang et al. (2020) Copyright Wiley-VCH.

further synthesized a linear liquid crystal copolymer (PABBP, M_n = 300 kg mol^{-1}) combining the photoresponsive azobenzenes and biphenyl moieties by ROMP (**Figure 2A**). By incorporating biphenyl mesogens, light can penetrate deeper in the PABBP layer. Thus, its photodeformability was improved due to the cooperative effect of the two mesogens (Xu et al., 2019). A long bilayer PFM actuator was constructed by the combination of PABBP and the commercially available ethylene-vinyl acetate (EVA) copolymer microtube (**Figure 2B**). The EVA microtube was selected as the supporting layer due to its good flexibility and comparable modulus. The isopropanol slug confined in PFM was manipulated to climb over a slope of 11° incline by the 470 nm light spot due to photodeformation-induced asymmetric capillary forces (**Figure 2C**). The PFM actuator was able to reprocess into arbitrary shapes, including knot, helix, and serpentine. Furthermore, the delaminated bilayer PFM can be healed by light due to the photofluidization mechanism of azobenzene moieties, which makes it possible to apply in wearable and integrated microfluidic systems.

Our group synthesized a series of linear liquid crystal azopolymers (P1) with different molecular weights by atom transfer radical polymerization (ATRP). High-molecular-weight entangled azopolymers were able to prepare photoactuators (Chen et al., 2020). These azopolymers showed photoinduced reversible solid-to-liquid transitions. *Trans* azopolymers are solids with glass transition temperature (T_g) values above room temperature, yet *cis* azopolymers are liquids with T_g values below room temperature (**Figure 2D**). Photoinduced reversible solid-to-liquid transitions of such azopolymers were applied to light-induced healing and reprocessing of actuators with high spatial resolution. The critical entanglement molecular weight of the azopolymer calculated using Wool's model (Wool, 1993) was 68 kg mol^{-1}. The low-molecular-weight azopolymers (5–53 kg mol^{-1}) were hard and brittle because their polymer chains lacked entanglements, whereas the high-molecular-weight azopolymers (80–100 kg mol^{-1}) entangled (**Figure 2E**). Thus, transparent (**Figure 2F**), flexible (**Figure 2G**), and stretchable (**Figure 2H**) actuators were fabricated by entangled azopolymers because of mechanical robustness. The photoactuators can be not only recycled and reshaped via solution processing but also reprocessed by light irradiation to produce microstructured actuators (Chen et al., 2020). The

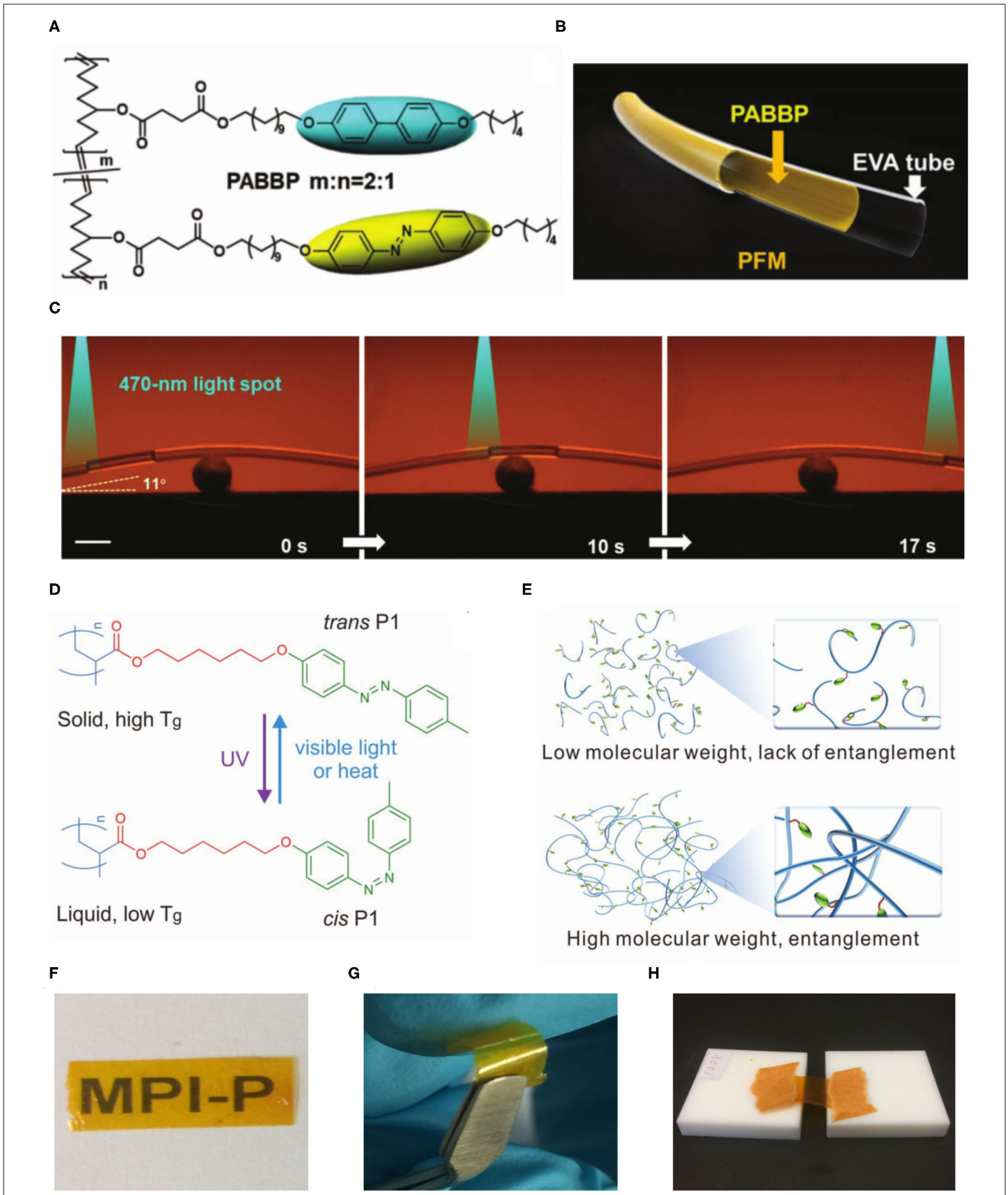

FIGURE 2 | (A) Chemical structure of the PABBP copolymer. **(B)** Schematic representation of the bilayer structure of the PFM. **(C)** Photographs of the light-controlled motion of an isopropanol slug climbing over a slope of 11° incline in a curved PFM. The intensity of the 470 nm point light was 120 mW cm^{-2}. The scale bar is 2 mm. **(A–C)** Reprinted with permission from Xu et al. (2019) Copyright Wiley-VCH. **(D)** The chemical structure and photoisomerization of P1. **(E)** Schematic representation of

(Continued)

FIGURE 2 | entanglement of polymer chains. The freestanding film of entangled P1 was highly transparent **(F)**, flexible **(G)**, and stretchable at 90°C **(H)**. **(D–H)** Reprinted with permission from Chen et al. (2020) Copyright Wiley-VCH.

combination of polymer chain entanglements and photoinduced reversible solid-to-liquid transitions provides a new strategy for designing actuators with good reprocessability and healability at room temperature.

CONCLUSIONS AND PERSPECTIVES

In this mini-review, we have summarized the recent progress on reconfigurable and recyclable photoactuators based on azopolymers. The incorporation of dynamic crosslinked networks based on exchangeable covalent bonds, Diels-Alder reactions, or non-covalently crosslinking has been made a breakthrough in the reprocessability of photoactuators. Photoactuators using exchangeable covalent bonds can be processed at high temperatures. Diels-Alder dynamic networks and non-covalently crosslinked networks make actuators recyclable and reprocessable directly from melt or solution processing at room temperature. With the development of improved processing techniques, it provides a new opportunity for designing programmable photoactuators involving the spatially modulation of the orientation of liquid crystals and the control over the geometry and composition. However, so far, the actual applications of photoactuators still face great challenges. In the future, more works should be done to address the following issues:

- Balance material (re) processability, mechanical robustness, and actuating stability: Obviously, crosslinking or entanglement affords mechanical toughness, but it hinders movements of polymer chains, and thus declines reprocessability. Dynamic crosslinked networks provide reprocessability and reconfigurability of the materials. However, during the long-term use of the materials, the dynamic reaction may lead to a reduction in its degree of orientation in actuators, and thus cause performance and reprocessability drops. Constructing new dynamic reaction systems and adjusting the material compositions to achieve a balance between reprocessability, mechanical toughness, and driving stability is of great significance for the practical applications of photoactuators.
- Develop novel non-covalently crosslinked systems and large-scale preparation on demands: The entangled azopolymer photoactuators cannot be large-scale prepared because it is difficult to polymerize high-molecular-weight azopolymers due to the large steric hindrance of azobenzene and other side reactions. In principle, each polymer has a characteristic average molecular weight between entanglements depending on the chemical structure of the repeating unit. This may also be taken into consideration in designing liquid crystal polymers that favor the use of chain entanglements. At present, the synthesis and design of non-covalently crosslinked photoactuators are still in the preliminary stage, and only a few cases are available. Since oriented polymer chains tend to relax in the isotropic state, the actuation degree may decrease after repeated order-disorder phase transition occurs. To exploit new synthetic methods and explore the impact of various chemical structures on their performance will facilitate the large-scale preparation of photoactuators on demand.
- Develop microstructured photoactuators: The recent studies showed that multi-smart functions or properties were accessible using microstructured photoactuators, while obtaining a specific function often required a specifically designed microstructure (Lahikainen et al., 2018; Chen et al., 2020; Ge and Zhao, 2020). Microstructured photoactuators will enable functions such as actuation, detection, transportation, and sensing with potential applications ranging from robotics and photonics to biomedical devices.

AUTHOR CONTRIBUTIONS

MC collected and read papers and wrote the manuscript. SL, CL, YL, and SW discussed and revised the manuscript. SW outlined the content of the manuscript. All authors contributed to the article and approved the submitted version.

ACKNOWLEDGMENTS

SW acknowledges the Thousand Talents Plan and Anhui Provincial Natural Science Foundation (No. 1908085MB38).

REFERENCES

Chakma, P., and Konkolewicz, D. (2019). Dynamic covalent bonds in polymeric materials. *Angew. Chem. Int. Ed.* 58, 9682–9695. doi: 10.1002/anie.201813525

Chen, M., Yao, B., Kappl, M., Liu, S., Yuan, J., Berger, R., et al. (2020). Entangled azobenzene-containing polymers with photoinduced reversible solid-to-liquid transitions for healable and reprocessable photoactuators. *Adv. Funct. Mater.* 30:1906752. doi: 10.1002/adfm.201906752

Choi, H. J., Jeong, K. U., Chien, L. C., and Lee, M. H. (2009). Photochromic 3-dimensional actuator based on an uncrosslinked liquid crystal elastomer. *J. Mater. Chem.* 19, 7124–7129. doi: 10.1039/b909494f

Finkelmann, H., Nishikawa, E., Pereira, G. G., and Warner, M. (2001). A new opto-mechanical effect in solids. *Phys. Rev. Lett.* 87:015501. doi: 10.1103/PhysRevLett.87.015501

Ge, F., and Zhao, Y. (2020). Microstructured actuation of liquid crystal polymer networks. *Adv. Funct. Mater.* 30:1901890. doi: 10.1002/adfm.201901890

Gelebart, A. H., Mulder, D. J., Vantomme, G., Schenning, A. P., and Broer, D. J. (2017a). A rewritable, reprogrammable, dual light-responsive polymer actuator. *Angew. Chem. Int. Ed.* 56, 13436–13439. doi: 10.1002/anie.201706793

Gelebart, A. H., Mulder, D. J., Varga, M., Konya, A., Vantomme, G., Meijer, E. W., et al. (2017b). Making waves in a photoactive polymer film. *Nature* 546, 632–636. doi: 10.1038/nature22987

Han, G., Nie, J., and Zhang, H. (2016). Facile preparation of recyclable photodeformable azobenzene polymer fibers with chemically crosslinked networks. *Polym. Chem.* 7, 5088–5092. doi: 10.1039/C6PY01100D

He, J., Zhao, Y., and Zhao, Y. (2009). Photoinduced bending of a coumarin-containing supramolecular polymer. *Soft Matter* 5, 308–310. doi: 10.1039/B814278E

Hines, L., Petersen, K., Lum, G. Z., and Sitti, M. (2017). Soft actuators for small-scale robotics. *Adv. Mater.* 29:1603483. doi: 10.1002/adma.201603483

Iamsaard, S., Aßhoff, S. J., Matt, B., Kudernac, T., Cornelissen, J. J., Fletcher, S. P., et al. (2014). Conversion of light into macroscopic helical motion. *Nat. Chem.* 6, 229–235. doi: 10.1038/nchem.1859

Jeon, S. J., Hauser, A. W., and Hayward, R. C. (2017). Shape-morphing materials from stimuli-responsive hydrogel hybrids. *Acc. Chem. Res.* 50, 161–169. doi: 10.1021/acs.accounts.6b00570

Jiang, Z. C., Xiao, Y. Y., Yin, L., Han, L., and Zhao, Y. (2020). "Self-Lockable" liquid crystalline diels-alder dynamic network actuators with room temperature programmability and solution reprocessability. *Angew. Chem. Int. Ed.* 132, 4955–4961. doi: 10.1002/ange.202000181

Kim, D. Y., Lee, S. A., Choi, H. J., Chien, L. C., Lee, M. H., and Jeong, K. U. (2013). Reversible actuating and writing behaviours of a head-to-side connected main-chain photochromic liquid crystalline polymer. *J. Mater. Chem. C* 1, 1375–1382. doi: 10.1039/c2tc00506a

Kumar, K., Knie, C., Bléger, D., Peletier, M. A., Friedrich, H., Hecht, S., et al. (2016). A chaotic self-oscillating sunlight-driven polymer actuator. *Nat. Commun.* 7:11975. doi: 10.1038/ncomms11975

Lahikainen, M., Zeng, H., and Priimagi, A. (2018). Reconfigurable photoactuator through synergistic use of photochemical and photothermal effects. *Nat. Commun.* 9:4148. doi: 10.1038/s41467-018-06647-7

Lu, X., Guo, S., Tong, X., Xia, H., and Zhao, Y. (2017). Tunable photocontrolled motions using stored strain energy in malleable azobenzene liquid crystalline polymer actuators. *Adv. Mater.* 29:1606467. doi: 10.1002/adma.201606467

Lv, J. A., Liu, Y., Wei, J., Chen, E., Qin, L., and Yu, Y. (2016). Photocontrol of fluid slugs in liquid crystal polymer microactuators. *Nature* 537, 179–184. doi: 10.1038/nature19344

Mamiya, J. I., Yoshitake, A., Kondo, M., Yu, Y., and Ikeda, T. (2008). Is chemical crosslinking necessary for the photoinduced bending of polymer films? *J. Mater. Chem.* 18, 63–65. doi: 10.1039/B715855F

Mauro, M. (2019). Gel-based soft actuators driven by light. *J. Mater. Chem. B* 7, 4234–4242. doi: 10.1039/C8TB01893F

McBride, M. K., Hendrikx, M., Liu, D., Worrell, B. T., Broer, D. J., and Bowman, C. N. (2017). Photoinduced plasticity in cross-linked liquid crystalline networks. *Adv. Mater.* 29:1606509. doi: 10.1002/adma.201606509

McBride, M. K., Martinez, A. M., Cox, L., Alim, M., Childress, K., Beiswinger, M., et al. (2018). A readily programmable, fully reversible shape-switching material. *Sci. Adv.* 4:eaat4634. doi: 10.1126/sciadv.aat4634

Merino, E. (2011). Synthesis of azobenzenes: the coloured pieces of molecular materials. *Chem. Soc. Rev.* 40, 3835–3853. doi: 10.1039/c0cs00183j

Ni, B., Xie, H. L., Tang, J., Zhang, H. L., and Chen, E. Q. (2016). A self-healing photoinduced-deformable material fabricated by liquid crystalline elastomers using multivalent hydrogen bonds as cross-linkers. *Chem. Commun.* 52, 10257–10260. doi: 10.1039/C6CC04199J

Nie, J., Liu, X., Yan, Y., and Zhang, H. (2017). Supramolecular hydrogen-bonded photodriven actuators based on an azobenzene-containing main-chain liquid crystalline poly (ester-amide). *J. Mater. Chem. C* 5, 10391–10398. doi: 10.1039/C7TC02943H

Pang, X., Lv, J. A., Zhu, C., Qin, L., and Yu, Y. (2019). Photodeformable azobenzene-containing liquid crystal polymers and soft actuators. *Adv. Mater.* 31:1904224. doi: 10.1002/adma.201904224

Saed, M. O., Gablier, A., and Terentejv, E. M. (2020). Liquid crystalline vitrimers with full or partial boronic-ester bond exchange. *Adv. Funct. Mater.* 30:1906458. doi: 10.1002/adfm.201906458

Si, Q., Feng, Y., Yang, W., Fu, L., Yan, Q., Dong, L., et al. (2018). Controllable and stable deformation of a self-healing photo-responsive supramolecular assembly for an optically actuated manipulator arm. *ACS Appl. Mater. Interfaces* 10, 29909–29917. doi: 10.1021/acsami.8b08025

Ube, T., Kawasaki, K., and Ikeda, T. (2016). Photomobile liquid-crystalline elastomers with rearrangeable networks. *Adv. Mater.* 28, 8212–8217. doi: 10.1002/adma.201602745

Wani, O. M., Verpaalen, R., Zeng, H., Priimagi, A., and Schenning, A. P. (2019). An artificial nocturnal flower via humidity-gated photoactuation in liquid crystal networks. *Adv. Mater.* 31:1805985. doi: 10.1002/adma.201805985

Wen, Z., McBride, M. K., Zhang, X., Han, X., Martinez, A. M., Shao, R., et al. (2018). Reconfigurable LC elastomers: using a thermally programmable monodomain to access two-way free-standing multiple shape memory polymers. *Macromolecules* 51, 5812–5819. doi: 10.1021/acs.macromol.8b01315

White, T. J. (2018). Photomechanical effects in liquid crystalline polymer networks and elastomers. *J. Polym. Sci. B Polym. Phys.* 56, 695–705. doi: 10.1002/polb.24576

Wool, R. P. (1993). Polymer entanglements. *Macromolecules* 26, 1564–1569. doi: 10.1021/ma00059a012

Xu, B., Zhu, C., Qin, L., Wei, J., and Yu, Y. (2019). Light-directed liquid manipulation in flexible bilayer microtubes. *Small* 15:1901847. doi: 10.1002/smll.201901847

Yang, Y., Pei, Z., Li, Z., Wei, Y., and Ji, Y. (2016). Making and remaking dynamic 3D structures by shining light on flat liquid crystalline vitrimer films without a mold. *J. Am. Chem. Soc.* 138, 2118–2121. doi: 10.1021/jacs.5b12531

Yoshino, T., Kondo, M., Mamiya, J. I., Kinoshita, M., Yu, Y., and Ikeda, T. (2010). Three-dimensional photomobility of crosslinked azobenzene liquid-crystalline polymer fibers. *Adv. Mater.* 22, 1361–1363. doi: 10.1002/adma.200902879

Yu, Y., Nakano, M., and Ikeda, T. (2003). Directed bending of a polymer film by light. *Nature* 425:145. doi: 10.1038/425145a

Conflict of Interest: The authors declare that the research was conducted in the absence of any commercial or financial relationships that could be construed as a potential conflict of interest.

Copyright © 2020 Chen, Liang, Liu, Liu and Wu. This is an open-access article distributed under the terms of the Creative Commons Attribution License (CC BY). The use, distribution or reproduction in other forums is permitted, provided the original author(s) and the copyright owner(s) are credited and that the original publication in this journal is cited, in accordance with accepted academic practice. No use, distribution or reproduction is permitted which does not comply with these terms.

frontiers in Chemistry

ORIGINAL RESEARCH
published: 16 October 2020
doi: 10.3389/fchem.2020.585569

A Degradable and Self-Healable Vitrimer Based on Non-isocyanate Polyurethane

Haitao Wu, Biqiang Jin, Hao Wang, Wenqiang Wu, Zhenxing Cao, Jinrong Wu and Guangsu Huang*

State Key Laboratory of Polymer Materials Engineering, College of Polymer Science and Engineering, Sichuan University, Chengdu, China

Developing degradable and self-healable elastomers composed of reusable resources is of great value but is rarely reported because of the undegradable molecular chains. Herein, we report a class of degradable and self-healable vitrimers based on non-isocyanate polyurethane elastomer. Such vitrimers are fabricated by copolymerizing *bis*(6-membered cyclic carbonate) and amino-terminated liquid nitrile rubber. The networks topologies can rearrange by transcarbonation exchange reactions between hydroxyl and carbonate groups at elevated temperatures; as such, vitrimers after reprocessing can recover 82.9–95.6% of initial tensile strength and 59–131% of initial storage modulus. Interestingly, the networks can be hydrolyzed and decarbonated in the strong acid solution to recover 75% of the pure di(trimethylolpropane) monomer. Additionally, the elastomer exhibits excellent self-healing efficiency (∼88%) and fracture strain (∼1,200%) by tuning the monomer feeding ratio. Therefore, this work provides a novel strategy to fabricate the sustainable elastomers with minimum environmental impact.

Keywords: vitrimer, non-isocyanate polyurethane, acid-degradation, strain-rate response, self-healing

OPEN ACCESS

Edited by:
Jie He,
University of Connecticut,
United States

Reviewed by:
Liheng Cai,
University of Virginia, United States
Si Wu,
University of Science and Technology of China, China
Guoliang Liu,
Virginia Tech, United States

****Correspondence:***
Jinrong Wu
wujinrong@scu.edu.cn

Specialty section:
This article was submitted to Green and Sustainable Chemistry, a section of the journal Frontiers in Chemistry

Received: *21 July 2020*
Accepted: *28 August 2020*
Published: *16 October 2020*

Citation:
Wu H, Jin B, Wang H, Wu W, Cao Z, Wu J and Huang G (2020) A Degradable and Self-Healable Vitrimer Based on Non-isocyanate Polyurethane. Front. Chem. 8:585569. doi: 10.3389/fchem.2020.585569

INTRODUCTION

Elastomers are a class of the most important polymer materials that have diverse applications in automobile, biomedical, and aerospace industries, as well as our daily life. Traditional covalently cross-linked elastomers display excellent mechanical properties and thermal and chemical stability (Tee et al., 2012; Tadakaluru et al., 2014; Wang and Loh, 2017). However, the irreversibility of chemical network prevents the recycling, reprocessing, and degradability of elastomer products, which puts a huge burden on ecology and environment.

One effective way to address this issue is to introduce dynamic covalent bonds into elastomer networks (Scott et al., 2005; Jin et al., 2013; Kloxin and Bowman, 2013; Garcia and Smulders, 2016; Chen et al., 2019; Jiang et al., 2020). The resulting dynamic networks can rearrange their topologies via exchange reactions under external stimuli, which imparts the elastomers with reprocessability and damage healability. Among various dynamic chemistries, vitrimers, a concept pioneered by Röttger et al. is particularly attractive because of associative topological rearrangement of the dynamic covalent networks (Montarnal et al., 2011; Röttger et al., 2017). As such, they hold huge potential in a variety of applications, such as recyclable thermoset polymers and self-healable polymers (Yang et al., 2014, 2016; Ube et al., 2016; Shi et al., 2017; Zhang and Xu, 2017). The fascinating performance of vitrimer was first demonstrated in a carboxylic acid cured epoxy network, which

undergoes transesterification under catalytic $Zn(OAc)_2$ (Montarnal et al., 2011). Currently, a variety of strategies have been adopted to design vitrimer or vitrimer-like materials, including carboxylate transesterification (Cromwell et al., 2015; Chen et al., 2018; Liu et al., 2018; Wang et al., 2019), transalkylation of triazolium salts (Obadia et al., 2015), transcarbamoylation (Fortman et al., 2015), olefin metathesis (Lu et al., 2012), boronic ester exchange (Röttger et al., 2017), disulfide exchange (Jian et al., 2018; Zhou et al., 2018), siloxane silanol exchange (Zheng and McCarthy, 2012), transamination (Denissen et al., 2017), etc. These strategies impart the vitrimer materials with reprocessable, recyclable, and repairable properties via bond exchange reactions at elevated temperatures; however, the products are usually non-degradable and insoluble, which causes serious ecological and environmental pollution at the end of the service life. Therefore, developing a degradable and self-healable vitrimer material is of great public value.

In this article, we develop a novel and efficient path to prepare a degradable and self-healable vitrimer based on non-isocyanate polyurethane elastomer (PU_E) by introducing carbonates that can undergo transcarbonation exchange reactions in **Figure 1**. The prepared elastomer can rearrange the network topology via transcarbonation exchange reactions, thus endowing the elastomer with vitrimer behaviors. In addition to being reprocessable and repairable, the networks can be hydrolyzed and decarbonated in hydrochloric acid solution to recover the di(trimethylolpropane) monomer and Pre-PU_E.

EXPERIMENTAL

Materials

Amino-terminated liquid nitrile rubber (ATBN, Mn = 402 g mol^{-1}) was purchased from Shandong Jining benoke Biotechnology Co., Ltd. Chloroformic acid–propylester (98%), n-methyl pyrrolidone (NMP), anhydrous tetrahydrofuran (THF), and di-trimethylolpropane (98%) were provided by Shanghai TITAN Technology Co., Ltd. Ethanol (AR grade), butyl titanate ($C_{16}H_{36}O_4Ti$), and triethylamine (Et_3N, AR grade) were supplied by Kelong Reagent Corp. (Chengdu, China). All of the raw materials were dried before use.

Synthesis of *bis*(6-Membered Cyclic Carbonate) (Bcc)

Bcc was successfully synthesized from di(trimethylolpropane) and chloroformic acid–propylester reaction procedure in **Figure 1A**. The details of the preparation were as follows: di-trimethylolpropane (10.0 g, 40 mmol) was dissolved in THF (250 mL) and transferred to three-neck round bottom flask with magnetic stirring 1 h under N_2 at 25°C, and then chloroformic acid–propylester (26 mL) was step-by-step drop added into a three-neck flask during stirring. Subsequently, catalyst Et_3N was added dropwise when the reaction temperature cooled to 0°C. Then, the reaction mixture was magnetic stirring for 5 h to form a white precipitate and removed by vacuum filtration, and solvent was removed via under rotary evaporation to yield a white solid. Finally, the white solid was recrystallized in THF (10 mL) to attain the pure product Bcc.

Preparation of Polymer PU_E

Attributing to the long molecular chain structure of ATBN, the end amino groups in long-chain molecule were surrounded by ATBN molecular chains, leading to a limited reactivity between amino and *bis*(6-membered cyclic carbonate). To improve the reactivity of the reaction, the low-molecular-weight ATBN was first chosen. Bcc (0.5 g, 1.65 mmol) and ATBN (29 g, 60 mmol) were added into three-neck round bottom under nitrogen atmosphere. Then, the reaction solvent NMP (60 mL) was added to the mixture, after nucleophilic addition reaction at 100°C with magnetic stirring for 24 h and formed prepolymer. Bcc can serve as cross-linker to realize cross-linking existed catalyst. For details, the cross-linked PU_E was synthesized by a one-step copolymerization existed catalyst $C_{16}H_{36}O_4Ti$ and THF at 25°C. Finally, the polymer PU_E was successfully prepared (**Figure 1B**). Because of existed substantial hydrogen bonds formed by hydroxyl and carbonate groups, dual cross-linked networks were thus formed during polymer preparation process in **Figure 1C**. Because the content of cross-linker Bcc and physical cross-links directly influences the polymer crosslinking density and thus has impact on the mechanical properties, a series of samples were synthesized by tuning the feed ratio. The feed ratios of PU_E—X (X = 1, 2, 3, 4, 5) are summarized in **Supplementary Table 1**.

Preparation of Polymer PU_E Film

The product PU_E solution was first put into a Teflon mold (30 × 50 × 10 mm) with a glass plate and was subsequently placed in an oven for 12 h at 40°C. Second, the product solution was heated from 40 to 50°C for 12 h. Additionally, the resulting polymer film was dried under vacuum at 50°C for 24 h. Finally, the film was taken out and cut into rectangles of 2 × 25 mm for further testing.

Characterization Methods

Prior to this, polymer PU_E samples were vacuum-dried at 50°C for 12 h.

Fourier Transform–Infrared Spectrometry (FT-IR)

FT-IR spectral analysis was recorded on a Fourier transform infrared spectrometer (Nicolet iS50) in a range of wavenumbers from 4,000 to 500 cm^{-1}.

Nuclear Magnetic Resonance Spectroscopy (NMR)

NMR spectra were recorded on a Bruker AV400 spectrometer (400 MHz, Germany) with dimethyl sulfoxide-d_6 and deuterated chloroform as the solvents and tetramethyl silane as the internal reference.

Dynamic Mechanical Analysis (DMA)

The dynamic mechanical analysis was studied using DMA Q800 (TA Instruments, USA), at a frequency of 1 Hz and then a heating rate of 3°C min^{-1} from −100 to 100°C.

Differential Scanning Calorimetry (DSC)

DSC was performed with a DSC-Q200 (TA Instrument, USA) over the temperature range from −60 to 60°C at a heating rate of 5°C min^{-1} under N_2 and empty aluminum as the reference.

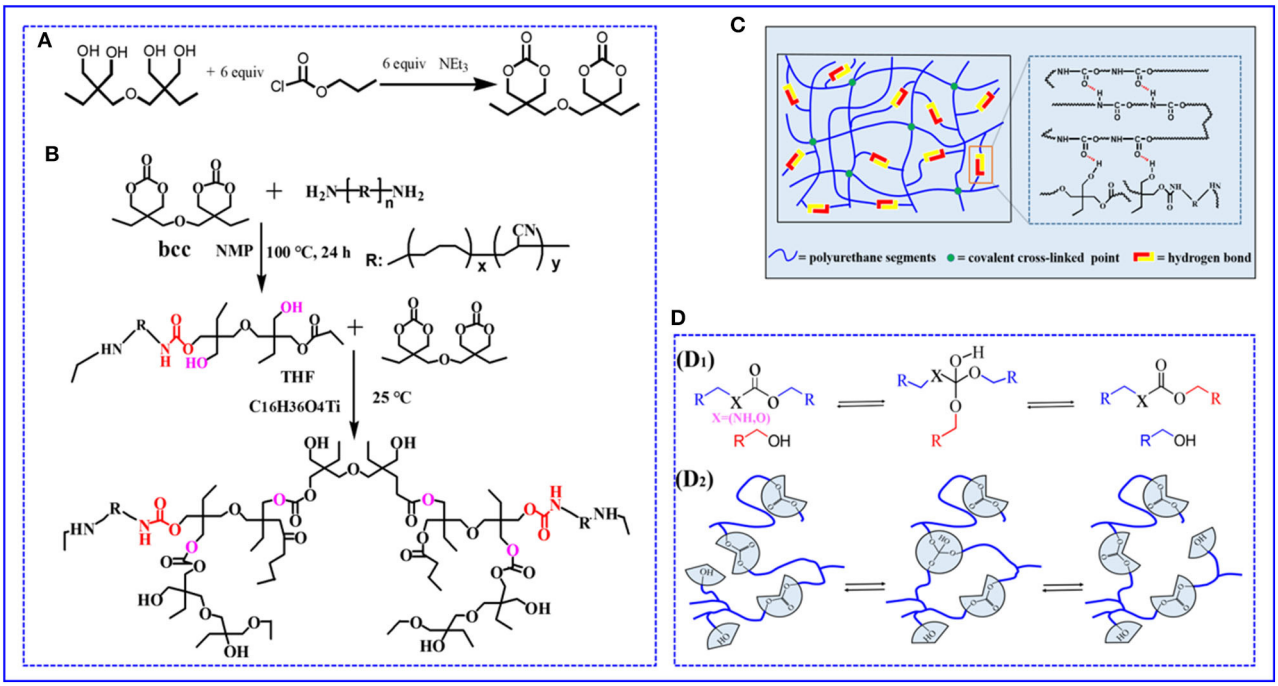

FIGURE 1 | (A,B) The chemical synthesis route and molecular design of non-isocyanate PU_E **(C)** Cartoon representation of the proposed cross-linked network structure for PU_E **(D)** Reprocessing mechanism of non-isocyanate PU_E (D_1). Transcarbonation exchange reaction whereby a hydroxyl nucleophile reacts with a carbonate, forming an associative intermediate, and releasing the exchanged carbonate and hydroxyl group. (D_2) Topology of a cross-linked elastomer network containing carbonates and hydroxyls can be adjusted via transcarbonation exchange reactions.

Scanning Electron Microscope (SEM)

A scanning electron microscope (Nova NanoSEM450) was used to trace the healing process of scratch immediately after making scratch by a blade.

Static Tensile Tests

The mechanical properties of the samples were investigated on an Instron Universal Testing Machine (Model 5967, Instron Crop) at a stretching rate of 0.083 s^{-1} at room temperature. The thickness and width of the specimens were 0.70 and 4 mm, respectively. The length of the sample between the two pneumatic grips of the testing machine was 20 mm. Three dumbbell-shaped specimens were tested in each sample.

Acid-Degradation Studies

To conduct swelling test, 0.5-g sample of polymer film was submerged in THF (15 mL) and then stirred for 24 h at room temperature until no obvious changes appear. It was shown that the cross-linked network only was swollen. For degradation studies, the same 0.5-g PU_E sample films were immersed in sealed vials containing 10 mL of HCl (1 M), KOH (1 M), and H_2O, respectively. The vial was heated in a drying oven to 100°C for 24 h. The sample was cleaned containing HCl solution with n-butanol (20 mL). The solvent was removed by rotary evaporation, and finally, the di(trimethylolpropane) monomer was obtained.

Reprocessing Recovery

To reprocess the PU_E materials, the sample films were ground to small pieces first, and second placed in a hot press at 130°C under the pressure of 5 to 10 MPa. These pieces were thermally equilibrated for 30 min and removed from the press to check for homogeneity of the film and then once again placed in a hot press at 130°C for 2 h under same pressure. Finally, uniaxial tensile tests and dynamic mechanical thermal analysis were carried out to determine the recovery efficiency of mechanical properties.

Self-Healing Tests

The elastomer sample was cut into two pieces at the center using a razor blade; the two pieces rejoin together to form nearly complete elastomer when contacting with each other at 100°C. Uniaxial tensile test was performed to determine the mechanical properties and healing efficiencies.

Polymer Characterization

The chemical structure of Pre-PU_E and PU_E samples was characterized using FT-IR spectra, as shown in **Supplementary Figure 3**. It can be found that the prepolymer sample exhibits several characteristics peaks: the absorption peak at 3,840 cm^{-1} indicates the presence of –OH; the peaks at 2,980 cm^{-1} can be attributed to the N-H bending vibration of the carbamate groups (–NHCOO) (Fan et al., 2019), and the peaks at 1,460 and 1,741 cm^{-1} can be assigned to the C–O stretching vibration and C = O stretching vibration of linear carbonate,

respectively (Snyder et al., 2018). These results illustrated that the presence of the carbamate and carbonate groups. It can be also seen that Pre-PU_E and PU_E samples basically showed similar FT-IR spectra. Swelling tests were performed; this Pre-PU_E and PU_E samples of 1.5 g were immersed in 10 mL THF for 36 h at room temperature in **Supplementary Figure 3**, respectively. The Pre-PU_E was dissolved, whereas PU_E is only swollen, which indicates that the PU_E is cross-linked under catalyst $C_{16}H_{36}O_4Ti$. These results suggest that the polymer PU_E was successfully prepared. Additionally, the temperature-dependent FT-IR spectra of PU_E were collected, as shown in **Supplementary Figure 4**. Upon heating from 10 to 150°C, the peak intensity at 1,741 cm^{-1} weakened, whereas the peak at 1,620 cm^{-1} (free urea C = O) intensified, which indicated that increasing the temperature can cause gradually dissociation of hydrogen bonds, which was consistent with the previously reported literature (Liu et al., 2019).

RESULTS AND DISCUSSION

Thermal Properties and Dynamic Nature of the Networks

The thermal properties of polymer materials play a dominant role in their topological rearrangement of networks. Therefore, differential scanning calorimetry (DSC) is performed. **Figure 2A** displays the DSC curves of PU_E samples. The relevant thermal parameters and their corresponding values are summarized in **Supplementary Table 2**. It is evident that the glass transition temperature (T_g) of PU_E samples increases with the increasing cross-linker Bcc amount. This suggests that the enhancement of the degree of cross-linking greatly restricts the mobility of chain segments, as shown in **Supplementary Figure 5A**. As is expected, there is no endothermic peak above T_g, which indicates that the material is amorphous. In addition, it can be found from **Supplementary Figure 5A** that the T_g values are lower than room temperature, indicating the material is an elastomer rather than plastic at room temperature. Meanwhile, thermogravimetric analysis measurements are conducted, and the values of thermal degradation temperatures are summarized in **Supplementary Table 2**. The elastomer network first lose mass around 214°C (5% mass loss), which is well above the temperature required for transcarbonation exchange reaction in **Supplementary Figure 5B**.

To better determine the network topology rearrangement via transcarbonation exchange reactions between free hydroxyl and carbonate groups at elevated temperatures and the rate of exchange reactions, the stress–relaxation measurements are performed by stretching the samples to a strain of 50% from 50 to 120°C. The strain is then maintained for 12 min, and the stress is recorded as a function of time in **Figure 2B**. The network characteristic relaxation time (τ) is defined as the time required for the elastomer to reach *1/e* (37%) of the initial stress and is used as a measure of the rate of transcarbonation exchange reactions under the testing conditions (Snyder et al., 2018). As illustrated by **Figure 2B**, it can be seen that PU_E-4 has a stress relaxation time of 547 s at 90°C. As the temperature increases to 120°C, the relaxation time decreases to 132 s. The result demonstrates that the exchange rate of elastomer network rearrangement largely depends on the temperature. As shown in **Figures 2B,C**, the temperature dependence of the relaxation time of PU_E-4 follows Arrhenius' law (Wu et al., 2020). According to Arrhenius' law:

$$\ln\tau = \ln\tau_0 + \frac{E_a}{RT} \quad (1)$$

The activation energy of the rearrangement network is determined to be 55.09 kJ mol^{-1}. As the temperature rises, the adaptivity of the PU_E-4 network is activated as a result of exchange reaction. Simultaneously, the samples with different cross-linker amount are fixed at 100°C and then maintained for 12 min; it can be seen that the residual stress of these samples lower than *1/e* of the initial stress undergoes stress relaxation within 4 min, illustrating that the network topologies of all these samples can be rearranged at elevated temperature in **Supplementary Figure 6**. Moreover, the storage modulus (E') and the loss factor (tanδ) of the elastomers as a function of temperature are recorded by DMA, as shown in **Figure 2D** and **Supplementary Figure 5D**. The samples exhibit a marked decrease of E' when the temperature exceeds T_g in **Figure 2D**. Interestingly, the rubber modulus decreases with temperature, indicating the dissociation of hydrogen bonds prior to dynamic network change. Not surprisingly, the sample with the higher cross-linker Bcc content possesses a higher E'-value. According to the E' value at T_g+ 30°C (Tang et al., 2020), the cross-linking density can be calculated in **Supplementary Equation 1** and shown in **Supplementary Table 2**.

Mechanical Properties

To investigate the mechanical properties of the elastomer, static tensile measurements are performed at a strain rate of 0.083 s^{-1}. **Figure 3A** displays the typical stress–strain curves for these samples, and mechanical properties are summarized in **Figure 3B** and **Supplementary Table 4**. PU_E-1 exhibits a tensile strength about 0.79 MPa and a strain at break of 1,696%, as the cross-linker Bcc content increases to 0.519 g (1.720 mmol), the tensile strength increases up to 2.09 MPa. The improved mechanical properties can be attributed to the synergistic effect of covalent cross-links and physical cross-links formed by substantial hydrogen bonds. The covalent bonds control the network elasticity and maintain the sample integrity at large deformation, whereas the recurrent dissociation/reassociation of the hydrogen bonds controls rigidity and toughness. Thus, when stretched, the hydrogen bonds fracture first to dissipate energy effectively, while the covalent bonds maintain a good strength of elastomer, as illustrated by **Figure 4A**. Interestingly, the stress–strain curves of these samples are relatively non-linear, and there is yielding point, which represents a non-classical rubberlike behavior.

To further explore the non-linear relationship between deforming and mechanical properties, we selected PU_E-4 as an example to perform the tensile tests at various straining rates, from 0.004 to 0.3 s^{-1}. **Figure 3C** manifests a unique strain-rate–responsive yield phenomenon. The yield stress strikingly with increasing strain rate, and meanwhile the Young's modulus

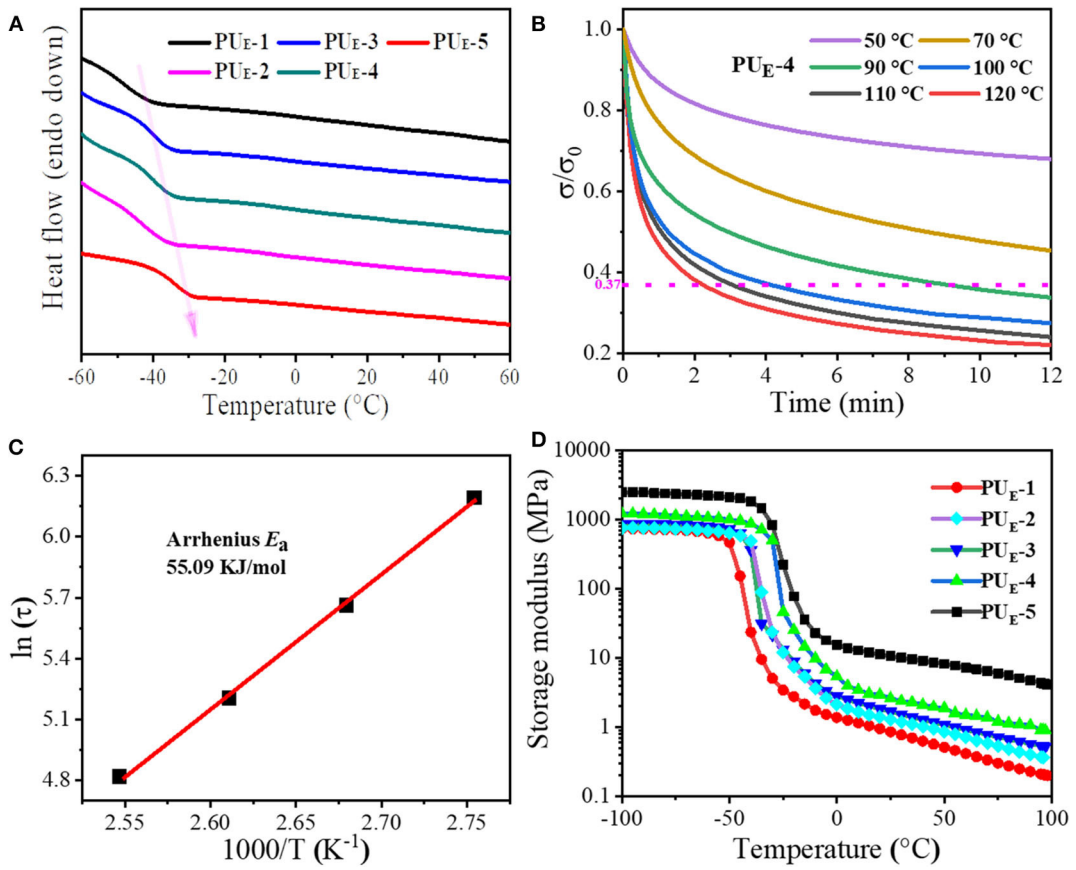

FIGURE 2 | Thermal properties and dynamic nature of the networks. **(A)** DSC curves of PU_E samples under N_2 in the temperature range of −60 to 60°C at a heating scan rate of 5°C min^{-1}. **(B)** Stress relaxation curves of PU_E-4 sample. The sample is stretched to a strain of 50% under different temperatures from 50 to 120°C and then maintained for 12 min. **(C)** Fitting of the relaxation times to the Arrhenius equation. **(D)** Dependence of the PU_E samples storage modulus *(E′)* on temperature.

obtained from the initial linear region of the stress–strain curves increases from 1.04 to 4.64 MPa in **Figure 3D**. Such a phenomenon demonstrates that the elastomers possess a self-stiffening ability with increasing strain rate (Wu et al., 2019). To explain the underlying mechanism governing this increasing yield phenomenon with strain rate, we need to consider the inherent (stress-free) dissociation rate constant (k_p) of the hydrogen bonds (Hu et al., 2017). At room temperature, k_p of the hydrogen bonds is much smaller than the strain rate. As a result, higher strain rates (>0.004 s^{-1}) tend to enhance the strain localization and thus promote yielding, which induces a slight drop in stress.

Additionally, the stretchability is highly dependent on the straining rate in **Supplementary Figure 7**, which is consistent with most elastomers (Li et al., 2016; Son et al., 2018; Lai et al., 2019). Surprisingly, unlike other super-stretchable elastomers with large residual strain after deformation, the non-isocyanate PU_E displays an excellent elastic behavior and can nearly completely restore its original shape even after they are subjected to large deformations. For an example, PU_E-4 can be stretched to a strain of 1,700%. After releasing the stress, the instantaneous residual strain is 70%, and it gradually decreases as a function of time, as shown in **Supplementary Figures 8A,B**. Prolonging the waiting time, the sample almost fully recovers its original shape without evident residue strain, which suggests both the robustness of the covalent network and reversibility of the physical network formed by hydrogen bonds. The performance comparison between this material and the existing literatures PU elastomer has been put into the (**Supplementary Figure 9**). (Yuan et al., 2014; Chen et al., 2016; Feula et al., 2016; Yang et al., 2017, 2020; Jin et al., 2020).

Acid-Degradation and Reprocessing

Compared with traditional isocyanate-based PU_Es, one degradation process allows the PU_E to recover the di(trimethylolpropane) monomer under acid hydrolysis condition at the end of service life. To illustrate the degradation process, the sample films of 0.5 g are immersed in sealed vials containing 10 mL of HCl (1 M), NaOH (1 M) and H_2O, respectively. The vials are heated in an oven to 100°C for 24 h. The sample films show no obvious changes in aqueous solution (H_2O) and slight degradation in basic solution (NaOH), while in strong acid solution (HCl), the sample can be fully dissolved into a homogenous solution after heating, as shown

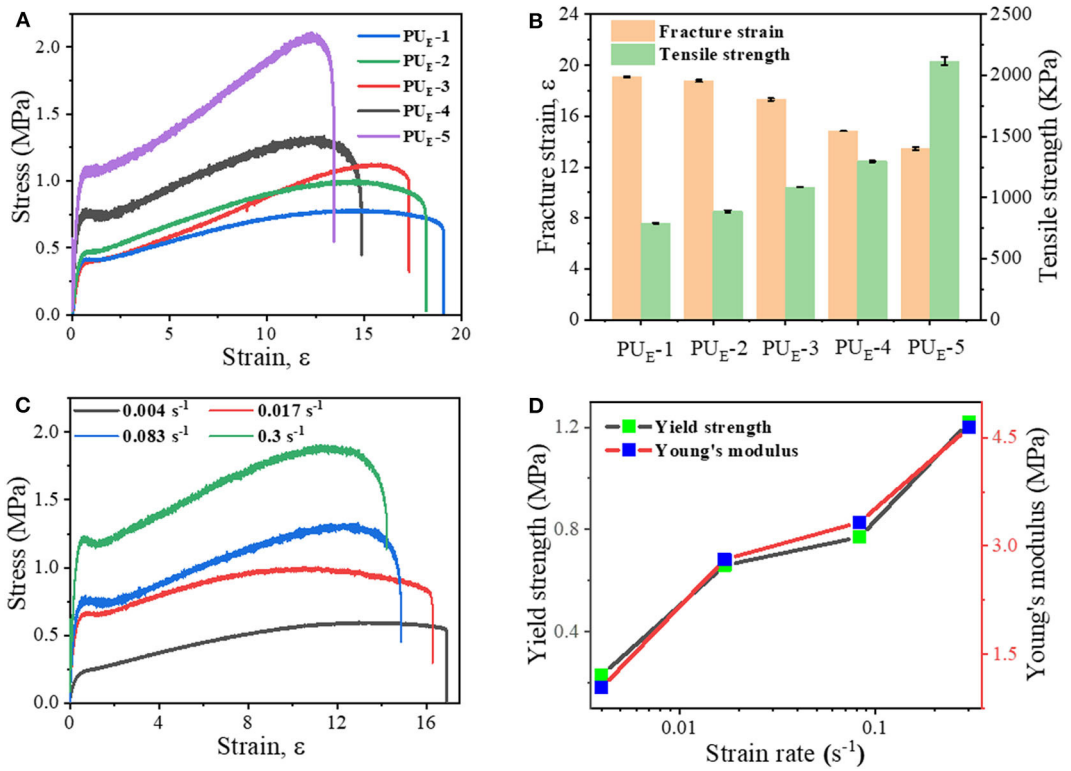

FIGURE 3 | Static tensile properties of the elastomers. **(A)** Tensile tests of as-prepared samples with various feeding ratios: the strain rate is 0.083 s^{-1}. **(B)** Summary of mechanical properties of the elastomers. **(C)** Stress—strain curves of the PU_E-4 sample at various strain rates. **(D)** Dependence of the yield strength and Young's modulus on the various strain rates.

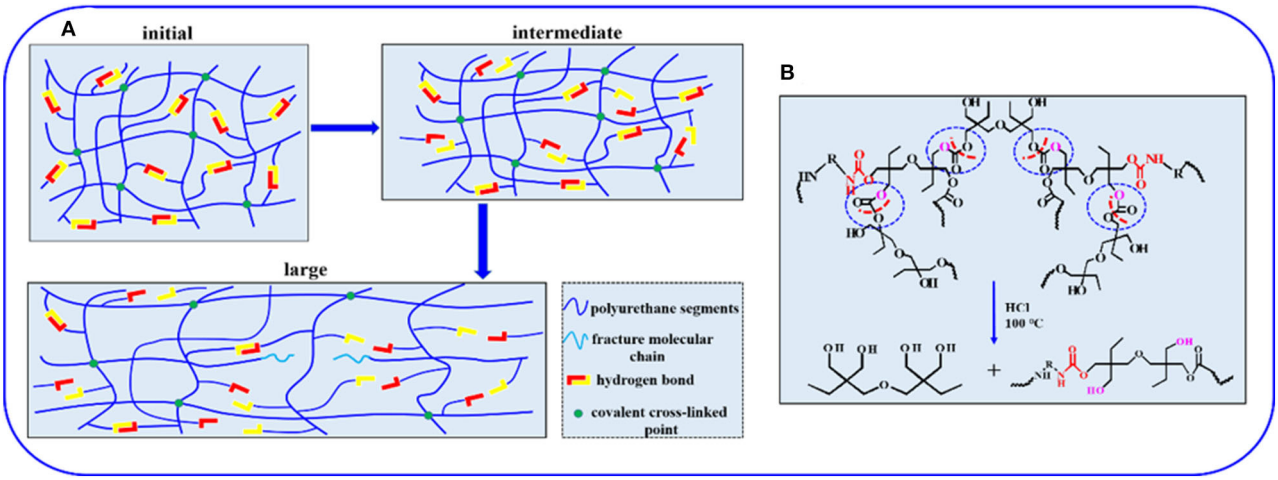

FIGURE 4 | (A) Illustration of the sequential breakage of networks in the elastomer during the stretching process. **(B)** The acid-degradation mechanism of non-isocyanate PU_E.

in **Figure 5A**. The acid-degradation mechanism is shown in **Figure 4B**: the carbonate bonds are broken in the strong acid solution. Extracting the acid-degraded solution containing HCl with *n*-butanol (20 mL) leads to 75% recovery of the pure di(trimethylolpropane) monomer. The product structure is not destroyed, as verified by NMR characterization in **Supplementary Figure 10**. In addition to being acid-degradable, the dynamic cross-linked network can reform once again at elevated temperatures owing to transcarbonation exchange reactions via free hydroxyl and carbonate groups. As such, the

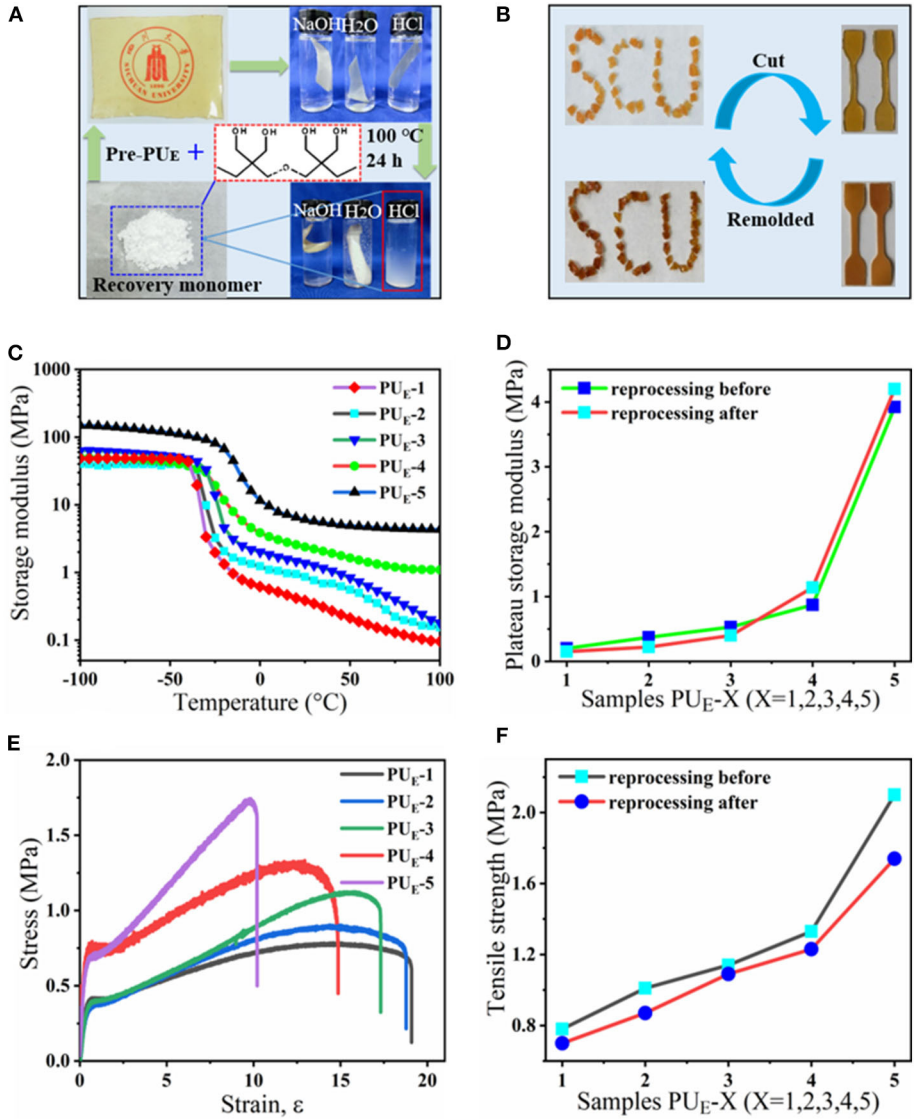

FIGURE 5 | The acid-degradation and reprocessing of the PU_E samples. **(A)** A sample film is hydrolyzed and decarbonated in hydrochloric acid, and the monomer can be recovered. **(B)** Hot reprocessing of the damaged sample films. **(C)** DMA curves of the samples after reprocessing. **(D)** The variation curves of the rubbery storage modulus at 50°C before and after reprocessing. **(E)** Stress-strain curves of the samples after reprocessing. **(F)** The variation curves of the tensile strength before and after reprocessing.

samples can be reprocessed. For example, the damaged samples are cut into small pieces and then hot pressed at 130°C under a pressure of 5 to 10 MPa. The sample can be fully restored after hot pressing in **Figure 5B**, indicating the excellent recyclability of the dynamically cross-linked elastomer.

The reprocessing mechanism relies on transcarbonation exchange reaction and is illustrated in **Figure 1D**: a hydroxyl nucleophile reacts with a carbonate at elevated temperature, forming an associative intermediate, and then the exchanged carbonate and hydroxyl groups are released, denoting completion of the network rearrangement process. Dynamic mechanical analysis and uniaxial tensile tests are carried out to determine the recovery efficiencies of the tensile strength and plateau storage modulus after reprocessing. The storage modulus of the samples after reprocessing as a function of temperature is recorded by DMA in **Figure 5C**. **Figure 5D** exhibits the plateau storage modulus at 50°C before and after reprocessing. The performance of the reprocessed material, which was better than its original form. Similar results have been found in previous literature (Snyder et al., 2018), and the mechanism is still unclear. Exploring the questions will require model networks of more controlled network structure and molar ratio between reversible

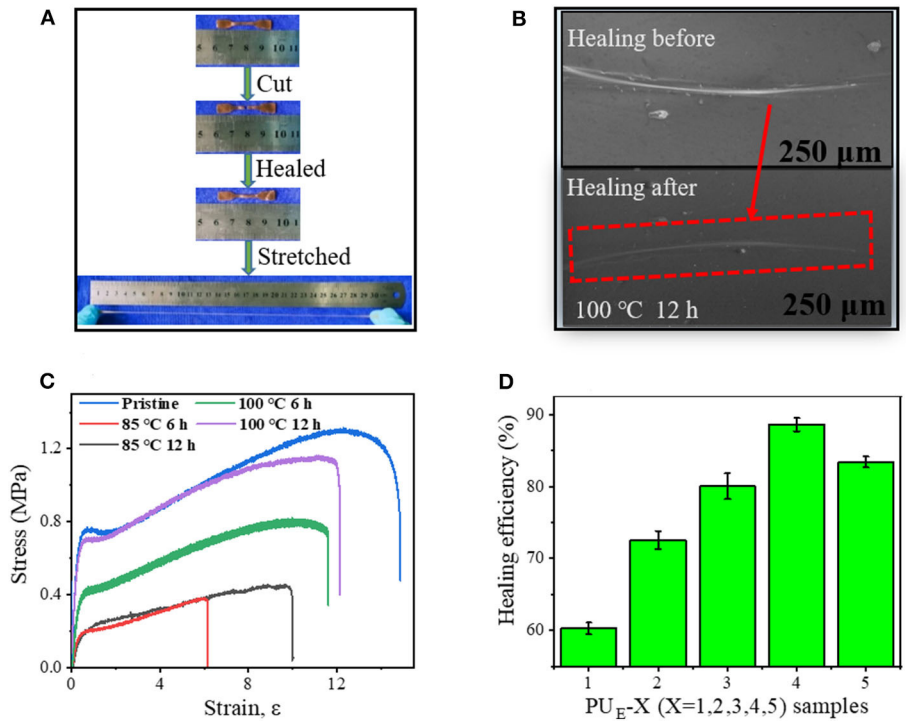

FIGURE 6 | Self-healing mechanism and properties of PU_E samples. **(A)** Pictures of before and after healing, and the healed sample under stretching. **(B)** SEM images of the damaged surfaces before and after healing at 100°C for 12 h. **(C)** Strain—stress curves of the healed at 85 and 100°C for various time. **(D)** Healing efficiency of $PU_{E\ S}$amples with various cross-linker bcc content (healed at 100°C for 12 h).

and covalent crosslinks. The typical stress–strain curves of these samples after hot pressing are illustrated by **Figure 5E**. The stress–strain curves of remolded samples also show the unique yield phenomenon. The tensile strength of the samples, however, decreases as reprocessing process in **Figure 5F**, suggesting that the reprocessing procedures would cause slightly decreases in tensile strength. Despite the slight decrease of mechanical properties, no changes in the chemical functionality are observed by FT-IR spectra in **Supplementary Figure 11**. Meanwhile, to quantify the reprocessing tensile strength recovery efficiency, we define it as ratio the tensile strength of before to after reprocessing in **Supplementary Equation 2**. The recovery efficiency of tensile strength is 82.9–95.6% after reprocessing in **Supplementary Figure 12**. Recovery of elastomers and avoidance of environmental pollution are the main research directions of soft materials. Although the degradation cost mentioned in this article is not the lowest, relatively speaking, it provides at least a feasible and easy to implement recycling strategy. How to reduce the cost and obtain the highest recovery product is the work we need to continue to carry out.

Self-Healing Properties

To demonstrate the self-healing behavior, tensile tests before and after self-healing are performed. As shown in **Figure 6A**, the healed sample can sustain a large strain after healing at 100°C for 12 h, indicating the excellent self-healing ability of the PU_E samples. **Figure 6C** exhibits the typical stress–strain curves of PU_E-4 healed at 85 and 100°C for various times. The self-healing efficiency is quantified by the ratio of the fracture stress of the healed to the pristine sample in **Supplementary Equation 3**. After being healed for at 85°C for 12 h, the healing efficiency is 34.9%. Significantly, the healing efficiency further increase to 62.8% and 88.4% after being healed at 100°C for 6 and 12 h, respectively. The self-healing fully demonstrates the reconstructing ability of network topologies and hydrogen bonds. **Figure 6D** shows the healing efficiencies of different PU_E samples. It is worth noting that the healing efficiency does not change monotonously with cross-linking density, and PU_E-4 sample exhibits the highest efficiency. In general, higher crosslinking density indicates restricted chain mobility, which is unfavorable for wetting and diffusion of rubber chains at interface and consequently leading to poor healing behavior (Cao et al., 2019). However, a higher cross-linking density means more carbonate bonds, which indicates that more covalent linkages can be reformed at interface via transcarbonation exchange reaction. The competition of these two effects leads to the highest healing efficiency of PU_E-4. To investigate the healing from microscopic scale, we prepare a scratch on a sample film and characterize the evolution of the scratch with scanning electron microscope (SEM). **Figure 6B** exhibits that the scratch on the film almost completely disappears after healing at 100°C for 12 h. This once again indicates the good self-healing behavior of the obtained PU_E samples.

CONCLUSIONS

In summary, we have designed and fabricated a novel acid-degradable and self-healable vitrimer based on non-isocyanate PU_E. Interestingly, the elastomer manifests a unique strain-rate–responsive yield phenomenon during stretching. The yield stress increases with increasing strain rate, as the increasing high strain rate ($>0.004\ s^{-1}$) tends to enhance the strain localization and promote yielding. Elevating the temperature can alter the networks topologies of the elastomer, which results in excellent reprocessing and self-healing behaviors. Simultaneously, the elastomer containing the dynamic networks can be hydrolyzed and decarbonated in the strong acid solution (HCl) to recovery 75 % of the pure di(trimethylolpropane) monomer. Therefore, we can envision that this non-isocyanate-based PU_E will manifest longer service life and decreased pollution to the environment.

DATA AVAILABILITY STATEMENT

All datasets generated for this study are included in the article/**Supplementary Material**.

AUTHOR CONTRIBUTIONS

HWu carried out experiment and wrote the manuscript. JW supervised the project and mainly revised the paper. All authors extensively reviewed the manuscript and approved the final version of the manuscript to be submitted.

FUNDING

This work was supported by National Natural Science Foundation of China (Grant No. 51673120), State Key Laboratory of Polymer Materials Engineering (Grant No. sklpme2019-2-14) and the Fundamental Research Funds for Central Universities.

SUPPLEMENTARY MATERIAL

The Supplementary Material for this article can be found online at: https://www.frontiersin.org/articles/10.3389/fchem.2020.585569/full#supplementary-material

REFERENCES

Cao, L., Fan, J., Huang, J., and Chen, Y. (2019). A robust and stretchable cross-linked rubber network with recyclable and self-healable capabilities based on dynamic covalent bonds. *J. Mater. Chem. A* 7, 4922–4933. doi: 10.1039/C8TA11587G

Chen, M., Yao, B., Kappl, M., Liu, S., Yuan, J., Berger, R., et al. (2019). Entangled azobenzene-containing polymers with photoinduced reversible solid-to-liquid transitions for healable and reprocessable photoactuators. *Adv. Funct. Mater*. 30:1906752. doi: 10.1002/adfm.201906752

Chen, W., Zhou, Y., Li, Y., Sun, J., Pan, X., Yu, Q., et al. (2016). Shape-memory and self-healing polyurethanes based on cyclic poly(ε-caprolactone). *Polym. Chem*. 7, 6789–6797. doi: 10.1039/C6PY01638C

Chen, Y., Tang, Z., Zhang, X., Liu, Y., Wu, S., and Guo, B. (2018). Covalently cross-linked elastomers with self-healing and malleable abilities enabled by boronic ester bonds. *ACS Appl. Mater. Interfaces* 10, 24224–24231. doi: 10.1021/acsami.8b09863

Cromwell, O. R., Chung, J., and Guan, Z. (2015). Malleable and self-healing covalent polymer networks through tunable dynamic boronic ester bonds. *J. Am. Chem. Soc*. 137, 6492–6495. doi: 10.1021/jacs.5b03551

Denissen, W., Droesbeke, M., Nicolay, R., Leibler, L., Winne, J. M., and Du Prez, F. E. (2017). Chemical control of the viscoelastic properties of vinylogous urethane vitrimers. *Nat. Commun*. 8:14857. doi: 10.1038/ncomms14857

Fan, C.-J., Huang, Z.-C., Li, B., Xiao, W.-X., Zheng, E., Yang, K.-K., et al. (2019). A robust self-healing polyurethane elastomer: from H-bonds and stacking interactions to well-defined microphase morphology. *Sci. China Mater*. 62, 1188–1198. doi: 10.1007/s40843-019-9422-7

Feula, A., Tang, X., Giannakopoulos, I., Chippindale, A. M., Hamley, I. W., Greco, F., et al. (2016). An adhesive elastomeric supramolecular polyurethane healable at body temperature. *Chem. Sci*. 7, 4291–4300. doi: 10.1039/C5SC04864H

Fortman, D. J., Brutman, J. P., Cramer, C. J., Hillmyer, M. A., and Dichtel, W. R. (2015). Mechanically activated, catalyst-free polyhydroxyurethane vitrimers. *J. Am. Chem. Soc*. 137, 14019–14022. doi: 10.1021/jacs.5b08084

Garcia, F., and Smulders, M. M. (2016). Dynamic covalent polymers. *J. Polym. Sci. A Polym. Chem*. 54, 3551–3577. doi: 10.1002/pola.28260

Hu, X., Zhou, J., Daniel, W. F. M., Vatankhah-Varnoosfaderani, M., Dobrynin, A. V., and Sheiko, S. S. (2017). Dynamics of dual networks: strain rate and temperature effects in hydrogels with reversible H-bonds. *Macromolecules* 50, 652–659. doi: 10.1021/acs.macromol.6b02422

Jian, X., Hu, Y., Zhou, W., and Xiao, L. (2018). Self-healing polyurethane based on disulfide bond and hydrogen bond. *Polym. Adv. Technol*. 29, 463–469. doi: 10.1002/pat.4135

Jiang, Z. C., Xiao, Y. Y., Yin, L., Han, L., and Zhao, Y. (2020). "Self-lockable" liquid crystalline diels-alder dynamic network actuators with room temperature programmability and solution reprocessability. *Angew. Chem. Int. Ed Engl*. 59, 4925–4931. doi: 10.1002/anie.202000181

Jin, C., Sinawang, G., Osaki, M., Zheng, Y., Yamaguchi, H., Harada, A., et al. (2020). Self-healing thermoplastic polyurethane linked via host-guest interactions. *Polymers* 12:1369. doi: 10.3390/polym12061393

Jin, Y., Yu, C., Denman, R. J., and Zhang, W. (2013). Recent advances in dynamic covalent chemistry. *Chem. Soc. Rev*. 42, 6634–6654. doi: 10.1039/c3cs60044k

Kloxin, C. J., and Bowman, C. N. (2013). Covalent adaptable networks: smart, reconfigurable and responsive network systems. *Chem. Soc. Rev*. 42, 7161–7173. doi: 10.1039/C3CS60046G

Lai, J. C., Jia, X. Y., Wang, D. P., Deng, Y. B., Zheng, P., Li, C. H., et al. (2019). Thermodynamically stable whilst kinetically labile coordination bonds lead to strong and tough self-healing polymers. *Nat. Commun*. 10:1164. doi: 10.1038/s41467-019-09130-z

Li, C. H., Wang, C., Keplinger, C., Zuo, J. L., Jin, L., Sun, Y., et al. (2016). A highly stretchable autonomous self-healing elastomer. *Nat. Chem*. 8, 618–624. doi: 10.1038/nchem.2492

Liu, W., Fang, C., Wang, S., Huang, J., and Qiu, X. (2019). High-performance lignin-containing polyurethane elastomers with dynamic covalent polymer networks. *Macromolecules* 52, 6474–6484. doi: 10.1021/acs.macromol.9b01413

Liu, Y., Tang, Z., Chen, Y., Zhang, C., and Guo, B. (2018). Engineering of beta-hydroxyl esters into elastomer-nanoparticle interface toward malleable, robust, and reprocessable vitrimer composites. *ACS Appl. Mater. Interfaces* 10, 2992–3001. doi: 10.1021/acsami.7b17465

Lu, Y. X., Tournilhac, F., Leibler, L., and Guan, Z. (2012). Making insoluble polymer networks malleable via olefin metathesis. *J. Am. Chem. Soc*. 134, 8424–8427. doi: 10.1021/ja303356z

Montarnal, D., Capelot, M., Tournilhac, F., and Leibler, L. (2011). Silica-like malleable materials from permanent organic networks. *Science* 334, 965–968. doi: 10.1126/science.1212648

Obadia, M. M., Mudraboyina, B. P., Serghei, A., Montarnal, D., and Drockenmuller, E. (2015). Reprocessing and recycling of highly cross-linked ion-conducting networks through transalkylation exchanges of C-N bonds. *J. Am. Chem. Soc*. 137, 6078–6083. doi: 10.1021/jacs.5b02653

Röttger, M., Domenech, T., van der Weegen, R., Breuillac, A., Nicolaÿ, R., and Leibler, L. (2017). High-performance vitrimers from commodity thermoplastics through dioxaborolane metathesis. *Science* 356, 62–65. doi: 10.1126/science.aah5281

Scott, T. F., Schneider, A. D., Cook, W. D., and Bowman, C. N. (2005). Photoinduced plasticity in cross-linked polymers. *Science* 308, 1615–1617. doi: 10.1126/science.1110505

Shi, Q., Yu, K., Kuang, X., Mu, X., Dunn, C. K., Dunn, M. L., et al. (2017). Recyclable 3D printing of vitrimer epoxy. *Mater Horiz.* 4, 598–607. doi: 10.1039/C7MH00043J

Snyder, R. L., Fortman, D. J., De Hoe, G. X., Hillmyer, M. A., and Dichtel, W. R. (2018). Reprocessable acid-degradable polycarbonate vitrimers. *Macromolecules* 51, 389–397. doi: 10.1021/acs.macromol.7b02299

Son, D., Kang, J., Vardoulis, O., Kim, Y., Matsuhisa, N., Oh, J. Y., et al. (2018). An integrated self-healable electronic skin system fabricated via dynamic reconstruction of a nanostructured conducting network. *Nat. Nanotechnol.* 13, 1057–1065. doi: 10.1038/s41565-018-0244-6

Tadakaluru, S., Thongsuwan, W., and Singjai, P. (2014). Stretchable and flexible high-strain sensors made using carbon nanotubes and graphite films on natural rubber. *Sensors.* 14, 868–876. doi: 10.3390/s140100868

Tang, L., Wang, Y., Zhou, T., Li, Y., and Li, Q. (2020). Enhanced toughness and mechanical property of epoxy resins with good shape memory behaviors. *Fibers Polym.* 21, 1187–1194. doi: 10.1007/s12221-020-9684-3

Tee, B. C., Wang, C., Allen, R., and Bao, Z. (2012). An electrically and mechanically self-healing composite with pressure- and flexion-sensitive properties for electronic skin applications. *Nat. Nanotechnol.* 7, 825–832. doi: 10.1038/nnano.2012.192

Ube, T., Kawasaki, K., and Ikeda, T. (2016). Photomobile liquid-crystalline elastomers with rearrangeable networks. *Adv. Mater.* 28, 8212–8217. doi: 10.1002/adma.201602745

Wang, L., and Loh, K. J. (2017). Wearable carbon nanotube-based fabric sensors for monitoring human physiological performance. *Smart Mater. Struct.* 26:055018. doi: 10.1088/1361-665X/aa6849

Wang, W., Song, Q., Liu, Q., Zheng, H., Li, C., Yan, Y., et al. (2019). A novel reprocessable and recyclable acrylonitrile-butadiene rubber based on dynamic oxime-carbamate bond. *Macromol. Rapid Commun.* 40:e1800733. doi: 10.1002/marc.201800733

Wu, B., Liu, Z., Lei, Y., Wang, Y., Liu, Q., Yuan, A., et al. (2020). Mutually-complementary structure design towards highly stretchable elastomers with robust strength and autonomous self-healing property. *Polymer* 186:122003. doi: 10.1016/j.polymer.2019.122003

Wu, Q., Xiong, H., Peng, Y., Yang, Y., Kang, J., Huang, G., et al. (2019). Highly stretchable and self-healing "solid-liquid" elastomer with strain-rate sensing capability. *ACS Appl. Mater. Interfaces* 11, 19534–19540. doi: 10.1021/acsami.9b05230

Yang, S., Wang, S., Du, X., Du, Z., Cheng, X., and Wang, H. (2020). Mechanically robust self-healing and recyclable flame-retarded polyurethane elastomer based on thermoreversible crosslinking network and multiple hydrogen bonds. *Chem. Eng. J.* 391:123544. doi: 10.1016/j.cej.2019.123544

Yang, Y., Lu, X., and Wang, W. (2017). A tough polyurethane elastomer with self-healing ability. *Mater. Des.* 127, 30–36. doi: 10.1016/j.matdes.2017.04.015

Yang, Y., Pei, Z., Li, Z., Wei, Y., and Ji, Y. (2016). Making and remaking dynamic 3D structures by shining light on flat liquid crystalline vitrimer films without a mold. *J. Am. Chem. Soc.* 138, 2118–2121. doi: 10.1021/jacs.5b12531

Yang, Y., Pei, Z., Zhang, X., Tao, L., Wei, Y., and Ji, Y. (2014). Carbon nanotube–vitrimer composite for facile and efficient photo-welding of epoxy. *Chem. Sci.* 5, 3486–3492. doi: 10.1039/C4SC00543K

Yuan, C. E., Rong, M. Z., and Zhang, M. Q. (2014). Self-healing polyurethane elastomer with thermally reversible alkoxyamines as crosslinkages. *Polymer* 55, 1782–1791. doi: 10.1016/j.polymer.2014.02.033

Zhang, H., and Xu, X. (2017). Improving the transesterification and electrical conductivity of vitrimers by doping with conductive polymer wrapped carbon nanotubes. *Compos. Part A Appl. Sci. Manuf.* 99, s15–22. doi: 10.1016/j.compositesa.2017.03.037

Zheng, P., and McCarthy, T. J. (2012). A surprise from 1954: siloxane equilibration is a simple, robust, and obvious polymer self-healing mechanism. *J. Am. Chem. Soc.* 134, 2024–2027. doi: 10.1021/ja2113257

Zhou, F., Guo, Z., Wang, W., Lei, X., Zhang, B., Zhang, H., et al. (2018). Preparation of self-healing, recyclable epoxy resins and low-electrical resistance composites based on double-disulfide bond exchange. *Compos. Sci. Technol.* 167, 79–85. doi: 10.1016/j.compscitech.2018.07.041

Conflict of Interest: The authors declare that the research was conducted in the absence of any commercial or financial relationships that could be construed as a potential conflict of interest.

The reviewer LC declared a past co-authorship with one of the authors JW to the handling editor.

Copyright © 2020 Wu, Jin, Wang, Wu, Cao, Wu and Huang. This is an open-access article distributed under the terms of the Creative Commons Attribution License (CC BY). The use, distribution or reproduction in other forums is permitted, provided the original author(s) and the copyright owner(s) are credited and that the original publication in this journal is cited, in accordance with accepted academic practice. No use, distribution or reproduction is permitted which does not comply with these terms.

frontiers in Chemistry

MINI REVIEW
published: 21 October 2020
doi: 10.3389/fchem.2020.595972

Advances of Carbon-Based Materials for Lithium Metal Anodes

Kaikai Tang[1], Jun Xiao[1], Xiao Li[1], Dandan Wang[1], Mengqi Long[1], Jun Chen[1], Hong Gao[1,2], Weihua Chen[3], Chuntai Liu[3] and Hao Liu[1,4]**

[1] Joint International Laboratory on Environmental and Energy Frontier Materials, School of Environmental and Chemical Engineering, Shanghai University, Shanghai, China, [2] State Key Laboratory of Advanced Special Steel, Shanghai Key Laboratory of Advanced Ferrometallurgy, Shanghai University, Shanghai, China, [3] Key Laboratory of Materials Processing and Mold (Zhengzhou University), Ministry of Education, Zhengzhou, China, [4] Centre for Clean Energy Technology, Faculty of Science, School of Mathematical and Physical Sciences, University of Technology Sydney, Sydney, NSW, Australia

Lithium metal with high theoretical specific capacity (3,860 mAh g^{-1}), low mass density, and low electrochemical potential (−3. 040 V vs. SHE) is an ideal candidate of the battery anode. However, the challenges including dendrite propagation, volume fluctuation, and unstable solid electrolyte interphase of lithium metal during the lithium plating impede the practical development of Lithium metal batteries (LMBs). Carbon-based materials with diverse structures and functions are ideal candidates to address the challenges in LMBs. Herein, we briefly summarize the main challenges as well as the recent achievements of lithium metal anode in terms of utilizing carbon-based materials as electrolyte additives, current collectors and composite anodes. Meanwhile, we propose the critical challenges that need to be addressed and perspectives for ways forward to boost the advancement of LMBs.

Keywords: composite anodes, current collectors, additives, carbon-based materials, lithium metal anodes, battereis

OPEN ACCESS

Edited by:
Jianping Yang,
Donghua University, China

Reviewed by:
Ji Liang,
University of Wollongong, Australia
Lei Zhang,
South China University of Technology, China
Bin Wang,
China Academy of Engineering Physics, China

Correspondence:
Hao Liu
hao.liu@uts.edu.au
Hong Gao
candy1122@shu.edu.cn

Specialty section:
This article was submitted to Green and Sustainable Chemistry, a section of the journal Frontiers in Chemistry

Received: *18 August 2020*
Accepted: *07 September 2020*
Published: *21 October 2020*

Citation:
Tang K, Xiao J, Li X, Wang D, Long M, Chen J, Gao H, Chen W, Liu C and Liu H (2020) Advances of Carbon-Based Materials for Lithium Metal Anodes. Front. Chem. 8:595972. doi: 10.3389/fchem.2020.595972

INTRODUCTION

Since Sony commercialized lithium-ion batteries (LIBs) in 1991, rechargeable LIBs have been successfully applied to portable electronics and electric vehicles (Yang G. et al., 2019; Yang T. et al., 2019; Lee et al., 2020; Maroufi et al., 2020; Pellow et al., 2020). However, the constrained energy density of the traditional LIBs based on intercalation chemistry are unable to meet the ever-growing requirement of high-energy-density batteries. Lithium metal batteries (LMBs) with high capacity and high energy density have attracted numerous attentions. Compared with commercial LIBs, LMBs employ metallic Li as an anode, which is based on a continuous plating/stripping mechanism, contributing to higher energy output (Chen C. et al., 2019; Zhang T. et al., 2019; Widijatmoko et al., 2020; Ye et al., 2020). Lithium metal anodes are known as the "Holy Grail" electrodes due to the unique advantages, such as the lowest density among metals, high theoretical specific capacity (3,860 mAh g^{-1}) and the lowest electrochemical potential (−3.040 V vs. standard hydrogen electrode) (Xie et al., 2019; Shi et al., 2020; Zhang Q. et al., 2020; Zhou Y. et al., 2020). Moreover, when LMBs collocate with high capacity cathodes, such as sulfur (S) and oxygen (O_2), it can achieve excellent specific energy and be regarded as promising next-generation energy storage systems beyond LIBs and other storage systems (Hong et al., 2019; Sloop et al., 2019; Xiao et al., 2019; Gan et al., 2020; Guo et al., 2020; Li W. T. et al., 2020). Unfortunately, the development of LMBs is hindered by the inevitable shortcomings of lithium metal anode, including dendrite propagation, volume fluctuation, and unstable solid electrolyte interphase (SEI), originating from the high chemical

reactivity and "hostless" nature of lithium metal during the plating/stripping process (Li Q. et al., 2018; Li Z. et al., 2020; Pan et al., 2020).

Carbon-based materials with good electrical and thermal conductivity, excellent structural stability, as well as high surface area and abundant surface functional groups have been extensively applied in numerous research fields (Liu et al., 2017; Yan et al., 2019; Tian et al., 2020). Even more noteworthy is that carbon-based materials offer a versatile platform to construct new architectures with interconnected porosity and active sites (Ge et al., 2018; Zhang Z. et al., 2018a; Zhang W. et al., 2019). The surface chemistry of carbon-based materials can be easily modified to improve the binding properties. Consequently, doping or co-doping with different heteroatoms (N, S, P) (Wei et al., 2019; Liu et al., 2020; Ma et al., 2020; Zhang D. M. et al., 2020) makes the carbon-based materials exhibit further enhancement of the electrocatalytic activity. Owing to these diversified functions of carbon-based materials, they have been intensively used to ameliorate the challenges of LMBs (Zuo et al., 2018; Xue et al., 2019; Huang et al., 2020).

Although there are many reported reviews on LMBs, very few reports that specifically describe carbon-based materials in addressing the challenges in LMBs. This review provides a comprehensive overview of the application of carbon-based materials in improving the performance of lithium metal anodes. In this review, we focus on the main challenges faced by lithium metal anodes and emphasize the effective strategies employing carbon-based materials as electrolyte additives, current collectors and composite anodes to achieve high performance lithium metal anodes. We believe that this review is informative and could offer some new insights for this exciting area.

CHALLENGES OF LITHIUM METAL ANODES

The LMBs were born in the 1970's. However, they have almost stagnated since then, lagging far behind the development of LIBs. As we all know, lithium metal is very active and can react with almost all organic electrolytes to form a SEI (**Figure 1**). An ideal SEI film should be electrically insulating and ionically conductive. Moreover, it should have good chemical and mechanical stability to withstand the volume change and protect the lithium metal from further exposure to the electrolyte. Nevertheless, due to the "hostless" property and unevenness of lithium metal surface, Li^+ preferentially deposits at the tips, resulting in uneven deposition of lithium and the formation of dendrites during the repeatedly stripping and plating process. The dendrites inevitably cause the electrode volume changes, which lead to the destruction of SEI film and then exposure of fresh lithium metal to the electrolyte. This is followed by continuous side reactions until the electrolyte is depleted, which have a negative impact on the Coulomb efficiency (CE). At the same time, the aforementioned process can in turn exacerbate the dendrite growth.

Eventually, there are two possibilities of the uncontrolled dendrites. Firstly, the dendrites may fall off from the anode surface to form "dead Li," causing the loss of active materials

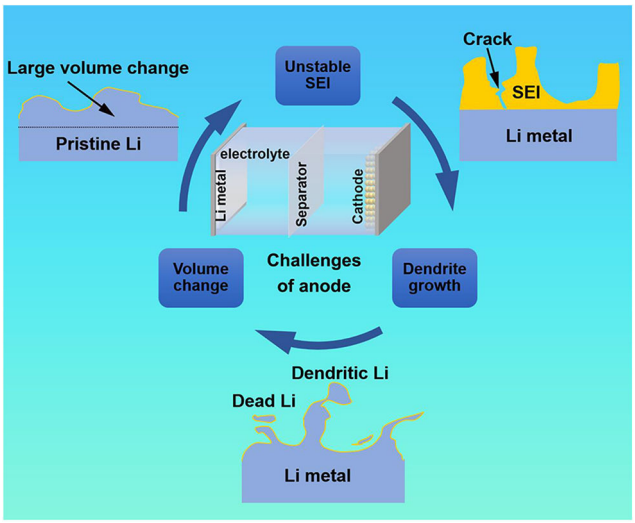

FIGURE 1 | Schematic diagram of the challenge of anode for LMBs.

and greatly reduce the utilization of Li. Secondly, the dendrites may pierce the separator to reach the cathode, causing a short circuit. These intrinsic challenges of lithium metal lead to many undesirable drawbacks such as unstable SEI, severe volume change and uncontrolled dendrite growth during electroplating/stripping in the rechargeable LMBs, which have been hindered their practical applications over the past 40 years (Zhang R. et al., 2017).

APPLICATION OF CARBON-BASED MATERIALS IN LITHIUM METAL ANODES

So far, tremendous strategies have been proposed to suppress the dendrites growth. These strategies can be classified into the following categories: (1) electrolyte manipulation, including modification of additives in the electrolyte (Zhang X. Q. et al., 2017; Huang et al., 2018; Li X. et al., 2018), and adoption of solid or polymer electrolytes (Aldalur et al., 2018; Girard et al., 2019; Huo et al., 2020; Hu Z. et al., 2020); (2) SEI engineering (Li C. et al., 2019; Yan et al., 2020), such as artificial SEI film (Zhu et al., 2019); (3) electrode structure design (Zhang Y. et al., 2018, 2019).

Carbon-based materials with unique physical and chemical properties can act as electrolyte additives to inhibit the dendrite growth. In addition, the various structures, high surface area and flexibility enable the carbon-based materials to be as hosts to accommodate the volume change (Jorge et al., 2019; Nan et al., 2019; Zhang X. et al., 2020).

Carbon-Based Materials to Construct Composite Anodes

On account of the intrinsic "hostless" of lithium metal, the lithium deposits on the planar electrode will undergo severe volume changes, resulting in continuous fracture and regeneration of the SEI film. Unstable SEI film will seriously

reduce the lifespan of the battery. Therefore, confining the lithium metal in scaffold is an effective way to accommodate the volume change (Yang et al., 2018; Pei et al., 2019; Tang et al., 2020). The as-prepared structured composite anode can regulate the Li^+ deposition and induce dendrite-free morphology, thereby achieving a high capacity and long cycle life lithium metal anode (Wang et al., 2017; Zhang R. et al., 2018a). The 3D porous scaffold with multiple ion and electron transfer paths and high surface area is often employed as host for lithium metal. Moreover, the current density can be dissipated by this 3D conductive porous scaffolds, resulting in a lower local current density (Chazalviel, 1990; Zhou T. et al., 2020), which can effectively control the growth rates of lithium dendrites.

The 3D porous scaffolds, such as copper foam (Yang et al., 2018; Yue et al., 2019b), nickel foam (Huang X. et al., 2019; Sun et al., 2019), mesoporous carbon (Zhang S. J. et al., 2019; Jeong et al., 2020), and carbon nanotube sponge (Yang G. et al., 2019), can accommodate infinite volume expansion and suppress dendrite growth during repeated electroplating/stripping processes. Besides, the composite electrode, assembled with a carbon-based skeleton, has good flexibility and can be used on wearable electronic devices. Nevertheless, most hosts need to be coated with a lithiophilic layer because of their poor lithiophilicity and the requirements of constructing a composite anode. Unlike metal frameworks that require complex processes to enhance lithiophilicity, carbon-based scaffolds have very significant advantages in practical applications. For example, some lithiophilic functional groups can be introduced into the most carbon hosts by facile surface chemistry approaches. Additionally, carbon-based materials with low density enable the high practical energy density batteries.

Tao et al. reported a simple surface ozonolysis and ammoniation treatment strategy to tune the lipophilicity of carbon scaffold (Tao et al., 2020). The flexible and lithiophilic carbon film (CF) is composed of multiple layered interwoven nanofibers. Due to the good mechanical strength and thermal stability, CF can be easily wetted by molten lithium to form a stable Li@CF composite anode. The as-prepared Li@CF composite electrode could deliver a high practical capacity of 3,222 mAh g^{-1} and behave a good rate performance. In addition, no obvious dendrites have been observed in the electrode.

Lithiophilic coating is an effective strategy to enhance the wettability between liquefied lithium and carbon matrix, because these coating layers can react with molten lithium to reduce the surface energy of carbon matrix or form alloys with lithium. Silicon can coat on the carbon-based materials via chemical vapor deposition to form the Li_xSi alloys (Liang et al., 2016; Hapuarachchi et al., 2018). Thus, the molten metallic lithium can easily and quickly flow into the scaffolds with silicon coating. Some metal oxides, such as ZnO (Zhao et al., 2019; Yue et al., 2020), CuO (Wu et al., 2018; Zhang C. et al., 2018; Huang K. et al., 2019), Co_3O_4 (Li S. Y. et al., 2019; Pan et al., 2019), can undergo redox reactions with molten lithium. Based on this fact, the scaffold coated with metal oxide can obtain enhanced lithiophilicity. Yue et al. coated Cu_xO (CFeltCu) on a porous carbon felt (CFelt) and prepared a stable

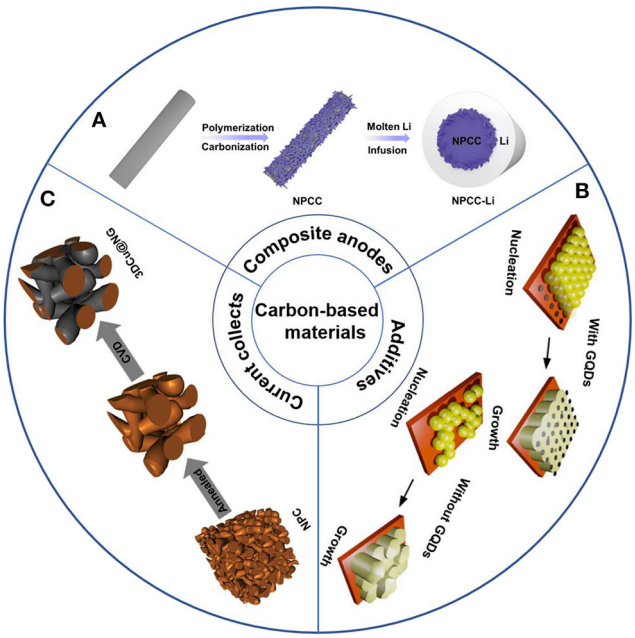

FIGURE 2 | Schematic diagram of the different strategies of carbon-based materials in addressing the challenges of lithium metal anodes: **(A)** Scheme illustration of the synthesis process of NPCC-Li. Li C. et al. (2019) with permission from WILEY-VCH. **(B)** Illustration of the GQDs regulated deposition processes Reprinted with permission from Hu Z. et al. (2020) with permission from Elsevier. **(C)** Schematic illustrations of the fabrication of 3D Cu@N-doped graphene. Reprinted with permission from Zhang Z. et al. (2018a) with permission from WILEY-VCH.

CFeltCu-Li composite anode via thermal infusion method (Yue et al., 2019a). During the thermal infusion process, the Cu nanoparticles derived from copper oxide reduced by molten lithium are evenly dispersed on the surface of the CFelt. To some extent, these Cu nanoparticles with high conductivity can not only regulate the Li stripping/plating behavior, but also reduce the local current density of anode. Therefore, the CFeltCu-Li composite anode presented outstanding cycle stability (over 1,000 h) and low overpotential (25 mV) without dendrite growth in symmetric cells.

Although the metal oxide coating can significantly improve the lithium affinity of carbon-based materials, the specific capacity and rate performance of lithium anodes have deteriorated to some extent. Carbon matrix with heteroatom co-doping can effectively overcome the above mentioned obstacle. A stable lithium composite anode that is composed of N and P co-doped carbon cloth and lithium metal, was presented by Li and coworkers (**Figure 2A**) (Li K. et al., 2019). N and P can provide enhanced surface lithiopholicity for carbon-based material, facilitating molten lithium diffusion and uniform coating. This composite anode delivered stable voltage hysteresis over 600 h at a current density of 3 mA cm^{-2}.

All the aforesaid approaches require complex preparation processes. In order to simplify the synthesis process, Go et al. made carbon cloth more affinity between lithium and carbon

by a facile heat treatment in air (Go et al., 2019). Numerous nanocrevasses can be introduced in carbon cloth during the heat treatment, allowing the successful infusion of molten lithium. As a result, the as-prepared composite anode with lower local current density presents long-term cycling and dendrite-free morphology.

Carbon-Based Materials as Additive

Liquid organic electrolytes play a vital role in LIBs, due to their good wettability with electrode and ionic conductivity. However, the side reaction between lithium metal and electrolyte has negative affect on the electrochemical performance of lithium metal anode. The liquid electrolyte is composed of solvent, lithium salt and additives, which determine the uniformity and stability of SEI film. Therefore, modifying the additives can improve the performance of the electrolyte, then changing the deposition morphology of lithium (Tao et al., 2017; Wang et al., 2020).

In general, soluble Li-containing compounds and organic compounds, such as $LiNO_3$ (Yan et al., 2018), LiF (Wang et al., 2019) and fluoroethylene carbonate (FEC) (Zhang R. et al., 2017), are commonly employed as additives. These additives are generally used as sacrifices to react with lithium metal in advance, forming a SEI film with controllable composition and good stability. On the contrary, when the carbon-based material is used as additive, it serves as the initial nucleation site for Li deposition instead of reacting with Li. Nanodiamond with a size of $\sim$ 5 nm and high crystallinity is an early member of the carbon-based material family (Cheng et al., 2017). The nanodiamond particles treated by octadecylamine (ODA) can be well-dispersed in the ester-based electrolyte. In Li||Cu half-cell batteries, due to the nanodiamonds inherit large surface area and strong binding energy with Li, the Li^+ can adsorb on the surface as the initial heterogeneous seeds instead of growing on the copper current collector. Moreover, nanodiamond-guided Li deposits are small enough to form a uniform distribution of deposition. When charging, the co-deposits of nanodiamond and Li can be stripped into the electrolyte to maintain a stable content of nanodiamond in the electrolyte, improving the cycling stability of the Li anode. Whereas, the nanodiamonds tend to aggregate and form clusters easily, which is negatively affect the long-term cycle.

With the development of technology, more and more new materials are recognized and applied in various fields. Graphene quantum dots (GQDs) with tiny size can be well-dispersed in the electrolyte without further modification (Deng et al., 2016; Park et al., 2016; Tam et al., 2019). Hu et al. directly added GQDs to the electrolyte, which is composed of Li bis (trifluoromethane)-sulfonimide (LiTFSI, 1.0 M), 2.0 wt% $LiNO_3$, 1,3-dioxolane (DOL) and 1,2-dimethoxyethane (DME; 1:1 by volume) (Hu Y. et al., 2020). Due to the quantum confinement effect (Zhang W. et al., 2018), GQDs act as the heterogeneous seeds enable continuously adjust ion dispersion and avoid high local electric field in the subsequent plating process, which is conducive to the uniform deposition and inhibit the dendrite growth (**Figure 2B**). However, the complex synthesis procedures and extreme conditions of GQDs leads to high costs, which limits its large-scale application.

Carbon-Based Materials as Current Collect

The current collector is one of the important components of LIBs. It is commonly used as a substrate to support active materials. During battery operation, the current collector not only transfer electrons between the active material and the external circuit, but also diffuse the heat generated inside the battery (Jin et al., 2018; Zhang Z. et al., 2018b). Generally, planar copper foil is used as anode current collector, while it is easy to cause severe dendrite formation. Due to the porosity, low cost, good electronic conductivity and confinement of 3D current collectors, they have attracted great attention from researchers. 3D metallic materials, such as copper foam, nickel foam and aluminum foam, with good electronic conductivity and high specific surface area have been regarded as the most competitive candidates. However, the nucleation overpotential of lithium deposited on the 3D metal structure is relatively higher than other current collectors, causing uneven nucleation and inhomogeneous lithium deposition. Carbon-based materials have good lithium affinity, and composite with metal materials can effectively improve battery performance. When N-doped graphene combined with 3D metal materials, an improving LMBs performance can be achieved. Zhang et al. prepared a 3D porous copper coated with N-doped graphene via a CVD process (**Figure 2C**) (Zhang R. et al., 2018b). Due to the presence of pyridinic and pyrrolic nitrogen, there is a strong interaction between N-doped graphene and Li^+, leading to homogeneous Li^+ flux and a uniform Li deposition.

The morphology of carbon-based material is critical to control the lithium loading and deposition location. The 3D carbon-based materials with random sponge-like structure lead to Li^+ preferentially deposit on the outer surface of the 3D framework. To solve this problem, a sequence of materials with regular structures have been investigated. A 3D construction is fabricated by vertically arranged nanofibers (VACNFs) directly grown on a planar copper foil. When it acts as a host for the lithium metal anode (Chen Y. et al., 2019), the special structure of VACNFs not only provides well-aligned brush-like space for Li^+ deposition, but also enhances the surface electrochemical activity because of the active graphitic edge sites. Therefore, this composite material can effectively decrease the local current density, suppress the lithium dendrite growth and result in dendrite-free Li deposits.

Although the 3D metal structure exhibits excellent performance as a current collector, the defects, such as high density and easy erosion, cannot meet the requirements of high-performance storage systems. Compared with active materials, the density of metal current collectors is generally higher, resulting in a low mass proportion of active materials in the entire electrode, which inhibits the improvement of the energy density of the entire battery (Zhou et al., 2018). During the repeated charge/discharge process, the metal current collector electrochemically eroded, resulting in a short cycle life. Carbon-based materials with light weight and good chemical stability can avoid the aforementioned problems encountered by metal current collectors. Among carbon-based materials, carbon

nanotubes (CNTs) are highly conductive and commercially available, and as an electrode behaving good lithium storage capacity (Che et al., 1998). Yang et al. used the commercial CNTs sponge as a current collector, which has high specific surface area and graphitic-amorphous carbon composite feature (Yang G. et al., 2019). In the initial stage of electroplating, the lithium-storage of the CNTs (above 0 V) makes it a "pre-lithiated" host, enhancing its wettability with subsequent lithium deposits (below 0 V) and lowering the lithium nucleation overpotential. More importantly, the high surface area of the porous CNTs sponge enable the increased density of lithium nucleation sites and reduced local current density on the carbon nanotubes as well as uniform lithium deposition.

CONCLUSIONS

In recent decades, researchers have been committed to developing more strategies to meet the safety and high energy storage requirements of lithium metal anodes. Carbon-based materials with various structures and unique chemical properties play a significant role in minimizing the shortcomings of lithium metal anodes. This review outlines the challenges of lithium metal anodes and the diverse strategies of carbon-based materials in advanced LMBs.

The diversity of carbon-based materials makes it play a specific role in different strategies to solve the safety issues of lithium metal anodes. Nanodiamonds and GQDs with a size of several nanometers can be used as electrolyte additives to form initial nucleation sites, guiding the uniform deposition of Li^+ on the electrode surface. As the size of the carbon-based material increases, it has greater flexibility, higher porosity and a larger surface area, which helps it be modified or composited with other materials. The abundant functional groups on the surface of the carbon-based material enable it combine with other metal oxides or as a coating material for other 3D porous frameworks. The 3D porous scaffolds composite constructed with lithiophilic materials can be used as a current collector for Li^+ deposition and be assembled with lithium metal to form a composite electrode. Therefore, the 3D porous scaffolds can effectively overcome the "hostless" problem of lithium metal, accommodate huge electrode volume changes during electrochemical process, as well as contribute to a stable cycle life.

On account of the special structural and morphological features, carbon-based materials are also widely used in other research fields. Carbon-based materials can not only be employed as the electrode materials for LIBs and supercapacitors, but also act as the metal-free electrocatalysts for oxygen reduction reaction, oxygen evolution reaction, and hydrogen evolution reaction, because of its large specific surface area, defective sites, as well as tunable electronic structure.

Carbon-based materials with low price, abundant nature reserves, versatile structure easy fabrication, have a significant impact in the field of electrocatalysis and energy storage, especially for large-scale high-energy-density batteries. It is believed that the development of carbon-based materials plays a significant role in the commercial application of LMBs.

AUTHOR CONTRIBUTIONS

All authors listed have made a substantial, direct and intellectual contribution to the work, and approved it for publication.

FUNDING

This project was financially supported by the Australian Research Council (ARC) through the ARC Discovery project (DP180102297) and Future Fellowship (FT180100705). HG and HL thank the Open Project of State Key Laboratory of Advanced Special Steel, Shanghai Key Laboratory of Advanced Ferrometallurgy and the Science and Technology Commission of Shanghai Municipality (No. 19DZ2270200). HG appreciates the support from the China Postdoctoral Science Foundation Funded Project (2019M661464). All authors thank the support from Joint International Laboratory on Environmental and Energy Frontier Materials and Innovation Research Team of High–Level Local Universities in Shanghai.

REFERENCES

Aldalur, I., Martinez-Ibanez, M., Piszcz, M., Zhang, H., and Armanda, M. (2018). Self-standing highly conductive solid electrolytes based on block copolymers for rechargeable all-solid-state lithium-metal batteries. *Batteries Supercaps* 1, 149–159. doi: 10.1002/batt.201800048

Chazalviel, J. (1990). Electrochemical aspects of the generation of ramified metallic electrodeposits. *Phys. Rev. A* 42, 7355–7367. doi: 10.1103/physreva.42.7355

Che, G., Lakshmi, B. B., Fisher, E. R., and Martin, C. R. (1998). Carbon nanotubule membranes for electrochemical energy storage and production. *Nature* 393, 346–349. doi: 10.1038/30694

Chen, C., Ma, Y., and Wang, C. (2019). Investigation of electrochemical performance of montmorillonite clay as Li-ion battery electrode. *Sustain. Mater. Techno.* 19:e00086. doi: 10.1016/j.susmat.2018.e00086

Chen, Y., Elangovan, A., Zeng, D., Zhang, Y., Ke, H., Li, J., et al. (2019). Vertically aligned carbon nanofibers on Cu foil as a 3D current collector for reversible Li plating/stripping toward high-performance Li-S batteries. *Adv. Funct. Mater.* 30:1906444. doi: 10.1002/adfm.201906444

Cheng, X. B., Zhao, M. Q., Chen, C., Pentecost, A., Maleski, K., Mathis, T., et al. (2017). Nanodiamonds suppress the growth of lithium dendrites. *Nat. Commun.* 8:336. doi: 10.1038/s41467-017-00519-2

Deng, G., Chao, D. L., Guo, Y. W., Chen, Z., Wang, H. H., Savilov, S. V., et al. (2016). Graphene quantum dots-shielded $Na_3(VO)_2(PO_4)_2F$@C nanocuboids as robust cathode for Na-ion battery. *Energy Storage Materials* 5, 198–204. doi: 10.1016/j.ensm.2016.07.007

Gan, B. L., Tang, K. K., Chen, Y. L., Wang, D. D., Wang, N., Li, W. X., et al. (2020). Concrete-like high sulfur content cathodes with enhanced electrochemical performance for lithium-sulfur batteries. *J. Energy Chem.* 42, 174–179. doi: 10.1016/j.jechem.2019.06.003

Ge, P., Hou, H. S., Li, S. J., Yang, L., and Ji, X. B. (2018). Tailoring rod-like $FeSe_2$ coated with nitrogen-doped carbon for high-performance sodium storage. *Adv. Funct. Mater.* 28:1801765. doi: 10.1002/adfm.201801765

Girard, G. M. A., Wang, X., Yunis, R., MacFarlane, D. R., Bhattacharyya, A. J., Forsyth, M., et al. (2019). Sustainable, dendrite free lithium-metal electrode cycling achieved with polymer composite electrolytes based on a poly(ionic liquid) host. *Batteries Supercaps* 2, 229–239. doi: 10.1002/batt.201800120

Go, W., Kim, M. H., Park, J., Lim, C. H., Joo, S. H., Kim, Y., et al. (2019). Nanocrevasse-rich carbon fibers for stable lithium and sodium metal anodes. *Nano Lett.* 19, 1504–1511. doi: 10.1021/acs.nanolett.8b04106

Guo, X., Zhang, W. X., Zhang, J. Q., Zhou, D., Tang, X., Xu, X. F., et al. (2020). Boosting sodium storage in two-dimensional phosphorene/$Ti_3C_2T_x$ MXene nanoarchitectures with stable fluorinated interphase. *ACS Nano* 14, 3651–3659. doi: 10.1021/acsnano.0c00177

Hapuarachchi, S. N. S., Nerkar, J. Y., Wasalathilake, K. C., Chen, H., Zhang, S., O'Mullane, A. P., et al. (2018). Utilizing room temperature liquid metals for mechanically robust silicon anodes in lithium-ion batteries. *Batteries Supercaps* 1, 122–128. doi: 10.1002/batt.201800047

Hong, Y. S., Zhao, C. Z., Xiao, Y., Xu, R., Xu, J. J., Huang, J. Q., et al. (2019). Safe lithium-metal anodes for Li-O_2 batteries: From fundamental chemistry to advanced characterization and effective protection. *Batteries Supercaps* 2, 638–658. doi: 10.1002/batt.201900031

Hu, Z., Li, G., Wang, A., Luo, J., and Liu, X. (2020). Recent progress of electrolyte design for lithium metal batteries. *Batteries Supercaps* 3, 331–335. doi: 10.1002/batt.201900191

Hu, Y., Chen, W., Lei, T. Y., Jiao, Y., Wang, H. B., Wang, X. P., et al. (2020). Graphene quantum dots as the nucleation sites and interfacial regulator to suppress lithium dendrites for high-loading lithium-sulfur battery. *Nano Energy* 68:104373. doi: 10.1016/j.nanoen.2019.104373

Huang, X., Feng, X., Zhang, B., Zhang, L., Zhang, S., Gao, B., et al. (2019). Lithiated $NiCo_2O_4$ nanorods anchored on 3D nickel foam enable homogeneous Li plating/stripping for high-power dendrite-free lithium metal anode. *ACS Appl. Mater. Inter.* 11, 31824–31831. doi: 10.1021/acsami.9b08438

Huang, Y., Chen, B., Duan, J., Yang, F., Wang, T., Wang, Z., et al. (2020). Graphitic carbon nitride (g-C_3N_4): An interface enabler for solid-state lithium metal batteries. *Angew. Chem. Int. Ed.* 59, 3699–3704. doi: 10.1002/anie.201914417

Huang, Z., Ren, J., Zhang, W., Xie, M., Li, Y., Sun, D., et al. (2018). Protecting the Li-metal anode in a Li-O_2 battery by using boric acid as an SEI-forming additive. *Adv. Mater.* 30:e1803270. doi: 10.1002/adma.201803270

Huang, K., Li, Z., Xu, Q. J., Liu, H. M., Li, H. X., and Wang, Y. G. (2019). Lithiophilic CuO nanoflowers on Ti-mesh inducing lithium lateral plating enabling stable lithium-metal anodes with ultrahigh rates and ultralong cycle life. *Adv. Energy Mater.* 9:1900853. doi: 10.1002/aenm.201900853

Huo, H., Li, X., Sun, Y., Lin, X., Doyle-Davis, K., Liang, J., et al. (2020). Li_2CO_3 effects: New insights into polymer/garnet electrolytes for dendrite-free solid lithium batteries. *Nano Energy* 73:104836. doi: 10.1016/j.nanoen.2020.104836

Jeong, J., Chun, J., Lim, W. G., Kim, W., Jo, C., and Lee, J. (2020). Mesoporous carbon host material for stable lithium metal anode. *Nanoscale* 12, 11818–11824. doi: 10.1039/d0nr02258f

Jin, S., Jiang, Y., Ji, H., and Yu, Y. (2018). Advanced 3D current collectors for lithium-based batteries. *Adv. Mater.* 30:e1802014. doi: 10.1002/adma.201802014

Jorge, A. B., Jervis, R., Periasamy, A. P., Qiao, M., Feng, J., Tran, L. N., et al. (2019). 3D carbon materials for efficient oxygen and hydrogen electrocatalysis. *Adv. Energy Mater.* 10:1902494. doi: 10.1002/aenm.201902494

Lee, J. I., Song, G., Cho, S., Han, D. Y., and Park, S. (2020). Lithium metal interface modification for high-energy batteries: approaches and characterization. *Batter. Supercaps.* 3, 828–859. doi: 10.1002/batt.202000016

Li, C., Liu, S., Shi, C., Liang, G., Lu, Z., Fu, R., et al. (2019). Two-dimensional molecular brush-functionalized porous bilayer composite separators toward ultrastable high-current density lithium metal anodes. *Nat. Commun.* 10:1363. doi: 10.1038/s41467-019-09211-z

Li, W. T., Zhang, Y. F., Li, H., Chen, Z. J., Shang, T. X., Wu, Z. T., et al. (2020). Layered MXene protected lithium metal anode as an efficient polysulfide blocker for lithium-sulfur batteries. *Batteries Supercaps* 3, 892–899. doi: 10.1002/batt.202000062

Li, X., Zheng, J. M., Ren, X. D., Engelhard, M. H., Zhao, W. G., Li, Q. Y., et al. (2018). Dendrite-free and performance-enhanced lithium metal batteries through optimizing solvent compositions and adding combinational additives. *Adv. Energy Mater.* 8:1703022. doi: 10.1002/aenm.201703022

Li, K., Hu, Z., Ma, J., Chen, S., Mu, D., and Zhang, J. (2019). A 3D and stable lithium anode for high-performance lithium-iodine batteries. *Adv. Mater.* 31:e1902399. doi: 10.1002/adma.201902399

Li, Q., Pan, H., Li, W., Wang, Y., Wang, J., Zheng, J., et al. (2018). Homogeneous interface conductivity for lithium dendrite-free anode. *ACS Energy Lett.* 3, 2259–2266. doi: 10.1021/acsenergylett.8b01244

Li, S. Y., Liu, Q. L., Zhou, J. J., Pan, T., Gao, L. N., Zhang, W. D., et al. (2019). Hierarchical Co_3O_4 nanofiber-carbon sheet skeleton with superior Na/Li-philic property enabling highly stable alkali metal batteries. *Adv. Funct. Mater.* 29:1808847. doi: 10.1002/adfm.201808847

Li, Z., Xu, N., Sha, Y., Ji, J., Liu, T., Yan, L., et al. (2020). Chitosan oligosaccharide derived polar host for lithium deposition in lithium metal batteries. *Sustain. Mater. Techno.* 24:e00158. doi: 10.1016/j.susmat.2020.e00158

Liang, Z., Lin, D., Zhao, J., Lu, Z., Liu, Y., Liu, C., et al. (2016). Composite lithium metal anode by melt infusion of lithium into a 3D conducting scaffold with lithiophilic coating. *Proc. Natl. Acad. Sci. U.S.A.* 113, 2862–2867. doi: 10.1073/pnas.1518188113

Liu, B., Wen, J., Chen, H., Yang, M., Liu, Y., and Li, H. (2020). O/N Co-doped, layered porous carbon with mesoporosity up to 99% for ultrahigh-rate capability supercapacitors. *Batteries Supercaps*. doi: 10.1002/batt.202000037

Liu, H., Liu, X. X., Li, W., Guo, X., Wang, Y., Wang, G. X., et al. (2017). Porous carbon composites for next generation rechargeable lithium batteries. *Adv. Energy Mater.* 7:1700283. doi: 10.1002/aenm.201700283

Ma, J., Gao, L., Li, S., Zeng, Z., Zhang, L., and Xie, J. (2020). Dual play of chitin-derived N-doped carbon nanosheets enabling high-performance Na-SeS_2 half/full cells. *Batteries Supercaps* 3, 165–173. doi: 10.1002/batt.201900159

Maroufi, S., Assefi, M., Nekouei, R. K., and Sahajwalla, V. (2020). Recovery of lithium and cobalt from waste lithium-ion batteries through a selective isolation-suspension approach. *Sustain. Mater. Techno.* 23:e00139. doi: 10.1016/j.susmat.2019.e00139

Nan, J. X., Guo, X., Xiao, J., Li, X., Chen, W. H., Wu, W. H., et al. (2019). Nanoengineering of 2D MXene-based materials for energy storage applications. *Small* e1902085. doi: 10.1002/smll.201902085

Pan, J., Tian, X. L., Zaman, S., Dong, Z., Liu, H., Park, H. S., et al. (2019). Recent progress on transition metal oxides as bifunctional catalysts for lithium-air and zinc-air batteries. *Batteries Supercaps* 2, 336–347. doi: 10.1002/batt.201800082

Pan, L., Wang, J., Luo, Z., Zhao, Z., Li, Y., Egun, I., et al. (2020). 3D periodic ion transport channel to suppress top deposition toward stable lithium metal anode. *Batteries Supercaps* 3, 773–779. doi: 10.1002/batt.202000001

Park, J., Moon, J., Kim, C., Kang, J. H., Lim, E., Park, J., et al. (2016). Graphene quantum dots: structural integrity and oxygen functional groups for high sulfur/sulfide utilization in lithium sulfur batteries. *Npg Asia Mater.* 8:e272. doi: 10.1038/am.2016.61

Pei, F., Fu, A., Ye, W., Peng, J., Fang, X., Wang, M. S., et al. (2019). Robust lithium metal anodes realized by lithiophilic 3D porous current collectors for constructing high-energy lithium-sulfur batteries. *ACS Nano* 13, 8337–8346. doi: 10.1021/acsnano.9b03784

Pellow, M. A., Ambrose, H., Mulvaney, D., Betita, R., and Shaw, S. (2020). Research gaps in environmental life cycle assessments of lithium ion batteries for grid-scale stationary energy storage systems: end-of-life options and other issues. *Sustain. Mater. Techno.* 23:e00120. doi: 10.1016/j.susmat.2019.e00120

Shi, Q. X., Guan, X., Pei, H. J., Chang, C., Qu, H., Xie, X. L., et al. (2020). Functional covalent triazine frameworks-based quasi-solid-state electrolyte used to enhance lithium metal battery safety. *Batteries Supercaps* 3, 936–945. doi: 10.1002/batt.202000069

Sloop, S. E., Crandon, L., Allen, M., Lerner, M. M., Zhang, H., Sirisaksoontorn, W., et al. (2019). Cathode healing methods for recycling of lithium-ion batteries. *Sustain. Mater. Techno.* 22:e00113. doi: 10.1016/j.susmat.2019.e00113

Sun, C., Li, Y., Jin, J., Yang, J., and Wen, Z. (2019). ZnO nanoarray-modified nickel foam as a lithiophilic skeleton to regulate lithium deposition for lithium-metal batteries. *J. Mater. Chem. A* 7, 7752–7759. doi: 10.1039/c9ta00862d

Tam, T. V., Kang, S. G., Kim, M. H., Lee, S. G., Hur, S. H., Chung, J. S., et al. (2019). Novel graphene hydrogel/B-doped graphene quantum dots composites as trifunctional electrocatalysts for Zn-Air batteries and overall water splitting. *Adv. Energy Mater.* 9:900945. doi: 10.1002/aenm.201900945

Tang, X., Zhou, D., Li, P., Guo, X., Sun, B., Liu, H., et al. (2020). MXene-based dendrite-free potassium metal batteries. *Adv. Mater.* 32:e1906739. doi: 10.1002/adma.201906739

Tao, L., Hu, A. Y., Yang, Z. J., Xu, Z. R., Wall, C. E., Esker, A. R., et al. (2020). A surface chemistry approach to tailoring the hydrophilicity and lithiophilicity of

carbon films for hosting high-performance lithium metal anodes. *Adv. Funct. Mater.* 30:2000585. doi: 10.1002/adfm.202000585

Tao, R., Bi, X. X., Li, S., Yao, Y., Wu, F., Wang, Q., et al. (2017). Kinetics Tuning the electrochemistry of lithium dendrites formation in lithium batteries through electrolytes. *ACS Appl. Mater. Inter.* 9, 7003–7008. doi: 10.1021/acsami.6b13859

Tian, H., Zhang, C., Su, P. P., Shen, Z. F., Liu, H., Wang, G. X., et al. (2020). Metal-organic-framework-derived formation of Co-N-doped carbon materials for efficient oxygen reduction reaction. *J. Energy Chem.* 40, 137–143. doi: 10.1016/j.jechem.2019.03.004

Wang, J., Huang, G., and Zhang, X. B. (2020). Interface between lithium metal and garnet electrolyte: Recent progress and perspective. *Batteries Supercaps*. doi: 10.1002/batt.202000082

Wang, M. Q., Peng, Z., Luo, W. W., Ren, F. H., Li, Z. D., Zhang, Q., et al. (2019). Tailoring lithium deposition via an SEI-functionalized membrane derived from LiF decorated layered carbon structure. *Adv. Energy Mater.* 9:1802912. doi: 10.1002/aenm.201802912

Wang, S. H., Yin, Y. X., Zuo, T. T., Dong, W., Li, J. Y., Shi, J. L., et al. (2017). Stable Li metal anodes via regulating lithium plating/stripping in vertically aligned microchannels. *Adv. Mater.* 29:1703729. doi: 10.1002/adma.201703729

Wei, X. J., Zhang, Y. B., Zhang, B. K., Lin, Z., Wang, X. P., Hu, P., et al. (2019). Yolk-shell-structured zinc-cobalt binary metal sulfide@N-doped carbon for enhanced lithium-ion storage. *Nano Energy* 64:103899. doi: 10.1016/j.nanoen.2019.103899

Widijatmoko, S. D., Gu, F., Wang, Z., and Hall, P. (2020). Selective liberation in dry milled spent lithium-ion batteries. *Sustain. Mater. Techno.* 23:e00134. doi: 10.1016/j.susmat.2019.e00134

Wu, S., Zhang, Z., Lan, M., Yang, S., Cheng, J., Cai, J., et al. (2018). Lithiophilic Cu-CuO-Ni hybrid structure: Advanced current collectors toward stable lithium metal anodes. *Adv. Mater.* 30:1705830. doi: 10.1002/adma.201705830

Xiao, J., Zhang, F., Tang, K., Li, X., Wang, D., Wang, Y., et al. (2019). Rational design of a P2-type spherical layered oxide cathode for high-performance sodium-ion batteries. *ACS Cent. Sci.* 5, 1937–1945. doi: 10.1021/acscentsci.9b00982

Xie, J., Li, B. Q., Song, Y. W., Peng, H. J., and Zhang, Q. (2019). A supramolecular electrolyte for lithium-metal batteries. *Batteries Supercaps* 3, 47–51. doi: 10.1002/batt.201900112

Xue, P., Sun, C., Li, H., Liang, J., and Lai, C. (2019). Superlithiophilic amorphous SiO_2-TiO_2 distributed into porous carbon skeleton enabling uniform lithium deposition for stable lithium metal batteries. *Adv. Sci.* 6:1900943. doi: 10.1002/advs.201900943

Yan, C., Yao, Y. X., Chen, X., Cheng, X. B., Zhang, X. Q., Huang, J. Q., et al. (2018). Lithium nitrate solvation chemistry in carbonate electrolyte sustains high-voltage lithium metal batteries. *Angew. Chem. Int. Ed.* 57, 14055–14059. doi: 10.1002/anie.201807034

Yan, J., Dong, K., Zhang, Y., Wang, X., Aboalhassan, A. A., Yu, J., et al. (2019). Multifunctional flexible membranes from sponge-like porous carbon nanofibers with high conductivity. *Nat. Commun.* 10:5584. doi: 10.1038/s41467-019-13430-9

Yan, J., Liu, F., Hu, Z., Gao, J., Zhou, W., Huo, H., et al. (2020). Realizing dendrite-free lithium deposition with a composite separator. *Nano Lett.* 20, 3798–3807. doi: 10.1021/acs.nanolett.0c00819

Yang, G., Chen, J., Xiao, P., Agboola, P. O., Shakir, I., and Xu, Y. (2018). Graphene anchored on Cu foam as a lithiophilic 3D current collector for a stable and dendrite-free lithium metal anode. *J. Mater. Chem. A* 6, 9899–9905. doi: 10.1039/c8ta02810a

Yang, G., Li, Y., Tong, Y., Qiu, J., Liu, S., Zhang, S., et al. (2019). Lithium plating and stripping on carbon nanotube sponge. *Nano Lett.* 19, 494–499. doi: 10.1021/acs.nanolett.8b04376

Yang, T., Liu, Y. G., Yang, D. X., Deng, B. B., Huang, Z. H., Ling, C. D., et al. (2019). Bimetallic metal-organic frameworks derived Ni-Co-Se@C hierarchical bundle-like nanostructures with high-rate pseudocapacitive lithium ion storage. *Energy Storage Mater.* 17, 374–384. doi: 10.1016/j.ensm.2018.05.024

Ye, H., Zhang, Y., Yin, Y. X., Cao, F. F., and Guo, Y. G. (2020). An outlook on low-volume-change lithium metal anodes for long-life batteries. *ACS Cent. Sci.* 6, 661–671. doi: 10.1021/acscentsci.0c00351

Yue, X. Y., Bao, J., Yang, S. Y., Luo, R. J., Wang, Q. C., Wu, X. J., et al. (2020). Petaloid-shaped ZnO coated carbon felt as a controllable host to construct hierarchical Li composite anode. *Nano Energy* 71:104614. doi: 10.1016/j.nanoen.2020.104614

Yue, X. Y., Wang, W. W., Wang, Q. C., Meng, J. K., Wang, X. X., Song, Y., et al. (2019b). Cuprite-coated Cu foam skeleton host enabling lateral growth of lithium dendrites for advanced Li metal batteries. *Energy Storage Mater.* 21, 180–189. doi: 10.1016/j.ensm.2018.12.007

Yue, X. Y., Li, X. L., Wang, W. W., Chen, D., Qiu, Q. Q., Wang, Q. C., et al. (2019a). Wettable carbon felt framework for high loading Li-metal composite anode. *Nano Energy* 60, 257–266. doi: 10.1016/j.nanoen.2019.03.057

Zhang, Q., Liu, S., Lin, Z., Wang, K., Chen, M., Xu, K., et al. (2020). Highly safe and cyclable Li-metal batteries with vinylethylene carbonate electrolyte. *Nano Energy* 74:104860. doi: 10.1016/j.nanoen.2020.104860

Zhang, R., Li, N. W., Cheng, X. B., Yin, Y. X., Zhang, Q., and Guo, Y. G. (2017). Advanced micro/nanostructures for lithium metal anodes. *Adv. Sci.* 4:1600445. doi: 10.1002/advs.201600445

Zhang, T., Han, S., Guo, W., Hou, F., Liu, J., Yan, X., et al. (2019). Continuous carbon nanotube composite fibers for flexible aqueous lithium-ion batteries. *Sustain. Mater. Techno.* 20:e00096. doi: 10.1016/j.susmat.2019.e00096

Zhang, X. Q., Cheng, X. B., Chen, X., Yan, C., and Zhang, Q. (2017). Fluoroethylene carbonate additives to render uniform Li deposits in lithium metal batteries. *Adv. Funct. Mater.* 27:1605989. doi: 10.1002/adfm.201605989

Zhang, Z., Sun, J., Wang, F., and Dai, L. (2018a). Efficient oxygen reduction reaction (ORR) catalysts based on single iron atoms dispersed on a hierarchically structured porous carbon framework. *Angew. Chem. Int. Ed.* 57, 9038–9043. doi: 10.1002/anie.201804958

Zhang, C., Lv, W., Zhou, G. M., Huang, Z. J., Zhang, Y. B., Lyu, R. Y., et al. (2018). Vertically aligned lithiophilic CuO nanosheets on a Cu collector to stabilize lithium deposition for lithium metal batteries. *Adv. Energy Mater.* 8:1703404. doi: 10.1002/aenm.201703404

Zhang, D. M., Chen, Z. W., Bai, J., Yang, C. C., and Jiang, Q. (2020). Highly nitrogen-doped porous carbon nanosheets as high-performance anode for potassium-ion batteries. *Batteries Supercaps* 3, 185–193. doi: 10.1002/batt.201900144

Zhang, R., Chen, X., Shen, X., Zhang, X. Q., Chen, X. R., Cheng, X. B., et al. (2018a). Coralloid carbon fiber-based composite lithium anode for robust lithium metal batteries. *Joule* 2, 764–777. doi: 10.1016/j.joule.2018.02.001

Zhang, R., Wen, S. W., Wang, N., Qin, K. Q., Liu, E. Z., Shi, C. S., et al. (2018b). N-doped graphene modified 3D porous Cu current collector toward microscale homogeneous Li deposition for Li metal anodes. *Adv. Energy Mater.* 8:1800914. doi: 10.1002/aenm.201800914

Zhang, S. J., You, J. H., Chen, J. D., Hu, Y. Y., Wang, C. W., Liu, Q., et al. (2019). Aluminum-based metal-organic frameworks derived Al_2O_3-loading mesoporous carbon as a host matrix for lithium-metal anodes. *ACS Appl. Mater. Inter.* 11, 47939–47947. doi: 10.1021/acsami.9b16363

Zhang, W., Fu, Y., Liu, W., Lim, L., Wang, X., and Yu, A. (2019). A general approach for fabricating 3D MFe_2O_4 (M = Mn, Ni, Cu, Co)/graphitic carbon nitride covalently functionalized nitrogen-doped graphene nanocomposites as advanced anodes for lithium-ion batteries. *Nano Energy* 57, 48–56. doi: 10.1016/j.nanoen.2018.12.005

Zhang, W., Xu, T., Liu, Z., Wu, N. L., and Wei, M. (2018). Hierarchical TiO_{2-x} imbedded with graphene quantum dots for high-performance lithium storage. *Chem. Commun.* 54, 1413–1416. doi: 10.1039/C7CC09406J

Zhang, X., Fan, Y., Khan, M. A., Zhao, H., Ye, D., Wang, J., et al. (2020). Co-Ni binary-metal oxide coated with porous carbon derived from metal-organic framework as host of nano-sulfur for lithium-sulfur batteries. *Batteries Supercaps* 3, 108–116. doi: 10.1002/batt.201900121

Zhang, Y., Shi, Y., Hu, X. C., Wang, W. P., Wen, R., Xin, S., et al. (2019). A 3D lithium/carbon fiber anode with sustained electrolyte contact for solid-state batteries. *Adv. Energy Mater.* 10:1903325. doi: 10.1002/aenm.201903325

Zhang, Y., Wang, C. W., Pastel, G., Kuang, Y. D., Xie, H., Li, Y. J., et al. (2018). 3D wettable framework for dendrite-free alkali metal anodes. *Adv. Energy Mater.* 8:1800635. doi: 10.1002/aenm.201800635

Zhang, Z., Wang, Z. L., and Lu, X. (2018b). Multishelled Si@Cu microparticles supported on 3D Cu current collectors for stable and binder-free anodes of lithium-ion batteries. *ACS Nano* 12, 3587–3599. doi: 10.1021/acsnano.8b00703

Zhao, F., Zhou, X. F., Deng, W., and Liu, Z. P. (2019). Entrapping lithium deposition in lithiophilic reservoir constructed by vertically aligned ZnO nanosheets for dendrite-free Li metal anodes. *Nano Energy* 62, 55–63. doi: 10.1016/j.nanoen.2019.04.087

Zhou, T., Shen, J. D., Wang, Z. S., Liu, J., Hu, R. Z., Ouyang, L. Z., et al. (2020). Regulating lithium nucleation and deposition via MOF-derived Co@C-modified carbon cloth for stable Li metal anode. *Adv. Funct. Mater.* 30, 1909159. doi: 10.1002/adfm.201909159

Zhou, Y., Doerrer, C., Kasemchainan, J., Bruce, P. G., Pasta, M., and Hardwick, L. J. (2020). Observation of interfacial degradation of Li_6PS_5Cl against lithium metal and $LiCoO_2$ via in situ electrochemical raman microscopy. *Batteries Supercaps* 3, 647–652. doi: 10.1002/batt.201900218

Zhou, Z. L., Li, N., Yang, Y. Z., Chen, H. S., Jiao, S. Q., Song, W. L., et al. (2018). Ultra-lightweight 3D carbon current collectors: constructing all-carbon electrodes for stable and high energy density dual-ion batteries. *Adv. Energy Mater.* 8:1801439. doi: 10.1002/aenm.201801439

Zhu, J. G., Li, P. K., Chen, X., Legut, D., Fan, Y. C., Zhang, R. F., et al. (2019). Rational design of graphitic-inorganic Bi-layer artificial SEI for stable lithium metal anode. *Energy Storage Mater.* 16, 426–433. doi: 10.1016/j.ensm.2018.06.023

Zuo, T. T., Yin, Y. X., Wang, S. H., Wang, P. F., Yang, X., Liu, J., et al. (2018). Trapping lithium into hollow silica microspheres with a carbon nanotube core for dendrite-free lithium metal anodes. *Nano Lett.* 18, 297–301. doi: 10.1021/acs.nanolett.7b04136

Conflict of Interest: The authors declare that the research was conducted in the absence of any commercial or financial relationships that could be construed as a potential conflict of interest.

Copyright © 2020 Tang, Xiao, Li, Wang, Long, Chen, Gao, Chen, Liu and Liu. This is an open-access article distributed under the terms of the Creative Commons Attribution License (CC BY). The use, distribution or reproduction in other forums is permitted, provided the original author(s) and the copyright owner(s) are credited and that the original publication in this journal is cited, in accordance with accepted academic practice. No use, distribution or reproduction is permitted which does not comply with these terms.

frontiers in Chemistry

ORIGINAL RESEARCH
published: 04 November 2020
doi: 10.3389/fchem.2020.604239

Two-Dimensional Metal Organic Framework Nanosheets as Bifunctional Catalyst for Electrochemical and Photoelectrochemical Water Oxidation

Chang Liu[1†], Xiaochen Shen[2†], Grayson Johnson[1], Yulu Zhang[1], Changlin Zhang[2], Jiafu Chen[2], Lingyan Li[2], Colton Sheehan[1], Zhenmeng Peng[2] and Sen Zhang[1*]*

[1] Department of Chemistry, University of Virginia, Charlottesville, VA, United States, [2] Department of Chemical and Biomolecular Engineering, University of Akron, Akron, OH, United States

OPEN ACCESS

Edited by:
Jie He,
University of Connecticut,
United States

Reviewed by:
Min-Rui Gao,
University of Science and Technology of China, China
Ben Liu,
Nanjing Normal University, China

***Correspondence:**
Zhenmeng Peng
zpeng@uakron.edu
Sen Zhang
sz3t@virginia.edu

† These authors have contributed equally to this work

Specialty section:
This article was submitted to Catalysis and Photocatalysis, a section of the journal Frontiers in Chemistry

Received: 09 September 2020
Accepted: 30 September 2020
Published: 04 November 2020

Citation:
Liu C, Shen X, Johnson G, Zhang Y, Zhang C, Chen J, Li L, Sheehan C, Peng Z and Zhang S (2020) Two-Dimensional Metal Organic Framework Nanosheets as Bifunctional Catalyst for Electrochemical and Photoelectrochemical Water Oxidation. Front. Chem. 8:604239. doi: 10.3389/fchem.2020.604239

Electrochemical (EC) and photoelectrochemical (PEC) water splitting represent promising strategies for renewable energy conversion and fuel production and require design of efficient catalysts for the oxygen evolution reaction (OER). Herein, we report the synthesis of two-dimensional (2D) Co-based metal organic framework (Co-MOF) nanosheets and their bifunctional catalytic properties for both EC and PEC OER. Benefiting from the large surface area and abundant isolated metal active sites, the Co-MOF nanosheets exhibited excellent OER activity and stability. The efficient electron–hole generation and separation of the nanosheets, owing to dimensional confinement, contributed to an improved visible light response in PEC OER. This study presents a new strategy to design EC/PEC bifunctional catalyst utilizing unique structural and electronic features of 2D MOF.

Keywords: metal organic framework, nanosheet, photoelectrochemical water oxidation, oxygen evolution reaction, bifunctional catalyst

INTRODUCTION

Electrochemical (EC) and photoelectrochemical (PEC) water splitting are recognized as two attractive processes for clean fuel hydrogen (H_2) generation via the conversion of renewable electrical energy into chemical energy and have aroused intense research interest in recent years (Fujishima and Honda, 1972; Zhong and Gamelin, 2010; Kim and Choi, 2014; Zhang et al., 2020). Nevertheless, the oxidative half-cell reaction at the anode, oxygen evolution reaction (OER), generally requires high overpotential as driving force owing to the intrinsically sluggish kinetics. To this end, electrocatalysts and photoelectrocatalysts have been extensively pursued to promote the reaction kinetics and improve the energy conversion efficiency. For practical purpose, efficient catalysts that work for both EC and PEC OER are required to allow the seamless operation of water splitting in the presence and absence of sunlight, maximizing the process efficiency. Such bifunctional catalyst development mainly resides in metal oxide nanomaterials, such as bismuth vanadate ($BiVO_4$) (Kim and Choi, 2014), hematite (α-Fe_2O_3) (Zhong and Gamelin, 2010), and tungsten trioxide (WO_3) (Sarnowska et al., 2016), most of which, however, still cannot achieve desirable properties for the two processes simultaneously.

Metal organic frameworks (MOFs) are a crystalline porous material with the coordinations of transitional metal nodes and organic linkers, which have attracted significant interest for applications in gas sorption, energy storage, and heterogeneous catalysis (Rodenas et al., 2015; Dhakshinamoorthy et al., 2016; Sheberla et al., 2017). A great variety of two-dimensional (2D) MOFs were also discovered with emergent physiochemical properties owing to the 2D confinement (Peng et al., 2014; Rodenas et al., 2015; Zhan and Zeng, 2016). In particular, 2D MOFs possess extremely large specific surface area and a high concentration of isolated metal ion sites on the surface, making them unique materials for the studies of heterogeneous catalysis (Li et al., 2011). Meanwhile, benefiting from an excess electron density of organic linkers, MOFs are endowed with semiconductor-like properties in which photons can be absorbed and transferred through organic linkers to bound metal ions, an important characteristic in photoelectrocatalysis (Dhakshinamoorthy et al., 2016; Zhang et al., 2016). Therefore, despite the lack of previous experimental report, 2D MOFs could potentially provide a catalytic structure that allows the dual-functionality in both EC and PEC OER catalysis.

Herein, we report, for the first time, the synthesis of 2D cobalt-based MOF (Co-MOF) nanosheets and their catalytic properties for EC and PEC OER. The Co-MOF nanosheets were obtained through the exfoliation treatment of premade MOF-71 bulk materials, with consecutive processes of hydrothermal reaction in water and sonication in isopropanol. The resultant Co-MOF nanosheets demonstrated high activity for EC OER and improved visible light response for PEC OER. The enhanced EC and PEC catalytic performances of 2D Co-MOF nanosheets, comparing to bulk MOF-71, is associated with the large surface area, abundant catalytic sites, and low-dimension confinement effect of 2D structure, suggesting the high potential of modulating 2D MOF-based catalysts for EC and PEC water electrolyzer or other energy/fuel production devices.

EXPERIMENTAL SECTION

Materials

All chemicals were used as received without further purification. Cobalt nitrate hexahydrate [$Co(NO_3)_2.6H_2O$, 98%], terephthalic acid (1,4-BDC, 98%), and dimethylformamide (DMF, 99.8%) were purchased from Millipore Sigma. Isopropanol (2-propanol, 99.9%) was purchased from Fisher Scientific.

Synthesis of Bulk MOF-71

Bulk MOF-71 was synthesized using the reported method (Rosi et al., 2005). In a typical synthesis, 389 mg of $Co(NO_3)_2 \cdot 6H_2O$, 74 mg of 1,4-BDC, and 20 ml of DMF were mixed together and transferred into an autoclave. The hydrothermal reaction in the autoclave took place at 110°C for 12 h. The resultant product was collected by centrifugation at 6,000 rpm for 5 min, and the powder was washed twice consecutively with DMF solvent for the removal of unreacted organic linker. Finally, the material was dried in an oven at 70°C overnight, in which it is stored and used in the subsequent experiment.

Synthesis of Co-MOF Nanosheets

Twenty milligrams of as-synthesized bulk MOF-71 and 20 ml of deionized water were mixed and transferred into an autoclave. The autoclave was maintained at 90°C for 12 h. The dispersion was then sonicated for 6 h and aged for 12 h. The sediment was collected and mixed with 10 ml of isopropanol. The mixture was then sonicated again for 6 h. Finally, the Co-MOF nanosheets were obtained by collecting the colloid dispersion with precipitation removal and evaporating the solvent at room temperature. The yield of Co-MOF nanosheets was 20% (4 mg of Co-MOF nanosheets can be obtained from 20 mg of bulk MOF-71).

Synthesis of $Co(OH)_2$ Nanosheets

Ten milliliters of 0.2 M $Co(NO_3)_2$ aqueous solution was purged under argon for the removal of oxygen, to which 2 ml of 1 M NaOH aqueous solution was dropwise added. The obtained dispersion was aged for 15 min. The product was then washed three times by adding deionized water and centrifuged at 6,000 rpm for 5 min. The material was dried at room temperature.

CHARACTERIZATION

The transmission electron microscopy (TEM) images of the prepared samples were obtained using a JEOL JEM-1230 microscope (acceleration voltage, 120 kV). High-resolution TEM (HRTEM) images were taken on a FEI Tecnai G2 F20 at 200 kV. X-ray diffraction (XRD) patterns were collected on a Bruker AXS Dimension D8 X-Ray diffractometer with a Cu Kα radiation source. The UV–Vis absorption spectra were recorded using an HP 8453 spectrometer. Fourier transform infrared (FTIR) spectroscopy experiments were conducted on a Thermo Scientific Nicolet 6700 spectrometer.

Rotating Disk Electrode Thin Film Preparation

Catalyst films were formed on a glassy carbon (GC) rotating disk electrode (RDE) (5 mm diameter) for electrochemical measurements. The catalyst ink was prepared by dispersing 2 mg of catalyst powders [bulk MOF-71, Co-MOF nanosheets or $Co(OH)_2$ nanosheets] in isopropanol (990 μl) and Nafion ionomer (10 μl) ($V_{isopropanol}/V_{nafion}$ = 99:1) and sonicating for 30 min. The GC-RDE was typically cleaned by sonication and rinsing in deionized water and polishing with alumina nanopowders for 2 min. The prepared catalyst ink (5 μl) was spin casted twice on the GC-RDE at 350 rpm, which contained 10 μg of catalyst.

Electrochemical Measurements

The electrochemical property of catalyst was evaluated using a CHI 760D potentiostat (CH Instrument, Inc.) and a rotating disk electrode controller (AFMSRCE, Pine Instrument Co.). A three-electrode system, consisting of a glassy carbon working electrode, platinum wire counter electrode, and Ag/AgCl reference electrode (CHI 111), was used in the study. The electrolyte was 1 M potassium hydroxide (KOH) aqueous solution. The Ag/AgCl reference electrode was calibrated vs.

reversible hydrogen electrode (RHE) potential by measuring the Pt electrode in hydrogen atmosphere. The OER overpotential (η) were calculated using η = E (vs. RHE) – 1.23 V. All potentials are reported vs. RHE. Linear sweep voltammetry (LSV) was collected in the potential window of 1.03–1.63 V at a scan rate of 5 mV s^{-1}. Electrochemical impedance spectroscopy (EIS) was measured at initial potential of 1.58 V from 1 to 105 Hz. Current–time (I–t) curve was collected at a potential of 1.58 V. For the photoelectrocatalytic property investigation, a Xeon solar simulator (PerfectLight, China) was used as a light source, with an AM 1.5 G filter and a power density at the RDE surface adjusted to 100 mW cm^{-2} before testing. The RDE would rotate at speed of 1,600 rpm during our measurement.

RESULTS AND DISCUSSION

Figure 1A shows the TEM image of as-synthesized Co-MOF nanosheets. The uniform and low contrast of individual nanosheet indicates its thinness. The observation of the Tyndall effect from a colloid suspension of the nanosheets was consistent with their nanoscale characteristics (**Supplementary Figure 1**). In comparison, the obtained bulk MOF-71 was comprised of closely stacking layers (**Supplementary Figure 2**), which was verified by TEM characterizations and suggested the exfoliation mechanism for the nanosheet formation. Careful HRTEM characterizations confirmed microporous characteristic of the Co-MOF nanosheets, with an average molecular channel spacing of 1.07 nm (**Figure 1B**). The nanosheet thickness was limited to a few nanometers based on atomic force microscopy (AFM) measurements (**Figure 1C**), in consistence with the TEM results. The XRD pattern indicated a crystalline structure of the as-synthesized bulk MOF-71 and was in agreement with that reported for MOF-71, which consists of Co^{II} square-pyramidal coordination geometry networks (**Figures 1D,E**) (Li et al., 2015; Chisca et al., 2016). In comparison, the XRD pattern of synthesized Co-MOF nanosheets shows fewer reflection peaks, which could be associated with favorable orientation along the basal plane (**Figure 1E**). The DMF ligand substitution with water during exfoliation could also introduce the new diffraction peaks at a large diffraction angle. **Figure 1F** shows the FTIR results of the Co-MOF nanosheets and the bulk MOF-71. The peaks at 3,072, 3,008, and 2,946 cm^{-1} were assigned to stretching vibration of =C–H in aromatic ring and –CH and $–CH_3$ stretching vibrations in DMF, respectively (Colthup et al., 1990). The band at 1,944 cm^{-1} was attributed to the aromatic carbon bond, corresponding to the spectrum of 1,4-BDC and confirming the ligands in the coordination network (**Supplementary Figure 3**) (Colthup et al., 1990). The bulk MOF-71 exhibited one absorbance band at 1,669 cm^{-1}, which was ascribed to the carboxyl group in DMF molecules (Colthup et al., 1990). The band at 1,669 cm^{-1} disappeared on the FTIR of the Co-MOF nanosheets. Instead, a new peak at 3,600 cm^{-1} together with a broad bump between 3,600 and 3,000 cm^{-1}, characteristics of hydroxyl groups, appeared after the bulk MOF-71 was exfoliated into nanosheets. These changes indicated that the DMF ligands were substituted with water molecules after the exfoliation process.

The catalytic properties of Co-MOF nanosheets for EC OER were investigated in 1 M KOH electrolyte. The LSV, with an onset potential at about 1.48 V and an exponential increase in current afterward, confirmed that the Co-MOF nanosheets were highly active for the OER (**Figure 2A**). The η required to achieve a current density of 10 mA cm^{-2} was determined to be 350 mV (**Supplementary Figure 4**) (McCrory et al., 2015). In comparison, 380 and 370 mV of η were needed for the bulk MOF-71 and the $Co(OH)_2$ nanosheets, respectively (**Supplementary Figures 5–7**), demonstrating an improved catalytic activity of the Co-MOF nanosheets. **Supplementary Table 1** summarizes EC OER performances of recently reported 2D MOF and MOF-derived materials, which also confirms the high activity of our Co-MOF nanosheets. Previous studies related to Co-based catalysts reported that high-valance state cobalt is responsible for OER electrocatalysis (Burke et al., 2015). A small oxidation peak prior to water oxidation was observed on the LSV of the Co-MOF nanosheets, which may be attributed to the transformation of surface Co^{II} to Co^{III}. The oxidation peak of the Co-MOF nanosheets was centered at around 1.17 V, significantly lower than that of the bulk MOF-71 (1.28 V) and the $Co(OH)_2$ nanosheets (1.30 V). This result suggested more efficient generation of Co^{III} sites on the 2D Co-MOF nanosheets and could partially account for their higher OER activity (**Supplementary Figures 8–10**). In addition, the larger electrochemical surface area of the Co-MOF nanosheets was beneficial to expose more active sites, thereby allowing for a higher activity than the bulk MOF-71. The larger electrochemical surface area was corroborated with an about 12-time increase in the double layer capacitance of the MOF nanosheets compared to the bulk MOF (**Supplementary Figure 11**). The Nyquist plots in **Figure 2B** show that the Co-MOF nanosheets possessed the smallest interfacial charge transfer resistance compared with the bulk MOF-71 and the $Co(OH)_2$ nanosheets, confirming the promoted OER kinetics. The Tafel slope is another important index for OER kinetic evaluation and a description for the relationship between electrode potential and OER current density. The Tafel data of the Co-MOF nanosheets, the bulk MOF-71, and the $Co(OH)_2$ nanosheets are shown in **Figure 2C**. The Tafel slopes of these catalysts were in the same range as that of the well-studied IrO_2 (49 mV dec^{-1}) and Ir/C (40 mV dec^{-1}) OER catalysts (Trotochaud et al., 2012; Gong et al., 2013). The Tafel slope of the Co-MOF nanosheets was measured to be 34.7 mV dec^{-1}, smaller than the other two samples [40.7 mV dec^{-1} for bulk MOF and 61.6 mV dec^{-1} for $Co(OH)_2$], which could suggest the varied OER mechanisms on their surfaces (Gong et al., 2013).

The PEC properties of the Co-MOF nanosheets were investigated in the same electrolyte. The PEC current profile was collected under AM 1.5 G visible light illumination at intervals of 20 s (**Figure 3A**). The immediate changes in the current density with on and off switches of the light demonstrated a significant photo response of the Co-MOF nanosheets (**Supplementary Figure 12**), suggesting that they are active for PEC OER. Under the specific testing condition, the OER current

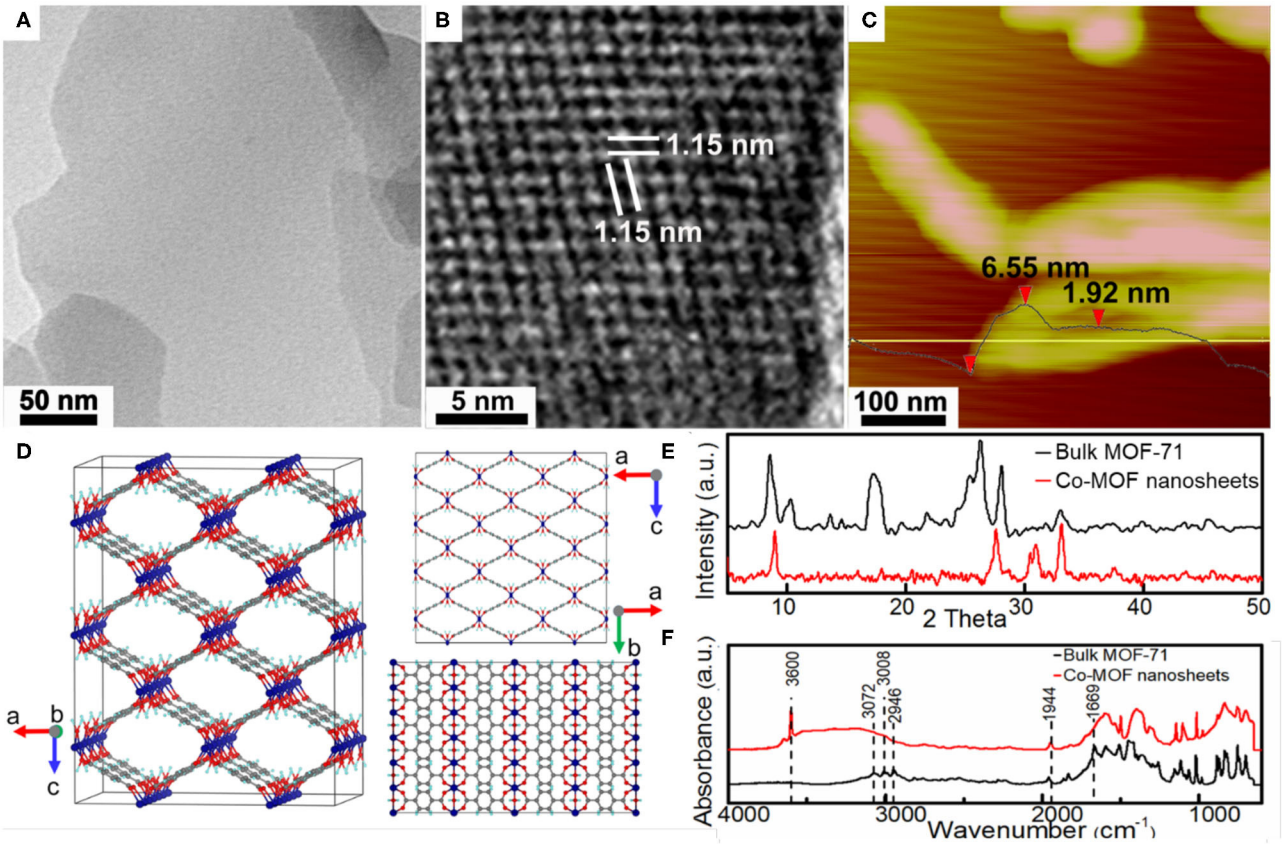

FIGURE 1 | Structural characterizations of the as-synthesized Co-based metal organic framework (Co-MOF) nanosheets: **(A)** transmission electron microscopy (TEM) image, **(B)** high-resolution TEM (HRTEM) image, **(C)** atomic force microscopy (AFM) image, and **(D)** crystalline structure of bulk MOF-71 (Co, C, O, and H atoms are shown in purple, gray, red, and blue) along different crystallographic axes; **(E)** X-ray diffraction (XRD) and **(F)** Fourier transform infrared (FTIR) of bulk MOF-71 and Co-MOF nanosheets.

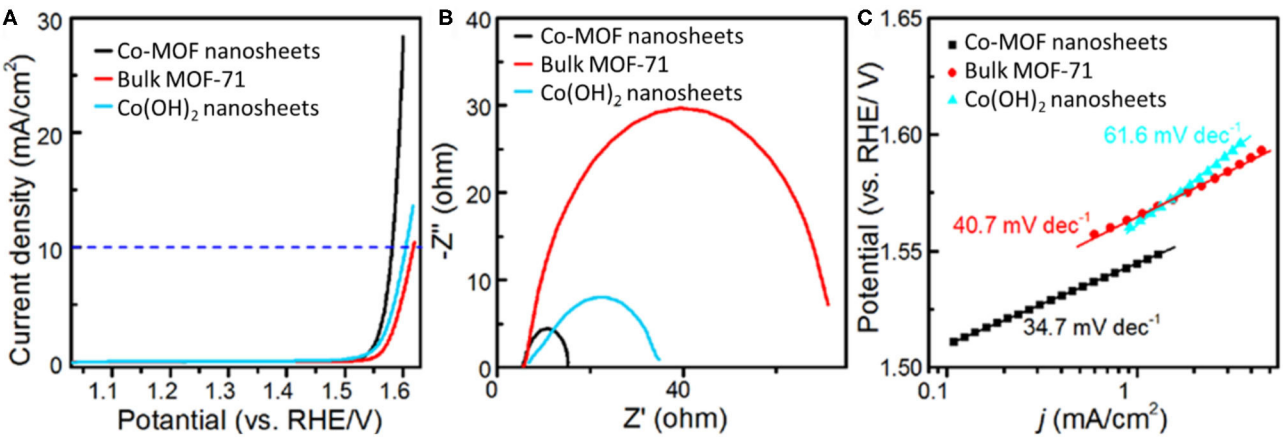

FIGURE 2 | Electrochemical measurements in 1 M KOH electrolyte: **(A)** iR-corrected linear sweep voltammetry (LSV), **(B)** Nyquist plots, and **(C)** Tafel plots of Co-MOF nanosheets, bulk MOF-71, and $Co(OH)_2$ nanosheets.

density increased by about 1.37 mA cm^{-2} under illumination. The photo response was larger than that using the bulk MOF-71 (1.23 mA cm^{-2}, **Supplementary Figure 13**). The increased PEC response of the Co-MOF nanosheets could be attributed to more efficient charge separation in 2D structure (O'Regan and Grätzel, 1990; King et al., 2013). The Co-MOF nanosheets

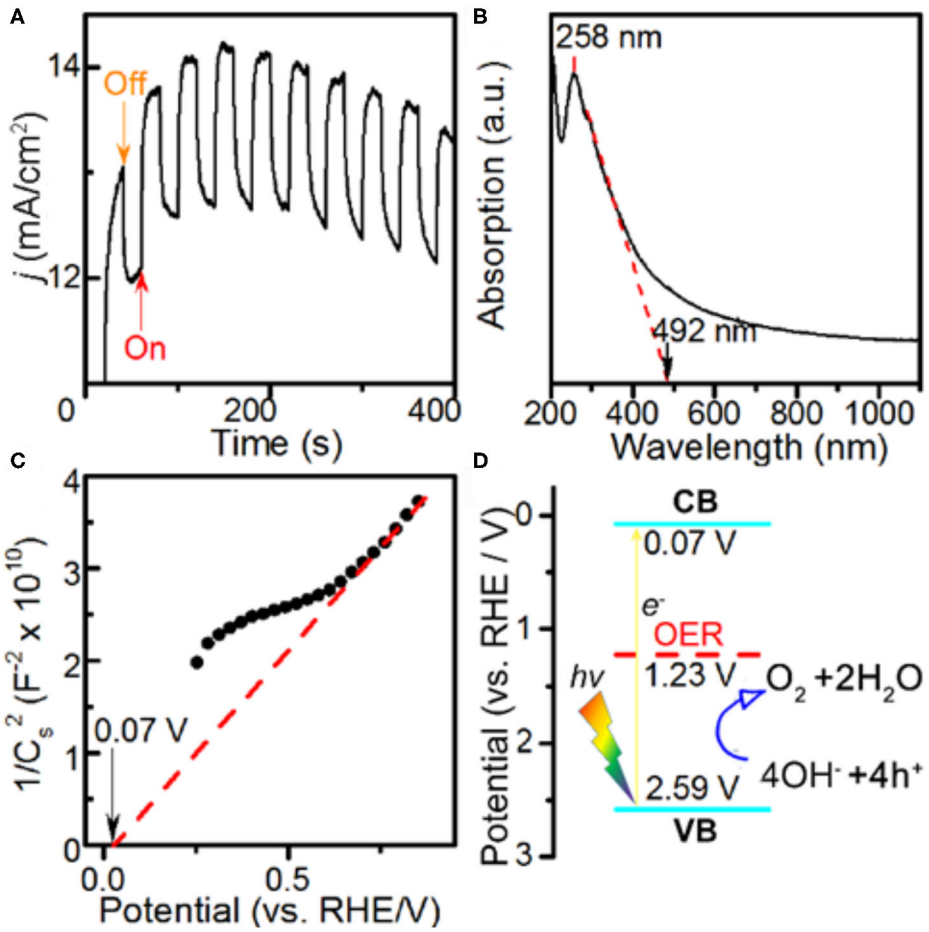

FIGURE 3 | Photoelectrochemical measurements in 1 M KOH electrolyte and characterizations: **(A)** potentiostatic current response at E = 1.582 V vs. reversible hydrogen electrode (RHE) with and without light illumination, **(B)** UV–Vis spectrum, **(C)** Mott–Schottky plot, and **(D)** band alignment of the Co-MOF nanosheets.

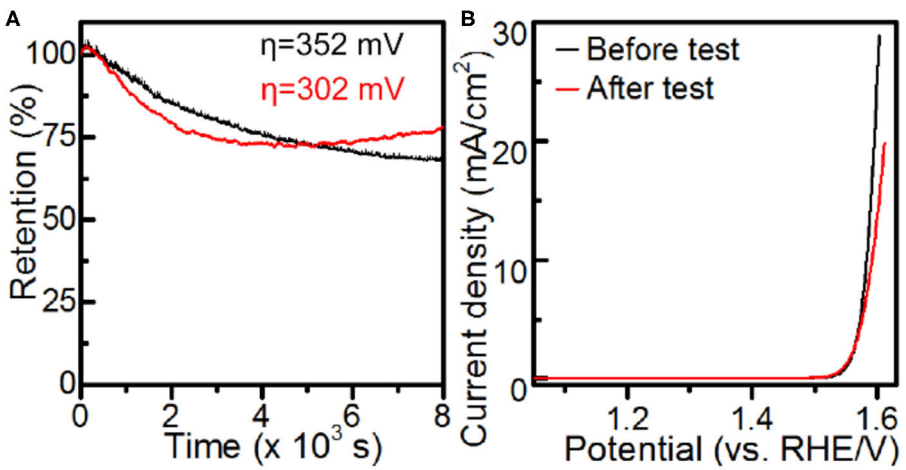

FIGURE 4 | Electrochemical measurements in 1 M KOH: **(A)** chronoamperometry and **(B)** iR-corrected LSV using Co-MOF nanosheets.

exhibited a mixed mode of absorbance, evidenced by the UV–Vis spectrum (**Figure 3B**). The peak at 258 nm could be assigned to the π-π transition in the conjugated ligand (Sarnowska et al., 2016). Besides, a small shoulder peak at around 300 nm was observed together with continuous absorption of light in a broad wavelength range, which was more like a semiconductor.

The band gap was determined to be 2.52 V based on the UV–Vis measurements. The flat band potential of the Co-MOF nanosheets was measured using the Mott–Schottky method (**Figure 3C**) (Gryse et al., 1975). The positive slope indicated that the Co-MOF nanosheets were an n-type semiconductor (Lin et al., 2014). The energy level of the conduction band (CB) bottom was determined to be 0.07 V vs. RHE. Based on the UV–Vis absorbance data and the Mott–Schottky plot, we could determine the energy level of the valence band (VB) top (2.59 V vs. RHE) and draw the energy level scheme (**Figure 3D**). The band alignment of bulk MOF-71 is shown in **Supplementary Figure 14**, which indicated a smaller band gap than Co-MOF nanosheets. Under the illumination of visible light, there would be excitation of electrons from the VB to CB band. Thus, the holes generated in the VB band possess a more positive potential than the Nernstian potential of 1.23 V for OER, which creates an additional driving force for the reaction and demonstrates that the PEC process is thermodynamically feasible on the Co-MOF nanosheets (Linic et al., 2015).

The catalytic durability of the Co-MOF nanosheets was evaluated by conducting chronoamperometry (CA) experiments at an η of 352 mV. The Co-MOF nanosheets exhibited a promising durability, with a gradual decrease in the current and 68% of the activity retained after 8,000 s of CA test (**Figure 4** and **Supplementary Figure 15**). The deactivation of the catalyst could be associated with oxidation and aggregation of surface active Co sites caused by the high overpotential, evidenced by an increase in the charge transfer resistance and formation of small nanoparticles on the tested Co-MOF nanosheets (**Supplementary Figures 16, 17**). The conclusion was supported by the durability experiments conducted at a lower overpotential of 302 mV, where the tested Co-MOF nanosheets retained 80% of the initial activity and showed significantly less generation of particles (**Supplementary Figures 17–19**). Moreover, the photo response was retained for the electrode after durability test (**Supplementary Figure 20**), which indicated an encouraging PEC stability of the Co-MOF nanosheets.

CONCLUSIONS

In summary, we synthesized Co-MOF nanosheets and studied their catalytic properties in EC and PEC OER processes. Characterizations showed that these Co-MOF nanosheets possessed the MOF-71 structure, with lattice DMF ligands substituted with water molecules in comparison with the bulk MOF-71. The Co-MOF nanosheets were found with interesting properties for both EC and PEC OER, demonstrating the potential use of 2D MOF structures as the bifunctional catalysts for water electrolyzers. The Co-MOF nanosheet catalyst exhibited a clear improvement in OER activity relative to the bulk MOF-71 (350 vs. 380 mV of η at 10 mA cm^{-2} current density), which was attributed to a significantly larger surface area and more efficient generation of high valence state Co active sites. The more intense response to visible light under the PEC condition comparing to its bulk counterpart was associated with more efficient charge separation in 2D structure. This work presents the first example of 2D MOF nanosheets for EC and PEC OER and suggests that the further tuning of 2D MOF nanostructures may lead to new opportunities in the design and construction of efficient catalysts for EC and PEC combined-mode water electrolyzers.

DATA AVAILABILITY STATEMENT

All datasets generated for this study are included in the article/**Supplementary Material**.

AUTHOR CONTRIBUTIONS

The project was conceived by CL under the supervision of ZP and SZ. Catalyst synthesis, structural characterization, and catalysis measurement were performed by CL, XS, GJ, YZ, and CS. The analysis and interpretation of all spectra were done by CL, CZ, and JC. The AFM image was taken by CL and LL. All authors contributed to the article and approved the submitted version.

FUNDING

This work was financially supported by the University of Akron fund (ZP) and the University of Virginia Faculty Start-up fund (SZ). TEM data were obtained at the (cryo) TEM facility at the Liquid Crystal Institute, Kent State University, supported by the Ohio Research Scholars Program Research Cluster on Surfaces in Advanced Materials.

SUPPLEMENTARY MATERIAL

The Supplementary Material for this article can be found online at: https://www.frontiersin.org/articles/10.3389/fchem.2020.604239/full#supplementary-material

REFERENCES

Burke, M. S., Kast, M. G., Trotochaud, L., Smith, A. M., and Boettcher, S. W. (2015). Cobalt-iron (oxy)hydroxide oxygen evolution electrocatalysts: the role of structure and composition on activity, stability, and mechanism. *J. Am. Chem. Soc.*137, 3638–3648. doi: 10.1021/jacs.5b00281

Chisca, D., Croitor, L., Petuhov, O., Coropceanu, E. B., and Fonari, M. S. (2016). MOF-71 as a degradation product in single crystal to single crystal transformation of new three-dimensional Co(ii) 1,4-benzenedicarboxylate. *CrystEngComm* 18, 38–41. doi: 10.1039/C5CE02094H

Colthup, N. B., Daly, L. H., and Wiberley, S. E. (1990). *Introduction to infrared and Raman spectroscopy*. San Diego, CA: Academic Press, 387–481.

Dhakshinamoorthy, A., Asiri, A. M., and Garcia, H. (2016). Metal–organic framework (MOF) compounds: photocatalysts for redox reactions and solar fuel production. *Angew. Chem. Int. Ed.* 55, 5414–5445. doi: 10.1002/anie.201505581

Fujishima, A., and Honda, K. (1972). Electrochemical photolysis of water at a semiconductor electrode. *Nature* 238, 37–38. doi: 10.1038/238037a0

Gong, M., Li, Y., Wang, H., Liang, Y., Wu, J. Z., Zhou, J., et al. (2013). An advanced Ni–Fe layered double hydroxide electrocatalyst for

water oxidation. *J. Am. Chem. Soc.* 135, 8452–8455. doi: 10.1021/ja4027715

Gryse, R. D., Gomes, W. P., Cardon, F., and Vennik, J. (1975). On the interpretation of Mott-Schottky plots determined at semiconductor/electrolyte systems. *J. Electrochem. Soc.* 122, 711–712. doi: 10.1149/1.2134298

Kim, T. W., and Choi, K. S. (2014). Nanoporous $BiVO_4$ photoanodes with dual-layer oxygen evolution catalysts for solar water splitting. *Science* 343, 990–994. doi: 10.1126/science.1246913

King, L. A., Zhao, W., Chhowalla, M., Riley, D. J., and Eda, G. (2013). Photoelectrochemical properties of chemically exfoliated MoS_2. *J. Mater. Chem. A* 1, 8935–8941. doi: 10.1039/c3ta11633f

Li, C., Chen, T., Xu, W., Lou, X., Pan, L., Chen, Q., et al. (2015). Mesoporous nanostructured Co_3O_4 derived from MOF template: a high-performance anode material for lithium-ion batteries. *J. Mater. Chem. A* 3, 5585–5591. doi: 10.1039/C4TA06914E

Li, P. Z., Maeda, Y., and Xu, Q. (2011). Top-down fabrication of crystalline metal–organic framework nanosheets. *Chem. Commun.* 47, 8436–8438. doi: 10.1039/c1cc12510a

Lin, R., Shen, L., Ren, Z., Wu, W., Tan, Y., and Fu, H., et al. (2014). Enhanced photocatalytic hydrogen production activity via dual modification of MOF and reduced graphene oxide on CdS. *Chem. Commun.* 50, 8533–8535. doi: 10.1039/C4CC01776E

Linic, S., Aslam, U., Boerigter, C., and Morabito, M. (2015). Photochemical transformations on plasmonic metal nanoparticles. *Nat. Mater.* 14, 567–576. doi: 10.1038/nmat4281

McCrory, C. C. L., Jung, S., Ferrer, I. M., Chatman, S. M., Peters, J. C., and Jaramillo, T. F. (2015). Benchmarking hydrogen evolving reaction and oxygen evolving reaction electrocatalysts for solar water splitting devices. *J. Am. Chem. Soc.* 137, 4347–4357. doi: 10.1021/ja510442p

O'Regan, B., and Grätzel, M. (1990). A low-cost, high-efficiency solar cell based on dye-sensitized colloidal TiO_2 films. *Nature* 353, 737–740. doi: 10.1038/353737a0

Peng, Y., Li, Y., Ban, Y., Jin, H., Jiao, W., Liu, X., et al. (2014). Metal-organic framework nanosheets as building blocks for molecular sieving membranes. *Science* 346, 1356–1359. doi: 10.1126/science.1254227

Rodenas, T., Luz, I., Prieto, G., Seoane, B., Miro, H., Corma, A., et al. (2015). Metal–organic framework nanosheets in polymer composite materials for gas separation. *Nat. Mater.* 14, 48–55. doi: 10.1038/nmat4113

Rosi, N. L., Kim, J., Eddaoudi, M., Chen, B., O'Keeffe, M., and Yaghi, O. M. (2005). Rod packings and metal– organic frameworks constructed from rod-shaped secondary building units. *J. Am. Chem. Soc.* 127, 1504–1518. doi: 10.1021/ja045123o

Sarnowska, M., Bienkowski, K., Barczuk, P. J., Solarska, R., and Augustynski, J. (2016). Highly efficient and stable solar water splitting at $(Na)WO_3$ photoanodes in acidic electrolyte assisted by non-noble metal oxygen evolution catalyst. *Adv. Energy Mater.* 6:1600526. doi: 10.1002/aenm.201600526

Sheberla, D., Bachman, J. C., Elias, J. S., Sun, C. J., Shao-Horn, Y., and Dinc,ă, M. (2017). Conductive MOF electrodes for stable supercapacitors with high areal capacitance. *Nat. Mater.* 16, 220–224. doi: 10.1038/nmat4766

Trotochaud, L., Ranney, J. K., Williams, K. N., and Boettcher, S. W. (2012). Solution-cast metal oxide thin film electrocatalysts for oxygen evolution. *J. Am. Chem. Soc.* 134, 17253–17261. doi: 10.1021/ja307507a

Zhan, G., and Zeng, H. C. (2016). Synthesis and functionalization of oriented metal-organic-framework nanosheets: toward a series of 2D catalysts. *Adv. Funct. Mater.* 26, 3268–3281. doi: 10.1002/adfm.201505380

Zhang, L., Cui, P., Yang, H., Chen, J., Xiao, F., Guo, Y., et al. (2016). Metal–organic frameworks as promising photosensitizers for photoelectrochemical water splitting. *Adv. Sci.* 3:1500243. doi: 10.1002/advs.201500243

Zhang, Y., Li, N., Zhang, Z., Li, S., Cui, M., Ma, L., et al. (2020). Programmable synthesis of multimetallic phosphide nanorods mediated by core/shell structure formation and conversion. *J. Am. Chem. Soc.* 142, 8490–8497. doi: 10.1021/jacs.0c02584

Zhong, D. K., and Gamelin, D. R. (2010). Photoelectrochemical water oxidation by cobalt catalyst ("Co–Pi")/α-Fe_2O_3 composite photoanodes: oxygen evolution and resolution of a kinetic bottleneck. *J. Am. Chem. Soc.* 132, 4202–4207. doi: 10.1021/ja908730h

Conflict of Interest: The authors declare that the research was conducted in the absence of any commercial or financial relationships that could be construed as a potential conflict of interest.

Copyright © 2020 Liu, Shen, Johnson, Zhang, Zhang, Chen, Li, Sheehan, Peng and Zhang. This is an open-access article distributed under the terms of the Creative Commons Attribution License (CC BY). The use, distribution or reproduction in other forums is permitted, provided the original author(s) and the copyright owner(s) are credited and that the original publication in this journal is cited, in accordance with accepted academic practice. No use, distribution or reproduction is permitted which does not comply with these terms.

frontiers in Chemistry

MINI REVIEW
published: 09 November 2020
doi: 10.3389/fchem.2020.596479

Nature's Chemists: The Discovery and Engineering of Phytochemical Biosynthesis

*Kaouthar Eljounaidi and Benjamin R. Lichman**

Centre for Novel Agricultural Products, Department of Biology, University of York, York, United Kingdom

Plants produce a diverse array of natural products, many of which have high pharmaceutical value or therapeutic potential. However, these compounds often occur at low concentrations in uncultivated species. Producing phytochemicals in heterologous systems has the potential to address the bioavailability issues related to obtaining these molecules from their natural source. Plants are suitable heterologous systems for the production of valuable phytochemicals as they are autotrophic, derive energy and carbon from photosynthesis, and have similar cellular context to native producer plants. In this review we highlight the methods that are used to elucidate natural product biosynthetic pathways, including the approaches leading to proposing the sequence of enzymatic steps, selecting enzyme candidates and characterizing gene function. We will also discuss the advantages of using plant chasses as production platforms for high value phytochemicals. In addition, through this report we will assess the emerging metabolic engineering strategies that have been developed to enhance and optimize the production of natural and novel bioactive phytochemicals in heterologous plant systems.

Keywords: phytochemicals, gene discovery, biosynthetic pathway, bioactive chemicals, synthetic biology, metabolic engineering, natural products, biosynthesis

OPEN ACCESS

Edited by:
Chun Xu,
The University of Queensland, Australia

Reviewed by:
Anne Osbourn,
John Innes Centre, United Kingdom
Paripok Phitsuwan,
King Mongkut's University of Technology Thonburi, Thailand

***Correspondence:**
Benjamin R. Lichman
benjamin.lichman@york.ac.uk

Specialty section:
This article was submitted to Chemical Biology, a section of the journal Frontiers in Chemistry

Received: *19 August 2020*
Accepted: *09 October 2020*
Published: *09 November 2020*

Citation:
Eljounaidi K and Lichman BR (2020) Nature's Chemists: The Discovery and Engineering of Phytochemical Biosynthesis. Front. Chem. 8:596479. doi: 10.3389/fchem.2020.596479

INTRODUCTION

Plants have a remarkable capacity to produce a wide array of specialized metabolites (also referred to as secondary metabolites or natural products), to support their defense and ecological adaptation. These phytochemicals exhibit a variety of bioactivities and many of them are of considerable pharmaceutical importance. Based on their biosynthetic origins, plant secondary metabolites can be divided into three major groups: terpenoids, alkaloids, and phenolics.

Terpenoids or isoprenoids are a structurally diverse class of plant specialized metabolites. They are derived by the repetitive fusion of branched five-carbon isopentanes, usually referred to as isoprene units. Many terpenoids have biological activities and are utilized as valuable pharmaceuticals. The most renowned terpenoid-based drugs include the antimalarial medicine artemisinin (*Artemisia annua*) and the anticancer drug Taxol (*Taxus brevifolia*) (**Figure 1A**). Another major class of secondary metabolites are alkaloids, nitrogen containing low-molecular-weight compounds, typically derived from amino acids (Lichman, 2020). Numerous alkaloids (or their derivatives) are employed as high value drugs, such as vincristine and vinblastine (anticancer) from Madagascar periwinkle (*Catharanthus roseus*), camptothecin (anticancer) from *Camptotheca acuminata* and morphine (analgesic drug) from opium poppy (**Figure 1B**). Phenolics are a large and diverse group of aromatic compounds which include the tannins, phenylpropanoid, anthocyanin and lignan subgroups. Etoposide and teniposide are among the

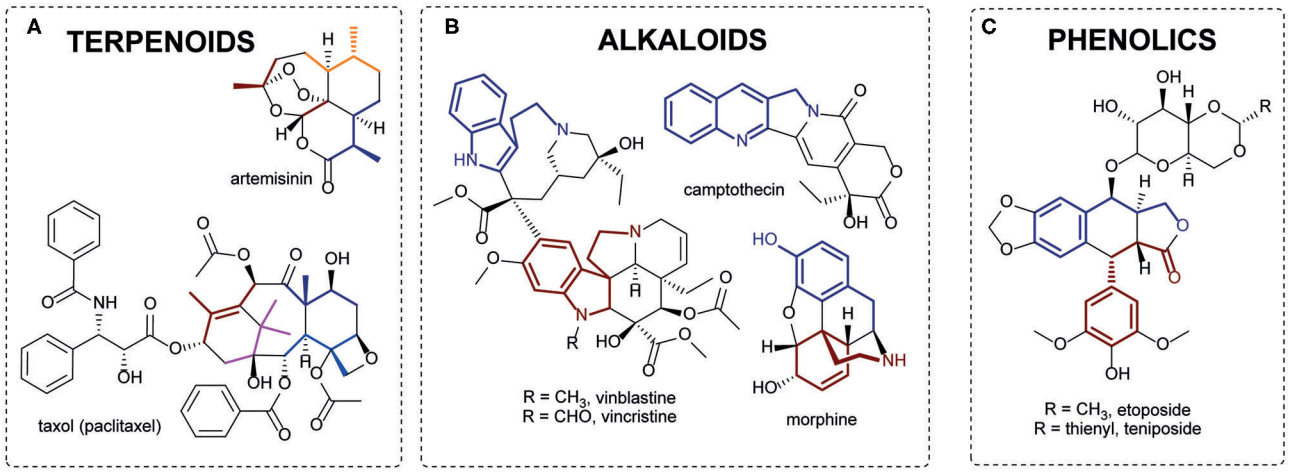

FIGURE 1 | Examples of plant specialized metabolites of pharmaceutical significance. **(A)** Terpenoids: artemisinin and taxol. Isoprene units are highlighted with colors. **(B)** Alkaloids: camptothecin, vinblastine, and vincristine with tryptophan precursor highlighted; morphine tyrosine precursors highlighted. **(C)** Phenolics: etoposide and teniposide with phenylpropanoid units highlighted.

most pharmaceutically important polyphenols (**Figure 1C**). These compounds are derivatives of podophyllotoxin, a lignan from mayapple (*Podophyllum peltatum*), and are widely used in chemotherapies. Alongside alkaloids, terpenoids, and phenolics, plants also produce other types of secondary metabolites, such as polyketides, cyanogenic glycosides and glucosinolates, of which many have pharmaceutical relevance.

Sourcing bioactive natural products from plants has many challenges. These metabolites are often found in low abundance or are produced in rare or slow-growing plant species, which limits the availability and accessibility of the active pharmaceutical agent and impacts market prices. In many cases, these molecules are very complex and are recalcitrant to chemical synthesis, as they contain many chiral centers or polycyclic rings (Nicolaou and Rigol, 2020). Even when synthesis is possible, it is not sustainable as it often relies on petrochemical feedstocks and/or environmentally unfriendly production processes (Lechner et al., 2016). This makes finding alternative sources for the supply of these valuable molecules necessary.

Increased access to phytochemicals can be achieved through a number of approaches. For instance, the biosynthetic capabilities of the natural producer may be enhanced through selective breeding programmes (Townsend et al., 2013) or through genetic modification and the creation of transgenic lines (Shen et al., 2018). Cell cultures may also enable greater control over the production of the compound of interest. For example, cambial meristematic cell cultures derived from *Taxus cuspidata* have been shown to produce high yields of the anticancer drug, paclitaxel (Taxol), while circumventing the obstacles routinely associated with the commercial growth of dedifferentiated plant cells (Lee et al., 2010).

Another alternative and increasingly popular approach is the transfer of biosynthetic pathways into heterologous systems such as plants (e.g., *Nicotiana benthamiana*) or microbes (e.g., *Saccharomyces cerevisiae* and *Escherichia coli*). The advantages of using microbes as production platforms for valuable chemicals include fast growth cycles, ease of genetic modification, and the fact that they offer a simplified product purification pipeline. The synthetic biology approaches used to produce plant metabolites in microbial organisms have been recently reviewed (Moses et al., 2017; Li et al., 2018). Plants, on the other hand, are photoautotrophs and do not require exogenous carbon sources, unlike typical microbial platforms. Plants also provide a cellular context similar to the native producer, which make them an attractive platform for the production of valuable chemicals.

In order to engineer valuable phytochemicals in microbe or plants, the first step is to uncover the biosynthetic pathway of the metabolite of interest. In this review we highlight the recent methods that have been used to elucidate natural product biosynthetic pathways, including the approaches leading to proposing the sequence of enzymatic steps, assigning enzyme family, as well as, gene function elucidation. We will also discuss the advantages of using plant chassis as a production platform for high value phytochemicals. In addition, through this report we will assess the emerging metabolic engineering strategies that have been developed to enhance and optimize the production of natural and novel bioactive phytochemicals in heterologous plant systems.

DISCOVERY OF SPECIALIZED METABOLIC PATHWAYS

Proposing a Biosynthetic Pathway

In order to identify the enzymes that underlie the biosynthesis of valuable plant natural products, it is first necessary to hypothesize a plausible sequence of enzyme catalyzed reactions that can lead from primary metabolism to the molecule of interest. Generally, biomimetic syntheses tend to use mild conditions and

harness cascade-like reactions commonly found in biosynthetic pathways, hence providing clues for pathway elucidation (Yoder and Johnston, 2005).

If the metabolic pathway is incompletely described, isotope-labeling studies can be used to identify the unknown steps. Primary metabolites, such as amino acids, sugars, or even dioxygen and carbon dioxide, labeled with stable isotopes (e.g. ^{2}H, ^{13}C, ^{15}N, and ^{18}O), can be fed to the plant. The target specialized metabolite can then be assessed for isotope labeling by mass spectrometry (MS) or nuclear magnetic resonance (NMR) (Freund and Hegeman, 2017). This allows us to establish the identity of the starting material and identify its mode of incorporation. Strategically positioned isotopic labels can be used to probe the transformations and structural rearrangements that occur along the biosynthetic pathway.

For example, the incompletely described biosynthesis of camptothecin, a monoterpene indole alkaloid (MIA) from *Camptotheca acuminata*, was investigated using metabolite profiling and isotope labeling studies. The approach led to the identification of plausible intermediates for missing pathway steps and demonstrated that nearly all camptothecin pathway intermediates were present as multiple isomers (Sadre et al., 2016). Therefore, these metabolite focused strategies can lead to a hypothetical biosynthetic pathway made up of a set of chemically reasonable enzymatic conversions.

The next step is to assign possible enzyme classes to each hypothesized reaction based on characterized enzyme activities. For instance, a hydroxylation step will probably involve a cytochrome P450 enzyme or a 2-oxoglutarate dependent oxygenase (Mitchell and Weng, 2019), whilst a transfer of an amine group onto a carbonyl is likely to involve a PLP-dependent enzyme (Lee and Facchini, 2011). Once the hypothetical pathway has been populated with proposed enzyme classes, the gene discovery effort can begin.

Integrative Approaches for Gene Identification

The discovery of genes involved in the biosynthesis of phytochemicals typically requires the use of multi-omics technologies such as genomics, transcriptomics, proteomics, and metabolomics. Analysis of these data enable the identification of candidate genes that encode enzymes that catalyze biosynthetic steps (**Figure 2**).

The biosynthesis of natural products is regulated both during development and in response to various environmental stimuli. Transcriptomics can pinpoint differentially expressed genes across different types of tissues (or cells), different developmental stages or in elicitor-treated material. Candidate genes involved in biosynthesis can be identified through correlation of expression with metabolite accumulation, or through identification of co-expressed clusters in which genes involved in the same pathway share expression patterns across tissues (**Figure 2A**).

The hormone methyl jasmonate (MeJA) is known to elicit various species-specific specialized metabolic pathways. This feature has often been used to identify genes involved in the biosynthesis of various natural products. Cytochrome P450 (CYP728B70) catalyzing the oxidation step in triptolide biosynthesis, an abietane-type diterpenoid from *Tripterygium wilfordii*, was identified through an integrative gene prioritization approach (Tu et al., 2020). The prioritized candidate genes were highly expressed in MeJA-induced cells and/or in the root bark (main accumulation site of the diterpene), as well as, exhibited similar expression patterns to already characterized enzymes in the pathway; copalyl diphosphate synthase and miltiradiene synthase (Tu et al., 2020).

Various valuable plant natural products have been shown to accumulate in specific specialized structures, such as artemisinin in the glandular trichomes of *Artemisia annua* (Duke et al., 1994) and morphine in the laticifers of the aerial organs of opium poppy (*Papaver somniferum*) (Facchini and De Luca, 1995). Generating multi-omic data from these structures allows the identification of new biosynthetic enzymes involved in pathways of interest. For example, comparative proteomic analysis of trichomes and trichome-depleted leaves in catmint (*Nepeta mussinii*) led to the discovery of the unusual nepetalactol-related short-chain dehydrogenase enzymes (NEPS), which are enriched in the trichome and involved in the biosynthesis of volatile nepetalactones (Lichman et al., 2019).

Phylogenetic analysis can provide valuable information to further guide the candidate gene prioritization process. Genes involved in a biosynthetic pathway unique to a particular species are likely to be phylogenetically distinct. Therefore, building phylogenetic trees containing candidate genes and homologous genes from other species may reveal subclades unique to the producer plant. Key oxidases in limonoid biosynthesis in *Melia azedarach*; CYP71BQ5 and CYP71CD2 were identified through this strategy. These cytochrome P450 enzymes were found in a distinct subclade within the phylogenetic tree, comprising only *Melia azedarach* sequences, suggesting their involvement in this lineage-specific pathway (Hodgson et al., 2019).

Candidate gene selection may also be supplemented by mining whole genomes or partial genome sequences for genes physically localized in the vicinity of previously characterized enzymes (**Figure 2B**). It has been reported that genes involved in biosynthetic pathways of a number of natural products are organized in functional clusters within plant genomes (Roselli et al., 2017; Lichman et al., 2020; Liu et al., 2020). Features of plant biosynthetic gene clusters, how they form and how they are regulated have been recently reviewed (Nützmann et al., 2016, 2018). Another approach is total protein purification and fractionation, from the native plant material, followed by functional assays (**Figure 2C**). Protein fractions demonstrating the desired enzyme activity can be analyzed through protein-mass spectrometry and the identity of the enzyme determined by comparison with a predicted peptide database. The formation of thebaine, the first opiate alkaloid in the biosynthesis of codeine and morphine in opium poppy, can occur spontaneously from (7*S*)-salutaridinol 7-O-acetate. However, functional assays with total soluble protein isolated from opium poppy latex resulted in a 10-fold increase in the formation of thebaine. After protein fractionation and subjecting the active protein fraction to LC-MS/MS proteomics analysis, candidate genes were identified and were then tested through enzymatic assays,

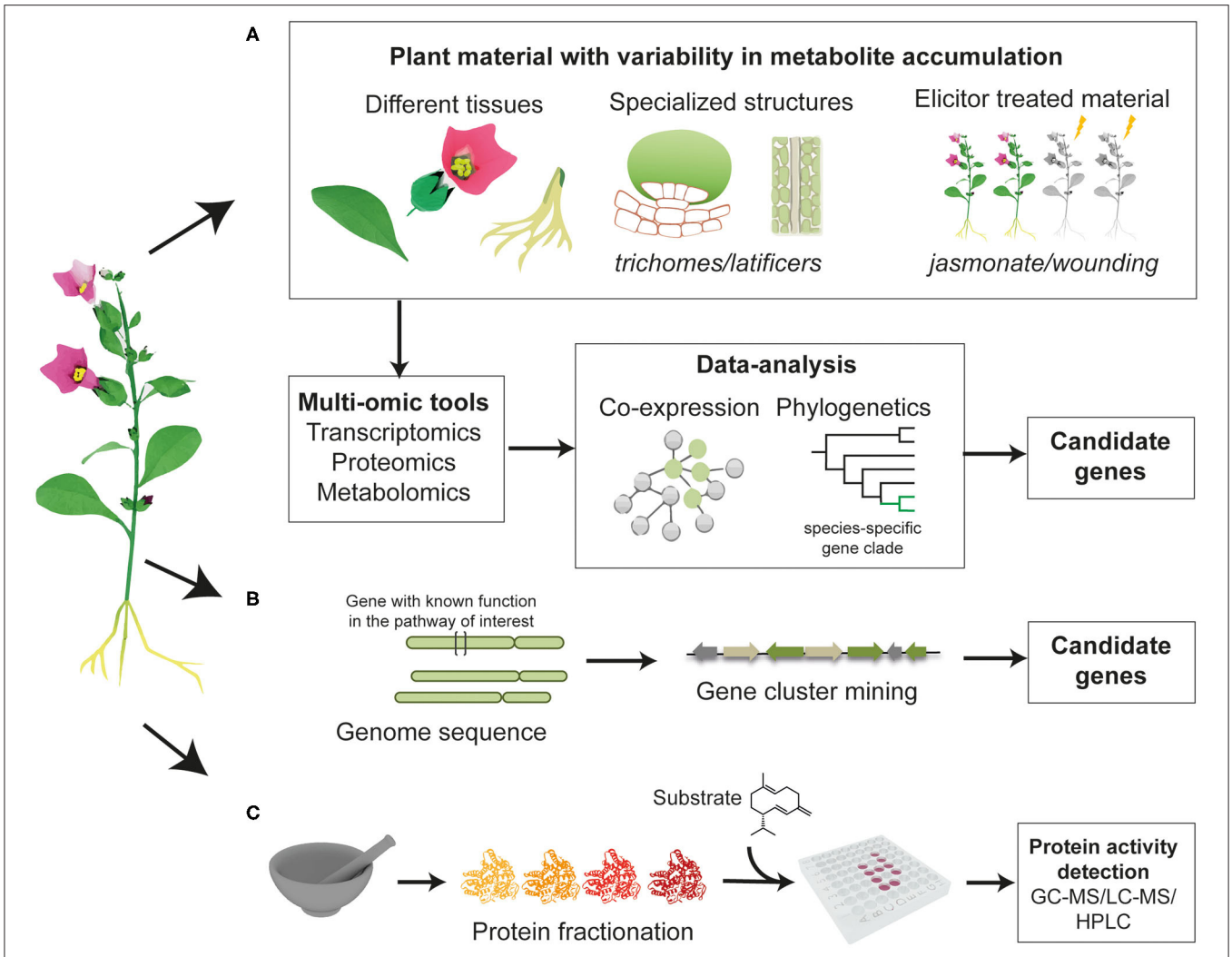

FIGURE 2 | Overview of the approaches that can be employed to discover unknown enzymes in a biosynthetic pathway of interest. **(A)** Identification of candidate genes in plant material with difference in metabolites accumulation, through co-expression analysis or phylogenetic analysis to examine whether a gene clade is specific to the native plant producer. **(B)** Mining genomic data to look for genes that are physically localized in the vicinity of previously characterized enzymes (gene clusters). **(C)** Total protein purification and fractionation from the native plant material, followed by functional assays and proteomic identification of the active fraction.

leading to the functional characterization of thebaine synthase (Chen et al., 2018).

Most of the aforementioned strategies, such as co-expression analysis, phylogenetics and genome mining, tend to be employed in an integrative way to allow efficient prioritization of candidate genes responsible for metabolic traits of interest. The next step is to verify the identity of the gene through functional assays.

Functional Characterization of Candidate Genes

Two types of experiments are typically required to ascribe a gene to a biosynthetic pathway: enzyme activity assays and reverse genetics gene function validation. The activity of the encoded enzyme must be characterized; this is typically achieved using recombinant expression. However, activity alone is not sufficient to determine *in planta* function. Here, reverse genetics approaches such as gene silencing are necessary to verify the role of the gene in a pathway.

Pathway Elucidation in Microbial Platforms

Recombinant protein expression in *Escherichia coli* has been extensively used for the enzymatic characterization of biosynthetic genes. The advantages of employing this prokaryotic organism include fast growth kinetics and well-established molecular tools. Protein expression in *E. coli* is often followed by enzyme purification and *in vitro* assays. This enables the assessment of the biochemical activities of the candidate enzymes outside the complex cellular context (Caputi et al., 2018; Torrens-Spence et al., 2018; Lichman et al., 2019; Kim et al., 2020) (**Figure 3**).

However, several enzyme families frequently involved in specialized metabolism in plants are membrane-associated, such

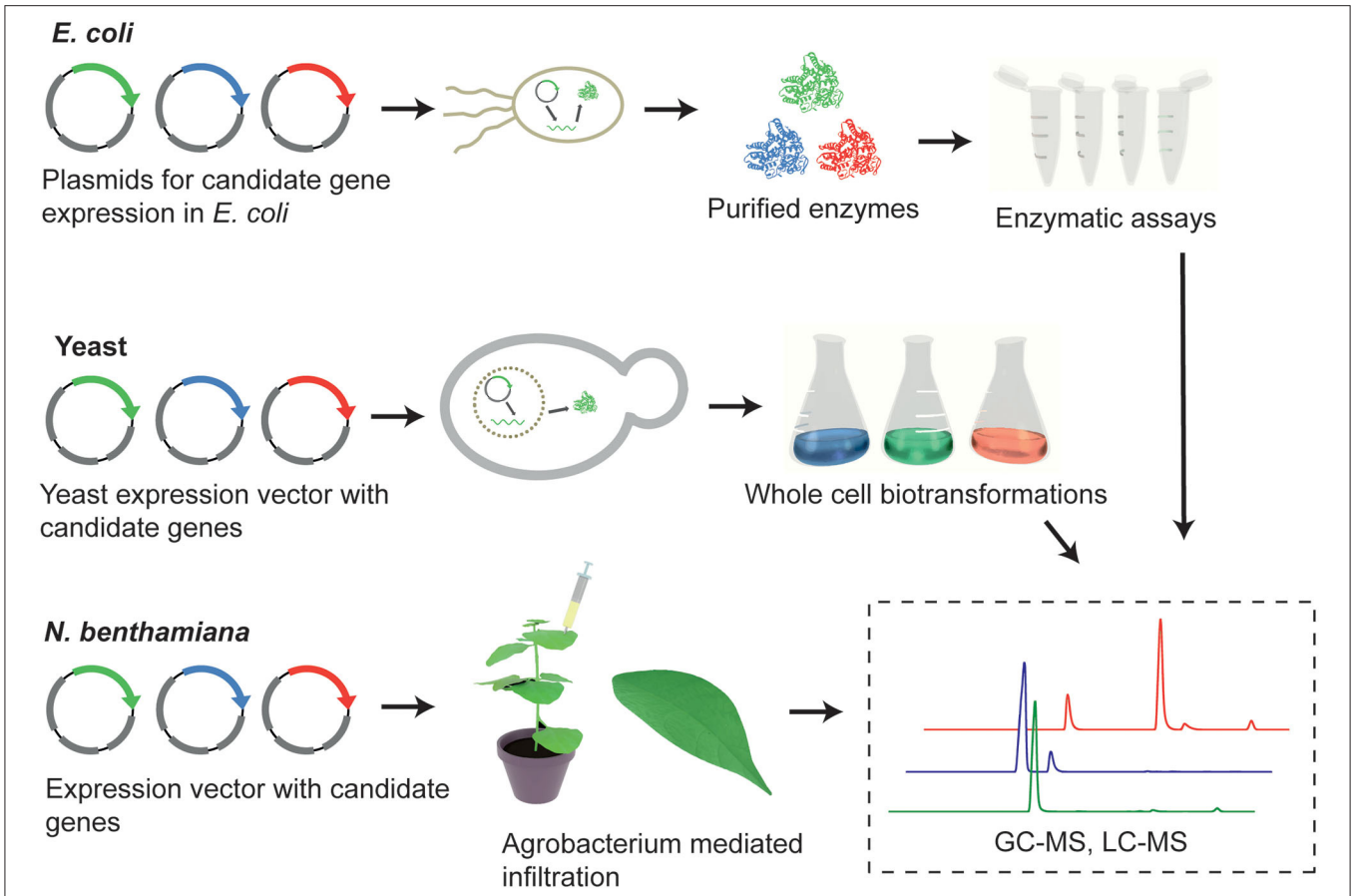

FIGURE 3 | Overview of the functional characterization methods that can be utilized to determine gene function; enzymatic assays, heterologous expression of candidate biosynthetic genes in microbial host (yeast cells), and heterologous expression *in planta* (*Nicotiana benthamiana*).

as cytochrome P450s and membrane-bound prenyltransferases, or require specific eukaryotic-type post-translational modifications. For expression of these proteins, *Saccharomyces cerevisiae* is preferred over *E. coli* because of its eukaryotic cell architecture, including the availability of more suitable protein post-translational mechanisms. Microsomal fractions of yeast cells containing active recombinant proteins can be prepared and utilized for subsequent biochemical assays (Levsh et al., 2019).

Alternatively, it is possible to exploit endogenous yeast metabolism and examine the enzymatic activity in an *in vivo* context, without purification. This method relies on the available precursors and substrates within native yeast pathways (**Figure 3**). This approach may be preferred over *in vitro* assays if enzyme purification is challenging or higher throughput is required. If the substrate of interest is not available in yeast, an exogenously supplied substrate can be used to build the desired secondary metabolite (Tu et al., 2020). Another option is to engineer yeast strains through genome engineering (e.g., CRISPR or homologous recombination) to accumulate specific precursors that are not naturally present in yeast (Luo et al., 2019; Munakata et al., 2019), or to shutdown endogenous competitive branches that deplete the precursor of interest (Moses et al., 2014).

Pathway Elucidation in *Nicotiana benthamiana*

Nicotiana benthamiana is a practical heterologous expression system for plant natural product biosynthetic pathways (**Figure 3**). It is highly amenable to *Agrobacterium*-mediated transformation, allowing the transient expression of one or, simultaneously, multiple gene(s) of interest. This plant also provides a cellular context that is similar to the native producer plant. This characteristic allows the expressed proteins to be properly folded and targeted to the correct subcellular compartment, as well as provides a natural supply of chemical precursors; coenzymes, and cofactors.

Heterologous expression of candidate genes in *N. benthama* has led to the discovery of a variety of enzymes underlying the biosynthesis of diverse high value plant-derived compounds (Levsh et al., 2019; Pluskal et al., 2019). The plant can also be used to reconstitute whole pathways for preparation of high-value compounds. For example, eight genes from *Gloriosa superba* involved in the biosynthesis of the alkaloid colchicine were discovered using *N. benthamiana* as a screening tool. Subsequently, the newly discovered genes plus eight previously described genes were used to engineer *N. benthamiana* to synthesise *N*-formyldemecolcine, a colchicine precursor, from

phenylalanine and tyrosine (Nett et al., 2020). The use of *N. benthamiana* for the heterologous production of whole pathways is discussed further in section Plants as Chasses for Production of High-Value Phytochemicals.

Virus Induced Gene Silencing

Virus-induced gene silencing (VIGS) is a reverse genetics approach commonly employed for the *in vivo* functional characterization of candidate biosynthetic genes (Moglia et al., 2016). VIGS provides direct evidence of the biological role of the gene through a loss-of-function mechanism. The system takes advantage of the plant's homology-dependent defense mechanisms in response to attack by viruses (Hileman et al., 2005). Inoculating the plant with a construct containing viral RNA and a fragment of the target gene will trigger the degradation or the inhibition of translation of the correspondent RNA, leading to the silencing of the gene of interest. The knock-down of specific genes through this system will reveal their involvement in the biosynthesis of the target natural product. The system was established and used in a variety of plants such as Madagascan periwinkle (*Catharanthus roseus*) (Qu et al., 2019) and opium poppy (Chen et al., 2018). However, a species-specific set up of the method is needed for each newly studied plant by, for instance, identifying suitable virus for the plant and efficient inoculation methods (Courdavault et al., 2020).

PLANTS AS CHASSES FOR THE PRODUCTION OF HIGH-VALUE PHYTOCHEMICALS

Expressing genes in heterologous plant systems not only enables pathway elucidation and gene function determination, but also provides new opportunities to increase and diversify the production of high-value bioactive phytochemicals. As mentioned above, *N. benthamiana* represents a valuable tool for the heterologous production of phytochemicals. For example, 16 biosynthetic genes from Himalayan mayapple (*Podophyllum hexandrum*) were transferred to *N. benthamiana* to produce precursors of the chemotherapeutic drug etoposide at milligram-scale (Schultz et al., 2019).

A major advantage of using *N. benthamina* as a production platform is the rapidity of the process; no transgenic plants need to be generated. Turnaround times are comparable to microbial systems, with the detection of products possible a few days after agroinfiltration. The process can be scaled up using vacuum agroinfiltration to reach gram-scale production of phytochemicals (Reed et al., 2017).

Optimizing Plant-Based Production of Phytochemicals

Diverse strategies have been used to enhance and optimize the production of phytochemicals *in planta*. Among these strategies include overexpressing yield-boosting enzymes such as tHMGR (truncated 3-hydroxy-3-methylglutaryl-CoA reductase, key rate-limiting enzyme in mevalonate pathway) (Reed et al., 2017) or 1-deoxy-d-xylulose 5-phosphate synthase (DXS), the first committed MEP pathway enzyme (Brückner and Tissier, 2013). Another method that can potentially lead to increased production is the suppression of competitive pathways through inactivation of endogenous genes by virus-induced gene silencing (Hasan et al., 2014) or RNA interference (Cankar et al., 2015).

The biosynthesis of natural products in plants is highly compartmentalized with different steps of biosynthetic pathways occurring in different subcellular localization (Heinig et al., 2013). To enhance the production of phytochemicals of interest, an alternative method is to alter the subcellular location of heterologously expressed enzymes by addition, removal or modification of target peptides (Reed and Osbourn, 2018). Various studies have shown the potential of this strategy in enhancing the production, with targeting biosynthetic enzymes in different subcellular compartments. Dong et al. (2016) reported that the targeting of geraniol synthase (GES) from *Valeriana officinalis* in the chloroplasts of *N. benthamina* increased the production of GES products compared to the mitochondrial- and cytosolic-targeted GES.

Emerging Metabolic Engineering Strategies

The ability of plant specialized structures, such as glandular trichomes, to synthesize and store hydrophobic and toxic metabolites has the potential to make engineering the production of these metabolites in plants more advantageous (Huchelmann et al., 2017). Conditions in trichomes and other structures may even be vital for the formation of the target compound: the final oxidative steps in the biosynthesis of artemisinin are non-enzymatic and require the non-aqueous environment of the subapical cavity of glandular trichomes to proceed (Czechowski et al., 2016). These findings highlight the challenges of producing specific secondary metabolites in microbial platforms that lack this level of structural complexity.

In addition, engineering metabolic pathways in plants is sometimes hindered by toxicity issues and growth defects, due to the cytotoxicity of the engineered compounds or the depleted pools of precursors, necessary for central metabolism. Expressing these pathways in a cell-type specific way, by taking advantage of the separation of trichomes from the rest of the plant, might offer a solution for these issues (Tissier et al., 2012). Efforts to produce secondary metabolites in trichomes through the use of trichome-specific promoters have been reported, such as; taxadiene in *N. sylvestris*, and casbene (diterpene from *Ricinus communis*), in *N. tabacum* (**Table 1**) (Rontein et al., 2008; Tissier et al., 2012).

Engineering plastids in order to optimize the yields of valuable phytochemicals has been explored. Plastid engineering has various advantages over nuclear genome engineering including an efficient homologous recombination machinery, as well as the potential for greater gene expression levels (Bock, 2015; Boehm and Bock, 2019). To enhance the yield of artemisinic acid production (the precursor for the anti-malaria drug: artemisinin), a synthetic biology strategy has been developed combining plastome and nuclear transformation (Fuentes et al., 2016). The artemisinic acid metabolic pathway was introduced into the chloroplast genome of *N. tabacum* plants. Subsequently,

TABLE 1 | Examples of engineered cellular/subcellular localization of phytochemical production in *Nicotiana* sp.

Host plant	Localization	Engineering strategy	Compound class	Compound accumulation	References
N. benthamiana	Synthetic hydrophobic organelles	Transient expression; fusing terpenoid enzymes to a microalgal lipid droplet surface protein	Diterpenoids	2.5 fold increase of target diterpenoids/diterpenoids acids	Sadre et al., 2019
N. benthamiana	Lipid bodies	Transient expression; Co-expression of α-bisabolol synthase with fatty acids biosynthesis regulators	Sesquiterpenoids	2–4 fold increase of; α-bisabolol, (E)-β -caryophyllene and α-barbatene.	Delatte et al., 2018
N. tabacum	Plastids	Stable transformation; plastome and nuclear transformation with artemisinic acid biosynthetic genes and other enzymes known to affect the metabolic flux	Sesquiterpenoids (artemisinic acid)	Accumulation of more than 120 mg/kg FW of Artemisinic acid.	Fuentes et al., 2016
N. tabacum	Glandular trichomes	Stable transformation; Casbene synthase/Trichome-specific promoters	Diterpenoids (casbene)	Accumulation of 1 mg/g FW of casbene	Tissier et al., 2012
N. sylvestris	Glandular trichomes	Stable transformation; taxadiene synthase/Trichome-specific promoters	Diterpenoids (Taxadiene)	Accumulation of 100 μg/g FW of taxadiene	Tissier et al., 2012

enzymes known to affect the metabolic flux were introduced through nuclear transformation (**Table 1**). This strategy led to identifying plants that produce high amounts of artemisinic acid (more than 120 mg of per kg biomass) (Fuentes et al., 2016; Jensen and Scharff, 2019).

A newly emerging metabolic engineering strategy is engineering synthetic hydrophobic droplets within cells that enable the accumulation and storage of lipophilic compounds such as terpenoids. For example, the synthesis of lipid droplets in transient *N. benthamiana* system was enhanced through the ectopic production of a regulator of plastid fatty acid biosynthesis and a microalgal lipid droplet surface protein. Biosynthetic steps were anchored onto the surface of the lipid droplets and high-value sesqui- or diterpenoids were efficiently produced. These engineered lipid droplets may potentially facilitate terpenoid extraction from the plant, through "trapping" of the target molecules in the oil fraction (**Table 1**) (Sadre et al., 2019). Another study demonstrated the potential of lipid bodies as hydrophobic storage organelle for sesquiterpenes molecules such as α-bisabolol (Delatte et al., 2018).

CRISPR and Cas9-associated protein systems are emerging as powerful tools to study gene function and to improve specific traits in plant species. Knocking out biosynthetic genes using CRISPR/Cas9 system has been reported in *Salvia miltiorrhiza* (tanshinone, diterpenoid) (Li et al., 2017) and *Papaver somniferum* L. (benzylisoquinoline alkaloids) (Alagoz et al., 2016). Setting up CRISPR/Cas9 systems in diverse plant species will be useful for gene function elucidation studies and will also guide future efforts to improve the yield of phytochemicals of interest in valuable medicinal plants. CRISPR/Cas9 systems also have the potential to shut down competing side branches of metabolic pathways within plants, leading to improved yields of the target compound.

Combinatorial Biosynthesis

Engineering new-to-nature metabolic pathways in plants offers the possibility to expand the natural chemical diversity of plants and create a subset of novel chemical structures with new or improved bioactivities. Combinatorial biosynthesis is an engineering strategy, based on combining biosynthetic genes from different sources in a single host, thereby establishing new enzyme–substrate combinations, that enables the generation of a suite of related compounds including many that are new-to-nature (Arendt et al., 2016). This strategy takes advantage of the hypothesis that enzymes involved in plant natural product biosynthesis have inherent relaxed substrate specificity and are often able to transform non-native substrates. Different studies aiming to explore the potential of this approach in creating novel compounds have been reported (**Table 2**).

Co-agroinfiltration of *N. benthamiana* with different expression constructs is an efficient method to test numerous enzyme combinations (Reed and Osbourn, 2018). This approach was used to generate novel β-amyrin derivatives through the expression of combinations of β-amyrin synthase and β-amyrin-oxidizing P450s from various plant species (Reed et al., 2017). In another study, the stereoselective biosynthesis of over 50 diterpene skeletons including natural variants and novel compounds was achieved *via* transient expression of combinations of class I and II diterpene synthases in *N. benthamiana* (Andersen-Ranberg et al., 2016). These terpene synthases were isolated from seven different diterpenoids producing plant species.

The generation of costunolide and parthenolide derivatives was achieved by applying a combinatorial metabolic engineering approach expressing different enzymes involved in sesquiterpenoids biosynthesis from *Tanacetum parthenium* and *Artemisia annua* (**Table 2**) (Kashkooli Beyraghdar et al., 2019). In a recent study, diverse cytochrome P450s from *Setaria*

TABLE 2 | Examples of novel compounds produced through combinatorial biosynthesis using transient expression in *N. benthamiana*.

Source of enzymes	Enzymes	Compound class	Obtained compounds	References
Tanacetum parthenium/Artemisia annua	Germacrene A synthase (GAS) Germacrene A oxidase (GAO) Costunolide synthase (COS) Parthenolide synthase (PTS) aldehyde Δ11(13) double bond reductase2 (DBR2)	Sesquiterpenoids	Costunolide and parthenolide derivatives	Kashkooli Beyraghdar et al., 2019
Oat, licorice, soy bean, barrel clover	β-amyrin synthase and β-amyrin-oxidizing P450s	Triterpenoids	β-amyrin derivatives	Reed et al., 2017
Various species	Class I/II diterpene synthases	Diterpenoids	Diverse diterpene skeletons	Andersen-Ranberg et al., 2016
Setaria italica, Sorghum bicolor, Lotus japonicus, Brassica rapa	Cytochrome P450s Glucosinolate biosynthetic genes	Isothiocyanate	Crucifalexins	Calgaro-Kozina et al., 2020

italica, *Sorghum bicolor*, *Lotus japonicus*, as well as glucosinolate biosynthetic genes from *Brassica rapa,* were heterologously expressed in *N. benthamiana*. This expression generated new-to-nature compounds with potent antifungal activity, called crucifalexins. This report showed that by broadening the set of primary metabolites that can be utilized by the core biosynthetic pathway of brassinin (isothiocyanate), it is possible to synthesize novel molecules with enhanced proprieties (Calgaro-Kozina et al., 2020).

CONCLUSION

Phytochemicals were foundational to the emergence of organic chemistry and the early development of pharmaceuticals. The structural complexity and bioactivity of phytochemicals will ensure their continued relevance in synthetic chemistry and drug discovery. With the maturity of genetic and biochemical tools for gene discovery, characterization and engineering, we are entering into a new synthetic era of phytochemistry, in which biosynthetic pathways are elucidated and high-value phytochemicals can be produced in synthetic biological chasses.

An integrative approach to gene prioritization, combining genomic transcriptomic and metabolomics, has become an efficient method for the identification of candidate biosynthetic genes. Characterization of genes through *in vitro* assays, coupled with *in vivo* validation through RNAi or VIGS, subsequently enables verification of candidate gene function. Once the pathway is uncovered, the heterologous *in planta* expression of the biosynthetic pathway is made possible, with many emerging engineering strategies available to enhance or diversify the production of the target compounds. These advances open the door to a future where diverse phytochemicals with new bioactivities and unusual structures can be routinely produced and purified from heterologous plant systems, aiding drug discovery efforts and leading to the scalable and sustainable production of valuable phytochemicals.

AUTHOR CONTRIBUTIONS

KE conceived of the manuscript and wrote the first draft. Both authors prepared figures, edited text, and approved the manuscript for submission.

FUNDING

This work was supported by a UK Research and Innovation Future Leaders Fellowship to BRL (MR/S01862X/1).

REFERENCES

Alagoz, Y., Gurkok, T., Zhang, B., and Unver, T. (2016). Manipulating the biosynthesis of bioactive compound alkaloids for next-generation metabolic engineering in opium poppy Using CRISPR-Cas 9 genome editing technology. *Sci. Rep.* 6:30910. doi: 10.1038/srep30910

Andersen-Ranberg, J., Kongstad, K. T., Nielsen, M. T., Jensen, N. B., Pateraki, I., Bach, S. S., et al. (2016). Expanding the landscape of diterpene structural diversity through stereochemically controlled combinatorial biosynthesis. *Angew. Chemie Int. Ed.* 55, 2142–2146. doi: 10.1002/anie.201510650

Arendt, P., Pollier, J., Callewaert, N., and Goossens, A. (2016). Synthetic biology for production of natural and new-to-nature terpenoids in photosynthetic organisms. *Plant J.* 87, 16–37. doi: 10.1111/tpj.13138

Bock, R. (2015). Engineering plastid genomes: methods, tools, and applications in basic research and biotechnology. *Annu. Rev. Plant Biol.* 66, 211–241. doi: 10.1146/annurev-arplant-050213-040212

Boehm, C. R., and Bock, R. (2019). Recent advances and current challenges in synthetic biology of the plastid genetic system and metabolism. *Plant Physiol.* 179, 794–802. doi: 10.1104/pp.18.00767

Brückner, K., and Tissier, A. (2013). High-level diterpene production by transient expression in *Nicotiana benthamiana*. *Plant Methods* 9:46. doi: 10.1186/1746-4811-9-46

Calgaro-Kozina, A., Vuu, K. M., Keasling, J. D., Loqué, D., Sattely, E. S., and Shih, P. M. (2020). Engineering plant synthetic pathways for the biosynthesis of novel antifungals. *ACS Cent. Sci.* 6, 1394–1400. doi: 10.1021/acscentsci.0c00241

Cankar, K., Jongedijk, E., Klompmaker, M., Majdic, T., Mumm, R., Bouwmeester, H., et al. (2015). (+)-Valencene production in *Nicotiana benthamiana* is increased by down-regulation of competing pathways. *Biotechnol. J.* 10, 180–189. doi: 10.1002/biot.201400288

Caputi, L., Franke, J., Farrow, S. C., Chung, K., Payne, R. M. E., Nguyen, T. D., et al. (2018). Missing enzymes in the biosynthesis of the anticancer drug vinblastine in Madagascar periwinkle. *Science* 360, 1235–1239. doi: 10.1126/science.aat4100

Chen, X., Hagel, J. M., Chang, L., Tucker, J. E., Shiigi, S. A., Yelpaala, Y., et al. (2018). A pathogenesis-related 10 protein catalyzes the final step in thebaine biosynthesis article. *Nat. Chem. Biol.* 14, 738–743. doi: 10.1038/s41589-018-0059-7

Courdavault, V., Besseau, S., Oudin, A., Papon, N., and O'Connor, S. E. (2020). Virus-induced gene silencing: hush genes to make them talk. *Trends Plant Sci.* 25, 714–715. doi: 10.1016/j.tplants.2020.02.013

Czechowski, T., Larson, T. R., Catania, T. M., Harvey, D., Brown, G. D., and Graham, I. A. (2016). *Artemisia annua* mutant impaired in Artemisinin synthesis demonstrates importance of nonenzymatic conversion in terpenoid metabolism. *Proc. Natl. Acad. Sci. U.S.A.* 113, 15150–15155. doi: 10.1073/pnas.1611567113

Delatte, T. L., Scaiola, G., Molenaar, J., de Sousa Farias, K., Alves Gomes Albertti, L., Busscher, J., et al. (2018). Engineering storage capacity for volatile sesquiterpenes in *Nicotiana benthamiana* leaves. *Plant Biotechnol. J.* 16, 1997–2006. doi: 10.1111/pbi.12933

Dong, L., Jongedijk, E., Bouwmeester, H., and Van Der Krol, A. (2016). Monoterpene biosynthesis potential of plant subcellular compartments. *New Phytol.* 209, 679–690. doi: 10.1111/nph.13629

Duke, M. V., Paul, R. N., Elsohly, H. N., Sturtz, G., and Duke, S. O. (1994). Localization of artemisinin and artemisitene in foliar tissues of glanded and glandless biotypes of *Artemisia annua* L. *Int. J. Plant Sci.* 155, 365–372. doi: 10.1086/297173

Facchini, P. J., and De Luca, V. (1995). Phloem-specific expression of tyrosine/dopa decarboxylase genes and the biosynthesis of isoquinoline alkaloids in opium poppy. *Plant Cell* 7, 1811–1821. doi: 10.2307/3870189

Freund, D. M., and Hegeman, A. D. (2017). Recent advances in stable isotope-enabled mass spectrometry-based plant metabolomics. *Curr. Opin. Biotechnol.* 43, 41–48. doi: 10.1016/j.copbio.2016.08.002

Fuentes, P., Zhou, F., Erban, A., Karcher, D., Kopka, J., and Bock, R. (2016). A new synthetic biology approach allows transfer of an entire metabolic pathway from a medicinal plant to a biomass crop. *Elife* 5:e13664. doi: 10.7554/eLife.13664.020

Hasan, M. M., Kim, H. S., Jeon, J. H., Kim, S. H., Moon, B. K., Song, J. Y., et al. (2014). Metabolic engineering of *Nicotiana benthamiana* for the increased production of taxadiene. *Plant Cell Rep.* 33, 895–904. doi: 10.1007/s00299-014-1568-9

Heinig, U., Gutensohn, M., Dudareva, N., and Aharoni, A. (2013). The challenges of cellular compartmentalization in plant metabolic engineering. *Curr. Opin. Biotechnol.* 24, 239–246. doi: 10.1016/j.copbio.2012.11.006

Hileman, L. C., Drea, S., De Martino, G., Litt, A., and Irish, V. F. (2005). Virus-induced gene silencing is an effective tool for assaying gene function in the basal eudicot species *Papaver somniferum* (opium poppy). *Plant J.* 44, 334–341. doi: 10.1111/j.1365-313X.2005.02520.x

Hodgson, H., De La Peña, R., Stephenson, M. J., Thimmappa, R., Vincent, J. L., Sattely, E. S., et al. (2019). Identification of key enzymes responsible for protolimonoid biosynthesis in plants: opening the door to azadirachtin production. *Proc. Natl. Acad. Sci. U.S.A.* 116, 17096–17104. doi: 10.1073/pnas.1906083116

Huchelmann, A., Boutry, M., and Hachez, C. (2017). Plant glandular trichomes: natural cell factories of high biotechnological interest. *Plant Physiol.* 175, 6–22. doi: 10.1104/pp.17.00727

Jensen, P. E., and Scharff, L. B. (2019). Engineering of plastids to optimize the production of high-value metabolites and proteins. *Curr. Opin. Biotechnol.* 59, 8–15. doi: 10.1016/j.copbio.2019.01.009

Kashkooli Beyraghdar, A., van der Krol, A. R., Rabe, P., Dickschat, J. S., and Bouwmeester, H. (2019). Substrate promiscuity of enzymes from the sesquiterpene biosynthetic pathways from *Artemisia annua* and *Tanacetum parthenium* allows for novel combinatorial sesquiterpene production. *Metab. Eng.* 54, 12–23. doi: 10.1016/j.ymben.2019.01.007

Kim, C. Y., Mitchell, A. J., Glinkerman, C. M., Li, F. S., Pluskal, T., and Weng, J. K. (2020). The chloroalkaloid (−)-acutumine is biosynthesized *via* a Fe(II)- and 2-oxoglutarate-dependent halogenase in Menispermaceae plants. *Nat. Commun.* 11:1867. doi: 10.1038/s41467-020-15777-w

Lechner, A., Brunk, E., and Keasling, J. D. (2016). The need for integrated approaches in metabolic engineering. *Cold Spring Harb. Perspect. Biol.* 8:a023903. doi: 10.1101/cshperspect.a023903

Lee, E. J., and Facchini, P. J. (2011). Tyrosine aminotransferase contributes to benzylisoquinoline alkaloid biosynthesis in opium poppy. *Plant Physiol.* 157, 1067–1078. doi: 10.1104/pp.111.185512

Lee, E. K., Jin, Y. W., Park, J. H., Yoo, Y. M., Hong, S. M., Amir, R., et al. (2010). Cultured cambial meristematic cells as a source of plant natural products. *Nat. Biotechnol.* 28, 1213–1217. doi: 10.1038/nbt.1693

Levsh, O., Pluskal, T., Carballo, V., Mitchell, A. J., and Weng, J. K. (2019). Independent evolution of rosmarinic acid biosynthesis in two sister families under the Lamiids clade of flowering plants. *J. Biol. Chem.* 294, 15193–15205. doi: 10.1074/jbc.RA119.010454

Li, B., Cui, G., Shen, G., Zhan, Z., Huang, L., Chen, J., et al. (2017). Targeted mutagenesis in the medicinal plant *Salvia miltiorrhiza*. *Sci. Rep.* 7:43320. doi: 10.1038/srep43320

Li, S., Li, Y., and Smolke, C. D. (2018). Strategies for microbial synthesis of high-value phytochemicals. *Nat. Chem.* 10, 395–404. doi: 10.1038/s41557-018-0013-z

Lichman, B. R. (2020). The scaffold-forming steps of plant alkaloid biosynthesis. *Nat. Prod. Rep.* doi: 10.1039/D0NP00031K

Lichman, B. R., Godden, G. T., Hamilton, J. P., Palmer, L., Kamileen, M. O., Zhao, D., et al. (2020). The evolutionary origins of the cat attractant nepetalactone in catnip. *Sci. Adv.* 6:eaba0721. doi: 10.1126/sciadv.aba0721

Lichman, B. R., Kamileen, M. O., Titchiner, G. R., Stevenson, C. E. M., Lawson, D. M., and Connor, S. E. O. (2019). Uncoupled activation and cyclization in catmint reductive terpenoid biosynthesis. *Nat. Chem. Biol.* 15, 71–79. doi: 10.1038/s41589-018-0185-2

Liu, Z., Suarez Duran, H. G., Harnvanichvech, Y., Stephenson, M. J., Schranz, M. E., Nelson, D., et al. (2020). Drivers of metabolic diversification: how dynamic genomic neighbourhoods generate new biosynthetic pathways in the Brassicaceae. *New Phytol.* 227, 1109–1123. doi: 10.1111/nph.16338

Luo, X., Reiter, M. A., d'Espaux, L., Wong, J., Denby, C. M., Lechner, A., et al. (2019). Complete biosynthesis of cannabinoids and their unnatural analogues in yeast. *Nature* 567, 123–126. doi: 10.1038/s41586-019-0978-9

Mitchell, A. J., and Weng, J. K. (2019). Unleashing the synthetic power of plant oxygenases: from mechanism to application. *Plant Physiol.* 179, 813–829. doi: 10.1104/pp.18.01223

Moglia, A., Acquadro, A., Eljounaidi, K., Milani, A. M., Cagliero, C., Rubiolo, P., et al. (2016). Genome-wide identification of BAHD acyltransferases and *in vivo* characterization of HQT-like enzymes involved in caffeoylquinic acid synthesis in globe artichoke. *Front. Plant Sci.* 7:1424. doi: 10.3389/fpls.2016.01424

Moses, T., Mehrshahi, P., Smith, A. G., and Goossens, A. (2017). Synthetic biology approaches for the production of plant metabolites in unicellular organisms. *J. Exp. Bot.* 68, 4057–4074. doi: 10.1093/jxb/erx119

Moses, T., Pollier, J., Almagro, L., Buyst, D., Van Montagu, M., Pedreño, M. A., et al. (2014). Combinatorial biosynthesis of sapogenins and saponins in *Saccharomyces cerevisiae* using a C-16α hydroxylase from *Bupleurum falcatum*. *Proc. Natl. Acad. Sci. U.S.A.* 111, 1634–1639. doi: 10.1073/pnas.1323369111

Munakata, R., Takemura, T., Tatsumi, K., Moriyoshi, E., Yanagihara, K., Sugiyama, A., et al. (2019). Isolation of *Artemisia capillaris* membrane-bound di-prenyltransferase for phenylpropanoids and redesign of artepillin C in yeast. *Commun. Biol.* 2:384. doi: 10.1038/s42003-019-0630-0

Nett, R. S., Lau, W., and Sattely, E. S. (2020). Discovery and engineering of colchicine alkaloid biosynthesis. *Nature* 584, 148–153. doi: 10.1038/s41586-020-2546-8

Nicolaou, K. C., and Rigol, S. (2020). Perspectives from nearly five decades of total synthesis of natural products and their analogues for biology and medicine. *Nat. Prod. Rep.* doi: 10.1039/D0NP00003E

Nützmann, H.-W., Scazzocchio, C., and Osbourn, A. (2018). Metabolic gene clusters in eukaryotes. *Annu. Rev. Genet.* 52, 159–183. doi: 10.1146/annurev-genet-120417-031237

Nützmann, H. W., Huang, A., and Osbourn, A. (2016). Plant metabolic clusters – from genetics to genomics. *New Phytol.* 211, 771–789. doi: 10.1111/nph.13981

Pluskal, T., Torrens-Spence, M. P., Fallon, T. R., De Abreu, A., Shi, C. H., and Weng, J. K. (2019). The biosynthetic origin of psychoactive kavalactones in kava. *Nat. Plants* 5, 867–878. doi: 10.1038/s41477-019-0474-0

Qu, Y., Safonova, O., and De Luca, V. (2019). Completion of the canonical pathway for assembly of anticancer drugs vincristine/vinblastine in *Catharanthus roseus*. *Plant J.* 97, 257–266. doi: 10.1111/tpj.14111

Reed, J., and Osbourn, A. (2018). Engineering terpenoid production through transient expression in *Nicotiana benthamiana*. *Plant Cell Rep.* 37, 1431–1441. doi: 10.1007/s00299-018-2296-3

Reed, J., Stephenson, M. J., Miettinen, K., Brouwer, B., Leveau, A., Brett, P., et al. (2017). A translational synthetic biology platform for rapid access to gram-scale quantities of novel drug-like molecules. *Metab. Eng.* 42, 185–193. doi: 10.1016/j.ymben.2017.06.012

Rontein, D., Onillon, S., Herbette, G., Lesot, A., Werck-Reichhart, D., Sallaud, C., et al. (2008). CYP725A4 from yew catalyzes complex structural rearrangement of taxa-4(5),11(12)-diene into the cyclic ether 5(12)-oxa-3(11)-cyclotaxane. *J. Biol. Chem.* 283, 6067–6075. doi: 10.1074/jbc.M708950200

Roselli, S., Olry, A., Vautrin, S., Coriton, O., Ritchie, D., Galati, G., et al. (2017). A bacterial artificial chromosome (BAC) genomic approach reveals partial clustering of the furanocoumarin pathway genes in parsnip. *Plant J.* 89, 1119–1132. doi: 10.1111/tpj.13450

Sadre, R., Kuo, P., Chen, J., Yang, Y., Banerjee, A., Benning, C., et al. (2019). Cytosolic lipid droplets as engineered organelles for production and accumulation of terpenoid biomaterials in leaves. *Nat. Commun.* 10:853. doi: 10.1038/s41467-019-08515-4

Sadre, R., Magallanes-Lundback, M., Pradhan, S., Salim, V., Mesberg, A., Jones, A. D., et al. (2016). Metabolite diversity in alkaloid biosynthesis: a multilane (diastereomer) highway for camptothecin synthesis in *camptotheca acuminata*. *Plant Cell* 28, 1926–1944. doi: 10.1105/tpc.16.00193

Schultz, B. J., Kim, S. Y., Lau, W., and Sattely, E. S. (2019). Total biosynthesis for milligram-scale production of etoposide intermediates in a plant chassis. *J. Am. Chem. Soc.* 141, 19231–19235. doi: 10.1021/jacs.9b10717

Shen, Q., Zhang, L., Liao, Z., Wang, S., Yan, T., Shi, P., et al. (2018). The genome of *Artemisia annua* provides insight into the evolution of asteraceae family and artemisinin biosynthesis. *Mol. Plant* 11, 776–788. doi: 10.1016/j.molp.2018.03.015

Tissier, A., Sallaud, C., and Rontein, D. (2012). "Tobacco trichomes as a platform for terpenoid biosynthesis engineering," in *Isoprenoid Synthesis in Plants and Microorganisms*, eds. T. Bach and M. Rohmer (New York, NY: Springer). p.271–283. doi: 10.1007/978-1-4614-4063-5_18

Torrens-Spence, M. P., Pluskal, T., Li, F. S., Carballo, V., and Weng, J. K. (2018). Complete pathway elucidation and heterologous reconstitution of rhodiola salidroside biosynthesis. *Mol. Plant* 11, 205–217. doi: 10.1016/j.molp.2017.12.007

Townsend, T., Segura, V., Chigeza, G., Penfield, T., Rae, A., Harvey, D., et al. (2013). The use of combining ability analysis to identify elite parents for *Artemisia annua* F1 hybrid production. *PLoS ONE* 8:e61989. doi: 10.1371/journal.pone.0061989

Tu, L., Su, P., Zhang, Z., Gao, L., Wang, J., Hu, T., et al. (2020). Genome of *Tripterygium wilfordii* and identification of cytochrome P450 involved in triptolide biosynthesis. *Nat. Commun.* 11:971. doi: 10.1038/s41467-020-14776-1

Yoder, R. A., and Johnston, J. N. (2005). A case study in biomimetic total synthesis: polyolefin carbocyclizations to terpenes and steroids. *Chem. Rev.* 105, 4730–4756. doi: 10.1021/cr040623l

Conflict of Interest: The authors declare that the research was conducted in the absence of any commercial or financial relationships that could be construed as a potential conflict of interest.

Copyright © 2020 Eljounaidi and Lichman. This is an open-access article distributed under the terms of the Creative Commons Attribution License (CC BY). The use, distribution or reproduction in other forums is permitted, provided the original author(s) and the copyright owner(s) are credited and that the original publication in this journal is cited, in accordance with accepted academic practice. No use, distribution or reproduction is permitted which does not comply with these terms.

frontiers in Chemistry

ORIGINAL RESEARCH
published: 10 November 2020
doi: 10.3389/fchem.2020.592904

Nitrogen-Doped Mesoporous Carbon Microspheres by Spray Drying-Vapor Deposition for High-Performance Supercapacitor

Xiaoran Sun[1,2], Yueqi Kong[2], Yang Liu[3], Liang Zhou[4], Ashok Kumar Nanjundan[2], Xiaodan Huang[2*] and Chengzhong Yu[2,3]*

[1] Institute of Photovoltaics, Southwest Petroleum University, Chengdu, China, [2] Australian Institute for Bioengineering and Nanotechnology, The University of Queensland, Brisbane, QLD, Australia, [3] School of Chemistry and Molecular Engineering, East China Normal University, Shanghai, China, [4] State Key Laboratory of Advanced Technology for Materials Synthesis and Processing, Wuhan University of Technology, Wuhan, China

OPEN ACCESS

Edited by:
Jianping Yang,
Donghua University, China

Reviewed by:
Yiyong Mai,
Shanghai Jiao Tong University, China
Guiyin Xu,
Massachusetts Institute of Technology, United States
Qin Yue,
University of Electronic Science and Technology of China, China

***Correspondence:**
Xiaodan Huang
x.huang@uq.edu.au
Ashok Kumar Nanjundan
ashok.nanjundan@uq.edu.au

Specialty section:
This article was submitted to Green and Sustainable Chemistry, a section of the journal Frontiers in Chemistry

Received: 08 August 2020
Accepted: 05 October 2020
Published: 10 November 2020

Citation:
Sun X, Kong Y, Liu Y, Zhou L, Nanjundan AK, Huang X and Yu C (2020) Nitrogen-Doped Mesoporous Carbon Microspheres by Spray Drying-Vapor Deposition for High-Performance Supercapacitor. Front. Chem. 8:592904. doi: 10.3389/fchem.2020.592904

Nitrogen-doped mesoporous carbon microspheres have been successfully synthesized via a spray drying-vapor deposition method for the first time, using commercial Ludox silica nanoparticles as hard templates. Compared to freeze-drying and air-drying methods, mesoporous carbon with a higher packing density can be achieved through the spray drying method. Vapor deposition of polypyrrole followed by carbonization and etching is beneficial for the generation of ultra-thin carbon network. The mesoporous carbon microspheres possess a mesopore-dominate (95%) high surface area of 1528 $m^2\ g^{-1}$, a wall thickness of 1.8 nm, and a nitrogen content of 8 at% in the framework. Benefiting from the increased apparent density, high mesopore surface area, and considerable nitrogen doping, the resultant mesoporous carbon microspheres show superior gravimetric/volumetric capacitance of 533.6 F g^{-1} and 208.1 F cm^{-3}, good rate performance and excellent cycling stability in electric double-layer capacitors.

Keywords: mesoporous carbon, microspheres, spray drying, vapor deposition, supercapacitor

INTRODUCTION

Electric double layer capacitors (EDLCs), a typical type of supercapacitors, are appealing power sources for consumer electronics and uninterruptible power supplies owing to their high power density, rapid charge/discharge, environmental friendliness, and long cycling life (Simon and Gogotsi, 2008, 2020; Choi et al., 2012; Wang et al., 2012; Liu et al., 2019, 2020; Noori et al., 2019; Li et al., 2020). Porous carbon materials have attracted tremendous attention as electrode materials for supercapacitors because of their high specific surface area, high conductivity, high chemical stability and tunable porous structures (Zhai et al., 2011; Tian et al., 2016, 2018; Hou et al., 2018; Wang et al., 2018; Liu et al., 2019; Shao et al., 2020). Microporous carbons with pore sizes smaller than 2 nm and high surface areas have been widely utilized in EDLCs (Zhang et al., 2009; Yan et al., 2014; Gadipelli et al., 2020). It was found that the capacitance reached a plateau when the microporous surface area went above 1,500 $m^2\ g^{-1}$ (Barbieri et al., 2005; Weingarth et al., 2014), indicating that the total surface area measured by gas sorption methods is not fully electrochemically accessible. The partially inaccessible small micropores also decreased the rate performance of microporous carbon (Zhang and Zhao, 2009). In the past decades, mesoporous carbon materials with pore sizes

of 2–50 nm have become promising candidates for EDLC applications (Simon and Gogotsi, 2008, 2020; Zhai et al., 2011; Choi et al., 2012; Wang et al., 2012, 2018; Tian et al., 2016, 2018; Hou et al., 2018; Liu et al., 2019, 2020; Noori et al., 2019; Li et al., 2020; Shao et al., 2020). Huang et al. (2008) demonstrated that the capacitance normalized by surface area was higher in mesoporous carbon compared to microporous carbon in aqueous solutions, suggesting a high capacitance can be achieved in carbon materials with high mesoporous surface area. Qian et al. reported the synthesis of mesoporous carbon with a high total surface area of 1,300 m^2 g^{-1} and a high percentage of mesopore surface area (1,200 m^2 g^{-1}). This material showed a high capacitance of 340 F g^{-1} at 1 A g^{-1} and 66% capacity retention at 10 A g^{-1} due to the small pore size of 2–3 nm (Qian et al., 2014). Li et al. (2013) reported the fabrication of protein-derived carbons with a high mesopore surface area percentage of ∼93% but a relatively small total surface area of 810 m^2 g^{-1}. There are few reports on the synthesis of mesoporous carbons with large mesopores and high mesopore surface areas (>1,400 m^2 g^{-1}) for supercapacitor applications.

In general, mesoporous carbons can be synthesized through soft-templating or hard-templating methods (Li et al., 2016). Surfactant molecules are generally used in the soft-templating method (Wei et al., 2013; Shen et al., 2015) and in the synthesis of mesoporous silicas as templates for the hard-templating approach (Ryoo et al., 1999). Instead of surfactants, using commercial Ludox silica nanoparticles as porogens is a convenient approach for the surfactant-free synthesis of mesoporous carbon (Han et al., 2000). However, the synthesis was usually conducted in solutions (Han and Hyeon, 1999), resulting in carbon materials with undefined morphology and relatively low packing density, unfavorable for the volumetric performance of EDLCs (Gogotsi and Simon, 2011; Wang et al., 2016). The packing density can be improved by controlling either the nanostructure or the micro-morphology (Li et al., 2015; Lin et al., 2016). Cui et al. reported the synthesis of porous carbon microspheres with increased packing density because small-sized spheres can be accommodated into the packing voids of large-sized spheres (Li et al., 2015). However, oil/water microemulsion was applied in the morphology control, not suitable for scalable synthesis. Spray drying, on the other hand, is a facile method for the synthesis of multi-shelled metal oxides (Zhou et al., 2013) and the assembly of colloidal silica nanoparticles into microspheres (Tan et al., 2012). When Ludox silica templates, resorcinol and formaldehyde as carbon precursors were used via the spray drying method, silica/polymer microspheres and subsequently mesoporous carbon microspheres were synthesized (Li et al., 2014), with a surface area below 1,200 m^2 g^{-1}. Wang et al. reported the synthesis of a partially graphitized porous carbon by spray drying Ludox silica with sucrose (Wang et al., 2015a,b). However, the capacitance of the obtained carbon microspheres is only 91 F g^{-1} at 10 mV s^{-1} due to the presence of a high proportion of micropores.

The choice of carbon precursors is crucial for replicating the template morphology with a homogenous carbon layer. Compared to resorcinol/formaldehyde or sucrose used in conventional infiltration and polyfurfuryl alcohol used in high-temperature chemical vapor deposition (CVD) (Lin et al., 2015), volatile precursors such as pyrrole applied in low-temperature vapor deposition achieved a uniform coating and maintained the structural stability of the template (Han et al., 2013). The high nitrogen content coming from carbonized polypyrrole contributed further to pseudo-capacitance and improved the overall capacitance of carbon materials (Shen and Fan, 2013; Wang et al., 2014). Ferrero et al. (2015) reported the preparation of N-doped hollow carbon nanospheres using vapor deposition of pyrrole on preformed silica nanoparticles, which have a faithfully replicated morphology of the silica template but a low packing density. It remains a challenge to use a convenient approach and synthesize mesoporous carbon microspheres with a high packing density, large mesopores and high mesopore surface areas for supercapacitors.

Herein, we report the preparation of nitrogen-doped mesoporous carbon microspheres by a spray drying-vapor deposition method for the first time, using commercial Ludox colloidal silica nanoparticles as porogens. The resultant mesoporous carbon microspheres have a mesopore-dominant (95%) high surface area (1,528 m^2 g^{-1}) with 8 At% nitrogen doping, an increased apparent density, and consequently excellent gravimetric/volumetric performance as an electrode material in EDLCs.

EXPERIMENTAL SECTION

Material Synthesis

Highly Nitrogen-doped mesoporous carbon microspheres were synthesized via spray drying and vapor deposition method. Typically, Ludox SM colloidal silica (40 g, 30 wt.% suspension in H_2O, Sigma-Aldrich) was mixed with iron chloride ($FeCl_3$) solution (0.3 M, 25 ml) and deionized water (200 ml). The mixture was ultrasonicated for over 1 h and kept stirring while spray drying. The suspension was spray dried at an inlet temperature of 220°C, a pump rate of 1.5 ml/min, and N_2 gas flow of 60 ml/min. The spray dried sample was coated with pyrrole vapor for 48 h in 50°C oven before carbonized at 800°C for 10 h in a nitrogen atmosphere. Then the composite was washed with 5 wt.% hydrofluoric acid (HF) to remove the sacrificial silica template. The resulting product was centrifuged and washed repeatedly with deionized water and dried in an oven (addressed as MC-7-SD). For comparison, all other procedures remained the same, but the suspension was dried using 50°C oven or freeze-drier after sonication. The resultant was addressed as MC-7-AD or MC-7-FD, respectively. Activated carbon Darco® G-60 (-100 mesh, Sigma-Aldrich) was also used for comparison.

Characterization

Field emission scanning electron microscopy (SEM) images were obtained using JEOL 7001. Transmission electron microscopy (TEM) images were taken using JEOL 1010 at 100 kV. High resolution transmission electron microscopy (HRTEM) was conducted under a Tecnai G2 F20 (FEI) operated at 200 kV. Nitrogen sorption isotherms were measured by Tristar II Surface

Area and Porosity analyser (Micromeritics). The sample was degassed at 180°C overnight under vacuum before the test. X-ray photoelectron spectroscopy (XPS) was recorded on a monochromatic Al Kα (1,486.6 eV) X-ray source and 165 mm hemispherical electron energy analyzer. The elemental analysis was carried out using a Thermo Flash EA-1112 Series NCHS-O analyzer. Dynamic light scattering (DLS) measurement was conducted on a Malvern Zetasizer Nano ZS instrument at room temperature. Thermogravimetric (TG) analysis was performed using METTLER TOLEDO TGA/DSC1 STAR^e System from 25 to 900°C in air with a heating rate of 5°C min^{-1}.

Electrochemical Measurements

A slurry composing of active material (80 wt.%), carbon black (10 wt.%), and polytetrafluoroethylene (PTFE, Sigma-Aldrich, 60 wt.% dispersion in H_2O) (10 wt.%) was mixed with ethanol. The working electrode was prepared by encapsulating mixture into Ni foam and dried at 100°C overnight. A three-electrode system was used to measure the electrochemical performance in 6 M KOH solution. Ni foam and Hg/HgO electrode were served as counter and reference electrode, respectively. Electrochemical measurements were carried out over a 1 V potential window (−1∼0 V vs. Hg/HgO) using Solartron Multistat 1480. According to the capacitance value, the energy density (E) and power density (P) can be calculated using the following equations:

$$E = CV^2/2$$

$$P = E/t$$

where C is the specific capacitance, V is the operating voltage, and t is the discharge time.

RESULTS AND DISCUSSION

Nitrogen-doped mesoporous carbon microspheres were synthesized by a spray drying-vapor deposition process (**Figure 1A**). Typically, commercially available colloidal silica nanoparticles (Ludox SM) with a diameter of around 7 nm (**Supplementary Figures 1a,b**) were dispersed in water. The suspension was atomized in the chamber of a spray drier to form droplets that were then dried in flight. Silica nanoparticles were agglomerated during the drying process, forming microspheres under contraction force. As a catalyst, iron chloride was added to the silica/water suspension and embedded in microspheres after spray drying for the oxidative polymerization of pyrrole. Then, pyrrole vapor was introduced to form a thin layer of polypyrrole coating on silica nanoparticles. After carbonization at 800°C in a nitrogen atmosphere and removing sacrificial silica template, N-doped mesoporous carbon microspheres were obtained (named as MC-7-SD). In order to highlight the advantage of spray drying method, silica aggregates were also synthesized using air-drying (Gierszal and Jaronic, 2007) and freeze-drying (Zhang et al., 2005) methods as reported in the literature for comparison. The resultant mesoporous carbons after 800°C carbonization and etching were denoted as MC-7-AD and MC-7-FD, respectively.

The apparent densities of MC-7-SD, MC-7-AD and MC-7-FD were measured as reported in the literature (Liu et al., 2016; Pei et al., 2016) and are shown in **Figure 1B**. MC-7-SD shows a higher apparent density (0.50 g cm^{-3}) compared to MC-7-AD (0.31 g cm^{-3}) and MC-7-FD (0.15 g cm^{-3}), slightly lower than that of a commercial activated carbon (0.54 g cm^{-3}). The obvious difference in apparent densities is explained in scanning electron microscopy (SEM) observations. The low magnification SEM image (**Figure 2a**) reveals that MC-7-SD has a micro-sized spherical morphology with a particle size of 700–5,000 nm (**Supplementary Figure 1c**). The invagination zones on the granules are probably caused by temperature (Biswas et al., 2016) and/or the polydispersity of constituent nanoparticles (Sen et al., 2012) during rapid spray drying. It is reported that the spherical morphology exhibits a higher packing density compared to other morphologies because the packing voids from large spheres accommodate smaller ones (Ying et al., 2004; Pan et al., 2020; Yue et al., 2020a,b). For comparison, MC-7-AD and MC-7-FD show fragmented morphologies with random particle packing (**Figures 2b,c**), leading to lower packing densities.

Transmission electron microscopy (TEM) was used to reveal the mesostructure of MC-7-SD, MC-7-AD, and MC-7-FD. TEM image of MC-7-SD (**Figure 2d**) shows a mesoporous micro-spherical morphology. As shown in **Figure 2d** inset, the thickness of the mesoporous carbon wall is around 1.8 nm. Different from MC-7-SD, the morphologies of MC-7-AD and MC-7-FD samples are monoliths with rich mesopores (**Figures 2e,f**). After measurement from the inset high magnification TEM images, the mesopore sizes in MC-7-AD and MC-7-FD are 7-8 nm, and the thicknesses of carbon layers are 3.0 and 3.1 nm, respectively. To fully characterize the porous structure of mesoporous carbon materials, nitrogen sorption analysis was employed. As shown in **Figure 3A**, all three samples show typical IV isotherms with H_2 hysteresis loops. The adsorption branches of MC-7-AD and MC-7-FD show major capillary condensation steps in relative pressure (P/P_0) range of 0.7–0.8 and >0.9, indicating the existence of large mesopores and packing voids. The adsorption isotherm of MC-7-SD shows a capillary condensation step at a relatively lower P/P_0 of 0.6–0.75, indicating a relatively small pore size. No capillary condensation is observed at $P/P_0 > 0.9$, suggesting small-sized spheres accommodates into the packing voids of large-sized spheres. The pore size distributions (PSD) calculated by Barrett–Joyner–Halanda (BJH) model from adsorption branches are shown in **Figure 3B**. The PSD of MC-7-AD and MC-7-FD show a peak centered at 7 nm, which is close to the size of Ludox silica templates (**Supplementary Figures 1a,b**). A shoulder peak at 2–5 nm can also be observed. Unlike MC-7-AD and MC-7-FD, MC-7-SD shows a wide PSD in the range of 2–9 nm, which can be attributed to the small mesoporous packing voids in the microspheres (Ying et al., 2004; Pan et al., 2020; Yue et al., 2020a,b).

As summarized in **Table 1**, the total pore volume of MC-7-AD, MC-7-FD, and MC-7-SD are 2.7, 2.3, and 1.6 cm^3 g^{-1}, respectively. MC-7-SD shows the lowest total pore volume because most of its pore volume is attributed by mesopores,

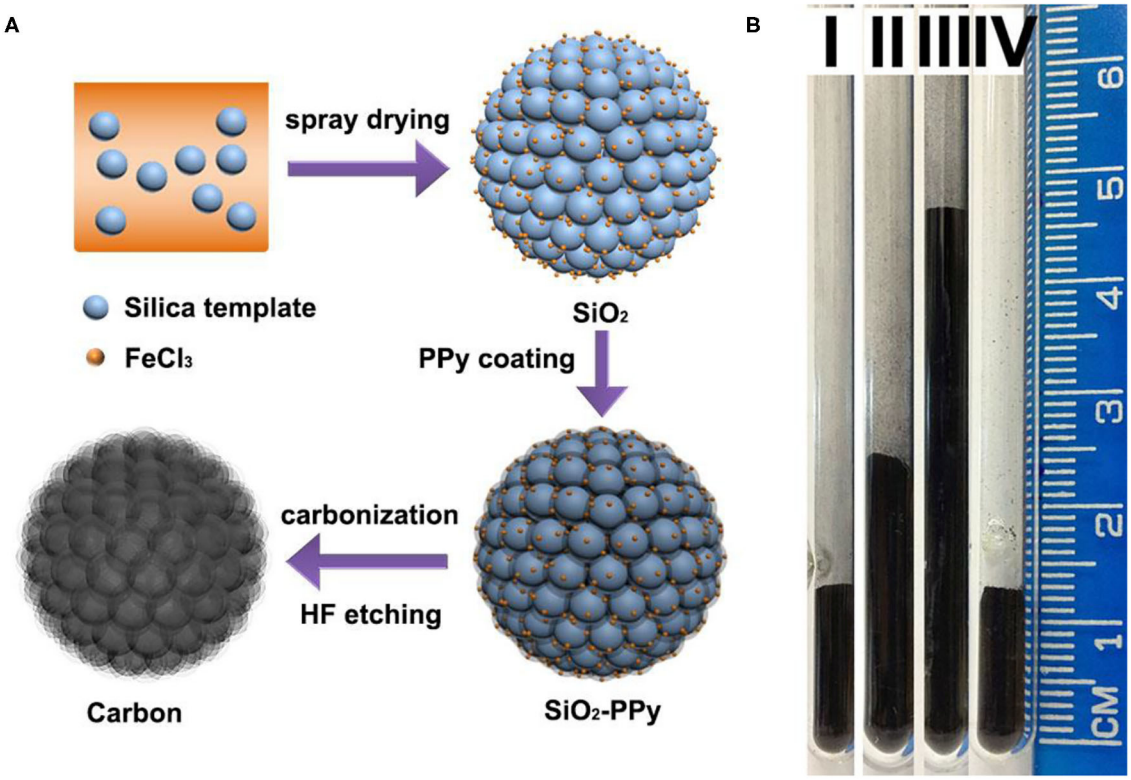

FIGURE 1 | (A) Illustration of the synthesis approach of MC-7-SD, **(B)** the apparent density of (I) MC-7-SD, (II) MC-7-AD, (III) MC-7-FD, and (IV) activated carbon materials. The mass of each material is 50 mg.

while the total pore volumes of MC-7-AD and MC-7-FD are combinations of mesopores and packing voids. In order to differentiate the contribution of pore volume from mesopores with different sizes, the pore volume of specific pore size range is calculated from the cumulative pore volume-pore size plots (**Figure 3C**). In MC-7-SD sample, 55% of total pore volume (0.8 $cm^3\ g^{-1}$) was attributed to mesopores with sizes of 2–5 nm, while only 20% of pore volume (0.3 $cm^3\ g^{-1}$) came from mesopores with sizes of 5–9 nm (**Table 1**). On the contrary, 0.3 $cm^3\ g^{-1}$ of pore volume of MC-7-AD and MC-7-FD was attributed to 2–5 nm mesopores (12 and 14%, respectively), and the majority of pore volume come from mesopores with sizes of 5–9 nm (1.3 $cm^3\ g^{-1}$ (52%) and 1.2 $cm^3\ g^{-1}$ (59%), respectively). MC-7-SD also shows the highest Brunauer-Emmett-Teller (BET) surface area (1,528 $m^2\ g^{-1}$, **Table 1**) with an extraordinary mesoporous surface ratio (95%) compared to MC-7-AD and MC-7-FD (1,338 and 1,229 $m^2\ g^{-1}$, respectively).

To investigate the formation of mesopores with sizes of 2–5 nm in MC-7-SD, MC-7-AD, and MC-7-FD, X-ray photoelectron spectroscopy (XPS) was conducted to analyze the Fe concentration on the surface of as-dried microspheres/aggregates. XPS spectra (**Supplementary Figure 2**) show the Fe/SiO_2 molar ratios of the as-dried aggregates are 3.4 and 3.6% after air-drying and freeze-drying method, respectively, similar to the feeding ratio in silica/water suspension (3.7%). However, the Fe/SiO_2 molar ratio of the as-dried microspheres after spray drying reduces to 1.1%, which is caused by the loss of Fe catalyst carried by inlet gas during spray drying (Wilkowska et al., 2016). As previously reported, the reduction of Fe catalyst results in less polypyrrole coated on the surface of spray-dried microspheres (Yang et al., 2005). The thermal gravimetric (TG) analysis of SiO_2/C composites after carbonization (**Supplementary Figure 3**) further supported our conclusion. The composite after spray-drying method shows 9.5 wt.% carbon, lower than those after air-drying (12.9 wt.%) and freeze-drying methods (13.0 wt.%). The smaller carbon coating amount is in accordance with the thinner carbon layer observed from HRTEM. It is reported that thin carbon layer ends up in an invaginated morphology with reduced pore size after etching (Zhang et al., 2015). The nitrogen sorption results show that the size-reduced mesopores exist in MC-7-SD, MC-7-AD, and MC-7-FD. With a thinner carbon layer, MC-7-SD exhibits a higher proportion of small-sized (2–5 nm) mesopores compared to MC-7-AD and MC-7-FD.

In order to investigate the structural change of mesoporous carbon microspheres as a function of carbonization temperature, MC-7-SD was carbonized at 650, 800, and 950°C. As shown in **Supplementary Figure 4**, a typical mesoporous micro-spherical morphology is well maintained despite various temperatures. A slight increase of the specific surface area

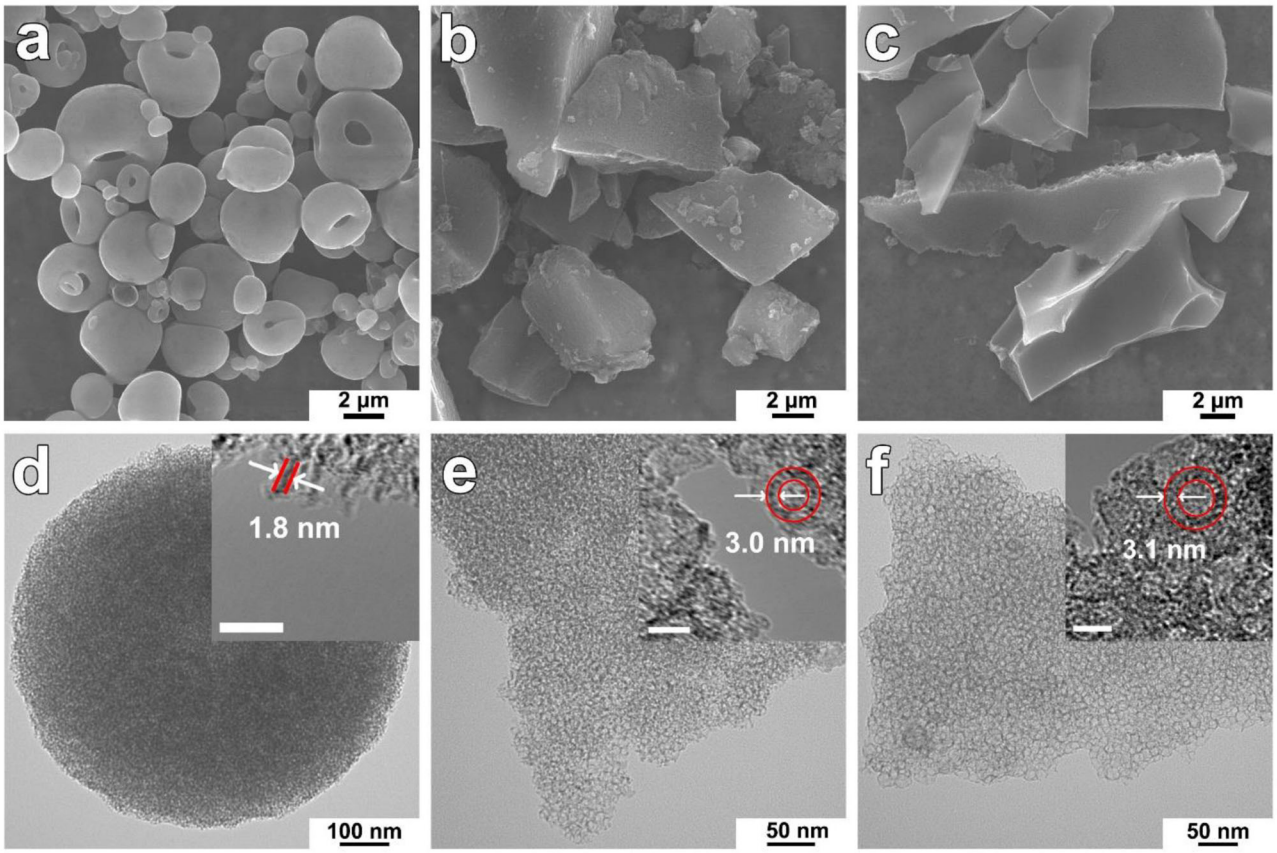

FIGURE 2 | (a–c) SEM and **(d–f)** TEM images of MC-7-SD, MC-7-AD, and MC-7-FD, respectively. **(d–f)** insets are HRTEM images of the edge of MC-7-SD, MC-7-AD, and MC-7-FD, respectively. The scale bars in insets are 10 nm.

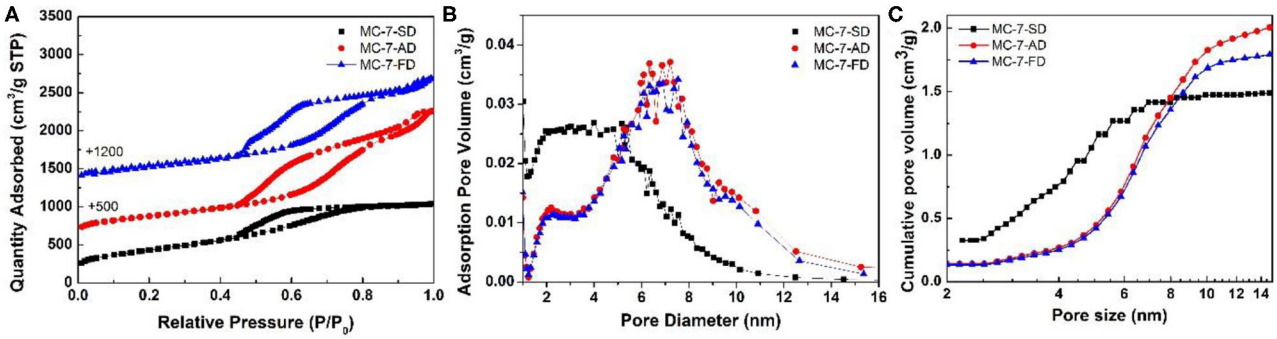

FIGURE 3 | (A) Nitrogen adsorption/desorption isotherm, **(B)** pore size distribution curves and **(C)** cumulative pore volume-pore size plots of MC-7-SD, MC-7-AD, and MC-7-FD.

and pore volume was observed with the rising of carbonized temperature (**Supplementary Table 1**). The increase in specific surface area and pore volume is similar to a previous report (Shen et al., 2015), which is mainly due to the higher degree of carbonization at increased temperature. Raman spectra (**Supplementary Figure 5**) show the graphitization of mesoporous carbons. The distinguishable peak at 1,360 cm^{-1} (D band) is associated with the structural imperfections due to the lack of long-range order in amorphous and quasi-crystalline forms of carbon materials; meanwhile, the peak at 1,592 cm^{-1} (G band) corresponds to the E_{2g} species (stretching vibrations) of the infinite crystalline graphite (Tuinstra and Koenig, 1970; Wang et al., 1990; He et al., 2013). The intensity ratio between D and G band (I_D/I_G) provides a meaningful

index for the crystallinity of carbon material. The I_D/I_G ratio slightly decreases from 0.90 to 0.88 with the increase of the carbonization temperature from 650 to 950°C, which is attributed to the increasing crystallinity of carbon at higher carbonization temperature. The nitrogen doping contents of MC-7-SD samples carbonized at 650, 800, and 950°C were also investigated. The XPS survey spectra (**Supplementary Figure 6**) show the surface chemistry is dominated by C, O, and N for all mesoporous carbons. The N content decreases from 13.21 to 5.57 at% with the ascending temperature from 650 to 950°C. Elemental analysis (**Supplementary Table 2**) was conducted to determine the nitrogen content in bulk material. It is also shown that the nitrogen content in MC-7-SD samples decreases from 13.29 to 6.47 wt.% when the carbonization temperature increases from 650 to 950°C, which is attributed to the decomposition of N-containing functional groups at elevated temperatures (Shen et al., 2015). The capacitive performances of MC-7-SD carbonized at 650, 800, and 950°C were tested in 6 M KOH (**Supplementary Figure 7**). The charge-discharge curves of three samples exhibit a typical EDLC behavior with triangular shapes. As mentioned before, MC-7-SD carbonized at higher temperature possesses a better crystallinity, but the N-doping content is decreased. Consequently, the capacitance of MC-7-SD is the lowest (242.5 F g^{-1}) carbonized at 650°C and the highest (362.8 F g^{-1}) at 800°C. Further increasing the carbonization temperature to 950°C leads to decreased capacitance of 330.1 F g^{-1} (all at 1 A g^{-1}). For this reason, 800°C was chosen as the optimized carbonization temperature of MC-7-SD, MC-7-AD, and MC-7-FD in the following studies.

Regardless of various drying method during synthesis, elemental analysis reveals that MC-7-SD, MC-7-AD, and MC-7-FD show similar nitrogen content after carbonization at 800°C (**Table 2**). XPS results further confirmed that about 8 at% nitrogen is accommodated in mesoporous carbons. Commonly, the high-resolution N1s spectra (**Figure 4**) include pyridinic-N (398.3 ± 0.1 eV), pyrrolic-N (399.7 ± 0.1 eV), quaternary-N (400.9 ± 0.1 eV), and pyridine N-oxide (402.2 ± 0.3 eV). Quaternary-N, also known as graphitic-N, has higher thermal stability by incorporating N atoms into graphitic carbon plane and bonded with three sp^2 carbon atoms. As shown in **Table 2**, MC-7-SD, MC-7-AD, and MC-7-FD samples possess 30.09, 40.61, and 39.65% of quaternary-N, respectively. The high proportions of quaternary-N in polypyrrole-derived carbon are beneficial for the electron transfer and electrical conductivity of carbons (Hou et al., 2015). On the other side, pyrrolic-N and pyridinic-N often considered electrochemically active in aqueous solution, contributing pseudo-capacitance due to the additional p-electron donation to the aromatic π system (Lai et al., 2012; Sun et al., 2014). The total proportion of pyrrolic-N and pyridinic-N in MC-7-SD (32.54 and 29.23 at%) are higher than those in MC-7-AD (28.97 and 22.51 at%) and MC-7-FD (33.76 and 19.19 at%), possibly due to more edges in the carbon framework. With more electrochemically active nitrogen, MC-7-SD is expected to show larger pseudo-capacitive contribution in capacitance.

The electrochemical performances of MC-7-SD, MC-7-AD, and MC-7-FD have been evaluated. **Figure 5A** shows the rectangular-shaped CV curves of MC-7-SD, MC-7-AD, and MC-7-FD. The broadened redox peaks in CV curves can be observed from −0.8 to −0.3 V. These wide and vague peaks are attributed to multiple faradaic peaks (Lin et al., 2015), partially associated with the pseudo-capacitance of pyrrolic-N/pyridinic-N (Xu et al., 2012). The representative galvanostatic charge-discharge curves of mesoporous carbons at a current density of 1 A g^{-1} are shown in **Figure 5B**. The charge-discharge curves are nearly linear and symmetric with a slight curvature, which suggests a good capacitive behavior and electrochemical reversibility (Zhang et al., 2016). The dependence of specific capacitances on the current density in **Figure 5C** shows that MC-7-SD delivers the highest specific capacitance (533.6 F g^{-1} at 0.1 A g^{-1}, 362.8 F g^{-1} at 1 A g^{-1}) with a high surface area normalized capacitance (23.74 μF cm^{-2} at 1 A g^{-1}), giving a high maximum energy density of 74 Wh kg^{-1} (at 0.1 A g^{-1}). The specific capacitance and surface area normalized capacitance of MC-7-SD are higher than those of micropore-dominate activated carbon (161.5 F g^{-1} and 19.22 μF cm^{-2} at 1 A g^{-1}, **Supplementary Figure 8**), revealing the high utilization efficiency of mesopore-dominate structure. With higher specific surface area and more electrochemically active nitrogen, the capacitance of MC-7-SD (362.8 F g^{-1}) is better than those of MC-7-AD and MC-7-FD (317.5 and 291.9 F g^{-1} at 1 A g^{-1}, respectively). Electrochemical impedance spectroscopy (EIS) measurements of MC-7 supercapacitors were also performed. Typical Nyquist plots in the frequency range of 0.01 to 100,000 Hz are shown in **Supplementary Figure 9**. The Nyquist plot, composed of a depressed semicircle in high frequency region and a sloping line in low frequency area, can be fitted using an equivalent circuit (**Supplementary Figure 9** inset). In

TABLE 1 | Textural properties of MC-7-SD, MC-7-AD, MC-7-FD and activated carbon.

Sample	S_{BET} (m^2 g^{-1})	S_{micro} (m^2 g^{-1})	S_{meso} (m^2 g^{-1})	V_t (cm^3 g^{-1})	V_{2-5nm} (cm^3 g^{-1})	V_{5-9nm} (cm^3 g^{-1})
MC-7-SD	1,528	69	1,459	1.6	0.8	0.3
MC-7-AD	1,338	55	1,338	2.7	0.3	1.3
MC-7-FD	1,229	66	1,229	2.3	0.3	1.2
Activated carbon	840	498	342	0.8	–	–

S_{BET} is BET surface area calculated from P/P_0 = 0.05–0.3, S_{micro} is t-plot micropore area, S_{meso} is mesopore area calculated from equation $S_{meso} = S_{BET}$-S_{micro}, V_t is total pore volume at P/P_0 = 0.995, V_{a-bnm} is the pore volume in the range of a–b nm, which is calculated from the cumulative pore volume.

TABLE 2 | The nitrogen-doping content of MC-7-SD, MC-7-AD, and MC-7-FD.

Sample	*N* (wt%)	*N* (at%)	Pyridinic-*N* (at%)	Pyrrolic-*N* (at%)	Quaternary-*N* (at%)	Pyridine *N*-oxide (at%)
MC-7-SD	9.46	8.67	32.54	29.23	30.09	8.14
MC-7-AD	9.75	7.05	28.97	22.51	40.61	7.91
MC-7-FD	9.33	8.50	33.76	19.19	39.65	7.40

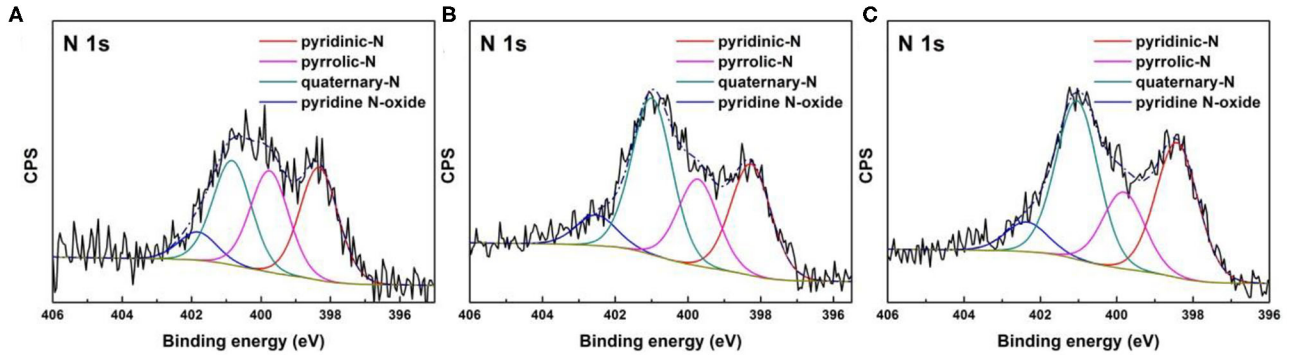

FIGURE 4 | High-resolution N1s spectra of **(A)** MC-7-SD, **(B)** MC-7-AD, and **(C)** MC-7-FD.

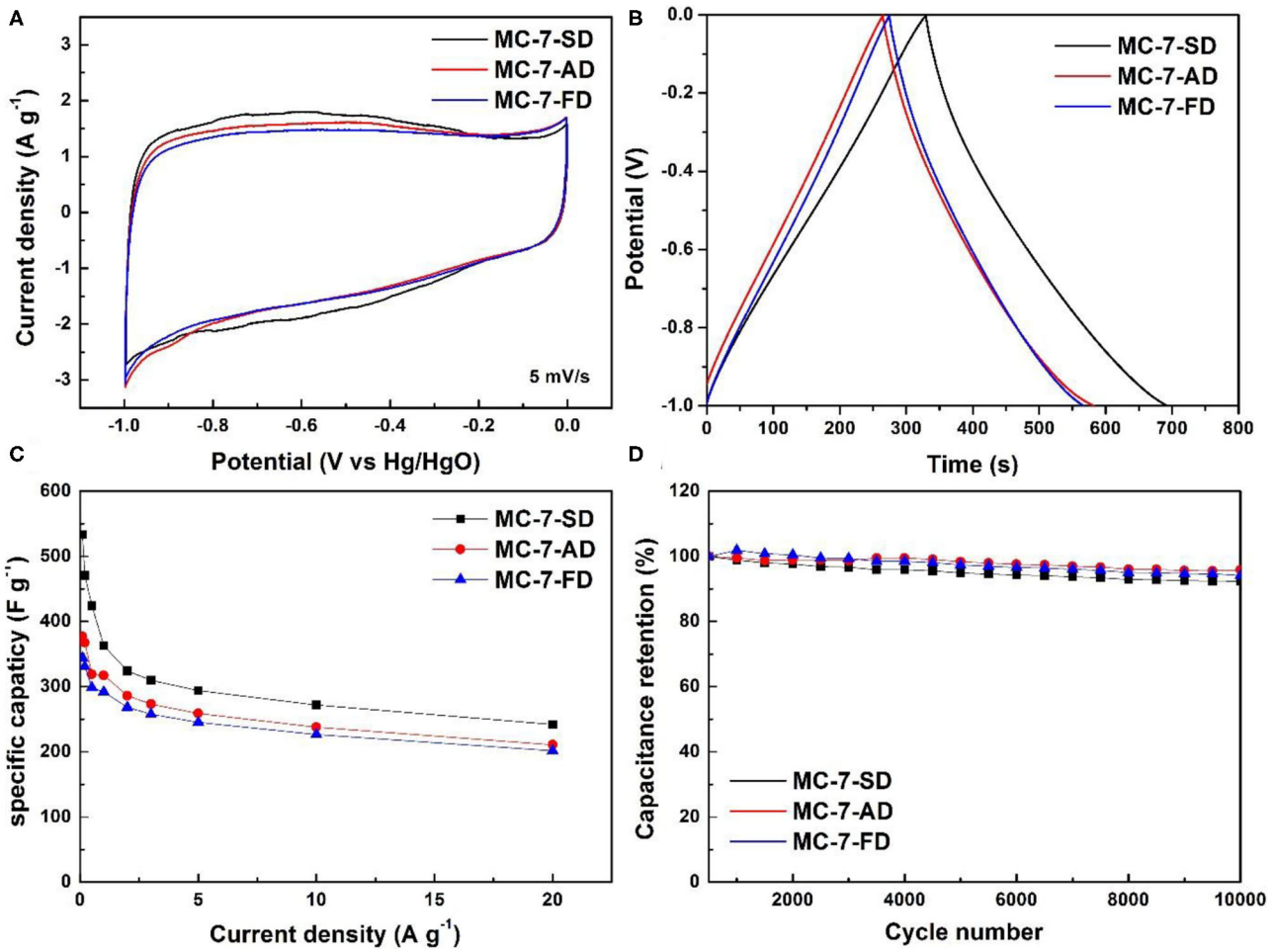

FIGURE 5 | (A) Cyclic voltammetry curves at 5 mV s^{-1}, **(B)** galvanostatic charge/discharge curves at 1 A g^{-1}, **(C)** specific capacitance of MC-7-SD, MC-7-AD, and MC-7-FD and **(D)** cycle performance of MC-7-SD, MC-7-AD, and MC-7-FD at 5 A g^{-1}.

the circuit, R_e represents the electrolyte and ohmic resistance, referring to the incept of the plot with Z' axis. R_{ct} and Q are the charge transfer resistance and double-layer capacitance, respectively, contributing to the depressed semicircle spanning Z' axis. The low frequency sloping line corresponds to the Warburg impedance (Z_w) that pertains the ion diffusion in the electrode. Comparison of R_{ct} values for three MC-7 materials reveals the lowest R_{ct} of MC-7-SD, corresponding to improved charge

transfer process due to efficient-packed carbon mesopores. After cycling, the plots maintained similar profiles.

It is noted the capacitance of MC-7-SD is comparable or better than those of mesoporous carbons reported in literature (**Supplementary Table 3**). Even at a high current density of 20 A g^{-1}, a capacitance of 242.2 F g^{-1} (10 kW kg^{-1} power density) can be maintained, corresponding to 66.8% of capacity retention. Compared to other mesopore-dominant carbon materials (Qian et al., 2014), the higher capacity retention of MC-7-SD indicates the advantage of large mesopore sizes favorable for rapid charge/discharge. A long-lasting cycle life with <8% capacitance loss after 10000 cycles is obtained in MC-7-SD under 5 A g^{-1} (**Figure 5D**), slightly weaker than those of MC-7-AD and MC-7-FD (5 and 6% capacitance loss, respectively). This observation is in accordance with a previous report: larger pores facilitate the ion transportation, resulting in better cycling stability under high current charge-discharge (Ma et al., 2014). Apart from high gravimetric performance, MC-7-SD also achieves a superior volumetric capacitive behavior (208.1 F cm^{-3} at 0.1 A g^{-1}) when calculating using an apparent density of 0.50 g cm^{-3}. The superior electrochemical performance of MC-7-SD for EDLCs can be attributed to its unique structural features. Firstly, the thin carbon layer coated by vapor deposition results in a high mesoporous surface area, which leads to a high accessible electrode-electrolyte interface for electric double layer formation. Secondly, the high content of nitrogen doping provides additional electrochemically active nitrogen for pseudo-capacitance. Thirdly, relatively large mesopores in the carbon framework are beneficial for the remarkable capacitance retention at high current densities. Fourthly, the micro-spherical morphology of MC-7-SD is ideal for effective packing and excellent volumetric capacitive performance.

CONCLUSION

In summary, nitrogen-doped mesoporous carbon microspheres have been successfully synthesized by spray drying-vapor deposition method. The resulting carbon microspheres possess a mesopore-dominate (95%) high surface area of 1528 m^2 g^{-1}, a nitrogen-doping of 8 at%, and an apparent density of 0.5 g cm^{-3}. Benefiting from its unique features, MC-7-SD manifests excellent gravimetric/volumetric performance (533.6 F g^{-1} and 208.1 F cm^{-3}). Our work opens up opportunities for the fabrication of efficient-packed porous carbon materials with heteroatom-doping for wide applications.

DATA AVAILABILITY STATEMENT

All datasets generated for this study are included in the article/**Supplementary Material**.

AUTHOR CONTRIBUTIONS

XS, LZ, XH, and CY designed the experiments. XS performed the material synthesis and electrochemical analysis. AN, YK, and YL performed material characterizations and electrochemical measurements. XS, XH, and CY co-wrote the manuscript. All the authors discussed the results, commented on the draft, and approved the final version of the manuscript.

FUNDING

We thank the funding support from the Australian Research Council, the Queensland Government, and the University of Queensland.

ACKNOWLEDGMENTS

We acknowledge the technical support from the Australian National Fabrication Facility, and the Australian Microscopy and Microanalysis Research Facility at the Centre for Microscopy and Microanalysis and the University of Queensland.

SUPPLEMENTARY MATERIAL

The Supplementary Material for this article can be found online at: https://www.frontiersin.org/articles/10.3389/fchem.2020.592904/full#supplementary-material

REFERENCES

Barbieri, O., Hahn, M., Herzog, A., and Kötz, R. (2005). Capacitance limits of high surface area activated carbons for double layer capacitors. *Carbon* 43, 1303–1310. doi: 10.1016/j.carbon.2005.01.001

Biswas, P., Sen, D., Mazumder, S., Basak, C. B., and Doshi, P. (2016). Temperature mediated morphological transition during drying of spray colloidal droplets. *Langmuir* 32, 2464–2473. doi: 10.1021/acs.langmuir.5b04171

Choi, N.-S., Chen, Z., Freunberger, S. A., Ji, X., Sun, Y.-K., Amine, K., et al. (2012). Challenges facing lithium batteries and electrical double-layer capacitors. *Angew. Chem. Int. Ed.* 51, 9994–10024. doi: 10.1002/anie.201201429

Ferrero, G. A., Fuertes, A. B., and Sevilla, M. (2015). N-doped porous carbon capsules with tunable porosity for high-performance supercapacitors. *J. Mater. Chem. A* 3, 2914–2923. doi: 10.1039/C4TA06022A

Gadipelli, S., Howard, C. A., Guo, J., Skipper, N. T., Zhang, H., Shearing, P. R., et al. (2020). Superior multifunctional activity of nanoporous carbons with widely tunable porosity: enhanced storage capacities for carbon-dioxide, hydrogen, water, and electric charge. *Adv. Energy Mater.* 10:1903649. doi: 10.1002/aenm.201903649

Gierszal, K. P., and Jaronic, M. (2007). Large pore volume carbons with uniform mesopores and macropores: synthesis, characterization, and relations between adsorption parameters of silica templates and their inverse carbon replicas. *J. Phys. Chem. C* 111, 9742–9748. doi: 10.1021/jp072067f

Gogotsi, Y., and Simon, P. (2011). True performance metrics in electrochemical energy storage. *Science* 334, 917–918. doi: 10.1126/science.1213003

Han, F., Li, D., Li, W.-C., Lei, C., Sun, Q., and Lu, A.-H. (2013). Nanoengineered polypyrrole-coated Fe2O3@C multifunctional composites with an improved cycle stability as lithium-ion anodes. *Adv. Funct. Mater.* 23, 1692–1700. doi: 10.1002/adfm.201202254

Han, S., and Hyeon, T. (1999). Simple silica-particle template synthesis of mesoporous carbons. *Chem. Comm.* 1999, 1955–1956. doi: 10.1039/a905848f

Han, S., Sohn, K., and Hyeon, T. (2000). Fabrication of new nanoporous carbons through silica templates and their application to the adsorption of bulky dyes. *Chem. Mater*. 12, 3337–3341. doi: 10.1021/cm000106t

He, C., Wu, S., Zhao, N., Shi, C., Liu, E., and Li, J. (2013). Carbon-encapsulated Fe_3O_4 nanoparticles as a high-rate lithium ion battery anode material. *ACS Nano* 7, 4459–4469. doi: 10.1021/nn401059h

Hou, D., Zhu, S. Y., Tian, H., Wei, H., Feng, X. L., and Mai, Y. Y. (2018). Two-dimensional sandwich-structured mesoporous Mo2C/carbon/graphene nanohybrids for efficient hydrogen production electrocatalysts. *ACS Appl. Mater. Interfaces* 10, 40800–40807. doi: 10.1021/acsami.8b15250

Hou, J., Cao, C., Idrees, F., and Ma, X. (2015). Hierarchical porous nitrogen-doped carbon nanosheets derived from silk for ultrahigh-capacity battery anodes and supercapacitors. *ACS Nano* 9, 2556–2564. doi: 10.1021/nn506394r

Huang, J., Sumpter, B. G., and Meunier, V. (2008). A universal model for nanoporous carbon supercapacitors applicable to diverse pore regimes, carbon materials, and electrolytes. *Chem. Eur. J.* 14, 6614–6626. doi: 10.1002/chem.200800639

Lai, L., Potts, J. R., Zhan, D., Wang, L., Poh, C. K., Tang, C., et al. (2012). Exploration of the active center structure of nitrogen-doped graphene-based catalysts for oxygen reduction reaction. *Energy Environ. Sci.* 5, 7936–7942. doi: 10.1039/c2ee21802j

Li, C., Li, Q., Kaneti, Y. V., Hou, D., Yamauchi, Y., and Mai, Y. Y. (2020). Self-assembly of block copolymers towards mesoporous materials for energy storage and conversion systems. *Chem. Soc. Rev*. 49, 4681–4736. doi: 10.1039/D0CS00021C

Li, W., Liang, Z., Lu, Z., Yao, H., Seh, Z. W., Yan, K., et al. (2015). A sulfur cathode with pomegranate-like cluster structure. *Adv. Energy Mater*. 5:1500211. doi: 10.1002/aenm.201500211

Li, W., Liu, J., and Zhao, D. Y. (2016). Mesoporous materials for energy conversion and storage devices. *Nat. Rev. Mater*. 1:16023. doi: 10.1038/natrevmats.2016.23

Li, X., Zhou, J., Wang, J., Qiao, W., Ling, L., and Long, D. (2014). Large-scale synthesis of mesoporous carbon microspheres with controllable structure and nitrogen doping using a spray drying method. *RSC Adv*. 4, 62662–62665. doi: 10.1039/C4RA11799A

Li, Z., Xu, Z., Tan, X., Wang, H., Holt, C. M. B., Stephenson, T., et al. (2013). Mesoporous nitrogen-rich carbons derived from protein for ultra-high capacity battery anodes and supercapacitors. *Energy Environ. Sci*. 6, 871–878. doi: 10.1039/c2ee23599d

Lin, T., Chen, I.-W., Liu, F., Yang, C., Bi, H., Xu, F., et al. (2015). Nitrogen-doped mesoporous carbon of extraordinary capacitance for electrochemical energy storage. *Science* 350, 1508–1513. doi: 10.1126/science.aab3798

Lin, Z. X., Tian, H., Xu, F. G., Yang, X. W., Mai, Y. Y., and Feng, X. L. (2016). Facile synthesis of bowl-shaped nitrogen-doped carbon hollow particles templated by block copolymer "kippah vesicles" for high performance supercapacitors. *Polym. Chem*. 7, 2092–2098. doi: 10.1039/C6PY00161K

Liu, C., Li, F., Ma, L.-P., and Cheng, H.-M. (2020). Advanced materials for energy storage. *Adv. Mater*. 22, E28–62. doi: 10.1002/adma.200903328

Liu, C. F., Liu, Y. C., Yi, T. Y., and Hu, C. C. (2019). Carbon materials for high-voltage supercapacitors. *Carbon*. 145, 529–548. doi: 10.1016/j.carbon.2018.12.009

Liu, Y., Zhang, H., Noonan, O., Xu, C., Niu, Y., Yang, Y., et al. (2016). Kinetically controlled assembly of nitrogen-doped invaginated carbon nanospheres with tunable mesopores. *Chem. Eur. J.* 22, 14962–14967. doi: 10.1002/chem.201602672

Ma, X., Gan, L., Liu, M., Tripathi, P. K., Zhao, Y., Xu, Z., et al. (2014). Mesoporous size controllable carbon microspheres and their electrochemical performances for supercapacitor electrodes. *J. Mater. Chem. A* 2, 8407–8415. doi: 10.1039/C4TA00333K

Noori, A., El-Kady, M. F., Rahmanifar, M. S., Kaner, R. B., and Mousavi, M. F. (2019). Towards establishing standard performance metrics for batteries, supercapacitors and beyond. *Chem. Soc. Rev*. 48, 1272–1341. doi: 10.1039/C8CS00581H

Pan, P. P., Zhang, T., Yue, Q., Elzatahry, A. A., Alghamdi, A., Cheng, X. W., et al. (2020). Interface co-assembly and polymerization on magnetic colloids: toward core–shell functional mesoporous polymer microspheres and their carbon derivatives. *Adv. Sci*. 7:2000443. doi: 10.1002/advs.202000443

Pei, F., An, T. H., Zang, J., Zhao, X. J., Fang, X. L., Zheng, M. S., et al. (2016). From hollow carbon spheres to N-doped hollow porous carbon bowls: rational design of hollow carbon host for Li-S batteries. *Adv. Energy Mater*. 6:1502539. doi: 10.1002/aenm.201502539

Qian, W., Sun, F., Xu, Y., Qiu, L., Liu, C., Wang, S., et al. (2014). Human hair-derived carbon flakes for electrochemical supercapacitors. *Energy Environ. Sci*. 7, 379–386. doi: 10.1039/C3EE43111H

Ryoo, R., Joo, S. H., and Jun, S. (1999). Synthesis of highly ordered carbon molecular sieves via template-mediated structural transformation. *J. Phys. Chem. B*. 103, 7743–7746. doi: 10.1021/jp991673a

Sen, D., Bahadur, J., Mazumder, S., and Bhattacharya, S. (2012). Formation of hollow spherical and doughnut microcapsules by evaporation induced self-assembly of nanoparticles: effects of particle size and polydispersity. *Soft Matter* 8, 10036–10044. doi: 10.1039/c2sm26493e

Shao, H., Wu, Y.-C., Lin, Z., Taberna, P.-L., and Simon, P. (2020). Nanoporous carbon for electrochemical capacitive energy storage. *Chem. Soc. Rev*. 49, 3005–3039. doi: 10.1039/D0CS00059K

Shen, G., Sun, X., Zhang, H., Liu, Y., Zhang, J., Meka, A., et al. (2015). Nitrogen-doped ordered mesoporous carbon single crystals: aqueous organic–organic self-assembly and superior supercapacitor performance. *J. Mater. Chem. A* 3, 24041–24048. doi: 10.1039/C5TA06129F

Shen, W., and Fan, W. (2013). Nitrogen-containing porous carbons: synthesis and application. *J. Mater. Chem. A* 1, 999–1013. doi: 10.1039/C2TA00028H

Simon, P., and Gogotsi, Y. (2008). Materials for electrochemical capacitors. *Nat. Mater*. 7, 845–854. doi: 10.1038/nmat2297

Simon, P., and Gogotsi, Y. (2020). Perspectives for electrochemical capacitors and related devices. *Nat. Mater*. 19, 1151–1163. doi: 10.1038/s41563-020-0747-z

Sun, L., Tian, C., Fu, Y., Yang, Y., Yin, J., Wang, L., et al. (2014). Nitrogen-doped porous graphitic carbon as an excellent electrode material for advanced supercapacitors. *Chem. Eur. J.* 20, 564–574. doi: 10.1002/chem.201303345

Tan, A., Martin, A., Nguyen, T.-H., Boyd, B. J., and Prestidge, C. A. (2012). Hybrid nanomaterials that mimic the food effect: controlling enzymatic digestion for enhanced oral drug absorption. *Angew. Chem. Int. Ed*. 51, 5475–5479. doi: 10.1002/anie.201200409

Tian, H., Lin, Z. X., Xu, F. G., Zheng, J. X., Zhuang, X. D., Mai, Y. Y., et al. (2016). Quantitative control of pore size of mesoporous carbon nanospheres through the self-assembly of diblock copolymer micelles in solution. *Small* 12, 3155–3163. doi: 10.1002/smll.201600364

Tian, H., Wang, N., Xu, F. G., Zhang, P. F., Hou, D., Mai, Y. Y., et al. (2018). Nitrogen-doped carbon nanosheets and nanoflowers with holey mesopores for efficient oxygen reduction catalysis. *J. Mater. Chem. A* 6, 10354–10360. doi: 10.1039/C8TA02319K

Tuinstra, F., and Koenig, J. L. (1970). Raman spectrum of graphite. *J. Chem. Phys*. 53, 1126–1130. doi: 10.1063/1.1674108

Wang, D., Fu, A., Li, H., Wang, Y., Guo, P., Liu, J., et al. (2015a). Mesoporous carbon spheres with controlled porosity for high-performance lithium–sulfur batteries. *J. Power Sources* 285, 469–477. doi: 10.1016/j.jpowsour.2015.03.135

Wang, G., Zhang, L., and Zhang, J. (2012). A review of electrode materials for electrochemical supercapacitors. *Chem. Soc. Rev*. 41, 797–828. doi: 10.1039/C1CS15060J

Wang, N., Tian, H., Zhu, S. Y., Yan, D.-Y., and Mai, Y.-Y. (2018). Two-dimensional nitrogen-doped mesoporous carbon/graphene nanocomposites from the self-assembly of block copolymer micelles in solution. *Chin. J. Polym. Sci*. 36, 266–272. doi: 10.1007/s10118-018-2091-1

Wang, Q., Yan, J., and Fan, Z. (2016). Carbon materials for high volumetric performance supercapacitors: design, progress, challenges and opportunities. *Energy Environ. Sci*. 9, 729–762. doi: 10.1039/C5EE03109E

Wang, X., Fan, X., Li, G., Li, M., Xiao, X., Yu, A., et al. (2015b). Composites of MnO2 nanocrystals and partially graphitized hierarchically porous carbon spheres with improved rate capability for high-performance supercapacitors. *Carbon* 93, 258–265. doi: 10.1016/j.carbon.2015.05.072

Wang, X., Sun, G., Routh, P., Kim, D.-H., Huang, W., and Chen, P. (2014). Heteroatom-doped graphene materials: syntheses, properties and applications. *Chem. Soc. Rev*. 43, 7067–7098. doi: 10.1039/C4CS00141A

Wang, Y., Alsmeyer, D. C., and McCreery, R. L. (1990). Raman spectroscopy of carbon materials: structural basis of observed spectra. *Chem. Mater*. 2, 557–563. doi: 10.1021/cm00011a018

Wei, J., Zhou, D., Sun, Z., Deng, Y., Xia, Y., and Zhao, D. (2013). A controllable synthesis of rich nitrogen-doped ordered mesoporous carbon

for CO_2 capture and supercapacitors. *Adv. Funct. Mater*. 23, 2322–2328. doi: 10.1002/adfm.201202764

Weingarth, D., Zeiger, M., Jäckel, N., Aslan, M., Feng, G., and Presser, V. (2014). Graphitization as a universal tool to tailor the potential-dependent capacitance of carbon supercapacitors. *Adv. Energy Mater*. 4:1400316. doi: 10.1002/aenm.201400316

Wilkowska, A., Ambroziak, W., Czyzowska, A., and Adamiec, J. (2016). Effect of microencapsulation by spray drying and freeze drying technique on the antioxidant properties of blueberry (*Vaccinium myrtillus*) juice polyphenolic compounds. *Pol. J. Food Nutr. Sci.* 66, 11–16. doi: 10.1515/pjfns-2015-0015

Xu, B., Hou, S., Cao, G., Wu, F., and Yang, Y. (2012). Sustainable nitrogen-doped porous carbon with high surface areas prepared from gelatin for supercapacitors. *J. Mater. Chem*. 22, 19088–19093. doi: 10.1039/c2jm32759g

Yan, J., Wang, Q., Wei, T., and Fan, Z. (2014). Recent advances in design and fabrication of electrochemical supercapacitors with high energy densities. *Adv. Energy Mater*. 4:1300816. doi: 10.1002/aenm.201300816

Yang, C.-M., Weidenthaler, C., Spliethoff, B., Mayanna, M., and Schüth, F. (2005). Facile template synthesis of ordered mesoporous carbon with polypyrrole as carbon precursor. *Chem. Mater*. 17, 355–358. doi: 10.1021/cm049164v

Ying, J., Jiang, C., and Wan, C. (2004). Preparation and characterization of high-density spherical $LiCoO_2$ cathode material for lithium ion batteries. *J. Power Sources* 129, 264–269. doi: 10.1016/j.jpowsour.2003.10.007

Yue, Q., Sun, J., Chen, S., Zhou, Y., Li, H. J., Chen, Y., et al. (2020b). Hierarchical mesoporous MXene–NiCoP electrocatalyst for water-splitting. *ACS Appl. Mater. Interfaces* 12, 18570–18577. doi: 10.1021/acsami.0c01303

Yue, Q., Sun, J. G., Kang, Y. J., and Deng, Y. H. (2020a). Advances in the interfacial assembly of mesoporous silica on magnetite particles. *Angew. Chem. Int. Ed*. 59, 15804–15817. doi: 10.1002/anie.201911690

Zhai, Y., Dou, Y., Zhao, D. Y., Fulvio, P. F., Mayes, R. T., and Dai, S. (2011). Carbon materials for chemical capacitive energy storage. *Adv. Mater*. 23, 4828–4850. doi: 10.1002/adma.201100984

Zhang, H., Hussain, I., Brust, M., Butler, M. F., Rannard, S. P., and Cooper, A. I. (2005). Aligned two- and three-dimensional structures by directional freezing of polymers and nanoparticles. *Nat. Mater*. 4, 787–793. doi: 10.1038/nmat1487

Zhang, H., Yu, M. H., Song, H., Noonan, O., Zhang, J., Yang, Y., et al. (2015). Self-organized mesostructured hollow carbon nanoparticles via a surfactant-free sequential heterogeneous nucleation pathway. *Chem. Mater*. 27, 6297–6304. doi: 10.1021/acs.chemmater.5b01993

Zhang, H. W., Noonan, O., Huang, X. D., Yang, Y. N., Xu, C., Zhou, L., et al. (2016). Surfactant-free assembly of mesoporous carbon hollow spheres with large tunable pore sizes. *ACS Nano* 10, 4579–4586. doi: 10.1021/acsnano.6b00723

Zhang, L. L., and Zhao, X. S. (2009). Carbon-based materials as supercapacitor electrodes. *Chem. Soc. Rev*. 38, 2520–2531. doi: 10.1039/b813846j

Zhang, Y., Feng, H., Wu, X., Wang, L., Zhang, A., Xia, T., et al. (2009). Progress of electrochemical capacitor electrode materials: a review. *Int. J. Hydrogen Energy*. 34, 4889–4899. doi: 10.1016/j.ijhydene.2009.04.005

Zhou, L., Xu, H., Zhang, H., Yang, J., Hartono, S. B., Qian, K., et al. (2013). Cheap and scalable synthesis of α-Fe2O3 multi-shelled hollow spheres as high-performance anode materials for lithium ion batteries. *Chem. Comm*. 49, 8695–8697. doi: 10.1039/c3cc43867h

Conflict of Interest: The authors declare that the research was conducted in the absence of any commercial or financial relationships that could be construed as a potential conflict of interest.

Copyright © 2020 Sun, Kong, Liu, Zhou, Nanjundan, Huang and Yu. This is an open-access article distributed under the terms of the Creative Commons Attribution License (CC BY). The use, distribution or reproduction in other forums is permitted, provided the original author(s) and the copyright owner(s) are credited and that the original publication in this journal is cited, in accordance with accepted academic practice. No use, distribution or reproduction is permitted which does not comply with these terms.

frontiers in Chemistry

REVIEW
published: 12 November 2020
doi: 10.3389/fchem.2020.583272

Applications of Thiol-Ene Chemistry for Peptide Science

*Mark D. Nolan and Eoin M. Scanlan**

School of Chemistry, Trinity College Dublin, Trinity Biomedical Sciences Institute, Dublin, Ireland

Radical thiol-ene chemistry has been demonstrated for a range of applications in peptide science, including macrocyclization, glycosylation and lipidation amongst a myriad of others. The thiol-ene reaction offers a number of advantages in this area, primarily those characteristic of "click" reactions. This provides a chemical approach to peptide modification that is compatible with aqueous conditions with high orthogonality and functional group tolerance. Additionally, the use of a chemical approach for peptide modification affords homogeneous peptides, compared to heterogeneous mixtures often obtained through biological methods. In addition to peptide modification, thiol-ene chemistry has been applied in novel approaches to biological studies through synthesis of mimetics and use in development of probes. This review will cover the range of applications of the radical-mediated thiol-ene reaction in peptide and protein science.

Keywords: peptides, bioconjugation, radical, thiol (-SH), protein

OPEN ACCESS

Edited by:
Chun Xu,
The University of Queensland, Australia

Reviewed by:
Junfeng Zhao,
Jiangxi Normal University, China
Mustafa O. Guler,
University of Chicago, United States

***Correspondence:**
Eoin M. Scanlan
eoin.scanlan@tcd.ie

Specialty section:
This article was submitted to Organic Chemistry, a section of the journal Frontiers in Chemistry

Received: *14 July 2020*
Accepted: *13 October 2020*
Published: *12 November 2020*

Citation:
Nolan MD and Scanlan EM (2020) Applications of Thiol-Ene Chemistry for Peptide Science. Front. Chem. 8:583272. doi: 10.3389/fchem.2020.583272

INTRODUCTION

Since its discovery by Posner (1905), the thiol-ene reaction has found many diverse applications in synthetic chemistry. This efficient process involves the generation of a thiyl radical from a thiol, which subsequently undergoes anti-Markovnikov addition to an alkene, furnishing a carbon-centered radical. The carbon-centered radical abstracts a hydrogen from another molecule of thiol to give the thioether product, along with facilitating propagation of the radical cycle through generation of a new thiyl radical (**Figure 1**). Thiyl radicals are readily formed through homolytic cleavage of the sulfhydryl S-H bond due to low bond dissociation energies of around 87 kcal mol^{-1} (Dénès et al., 2014). However, both thermal and photochemical radical initiators are often applied to aid in radical formation. In particular, applications of the thiol-ene reaction in peptide chemistry often make use of 2,2-dimethoxy-2-phenylacetophenone (DPAP) **1** or the water-soluble 2,2'-azobis[2-(2-imidazolin-2-yl)propane]-dihydrochloride (VA044) **2** radical initiator (**Figure 1**). Radical thiol-ene chemistry has been demonstrated for many applications including, but not limited to thiosugar synthesis and carbohydrate chemistry (McSweeney et al., 2016), polymerisations (Hoyle et al., 2004), surface chemistry (Hoyle and Bowman, 2010), synthetic chemistry (Dénès et al., 2014) and in peptide chemistry, the latter being the focus of this review.

The thiol-ene reaction, or thiol-ene coupling (TEC) is considered a "click" reaction (Hoyle and Bowman, 2010) as originally defined by Shapless in Kolb et al. (2001). Notable features of such "click" reactions include high yields, lack of side products, compatibility with aqueous conditions and orthogonality to many other synthetic reactions. These "click" characteristics prove ideal for application to peptide science. Whilst high yields mean valuable starting material is not wasted and the lack of side products allows easier purification, the compatibility with aqueous conditions is ideal for peptide dissolution and reaction orthogonality allows for minimal or no use of side-chain protecting groups. In addition, the thioether linkage produced in the reaction is stable in a range of chemical environments, tolerating pH ranges.

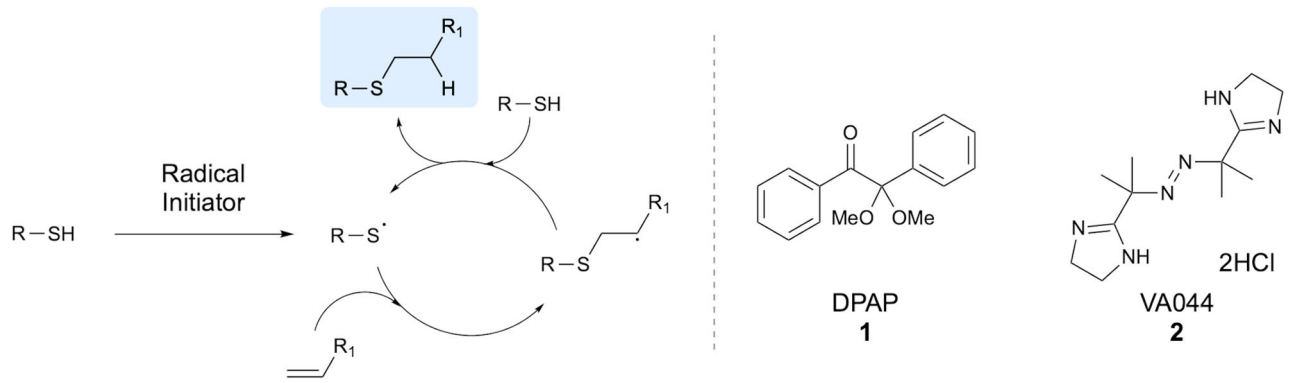

FIGURE 1 | Radical cycle of thiol-ene coupling and structures of two common initiators. The radical cycle for a generalized thiol-ene coupling reaction is shown, along with the commonly applied radical initiators DPAP and VA044.

The absence of any requirement for metal catalysts in the thiol-ene reaction is of particular advantage in peptide chemistry. This avoids the need for removal of often toxic metals for biological applications. This is in contrast to the widely utilized copper-catalyzed azide-alkyne cycloaddition (CuAAC) reaction commonly applied in bioconjugate chemistry, in which the copper catalyst demonstrates *in vivo* toxicity.

The thiol-ene reaction may also proceed via an ionic mechanism when the alkene is part of a Michael acceptor system. The use of dehydroalanine (Dha) in a peptide sequence provides an ideal target for Michael addition, and has been demonstrated as a handle for peptide modification (Zhu and van Der Donk, 2001; Bernardes et al., 2008). Furthermore, the alkene of the maleimide moiety has been utilized as a target for peptide modification in formation of the thiosuccinimide bond (Elduque et al., 2014; Forner et al., 2020). However, this review will focus exclusively on radical-mediated thiol-ene chemistry. Ionic thiol-Michael peptide modifications have been reviewed elsewhere (Hoyle and Bowman, 2010; Tang and Becker, 2014; Gunnoo and Madder, 2016).

The use of the thiol-ene "click" reaction facilitates highly efficient application with high selectivity and little side products. The use of single electron radical chemistry provides superior selectivity in the presence of unprotected amino acid functional groups, which can include both nucleophilic and electrophilic groups prone to side reactions in two-electron approaches. A potential issue with the formation of thioether linkages is their subsequent oxidation to the corresponding sulfoxide. However, in all of the works included in this review, only Hoppmann et al. reported formation of the sulfoxide, which was attributed to the proximal photoactive azobenzene moiety facilitating further redox processes (Hoppmann et al., 2011, 2012). The sulfoxide linkage may also be seen as an advantage if increased water solubility is desired.

In the development of homogenously modified peptides and proteins, chemical modification has proven an essential tool. In nature, a variety of post-translational modifications (PTMs) of peptides and proteins result in vastly increased diversity from the 20 naturally-occurring amino acids. However, biological PTM often results in non-homogeneous mixtures through non-uniform modification, posing complications for manufacturing and production (Chalker, 2013). Chemical modifications enable precise, uniform modification of peptides for study of function and development of therapeutics. One approach for such modifications involves incorporation of unnatural amino acids or modifications to facilitate bioorthogonal reactions. Incorporation of functional groups that undergo click reactions is of particular use for the aforementioned reasons. The other approach involves targeting of native amino acid functional groups. Cys and Lys residues offer the advantage of the nucleophilic thiol and amine side-chain functional groups and their use in such modifications has been reviewed (Boutureira and Bernardes, 2015; Gunnoo and Madder, 2016). Cys residues, in particular, have a relatively low frequency of occurrence in naturally occurring sequences, at 1.48% (Agouridas et al., 2017). Development of an arsenal of varied and specific methodologies for peptide modification allows chemoselective targeting of specific residues or functional groups and is therefore of utmost importance in peptide science. An additional advantage of thiol-ene chemistry over other methodologies is in the formation of the naturally occurring thioether linkage. This is in contrast to commonly utilized linkages such as the triazole formed via CuAAC or other heterocycle-based linkers (Montgomery et al., 2019; Zhang et al., 2019).

Thiol-ene chemistry has been utilized in performing some of the most common naturally occurring PTMs through chemical modification, namely cyclization, glycosylation and lipidation. In addition to cyclization, installation of non-natural staples to α-helical peptide sequences has been demonstrated through thiol-ene chemistry. Thiol-ene chemistry has been applied less extensively in other areas of peptide science such as tagging of peptides or in probes. This review will focus on the applications of thiol-ene based modifications of peptides. Applications for polypeptide modifications and in hydrogel-peptide conjugates have been reviewed elsewhere (Hoyle and Bowman, 2010; Brosnan and Schlaad, 2014; Deming, 2016).

CYCLIZATION AND STAPLING OF PEPTIDES

Peptide cyclization is a naturally occurring PTM, with cyclizations occurring between *N*- and *C*-termini, between side chains or between the side chain and either the *N*- or *C*-terminus of the peptide chain. Cyclization is an approach often undertaken in improving therapeutic properties of peptide drugs. This is often particularly aimed at stabilizing the active conformation of the peptide, as cyclization imparts conformational constraint which reduces the entropic cost of binding, resulting in stronger, more selective target interactions (Zorzi et al., 2017; Vinogradov et al., 2019). A further advantage often observed is improved proteolytic stability, allowing improved *in vivo* half-life of therapeutics (Byk et al., 1996; Hess et al., 2008).

Cyclic peptides have been in therapeutic use since the mid Twentieth century, with the use of Gramicidin S for treatment of infected wounds in the Second World War (Gause and Brazhnikova, 1944). Octreotide presents an example with extensive modern use in oncology, with sales of USD 1.585 billion in 2019 under the brand name Sandostatin (Jón Tryggvi Njardarson, 2000; McGrath et al., 2010).

Thiol-ene chemistry has been utilized in peptide cyclization and stapling in both one- and two-component systems. Existing methods for one-component macrocyclizations involve activated alkenes or long aliphatic alkene side chains, whilst two-component stapling methodologies use dienes of varying length with native Cys residues. Examples involving thiol-yne reactions are sparsely studied and therefore beyond the scope of this review.

One-Component Systems

One-component systems for peptide cyclization make use of at least one unnatural or modified amino acid residue, along with a complimentary functional group located on the side-chain of another amino acid that may or may not be proteinogenic (e.g., Cys, Lys). This facilitates control of the macrocyclization reaction through the introduction of the necessary amino acids or modifications in linear peptide synthesis. The direct reaction of these side chain functional groups results in macrocycle formation, with no introduction of additional linkers. The main potential issue with one-component systems is in the formation of dimers, where the intermolecular reaction occurs. This has been overcome primarily through use of dilute conditions and on-resin cyclizations which benefit from a *pseudo*-dilution effect.

In 2010, Aimetti et al. published the first reported methodology for on-resin macrocyclization of peptides via thiol-ene reaction (Aimetti et al., 2010). To incorporate an alkene group into the linear peptide sequence, a Lys side chain amino group was modified with either an allyloxycarbonyl (alloc) group or a norbornene group (**Figure 2A**). These functional handles were reacted with the thiol groups of Cys residues through photoinitiated thiol-ene reaction using the type I photoinitiator DPAP in DMF. This macrocyclization approach gave yields of 24 and 37% for the alloc and norbornene precursors, respectively. It was noted that the norbornene-containing peptide underwent cyclization in as little as 20 min due to the heightened reactivity of the alkene resulting from the strained bicyclic structure. NMR spectra of the norbornane-containing cyclic peptide showed diastereotopic protons at the cysteine β-position which were attributed to formation of *endo* and *exo* conformations at the norbornane. The authors investigated the thermal initiation process but found that even with extended reaction times, lower yields were achieved. Additionally, the solution-phase reaction was only briefly investigated due to the requirement for additional purification steps and work up, which gave reduced yields. The Arg-Gly-Asp (RGD) cyclic peptides produced using this methodology were evaluated for bioactivity, demonstrating improved activity upon cyclization.

A further demonstration of the use of thiol-ene reaction between a Cys thiol and the alkene of an alloc *N*-protecting group in peptide macrocyclization was carried out by Levalley et al. in tandem with strain-promoted azide-alkyne cycloaddition for additional conjugation (Levalley et al., 2018). As in the previous work, this study focused on an RGD peptide containing the Cys and alloc groups for cyclization as well as an azide for subsequent functionalization. The authors reported low yields when the cyclization was attempted on resin and so a solution-phase approach was adopted using the lithium phenyl-2,4,6-trimethylbenzoylphosphinate (LAP) photoinitiator in water. This approach gave cyclized peptide in yields of approximately 70%, and importantly retained the azide functionality. This azide group was then used for hydrogel and fluorophore conjugation.

Application of the thiol-ene reaction for installation of photoswitchable linkages in α-helical peptides was demonstrated by Hoppmann et al. using a photoswitchable click amino acid (PSCaa) containing both an azobenzene unit and an alkene handle (Hoppmann et al., 2011, 2012). Incorporation of this PSCaa into the linear sequence along with a Cys residue preceded cyclization in solution through irradiation in the presence of the photoinitiator 2-hydroxy-1-[4-(2- hydroxyethoxy)phenyl]-2-methyl-1-propanone **3**, along with *trans*-to-*cis* isomerization of the azo group (**Figure 2B**). The authors further investigated the cyclization reaction in presence of Cys-containing glutathione (GSH), demonstrating a preference for the intramolecular thiol-ene reaction over the intermolecular reaction of the PSCaa alkene with GSH. The authors also made the unique observation of formation of the sulfoxide linkage, previously unreported in thiol-ene reactions of peptides. This is assumed to have occurred due to further light-induced redox with the proximal azobenzene group, and provides increased solubility in aqueous media.

The work of Zhao et al. demonstrated on-resin peptide macrocyclization via thiol-ene reaction between Cys and terminal alkene bearing side chains of four to six carbons in length (Zhao et al., 2016). After optimization of the reaction conditions using a model pentapeptide bearing only Ala and the desired Cys and unnatural amino acid residues (**Figure 2C**), sequence compatibility was investigated through variations of the pentapeptide model to include Arg, Glu, Gly, Lys, Pro, Trp, and Tyr in varying combinations with four and five carbon alkene side chain bearing unnatural amino acids. In order to demonstrate potential for biological applications, along with compatibility with longer peptides, an *i,i+4* stapled analog of the

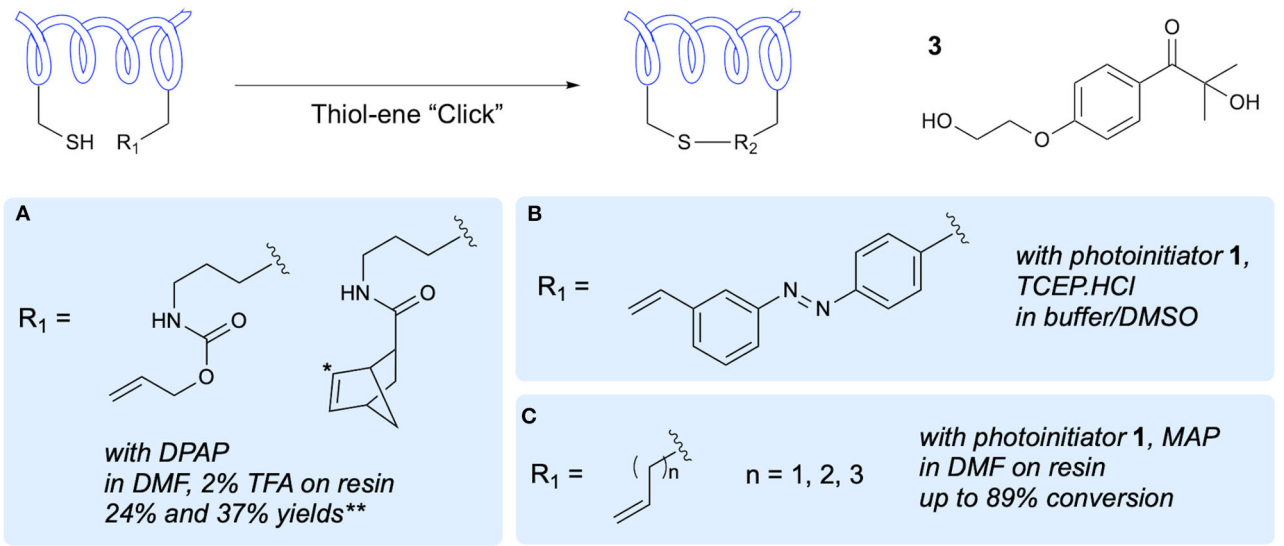

FIGURE 2 | One-component peptide stapling/cyclization. Alkene-containing side-chains and side-chain modifications that have been used to demonstrate peptide stapling and cyclization and the conditions reported. *Prochiral C center at which thiyl attack takes place resulting in diastereoisomers. **Yield based on initial resin loading. **(A)** Anseth's activated alkenes. **(B)** Photoswitchable linker. **(C)** Simple alkene side chains.

11-mer linear peptide ligand that binds the co-activator binding site of estrogen receptor was synthesized. In a fluorescence polarization assay, the cyclic peptide analog showed higher binding affinity than the linear peptide, whilst both synthetic peptides have higher affinities than the native ligand.

The one-component peptide cyclization/stapling methodologies discussed demonstrate the potential for use of thiol-ene chemistry for synthesis of cyclic peptides either on-resin or in solution as well as its utility in installation of either simple aliphatic linkers or more specialized linkers with additional functionality. A notable advantage is the need for one unnatural amino acid at most, as Cys serves as a reactive partner. However, this raises the question of selectivity where a peptide chain has more than one Cys residue. Little investigation has been performed on this potential caveat through either selectivity studies or protecting group chemistry. Nevertheless, one-component thiol-ene chemistry provides rapid access to cyclic peptides via "click" chemistry and shows potential for further study in selectivities and linker variation, aided in part by the orthogonality of the thiol-ene reaction.

Two-Component Systems

Two-component peptide stapling involves the reaction of the peptide substrate with an external linker or staple bearing two functional groups, each with complementary reaction partners on the peptide chain. Often, the amino acids in the stapling positions must be replaced with one bearing a side chain with a suitable reaction partner for the staple. Cys is a common choice as a stapling site due the potential for reaction of the thiol group with a suitable electrophile. Additionally, as is the subject of this section, the formation of radicals at the Cys sulfhydryl can facilitate reaction with external staples. The primary challenge with two-component systems is the formation of side products, whereby the peptide chain reacts with two different linkers molecules to form a *bis*-adduct. This has been overcome through various methods that favor the intramolecular reaction over the intermolecular variant, such as selection of reactive amino acid positioning in relation to the linker or preorganization of the peptide chain.

The first demonstration of two-component peptide stapling using thiol-ene chemistry was reported by Chou in their study of the use of thiol-ene chemistry for stapling of peptides at two Cys residues using diene staples (Wang and Chou, 2015). Importantly, this study showed the use of thiol-ene chemistry in macrocyclization of native, unmodified peptide sequences. Initial investigation of reaction conditions focused on the reaction between 1,7-octadiene and *N*-acetyl-Cys methyl ester in DMF, with DPAP proving to be the most suitable radical initiator (**Figure 3A**). It was subsequently found that for peptide substrates use of *N*-methyl-2-pyrrolidone (NMP) as a solvent offered improved yields. The stapling reactions for peptide examples using the DPAP photoinitiator in NMP gave yields of up to 92% for a variety of diene lengths and heteroatom substitutions for *i,i+4* and *i,i+7* Cys arrangements. To investigate the application of this stapling methodology in biologically active peptides, an *i,i+4*-stapled Axin mimetic **10** developed by the Verdine group using ring-closing metathesis (RCM) (Grossmann et al., 2012) was synthesized, along with the dithioether-stapled analog (**Figure 4**). Circular dichroism (CD) experiments showed comparable α-helicity in the reported peptide and newly synthesized dithioether-stapled peptide **12a**. Next, an *i,i+7*-stapled p53 mimetic developed by Bernal et al. using RCM (Bernal et al., 2007) was synthesized along with the equivalent dithioether-stapled peptide obtained via thiol-ene stapling. It was found that the dithioether stapled

peptide obtained from reaction with 1,8-non-adiene showed similar α-helical properties to the previously reported peptide. Additionally the results of an ELISA assay for quantification of the efficacy of the newly obtained peptides in blocking p53-MDM2 interactions showed the dithioether-stapled peptides to be just as effective as the reported RCM-stapled peptides, whilst the unstapled peptide did not block the interaction. Importantly, the authors highlight the compatibility of this methodology with unprotected peptides without the requirement for unnatural amino acids. Further work by Wang et al. on this methodology has adapted this stapling reaction for aqueous conditions (Wang et al., 2017) **Figure 3B**. This was achieved through use of the water-soluble VA044 radical initiator in combination with water-soluble diallylurea staples. A notable achievement of this study is the use of otherwise unfunctionalised diene staples, as equivalent dihalogan synthons show insufficient reactivity.

Recently the Brimble group have applied divinyl diester staples to thiol-ene peptide stapling of Cys-containing peptides, providing access to a significantly more hydrophilic staple than traditional hydrocarbon staples (**Figure 3C**). Having previously developed their Cysteine Lipidation of a Peptide or Amino acid (CLipPA) methodology (see section Amino Acid and Peptide Lipidation), the authors demonstrated a comparable peptide stapling methodology. A linear Axin analog containing two Cys residues previously discussed in the work of Wang and Chou (2015) and based on the work of Grossmann et al. was synthesized (Grossmann et al., 2012) and used for optimization of reaction conditions for *i,i+4* stapling (**Figure 4**). Confirmation of successful stapling was achieved by mass shift experiments. Similar α-helical content to that of Chou's mimetic **12a** (88%) was observed in the diester stapled peptides, at 89% α-helical content. Further demonstration of *i,i+4* stapling was achieved in synthesis of SIGK stapled analogs. These are binders of Gβγ complex involved in the G protein coupled receptor signaling cascade. An additional Lys residue was incorporated into the sequence allowing attachment of fluorescein prior to stapling. Cell uptake was measured using BT549 breast cancer cells via confocal microscopy, showing uptake after 7 h incubation. In examination of potential for *i,i+7* stapling an analog of an IRS1-targeting peptide developed by Hu et al. was synthesized (Hu et al., 2017). Successful stapling resulted in an increase in α-helicity from 2 to 44%, representing the greatest improvement for the examples chosen.

As exemplified in the studies discussed, two-component stapling via thiol-ene chemistry allows successful and beneficial stapling of peptides using a variety of linkers. Whilst many other methods rely on predominantly aliphatic or unfunctionalised staples, thiol-ene methodology has been used to incorporate linkers containing ester, ether and urea functionalities. These staples impart different solubilities to traditional hydrophobic staples and therefore will impact overall peptide structure and solubility. Again, the use of Cys residues at the stapling locations is notable as no unnatural amino acids are required and Cys residues can be easily introduced in the desired position.

AMINO ACID, PEPTIDE AND PROTEIN GLYCOSYLATION

It has been estimated that over half of all proteins are glycoproteins, while almost two thirds have potential *N*-glycosylation sites (Apweiler et al., 1999). The glycosylation of proteins *in vivo* results in a large degree of heterogeneity. As previously discussed, this heterogeneity proposes issues for use in syntheses. This has led to the requirement for chemical methods for selective glycosylation or other approaches for synthesis of glycopeptides. Thiol-ene chemistry has demonstrated utility in glycosylation of individual amino acids for use in solid phase peptide synthesis (SPPS) as well as modification of larger proteins. This has been approached using thiosugars and alkene-containing peptide chains as well as using alkene-functionalised sugars with native proteins. Additionally, the orthogonality of the thiol-ene reaction leads to potential for use in tandem functionalizations to introduce more than one different sugar modification. The general use of thiyl radicals in glycopeptide and glycoprotein synthesis was also reviewed by the Scanlan group in 2016 (McSweeney et al., 2016).

Early work in the use of the thiol-ene reaction in glycosylation was performed by Dondoni et al. (2009), with initial investigation focusing on reaction of Fmoc-protected cysteine with a variety of monosaccharides bearing a terminal alkene-containing chain at the anomeric position. The photoinitiated reaction using DPAP in DMF with an excess of Cys provided conversion of >95%, without loss of the Cys stereochemistry. GSH was selected as a model peptide for further development of the methodology. Use of a DMF/H_2O (1:2) solvent system facilitated glycosylation with 81% isolated yield. Application to a model nonapeptide bearing a single Cys residue was achieved via addition of a solution of the allyl α-*C*-galactoside and DPAP in DMSO to a phosphate-buffered solution of the peptide. With the goal of the study being to apply the methodology to protein glycosylation, globular bovine serum albumin (BSA) was selected as a model substrate. Modification of BSA (Bujacz, 2012) with alkene-containing glycopeptides had previously been demonstrated by Wittrock et al. (2007). Application of the conditions obtained for the nonapeptide example resulted in the addition of 3 equivalents of galactoside with cleavage of the 75↔91 disulphide bond (**Figure 5A**).

Also in 2009, Floyd et al. applied a "tag-modify" strategy to the thiol-ene mediated glycosylation of amino acids and proteins (Floyd et al., 2009). This involved the use of alkene-containing amino acids and a range of glycosyl thiols. Homoallylglycine (Hag) was used as a "tag" to introduce the alkene group into the protein substrate, allowing glycosylation through thiol-ene reaction with the glycosyl thiol. Initial investigation focused on single amino acid models, with the aim of optimizing the reaction for mild, aqueous conditions. To this end, the water-soluble VA044 initiator was applied at pHs ranging from 4 to 7, furnishing conversions >98% with retention of the anomeric configuration. This included a single Gal-Glc thiol disaccharide example for which >98% conversion was achieved. The authors subsequently applied their methodology to 3 model protein

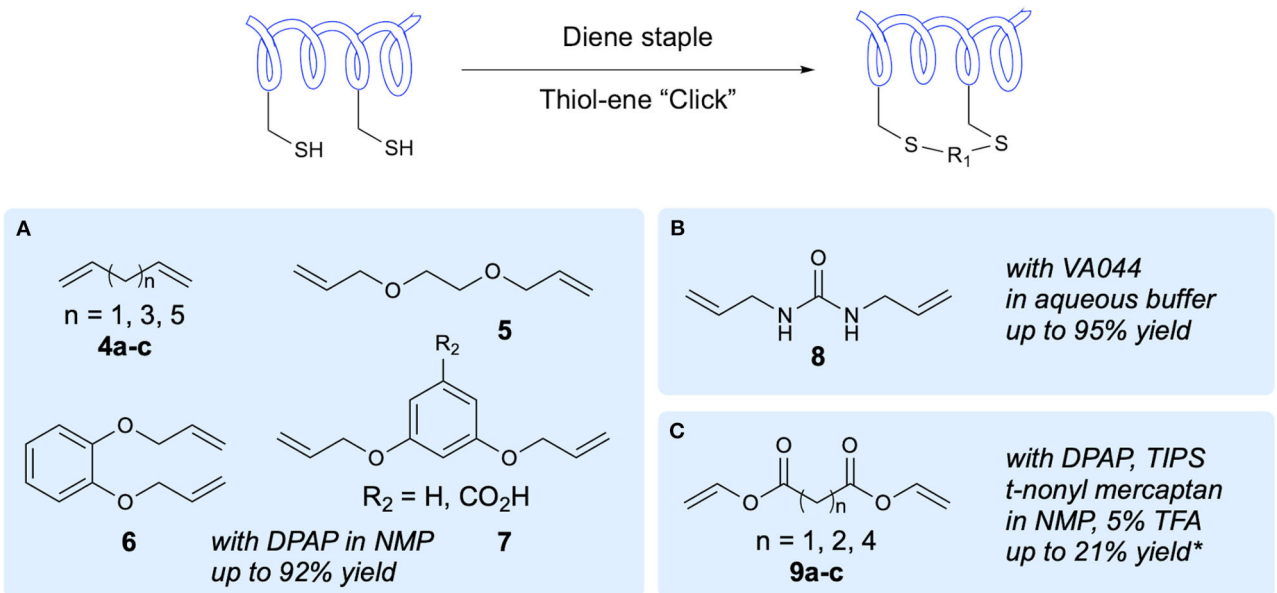

FIGURE 3 | Two-component peptide stapling. A range of staples that have been applied in two-component peptide stapling via thiol-ene reaction and the conditions reported. *Yield based on initial resin loading. **(A)** Staples used in Chou's initial study. **(B)** Chou's water-compatible stapling. **(C)** Brimble's divinyl diester staples.

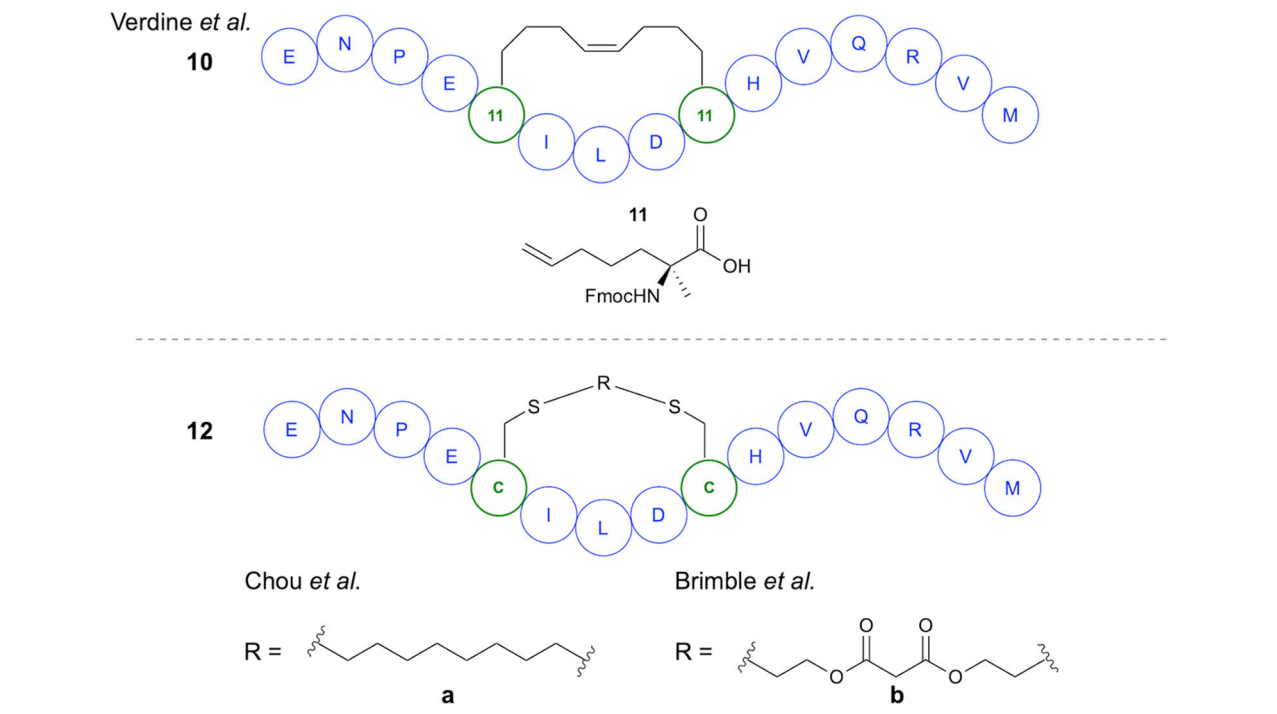

FIGURE 4 | Stapled Axin mimetics. Comparison of structures of axin mimetics developed using RCM and using thiol-ene chemistry.

systems; TIM-barrell protein (*Ss* βG), (Aguilar et al., 1997) the β-helix Np276 protein and virus-like bacteriophage particle Qβ. Each protein was expressed in an *E. coli* strain, with Hag introduced in a site-specific manner through the "Met" ATG codon. Incorporation of a single Hag residue into the *Ss*βG sequence allowed reaction optimization to achieve >95% conversion at pH < 7 using VA044 (**Figure 5B**). Similar results were achieved for the Np276 cuboid protein, with reactions at pH 4 and 6 giving >95% conversion. For the virus-like bacteriophage particle Qβ, 180 Hag residues were incorporated.

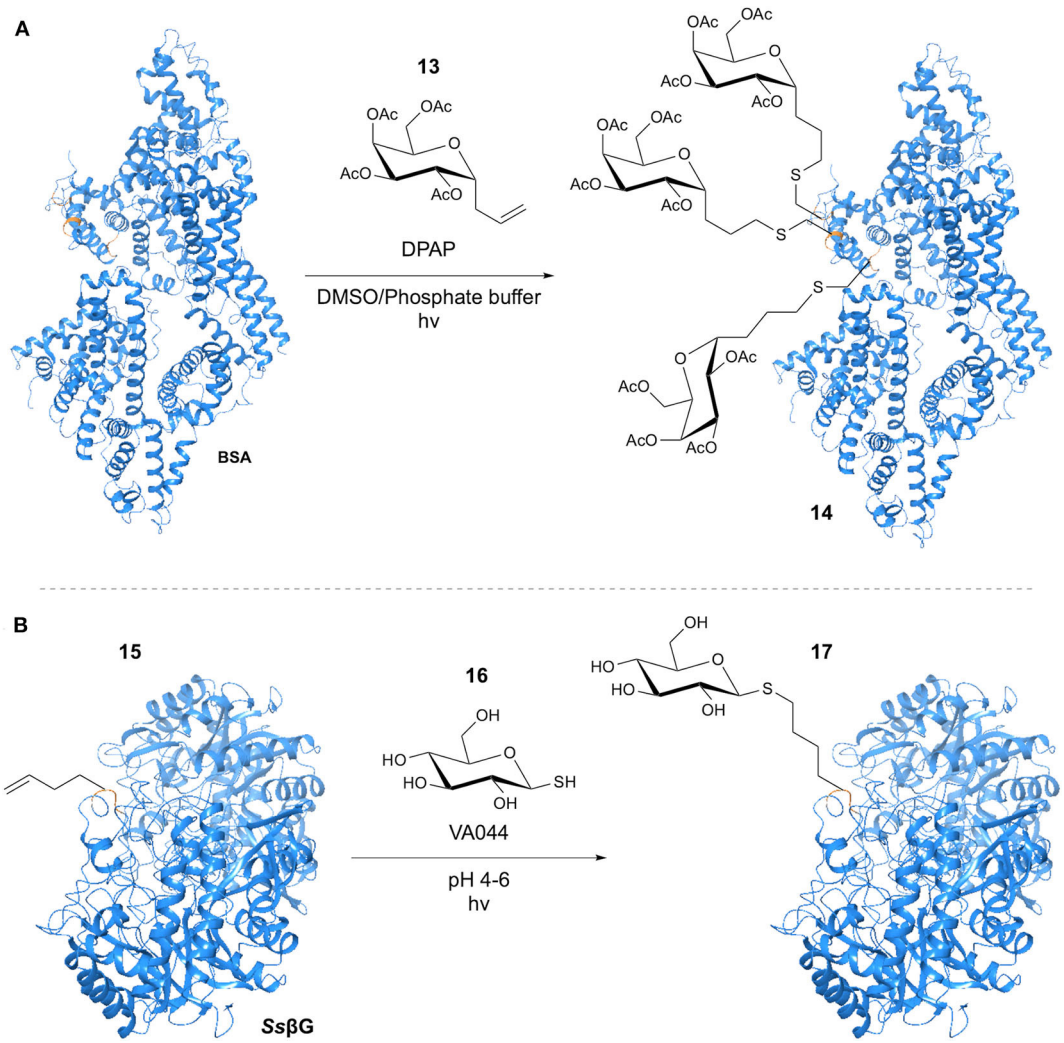

FIGURE 5 | TEC-mediated protein glycosylation. **(A)** Glycosylation of the Cys residues at positions 34, 75 and 91 of BSA. **(B)** Glycosylation of Hag tag installed in β-Glycosidase.

Glycosylation of all 180 alkenes was observed, with conservation of the structurally integral protein disulphide bonds and again > 95% conversion.

Conte et al. later expanded on Conte et al. earlier studies with the double glycosylation of cysteine-containing peptides via installation of an alkyne at the Cys thiol using propargyl bromide, followed by sequential thiol-yne-thiol-ene couplings (Conte et al., 2010). In further studies, Fiore et al. reversed the functional handles of the amino acid and carbohydrate reactants, demonstrating DPAP initiated glycosylation of alkene-containing amino acids using glycosyl thiols (**Figure 6A**) (Fiore et al., 2011). Solution-phase peptide synthesis using a glycosylated amino acid then yielded a glycosylated tripeptide with overall 61.5% yield, demonstrating coupling at both the *N* and *C* terminus. An alternative approach to synthesis of glycosylated Cys was also presented via an initial reaction of Boc-protected Cys with 4-bromo-1-butene to give an alkene functionalized amino acid, followed by TEC with the glycosyl thiol. This approach was further applied to modification of GSH, where modification with 4-bromo-1-butene, followed by TEC afforded glycosylated GSH with 97% yield.

Conte et al. later investigated the modification of BSA first with a sugar alkyne at Cys residues via thiol-yne coupling, followed by fluorescent labeling via TEC (Conte et al., 2011). This study primarily focused on the use of thiol-yne coupling to introduce alkynes bearing sugars or other linkers.

Lázár et al. demonstrated an alternative approach through the use of enoses as the alkene component of the TEC reaction (Lázár et al., 2012). Though the majority of this work focused on non-peptidic thiols, the reaction was demonstrated using *N*-Acetyl-Cys and also the GSH tripeptide using DPAP in DMF.

The synthesis of glycosylated amino acids and their application in SPPS was also investigated by Piccirillo et al., using TEC between Fmoc-Cys and various *O*-allyl glycosides (Piccirillo

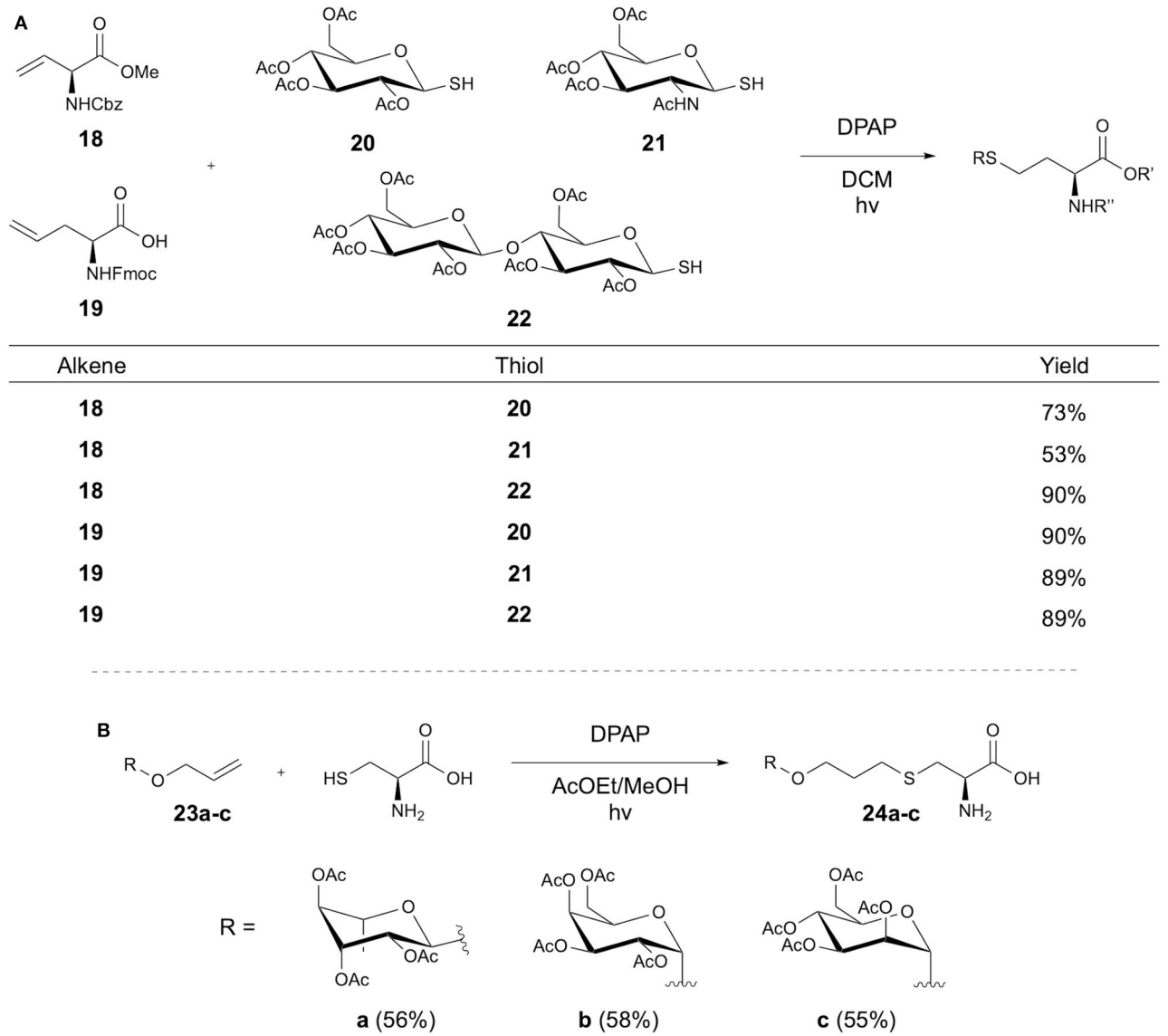

Alkene	Thiol	Yield
18	**20**	73%
18	**21**	53%
18	**22**	90%
19	**20**	90%
19	**21**	89%
19	**22**	89%

FIGURE 6 | Synthesis of glycosyl amino acids via TEC. Synthesis of glycosyl amino acids achieved via **(A)** coupling of alkene-containing amino acids and glycosyl thiols or **(B)** using cysteine and an alkene-linked sugar.

et al., 2017). Elastin-derived peptides were synthesized with an *N*-terminal Cys residue, but attempts to perform TEC with the peptide gave low yields (26%), inspiring the alternative approach of SPPS using glycosyl amino acids **23a-c**. Acetyl-protected allyl carbohydrates underwent TEC with Fmoc-Cys using DPAP in an ethyl acetate/methanol solvent mix (**Figure 6B**). These were then applied in SPPS using racemization-reducing conditions. Cleavage from the resin followed by deprotection of the carbohydrate then followed to yield the desired glycopeptides.

The work of Rojas-Ocáriz et al. aimed to provide application of glycopeptides synthesized via thiol-ene chemistry as potential vaccines (Rojas-Ocáriz et al., 2016). The authors utilize TEC for synthesis of glycosyl amino acids for incorporation of carbohydrate antigens to MUC1 sequences via linkers of varying length to favor antigen presentation. Somewhat surprisingly, compared to previous studies, thermal initiation proved more effective, providing glycosyl amino acids with a range of linkers.

The Scanlan group has reported the modification of Cys residues re-formed after native chemical ligation (NCL) using thiol-ene chemistry (Markey et al., 2013). The aim of the study was to demonstrate three sequential NCL-Thiyl radical modification cycles to produce highly functionalized peptides (**Figure 7A**). The first cycle was applied to a Boc-protected alanine thioester 25 and cysteine, followed by functionalization through TEC with a glycan **27** bearing a vinyl ether group in the anomeric position. Use of the photosensitizer 4-methoxyacetophenone (MAP) and DPAP initiator afforded the glycopeptide **28** in 95% yield. Conversion of the peptide to

the *C*-terminal thioester allowed a second NCL cycle with Cys, which then underwent radical-mediated desulfurization following Danishefsky's method (Wan and Danishefsky, 2007). Conversion again to the thioester allowed a third NCL, followed by thiol-ene coupling to introduce an azido group, facilitating fluorescein labeling via CuAAC. This afforded doubly functionalised tripeptide **29**, bearing a carbohydrate and fluorescein modification.

Fiore et al. applied TEC, among other approaches, to the synthesis of tetravalent glycocyclopeptides (Fiore et al., 2013). Synthesis of 10-mer cyclic peptides containing four Lys residues provided the peptidic core structure. For the thiol-ene substrates, the Lys side chains were modified with pentenyl or alloc groups, providing the alkene handle. Conversions of 82 and 85%, respectively, were achieved in coupling with the glycosyl thiol model using DPAP. This methodology was later expanded on by Fiore et al. in a one-pot procedure for synthesis of heteroglycoclusters (Fiore et al., 2014) **33a-b** via tandem thiol-chloroacetyl coupling (TCC) and TEC (**Figure 7B**). Orthogonality of these reactions had been previously demonstrated (Kottari et al., 2014) and therefore allowed selective functionalization of either the alloc alkene or the chloroacetyl groups using glycosyl thiols.

In 2017, Su et al. demonstrated the formation of a covalent attachment between chitosan and the antimicrobial peptide (AMP) α-poly-L-lysine (EPL), showing application with large polysaccharides (Su et al., 2017). Modification of the peptide *N*-terminus to include a homocysteine residue provided the thiol group, whilst modification of the chitosan amino group with methacrylic acid provided an alkene handle (**Figure 8**). TEC was initiated using DPAP in ddH_2O, resulting in radical addition over possible thiol-michael coupling. Chen et al. later expanded on the utilization of thiol-ene chemistry for attachment of AMPs to polysaccharides, using thiolated polysaccharides and alkene-modified peptides (Chen et al., 2019). Thiolated dextran was coupled with aminoethyl methacrylate modified AMPs to give multiple examples of peptidopolysaccharides through TEC using DPAP in ddH_2O.

These examples serve to highlight the broad range of approaches through which thiol-ene chemistry has been integrated in the synthesis of glycopeptides. The approach taken by Davis and co-workers in the glycosylation of 180 sites on a single protein particle allows controlled, large-scale glycosylation across proteins, utilizing a "tag-modify" strategy. In contrast, the same methodology can allow glycosylation of a single site in a protein by incorporating only one "tag." Intermediate levels of glycosylation are also facilitated via TEC, as shown by Dondoni and co-workers using native BSA. Additionally, glycosylation has been performed using both protected and unprotected sugars. This demonstrates the range of glycosylations that have so far been achieved using thiol-ene chemistry.

AMINO ACID AND PEPTIDE LIPIDATION

Recombinant access to lipopeptides is severely restricted due to heterogeneity in the lipid chains, necessitating development of chemical methods for homogenous peptide modification or other synthetic methods for access to lipopeptides. Incorporation of a lipid moiety onto the peptide backbone has been shown to impart a number of therapeutically-relevant advantages such as enzymatic stability, bioavailability and membrane permeability (Hamman et al., 2005; Simerska et al., 2011; Zhang and Bulaj, 2012). Additionally, a number of lipopeptides isolated from nature show promise as potential therapeutics, including novel antimicrobial agents (Cochrane and Vederas, 2016). Approaches to chemical synthesis of lipopeptides include synthesis of lipid containing amino acids or modification of peptide chains to attach a lipid moiety, both of which have been achieved through application of thiol-ene chemistry. Modification of peptide chains via thiol-ene chemistry has been widely studied in the context of the CLipPA methodology developed by the Brimble group, involving use of fatty acid vinyl esters for attachment at Cys residues (Kowalczyk et al., 2017; Hermant et al., 2020).

Triola et al. investigated the thiol-ene reaction for synthesis of lipidated Cys residues for use in preparation of lipid-modified Ras protein analogs, with particular focus on introducing non-natural hexadecylated Cys (Triola et al., 2008). The aim of the study was to provide a more efficient synthetic route to access alkylated Cys residues, as previously reported methods relying on use of basic conditions for Cys alkylation furnished yields below 30% and required extensive purification, along with significant racemization. To avoid racemization, the authors focused on the thiol-ene reaction between cysteine residues bearing varying protecting groups and 1-hexadecene, with the end goal of synthesis of Fmoc-Cys(hexadecane)-OH **43** (**Figure 9**). Alkylation of the Cys methyl ester provided the product in 91% yield through TEC using AIBN as the initiator, followed by Fmoc protection to give intermediate **42** in overall 74% yield. Cleavage of the methyl ester presented a problematic step, inducing racemization and resulting in an ee of only 86%. To avoid this step, the use of different protecting groups was explored. The most efficient route, giving an overall yield of 57% in four steps, employed Cystine-O^{t}Bu as a starting material in which the disulphide bond was reduced using dithiothreitol (DTT), followed by TEC, Fmoc-protection and ester hydrolysis using TFA. Stereochemistry was retained to afford 99% ee in the product **36**. Various other protecting groups were also investigated, giving a range of overall yields from 42 to 55%. Notably, use of Fmoc-Cys(Trt)-OH **47** gave 55% yield in only two steps. To demonstrate wider application, **47** was reacted with a range of other alkenes including 1-octene, 2-methyl-1-hexene and *trans*-2-octene as well as a dansyl derivative and biotin marker, providing yields ranging from 35 to 91%.

Lipidation of Cys residues through TEC with vinyl esters has been extensively investigated by the Brimble group. In 2013, the Brimble group investigated the "post-translational" TEC of vinyl palmitate with Cys residues (Wright et al., 2013), noting the poor efficiency of using lipidated amino acids in SPPS. Initial investigations focused on reaction between Fmoc-Cys-OH and vinyl palmitate **48a**. Notably, thermal initiation using AIBN resulted in a complex mixture of products, whereas photoinitiation using DPAP offered an improved profile with yield of 44%. The reaction was then applied to

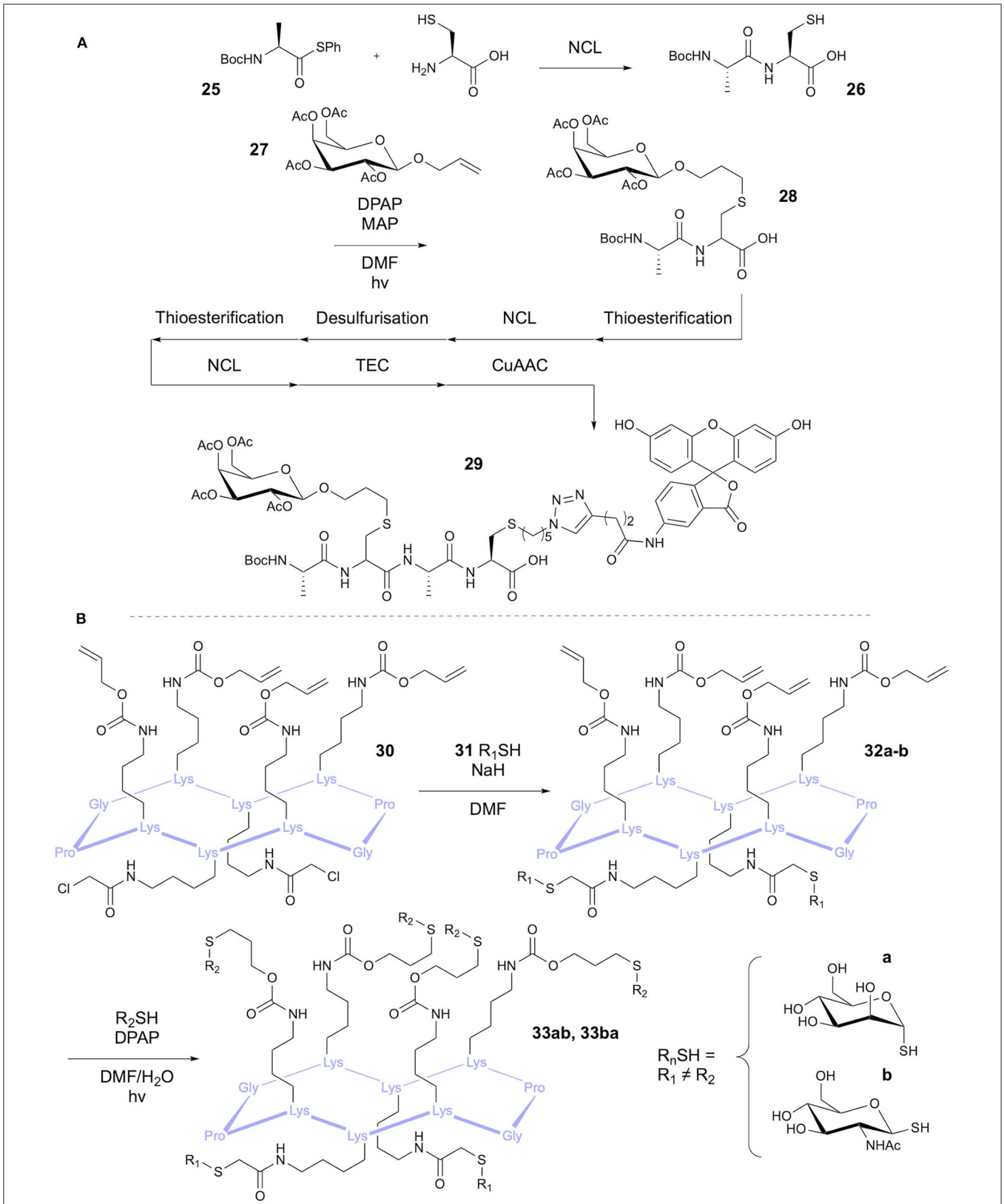

FIGURE 7 | Synthesis of heterofunctionalised peptides. **(A)** Cycles of NCL and thiyl radical reactions have been used to synthesize a tripeptide with different modifications. **(B)** TEC and TCC has been used in a one-pot reaction to give heteroglycosylated peptides.

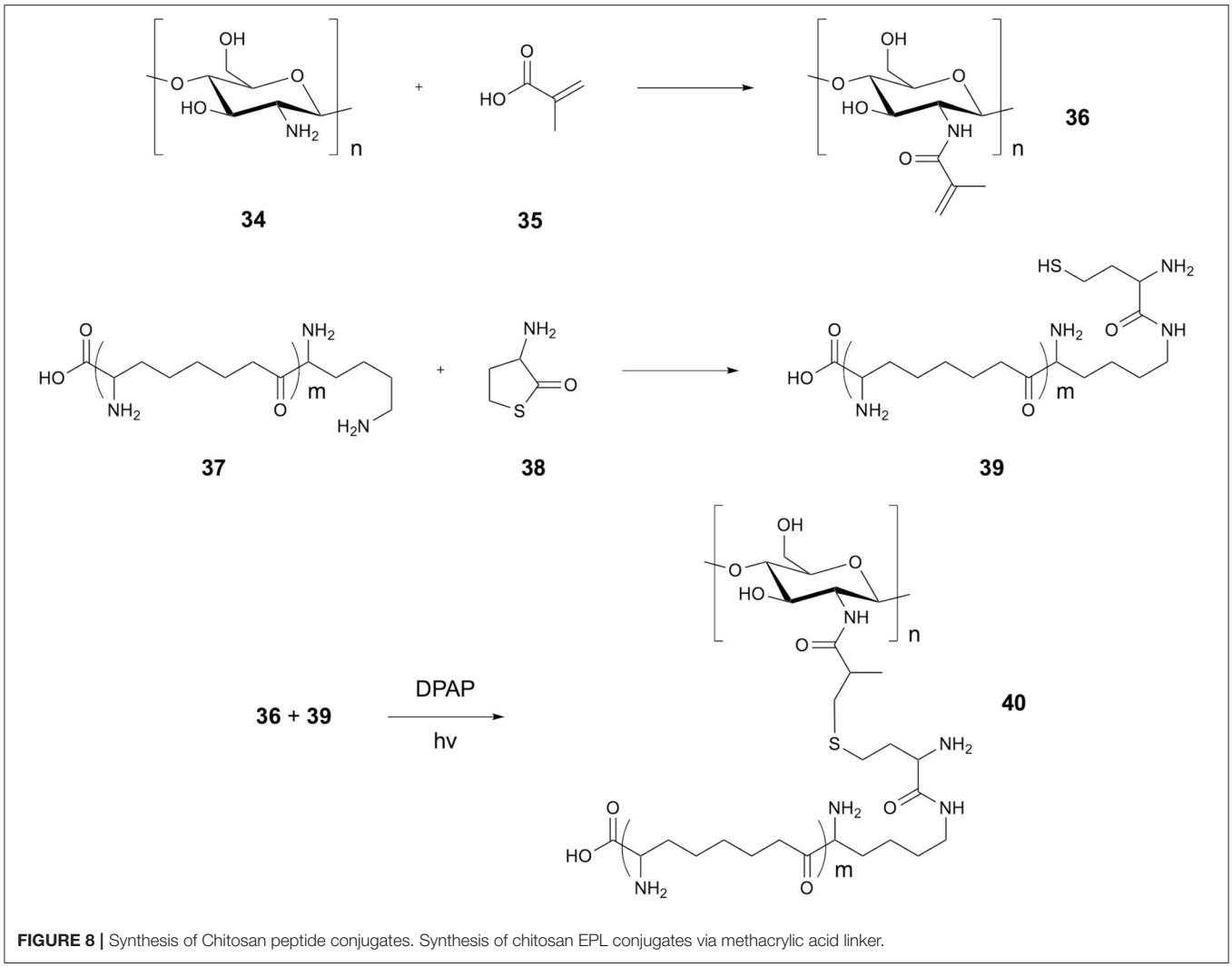

FIGURE 8 | Synthesis of Chitosan peptide conjugates. Synthesis of chitosan EPL conjugates via methacrylic acid linker.

an unprotected hexapeptide example, with thermal initiation providing no desired product, whilst photochemical conditions gave over 90% conversion via use of DPAP in NMP, with 5 equivalents of **48a**. However, significant amounts of by-products were observed due to polymerization of the vinyl palmitate. To reduce this polymerization, DTT was added to provide more efficient chain transfer via reaction with the C-centered radical resulting from thiyl radical attack on the alkene. This resulted in elimination of such polymerization by-products with conversions >90%. The reaction with a 15-mer peptide containing a terminal Cys, solubilizing polylysine tag and 9-mer epitope (CSKKKKNLVPMVATV) known to activate cytotoxic T-cells was then investigated. The lipopeptide target was obtained in >95% purity after RP-HPLC, though no yield is reported. Notably, lipopeptides prepared via this method showed comparable bioactivity to naturally occurring analogs.

Yang et al. later provided detailed insight into the methodology, which they termed Cysteine Lipidation on a Peptide or Amino acid (ClipPA) (Yang et al., 2016). This study aimed to vary the *N*-protecting group (Fmoc, Boc, Ac), radical initiator (DPAP, AIBN) and activation method (thermal, UV, microwave). For the Fmoc- and Boc-protected residues, photoinitiation using DPAP gave the best results at 82% isolated yield in both cases. In the case of Ac-Cys, microwave irradiation with AIBN gave the best result, with >99% yield, although other initiation conditions gave high yields of 74 to 95%. The authors then investigated the coupling of N^{α}-protected *S*-palmitoylated Cys to a peptide in SPPS. To this end, a 14-mer sequence corresponding to that utilized in the previous study was constructed on-resin (SKKKKNLVPCVATV). Incorporation of Cys(^{t}Bu) demonstrated tolerance for suitably protected sulfhydryl groups within the sequence. Coupling was performed using (benzotri-azol-1-yloxy)tripyrrolidinophosphonium hexafluorophosphate (PyBop) and 2,4,6-trimethylpyridine (TMP). When using the acetyl-protected amino acid a 1:1 mixture of epimers was obtained due to racemization during the formation of the activated ester. In contrast, the Fmoc protection resulted in no detectable racemization. A convergent approach for synthesis of this lipopeptide was then investigated, in which the full 15-mer sequence

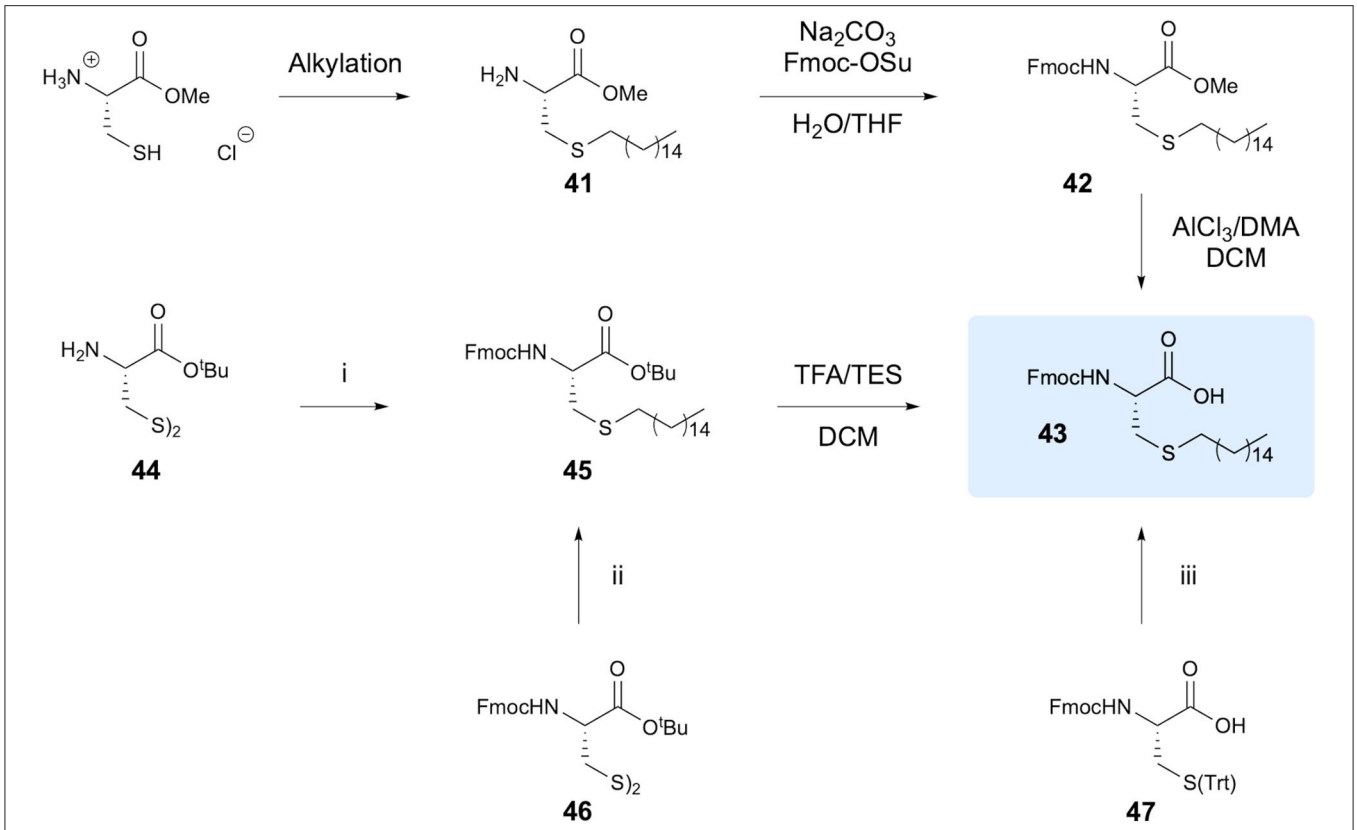

FIGURE 9 | Synthesis of alkylated Cys amino acids. The various approaches to synthesis of Fmoc-Cys(hexadecane)-OH investigated are shown. (i) 1. DTT, DCM. 2. 1-Hexadecene, AIBN, DCE. 3. Na_2CO_3, Fmoc-OSu, H_2O/THF. (ii) 1. DTT, DCM. 2. 1- Hexadecene, AIBN, DCE. (iii) 1. TFA/TES, DCM. 2. 1-Hexadecene, AIBN, DCE.

(AcHN-SKKKKNLVPCVATV) was constructed on resin and cleaved prior to lipidation. Optimisation of the conditions previously reported, along with addition of triisopropylsilane (TIPS) provided the desired monopalmitoylated product (**Figure 10**) in 88% yield, with 12% *bis*-palmitoylated by-product and overall >95% conversion. Application of the methodology to longer peptides, a 44-mer and 32-mer (AcHN-CSKKKKGARGPESRLLEFYLAMPFATPMEAELARRSLAQDA PPL-OH and H_2N-CSKKKKVPGVLLKEFTVSGNILTIRLTAAD HR-OH), gave exclusively monopalmitoylated product in yields of 81 and 46%, respectively. The authors assign high importance to the use of the dual-reducatant ^{t}BuSH-TIPS system in prevention of formation of *bis*-adducts through efficient propogation of the radical chain.

In 2018, Williams et al. reported further development of the CLipPA methodology in adaptation for on-resin lipidation (SP-CLipPA) through the synthesis of a CGRP receptor antagonist (Williams et al., 2018). This was necessitated by poor conversion and complex reaction profile when lipidation was performed in solution, as in the lipidated amino acid approach. Synthesis of the linear peptide (THRLAGLLSRSGGVVKNNFVPTNVGSKAF-RA-Resin) on resin was carried out, incorporating orthogonally protected Cys(Mmt)-OH at the *N*-terminus to allow for selective sulfhydryl deprotection. Application of previously optimized CLipPA conditions furnished the desired lipopeptide, albeit with only 20% conversion. Optimisation of reaction conditions using 70 equivalents of vinyl palmitate, one equivalent of DPAP and DMF solvent, resulted in 91% conversion, with 97:3 ratio of *mono*- to *bis*-palmitoylated product. The desired lipopeptide was obtained in 30% yield with 97% purity. This lipopeptide CGRP receptor antagonist gave equivalent antagonism to CGRP in cell studies.

Yim et al. recently applied CLipPA chemistry to the lipidation of cyclic peptides obtained via native chemical ligation (NCL) (Yim et al., 2020b). This NCL-CLipPA approach involved reaction of the Cys residue regenerated following NCL with lipid vinyl esters to afford the cyclic lipopeptide products (**Figure 10**). This study focused on the synthesis of an analog of iturin A, a broad spectrum antifungal cyclic lipopeptide, bearing a β-amino acid with a lipid side chain. Replacement of the α-amino acid with a lipidated Cys residue provided an analog suitable for the NCL-CLipPA synthetic approach. Boc-SPPS provided the linear peptide *C*-terminal thioester, which underwent NCL in solution upon unmasking of the D-1,3-thiazolidine-4-carboxylic acid (D-Thz) to give the *N*-terminal Cys, followed by adjustment to pH 7.5, affording the cyclic peptide **51** in 38% yield. Lipidation of the Cys was performed using vinyl palmitate **48**, TIPS/*tert*-nonylthiol (^{t}NonSH), and DPAP, giving 82% conversion. This approach was subsequently applied to synthesis of six iturin A analogs **52a-f**. Cysteine modifications included short (propyl),

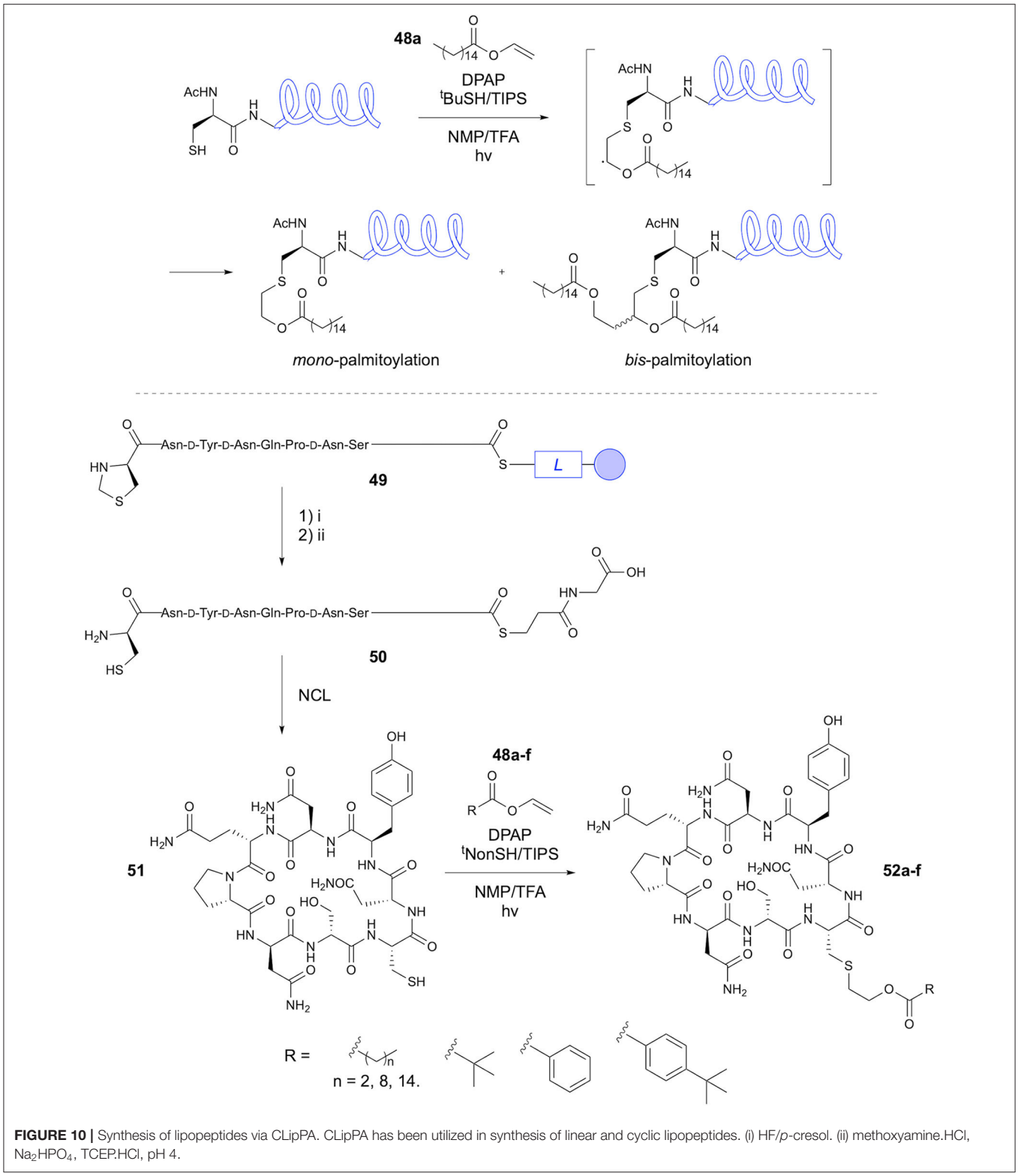

FIGURE 10 | Synthesis of lipopeptides via CLipPA. CLipPA has been utilized in synthesis of linear and cyclic lipopeptides. (i) HF/*p*-cresol. (ii) methoxyamine.HCl, Na_2HPO_4, TCEP.HCl, pH 4.

medium (nonyl) and long (palmityl) lipid chains, a branched (^{t}Bu) chain, phenyl group and *para*-^{t}Bu substituted phenyl group attached via the ester linkage. Conversions achieved for the CLipPA step were high, ranging from 81 to 85%. Unfortunately, the analogs prepared did not show biological activity. The authors hypothesize that this is due to the smaller macrocycle compared to iturin A. However, this is an important demonstration of the use of natural amino acids and modification of the peptide chain

to negate the challenging synthesis of chiral lipid-containing amino acids for synthesis of lipopeptides.

Yang et al. further investigated the application of alternative thiol radical chain propagators in their CLipPA methodology in place of ^{t}BuSH (Yang et al., 2020b). This investigation was motivated by the desire to replace the volatile, odorous ^{t}BuSH, of which approximately 80 equivalents are required for high conversions. The authors defined two selection criteria; that the thiol be sufficiently bulky to prevent *S*-alkylation, and that it should be less volatile than ^{t}BuSH. Two alternatives were therefore investigated. Trityl thiol (TrtSH) is a solid and the radical generated is stabilized by the phenyl groups. ^{t}NonSH is significantly less volatile and has sufficient steric bulk to prevent *S*-alkylation. Initial screening using TrtSH gave complicated product mixtures, whereas those using ^{t}NonSH gave comparable results to ^{t}BuSH. A number of examples using ^{t}NonSH gave conversions mostly of >95%, with one example at 82%.

In their recent studies utilizing the CLipPA methodology, Yim et al. synthesized a number of linear Battacin analogs with varying lipid chains (Yim et al., 2020a). The previously developed system utilizing DPAP, TIPS and ^{t}NonSH in NMP afforded lipopeptides in yields ranging from 1 to 32%, with >94% purity via either an *N*-terminal Cys or 3-mercaptopropionate (MPA) handle. Antimicrobial properties of the synthesized peptides were evaluated via minimum inhibitory concentration (MIC) values against *E. coli*, *P. aeruginosa*, and *A. calcoaceticus* Gram-negative bacteria, as well as Gram positive *S. Aureus*. Additionally, molecular dynamics (MD) simulations were used to study the mechanism of action. The MPA-linked lipopeptides were found to possess MICs equal to or lower than their Cys-linked counterparts bearing the same lipid. Lowest MICs were observed for the peptides baring long alkyl chains (9 carbons) or substituted aromatic moieties. This study is an important demonstration of use of the CLipPA methodology to afford a library of biologically active synthetic peptides. The group also published a study on synthesis of Paenipeptin C' analogs bearing a range of lipid moieties via CLipPA using the MPA handle (Tong et al., 2020). A number of analogs obtained showed comparable or improved activity to Paenipeptin C' against *E. coli* and *S. aureus*, again demonstrating the utility of the CLipPA methodology in preparation of a library of biologically active synthetic lipopeptides.

The CLipPA methodology was also applied to the synthesis of Connexin 43 channel inhibitory Peptide5 analogs (Yang et al., 2020a). Peptide5 moderates hemichannels and gap junctions, with implication in the progression of neurological disease. It was hypothesized that addition of a lipid moiety would help in anchoring of the peptide to the cell membrane, thus aiding function. Six peptide thiol analogs were synthesized through use of a Cys handle in place of a single native amino acid residue. One further peptide thiol was synthesized via capping of the *N*-terminus using 3-mercaptopropionic acid to provide the thiol handle. The native Cys residue in the 3-position was protected using a temporary acetamidomethyl (Acm) group, which was removed after *S*-lipidation. Previously optimized conditions for the CLipPA methodology were applied to synthesis of a total of 42 lipopeptide analogs. Biological evaluation of these lipopeptides showed no improvement in half-life compared to the natural Peptide5, but did exhibit improved functional efficacy where short lipid chains were used. This study importantly demonstrated further that the CLipPA methodology can be used in preparation of biologically active lipopeptides.

The most recent demonstration of the use of the CLipPA methodology from the Brimble group was in the synthesis of truncated *S*-lipidated teixobactin analogs (Yim et al., 2020c). Capping of the *N*-terminal of truncated teixobactin with 3-mercaptopropionic acid provided the thiol handle for CLipPA. Lipids of varying length were attached via this methodology, but unfortunately no activity was observed against *S. aureus*. It was hypothesized that the lack of activity was due to the increased hydrophilicity provided by the sulfur-containing bridging unit when compared to the control analog used, lipobactin, in which the lipid is attached directly to the *N*-terminus.

The studies discussed herein illustrate the two approaches to lipopeptide synthesis via thiol-ene chemistry, namely through incorporation of lipidated amino acids or via modification of peptide sequences. The CLipPA methodology has been extensively studied and developed, providing access to examples of biologically active linear peptides, as well as methodology for synthesis of cyclic lipopeptides. The methodology has shown compatibility with a range of sequences, producing high conversions, whilst on-resin modifications allow for greater ease of purification.

OTHER FUNCTIONALIZATIONS AND APPLICATIONS

Thiol-ene chemistry has been used for a number of functionalizations that do not fall into the previous categories. Whilst many biological applications particularly necessitate cyclization, glycosylation and lipidation of peptides and proteins, other synthetic modifications provide useful applications for chemical biology. Modifications including attachment of small alkenes can be used as handles for further conjugation or study of peptide binding. Innovative approaches to biological studies have also incorporated radical thiol-ene chemistry for the study of protein modifications and enzyme activity.

Karmann and Kazmier have investigated the use of TEC for the synthesis of modified amino acids, using allylglycine and a variety of thiols (Karmann and Kazmaier, 2013). Initial studies utilized Boc-protected allylglycine, which was reacted with a range of thiols using EtOH as a solvent under UV irradiation. High yields, mostly over 90%, were achieved and thiols bearing simple alkanes, alcohols, carboxylic acids, amines and a trimethoxy silicate group were coupled, along with thioacetic acid and Boc-Cys. The reaction was then applied to two further substituted alkene containing amino acids **56** and **58** (**Figure 11A**). The terminal alkene still provided comparable results to allylglycine, but the linear side chain amino acid did not react. The authors suggest that this is a steric effect. Investigation of the effect on the enantiomeric purity was carried out, showing reduction from 86 to 80% ee in the TEC reaction. This was

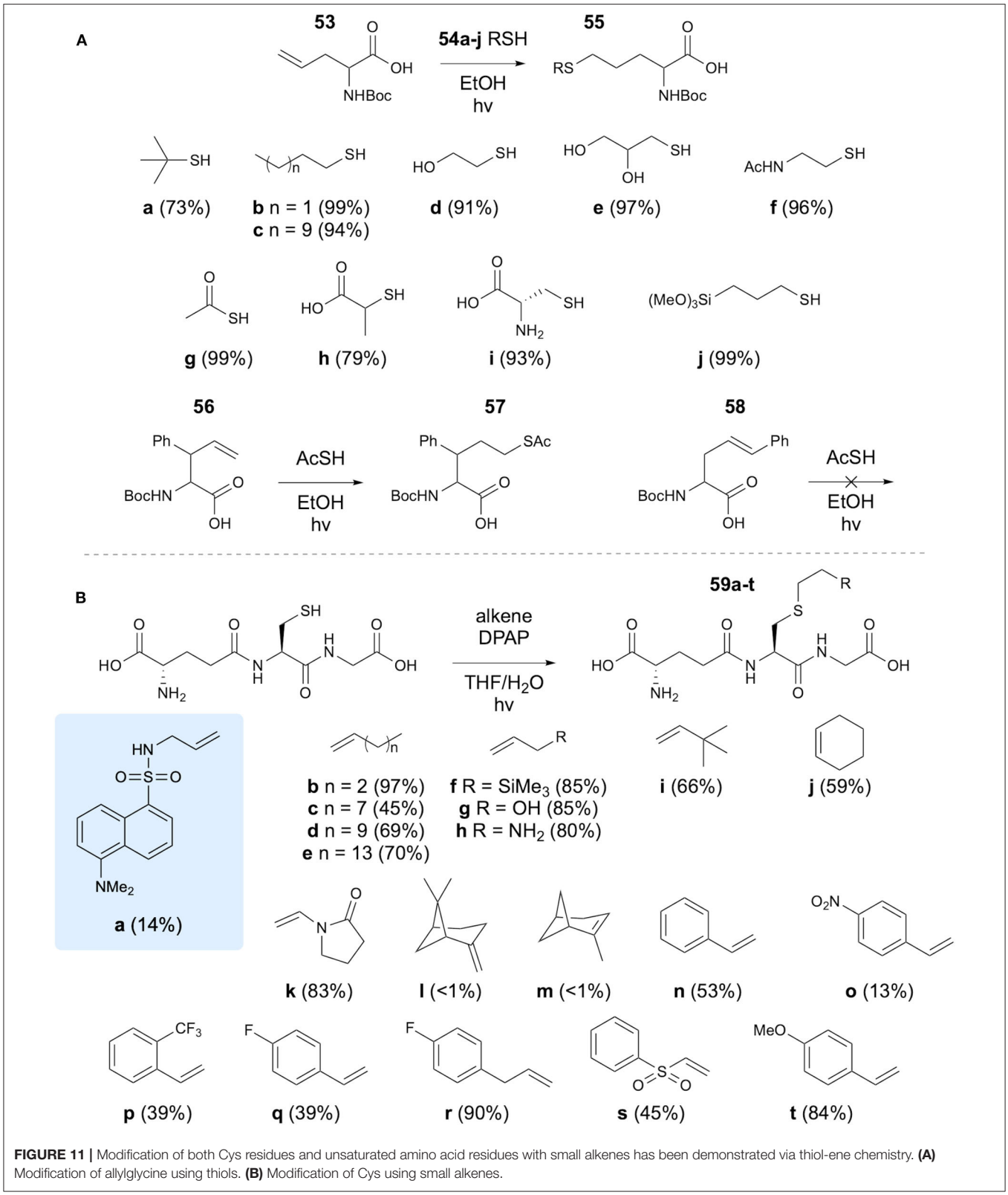

FIGURE 11 | Modification of both Cys residues and unsaturated amino acid residues with small alkenes has been demonstrated via thiol-ene chemistry. **(A)** Modification of allylglycine using thiols. **(B)** Modification of Cys using small alkenes.

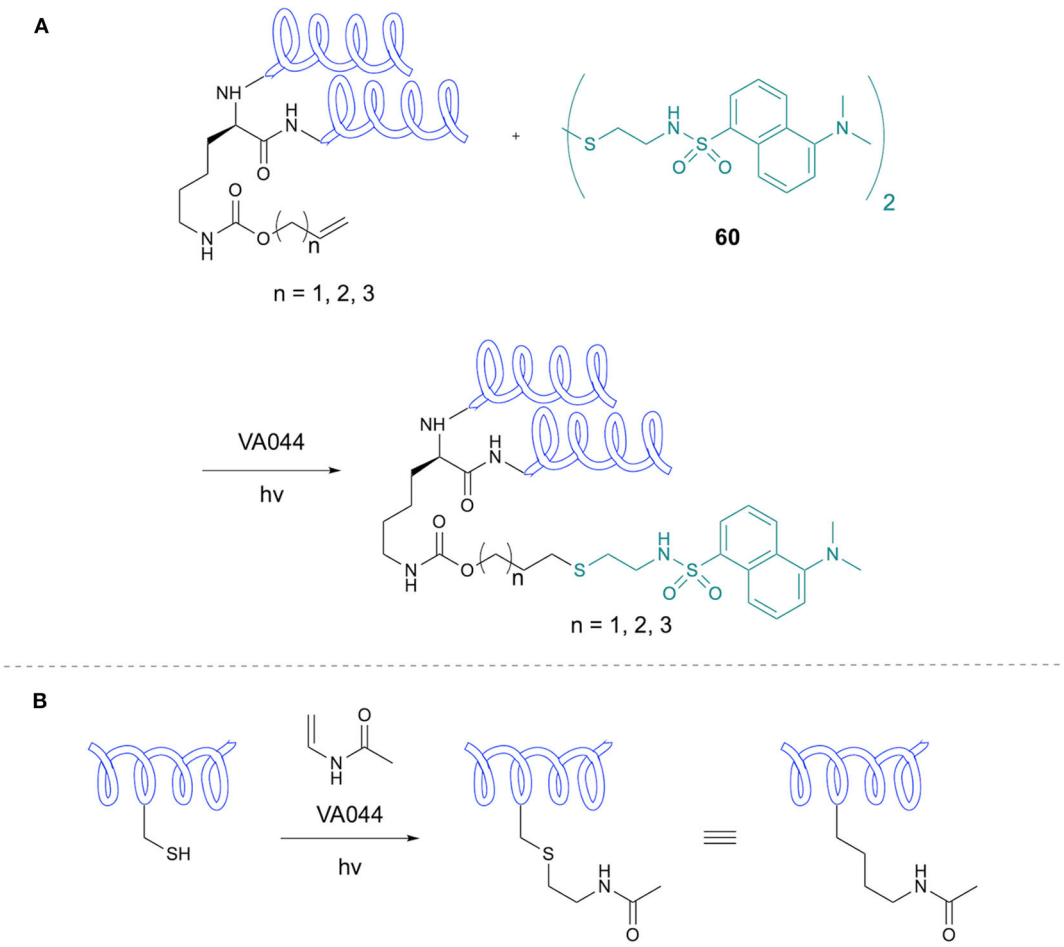

FIGURE 12 | Lysine modification and Acetylated Analogs. **(A)** Synthesis of di-dansyl-tagged peptides via genetically-encoded lysine alkene modification. **(B)** Synthesis of acetylated Lys analogs through thiol-ene chemistry.

further investigated in dipeptides, where no epimerization was detected. Furthermore, an allylglcine containing tetrapeptide and a tetrapeptide containing a vinyl ether side chain amino acid were successfully reacted with a selection of thiols.

Healy et al. have applied TEC to the synthesis of glutathione conjugates for study of binding to bacterial glutathione-binding protein Kef (Healy et al., 2016). Initial motivation for this study involved the synthesis of a dansyl labeled GSH analog **59a**. To this end, dansyl chloride was reacted with allylamine to introduce an alkene group, which was subsequently reacted with the Cys thiol of GSH using DPAP initiator in THF/H_2O solvent mixture. It was found that TCEP.HCl was also required as a reducing agent to prevent formation of the disulfide, though for simpler alkenes this was excluded. A variety of alkenes were coupled with GSH with varying yields (**Figure 11B**). Analogs synthesized using this approach were subsequently investigated in binding studies.

Recently, the Scanlan group applied radical TEC coupling to dehydroalanine (Dha) for synthesis of *N*-terminal cysteinyl thioesters suitable for *S*, *N*-acyl transfer (Petracca et al., 2019). Radical TEC between *N*-protected Dha and either thioacetic acid or a glycine thioacid was effected using DPAP and MAP in aqueous buffer at pH 6. An azido Dha derivative was also utilized in reaction with thioacetic acid with full conversion, having previously failed to react under ionic conditions. The doubly Boc-protected Dha was found to be the most efficient Dha derivative in the radical process, whilst derivatives protected with a single Boc group or with a Boc and Ac group gave no conversion.

Valkevich et al. have reported the use of thiol-ene chemistry in the synthesis of branched Ubiquitin (Ub) trimers for study of isopeptidase activity (Valkevich et al., 2012). Site-directed mutagenesis was used to generate Ub monomers with a Cys residue in place of a Lys, whilst the *C*-terminus of another Ub monomer was modified with allylamine, furnishing an *Nε*-Gly-L-homothiaLys isopeptide bond upon TEC. Initial studies on dimer formation found lithium acyl phosphinate (LAP) photoinitiator to be the most effective initiator. Topoisomers, linked via different Lys position mutations were produced, with varying results due to lower conversions with increasing steric bulk surrounding the position at which the radical is generated. To investigate the function of these dimers, hydrolytic cleavage

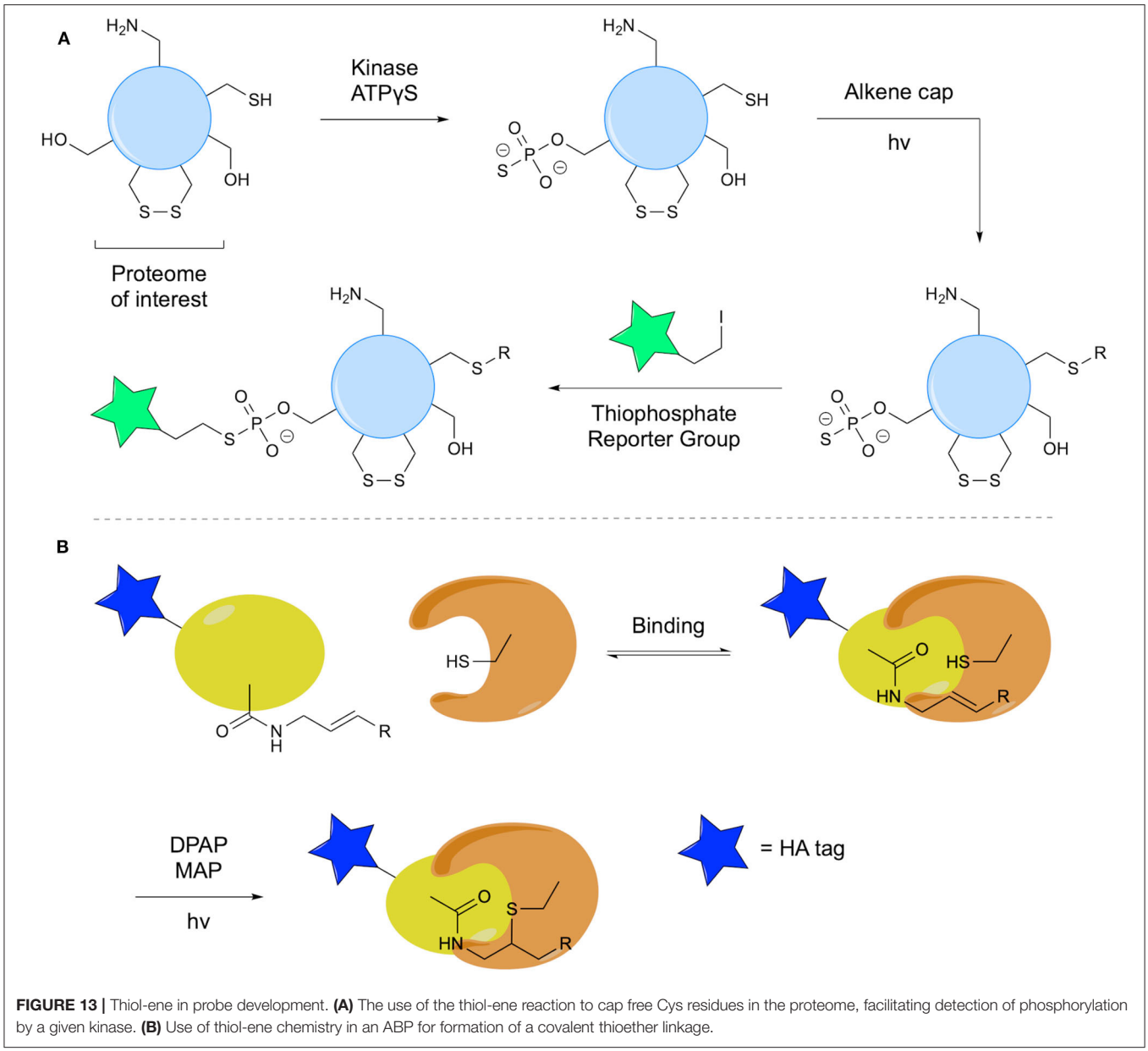

FIGURE 13 | Thiol-ene in probe development. **(A)** The use of the thiol-ene reaction to cap free Cys residues in the proteome, facilitating detection of phosphorylation by a given kinase. **(B)** Use of thiol-ene chemistry in an ABP for formation of a covalent thioether linkage.

of the *N*ε-Gly-L-homothiaLys isopeptide links was investigated using isopeptidases. The authors observed a nearly identical half-life for *N*ε-Gly-L-homothiaLys and naturally occurring *N*ε-Gly-L-Lys, with site selectivity maintained for different isopeptidases. TEC was then applied in the synthesis of three Ub_3 topoisomers. Different deubiquitinases (DUBs) were applied to hydrolysis of trimers, again showing selectivity for different linkages depending on the DUB applied.

Rafie et al. have applied TEC in the synthesis of uridine diphosphate (UDP) peptide conjugates for application as β-*N*-acetylglucosamine transferase (OGT) inhibitors (Rafie et al., 2018). To this end, allyl-UDP was reacted with Cys-containing cell penetrating peptides (CPPs) through TEC. Michael addition and disulfide exchange pathways were also investigated but proved less ideal due to need for an additional electron-withdrawing group and racemization of the Cys linker, respectively. For TEC, the initiators VA044, DPAP, and MAP were investigated, with LAP giving best results. The conjugates were shown to have activity toward human OGT *in vitro*.

Li et al. applied TEC to introduction of fluorescent dyes to proteins incorporating genetically encoded alkene handles in an example of a "tag-modify" approach (**Figure 12A**) (Li et al., 2012). The authors incorporated alkene-bearing lysine derivatives into protein sequences using a mutant pyrolysyl-tRNA-synthetase (PylRS). Thiol-ene modification was applied to HdeA, an *E. coli* acid-chaperone, modified with an alkene-containing residue at the 58 position. The tagged protein was reacted with bi-dansyl-cystamine using VA044 initiation

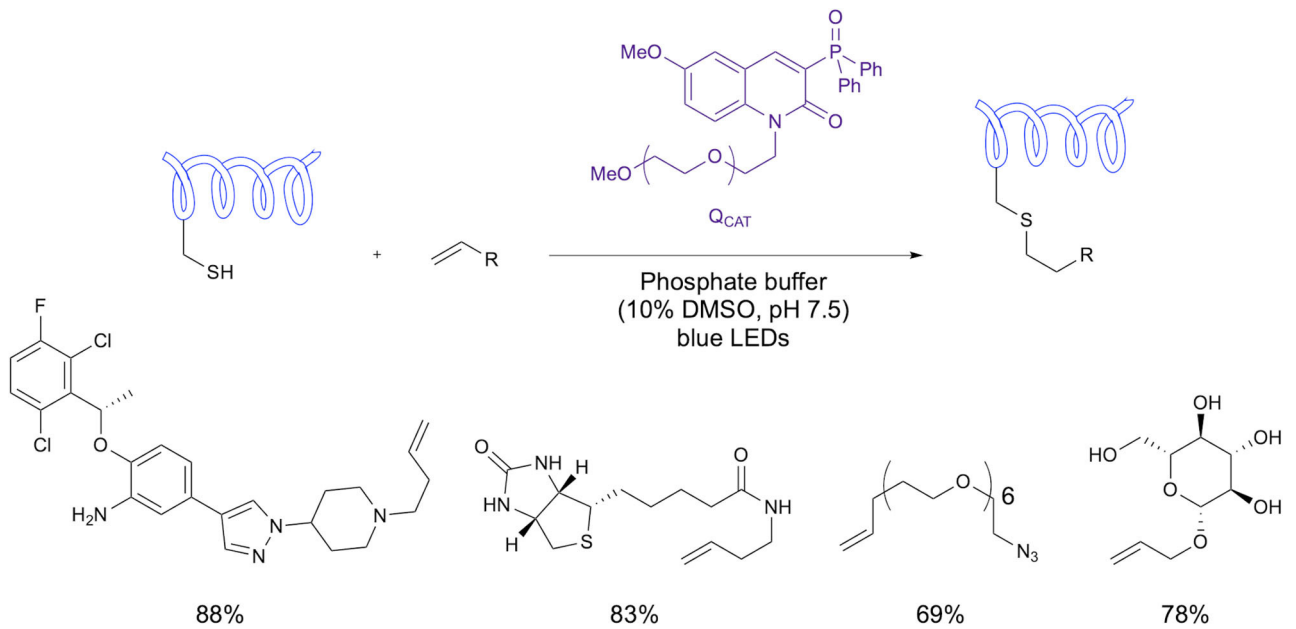

FIGURE 14 | Visible light thiol-ene bioconjugation. Use of an organic photosensitizing fluorophore to facilitate bioconjugation under illumination with blue LEDS.

in the presence of reduced GSH. Biological studies suggested a similar activity of this modified protein to its natural analog. Modification of two sites of HdeA was then studied, with successful double ligation of bi-dansyl-cystamine. To demonstrate application to larger proteins, 36 KDa asparaginase II was tagged at the 79 position and successfully modified with the dansyl thiol without effect on the protein Cys residues.

Li et al. demonstrated the application of TEC for site-specific protein acetylation, with the aim of application in study of Lys acetylation biology (Li et al., 2011). A major challenge in this field is obtaining homogeneous protein samples with acetylation of the Lys residue of interest. The authors therefore envisaged selective modification of a Cys residue via TEC to afford a *N*-acetyl-thialysine [sLys(AC)] residue to act as Lys(Ac) mimetic (**Figure 12B**). The methodology was applied to synthetic Cys-tagged peptides via TEC with *N*-vinyl acetamide in the presence of VA044 as initiator, along with reduced GSH to encourage radical chain transfer, giving products in near quantitative yields. Control peptides with no Cys residue did not react under the same conditions or in absence of UV or VA044. Application to a peptide containing four Cys residues gave tetra-alkylation in 95% yield. Mutant protein examples including Ub and histones were also successfully reacted with *N*-vinyl acetamide to give the desired alkylation products. The sLys(Ac) residues proved to be suitable mimetics of Lys(Ac) in biological studies.

An interesting application of thiol-ene chemistry in detection of phosphorylated proteins was reported by Garber and Carlson using TEC to mask cysteine residues (Garber and Carlson, 2013). In this methodology, adenosine 5′-*O*-(3-thiophosphate) (ATPγS) facilitates transfer of a thiophosphate by an appropriate kinase. This group is subsequently employed as a nucleophile for detection of protein phosphorylation. However, to facilitate use of this nucleophilic handle, other Cys residues must be blocked. TEC was used, as it is selective for Cys thiols over thiophosphorylated residues due to differences in pK_a, facilitating selective radical formation. In the capping of the Cys thiols, 1-(2-methoxyphenyl)-3-buten-1-ol was reacted with the protein using the LAP photoinitiator. A thiophosphorylated derivative showed no reaction under the same conditions (**Figure 13A**). This methodology was applied to a cancer cell proteome using three different kinases, facilitating detection of thiophosphorylated species.

Taylor et al. recently applied thiol-ene chemistry in their development of activity-based probes (ABPs) to target DUBs with the additional advantage of control over initiation of the enzyme-probe reaction (Taylor et al., 2020). Radical formation occurs at an active site Cys, triggered by UV irradiation in presence of an initiator, which in turn will react with the alkene of the probe to form a covalent enzyme-probe linkage (**Figure 13B**). The probe used consisted of a human influenza hemagglutinin (HA) tag linked to Ub, the *C*-terminal of which was modified with a terminal alkene. This probe was tested via incubation with recombinant DUB for 1 h, followed by addition of DPAP and MAP, degassing and UV irradiation to successfully effect TEC. A denaturation experiment confirmed the necessity for specific binding interaction prior to TEC. A short irradiation time of only 1 min was required to achieve complete labeling due to the pre-organization afforded by the binding interaction. Further, a phenyl-substituted *trans*-alkene probe was synthesized to elucidate effects on reactivity and selectivity. Comparative

studies with the terminal alkene probe showed reduced labeling of protein targets.

In a recent study from Choi et al., a water soluble fluorescent photosensitizer was utilized in visible-light-induced thiol-ene bioconjugation (Choi et al., 2020). The study demonstrated conjugation of the photosensitizer (Q_{PEG}) via a PEG linker and also of biologically relevant groups (using their catalyst denoted Q_{CAT}) including biotin, an azide group, a drug example and carbohydrate example (**Figure 14**). The reaction proceeded in phosphate buffer under irradiation with blue LEDs. Most notably, this study demonstrates the use of visible light in place of uv irradiation with both peptide and protein examples without the use of a metal catalyst.

These examples serve to highlight the broad range of applications that TEC has found in peptide and protein science, outside of the "traditional" peptide modifications of cyclization, glycosylation and lipidation. In particular, applications in biological studies show the considerable potential of innovative chemical methodologies for probing problems in biology through development of biomimietics, conjugates and probes. The "click" characteristics of the thiol-ene reaction make it an attractive tool for probe development. The highly efficient reaction, as demonstrated by very short reaction times reported by Taylor et al., allows for complete reaction with the relevant biological targets. A less efficient reaction may not provide full coverage of the groups to be investigated using the probe. Similarly, the lack of side products facilitates probe selectivity for thiol residues in targets possessing multiple varying functional groups.

CONCLUSIONS AND OUTLOOK

Radical thiol-ene chemistry has been applied extensively to the field of peptide science. The methodology is highly compatible with sensitive biomolecules and the diverse range of functional groups found in nature. The methodology is tolerant of aqueous conditions and generally high yielding, offering unprecedented chemo- and regioselectivity in modification of peptides and proteins. Peptide stapling achieved via TEC offers considerable promise for further development of novel stapled peptides for therapeutic use, in particular with variation of the staple architecture. Glycosylation methodologies have been extensively developed, incorporating direct peptide-glycan conjugation and use of linkers. Use of the CLipPA methodology for synthesis of lipopeptides has been extensively developed. However, lipidation without use of vinyl esters is relatively poorly studied. A wide range of smaller alkenes have been conjugated to peptides through TEC for varying purposes. The use of thiol-ene chemistry in biological studies has shown particular ingenuity, demonstrating extensive potential for development of TEC-based methodologies to overcome biological problems and for biological applications. For a large number of these applications, the attraction of thiol-ene chemistry lies in its "click" characteristics. The ability to selectively react a thiol and alkene in presence of mixtures of nucleophiles and electrophiles lends itself particularly well to peptide science. The ability to incorporate unsaturated amino acids into peptide and protein sequences has been instrumental in these selective modification approaches.

Despite recent advances, thiol-ene chemistry continues to be underutilized across peptide science and in the wider context of chemical biology, certainly in comparison to the analogous Michael addition. Technical challenges associated with the photochemical nature of the process have largely been ameliorated and the methodology is now well within the means of non-specialist labs. Further innovative applications of thiol-ene in peptide science, in particular, under continuous-flow conditions, will no doubt accelerate interest in the field. The considerable advantages of this approach lend it great potential in future development of peptide modifications and applications in peptide science.

AUTHOR CONTRIBUTIONS

MN performed literature searches. MN and ES prepared the manuscript. All authors contributed to the article and approved the submitted version.

FUNDING

This work was supported by Science Foundation Ireland (SFI) under Grant No. 15/CDA/3310 (ES), SFI Frontiers Award Grant No. 19/FFP/6667 (ES) and SSPC, The SFI Research Center for Pharmaceuticals, Grant No. 12/RC/2275_p2 (MN) and (ES).

REFERENCES

Agouridas, V., El Mahdi, O., Cargoët, M., and Melnyk, O. (2017). A statistical view of protein chemical synthesis using NCL and extended methodologies. *Bioorganic Med. Chem.* 25, 4938–4945. doi: 10.1016/j.bmc.2017.05.050

Aguilar, C. F., Sanderson, I., Moracci, M., Ciaramella, M., Nucci, R., Rossi, M., et al. (1997). Crystal structure of the β-glycosidase from the hyperthermophilic archeon sulfolobus solfataricus: resilience as a key factor in thermostability. *J. Mol. Biol.* 271, 789–802. doi: 10.1006/jmbi.1997.1215

Aimetti, A. A., Shoemaker, R. K., Lin, C.-C., and Anseth, K. S. (2010). On-resin peptide macrocyclization using thiol–ene click chemistry. *Chem. Commun.* 46, 4061–4063. doi: 10.1039/c001375g

Apweiler, R., Hermjakob, H., and Sharon, N. (1999). On the frequency of protein glycosylation, as deduced from analysis of the SWISS-PROT database. *Biochim. Biophys. Acta Gen. Subj.* 1473, 4–8. doi: 10.1016/S0304-4165(99)00165-8

Bernal, F., Tyler, A. F., Korsmeyer, S. J., Walensky, L. D., and Verdine, G. L. (2007). Reactivation of the p53 tumor suppressor pathway by a stapled p53 peptide. *J. Am. Chem. Soc.* 129, 2456–2457. doi: 10.1021/ja0693587

Bernardes, G. J. L., Chalker, J. M., Errey, J. C., and Davis, B. G. (2008). Facile conversion of cysteine and alkyl cysteines to dehydroalanine on protein surfaces: versatile and switchable access to functionalized proteins. *J. Am. Chem. Soc.* 130, 5052–5053. doi: 10.1021/ja800800p

Boutureira, O., and Bernardes, G. J. L. (2015). Advances in chemical protein modification. *Chem. Rev.* 115, 2174–2195. doi: 10.1021/cr500399p

Brosnan, S. M., and Schlaad, H. (2014). Modification of polypeptide materials by Thiol-X chemistry. *Polymer* 55, 5511–5516. doi: 10.1016/j.polymer.2014.08.067

Bujacz, A. (2012). Structures of bovine, equine and leporine serum albumin. *Acta Crystallogr. Sect. D Biol. Crystallogr.* 68, 1278–1289. doi: 10.1107/S0907444912027047

Byk, G., Halle, D., Zeltser, I., Bitan, G., Selinger, Z., and Gilon, C. (1996). Synthesis and biological activity of NK-1 selective, N-backbone cyclic analogs of the C-terminal hexapeptide of substance P. *J. Med. Chem.* 39, 3174–3178. doi: 10.1021/jm960154i

Chalker, J. M. (2013). Prospects in the total synthesis of protein therapeutics. *Chem. Biol. Drug Des.* 81, 122–135. doi: 10.1111/cbdd.12007

Chen, Y., Yu, L., Zhang, B., Feng, W., Xu, M., Gao, L., et al. (2019). Design and synthesis of biocompatible, hemocompatible, and highly selective antimicrobial cationic peptidopolysaccharides via click chemistry. *Biomacromolecules* 20, 2230–2240. doi: 10.1021/acs.biomac.9b00179

Choi, H., Kim, M., Jang, J., and Hong, S. (2020). *Visible-light-induced cysteine-specific* bioconjugation: biocompatible Thiol-Ene click chemistry. *Angew. Chem. Int. Ed.* 59, 2–10. doi: 10.1002/anie.202010217

Cochrane, S. A., and Vederas, J. C. (2016). Lipopeptides from bacillus and Paenibacillus spp.: a gold mine of antibiotic candidates. *Med. Res. Rev.* 36, 4–31. doi: 10.1002/med.21321

Conte, M. L., Pacifico, S., Chambery, A., Marra, A., and Dondoni, A. (2010). Photoinduced addition of glycosyl thiols to alkynyl peptides: use of free-radical Thiol-yne coupling for post-translational double-glycosylation of peptides. *J. Org. Chem.* 75, 4644–4647. doi: 10.1021/jo1008178

Conte, M. L., Staderini, S., Marra, A., Sanchez-Navarro, M., Davis, B. G., and Dondoni, A. (2011). Multi-molecule reaction of serum albumin can occur through thiol-yne coupling. *Chem. Commun.* 47, 11086–11088. doi: 10.1039/c1cc14402b

Deming, T. J. (2016). Synthesis of side-chain modified polypeptides. *Chem. Rev.* 116, 786–808. doi: 10.1021/acs.chemrev.5b00292

Dénès, F., Pichowicz, M., Povie, G., and Renaud, P. (2014). Thiyl radicals in organic synthesis. *Chem. Rev.* 114, 2587–2693. doi: 10.1021/cr400441m

Dondoni, A., Massi, A., Nanni, P., and Roda, A. (2009). A new ligation strategy for peptide and protein glycosylation: photoinduced thiol-ene coupling. *Chem. A Eur. J.* 15, 11444–11449. doi: 10.1002/chem.200901746

Elduque, X., Pedroso, E., and Grandas, A. (2014). Orthogonal protection of peptides and peptoids for cyclization by the thiol-ene reaction and conjugation. *J. Org. Chem.* 79, 2843–2853. doi: 10.1021/jo500427c

Fiore, M., Berthet, N., Marra, A., Gillon, E., Dumy, P., Dondoni, A., et al. (2013). Tetravalent glycocyclopeptide with nanomolar affinity to wheat germ agglutinin. *Org. Biomol. Chem.* 11, 7113–7122. doi: 10.1039/c3ob41203b

Fiore, M., Chand Daskhan, G., Thomas, B., and Renaudet, O. (2014). Orthogonal dual thiol-chloroacetyl and thiol-ene couplings for the sequential one-pot assembly of heteroglycoclusters. *Beilstein J. Org. Chem.* 10, 1557–1563. doi: 10.3762/bjoc.10.160

Fiore, M., Lo Conte, M., Pacifico, S., Marra, A., and Dondoni, A. (2011). Synthesis of S-glycosyl amino acids and S-glycopeptides via photoinduced click thiol-ene coupling. *Tetrahedron Lett.* 52, 444–447. doi: 10.1016/j.tetlet.2010.11.097

Floyd, N., Vijayakrishnan, B., Koeppe, J. R., and Davis, B. G. (2009). Thiyl glycosylate of olefinic proteins: S-linked glycoconjugate synthesis. *Angew. Chem. Int. Ed.* 48, 7798–7802. doi: 10.1002/anie.200903135

Forner, M., Defaus, S., and Andreu, D. (2020). Peptide-based multiepitopic vaccine platforms via click reactions. *J. Org. Chem.* 85, 1626–1634. doi: 10.1021/acs.joc.9b02798

Garber, K. C. A., and Carlson, E. E. (2013). Thiol-ene enabled detection of thiophosphorylated kinase substrates. *ACS Chem. Biol.* 8, 1671–1676. doi: 10.1021/cb400184v

Gause, G. F., and Brazhnikova, M. G. (1944). Gramicidin S and its use in the treatment of infected wounds [3]. *Nature* 154, 703. doi: 10.1038/154703a0

Grossmann, T. N., Yeh, J. T. H., Bowman, B. R., Chu, Q., Moellering, R. E., and Verdine, G. L. (2012). Inhibition of oncogenic Wnt signaling through direct targeting of β-catenin. *Proc. Natl. Acad. Sci. U. S. A.* 109, 17942–17947. doi: 10.1073/pnas.1208396109

Gunnoo, S. B., and Madder, A. (2016). Chemical protein modification through cysteine. *ChemBioChem* 17, 529–553. doi: 10.1002/cbic.201500667

Hamman, J. H., Enslin, G. M., and Kotzé, A. F. (2005). Oral delivery of peptide drugs: barriers and developments. *BioDrugs* 19, 165–177. doi: 10.2165/00063030-200519030-00003

Healy, J., Rasmussen, T., Miller, S., Booth, I. R., and Conway, S. J. (2016). The photochemical thiol-ene reaction as a versatile method for the synthesis of glutathione S-conjugates targeting the bacterial potassium efflux system Kef. *Org. Chem. Front.* 3, 439–446. doi: 10.1039/C5QO00436E

Hermant, Y. O., Cameron, A. J., Harris, P. W. R., and Brimble, M. A. (2020). Synthesis of antimicrobial lipopeptides using the 'CLipPA' thiol-ene reaction. *Methods Mol. Biol.* 2103, 263–274. doi: 10.1007/978-1-0716-0227-0_18

Hess, S., Linde, Y., Ovadia, O., Safrai, E., Shalev, D. E., Swed, A., et al. (2008). Backbone cyclic peptidomimetic melanocortin-4 receptor agonist as a novel orally administrated drug lead for treating obesity. *J. Med. Chem.* 51, 1026–1034. doi: 10.1021/jm701093y

Hoppmann, C., Kühne, R., and Beyermann, M. (2012). Intramolecular bridges formed by photoswitchable click amino acids. *Beilstein J. Org. Chem.* 8, 884–889. doi: 10.3762/bjoc.8.100

Hoppmann, C., Schmieder, P., Heinrich, N., and Beyermann, M. (2011). Photoswitchable click amino acids: light control of conformation and bioactivity. *ChemBioChem* 12, 2555–2559. doi: 10.1002/cbic.201100578

Hoyle, C. E., and Bowman, C. N. (2010). Thiol-ene click chemistry. *Angew. Chem. Int. Ed.* 49, 1540–1573. doi: 10.1002/anie.200903924

Hoyle, C. E., Lee, T. Y., and Roper, T. (2004). Thiol-enes: chemistry of the past with promise for the future. *J. Polym. Sci. Part A Polym. Chem.* 42, 5301–5338. doi: 10.1002/pola.20366

Hu, X., He, Y., Wu, L., Hao, Y., Wang, Z., and Zheng, W. (2017). Novel all-hydrocarbon stapled p110α[E545K] peptides as blockers of the oncogenic p110α[E545K]-IRS1 interaction. *Bioorganic Med. Chem. Lett.* 27, 5446–5449. doi: 10.1016/j.bmcl.2017.10.076

Jón Tryggvi Njardarson (2000). *Jón Tryggvi Njardarson Top Pharmaceuticals Poster | Njarðarson.* Available online at: https://njardarson.lab.arizona.edu/content/top-pharmaceuticals-poster (accessed May 13, 2020).

Karmann, L., and Kazmaier, U. (2013). Thiol-Ene click reactions - versatile tools for the modification of unsaturated amino acids and peptides. *Eur. J. Org. Chem.* 2013, 7101–7109. doi: 10.1002/ejoc.201300672

Kolb, H. C., Finn, M. G., and Sharpless, K. B. (2001). Click chemistry: diverse chemical function from a few good reactions. *Angew. Chem. Int. Ed.* 40, 2004–2021. doi: 10.1002/1521-3773(20010601)40:11<2004::aid-anie2004>3.3.co;2-x

Kottari, N., Chabre, Y. M., Shiao, T. C., Rej, R., and Roy, R. (2014). Efficient and accelerated growth of multifunctional dendrimers using orthogonal thiol–ene and SN2 reactions. *Chem. Commun.* 50, 1983–1985. doi: 10.1039/c3cc46633g

Kowalczyk, R., Harris, P. W. R., Williams, G. M., Yang, S. H., and Brimble, M. A. (2017). Peptide lipidation - a synthetic strategy to afford peptide based therapeutics. *Adv. Exp. Med. Biol.* 1030, 185–227. doi: 10.1007/978-3-319-66095-0_9

Lázár, L., Csávás, M., Herczeg, M., Herczegh, P., and Borbás, A. (2012). Synthesis of S-linked glycoconjugates and S-disaccharides by thiol-ene coupling reaction of enoses. *Org. Lett.* 14, 4650–4653. doi: 10.1021/ol302098u

Levalley, P. J., Ovadia, E. M., Bresette, C. A., Sawicki, L. A., Maverakis, E., Bai, S., et al. (2018). Design of functionalized cyclic peptides through orthogonal click reactions for cell culture and targeting applications. *Chem. Commun.* 54, 6923–6926. doi: 10.1039/C8CC03218A

Li, F., Allahverdi, A., Yang, R., Lua, G. B. J., Zhang, X., Cao, Y., et al. (2011). A direct method for site-specific protein acetylation. *Angew. Chem. Int. Ed.* 50, 9611–9614. doi: 10.1002/anie.201103754

Li, Y., Yang, M., Huang, Y., Song, X., Liu, L., and Chen, P. R. (2012). Genetically encoded alkenyl-pyrrolysine analogues for thiol-ene reaction mediated site-specific protein labeling. *Chem. Sci.* 3, 2766–2770. doi: 10.1039/c2sc20433a

Markey, L., Giordani, S., and Scanlan, E. M. (2013). Native chemical ligation,Thiol–Ene click: a methodology for the synthesis of functionalized peptides. *J. Org. Chem* 78, 4270–4277. doi: 10.1021/jo4001542

McGrath, N. A., Brichacek, M., and Njardarson, J. T. (2010). A graphical journey of innovative organic architectures that have improved our lives. *J. Chem. Educ.* 87, 1348–1349. doi: 10.1021/ed1003806

McSweeney, L., Dénès, F., and Scanlan, E. M. (2016). Thiyl-radical reactions in carbohydrate chemistry: from thiosugars to glycoconjugate synthesis. *Eur. J. Org. Chem.* 2016, 2080–2095. doi: 10.1002/ejoc.201501543

Montgomery, J. E., Donnelly, J. A., Fanning, S. W., Speltz, T. E., Shangguan, X., Coukos, J. S., et al. (2019). Versatile peptide macrocyclization with diels-alder cycloadditions. *J. Am. Chem. Soc.* 141, 16374–16381. doi: 10.1021/jacs.9b07578

Petracca, R., Bowen, K. A., McSweeney, L., O'Flaherty, S., Genna, V., Twamley, B., et al. (2019). Chemoselective synthesis of N-terminal cysteinyl thioesters via β,γ-C,S thiol-michael addition. *Org. Lett.* 21, 3281–3285. doi: 10.1021/acs.orglett.9b01013

Piccirillo, G., Pepe, A., Bedini, E., and Bochicchio, B. (2017). Photoinduced thiol-ene chemistry applied to the synthesis of self-assembling elastin-inspired glycopeptides. *Chem. A Eur. J.* 23, 2648–2659. doi: 10.1002/chem.201604831

Posner, T. (1905). Beiträge zur Kenntniss der ungesättigten Verbindungen. II. Ueber die Addition von Mercaptanen an ungesättigte Kohlenwasserstoffe. *Berichte der Dtsch. Chem. Gesellschaft* 38, 646–657. doi: 10.1002/cber.190503801106

Rafie, K., Gorelik, A., Trapannone, R., Borodkin, V. S., and van Aalten, D. M. F. (2018). Thio-linked UDP-peptide conjugates as O-GlcNAc transferase inhibitors. *Bioconjug. Chem.* 29, 1834–1840. doi: 10.1021/acs.bioconjchem.8b00194

Rojas-Ocáriz, V., Compañón, I., Aydillo, C., Castro-Lo?ez, J., Jiménez-Barbero, J., Hurtado-Guerrero, R., et al. (2016). Design of α-S-neoglycopeptides derived from MUC1 with a flexible and solvent-exposed sugar moiety. *J. Org. Chem.* 81, 5929–5941. doi: 10.1021/acs.joc.6b00833

Simerska, P., Moyle, P. M., and Toth, I. (2011). Modern lipid-, carbohydrate-, and peptide-based delivery systems for peptide, vaccine, and gene products. *Med. Res. Rev.* 31, 520–547. doi: 10.1002/med.20191

Su, Y., Tian, L., Yu, M., Gao, Q., Wang, D., Xi, Y., et al. (2017). Cationic peptidopolysaccharides synthesized by "click" chemistry with enhanced broad-spectrum antimicrobial activities. *Polym. Chem.* 8, 3788–3800. doi: 10.1039/C7PY00528H

Tang, W., and Becker, M. L. (2014). "click" reactions: a versatile toolbox for the synthesis of peptide-conjugates. *Chem. Soc. Rev.* 43, 7013–7039. doi: 10.1039/C4CS00139G

Taylor, N. C., Hessman, G., Kramer, H. B., and McGouran, J. F. (2020). Probing enzymatic activity-a radical approach. *Chem. Sci.* 11, 2967–2972. doi: 10.1039/C9SC05258E

Tong, J. T. W., Kavianinia, I., Ferguson, S. A., Cook, G. M., Harris, P. W. R., and Brimble, M. A. (2020). Synthesis of paenipeptin C′ analogues employing solution-phase CLipPA chemistry. *Org. Biomol. Chem.* 18, 4381–4385. doi: 10.1039/D0OB00950D

Triola, G., Brunsveld, L., and Waldmann, H. (2008). Racemization-free synthesis of S-alkylated cysteines via thiol-ene reaction. *J. Org. Chem.* 73, 3646–3649. doi: 10.1021/jo800198s

Valkevich, E. M., Guenette, R. G., Sanchez, N. A., Chen, Y. C., Ge, Y., and Strieter, E. R. (2012). Forging isopeptide bonds using thiol-ene chemistry: Site-specific coupling of ubiquitin molecules for studying the activity of isopeptidases. *J. Am. Chem. Soc.* 134, 6916–6919. doi: 10.1021/ja300500a

Vinogradov, A. A., Yin, Y., and Suga, H. (2019). Macrocyclic peptides as drug candidates: recent progress and remaining challenges. *J. Am. Chem. Soc.* 141, 4167–4181. doi: 10.1021/jacs.8b13178

Wan, Q., and Danishefsky, S. J. (2007). Free-radical-based, specific desulfurization of cysteine: a powerful advance in the synthesis of polypeptides and glycopolypeptides. *Angew. Chem. Int. Ed.* 46, 9248–9252. doi: 10.1002/anie.200704195

Wang, Y., Bruno, B. J., Cornillie, S., Nogieira, J. M., Chen, D., Cheatham, T. E., et al. (2017). Application of Thiol–yne/Thiol–ene reactions for peptide and protein macrocyclizations. *Chem. A Eur. J.* 23, 7087–7092. doi: 10.1002/chem.201700572

Wang, Y., and Chou, D. H. C. (2015). A thiol-ene coupling approach to native peptide stapling and macrocyclization. *Angew. Chem. Int. Ed.* 54, 10931–10934. doi: 10.1002/anie.201503975

Williams, E. T., Harris, P. W. R., Jamaluddin, M. A., Loomes, K. M., Hay, D. L., and Brimble, M. A. (2018). Solid-phase thiol–ene lipidation of peptides for the synthesis of a potent CGRP receptor antagonist. *Angew. Chem. Int. Ed.* 57, 11640–11643. doi: 10.1002/anie.201805208

Wittrock, S., Becker, T., and Kunz, H. (2007). Synthetic vaccines of tumor-associated glycopeptide antigens by immune-compatible thioether linkage to bovine serum albumin. *Angew. Chem. Int. Ed.* 46, 5226–5230. doi: 10.1002/anie.200700964

Wright, T. H., Brooks, A. E. S., Didsbury, A. J., Williams, G. M., Harris, P. W. R., Dunbar, P. R., et al. (2013). Direct peptide lipidation through thiol-ene coupling enables rapid synthesis and evaluation of self-adjuvanting vaccine candidates. *Angew. Chem. Int. Ed.* 52, 10616–10619. doi: 10.1002/anie.201305620

Yang, S.-H., Hermant, Y. O. J., Harris, P. W. R., and Brimble, M. A. (2020b). Replacement of the acrid tert-butylthiol and an improved isolation protocol for cysteine lipidation on a peptide or amino acid (CLipPA). *Eur. J. Org. Chem.* 2020, 944–947. doi: 10.1002/ejoc.201901696

Yang, S. H., Harris, P. W. R., Williams, G. M., and Brimble, M. A. (2016). Lipidation of cysteine or cysteine-containing peptides using the Thiol-ene reaction (CLipPA). *Eur. J. Org. Chem.* 2016, 2608–2616. doi: 10.1002/ejoc.201501375

Yang, S.-H., Clemett, C., Brimble, M., O'Carroll, S., and Harris, P. (2020a). *Synthesis and biological evaluation of S-lipidated lipopeptides of a connexin 43 channel inhibitory peptide. RSC Med. Chem.* 11, 1041–1047. doi: 10.1039/D0MD00172D

Yim, V. V., Cameron, A. J., Kavianinia, I., Harris, P. W. R., and Brimble, M. A. (2020c). Thiol-ene enabled chemical synthesis of truncated S-lipidated teixobactin analogs. *Front. Chem.* 8:568. doi: 10.3389/fchem.2020.00568

Yim, V. V., Kavianinia, I., Cameron, A. J., Harris, P. W. R., and Brimble, M. A. (2020b). Direct synthesis of cyclic lipopeptides using intramolecular native chemical ligation and thiol-ene CLipPA chemistry. *Org. Biomol. Chem.* 18, 2838–2844. doi: 10.1039/D0OB00203H

Yim, V. V., Kavianinia, I., Knottenbelt, M. K., Ferguson, S. A., Cook, G. M., Swift, S., et al. (2020a). *"CLipP"ing on lipids to generate antibacterial lipopeptides. Chem. Sci.* 11, 5759–5765. doi: 10.1039/D0SC01814G

Zhang, L., and Bulaj, G. (2012). Converting peptides into drug leads by lipidation. *Curr. Med. Chem.* 19, 1602–1618. doi: 10.2174/092986712799945003

Zhang, Y., Zhang, Q., Wong, C. T. T., and Li, X. (2019). Chemoselective peptide cyclization and bicyclization directly on unprotected peptides. *J. Am. Chem. Soc.* 141, 12274–12279. doi: 10.1021/jacs.9b03623

Zhao, B., Zhang, Q., and Li, Z. (2016). Constructing thioether-tethered cyclic peptides via on-resin intra-molecular thiol–ene reaction. *J. Pept. Sci.* 540–544. doi: 10.1002/psc.2902

Zhu, Y., and van Der Donk, W. A. (2001). Convergent synthesis of peptide conjugates using dehydroalanines for chemoselective ligations. *Org. Lett.* 3, 1189–1192. doi: 10.1021/ol015648a

Zorzi, A., Deyle, K., and Heinis, C. (2017). Cyclic peptide therapeutics: past, present and future. *Curr. Opin. Chem. Biol.* 38, 24–29. doi: 10.1016/j.cbpa.2017.02.006

Conflict of Interest: The authors declare that the research was conducted in the absence of any commercial or financial relationships that could be construed as a potential conflict of interest.

Copyright © 2020 Nolan and Scanlan. This is an open-access article distributed under the terms of the Creative Commons Attribution License (CC BY). The use, distribution or reproduction in other forums is permitted, provided the original author(s) and the copyright owner(s) are credited and that the original publication in this journal is cited, in accordance with accepted academic practice. No use, distribution or reproduction is permitted which does not comply with these terms.

frontiers in Chemistry

ORIGINAL RESEARCH
published: 17 November 2020
doi: 10.3389/fchem.2020.581512

Supported Pt Nanoparticles on Mesoporous Titania for Selective Hydrogenation of Phenylacetylene

*Mingzhen Hu[1,2], Lei Jin[2], Yanliu Dang[3], Steven L. Suib[2,3], Jie He[2,3] and Ben Liu[1]**

[1] Jiangsu Key Laboratory of New Power Batteries, Collaborative Innovation Center of Biomedical Functional Materials, School of Chemistry and Materials Science, Nanjing Normal University, Nanjing, China, [2] Department of Chemistry, University of Connecticut, Mansfield, CT, United States, [3] Institute of Materials Science, University of Connecticut, Mansfield, CT, United States

Semi-hydrogenation of alkynes to alkenes is one of the most important industrial reactions. However, it remains technically challenging to obtain high alkene selectivity especially at a high alkyne conversion because of kinetically favorable over hydrogenation. In this contribution, we show that supported ultrasmall Pt nanoparticles (2.5 nm) on mesoporous TiO_2 (Pt@mTiO_2) remarkably improve catalytic performance toward semi-hydrogenation of phenylacetylene. Pt@mTiO_2 is prepared by co-assembly of Pt and Ti precursors with silica colloidal templates *via* an evaporation-induced self-assembly process, followed by further calcination for thermal decomposition of Pt precursors and crystallization of mTiO_2 simultaneously. As-resultant Pt@mTiO_2 discloses a high hydrogenation activity of phenylacetylene, which is 2.5 times higher than that of commercial Pt/C. More interestingly, styrene selectivity over Pt@mTiO_2 remains 100% in a wide phenylacetylene conversion window (20–75%). The styrene selectivity is >80% even at 100% phenylacetylene conversion while that of the commercial Pt/C is 0%. The remarkable styrene selectivity of the Pt@mTiO_2 is derived from the weakened styrene adsorption strength on the atop Pt sites as observed by diffuse reflectance infrared Fourier transform spectroscopy with CO as a probe molecule (CO-DRIFTS). Our strategy provides a new avenue for promoting alkyne to alkene transformation in the kinetically unfavorable region through novel catalyst preparation.

Keywords: TiO_2, Pt nanocatalysts, mesoporous chemistry, selective hydrogenation, phenylacetylene

OPEN ACCESS

Edited by:
Marc Pera-Titus, Fudan University, China

Reviewed by:
Konstantinos Triantafyllidis, Aristotle University of Thessaloniki, Greece
Mattia Bartoli, Politecnico di Torino, Italy

***Correspondence:**
Ben Liu
ben.liu@njnu.edu.cn

Specialty section:
This article was submitted to Green and Sustainable Chemistry, a section of the journal Frontiers in Chemistry

Received: *09 July 2020*
Accepted: *14 September 2020*
Published: *17 November 2020*

Citation:
Hu M, Jin L, Dang Y, Suib SL, He J and Liu B (2020) Supported Pt Nanoparticles on Mesoporous Titania for Selective Hydrogenation of Phenylacetylene. Front. Chem. 8:581512. doi: 10.3389/fchem.2020.581512

INTRODUCTION

Selective hydrogenation of alkynes to alkenes is one of the most industrially important reactions (Yang et al., 1998, 2019; Mastalir et al., 2000; Huang et al., 2007; Studt et al., 2008; Yuan et al., 2009; Liu H. et al., 2012; Sheng et al., 2012; Tüysüz et al., 2013; Zhao et al., 2015, 2019; Xie et al., 2016; Xiao et al., 2017; Zhan et al., 2017). The increase of alkene selectivity not only benefits high quality of the downstream polyene products but greatly improves the alkene yields and profitability (Borodziński and Bond, 2006, 2008; McCue and Anderson, 2015; Hu et al., 2018a). Pt-based catalysts still suffer from low selectivity to alkenes especially in higher alkyne conversion windows, despite its high activity for hydrogenation (Li et al., 2017; Tang et al., 2017; Wang et al., 2018). In theory, the adsorption and activation of alkynes are favored thermodynamically over Pt compared to alkenes. However, as alkynes approach a high conversion, alkenes become kinetically favorable to adsorb on

Pt, leading to a full hydrogenation to alkanes and thus a sharp decrease in alkene selectivity (Yang et al., 2012; McCue and Anderson, 2015). For example, commercial Pd/C or Pt/C catalysts generally produce alkane at 100% alkyne conversion (Li et al., 2012). The lack of control of alkene selectivity at higher alkyne conversions greatly limits alkene yields. As a result, selective hydrogenation of alkynes is generally conducted at low alkyne conversions to generate enhanced yields of alkenes.

The key to solving this problem lies in developing more efficient Pt-group metal catalysts with weakened alkene adsorption strength, which facilitates the alkenes desorption rather than over hydrogenation to alkanes. Compared with strong σ-bonded alkenes, π-bonded alkenes are more favorable to desorb from the active Pt-group metal (Wan and Zhao, 2007; Armbrüster et al., 2010; Mitsudome et al., 2016; Feng et al., 2017). For example, Li et al. found that the π-bonded ethylene was 0.75 eV more facile than the σ-bonded ethylene to desorb from Pd surfaces based on density-functional theory (DFT) calculations (Feng et al., 2017). This in turn greatly favors high ethylene selectivity where 80% ethylene selectivity is achieved, even when acetylene is fully converted. The π-mode alkene adsorption is mainly on atop metal sites (Pei et al., 2017). To improve the alkene selectivity in selective hydrogenation of alkyne, both nanoparticles (NPs) downsizing and alloying strategies have been carried out to enrich the atop sites of Pt-group metal catalysts (Hu et al., 2018b). On the other hand, metal-support interaction has long been employed to tune catalytic properties of catalysts especially the small NPs with strong interactions with supports (Teschner et al., 2008). A reduced hydrogen reduction temperature is generally observed on the small NPs functionalized supports, which greatly benefits hydrogenation activity by virtue of strong hydrogen spillover (Wang et al., 2015; Wei et al., 2018). The decrease of particle sizes also enables more surface-exposed and low-coordinated active sites in the form of corner or edge sites, potentially favoring weak π-adsorbed alkenes (Kleis et al., 2011; Yang et al., 2013; Wu et al., 2019). Thus, smaller Pt NPs hold great potential to catalyze semi-hydrogenation of alkynes with high catalytic activity and alkene selectivity.

In the current study, we present a highly selective catalyst that contains ultrasmall Pt NPs (2.5 nm), strong Pt-support (Pt-TiO$_2$) interaction, and high surface area (mesoporous framework) for selective hydrogenation of phenylacetylene to styrene. Supporting ultrasmall Pt NPs on mesoporous TiO$_2$ (Pt@mTiO$_2$) were prepared using an evaporation-induced self-assembly (EISA) method (**Figure 1a**). For this synthesis, platinum acetylacetonate (Pt(acac)$_2$) was mixed with titanium sources and structure-directing polymers in EISA (Liu X. et al., 2012). Upon annealing, ultrasmall Pt NPs were synthesized and encapsulated within the ordered mTiO$_2$ support. The ordered mesopores of mTiO$_2$ provide a powerful nanoconfinement and endow the ultrasmall Pt nanoparticles with excellent size uniformity and thermal stability. The monodisperse Pt NPs with sizes of around 2.5 nm remained stable after calcination at 450°C. Pt NPs supported on mTiO$_2$ (Pt@TiO$_2$) exhibited excellent catalytic properties toward selective hydrogenation of phenylacetylene. The selectivity to styrene remained at 100% in the phenylacetylene conversion range of 20–75%. Even at 100% phenylacetylene conversion, Pt@TiO$_2$ exhibited >80% styrene selectivity. The abundant surface atop Pt sites of the Pt@mTiO$_2$ accounted for the high styrene selectivity as revealed by CO-DRIFTS. In addition, the specific mass activity of the 2.5 nm Pt@mTiO$_2$ reached as high as 0.5 mol h^{-1} per gram of Pt metal, which is 2.5 times higher than that of the commercial Pt/C catalyst (0.2 mol h^{-1} per gram of Pt metal).

EXPERIMENTAL SECTION

Chemicals and Materials

Titanium chloride (TiCl$_4$), titanium tetraisopropoxide (TIPO), 1,4-dioxane, phenylacetylene, commercial Pt/C (5 wt%) and platinum acetylacetonate (Pt(acac)$_2$) were purchased from Sigma-Aldrich. The CDCl$_3$ was purchased from Cambridge Isotope Laboratories, Inc. All the chemicals were used without further purification unless otherwise noted. Silane-containing block copolymers of poly(ethylene oxide)-*block*-poly(3-(trimethoxysilyl)propyl methacrylate) (PEO-*b*-PTMSPMA, M_n = 56.9 kg mol^{-1}) was prepared through atom transfer radical polymerization (ATPR) method as described in our previous reports (Tauster et al., 1978; Wang et al., 2015; Zhang et al., 2015; Feng et al., 2017; Hu et al., 2020). The polymer micelles were prepared in water/ethanol mixtures and dialyzed in ethanol prior to use. Deionized water (High-Q, Inc. 103S Stills) with a resistivity of >10.0 MΩ was used in all experiments.

Synthesis of Pt@mTiO$_2$

Pt@mTiO$_2$ was prepared using an EISA method. In a typical synthesis, 400 μL of newly prepared TiCl$_4$ solution (10 % in ethanol, volume ratio) was added to 5.0 mL of PEO-*b*-PTMSPMA micelles solution (15.0 mg mL^{-1} in ethanol) under stirring. Two hundred and seventy micro liter of TIPO was then added into the above solution, followed by mild stirring for 30 min. 2.0 mg of Pt(acac)$_2$ dissolved in 1.0 mL of ethanol was added dropwise where the theoretical mole ratio of Pt to Ti is 0.004 (corresponding to 1.0 wt% Pt loading in the obtained Pt@mTiO$_2$). After sufficient stirring for 30 min, the mixture solution was transferred into a Petri dish to evaporate the solvent at 40°C for 24 h and 100°C for another 12 h. After this procedure, the obtained intermediates were allowed for calcination at 450°C under air for 2 h. A template removal process is further carried out by washing with hot 2.0 M NaOH solution for 30 min at 50°C. The Pt loading given by EDS measurements is 1 wt%, agreeing well with the initial Pt feed ratio. Through subsequent drying in vacuum at 50°C overnight, Pt@mTiO$_2$ was finally obtained. About 3.6 nm Pt NPs on mesoporous TiO$_2$ is also prepared as a control using similar procedures except that the thermal calcination is carried out at 650°C for 2 h.

Selective Hydrogenation of Phenylacetylene Catalytic Evaluations

Selective hydrogenation of phenylacetylene over the Pt@mTiO$_2$ catalysts was carried out by the following procedures. Firstly, 10.0 mg of catalyst was added to 3.0 mL of 1,4-dioxane in a 15 mL processed glass bottle. After 20 min sonication, 100.0 mg (1.0

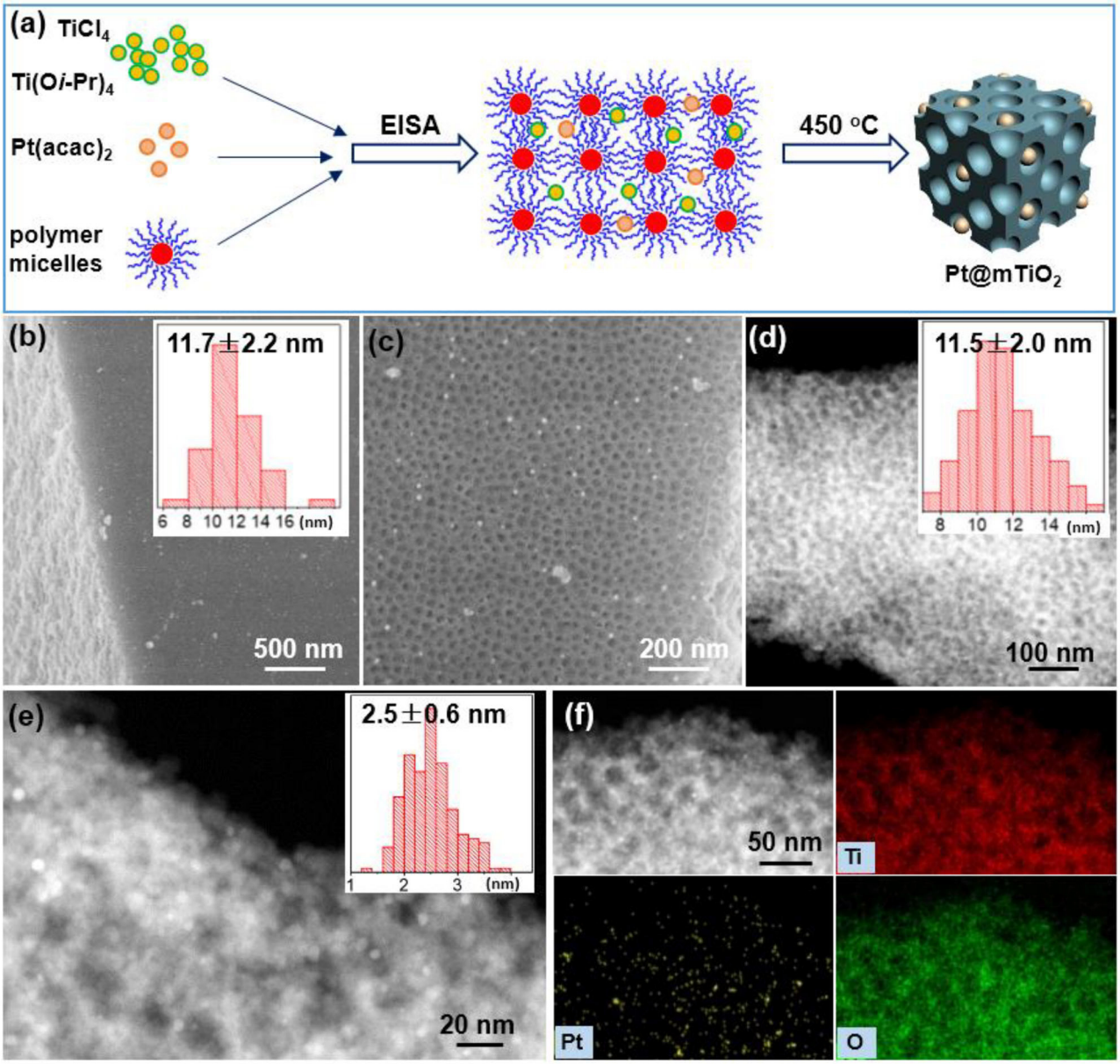

FIGURE 1 | (a) Schematic illustration of preparing 2.5 nm Pt NPs supported within the mesoporous TiO_2. **(b,c)** SEM images, **(d,e)** HAADF-STEM images, and **(f)** EDS mapping images of Pt@mTiO_2. The inset of **(b,d,e)** are size/diameter distributions of mesopores from SEM, mesopores from TEM, and Pt NPs from STEM.

mmol) of phenylacetylene was further added to the homogeneous suspension and stirred for another 30 min. Before transferring the processed bottle to a 25 mL high-pressure stainless-steel reactor, the magnet is taken out, leaving the reaction happen at static conditions without stirring. After purging with hydrogen several times, the reactor was pressurized with 50 psi (pounds per square inch) hydrogen and reacted for varied times. After the reaction finished, the whole reactor was cooled down in an ice bath. The postreaction suspension was separated by centrifugation at 8,000 rpm. The resultant product was kept in a 5 mL test tube and the proton nuclear magnetic resonance (^{1}H NMR) analysis was carried out using $CDCl_3$ as solvent to calculate the conversion of phenylacetylene and the selectivity to styrene. The reaction kinetics were measured both for the Pt@mTiO_2 and commercial Pt/C catalysts. The specific reaction rate was determined as the consumption rate of the phenylacetylene (normalized to the mass of Pt metal per hour) by controlling the phenylacetylene conversion in the kinetic region. The specific rate in this work was calculated using the following equation:

$$r = \frac{N}{w*t} \tag{1}$$

where r is the specific rate, N is the converted phenylacetylene amount in mole, w is supported metal loading weight (gram), and t is the reaction (minute).

The turnover frequency (TOF) is calculated based on the following equation:

$$TOF = \frac{N}{(w/M)*D*t} \quad (2)$$

where N is the converted phenylacetylene amount in mole, w is supported Pt loading weight (gram), M is the molar mass of Pt, D is metal dispersion of Pt and t is the reaction (second). The metal dispersion is calculated according to previous reports (Dominguez-Dominguez et al., 2008; Qiao et al., 2011).

The stability tests of the Pt@mTiO$_2$ and the commercial Pt/C were carried out by recycling the catalyst for 5 consecutive cycles.

Characterization

Scanning electron microscopy (SEM) was conducted on a FEI Nova NanoSEM 450. Bright and dark-field transmission electron microscopy (TEM) was performed on JEM-2100F FETEM. The X-ray diffraction (XRD) patterns were collected on a Bruker D2 Phaser. The small angle X-ray scattering (SAXS) patterns were recorded on a Bruker Nano STAR instrument. X-ray photoelectron spectroscopy (XPS) analysis was conducted on ESCALAB 250 Xi X-ray photoelectron spectrometer with Al Kα radiation. The N_2 sorption measurements were conducted on a Micromeritics ASAP 2020 Surface Area and Porosity Analyzer. ^{1}H NMR spectroscopy was collected on a Bruker Avance 300 MHz spectrometer. Diffuse reflectance Fourier transform infrared (DRIFT) spectroscopy was carried out using a Nicolet IS50 spectrometer using CO as a probe molecule. The DRIFT cell was filled with 20 mg of catalysts and was treated at 100°C with nitrogen before CO was introduced.

RESULTS AND DISCUSSION

Mesoscopic and microscopic structures of the Pt@mTiO$_2$ were thoroughly characterized with SEM and high-angle annular dark field scanning TEM (HAADF-STEM) (**Figure 1**). The SEM image in **Figure 1b** shows the mesopores throughout entire mTiO$_2$ support. **Supplementary Figure 1** shows that mTiO$_2$ displays bulk cubic morphology with a broad side length distribution. The zoomed-in SEM picture in **Figure 1c** confirms the uniform distribution of mesopores. The average pore size of mTiO$_2$ is 11.7 ± 2.2 nm as given in the inset of **Figure 1b**. Since Pt NPs are small, there is no obvious contrast on bright field TEM. The HAADF-STEM technique is further used to identify the ultrasmall Pt NPs. The HAADF-STEM images of Pt@mTiO$_2$ in **Figures 1d–f** reveal the well-dispersed Pt NPs. Pt NPs with a higher electron density are brighter under dark-field STEM image while TiO$_2$ is darker. The average size of Pt NPs is 2.5 ± 0.5 nm as plotted in **Figure 1e**. The pore size of mTiO$_2$ is about 11 nm from HAADF-STEM characterization, which agrees well with the above SEM observations. **Figure 1f** shows energy dispersive X-ray spectroscopy (EDS) mapping images of Pt@mTiO$_2$, further confirming fine dispersion of these 2.5 nm Pt NPs in mTiO$_2$ support. The Pt loading of Pt@mTiO$_2$ is further determined by EDS measurements. As show in **Supplementary Figure 2** and **Supplementary Table 1**, the Pt loadings obtained by EDS measurements of Pt@mTiO$_2$ are about 1 wt%, agreeing well with the initial feed ratio (1 wt%). This observation implies no loss of Pt during preparation processes. By comparison, we have also carried out TEM observations of the commercial Pt/C catalyst. As displayed in **Supplementary Figure 3**, the Pt NPs in commercial Pt/C show a very wide size distribution averaging about 3 nm as reported previously (Cui et al., 2019). The Pt loading of the commercial Pt/C is 5 wt% as received.

To examine the mesoporous structures and crystallographic information of the Pt@mTiO$_2$, we carried out small-angle X-ray scattering (SAXS) and wide-angle X-ray diffraction (XRD) characterization. **Figure 2A** is the SAXS patterns of the Pt@mTiO$_2$ and the pure mTiO$_2$ support. These data show a set of strong scattering peaks that are clearly identified and assigned to (111), (311), and (500) reflections of the face-centered cubic (fcc) mesostructure. The average cell parameters were calculated to be 38 nm as displayed in **Supplementary Table 2**. The SAXS signals are almost the same for Pt@mTiO$_2$ and mTiO$_2$, indicating well-defined mesoporous structures. **Figure 2B** displayed the wide-angle XRD patterns, suggesting the anatase TiO$_2$ phase for both Pt@mTiO$_2$ and mTiO$_2$ (JCPDS 00-064-0863). Unfortunately, due to the ultrasmall size, metallic Pt NPs (JCPDS 04-0802) only showed very broad and weak XRD diffraction (Xiang et al., 2011; Prinz et al., 2014). Benefiting from the well-defined mesoporous structures, the BET specific surface area of the Pt@TiO$_2$ is 42 m^2g^{-1} with an average of pore size of 14 nm as displayed in **Figures 2C,D**.

Pt@mTiO$_2$ has multiple advantageous properties, including ultrasmall Pt NPs and mesoporous framework with high surface area, which possibly benefit the selective hydrogenation of alkynes to alkenes. In this manuscript, selective hydrogenation of phenylacetylene was chosen as a probe reaction since the semi-hydrogenation product of styrene is industrially important (**Figure 3A**). As a control, commercial Pt/C was also investigated. Pt@mTiO$_2$ was favorable for catalyzing the hydrogenation of phenylacetylene to styrene, while commercial Pt/C fully hydrogenated phenylacetylene to ethylbenzene. **Figure 3B** showed the phenylacetylene conversion and the styrene selectivity over Pt@mTiO$_2$ as a function of reaction time. Phenylacetylene was selectively converted to styrene in a wide phenylacetylene conversion window (20–75%), only when phenylacetylene reached full conversion, styrene selectivity slightly dropped to 80.3%. This result (80.3% styrene selectivity at 100% phenylacetylene conversion) is among the best reported to date as demonstrated in **Supplementary Table 3** (Zhao et al., 1998; Kleis et al., 2011; Behrens et al., 2012; Montesano Lopez, 2014; Alig et al., 2019; Han et al., 2019). By comparison, pure mTiO$_2$ is inactive and shows no activity to convert phenylacetylene in the reaction time range from 7 to 26 h (**Supplementary Figure 4**). We have also compared the catalytic properties of Pt@mTiO$_2$ with commercial Pt/C catalysts. Phenylacetylene was fully over hydrogenated to ethylbenzene in the measuring time range from

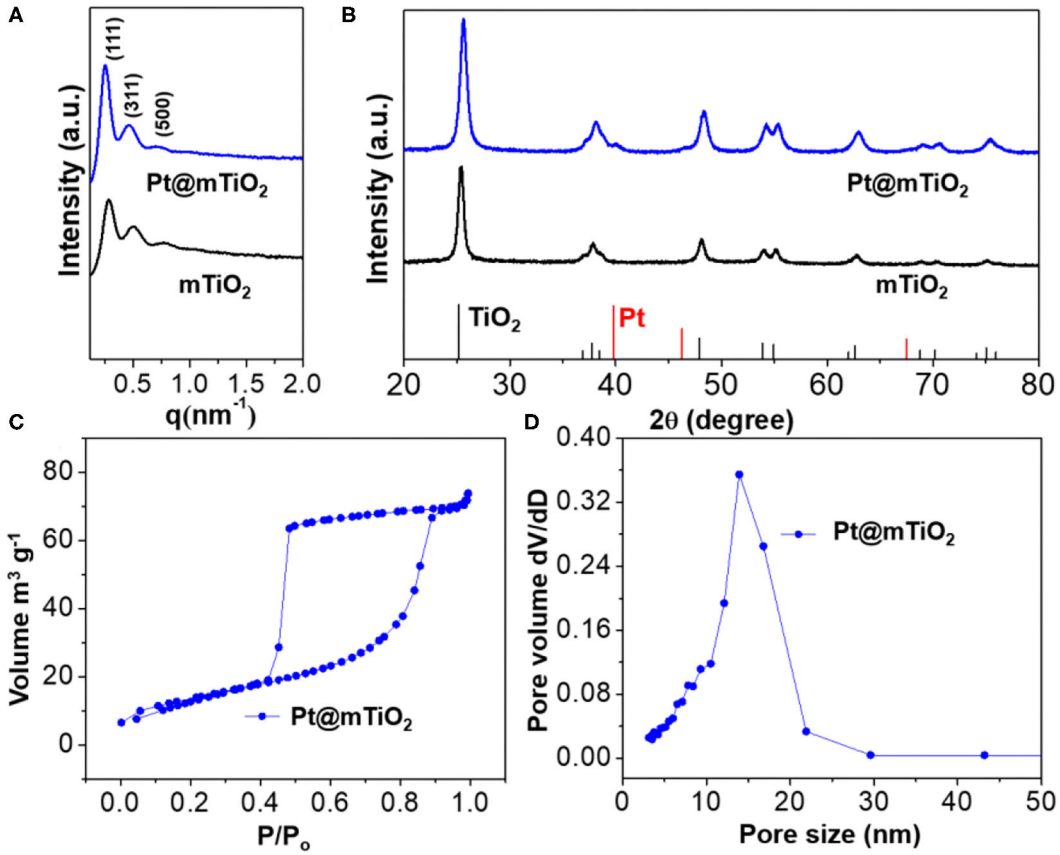

FIGURE 2 | (A) SAXS, and **(B)** wide-angle XRD of Pt@mTiO$_2$ and pure mTiO$_2$. **(C)** N$_2$ adsorption-desorption isotherms, and **(D)** pore size distributions of Pt@mTiO$_2$.

7 to 26 h with a 100% ethylbenzene selectivity as shown in **Supplementary Figure 5**.

Figure 3C shows the catalytic rates of Pt@mTiO$_2$ and commercial Pt/C normalized to the Pt mass per unit time. By controlling the phenylacetylene conversion in the kinetic region (10–20% of conversion), the rate characterizes the intrinsic activity of the catalyst. The catalytic rate of Pt@mTiO$_2$ is 0.5 mol g_{Pt}^{-1} h^{-1}, 2.5 times higher than that of commercial Pt/C (0.2 mol g_{Pt}^{-1} h^{-1}). In addition, the TOF value of the Pt@mTiO$_2$ is calculated to be 4.1 s^{-1}, which is more than 2 times that of the commercial Pt/C (2.0 s^{-1}), demonstrating a higher intrinsic activity. According to previous results, the particle size of Pt NPs is intimately connected with the amount of surface-exposed active sites, which in turn affects the activity (Zhang et al., 2007; Qiao et al., 2011). The smaller sized Pt in Pt@mTiO$_2$ results in more exposed surface Pt sites compared with commercial Pt/C (average size of 3 nm), which benefits high catalytic activity. Catalytic stability is another concern for practical applications. To test the catalytic stability of Pt@mTiO$_2$, we have carried out recycling experiments of the post-reacted Pt@mTiO$_2$ at 50°C and 50 psi hydrogen. As shown in **Figure 3D**, styrene selectivity remains around 80% over the Pt@mTiO$_2$ while phenylacetylene conversion remains at 100% even after five catalytic recycles, showing excellent catalytic stability. By comparison, styrene selectivity over the commercial Pt/C is 0% for the five consecutive measurements at 100% phenylacetylene conversion as displayed in **Supplementary Figure 6**. By virtue of the nanoconfinment enabled by mesoporous mTiO$_2$ supports, the average particle size of the post-reacted Pt@mTiO$_2$ remains the same without any growth or aggregation as displayed in **Supplementary Figure 7**.

To reveal the intrinsic nature why Pt@mTiO$_2$ presented excellent catalytic properties for the selective hydrogenation of phenylacetylene, the surface properties of Pt were carefully studied. We first carried out X-ray photoelectron spectroscopy (XPS) for Pt@mTiO$_2$. **Figure 4A** is the high-resolution Pt 4f XPS spectra of Pt@mTiO$_2$ and commercial Pt/C. The well-resolved XPS binding energy peaks centered at 71.9 and 75.3 eV of Pt@mTiO$_2$ are ascribed to metallic Pt $4f_{7/2}$ and Pt $4f_{5/2}$, respectively. For the commercial Pt/C, the Pt $4f_{7/2}$ and Pt $4f_{5/2}$ shifted to a slightly higher binding energy at 72 and 75.4 eV, respectively. The shift of Pt 4f peaks is indicative of the surface electron density difference of the two samples. 2.5 nm Pt NPs is slightly electron-rich compared to that of the commercial Pt/C. The electron-rich 2.5 nm Pt NPs are more effective to transfer electrons to the π^* molecular orbitals of phenylacetylene, which in turn promotes phenylacetylene activation and improves catalytic reactivity (Wan and Zhao, 2007). Both the Pt@mTiO$_2$ and commercial Pt/C show existence of Pt^{2+} species as identified

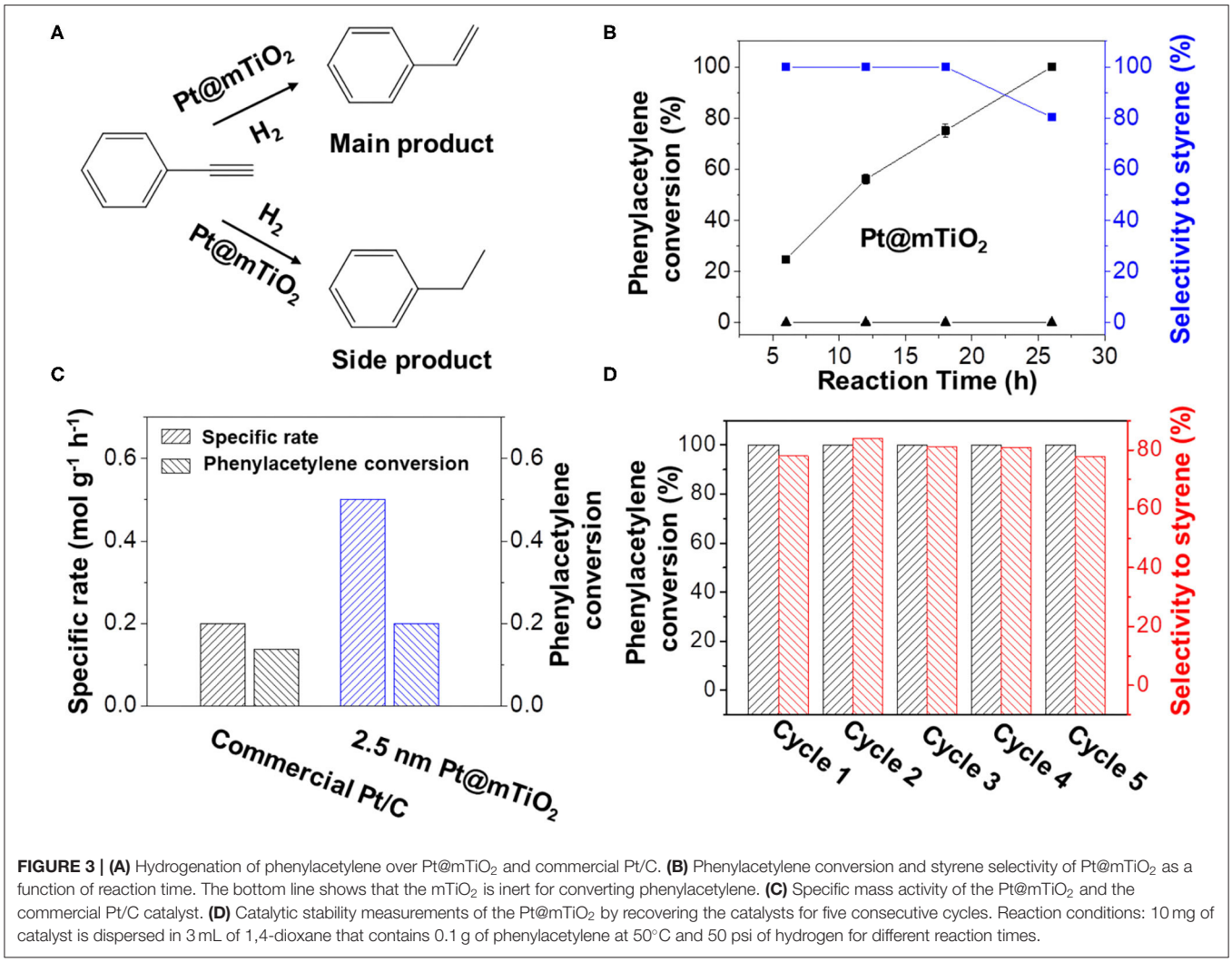

FIGURE 3 | (A) Hydrogenation of phenylacetylene over Pt@mTiO$_2$ and commercial Pt/C. **(B)** Phenylacetylene conversion and styrene selectivity of Pt@mTiO$_2$ as a function of reaction time. The bottom line shows that the mTiO$_2$ is inert for converting phenylacetylene. **(C)** Specific mass activity of the Pt@mTiO$_2$ and the commercial Pt/C catalyst. **(D)** Catalytic stability measurements of the Pt@mTiO$_2$ by recovering the catalysts for five consecutive cycles. Reaction conditions: 10 mg of catalyst is dispersed in 3 mL of 1,4-dioxane that contains 0.1 g of phenylacetylene at 50°C and 50 psi of hydrogen for different reaction times.

at around 73.1 and 77.1 eV, respectively, which may derive from surface oxidation (Miller et al., 2014). The Pt^{2+}/Pt^0 ratio, as measured from the integration areas in the fitting cure, is 0.43 for 2.5 nm Pt NPs. By comparison, this is much lower for commercial Pt/C with a Pt^{2+}/Pt^0 ratio of 0.35. This result implies that Pt is more surface oxidized in 2.5 nm Pt NPs, which is further evidenced in Ti 2p XPS spectra. As shown in **Figure 4B**, a strong Ti^{3+} XPS binding energy peak at around 458.2 eV is found in 2.5 nm Pt NPs on mTiO$_2$, which is absent in the pure mTiO$_2$ (Yang et al., 2017; Ou et al., 2018). These results show that 2.5 nm Pt NPs have a stronger interaction with the mTiO$_2$ support where Pt NPs are partially oxidized and demonstrate electron back-donation to reduce Ti^{4+} to Ti^{3+} of mTiO$_2$. The stronger metal-support interaction is of great importance in stabilizing small NPs as revealed by a series of reports (Lu and Schüth, 2006). In the current case, the excellent thermal stability of 2.5 nm Pt NPs supported on mTiO$_2$ may also derive from strong metal-support interactions.

Small NPs afford abundant surface low-coordinated corner or edge sites, which potentially modifies reactant/product adsorption modes that are quite different from that on larger ones (Zelcer and Soler-Illia, 2013). For example, alkenes prefer a weak π adsorption on low-coordinated Pt sites such as corner, edge, or single atom sites of small Pt NPs rather than a strong σ adsorption on continuous Pt lattices of larger Pt NPs. The weakening of alkene adsorption strength greatly favors high alkene selectivity (Yang et al., 2013; Zhang et al., 2019). To this end, CO-DRIFTS was further carried out to understand the high selectivity to styrene on Pt@mTiO$_2$. For the commercial Pt/C, it is very difficult to collect CO-DRIFT spectra because of signal blocking of carbon supports. Thus, we further prepared 3.6 nm Pt supported on mTiO$_2$ by calcination at a higher annealing temperature (650°C), which preserved the mesoporous structure but with slightly larger Pt NPs (3.6 nm) (**Supplementary Figure 8**). **Supplementary Figure 9** shows that both the catalytic activity and styrene selectivity of the 3.6 nm Pt NPs on mTiO$_2$ are much lower than that of the 2.5 nm Pt NPs on mTiO$_2$. **Figure 5** shows the CO-DRIFTS curve of 2.5 nm Pt NPs and 3.6 nm Pt NPs on mTiO$_2$, respectively. The CO adsorption models on 2.5 nm Pt NPs are quite different from

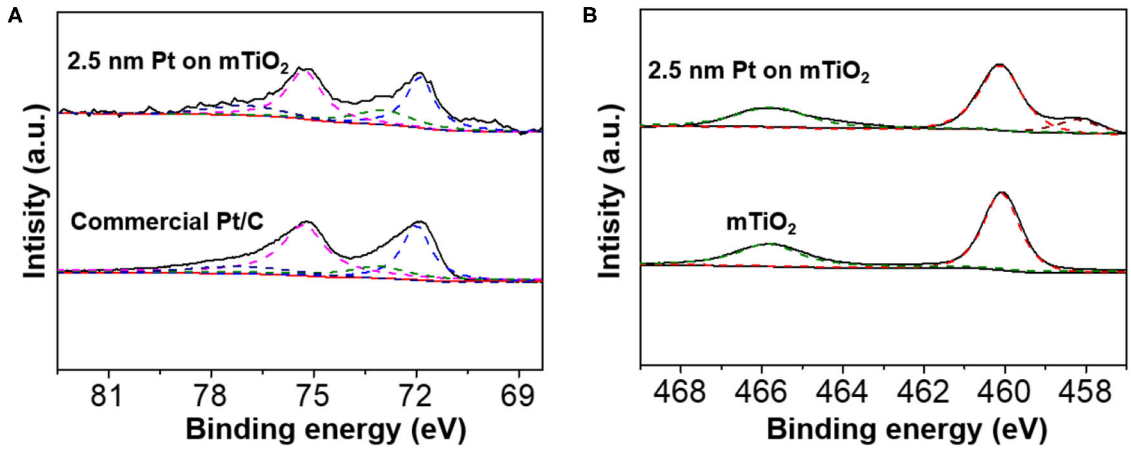

FIGURE 4 | (A) High-resolution Pt 4f XPS spectra of the 2.5 nm Pt NPs on mTiO$_2$ and commercial Pt/C. **(B)** High-resolution Ti 2p XPS spectra of the 2.5 nm Pt NPs on mTiO$_2$, and pure mTiO$_2$.

that on 3.6 nm Pt NPs. The fitted results show that only the linear CO adsorption mode is observed on the 2.5 nm Pt NPs on mTiO$_2$ while the 3.6 nm Pt NPs on mTiO$_2$ display both linear CO adsorption and bridged CO adsorption modes in the wavenumber window between 1,800 and 2,200 cm^{-1} (Singh et al., 2018). The linear CO adsorption of both 2.5 nm Pt NPs on mTiO$_2$ and 3.6 nm Pt NPs on mTiO$_2$ are related to the surface atop Pt sites (Wieckowski, 1999). Due to the Pt coordination differences, the linear CO adsorption bands of the 2.5 nm Pt NPs on mTiO$_2$ and the 3.6 nm Pt NPs on mTiO$_2$ are divided into two regions that are referred to as the low-coordination Pt-CO linear adsorption band and high-coordination Pt-CO linear adsorption band centered at around 2,004 and 2,160 cm^{-1}, respectively (Redina et al., 2015; Singh et al., 2018). The low-coordination Pt-CO linear adsorption to high-coordination Pt-CO linear adsorption ratio of 2.5 nm Pt NPs on mTiO$_2$ is calculated to be 4.8, which is 6 times higher than that of 3.6 nm Pt NPs on mTiO$_2$. This result demonstrates high unsaturated coordination of the Pt sites in 2.5 nm Pt NPs on mTiO$_2$ due to the smaller Pt NPs size as compared with 3.6 nm Pt NPs on mTiO$_2$, which agrees well with the above HAADF-STEM observations. The schematic models of Pt NPs with diameters of 2.5 and 3.6 nm are also constructed, respectively, as displayed in **Supplementary Figure 10**. Smaller Pt NPs show more abundant surface corner and edge sites, which accounts for the pure linear CO adsorption revealed via CO-DRIFTS measurements. The unique surface structures of the 2.5 nm Pt NPs on mTiO$_2$ greatly benefit weak styrene adsorption in selective hydrogenation of phenylacetylene through a π adsorption mode, which favors styrene desorption and high styrene selectivity.

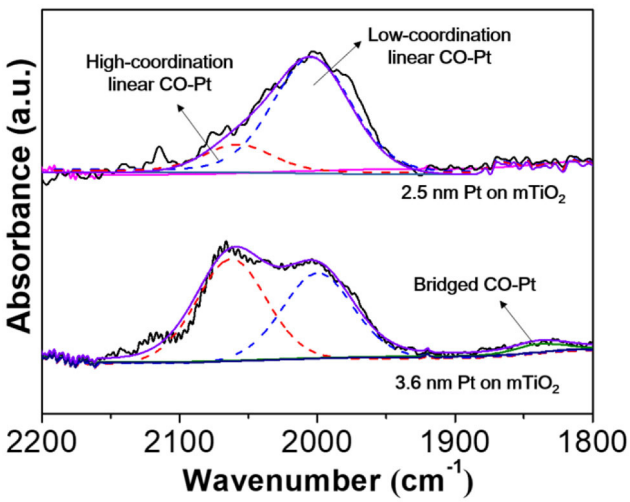

FIGURE 5 | Diffuse reflectance infrared Fourier transform spectroscopy with CO molecules of the 2.5 nm Pt NPs on mTiO$_2$ and the 3.6 nm Pt NPs on mTiO$_2$.

CONCLUSION

To summarize, we report the preparation of mesoporous TiO$_2$ confined ultrasmall Pt nanoparticles with an average particle size of 2.5 ± 0.5 nm using an EISA method. As-resulted Pt@mTiO$_2$ displayed excellent catalytic activity and styrene selectivity in semi-hydrogenation of phenylacetylene. The hydrogenation activity of Pt@mTiO$_2$ displays a 2.5-fold increase over that of the commercial Pt/C. A 100% styrene selectivity is also obtained over the Pt@mTiO$_2$ in a wide phenylacetylene conversion range of 20–75%. The styrene selectivity is remarkably above 80% even at full phenylacetylene conversion. The excellent styrene selectivity is ascribed to the abundant surface atop Pt sites as given by the CO-DRIFTS. In addition, the Pt@mTiO$_2$ also shows excellent catalytic stability as demonstrated in five consecutive recycling experiments, which shows great potential for practical

applications. Our work is expected to open up new opportunities for developing highly efficient alkene-to-alkene conversion catalysts by novel synthesis.

DATA AVAILABILITY STATEMENT

The original contributions presented in the study are included in the article/**Supplementary Material**, further inquiries can be directed to the corresponding author.

AUTHOR CONTRIBUTIONS

MH, SS, JH, and BL conceived the projects. MH carried out the experiments and analyzed data in the assist of LJ. YD did high-resolution TEM and analyzed the data. All authors co-wrote the manuscript.

ACKNOWLEDGMENTS

JH is grateful for the financial support from the University of Connecticut. The SEM/TEM studies were performed using the facilities in the UConn/Thermo Fisher Scientific Center for Advanced Microscopy and Materials Analysis (CAMMA). SS thanks the US Department of Energy, Office of Basic Energy Sciences, Division of Chemical, Biological and Geological Sciences under grant DE-FG02-86ER13622 for support of this research.

SUPPLEMENTARY MATERIAL

The Supplementary Material for this article can be found online at: https://www.frontiersin.org/articles/10.3389/fchem.2020.581512/full#supplementary-material

REFERENCES

Alig, L., Fritz, M., and Schneider, S. (2019). First-row transition metal (De)hydrogenation catalysis based on functional pincer ligands. *Chem. Rev.* 119, 2681–2751. doi: 10.1021/acs.chemrev.8b00555

Armbrüster, M., Kovnir, K., Behrens, M., Teschner, D., Grin, Y., and Schlögl, R. (2010). Pd–Ga intermetallic compounds as highly selective semihydrogenation catalysts. *J. Am. Chem. Soc.* 132, 14745–14747. doi: 10.1021/ja106568t

Behrens, M., Studt, F., Kasatkin, I., Kühl, S., Hävecker, M., Abild-Pedersen, F., et al. (2012). The active site of methanol synthesis over Cu/ZnO/Al_2O_3 industrial catalysts. *Science* 336, 893–897. doi: 10.1126/science.1219831

Borodziński, A., and Bond, G. C. (2006). Selective hydrogenation of ethyne in ethene-rich streams on palladium catalysts. Part 1. effect of changes to the catalyst during reaction. *Catal. Rev.* 48, 91–144. doi: 10.1080/01614940500364909

Borodziński, A., and Bond, G. C. (2008). Selective hydrogenation of ethyne in ethene-rich streams on palladium catalysts, Part 2: steady-state kinetics and effects of palladium particle size, carbon monoxide, and promoters. *Catal. Rev.* 50, 379–469. doi: 10.1080/01614940802142102

Cui, Y., Lian, X., Xu, L., Chen, M., Yang, B., Wu, C.-e., et al. (2019). Designing and fabricating ordered mesoporous metal oxides for CO_2 catalytic conversion: a review and prospect. *Materials* 12:276. doi: 10.3390/ma12020276

Dominguez-Dominguez, S., Berenguer-Murcia, A., Pradhan, B. K., Linares-Solano, A., and Cazorla-Amoros, D. (2008). Semihydrogenation of phenylacetylene catalyzed by palladium nanoparticles supported on carbon materials. *J. Phys. Chem. C* 112, 3827–3834. doi: 10.1021/jp710693u

Feng, Q., Zhao, S., Wang, Y., Dong, J., Chen, W., He, D., et al. (2017). Isolated single-atom pd sites in intermetallic nanostructures: high catalytic selectivity for semihydrogenation of alkynes. *J. Am. Chem. Soc.* 139, 7294–7301. doi: 10.1021/jacs.7b01471

Han, A., Zhang, J., Sun, W., Chen, W., Zhang, S., Han, Y., et al. (2019). Isolating contiguous Pt atoms and forming Pt-Zn intermetallic nanoparticles to regulate selectivity in 4-nitrophenylacetylene hydrogenation. *Nat. Commun.* 10:3787. doi: 10.1038/s41467-019-11794-6

Hu, M., Jin, L., Su, X., Bamonte, S., Lu, X., Gao, P., et al. (2020). Polymer-assisted co-assembly towards synthesis of mesoporous titania encapsulated monodisperse PdAu for highly selective hydrogenation of phenylacetylene. *ChemCatChem* 12, 1476–1482. doi: 10.1002/cctc.201901957

Hu, M., Zhang, J., Zhu, W., Chen, Z., Gao, X., Du, X., et al. (2018a). 50 ppm of Pd dispersed on Ni(OH)2 nanosheets catalyzing semi-hydrogenation of acetylene with high activity and selectivity. *Nano Res.* 11, 905–912. doi: 10.1007/s12274-017-1701-5

Hu, M., Zhao, S., Liu, S., Chen, C., Chen, W., Zhu, W., et al. (2018b). MOF-confined Sub-2 nm atomically ordered intermetallic PdZn nanoparticles as high-performance catalysts for selective hydrogenation of acetylene. *Adv. Mater.* 30:1801878. doi: 10.1002/adma.201801878

Huang, W., McCormick, J. R., Lobo, R. F., and Chen, J. G. (2007). Selective hydrogenation of acetylene in the presence of ethylene on zeolite-supported bimetallic catalysts. *J. Catal.* 246, 40–51. doi: 10.1016/j.jcat.2006.11.013

Kleis, J., Greeley, J., Romero, N., Morozov, V., Falsig, H., Larsen, A. H., et al. (2011). Finite size effects in chemical bonding: from small clusters to solids. *Catal. Lett.* 141, 1067–1071. doi: 10.1007/s10562-011-0632-0

Li, C., Shao, Z., Pang, M., Williams, C. T., and Liang, C. (2012). Carbon nanotubes supported Pt catalysts for phenylacetylene hydrogenation: effects of oxygen containing surface groups on Pt dispersion and catalytic performance. *Catal. Today.* 186, 69–75. doi: 10.1016/j.cattod.2011.09.005

Li, K., Zhao, Y., Song, C., and Guo, X. (2017). Magnetic ordered mesoporous Fe_3O_4/CeO_2 composites with synergy of adsorption and fenton catalysis. *Appl. Surf. Sci.* 425, 526–534. doi: 10.1016/j.apsusc.2017.07.041

Liu, H., Du, X., Xing, X., Wang, G., and Qiao, S. Z. (2012). Highly ordered mesoporous Cr_2O_3 materials with enhanced performance for gas sensors and lithium ion batteries. *Chem. Commun.* 48, 865–867. doi: 10.1039/C1CC16341H

Liu, X., Mou, C.-Y., Lee, S., Li, Y., Secrest, J., and Jang, B. W.-L. (2012). Room temperature O_2 plasma treatment of SiO_2 supported Au catalysts for selective hydrogenation of acetylene in the presence of large excess of ethylene. *J. Catal.* 285, 152–159. doi: 10.1016/j.jcat.2011.09.025

Lu, A.-H., and Schüth, F. (2006). Nanocasting: a versatile strategy for creating nanostructured porous materials. *Adv. Mater.* 18, 1793–1805. doi: 10.1002/adma.200600148

Mastalir, A., Király, Z., Szöllosi, G., and Bartok, M. (2000). Preparation of organophilic Pd–montmorillonite, an efficient catalyst in alkyne semihydrogenation. *J. Catal.* 194, 146–152. doi: 10.1006/jcat.2000.2929

McCue, A. J., and Anderson, J. A. (2015). Recent advances in selective acetylene hydrogenation using palladium containing catalysts. *Front. Chem. Sci. Eng.* 9, 142–153. doi: 10.1007/s11705-015-1516-4

Miller, D., Sanchez Casalongue, H., Bluhm, H., Ogasawara, H., Nilsson, A., and Kaya, S. (2014). Different reactivity of the various platinum oxides and chemisorbed oxygen in CO oxidation on Pt(111). *J. Am. Chem. Soc.* 136, 6340–6347. doi: 10.1021/ja413125q

Mitsudome, T., Urayama, T., Yamazaki, K., Maehara, Y., Yamasaki, J., Gohara, K., et al. (2016). Design of core-Pd/shell-Ag nanocomposite catalyst for selective semihydrogenation of alkynes. *ACS Catal.* 6, 666–670. doi: 10.1021/acscatal.5b02518

Montesano Lopez, R. (2014). *Selectivity and Deactivation in the Single-stage Synthesis of Dimethyl Ether from $CO_2/CO/H_2$*. Imperial College London. doi: 10.25560/26597

Ou, G., Xu, Y., Wen, B., Lin, R., Ge, B., Tang, Y., et al. (2018). Tuning defects in oxides at room temperature by lithium reduction. *Nat. Commun.* 9:1302. doi: 10.1038/s41467-018-03765-0

Pei, G. X., Liu, X. Y., Yang, X., Zhang, L., Wang, A., Li, L., et al. (2017). Performance of Cu-alloyed pd single-atom catalyst for semihydrogenation of acetylene under simulated front-end conditions. *ACS Catal.* 7, 1491–1500. doi: 10.1021/acscatal.6b03293

Prinz, J., Pignedoli, C. A., Stöckl, Q. S., ArmbrÃster, M., Brune, H., Gröning, O., et al. (2014). Adsorption of small hydrocarbons on the three-fold PdGa surfaces: the road to selective hydrogenation. *J. Am. Chem. Soc.* 136, 11792–11798. doi: 10.1021/ja505936b

Qiao, B., Wang, A., Yang, X., Allard, L. F., and Zhang, T. (2011). Single-atom catalysis of CO oxidation using Pt_1/FeO_x. *Nat. Chem.* 3, 634–641. doi: 10.1038/nchem.1095

Redina, E., Greish, A., Novikov, R., Strelkova, A., Kirichenko, O., Tkachenko, O., et al. (2015). Au/Pt/TiO_2 catalysts prepared by redox method for the chemoselective 1,2-propanediol oxidation to lactic acid and an NMR spectroscopy approach for analyzing the product mixture. *Appl. Catal. A* 491, 170–183. doi: 10.1016/j.apcata.2014.11.039

Sheng, B., Hu, L., Yu, T., Cao, X., and Gu, H. (2012). Highly-dispersed ultrafine Pt nanoparticles on graphene as effective hydrogenation catalysts. *RSC Adv.* 2, 5520–5523. doi: 10.1039/c2ra20400b

Singh, J. A., Yang, N., Liu, X., Tsai, C., Stone, K. H., Johnson, B., et al. (2018). Understanding the active sites of CO hydrogenation on Pt–Co catalysts prepared using atomic layer deposition. *J. Phys. Chem. C* 122, 2184–2194. doi: 10.1021/acs.jpcc.7b10541

Studt, F., Abild-Pedersen, F., Bligaard, T., Sørensen, R. Z., Christensen, C. H., and Nørskov, J. K. (2008). Identification of non-precious metal alloy catalysts for selective hydrogenation of acetylene. *Science* 320, 1320–1322. doi: 10.1126/science.1156660

Tang, Q., Angelomé, P. C., Soler-Illia, G. J., and Müller, M. (2017). Formation of ordered mesostructured TiO_2 thin films: a soft coarse-grained simulation study. *Phys. Chem. Chem. Phys.* 19, 28249–28262. doi: 10.1039/C7CP05304E

Tauster, S. J., Fung, S. C., and Garten, R. L. (1978). Strong metal-support interactions. Group 8 noble metals supported on titanium dioxide. *J. Am. Chem. Soc.* 100, 170–175. doi: 10.1021/ja00469a029

Teschner, D., Borsodi, J., Wootsch, A., Révay, Z., Hävecker, M., Knop-Gericke, A., et al. (2008). The roles of subsurface carbon and hydrogen in palladium-catalyzed alkyne hydrogenation. *Science* 320, 86–89. doi: 10.1126/science.1155200

Tüysüz, H., Hwang, Y. J., Khan, S. B., Asiri, A. M., and Yang, P. (2013). Mesoporous CO_3O_4 as an electrocatalyst for water oxidation. *Nano Res.* 6, 47–54. doi: 10.1007/s12274-012-0280-8

Wan, Y., and Zhao, D. (2007). On the controllable soft-templating approach to mesoporous silicates. *Chem. Rev.* 107, 2821–2860. doi: 10.1021/cr068020s

Wang, H., Guo, W., Jiang, Z., Yang, R., Jiang, Z., Pan, Y., et al. (2018). New insight into the enhanced activity of ordered mesoporous nickel oxide in formaldehyde catalytic oxidation reactions. *J. Catal.* 361, 370–383. doi: 10.1016/j.jcat.2018.02.023

Wang, J., Tan, H., Yu, S., and Zhou, K. (2015). Morphological effects of gold clusters on the reactivity of ceria surface oxygen. *ACS Catal.* 5, 2873–2881. doi: 10.1021/cs502055r

Wei, X., Shao, B., Zhou, Y., Li, Y., Jin, C., Liu, J., et al. (2018). Geometrical structure of the gold–iron(III) oxide interfacial perimeter for CO oxidation. *Angew. Chem. Int. Edit.* 57, 11289–11293. doi: 10.1002/anie.201805975

Wieckowski, A. (1999). *Interfacial Electrochemistry: Theory: Experiment, and Applications*. New York, NY: CRC Press.

Wu, S. M., Yang, X. Y., and Janiak, C. (2019). Confinement effects in zeolite-confined noble metals. *Angew. Chem. Int. Edit.* 131, 12468–12482. doi: 10.1002/ange.201900013

Xiang, S.-C., Zhang, Z., Zhao, C.-G., Hong, K., Zhao, X., Ding, D.-R., et al. (2011). Rationally tuned micropores within enantiopure metal-organic frameworks for highly selective separation of acetylene and ethylene. *Nat. Commun.* 2:204. doi: 10.1038/ncomms1206

Xiao, Y., Zheng, X., Chen, X., Jiang, L., and Zheng, Y. (2017). Synthesis of Mg-doped ordered mesoporous Pd–Al_2O_3 with different basicity for CO, NO, and HC elimination. *Ind. Eng. Chem. Res.* 56, 1687–1695. doi: 10.1021/acs.iecr.6b03799

Xie, Y., Kocaefe, D., Chen, C., and Kocaefe, Y. (2016). Review of research on template methods in preparation of nanomaterials. *J. Nanomater.* 2016:2302595. doi: 10.1155/2016/2302595

Yang, B., Burch, R., Hardacre, C., Headdock, G., and Hu, P. (2012). Origin of the increase of activity and selectivity of nickel doped by Au, Ag, and Cu for acetylene hydrogenation. *ACS Catal.* 2, 1027–1032. doi: 10.1021/cs2006789

Yang, J., Zhu, Y., Fan, M., Sun, X., Wang, W. D., and Dong, Z. (2019). Ultrafine palladium nanoparticles confined in core–shell magnetic porous organic polymer nanospheres as highly efficient hydrogenation catalyst. *J. Colloid Interface Sci.* 554, 157–165. doi: 10.1016/j.jcis.2019.07.006

Yang, P., Zhao, D., Margolese, D. I., Chmelka, B. F., and Stucky, G. D. (1998). Generalized syntheses of large-pore mesoporous metal oxides with semicrystalline frameworks. *Nature* 396, 152–155. doi: 10.1038/24132

Yang, X.-F., Wang, A., Qiao, B., Li, J., Liu, J., and Zhang, T. (2013). Single-atom catalysts: a new frontier in heterogeneous catalysis. *Acc. Chem. Res.* 46, 1740–1748. doi: 10.1021/ar300361m

Yang, Y., Gao, P., Ren, X., Sha, L., Yang, P., Zhang, J., et al. (2017). Massive Ti^{3+} self-doped by the injected electrons from external Pt and the efficient photocatalytic hydrogen production under visible-light. *Appl. Catal. B Environ.* 218, 751–757. doi: 10.1016/j.apcatb.2017.07.014

Yuan, Q., Li, L.-L., Lu, S.-L., Duan, H.-H., Li, Z.-X., Zhu, Y.-X., et al. (2009). Facile synthesis of Zr-based functional materials with highly ordered mesoporous structures. *J. Phys. Chem. C* 113, 4117–4124. doi: 10.1021/jp806467c

Zelcer, A., and Soler-Illia, G. J. A. A. (2013). One-step preparation of UV transparent highly ordered mesoporous zirconia thin films. *J. Mater. Chem. C* 1, 1359–1367. doi: 10.1039/C2TC00319H

Zhan, S., Zhang, H., Zhang, Y., Shi, Q., Li, Y., and Li, X. (2017). Efficient NH_3-SCR removal of NO_x with highly ordered mesoporous WO_3-CeO_2 at low temperatures. *Appl. Catal. B-Environ.* 203, 199–209. doi: 10.1016/j.apcatb.2016.10.010

Zhang, G., Yang, D., and Sacher, E. (2007). X-ray photoelectron spectroscopic analysis of Pt nanoparticles on highly oriented pyrolytic graphite, using symmetric component line shapes. *J. Phys. Chem. C* 111, 565–570. doi: 10.1021/jp065606+

Zhang, J., Li, Y., Zhang, Y., Chen, M., Wang, L., Zhang, C., et al. (2015). Effect of support on the activity of ag-based catalysts for formaldehyde oxidation. *Sci. Rep.* 5:12950. doi: 10.1038/srep12950

Zhang, L., Jin, L., Liu, B., and He, J. (2019). Templated growth of crystalline mesoporous materials: from soft/hard templates to colloidal templates. *Front. Chem.* 7:22. doi: 10.3389/fchem.2019.00022

Zhao, D., Feng, J., Huo, Q., Melosh, N., Fredrickson, G. H., Chmelka, B. F., et al. (1998). Triblock copolymer syntheses of mesoporous silica with periodic 50 to 300 angstrom pores. *Science* 279, 548–552. doi: 10.1126/science.279.5350.548

Zhao, Y., Dong, F., Han, W., Zhao, H., and Tang, Z. (2019). The synergistic catalytic effect between graphene oxide and three-dimensional ordered mesoporous CO_3O_4 nanoparticles for low-temperature CO oxidation. *Microporous Mesoporous Mat.* 273, 1–9. doi: 10.1016/j.micromeso.2018.06.042

Zhao, Y., Tian, H., He, J., and Yang, Q. (2015). Catalytic oxidation of formaldehyde over mesoporous MnO_x-CeO_2 catalysts. *Int. J. Nanosci.* 14:1460028. doi: 10.1142/S0219581X1460028X

Conflict of Interest: The authors declare that the research was conducted in the absence of any commercial or financial relationships that could be construed as a potential conflict of interest.

Copyright © 2020 Hu, Jin, Dang, Suib, He and Liu. This is an open-access article distributed under the terms of the Creative Commons Attribution License (CC BY). The use, distribution or reproduction in other forums is permitted, provided the original author(s) and the copyright owner(s) are credited and that the original publication in this journal is cited, in accordance with accepted academic practice. No use, distribution or reproduction is permitted which does not comply with these terms.

frontiers in Chemistry

REVIEW
published: 20 November 2020
doi: 10.3389/fchem.2020.592915

Cobalt-Based Metal-Organic Frameworks and Their Derivatives for Hydrogen Evolution Reaction

Wenjuan Han, Minhan Li, Yuanyuan Ma and Jianping Yang**

State Key Laboratory for Modification of Chemical Fibers and Polymer Materials, College of Materials Science and Engineering, Donghua University, Shanghai, China

Hydrogen has been considered as a promising alternative energy to replace fossil fuels. Electrochemical water splitting, as a green and renewable method for hydrogen production, has been drawing more and more attention. In order to improve hydrogen production efficiency and lower energy consumption, efficient catalysts are required to drive the hydrogen evolution reaction (HER). Cobalt (Co)-based metal-organic frameworks (MOFs) are porous materials with tunable structure, adjustable pores and large specific surface areas, which has attracted great attention in the field of electrocatalysis. In this review, we focus on the recent progress of Co-based metal-organic frameworks and their derivatives, including their compositions, morphologies, architectures and electrochemical performances. The challenges and development prospects related to Co-based metal-organic frameworks as HER electrocatalysts are also discussed, which might provide some insight in electrochemical water splitting for future development.

Keywords: electrocatalysts, metal-organic frameworks, cobalt-base catalysts, hydrogen evolution reaction, water electrolysis

OPEN ACCESS

Edited by:
Xiaopeng Han,
Tianjin University, China

Reviewed by:
Bao Yu Xia,
Huazhong University of Science and Technology, China
Mingchuan Luo,
Leiden University, Netherlands
Yongchang Liu,
University of Science and Technology Beijing, China

****Correspondence:***
Yuanyuan Ma
yyma@dhu.edu.cn
Jianping Yang
jianpingyang@dhu.edu.cn

Specialty section:
This article was submitted to Electrochemistry, a section of the journal Frontiers in Chemistry

Received: *08 August 2020*
Accepted: *07 October 2020*
Published: *20 November 2020*

Citation:
Han W, Li M, Ma Y and Yang J (2020) Cobalt-Based Metal-Organic Frameworks and Their Derivatives for Hydrogen Evolution Reaction. Front. Chem. 8:592915. doi: 10.3389/fchem.2020.592915

INTRODUCTION

With the rapid development of economy, energy and environmental problems have raised increasing concerns in recent years (Su et al., 2019; Lin et al., 2020; Liu H. et al., 2020; Liu S. et al., 2020b). To reduce the fossil fuels reliance and lower greenhouse gas emission, there is an urgent need to develop clean and sustainable energy resources. Hydrogen, which possesses high gravimetric energy density, has been considered as an ideal alternative energy carrier to fossil fuels (He et al., 2020). The green and sustainable supply of hydrogen is essential for the hydrogen economy. At present, hydrogen is mainly obtained through a steam reforming of fossil fuels, which not only consumes a large amount of non-renewable energy, but also increases CO_2 emissions (Qin et al., 2016; Li M. et al., 2017a,b). Therefore, to produce hydrogen in a clean and renewable way is urgently required. Water electrolysis, featuring high energy conversion efficiency, high hydrogen production rate and compact devices, has been regarded as an ideal method for hydrogen production in the future (He et al., 2020).

The electrochemical water splitting is composed of two half reactions (**Figure 1**): HER on cathode and oxygen evolution reaction (OER) on anode. Two electrodes of the electrolysis system will play a key role in the hydrogen production. In theory, the decomposition voltage of water is 1.23 V. However, in order to overcome the thermodynamic equilibrium potential, a certain overpotential (η) is required during the practical electrolytic process, which will increase

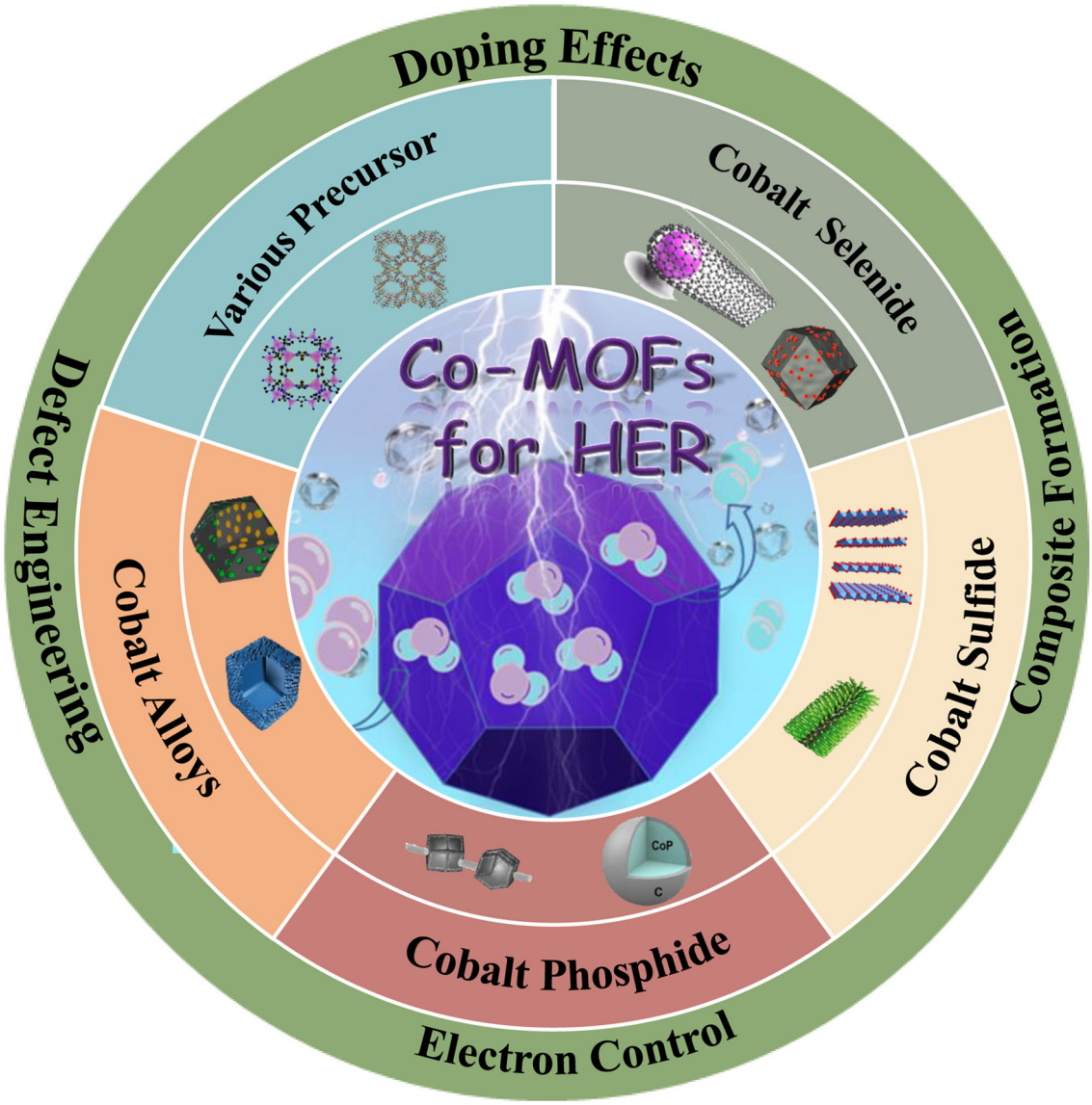

Graphical Abstract |

energy consumption (Xiang et al., 2020). Generally, highly efficient electrocatalysts could reduce the overpotential and increase the current density of these catalytic reactions (Karmodak and Andreussi, 2020; Xu et al., 2020). It is well-known that platinum group metals are the most efficient catalysts for HER (Tian et al., 2019; Huang C. et al., 2020; Huang H. et al., 2020b; Lan et al., 2020; Liu Z. et al., 2020). However, the scarcity and high cost of these precious metals impede their large-scale applications. Therefore, it is pressingly needed to develop low platinum or non-precious metal electrocatalysts with high catalytic activity and long cycle stability for hydrogen production, which will facilitate the realization of hydrogen economy.

During the past few years, a variety of electrocatalysts have been studied for HER, mainly including metals (Xiu et al., 2020), metal sulfides (Huang H. et al., 2020b), metal phosphides (Zhou et al., 2020), metal carbides (Ma X. C. et al., 2020; Yu H. et al., 2020; Yu Y. et al., 2020) and carbon-based materials (Wang H.-F. et al., 2020; Wang J. et al., 2020; Wang X. et al., 2020). In general, the electrocatalysis properties could be improved through increasing the number of active sites and the intrinsic activity of each active site (Huang H. et al., 2020b; Huang Z. et al., 2020). It is worth noting that the concentration and intrinsic activity of active sites can be simultaneously improved by increasing the specific surface area of catalyst (Eiler et al., 2020). In addition, regulating the electronic structure of catalysts could also increase the intrinsic activity, such as heteroatom doping (Liu et al., 2015; Nan et al., 2019; Liu H. et al., 2020), defect engineering (Yilmaz et al., 2018), alloying (Yang et al.,

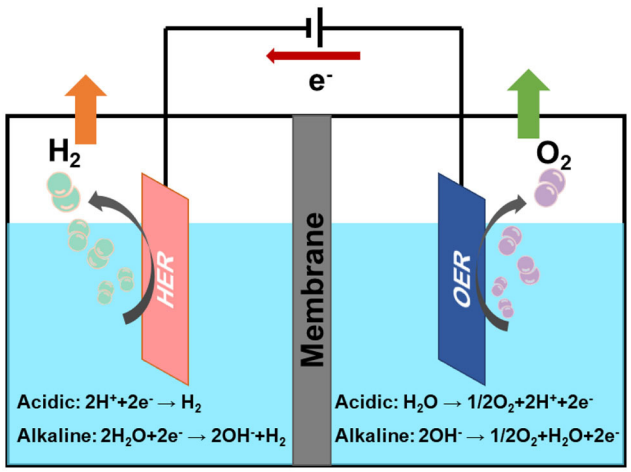

FIGURE 1 | Schematic of water electrolysis system.

2015). Co is plentiful and low cost compared with noble metals. It also has high theoretical catalytic activity due to Co have a low energy barrier for H adsorption, making Co-based composites to be excellent candidates for HER (Chai et al., 2020). Therefore, Co-based catalysts have been widely investigated as the catalysts for HER (Wang H. et al., 2018; Wang X. et al., 2018a; Kuznetsov et al., 2019). Metal-organic frameworks are a porous material consisted of metal nodes and organic linkers, and their derived composites exhibit tunable structure, adjustable pores and large specific surface area (Huang H. et al., 2020a,b). Moreover, the high specific surface can provide a huge number of active sites and the open pore structure in the catalytic process, which is very important to increase the catalytic activity. Therefore, a large number of MOFs have been exploited and classified according to their structural characteristics in recent years, such as zeolitic imidazolate frameworks (ZIFs) (Liu H. et al., 2020), boron imidazolate frameworks (BIFs) (Liu et al., 2018), materials of institute lavoisier (MIL) (Chen J. et al., 2019; Chen W. et al., 2019) and so on. Through the pyrolysis process, these materials can convert into various metals, metal sulfides/phosphides/carbides, carbon-based materials, and other metal structures. Co-MOFs, showing excellent performance for the HER, has sprung up due to its intriguing advantages: (1) Co metal has a proper binding energy for hydrogen atom (close to Pt) (Jin et al., 2015; Huang et al., 2017); (2) the porosity of MOFs can improve the exposure of active sites and electron/mass transfer (Jia et al., 2017; Wang X. et al., 2020); (3) the organic linkers can serve as the source of N-doping which facilitates to maximize conductivity of carbon matrix (Li D. et al., 2018; Weng et al., 2018). In light of the above unique characteristics, Co-based MOFs have attracted great attention for obtaining highly efficient catalysts for HER.

In this review, we present an overview of Co-based MOFs for HER in the past few years. Firstly, the reaction mechanisms of hydrogen evolution reaction were briefly summarized, and also giving the design strategy of Co-based MOFs electrocatalysts. According to the related research works, we discussed the current progress of Co-based MOFs electrocatalysts. In addition, the challenges and perspectives for Co-based MOFs HER catalysts were also discussed, which might provide some insight in electrochemical water splitting for future development.

REACTION MECHANISM FOR HER

The reaction mechanism of HER has been extensively studied (Chen et al., 2020). It is generally carried out in acidic condition or alkaline condition. HER is a two-electron transfer process, includes three possible reaction steps. The specific reaction steps are as follows:

(1) Volmer reaction:

$$H_3O^+ + M + e^- \leftrightarrow M -^* H + H_2O \text{ (acidic medium)} \quad (1)$$

$$H_2O + M + e^- \leftrightarrow M -^* H + OH^- \text{(alkaline medium)} \quad (2)$$

(2) Heyrovsky reaction:

$$H^+ + e^- + M -^* H \leftrightarrow H_2 + M \text{ (acidicmedium)} \quad (3)$$

$$H_2O + e^- + M -^* H \leftrightarrow H_2 + OH^- + M\text{(alkaline medium)} \quad (4)$$

(3) Tafel reaction:

$$2M -^* H \leftrightarrow H_2 + 2M \text{ (acidic and alkaline medium)} \quad (5)$$

M represents the hydrogen adsorption sites, *H represents the reaction intermediates of hydrogen atom on catalyst. From the above reaction steps, the reaction mechanism of HER in acidic electrolyte and alkaline electrolyte is much more different. In acidic electrolyte, the formation of *H is come from hydronium-ion (H_3O^+) during Volmer process, while in alkaline electrolyte *H is formed by the dissociation of water molecules (H_2O). Subsequently, the adsorbed *H will react with H^+ or H_2O to produce H_2 via Heyrovsky process, or combined with another *H to generate H_2 through Tafel process. The whole process of HER includes the *H adsorption and hydrogen desorption from the active sites on the surface of electrocatalysts. Generally, the rate-determining step of HER is the adsorption free energy of hydrogen (ΔG_{H^*}) (Nørskov et al., 2005). For excellent HER electrocatalysts, the bonding strength of the adsorbed hydrogen atom with catalyst should be appropriate. In alkaline media, however, it will introduce an additional energy barrier due to the dissociation of water molecule, which may lower the reaction rate of alkaline HER. It is obvious that the hydrogen adsorption and dissociation on the electrode surface are two consecutive steps in the electrocatalysis process (Li et al., 2020). However, they are inherently competitive. If the bonding strength between the catalyst and hydrogen atom is too weakly, it cannot effectively

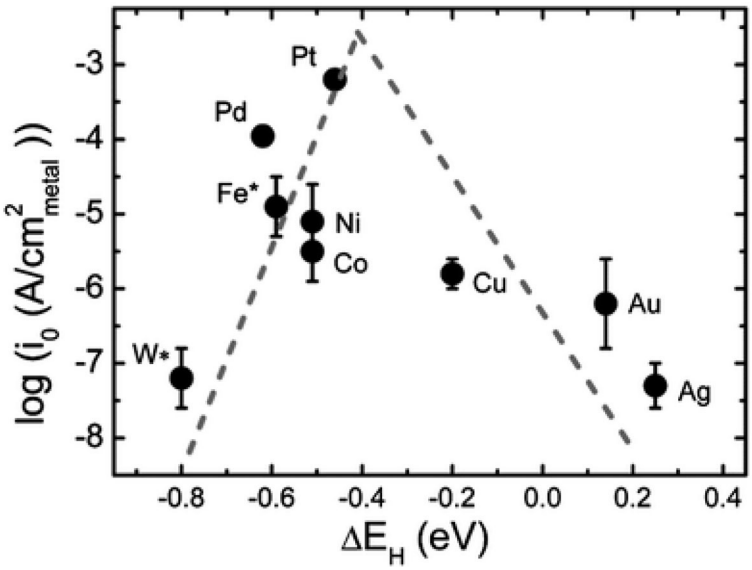

FIGURE 2 | Volcano plot for HER in alkaline medium for various metals. Reproduced with permission (Sheng et al., 2013). Copyright © 2013, Energy Environ. Sci. All rights reserved.

adsorb hydrogen proton intermediates. On the contrary, if the bonding strength between the catalyst and hydrogen atom is too strongly, the generated hydrogen is difficult to desorb from the catalyst. Therefore, only when the adsorption and desorption reach a balance, the HER performance can achieve the most excellent (Hossain et al., 2019). Skúlason et al. (2010) calculated the free energy of hydrogen adsorption of different transition metals using density functional theory, the results are consistent with the Sabatier principle. Sheng has summarized the volcano plots of various metals under alkaline conditions for the HER, which is shown in **Figure 2** (Sheng et al., 2013). This volcano plot is a useful descriptor of hydrogen evolution activity for various metals. When the position of metal is close to the apex of volcano chart, the catalyst reaches the best balance of adsorption and desorption of hydrogen, which has a best HER performance.

According to the volcano plot, Co has a lower adsorption free energy of hydrogen, which should have excellent HER performance. However, there is still a certain gap between Co and precious metals, i.e., Pt, Pd. Hence, to improve the HER performance of Co-based catalysts are necessary. In view of the intrinsic features of large pore volumes, high specific surface area, tunable chemical constituents, and adjustable crystalline porous frameworks, Co-based MOFs have become an increasingly important catalysts in the field of HER. However, insufficient electrical conductivity and low chemical stability seriously limit their applications. Thus, to improve the HER performance of Co-based MOFs catalysts are of great importance. In recent years, various strategies have been adopted to improve the HER performance, including adjusting precursors and synthetic methods, doping heteroatoms, and alloying. Therefore, a reasonable design of Co-based MOFs catalysts can be an effective method to improve the electrocatalytic performance.

CO-BASED MOFs MATERIALS FOR HER

Co-based MOFs has been proved to have a low energy barrier for HER (Jin et al., 2015). However, it still has much room for improvement. Up to now, various strategies have been adopted to improve its electrocatalytic performance, such as choosing different precursor, selenizing, vulcanizing, phosphating, and alloying.

Co-MOFs Derivatives Catalysts From Various Precursor

MOFs and MOFs-derived materials are excellent catalytic materials (Pan et al., 2018; Ma X. C. et al., 2020; Ma Y. et al., 2020). They have attracted much attention because of their designability and adjustability. The structure of MOFs depending on the bridging metal ions and organic linkers. In the past several years, various Co-MOFs derived materials have been extensively developed and used as electrocatalysts for HER (Huang et al., 2017; Li M. et al., 2017b; Tabassum et al., 2017).

With the development of B-H key function research (Zhang et al., 2014), BIFs are widely used in HER. There are two types of tetrahedral centers in BIFs: B (boron) and M (metal) (Zhang H. X. et al., 2016b; Zhang X. et al., 2016). BIFs are generally using lightweight main group metals to build the vertices of the framework and using light elements B to construct polyhedral nodes (Zhang et al., 2009; Zhang H. X. et al., 2016a; Zhang X. et al., 2016; Zhu et al., 2020). Liu et al. (2018) prepared Co/NBC by carbonization of a cobalt-based boron imidazolate frameworks (BIF-82-Co) under various pyrolysis temperature. In 1.0 M KOH solution, Co/NBC-900 required a lower overpotential of 117 mV to achieve the current density of 10 mA cm^{-2} for HER, and a small Tafel slope of 146 mV dec^{-1}.

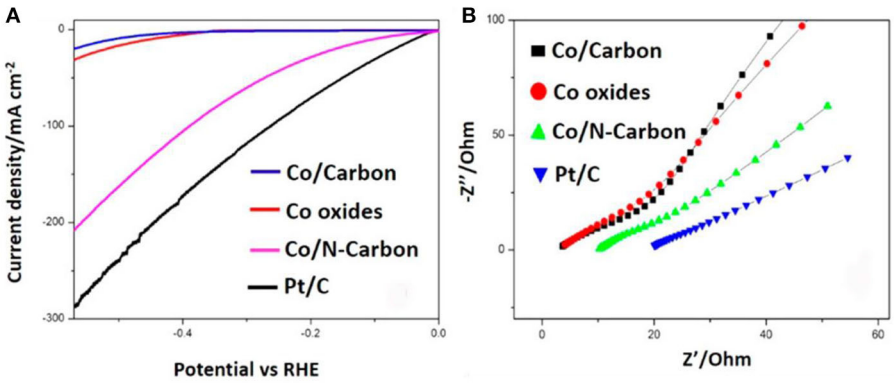

FIGURE 3 | N-Doped carbon material derived Co/N-Carbon as an electrocatalyst for HER in 1 M KOH solution. **(A)** LSV of different electrocatalysts with rotation disk electrode at 1,600 rpm. **(B)** EIS of different electrocatalysts. Reproduced with permission (Huang et al., 2017). © 2017 ACS Sustain. Chem. Eng. All rights reserved.

However, the poor stability (10 h) of these catalysts seriously limits their practical applications.

ZIFs, which is based on imidazolate complexes, can serve as an excellent precursor for non-precious Co-MOFs catalysts. Yang et al. (2017) proposed CoP nanoparticles encapsulated in ultrathin nitrogen-doped porous carbon (CoP@NC) with ZIF-9 as the precursor. The CoP@NC catalyst exhibits outstanding HER catalytic activities in alkaline and acidic conditions. Remarkably, the CoP@NC achieves a current density of 10 mA cm^{-2} at an extremely low overpotentials of 129 and 78 mV in 1.0 M KOH and 0.5 M H_2SO_4 solutions, respectively. More recently, Sun et al. (2016) prepared the $CoSe_2$/CF from zeolitic imidazolate framework-67 (ZIF-67) through pyrolysis and selenizing process. $CoSe_2$/CF delivers a smaller Tafel slope of ∼52 mV dec^{-1}. In addition, $CoSe_2$/CF also shows a better long-term stability than commercial Pt/C.

Apart from MOFs precursors, carbon matrix also plays a decisive role of Co-MOFs derived HER catalysts. To date, most MOF-derived catalysts are modified via the heteroatom doping strategy. When the electronegativity of doping atoms is larger than that of carbon atoms, they will act as electron acceptors (i.e., N, O), on the contrary, they are called electron donors (i.e., F, S, P, B) (Zhang K. et al., 2017; Zhang L. et al., 2017). Nitrogen atom has a similar atomic size but one more shell electron compared with carbon. Therefore, N is the most common doping element among the above elements. The N doping can promote the electrocatalytic activity by increasing the conductivity, enhancing the adsorption strength of anion group (-OH), reducing the reaction energy barrier and accelerating the reaction kinetics (Li D. et al., 2018). Generally, there are two ways to introduce nitrogen atom: one is to select a precursor containing N elements, the other is to combine MOFs with N-containing materials, then allowing the heteroatomic doping of N in the post-processing process (Oh et al., 2019). With the study of N doping, the content of N doping is a key factor to affect the performance of catalyst. For example, Huang et al. (2017) reported a facile one-step pyrolysis strategy to synthesize Co/N-carbon in argon atmosphere. As illustrated in **Figure 3A**, the overpotential of Co/N-carbon is 103 mV (vs. RHE) at 10 mA cm^{-2}. The dramatic enhancement of catalytic activity was even more apparent of charge-transfer resistance (R_{ct}) for the Co/N-carbon (45 Ω) (**Figure 3B**). Experimental results prove that after doping with N, HER performance of Co/N-carbon has been significantly improved. There is almost no HER polarization curve shift for Co/N-carbon after 2,000 cycles, demonstrating their superior cycling durability. To further investigate the effect of N doping, they prepared various catalysts with different N contents. According to the linear sweep voltammetry (LSV) curves, the catalyst of N with 30 mg dosage shows the best HER performance, which further illustrated that the less dosage of N atom can't provide enough rich electronic. However, excessive dopant will reduce the graphitic carbon, and degrade the performance of HER. Therefore, the content of N is an important factor affecting the HER performance.

Dual-heteroatom-doped has become a burgeoning research topic to further boost the HER performance of Co-MOFs derived catalysts. Experimental results revealed that co-doped can downshift the valence bands of carbon matrix and reduce HER overpotential (Zheng et al., 2014; Jiao et al., 2016). In order to improve the catalytic performance of N doping, the use of co-doped is generally required. In the co-doped system, the second doping element is one of key problems needs to be tackled. A simple and effective strategy to solve such a problem is using two doping elements which play different roles on the carbon matrix. N-doping can promote electrocatalytic performance by enhancing the adsorption strength of anionic groups (-OH), optimizing the ΔG_{H*} and ΔG_{H2O}. For S doping, the electronegativity is almost the same as carbon, mainly by changing the electron spin density to improve the performance of the carbon matrix. The enhanced electrocatalytic activity of catalysts was ascribed to the optimized water and hydrogen adsorption free energy by N, S atoms co-doping (Weng et al., 2018). Weng et al. (2018) demonstrated a facile preparation of S-doping CoWP nanoparticles embedded in S- and N-doped carbon matrix [S-CoWP@ (S, N)-C] and further proved the synergistic effects between S and N. In addition, doping B and N into the carbon matrix is another effective approach. When one carbon atom is adjacent to two different doping atoms which have

the same electron-absorbing or electron-giving effects on the middle carbon atom, it will not be conducive to the polarization of the electron cloud of the middle carbon atom. On the contrary, if the heteroatoms on the one side of the carbon atom are pushing electrons on the other side of carbon, it will promote the polarization of the electron cloud of the middle carbon atom (Liu et al., 2018). Therefore, through the synergistic effect of B and N, the catalytic performance of materials can be improved (Liu et al., 2018).

To summarize, both BIFs and ZIFs are bridged by imidazolate. Their derivatives are naturally B-or/and N-doping materials. According to the above description, optimum N-doping content and co-doping play a significant role for boosting the performance of HER. However, to elucidate the synergistic effect of heteroatomic doping remains a challenge.

Co-MOFs Derived Metal Selenide

Cobalt selenide has been attracted considerable attention in the field of water electrolysis due to its excellent performance, high stability and low cost (Liu Y. et al., 2014; Wang et al., 2015; Li K. et al., 2016; Ao et al., 2018; Wang X. et al., 2018a,b; Yi et al., 2020). The electrocatalysis activity of cobalt selenide is mainly attributed to the number of active sites. Moreover, the density of states (DOS) could also determine material properties. For electrocatalysts, the DOS near Fermi level is responsible for the adsorption strength of catalysts. Kong et al. (2013) has prepared a various of first-row transition metal dichalcogenides (ME_2, M = Fe, Co, Ni; E =S, Se) as HER catalysts in acidic media. For all samples, $CoSe_2$ exhibits a high HER performance and shows a small Tafel slope (42.175 mV dec^{-1}), which may be related to its unique electronic structure.

However, $CoSe_2$ has fewer active sites due to easy agglomeration, which limits its application (Liu Y. et al., 2014; Kim et al., 2017; Wang F. et al., 2019; Wang X. et al., 2019; Ding et al., 2020). To overcome this drawback, assembling catalysts with conductive carbon, such as carbon fiber paper (Park and Kang, 2018), carbon nanotubes (Zhou W. et al., 2016; Park and Kang, 2018; Ding et al., 2020), has been demonstrated to be an effective approach. However, the uniform dispersion of nanoparticle catalysts on carbon matrix is still a great challenge. Thus, using MOFs as precursors to introduce carbon nanomaterials has become a popular research subject. According to the morphological relationship between the carbon material and $CoSe_2$, it can be divided into coating (Zhou W. et al., 2016; Meng et al., 2017; Lu et al., 2019; Ding et al., 2020) and loading (Park and Kang, 2018). By coating with carbon materials, the agglomeration and corrosion of $CoSe_2$ can be largely restricted (Zhang F. et al., 2019; Zhang L. et al., 2019; Ding et al., 2020). Zhou W. et al. (2016) prepared the core-shell structure of $CoSe_2$@DC with $CoSe_2$ as the core and embedded $CoSe_2$ with defective carbon nanotubes by a carbonization-oxidation-sialylation strategies. Polarization curves of the materials are shown in **Figures 4A,B**. The overpotential of $CoSe_2$@DC is 132 mV at 10 mA cm^{-2}. Additionally, the Tafel slopes are drawn to study the HER kinetics of the products (**Figure 4C**). The $CoSe_2$@DC exhibits a Tafel slope of 82 mV dec^{-1}, which is lower than that of other materials. Nyquist plots of all catalysts are given in **Figure 4D**, obviously, the R_{ct} of $CoSe_2$@DC is far smaller than the other catalysts. In addition, Ding et al. (2020) synthesized a $CoSe_2$@N/C-CNT catalyst by self-assembling Co^{2+} ions in Adenine (Ade) which is the source of C and N. N-doping bamboo-like carbon nanotubes is also used to prevent the agglomeration and corrosion of catalyst. This method provides strong inspiration for design encased core-shell structure, which might eliminate the issue of the agglomeration. Loading the sample on a carbon substrate is another method to mitigate the agglomeration (Sun et al., 2016; Park and Kang, 2018). Sun et al. (2016) reported that Co^{2+} and organic ligand are repeatedly introduced on the carbon fiber paper. Then, Co-MOFs is formed through the heterosexual attraction between the positively charged Co^{2+} and the negatively charged -COOH group on the carbon fiber paper. Because of the high conductivity of carbon fiber paper, this material exhibits excellent electrocatalytic activity of HER. The time of introducing Co^{2+} and organic ligand was controlled in the synthesis process, which can avoid the agglomeration and produce the optimal loading catalyst with high performance.

Co-MOFs Derived Metal Sulfide

Cobalt sulfides have got tremendous attention due to their intrinsic merits including low cost, easy synthesis and remarkable chemical bond between Co and S (Li K. et al., 2016; Li Z. Q. et al., 2016). The importance of S species in improving the HER performance of Co-based MOFs materials has been confirmed by Staszak-Jirkovsky et al. (2016). It has been known that the electronegativity of S is larger than that of Co (Liu et al., 2019b), the electron transfer from Co to S will increase the electron cloud density around S atoms (Liu S. et al., 2020a). The integrated effects of these factors in Co-MOFs derived metal sulfide ensure its excellent performances. Chen W. et al. (2019) fabricated the flower-like hybrid materials NCO@M (M = Co_3O_4, C, CoS, and CoSe) by ZIF-67 supported of Ni-Fe foam. From the SEM and TEM images, the morphology of NCO@CoS retains the flower-like structure while other samples are changed, suggesting that NCO@CoS has the strong chemical bond between Co and S elements. In addition, NCO@CoS also shows the excellent HER performances compared with the other three samples.

Cobalt sulfides have good corrosion resistance in alkaline solution, and the valence state of cobalt is abundant. Co and S can form various compounds, such as CoS, CoS_2, Co_2S_3, Co_3S_4, Co_9S_8 (Chandrasekaran et al., 2019). The calcination time and atmosphere have been described as key conditions to determine the valence states of the cobalt. Sulfur could sublimate at high temperature, increasing the calcination time can reduce the sulfur content. When the experimental atmosphere is changed from Ar to H_2/Ar, the S content will be further reduced. This might be ascribed to that S can react with H_2 and thus reduce the content of S (Sun et al., 2018). However, most metal sulfide are semiconductors, when they are used as HER catalysts in acidic or alkaline solutions, insufficient conductivity and low stability seriously will degrade their electrocatalytic performance (Li H. et al., 2017; Li M. et al., 2017b). Incorporating carbon materials (e.g., carbon cloth and graphene oxide sheets)

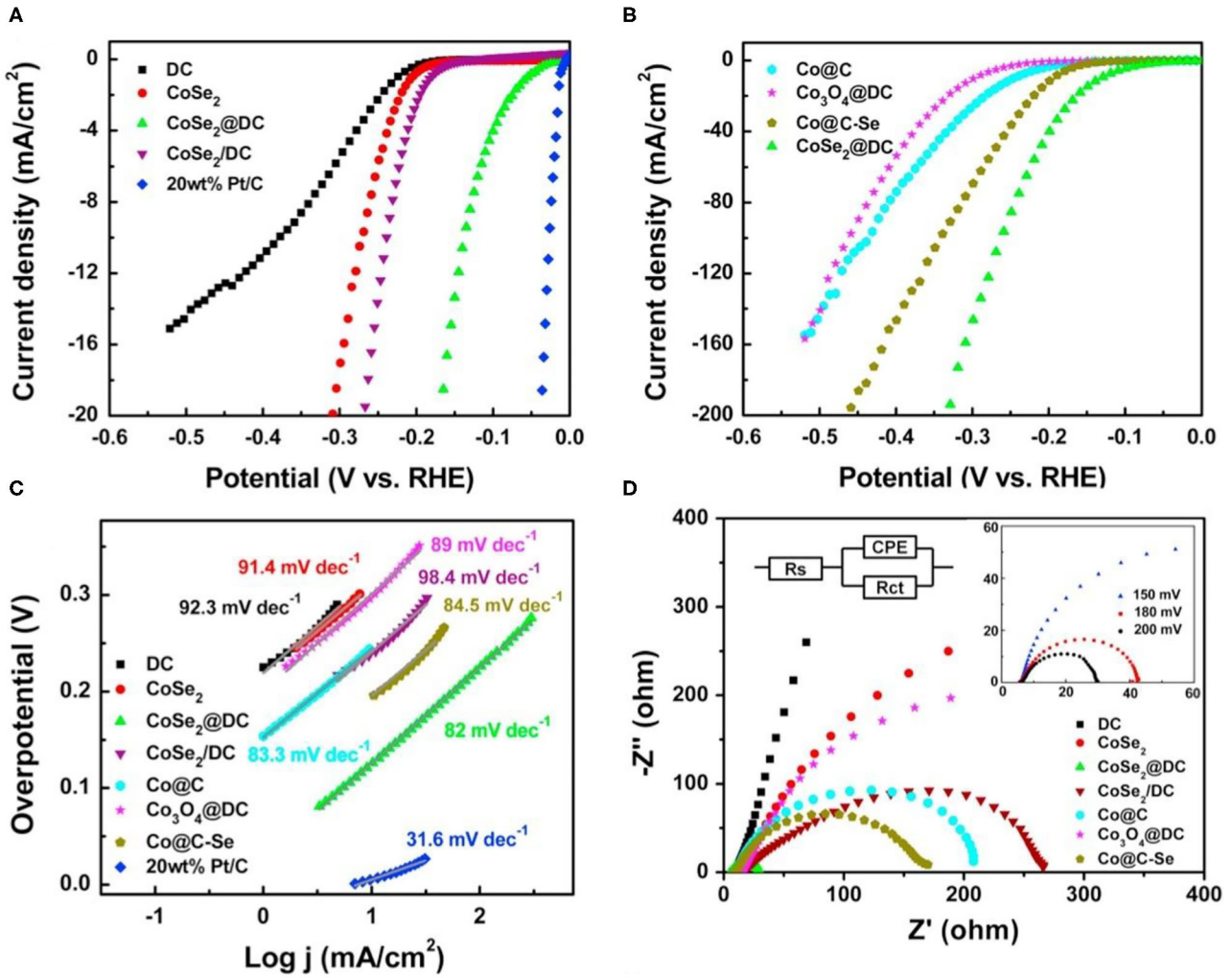

FIGURE 4 | HER performances of Co-MOFs derived metal selenide ($CoSe_2$@DC) in 0.5 M H_2SO_4. **(A,B)** Polarization curves of the different samples, **(C)** the Tafel plots from **(A,B,D)** Nyquist plots of the different samples. Reproduced with permission (Zhou W. et al., 2016). © 2016 Nano Energy. All rights reserved.

is a well-established strategy to enhance the conductivity of the electrocatalysts.

When the catalyst loading on the carbon matrix, the additional sulfur source will be partially doped in the carbon material (Wu et al., 2015). Since most organic ligands are rich in N, S, and N are usually co-doped in the carbon matrix (Li M. et al., 2017b; Wu et al., 2017b). Recently, S, N co-doping has stimulated intensive interest as an emerging method (Wang et al., 2017). Zhang X. et al. (2016) used S- and N-containing chemicals with fixed S/N atomic ratios as precursors to precisely control the doping of S and N in the carbon structure. As shown in **Figure 5A**, the Co/Co_9S_8@SNGS catalyst was synthesized by Co ions with S containing thiophene-2,5-dicarboxylate (Tdc) and N-containing 4,4′-bipyridine (Bpy) (**Figure 5A**). The two-dimensional network layer is formed by Tdc in the sample, and the connection between the two-dimensional network structure is realized by Bpy. The experimental results show that due to the periodic arrangement of the two connectors, the precise ratio of N and S can be achieved to 2.4:1. The electrocatalytic performance of the Co/Co_9S_8@SNGS-T (T = 900, 1,000, 1,100°C) and Co@SNGS-800 was evaluated in 0.1 M KOH solution. The onset potentials of the Co@SNGS-800, Co/Co_9S_8@SNGS-900, Co/Co_9S_8@SNGS-1000, Co/Co_9S_8@SNGS-1100, and Pt/C are 320, 250, 150, 240, and 0 mV (vs. RHE), respectively (**Figure 5B**). Additionally, Co/Co_9S_8@SNGS-T shows the smaller Tafel slope than that of Co@SNGS-800 (125.9 mV dec^{-1}) (**Figure 5C**). The above HER results further confirmed that the interaction between Co and S can promote the performance of HER.

Co-MOFs Derived Metal Phosphide

Recent years, transition metal phosphides (TMPs) have attracted wide attention due to their excellent HER activity, low cost and stability in acidic environments (Tabassum et al., 2017; Wang Q. et al., 2018; Wang X. et al., 2018a; Zhang et al., 2018; Ma X. C. et al., 2020). Unlike the typical layer-structured metal sulfides,

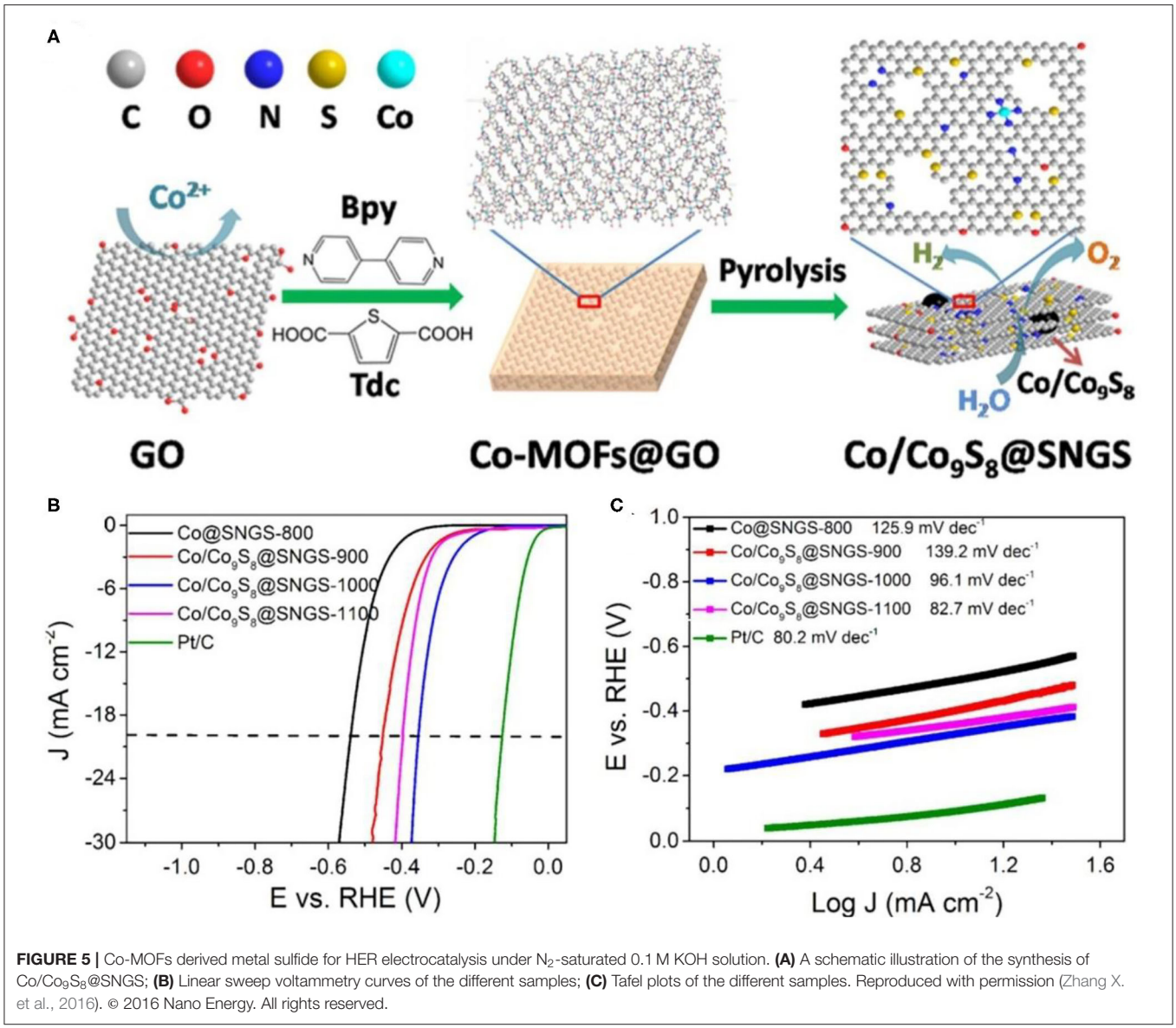

FIGURE 5 | Co-MOFs derived metal sulfide for HER electrocatalysis under N_2-saturated 0.1 M KOH solution. **(A)** A schematic illustration of the synthesis of Co/Co_9S_8@SNGS; **(B)** Linear sweep voltammetry curves of the different samples; **(C)** Tafel plots of the different samples. Reproduced with permission (Zhang X. et al., 2016). © 2016 Nano Energy. All rights reserved.

TMPs tend to form more isotropic crystal structures. Due to the unique structure, metal phosphides usually exhibit abundant unsaturated coordination atoms on the surface. Therefore, TMPs are believed to have higher activity for HER than transition metal sulfides (Das and Nanda, 2016). P vapor is often used for TMP preparation, but it usually requires very high temperature (>500°C) due to the non-reactivity of P_4 molecules (Zhang K. et al., 2017). While, such high temperature will cause the collapse of MOFs, thereby reducing the exposure of active sites and hindering electrons transport (Zhang L. et al., 2019). Hence, it is important to select an appropriate phosphorus source (Jia et al., 2017; Yang et al., 2017; Liu et al., 2019b). PH_3 with high reactivity seems to be a better choice than P vapor, but it is extremely toxic, and has high risk during the experiment. In order to solve this problem, the use of NaH_2PO_2 as a phosphorus source can not only achieve low temperature phosphating (∼300°C) but also ensure safety during the experiment (Liu Q. et al., 2014; Liu Y. et al., 2014; Zhang et al., 2015).

The low conductivity of cobalt phosphides, however, seriously limits their widespread application (Zhou D. et al., 2016; Zhou W. et al., 2016; Wu et al., 2017a; Zhang K. et al., 2017; Pan et al., 2018). Co-MOFs derived cobalt phosphides feature highly dispersed active phases in carbon matrix, which improving the conductivity of materials and making Co-MOFs derived cobalt phosphide an ideal catalyst for HER. In 2018, Hao et al. (2018) successfully embedded Co/CoP into a hairy N-doping carbon polyhedron (Co/CoP HNC). The N-doping carbon nanotube structure not only enhances the interface contact between catalyst and electrolyte, but also facilitates the charge transfer. Inspired by this structure, Pan et al. (2018) prepared the similar structure sample with core shell ZIF-8@ZIF-67 as the precursor to the CoP nanoparticles (NPs) into the hollow polyhedron N-doping

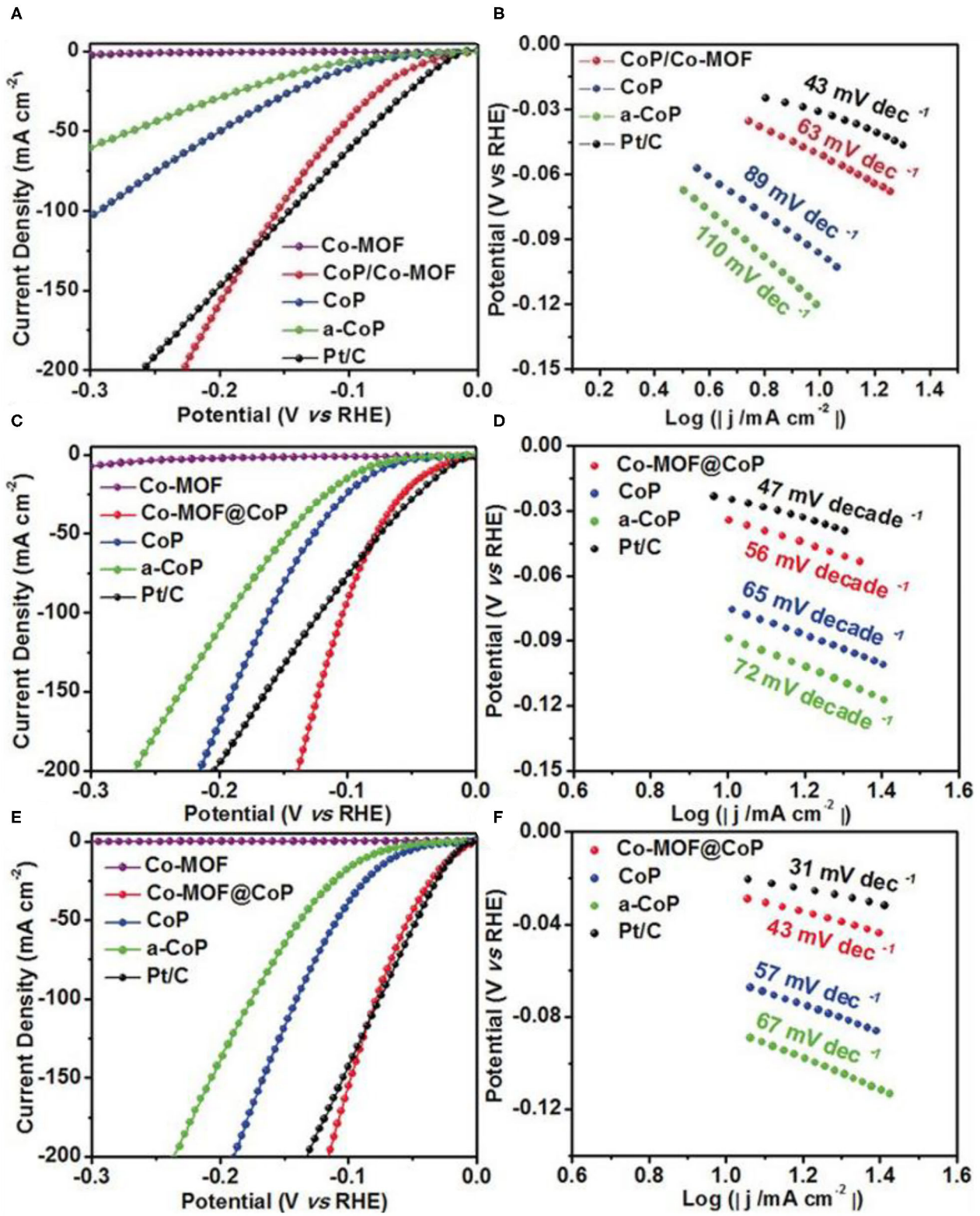

FIGURE 6 | HER performances of Co-MOF derived metal phosphide. LSV curves **(A)**, Tafel slope **(B)** in 1 M PBS, LSV curves **(C)**, Tafel slope **(D)** in 1 M KOH and LSV curves **(E)**, Tafel slope **(F)** in 0.5 M H_2SO_4 of the different samples. Reproduced with permission (Liu et al., 2019a) © 2019 Angew. Chem. Int. Edit. All rights reserved.

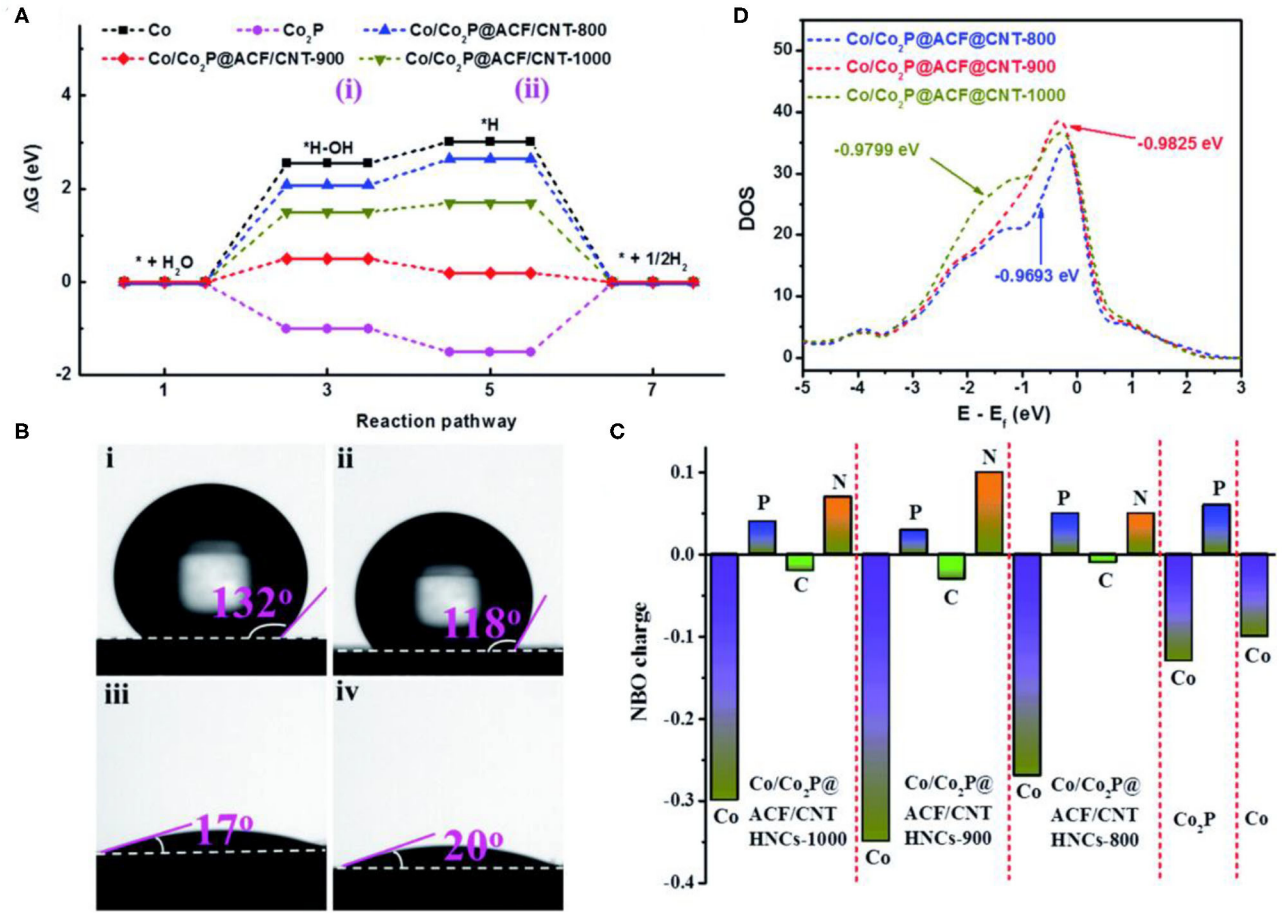

FIGURE 7 | HER performances of Co-MOFs derived metal phosphide synthesized by controlling the pyrolysis temperature. **(A)** Calculated free energy diagram of the HER for (i) $*H_2O$ and (ii) $*1/2H_2$ on the different samples, **(B)** The contact angles of a drop of 1.0 M KOH on (i): ZIF67 precursor, (ii): Co/Co_2P@ACF/CNT HNCs-800, (iii): Co/Co_2P@ACF/CNT HNCs-900, and (iv): Co/Co_2P@ACF/CNT HNCs-1000, **(C)** Calculated DOS of the different samples, **(D)** NBO charge distribution. Reproduced with permission (Wang F. et al., 2019). © 2019 J. Mater. Chem. A. All rights reserved.

carbon nanotubes (NCNHP). It is found that the CoP/NCHNP has high conductivity, which can be ascribed to the hollow polyhedron unique N-doping carbon nanotubes.

The hybridization of Co and cobalt phosphides is another effective approach to enhance the conductivity (Masa et al., 2016; Xue et al., 2017). However, the higher concentration of P in the catalysts impedes the delocalization of cobalt atoms (Wang F. et al., 2019), which is a major reason why it has a low performance of HER. Hence, to control the concentration of P is still an urgent task. Liu et al. (2019a) proposed CoP/Co-MOF on a carbon fiber paper (CF) through a controllable partial phosphorization strategy. The optimized CoP/Co-MOF/CF exhibits outstanding HER performance in alkaline, acidic, and neutral conditions. Remarkably, the CoP/Co-MOF/CF achieves a current density of 10 mA cm^{-2} at an extremely low overpotential of 49, 34, and 21 mV in 1.0 M PBS, 1.0 M KOH, and 0.5 M H_2SO_4 solutions, respectively (**Figures 6A,C,E**). **Figures 6B,D,F** indicate that CoP/Co-MOF possesses the fast dynamics with the Tafel slope of 63, 56, and 43 mV dec^{-1} in 1.0 M PBS, 1.0 M KOH, and 0.5 M H_2SO_4 solutions, respectively. Both experiment and density functional theory (DFT) results show that the N atom in Co-MOF has large electronegativity, the electrons transfer from CoP to Co-MOF increases the positive charge of Co atoms. Positive charge Co atoms interact with the negative charge oxygen atoms in water is conducive to the adsorption and activation of water molecules, thus improve the performance of HER.

In addition to partial phosphorization strategy, annealing temperature is another method to control the doping content of P. High temperature annealing could accelerate the loss of phosphorus and increase the content of Co (Wang F. et al., 2019). Wang F. et al. (2019) prepared the component controllable Co/Co_2P@ACF/CNT HNCs materials through simple etching-pyrolysis-phosphate process. From the free energy calculation results (**Figure 7A**), Co/Co_2P@ACF/CNT-900 has an optimal adsorption energy for water activation. The water contact angle (**Figure 7B**) shows that Co/Co_2P@ACF/CNT-900 has

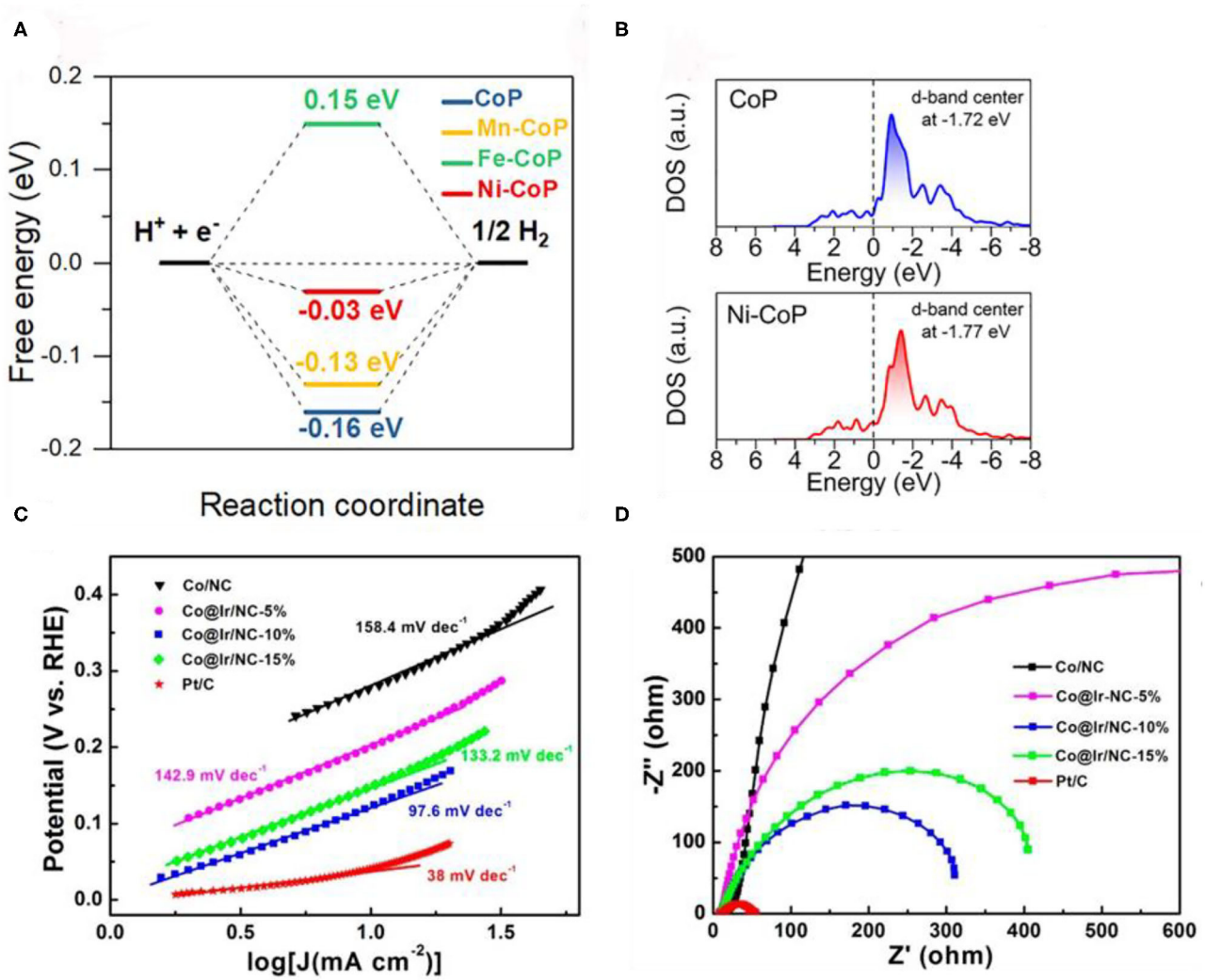

FIGURE 8 | (A) The calculated free-energy diagram of the different samples, **(B)** Calculated DOS curves for CoP and Ni-CoP. Adapted with permission from Pan et al. (2019). © 2019 Nano Energy. All rights reserved. **(C)** Tafel plots of different catalysts in 1 M KOH solution. **(D)** Electrochemical impedance spectra of various catalysts at −0.07 V vs. RHE in 1 M KOH solution. Reproduced with permission (Li D. et al., 2018). © 2018 ACS Sustain. Chem. Eng. All rights reserved.

a lower H* intermediate adsorption energy. This indicates that Co/Co_2P@ACF/CNT-900 is conducive to the adsorption of water, and promotes the Volmer steps, further enhances the HER performance. In addition, the d-band center of Co/Co_2P@ACF/CNT-900 is close to the Fermi level, which possess the moderate H adsorption energy (**Figures 7C,D**). The subsequent electrochemical test was consistent with the above calculations, Co/Co_2P-@ACF/CNT HNCS-900 exhibits the best HER performance. What's more, the phosphating degree could be controlled by changing the mass ratio of phosphorus source and Co during the experiment. Xue et al. (2017) synthesized a novel Mott–Schottky Co/Co_2P microspheres (Co/Co_2P@C) catalyst through carbonization and gradual phosphorization of Co-based MOFs. The hybridization between cobalt and Co_2P can form the Mott-Schottky effect, which could effectively promote the electron transfer.

Synergies With Other Metals

In addition to Co ion, the presence of other metals in the nodes or anchoring other metal ions into MOFs pores can obtain mixed Co-metal MOFs (CoM-MOFs). Compared with single metal Co-MOFs, CoM-MOFs exhibits better HER performance due to the increased active sites (Singh et al., 2019) or optimized absorption and desorption of hydrogen intermediates (Yilmaz et al., 2017; Li D. et al., 2018; Li X. et al., 2018; Yu et al., 2018; Chen W. et al., 2019; Feng et al., 2019; Zhang L. et al., 2019). In order to further improve the performance of the CoM-MOFs, it is important to understand the reaction mechanism of this materials. Increasing the level of the d-band center of metal ions could enhance the interaction between metal and the adsorbed molecules (Hammer and Norskov, 1995; Skúlason et al., 2010; Zheng et al., 2014; Chen et al., 2018). Therefore, regulating the d band center of Co can adjust the interaction between catalysts

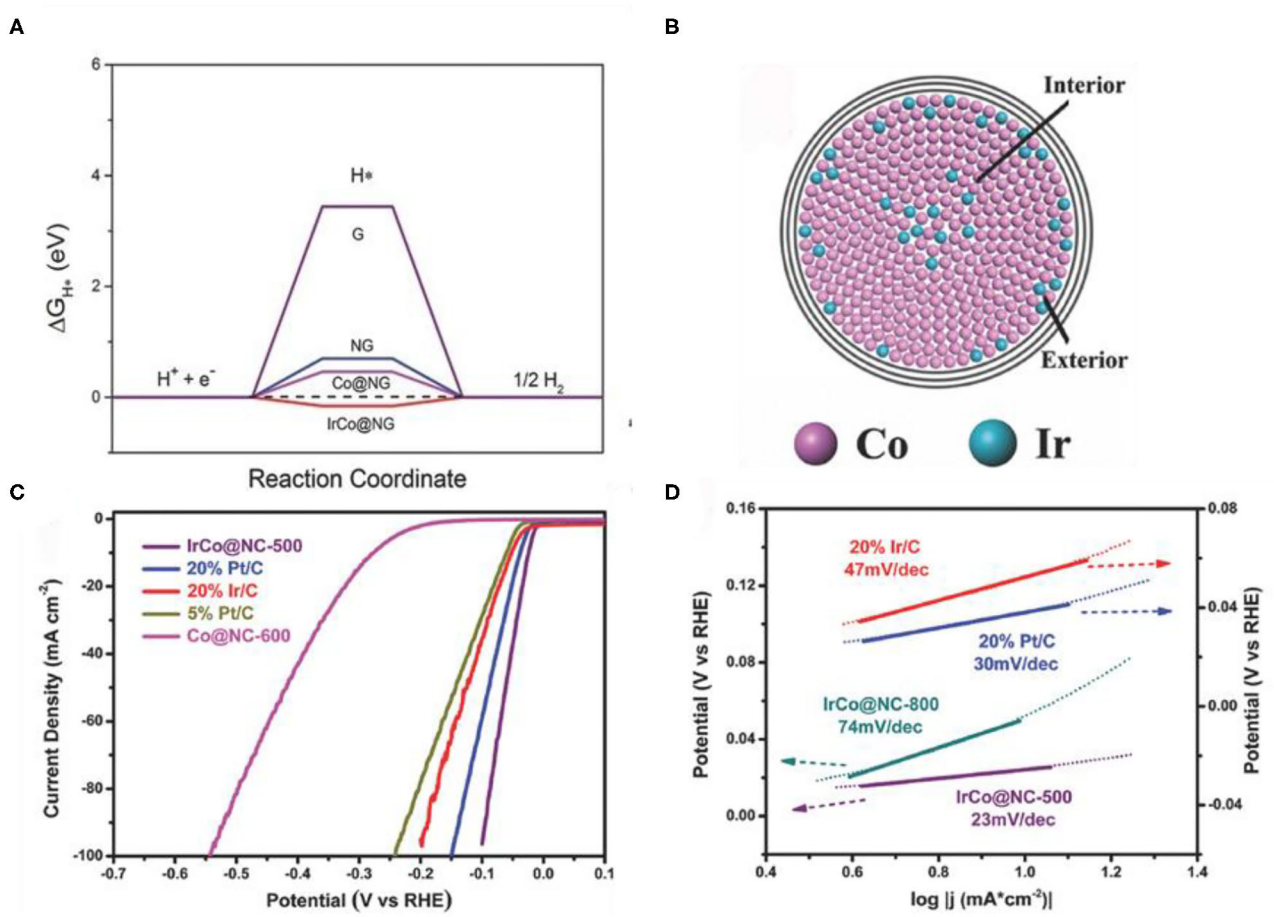

FIGURE 9 | (A) Calculated free-energy diagram of HER at the equilibrium potential for different models, **(B)** Tentative model of an alloy core particle consisting of Co and Ir, **(C,D)** Electrocatalytic HER performance of the catalysts in N_2-saturated 0.5 M H_2SO_4 solution. **(C)** Polarization curves of the different samples, **(D)** Tafel plots of the different catalysts. Reproduced with permission (Jiang et al., 2018). © 2018 Adv. Mater. All rights reserved.

and hydrogen intermediates, optimize the ΔG_{H^*} (Ahn et al., 2018). There are two strategies to modulate the d-band center of Co: (1) adopting two metals with different electronegativities to promote the electron transfer, and adjusting the level of the d-band center of Co (Xu et al., 2018; Lian et al., 2019; Qiao et al., 2020). (2) regulating the lattice parameters and bandwidth of Co, thereby changing the height of the d-band center of Co (Lai et al., 2019; Wang X. et al., 2020; Zhang et al., 2020).

Recently, Pan et al. (2019) prepared M-doped CoP (M = Ni, Mn, Fe) on a hollow polyhedral framework (HPFs) by self-template transformation (STT) strategy. With Fe, Mn, and Ni doping, the doping ions substituted some Co^{2+} ions in CoP. DFT study (**Figure 8A**) suggested that Ni-doped CoP had the optimal hydrogen adsorption free energy. The doping of Ni atoms will lead to the transfer of electron from doping metal to Co atoms, and could improve the performance of HER. DOS calculation further proved how it changes the electronic structure of CoP. As shown in **Figure 8B**, the d-band center decreases as Ni doping in CoP, thus decrease the binding strength of H. These studies indicate that the downshift of d-band center reduces the adsorption of H and increase the desorption of H, which can improve the HER performance. Similarly, doping of other metals could also adjust the d-band center of Co. Li D. et al. (2018), Li X. et al. (2018) prepared Co@Ir/NC-*x* catalyst through a galvanic replacement reaction between $IrCl_3$ and Co/NC. According to the X-ray photoelectron spectroscopy (XPS) analysis, the binding energy of the Co 2p electrons of Co@Ir/NC-10% (781.9 eV) is higher than that of Co/NC (780.0 eV). This indicates that the electron transferred from the Co core to the Ir shell, which can significantly optimize the electrocatalytic performance. According to **Figure 8C**, the Tafel slopes of Co/NC, Co@Ir/NC-5%, Co@Ir/NC-10%, Co@Ir/NC-15%, and Pt/C are measured to be 158.4, 142.9, 97.6, 133.2, and 38 mV dec^{-1}, respectively. The Co@Ir/NC-10% also shows the lowest charge transfer resistance (**Figure 8D**). Unlike the above post-modification method, Chen W. et al. (2019) used two metal salts as metal sources and 1,4-benzenedicarboxylic acid (1,4-BDC) as a linker to synthesize Co-Fe-P nanotubes. The charge transfer from Fe to Co of Co-Fe-P catalyst

TABLE 1 | Summary of Co-MOFs derived electrocatalysts for HER.

	Precursor	Loading amount [mg cm^{-2}]	Electrolytes	Overpotential at 10 mA cm^{-2} [mV]	Tafel slope [mV dec^{-1}]	References
FeCo-600	ZIF-67	0.285	0.5 M H_2SO_4	262		Yang et al., 2015
Co/Co_2P@C-10	ZIF-67	0.2	0.5 M H_2SO_4	192		Yu H. et al., 2020
			1.0 M KOH	158	56.35	
CoP@BCN	ZIF-67	0.4	0.5 M H_2SO_4	87	46	Tabassum et al., 2017
			1.0 M KOH	215	52	
			1M PBS	122	59	
Co-NC/CF	ZIF-67	0.649	1.0 M KOH	103	109	Huang et al., 2017
Co/NBC-900	BIF	2	1.0 M KOH	117	146	Liu et al., 2018
$CoSe_2$/CF	ZIF-67	2.9	1.0 M KOH	52	95	Sun et al., 2016
S-CoWP@(S, N)-C	ZIF-67	0.75	1.0 M KOH	35	35	Weng et al., 2018
$CoSe_2$@N/C-CNT	ZIF-67	0.255	0.5 M H_2SO_4	185	98	Ding et al., 2020
$CoSe_2$@NC-NR/CNT	ZIF-67	1.3	0.5 M H_2SO_4		49.8	Park and Kang, 2018
$CoSe_2$@DC	ZIF-67	0.357	0.5 M H_2SO_4	132	82	Zhou W. et al., 2016
$CoSe_2$(400)-NC-800	ZIF-67	0.212	0.5 M H_2SO_4	234	95	Lu et al., 2019
NCO@CoS	ZIF-67	/	1.0 M KOH	100	68	Chen W. et al., 2019
Co_9S_8/$CoS_{1.097}$/rGO	ZIF-67	1.684	0.5 M H_2SO_4	188	96	Sun et al., 2018
Co/Co9S8@SNGS-1000	ZIF-67	1	0.1 M KOH	350	96.1	Zhang X. et al., 2016
CoP/Co-MOF/CF	ZIF-67	5	0.5 M H_2SO_4	21	43	Liu et al., 2019a
			1.0 M KOH	34	56	
			1M PBS	49	63	
CoP–CNTs	ZIF-67	0.267	0.5 M H_2SO_4	139	52	Wu et al., 2017a
Co/CoP–HNC	ZIF-67	0.19	1.0 M KOH	180	105.6	Hao et al., 2018
CoP/NCNHP	ZIF-67	0.390	0.5 M H_2SO_4	140	53	Pan et al., 2018
		0.390	1.0 M KOH	115	66	
FexCo_2-xP	ZIF-67	4	1.0 M KOH	114	97	Singh et al., 2019
Co@Ir/NC-10%	ZIF-67	0.202	0.5 M H_2SO_4	29.4	41.9	Li D. et al., 2018; Li X. et al., 2018
			1.0 M KOH	121	97.6	
NC@Cu-Co-W-C-700	ZIF-67	2	1.0 M KOH	98	50	Qiao et al., 2020
$Co_{0.6}Fe_{0.4}P$-1.125		0.270	0.5 M H_2SO_4	97		Lian et al., 2019
	ZIF-67		1.0 M KOH	133	61	
			1M PBS	140		
NiCoN/C	ZIF-67	/	1.0 M KOH	103		Lai et al., 2019
Co-NCF@600-Ni	ZIF-67	0.28	1.0 M KOH	157	112	Zhang et al., 2020
Ni-CoP/HPFs	ZIF-67	0.796	0.5 M H_2SO_4	144	52	Pan et al., 2019
			1.0 M KOH	92	71	
IrCo@NC-500	ZIF-67	0.285	0.5 M H_2SO_4	24	23	Jiang et al., 2018
N/Co-PCP//NRGO	ZIF-67	0.714	0.5 M H_2SO_4		126	Hou et al., 2015
Co-NC/CF	ZIF-67	1	1.0 M KOH	157	109	Huang H. et al., 2020b
Co/Co_9S_8	ZIF-67	0.64	1.0 M KOH	216	80	Du et al., 2019
MOF-$CoSe_2$	ZIF-67	0.539	0.5 M H_2SO_4		42	Lin et al., 2017
CoP - NB	ZIF-67	0.707	0.5 M H_2SO_4		51	Wang X. et al., 2018a
CoPS@NPS-C (4 wt%)	ZIF-67	0.357	0.5 M H_2SO_4	93	63	Hu et al., 2018
$Co_{0.75}Fe_{0.25}$-NC	ZIF-67	0.212	1.0 M KOH	202	67.96	Feng et al., 2018
$Zn_{0.3}0Co_{2.70}S_4$	ZIF-67	0.285	0.5 M H_2SO_4	80	47.5	Huang et al., 2016

achieved the desirable electronic configuration and boost the HER performance.

Alloying is another simple and feasible strategy to adjust the d-band center (Wang X. et al., 2020). After alloying, the electronic structure of Co was altered, and hydrogen bonding energy was optimized, thus the HER performance was promoted (Greeley and Mavrikakis, 2004). The surface lattice strain and the coordination environment can be changed by adjusting

the ratio of two kinds of metal atoms, thereby optimizing the d-band center of Co (Pan et al., 2019). Yang et al. (2015) prepared FeCo alloy nanoparticles by annealing of MOFs nanoparticles. Raising the annealing temperature, the average crystallite sizes of the crystal grain increases. After forming the alloy, the bond length of Fe-Co (2.18 Å) is lower than that of Co-Co, suggesting that the doping of Fe could result in strain effects. These results help to shift the d-band center of Co and increases the ΔG_{H^*}. Jiang et al. (2018) prepared IrCo alloys (IrCo@NC) with a simple annealing strategy from Ir-doped Co-based MOFs. Compared with Co@NC, the d-band center of the IrCo@NC located in the vicinity of the Fermi level, which lead to the IrCo@NC has a moderate ΔG_{H^*} (**Figure 9A**). Due to the different atomic radius of Co and Ir, the lattice parameters of Co will be changed when Ir is introduced into the Co core (**Figure 9B**). From the electrochemical test, the IrCo@NC catalyst shows a low onset overpotential (24 mV) (**Figure 9C**) and a small Tafel slope (23 mV dec^{-1}) (**Figure 9D**) than that of commercial Pt/C (30 mV dec^{-1}).

CoM-MOFs is expected to provide a promising avenue in designing and developing novel catalysts, which can improve the performance by offering two different catalytic centers. Apart from doping other metals with different electronegativity, adjusting the lattice parameters of cobalt is another method to achieve the goals. However, how to control the distribution of metals in the catalyst is worth exploring.

CONCLUSIONS AND PERSPECTIVES

In summary, due to porous structures and variable chemical compositions, Co-MOFs have been proved to be an effective catalyst for HER. However, the HER performance of the original Co-based MOFs is still not very well. In this review, we summarize the recent efforts of Co-MOFs derived materials for HER: (1) Co-MOFs derivatives from various precursor; (2) Co-MOFs derived metal selenide; (3) Co-MOFs derived metal sulfide; (4) Co-MOFs derived metal phosphide; (5) synergies with other metals. To better understand the advantages of the above strategies, the HER performances of Co-MOFs derivatives catalysts are listed in **Table 1**. Those studies will provide some new insight in the development of Co-based catalysts for HER. Despite the impressive progress of Co-MOFs in this field, there are still many issues to be solved. In the end, to improve the catalytic performance of Co-MOFs derived materials for HER, the following urgent issues should be rationally considered.

1) It is important to explore various novel Co-based MOFs precursors. Currently, the preparation of Co-based MOFs is mainly come from ZIF-67 (**Table 1**), which possess chemical and thermal stability, and rich topological diversity. Nonetheless, exploring novel precursors to obtain more excellent Co-MOFs catalysts is of great significant for the development of hydrogen production in the future.
2) Optimizing the preparation condition of Co-based MOFs electrocatalysts is crucial. Although most MOFs are crystals, the conductivity of these materials are poorly or scarcely existing due to the insulating character of ligands. High temperature pyrolysis is necessary for MOFs precursor to improve the conductivity. However, the high temperature often leads to the aggregation of metal atoms and collapse of porous network of the MOFs-derived materials. Therefore, achieving an optimal balance among pyrolysis temperature, conductivity, metal particles distribution and surface structure of MOFs-based catalysts is still challenging.
3) The synergistic effect between Co and other metals can reduce the HER energy barrier and improve the catalysts performance. However, the existence of multiple metals increases the complexity of designing MOFs-based materials. The main challenge is how to control the synthesis of Co with other metals, including optimizing of the ratio of metal ions. In addition, the precise reaction mechanism of CoM-MOFs based catalysts is unclear. Hence, to obtain a high performance HER catalysts, it is necessary to have a fundamental understanding of the reaction mechanism for CoM-MOFs based materials.

AUTHOR CONTRIBUTIONS

YM prepared the outline of the review article and guided WH in preparing the first draft to final version. ML was responsible for the modification of language. JY put forward the central idea of the manuscript and gives final modification. All authors listed have made a substantial, direct and intellectual contribution to the work, and approved it for publication.

ACKNOWLEDGMENTS

The authors acknowledge financial support from the Fok Ying-Tong Education Foundation of China (No. 171041), the Program for Professor of Special Appointment (Eastern Scholar), the Initial Research Funds for Young Teachers of Donghua University, Chenguang Program supported by Shanghai Education Development Foundation and Shanghai Municipal Education Commission.

REFERENCES

Ahn, W., Park, M. G., Lee, D. U., Seo, M. H., Jiang, G., Cano, Z. P., et al. (2018). Hollow multivoid nanocuboids derived from ternary Ni–Co–Fe prussian blue analog for dual-electrocatalysis of oxygen and hydrogen evolution reactions. *Adv. Funct. Mater.* 28:1802129. doi: 10.1002/adfm.201802129

Ao, K., Dong, J., Fan, C., Wang, D., Cai, Y., Li, D., et al. (2018). Formation of yolk–shelled nickel–cobalt selenide dodecahedral nanocages from metal–organic frameworks for efficient hydrogen and oxygen evolution. *ACS Sustain. Chem. Eng.* 6, 10952–10959. doi: 10.1021/acssuschemeng.8b02343

Chai, L., Hu, Z., Wang, X., Xu, Y., Zhang, L., Li, T.-T., et al. (2020). Stringing bimetallic metal–organic framework-derived cobalt phosphide

composite for high-efficiency overall water splitting. *Adv. Sci.* 7:1903195. doi: 10.1002/advs.201903195

Chandrasekaran, S., Yao, L., Deng, L., Bowen, C., Zhang, Y., Chen, S., et al. (2019). Recent advances in metal sulfides: from controlled fabrication to electrocatalytic, photocatalytic and photoelectrochemical water splitting and beyond. *Chem. Soc. Rev*. 48, 4178–4280. doi: 10.1039/C8CS00664D

Chen, J., Liu, J., Xie, J.-Q., Ye, H., Fu, X.-Z., Sun, R., et al. (2019). Co-Fe-P nanotubes electrocatalysts derived from metal-organic frameworks for efficient hydrogen evolution reaction under wide pH range. *Nano Energy* 56, 225–233. doi: 10.1016/j.nanoen.2018.11.051

Chen, W., Zhang, Y., Chen, G., Zhou, Y., Xiang, X., and Ostrikov, K. K. (2019). Interface coupling of Ni–Co layered double hydroxide nanowires and cobalt-based zeolite organic frameworks for efficient overall water splitting. *ACS Sustain. Chem. Eng.* 7, 8255–8264. doi: 10.1021/acssuschemeng.8b06627

Chen, Z., Qing, H., Zhou, K., Sun, D., and Wu, R. (2020). Metal-organic framework-derived nanocomposites for electrocatalytic hydrogen evolution reaction. *Prog. Mater. Sci*. 108:100618. doi: 10.1016/j.pmatsci.2019.100618

Chen, Z., Song, Y., Cai, J., Zheng, X., Han, D., Wu, Y., et al. (2018). Tailoring the d-band centers enables Co4 N nanosheets to be highly active for hydrogen evolution catalysis. *Angew. Chem. Int. Ed. Engl.* 57, 5076–5080. doi: 10.1002/anie.201801834

Das, D., and Nanda, K. K. (2016). One-step, integrated fabrication of Co2P nanoparticles encapsulated N, P dual-doped CNTs for highly advanced total water splitting. *Nano Energy* 30, 303–311. doi: 10.1016/j.nanoen.2016.10.024

Ding, H., Xu, G., Zhang, L., Wei, B., Hei, J., and Chen, L. (2020). A highly effective bifunctional catalyst of cobalt selenide nanoparticles embedded nitrogen-doped bamboo-like carbon nanotubes toward hydrogen and oxygen evolution reactions based on metal-organic framework. *J. Colloid. Interface. Sci*. 566, 296–303. doi: 10.1016/j.jcis.2020.01.096

Du, J., Wang, R., Lv, Y.-R., Wei, Y.-L., and Zang, S.-Q. (2019). One-step MOF-derived Co/Co9S8 nanoparticles embedded in nitrogen, sulfur and oxygen ternary-doped porous carbon: an efficient electrocatalyst for overall water splitting. *Chem. Commun*. 55, 3203–3206. doi: 10.1039/c9cc00196d

Eiler, K., Suriñach, S., Sort, J., and Pellicer, E. (2020). Mesoporous Ni-rich Ni–Pt thin films: electrodeposition, characterization and performance toward hydrogen evolution reaction in acidic media. *Appl. Catal. B* 265:118597. doi: 10.1016/j.apcatb.2020.118597

Feng, X., Bo, X., and Guo, L. (2018). CoM(M=Fe,Cu,Ni)-embedded nitrogen-enriched porous carbon framework for efficient oxygen and hydrogen evolution reactions. *J. Power Sources* 389, 249–259. doi: 10.1016/j.jpowsour.2018.04.027

Feng, X., Wang, H., Bo, X., and Guo, L. (2019). Bimetal–organic framework-derived porous rodlike Cobalt/Nickel nitride for All-pH value electrochemical hydrogen evolution. *ACS Appl. Mater. Interfaces* 11, 8018–8024. doi: 10.1021/acsami.8b21369

Greeley, J., and Mavrikakis, M. (2004). Alloy catalysts designed from first principles. *Nat. Mater*. 3, 810–815. doi: 10.1038/nmat1223

Hammer, B., and Norskov, J. K. (1995). Why gold is the noblest of all the metals. *Nature* 376, 238–240. doi: 10.1038/376238a0

Hao, Y. C., Xu, Y. Q., Liu, W., and Sun, X. M. (2018). Co/CoP embedded in a hairy nitrogen-doped carbon polyhedron as an advanced tri-functional electrocatalyst. *Mater. Horizons* 5, 108–115. doi: 10.1039/c7mh00706j

He, Q., Tian, D., Jiang, H., Cao, D., Wei, S., Liu, D., et al. (2020). Achieving efficient alkaline hydrogen evolution reaction over a Ni5P4 catalyst incorporating single-atomic Ru sites. *Adv. Mater*. 32:1906972. doi: 10.1002/adma.201906972

Hossain, M. D., Liu, Z., Zhuang, M., Yan, X., Xu, G.-L., Gadre, C. A., et al. (2019). Rational design of graphene-supported single atom catalysts for hydrogen evolution reaction. *Adv. Energy. Mater*. 9:1803689. doi: 10.1002/aenm.201803689

Hou, Y., Wen, Z., Cui, S., Ci, S., Mao, S., and Chen, J. (2015). An advanced nitrogen-doped graphene/cobalt-embedded porous carbon polyhedron hybrid for efficient catalysis of oxygen reduction and water splitting. *Adv. Funct. Mater*. 25, 872–882. doi: 10.1002/adfm.201403657

Hu, Y., Li, F., Long, Y., Yang, H., Gao, L., Long, X., et al. (2018). Ultrafine CoPS nanoparticles encapsulated in N, P, and S tri-doped porous carbon as an efficient bifunctional water splitting electrocatalyst in both acid and alkaline solutions. *J. Mater. Chem. A*. 6, 10433–10440. doi: 10.1039/C8TA01310A

Huang, C., Yu, L., Zhang, W., Xiao, Q., Zhou, J., Zhang, Y., et al. (2020). N-doped Ni-Mo based sulfides for high-efficiency and stable hydrogen evolution reaction. *Appl. Catal. B*. 276:119137. doi: 10.1016/j.apcatb.2020.119137

Huang, H., Zhao, Y., Bai, Y., Li, F., Zhang, Y., and Chen, Y. (2020a). Conductive metal–organic frameworks with extra metallic sites as an efficient electrocatalyst for the hydrogen evolution reaction. *Adv. Sci*. 7:2000012. doi: 10.1002/advs.202000012

Huang, H., Zhou, S., Yu, C., Huang, H., Zhao, J., Dai, L., et al. (2020b). Rapid and energy-efficient microwave pyrolysis for high-yield production of highly-active bifunctional electrocatalysts for water splitting. *Energy Environ. Sci.* 13, 545–553. doi: 10.1039/C9EE03273H

Huang, T., Chen, Y., and Lee, J.-M. (2017). Two-dimensional cobalt/N-doped carbon hybrid structure derived from metal–organic frameworks as efficient electrocatalysts for hydrogen evolution. *ACS Sustain. Chem. Eng.* 5, 5646–5650. doi: 10.1021/acssuschemeng.7b00598

Huang, Z., Yuan, S., Zhang, T., Cai, B., Xu, B., Lu, X., et al. (2020). Selective selenization of mixed-linker Ni-MOFs: NiSe2@NC core-shell nano-octahedrons with tunable interfacial electronic structure for hydrogen evolution reaction. *Appl. Catal. B* 272:118976. doi: 10.1016/j.apcatb.2020.118976

Huang, Z.-F., Song, J., Li, K., Tahir, M., Wang, Y.-T., Pan, L., et al. (2016). Hollow cobalt-based bimetallic sulfide polyhedra for efficient all-pH-value electrochemical and photocatalytic hydrogen evolution. *J. Am. Chem. Soc*. 138, 1359–1365. doi: 10.1021/jacs.5b11986

Jia, G., Zhang, W., Fan, G., Li, Z., Fu, D., Hao, W., et al. (2017). Three-dimensional hierarchical architectures derived from surface-mounted metal-organic framework membranes for enhanced electrocatalysis. *Angew. Chem. Int. Ed. Engl.* 56, 13781–13785. doi: 10.1002/anie.201708385

Jiang, P., Chen, J., Wang, C., Yang, K., Gong, S., Liu, S., et al. (2018). Tuning the activity of carbon for electrocatalytic hydrogen evolution via an iridium-cobalt alloy core encapsulated in nitrogen-doped carbon cages. *Adv. Mater*. 30:1705324. doi: 10.1002/adma.201705324

Jiao, Y., Zheng, Y., Davey, K., and Qiao, S.-Z. (2016). Activity origin and catalyst design principles for electrocatalytic hydrogen evolution on heteroatom-doped graphene. *Nat. Energy* 1:16130. doi: 10.1038/nenergy.2016.130

Jin, H., Wang, J., Su, D., Wei, Z., Pang, Z., and Wang, Y. (2015). *In situ* cobalt–cobalt oxide/N-doped carbon hybrids as superior bifunctional electrocatalysts for hydrogen and oxygen evolution. *J. Am. Chem. Soc*. 137, 2688–2694. doi: 10.1021/ja5127165

Karmodak, N., and Andreussi, O. (2020). Catalytic activity and stability of two-dimensional materials for the hydrogen evolution reaction. *ACS Energy Lett*. 5, 885–891. doi: 10.1021/acsenergylett.9b02689

Kim, J. K., Park, G. D., Kim, J. H., Park, S.-K., and Kang, Y. C. (2017). Rational design and synthesis of extremely efficient macroporous CoSe2–CNT composite microspheres for hydrogen evolution reaction. *Small* 13:1700068. doi: 10.1002/smll.201700068

Kong, D., Cha, J. J., Wang, H., Lee, H. R., and Cui, Y. (2013). First-row transition metal dichalcogenide catalysts for hydrogen evolution reaction. *Energy Environ. Sci*. 6, 3553–3558. doi: 10.1039/c3ee42413h

Kuznetsov, D. A., Chen, Z., Kumar, P. V., Tsoukalou, A., Kierzkowska, A., Abdala, P. M., et al. (2019). Single site cobalt substitution in 2D molybdenum carbide (MXene) enhances catalytic activity in the hydrogen evolution reaction. *J. Am. Chem. Soc*. 141, 17809–17816. doi: 10.1021/jacs.9b08897

Lai, J., Huang, B., Chao, Y., Chen, X., and Guo, S. (2019). Strongly coupled nickel–cobalt nitrides/carbon hybrid nanocages with Pt-like activity for hydrogen evolution catalysis. *Adv. Mater*. 31:1805541. doi: 10.1002/adma.201805541

Lan, Y., Chen, J., Zhang, H., Zhang, W. X., and Yang, J. (2020). Fe/Fe3C nanoparticle-decorated N-doped carbon nanofibers for improving the nitrogen selectivity of electrocatalytic nitrate reduction. *J. Mater. Chem. A* 8, 15853–15863. doi: 10.1039/D0TA02317E

Li, D., Zong, Z., Tang, Z., Liu, Z., Chen, S., Tian, Y., et al. (2018). Total water splitting catalyzed by Co@Ir core–shell nanoparticles encapsulated in nitrogen-doped porous carbon derived from metal–organic frameworks. *ACS Sustain. Chem. Eng.* 6, 5105–5114. doi: 10.1021/acssuschemeng.7b04777

Li, H., Qian, X., Xu, C., Huang, S., Zhu, C., Jiang, X., et al. (2017). Hierarchical porous Co9S8/nitrogen-doped carbon@MoS2 polyhedrons as pH universal electrocatalysts for highly efficient hydrogen evolution reaction. *ACS Appl. Mater. Interfaces* 9, 28394–28405. doi: 10.1021/acsami.7b06384

Li, K., Zhang, J., Wu, R., Yu, Y., and Zhang, B. (2016). Anchoring CoO domains on CoSe2 nanobelts as bifunctional electrocatalysts for overall water splitting in neutral media. 3:1500426. doi: 10.1002/advs.201500426

Li, M., Wang, H., Luo, W., Sherrell, P. C., Chen, J., and Yang, J. (2017a). Heterogeneous single-atom catalysts for electrochemical CO2 reduction reaction. *Acs Energy Lett*. 32:2001848. doi: 10.1002/adma.202001848

Li, M., Zhou, H., Yang, W., Chen, L., Huang, Z., Zhang, N., et al. (2017b). Co9S8 nanoparticles embedded in a N, S co-doped graphene-unzipped carbon nanotube composite as a high performance electrocatalyst for the hydrogen evolution reaction. *J. Mater. Chem. A* 5, 1014–1021. doi: 10.1039/C6TA08955K

Li, X., Wei, J., Li, Q., Zheng, S., Xu, Y., Du, P., et al. (2018). Nitrogen-doped cobalt oxide nanostructures derived from cobalt–alanine complexes for high-performance oxygen evolution reactions. *Adv. Funct. Mater*. 28:1800886. doi: 10.1002/adfm.201800886

Li, Z., Feng, Y., Liang, Y.-L., Cheng, C.-Q., Dong, C.-K., Liu, H., et al. (2020). Stable rhodium (IV) oxide for alkaline hydrogen evolution reaction. *Adv. Mater*. 32:1908521. doi: 10.1002/adma.201908521

Li, Z. Q., Li, C. X., Ge, X. L., Ma, J. Y., Zhang, Z. W., Li, Q., et al. (2016). Reduced graphene oxide wrapped MOFs-derived cobalt-doped porous carbon polyhedrons as sulfur immobilizers as cathodes for high performance lithium sulfur batteries. *Nano Energy* 23, 15–26. doi: 10.1016/j.nanoen.2016.02.049

Lian, Y., Sun, H., Wang, X., Qi, P., Mu, Q., Chen, Y., et al. (2019). Carved nanoframes of cobalt-iron bimetal phosphide as a bifunctional electrocatalyst for efficient overall water splitting. *Chem. Sci*. 10, 464–474. doi: 10.1039/c8sc03877e

Lin, J., He, J., Qi, F., Zheng, B., Wang, X., Yu, B., et al. (2017). *In-situ* selenization of Co-based metal-organic frameworks as a highly efficient electrocatalyst for hydrogen evolution reaction. *Electrochim. Acta* 247, 258–264. doi: 10.1016/j.electacta.2017.06.179

Lin, L., Sherrell, P., Liu, Y., Lei, W., Zhang, S., Zhang, H., et al. (2020). Engineered 2D transition metal dichalcogenides—a vision of viable hydrogen evolution reaction catalysis. *Adv. Energy. Mater*. 10:1903870. doi: 10.1002/aenm.201903870

Liu, H., Jin, M., Zhan, D., Wang, J., Cai, X., Qiu, Y., et al. (2020). Stacking faults triggered strain engineering of ZIF-67 derived Ni-Co bimetal phosphide for enhanced overall water splitting. *Appl. Catal. B. Environ*. 272:118951. doi: 10.1016/j.apcatb.2020.118951

Liu, J., Wickramaratne, N. P., Qiao, S. Z., and Jaroniec, M. (2015). Molecular-based design and emerging applications of nanoporous carbon spheres. *Nat. Mater*. 14, 763–774. doi: 10.1038/nmat4317

Liu, M.-R., Hong, Q.-L., Li, Q.-H., Du, Y., Zhang, H.-X., Chen, S., et al. (2018). Cobalt boron imidazolate framework derived cobalt nanoparticles encapsulated in B/N codoped nanocarbon as efficient bifunctional electrocatalysts for overall water splitting. *Adv. Funct. Mater*. 28:1801136. doi: 10.1002/adfm.201801136

Liu, Q., Tian, J., Cui, W., Jiang, P., Cheng, N., Asiri, A. M., et al. (2014). Carbon nanotubes decorated with CoP nanocrystals: a highly active non-noble-metal nanohybrid electrocatalyst for hydrogen evolution. *Angew. Chem. Int. Ed. Engl*. 53, 6710–6714. doi: 10.1002/anie.201404161

Liu, S., Che, C., Jing, H., Zhao, J., Mu, X., Zhang, S., et al. (2020a). Phosphorus-triggered synergy of phase transformation and chalcogenide vacancy migration in cobalt sulfide for an efficient oxygen evolution reaction. *Nanoscale* 12, 3129–3134. doi: 10.1039/C9NR09203J

Liu, S., Mao, J., Zhang, Q., Wang, Z., Pang, W. K., Zhang, L., et al. (2020b). An intrinsically non-flammable electrolyte for high-performance potassium batteries. *Angew. Chem. Int. Ed*. 59, 3638–3644. doi: 10.1002/anie.201913174

Liu, T., Li, P., Yao, N., Cheng, G., Chen, S., Luo, W., et al. (2019a). CoP-doped MOF-based electrocatalyst for ph-universal hydrogen evolution reaction. *Angew. Chem. Int. Edit*. 58, 4679–4684. doi: 10.1002/anie.201901409

Liu, T., Li, P., Yao, N., Kong, T., Cheng, G., Chen, S., et al. (2019b). Self-sacrificial template-directed vapor-phase growth of MOF assemblies and surface vulcanization for efficient water splitting. *Adv. Mater*. 31:1806672. doi: 10.1002/adma.201806672

Liu, Y., Cheng, H., Lyu, M., Fan, S., Liu, Q., Zhang, W., et al. (2014). Low overpotential in vacancy-rich ultrathin CoSe2 nanosheets for water oxidation. *J. Am. Chem. Soc*. 136, 15670–15675. doi: 10.1021/ja5085157

Liu, Z., Ai, J., Sun, M., Han, F., Li, Z., Peng, Q., et al. (2020). Phosphorous-doped graphite layers with outstanding electrocatalytic activities for the oxygen and hydrogen evolution reactions in water electrolysis. *Adv. Funct. Mater*. 30:1910741. doi: 10.1002/adfm.201910741

Lu, H., Zhang, Y., Huang, Y., Zhang, C., and Liu, T. (2019). Reaction packaging CoSe2 nanoparticles in N-doped carbon polyhedra with bifunctionality for overall water splitting. *ACS Appl. Mater. Interfaces* 11, 3372–3381. doi: 10.1021/acsami.8b20184

Ma, X. C., He, Y. Y., Zhang, D. X., Chen, M. J., Ke, S. C., Yin, Y. X., et al. (2020). Cobalt-based MOF-derived CoP/Hierarchical Porous Carbon (HPC) composites as robust catalyst for efficient dehydrogenation of ammonia-borane. *Chemistry. Select*. 5, 2190–2196. doi: 10.1002/slct.201904481

Ma, Y., Chen, M., Geng, H., Dong, H., Wu, P., Li, X., et al. (2020). Synergistically tuning electronic structure of porous β-Mo2C spheres by Co doping and Mo-vacancies defect engineering for optimizing hydrogen evolution reaction activity. *Adv. Funct. Mater*. 30:2000561. doi: 10.1002/adfm.202000561

Masa, J., Barwe, S., Andronescu, C., Sinev, I., Ruff, A., Jayaramulu, K., et al. (2016). Low overpotential water splitting using cobalt–cobalt phosphide nanoparticles supported on nickel foam. *Acs Energy Lett*. 1, 1192–1198. doi: 10.1021/acsenergylett.6b00532

Meng, T., Qin, J., Wang, S., Zhao, D., Mao, B., and Cao, M. (2017). *In Situ* coupling of Co0.85Se and N-doped carbon via one-step selenization of metal–organic frameworks as a trifunctional catalyst for overall water splitting and Zn–air batteries. *J. Mater. Chem. A* 5, 7001–7014. doi: 10.1039/C7TA01453H

Nan, J., Guo, X., Xiao, J., Li, X., Chen, W., Wu, W., et al. (2019). Nanoengineering of 2D MXene-based materials for energy storage applications. *Small*. doi: 10.1002/smll.201902085. [Epub ahead of print].

Nørskov, J. K., Bligaard, T., Logadottir, A., Kitchin, J. R., Chen, J. G., Pandelov, S., et al. (2005). Trends in the exchange current for hydrogen evolution. *J. Electrochem. Soc*. 152, J23–J26. doi: 10.1149/1.1856988

Oh, J., Park, S., Jang, D., Shin, Y., Lim, D., and Park, S. (2019). Metal-free N-doped carbon blacks as excellent electrocatalysts for oxygen reduction reactions. *Carbon* 145, 481–487. doi: 10.1016/j.carbon.2019.01.056

Pan, Y., Sun, K., Lin, Y., Cao, X., Cheng, Y., Liu, S., et al. (2019). Electronic structure and d-band center control engineering over M-doped CoP (M = Ni, Mn, Fe) hollow polyhedron frames for boosting hydrogen production. *Nano Energy* 56, 411–419. doi: 10.1016/j.nanoen.2018.11.034

Pan, Y., Sun, K., Liu, S., Cao, X., Wu, K., Cheong, W. C., et al. (2018). Core-Shell ZIF-8@ZIF-67-derived CoP nanoparticle-embedded N-doped carbon nanotube hollow polyhedron for efficient overall water splitting. *J. Am. Chem. Soc*. 140, 2610–2618. doi: 10.1021/jacs.7b12420

Park, S. K., and Kang, Y. C. (2018). MOF-templated N-doped carbon-coated CoSe2 nanorods supported on porous CNT microspheres with excellent sodium-ion storage and electrocatalytic properties. *ACS Appl. Mater. Interfaces* 10, 17203–17213. doi: 10.1021/acsami.8b03607

Qiao, L., Zhu, A., Zeng, W., Dong, R., Tan, P., Ding, Z., et al. (2020). Achieving electronic structure reconfiguration in metallic carbides for robust electrochemical water splitting. *J. Mater. Chem. A* 8, 2453–2462. doi: 10.1039/c9ta10682k

Qin, Z., Chen, Y., Huang, Z., Su, J., Diao, Z., and Guo, L. (2016). Composition-dependent catalytic activities of noble-metal-free NiS/Ni3S4 for hydrogen evolution reaction. *J. Phys. Chem. C* 120, 14581–14589. doi: 10.1021/acs.jpcc.6b05230

Sheng, W., Myint, M., Chen, J. G., and Yan, Y. (2013). Correlating the hydrogen evolution reaction activity in alkaline electrolytes with the hydrogen binding energy on monometallic surfaces. *Energy Environ. Sci*. 6, 1509–1512. doi: 10.1039/C3EE00045A

Singh, T. I., Rajeshkhanna, G., Singh, S. B., Kshetri, T., Kim, N. H., and Lee, J. H. (2019). Metal-organic framework-derived Fe/Co-based bifunctional electrode for H2 production through water and urea electrolysis. *Chem. Sus. Chem*. 12, 4810–4823. doi: 10.1002/cssc.201902232

Skúlason, E., Tripkovic, V., Björketun, M. E., Gudmundsdóttir, S., Karlberg, G., Rossmeisl, J., et al. (2010). Modeling the electrochemical hydrogen oxidation and evolution reactions on the basis of density functional theory calculations. *J. Phys. Chem. C*. 114, 18182–18197. doi: 10.1021/jp1048887

Staszak-Jirkovsky, J., Malliakas, C. D., Lopes, P. P., Danilovic, N., Kota, S. S., Chang, K. C., et al. (2016). Design of active and stable Co-Mo-Sx chalcogels

as pH-universal catalysts for the hydrogen evolution reaction. *Nat. Mater*. 15, 197–203. doi: 10.1038/nmat4481

Su, L., Han, D., Zhu, G., Xu, H., Luo, W., Wang, L., et al. (2019). Tailoring the assembly of iron nanoparticles in carbon microspheres toward high-performance electrocatalytic denitrification. *Nano Lett*. 19, 5423–5430. doi: 10.1021/acs.nanolett.9b01925

Sun, C., Dong, Q., Yang, J., Dai, Z., Lin, J., Chen, P., et al. (2016). Metal–organic framework derived CoSe2 nanoparticles anchored on carbon fibers as bifunctional electrocatalysts for efficient overall water splitting. *Nano Res*. 9, 2234–2243. doi: 10.1007/s12274-016-1110-1

Sun, X., Huang, H., Wang, C., Liu, Y., Hu, T.-L., and Bu, X.-H. (2018). Effective CoxSy HER electrocatalysts fabricated by *in-situ* sulfuration of a metal-organic framework. *Chem. Electro. Chem*. 5, 3639–3644. doi: 10.1002/celc.201801238

Tabassum, H., Guo, W., Meng, W., Mahmood, A., Zhao, R., Wang, Q., et al. (2017). Metal–Organic frameworks derived cobalt phosphide architecture encapsulated into B/N Co-doped graphene nanotubes for all pH value electrochemical hydrogen evolution. *Adv. Energy Mater*. 7:1601671. doi: 10.1002/aenm.201601671

Tian, H., Liu, X., Dong, L., Ren, X., Liu, H., Price, C. A. H., et al. (2019). Enhanced hydrogenation performance over hollow structured Co-CoOx@N-C capsules. *Adv. Sci*. 6:1900807. doi: 10.1002/advs.201900807

Wang, F., Hu, L., Liu, R., Yang, H., Xiong, T., Mao, Y., et al. (2019). Hybrid implanted hybrid hollow nanocube electrocatalyst facilitates efficient hydrogen evolution activity. *J. Mater. Chem. A* 7, 11150–11159. doi: 10.1039/c9ta00931k

Wang, H., Yang, N., Li, W., Ding, W., Chen, K., Li, J., et al. (2018). Understanding the roles of nitrogen configurations in hydrogen evolution: trace atomic cobalt boosts the activity of planar nitrogen-doped graphene. *ACS Energy Lett*. 3, 1345–1352. doi: 10.1021/acsenergylett.8b00522

Wang, H.-F., Chen, L., Pang, H., Kaskel, S., and Xu, Q. (2020). MOF-derived electrocatalysts for oxygen reduction, oxygen evolution and hydrogen evolution reactions. *Chem. Soc. Rev*. 49, 1414–1448. doi: 10.1039/C9CS00906J

Wang, J., Kong, H., Zhang, J., Hao, Y., Shao, Z., and Ciucci, F. (2020). Carbon-based electrocatalysts for sustainable energy applications. *Prog. Mater. Sci*. 100717. doi: 10.1016/j.pmatsci.2020.100717

Wang, K., Xi, D., Zhou, C., Shi, Z., Xia, H., Liu, G., et al. (2015). CoSe2 necklace-like nanowires supported by carbon fiber paper: a 3D integrated electrode for the hydrogen evolution reaction. *J. Mater. Chem. A* 3, 9415–9420. doi: 10.1039/C5TA01143D

Wang, L., Wu, X., Guo, S., Han, M., Zhou, Y., Sun, Y., et al. (2017). Mesoporous nitrogen, sulfur co-doped carbon dots/CoS hybrid as an efficient electrocatalyst for hydrogen evolution. *J. Mater. Chem. A* 5, 2717–2723. doi: 10.1039/C6TA09580A

Wang, Q., Fan, Y., Wang, K. K., Shen, H. M., Li, G. J., Fu, H. Y., et al. (2018). Hierarchical tubular structures composed of CoPx and carbon nanotubes: highly effective electrocatalyst for oxygen reduction. *Carbon* 130, 241–249. doi: 10.1016/j.carbon.2018.01.005

Wang, X., He, J., Yu, B., Sun, B., Yang, D., Zhang, X., et al. (2019). CoSe2 nanoparticles embedded MOF-derived Co-N-C nanoflake arrays as efficient and stable electrocatalyst for hydrogen evolution reaction. *Appl. Catal. B Environ*. 258:117996. doi: 10.1016/j.apcatb.2019.117996

Wang, X., Na, Z., Yin, D., Wang, C., Wu, Y., Huang, G., et al. (2018a). Phytic acid-assisted formation of hierarchical porous CoP/C nanoboxes for enhanced lithium storage and hydrogen generation. *ACS Nano* 12, 12238–12246. doi: 10.1021/acsnano.8b06039

Wang, X., Zheng, B., Yu, B., Wang, B., Hou, W., Zhang, W., et al. (2018b). *In situ* synthesis of hierarchical MoSe2–CoSe2 nanotubes as an efficient electrocatalyst for the hydrogen evolution reaction in both acidic and alkaline media. *J. Mater. Chem. A* 6, 7842–7850. doi: 10.1039/C8TA01552J

Wang, X., Zheng, Y., Sheng, W., Xu, Z. J., Jaroniec, M., and Qiao, S.-Z. (2020). Strategies for design of electrocatalysts for hydrogen evolution under alkaline conditions. *Mater. Today* 36, 125–138. doi: 10.1016/j.mattod.2019.12.003

Weng, B., Grice, C. R., Meng, W., Guan, L., Xu, F., Yu, Y., et al. (2018). Metal–organic framework-derived CoWP@C composite nanowire electrocatalyst for efficient water splitting. *ACS Energy Lett*. 3, 1434–1442. doi: 10.1021/acsenergylett.8b00584

Wu, C., Yang, Y., Dong, D., Zhang, Y., and Li, J. (2017a). *In situ* coupling of CoP polyhedrons and carbon nanotubes as highly efficient hydrogen evolution reaction electrocatalyst. *Small* 13:1602873. doi: 10.1002/smll.201602873

Wu, C., Zhang, Y., Dong, D., Xie, H., and Li, J. (2017b). Co9S8 nanoparticles anchored on nitrogen and sulfur dual-doped carbon nanosheets as highly efficient bifunctional electrocatalyst for oxygen evolution and reduction reactions. *Nanoscale* 9, 12432–12440. doi: 10.1039/C7NR03950F

Wu, R., Wang, D. P., Rui, X., Liu, B., Zhou, K., Law, A. W. K., et al. (2015). *In-situ* formation of hollow hybrids composed of cobalt sulfides embedded within porous carbon polyhedra/carbon nanotubes for high-performance lithium-ion batteries. *Adv. Mater*. 27, 3038–3044. doi: 10.1002/adma.201500783

Xiang, K., Wu, D., Deng, X., Li, M., Chen, S., Hao, P., et al. (2020). Boosting H2 generation coupled with selective oxidation of methanol into value-added chemical over cobalt hydroxide@hydroxysulfide nanosheets electrocatalysts. *Adv. Funct. Mater*. 30:1909610. doi: 10.1002/adfm.201909610

Xiu, L., Pei, W., Zhou, S., Wang, Z., Yang, P., Zhao, J., et al. (2020). Multilevel hollow MXene tailored low-Pt catalyst for efficient hydrogen evolution in full-pH range and seawater. *Adv. Funct. Mater*. 1910028. doi: 10.1002/adfm.201910028

Xu, H., Shi, Z.-X., Tong, Y.-X., and Li, G.-R. (2018). Porous microrod arrays constructed by carbon-confined NiCo@NiCoO2 Core@shell nanoparticles as efficient electrocatalysts for oxygen evolution. *Adv. Mater*. 30:1705442. doi: 10.1002/adma.201705442

Xu, H., Wu, J., Luo, W., Li, Q., Zhang, W., and Yang, J. (2020). Dendritic cell-inspired designed architectures toward highly efficient electrocatalysts for nitrate reduction reaction. *Small* 16:2001775. doi: 10.1002/smll.202001775

Xue, Z.-H., Su, H., Yu, Q.-Y., Zhang, B., Wang, H.-H., Li, X.-H., et al. (2017). Janus Co/CoP nanoparticles as efficient mott-schottky electrocatalysts for overall water splitting in wide pH range. *Adv Energy Mater*. 7:1602355. doi: 10.1002/aenm.201602355

Yang, F., Chen, Y., Cheng, G., Chen, S., and Luo, W. (2017). Ultrathin nitrogen-doped carbon coated with CoP for efficient hydrogen evolution. *ACS Catal*. 7, 3824–3831. doi: 10.1021/acscatal.7b00587

Yang, Y., Lun, Z., Xia, G., Zheng, F., He, M., and Chen, Q. (2015). Non-precious alloy encapsulated in nitrogen-doped graphene layers derived from MOFs as an active and durable hydrogen evolution reaction catalyst. *Energy Environ. Sci*. 8, 3563–3571. doi: 10.1039/c5ee02460a

Yi, J., Zhu, X., Zhou, M., Zhang, S., Li, L., Song, Y., et al. (2020). Crystal phase dependent solar driven hydrogen evolution catalysis over cobalt diselenide. *Chem. Eng. J*. 396:125244. doi: 10.1016/j.cej.2020.125244

Yilmaz, G., Tan, C. F., Hong, M., and Ho, G. W. (2018). Functional defective metal-organic coordinated network of mesostructured nanoframes for enhanced electrocatalysis. *Adv. Funct. Mater*. 28:1704177. doi: 10.1002/adfm.201704177

Yilmaz, G., Yam, K. M., Zhang, C., Fan, H. J., and Ho, G. W. (2017). *In situ* transformation of MOFs into layered double hydroxide embedded metal sulfides for improved electrocatalytic and supercapacitive performance. *Adv. Mater*. 29:1606814. doi: 10.1002/adma.201606814

Yu, H., Li, J., Gao, G., Zhu, G., Wang, X., Lu, T., et al. (2020). Metal-organic frameworks derived carbon-incorporated cobalt/dicobalt phosphide microspheres as Mott–Schottky electrocatalyst for efficient and stable hydrogen evolution reaction in wide-pH environment. *J. Colloid Interface Sci*. 565, 513–522. doi: 10.1016/j.jcis.2020.01.059

Yu, Y., Zhou, J., and Sun, Z. (2020). Novel 2D Transition-metal carbides: ultrahigh performance electrocatalysts for overall water splitting and oxygen reduction. *Adv. Funct. Mater*. 2000570. doi: 10.1002/adfm.202000570

Yu, Z., Bai, Y., Zhang, S., Liu, Y., Zhang, N., and Sun, K. (2018). Metal–organic framework-derived Zn0.975Co0.025S/CoS2 embedded in N,S-codoped carbon nanotube/nanopolyhedra as an efficient electrocatalyst for overall water splitting. *J. Mater. Chem. A* 6, 10441–10446. doi: 10.1039/C8TA01370E

Zhang, F., Zhu, G., Wang, K., Qian, X., Zhao, Y., Luo, W., et al. (2019). Boosting the initial coulombic efficiency in silicon anodes through interfacial incorporation of metal nanocrystals. *J. Mater. Chem. A* 7, 17426–17434. doi: 10.1039/C9TA05340A

Zhang, H. X., Liu, M., Bu, X., and Zhang, J. (2014). Zeolitic BIF crystal directly producing noble-metal nanoparticles in its pores for catalysis. *Sci. Rep*. 4:3923. doi: 10.1038/srep03923

Zhang, H. X., Liu, M., Wen, T., and Zhang, J. (2016a). Synthetic design of functional boron imidazolate frameworks. *Coord. Chem. Rev*. 307, 255–266. doi: 10.1016/j.ccr.2015.08.003

Zhang, H. X., Liu, M., Xu, G., Liu, L., and Zhang, J. (2016b). Selectivity of CO_2 via pore space partition in zeolitic boron imidazolate frameworks. *Chem. Commun.* 52, 3552–3555. doi: 10.1039/c6cc00185h

Zhang, J., Wu, T., Zhou, C., Chen, S., Feng, P., and Bu, X. (2009). Zeolitic boron imidazolate frameworks. *Angew. Chem. Int. Ed. Engl.* 48, 2542–2545. doi: 10.1002/anie.200804169

Zhang, K., Park, M., Zhang, J., Lee, G.-H., Shin, J., and Kang, Y.-M. (2017). Cobalt phosphide nanoparticles embedded in nitrogen-doped carbon nanosheets: promising anode material with high rate capability and long cycle life for sodium-ion batteries. *Nano Res.* 10, 4337–4350. doi: 10.1007/s12274-017-1649-5

Zhang, L., Wang, X., Li, A., Zheng, X., Peng, L., Huang, J., et al. (2019). Rational construction of macroporous CoFeP triangular plate arrays from bimetal–organic frameworks as high-performance overall water-splitting catalysts. *J. Mater. Chem. A* 7, 17529–17535. doi: 10.1039/C9TA05282H

Zhang, L., Xiao, J., Wang, H., and Shao, M. (2017). Carbon-based electrocatalysts for hydrogen and oxygen evolution reactions. *ACS Catal.* 7, 7855–7865. doi: 10.1021/acscatal.7b02718

Zhang, X., Liu, S., Zang, Y., Liu, R., Liu, G., Wang, G., et al. (2016). Co/Co9S8@S,N-doped porous graphene sheets derived from S, N dual organic ligands assembled Co-MOFs as superior electrocatalysts for full water splitting in alkaline media. *Nano Energy* 30, 93–102. doi: 10.1016/j.nanoen.2016.09.040

Zhang, Y., Gao, L., Hensen, E. J. M., and Hofmann, J. P. (2018). Evaluating the stability of Co2P electrocatalysts in the hydrogen evolution reaction for both acidic and alkaline electrolytes. *ACS Energy Lett.* 3, 1360–1365. doi: 10.1021/acsenergylett.8b00514

Zhang, Z., Deng, L., Zhao, Z., Zhao, Y., Yang, J., Jiang, J., et al. (2020). Nickel nanograins anchored on a carbon framework for an efficient hydrogen evolution electrocatalyst and a flexible electrode. *J. Mater. Chem. A* 8, 3499–3508. doi: 10.1039/C9TA13632K

Zhang, Z., Hao, J., Yang, W., and Tang, J. (2015). Defect-Rich CoP/nitrogen-doped carbon composites derived from a metal–organic framework: high-performance electrocatalysts for the hydrogen evolution reaction. *Chem. Cat. Chem.* 7, 1920–1925. doi: 10.1002/cctc.201500398

Zheng, Y., Jiao, Y., Li, L. H., Xing, T., Chen, Y., Jaroniec, M., et al. (2014). Toward design of synergistically active carbon-based catalysts for electrocatalytic hydrogen evolution. *ACS Nano* 8, 5290–5296. doi: 10.1021/nn501434a

Zhou, D., He, L., Zhu, W., Hou, X., Wang, K., Du, G., et al. (2016). Interconnected urchin-like cobalt phosphide microspheres film for highly efficient electrochemical hydrogen evolution in both acidic and basic media. *J. Mater. Chem. A* 4, 10114–10117. doi: 10.1039/c6ta03628g

Zhou, F., Sa, R., Zhang, X., Zhang, S., Wen, Z., and Wang, R. (2020). Robust ruthenium diphosphide nanoparticles for pH-universal hydrogen evolution reaction with platinum-like activity. *Appl. Catal. B* 274:119092. doi: 10.1016/j.apcatb.2020.119092

Zhou, W., Lu, J., Zhou, K., Yang, L., Ke, Y., Tang, Z., et al. (2016). CoSe2 nanoparticles embedded defective carbon nanotubes derived from MOFs as efficient electrocatalyst for hydrogen evolution reaction. *Nano Energy* 28, 143–150. doi: 10.1016/j.nanoen.2016.08.040

Zhu, G., Guo, R., Luo, W., Liu, H. K., Jiang, W., Dou, S. X., et al. (2020). Boron doping-induced interconnected assembly approach for mesoporous silicon oxycarbide architecture. *Natl. Sci. Rev.* nwaa152. doi: 10.1093/nsr/nwaa152

Conflict of Interest: The authors declare that the research was conducted in the absence of any commercial or financial relationships that could be construed as a potential conflict of interest.

Copyright © 2020 Han, Li, Ma and Yang. This is an open-access article distributed under the terms of the Creative Commons Attribution License (CC BY). The use, distribution or reproduction in other forums is permitted, provided the original author(s) and the copyright owner(s) are credited and that the original publication in this journal is cited, in accordance with accepted academic practice. No use, distribution or reproduction is permitted which does not comply with these terms.

frontiers in Chemistry

REVIEW
published: 20 November 2020
doi: 10.3389/fchem.2020.577327

Leverage Surface Chemistry for High-Performance Triboelectric Nanogenerators

*Jing Xu, Yongjiu Zou, Ardo Nashalian and Jun Chen**

Department of Bioengineering, University of California, Los Angeles, Los Angeles, CA, United States

Triboelectric Nanogenerators (TENGs) are a highly efficient approach for mechanical-to-electrical energy conversion based on the coupling effects of contact electrification and electrostatic induction. TENGs have been intensively applied as both sustainable power sources and self-powered active sensors with a collection of compelling features, including lightweight, low cost, flexible structures, extensive material selections, and high performances at low operating frequencies. The output performance of TENGs is largely determined by the surface triboelectric charges density. Thus, manipulating the surface chemical properties via appropriate modification methods is one of the most fundamental strategies to improve the output performances of TENGs. This article systematically reviews the recently reported chemical modification methods for building up high-performance TENGs from four aspects: functional groups modification, ion implantation and decoration, dielectric property engineering, and functional sublayers insertion. This review will highlight the contribution of surface chemistry to the field of triboelectric nanogenerators by assessing the problems that are in desperate need of solving and discussing the field's future directions.

Keywords: surface chemistry, surface engineering, triboelectric nanogenerator, wearable electronics, Internet of Things

OPEN ACCESS

Edited by:
Jianping Yang,
Donghua University, China

Reviewed by:
Weiqing Yang,
Southwest Jiaotong University, China
Tao Huang,
Donghua University, China

Correspondence:
Jun Chen
jun.chen@ucla.edu

Specialty section:
This article was submitted to Nanoscience, a section of the journal Frontiers in Chemistry

Received: *30 June 2020*
Accepted: *15 September 2020*
Published: *20 November 2020*

Citation:
Xu J, Zou Y, Nashalian A and Chen J (2020) Leverage Surface Chemistry for High-Performance Triboelectric Nanogenerators. Front. Chem. 8:577327. doi: 10.3389/fchem.2020.577327

INTRODUCTION

The rapid development of wearable and portable electronic devices is greatly revolutionizing our conventional means of energy generation and consumption (Gubbi et al., 2013; Lee and Lee, 2015; Zhou et al., 2020a; Zou et al., 2020). Miniaturized energy sources with high portability and sustainability are eagerly desired for powering billions of distributed devices in the era of the Internet of Things (Bai et al., 2014; Yang et al., 2015; Lin et al., 2017; Xu et al., 2017; Bedi et al., 2018; Wang, 2019). In the modern world, portable energy storage units, such as batteries, seem like the intuitive and most widely used solution to meet the power consumption needs of electronic devices (Grey and Tarascon, 2017; Gu et al., 2017; Liu W. et al., 2017; He et al., 2018; Zan et al., 2020). However, their limited lifetime (Ponrouch et al., 2016; Placke et al., 2017; Liu K. et al., 2018; Wan et al., 2019; Xu et al., 2019), rigid structure, toxic chemical components, and unsustainable working mode, which includes periodically recharging or even replacing the battery unit, deems portable energy storage units obsolete for wide-range adoption to mobile electronics, and more specifically wearable devices (Wang, 2013; Zang et al., 2015; Gao et al., 2016; Kenry and Lim, 2016; Trung and Lee, 2016; Liu Y. et al., 2017; Seneviratne et al., 2017; Gür, 2018; Kim et al., 2019; Yan et al., 2020; Zhang et al., 2020) and bio-integrated applications (Kang et al., 2013; Slater et al., 2013; Li and Dai, 2014; Yabuuchi et al., 2014; Fu et al., 2017; Zhang et al., 2017; Lin et al., 2018; Yan et al., 2018; Meng et al., 2019; Zhou et al., 2020b). Converting the accessible, renewable energy from the human body

and its surroundings into electricity is considered a great alternative solution (Wang Z. L. et al., 2015; Chen et al., 2020; Su et al., 2020). Electricity generation from biomechanical motions (Qin et al., 2008; Sun et al., 2011; Lee et al., 2012; Yang W. et al., 2013; Yi et al., 2015; Chen and Wang, 2017; Zhao et al., 2019), acoustic waves (Wang et al., 2007; Cha et al., 2010; Yang J. et al., 2014a), solar irradiance (Stephen, 2006; Zheng et al., 2015; Chen et al., 2016b; Dagdeviren et al., 2017), body heat (Niu et al., 2009; Yang et al., 2013b; Zi et al., 2015a; Wang et al., 2019), and biofuels (Zou et al., 2016), are just some examples of the conversion of energy from and around the human body. In 2012, the triboelectric nanogenerator (TENG) was invented as a highly efficient energy harvesting technology from human biomechanical motions (Bai et al., 2013a; Chen et al., 2013; Hou et al., 2013; Zhu et al., 2013a, 2014b; Yang J. et al., 2014b; Cheng et al., 2015b; Jeong et al., 2015; Chen, 2016; Jin et al., 2016; Wang Z. L. et al., 2016). Compared to other energy harvesting approaches, TENG has several advantages: light weight, low cost, flexible structures, extensive material selection, and great efficiency at low operating frequencies, all of which make TENGs one of the mainstream power supplies for self-powered devices (Jing et al., 2014; Yang W. et al., 2014a,b; Kuang et al., 2015; Lin et al., 2016; Liu R. et al., 2018; Chu et al., 2020; Pu et al., 2020a). TENGs is feasible for driving various electronic devices, ranging from light-emitting diodes (LEDs) (Yang et al., 2013d; Lin et al., 2014; Chun et al., 2015; Kanik et al., 2015; Mao et al., 2015; Wu et al., 2016) to cell phones (Wang et al., 2012; Zhu et al., 2014c) and from a large number of bio-sensors (Fan et al., 2015; Wen et al., 2015; Cai et al., 2018; Su et al., 2018, 2020a,b; Davoodi et al., 2020; Meng et al., 2020) to pacemakers (Zheng Q. et al., 2014). This shows showing their remarkable compatibility with a wide range of application in different settings, displaying that plentiful possibilities are remaining to be further explored (Wang, 2014; Hinchet et al., 2015; Wang S. et al., 2015; Zhang et al., 2015; Zhu et al., 2015; Zhang B. et al., 2016; Pu et al., 2020b).

Note that the triboelectric effect is a well-known phenomenon, in which two surfaces, having different triboelectric properties, become electrically charged during physical contact (Mizes et al., 1990; Liu and Bard, 2009). The principle of TENG is based on the coupling effect of contact electrification and electrostatic induction (Yang et al., 2013c; Su et al., 2014b; Wu et al., 2015; Li Z. et al., 2016; Zhang L. et al., 2016). The static polarized charges, resulting from the contact between the two friction surfaces with different charge affinities, are generated on the friction surfaces and cause different surface potentials, thereby bringing about inductive charges among the two attached electrodes (Su et al., 2014a; Zhu et al., 2014a; Chen et al., 2015a,b). Then the inductive electrons are driven to flow between two electrodes via an external circuit to fulfill the conversion process from mechanical energy to electricity (Niu et al., 2013a,b, 2014a; Chen et al., 2015c; Niu and Wang, 2015; Zi et al., 2015b). The output performance of TENGs is determined by the triboelectric charge density on the triboelectric material surfaces (Dharmasena et al., 2018). Thus, increasing the triboelectric charge density is the most fundamental strategy for building high-performance TENGs. Considerable efforts have been made to increase the triboelectric charge density of TENGs, including proper triboelectric materials selection (Zenkiewicz et al., 2015; Zhao et al., 2015; Kim et al., 2017; Lee et al., 2018), advanced device structural design (Bai et al., 2013b; Lin L. et al., 2013; Wang et al., 2013; Yang et al., 2013a; Zhang H. et al., 2014; Deng et al., 2020), and triboelectric materials surface physical/chemical modifications (Lin et al., 2009; Lin Z. H. et al., 2013; Niu et al., 2014b; Jing and Kar-Narayan, 2018; Zhou Y. et al., 2020). The surface physical modification is primarily realized via material morphological manipulation. Namely, increasing the effective friction area through incorporating surface micro-/nano-structures (Jeong et al., 2014; Kim et al., 2015; Feng et al., 2016; Wang et al., 2017), such as nanowires (Zheng et al., 2014; Lin et al., 2015), nanoparticles (Zhu et al., 2013b) and other nanoscale patterns (Zhang et al., 2013; Lee et al., 2014; Choi et al., 2015; Dudem et al., 2015). Furthermore, manipulating the surface chemistry of the friction layers through chemical modifications and consequent changes in surface potentials will enlarge the polarity between the two friction surfaces therefore contributing to the high-performance of TENGs (Wang S. et al., 2016).

This review systematically reports the current advances in surface chemistry for high-performance TENGs. As shown in **Figure 1**, the chemical modification methods can be summarized and classified into four categories: functional groups grafting, ion implantation and decoration, dielectric property engineering, and functional sublayers insertion. In addition, this review provides a critical analysis of surface chemistry for TENG and insights into remaining challenges and future directions. With worldwide efforts in innovations in chemistry and materials elaborated in this review, the frontiers of high-performance TENGs will be pushed forward, which could offer the era of Internet of Things a compelling pervasive energy solution.

FUNCTIONAL GROUPS GRAFTING

Functional groups grafting is a straightforward and efficient method to fabricate high-performance TENG with finely tunable triboelectric properties. By simply introducing electron-accepting and electron-donating groups onto triboelectric material surfaces, functional group grafting outperforms complicated bulk engineering. It indicates that TENGs can be built with a wider range of polymeric surfaces even if they are originally inefficient for triboelectric energy harvesting. This indication unlocks the limitations of triboelectric materials choice for designing high-performance TENGs. In principle, surface functional groups grafting is achieved by chemically grafting target element-containing groups, such as $-CF_3$ and $-NH_2$ groups, generally through either solution reactions or vapor treatments. By introducing functional groups with high tendency to gain or loss electrons onto the triboelectric surfaces, the negative or positive potential of the surface will be increased and manipulated. This manipulation contributes to a greater transfer charge density during the cyclic contact-and-separate movement between two triboelectric materials and therefore improves the output performance of TENGs. Moreover, applying some surface treatments for functional groups grafting such as the plasma process, can chemically and morphologically modify

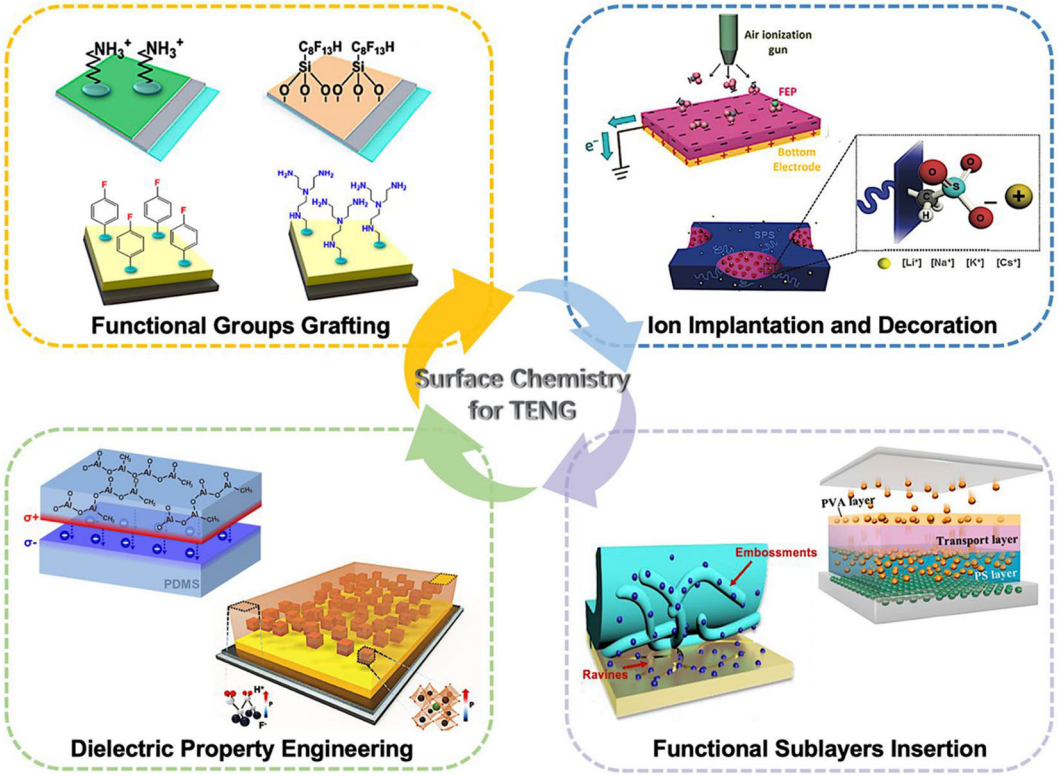

FIGURE 1 | Surface chemistry for high-performance triboelectric nanogenerators. Reprinted with permission from Shin et al. (2017). Copyright 2017 American Chemical Society. Reprinted with permission from Shin and Kwon (2015). Copyright 2015 American Chemical Society. Reprinted with permission from Wang et al. (2014). Copyright 2014 Wiley-VCH. Reprinted with permission from Park et al. (2017). Copyright 2017 WILEY-VCH. Reprinted with permission from Yu et al. (2015). Copyright 2015 Wiley-VCH. Reprinted with permission from Seung et al. (2017). Copyright 2017 Wiley-VCH. Reprinted with permission from Lai et al. (2018). Copyright 2018 American Chemical Society. Reprinted with permission from Cui et al. (2018). Copyright 2018 American Chemical Society.

surfaces simultaneously (Zhang X. et al., 2014; Cheng et al., 2015a; Li et al., 2015), which can further improve the output performance of TENGs. In this section, methods concerning functional groups grafting on the triboelectric material surfaces are introduced, including their enhancement mechanism toward TENG performance.

Self-Assembled Monolayer

The self-assembled monolayer (SAM) method, wherein the chemical adsorption of an active surfactant on a solid surface is used to realize well-ordered molecular assembly can be easily performed and widely used on various kinds of surfaces (Ulman, 1996; Song et al., 2015). Using the SAM method in surface functionalization of TENGs, the target functional groups can be anchored onto the material surfaces through forming strong chemical bonds, effectively altering the surface potential of contact materials. Unlike simply functionalized surface via one-step solution reactions or vapor treatments (Yao et al., 2017), this method is effective not only on noble-metal substrates but also on insulating substrates, such as SiO_2 and Kapton. Moreover, the uniform and well-ordered SAMs in nanoscale effectively controlled surface defects and reduced the adsorption of additional adsorbates in the air (Rimola et al., 2013). In this way, the SAM method can extensively expand the scope of triboelectric material choices and enhance the performance of TENGs.

Byun et al. systematically modulated the triboelectric polarities of SiO_2 layers by functionalizing the surfaces with various electron-donating functional groups, including $-NH_2$, –SH, a neutral group $-CH_3$, and an electron-accepting functional group, $-CF_3$ (Byun et al., 2016) **Figure 2A** shows a schematic diagram depicting the triboelectrification of these various SAM-modified SiO_2 layers. The modification process started with treating the substrates, a wafer with a 100 nm-thick SiO_2 layer, by ultraviolet/ ozone plasma for 10 min to prepare for functional group anchoring. After that, in the lone case of $-NH_2$, the substrate was immersed in a 1% (v/v) (3-aminopropyl) triethoxysilane (APTES)/ethanol solution for 1 h. The other three functional groups, –SH, $-CH_3$, and $-CF_3$, were all formed by the chemical vapor deposition method (Hozumi et al., 1999; Hayashi et al., 2002). During these processes, target functional groups were anchored on the surface of triboelectric materials, which altered the conventional triboelectric series of original substrates, leading to a higher tendency of triboelectric surfaces to lose or gain electrons. **Figures 2B,C** show energy band diagrams of surface modified with an electron-donating and an electron-accepting functional groups. Among these functional groups, the negative and positive surface dipoles introduced by the

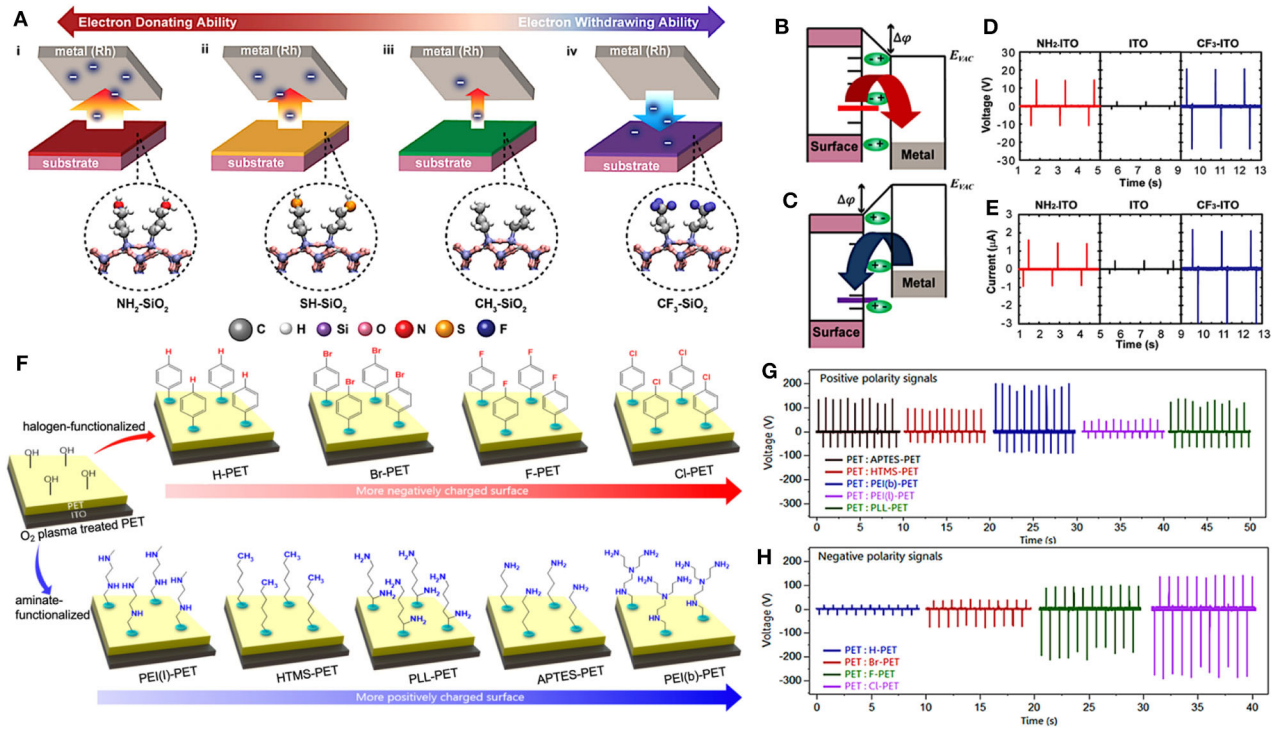

FIGURE 2 | Schematic representations of SAM-modified triboelectric materials and their output performance before and after functionalization. **(A)** Schematic diagram showing the propensity of the triboelectrification on (i) a strongly electron-donating layer (–NH_2), (ii) a moderate electron-donating layer (–SH), (iii) a neutral layer (–CH_3), and (iv) an electron-accepting layer (–CF_3). **(B)** Energy band diagrams of substrates modified with an electron-donating layer and **(C)** with an electron-accepting layer and that of the metal. **(D)** Open-circuit voltage and **(E)** short-circuit current of the triboelectric device composed of PI and SAM-modified ITO. Reprinted with permission from Byun et al. (2016). Copyright 2016 American Chemical Society. **(F)** Schematic illustrations of surface functionalized polyethylene terephthalate (PET) substrates with various halogen-containing and aminated molecules. **(G)** Output voltage generated by cyclic contacts between bare PET:aminated-PET pairs and **(H)** bare PET:halogenated-PET pairs. Reprinted with permission from Shin et al. (2017). Copyright 2017 American Chemical Society.

strong electron-donating –NH_2 groups and electron-accepting –CF_3 groups can significantly decrease or increase the surface potential. The relative position of the as-functionalized surfaces and the counter materials in energy level affects the direction of electrons flow. It reveals that by modulating the surfaces with various electron-donating and -withdrawing functional groups, the polarity and the amount of triboelectric charge on the material surfaces can be well-controlled. In principle, TENG with as-SAMs-modified surfaces should deliver significant electric output considering the enlarged difference of friction surfaces potential. **Figures 2D,E** compare the open-circuit voltage and the short-circuit current of TENGs consisting of the SAMs-modified indium tin oxide (ITO) and polyimide (PI). With SAMs-modified surfaces: NH_2-ITO and CF_3-ITO, the output performance of as-fabricated TENGs have remarkable enlargement in both V_{oc} and I_{sc}, compared to that of using a bare ITO surface.

Similar SAMs functionalization was applied to conventional TENG materials, such as polyethylene terephthalate (PET) substrates through a series of halogens and amines. Shin et al. obtained a wide spectrum of tunable triboelectric polarity through chemical surface functionalization with the halogen-containing molecules and the aminated molecules (Shin et al., 2017). Before anchoring functional groups to the PET surfaces, the PET substrates were first treated by oxygen plasma to form hydroxyl groups (–OH) on the surfaces, as shown in **Figure 2F**. Here, the –OH groups played a crucial role as strong chemical bonds between the surfaces of PET substrates and the target functional molecules. The surface was then functionalized with electron-accepting elements, halogens (Br, F, and Cl)-terminated phenyl derivatives and several aminated molecules to induce triboelectrically negative or positive property on PET substrates. **Figures 2G,H** show the output voltages of TENGs with bare PET:aminated-PET contact pairs and bare PET:halogenated-PET contact pairs, respectively. The result shows a significant variation in the output performance. The TENGs with the aminated-PET surfaces generated strong positive polarity signals, while negative polarity signals were generated from the TENGs with halogenated-surfaces in contrast. Among them, the PEI(b)-PET:PET and Cl-PET:PET contact pairs generated the maximum output voltage, exceeding 300 and 200 V, respectively.

For high-performance TENGs designation, SAM method, cooperating with other efficient surface functionalization approaches, is applied flexibly to modulate the triboelectric polarities of both triboelectric materials. Shin et al. engineered the surfaces of triboelectric materials with a negatively charged –CF_3 group via self-assembling deposition and with positively

charged $-NH_3$ group through dip-coating (Shin and Kwon, 2015). **Figures 3A,B** display the surface modification process, where firstly PET substrates were treated by oxygen plasma for 100 s to form reactive –OH groups strongly binding on their surfaces. Subsequently, one plasma-treated PET film was dipped in the poly-l-lysine (PLL) solution for 5 min, while the other side was exposed in trichloro(1H,1H,2H,2H-perfluorooctyl) silane FOTS vapor environment at 95°C for 1 h. During this processing step, target molecules (PLL and FOTS) are anchored onto the surfaces of PETs through covalent bonding with –OH groups. Consequently, the PPL-coated PET (P-PET) surface is positively charged by $-NH_3$ groups and the self-assembling chemical vapor treated PET (F-PET) surface is negatively charged by $-CF_3$ groups. **Figure 3C** displays the schematic of TENGs fabricated with various triboelectric material pairs: (i) bare PET:bare PET, (ii) bare PET:P-PET, (iii) bare PET:F-PET, (iv) P-PET:F-PET. Furthermore, the comparisons of their open-circuit voltages are shown in **Figures 3D,E**. Among these TENGs, the generated output voltages increase from ∼4 V in the device with PET:PET contact pair to ∼330 V with P-PET:F-PET pair. Thus, the output performance of TENGs can be greatly enhanced by modulating both friction surfaces and corresponding triboelectric polarities, implying the outstanding effectiveness of these functional group modification methods. In addition, the surface of the functionalized PET demonstrates superior stability, which is attributed to its tight chemical bonds with surface functional groups.

Ultraviolet-Ozone Irradiation

In addition to the SAM method, Ultraviolet-ozone (UVO) irradiation is another facile method to enhance the triboelectric charge of triboelectric material surfaces via tailoring the chemical functional groups (Hoek et al., 2010; Fan et al., 2014). Unlike the SAM method, UVO irradiation creates desired functional groups by substituting the existing chemical elements and bonds on the surface with target elements and new bonds, instead of directly introducing new chemical functional groups onto the material surfaces. Yun et al. increased the triboelectric surface charge of polydimethylsiloxane (PDMS) via the UVO irradiation method. After that, by simply sprinkling NaOH or HCl solution onto the UVO-irradiated PDMS surfaces, the triboelectric surface charge was further changed significantly (Yun et al., 2015). As shown in **Figure 4A**, the fresh PDMS surface consists of mainly non-polar $Si-CH_3$ bonds (Cole et al., 2011). During UVO irradiation, the previous $Si-CH_3$ bonds are broken and converted to polar Si–O, Si–OH, and Si–COOH bonds, obtaining a mildly base and polar surface. Further NaOH treatment by simply sprinkling NaOH solution onto the UVO-treated PDMS surface results in an additional increase of the amount of Si–O bonds at the expense of $Si-CH_3$ bonds. When adopting the HCl treatment, on the other hand, the Si–O bonds are changed to Si–OH bonds (Lai et al., 2012). Due to a large amount of polar Si–O bonds on the UVO- and NaOH-treated PDMS surface, a greater triboelectric charge was generated, leading to higher output performance of as-treated PDMS based TENGs. As for the UVO- and HCl-treated PDMS surface, the result showed relatively little triboelectric charge and lower output performance of as-fabricated TENGs. **Figure 4B** compares the output performance of fresh and surface-treated PDMS-based TENGs. After surface treatment with NaOH for 2 h and UVO irradiation for 1 h, the open-circuit voltage and short-circuit current exhibited an almost 15-fold enhancement than those of fresh PDMS-based TENGs reaching 49.3 V and 1.2 μA, respectively. Note that, the output voltage and current of TENGs can be improved by simple UVO treatment for 1 h, shown in **Figure 4B** with red lines. However, when increasing the exposure time to 2 h, the output voltage and current showed no further enhancement, as shown with blue lines. An in-depth

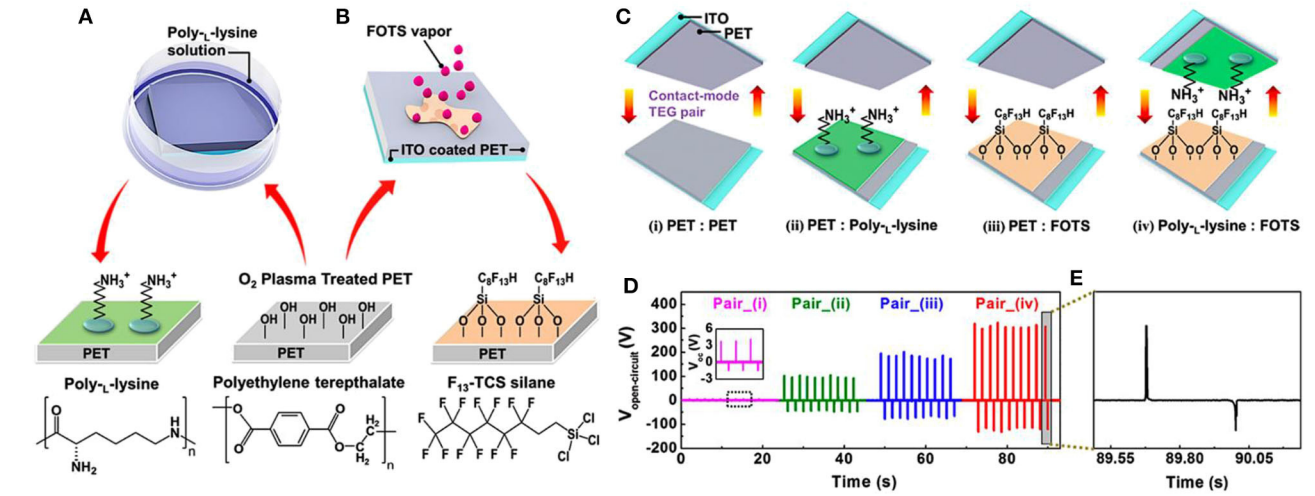

FIGURE 3 | Schematic illustration of modification processes and output performance of TENGs with functionalized-surfaces. **(A)** The surface modification process by dip-coating and **(B)** self-assembling deposition. **(C)** Schematic of TENGs fabricated with different contact pairs. **(D)** Open-circuit voltage of corresponding TENGs. **(E)** Local enlarged peaks of the open-circuit voltage. Reprinted with permission from Shin and Kwon (2015). Copyright 2015 American Chemical Society.

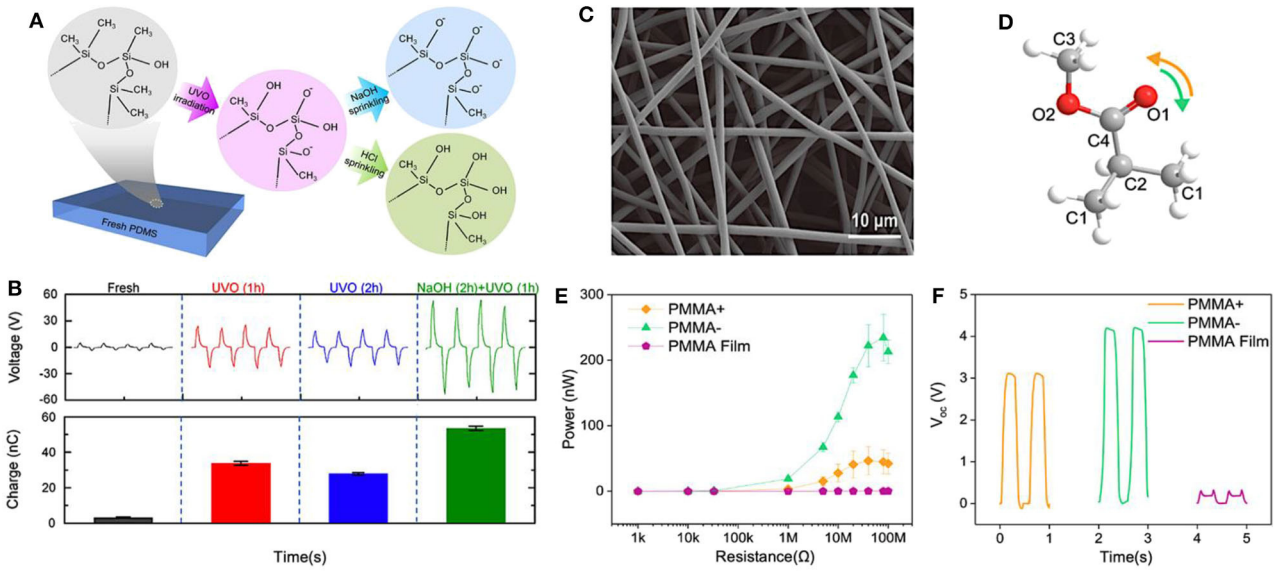

FIGURE 4 | Schematic diagrams and output performance of functionalized triboelectric materials surfaces via UVO irradiation or electrospinnig. **(A)** Schematic diagram about suggested mechanism of chemical elements and bonds of PDMS surface after UVO irradiation and NaOH treatment. **(B)** Comparison of the open-circuit voltage and induced triboelectric surface charge of surface-treated TENGs based on fresh PDMS, UVO-irradiated PDMS for 1 h [UVO (1 h)] and 2 h [UVO (2 h)], and NaOH-treated PDMS for 2 h after UVO irradiation for 1 h [NaOH (2 h)+UVO (1 h)]. Reprinted with permission from Yun et al. (2015). Copyright 2015 Elsevier. **(C)** SEM image of electrospun PMMA fibers. **(D)** Schematic structure of a single unit of PMMA polymer chain. **(E)** Output power and **(F)** open-circuit voltage of electrospun PMMA-based TENGs. Reprinted with permission from Busolo et al. (2018). Copyright 2018 Elsevier.

comparison of triboelectric surface charge induced from fresh and surface-treated PDMS-based TENGs is displayed too. The triboelectric charges of UVO (1 h) and NaOH (2 h)+UVO (1 h) treated PDMS were enhanced significantly, with ∼33.9 and 53.5 nC respectively, when compared to that of fresh PDMS with merely 3.17 nC. While increasing the UVO treatment time to 2 h, the surface-induced charge decreases. It implies that NaOH solution treatment after UVO irradiation is an easy-achieved and efficient method to enhance the output performance of TENGs, but controlling the UVO irradiation time is critical to optimize efficiency.

Electrospinning

The electrospinning technique is a one-step method to tailor the surface potential of triboelectric materials and consequently improve TENGs triboelectric output performance. Electrospinning is applied in the materials fabrication process; a high voltage is applied between the nozzle of a syringe filled with a polymer solution and the grounded substrate to produce solid fibers on the substrate. In this case, through applying a positive or negative voltage to the nozzle during the electrospinning process, charges of equivalent polarity are generated at the liquid jet–air interface, altering the surface chemical properties of materials (Stachewicz et al., 2012). Busolo et al. altered the surface chemistry of polymethylmethacrylate (PMMA) fibers via electrospinning and substantially improved triboelectric output performance of electrospun PMMA based TENGs (Busolo et al., 2018). The PMMA fibers altered by polarized charges were successfully fabricated as scanning electron microscopy (SEM) images shown in **Figure 4C**. Positive ($PMMA^+$) and negative ($PMMA^-$) charges were generated by applying a positive and negative voltage to the nozzle, respectively, to modify the surface chemistry. The changes in surface chemistry were analyzed by using X-ray photoelectron spectroscopy and the result data indicated that the variation of the surface potential properties between $PMMA^+$ and $PMMA^-$ fibers were directly related to the distinct contents of chemical bonds in the units of PMMA polymer chain, as shown in **Figure 4D**. In the case of positive voltage polarity applied during electrospinning, more oxygen-containing groups were present at the O1 and O2 regions, whereas, in the case of negative voltage polarity applied, the units contained more C–C chemical bonds. Thus, due to the high electronegativity of oxygen, $PMMA^+$ fibers exhibited a lower surface potential when compared to $PMMA^-$ fibers. The changes in surface potential were correlated with variations of charge transfer affinity and triboelectric performance. To investigate the output performance of as-fabricated TENGs, $PMMA^+$ and $PMMA^-$ fibers were deposited onto an aluminum foil by electrospinning. The modified aluminum foil served as one of the triboelectric material. Via periodically stimulating the contact-and-separate movement with the counter-electrode (copper substrate), the output power and voltage of $PMMA^+$ fiber, $PMMA^-$ fiber, and pure PMMA film are obtained and compared in **Figures 4E,F**. Contact pairs based on $PMMA^+$ and $PMMA^-$ fibers significantly outperformed PMMA film-based TENGs in both output power and open-circuit voltage. The $PMMA^-$ fibers produced a maximum power output of 234.4 nW at a load resistance of 80 MΩ and obtaining a

nearly 10-fold enhancement in voltage. These results indicated that the electrospinning technique can be adopted to effectively manipulate the surface potential of fibers by alternating the polarity of applied voltage in a simple manufacturing process; therefore, substantially improving the triboelectric output.

In conclusion, functional groups grafting is a straightforward, cost-efficient and easy-to-implement method to manipulate the surface chemical properties, by breaking and forming new chemical bonds on triboelectric materials' surfaces. New functional groups with strong electron-donating or electron-accepting ability are anchored onto the materials surface, giving rise to drastic performance enhancement of TENGs. However, since the functional groups grafting is just taken place on the surfaces rather than deep into the bulk of tribo-materials, the results may lose its effectiveness if the surface is polished or worn out during the friction.

ION IMPLANTATION AND DECORATION

Ion implantation and decoration, is the method that directly adds ions or single-polarity charged particles on or inside the triboelectric materials of interest. This can be an efficient way to increase the charge density of the triboelectric surfaces and thus enhance the output performance of TENGs. Such methods, including ion injection and irradiation, usually are achieved with the assistance of special instruments, such as, an air-ionization gun. Additionally, the modifications do not only take place on the material surfaces, but also affect both surface and bulk regions. This indicates that the results can be maintained for several months or even longer (Wang et al., 2014), implying that the as-fabricated high-performance TENGs will have better output stability.

Ion Injection

The ion injection technique, which is applicable to various triboelectric polymers, is an effective and the most commonly adopted way to introduce surface charges for enhancing TENGs' output performance. The ions with negative or positive polarities are generated and subsequently implanted onto the material surfaces by triggering the discharge of air in the air-ionization gun. Wang et al. adopted this method to create negative charges CO_3^-, NO_3^-, NO_2^-, O_3^-, and O_2^-, and injected them onto the fluorinated ethylene propylene (FEP) surface (Baytekin et al., 2011). In order to achieve the maximum surface charge density for high-performance TENG, the bottom electrode attached to the back of the FEP film was grounded, as shown in **Figure 5A**. In this way, the negative charges introduced by ion injection will drive equal quantities of electrons away from the bottom electron to the ground, leaving positive charges in the electrode. The grounded connection of the bottom electron will lead to a higher surface charge density when compared with the electrode-free FEP layer, because FEP has a much larger dielectric property than air. By repeating this procedure multiple times, the negative charge density on the material surface can be controlled to reach any desired level. The large amount of the negative or positive polarities charges distributed on the surface of the contact materials through the ion injection can lead to a strong driving force for the high-output voltage and current. In this work the results showed a five-fold enhancement of the surface charge density is obtained by the ion injection. **Figures 5B,C** compare the V_{oc} of TENGs fabricated with FEP films before and after ion injection, respectively. The FEP film is assembled with an Al layer, as a pair of triboelectric materials, to form a contact-mode TENG. Before injection, as-fabricated TENG can only produce a V_{oc} of ~200 V, because its surface charges are generated merely

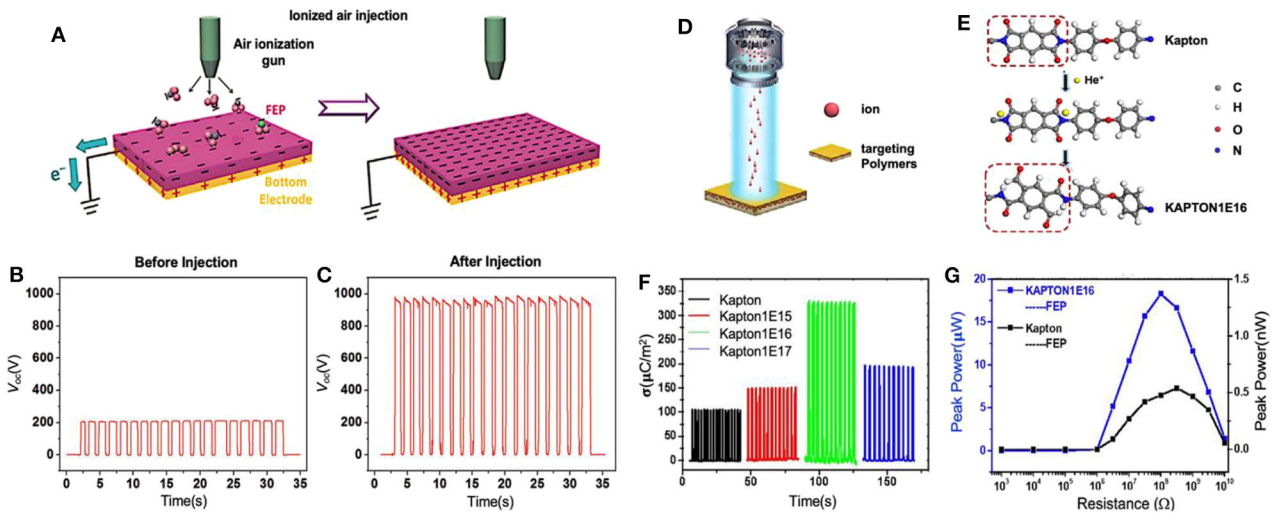

FIGURE 5 | Basic modification processes and output enhancement of triboelectric materials surfaces via ion injection and ion irradiation. **(A)** Schematic diagram of the ionized ion injection applying onto FEP surface with air ionization gun. **(B,C)** Open-circuit voltage of TENGs based on FEP films **(B)** before and **(C)** after the ion injection process. Reprinted with permission from Wang et al. (2014). Copyright 2014 Wiley-VCH. **(D)** Schematic diagram of ion irradiation simulation. **(E)** Schematic diagram of chemical structure changes of Kapton. **(F)** Transferred charge density and **(G)** output power of different ion concentration irradiated Kapton contracting with fluorinated ethylene propylene (FEP) films. Reprinted with permission from Li et al. (2020). Copyright 2019 Royal Society of Chemistry.

by the triboelectrification. After the injection, which introduced a large number of external charges onto the surface, the V_{oc} was enhanced to ∼1,000 V. Moreover, the output power of the modified-TENGs was elevated by 25 times, which was also proven to be stable over 5 months and 400,000 continuous operating cycles.

Ion Irradiation

Ion irradiation is a widely used method for many materials such as metals, superconductors and semiconductors, etc., owing to its controllable applied area, adjustable ion dose, and uniform treated results (Dong and Bell, 1999; Awasthi et al., 2010; Kumar et al., 2013; Kumar and Singh, 2015; Wang et al., 2015). Via low-energy ion irradiation, Li et al. proposed a novel surface modification process to effectively modulate the chemical structures of the target polymer, Kapton (Li et al., 2020). Unlike the Ion Injection method mentioned above, which can significantly improve the achievable maximum charge density on the tribo-materials surfaces by electrostatically inducing the same amount of electrons flowing from the bottom electrode to the ground, Ion Irradiation mainly changes the crystal structure of the target materials and consequently changes its surface properties via inducing the breaking and rearrangement of chemical bonds. **Figure 5D** shows a schematic diagram of ion irradiation simulation, where a low-energy ion beam of 50 keV He was used to irradiate the Kapton surface. Meanwhile, various ion irradiation concentrations are adopted on the polymer, changing from 1×10^{15} to 1×10^{17} ions/cm^2 (as-treated Kapton polymers were named Kapton1E15, Kapton1E16, and Kapton1E17, correspondingly). The collisions produced by ion irradiation cause macromolecules in the polymer to reach a chemical bond energy barrier and finally break. After that, the implanted ions combine onto polymer surfaces by forming new chemical bonds. Take the ion irradiation process of Kapton1E16 as an example, shown in **Figure 5E**. The original C-N bonds were broken and C-H and N-H bonds were formed instead after low-energy He ion implantation. In this way, the -NHCOR bond, which is a very strong electron donating group when conjugated with a benzene ring, was established on the surface of the polymer. This is circled out with the red dotted line in the Kapton1E16 molecular formula. As a result, Kapton film modified by ion irradiation shows higher surface charge density, excellent stability, and ultrahigh electron-donating capability. Therefore, this provides a good demonstration for manipulating the output performance of TENGs based on controllable chemical structure change. The transferred charge density of different ion concentration irradiated Kapton contracting with fluorinated ethylene propylene (FEP) films were shown in **Figure 5F**. Among these four samples, Kapton1E16 film achieved the maximum transferred charge density with 332 μC/m^2. Moreover, the output power of Kapton1E16 and pre-irradiated Kapton polymer are compared in **Figure 5G**, implying a significant enhancement in maximum peak power after ion irradiation treatment, from 0.5 nW to 18 μW. To further verify the stability of Kapton1E16, the as-fabricated TENG was tested for more than 60 days without output degradation, which proved that the chemical modification of Kapton film induced by ion irradiation is quite stable and effective.

Ion Absorption

Alkali Metal ions can also be used to modify the surface chemistry of some types of triboelectric materials by simple solution-processed alkali metal ion absorption. As shown in **Figure 6A**, Li et al. chose SAM-modified PDMS and the

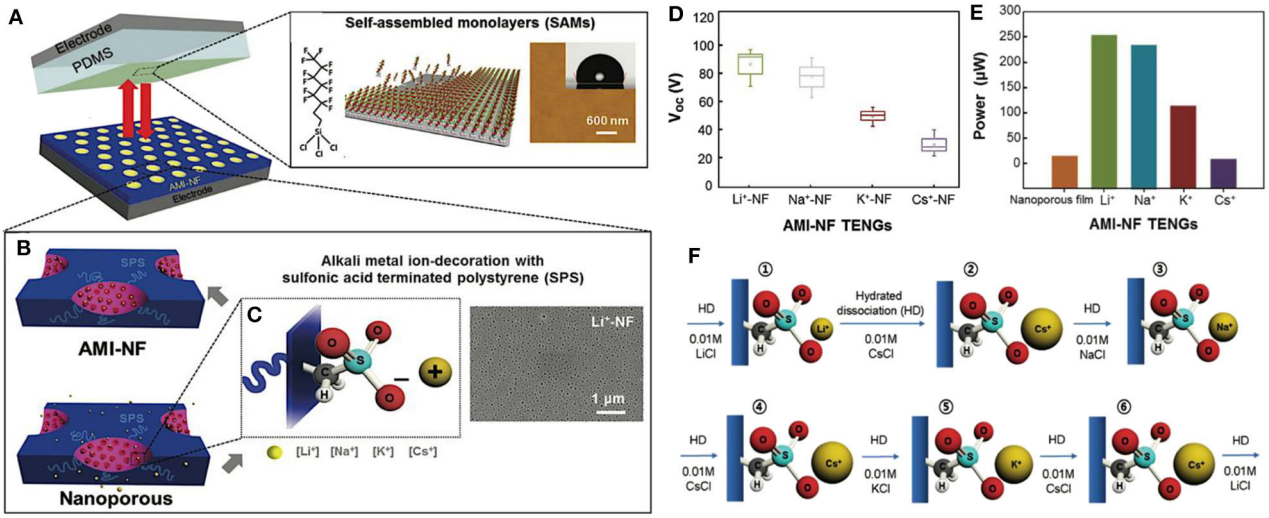

FIGURE 6 | Schematic diagrams and output performance of TENGs with ion-decorated triboelectric materials. **(A)** Schematic diagram of the structure of an AMI-NF TENG. **(B)** Schematic diagram of nanoporous structure on the surface of AMI-NF. **(C)** Partial enlarged schematics of alkali metal ion (Li^+, Na^+, K^+, and Cs^+) association with sulfonate (SO_3^-) functional groups on the surface of the nanopores. **(D)** Average V_{oc} and **(E)** averaged maximum power of AMI-NF with various alkali metal ions. **(F)** Schematics of sequential alkali metal ion exchange on a nanoporous surface: ① Li^+→ ② Cs^+→ ③ Na^+→ ④ Cs^+→ ⑤K^+→ ⑥ Cs^+→ ① Li^+. Reprinted with permission from Park et al. (2017). Copyright 2017 WILEY-VCH.

alkali-metal-ion-decorated nanoporous film (AMI-NF) as a pair of triboelectric materials for TENGs fabrication (Park et al., 2017). The modification process started from the preparation of the supramolecular-assembled nanoporous film, where 6:4 w/w blends of sulfonic-acid-terminated poly(styrene) (SPS) and poly(2-vinylpyridine) (P2VP) were used as a precursor. The subsequent removal of P2VP from the precursor, where the pyridine nitrogen atoms of P2VP had been ionically linked to the sulfonic acid groups of SPS by acid-base interaction, resulted in a nanoporous surface enriched with sulfonic acids (SO_3^- groups) that could be used for binding alkali metal ions, as shown in the diagram in **Figure 6B**. On the other side, PDMS film was modified via vapor deposition to form a layer of uniform FOTS on the surface. Following the procedures, we introduced before in the section of the SAM method, as-modified PDMS film obtains a fluorinated surface that has a strong tendency to attract electrons. Next, the ions chosen in the work to modify the nanoporous friction film were alkali metal ions, including Li^+, Na^+, K^+, and Cs^+. By simply immersing the nanoporous film into an aqueous solution containing these alkali metal ions, Li^+, Na^+, K^+, and Cs^+ ions can be absorbed into the nanopores of the materials and selectively bind with SO_3^- groups, as schematically shown in **Figure 6C**. Since the electrostatic field built by cation field can lead to the polarization effect of the sulfonate group (Kujawski et al., 1992; Salis and Ninham, 2014), the electron transfer ability from AMI-NF to PDMS increases upon the tribo-contact after metal ions decoration, allowing us to fabricate alkali-metal-ion-decorated TENGs with better output performance and mechanical properties. **Figures 6D,E** show the average open-circuit voltage and the maximum power of AMI-NFs modified with various alkali metal ions. The average V_{oc} values of AMI-NF TENGs with Li+, Na+, K+, and Cs+ ions were −90, −79, −49.2, and −27.4 V, respectively. For comparison, the output power of nanoporous film without alkali-metal-ions absorption was examined with AMI-NF TENGs, showing that the power generated from the bare nanoporous film was much poorer than that of the Li^+, Na^+, K^+-NF TENGs. The averaged maximum power of Li^+, Na^+, K^+-NF TENGs was 256.5, 238.4, 115.7, and 11.5 μW, respectively. The value of 256.5 μW in the case of Li + -NF is notably high and 20 times higher than that of the bare nanoporous film with a value of only 12.8 μW. The lowest output performance of bare nanoporous film attributes to the weakest polarization without alkali metal ions effect. Therefore, the friction film obtains the least effective electron transfer ability when in contact with the PDMS friction film, resulting in a TENG with the lowest output performance. Furthermore, in the stability test of as-modified TENGs, the device with a size of 2 × 3 cm was mechanically robust and could be operated without performance degradation under repetitive contacts (1.25 Hz, 5 N) for more than 50,000 cycles. The results suggest that chemical modification of the triboelectric material surface with alkali metal salts is crucial for high-performance TENGs with relatively long effective duration.

Interestingly, as-fabricated AMI-NF TENGs offers a convenient means to switch the triboelectric properties via a simple solution treatment, since alkali metal ions bound with SO_3^- groups on the nanoporous surface can be readily exchanged from one to another, as shown in **Figure 6F**. Each step (from ① to ⑥) shown in the diagram involves the hydrated dissociation (HD) of the alkali metal ions from the SO_3^- groups with AMI-Cl solution. In this way, a controllable V_{oc} and output power, ranging from −90 to −27.4 V and 11.5–256.5 μW, respectively, were obtained simply by a conventional ion exchange process in a reversible manner. Thereby, wide-range tuning of triboelectric output performance can be achieved.

In summary, the ion injection and decoration methods provide effective approaches for improving the TENG's output performance. Since modification took place upon both the surface and near-surface regions, the enhanced output performance can last stably at least for months and will not suffer from the polish of the surfaces. Thus, it is the most commonly adopted method of materials surface modification for improving TENGs' output performance by far. Nevertheless, the fabrication processes are relatively complicated and the instrument used during the process adds extra cost, which may bring obstacles for further scaling up.

DIELECTRIC PROPERTY ENGINEERING

Controlling the dielectric property of triboelectric materials can also effectively enhance the output performance of TENGs. The underlying mechanism of the dielectric property engineering shares similarities with the above-mentioned ion implantation and decoration methods. Both of them manipulate the output performance of TENGs by controlling the surface charge density of triboelectric materials or introducing extra charged ions or molecules. Compared to other chemical modification methods, the dielectric property engineering improves the triboelectric materials' binding force and holding capacity of electrons. This method achieves such characteristic enhancements by doping high dielectric nanomaterials into its bulk region. This bulk modification, which manipulates the chemical properties of the material itself instead of just modifying the outermost surface, will then be reflected on the changes in surfaces' charge density. Certainly, this approach also contributes to developing high-performance TENGs with good resistance to the surface wearing issue. Moreover, dielectric property modification is versatile in tailoring a broad range of triboelectric materials since a variety of metalorganic molecules possess high permittivity in most polymer chains (George, 2010; Jin et al., 2020). With proper selection of dopants and precise control of the dose, dielectric property modification could be a promising approach to improve the output performance of TENGs.

Sequential Infiltration Synthesis

Sequential infiltration synthesis (SIS) is a molecular infiltration process on the basis of the atomic layer deposition (ALD) technique (Wilson et al., 2005; Peng et al., 2011; Biswas et al., 2015). The method is applied in the process of polymer fabrication; the larger permittivity of metalorganic ALD precursors allows deep infiltration of inorganic compounds during the ALD process, leading to inorganic-and-organic hybrid materials (Ferguson et al., 2004; Gong et al., 2012a,b; Moghaddam et al., 2013; Padbury and Jur, 2014). Through

deep infiltration of some high dielectric inorganic molecules, such as AlO_x, the SIS technique was expected to be an effective means to tailor the dielectric and electrical properties of the polymer of interest and therefore provide a solution for modifying triboelectric materials in bulk volume. Based on the SIS technique, Yu et al. proposed an internal AlO_x doping method of several triboelectric polymers, including PDMS, Kapton and PMMA (Yu et al., 2015). AlO_x was selected as the dopant since trimethylaluminum (TMA, ALD precursor of Al_2O_3) has desirable permittivity in a number of polymers such as polystyrene (PS), polypropylene (PP), polyethylene (PE), and poly (vinyl chloride) (PVC) and PMMA (Seung et al., 2015). The modification results of the PDMS film serves as a good as simultaneous surface and bulk modification of the PDMS films' dielectric and electrical properties were achieved, the schematic diagram is shown in **Figure 7A**. The AlO_x-doped PDMS is capable of storing a greater volume of charges compared with the pristine one. Moreover, the surface potential of the AlO_x-doped PDMS film was changed due to the injection of electrons from AlO_x-doped PDMS film to pristine PDMS film upon their friction. This subsequently leads to a positively charged surface in the doped PDMS film and negatively charged surface in the pristine PDMS film. As we know, such a charge redistribution will not happen between two PDMS films without modification, due to their identical surface potential. Therefore, the AlO_x doping process via the SIS technique should be able to significantly raise the output performance of TENGs.

As a consequence of the modification, **Figures 7B,C** show the cross-sectional SEM images and corresponding energy dispersive spectroscopy (EDS) elemental mappings of the pristine PDMS film and the AlO_x-doped PDMS film after 5-cycle sequential TMA/H_2O infiltration, respectively. This elemental distribution analysis indicated the successful deep infiltration of molecules in the PDMS film rather than the surface coating of Al_2O_3 molecules. From these diagrams, AlO_x molecules were found to be capable of penetrating as deep as ~3 μm into PDMS film, since there was a high concentration of ions gathering within this region. This bulk modification attributed to the deep doping method, allows the enhanced performance of TENGs to survive even after polishing off 2 μm-thick polymer materials, leading to a longer duration of effective time. **Figure 7D** displays the dielectric constant of pristine PDMS film and AlOx-doped PDMS film. The dielectric constant of PDMS films increased from ~2.4 to ~2.7 after the SIS doping technique, implying

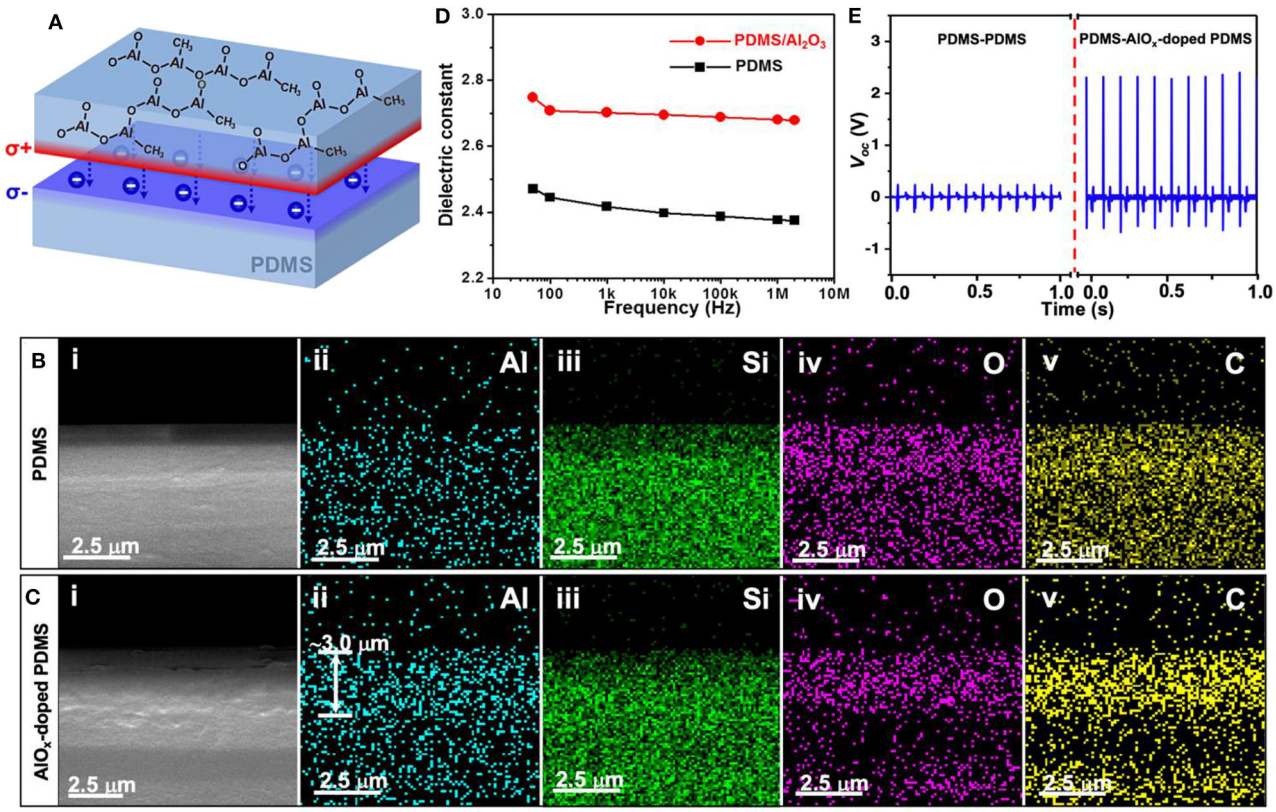

FIGURE 7 | SEM images of SIS-modified triboelectric materials and output performance of as-fabricated TENG. **(A)** Schematic diagram of triboelectrification induced charge redistribution between pristine PDMS and AlO_x-doped PDMS films upon contact. **(B,C)** Cross-sectional SEM images (i) and corresponding energy dispersive spectroscopy (EDS) mappings of a pristine PDMS film and an AlO_x-doped PDMS film for Al, Si, O, and C elements (ii–v). **(D)** Dielectric constant of pristine PDMS film and AlO_x-doped PDMS film. **(E)** V_{oc} of TENGs based on the PDMS with and without AlO_x doping. Reprinted with permission from Yu et al. (2015). Copyright 2015 Wiley-VCH.

that AlO_x-doped PDMS was capable of storing more charges than the pristine one. By controlling the types and doses of dopant and modified triboelectric materials, the SIS doping could also arbitrarily tune the charge attraction or repulsion ability of the polymer, therefore, successfully manipulating the output performance of TENGs, similar to previously discussed modification strategies. The average peak values of the V_{oc} of TENGs fabricated with the two pristine PDMS pair and AlO_x-doped PDMS: PDMS pairs are shown in **Figure 7E**. The value reached 2.3 V in the AlO_x-doped pair which were comparable to TENGs based on typical triboelectric pairs with distinct electron affinities, such as PDMS-ITO and Teflon-metal pairs (Fan et al., 2012), while the untreated PDMS pair generated only 0.3 V in the same testing condition.

High Dielectric Nanoparticles Doping

Nanoparticles with high permittivity are also doped inside the triboelectric materials to increase its dielectric constant, and therefore, to improve the output performance of the TENGs (Liu et al., 2017). Chen et al. filled the triboelectric materials, PDMS matrices, with high permittivity nanoparticles, such as SiO_2, TiO_2, $BaTiO_3$, and $SrTiO_3$ (Chen et al., 2016a), as shown in **Figure 8A**. The relative permittivity of these nanoparticles is demonstrated in **Figure 8B**. Among them, the TENGs doped with $SrTiO_3$ particles generated the highest output voltage due to its highest relative permittivity of 300. **Figure 8C** displays the open-circuit voltage of TENGs fabricated with different dielectric-nanoparticles-doped PDMS films. The voltage was greatly enhanced after doping and reached a peak value of 305 V generated from the composite PDMS film containing 10 vol % $SrTiO_3$ nanoparticles, while only 172 V can be obtained from the original PDMS. As a result, the peak voltage and current density for the TENG with composite PDMS film are 1.8 and 2.4 times as much as that of the original one.

In order to modulate the permittivity, a porous structure was formed inside the PDMS film by the process of simply and feasibly mixing and removing NaCl particles, as displayed in **Figure 8D**. When the TENG is pressed by a cyclic external force during the contact-and-separate movement, the triboelectric materials will shrink to minimum thickness, which increases the electrical output of the TENG due to the enlarged capacitance. Thus, the reason for introducing pores into triboelectric materials is that the effective thickness of the triboelectric materials can be reduced and the surface area can be enlarged simultaneously by forming sponge structure. However, adding pores into triboelectric materials, which can be regarded as filling particles with the permittivity of the air (even lower than the original triboelectric materials, PDMS), will have an adverse influence on the effective permittivity. The effective permittivity of PDMS film with sponge structure drops from 3 to 1.83 when the volume fraction of pores increases from 0 to 45%, verifying that filling with lower dielectric particles into the PDMS film causes a reduction in its effective permittivity. After comparing and balancing the three factors: effective thickness, top surface area, and permittivity of the PDMS film with sponge structure, the investigations found that the TENG based on the sponge PDMS friction film doped with 10 vol % $SrTiO_3$ NPs and 15 vol % pores can provide an optimal output performance, reaching up to 9.06 $\mu A/cm^2$ and 338 V in short-current density and open-circuit voltage, respectively. The as-modified TENG achieved over 5-fold power enhancement when compared with the TENG based on the pure PDMS film.

However, some researchers reported that the agglomeration effect, due to the high surface energy of nanoparticles doped

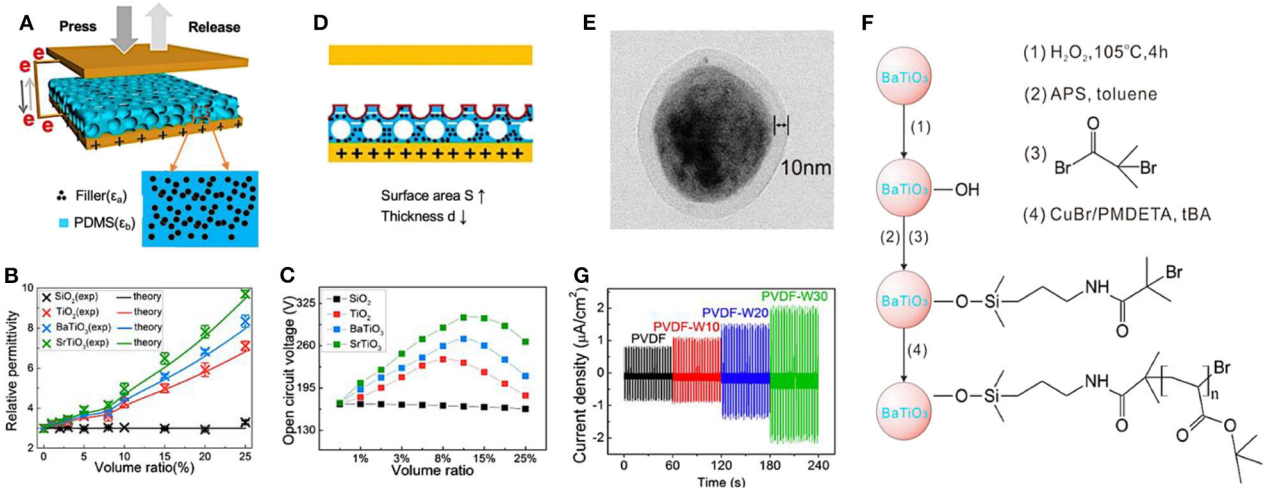

FIGURE 8 | Schematic diagrams and output performance of nanoparticles-doped TENGs. **(A)** Structure and working principle of as-fabricated TENG. **(B)** The relative permittivity and **(C)** open circuit voltage of TENGs fabricated with different dielectric-nanoparticles-doped PDMS films. **(D)** Schematic diagram of TENG with sponge structure PDMS composite film. Reprinted with permission from Chen et al. (2016a). Copyright 2016 American Chemical Society. **(E)** TEM images of the core-shell-structured $BaTiO_3$-PtBA nanoparticles. **(F)** Schematic diagram illustrating the preparation process of the core-shell-structured $BaTiO_3$-PtBA nanoparticles. **(G)** Output current densities generated by the PVDF-based TENGs with different percentage of the $BaTiO_3$-PtBA nanoparticles (ranging from 0 to 30%). Reprinted with permission from Du et al. (2018). Copyright 2018 American Chemical Society.

into the triboelectric materials, might yield poor mechanical properties and high dielectric loss (Kim et al., 2007). Surface treatments should be applied in advance to reduce the surface energy and enhance the dispersity of nanoparticles to overcome the shortcoming of directly doping the high dielectric nanoparticle in the polymer matrix. Du et al. modified the surface of $BaTiO_3$ nanoparticles with polymer polypoly(tert-butyl acrylate) (PtBA) and created core-shell-structured $BaTiO_3$-PtBA nanoparticles by the atom transfer radical polymerization (ATRP) technique (Du et al., 2018). The transmission electron microscopy (TEM) images of the core-shell-structure $BaTiO_3$ nanoparticles and the flow chart of the modification process are shown in **Figures 8E,F**. This PtBA shell can effectively reduce the surface energy of the nanoparticles in order to avoid aggregation in friction polymers, and therefore make the $BaTiO_3$ nanoparticles maintain high flexibility with low dielectric loss. As demonstrated in **Figure 8G**, the TENG with $BaTiO_3$-PtBA doped PVDF film generated a short-circuit current in the range from 1.1 to 2.1 $\mu A/cm^2$, according to the weight percent of the $BaTiO_3$-PtBA nanoparticles ranging from 0 to 30%, while the TENG with pure PVDF film generated only 0.8 $\mu A/cm^2$. The as-modified nanocomposites have a high breakdown field, a high dielectric constant, and good mechanical properties. These favorable characteristics further improve the output performance of TENGs that are modified with the high dielectric nanoparticles doping method.

Aside from forming a sponge structure, there is another method, working together with nanoparticles doping, to further enhance the output performance of TENGs. Seung et al. applied both the relative permittivity effects and the polarization effects to modify the triboelectric materials (Seung et al., 2017). As displayed in **Figure 9A**, the triboelectric materials in this work are composed of poled ferroelectric copolymer matrix, poly(vinylidenefluoride-co-trifluoroethylene) [P(VDF-TrFE)] (Lee et al., 2015a,b), doped with high dielectric nanoparticles, $BaTiO_3$ (BTO) (Wu et al., 2009; Kim et al., 2014). The poled ferroelectric P(VDF-TrFE) matrix could attract a large number of electrons from the opposite triboelectric material during the cyclic contact-and-separate movement. Moreover, the embedded $BaTiO_3$ nanoparticles, with a high dielectric property, acting as a strong charge-trapping site of TENGs, can greatly increase the capacitance of triboelectric material (Wolters and van der Schoot, 1985). In this way, by embedding dielectric $BaTiO_3$ nanoparticles inside the poled ferroelectric P(VDF-TrFE) copolymer matrix, TENGs with as-modified composite triboelectric materials can exhibit a dramatic increase in output performance (Zhong et al., 2015; Li W. et al., 2016; Wang et al., 2016). The charge transfer behavior between aluminum film and three different P(VDF-TrFE)-based surfaces, including non-poled P(VDF-TrFE), poled P(VDF-TrFE), and poled P(VDF-TrFE):BTO, are shown in **Figure 9B**. Among the three pairs, no significant charge transfer occurred between Al and non-poled P(VDF-TrFE). While in the pair of Al and poled P(VDF-TrFE):BTO, the band shifted steeply and a huge charge transfer occurred on the surface, owing to both the polarization of P(VDF-TrFE) (Shin et al., 2014) and the dielectric properties of the embedded nanoparticles. **Figure 9C** compared the dielectric constant between poled P(VDF-TrFE) and poled P(VDF-TrFE):BTO in order to visually display the electrical impacts brought from the introduction of high dielectric nanoparticles. For the whole measured range, the dielectric constant of the poled P(VDF-TrFE):BTO film

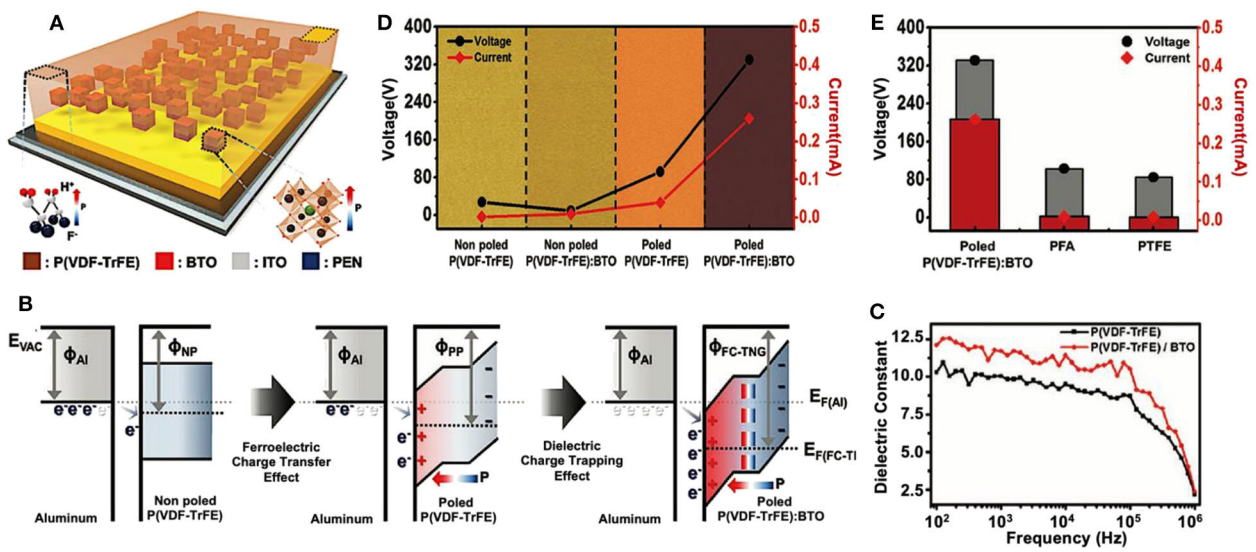

FIGURE 9 | Schematic diagrams and output performance of a ferroelectric composite-based TENG with dielectric nanoparticles BTO. **(A)** Schematic representations of the structure of as-modified TENG. **(B)** The charge transfer behavior between two different material surfaces and its corresponding energy band modification. **(C)** The dielectric constant of P(VDF-TrFE) with and without dielectric nanoparticles BTO. **(D)** The output voltage and current of TENGs with different modification depending on with or without two effects: ferroelectric and dielectric. **(E)** Output performance comparison between ferroelectric composite-based TENG with BTO nanoparticles and TENGs with traditional polymer films. Reprinted with permission from Seung et al. (2017). Copyright 2017 John Wiley & Sons.

was larger than the poled P(VDF-TrFE) film. The output voltage and current of TENGs based on different triboelectric materials, depending on with or without ferroelectric and dielectric effects, are shown in **Figure 9D**. Note that after embedding the $BaTiO_3$ nanoparticles into the poled P(VDF-TrFE) rather than the non-poled P(VDF-TrFE), both the output voltage and current increased significantly, reaching nearly 360 V and 0.3 mA, respectively. That means the as-fabricated TENGs can only provide the maximum electrical output by introducing high dielectric nanoparticles and poling the matrix simultaneously. When compared with typical triboelectric material-based TENGs, as shown in **Figure 9E**, the as-fabricated TENG with poled P(VDF-TrFE):BTO film had a boosted output performance which was improved by about ∼150 times.

Generally speaking, dielectric property modification is an effective and simple approach to fabricate high-performance TENGs. However, the percentage of nanoparticles embedded into the triboelectric material should be precisely controlled, since the introduction of new contents may affect other chemical or physical properties of the material itself including: surface effective area, material effective thickness and so on. In fact, the correlation between tribo-materials' dielectric properties and the output performance of TENGs is not clearly understood yet. Therefore, more investigations should be done to further improve the performance of energy harvesting.

FUNCTIONAL SUBLAYERS INSERTION

Functional sublayers insertion is another effective way to increase the charge density of triboelectric materials and thus improve the output performance of the TENGs. By adding sublayers with different electrical properties into the TENG structure, the triboelectric charges in the bulk of triboelectric materials will redistribute to avoid the unnecessary loss of electrons. Furthermore, they will enlarge the friction layers' capacity of triboelectric electrons. Take the triboelectric electrons in a negative triboelectric material e.g., the original transport and storage process is as follows: when the electrons are accumulated on the contact surface after the cyclic contact between the positive and negative friction layers, the positive charges can be induced in the electrode. Due to this separate accumulation of opposite charges, a vertical upward electric field will be established between the friction surface and the bottom electrode. Therefore, the electrons will be transported deeper into the bulk of the triboelectric material, rather than stay on the friction surface through a drift process caused by the vertical electric field and a diffusion process caused by the concentration gradient of electrons. However, the loss of electrons may occur during the transport process. The positively charged ions or particles in the air may also be absorbed onto the friction surface, causing a decrease in the number of surface triboelectric electrons. Moreover, for the triboelectric electrons that transport deep into the bulk area, they may reach the bottom electrode and recombine with the induced positive charges. Furthermore, the triboelectric charges gathered on the surface will hinder the subsequent triboelectric charges from entering into the friction layer and cause a decline in charge density. In this case, one intuitive solution to the problem is to transport and trap triboelectric electrons into a specific middle layer of the triboelectric material, which is far from the friction surface. To store more charges, the sublayers used to trap the triboelectric electrons should have a higher dielectric constant. For the reasons above, adding multiple functional sublayers, including the charge transport layer with high electric conductivity and the charge storage layer with high dielectric property, etc., seems like a promising way to realize the electronic redistribution inside the triboelectric materials and therefore increase the charge density, which plays a vital role in improving the output performance of TENGs.

Electrons Capture Layer Insertion

Typically, monolayer molybdenum disulfide (MoS_2), similar to the reduced graphene oxide (GO) sheet, is a competitive candidate as the charge-trapping agent due to its quantum confinement effect, large specific surface area, and appropriate energy level (Liu et al., 2012; Shin et al., 2016). Therefore, Wu et al. introduced 2D MoS_2 monolayer sheets inside the triboelectric materials of TENG in an attempt to dramatically enhance its output performance, as displayed in **Figure 10A** (Wu et al., 2017). In the structure of TENG, a PI layer and Al film were chosen as the negative and the positive triboelectric material. Based on this, a MoS_2 monolayer sheet was inserted into the bulk of the PI material by spin-coating and subsequent imidization (Wu et al., 2011), to create a uniform MoS_2-inserted PI layer. During the cyclic contact-and-separate movement of as-fabricated TENG, the triboelectric electrons generated on the surface of the PI may be transferred into the MoS_2 monolayer. Furthermore, they may also be stored inside the negative friction layer rather than on its surface; the aforementioned transfer and storage of electrons within this system are displayed in **Figure 10B**. This phenomenon can be attributed to the high charge-trapping property of the MoS_2 monolayer. Therefore, the static electron density on the negative triboelectric surfaces is decreased, increasing the gap between the positive and the negative charges. The high electron-capture properties of the monolayer MoS_2 can weaken the air breakdown effect, the recombination process between triboelectric electrons, and the later absorbed positive charges, which can both cause the loss of generated triboelectric electrons. Additionally, the monolayer MoS_2 can also suppress the drift and the diffusion effects of electrons. The electrons in the friction layer serve as an electrostatic induction source for the electricity generation process of the TENGs, which has a great impact on the output performances of TENGs. As a result, the electrical output performance of as-fabricated TENG can be enhanced by the dramatic increase in the density of triboelectric electrons.

To verify the impact of MoS_2 monolayer insertion, a vertical contact-separation mode TENG containing MoS_2 monolayer as an electron-acceptor layer was fabricated. **Figure 10C** shows that the open-circuit voltage of the TENG without MoS_2 monolayer is about 30 V, however, that of the TENG equipped with MoS_2 is as high as 400 V. Furthermore, the as-fabricated TENG exhibited a dramatic enhancement in its short-circuit current density and

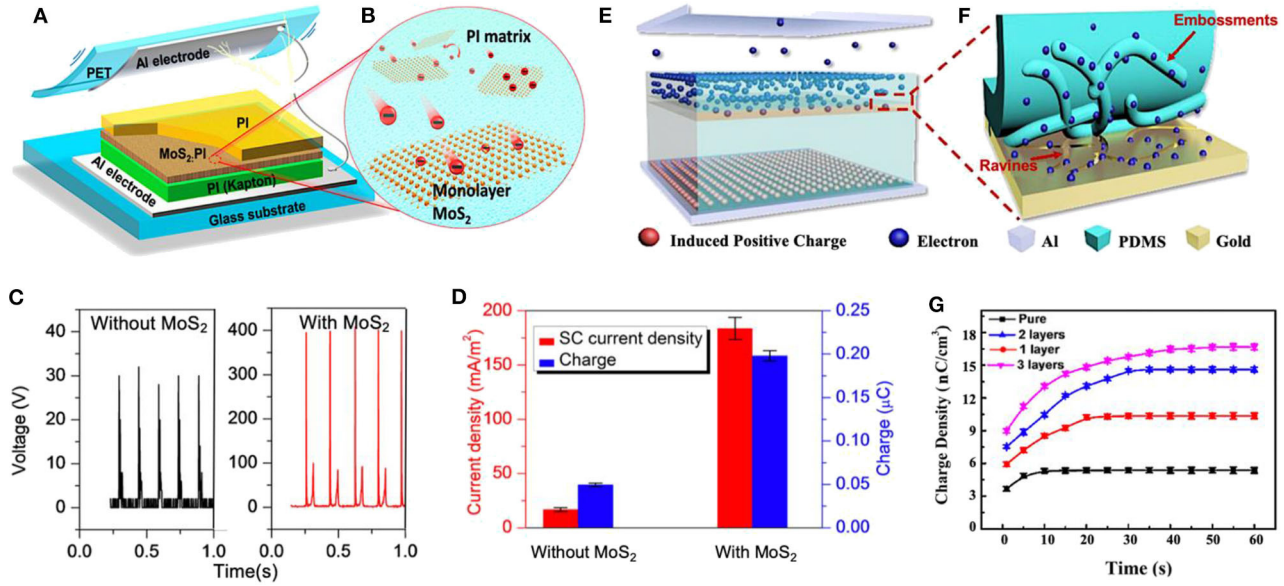

FIGURE 10 | Schematic diagrams and output performance of TENGs with dielectric monolayers. **(A)** Schematic diagram of a vertical contact-separation mode TENGs based on the MoS_2-inserted PI layer. **(B)** Schematic views of the electron transfer from the PI layer to the MoS_2 monolayer. **(C)** Rectified open-circuit voltage of the TENGs without and with MoS_2 monolayer. **(D)** Short-circuit current density and the amount of charge generated during a press-release cycle for the TENGs with and without monolayer. Reprinted with permission from Wu et al. (2017). Copyright 2017 American Chemical Society. **(E)** Illustrations of electrons' drift process in the TENG based on Au film. **(F)** Schematic diagram of electrons tunnel from PDMS to the Au film. **(G)** Transfer charge densities of TENGs. Reprinted with permission from Lai et al. (2018). Copyright 2018 American Chemical Society.

the amount of charge generated by the TENG, as displayed in **Figure 10D**. The total amount of charge generated by TENG with MoS_2 monolayer reached ~0.2 μC, which was much larger than that generated by using a TENG without MoS_2 monolayer with a value of 20.05 μC. Moreover, the peak power density of modified TENG was as large as 25.7 W/m^2, which is 120 times larger than that of the pristine TENG. These performance enhancements are attributed to the highly efficient electrons-captured ability of some novel 2D materials, which can provide direction to a frontier inactive material selection and device structure design for high efficiency triboelectric devices.

Electrons Trapping Layer Insertion

In addition to a MoS2 monolayer, the conductive materials serving as sublayers have also been reported. These materials are normally inserted in a bulk triboelectric material as transport layers and form sandwich structures. Lai et al. embedded ravines, gullies, and crisscrossed Au layers into the near-surface region of the negative triboelectric material of PDMS, as shown in **Figure 10E** (Lai et al., 2018). In order to obtain the PDMS triboelectric material equipped with the Au layer, gold was coated on the surface of PDMS via magnetron sputtering deposition. It was determined, through theoretical analysis, that when the negative triboelectric material, PDMS, captures the triboelectric charges from the positive triboelectric material, Al film, the charges drift from the surface to the internal bulk of the triboelectric material. This can be credited to the diffusion process caused by the concentration gradient of electrodes and the strong electric field between the friction surface and the bottom electrode. The Au layers applied in the work act as the passageways and trapping agent of the triboelectric charges during the drifting process. When the triboelectric charges reach the interface between the PDMS and the Au layer, owing to the strong electric field, the triboelectric charges will tunnel from the PDMS to the gold. In this way, the internal-space-charge zone is built. Moreover, the existence of ravines and gullies in PDMS and crisscrosses in the Au layers jointly benefit from the tunneling of charges. Owing to the existence of ravines in the gold layer, formed by plasma treatment, there are many embossments similar to those in mountain chain formation via PDMS, as shown in **Figure 10F**. As we know, for a charged object, the charge surface density is proportional to the curvature. Thus, electrons will assemble in the embossments, resulting in an increase of the local electric field strength. Accordingly, the increased strength of the local electric field leads to an increase in the probability of tunneling. Through embedding ravines and gullies, the crisscrossed gold layer has an improved charge storage capability and enhanced storage depth of the triboelectric charge, which leads to the high output performance of TENG. **Figure 10G** displays the transfer charge densities of TENGs, where the charge density of the TENG with Au trapping layer increases to 16.8 nC/cm^2 which is ~3 times higher than that of the pure TENG without the Au layer. TENGs equipped with multiple gold layers were built in the work to investigate the changing tendency of triboelectric charge densities. With the increasing number of inserted gold layers, from 0 to 4, the value of transfer charge density is about 5.4, 9.7, 14.5, 16.7, and 16.8 nC/cm^2, respectively, showing a gradual steady tendency at

around 16.8 nC/cm^2 when the number of layers reaches three. This observation implies that the charges cannot drift much, because they are being restricted by the depth of the drift and depressed by the product of the probabilities of tunneling in each interface. Overall, this study paves a novel way to enhance the charge density of the triboelectric materials and, therefore, improve TENG's output performance.

Multiple Layers Structure

Based on the electrons trapping layer insertion method mentioned above, a composite multiple-layer structure was built in the triboelectric materials, in order to adjust the internal distribution of the triboelectric charges and therefore improve the output performance of TENGs. The structure was formed by the stacking of a charge capture layer, a charge transport layer, and a charge storage layer from the friction surface to the bottom electrode. Among these three sublayers, the charge capture layer was used as the fundamental friction layer that was equipped in all of the structures of TENGs demonstrated in **Figure 11A**. Furthermore, the charge capture layer was used for robbing charges effectively from the opposite friction layer during the cyclic contact-separate-movement. In contrast, the charge transport sublayer was inserted to transport the generated triboelectric charges on the surface to deeper inside the material. Finally, the charge storage layer was added in order to hold more charges in the triboelectric materials. For these purposes, the transport sublayer should use materials with high conductivity in order to allow for triboelectric charges to pass through this layer quickly and hardly reside in it. This passageway for charge can not only help the generated triboelectric charges on the surface transport deeper into the bulk area, but also weaken the repulsive force for the later coming charges as well. As for the charge storage sublayer, it should be made of materials with lower carrier mobility, low intrinsic carrier concentration, and rich defects, which can all contribute to a larger charge capacity. As we all know, increasing the triboelectric charge density of a friction layer is one of the most basic approaches to improve the electrical output performance of TENGs.

On the basis of the theoretical analysis, Cui et al. fabricated TENGs based on the above three-sublayers structure (Cui et al., 2016). The negative and positive friction layers of TENGs fabricated in this work were polyvinylidene fluoride (PVDF) and aluminum foils. Firstly, the PS dielectric sublayer was added into the negative triboelectric material, as a charge storage layer between the bottom aluminum electrode and PVDF friction layer. The intrinsic carrier density and electron mobility of PS are both smaller than that of PVDF, due to its abundant trap levels of electrons, making PS one of the most suitable dielectric materials for acting as a storage layer. The short-circuit currents performances, compared in **Figures 11B,C**, indicate that the TENG with the PS sublayer demonstrated a dramatically enhanced short-circuit current value with nearly 600 nA, which is over 8 times greater than that of the TENG without the sublayer. The triboelectric charge density of the triboelectric material with this new structure is 7 times larger than that with the pure PVDF layer, as shown in **Figure 11D**. To further enhance the output performance of TENGs, a charge transport layer made of a small number of carbon nanotubes was inserted between the PVDF friction layer and the PS storage layer, in order to increase the conductivity of the near-surface area in triboelectric material. The transport sublayer is formed by adding a small number of carbon nanotubes (CNTs) into a PS or poly(vinyl alcohol) (PVA) layer. In this way, the transport process of the triboelectric charge in the negative triboelectric materials was improved as

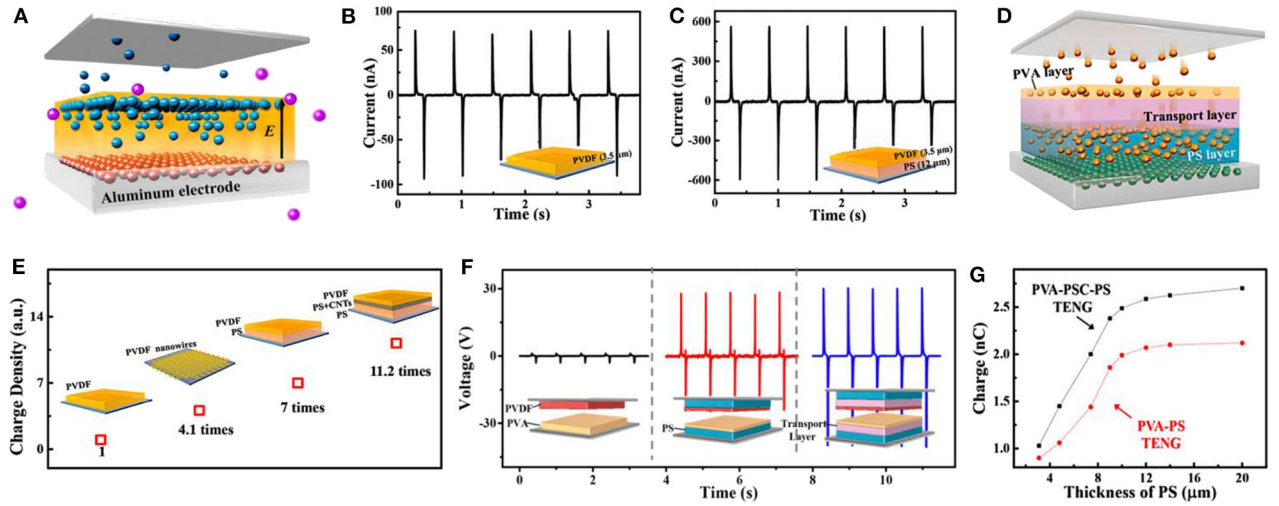

FIGURE 11 | Schematic diagrams and output performance of TENGs with multiple functional sublayers. **(A)** Schematic diagram of the transport process of triboelectric electrons in the negative triboelectric material of TENG. **(B,C)** The output comparation of short current generated from TENG **(B)** without and **(C)** with PS dielectric sublayer. **(D)** Improvement effects of different composite friction layer structure. Reprinted with permission from Cui et al. (2016). Copyright 2016 American Chemical Society. **(E)** Schematic of the electrons transport process of TENG with three-sublayers structure. **(F)** The voltage of TENG with different sublayers applied in both the positive and negative triboelectric materials. **(G)** The charge capacity of TENGs fabricated with different thicknesses of PS dielectric layers. Reprinted with permission from Cui et al. (2018). Copyright 2018 American Chemical Society.

follows: triboelectric charges from the positive friction layer was first captured by the outermost PEDF layer and entered the friction surface. Under the force of a built-in electric field between the negative triboelectric charges on the friction surface and the positive induced charges in the electrode, these charges migrated deeper into the bulk area through the CNTs-based PS layer and finally remained in the PS dielectric layer. This further introduction of the charge transport layer can increase the triboelectric charge yield effectively. And in this way, the total charge quantity in the friction layer could be increased again by a factor of 1.6. Overall, these multiple-layer structures of negative triboelectric material provided a factor of 11.2 improvement of the charge density produced from as-fabricated TENG when compared to the original non-modified one.

Based on the previous work, it can be speculated that the introduction of the charge transport and storage sublayers, which has been proved to be effective in improving the electron storage capacity for the negative triboelectric materials, may also take effect in the positive triboelectric materials. As demonstrated in **Figure 11E**, Cui et al. also introduced a similar multilayer structure to the positive triboelectric material, PVA layer (Cui et al., 2018). The three-sublayers structure are, in this case, from the friction surface to the bottom electrode, a 2 μm thick PVA layer, a 5 μm thick PS-doped 0.7 wt % CNTs layer (PSC), and PS layer ranging from 3 to 20 μm, working as the positive charge capture layer, the charge transport layer and the storage layer, respectively. Actually, to achieve the optical output performance of TENG, the structure with three collaborative sublayers may well be applied to both the negative and positive friction layer. Therefore, three TENGs equipped with different sublayers are built to investigate their output performance, including a TENG with a PVA positive friction layer and a PVDF negative friction layer, the second TENG with the same pair of friction layer and an inserted PS storage layer, the third TENG added both the PSC transport layer and PS storage layer into the same friction pair. The schematic diagram of these structures and the output voltage are shown in **Figure 11F**. The TENG with multiple functional sublayers exhibited a dramatic enhancement on output performance when compared to the original TENG. Moreover, by introducing the PSC layer into the positive friction layer, the charge capacity of TENG could be improved by 3.7-fold, from 0.37 to 2.7 nC/cm^2, as displayed in **Figure 11G**. By properly applying this three-sublayers structure to both positive and negative friction layers, the charge capacity of the designed TENG would be able to improve by 16.5-fold, which results in an outstanding promotion in the performance of the as-fabricated TENG.

Furthermore, in this multiple-layer structure, the thickness of each inserted sublayer has a vital relationship with the total charge capacity of the triboelectric materials and their inner charge distribution. **Figure 11G** shows the charge capacity of TENG with the bottom PS charge storage layer of different thicknesses, ranging from 3 to 20 μm, while the devices' top PVA layers are all 2 μm and PSC layers are 5 μm. From the output performance test, it can be found that with the increase of the PS layer's thickness, the charge capacity reveals an initial trend of rapid rising and finally becoming stable finally, at about 12 μm. The same trend of output performance can also be found in the structure with a charge capture layer or transport layer of changing thickness. The charge capacity of the inserted capture layer PVA and the inserted transport layer PSC continues to increase with the increase of the thickness of each layer, respectively, but the increasing rate decreases gradually. This means that an excess of thickness for these sublayers will not supply more extra effective storage space for the triboelectric charges. When comparing the performance difference between devices with (shown in black line) and without (shown in red line) a charge transport layer in this multiple-layer structure, it can also be found that the thicker the PS layer, the greater the influence of the charge transport layer. This is because, for a PVA–PSC–PS three-layers structure TENG with a thicker PS layer, a greater proportion of positive charges is separated from the surface by the transport layer. Therefore, the function of the inserted charge transport layer certainly becomes more obvious.

In general, adding additional sublayers with different electrical properties into the TENG structure yields an active intervention to the electrons transport and storage process; therefore, functional sublayers insertion is a promising way to improve the output performance of the TENGs. The triboelectric charges in the bulk of triboelectric materials were redistributed, in order to avoid the unnecessary loss of triboelectric electrons. Furthermore, this enlarges the friction layers' capacity of triboelectric electrons. However, the mechanism of the collaborative effect from the inserted sublayers, inner interfaces, and the triboelectric material, which, respectively, enhances the effective capture, transfer and storage of triboelectric charges has not yet been well-studied. Accordingly, future studies in this field will have great guiding significance for improving the performance and stability of TENGs.

CONCLUSIONS

In this review, surface chemistry was systematically introduced to promote the mechanical to electrical energy conversion via triboelectric nanogenerators. Through chemical modifications and approaches, triboelectric materials' surface charge densities have been proven to be modulated and thus the output performances of TENGs are improved. **Table 1** systematically summarizes the performance enhancements and mechanical durability of each chemical-modified TENGs. Methods that have been discussed in this review include functional groups grafting, ion implantation and decoration, dielectric properties engineering, and sublayers insertion. TENGs with broadened material choices, diversified operation modes and structural design have fully displayed the advantages in a variety of application scenarios, comparing with other mechanical energy harvesting techniques. Many challenges are waiting to be overcome to advance the field of surface chemistry for high-performance TENGs, as follows.

(1) Enhance the chemical stability of the surface chemical functional group grafting. Functional group grafting is a straightforward, cost-efficient, and easy-to-implement way to efficiently enhance the output performance of TENGs.

TABLE 1 | A summary of typical chemical modification methods for TENGs.

Tribo-materials	Modification method	Output performance enhancement[b]				Duration[c]	References
		Charge	Voltage	Current	Power		
Cl-PET, PEI(b)-PET	Self-assembled monolayer	-	19.80 [a]	21 [a]	-	5,000	Shin et al., 2017
PDMS, ITO	UVO-irradiation	15.88	11.97	17.46	-	20,000	Yun et al., 2015
$PMMA^-$ fiber, Cu	Electrospinning	-	1.28 [a]	147 [a]	585 [a]	125,000	Busolo et al., 2018
FEP, Al	Ion Injection	5	5	3.33	25	400,000	Wang et al., 2014
FEP, Kapton	Ion Irradiation	2.32 [a]	-	-	35,999	-	Li et al., 2020
FOTS-PDMS, Li^+ film	Ion Absorption	-	2.40	5.25	20	50,000	Park et al., 2017
AlO_X-PDMS, PDMS	Sequential Infiltration Synthesis	8	6.67	6.33	-	-	Yu et al., 2015
$BaTiO_3$-doped(PVDF-TrFE), Al	High Dielectric Doping	2.52	2 [a]	5 [a]	150	-	Seung et al., 2017
PI/MoS_2:PI/PI, Al	Caption-Layer Insertion	3	12.33	6 [a]	120	-	Wu et al., 2017
PDMS-Au layer, Al	Trapping-Layer Insertion	4	-	-	-	-	Lai et al., 2018
PVA-PSC-PS, PVDF-PSC-PS	Multiple-Layer Structure	16.5	9 [a]	9 [a]	-	-	Cui et al., 2018

[a] *Estimated value.* [b] *Multiple of Enhancement.* [c] *Testing Cycle of Duration.*

Although that may be true, the results may lose its effectiveness if the surface is polished or worn out during the friction since the modification just takes place on the surfaces rather than deep into the bulk of triboelectric materials. To overcome this difficulty and limitation, further improvements should be found to enhance stability and effective duration of the method.

(2) Reduce the cost of ion injection and decoration methods for further scaling up. The ion injection and decoration methods provide effective approaches for improving the TENG's output performance with relatively high stability. However, the fabrication processes are relatively complicated and the instruments used during the processes, such as air-ionization guns, add extra cost. It may bring obstacles for further scaling up. Consequently, more flexible and cost-efficient techniques should be explored for ion implantation promotion.

(3) Deeply explore the mechanisms of dielectric engineering. Although the dielectric property modification is experimentally proven to be an effective and simple approach for obtaining high-performance TENGs, the correlation between dielectric properties of triboelectric materials and output performance of as-fabricated TENGs is not clearly unveiled yet. Further investigation should be done to explore the mechanisms of dielectric engineering and reveal the coefficient between embedded nanoparticles and other chemical and physical properties of the material itself, therefore optimizing the dose of dopants for high-performance TENGs.

(4) Investigate the inner mechanism of functional sublayers insertion. Functional sublayers insertion is a promising way to improve the output performance of the TENGs because it can provide an active intervention to the electrons transport and storage process. Nevertheless, the mechanism of the collaborative effect from the inserted sublayers, inner interfaces, and the triboelectric material has not yet been well-studied. Thus, further studies investigating the inner mechanism will have great guiding significance to further improve the output performance of TENGs.

(5) Incorporation of chemical and physical modifications. The synergy of chemical and physical modifications could be an effective approach to build up a high-performance TENGs. Applying them to a material of interest can not only increase the effective contact area between the two triboelectric surfaces by various surface morphologies, but also increase the gap between the two triboelectric materials' ability to gain or lose electrons as well. Therefore, more attempts should be done to apply both chemical and physical modifications together to triboelectric materials or to explore new techniques that can modify surface morphologies and chemical properties simultaneously.

(6) Seek for possible biochemical approaches. Chemical and biological approaches are usually highly correlated with each other. By introducing biomaterials as novel triboelectric materials, like silk fibroin film, TENG may have some satisfying superiorities, such as flexible, stretchable, bio-friendly and preferably transparent. Therefore, it should be wearable (or even implantable) to the human body. Through applying proper chemical modifications to these biomaterials, higher electrical performance and working stability can also be achieved, making TENG an efficient and reliable power source with wider application prospects.

(7) Explorations of versatile TENG-based self-powered devices. Both theoretical calculations and experimental endeavors are highly in need for promoting existing materials or potentially discovering new materials. which are not only with high triboelectric properties but also compatibility with various application scenarios, which seem to be a basis for the development of versatile TENG-based self-powered devices.

Overall, the utilization of surface chemistry opens an emerging and effective route to build up high-performance triboelectric nanogenerator as a pervasive energy solution in the upcoming era of the Internet of Things. Challenges coexist with opportunities, and much more research efforts remain desired to improve surface chemical modification with the goals of improved stability, robustness, scalable and advanced surface modification.

We anticipate that the wide application of surface chemistry can contribute largely to develop high-performance TENGs as both sustainable power sources and active sensors.

AUTHOR CONTRIBUTIONS

JC: supervision, visualization, and funding acquisition. JC and JX: conceptualization and writing-original draft. JX, JC, YZ, and AN: writing-review and editing. All authors contributed to the article and approved the submitted version.

FUNDING

Startup support from the University of California, Los Angeles and the 2020 Okawa Foundation Research Grant.

ACKNOWLEDGMENTS

We acknowledge the Henry Samueli School of Engineering & Applied Science and the Department of Bioengineering at the University of California, Los Angeles for the startup support. JC also acknowledges the 2020 Okawa Foundation Research Grant.

REFERENCES

Awasthi, K. Kulshrestha, V., Avasthi, D. K., and Vijay, Y. K. (2010). Optical, chemical and structural modification of oxygen irradiated PET. *Radiat. Meas.* 45, 850–855. doi: 10.1016/j.radmeas.2010.03.002

Bai, P., Zhu, G., Jing, Q., Yang, J., Chen, J., Su, Y., et al. (2014). Membrane-based self-powered triboelectric sensors for pressure change detection and its uses in security surveillance and healthcare monitoring. *Adv. Funct. Mater.* 24, 5807–5813. doi: 10.1002/adfm.201401267

Bai, P., Zhu, G., Lin, Z., Jing, Q., Chen, J., Zhang, G., et al. (2013a). Integrated multilayered triboelectric nanogenerator for harvesting biomechanical energy from human motions. *ACS Nano* 7, 3713–3719. doi: 10.1021/nn4007708

Bai, P., Zhu, G., Liu, Y., Chen,. J., Jing, Q., Yang, W., et al. (2013b). Cylindrical rotating triboelectric nanogenerator. *ACS Nano* 7, 6361–6366. doi: 10.1021/nn402491y

Baytekin, H. T., Patashinski, A. Z., Branicki, M., Baytekin, B., Soh, S., and Grzybowski, B. A. (2011). The mosaic of surface charge in contact electrification. *Science* 333, 308–312. doi: 10.1126/science.1201512

Bedi, G., Venayagamoorthy, G. K., Singh, R., Brooks, R. R., and Wang, K. (2018). Review of internet of things (IoT) in electric power and energy systems. *IEEE Internet Things J.* 5, 847–870. doi: 10.1109/JIOT.2018.2802704

Biswas, M., Libera, J. A., Darling, S. B., and Elam, J. W. (2015). Kinetics for the sequential infiltration synthesis of alumina in poly (methyl methacrylate): an infrared spectroscopic study. *J. Phys. Chem. C* 119, 14585–14592. doi: 10.1021/jp511939j

Busolo, T., Ura, D. P., Kim, S. K., Marzec, M. M., Bernasik, A., Stachewicz, U., et al. (2018). Surface potential tailoring of PMMA fibers by electrospinning for enhanced triboelectric performance. *Nano Energy* 57, 500–506. doi: 10.1016/j.nanoen.2018.12.037

Byun, K. E., Cho, Y., Seol, M., Kim, S., Kim, S. W., Shin, H. J., et al. (2016). Control of triboelectrification by engineering surface dipole and surface electronic state. *ACS Appl. Mater. Interfaces* 8, 18519–18525. doi: 10.1021/acsami.6b02802

Cai, L., Song, A. Y., Li, W., Hsu, P. C., Lin, D., Catrysse, P. B., et al. (2018). Spectrally selective nanocomposite textile for outdoor personal cooling. *Adv. Mater.* 30:1802152. doi: 10.1002/adma.201802152

Cha, S. N., Seo, J. S., Kim, S. M., Kim, H. J., Park, Y. J., Kim, S. W., et al. (2010). Sound-driven piezoelectric nanowire-based nanogenerators. *Adv. Mater.* 22, 4726–4730. doi: 10.1002/adma.201001169

Chen, G., Li, Y., Bick, M., and Chen, J. (2020). Smart textiles for electricity generation. *Chem. Rev.* 120, 3668–3720. doi: 10.1021/acs.chemrev.9b00821

Chen, J. (2016). *Triboelectric Nanogenerators.* Atlanta, GA: Georgia Institute of Technology. Available online at: http://hdl.handle.net/1853/54956

Chen, J., Guo, H., He, X., Liu, G., Xi, Y., Shi, H., et al. (2016a). Enhancing performance of triboelectric nanogenerator by filling high dielectric nanoparticles into sponge PDMS film. *ACS Appl. Mater. Interfaces* 8, 736–744. doi: 10.1021/acsami.5b09907

Chen, J., Huang, Y., Zhang, N., Zou, H., Liu, R., Tao, C., et al. (2016b). Micro-cable structured textile for simultaneously harvesting solar and mechanical energy. *Nat. Energy* 1:16138. doi: 10.1038/nenergy.2016.138

Chen, J., and Wang, Z. L. (2017). Reviving vibration energy harvesting and self-powered sensing by a triboelectric nanogenerator. *Joule* 1, 480–521. doi: 10.1016/j.joule.2017.09.004

Chen, J., Yang, J., Guo, H., Li, Z., Zheng, L., Su, Y., et al. (2015a). Automatic mode transition enabled robust triboelectric nanogenerators. *ACS Nano* 9, 12334–12343. doi: 10.1021/acsnano.5b05618

Chen, J., Yang, J., Li, Z., Fan, X., Zi, Y., Jing, Q., et al. (2015b). Networks of triboelectric nanogenerators for harvesting water wave energy: a potential approach toward blue energy. *ACS Nano* 9, 3324–3331. doi: 10.1021/acsnano.5b00534

Chen, J., Zhu, G., Yang, J., Jing, Q., Bai, P., Yang, W., et al. (2015c). Personalized keystroke dynamics for self-powered human-machine interfacing. *ACS Nano* 9:105. doi: 10.1021/nn506832w

Chen, J., Zhu, G., Yang, W., Jing, Q., Bai, P., Yang, Y., et al. (2013). Harmonic-resonator-based triboelectric nanogenerator as a sustainable power source and a self-powered active vibration sensor. *Adv. Mater.* 25, 6094–6099. doi: 10.1002/adma.201302397

Cheng, X., Meng, B., Chen, X., Han, M., Chen, H., Su, Z., et al. (2015a). Single-step fluorocarbon plasma treatment-induced wrinkle structure for high-performance triboelectric nanogenerator. *Small* 12, 229–236. doi: 10.1002/smll.201502720

Cheng, X., Meng, B., Zhang, X., Han, M., Su, Z., and Zhang, H. (2015b). Wearable electrode-free triboelectric generator for harvesting biomechanical energy. *Nano Energy* 12, 19–25. doi: 10.1016/j.nanoen.2014.12.009

Choi, D., Yoo, D., and Kim, D. S. (2015). One-step fabrication of transparent and flexible nanotopographical-triboelectric nanogenerators via thermal nanoimprinting of thermoplastic fluoropolymers. *Adv. Mater.* 27, 7386–7394. doi: 10.1002/adma.201503802

Chu, X., Zhao, X., Zhou, Y., Wang, Y., Han, X., Zhou, Y., et al. (2020). An ultrathin robust polymer membrane for wearable solid-state electrochemical energy storage. *Nano Energy* 76:105179. doi: 10.1016/j.nanoen.2020.105179

Chun, J., Kim, J. W., Jung, W. S., Kang, C. Y., Kim, S. W., Wang, Z. L., et al. (2015). Mesoporous pores impregnated with Au nanoparticles as effective dielectrics for enhancing triboelectric nanogenerator performance in harsh environments. *Energy Environ. Sci.* 8, 3006–3012. doi: 10.1039/C5EE01705J

Cole, J. J., Barry, C. R., Knuesel, R. J., Wang, X., and Jacobs,. H. O. (2011). Nanocontact electrification: patterned surface charges affecting adhesion, transfer, and printing. *Langmuir* 27, 7321–7329. doi: 10.1021/la200773x

Cui, N., Gu, L., Lei, Y., Liu, J., Qin, Y., Ma, X., et al. (2016). Dynamic behavior of the triboelectric charges and structural optimization of the friction layer for a triboelectric nanogenerator. *ACS Nano* 10, 6131–6138. doi: 10.1021/acsnano.6b02076

Cui, N., Liu, J., Lei, Y., Gu, L., Xu, Q., Liu, S., et al. (2018). High-performance triboelectric nanogenerator with a rationally designed friction layer structure. *ACS Appl. Energy Mater.* 1, 2891–2897. doi: 10.1021/acsaem.8b00530

Dagdeviren, C. N., Li, Z., and Wang, Z. L. (2017). Energy harvesting from the animal/human body for self-powered electronics. *Annu. Rev. Biomed. Eng.* 19, 85–108. doi: 10.1146/annurev-bioeng-071516-044517

Davoodi, E., Montazerian, H., Haghniaz, R., Rashidi, A., Ahadian, S., Sheikhi, A., et al. (2020). 3D-printed ultra-robust surface-doped porous silicone sensors for wearable biomonitoring. *ACS Nano* 14, 1520–1532. doi: 10.1021/acsnano.9b06283

Deng, W., Zhou, Y., Zhao, X., Zhang, S., Zou, Y., Xu, J., et al. (2020). Ternary electrification layered architecture for high-performance triboelectric nanogenerators. *ACS Nano* 14, 9050–9058. doi: 10.1021/acsnano.0c04113

Dharmasena, R. D. I. G., Deane, J. H. B., and Silva, S. R. P. (2018). Nature of power generation and output optimization criteria for triboelectric nanogenerators. *Adv. Energy Mater.* 8:1802190. doi: 10.1002/aenm.201802190

Dong, H., and Bell, T. (1999). State-of-the-art overview: ion beam surface modification of polymers towards improving tribological properties. *Surf. Coat. Technol.* 111, 29–40. doi: 10.1016/S0257-8972(98)00698-7

Du, X., Liu, Y., Wang, J., Niu, H., Yuan, Z., Zhao, S., et al. (2018). Improved triboelectric nanogenerator output performance through polymer nanocomposites filled with core–shell–structured particles. *ACS Appl. Mater. Interfaces* 10, 25683–25688. doi: 10.1021/acsami.8b05966

Dudem, B., Ko, Y. H., Leem, J. W., Lee, S. H., and Yu, J. S. (2015). Highly transparent and flexible triboelectric nanogenerators with subwave length architectured polydimethylsiloxane by a nanoporous anodic aluminum oxide Template. *ACS Appl. Mater. Interfaces* 7, 20520–20529. doi: 10.1021/acsami.5b05842

Fan, F., Lin, L., Zhu, G., Wu, W., Zhang, R., and Wang, Z. L. (2012). Transparent triboelectric nanogenerators and self-powered pressure sensors based on micropatterned plastic films. *Nano Lett.* 12, 3109–3114. doi: 10.1021/nl300988z

Fan, F. R., Luo, J., Tang, W., Li, C., Zhang, C., Tian, Z., et al. (2014). Highly transparent and flexible triboelectric nanogenerators: performance improvements and fundamental mechanisms. *J. Mater. Chem. A* 2, 13219–13225. doi: 10.1039/C4TA02747G

Fan, X., Chen, J., Yang, J., Bai, P., Li, Z., and Wang, Z. L. (2015). Ultrathin, rollable, paper-based triboelectric nanogenerator for acoustic energy harvesting and self-powered sound recording. *ACS Nano* 9, 4236–4243. doi: 10.1021/acsnano.5b00618

Feng, Y., Zheng, Y., Ma, S., Wang, D., Zhou, F., and Liu, W. (2016). High output polypropylene nanowire array triboelectric nanogenerator through surface structural control and chemical modification. *Nano Energy* 19, 48–57. doi: 10.1016/j.nanoen.2015.11.017

Ferguson, J. D., Weimer, A. W., and George, S. M. (2004). Atomic layer deposition of Al_2O_3 films on Polyethylene particles. *Chem. Mater.* 16, 5602–5609. doi: 10.1021/cm040008y

Fu, J., Cano, Z. P., Park, M. G., Yu, A., Fowler, M., and Chen, Z. (2017). Electrically rechargeable zinc-air batteries: progress, challenges, and perspectives. *Adv. Mater.* 29:1604685. doi: 10.1002/adma.201604685

Gao, W., Emaminejad, S., Nyein, H. Y. Y., Challa, S., Chen, K., Peck, A., et al. (2016). Fully integrated wearable sensor arrays for multiplexed *in situ* perspiration analysis. *Nature* 529, 509–514. doi: 10.1038/nature16521

George, S. M. (2010). Atomic layer deposition: an overview. *Chem. Rev.* 110, 111–131. doi: 10.1021/cr900056b

Gong, B., Kim, D. H., and Parsons, G. N. (2012a). Mesoporous metal oxides by vapor infiltration and atomic layer deposition on ordered surfactant polymer films. *Langmuir* 28, 11906–11913. doi: 10.1021/la302027b

Gong, B., Spagnola, J. C., Arvidson, S. A., Khan, S. A., and Parsons, G. N. (2012b). Directed inorganic modification of bi-component polymer fibers by selective vapor reaction and atomic layer deposition. *Polymer* 53, 4631–4636. doi: 10.1016/j.polymer.2012.08.018

Grey, C. P., and Tarascon, J. M. (2017). Sustainability and in situ monitoring in battery development. *Nat. Mater.* 16, 45–56. doi: 10.1038/nmat4777

Gu, P., Zheng, M., Zhao, Q., Xiao, X., Xue, H., and Pang, H. (2017). Rechargeable zinc-air batteries: a promising way to green energy. *J. Mater. Chem. A* 5, 7651–7666. doi: 10.1039/C7TA01693J

Gubbi, J., Buyya, R., Marusic, S., and Palaniswami, M. (2013). Internet of things (IoT): a vision, architectural elements, and future directions. *Future Gener. Comput. Syst.* 29, 1645–1660. doi: 10.1016/j.future.2013.01.010

Gür, T. M. (2018). Review of electrical energy storage technologies, materials and systems: challenges and prospects for large-scale grid storage. *Energy Environ. Sci.* 11, 2696–2767. doi: 10.1039/C8EE01419A

Hayashi, K., Saito, N., Sugimura, H., Takai, O., and Nakagiri, N. (2002). Surface potential contrasts between silicon surfaces covered and uncovered with an organosilane self-assembled monolayer. *Ultramicroscopy* 91, 151–156. doi: 10.1016/S0304-3991(02)00094-3

He, Y., Matthews, B., Wang, J., Song, L., Wang, X., and Wu, G. (2018). Innovation and challenges in materials design for flexible rechargeable batteries: from 1D to 3D. *J. Mater. Chem. A* 6, 735–753. doi: 10.1039/C7TA09301B

Hinchet, R., Seung, W., and Kim, S. W. (2015). Recent progress on flexible triboelectric nanogenerators for self-powered electronics. *ChemSusChem* 8, 2327–2344. doi: 10.1002/cssc.201403481

Hoek, I., Tho, F., and Arnold, W. M. (2010). Sodium hydroxide treatment of PDMS based microfluidic devices. *Lab Chip* 10, 2283–2285. doi: 10.1039/c004769d

Hou, T., Yang, Y., Zhang, H., Chen, J., Chen, L., and Wang, Z. L. (2013). Triboelectric nanogenerator built inside shoe insole for harvesting walking energy. *Nano Energy* 2, 856–862. doi: 10.1016/j.nanoen.2013.03.001

Hozumi, A., Ushiyama, K., Sugimura, H., and Takai, O. (1999). Langmuir fluoroalkylsilane monolayers formed by chemical vapor surface modification on hydroxylated oxide surfaces. *Langmuir* 15, 7600–7604. doi: 10.1021/la9809067

Jeong, C. K., Baek, K. M., Niu, S., Nam, T. W., Hur, Y. H., Park, D. Y., et al. (2014). Topographically designed triboelectric nanogenerator via block copolymer self-assembly. *Nano Lett.* 14, 7031–7038. doi: 10.1021/nl503402c

Jeong, C. K., Lee, J., Han, S., Ryu, J., Hwang, G. T., Park, D. Y., et al. (2015). A hyper-stretchable elastic-composite energy harvester. *Adv. Mater.* 27, 2866–2875. doi: 10.1002/adma.201500367

Jin, L., Chen, J., Zhang, B., Deng, W., Zhang, L., Zhang, H., et al. (2016). Self-powered safety helmet based on hybridized nanogenerator for emergency. *ACS Nano* 10, 7874–7881. doi: 10.1021/acsnano.6b03760

Jin, L., Xiao, X., Deng, W., Nashalian, A., He, D., Yan, C., et al. (2020). Manipulating relative permittivity for high-performance wearable triboelectric nanogenerators. *Nano Lett.* 9, 6404–6411. doi: 10.1021/acs.nanolett.0c01987

Jing, Q., and Kar-Narayan, S. (2018). Nanostructured polymer-based piezoelectric and triboelectric materials and devices for energy harvesting applications. *J. Phys. D Appl. Phys.* 51:303001. doi: 10.1088/1361-6463/aac827

Jing, Q., Zhu, G., Bai, P., Xie, Y., Chen, J., Han, R. P. S., et al. (2014). Case-encapsulated triboelectric nanogenerator for harvesting energy from reciprocating sliding motion. *ACS Nano* 8, 3836–3842. doi: 10.1021/nn500694y

Kang, D. H. P., Chen, M. J., and Ogunseitan, O. A. (2013). Potential environmental and human health impacts of rechargeable lithium batteries in electronic waste. *Environ. Sci. Technol.* 47, 5495–5503. doi: 10.1021/es400614y

Kanik, M., Say, M. G., Daglar, B., Yavuz, A. F., Dolas, M. H., El-Ashry, M. M., et al. (2015). A motion-and sound-activated, 3D-printed, chalcogenide-based triboelectric nanogenerator. *Adv. Mater.* 27, 2367–2376. doi: 10.1002/adma.201405944

Kenry, Y. J. C., and Lim, C. T. (2016). Emerging flexible and wearable physical sensing platforms for healthcare and biomedical applications. *Microsyst. Nanoeng.* 2:16043. doi: 10.1038/micronano.2016.43

Kim, D., Jeon, S. B., Kim, J. Y., Seol, M. L., Kim, S. O., and Choi, Y. K. (2015). High-performance nanopattern triboelectric generator by block copolymer lithography. *Nano Energy* 12, 331–338. doi: 10.1016/j.nanoen.2015.01.008

Kim, J., Campbell, A. S., Avila, B. E., and de Wang, J. (2019). Wearable biosensors for healthcare monitoring. *Nat. Biotechnol.* 37, 389–406. doi: 10.1038/s41587-019-0045-y

Kim, P., Jones, S. C., Hotchkiss, P. J., Haddock, J. N., Kippelen, B., Marder, S. R., et al. (2007). Phosphonic acid-modified barium titanate polymer nanocomposites with high permittivity and dielectric strength. *Adv. Mater.* 19, 1001–1005. doi: 10.1002/adma.200602422

Kim, Y., Lee, K. Y., Hwang, S. K., Park, C., Kim, S. W., and Cho, J. (2014). Layer-by-layer controlled perovskite nanocomposite thin films for piezoelectric nanogenerators. *Adv. Funct. Mater.* 24, 6262–6269. doi: 10.1002/adfm.201401599

Kim, Y. J., Lee, J., Park, S., Park, C., Park, C., and Choi, H. (2017). Effect of the relative permittivity of oxides on the performance of triboelectric nanogenerators. *RSC Adv.* 7, 49368–49373. doi: 10.1039/C7RA07274K

Kuang, S. Y., Chen, J., Cheng, X., Zhu, G., and Wang, Z. L. (2015). Two-dimensional rotary triboelectric nanogenerator as a portable and wearable power source for electronics. *Nano Energy* 17, 10–16. doi: 10.1016/j.nanoen.2015.07.011

Kujawski, W., Nguyen, Q. T., and Neel, J. (1992). Infrared investigations of sulfonated ionomer membranes. I. Water–alcohol compositions and counterions effects. *Appl. Polym. Sci.* 44, 951–958. doi: 10.1002/app.1992.070440603

Kumar, R., and Singh, P. (2015). Influence of SHI upon nanohole free volume and micro scale level surface modifications of polyethyleneterephthalate polymer films. *Appl. Surf. Sci.* 337, 19–26. doi: 10.1016/j.apsusc.2015.02.043

Kumar, S., Surendar, T., Baruah, A., and Shanker, V. (2013). Synthesis of a novel and stable g-C_3N_4-Ag_3PO_4 hybrid nanocomposite photocatalyst and study of the photocatalytic activity under visible light irradiation. *J. Mater. Chem. A* 1, 5333–5340. doi: 10.1039/c3ta00186e

Lai, C., Fu, Y., Chen, J., An, Q., Liao, K., Fang, S., et al. (2012). Pervaporation separation of ethanol/water mixture by UV/O_3-modified PDMS membranes. *Sep. Purif. Technol.* 100, 15–21. doi: 10.1016/j.seppur.2012.07.018

Lai, M., Du, B., Guo, H., Xi, Y., Yang, H., Hu, C., et al. (2018). Enhancing the output charge density of TENG via building longitudinal paths of electrostatic charges in the contacting layers. *ACS Appl. Mater. Interfaces* 10, 2158–2165. doi: 10.1021/acsami.7b15238

Lee, B. Y., Kim, S. U., Kang, S., and Lee, S. D. (2018). Transparent and flexible high power triboelectric nanogenerator with metallic nanowire-embedded tribonegative conducting polymer. *Nano Energy* 53, 152–159. doi: 10.1016/j.nanoen.2018.08.048

Lee, I. K., and Lee, K. (2015). The internet of things (IoT): applications, investments, and challenges for enterprises. *Bus. Horiz.* 58, 431–440. doi: 10.1016/j.bushor.2015.03.008

Lee, J. H., Hinchet, R., Kim, T. Y., Ryu, H., Seung, W., Yoon, H. J., et al. (2015a). Control of skin potential by triboelectrification with ferroelectric polymers. *Adv. Mater.* 27, 5553–5558. doi: 10.1002/adma.201502463

Lee, J. H., Yoon, H. J., Kim, T. Y., Gupta, M. K., Lee, J. H., Seung, W., et al. (2015b). Micropatterned P(VDF-TrFE) film-based piezoelectric nanogenerators for highly sensitive self-powered pressure sensors. *Adv. Funct. Mater.* 25, 3203–3209. doi: 10.1002/adfm.201500856

Lee, K. Y., Chun, J., Lee, J. H., Kim, K. N., Kang, N. R., Kim, J. Y., et al. (2014). Hydrophobic sponge structure-based triboelectric nanogenerator. *Adv. Mater.* 26, 5037–5042. doi: 10.1002/adma.201401184

Lee, M., Chen, C., Wang, S., Cha, S. N., Park, Y. J., Kim, J. M., et al. (2012). A hybrid piezoelectric structure for wearable nanogenerators. *Adv. Mater.* 24, 1759–1764. doi: 10.1002/adma.201200150

Li, H., Su, L., Kuang, S., Pan, C., Zhu, G., and Wang, Z. L. (2015). Significant enhancement of triboelectric charge density by fluorinated surface modification in nanoscale for converting mechanical energy. *Adv. Funct. Mater.* 25, 5691–5697. doi: 10.1002/adfm.201502318

Li, S., Fan, Y., Chen, H., Nie, J., Liang, Y., Tao, X., et al. (2020). Manipulating the triboelectric surface charge density of polymers by low-energy helium ion irradiation/implantation. *Energy Environ. Sci.* 13, 896–907. doi: 10.1039/C9EE03307F

Li, W., Wu, N., Zhong, J., Zhong, Q., Zhao, S., Wang, B., et al. (2016). Theoretical study of cellular piezoelectret generators. *Adv. Funct. Mater.* 26, 1964–1974. doi: 10.1002/adfm.201503704

Li, Y., and Dai, H. (2014). Recent advances in zinc-air batteries. *Chem. Soc. Rev.* 43, 5257–5275. doi: 10.1039/C4CS00015C

Li, Z., Chen, J., Guo, H., Fan, X., Wen, Z., Yeh, M.-H., et al. (2016). Triboelectrification-enabled self-powered detection and removal of heavy metal ions in wastewater. *Adv. Mater.* 28, 2983–2991. doi: 10.1002/adma.201504356

Lin, L., Wang, S., Xie, Y., Jing, Q., Niu, S., Hu, Y., et al. (2013). Segmentally structured disk triboelectric nanogenerator for harvesting rotational mechanical energy. *Nano Lett.* 13, 2916–2923. doi: 10.1021/nl4013002

Lin, L., Xie, Y., Niu, S., Wang, S., Yang, P., and Wang, Z. L. (2015). Robust triboelectric nanogenerator based on rolling electrification and electrostatic induction at an instantaneous energy conversion efficiency of approximately 55%. *ACS Nano* 9, 922–930. doi: 10.1021/nn506673x

Lin, W. C., Lee, S. H., Karakachian, M., Yu, B., Chen, Y., Lin, Y., et al. (2009). Tuning the surface potential of gold substrates arbitrarily with self-assembled monolayers with mixed functional groups. *Phys. Chem. Chem. Phys.* 11, 6199–6204. doi: 10.1039/b902044f

Lin, Z., Chen, J., Li, X., Zhou, Z., Meng, K., Wei, W., et al. (2017). Triboelectric nanogenerator enabled body sensor network for self-powered human heart-rate monitoring. *ACS Nano* 11, 8830–8837. doi: 10.1021/acsnano.7b02975

Lin, Z., Chen, J., and Yang, J. (2016). Recent progress in triboelectric nanogenerators as a renewable and sustainable power source. *J. Nanomater.* 2016:5651613. doi: 10.1155/2016/5651613

Lin, Z., Yang, J., Li, X., Wu, Y., Wei, W., Liu, J., et al. (2018). Large-scale and washable smart textiles based on triboelectric nanogenerator arrays for self-powered sleeping monitoring. *Adv. Funct. Mater.* 28:1704112. doi: 10.1002/adfm.201704112

Lin, Z. H., Cheng, G., Lee, S., Pradel, K. C., and Wang, Z. L. (2014). Harvesting water drop energy by a sequential contact-electrification and electrostatic induction process. *Adv. Mater.* 26, 4690–4696. doi: 10.1002/adma.201400373

Lin, Z. H., Xie, Y., Yang, Y., Wang, S., Zhu, G., and Wang, Z. L. (2013). Enhanced triboelectric nanogenerators and triboelectric nanosensor using chemically modified TiO_2 nanomaterials. *ACS Nano* 7, 4554–4560. doi: 10.1021/nn401256w

Liu, C., and Bard, A. J. (2009). Electrons on dielectrics and contact electrification. *Chem. Phys. Lett.* 480, 145–156. doi: 10.1016/j.cplett.2009.08.045

Liu, D., Hoang, A. T., Pourrahimi, A. M., Pallon, L. K. H., Nilsson, F., Gubanski, S. M., et al. (2017). Influence of nanoparticle surface coating on electrical conductivity of LDPE/Al_2O_3 nanocomposites for HVDC cable insulations. *IEEE Trans. Dielectr. Electr. Insul.* 24, 1396–1404. doi: 10.1109/TDEI.2017.006310

Liu, J., Zeng, Z., Cao, X., Lu, G., Wang, L., Fan, Q., et al. (2012). Preparation of MoS2-Polyvinylpyrrolidone nanocomposites for flexible nonvolatile rewritable memory devices with reduced graphene oxide electrodes. *Small* 8, 3517–3522. doi: 10.1002/smll.201200999

Liu, K., Kong, B., Liu, W., Sun, Y., Song, M., Chen, J., et al. (2018). Stretchable lithium metal anode with improved mechanical and electrochemical cycling stability. *Joule* 2, 1857–1865. doi: 10.1016/j.joule.2018.06.003

Liu, R., Kuang, X., Deng, J., Wang, Y., Wang, A., Ding, W., et al. (2018b). Shape memory polymers for body motion energy harvesting and self-powered mechanosensing. *Adv. Mater.* 30:1705195. doi: 10.1002/adma.201705195

Liu, W., Chen, J., Chen, Z., Liu, K., Zhou, G., Sun, Y., et al. (2017). Stretchable lithium-ion batteries enabled by device-scaled wavy structure and elastic-sticky separator. *Adv. Energy Mater.* 7:1701076. doi: 10.1002/aenm.201701076

Liu, Y., Pharr, M., and Salvatore, G. A. (2017). Lab-on-skin: a review of flexible and stretchable electronics for wearable health monitoring. *ACS Nano* 11, 9614–9635. doi: 10.1021/acsnano.7b04898

Mao, Y., Geng, D., Liang, E., and Wang, X. (2015). Single-electrode triboelectric nanogenerator for scavenging friction energy from rolling tires. *Nano Energy* 15, 227–234. doi: 10.1016/j.nanoen.2015.04.026

Meng, K., Chen, J., Li, X., Wu, Y., Fan, W., Zhou, Z., et al. (2019). Flexible weaving constructed self-powered pressure sensor enabling continuous diagnosis of cardiovascular disease and measurement of cuffless blood pressure. *Adv. Funct. Mater.* 29:1806388. doi: 10.1002/adfm.201806388

Meng, K., Zhao, S., Zhou, Y., Wu, Y., Zhang, S., He, Q., et al. (2020). A wireless textile-based sensor system for self-powered personalized health care. *Matter* 2, 896–907. doi: 10.1016/j.matt.2019.12.025

Mizes, H. A., Conwell, E. M., and Salamida, D. P. (1990). Direct observation of ion transfer in contact charging between a metal and a polymer. *Appl. Phys. Lett.* 56, 1597–1599. doi: 10.1063/1.103139

Moghaddam, R. S., Huettner, S., Vaynzof, V., Divitini, C. D. G., Lohwasser, R. H., Musselman, K. P., et al. (2013). Polymer crystallization as a tool to pattern hybrid nanostructures: growth of 12 nm ZnO arrays in Poly(3-hexylthiophene). *Nano Lett.* 13, 4499–4504. doi: 10.1021/nl4024275

Niu, S., Liu, Y., Wang, S., Lin, L., Zhou, Y., Hu, Y., et al. (2014a). Theoretical investigation and structural optimization of single-electrode triboelectric nanogenerators. *Adv. Funct. Mater.* 24, 3332–3340. doi: 10.1002/adfm.201303799

Niu, S., Liu, Y., Wang, S., Lin, L., Zhou,. Y., Hu, Y., et al. (2013a). Theory of sliding-mode triboelectric nanogenerators. *Adv. Mater.* 25, 6184–6193. doi: 10.1002/adma.201302808

Niu, S., Wang, S., Lin, L., Liu, Y., Zhou, Y., Hu, Y., et al. (2013b). Theoretical study of contact-mode triboelectric nanogenerators as an effective power source. *Energy Environ. Sci.* 6, 3576–3583. doi: 10.1039/c3ee42571a

Niu, S., Wang, S., Liu, Y., Zhou, Y., Lin, L., Hu, Y., et al. (2014b). A Theoretical study of grating structured triboelectric nanogenerators. *Energy Environ. Sci.* 7, 2339–2349. doi: 10.1039/C4EE00498A

Niu, S., and Wang, Z. L. (2015). Theoretical systems of triboelectric nanogenerators. *Nano Energy* 14, 161–192. doi: 10.1016/j.nanoen.2014.11.034

Niu, X., Yu, J., and Wang, S. (2009). Experimental study on low-temperature waste heat thermoelectric generator. *J. Power Sources* 188, 621–626. doi: 10.1016/j.jpowsour.2008.12.067

Padbury, R. P., and Jur, J. S. (2014). Comparison of precursor infiltration into polymer thin films via atomic layer deposition and sequential vapor infiltration using *in-situ* quartz crystal microgravimetry. *J. Vac. Sci. Technol. A* 32:041602. doi: 10.1116/1.4882654

Park, C., Song, G., Cho, S. M., Chung, J., Lee, Y., Kim, E. H., et al. (2017). Supramolecular-assembled nanoporous film with switchable metal salts for a triboelectric nanogenerator. *Adv. Funct. Mater*. 27:1701367. doi: 10.1002/adfm.201701367

Peng, Q., Tseng, Y. C., Darling, S. B., and Elam, J. W. (2011). A route to nanoscopic materials via sequential infiltration synthesis on block copolymer templates. *ACS Nano* 5, 4600–4606. doi: 10.1021/nn2003234

Placke, T., Kloepsch, R., Duhnen, S., and Winter, M. A. (2017). Lithium ion, lithium metal, and alternative rechargeable battery technologies: the odyssey for high energy density. *J. Solid State Electrochem*. 21, 1939–1964. doi: 10.1007/s10008-017-3610-7

Ponrouch, A., Frontera, C., Barde, F., and Palacin, M. R. (2016). Towards a calcium-based rechargeable battery. *Nat. Mater*. 15, 169–172. doi: 10.1038/nmat4462

Pu, S., Fu, J., Liao, Y., Ge, L., Zhou, Y., Zhang, S., et al. (2020a). Promoting energy efficiency via a self-adaptive evaporative cooling hydrogel. *Adv. Mater*. 32:1907307. doi: 10.1002/adma.201907307

Pu, S., Liao, Y., Chen, K., Fu, J., Zhang, S., Ge, L., et al. (2020b). Thermogalvanic hydrogel for synchronous evaporative cooling and low-grade heat energy harvesting. *Nano Lett*. 20, 3791–3797. doi: 10.1021/acs.nanolett.0c00800

Qin, Y., Wang, X., and Wang, Z. L. (2008). Microfibre-nanowire hybrid structure for energy scavenging. *Nature* 451, 809–813. doi: 10.1038/nature06601

Rimola, A., Costa, D., Sodupe, M., Lambert, J. F., and Ugliengo, P. (2013). Silica surface features and their role in the adsorption of biomolecules: computational modeling and experiments. *Chem. Rev*. 113, 4216–4313. doi: 10.1021/cr3003054

Salis, A., and Ninham, B. W. (2014). Models and mechanisms of hofmeister effects in electrolyte solutions, and colloid and protein systems revisited. *Chem. Soc. Rev*. 43, 7358–7377. doi: 10.1039/C4CS00144C

Seneviratne, S., Hu, Y., Nguyen, T., Lan, G., Khalifa, S., and Thilakarathna, K. (2017). A survey of wearable devices and challenges. *IEEE Commun. Surv. Tut*. 19, 2573–2620. doi: 10.1109/COMST.2017.2731979

Seung, W., Gupta, M. K., Lee, K. Y., Shin, K. S., Lee, J. H., Kim, T. Y., et al. (2015). Nanopatterned textile-based wearable triboelectric nanogenerator. *ACS Nano* 9, 3501–3509. doi: 10.1021/nn507221f

Seung, W., Yoon, H. J., Kim, T. Y., Ryu, H., Kim, J., Lee, J. H., et al. (2017). Boosting power-generating performance of triboelectric nanogenerators via artificial control of ferroelectric polarization and dielectric properties. *Adv. Energy Mater*. 7:1600988. doi: 10.1002/aenm.201600988

Shin, G. H., Kim, C. K., Bang, G. S., Kim, J. Y., Jang, B. C., Koo, B. J., et al. (2016). Multilevel resistive switching nonvolatile memory based on MoS2 nanosheet-embedded graphene oxide. *2D Mater*. 3:034002. doi: 10.1088/2053-1583/3/3/034002

Shin, K.-S., Kim, T. Y., Yoon, G. C., Gupta, M. K., Kim, S. K., Seung, W., et al. (2014). Ferroelectric coupling effect on the energy-band structure of hybrid heterojunctions with self-organized P(VDF-TrFE) nanomatrices. *Adv. Mater*. 26, 5619–5625. doi: 10.1002/adma.201400405

Shin, S. H., Bae, Y. E., Moon, H. K., Kim, J., Choi, S. H., Kim, Y., et al. (2017). Formation of triboelectric series via atomic-level surface functionalization for triboelectric energy harvesting. *ACS Nano* 11, 6131–6138. doi: 10.1021/acsnano.7b02156

Shin, S. H., and Kwon, Y. H. (2015). Triboelectric charging sequence induced by surface functionalization as a method to fabricate high performance triboelectric generators. *ACS Nano* 9, 4621–4627. doi: 10.1021/acsnano.5b01340

Slater, M. D., Kim, D. H., Lee, E., and Johnson, C. S. (2013). Sodium-ion batteries. *Adv. Funct. Mater*. 23, 947–958. doi: 10.1002/adfm.201200691

Song, G., Kim, Y., Yu, S., Kim, M. O., Park, S. H., Cho, S. M., et al. (2015). Molecularly engineered surface triboelectric nanogenerator by self-assembled monolayers (METS). *Chem. Mater*. 27, 4749–4755. doi: 10.1021/acs.chemmater.5b01507

Stachewicz, U., Stone, C. A., Willis, C. R., and Barber, A. H. (2012). Charge assisted tailoring of chemical functionality at electrospun nanofiber surfaces. *J. Mater. Chem*. 22, 22935–22941. doi: 10.1039/c2jm33807f

Stephen, N. G. (2006). On energy harvesting from ambient vibration. *J. Sound Vibr*. 293, 409–425. doi: 10.1016/j.jsv.2005.10.003

Su, H., Huang, H., Zhang, H., Chu, X., Zhang, B., Gu, B., et al. (2018). *In situ* direct method to massively prepare hydrophilic porous carbide-derived carbons for high-performance supercapacitors. *ACS Appl. Energy Mater*. 1, 3544–3553. doi: 10.1021/acsaem.8b00764

Su, H., Huang, H., Zhao, S., Zhou, Y., Xu, S., Pan, H., et al. (2020). Understanding the ion-sorption dynamics in functionalized porous carbons for enhanced capacitive energy storage. *ACS Appl. Mater. Interfaces* 12, 2773–2782. doi: 10.1021/acsami.9b15781

Su, Y., Wang, J., Wang, B., Yang, T., Yang, B., Xie, G., et al. (2020a). Alveolus-inspired active membrane sensors for self-powered wearable chemical sensing and breath analysis. *ACS Nano* 14, 6067–6075. doi: 10.1021/acsnano.0c01804

Su, Y., Wen, X., Zhu, G., Yang, J., Chen, J., Bai, P., et al. (2014a). Hybrid triboelectric nanogenerator for harvesting water wave energy and as a self-powered distress signal emitter. *Nano Energy* 2014, 186–195. doi: 10.1016/j.nanoen.2014.07.006

Su, Y., Yang, T., Zhao, X., Cai, Z., Chen, G., Yao, M., et al. (2020b). A wireless energy transmission enabled wearable active acetone biosensor for non-invasive prediabetes diagnosis. *Nano Energy* 74:104941. doi: 10.1016/j.nanoen.2020.104941

Su, Y., Zhu, G., Yang, W., Yang, J., Chen, J., Jing, Q., et al. (2014b). Triboelectric sensor for self-powered tracking of object motion inside tubing. *ACS Nano* 8, 3843–3850. doi: 10.1021/nn500695q

Sun, C., Shi, J., Bayerl, D. J., and Wang, X. (2011). PVDF microbelts for harvesting energy from respiration. *Energy Environ. Sci*. 4, 4508–4512. doi: 10.1039/c1ee02241e

Trung, T. Q., and Lee, N. E. (2016). Flexible and stretchable physical sensor integrated platforms for wearable human-activity monitoringand personal healthcare. *Adv. Mater*. 28, 4338–4372. doi: 10.1002/adma.201504244

Ulman, A. (1996). Formation and structure of self-assembled monolayers. *Chem. Rev*. 96, 1533–1554. doi: 10.1021/cr9502357

Wan, J., Xie, J., Kong, X., Liu, Z., Liu, K., Shi, F., et al. (2019). Ultrathin, flexible, solid polymer composite electrolyte enabled with aligned nanoporous host for lithium batteries. *Nat. Nanotechnol*. 14, 705–711. doi: 10.1038/s41565-019-0465-3

Wang, B., Zhong, J., Zhong, Z., Wu, N., Cheng, X., Li, W., et al. (2016). Sandwiched composite fluorocarbon film for flexible electret generator. *Adv. Electron. Mater*. 2:1500408. doi: 10.1002/aelm.201500408

Wang, C., Yang, T., Xiao, J., Liu, S., Xue, J., Wang, J., et al. (2015). Irradiation-induced structural transitions in Ti2AlC. *Acta Mater*. 98, 197–205. doi: 10.1016/j.actamat.2015.07.043

Wang, H. S., Jeong, C. K., Seo, M. H., Joe, D. J., Han, J. H., Yoon, J. B., et al. (2017). Performance enhanced triboelectric nanogenerator enabled by wafer-scale nanograts of multistep pattern downscaling. *Nano Energy* 35, 415–423. doi: 10.1016/j.nanoen.2017.04.012

Wang, Q., Bowen, C. R., Lewis, R., Chen, J., Lei, W., Zhang, H., et al. (2019). Hexagonal boron nitride nanosheets doped pyroelectric ceramic composite for high-performance thermal energy harvesting. *Nano Energy* 60, 144–152. doi: 10.1016/j.nanoen.2019.03.037

Wang, S., Lin, L., and Wang, Z. L. (2012). Nanoscale triboelectric-effect-enabled energy conversion for sustainably powering portable electronics. *Nano Lett*. 12, 6339–6346. doi: 10.1021/nl303573d

Wang, S., Lin, L., and Wang, Z. L. (2015). Triboelectric nanogenerators as self-powered active sensors. *Nano Energy* 11, 436–462. doi: 10.1016/j.nanoen.2014.10.034

Wang, S., Lin, L., Xie, Y., Jing, Q., Niu, S., and Wang, Z. L. (2013). Sliding-triboelectric nanogenerators based on in-plane charge-separation mechanism. *Nano Lett*. 13, 2226–2233. doi: 10.1021/nl400738p

Wang, S., Xie, Y., Niu, S., Lin, L., Liu, C., Zhou, Y., et al. (2014). Maximum surface charge density for triboelectric nanogenerators achieved by ionized-air injection: methodology and theoretical understanding. *Adv. Mater*. 26, 6720–6728. doi: 10.1002/adma.201402491

Wang, S., Zi, Y., Zhou, Y., Li, S., Fan, F., Lin, L., et al. (2016). Molecular surface functionalization to enhance the power output of triboelectric nanogenerators. *J. Mater. Chem. A* 4, 3728–3734. doi: 10.1039/C5TA10239A

Wang, X., Song, J., Liu, J., and Wang, Z. L. (2007). Direct-current nanogenerator driven by ultrasonic waves. *Science* 316, 102–105. doi: 10.1126/science.1139366

Wang, Z. L. (2013). Triboelectric nanogenerators as new energy technology for self-powered systems and as active mechanical and chemical sensors. *ACS Nano* 7, 9533–9557. doi: 10.1021/nn404614z

Wang, Z. L. (2014). Triboelectric nanogenerators as new energy technology and self-powered sensors-principles, problems and perspectives. *Faraday Discuss*. 176, 447–458. doi: 10.1039/C4FD00159A

Wang, Z. L. (2019). Entropy theory of distributed energy for internet of things. *Nano Energy* 58, 669–672. doi: 10.1016/j.nanoen.2019.02.012

Wang, Z. L., Chen, J., and Lin, L. (2015). Progress in triboelectric nanogenerators as a new energy technology and self-powered sensors. *Energy Environ. Sci*. 8, 2250–2282. doi: 10.1039/C5EE01532D

Wang, Z. L., Lin, L., Chen, J., Niu, S., and Zi, Y. (2016). "Self-powered sensing for human-machine interface," in *Green Energy and Technology* (Cham: Springer) 401–429. doi: 10.1007/978-3-319-40039-6_14

Wen, Z., Chen, J., Yeh, M. H., Guo, H., Li, Z., Fan, X., et al. (2015). Blow-driven triboelectric nanogenerator as an active alcohol breath analyzer. *Nano Energy* 16, 38–46. doi: 10.1016/j.nanoen.2015.06.006

Wilson, C. A., Grubbs, R. K., and George, S. M. (2005). Nucleation and growth during Al2O3 atomic layer deposition on polymers. *Chem. Mater.* 17, 5625–5634. doi: 10.1021/cm050704d

Wolters, D. R., and van der Schoot, J. J. (1985). Kinetics of charge trapping in dielectrics. *J. Appl. Phys*. 58:831. doi: 10.1063/1.336152

Wu, C., Kim, T. W., Park, J. H., An, H., Shao, J., Chen, X., et al. (2017). Enhanced triboelectric nanogenerators based on MoS_2 monolayer nanocomposites acting as electron-acceptor layers. *ACS Nano* 11, 8356–8363. doi: 10.1021/acsnano.7b03657

Wu, C., Li, F., Zhang, Y., Guo, T., and Chen, T. (2011). Highly reproducible memory effect of organic multilevel resistive-switch device utilizing graphene oxide sheets/polyimide hybrid nanocomposite. *Appl. Phys. Lett*. 99:042108. doi: 10.1063/1.3619815

Wu, J., Chang, C., and Chang, Y. (2016). High-output current density of the triboelectric nanogenerator made from recycling rice husks. *Nano Energy* 19, 39–47. doi: 10.1016/j.nanoen.2015.11.014

Wu, L., Chure, M. C., Wu, K., Chang, W., Yang, M., Liu, W., et al. (2009). Dielectric properties of barium titanate ceramics with different materials powder size. *Ceram. Int.* 35, 957–960. doi: 10.1016/j.ceramint.2008.04.030

Wu, Y., Jing, Q., Chen, J., Bai, P., Bai, J., Zhu, G., et al. (2015). A self-powered angle measurement sensor based on triboelectric nanogenerator. *Adv. Funct. Mater*. 25, 2166–2174. doi: 10.1002/adfm.201403828

Xu, G., Yu, W., Griffith, D., Golmie, N., and Moulema, P. (2017). Toward integrating distributed energy resources and storage devices in smart grid. *IEEE Internet Things J*. 4, 192–204. doi: 10.1109/JIOT.2016.2640563

Xu, S., Liang, X., Wu, X., Zhao, S., Chen, J., Wang, K., et al. (2019). Multistaged discharge constructing heterostructure with enhanced solid-solution behavior for long-life lithium-oxygen batteries. *Nat. Commun*. 10:5810. doi: 10.1038/s41467-019-13712-2

Yabuuchi, N., Kubota, K., Dahbi, M., and Komaba, S. (2014). Research development on sodium ion batteries. *Chem. Rev*. 114, 11636–11682. doi: 10.1021/cr500192f

Yan, C., Deng, W., Jin, L., Yang, T., Wang, Z., Chu, X., et al. (2018). Epidermis-inspired ultrathin 3D cellular sensor array for self-powered biomedical monitoring. *ACS Appl. Mater. Interfaces* 10, 41070–41075. doi: 10.1021/acsami.8b14514

Yan, C., Gao, Y., Zhao, S., Zhang, S., Zhou, Y., Deng, W., et al. (2020). A linear-to-rotary hybrid nanogenerator for high-performance wearable biomechanical energy harvesting. *Nano Energy* 67:104235. doi: 10.1016/j.nanoen.2019.104235

Yang, J., Chen, J., Liu, Y., Yang, W., Su, Y., and Wang, Z. L. (2014a). Triboelectrification-based organic film nanogenerator for acoustic energy harvesting and self-powered active acoustic sensing. *ACS Nano* 8, 2649–2657. doi: 10.1021/nn4063616

Yang, J., Chen, J., Su, Y., Jing, Q., Li, Z., Yi, F., et al. (2015). Eardrum-inspired active sensors for self-powered cardiovascular system characterization and throat-attached anti-interference voice recognition. *Adv. Mater*. 27, 1316–1326. doi: 10.1002/adma.201404794

Yang, J., Chen, J., Yang, Y., Zhang, H., Yang, W., Bai, P., et al. (2014b). Broadband vibrational energy harvesting based on a triboelectric nanogenerator. *Adv. Energy Mater*. 4:1301322. doi: 10.1002/aenm.201301322

Yang, W., Chen, J., Jing, Q., Yang, J., Wen, X., Su, Y., et al. (2014a). 3D stack integrated triboelectric nanogenerator for harvesting vibration energy. *Adv. Funct. Mater*. 24, 4090–4096. doi: 10.1002/adfm.201304211

Yang, W., Chen, J., Wen, X., Jing, Q., Yang, J., Su, Y., et al. (2014b). Triboelectrification based motion sensor for human-machine interfacing. *ACS Appl. Mater. Interfaces*. 6, 7479–7484. doi: 10.1021/am500864t

Yang, W., Chen, J., Zhu, G., Yang, J., Bai, P., Su, Y., et al. (2013). Harvesting energy from the natural vibration of human walking. *ACS Nano*7, 11317–11324. doi: 10.1021/nn405175z

Yang, Y., Zhang, H., Chen, J., Jing, Q., Zhou, Y., Wen, X., et al. (2013a). Single-electrode based sliding triboelectric nanogenerator for self-powered displacement vector sensor system. *ACS Nano* 7, 7342–7351. doi: 10.1021/nn403021m

Yang, Y., Zhang, H., Lin, Z., Liu, Y., Chen, J., Lin, Z., et al. (2013b). A hybrid energy cell for self-powered water splitting. *Energy Environ. Sci*. 6, 2429–2434. doi: 10.1039/c3ee41485j

Yang, Y., Zhang, H., Lin, Z., Zhou, Y., Jing, Q., Su, Y., et al. (2013c). Human skin based triboelectric nanogenerators for harvesting biomechanical energy and as self-powered active tactile sensor system. *ACS Nano* 7, 9213–9222. doi: 10.1021/nn403838y

Yang, Y., Zhu, G., Zhang, H., Chen, J., Zhong, X., Lin, Z., et al. (2013d). Triboelectric nanogenerator for harvesting wind energy and as self-powered wind vector sensor system. *ACS Nano* 7, 9461–9468. doi: 10.1021/nn4043157

Yao, C., Yin, X., Yu, Y., Cai, Z., and Wang, X. (2017). Chemically functionalized natural cellulose materials for effective triboelectric nanogenerator development. *Adv. Funct. Mater*. 27, 1700794. doi: 10.1002/adfm.201700794

Yi, F., Lin, L., Niu, S., Yang, P. K., Wang, Z., Chen, J., et al. (2015). Stretchable-rubber-based triboelectric nanogenerator and its application as self-powered body motion sensors. *Adv. Funct. Mater*. 25, 3688–3696. doi: 10.1002/adfm.201500428

Yu, Y., Li, Z., Wang, Y., Gong, S., and Wang, X. (2015). Sequential infiltration synthesis of doped polymer films with tunable electrical properties for efficient triboelectric nanogenerator development. *Adv. Mater*. 27, 4938–4944. doi: 10.1002/adma.201502546

Yun, B. K., Kim, J. W., Kim, H. S., Jung, K. W., Yi, Y., Jeong, M. S., et al. (2015). Base-treated polydimethylsiloxane surfaces as enhanced triboelectric nanogenerators. *Nano Energy* 15, 523–529. doi: 10.1016/j.nanoen.2015.05.018

Zan, G., Wu, T., Hu, P., Zhou, Y., Zhao, S., Xu, S., et al. (2020). An approaching theoretical-capacity anode material for aqueous battery: hollow hexagonal prism Bi_2O_3 assembled by nanoparticles. *Energy Stor. Mater*. 28, 82–90. doi: 10.1016/j.ensm.2020.02.027

Zang, Y., Zhang, F., Di, C., and Zhu, D. (2015). Advances of flexible pressure sensors toward artificial intelligence and health care applications. *Mater. Horiz*. 2, 140–156. doi: 10.1039/C4MH00147H

Zenkiewicz, M., Zuk, T., and Markiewicz, E. (2015). Triboelectric series and electrostatic separation of some biopolymers. *Polym. Test*. 42, 192–198. doi: 10.1016/j.polymertesting.2015.01.009

Zhang, B., Chen, J., Jin, L., Deng, W., Zhang, L., Zhang, H., et al. (2016). Rotating-disk-based hybridized electromagnetic-triboelectric nanogenerator for sustainably powering wireless traffic volume sensors. *ACS Nano* 10, 6241–6247. doi: 10.1021/acsnano.6b02384

Zhang, H., Yang, Y., Su, Y., Chen, J., Adams, K., Lee, S., et al. (2014). Triboelectric nanogenerator for harvesting vibration energy in full space and as self-powered acceleration sensor. *Adv. Funct. Mater*. 24, 1401–1407. doi: 10.1002/adfm.201302453

Zhang, L., Zhang, B., Chen, J., Jin, L., Deng, W., Tang, J., et al. (2016). Lawn structured triboelectric nanogenerators for scavenging sweeping wind energy on rooftops. *Adv. Mater*. 28, 1650–1656. doi: 10.1002/adma.201504462

Zhang, N., Huang, F., Zhao, S., Lv, X., Zhou, Y., Xiang, S., et al. (2020). Photo-rechargeable fabrics as sustainable and robust power sources for wearable bioelectronics. *Matter* 2, 1260–1269. doi: 10.1016/j.matt.2020.01.022

Zhang, N., Tao, C., Fan, X., and Chen, J. (2017). Progress in triboelectric nanogenerators as self-powered smart sensors. *J. Mater. Res*. 32, 1628–1646. doi: 10.1557/jmr.2017.162

Zhang, X., Han, M., Meng, B., and Zhang, X. (2015). High performance triboelectric nanogenerators based on large-scale mass-fabrication technologies. *Nano Energy* 11, 304–322. doi: 10.1016/j.nanoen.2014.11.012

Zhang, X., Han, M., Wang, R., Meng, B., Zhu, F., Sun, X., et al. (2014). High-performance triboelectric nanogenerator with enhanced energy density based on single-step fluorocarbon plasma treatment. *Nano Energy* 4, 123–131. doi: 10.1016/j.nanoen.2013.12.016

Zhang, X., Han, M., Wang, R., Zhu, F., Li, Z., Wang, W., et al. (2013). Frequency-multiplication high-output triboelectric nanogenerator for sustainably powering biomedical microsystems. *Nano Lett*. 13, 1168–1172. doi: 10.1021/nl3045684

Zhao, G., Yang, J., Chen, J., Zhu, G., Jiang, Z., Liu, X., et al. (2019). Keystroke dynamics identification based on triboelectric nanogenerator for intelligent keyboard using deep learning method. *Adv. Mater. Technol*. 4:1800167. doi: 10.1002/admt.201800167

Zhao, X. J., Zhu, G., and Wang, Z. L. (2015). Coplanar induction enabled by asymmetric permittivity of dielectric materials for mechanical energy conversion. *ACS Appl. Mater. Interfaces* 7, 6025–6029. doi: 10.1021/acsami.5b00019

Zheng, L., Cheng, G., Chen, J., Lin, L., Wang, J., Liu, Y., et al. (2015). A hybridized power panel to simultaneously generate electricity from sunlight, raindrops, and wind around the clock. *Adv. Energy Mater*. 5:1501152. doi: 10.1002/aenm.201501152

Zheng, L., Lin, Z., Cheng, G., Wu, W., Wen, X., Lee, S., et al. (2014). Silicon-based hybrid cell for harvesting solar energy and raindrop electrostatic energy. *Nano Energy* 9, 291–300. doi: 10.1016/j.nanoen.2014.07.024

Zheng, Q., Shi, B., Fan, F., Wang, X., Yan, L., Yuan, W., et al. (2014). *In vivo* powering of pacemaker by breathing driven implanted triboelectric nanogenerator. *Adv. Mater*. 26, 5851–5856. doi: 10.1002/adma.201402064

Zhong, Q., Zhong, J., Cheng, X., Yao, X., Wang, B., Li, W., et al. (2015). Paper-based active tactile sensor array. *Adv. Mater*. 27, 7130–7136. doi: 10.1002/adma.201502470

Zhou, Y., Deng, W., Xu, J., and Chen, J. (2020). Engineering materials at the nanoscale for triboelectric nanogenerators. *Cell Rep. Phys. Sci*. 1:100142. doi: 10.1016/j.xcrp.2020.100142

Zhou, Z., Chen, K., Li, X., Zhang, S., Wu, Y., Zhou, Y., et al. (2020a). Sign-to-speech translation using machine-learning-assisted stretchable sensor arrays. *Nat. Electron*. 3, 571–578. doi: 10.1038/s41928-020-0428-6

Zhou, Z., Padgett, S., Cai, A., Conta, G., Wu, Y., He, Q., et al. (2020b). Single-layered ultra-soft washable smart textiles for all-around ballistocardiograph, respiration, and posture monitoring during sleep. *Biosens. Bioelectron*. 155:12064. doi: 10.1016/j.bios.2020.112064

Zhu, G., Bai, P., Chen, J., and Wang, Z. L. (2013a). Power-generating shoe insole based on triboelectric nanogenerators for self-powered consumer electronics. *Nano Energy* 2, 688–692. doi: 10.1016/j.nanoen.2013.08.002

Zhu, G., Chen, J., Zhang, T., Jing, Q., and Wang, Z. L. (2014c). Radial-arrayed rotary electrification for high performance triboelectric generator. *Nat. Commun*. 5:3426. doi: 10.1038/ncomms4426

Zhu, G., Lin, Z., Jing, Q., Bai, P., Pan, C., Yang, Y., et al. (2013b). Toward large-scale energy harvesting by a nanoparticle-enhanced triboelectric nanogenerator. *Nano Lett*. 13, 847–853. doi: 10.1021/nl4001053

Zhu, G., Peng, B., Chen, J., Jing, Q., and Wang, Z. L. (2015). Triboelectric nanogenerators as a new energy technology: From fundamentals, devices, to applications. *Nano Energy* 14, 126–138. doi: 10.1016/j.nanoen.2014.11.050

Zhu, G., Su, Y., Bai, P., Chen, J., Jing, Q., Yang, W., et al. (2014a). Harvesting water wave energy by asymmetric screening of electrostatic charges on a nanostructured hydrophobic thin-film surface. *ACS Nano* 8, 6031–6037. doi: 10.1021/nn5012732

Zhu, G., Yang, W., Zhang, T., Jing, Q., Chen, J., Zhou, Y., et al. (2014b). Self-powered, ultrasensitive, flexible tactile sensors based on contact electrification. *Nano Lett*. 14, 3208–3213. doi: 10.1021/nl5005652

Zi, Y., Lin, L., Wang, J., Wang, S., Chen, J., Fan, X., et al. (2015a). Triboelectric-pyroelectric-piezoelectric hybrid cell for high-efficiency energy-harvesting and self-powered sensing. *Adv. Mater*. 27, 2340–2347. doi: 10.1002/adma.201500121

Zi, Y., Niu, S., Wang, J., Wen, Z., Tang, W., and Wang, Z. L. (2015b). Standards and figure-of-merits for quantifying the performance of triboelectric nanogenerators. *Nat. Commun*. 6:8376. doi: 10.1038/ncomms9376

Zou, H., Chen, J., Fang, Y., Ding, J., Peng, W., and Liu, R. (2016). A dual-electrolyte based air-breathing regenerative microfluidic fuel cell with 1.76V open-circuit-voltage and 0.74V water-splitting voltage. *Nano Energy* 27, 619–626. doi: 10.1016/j.nanoen.2016.07.036

Zou, Y., Raveendran, V., and Chen, J. (2020). Wearable triboelectric nanogenerators for biomechanical energy harvesting. *Nano Energy* 77:105303. doi: 10.1016/j.nanoen.2020.105303

Conflict of Interest: The authors declare that the research was conducted in the absence of any commercial or financial relationships that could be construed as a potential conflict of interest.

Copyright © 2020 Xu, Zou, Nashalian and Chen. This is an open-access article distributed under the terms of the Creative Commons Attribution License (CC BY). The use, distribution or reproduction in other forums is permitted, provided the original author(s) and the copyright owner(s) are credited and that the original publication in this journal is cited, in accordance with accepted academic practice. No use, distribution or reproduction is permitted which does not comply with these terms.

frontiers in Chemistry

ORIGINAL RESEARCH
published: 03 December 2020
doi: 10.3389/fchem.2020.597980

Influence of Solvents' Polarity on the Physicochemical Properties and Photocatalytic Activity of Titania Synthesized Using *Deinbollia pinnata* Leaves

Yakubu Rufai[1,2], *Sheela Chandren*[1,3]* and *Norazah Basar*[1]

[1] Department of Chemistry, Faculty of Science, Universiti Teknologi Malaysia, Johor Bahru, Malaysia, [2] Department of Chemistry, Federal College of Education (FCE), Okene, Nigeria, [3] Centre for Sustainable Nanomaterials, Ibnu Sina Institute for Scientific and Industrial Research, Universiti Teknologi Malaysia, Johor Bahru, Malaysia

Nanotechnology is one of the most interesting areas of research due to its flexibility to improve or form new products from nanoparticles (NPs), and as a fast, greener, more eco-friendly and sustainable solution to technological and environmental challenges. Among metal oxides of photocatalytic performance, the use of titania (TiO_2) as photocatalyst is most popular due to its unique optical and electronic properties. Despite the wide utilization, the synthesis of TiO_2 NPs bears many disadvantages: it utilizes various less environmental-friendly chemicals, high cost, requires high pressure and energy, and potentially hazardous physical and chemical methods. Hence, the development of green synthesis approach with eco-friendly natural products can be used to overcome these adverse effects. In this work, TiO_2 NPs have been prepared by using *Deinbollia pinnata* leaves extracts, obtained by different solvents (*n*-hexane, ethyl acetate, and ethanol) with different polarities. The extracts acted as the reducing agent, while titanium isopropoxide as the precursor and water as the solvent. X-ray diffraction (XRD) pattern confirmed the synthesized TiO_2 consist of anatase phase in high purity, with average crystallite size in the range of 19–21 nm. Characterization by using field emission scanning electron microscopy (FESEM) showed the TiO_2 NPs possess a uniform semi-spherical shape in the size range of 33–48 nm. The energy dispersive X-ray (EDX) spectra of green TiO_2 NPs showed two peaks for the main elements of Ti (61 Wt.%) and O (35 Wt.%). The band-gap energy of 3.2 eV was determined using UV-Vis spectroscopy. From the nitrogen sorption analysis, type V isotherm of the material was obtained, with BET surface area of 31.77 m^2/g. The photocatalytic activity of synthesized TiO_2 was evaluated for photodegradation of methyl orange (MO) under UV light irradiation. Based on the results, it is shown that TiO_2 NPs synthesized with *D. pinnata* leaves extracted using ethyl acetate showed the most effective photodegradation performance, achieving 98.7% of MO conversion within 150 min. It can be concluded that the use of plant extracts in synthesis with TiO_2 managed to produce highly crystalline anatase TiO_2 with superior photocatalytic activity in the photodegradation of organic dye.

Keywords: TiO_2, green synthesis, *Deinbollia pinnata*, solvents polarities, methyl orange, photodegradation

OPEN ACCESS

Edited by:
Chun Xu,
The University of Queensland, Australia

Reviewed by:
K. M. Garadkar,
Shivaji University, India
Vincenzo Vaiano,
University of Salerno, Italy

****Correspondence:***
Sheela Chandren
sheela@utm.my

Specialty section:
This article was submitted to Catalysis and Photocatalysis, a section of the journal Frontiers in Chemistry

Received: *23 August 2020*
Accepted: *09 November 2020*
Published: *03 December 2020*

Citation:
Rufai Y, Chandren S and Basar N (2020) Influence of Solvents' Polarity on the Physicochemical Properties and Photocatalytic Activity of Titania Synthesized Using Deinbollia pinnata Leaves. Front. Chem. 8:597980. doi: 10.3389/fchem.2020.597980

INTRODUCTION

The nature of nanostructured materials has prompted natural product researchers' attention to this field. The naturally occurring oxide of titanium (IV) oxide or titania (TiO_2) possesses unique optical and electronic properties (Ahmad et al., 2019). The surface chemistry of nanostructures in terms of smaller size and uniqueness have already been utilized in medicine, nutrition, energy (Venugopal et al., 2017; Agarwal et al., 2018; Kim et al., 2018) and in the biosynthesis of TiO_2 NPs with metabolites present in plants extract to reduce and stabilize bulk metal into elemental forms (Mohamad et al., 2014). Plants are a major segment of biodiversity affected by many living and non-living components with their medicinal values. This is due to the presence of certain chemicals/active ingredients used for the treatment of disorders, with low cost, eco-friendliness and easy availability in the forest (Patel, 2015). Stable biological NPs are achieved with appropriate choice of solvents polarity for plant extraction (reducing agents) and as toxic-free material (Raghad et al., 2016). Fungi, actinomycetes, bacteria, and plant extracts (Órdenes-Aenishanslins et al., 2014) have replaced chemical agents in the green synthesis materials. Furthermore, the usage of these materials can enhance the photocatalytic and pharmacological properties of the NPs produced. Bio-mediated TiO_2 NPs have also been obtained from the extracts of *Morinda citrifolia L.* (Sundrarajan et al., 2017), *Tamarindus indica* (Hiremath et al., 2018); and *Azadirachta indica* (Thakur et al., 2019). The roots and leaves of *D. pinnata* are used in folkloric medicine as remedy for febrifuge, analgesic, bronchiasis intercostals, intestinal pains, jaundice, cough, asthma, and infections (Sotubo et al., 2016). Leaf extracts are used in fetus positioning during child birth (Kankara et al., 2015). The root act as an antibacterial agent (Sotubo et al., 2016).

Various synthesis methods of TiO_2 NPs are available, such as solution combustion (Kitamura et al., 2007), sol-gel (Elbushra et al., 2018), hydrothermal (Bregadiolli et al., 2017), solvothermal (Dinh et al., 2012), microwave-assisted (May-Masnou et al., 2018), co-precipitation (Rab et al., 2018), and chemical vapor deposition (Lee et al., 2011). However, the sol-gel process clearly stood out due to the lower processing temperature ($<100°C$), which can produce highly crystalline particles with small sizes and high surface area. In addition, this method is also low in cost and can give fast composition homogeneity.

Dyes are major coloring agents used in industries for precious stones, paper, leather, plastic, textile, and food production. Hazardous waste water from dyeing process act as a major contaminant to the environment (Murugan and Parimelazhagan, 2014; Hejazi et al., 2020). The dye effluents are usually non-biodegradable, highly oxidizing, and stable to heat and light (Khataee and Mirzajani, 2010; Khataee et al., 2010) which attributed to their toxicity, undesirable aesthetic, and carcinogenicity (Khalik et al., 2017). This is due to their diversity and complex structure (Benkhaya et al., 2017), which need to be degraded. One example is methyl orange (MO), which is a commonly used dye.

Methyl orange dyes are stable under visible light, which can be easily degraded in the presence of catalyst (Chiu et al., 2019). It is known to cause irritation to reproductive, excretory, respiratory. and central nervous systems when in contact or consumed (Parida et al., 2013; Ljubas et al., 2015). Among all other methods to overcome its environmental hazard, photocatalysis has been proven effective for its degradation and removal of azo dyes in a less harmful (greener) method (Guettaï and Ait Amar, 2005). This present work focuses on the sol-gel green synthesis of TiO_2 NPs using *D. pinnata* plant extracts obtained by different solvents with different polarities (*n*-hexane, ethyl acetate, and methanol). Their multi-functional group in the ethyl acetate crude extracts were characterized by Fourier transform infrared (FTIR) spectroscopy. The TiO_2 NPs obtained were then characterized using X-ray diffraction (XRD), field emission scanning electron microscopy (FESEM), the energy dispersive X-ray (EDX), ultraviolet-visible light analysis (UV-Visible), nitrogen sorption analysis (N_2 sorption), and photoluminescence analysis (PL). Following that, the photocatalytic activity of the synthesized TiO_2 NPs was evaluated for the photocatalytic degradation of MO under UV light irradiation. This current work further shows the potential of utilizing plants extract in multi-fold directions, but such as in the case of biosynthesis.

EXPERIMENTAL

Materials

The materials used in this research were titanium isopropoxide (TTIP), $C_{12}H_{28}O_4Ti$ [Aldrich (97%)], methyl orange (MO) $C_{14}H_{14}N_3NaO_3S$ [Aldrich (85%)], absolute ethanol (EtOH) C_2H_6O [MERK (100%)]. All materials were used as-received without further purification. Deionized water (MQ-H_2O) was used throughout the experiments. Mettler H10, photoreactor chamber, membrane filter, syringe, centrifuge, UV lamp 1,200 W, glass beaker, cuvette, aluminum foil, and glass petri-dish were used as the apparatus in this work.

The *D. pinnata* (Poir.) Schumach. and Thonn leaves were collected from Okehi Local Government Area of Kogi State, Nigeria during dry season, early January, for 1 week (daytime temperature ranges from 28°C in January to 32°C). The plant was identified and confirmed at the Biological Department, Federal College of Education Okene Kogi State by Mrs. Aniama S.O.A., a botanist. The plant material was authenticated at Forestry Research Institute of Nigeria Ibadan through comparison with voucher specimen under accession number of FHI 3251. The leaves were collected, washed and air dried at room temperature for 1 month.

Extraction

Powdered plant material of *D. pinnata* (Poir.) Schumach. and Thonn was extracted using sonication method as shown in **Figure 1**. Briefly, the leaf samples were placed into several conical flasks (30 g each) and extracted with organic solvents (150 mL), which were *n*-hexane, ethyl acetate, and methanol, in a sonicator using ultrasonic-assisted extraction method for 10 min with agitation. This method utilizes the following software conditions of time, temperature, and solvent ratio. Upon completion, the samples were filtered into bottles and allowed to settle for 24 h.

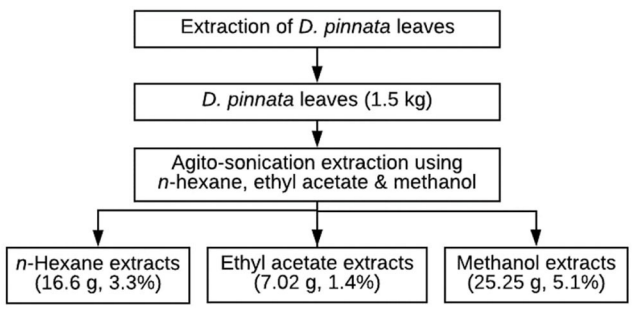

FIGURE 1 | Extraction steps of *D. pinnata* leaves.

The combined filtrates were then concentrated in *vacuo* at 40°C using a rotary evaporator.

Qualitative Phytochemical Screening of Extract

The *D. pinnata* ethyl acetate extract was subjected to chemical tests for the identification of their active constituents. The chemical tests were performed using the methods reported by Samkeliso et al. (2018).

Test for Phenols

Five percent ferric chloride was added to 2 mL of the leaf extract, which will show black coloration. This indicates the presence of phenols.

Test for Flavonoids

Ten milliliters of ethyl acetate was added to the leaf extract and the test tube containing this mixture was heated in the water bath. One milliliter of diluted ammonia was added to this mixture, which will give yellow color, showing the presence of flavonoids.

Test for Alkaloids (Mayer's Test)

Mayer's test reagent was added to 2 mL of the leaf extract, which will then give cream colored precipitation, indicating the presence of alkaloids.

Test for Steroids

Two milliliters of concentrated H_2SO_4 was added to 1 mL of the extract. Following that, 2 mL of acetic anhydride was added. The change in the color of extract from violet to blue or green will take place if steroids are present.

Test for Coumarins

Ten percent of the NaOH was added to the extract and chloroform was added. Formation of yellow color will show the presence of coumarin.

Synthesis of Green TiO_2 NPs

The synthesis was carried out using the sol-gel method, where titanium (IV) isopropoxide (TTIP) was utilized as the precursor, *D. pinnata* extracts [1 g/5 mL] and deionized (DI) water as the medium. TiO_2 NP_S were prepared by dissolving 4 mL TTIP with 20 mL of DI water under constant stirring for 30 min at 30°C. This was followed by the gradual addition of 0.2 g/mL of *DP* extracts (either by *n*-hexane, ethyl acetate, or ethanol) with constant stirring at 50°C for 4 h before kept at room condition for 48 h of aging process. The resulting colloidal suspension was washed with ethanol and centrifuged three times at 10,000 rpm for 30 min. The samples were then dried at 95°C for 24 h in an oven, before being calcined at 500°C in a muffle furnace for 5 h. The calcined TiO_2 NPs powder was further characterized spectroscopically.

Characterizations of Green TiO_2 NPs

The crystallinity of the synthesized TiO_2 NPs were performed by Rigaku Smart Lab, Germany with Cu Kα radiation (λ = 1.5418 Å) operated at 40 kV and 30 mA. The diffraction pattern was scanned in the 2θ range of 20–90°. The morphological features and surface characteristics of the photocatalyst were characterized using field emission scanning electron microscopy (FESEM) (JEOL JSM 6710F) equipped with EDX, at an accelerating voltage of 0.5–30 kV to determine the surface chemical element contents of the photocatalysts. The band gap energy of the TiO_2 NPs were determined using UV-Vis near-IR (UV-Vis-NIR) spectrophometer (Shimadzu UV-3600 Plus UV-VIS-NIR). The spectra were recorded in the range of 300–500 nm at temperature rate/hold/time of 10:1,000:1.The specific surface area, micropore and pore size distribution of the TiO_2 NPs were obtained using a multipoint Brunauer–Emmett–Teller (BET) analysis through the measurement of nitrogen adsorption–desorption isotherm as a function of relative pressure from a Quantachrome NOVA-4LX firmware with helium gas, and ambient temperature of 30.06°C. The thermal stability and heat flow were examined using thermogravimetric-differential scanning calorimetry analyzer (TGA-DSC, SHIMADZU DTG-60H). The scanning was performed within the furnace temperature range of 20–800°C with a heating rate and air flow rate of 10°C min^{-1} and 20 mL min^{-1}, respectively. The electrons-holes recombination's of the photocatalysts through discrete electronic states were analyzed by Photoluminescence (Horiba-fluoroMax-4C spectrofluorometer) with emission of full spectrum range between 400 and 800 nm. The chemical functional groups were detected by Fourier transform infrared spectroscopy (1600 FT-IR). The spectra were recorded in the range of 400–4,000 cm^{-1} using PerkinElmer Spectrum One Spectrometer.

Photocatalytic Testing

The photocatalytic activity of the green TiO_2 NPs was tested out in the degradation of methyl orange (MO, Aldrich 85%) using a 1,200 W lamp UV light source spaced at 3 cm horizontally. Prior to the test the stock solution of the water-based MO was prepared at 1,000 ppm in 100 mL and allowed to stand for 24 h. This was then followed by serial dilutions of 5, 10, 15, 20, 25, and 30 ppm. Five dilutions were used for the calibration curve, as shown in **Figure 2**, where $R^2 = 0.9999$ was obtained from the straight line. For the reaction using the synthesized photocatalyst, the green TiO_2 NPs synthesized was added to MO solution (50 mL) and sonicated. The solution was stirred using a magnetic stirrer in the dark condition for 1 h in order to

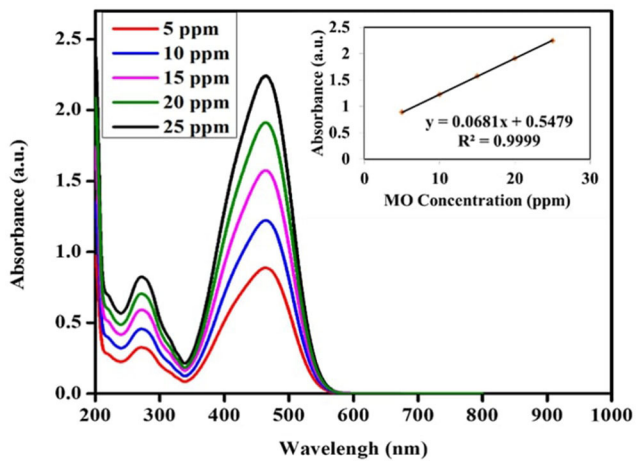

FIGURE 2 | Calibration curve spectra and line graph of M.O. Solution.

reach the adsorption equilibrium. After reaching the adsorption equilibrium, the UV light was switched on 3 mL of the treated MO was collected after interval of 30, 60, 90, 120, and 150 min of reaction. The concentration of the MO from the withdrawn aliquot was analyzed using a UV-Vis spectrophotometer.

RESULTS AND DISCUSSION

Possible Mechanism for the Formation of TiO_2 NPs

Preliminary phytochemical screening was done using standard procedures to identify the constituents present in the extract, as described by Samkeliso et al. (2018). It involves observing plant samples for different classes of phytochemicals. This qualitative tests were used to provide an indication of the nature of phytochemicals present in D. *pinnata* (Poir.) Schumach. and Thonn's extract, as shown in **Table 1**.

Table 1 shows that the plant of *D. pinnata* contains high amount of flavonoids and phenols that are important as surfactants and stabilizers. These constituents are able to prevent excessive agglomeration of the nanoparticulate material during the synthesis process. Other phyto-constituents present in the leaf extract were alkaloids, stereoids, and coumarins.

The mechanism for the formation of TiO_2 is shown in **Figure 3**. TiO_2 synthesis begins with complete hydrolysis of the precursor used [titanium isopropoxide, Ti(*i*-OPr)$_4$] by direct interaction of the titanium source with water. Titanyl hydroxide was obtained according to the following reaction (Solano et al., 2019):

$$Ti(i-OC_3H_7)_4 + 3H_2O \rightarrow TiO(OH)_2 + 4C_3H_7OH$$

The FTIR data of *D. pinnata* ethyl acetate leaf extract displays the presence of a broad peak for OH functional group in the spectrum (**Figure 13**). It shows that the extract contains compounds having hydroxyl group as a functional group in the structure. Titanyl hydroxide can be dehydrated to give TiO_2 nanoparticles by heating it with ethyl acetate leaf extracts of *D. pinnata* at about 50°C. In this process, *D. pinnata* extract serves as catalysts due to the present of compounds having hydroxyl group as a functional group in the structures (Selvaraj et al., 2012). Hence the reaction between *D. pinnata* extract and $TiO(OH)_2$ might occur through the possible pathway which is described in **Figure 3**. Hence, water soluble compounds containing hydroxyl functional group are reported to be responsible for the stabilization of TiO_2 nanoparticles.

TABLE 1 | Phytochemical constituents present in ethyl acetate leaf extracts of *D. pinnata*.

Constituents	Results
Phenolics	+++
Flavonoids	+++
Alkaloids	++
Steroids	++
Coumarins	++

Physicochemical Properties Green TiO_2 NPs

In this research, green TiO_2 NPs were successfully prepared by the sol-gel method using *D. pinnata* plant, extracted by different solvents with different polarities (*n*-hexane, ethyl acetate, and methanol). First, the preparation of green TiO_2 NPs colloid was obtained by gradual addition of extracts into the continuously stirred titanium isopropoxide in distilled water. Subsequently, TiO_2 NPs were washed with absolute ethanol several times and calcined at 500°C, before being characterized.

For the crystallinity studies done using XRD, as shown in **Figure 4**, the major peaks were at 2θ values of 25.18° (101), 37.73° (004), 47.94° (200), 53.76° (105), and 54.96° (211), which indicated the successful synthesis of anatase TiO_2 NP_S. The XRD pattern confirmed the synthesized TiO_2 consist of anatase phase in high purity, with average crystallite size in the range of 19–21 nm. Scherer's equation (Lima et al., 2018), which relates the size of sub-micrometer crystallites in a solid to broadening of a sample peak in a diffraction pattern' illustrated as; $D = K\lambda/\beta \cos\theta$ where (D) is average crystal size for the main broadening anatase peak; K = Scherrer's coefficient constant (0.89) which depend on the crystallite shape, λ = X-ray wavelength; β = full width at half maximum intensity (FWHM) of diffraction peaks in radians and θ = Bragg's angle, has been used to correlate the sample analysis reference pattern. The average crystallite size of the synthesized TiO_2 was 11 nm, which showed similarity with TiO_2 NPs synthesis using the extracts of *Syzygium cumini*, as reported by Sethy et al. (2020). The order of their lattice parameters is as follows: the fraction from ethyl acetate (a = 3.79632, b = 9.52847) > *n*-hexane (a = 3.79223, b = 9.51600) > methanol (a = 3.79237, b = 9.51330), which indicates the qualitative merit for the fraction obtained by ethyl acetate [(0.149) > *n*-hexane fraction (0.136) >methanol extracts (0.121)]. This is indirectly proportional to their 2θ vales of (101), where ethyl acetate fractions with 25.2324 < *n*-hexane fractions at 25.2607

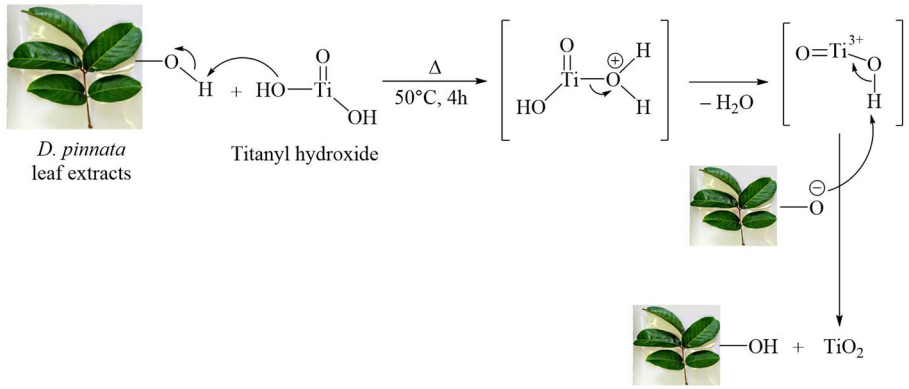

FIGURE 3 | Possible reaction mechanism for the formation of TiO_2 NPs in presence of hydroxyl group (–OH) of leaf extract of *D. pinnata*.

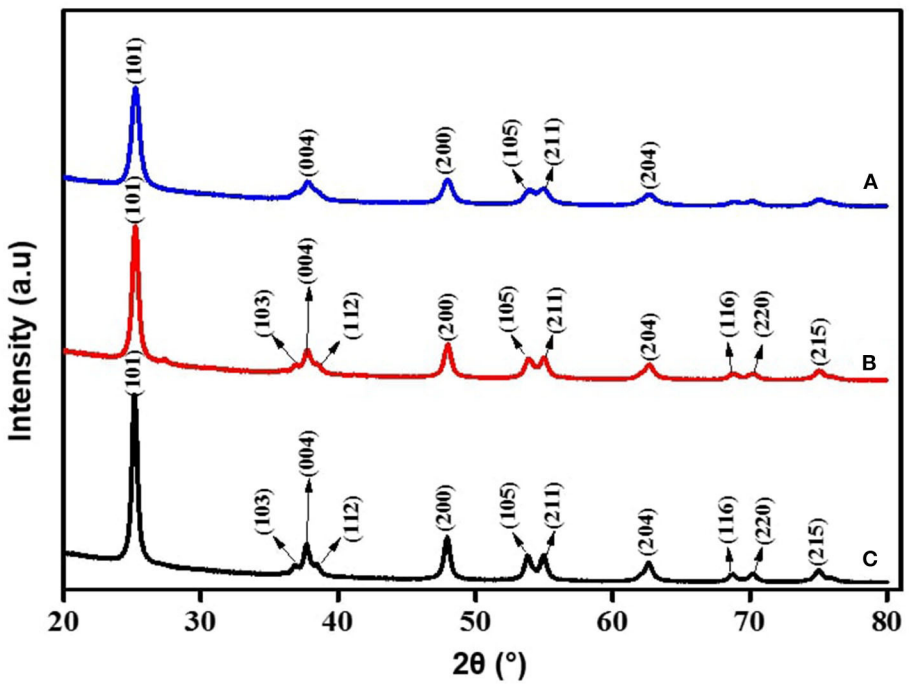

FIGURE 4 | XRD patterns of green TiO_2 NPs synthesized from the extracts of *D. pinnata* plant using **(A)** methanol, **(B)** *n*-hexane, and **(C)** ethyl acetate as the extraction solvents.

< methanol fractions at the value of 25.2608. Thus, XRD morphological studies showed significant crystallinity, crystal phase, and peak sharpness of green TiO_2 obtained using ethyl acetate plant extracts compared to those of methanol and *n*-hexane fractions, by comparing their major peaks, lattice parameter, and qualitative merit. Since TiO_2 synthesized with the extracts of *D. pinnata* plant using ethyl acetate as solvent showed better results, further characterizations were focused on the ethyl acetate green TiO_2 NP_S. The crystallographic database (DB card number 5000223) did match with the tetragonal anatase of high purity indexed at 97.55 (15%), as displayed in **Figure 5**. The 3D-tetragonal crystal structure showed a supportive lattice parameter at a = 3.7963Å and c = 9.52847Å with angle of 90°.The quantitative analysis showed a figure of merit at 0.149 with a space group at 141: 141/amd:1. Such crystallinity, crystal phase, and peak sharpness of green TiO_2 NP_S anatase were reported to influence their application as catalyst (Kim et al., 2018) or as support (Bagheri et al., 2014), acting as gas sensor (Zakrzewska and Radecka, 2017), degradation of pollutants (Phuinthiang and Kajitvichyanukul, 2019) and in solar cell (Kang et al., 2019).

The FESEM images of green TiO_2 NP_S synthesized from the extracts of *D. pinnata* plant, obtained by ethyl acetate, with different magnifications, are shown in **Figure 6**. The size of the particles were in the range of 19–21 nm, and the particles were

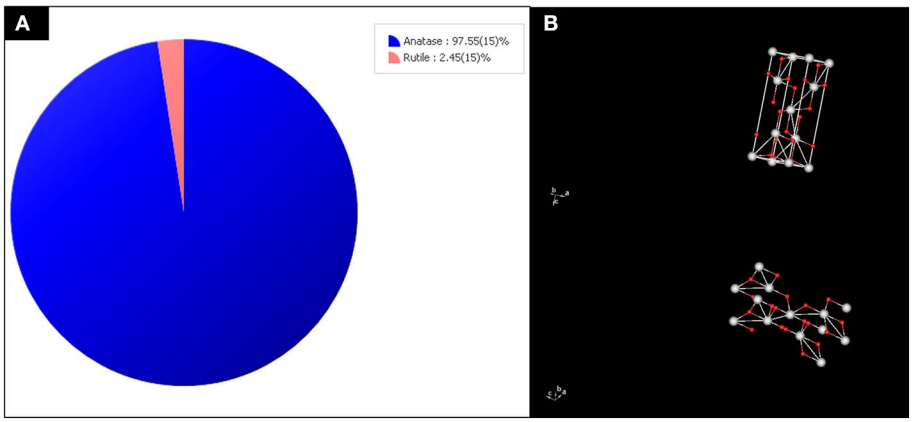

FIGURE 5 | (A) The purity index and **(B)** 3D-tetragonal structure of anatase TiO_2 obtained from the XRD results.

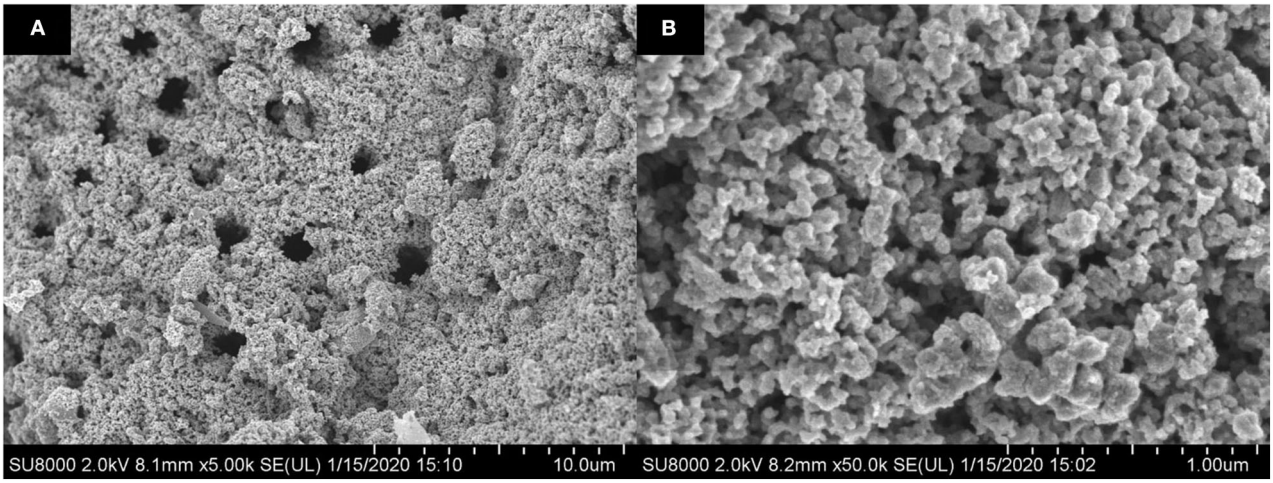

FIGURE 6 | FESEM images of synthesized green TiO_2 NPs with magnifications of **(A)** 5,000 times and **(B)** 50,000 times.

densely aggregated, with non-uniformed semi-spherical shapes. This also proved that TiO_2 particles in nano-sized have been successfully obtained.

The elemental analysis was performed via EDX. The EDX line scan spectrum of calcined TiO_2 NPs in **Figure 7** shows two peaks as the main chemical composition, which were Ti (61 wt.%) and O (35 wt.%). This is also consistent with the results obtained in the XRD analysis. The non-stoichiometric of TiO_2 with the presence of oxygen can contribute to high performance in photocatalytic activity (Liu et al., 2012) with intense peak as bulk TiO_2 and less intense peak as surface TiO_2 (Ebrahimian et al., 2017). The EDX spectrum analysis showed that no other impurities were present in the synthesized green TiO_2 NPs, which proved its high purity level.

The optical absorption properties of the green TiO_2 NPs were studied by UV-Vis-NIR as the absorption potential is an important factor to reflect its photocatalysis. The wavelength dependent absorbance was within the range of 300–500 nm. The band gap energy (E_g) was calculated using this equation; $E_g = 1239.8/\lambda$ in (Parida et al., 2013; Ljubas et al., 2015) where the absorption spectrum has a wavelength value of 378 nm, which indicated typical TiO_2 anatase with high crystallinity as also reported by (Li et al., 2019), and band gap energy of 3.2 eV, as shown in **Figure 8**.

The N_2 isotherm and pore size distribution (inset) of the synthesized TiO_2 NPs are shown in **Figure 9**. The isotherm is of type V isotherm, where a hysteresis loop can be seen. This indicates that the distribution of pores in an irregular flow rate (Tan et al., 2012). The BJH pore size distribution based on desorption branch showed major peaks starting from 2.02 to 6.00 nm with a broad peak at 3.98 nm, showing the mesoporosity. As for the specific surface area of synthesized TiO_2 NPs, it was examined through BET multipoint graph, as shown in **Figure 10**. The BET surface area of the green TiO_2 NPs was found to be 31.77 m^2/g, which corresponds to correlation coefficient (r) of 0.99, as a liner graph (Ahmad et al., 2017).

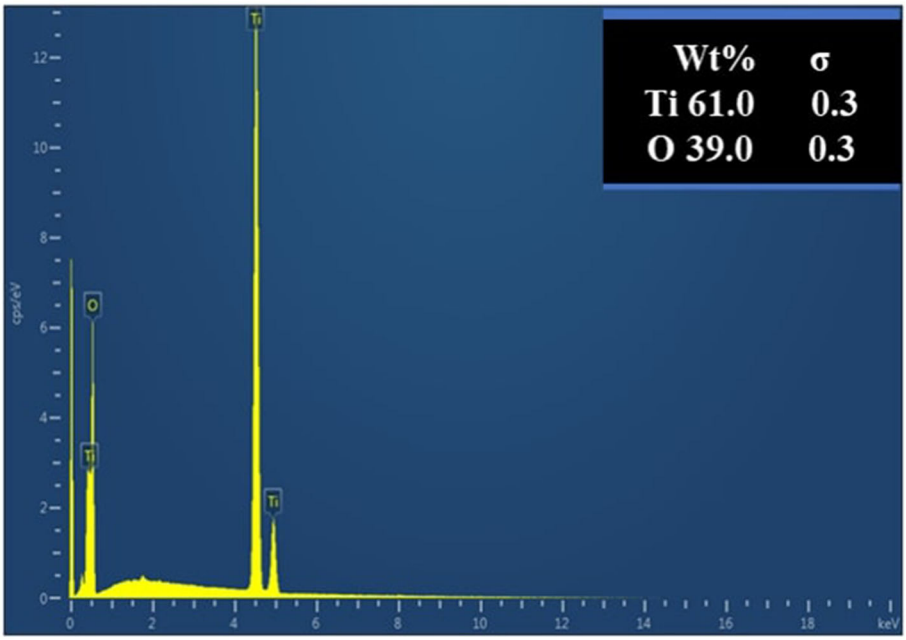

FIGURE 7 | EDX spectrum of green TiO_2 NPs synthesized from the extracts of *D. pinnata* plant using ethyl acetate as the extraction solvent.

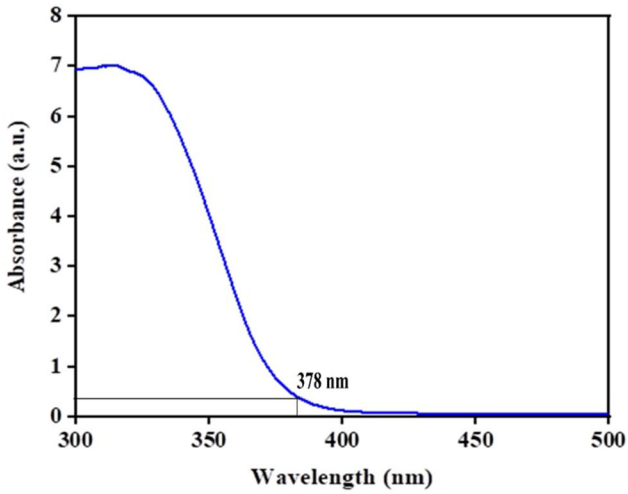

FIGURE 8 | UV-Vis of green TiO_2 NPs.

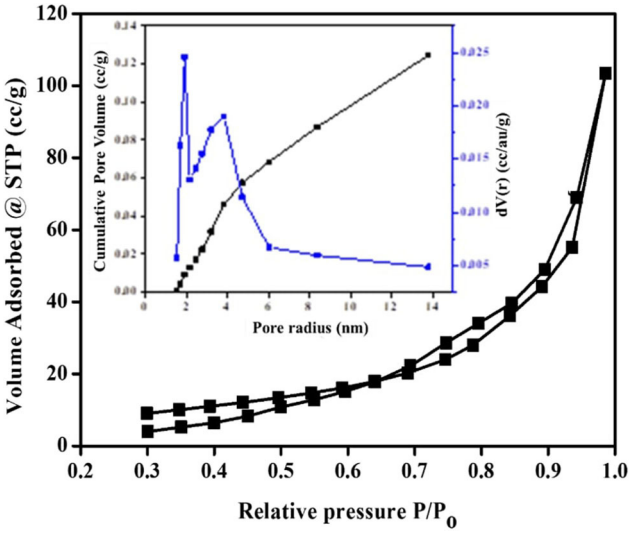

FIGURE 9 | N_2 isotherm and pore size distribution (inset) of the synthesized TiO_2 NPs.

Thermogravimetric analysis is a method used to determine thermal stability and the fractions of volatile components by monitoring the weight changes at a constant heating rate (Pintana and Tippayawong, 2013). The differential scanning calorimetry deals with the heat flow-temperature and this analysis has been carried out in the temperature range of 20–800°C using the uncalcined sample, as shown in **Figure 11.** The first weight loss band can be seen at 102°C, which is attributed to the loss of adsorbed atmospheric water (Yang et al., 2017). The second noticeable peak at 278°C was assigned to lower molecular weight metabolites, such as long chain fatty acids, galloyl ester or long chain esters. The last weight loss at 503°C marked the decomposition of all organic compounds (Kim et al., 2018). The irregular band line shown in the spectrum may be attributed to the nature of the products formed. The higher percentage mass loss (70%) was found for lower molecular weight constituents. The temperature at 106 and 288°C are associated with the loss of ethanol-water mixtures residue and

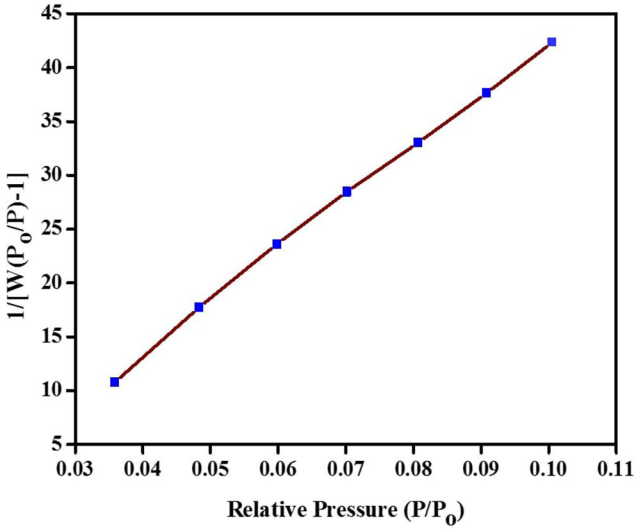

FIGURE 10 | BET plot of the synthesized green TiO_2 NPs.

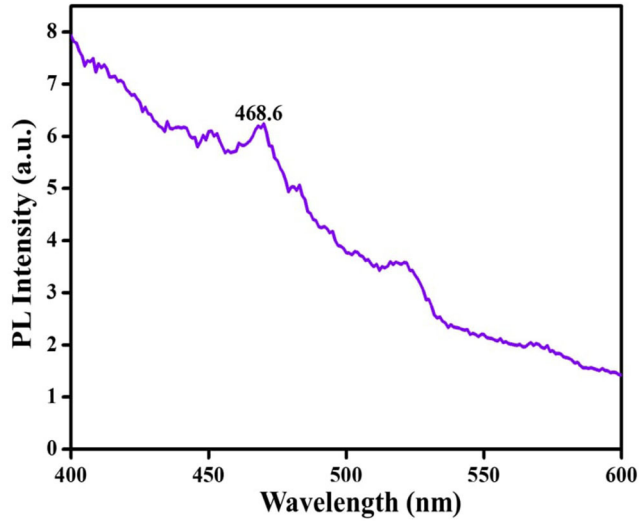

FIGURE 12 | PL spectrum of the synthesized green TiO_2 NPs.

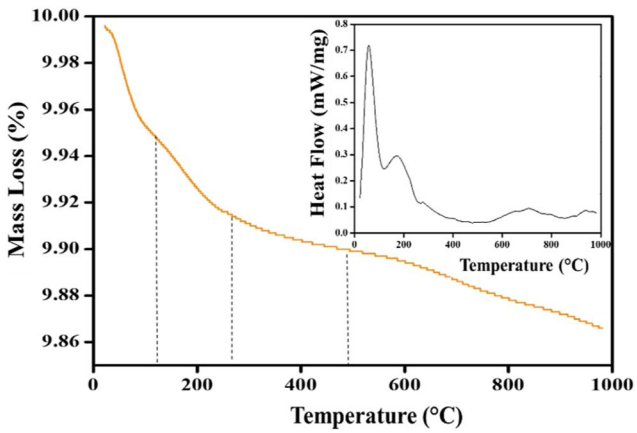

FIGURE 11 | The TGA and DSC (inset) curves of the synthesized green TiO_2 NPs.

fatty acids/ester endothermically. The exothermic peaks at 98 and 180°C seen on the DSC curve may be attributed to early phase transformation (Marinescu and Sofronia, 2011). The third region at 500°C justified total phase transformation of residual organic constituents of high molecular weight strongly coordinated to TiO_2 atoms such as triterpenoids.

Photoluminescence (PL) is also an important technique to study the optical properties of the synthesized TiO_2 NPs. **Figure 12** shows the p spectrum of the synthesized green TiO_2 NPs. These NPs show a strong luminescent emission peak at 520.3 nm with irregular broad peak surfaces, in the green region, and a weak emission peak at 468.6 nm at room temperature. These transitions could be attributed to the complete inter-band formation in dxy orbital with phytoconstituents, implying $3d^2$ $4s^2$, and $3d^0$ in the Ti^{4+} ions (Yin et al., 2013). It was also observed that the second luminescence peak shifted toward the lower energy region. This may be attributed to the inter bonding of Ti-O from the carbonyl components in the plant signifying active anatase TiO_2 of good light-response (Haghighatmamaghani et al., 2018). Furthermore, the shift toward the blue region may indicate a slight decrease in the particle sizes (Haque et al., 2017).

The FTIR spectrum of *D. pinnata* ethyl acetate extract and TiO_2 NPs were indicated by **Figures 13A,B**, respectively. Absorption bands at 3,386, 2,927, 1,710, 1,612, 1,446, 1,043, and 756 cm^{-1} are due to O-H bond stretching, C-H bond stretching, C=O bond stretching of carbonyl groups, C=C bond stretching, C-O bond bending vibration on phenolic compound, C-O bond stretching of the hydroxyl group, and out-of-plane C-H bending for aromatic ring. These functional groups represent the phytochemicals present in the extract. In **Figure 12B**, the broad absorption band observed at 3,386 cm^{-1} represents O-H bond stretching due to adsorbed moisture at the surface of TiO_2 NPs. The broad band at 537 cm^{-1} represents a characteristic peak of Ti-O-Ti bending mode of vibration which confirms the formation of metal oxygen bonding (Catauro et al., 2018). The TiO_2 NPs calcined at 500°C showed no traces of organic components functional groups, which justified complete calcination.

Photocatalytic Activity

The photocatalytic activity of the green TiO_2 NPs synthesized using the extracts of *D. pinnata* leaves with ethyl acetate as the solvent was tested out in the photodegradation of MO under UV light irradiation (1,200 W). The light source played a vital role in photocatalytic degradation as semiconductor compounds, such as TiO_2, degrades volatile and organic pollutants under UV light

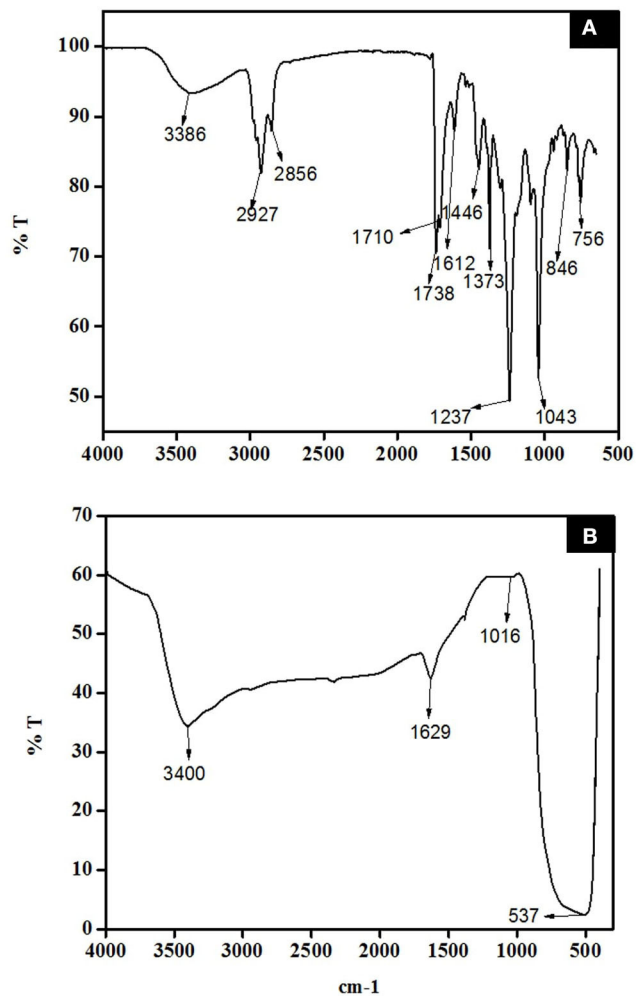

FIGURE 13 | FTIR spectra of (**A**) *D. pinnata* crude extract and **(B)** synthesized TiO_2 NPs.

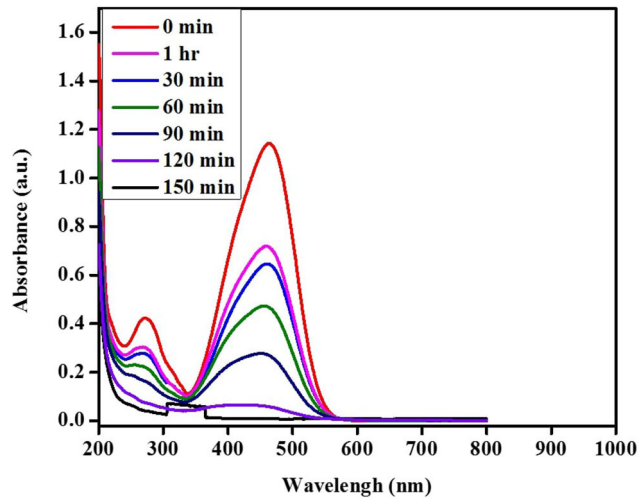

FIGURE 14 | Absorbance spectra of photocatalytic degradation pattern of MO solution.

irradiation (Cun et al., 2002; Laoufi and Bentahar, 2014; Luan et al., 2014). MO dye was chosen as the model organic pollutant and the photodegradation process was monitored by UV-visible spectrophotometer in the range of 800–200 nm. The degradation percentage was calculated using the following equation: D (%) $= (C_i\text{-}C_f)/C_i \times 100$ where C_i is initial concentration, $C_f$is final concentration of MO at time (t) (Haque et al., 2017). **Figure 14** shows the spectra of the reaction mixture withdrawn at intervals of 30, 60, 90, 120, and 150 min. After only 90 min, 51.72% of MO has been degraded. It was also observed that at 120 min, the photodegradation reached 81.36%, while at 150 min, 97.53% of MO photodegradation was obtained. It is evident that the rate of photodegradation of green TiO_2 NPs photocatalyst on MO increased with longer irradiation time. This indicate faster interaction between the photons and green TiO_2 NPs, which showed direct proportionality to the duration of irradiation. Therefore, MO (20 ppm) showed optimum irradiation duration of 150 min (97.53%). This can signify rapid formation of •OH radicals as active sites on the TiO_2 NPs' surface for effective adsorption throughout the reaction (Youssef et al., 2016). Based on these results, it can be seen that an optimal performance of green TiO_2 NPs can be achieved within a short time. This may indicate that extracts from plants as green substitute for the synthesis of NPs has the benefits of enhancing the charge carrier's separation (Solano et al., 2019), increasing specific surface area and overall photocatalytic performance. The physicochemical properties and photocatalytic activity have justified the efficient performance of green synthesized TiO_2 NPs from *D. pinnata* plant for the photodegradation of MO.

CONCLUSION

Based on the physicochemical characterization, TiO_2 NPs have been successfully synthesized using the extracts of *D. pinnata* leaves. Different solvents used in the extraction also showed the contributions of solvents polarity in the extractions, where in this work, extracts using ethyl acetate showed superior characteristics. The synthesized green TiO_2 NPs also showed good photocatalytic activity in the photodegradation of methyl orange dye under UV light irradiation. The work here showed that TiO_2 NPs with good physicochemical properties and photocatalytic activity can be synthesized using extracts of plants, which can reduce or eliminate the use of harmful chemicals. Further work on the physicochemical properties and photocatalytic activity of TiO_2 NPs obtained using extracts from *n*-hexane and methanol will be carried out.

DATA AVAILABILITY STATEMENT

The original contributions presented in the study are included in the article/supplementary materials, further inquiries can be directed to the corresponding author/s.

AUTHOR CONTRIBUTIONS

All authors listed have made a substantial, direct and intellectual contribution to the work, and approved it for publication.

FUNDING

This research received funding from Ministry of Higher Education (MOHE) under the Fundamental Research Grant Scheme (R.J130000.7854.5F242) and Collaborative Research Grant (R.J130000.7354.4B502), Research Grant from Nippon Sheet Glass Foundation for Materials Science and Engineering (R.J130000.7354.4B515) and Universiti Teknologi Malaysia for Industry-International Incentive Grant (Q.J130000.3654.02M62). A great appreciation to Tertiary Education Trust Fund-Nigeria (TET Fund) for doctoral study support and Faculty of Science, Universiti Teknologi Malaysia for the research facilities.

REFERENCES

Agarwal, H., Nakara, A., and Shanmugam, V. K. (2018). Anti-inflammatory mechanism of various metal and metal oxide nanoparticles synthesized using plant extracts: a review. *Biomed. Pharmacother.* 109, 2561–2572. doi: 10.1016/j.biopha.2018.11.116

Ahmad, S., Munir, S., Zeb, N., Ullah, A., Khan, B., Ali, J., et al. (2019). Green nanotechnology: a review on green synthesis of silver nanoparticles—an ecofriendly approach. *Int. J. Nanomed.* 14, 5087–5107. doi: 10.2147/IJN.S200254

Ahmad, T., Phul, R., Alam, P., Lone, I. H., Shahazad, M., Ahmed, J., et al. (2017). Dielectric, optical and enhanced photocatalytic properties of $CuCrO_2$ nanoparticles. *RSC Adv.* 7, 27549–27557. doi: 10.1039/C6RA26888A

Bagheri, S., Muhd Julkapli, N., and Bee Abd Hamid, S. (2014). Titanium dioxide as a catalyst support in heterogeneous catalysis. *Sci. World J.* 2014, 1–21. doi: 10.1155/2014/727496

Benkhaya, S., El Harfi, S., and Elharfi, A. (2017). Classifications, properties and applications of textile dyes : a review. *Appl. J. Environ. Eng. Sci.* 3, 311–320. doi: 10.1016/j.heliyon.2020.e03271

Bregadiolli, B. A., Fernandes, S. L., and De Oliveira Graeff, C. F. (2017). Easy and fast preparation of TiO_2-based nanostructures using microwave assisted hydrothermal synthesis. *Mater. Res.* 20, 912–919. doi: 10.1590/1980-5373-mr-2016-0684

Catauro, M., Tranquillo, E., Dal Poggetto, G., Pasquali, M., Dell'Era, A., and Ciprioti, S. V. (2018). Influence of the heat treatment on the particles size and on the crystalline phase of TiO_2 synthesized by the sol-gel method. *Materials* 11, 2364–2375. doi: 10.3390/ma11122364

Chiu, Y. H., Chang, T. F. M., Chen, C. Y., Sone, M., and Hsu, Y. J. (2019). Mechanistic insights into photodegradation of organic dyes using heterostructure photocatalysts. *Catalysts* 9:430. doi: 10.3390/catal9050430

Cun, W., Jincai, Z., Xinming, W., Bixian, M., Guoying, S., Ping'an, P., et al. (2002). Preparation, characterization and photocatalytic activity of nano-sized ZnO/SnO_2 coupled photocatalysts. *Appl. Catal. B Environ.* 39, 269–279. doi: 10.1016/S0926-3373(02)00115-7

Dinh, C. T., Nguyen, T. D., Kleitz, F., and Do, T. O. (2012). A solvothermal single-step route towards shape-controlled titanium dioxide nanocrystals. *Can. J. Chem. Eng.* 90, 8–17. doi: 10.1002/cjce.20574

Ebrahimian, A., Monazzam, P., and Fakhari, B. (2017). Co/TiO_2 nanoparticles : preparation, characterization and its application for photocatalytic degradation of methylene blue. *Desalin. Publ.* 63, 283–292. doi: 10.5004/dwt.2017.20205

Elbushra, H., Ahmed, M., Wardi, H., and Eassa, N. (2018). Synthesis and characterization of TiO_2 using sol-gel method at different annealing temperature. *MRS Advances.* 3, 2527–2535. doi: 10.1557/adv.2018.23

Guettaï, N., and Ait Amar, H. (2005). Photocatalytic oxidation of methyl orange in presence of titanium dioxide in aqueous suspension. Part I: parametric study. *Desalination* 185, 427–437. doi: 10.1016/j.desal.2005.04.048

Haghighatmamaghani, A., Haghighat, F., and Lee, C. (2018). Performance of various commercial TiO_2 in photocatalytic degradation of a mixture of indoor air pollutants: effect of photocatalyst and operating parameters. *Sci. Technol. Built Environ.* 4731, 1–41. doi: 10.1080/23744731.2018.1556051

Haque, F. Z., Nandanwar, R., and Singh, P. (2017). Evaluating photodegradation properties of anatase and rutile TiO_2 nanoparticles for organic compounds. *Optik* 128, 191–200. doi: 10.1016/j.ijleo.2016.10.025

Hejazi, S., Mohajernia, S., Osuagwu, B., Zoppellaro, G., Andryskova, P., Tomanec, O., et al. (2020). On the controlled loading of single platinum atoms as a co-catalyst on TiO_2 anatase for optimized photocatalytic H2 generation. *Advan. Mater.* 32:1908505. doi: 10.1002/adma.201908505

Hiremath, S., Antony Raj, M. A. L., Chandra Prabha, M. N., and Vidya, C. (2018). *Tamarindus indica* mediated biosynthesis of nano TiO_2 and its application in photocatalytic degradation of Titan yellow. *J. Environ. Chem. Eng.* 6, 7338–7346. doi: 10.1016/j.jece.2018.08.052

Kang, X., Liu, S., Dai, Z., He, Y., Song, X., and Tan, Z. (2019). Titanium dioxide: from engineering to applications. *Catalysts* 9, 191–223. doi: 10.3390/catal9020191

Kankara, S. S., Ibrahim, M. H., Mustafa, M., and Go, R. (2015). Ethnobotanical survey of medicinal plants used for traditional maternal healthcare in Katsina state, Nigeria. *S. Afr. J. Bot.* 97, 165–175. doi: 10.1016/j.sajb.2015.01.007

Khalik, W. F., Ong, S. A., Ho, L. N., Voon, C. H., Wong, Y. S., Yusoff, N. A., et al. (2017). Comparison the performance of carbon plate and Pt-loaded carbon in photocatalytic fuel cell (PFC) process. *AIP Conf. Proceed.* 1828:020014. doi: 10.1063/1.4979385

Khataee, A. R., and Mirzajani, O. (2010). UV/peroxydisulfate oxidation of C. I. Basic Blue 3: modeling of key factors by artificial neural network. *Desalination* 251, 64–69. doi: 10.1016/j.desal.2009.09.142

Khataee, A. R., Pons, M. N., and Zahraa, O. (2010). Photocatalytic decolorisation and mineralisation of orange dyes on immobilised titanium dioxide nanoparticles. *Water Sci. Technol.* 62, 1112–1120. doi: 10.2166/wst.2010.438

Kim, T. H., Go, G. M., Cho, H. B., Song, Y., Lee, C. G., and Choa, Y. H. (2018). A novel synthetic method for N doped TiO_2 nanoparticles through plasma-assisted electrolysis and photocatalytic activity in the visible region. *Front. Chem.* 6, 1–10. doi: 10.3389/fchem.2018.00458

Kitamura, Y., Okinaka, N., Shibayama, T., Mahaney, O. O. P., Kusano, D., Ohtani, B., et al. (2007). Combustion synthesis of TiO_2 nanoparticles as photocatalyst. *Powder Technol.* 176, 93–98. doi: 10.1016/j.powtec.2007.02.009

Laoufi, N. A., and Bentahar, F. (2014). Pesticide removal from water suspension by UV/TiO_2 process : a parametric study. *Desalin. Water Treat.* 52, 1947–1955. doi: 10.1080/19443994.2013.804453

Lee, H., Song, M. Y., Jurng, J., and Park, Y. K. (2011). The synthesis and coating process of TiO_2 nanoparticles using CVD process. *Powder Technol.* 214, 64–68. doi: 10.1016/j.powtec.2011.07.036

Li, Y., Fu, Y., and Zhu, M. (2019). Green synthesis of 3D tripyramid TiO_2 architectures with assistance of aloe extracts for highly efficient photocatalytic degradation of antibiotic ciprofloxacin. *Appl.Catal. B Environ.* 260, 1–9. doi: 10.1016/j.apcatb.2019.118149

Lima, F. M., Martins, F. M., Herbert, P., Maia, F., Fabíola, A., Almeida, L., et al. (2018). Nanostructured titanium dioxide average size from alternative analysis of Scherrer' s. *Rev. Mat.* 23, 1–10. doi: 10.1590/s1517-707620170001.0301

Liu, F., Lu, L., Xiao, P., He, H., Qiao, L., and Zhang, Y. (2012). Effect of oxygen vacancies on photocatalytic efficiency of TiO_2 nanotubes aggregation. *Bull. Korean Chem. Soc.* 33, 2255–2259. doi: 10.5012/bkcs.2012.33.7.2255

Ljubas, D., Smoljanić, G., and Juretić, H. (2015). Degradation of methyl orange and congo red dyes by using TiO_2 nanoparticles activated by the solar and the solar-like radiation. *J. Environ. Manage.* 161, 83–91. doi: 10.1016/j.jenvman.2015.06.042

Luan, J., Chen, M., and Hu, W. (2014). Synthesis, characterization and photocatalytic activity of new photocatalyst $ZnBiSbO_4$ under visible light irradiation. *Int. J. Mol. Sci.* 15, 9459–9480. doi: 10.3390/ijms15069459

Marinescu, C., and Sofronia, A. (2011). DSC investigation of nanocrystalline TiO_2 powder. *J. Therm. Anal. Calorim.* 103, 49–57. doi: 10.1007/s10973-010-1072-6

May-Masnou, A., Soler, L., Torras, M., Salles, P., Llorca, J., and Roig, A. (2018). Fast and simple microwave synthesis of TiO_2/Au nanoparticles for gas-phase photocatalytic hydrogen generation. *Front. Chem.* 6, 1–13. doi: 10.3389/fchem.2018.00110

Mohamad, N. A. N., Arham, N. A., Jai, J., and Hadi, A. (2014). Plant extract as reducing agent in synthesis of metallic nanoparticles: a review. *Advan. Mater. Res.* 832, 350–355. doi: 10.4028/www.scientific.net/AMR.832.350

Murugan, R., and Parimelazhagan, T. (2014). Comparative evaluation of different extraction methods for antioxidant and anti-inflammatory properties from *Osbeckia parvifolia* Arn.–an *in vitro* approach. *J. King Saud Univ.* 26, 267–275. doi: 10.1016/j.jksus.2013.09.006

Órdenes-Aenishanslins, N. A., Saona, L. A., Durán-Toro, V. M., Monrás, J. P., Bravo, D. M., and Pérez-Donoso, J. M. (2014). Use of titanium dioxide nanoparticles biosynthesized by Bacillus mycoides in quantum dot sensitized solar cells. *Microb. Cell Fac.* 13:90. doi: 10.1186/s12934-014-0090-7

Parida, K. M., Pany, S., and Naik, B. (2013). Green synthesis of fibrous hierarchical meso-macroporous N doped TiO_2 nanophotocatalyst with enhanced photocatalytic H2 production. *Int. J. Hydrog. Energy* 38, 3545–3553. doi: 10.1016/j.ijhydene.2012.12.118

Patel, D. K. (2015). Plants as a source of medicine. *Med. Aromat. Plants* S3:2167. doi: 10.4172/2167-0412.S3-e001

Phuinthiang, P., and Kajitvichyanukul, P. (2019). Degradation of paraquat from contaminated water using green TiO_2 nanoparticles synthesized from *Coffea arabica* L. in photocatalytic process. *Water Sci. Technol.* 79, 905–910. doi: 10.2166/wst.2018.493

Pintana, P., and Tippayawong, N. (2013). Nonisothermal thermogravimetric analysis of Thai Lignite with high CaO content. *Sci. World J.* 2013, 1–7. doi: 10.1155/2013/216975

Rab, N., Chong, F. K., Mohamed, H. I., and Lim, W. H. (2018). Preparation of TiO_2 nanoparticles by hydrolysis of TiCl 4 using water and glycerol solvent system. *J. Phys. Conf. Ser.* 1123, 1–8. doi: 10.1088/1742-6596/1123/1/012065

Raghad, D. H., Abdul, J., Nuaman, R. S., and Abd, A. N. (2016). Biological synthesis of titanium dioxide nanoparticles by *Curcuma longa* plant extract and study its biological properties. *World Sci. News* 49, 204–222. Available online at: www.worldscientificnews.com

Samkeliso, T., Fanyana, M., and Michael, P. (2018). Analysis of the phytochemical contents and antioxidant activities of crude extracts from Tulbaghia species. *J. Tradit. Chin. Med.* 38, 272–729. doi: 10.1016/j.jtcm.2018.04.005

Selvaraj, M. R., Bharathia, A., Prabhakarn, A., Abdul Rahuman, A., Velayutham, K., Rajakumar, G., et al. (2012). Efficient phytosynthesis and structural characterization of rutile TiO_2 nanoparticles using *Annona squamosa* peel extract. *Spectrochim. Acta A Mol. Biomol. Spectrosc.* 98, 86–90. doi: 10.1016/j.saa.2012.08.055

Sethy, N. K., Arif, Z., Mishra, P. K., and Kumar, P. (2020). Green synthesis of TiO_2 nanoparticles from Syzygium cumini extract for photo-catalytic removal of lead (Pb) in explosive industrial wastewater. *De Gruyter* 9, 171–181. doi: 10.1515/gps-2020-0018

Solano, R. A., Herrera, A. P., Maestre, D., and Cremades, A. (2019). Fe-TiO_2 nanoparticles synthesized by green chemistry for potential application in waste water photocatalytic treatment. *J. Nanotechnol.* 2019, 1–11. doi: 10.1155/2019/4571848

Sotubo, S. E., Lawal, O. A., Osunsami, A. A., and Ogunwande, I. A. (2016). Constituents and insecticidal activity of Deinbollia pinnata essential oil. *Nat. Prod. Commun.* 11:1889. doi: 10.1177/1934578x1601101228

Sundrarajan, M., Bama, K., Bhavani, M., Jegatheeswaran, S., Ambika, S., Sangili, A., et al. (2017). Obtaining titanium dioxide nanoparticles with spherical shape and antimicrobial properties using M. citrifolia leaves extract by hydrothermal method. *J. Photochem Photobiol. B Biol.* 171, 117–124. doi: 10.1016/j.jphotobiol.2017.05.003

Tan, Y. H., Davisa, J. A., Fujikawaa, K., Ganesh, N. V., Demchenko, A. V., and Stine, K. J. (2012). Surface area and pore size characteristics of nanoporous gold subjected to thermal, mechanical, or surface modification studied using gas adsorption isotherms, cyclic voltammetry, thermogravimetric analysis, and scanning electron microscopy. *J. Mater.Chem.* 22, 6733–6745. doi: 10.1039/c2jm16633j

Thakur, B. K., Kumar, A., and Kumar, D. (2019). Green synthesis of titanium dioxide nanoparticles using *Azadirachta indica* leaf extract and evaluation of their antibacterial activity. *S. Afr. J. Bot.* 124, 223–227. doi: 10.1016/j.sajb.2019.05.024

Venugopal, K., Ahmad, H., Manikandan, E., Thanigai Arul, K., Kavitha, K., Moodley, M. K., et al. (2017). The impact of anticancer activity upon beta vulgaris extract mediated biosynthesized silver nanoparticles (Ag-NPs) against human breast (MCF-7), lung (A549) and pharynx (Hep-2) cancer cell lines. *J. Photochem. Photobiol. B Biol.* 173, 99–107. doi: 10.1016/j.jphotobiol.2017.05.031

Yang, C., Dong, W., Cui, G., Zhao, Y., Shi, X., and Xia, X. (2017). Highly-efficient photocatalytic degradation of methylene blue by PoPD-modified TiO_2 nanocomposites due to effect of TiO_2 with PoPD. *Sci. Rep.* 7, 1–12. doi: 10.1038/s41598-017-04398-x

Yin, W., Zhang, L., Wang, Z., Wang, T., Zhou, C., Selloni, A., et al. (2013). Electronic structure and photoabsorption of Ti3+ ions in reduced anatase and rutile TiO_2. *Physical Chem. Chem. Phys.* 1, 1–9. doi: 10.1039/c8cp02648c

Youssef, N. A., Shaban, S. A., Ibrahim, F. A., and Mahmoud, A. S. (2016). Degradation of methyl orange using Fenton catalytic reaction. *Egypt. J. Pet.* 25, 317–321. doi: 10.1016/j.ejpe.2015.07.017

Zakrzewska, K., and Radecka, M. (2017). TiO_2-based nanomaterials for gas sensing- influence of anatase and rutile contributions. *Nanoscale Res. Lett.* 12, 1–8. doi: 10.1186/s11671-017-1875-5

Conflict of Interest: The authors declare that the research was conducted in the absence of any commercial or financial relationships that could be construed as a potential conflict of interest.

Copyright © 2020 Rufai, Chandren and Basar. This is an open-access article distributed under the terms of the Creative Commons Attribution License (CC BY). The use, distribution or reproduction in other forums is permitted, provided the original author(s) and the copyright owner(s) are credited and that the original publication in this journal is cited, in accordance with accepted academic practice. No use, distribution or reproduction is permitted which does not comply with these terms.

frontiers in Chemistry

REVIEW
published: 07 December 2020
doi: 10.3389/fchem.2020.603259

Current Methods for Detecting Cell Membrane Transient Interactions

*Yousef Bagheri†, Ahsan Ausaf Ali† and Mingxu You**

Department of Chemistry, University of Massachusetts, Amherst, MA, United States

Short-lived cell membrane complexes play a key role in regulating cell signaling and communication. Many of these complexes are formed based on low-affinity and transient interactions among various lipids and proteins. New techniques have emerged to study these previously overlooked membrane transient interactions. Exciting functions of these transient interactions have been discovered in cellular events such as immune signaling, host–pathogen interactions, and diseases such as cancer. In this review, we have summarized current experimental methods that allow us to detect and analyze short-lived cell membrane protein–protein, lipid–protein, and lipid–lipid interactions. These methods can provide useful information about the strengths, kinetics, and/or spatial patterns of membrane transient interactions. However, each method also has its own limitations. We hope this review can be used as a guideline to help the audience to choose proper approaches for studying membrane transient interactions in different membrane trafficking and cell signaling events.

Keywords: membrane biology, cell signaling, transient interactions, lipids, proteins, membrane probes

OPEN ACCESS

Edited by:
Jianping Yang,
Donghua University, China

Reviewed by:
Quezia B. Cass,
Federal University of São Carlos, Brazil
Huawen Wu,
Hitronics Technologies, Inc,
United States

***Correspondence:**
Mingxu You
mingxuyou@chem.umass.edu

†These authors have contributed equally to this work

Specialty section:
This article was submitted to Analytical Chemistry, a section of the journal Frontiers in Chemistry

Received: *06 September 2020*
Accepted: *16 October 2020*
Published: *07 December 2020*

Citation:
Bagheri Y, Ali AA and You M (2020) Current Methods for Detecting Cell Membrane Transient Interactions. Front. Chem. 8:603259. doi: 10.3389/fchem.2020.603259

INTRODUCTION

Cell membranes are composed of various lipid, protein, and carbohydrate compounds. These membrane components dynamically interact with each other to regulate cell cycles and communications (Lee, 2003; Contreras et al., 2011; Varshney et al., 2016; Sezgin et al., 2017). Based on the affinity and duration of these interactions, there are two types of membrane interactions: strong/stable and weak/transient. Strong/stable interactions last for a long time with binding affinities in the range of fM to nM. In contrast, weak/transient interactions happen only in the range of microseconds to seconds, with a μM–mM binding affinity (De Keersmaecker et al., 2018; Corradi et al., 2019). While it is worth mentioning that there is no absolute clear cut between these two types of membrane interactions, many membrane stable interactions have been well-studied, whereas in comparison, those transient interactions are often more challenging to investigate. This is because at any given time, only a small number of membrane transient interactions happen. The formed short-lived complexes are always under a dynamic equilibrium with monomers that will freely diffuse in the membrane. Meanwhile, these transient complexes are often disrupted or overlooked during *in vitro* isolation and purification processes.

In this review, we will first discuss the biological importance of these membrane transient interactions in regulating cellular functions. We will then focus on available experimental methods that can be used to study these transient interactions, especially in living cell membranes. We hope this review can provide some useful guidelines for future cell membrane studies.

IMPORTANCE OF MEMBRANE TRANSIENT INTERACTIONS

The first role of membrane transient interactions is to regulate the activation or suppression of many membrane protein complexes (Ikonen, 2008; Larsen et al., 2015; Sezgin et al., 2017). These protein complexes or oligomerizations cannot function without transient binding and interactions (Heldin et al., 1997; James et al., 2006). In membrane signaling network, the same protein is often involved in forming more than one complex and need to interact with different membrane partners. Weak and transient interactions will allow these membrane proteins to function in several signaling and trafficking pathways simultaneously. In addition, intracellular proteins can also be transiently recruited to the membrane to form dynamic receptor complexes (Sezgin et al., 2017; Corradi et al., 2019). Disruption of these fine-regulated membrane dynamic network will result in ineffective signal transduction and cell damage (Wymann and Schneiter, 2008).

For example, the oligomerizations and functions of G-proteins and some electron transport complexes are controlled by membrane local environment (Nooren and Thornton, 2003; Acuner Ozbabacan et al., 2011; Sevcsik et al., 2015). G-proteins regulate various metabolic, developmental, humoral, and neuronal functions (Simon et al., 1991). Dependent on GTP and GDP levels, G-protein subunits (α, β, γ) can switch between stable binding and transient interaction to modulate cellular reactions (Neer and Clapham, 1988; Ritter and Hall, 2009). T-cell receptor (TCR) activation is also fundamentally regulated by membrane transient interactions of several protein subunits (**Figure 1A**). Immediately after T-cell engagement to the activating antigens, nanometer-sized TCR clusters are formed to function as a platform for the recruitment and activation of downstream effectors such as LAT and SLP-76 (Bunnell et al., 2002; Zal and Gascoigne, 2004; Yi et al., 2019).

In addition to these transient protein–protein interactions, lipid–protein and lipid–lipid interactions also play a major role in the cell membrane fluidity, curvature, and domain

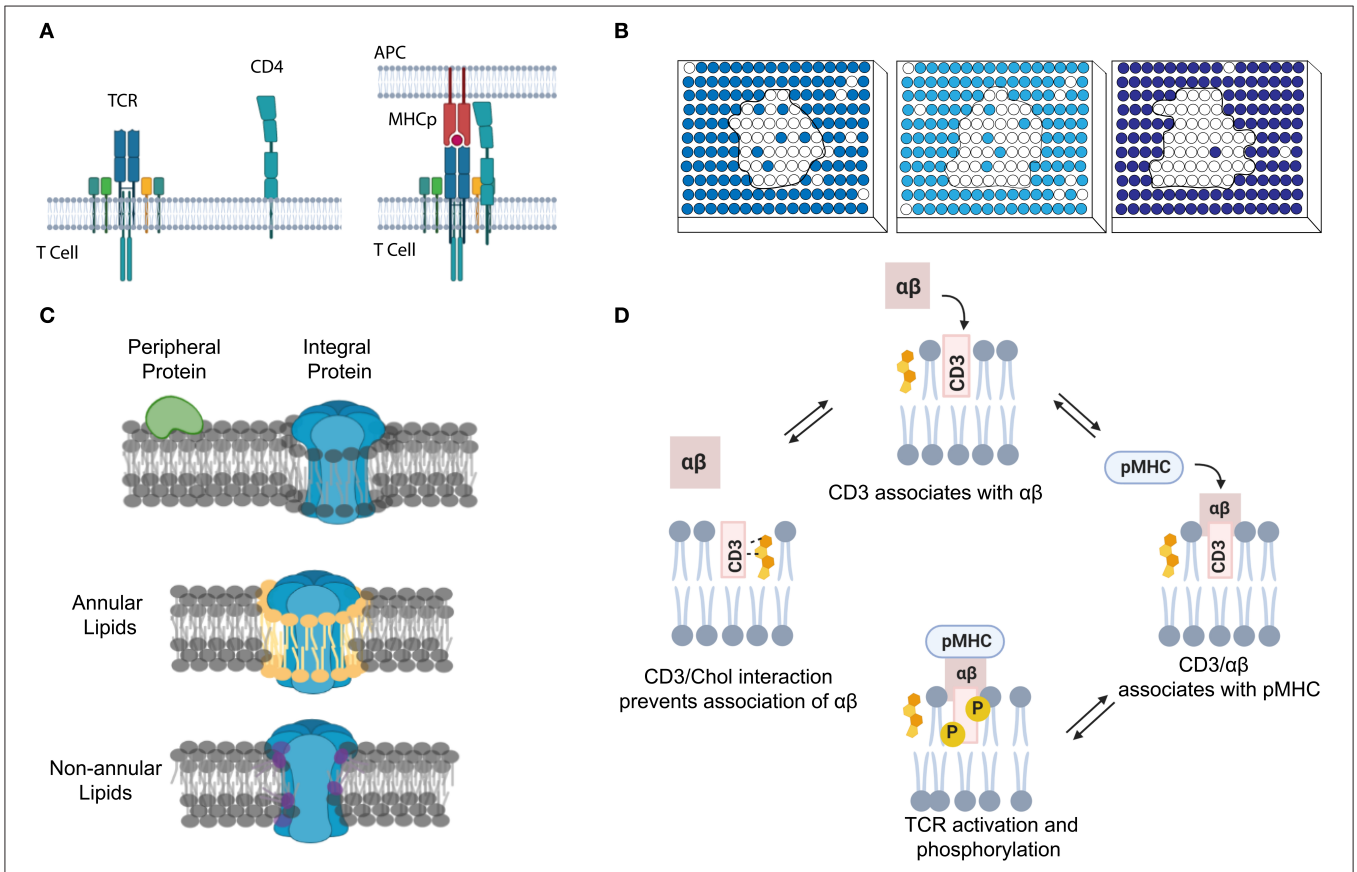

FIGURE 1 | Transient interactions control membrane functions. **(A)** During T-cell signaling, the MHCp ligand binding induces dynamic protein–protein interactions between T-cell receptor (TCR) and CD4. **(B)** The strength of lipid–lipid interactions regulates membrane phase separation and domain formation. White circles represent that lipids prefer ordered domain. The darker the blue shading of circles, the poorer the ability of these disordered phase-preferred lipids to pack tightly. **(C)** The correlation between membrane protein location and their interactions with lipids. Membrane lipids can be thus categorized into three groups: bulk, annular, and non-annular. **(D)** Dynamic cholesterol interaction with TCR regulates its activation and prevents non-specific responses.

formation (Leikin et al., 1996; Aimon et al., 2014; McMahon and Boucrot, 2015). These short-lived and transient lipid-mediated interactions provide a mechanism allowing membrane compounds to quickly respond to stimuli, yet retain the ability to return to their original state. Based on the structure and degree of saturation, lipids tend to arrange themselves into either ordered or disordered domains (Bakht et al., 2007; Kaiser et al., 2009; **Figure 1B**). In the case that a membrane compound has similar binding affinities with several binding partners, by forming these lipid domains, the high chance of colocalization with a particular partner will clearly increase their opportunity of interactions. As a result, specific membrane complexes can form because of high local concentrations, despite their weak binding affinities.

For example, transient lipid interactions (in the range of μs–ms) have resulted in the formation of lipid rafts, i.e., small membrane domains that are usually <200 nm in diameter (Kolmakov et al., 2010; Smith, 2012; Sezgin et al., 2017; Bolmatov et al., 2020). Cholesterols, sphingolipids, and various proteins participate in these raft-like structures and regulate cellular processes such as in immune signaling, host–pathogen interaction, cancer, and cardiovascular diseases (Lorizate et al., 2013; Larsen et al., 2015; Varshney et al., 2016; Stone et al., 2017; Bolmatov et al., 2020).

Lipids can also directly interact with proteins to define their membrane structures and locations (Sezgin et al., 2017; Bolla et al., 2019). Dependent on the relative position of lipids to proteins, membrane lipids can be categorized into three groups: annular, non-annular, and bulk (**Figure 1C**; Lee, 2003; Contreras et al., 2011; Marius et al., 2012). Bulk lipids function as general membrane composition and usually have minimal interactions with membrane proteins (Lee, 2004). Annular lipids can form a ring-shaped shell that non-specifically surrounds membrane proteins (Contreras et al., 2011). In contrast, non-annular lipids can selectively occupy the cavities of proteins and function as specific building blocks or cofactors for the target proteins. Both annular and non-annular lipid–protein interactions are largely mediated by hydrophobic interactions. Meanwhile, hydrophilic interactions between polar amino acid chains and lipids' head groups have further increased the affinity and specificity of these lipid–protein conjugates (Lee, 2004; Contreras et al., 2011). Compared to the transient annular lipid–protein interactions, many non-annular lipid–protein interactions are more stable and long-lasting (Lee, 2011; Marius et al., 2012), e.g., as that happens during the selective interactions between phosphatidylglycerol and the homotetrameric potassium channel KcsA (Heginbotham et al., 1998; Valiyaveetil et al., 2002).

We can also distinguish membrane lipid–protein interactions based on the different categories of membrane proteins (**Figure 1C**). Integral membrane proteins and lipid-anchored proteins can interact with lipids through hydrophobic interactions. While peripheral proteins will normally interact with lipids through transient binding with lipids' head groups, different strengths of these interactions can be used to define proteins' locations and functions. For example, proteins that specifically bind glycosphingolipids or sphingomyelin can be recruited to the aforementioned membrane nanodomains (Fantini and Yahi, 2010; Pontier and Schweisguth, 2012; Sezgin et al., 2017). During T-cell activation, cholesterol can selectively bind to the resting TCR and activate the allosteric transition of the TCR complex (Swamy et al., 2016; **Figure 1D**). Meanwhile, the dynamic interactions between CD28 and cholesterol or sphingomyelin also help recruit these membrane proteins into the same submembrane domains of the TCR complex for the efficient T-cell activation (Kabouridis et al., 2000; Yang et al., 2017). These transient lipid–protein interactions are required to prevent spurious TCR activation and ensure accurate membrane functions.

Membrane lipid domains are also involved in cancer development and progression. It has been shown that oncogenic proteins such as mucin 1 and urokinase plasminogen activator surface receptor are centered in raft-like domains (Staubach et al., 2009). Mitogenic signaling is also initiated from cell surface receptors in the lipid domains (Heldin et al., 2016; Varshney et al., 2016). In addition, by disrupting raft-like membrane domains, anticancer drugs can be developed (Gajate and Mollinedo, 2007). Similarly, lipid domain partitions have also been observed in other health threats such as vascular diseases (Maguy et al., 2006). Membrane transient interactions are indeed important cellular events that require better understanding.

METHODS TO STUDY MEMBRANE TRANSIENT INTERACTIONS

In the past few decades, several computational and experimental methods have been developed to study membrane transient interactions (Loura et al., 2010; Smith, 2012; Corradi et al., 2019). With significant improvement in the computing power and theoretical models, computational approaches can now predict and explain many membrane short-lived interactions. Dynamic simulations have been applied to study various membrane interactions (Corradi et al., 2019; Muller et al., 2019), such as the effect of lipid environment on membrane channel functions (Gu and de Groot, 2020), the impact of polyunsaturated fatty acids on lipid raft structure and distribution (Levental et al., 2016), and lipid-induced cross-talk through the leaflets (Bossa et al., 2015). There are several great reviews on using computational methods to study membrane dynamic interactions (Corradi et al., 2019; Muller et al., 2019; Siebenmorgen and Zacharias, 2020). Here, we will mainly discuss experimental methods that can be used to really detect and analyze transient interactions in the cell membranes.

Nuclear Magnetic Resonance Spectroscopy

X-ray crystallography and electron microscopy can provide valuable structural information about stable membrane protein–lipid complexes (Zhou et al., 2001; Nooren and Thornton, 2003). However, these methods are normally not suitable for studying transient interactions or conformational changes. In comparison, nuclear magnetic resonance (NMR) spectroscopy is better for analyzing structure and dynamics of membrane transient complexes (Díaz-Moreno et al., 2005; Dannatt et al., 2016; Purslow et al., 2020). Thermodynamic information such as

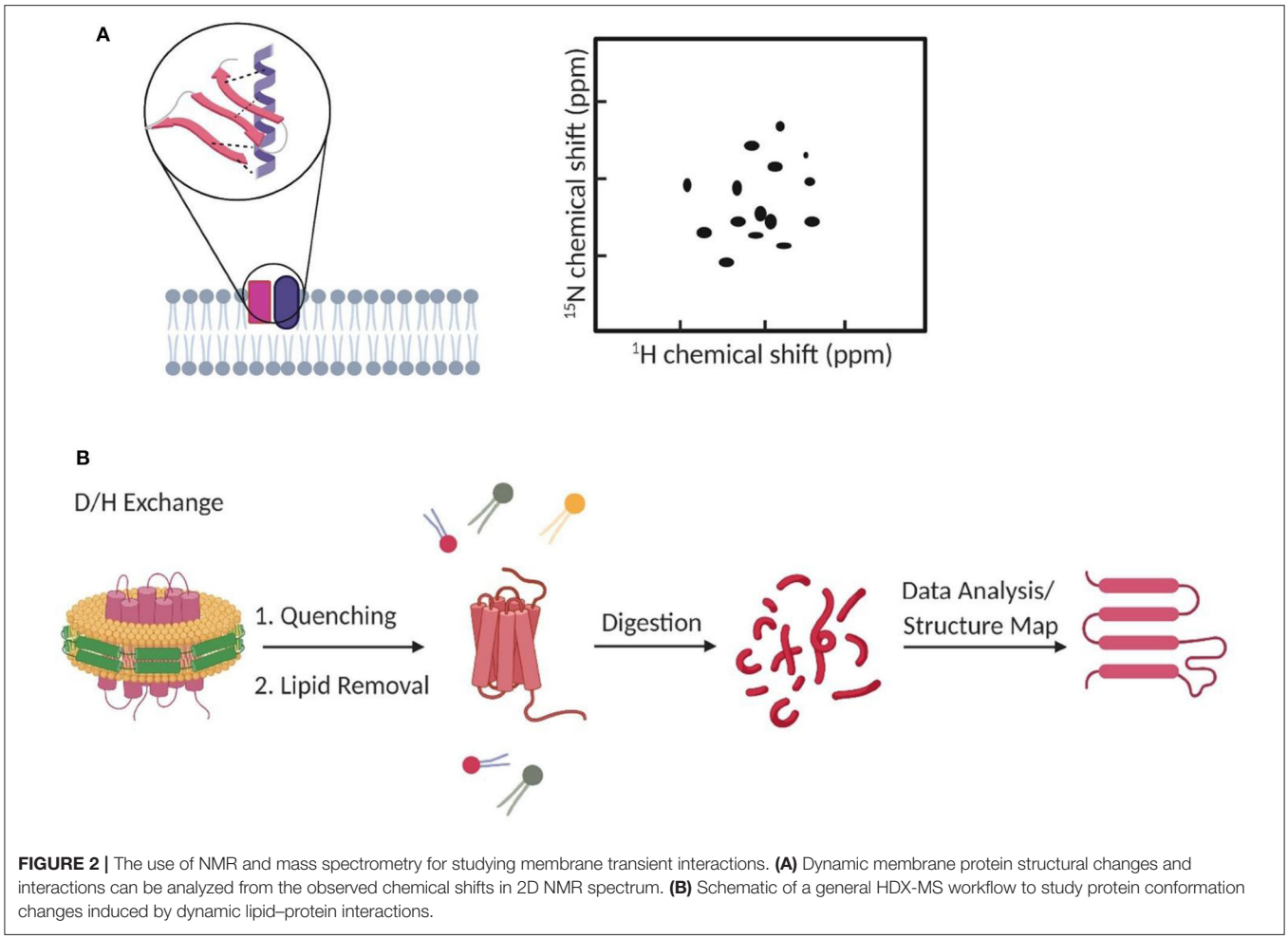

FIGURE 2 | The use of NMR and mass spectrometry for studying membrane transient interactions. **(A)** Dynamic membrane protein structural changes and interactions can be analyzed from the observed chemical shifts in 2D NMR spectrum. **(B)** Schematic of a general HDX-MS workflow to study protein conformation changes induced by dynamic lipid–protein interactions.

the binding affinities of membrane partners can also be measured in NMR (Purslow et al., 2020). NMR is a powerful technique for studying membrane transient interactions, especially if atomic-level structural information is needed.

Chemical shift of proteins is very sensitive to the local electronic environment. As a result, changes in the chemical shift can be used for the NMR analysis of protein complex formation and structure (Ahuja et al., 2013; **Figure 2A**). For example, chemical shift perturbation is a suitable method for studying transient interactions with μM–mM binding affinities (Acuner Ozbabacan et al., 2011). In this method, a ^{15}N- or ^{13}C-labeled target protein is titrated with different amounts of unlabeled binding partner. Changes in the two-dimensional (2D) heteronuclear single-quantum coherence spectra are then used to calculate the binding affinity and binding site of the protein complex. Several other NMR-based methods have also been developed to study membrane dynamic protein–protein interactions, such as solvent paramagnetic relaxation enhancement, residual dipolar coupling, and nuclear Overhauser effect (Vinogradova and Qin, 2012; Gell et al., 2017; Larsen et al., 2018).

However, it is still difficult to use NMR to characterize structures of large-molecular-weight complexes. Appropriate kinetic models should also be carefully chosen to convert the obtained NMR data into accurate interaction parameters (Furukawa et al., 2016). In this regard, a relevant strategy based on site-directed spin labeling electron paramagnetic resonance (EPR) spectroscopy can be advantageous for the more direct study of membrane transient interactions (Subczynski et al., 2010; Zhang et al., 2011). However, both NMR and EPR are still challenging to be directly applied for studying interactions in live cell membranes. The differences between real cell membrane environment and *in vitro* conditions have to be considered.

Mass Spectrometry

Mass spectrometry (MS) is another common method to study membrane dynamic interactions (Konijnenberg et al., 2014; Gupta et al., 2017, 2018; Bolla et al., 2019; Frick and Schmidt, 2019). MS does not provide high-resolution target structure, but it can measure the mass and stoichiometry of the complex (Pyle et al., 2018; Frick and Schmidt, 2019). Among different types of MS, hydrogen–deuterium exchange MS (HDX-MS) has gained much attention for studying transient (millisecond range) protein conformational changes (Rist et al., 2005; Giladi and Khananshvili, 2020). For example, HDX-MS has been used to study how transient lipid–protein interactions can induce

conformational and functional changes of bacterial leucine transporter LeuT (Adhikary et al., 2017), rhomboid protease GlpG (Reading et al., 2017), and various secondary transporters (Martens et al., 2018). In HDX-MS, labile hydrogens in the protein complex can be exchanged with deuterium. The mass uptake at different locations of the complex will then be measured and mapped to allow visualization of its structural dynamics (**Figure 2B**; Martens et al., 2019; Giladi and Khananshvili, 2020). High-purity samples are desirable but not essential, because the contaminants can be easily ruled out during data processing (Martens et al., 2019).

HDX-MS is still limited with some shortcomings. First, HDX-MS reports the changes in the protein uptake of deuterium, not directly the complex conformation. For a 50-kDa protein, analyzing and converting one set of data to the conformational changes may take ∼2 days (Martens et al., 2019). Detergents are normally used to extract membrane protein complexes in MS studies. However, affected by the choice of detergent, the obtained results may not represent the native structure of membrane complexes. Membrane-mimic lipid nanostructures, such as picodiscs, nanodiscs, styrene maleic acid lipid particles, bicelles, and liposomes (Grinkova et al., 2010; Dürr et al., 2012; Marty et al., 2016; Frick and Schmidt, 2019), have been developed to alleviate this problem, while the effect of these artificial lipid structures should be still carefully considered.

Secondary ion MS (SIMS) has been used to image lipid distributions in the cell membranes. For example, by metabolically incorporating isotopic form of lipids, SIMS allows the imaging of sphingolipid and cholesterol distributions in the membrane domains, with a resolution of <100 nm (McQuaw et al., 2007; He et al., 2017; Kraft, 2017). Compared to fluorescent labeling as mentioned below, such isotope labeling has less impact on the natural membrane properties of the target lipids. SIMS can indirectly verify lipid–lipid or lipid–protein interactions by quantifying target lipid distributions and transitions upon addition and depletion of the partner lipids or proteins (McQuaw et al., 2007; He et al., 2017). However, SIMS cannot directly assess membrane interactions, especially those being transient. In addition, SIMS is not suitable for live-cell studies. Cells need to be dehydrated first, and the measurements are performed in vacuum.

Fluorescence Correlation Spectroscopy and Cross-Correlation Spectroscopy

The development of fluorescence techniques has revolutionized membrane biophysical studies (Triffo et al., 2012; Martinez-Moro et al., 2019). Fluorescence methods enable the real-time study of dynamic phenomena in living cell membranes with high temporal and spatial resolution. Here, we will discuss some fluorescence spectroscopy and microscopy approaches that have been used to study transient interactions in the cell membranes.

The first method is based on fluorescence correlation spectroscopy (FCS). FCS can be used to analyze the concentrations, motilities, and interactions of membrane fluorescent-labeled compounds (Haustein and Schwille, 2003; Bacia et al., 2006). It works by measuring fluorescence fluctuations in a tiny focal spot. Membrane complex formation results in changes in the mobility. In order to obtain reliable interaction information in FCS, a large-molecular-weight difference (usually >eight-fold) between bound and unbound state is needed. To study membrane interactions between molecules of similar molecular weight, fluorescence cross-correlation spectroscopy (FCCS) can be a good option. FCCS measures the fluctuations and correlations of two fluorescent-labeled partners in the same focal spot (Bacia et al., 2006; Bacia and Schwille, 2007). If these two molecules interact, even transiently, they will diffuse together and exhibit a positive cross-correlation signal.

FCCS has become a popular method to study, at the single-molecule level, membrane dynamic interactions (Bacia et al., 2006; Sadamoto and Muto, 2013; Ma et al., 2014; Martinez-Moro et al., 2019). FCCS is able to report the correlated diffusion and binding stoichiometry over multiple time scales (10^{-7}-10^{1} s) (Bacia et al., 2006). For example, FCCS has been used to study the regulation effect of cardiolipin and phosphatidylglycerol on the dynamic oligomerization of mitochondrial membrane voltage-dependent anion channel (Betaneli et al., 2012). In another example, SNARE proteins were found to prefer incorporating into disordered membrane domains (Bacia et al., 2004). As an example for measuring transient protein–protein interactions in live cell membranes, pulsed-interleaved excitation FCCS was used to investigate anchor-mediated dynamic colocalization of lymphocyte cell kinase, RhoA, and K-Ras proteins (**Figure 3A**; Triffo et al., 2012).

FCS and FCCS are not suitable for monitoring slowly moving membrane particles, though. In this case, the number of interactions within the focal spot is hardly sufficient to obtain good statistics; meanwhile, the fluorophores can be easily bleached before leaving the focal spot (Triffo et al., 2012). Traditional FCCS can assess only tiny focal spots rather than the whole membrane area. To assess a large membrane, temporal and spatial correlation analysis can be combined with scanning FCS/FCCS now (Ruan et al., 2004).

Super-Resolution Microscopy

FCS and FCCS normally operate on a confocal microscope. However, limited by the relatively big focal spot (∼200 nm in diameter), it is challenging to validate if these membrane interactions indeed happen on the molecular level, especially in those small nanodomains. Stimulated emission depletion (STED) microscopy is a super-resolution approach that can be combined with FCS to image interactions below the diffraction limit (Honigmann et al., 2014; Saka et al., 2014; Sevcsik et al., 2015; Sezgin et al., 2019). Using STED-FCS, a 20-nm focal spot is accessible, which allows a better distinction between membrane free diffusion and transient interactions (Eggeling et al., 2009).

STED-FCS has been used to monitor cholesterol-dependent membrane diffusion and colocalization of sphingolipids and glycosylphosphatidylinositol (GPI)–anchored proteins in living cells (Eggeling et al., 2009; **Figure 3B**). These lipid moieties were found to be transiently trapped in cholesterol-mediated complexes in a <20-nm-diameter area. In a more recent study, the same authors applied scanning STED-FCS to investigate

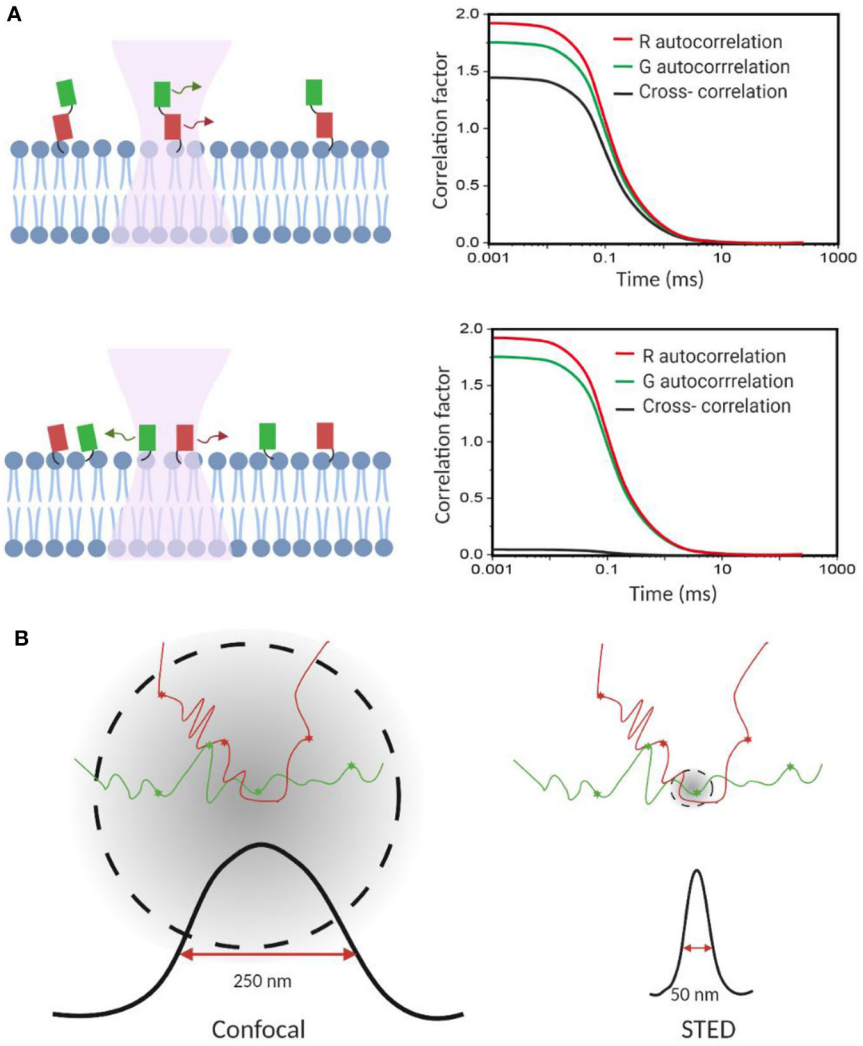

FIGURE 3 | Fluorescence correlation spectroscopy measures membrane transient interactions at the single-molecule level. **(A)** Schematic of fluorescence cross-correlation of correlated and uncorrelated protein diffusions in the membrane. Increase in correlation among targets results in higher cross-correlation. **(B)** STED-FCS provides better spatial resolution to distinguish target interactions than the conventional confocal FCS.

the spatial distributions of these membrane cholesterol–lipid interactions. Again, transient interaction hotspots across the cell membrane were observed (Honigmann et al., 2014). Dynamic cholesterol-dependent multiprotein membrane assemblies can also be visualized with STED-FCS (Saka et al., 2014).

In addition to STED, other single-molecule imaging and super-resolution techniques, such as total internal reflection fluorescence (TIRF) microscopy, structured illumination microscopy, and photoactivated localization microscopy, have also been used to study membrane transient interactions (Hess et al., 2007; Galbraith and Galbraith, 2011). Considering that the short-lived interactions usually do not result in many accumulated signals over a large membrane plane, microscopes of high spatial resolution and single-molecule sensitivity are useful techniques in our understanding of these heterogeneous and transient interactions. However, μs–ms range membrane transient interactions are often still too fast to be analyzed based on single-molecule imaging or colocalization methods. Many super-resolution techniques have to sacrifice the temporal resolution to obtain spatially resolved information (Westphal et al., 2008; Galbraith and Galbraith, 2011).

With fast image acquisition, high signal-to-noise ratio, and spatial resolution, TIRF is a popular approach to monitor dynamic motions and interactions in live cell (Suzuki et al., 2012; Stender et al., 2013). Using bright and photostable fluorophores, transient colocalization as short as microseconds can be detected in TIRF. For example, transient homodimerization of GPI-anchored proteins was found as critical organization unit for membrane domain formation (Suzuki et al., 2012; **Figure 4A**). While, interestingly, somewhat controversial result was shown in another TIRF-based study, which indicated that GPI-anchored proteins were not found to partition in the membrane domains

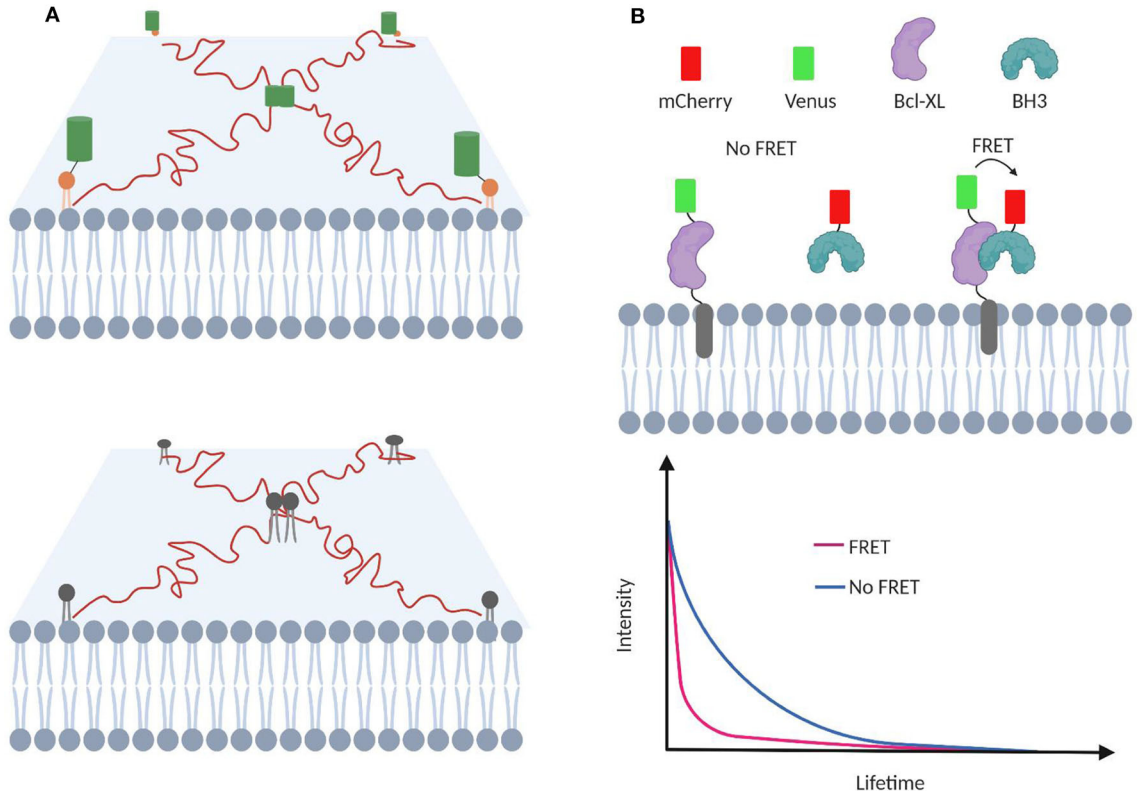

FIGURE 4 | TIRF-based single-molecule tracking to investigate membrane transient interactions. **(A)** Protein homodimerization and lipid–lipid interactions are transient process that can be studied with TIRF. **(B)** Transient interactions between proapoptotic BH3 protein and membrane-bound antiapoptotic Bcl-2 proteins can be studied using FLIM-FRET. FRET among Venus and mCherry facilitates Venus relaxation and lowers its lifetime.

(Sevcsik et al., 2015), this discrepancy may indicate that it is still challenging to precisely measure membrane transient interactions based on simply monitoring the trajectory of each single molecule.

Meanwhile, because normally TIRF is performed close to the surface of the coverslip, it is mainly capable of studying the surface-attached part of the target cells (Hell et al., 2015), e.g., the basal surface of epithelial cells but not the apical side. Considering that basal and apical cell membrane may have different compositions and functions, TIRF may only provide partially representative information about the whole cell membrane. Furthermore, close proximity with the glass surface may also induce non-natural protein/lipid organization and diffusion patterns.

Förster Resonance Energy Transfer

Förster resonance energy transfer (FRET) is another powerful technique to investigate membrane molecular interactions (Rao and Mayor, 2005; Loura et al., 2010; Loura and Prieto, 2011). By modifying the target membrane partner with a donor and acceptor fluorophore, respectively, once two molecules are in close proximity (<10 nm), the energy transfer between the donor and acceptor results in a strong FRET signal. For example, FRET has been used to discover specific membrane interactions between sphingomyelin and the p24 protein (Contreras et al., 2012), as well as the membrane domain formation during the interactions of N-Ras and K-Ras4B oncoproteins (Li et al., 2019).

FRET is often combined with fluorescence lifetime imaging microscopy (FLIM) to study membrane transient interactions (Llères et al., 2007; Liu et al., 2012; Gagnon et al., 2017). In FLIM-FRET, the energy transfer between the FRET donor and acceptor results in a fluorescence lifetime decrease of the donor fluorophore. Compared with fluorescence intensity-based measurement, FLIM-FRET is advantageous of being independent of the membrane concentration of target molecules (Wallrabe and Periasamy, 2005). This feature is critical considering the heterogeneity and diverse distribution patterns of lipids and proteins. For example, the effect of various mutations and chemical inhibitors in modulating transient interactions between membrane-bound antiapoptotic Bcl-2 protein and proapoptotic BH3 protein has been measured using FLIM-FRET (Liu et al., 2012; Osterlund et al., 2015; **Figure 4B**).

In addition to FRET, distance-dependent non-FRET quenching has also been used to track transient interactions in live cell membranes (Artetxe et al., 2013). For example, fluorophore- and quencher-labeled lipid pairs were used to study the impact of head group size of sphingolipids and ceramide on their interactions with membrane cholesterols (Artetxe

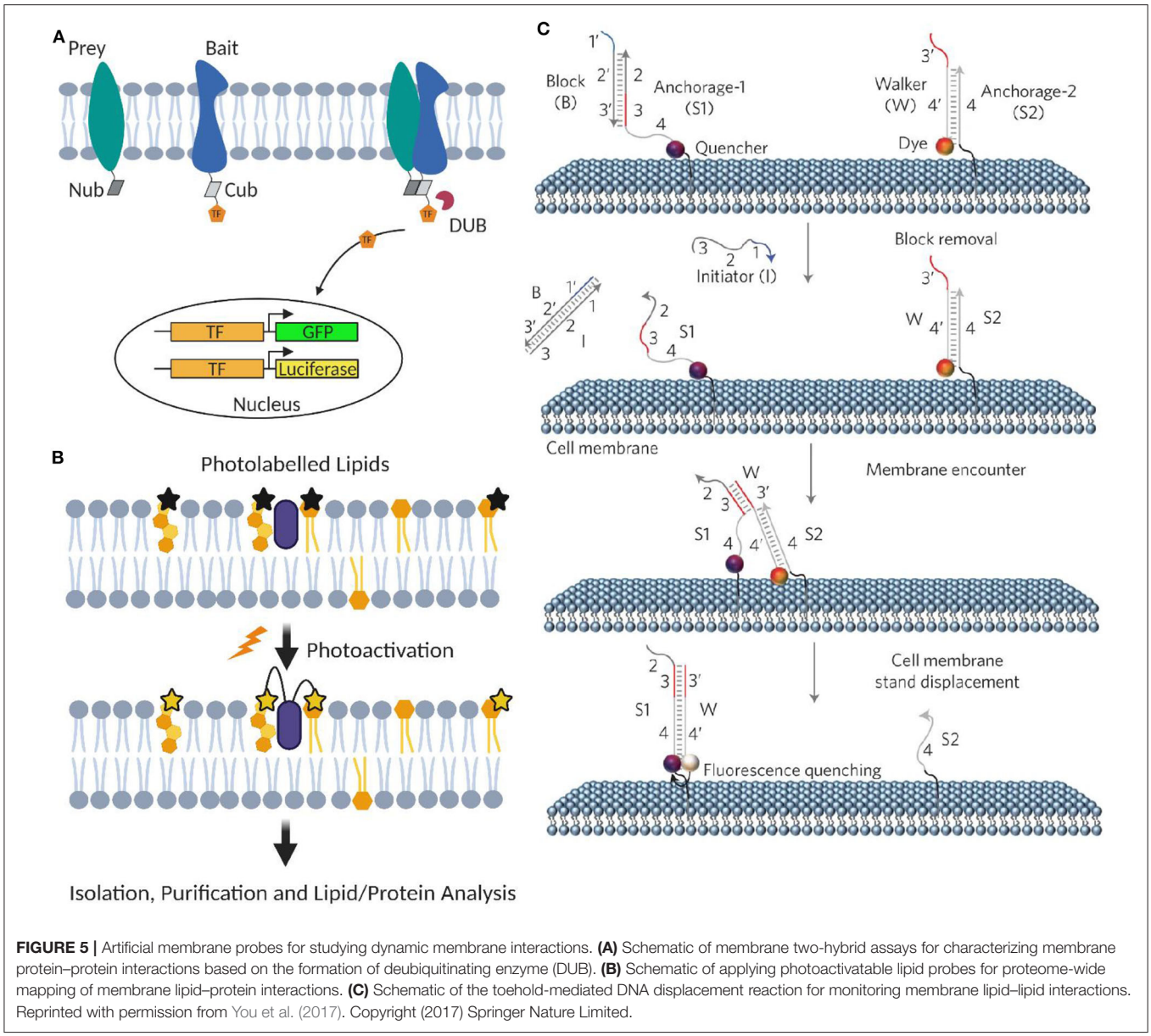

FIGURE 5 | Artificial membrane probes for studying dynamic membrane interactions. **(A)** Schematic of membrane two-hybrid assays for characterizing membrane protein–protein interactions based on the formation of deubiquitinating enzyme (DUB). **(B)** Schematic of applying photoactivatable lipid probes for proteome-wide mapping of membrane lipid–protein interactions. **(C)** Schematic of the toehold-mediated DNA displacement reaction for monitoring membrane lipid–lipid interactions. Reprinted with permission from You et al. (2017). Copyright (2017) Springer Nature Limited.

et al., 2013). In these FRET or quencher approaches, both target molecules are needed to be fused with fluorophore or quencher at a specific location to ensure close proximity during interactions. Meanwhile, the limited signal-to-noise ratio has prevented the application of these FRET methods for imaging some really transient (submillisecond) membrane interactions.

Membrane Two-Hybrid Assays

Yeast and mammalian two-hybrid assays have been developed to characterize membrane protein–protein interactions, including transient ones (Snider et al., 2010; Petschnigg et al., 2014). In these assays, each half of a split ubiquitin is tagged, respectively, to the target membrane protein (named as bait and prey). Once bait and prey proteins interact, a pseudoubiquitin is formed and then cleaved by cytosolic deubiquitinating enzymes to release a reporter protein, such as a transcription factor for generating fluorescent proteins or luciferases (Petschnigg et al., 2014; **Figure 5A**).

One major advantage of membrane two-hybrid assay is that it can be used for high-throughput screening. For example, using this approach, CRKII has been identified as a new adaptor protein that can dynamically interact with membrane epidermal growth factor receptor in oncogenic signaling (Petschnigg et al., 2014). These membrane two-hybrid assays can also potentially be useful in discovering drug molecules that can interfere with transient protein interactions during membrane signaling.

On the other hand, compared with the reversible FRET interactions, these membrane two-hybrid assays are normally irreversible and not suitable to image the location or dynamics of membrane interactions. The relatively high rate of false-positive

signals, e.g., from protein overexpression, requires careful data analysis and validation. In theory, other methods that can convert dynamic interactions into permanent signals, such as *in situ* proximity ligation assay (Petschnigg et al., 2014) and bimolecular fluorescence complementation (Kodama and Hu, 2012), may also be useful for characterizing membrane transient interactions. However, the interaction time required for the proximity-based ligation or reconstitution of fluorescent proteins made these methods practically challenging to study short-lived membrane interaction events.

Photoactivatable Lipid Probes

A powerful method to profile proteome-wide membrane lipid–protein interactions is based on photoactivatable lipid probes (Xia and Peng, 2013; Peng et al., 2014). In this method, after incorporating into the membranes and upon light irradiation, photoactivatable lipids can be activated and cross-linked with their interacting membrane protein partners (**Figure 5B**). Transiently formed membrane lipid–protein complexes can thus be covalently stabilized. After separation and purification, different approaches such as MS, autoradiography, high-performance liquid chromatography, and gel electrophoresis can be used to analyze the cross-linked membrane complexes.

These photoactivatable lipid probes can be used in both artificial and live cell membranes. They have been used to proteome-wide map and identify new membrane proteins that can transiently bind target lipids (Niphakis et al., 2015). Without prior knowledge, unlabeled endogenous membrane proteins can be directly cross-linked with the photoactivatable lipid probes once an interaction happens. Meanwhile, with the help of bifunctional lipid probes, the binding sites of these lipid–protein complexes can also be determined (Xia and Peng, 2013; Peng et al., 2014). In addition to membrane lipid–protein interactions, these photoactivatable probes can also be used to map dynamic lipid-anchored protein–protein interactions.

On the other hand, by introducing several functional groups in the lipid molecules, the natural interaction pattern of the target lipid may be disrupted. In addition, the crosslinking efficiency is highly dependent on the activity and position of the functional group. As a result, the choice of bio-orthogonal crosslinking moiety and tagging site in lipids is critical in developing accurate and efficient photoactivatable probes. A series of photoactivatable lipid probes have been developed (Xia and Peng, 2013). With continuous efforts in the characterization and optimization of these functional probes, the photo-crosslinking approach can play a critical role in profiling membrane transient interactions.

DNA-Based Membrane Probes

We have recently developed a DNA-based approach to image transient interactions in live cell membranes (You et al., 2017). In this approach, individual membrane lipid–lipid and protein–protein interactions are converted into changes in the collective fluorescence signal, which can be easily detected by fluorescence microscopes. DNA probes can be covalently modified onto target membrane lipids without affecting their lateral diffusion and domain partition (You et al., 2017; Bagheri et al., 2019a). The highly precise and controllable DNA hybridizations have further allowed programmable manipulation and function of these membrane-anchored DNA probes (Bagheri et al., 2019b; Zhao et al., 2020).

Our DNA probe is realized through a toehold-mediated strand displacement reaction (**Figure 5C**). To measure membrane transient lipid–lipid interactions, two target lipids were modified with a quencher strand (S_1) and an unmodified anchor strand (S_2), respectively. Once two lipids are located within ∼5 nm, a fluorophore-labeled DNA probe (W) will translocate from S2 to S1, resulting in a fluorescence quenching. By monitoring membrane fluorescence signal changes, this approach allows live-cell imaging of μs-to-ms-range lipid–lipid interactions using common fluorescence microscope and flow cytometer. Similar strategy can also be applied to monitor membrane protein–protein interactions using target protein-specific DNA aptamers (You et al., 2017).

This modular DNA-based approach can be easily adopted to different targets on the cell membrane. However, it is necessary to carefully evaluate the effect of DNA modification on the membrane properties and behaviors of the target molecules. Furthermore, the membrane densities of the DNA probes should be kept in the minimum possible level to provide enough fluorescence signals but also avoid membrane interruptions.

DISCUSSION

Membrane transient interactions are important biophysical events for membrane trafficking, signal transduction, and cell proliferation (Ikonen, 2008; Kraft, 2013; Sezgin et al., 2017; Martens et al., 2018; Yi et al., 2019). With fast emergence of new powerful methods and tremendous advancement in instrumentations, our understanding of these short-lived events has been significantly improved. As shown in **Table 1**, we have summarized and compared different properties and applications of these variant experimental methods in studying membrane transient interactions. We will discuss as follows our view on how to further advance these methods, as well as future directions in membrane interaction studies.

NMR and MS are both almost label-free approaches that can measure membrane interactions in their natural forms. However, direct *in situ* analysis in live cell membranes is still difficult for both methods. The recent development of SIMS seems to provide a promising solution for this issue. Furthermore, it is challenging to apply NMR and MS to study really fast (<ms) membrane interactions or conformational changes. Indeed, efforts have been taken to improve the temporal resolution of MS, for example, by conjugating with a flow quenching system (Rist et al., 2005; Giladi and Khananshvili, 2020).

NMR provides great spatial resolution for structural studies. In comparison, MS and other methods usually suffer from low spatial resolutions. To potentially improve their resolution, complementing the experimental data with computational simulations can be an effective approach to obtain molecular-level structural information (Martens et al., 2019).

Fluorescence-based methods allow direct and real-time visualization of transient interactions in live cell membranes.

TABLE 1 | Currently available methods for studying cell membrane transient interactions.

Method	Resolution		Membranes applied		Interactions studied	Interaction information provided
	Temporal	Spatial	Cell	Synthetic		
NMR	ms	Atomic	No	Yes	Lipid–protein Protein–protein	Structure and conformation Kinetic and equilibrium constant
HDX-MS	ms	μm	No	Yes	Lipid–protein Protein–protein	Protein conformation Stoichiometry
SIMS	min	100 nm	Yes	Yes	Lipid–lipid Lipid–protein	Membrane distribution
FCS and FCCS	μs	200 nm	Yes	Yes	Lipid–lipid Lipid–protein Protein–protein	Membrane concentration Membrane distribution Kinetic and equilibrium constant
STED-FCS	μs	20 nm	Yes	Yes	Lipid–lipid Lipid–protein Protein–protein	Membrane concentration Membrane distribution Kinetic and equilibrium constant
TIRF	μs	20 nm	Yes	Yes	Lipid–lipid Lipid–protein Protein–protein	Membrane distribution Kinetic and equilibrium constant
FRET	μs	10 nm	Yes	Yes	Lipid–lipid Lipid–protein Protein–protein	Membrane distribution Kinetic and equilibrium constant
FLIM-FRET	s	10 nm	Yes	Yes	Protein–protein	Membrane distribution Kinetic and equilibrium constant
MTH	s	200 nm	Yes	Yes	Protein–protein	High-throughput screening
PAL	ms	μm	Yes	Yes	Lipid–protein	Proteome-wide profiling Protein–lipid complex structure
DNA probe	μs	10 nm	Yes	Yes	Lipid–lipid Protein–protein	Membrane distribution Kinetic and equilibrium constant

MTH, membrane two-hybrid assay; PAL, photoactivable lipid probe.

Using commercially available microscopes, currently it is easy to precisely measure ms–s range membrane interactions. Meanwhile, advanced imaging systems have been designed and applied for detecting even faster ($< \mu s$) interactions (Simmons and Konermann, 2002; Rist et al., 2005; Honigmann et al., 2014; Sezgin et al., 2019). We are expecting these advanced systems to be more readily available to the broad community of researchers in the future.

With the development of versatile fluorescent membrane probes, advanced fluorescence microscopes have genuinely reshaped our perception of membrane transient interactions. However, methods that allow high-throughput and quantitative analysis are still limited, especially for screening compounds that can potentially regulate critical transient interactions in diseases. As a result, membrane heterogeneities and cell-to-cell variations of these dynamic interactions or so-called membrane "interactome" are largely unknown.

Even using the same method, contradictory results have been obtained for many transient interactions such as in the case of membrane nanodomains. This inconsistency may result from the limited precision of the methods, but also is likely due to the dynamic nature of these transient interactions. Under different cellular environment and conditions, the lifetime of membrane interactions can be varied dramatically. Standard experimental procedure and statistical data analysis should be established. Meanwhile, it will be helpful to use more than one method to validate the observed results for membrane transient interactions.

A systematic comparison of the accuracy and performance of available methods in analyzing membrane transient interactions is highly desired. Most laboratories chose the methods based on their own experience and expertise. One goal of this review is to provide the first step in initiating such comparison. We believe once a well-accepted membrane model and standard approach were established, versatile functions of transient interactions in regulating membrane trafficking and cell signaling can be discovered in both healthy and diseased cell conditions.

This review has been focusing on major methods in studying transient membrane interactions among individual lipids and proteins. Other interesting membrane interactions, such as membrane vesicle formation, transportation, and fusion, are also critical for various cellular functions such as cell growth, hormone secretion, and neurotransmission (Novick and Schekman, 1979; Wickner and Schekman, 2008; Rupert et al., 2017; Welsh et al., 2017). Unfortunately, because of the limited space in this article, we are not able to cover all these topics. We would like to refer interested audience to those reports mentioned above.

In short, the introduction of new methodologies has been continuously improving our knowledge of transient membrane interactions. It is important that researchers with different expertise to collaboratively work together in developing more

powerful toolkits. We believe that future evolution of methods and instrumentations will continue to play a major role in advancing our understanding of the dynamic nature of cells and other biological system.

AUTHOR CONTRIBUTIONS

MY provided the guidance for the whole project and revised the manuscript. YB and AA searched the literature and wrote the manuscript. All the authors have reviewed, edited, and approved the manuscript before submission.

FUNDING

The authors gratefully acknowledge NIH R35GM133507, Sloan Research Fellowship, a start-up grant from UMass Amherst, and an IALS M2M seed grant to MY.

REFERENCES

Acuner Ozbabacan, S. E., Engin, H. B., Gursoy, A., and Keskin, O. (2011). Transient protein-protein interactions. *Protein Eng. Des. Sel.* 24, 635–648. doi: 10.1093/protein/gzr025

Adhikary, S., Deredge, D. J., Nagarajan, A., Forrest, L. R., Wintrode, P. L., and Singh, S. K. (2017). Conformational dynamics of a neurotransmitter:sodium symporter in a lipid bilayer. *Proc. Natl. Acad. Sci. U.S.A.* 114, E1786–E1795. doi: 10.1073/pnas.1613293114

Ahuja, S., Jahr, N., Im, S. C., Vivekanandan, S., Popovych, N., Le Clair, S. V., et al. (2013). A model of the membrane-bound cytochrome b5-cytochrome P450 complex from NMR and mutagenesis data. *J. Biol. Chem.* 288, 22080–22095. doi: 10.1074/jbc.M112.448225

Aimon, S., Callan-Jones, A., Berthaud, A., Pinot, M., Toombes, G. E. S., and Bassereau, P. (2014). Membrane shape modulates transmembrane protein distribution. *Dev. Cell* 28, 212–218. doi: 10.1016/j.devcel.2013.12.012

Artetxe, I., Sergelius, C., Kurita, M., Yamaguchi, S., Katsumura, S., Slotte, J. P., et al. (2013). Effects of sphingomyelin headgroup size on interactions with ceramide. *Biophys. J.* 104, 604–612. doi: 10.1016/j.bpj.2012.12.026

Bacia, K., Kim, S. A., and Schwille, P. (2006). Fluorescence cross-correlation spectroscopy in living cells. *Nat. Methods* 3, 83–89. doi: 10.1038/nmeth822

Bacia, K., Schuette, C. G., Kahya, N., Jahn, R., and Schwille, P. (2004). SNAREs prefer liquid-disordered over "raft" (liquid-ordered) domains when reconstituted into giant unilamellar vesicles. *J. Biol. Chem.* 279, 37951–37955. doi: 10.1074/jbc.M407020200

Bacia, K., and Schwille, P. (2007). Practical guidelines for dual-color fluorescence cross-correlation spectroscopy. *Nat. Protoc.* 2, 2842–2856. doi: 10.1038/nprot.2007.410

Bagheri, Y., Chedid, S., Shafiei, F., Zhao, B., and You, M. (2019a). A quantitative assessment of the dynamic modification of lipid–DNA probes on live cell membranes. *Chem. Sci.* 10, 11030–11040. doi: 10.1039/C9SC04251B

Bagheri, Y., Shafiei, F., Chedid, S., Zhao, B., and You, M. (2019b). Lipid-DNA conjugates for cell membrane modification, analysis, and regulation. *Supramol. Chem.* 31, 532–544. doi: 10.1080/10610278.2019.1632454

Bakht, O., Pathak, P., and London, E. (2007). Effect of the structure of lipids favoring disordered domain formation on the stability of cholesterol-containing ordered domains (lipid rafts): identification of multiple raft-stabilization mechanisms. *Biophys. J.* 93, 4307–4318. doi: 10.1529/biophysj.107.114967

Betaneli, V., Petrov, E. P., and Schwille, P. (2012). The role of lipids in VDAC oligomerization. *Biophys. J.* 102, 523–531. doi: 10.1016/j.bpj.2011.12.049

Bolla, J. R., Agasid, M. T., Mehmood, S., and Robinson, C. V. (2019). Membrane protein–lipid interactions probed using mass spectrometry. *Annu. Rev. Biochem.* 88, 85–111. doi: 10.1146/annurev-biochem-013118-111508

Bolmatov, D., Soloviov, D., Zhernenkov, M., Zav'yalov, D., Mamontov, E., Suvorov, A., et al. (2020). Molecular picture of the transient nature of lipid rafts. *Langmuir* 36, 4887–4896. doi: 10.1021/acs.langmuir.0c00125

Bossa, G. V., Roth, J., and May, S. (2015). Modeling lipid–lipid correlations across a bilayer membrane using the quasi-chemical approximation. *Langmuir* 31, 9924–9932. doi: 10.1021/acs.langmuir.5b01719

Bunnell, S. C., Hong, D. I., Kardon, J. R., Yamazaki, T., McGlade, C. J., Barr, V. A., et al. (2002). T cell receptor ligation induces the formation of dynamically regulated signaling assemblies. *J. Cell Biol.* 158, 1263–1275. doi: 10.1083/jcb.200203043

Contreras, F.-X., Ernst, A. M., Haberkant, P., Björkholm, P., Lindahl, E., Gönen, B., et al. (2012). Molecular recognition of a single sphingolipid species by a protein's transmembrane domain. *Nature* 481, 525–529. doi: 10.1038/nature10742

Contreras, F.-X., Ernst, A. M., Wieland, F., and Brügger, B. (2011). Specificity of intramembrane protein–lipid interactions. *Cold Spring Harb. Perspect. Biol.* 3:a004705. doi: 10.1101/cshperspect.a004705

Corradi, V., Sejdiu, B. I., Mesa-Galloso, H., Abdizadeh, H., Noskov, S. Y., Marrink, S. J., et al. (2019). Emerging diversity in lipid–protein interactions. *Chem. Rev.* 119, 5775–5848. doi: 10.1021/acs.chemrev.8b00451

Dannatt, H. R. W., Felletti, M., Jehle, S., Wang, Y., Emsley, L., Dixon, N. E., et al. (2016). Weak and transient protein interactions determined by solid-state NMR. *Angew. Chemie Int. Ed.* 55, 6638–6641. doi: 10.1002/anie.201511609

De Keersmaecker, H., Camacho, R., Rantasa, D. M., Fron, E., Uji-I, H., Mizuno, H., et al. (2018). Mapping transient protein interactions at the nanoscale in living mammalian cells. *ACS Nano* 12, 9842–9854. doi: 10.1021/acsnano.8b01227

Díaz-Moreno, I., Díaz-Quintana, A., Molina-Heredia, F. P., Nieto, P. M., Hansson, Ö., De La Rosa, M. A., et al. (2005). NMR analysis of the transient complex between membrane photosystem I and soluble cytochrome c6. *J. Biol. Chem.* 280, 7925–7931. doi: 10.1074/jbc.M412422200

Dürr, U. H. N., Gildenberg, M., and Ramamoorthy, A. (2012). The magic of bicelles lights up membrane protein structure. *Chem. Rev.* 112, 6054–6074. doi: 10.1021/cr300061w

Eggeling, C., Ringemann, C., Medda, R., Schwarzmann, G., Sandhoff, K., Polyakova, S., et al. (2009). Direct observation of the nanoscale dynamics of membrane lipids in a living cell. *Nature* 457, 1159–1162. doi: 10.1038/nature07596

Fantini, J., and Yahi, N. (2010). Molecular insights into amyloid regulation by membrane cholesterol and sphingolipids: common mechanisms in neurodegenerative diseases. *Expert Rev. Mol. Med.* 12:e27. doi: 10.1017/S1462399410001602

Frick, M., and Schmidt, C. (2019). Mass spectrometry—A versatile tool for characterising the lipid environment of membrane protein assemblies. *Chem. Phys. Lipids* 221, 145–157. doi: 10.1016/j.chemphyslip.2019.4.001

Furukawa, A., Konuma, T., Yanaka, S., and Sugase, K. (2016). Quantitative analysis of protein-ligand interactions by NMR. *Prog. Nucl. Magn. Reson. Spectrosc.* 96, 47–57. doi: 10.1016/j.pnmrs.2016.02.002

Gagnon, E., Connolly, A., Dobbins, J., and Wucherpfennig, K. W. (2017). Studying dynamic plasma membrane binding of TCR-CD3 chains during immunological synapse formation using donor-quenching FRET and FLIM-FRET. *Methods Mol. Biol.* 1584, 259–289. doi: 10.1007/978-1-4939-6881-7_16

Gajate, C., and Mollinedo, F. (2007). Edelfosine and perifosine induce selective apoptosis in multiple myeloma by recruitment of death receptors and downstream signaling molecules into lipid rafts. *Blood* 109, 711–719. doi: 10.1182/blood-2006-04-016824

Galbraith, C. G., and Galbraith, J. A. (2011). Super-resolution microscopy at a glance. *J. Cell Sci.* 124, 1607–11. doi: 10.1242/jcs.080085

Gell, D. A., Kwan, A. H., and Mackay, J. P. (2017). "NMR spectroscopy in the analysis of protein-protein interactions," in *Modern Magnetic Resonance,* ed G. A. Webb (London: Springer International Publishing), 1–34. doi: 10.1007/978-3-319-28275-6_121-1

Giladi, M., and Khananshvili, D. (2020). Hydrogen-deuterium exchange mass-spectrometry of secondary active transporters: from structural

dynamics to molecular mechanisms. *Front. Pharmacol.* 11:70. doi: 10.3389/fphar.2020.00070

Grinkova, Y. V., Denisov, I. G., and Sligar, S. G. (2010). Engineering extended membrane scaffold proteins for self-assembly of soluble nanoscale lipid bilayers. *Protein Eng. Des. Sel.* 23, 843–848. doi: 10.1093/protein/gzq060

Gu, R.-X., and de Groot, B. L. (2020). Lipid-protein interactions modulate the conformational equilibrium of a potassium channel. *Nat. Commun.* 11:2162. doi: 10.1038/s41467-020-15741-8

Gupta, K., Donlan, J. A. C., Hopper, J. T. S., Uzdavinys, P., Landreh, M., Struwe, W. B., et al. (2017). The role of interfacial lipids in stabilizing membrane protein oligomers. *Nature* 541, 421–424. doi: 10.1038/nature20820

Gupta, K., Li, J., Liko, I., Gault, J., Bechara, C., Wu, D., et al. (2018). Identifying key membrane protein lipid interactions using mass spectrometry. *Nat. Protoc.* 13, 1106–1120. doi: 10.1038/nprot.2018.014

Haustein, E., and Schwille, P. (2003). Ultrasensitive investigations of biological systems by fluorescence correlation spectroscopy. *Methods* 29, 153–166. doi: 10.1016/S1046-2023(02)00306-7

He, C., Hu, X., Jung, R. S., Weston, T. A., Sandoval, N. P., Tontonoz, P., et al. (2017). High-resolution imaging and quantification of plasma membrane cholesterol by NanoSIMS. *Proc. Natl. Acad. Sci. U.S.A.* 114, 2000–2005. doi: 10.1073/pnas.1621432114

Heginbotham, L., Kolmakova-Partensky, L., and Miller, C. (1998). Functional reconstitution of a prokaryotic K^+ channel. *J. Gen. Physiol.* 111, 741–749. doi: 10.1085/jgp.111.6.741

Heldin, C.-H., Miyazono, K., and ten Dijke, P. (1997). TGF-β signalling from cell membrane to nucleus through SMAD proteins. *Nature* 390, 465–471. doi: 10.1038/37284

Heldin, C. H., Lu, B., Evans, R., and Gutkind, J. S. (2016). Signals and receptors. *Cold Spring Harb. Perspect. Biol.* 8:a005900. doi: 10.1101/cshperspect.a005900

Hell, S. W., Sahl, S. J., Bates, M., Zhuang, X., Heintzmann, R., Booth, M. J., et al. (2015). The 2015 super-resolution microscopy roadmap. *J. Phys. D. Appl. Phys.* 48:443001. doi: 10.1088/0022-3727/48/44/443001

Hess, S. T., Gould, T. J., Gudheti, M. V., Maas, S. A., Mills, K. D., and Zimmerberg, J. (2007). Dynamic clustered distribution of hemagglutinin resolved at 40 nm in living cell membranes discriminates between raft theories. *Proc. Natl. Acad. Sci. U.S.A.* 104, 17370–5. doi: 10.1073/pnas.0708066104

Honigmann, A., Mueller, V., Ta, H., Schoenle, A., Sezgin, E., Hell, S. W., et al. (2014). Scanning STED-FCS reveals spatiotemporal heterogeneity of lipid interaction in the plasma membrane of living cells. *Nat. Commun.* 5:5412. doi: 10.1038/ncomms6412

Ikonen, E. (2008). Cellular cholesterol trafficking and compartmentalization. *Nat. Rev. Mol. Cell Biol.* 9, 125–138. doi: 10.1038/nrm2336

James, J. R., Oliveira, M. I., Carmo, A. M., Iaboni, A., and Davis, S. J. (2006). A rigorous experimental framework for detecting protein oligomerization using bioluminescence resonance energy transfer. *Nat. Methods* 3, 1001–1006. doi: 10.1038/nmeth978

Kabouridis, P. S., Janzen, J., Magee, A. L., and Ley, S. C. (2000). Cholesterol depletion disrupts lipid rafts and modulates the activity of multiple signaling pathways in T lymphocytes. *Eur. J. Immunol.* 30, 954–963. doi: 10.1002/1521-4141(200003)30:3<954::AID-IMMU954>3.0.CO;2-Y

Kaiser, H.-J., Lingwood, D., Levental, I., Sampaio, J. L., Kalvodova, L., Rajendran, L., et al. (2009). Order of lipid phases in model and plasma membranes. *Proc. Natl. Acad. Sci. U.S.A.* 106, 16645–50. doi: 10.1073/pnas.0908987106

Kodama, Y., and Hu, C. D. (2012). Bimolecular fluorescence complementation (BiFC): a 5-year update and future perspectives. *Biotechniques* 53, 285–298. doi: 10.2144/000113943

Kolmakov, K., Belov, V., Bierwagen, J., Ringemann, C., Müller, V., Eggeling, C., et al. (2010). Red-emitting rhodamine dyes for fluorescence microscopy and nanoscopy. *Chem. A Eur. J.* 16, 158–166. doi: 10.1002/chem.200902309

Konijnenberg, A., Yilmaz, D., Ingólfsson, H. I., Dimitrova, A., Marrink, S. J., Li, Z., et al. (2014). Global structural changes of an ion channel during its gating are followed by ion mobility mass spectrometry. *Proc. Natl. Acad. Sci. U.S.A.* 111, 17170–5. doi: 10.1073/pnas.1413118111

Kraft, M. L. (2013). Plasma membrane organization and function: moving past lipid rafts. *Mol. Biol. Cell* 24, 2765–2768. doi: 10.1091/mbc.e13-03-0165

Kraft, M. L. (2017). Sphingolipid organization in the plasma membrane and the mechanisms that influence it. *Front. Cell Dev. Biol.* 4:154. doi: 10.3389/fcell.2016.00154

Larsen, E., Olivieri, C., Walker, C., Manu, V. S., Gao, J., Bernlohr, D. A., et al. (2018). Probing protein-protein interactions using asymmetric labeling and carbonyl-carbon selective heteronuclear NMR spectroscopy. *Molecules* 23:1937. doi: 10.3390/molecules23081937

Larsen, J. B., Jensen, M. B., Bhatia, V. K., Pedersen, S. L., Bjørnholm, T., Iversen, L., et al. (2015). Membrane curvature enables N-Ras lipid anchor sorting to liquid-ordered membrane phases. *Nat. Chem. Biol.* 11, 192–194. doi: 10.1038/nchembio.1733

Lee, A. (2003). Lipid–protein interactions in biological membranes: a structural perspective. *Biochim. Biophys. Acta Biomembr.* 1612, 1–40. doi: 10.1016/S0005-2736(03)00056-7

Lee, A. G. (2004). How lipids affect the activities of integral membrane proteins. *Biochim. Biophys. Acta Biomembr.* 1666, 62–87. doi: 10.1016/j.bbamem.2004.05.012

Lee, A. G. (2011). Lipid–protein interactions. *Biochem. Soc. Trans.* 39, 761–766. doi: 10.1042/BST0390761

Leikin, S., Kozlov, M. M., Fuller, N. L., and Rand, R. P. (1996). Measured effects of diacylglycerol on structural and elastic properties of phospholipid membranes. *Biophys. J.* 71, 2623–2632. doi: 10.1016/S0006-3495(96)79454-7

Levental, K. R., Lorent, J. H., Lin, X., Skinkle, A. D., Surma, M. A., Stockenbojer, E. A., et al. (2016). Polyunsaturated lipids regulate membrane domain stability by tuning membrane order. *Biophys. J.* 110, 1800–1810. doi: 10.1016/j.bpj.2016.03.012

Li, L., Dwivedi, M., Patra, S., Erwin, N., Möbitz, S., and Winter, R. (2019). Probing colocalization of N-Ras and K-Ras4B lipoproteins in model biomembranes. *ChemBioChem* 20, 1190–1195. doi: 10.1002/cbic.201800776

Liu, Q., Leber, B., and Andrews, D. W. (2012). Interactions of pro-apoptotic BH3 proteins with anti-apoptotic Bcl-2 family proteins measured in live MCF-7 cells using FLIM FRET. *Cell Cycle* 11, 3536–3542. doi: 10.4161/cc.21462

Llères, D., Swift, S., and Lamond, A. I. (2007). Detecting protein-protein interactions *in vivo* with FRET using multiphoton fluorescence lifetime imaging microscopy (FLIM). *Curr. Protoc. Cytom.* 42, 12.10.1–12.10.19. doi: 10.1002/0471142956.cy1210s42

Lorizate, M., Sachsenheimer, T., Glass, B., Habermann, A., Gerl, M. J., Kräusslich, H.-G., et al. (2013). Comparative lipidomics analysis of HIV-1 particles and their producer cell membrane in different cell lines. *Cell. Microbiol.* 15, 292–304. doi: 10.1111/cmi.12101

Loura, L., and Prieto, M. J. (2011). FRET in membrane biophysics: an overview. *Front. Physiol.* 2:82. doi: 10.3389/fphys.2011.00082

Loura, L. M. S., Prieto, M., and Fernandes, F. (2010). Quantification of protein–lipid selectivity using FRET. *Eur. Biophys. J.* 39, 565–578. doi: 10.1007/s00249-009-0532-z

Ma, X., Foo, Y. H., and Wohland, T. (2014). Fluorescence cross-correlation spectroscopy (FCCS) in living cells. *Nature Methods* 3, 557–573. doi: 10.1007/978-1-62703-649-8_25

Maguy, A., Hebert, T., and Nattel, S. (2006). Involvement of lipid rafts and caveolae in cardiac ion channel function. *Cardiovasc. Res.* 69, 798–807. doi: 10.1016/j.cardiores.2005.11.013

Marius, P., de Planque, M. R. R., and Williamson, P. T. F. (2012). Probing the interaction of lipids with the non-annular binding sites of the potassium channel KcsA by magic-angle spinning NMR. *Biochim. Biophys. Acta Biomembr.* 1818, 90–96. doi: 10.1016/j.bbamem.2011.09.017

Martens, C., Shekhar, M., Borysik, A. J., Lau, A. M., Reading, E., Tajkhorshid, E., et al. (2018). Direct protein-lipid interactions shape the conformational landscape of secondary transporters. *Nat. Commun.* 9:4151. doi: 10.1038/s41467-018-06704-1

Martens, C., Shekhar, M., Lau, A. M., Tajkhorshid, E., and Politis, A. (2019). Integrating hydrogen–deuterium exchange mass spectrometry with molecular dynamics simulations to probe lipid-modulated conformational changes in membrane proteins. *Nat. Protoc.* 14, 3183–3204. doi: 10.1038/s41596-019-0219-6

Martinez-Moro, M., Di Silvio, D., and Moya, S. E. (2019). Fluorescence correlation spectroscopy as a tool for the study of the intracellular dynamics and biological fate of protein corona. *Biophys. Chem.* 253:106218. doi: 10.1016/j.bpc.2019.106218

Marty, M. T., Hoi, K. K., and Robinson, C. V. (2016). Interfacing membrane mimetics with mass spectrometry. *Acc. Chem. Res.* 49, 2459–2467. doi: 10.1021/acs.accounts.6b00379

McMahon, H. T., and Boucrot, E. (2015). Membrane curvature at a glance. *J. Cell Sci.* 128, 1065–70. doi: 10.1242/jcs.114454

McQuaw, C. M., Zheng, L., Ewing, A. G., and Winograd, N. (2007). Localization of sphingomyelin in cholesterol domains by imaging mass spectrometry. *Langmuir* 23, 5645–50. doi: 10.1021/la063251f

Muller, M. P., Jiang, T., Sun, C., Lihan, M., Pant, S., Mahinthichaichan, P., et al. (2019). Characterization of lipid–protein interactions and lipid-mediated modulation of membrane protein function through molecular simulation. *Chem. Rev.* 119, 6086–6161. doi: 10.1021/acs.chemrev.8b00608

Neer, E. J., and Clapham, D. E. (1988). Roles of G protein subunits in transmembrane signalling. *Nature* 333, 129–134. doi: 10.1038/333129a0

Niphakis, M. J., Lum, K. M., Cognetta, A. B., Correia, B. E., Ichu, T. A., Olucha, J., et al. (2015). A global map of lipid-binding proteins and their ligandability in cells. *Cell* 161, 1668–1680. doi: 10.1016/j.cell.2015.05.045

Nooren, I. M., and Thornton, J. M. (2003). Structural characterisation and functional significance of transient protein–protein interactions. *J. Mol. Biol.* 325, 991–1018. doi: 10.1016/S0022-2836(02)01281-0

Novick, P., and Schekman, R. (1979). Secretion and cell-surface growth are blocked in a temperature-sensitive mutant of saccharomyces cerevisiae. *Proc. Natl. Acad. Sci. U.S.A.* 76, 1858–1862. doi: 10.1073/pnas.76.4.1858

Osterlund, E. J., Liu, Q., and Andrews, D. W. (2015). The use of FLIM-FRET for the Detection of mitochondria-associated protein interactions. *Methods Mol. Biol.* 1264, 395–419. doi: 10.1007/978-1-4939-2257-4_34

Peng, T., Yuan, X., and Hang, H. C. (2014). Turning the spotlight on protein-lipid interactions in cells. *Curr. Opin. Chem. Biol.* 21, 144–153. doi: 10.1016/j.cbpa.2014.07.015

Petschnigg, J., Groisman, B., Kotlyar, M., Taipale, M., Zheng, Y., Kurat, C. F., et al. (2014). The mammalian-membrane two-hybrid assay (MaMTH) for probing membrane-protein interactions in human cells. *Nat. Methods* 11, 585–592. doi: 10.1038/nmeth.2895

Pontier, S. M., and Schweisguth, F. (2012). Glycosphingolipids in signaling and development: from liposomes to model organisms. *Dev. Dyn.* 241, 92–106. doi: 10.1002/dvdy.22766

Purslow, J. A., Khatiwada, B., Bayro, M. J., and Venditti, V. (2020). NMR methods for structural characterization of protein-protein complexes. *Front. Mol. Biosci.* 7:9. doi: 10.3389/fmolb.2020.00009

Pyle, E., Kalli, A. C., Amillis, S., Hall, Z., Lau, A. M., Hanyaloglu, A. C., et al. (2018). Structural lipids enable the formation of functional oligomers of the eukaryotic purine symporter UapA. *Cell Chem. Biol.* 25, 840–848.e4. doi: 10.1016/j.chembiol.2018.03.011

Rao, M., and Mayor, S. (2005). Use of forster's resonance energy transfer microscopy to study lipid rafts. *Biochim. Biophys. Acta Mol. Cell Res.* 1746, 221–233. doi: 10.1016/j.bbamcr.2005.08.002

Reading, E., Hall, Z., Martens, C., Haghighi, T., Findlay, H., Ahdash, Z., et al. (2017). Interrogating membrane protein conformational dynamics within native lipid compositions. *Angew. Chem. Int. Ed. Engl.* 56, 15654–15657. doi: 10.1002/anie.201709657

Rist, W., Rodriguez, F., Jørgensen, T. J. D., and Mayer, M. P. (2005). Analysis of subsecond protein dynamics by amide hydrogen exchange and mass spectrometry using a quenched-flow setup. *Protein Sci.* 14, 626–632. doi: 10.1110/ps.041098305

Ritter, S. L., and Hall, R. A. (2009). Fine-tuning of GPCR activity by receptor-interacting proteins. *Nat. Rev. Mol. Cell Biol.* 10, 819–830. doi: 10.1038/nrm2803

Ruan, Q., Cheng, M. A., Levi, M., Gratton, E., and Mantulin, W. W. (2004). Spatial-temporal studies of membrane dynamics: scanning fluorescence correlation spectroscopy (SFCS). *Biophys. J.* 87, 1260–1267. doi: 10.1529/biophysj.103.036483

Rupert, D. L. M., Claudio, V., Lässer, C., and Bally, M. (2017). Methods for the physical characterization and quantification of extracellular vesicles in biological samples. *Biochim. Biophys. Acta Gen. Subj.* 1861, 3164–3179. doi: 10.1016/j.bbagen.2016.07.028

Sadamoto, H., and Muto, H. (2013). "Fluorescence cross-correlation spectroscopy (FCCS) to observe dimerization of transcription factors in living cells," *Gene Regulation. Methods in Molecular Biology (Methods and Protocols*) (Totowa, *NJ*: Humana Press*)*, 229–241. doi: 10.1007/978-1-62703-284-1_18

Saka, S. K., Honigmann, A., Eggeling, C., Hell, S. W., Lang, T., and Rizzoli, S. O. (2014). Multi-protein assemblies underlie the mesoscale organization of the plasma membrane. *Nat. Commun.* 5:4509. doi: 10.1038/ncomms5509

Sevcsik, E., Brameshuber, M., Fölser, M., Weghuber, J., Honigmann, A., and Schütz, G. J. (2015). GPI-anchored proteins do not reside in ordered domains in the live cell plasma membrane. *Nat. Commun.* 6:6969. doi: 10.1038/ncomms7969

Sezgin, E., Levental, I., Mayor, S., and Eggeling, C. (2017). The mystery of membrane organization: composition, regulation and roles of lipid rafts. *Nat. Rev. Mol. Cell Biol.* 18, 361–374. doi: 10.1038/nrm.2017.16

Sezgin, E., Schneider, F., Galiani, S., Urbančič, I., Waithe, D., Lagerholm, B. C., et al. (2019). Measuring nanoscale diffusion dynamics in cellular membranes with super-resolution STED–FCS. *Nat. Protoc.* 14, 1054–1083. doi: 10.1038/s41596-019-0127-9

Siebenmorgen, T., and Zacharias, M. (2020). Computational prediction of protein–protein binding affinities. *WIREs Comput. Mol. Sci.* 10:e1448. doi: 10.1002/wcms.1448

Simmons, D. A., and Konermann, L. (2002). *Characterization of transient protein folding intermediates during myoglobin reconstitution by time-resolved electrospray mass spectrometry with on-line isotopic pulse* labeling. *Biochemistry* 41, 1906–1914. doi: 10.1021/bi011697j

Simon, M. I., Strathmann, M. P., and Gautam, N. (1991). Diversity of G proteins in signal transduction. *Science* 252, 802–808. doi: 10.1126/science.1902986

Smith, A. W. (2012). Lipid–protein interactions in biological membranes: a dynamic perspective. *Biochim. Biophys. Acta Biomembr.* 1818, 172–177. doi: 10.1016/j.bbamem.2011.06.015

Snider, J., Kittanakom, S., Damjanovic, D., Curak, J., Wong, V., and Stagljar, I. (2010). Detecting interactions with membrane proteins using a membrane two-hybrid assay in yeast. *Nat. Protoc.* 5, 1281–1293. doi: 10.1038/nprot.2010.83

Staubach, S., Razawi, H., and Hanisch, F.-G. (2009). Proteomics of MUC1-containing lipid rafts from plasma membranes and exosomes of human breast carcinoma cells MCF-7. *Proteomics* 9, 2820–2835. doi: 10.1002/pmic.200800793

Stender, A. S., Marchuk, K., Liu, C., Sander, S., Meyer, M. W., Smith, E. A., et al. (2013). Single cell optical imaging and spectroscopy. *Chem. Rev.* 113, 2469–2527. doi: 10.1021/cr300336e

Stone, M. B., Shelby, S. A., Núñez, M. F., Wisser, K., and Veatch, S. L. (2017). Protein sorting by lipid phase-like domains supports emergent signaling function in B lymphocyte plasma membranes. *Elife* 6:e19891. doi: 10.7554/eLife.19891

Subczynski, W. K., Raguz, M., and Widomska, J. (2010). Studying lipid organization in biological membranes using liposomes and EPR spin labeling. *Methods Mol. Biol.* 606, 247–269. doi: 10.1007/978-1-60761-447-0_18

Suzuki, K. G. N., Kasai, R. S., Hirosawa, K. M., Nemoto, Y. L., Ishibashi, M., Miwa, Y., et al. (2012). Transient GPI-anchored protein homodimers are units for raft organization and function. *Nat. Chem. Biol.* 8, 774–783. doi: 10.1038/nchembio.1028

Swamy, M., Beck-Garcia, K., Beck-Garcia, E., Hartl, F. A., Morath, A., Yousefi, O. S., et al. (2016). A cholesterol-based allostery model of T cell receptor phosphorylation. *Immunity* 44, 1091–1101. doi: 10.1016/j.immuni.2016.04.011

Triffo, S. B., Huang, H. H., Smith, A. W., Chou, E. T., and Groves, J. T. (2012). Monitoring lipid anchor organization in cell membranes by PIE-FCCS. *J. Am. Chem. Soc.* 134, 10833–10842. doi: 10.1021/ja300374c

Valiyaveetil, F. I., Zhou, Y., and MacKinnon, R. (2002). Lipids in the structure, folding, and function of the KcsA K^+ *channel*. *Biochemistry* 41, 1071–7. doi: 10.1021/bi026215y

Varshney, P., Yadav, V., and Saini, N. (2016). Lipid rafts in immune signalling: current progress and future perspective. *Immunology* 149, 13–24. doi: 10.1111/imm.12617

Vinogradova, O., and Qin, J. (2012). NMR as a unique tool in assessment and complex determination of weak protein-protein interactions. *Top. Curr. Chem.* 326, 35–46. doi: 10.1007/128_2011_216

Wallrabe, H., and Periasamy, A. (2005). Imaging protein molecules using FRET and FLIM microscopy. *Curr. Opin. Biotechnol.* 16, 19–27. doi: 10.1016/j.copbio.2004.12.002

Welsh, J. A., Holloway, J. A., Wilkinson, J. S., and Englyst, N. A. (2017). Extracellular vesicle flow cytometry analysis and standardization. *Front. Cell Dev. Biol.* 5:78. doi: 10.3389/fcell.2017.00078

Westphal, V., Rizzoli, S. O., Lauterbach, M. A., Kamin, D., Jahn, R., and Hell, S. W. (2008). Video-rate far-field optical nanoscopy dissects synaptic vesicle movement. *Science* 320, 246–9. doi: 10.1126/science.1154228

Wickner, W., and Schekman, R. (2008). Membrane fusion. *Nat. Struct. Mol. Biol.* 15, 658–664. doi: 10.1038/nsmb.1451

Wymann, M. P., and Schneiter, R. (2008). Lipid signalling in disease. *Nat. Rev. Mol. Cell Biol.* 9, 162–176. doi: 10.1038/nrm2335

Xia, Y., and Peng, L. (2013). Photoactivatable lipid probes for studying biomembranes by photoaffinity labeling. *Chem. Rev.* 113, 7880–7929. doi: 10.1021/cr300419p

Yang, W., Pan, W., Chen, S., Trendel, N., Jiang, S., Xiao, F., et al. (2017). Dynamic regulation of CD28 conformation and signaling by charged lipids and ions. *Nat. Struct. Mol. Biol.* 24, 1081–1092. doi: 10.1038/nsmb.3489

Yi, J., Balagopalan, L., Nguyen, T., McIntire, K. M., and Samelson, L. E. (2019). TCR microclusters form spatially segregated domains and sequentially assemble in calcium-dependent kinetic steps. *Nat. Commun.* 10:277. doi: 10.1038/s41467-018-08064-2

You, M., Lyu, Y., Han, D., Qiu, L., Liu, Q., Chen, T., et al. (2017). DNA probes for monitoring dynamic and transient molecular encounters on live cell membranes. *Nat. Nanotechnol.* 12, 453–459. doi: 10.1038/nnano.2017.23

Zal, T., and Gascoigne, N. R. (2004). Using live FRET imaging to reveal early protein–protein interactions during T cell activation. *Curr. Opin. Immunol.* 16, 418–427. doi: 10.1016/j.coi.2004.05.019

Zhang, X., Lam, V. Q., Mou, Y., Kimura, T., Chung, J., Chandrasekar, S., et al. (2011). Direct visualization reveals dynamics of a transient intermediate during protein assembly. *Proc. Natl. Acad. Sci. U.S.A.* 108, 6450–6455. doi: 10.1073/pnas.1019051108

Zhao, B., Tian, Q., Bagheri, Y., and You, M. (2020). Lipid–oligonucleotide conjugates for simple and efficient cell membrane engineering and bioanalysis. *Curr. Opin. Biomed. Eng.* 13, 76–83. doi: 10.1016/j.cobme.2019.12.006

Zhou, Y., Morais-Cabral, J. H., Kaufman, A., and Mackinnon, R. (2001). Chemistry of ion coordination and hydration revealed by a K+ channel-Fab complex at 2.0 Å resolution. *Nature* 414, 43–48. doi: 10.1038/35102009

Conflict of Interest: The authors declare that the research was conducted in the absence of any commercial or financial relationships that could be construed as a potential conflict of interest.

Copyright © 2020 Bagheri, Ali and You. This is an open-access article distributed under the terms of the Creative Commons Attribution License (CC BY). The use, distribution or reproduction in other forums is permitted, provided the original author(s) and the copyright owner(s) are credited and that the original publication in this journal is cited, in accordance with accepted academic practice. No use, distribution or reproduction is permitted which does not comply with these terms.

frontiers in Chemistry

MINI REVIEW
published: 11 December 2020
doi: 10.3389/fchem.2020.598013

Functional Nucleic Acid-Based Live-Cell Fluorescence Imaging

Yutong Zhang[1], *Yulin Du*[1], *Yuting Zhuo*[1,2] *and Liping Qiu*[1,2]*

[1] *Molecular Science and Biomedicine Laboratory (MBL), State Key Laboratory of Chemo/Bio-Sensing and Chemometrics, College of Chemistry and Chemical Engineering, College of Biology, Aptamer Engineering Center of Hunan Province, Hunan University, Changsha, China,* [2] *NHC Key Laboratory of Birth Defect for Research and Prevention, Hunan Provincial Maternal and Child Health Care Hospital, Changsha, China*

Cell is the structural and functional unit of organism. It serves as a key research object in various biological processes, such as growth, ontogeny, metabolism and stress. Studying the spatiotemporal distribution and functional activity of specific biological molecules in living cells is crucial for exploring the mechanism governing life. It also facilitates the elucidation of pathogenesis, clinical prevention and disease theranostics. In recent years, the fluorescence imaging technique has been greatly exploited for live-cell imaging. However, the development of molecular probes has lagged far behind. Functional nucleic acids (FNAs), for example, aptamer and DNAzyme, possess special chemical and/or biological functions, hence severing as promising molecular tools for cellular imaging. The current mini review focuses on the applications of FNAs in live-cell fluorescence imaging.

Keywords: live-cell imaging, aptamer, DNAzyme, fluorescence probe, functional nucleic acid

OPEN ACCESS

Edited by:
Jianping Yang,
Donghua University, China

Reviewed by:
Hongyan Sun,
City University of Hong Kong,
Hong Kong
Giovanni Signore,
Fondazione Pisana per la Scienza
Onlus, Italy

****Correspondence:***
Liping Qiu
qiuliping@hnu.edu.cn

Specialty section:
This article was submitted to
Chemical Biology,
a section of the journal
Frontiers in Chemistry

Received: *24 August 2020*
Accepted: *16 November 2020*
Published: *11 December 2020*

Citation:
Zhang Y, Du Y, Zhuo Y and Qiu L (2020) Functional Nucleic Acid-Based Live-Cell Fluorescence Imaging. Front. Chem. 8:598013. doi: 10.3389/fchem.2020.598013

INTRODUCTION

Cell, as the fundamental unit of life, was composed of a highly complex but ordered structure. It could be elaborately subdivided into functionally distinct compartments and contained various biological molecules, e.g., small molecules, nucleic acids and proteins. The capability to monitor specific molecules with high spatiotemporal resolution would be significant to unravel the mechanism underlying related physiological processes (Cooper and Hausman, 2000).

Live-cell imaging was emerging as a significant strategy to study the cellular physiological process, enabling capture of dynamic information for specific molecules (Ebrahimi et al., 2020). As one of the most attracted imaging techniques, fluorescence imaging has been widely applied in areas of biomedical and biological research (Sokolov et al., 2003; Imamura et al., 2018). Specially, advances in fluorescence microscopy had allowed great progresses in the study of cellular biology. On the other hand, the application of such imaging techniques might be confounded by the lack of appropriate molecular probes.

In recent decades, various small molecules (Liu et al., 2018), peptides (Tung, 2004) and nucleic acids have been developed as fluorescence probes and utilized in the realm of live-cell analysis. Particularly, nucleic acid-based probes, were booming as attractive candidates owing to their advantages of good biocompatibility, low immunogenicity, easy synthesis, and convenient modification.

Typically, it has been discovered that nucleic acids can bind with specific molecules or function as catalysis like protease (Lu and Liu, 2006). These nucleic acid molecules with specific functions were regarded as functional nucleic acids (FNAs), in which aptamer and DNAzyme were considered as two typical representatives. Several decades in the past have witnessed the exponential rise in the application of FNAs in biological and biomedical research.

FUNCTIONAL NUCLEIC ACIDS (FNAs)

In 1990, Andrew D. Ellington et al. postulated the concept of aptamer, a term derived from the combination of "aptus" in Latin and "meros" in Greek (Ellington and Szostak, 1990; Tuerk and Gold, 1990). Aptamers were single-stranded oligonucleotides (DNA or RNA) that bound to target cargos through folding into specific secondary/tertiary conformation. The process in which aptamers bound to the target cargos was similar to the interaction between antibody and antigen, thus aptamers were referred as "chemical antibody" (Fang and Tan, 2010). Compared with antibodies, aptamers had several advantages including easy modification, reversible manipulation, low immunogenicity, fast penetration and so on.

As reported by Gerald. F. Joyce et al. in 1994, DNAzymes were a member of metalloenzyme family and functioned as catalysis in the presence of co-factors (Breaker and Joyce, 1994). They could modulate DNA and RNA cleavage, DNA ligation, peroxidase activity and so on. Their catalytic ability could be activated in conjunction with specific co-factors, such as metal ions. Studies over the past several decades have provided various applications of DNAzymes in bioanalysis and biomedicine (Scott, 2017).

Both aptamers and DNAzymes were screened by the *in vitro* competitive process termed Systematic Evolution of Ligands by Exponential Enrichment (SELEX). In the process of SELEX, target molecules were incubated with the nucleic acid library. Then unbounded nucleic acids were washed away, and bounded ones were extracted and amplified through polymerase chain reaction (PCR). At last, nucleic acids that had a high affinity with target molecules were isolated and enriched through repeated cycles. During the past decades, a wide range of SELEX techniques have been developed. Especially, Cell-SELEX was developed by using intact living cells as the selection target, with no need to involve prior knowledge of the membrane protein (Shangguan et al., 2006), providing a novel technology for screening molecular tools for cell analysis.

The past few decades have witnessed the applications of FNAs-based fluorescent probes in live-cell imaging. In this mini review, we focused on the application of FNAs for fluorescence imaging at the cellular and subcellular level.

LIVE-CELL FLUORESCENCE IMAGING WITH FUNCTIONAL NUCLEIC ACID-BASED PROBES

Cell Recognition and Detection

Cell recognition with high specificity was a primary requirement in precision medicine, which mainly relied on recognition of proteins expressed on the cell membrane. Membrane proteins accounted for one third of all human proteins, and represented nearly 50% of therapeutic targets (Overington et al., 2006). One major advantage of Cell-SELEX was to maintain the native state of membrane proteins during the selection process.

By conjugating these aptamers with fluorescent dyes, target cells could be directly visualized with fluorescence imaging (Cerchia and de Franciscis, 2010). For example, Wu et al. identified an aptamer XQ-2d for specifically targeting a pancreatic ductal adenocarcinoma cell line, PL45, with an affinity of 82.5 nM (Wu et al., 2015). By linking a fluorescein (FAM) dye to aptamer QX-2d, the specific fluorescence imaging of PL45 was realized. Additionally, owing to the plasmon resonance, gold nanoparticles aggregated with accompany of a spectrum shift, resulting in a color change from red to blue/purple. Based on this principle, Medley et al. developed aptamer-functionalized AuNPs to enable cancer cell detection with naked eyes (Medley et al., 2008). Despite positive preliminary results, these aptamer probes were "always on," potentially leading to a high background signal. To improve the imaging sensitivity, Shi et al. designed an activable aptamer probe (AA2) based on the conformational changes (Shi et al., 2011). In the absence of the target, AA2 was maintained in a harpin conformation where the fluorophore was approaching to the quencher, resulting in fluorescence quenching. Upon binding with the target, acute lymphoblastic leukemia cell line, CCRF-CEM, the hairpin conformation of AA2 was unfolded, resulting in a fluorescence restoration. As such, recognition-induced signal from "off" to "on" could be achieved, thus enhancing the signal-to-noise ratio of target cell imaging both *in vitro* and *in vivo*.

Normally, cells were highly heterogeneous, it was difficult to achieve precise cellular identification through a single-parameter detection. For example, human epidermal growth factor receptor-2 (HER2) protein was not merely expressed on cancer cells, but also expressed on normal cells with a relatively low content. Herein, it was challenging to distinguish cancer cells from normal cells in terms of HER2 only. To improve the accuracy of cellular identification, multiparameter-based cell recognition strategies were developed. In 2014, Wang et al. used three different aptamers which were separately labeled with three different fluorophores to develop a multicolor imaging method for distinguishing different types of cancer cells (Wang et al., 2014). Taking advantages of three detection parameters on individual cells, the accuracy of cellular identification could be remarkably improved. In addition to targeting cells, exosome, a cell-excreted vesicle that maintained similar membrane characteristics could serve as an alternative marker for fluid biopsy of cancers. Jiang et al. designed an aptamer-functionalized AuNP platform capable of identifying exosomes with naked eyes (Jiang et al., 2017). On sensing the target exosome, aptamer would fold into specific tertiary conformation and thus dissociate from AuNPs, leading to particle aggregation accompanied with a change of absorption spectrum. Furthermore, by using multiple aptamers, the profiling of exosome could be realized. To achieve simple operation and low-cost testing, Liu et al. reported an aptamer-based thermophoretic sensor for collecting and detecting exosomes from minute amounts of serum (Liu et al., 2019). Finally, in the combination with machine learning algorithm, the membrane protein information of exosomes was utilized for early profiling detection of six types of cancer.

To achieve intelligent diagnosis, multiple aptamers were used to construct DNA circuits for analyzing the expression pattern of cancer membrane proteins. For example, You et al. (2015) designed a programmable DNA-based nanoplatform and constructed both "AND" and "OR" logic gates to improve the recognition specificity of CCRF-CEM (**Figure 1A**). In subsequent studies, Chang et al. introduced the hybridization chain reaction

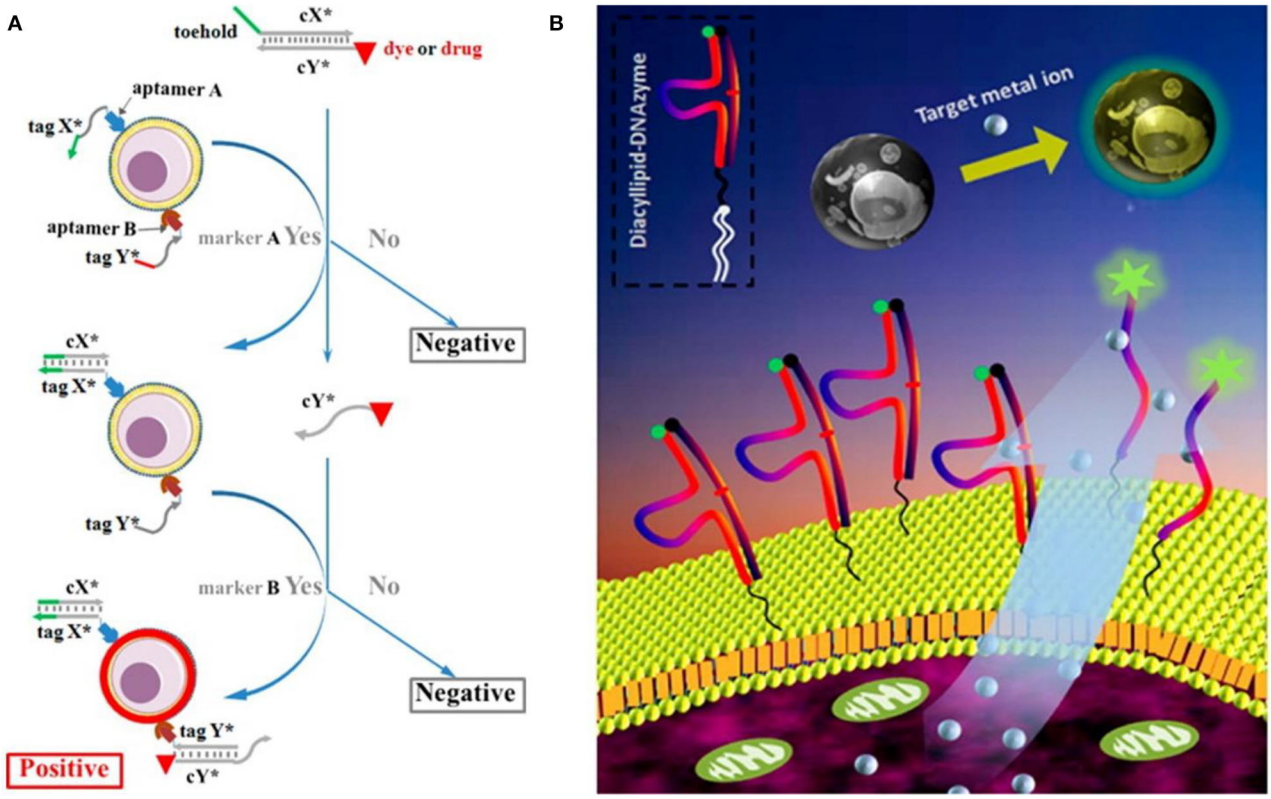

FIGURE 1 | (A) Scheme of DNA-based logic platform for multiparameter cancer cell recognition (You et al., 2015); **(B)** Scheme of diacyllipid-conjuageted DNAzyme fluorescence probe (Qiu et al., 2014). Reproduced with the permission of American Chemical Society.

(HCR) to amplify the recognition signal generated in the logic gate operation (Chang et al., 2019).

Notably, one major advantage of aptamers was their reversible recognition capability, which made them flexible tools for cell type-specific capture and release. Kacherovsky et al. screened an anti-CD8 aptamer via Cell-SELEX and used this aptamer to specifically capture $CD8^+$ T cells from peripheral blood (Kacherovsky et al., 2019). The captured T cells were released through the strand displacement reaction with addition of a complementary DNA, offering a traceless way for $CD8^+$ T cell isolation with high purity and high yield. They also demonstrated that $CD8^+$ T cells isolated with this strategy had the same functional effector as that isolated with the antibody-based strategy. Furthermore, Li et al. thoroughly studied different kinetic mechanisms governing the disassociation of aptamers from the cellular surface using complement DNA (cDNA), toehold-labeled cDNA (tcDNA) and single-stranded binding protein (SSB), laying a solid foundation for aptamer-based capture and isolation of target cells (Li L. et al., 2019).

Subcellular Imaging

Cell Membrane-Based Microenvironment Imaging

The cellular microenvironment referred to a local and dynamic surrounding around the cell that exerted a vital influence on the cellular behavior through transmission of either physical, chemical, or biological signals. It played a critical role in regulation of various cellular functions, such as metabolism, reproduction, differentiation, apoptosis, and communication (Joyce and Pollard, 2009). Real-time monitoring of specific molecules in such a microenvironment would provide essential information to understand the mechanism governing many biological processes.

In 2011, Zhao et al. covalently modified an aptamer probe on the surface of mesenchymal stem cells for real-time monitoring of platelet-derived growth factor (PDGF) in the cellular microenvironment (Zhao et al., 2011). In despite of considerable interest, the covalent modifications of the cell membrane could potentially affect the natural cellular state, which would limit their applications, to some extent. To address this issue, non-covalent cellular modification methods, especially the hydrophobic interaction-based strategy, have emerged as attracted alternatives. In this light, a variety of amphiphilic DNA probes, which were composed of a hydrophobic fragment, a DNA fragment and a linker in between, were developed for cell surface engineering.

For example, Qiu et al. designed and synthesized a diacyllipid-conjugated DNAzyme probe for real-time monitoring of target metal ions in the cellular microenvironment (Qiu et al., 2014). Based on the hydrophobic interaction between the diacyllipid fragment and the phospholipid bilayer, this amphiphilic probe

could be effectively anchored onto the cell membrane without affecting the cellular activity (**Figure 1B**). In addition to excellent membrane decoration efficiency, it was endowed with several advantages, including good biocompatibility, simple operation, and general applicability. The results also demonstrated that this membrane-anchored DNAzyme probe was able to dynamically monitor the cellular secretion process of target ions. In order to enhance the membrane-anchoring stability of DNA probes, Li et al. continued to develop an amphiphilic three-dimensional (3D) DNA probe using DNA tetrahedrons with three hydrophobic vertexes as the scaffold. This 3D DNA probe showed nearly 100-fold improvement on the membrane-anchoring stability, compared with that of the linear one (Li J. et al., 2019).

In addition, membrane-anchored DNA probes have been used to study the dynamic nature of the plasma membrane. You et al. used amphiphilic DNA probes as the building block and developed DNA-based reaction circuits to investigate the membrane locomotion through toehold-mediated strand displacement. The transient encounters between the membrane-anchored DNA probes could translate the membrane movement into fluorescent signals, thus providing a powerful platform to study molecular interactions of the cellular interface (You et al., 2017).

To improve the spatial resolution of imaging, super-resolution imaging techniques have been actively applied for fluorescence imaging of receptor proteins on the cell membrane. In 2006, Hochstrasser et al. developed the point accumulation for imaging in nanoscale topography (PAINT), based on the instant collision between the probe and the target, and achieved significant improvement on the spatial resolution of fluorescence imaging (Sharonov and Hochstrasser, 2006). Since the working principle of PAINT mainly relied on the molecular thermal motion, the imaging resolution was rarely linked with the density of the probe. DNA, owing to its predictable and controllable hybridization, showed great potential in PAINT. In 2010, Jungmann et at. developed a technique of DNA-PAINT (Jungmann et al., 2010), where a DNA docking strand was bounded to the target molecule, and a fluorescent dye-labeled DNA imaging strand contained a complementary sequence of the docking strand. When the imaging strand was in instant contact with the docking strand, a scintillating fluorescence signal would be generated. Aptamer, because of its small size, quantitative labeling as well as fast diffusion, held great potential in this aspect. In 2018, Strauss et al. (2018) utilized aptamer to realize the super-resolution imaging for seven different proteins for both cellular membrane and cytoplasm.

Cytoplasm Imaging

The cytoplasm was a primary site for cell metabolism and many biochemical reactions. Studying the dynamic distribution of specific components in the cytoplasm would definitely offer important information for study of various cellular processes. FNAs have attracted wide attention in intracellular fluorescence imaging with their excellent specificity, easy modification, and high programmability. Conversely, nucleic acids, which were negatively charged, couldn't easily penetrate the cell membrane due to the electrostatic repulsion, thus limiting their applications in the cytoplasm. Recently, great progress has been made to overcome this drawback via development of many cellular delivery methods.

Inorganic nanomaterial-based delivery

Inorganic nanomaterials with large surface area and rigid structures have been widely used in nucleic acid delivery. As a notable example, in 1996, Mirkin et al. reported spherical nucleic acid (SNAs) composed of inorganic core and DNA shell (Mirkin et al., 1996). Rosi et al. then proved that the cellular uptake efficiency of SNAs could reach as high as 99% (Rosi et al., 2006). Furthermore, Seferos et al. reported live-cell imaging of mRNA based on SNAs functionalized with recognition DNA and reporter DNA (Seferos et al., 2007).

Apart from 3D inorganic nanoparticles, 2D nanosheets, have been used as a delivery carrier for nucleic acids through π-π interactions. Wang et al. reported a Graphene Oxide (GO)-based strategy for the cellular delivery of fluorophore-labeled aptamer that could specifically recognize ATP (Wang et al., 2010). On sensing intracellular ATP, the aptamer could form a specific tertiary structure and then liberate from the GO. In this way, the fluorescence would be recovered for indicating the presence of ATP. By combining with unique physical and chemical features of inorganic nanomaterials, not only could the cellular uptake efficiency of FNAs be improved, but also multi-functions could be realized.

DNA nanostructure-based delivery

In recent years, an interesting phenomenon was frequently reported that DNA molecules can effectively enter living cells through forming rigid 3D nanostructures. In addition, formation of DNA nanostructures could protect DNA molecules from nuclease digestion, which would be beneficial for the reduction of false-positive signals. In 2017, He et al. designed and synthesized DNA tetrahedron nanotweezers (DTNTs) based on Fluorescence Resonance Energy Transfer (FRET) for live-cell imaging of tumor-related mRNA (He et al., 2017). After the cellular entry, DTNTs could bind with target mRNA to "turn off" the FRET signal. With introduction of the entropy-driven amplification strategy, the target-responsive fluorescence signal could be effectively amplified to improve the imaging sensitivity (He et al., 2018).

Internalized aptamer-based delivery

Aptamers screened from Cell-SELEX could specifically bind with the membrane proteins, and some of them could be driven into the cells by the translocation behavior of the target protein, thus providing an excellent ligand for cell-specific delivery (Yoon and Rossi, 2018). For example, aptamer AS1411 could specifically bind with nucleolin that were overexpressed on the membrane of many cancer cell lines. Based on the shuttle behavior of nucleolin between the cytoplasm and the nucleus, AS1411 could be efficiently internalized by cancer cells. By using AS1411 as the targeting ligand, Qiu et al. developed a self-delivered and photo-controlled molecular beacon (MB) for intracellular mRNA analysis (Qiu et al., 2013). After entering the cell, the PC

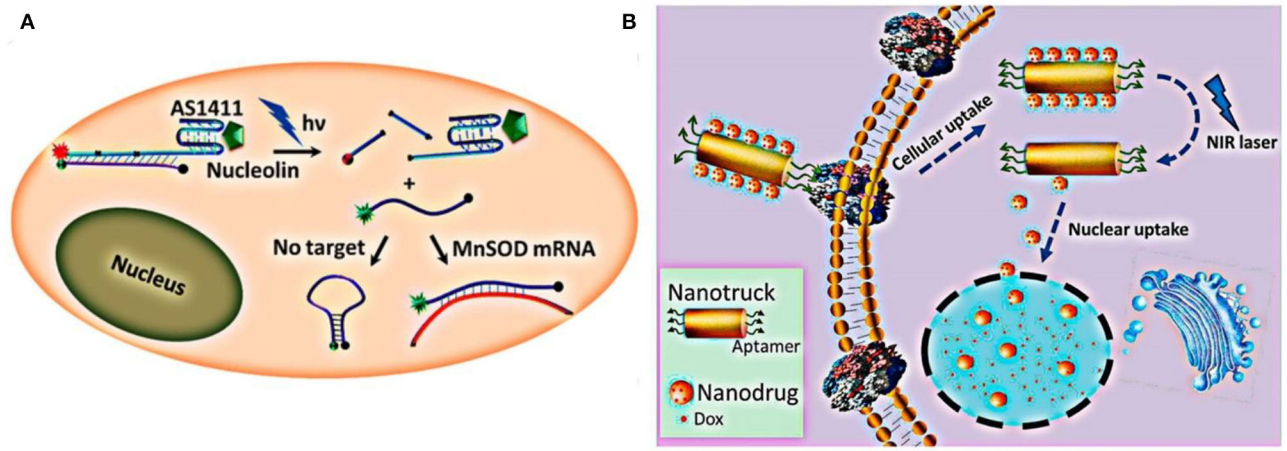

FIGURE 2 | Strategies for intracellular imaging of biological molecules **(A)** AS1411-based internalized strategy for mRNA imaging (Qiu et al., 2013); **(B)** Smart nanodrug delivery system with nuclear uptake (Qiu et al., 2015); Reproduced with the permission of American Chemical Society.

linker was cleaved upon light irradiation, thus releasing MBs to sense the target mRNA accomplished with fluorescent recovery (**Figure 2A**).

Nucleus Imaging

Nucleus was the control center of the cell. The live-cell imaging of specific components in the nucleus would be of great importance. Based on the nucleolus-targeting property of AS1411, Sun et al. designed an aptamer-functionalized Ag cluster for nucleus imaging (Sun et al., 2011). In addition, aptamer Ch4-1 screened by Shen et al. was validated to bind the nucleus with high affinity ($K_d = 6.65 \pm 3.40$ nM), which was used for identification of dead cells through nucleus imaging in an apoptosis assay (Shen et al., 2019). To make the cellular delivery smarter, Qiu et al. developed an aptamer-functionalized photo-responsive nano-assembly system (Qiu et al., 2015). After the nano-assembly was internalized into the cell, small-sized nanodrugs could be accumulated in the nucleus upon exposure of near-infrared (NIR) light (**Figure 2B**). Their results demonstrated that this delivery system held great promise in overcoming the P-glycoprotein-mediated multidrug resistance (MDR).

SUMMARY AND OUTLOOK

The past 20 years have witnessed the rapid advances of FNAs in interdisciplinary areas of chemistry, biology and medicine. Based on the *in vitro* screening technology, a large number of FNAs have been screened against diverse specific target molecules, providing excellent tools for biological and biomedical applications. Meanwhile, taking advantage of high programmability, good biocompatibility, easy synthesis and convenient modification, FNAs have gained considerable attention and shown great potential in live-cell study. On the other hand, FNAs were still in the preliminary stage, challenges remained for practical applications. First, FNAs could be easily digested by nucleases, their biostability could be a primary concern. Many strategies, such as utility of artificial bases and terminal-blocked scheme, have been developed to solve this issue though, there was still plenty of room for improvement. Second, FNAs that possessed high specificity and high affinity to their targets were relatively lacking. The innovation of the SELEX technique to generate high-performance FNAs would be desirable. Third, the recognition mechanism of most aptamers with their target molecules remained unclear, which would apparently hinder the application scopes. This was a major reason why only several aptamers, e.g., anti-ATP and anti-thrombin aptamers, have been frequently used in fundamental research. Meanwhile, to achieve subcellular imaging with high spatiotemporal resolution, FNAs capable of targeting different organelles should be exploited.

AUTHOR CONTRIBUTIONS

YZha drafted the manuscript. LQ guided and amended the manuscript. YD and YZhu helped to review the manuscript. All authors contributed to the manuscript.

FUNDING

This work was supported by NSFC grants (NSFC 91753109, 21922404), the National Key Research Program (2018YFC1602900), the Science and Technology Project of Hunan Province (2018RS3035 and 2018JJ3034).

REFERENCES

Breaker, R. R., and Joyce, G. F. (1994). A DNA enzyme that cleaves RNA. *Chem. Biol.* 1, 223–229. doi: 10.1016/1074-5521(94)90014-0

Cerchia, L., and de Franciscis, V. (2010). Targeting cancer cells with nucleic acid aptamers. *Trends Biotechnol.* 28, 517–525. doi: 10.1016/j.tibtech.2010.07.005

Chang, X., Zhang, C., Lv, C., Sun, Y., Zhang, M., Zhao, Y., et al. (2019). Construction of a multiple-aptamer-based DNA logic device on live cell membranes via associative toehold activation for accurate cancer cell identification. *J. Am. Chem. Soc.* 141, 12738–12743. doi: 10.1021/jacs.9b05470

Cooper, G. M., and Hausman, R. E. (2000). *The Cell: A Molecular Approach*. Washington, DC: ASM press.

Ebrahimi, S. B., Samanta, D., and Mirkin, C. A. (2020). DNA-based nanostructures for live-cell analysis. *J. Am. Chem. Soc.* 142, 11343–11356. doi: 10.1021/jacs.0c04978

Ellington, A. D., and Szostak, J. W. (1990). *In vitro* selection of RNA molecules that bind specific ligands. *Nature*. 346, 818–822. doi: 10.1038/346818a0

Fang, X., and Tan, W. (2010). Aptamers generated from cell-SELEX for molecular medicine: a chemical biology approach. *Acc. Chem. Res.* 43, 48–57. doi: 10.1021/ar900101s,

He, L., Lu, D., Liang, H., Xie, S., Zhang, X., Liu, Q., et al. (2018). mRNA-initiated, three-dimensional DNA amplifier able to function inside living cells. *J. Am. Chem. Soc.* 140, 258–263. doi: 10.1021/jacs.7b09789

He, L., Lu, D. Q., Liang, H., Xie, S., Luo, C., Hu, M., et al. (2017). fluorescence resonance energy transfer-based DNA tetrahedron nanotweezer for highly reliable detection of tumor-related mRNA in living cells. *ACS Nano*. 11, 4060–4066. doi: 10.1021/acsnano.7b00725

Imamura, T., Saitou, T., and Kawakami, R. (2018). *In vivo* optical imaging of cancer cell function and tumor microenvironment. *Cancer Sci.* 109, 912–918. doi: 10.1111/cas.13544

Jiang, Y., Shi, M., Liu, Y., Wan, S., Cui, C., Zhang, L., et al. (2017). Aptamer/AuNP biosensor for colorimetric profiling of exosomal proteins. *Angew.Chemie Int. Ed*. 56, 11916–11920. doi: 10.1002/anie.201703807

Joyce, J. A., and Pollard, J. W. (2009). Microenvironmental regulation of metastasis. *Nat. Rev. Cancer*. 9, 239–252. doi: 10.1038/nrc2618

Jungmann, R., Steinhauer, C., Scheible, M., Kuzyk, A., Tinnefeld, P., and Simmel, F. C. (2010). Single-molecule kinetics and super-resolution microscopy by fluorescence imaging of transient binding on DNA origami. *Nano Lett.* 10, 4756–4761. doi: 10.1021/nl103427w

Kacherovsky, N., Cardle, I. I., Cheng, E. L., Yu, J. L., Baldwin, M. L., Salipante, S. J., et al. (2019). Traceless aptamer-mediated isolation of CD8+ T cells for chimeric antigen receptor T-cell therapy. *Nat. Biomed. Eng.* 3, 783–795. doi: 10.1038/s41551-019-0411-6

Li, J., Xun, K., Pei, K., Liu, X., Peng, X., Du, Y., et al. (2019). Cell-membrane-anchored DNA nanoplatform for programming cellular interactions. *J. Am. Chem. Soc.* 141, 18013–18020. doi: 10.1021/jacs.9b04725

Li, L., Chen, X., Cui, C., Pan, X., Li, X., Yazd, H. S., et al. (2019). Aptamer displacement reaction from live-cell surfaces and its applications. *J. Am. Chem. Soc.* 141, 17174–17179. doi: 10.1021/jacs.9b07191

Liu, C., Zhao, J., Tian, F., Cai, L., Zhang, W., Feng, Q., et al. (2019). Low-cost thermophoretic profiling of extracellular-vesicle surface proteins for the early detection and classification of cancers. *Nat. Biomed. Eng.* 3, 183–193. doi: 10.1038/s41551-018-0343-6

Liu, H. W., Chen, L., Xu, C., Li, Z., Zhang, H., Zhang, X. B., et al. (2018). Recent progresses in small-molecule enzymatic fluorescent probes for cancer imaging. *Chem. Soc. Rev.* 47, 7140–7180. doi: 10.1039/C7CS00862G

Lu, Y., and Liu, J. (2006). Functional DNA nanotechnology: emerging applications of DNAzymes and aptamers. *Curr. Opin. Biotechnol.* 17, 580–588. doi: 10.1016/j.copbio.2006.10.004

Medley, C. D., Smith, J. E., Tang, Z., Wu, Y., Bamrungsap, S., and Tan, W. (2008). Gold nanoparticle-based colorimetric assay for the direct detection of cancerous cells. *Anal. Chem.* 80, 1067–1072. doi: 10.1021/ac702037y

Mirkin, C. A., Letsinger, R. L., Mucic, R. C., and Storhoff, J. J. (1996). A DNA-based method for rationally assembling nanoparticles into macroscopic materials. *Nature*. 382, 607–609.doi: 10.1038/382607a0

Overington, J. P., Al-Lazikani, B., and Hopkins, A. L. (2006). How many drug targets are there? *Nat. Rev. Drug Discov*. 5, 993–996. doi: 10.1038/nrd2199

Qiu, L., Chen, T., Öçsoy, I., Yasun, E., and Wu, C., Zhu, G., et al. (2015). A cell-targeted, size-photocontrollable, nuclear-uptake nanodrug delivery system for drug-resistant cancer therapy. *Nano Lett.* 15, 457–463. doi: 10.1021/nl503777s

Qiu, L., Wu, C., You, M., Han, D., Chen, T., Zhu, G., et al. (2013). Cell membrane-anchored biosensors for real-time monitoring of the cellular microenvironment. *J. Am. Chem. Soc.* 135, 12952–12955. doi: 10.1021/ja406252w

Qiu, L., Zhang, T., Jiang, J., Wu, C., Zhu, G., You, M., et al. (2014). Cell membrane-anchored biosensors for real-time monitoring of the cellular microenvironment. *J. Am. Chem. Soc.* 136, 13090–13093. doi: 10.1021/ja5047389

Rosi, N. L., Giljohann, D. A., Thaxton, C. S., Lytton-Jean, A. K. R., Han, M. S., and Mirkin, C. A. (2006). Oligonucleotide-modified gold nanoparticles for infracellular gene regulation. *Science* 312, 1027–1030. doi: 10.1126/science.1125559

Scott, K. S. (2017). Catalytic DNA: scope, applications, and biochemistry of deoxyribozymes. *Trends Biochem. Sci.* 176, 139–148. doi: 10.1016/j.tibs.2016.04.010

Seferos, D. S., Giljohann, D. A., Hill, H. D., Prigodich, A. E., and Mirkin, C. A. (2007). Nano-flares: probes for transfection and mRNA detection in living cells. *J. Am. Chem. Soc.* 129, 15477–15479. doi: 10.1021/ja0776529

Shangguan, D., Li, Y., Tang, Z., Cao, Z. C., Chen, H. W., Mallikaratchy, P., et al. (2006). Aptamers evolved from live cells as effective molecular probes for cancer study. *Proc. Natl. Acad. Sci. U. S. A.* 103, 11838–11843.

Sharonov, A., and Hochstrasser, R. M. (2006). Wide-field subdiffraction imaging by accumulated binding of diffusing probes. *Proc. Natl. Acad. Sci. U.S.A.* 103, 18911–18916. doi: 10.1073/pnas.0609643104

Shen, L., Bing, T., Zhang, N., Wang, L., Wang, J., Liu, X., et al. (2019). A nucleus-targeting DNA aptamer for dead cell indication. *ACS Sens.* 4, 1612–1618. doi: 10.1021/acssensors.9b00342

Shi, H., He, X., Wang, K., Wu, X., Ye, X., Guo, Q., et al. (2011). Activatable aptamer probe for contrast-enhanced *in vivo* cancer imaging based on cell membrane protein-triggered conformation alteration. *Proc. Natl. Acad. Sci. U.S.A.* 108, 3900–3905. doi: 10.1073/pnas.1016197108

Sokolov, K., Aaron, J., Hsu, B., Nida, D., Gillenwater, A., Follen, M., et al. (2003). Optical systems for *in vivo* molecular imaging of cancer. *Technol. Cancer Res. Treat.* 2, 491–504. doi: 10.1177/153303460300200602

Strauss, S., Nickels, P. C., Strauss, M. T., Jimenez Sabinina, V., Ellenberg, J., Carter, J. D., et al. (2018). Modified aptamers enable quantitative sub-10-nm cellular DNA-PAINT imaging. *Nat. Methods* 15, 685–688. doi: 10.1038/s41592-018-0105-0

Sun, Z., Wang, Y., Wei, Y., Liu, R., Zhu, H., Cui, Y., et al. (2011). Ag cluster-aptamer hybrid: specifically marking the nucleus of live cells. *Chem. Commun.* 47, 11960–11962. doi: 10.1039/c1cc14652a

Tuerk, C., and Gold, L. (1990). Systematic evolution of ligands by exponential enrichment: RNA ligands to bacteriophage T4 DNA polymerase. *Science* 249, 505–510. doi: 10.1126/science.2200121

Tung, C. H. (2004). Fluorescent peptide probes for *in vivo* diagnostic imaging. *Biopolym. Pept. Sci. Sect.* 76, 391–403. doi: 10.1002/bip.20139

Wang, S., Kong, H., Gong, X., Zhang, S., and Zhang, X. (2014). Multicolor imaging of cancer cells with fluorophore-tagged aptamers for single cell typing. *Anal. Chem.* 86, 8261–8266. doi: 10.1021/ac501657g

Wang, Y., Li, Z., Hu, D., Lin, C., Li, J., and Lin, Y. (2010). Aptamer/graphene oxide nanocomplex for *in situ* molecular probing in living cells ying. *J. Am. Chem. Soc.* 9274–9276. doi: 10.1021/ja103169v

Wu, X., Zhao, Z., Bai, H., Fu, T., Yang, C., Hu, X., et al. (2015). DNA aptamer selected against pancreatic ductal adenocarcinoma for *in vivo* imaging and clinical tissue recognition. *Theranostics*. 5, 985–994. doi: 10.7150/thno.11938

Yoon, S., and Rossi, J. J. (2018). Aptamers: uptake mechanisms and intracellular applications. *Adv. Drug Deliv. Rev.* 134, 22–35. doi: 10.1016/j.addr.2018.07.003

You, M., Lyu, Y., Han, D., Qiu, L., Liu, Q., Chen, T., et al. (2017). DNA probes for monitoring dynamic and transient molecular encounters on live cell membranes. *Nat. Nanotechnol.* 12, 453–459. doi: 10.1038/nnano.2017.23

You, M., Zhu, G., Chen, T., Donovan, M. J., and Tan, W. (2015). Programmable and multiparameter DNA-based logic platform for cancer recognition and targeted therapy. *J. Am. Chem. Soc.* 137, 667–674. doi: 10.1021/ja509263k

Zhao, W., Schafer, S., Choi, J., Yamanaka, Y. J., Lombardi, M. L., Bose, S., et al. (2011). Cell-surface sensors for real-time probing of cellular environments. *Nat. Nanotechnol.* 6, 524–531. doi: 10.1038/nnano.2011.101

Conflict of Interest: The authors declare that the research was conducted in the absence of any commercial or financial relationships that could be construed as a potential conflict of interest.

Copyright © 2020 Zhang, Du, Zhuo and Qiu. This is an open-access article distributed under the terms of the Creative Commons Attribution License (CC BY). The use, distribution or reproduction in other forums is permitted, provided the original author(s) and the copyright owner(s) are credited and that the original publication in this journal is cited, in accordance with accepted academic practice. No use, distribution or reproduction is permitted which does not comply with these terms.

frontiers in Chemistry

REVIEW
published: 11 December 2020
doi: 10.3389/fchem.2020.604236

Controlling Experimental Parameters to Improve Characterization of Biomaterial Fouling

Alexander H. Jesmer[1] *and Ryan G. Wylie*[1,2]*

[1] Department of Chemistry and Chemical Biology, Hamilton, ON, Canada, [2] School of Biomedical Engineering, McMaster University, Hamilton, ON, Canada

Uncontrolled protein adsorption and cell binding to biomaterial surfaces may lead to degradation, implant failure, infection, and deleterious inflammatory and immune responses. The accurate characterization of biofouling is therefore crucial for the optimization of biomaterials and devices that interface with complex biological environments composed of macromolecules, fluids, and cells. Currently, a diverse array of experimental conditions and characterization techniques are utilized, making it difficult to compare reported fouling values between similar or different biomaterials. This review aims to help scientists and engineers appreciate current limitations and conduct fouling experiments to facilitate the comparison of reported values and expedite the development of low-fouling materials. Recent advancements in the understanding of protein–interface interactions and fouling variability due to experiment conditions will be highlighted to discuss protein adsorption and cell adhesion and activation on biomaterial surfaces.

Keywords: biomaterials, low-fouling, protein interactions, cell adhesion, non-specific binding

OPEN ACCESS

Edited by:
Chun Xu,
The University of Queensland, Australia

Reviewed by:
Henny C. Van Der Mei,
University Medical Center Groningen, Netherlands
Nicholas G. Welch,
University of Melbourne, Australia

***Correspondence:**
Ryan G. Wylie
wylier@mcmaster.ca

Specialty section:
This article was submitted to Chemical Biology, a section of the journal Frontiers in Chemistry

Received: *09 September 2020*
Accepted: *30 October 2020*
Published: *11 December 2020*

Citation:
Jesmer AH and Wylie RG (2020) Controlling Experimental Parameters to Improve Characterization of Biomaterial Fouling. Front. Chem. 8:604236. doi: 10.3389/fchem.2020.604236

INTRODUCTION

In vitro biofouling characterization is crucial for the discovery of materials for medical implants and other blood or tissue contacting devices. Inaccurate or incomplete biofouling characterization may hinder the discovery of promising biomaterials as initial results may not translate to *in vivo* tests (Ratner, 2019). Because of the difficult nature of executing comparable biofouling experiments between the ever-expanding library of biomaterials and many different procedures and techniques, data comparison between reported values remains difficult or impossible (Heggestad et al., 2019). The following will therefore discuss the unwanted biological outcomes from biofouling, interactions of proteins and cells with material interfaces as a function of experimental conditions, and fouling characterization techniques, all with respect to prominent biomaterial applications.

Surfaces of implanted and biofluid contacting materials are subject to interactions with biological macromolecules, cells, and tissues (Anderson et al., 2008). Left uncontrolled, these interactions can lead to deleterious inflammatory responses, infections (Busscher et al., 2012), implant failures (Trindade et al., 2014), and loss of material performance. Protein interactions with biomaterial surfaces can lead to thrombus formation (Gorbet and Sefton, 2004), degradation of performance (Xie et al., 2018), and cell adhesion, where the identity (Swartzlander et al., 2015; Vu et al., 2019) and state of adsorbed proteins dictate downstream cell responses (Veiseh and Vegas, 2019).

Host mammalian cells can encapsulate, or fibrose, the implanted material leading to poor integration, loss of function in implanted sensors, or drug delivery vehicles or degrade the biomaterial itself via reactive oxygen species (Welch et al., 2020). For example, fibrotic responses to implanted pacemakers can lead to fatal outcomes in nearly 2% of removal procedures despite advances (Rennert et al., 2014) and can degrade hearing and cause device failure in 1% of cochlear implants (Foggia et al., 2019).

Bacterial adhesion to biomaterials can lead to persistent and difficult-to-treat infections through the production of biofilms, which increases antibiotic resistance, as well as the failure of implants altogether (Arciola et al., 2018). With respect to bacterial complications, approximately two catheter-associated urinary tract infections occur every 1,000 days of catheter use, contributing to urinary tract infections being the most common hospital acquired infection (Saint et al., 2016). Furthermore, there are 100,000–200,000 central line–associated blood infections per year in the United States, even after the widespread implementation of guidelines to reduce infections over the last two decades (Bell and O'Grady, 2018).

To control (Vishwakarma et al., 2016) non-specific biomolecule adsorption or cellular interactions with material interfaces and identify promising low-fouling materials, we must first select appropriate conditions for *in vitro* fouling experiments. For non-specific adsorption and adhesion measurements, we must carefully select the protein or biofluid source, experimental conditions, and characterization methods,

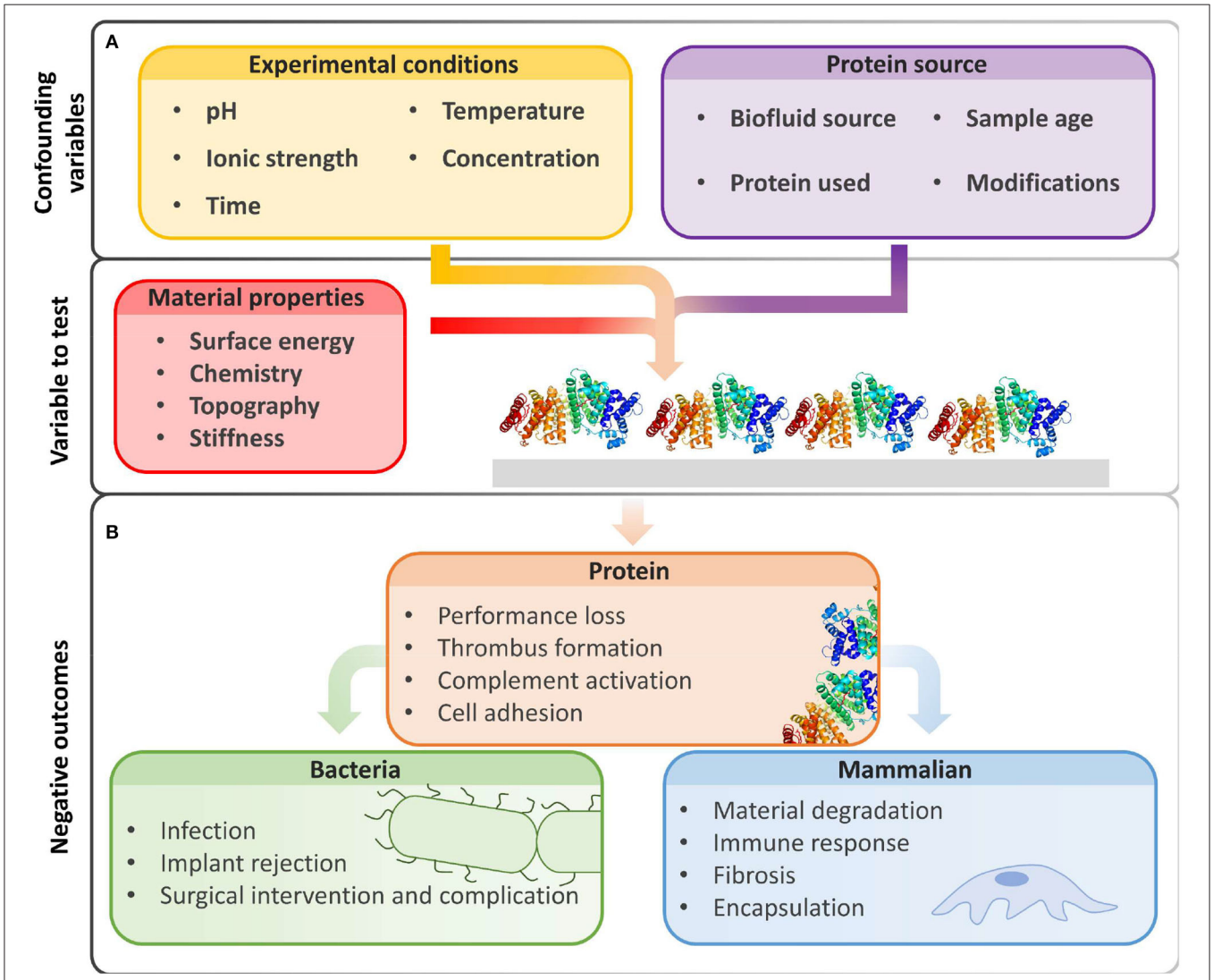

FIGURE 1 | Beyond intrinsic material properties, experimental conditions and biological reagents greatly influence fouling results. **(A)** The amount of non-specific protein adsorption on biomaterial surfaces is influenced by experimental conditions and protein sources chosen by the user. **(B)** Biofouling may hinder device performance and produce unwanted biological events due to non-specific protein adsorption, increased bacterial adhesion, and deleterious interactions with mammalian cells. Image of PDB ID 1BJ5 (Curry et al., 1998) created with (PyMol, 2015).

as they all influence protein adsorption and cell adhesion (**Figure 1**). Because of the great number of variables, it is often difficult to compare reported results between experiments (Heggestad et al., 2019). It is therefore useful to include controls and highlight limitations to prevent problematic comparisons.

Ultimately, the material and intended application should guide the selection of biofouling experiments. As best as possible, *in vitro* testing should recapitulate the biological conditions, and the influence of any deviations should be considered. The characterization tool will depend on intrinsic material properties and the biological environment needed for the experiment. The following will provide a brief overview of factors that influence protein and cell adhesion on biomaterial surfaces and cover common biofouling characterization methods.

NON-SPECIFIC ADSORPTION AND ADHESION

Protein Adsorption

The interaction of proteins with surfaces is common in biological environments, and their understanding is required to design low-fouling biomaterials. Controlled and specific protein–surface interactions are essential for non-medical and medical devices for implant integration and tissue engineering (Fernandez-yague et al., 2015). Protein–surface interactions can also be harmful; they may prevent integration with host tissue for functional recovery, as well as promote harmful blood clots and immune responses (Vishwakarma et al., 2016).

Proteins adsorbing to biomaterial surfaces displace water molecules (Chen et al., 2010) and interact with the material through non-covalent Van der Waals, hydrogen bonds, electrostatics, and hydrophobic interactions (Norde, 1996). Proteins can then unfold or rearrange on the surface at different rates (Roach et al., 2005). This process of adsorption, conformational change, and displacement may be dynamic and competitive. For example, the Vroman effect describes the competitive displacement of abundant and high-mobility proteins with proteins that have higher surface affinity and lower mobility (Vroman et al., 1980). The rate of displacement is dependent on protein concentration and material properties (Horbett, 2018).

Because of limitations in experimental techniques, quantification of protein adsorption cannot always be conducted under physiological conditions. However, any deviations from physiological conditions may change the amount of protein adsorption (**Figure 1A**). Experimental factors that alter protein interactions with materials include (1) protein concentration and protein source (e.g., solution vs. serum), (2) charge screening by ionic strength or pH changes, (3) fluorescent labels that increase hydrophobicity, and (4) temperature.

The concentration of protein in solution impacts the amount of non-specific protein adsorption on surfaces (Chandrasekaran et al., 2013; Hedayati et al., 2020). Protein concentration can also influence protein stability and rates of unfolding and surface displacement, leading to dynamic changes in adsorbed protein populations (Hedayati et al., 2020). For example, increasing the concentration of milk or blood-sourced proteins from 0.1 to 2 mg mL^{-1} led to greater adsorption on stainless steel (Chandrasekaran et al., 2013). At lower concentrations, the trend may be reversed; fibrinogen and albumin adsorption was greater with ∼1 μg mL^{-1} than 1 mg mL^{-1} solutions (Hedayati et al., 2020). The wide variation of utilized protein concentrations also complicates comparisons. As determined through observations and a selection of reports, protocols without fluorescent or radioactive proteins typically use concentrations of 1 (Dong et al., 2016; Yu et al., 2017) to 80 mg mL^{-1} (undiluted blood serum), whereas protocols with fluorescently labeled proteins regularly use 0.1–10 mg mL^{-1} (Sundaram et al., 2011; Liu et al., 2017; Yang et al., 2018; Feng et al., 2019), ranges that may be well below or above physiological concentrations.

The amount and identity of adsorbed proteins can also change with biofluid source; even pooled blood samples vary in protein adsorption (Pereira et al., 2014). Age of biofluid samples modifies protein conformation, leading generally to higher levels of non-specific adsorption (Yang et al., 2009). Fluorescent labels on protein surfaces may influence the orientation of proteins on surface, modifying downstream cell adhesion. Finally, adsorbed proteins may be displaced by other proteins over time when using complex protein solutions, which introduces time as a variable.

Cell Adhesion to Protein Covered Surfaces

Cell adhesion to surfaces with adsorbed proteins is controlled by protein identity, density (i.e., ng cm^{-2}), conformation, and orientation (Felgueiras et al., 2018) (**Figure 2**). For non-adhesive proteins, proteins partially or fully denatured may result in greater cell or bacteria adhesion by modifying surface hydrophobicity. For adhesive proteins, the folded protein will likely result in greater mammalian cell adhesion due to cell surface integrins (Anselme et al., 2010). For example, only ∼10 ng cm^{-2} of fibrinogen is required for most cells to adhere, and even less for monocytes (Shen et al., 2001). Beyond the protein coating, adhesion is also dependent on surface biomaterial properties, cell cycle stage, and environmental factors such as pH.

Cell adhesion to surfaces is also driven by material properties independent of protein adsorption (Rahmati et al., 2020) (**Figure 2**). Surface stiffness can control the adhesion of cells *in vitro* (Yeung et al., 2005) and influence cell signaling and differentiation *in vivo* (Miller and Davidson, 2013). Surface structure, roughness, and engineered structures can also influence cell adhesion (Graham and Cady, 2014), whereas patterns direct cell alignment (Nguyen et al., 2016). Selective cell adhesion has been demonstrated by controlling feature size on surfaces. For example, surface features smaller than the footprint of mammalian cells can prevent non-specific adhesion of osteoblasts and promote bacterial adhesion (Wu et al., 2011).

Potential Unwanted Events Due to Cell Adhesion

Because protein adsorption onto low-fouling materials is often below detection limits, quantifying cell adhesion to surfaces may be necessary to contextualize protein fouling data and investigate potential cell-based biofouling events. Host cell interactions with biomaterials may result in a range of biochemical processes such as macrophage activation [and the foreign body response (FBR)], platelet activation, and thrombus formation. The FBR is initiated

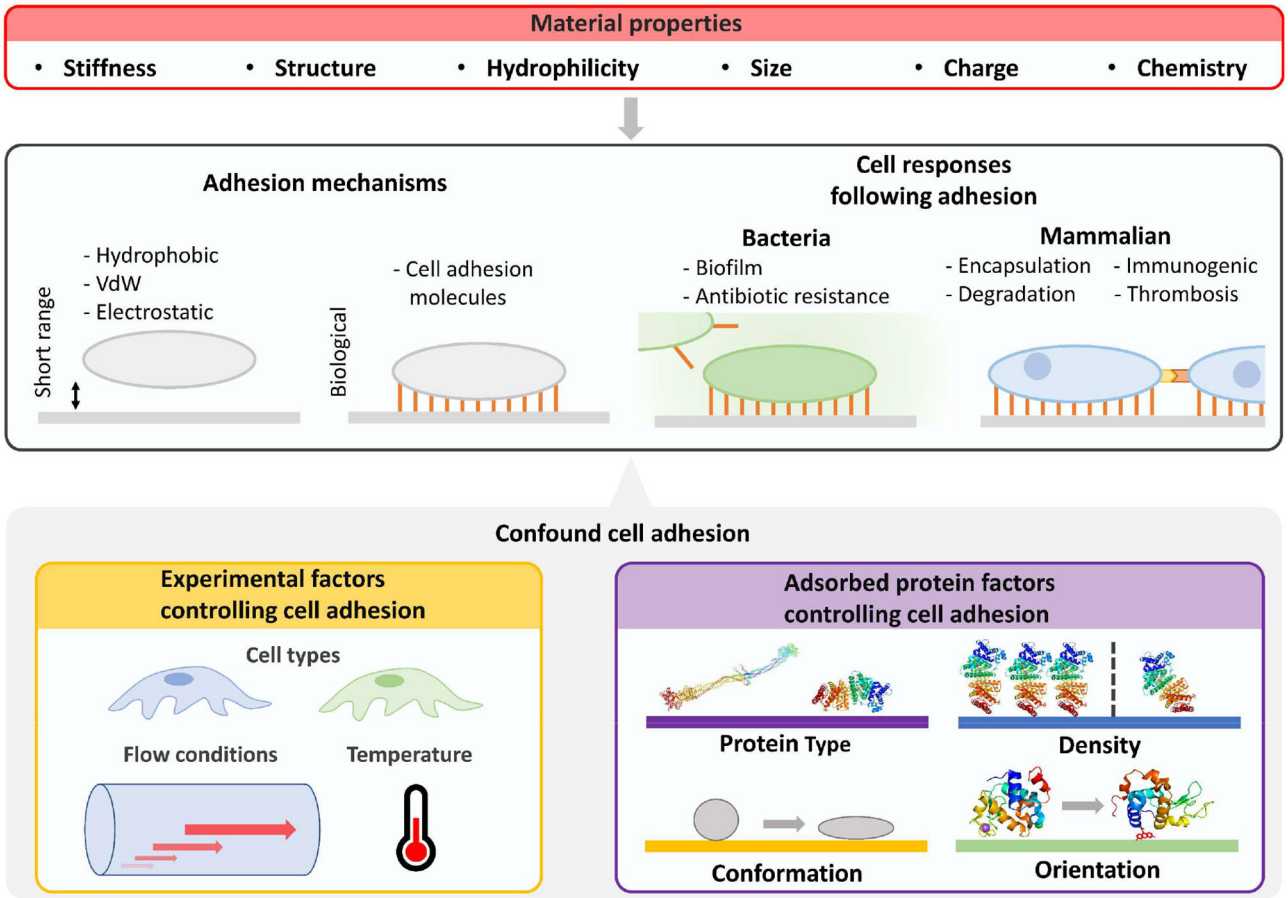

FIGURE 2 | Characterization of cellular fouling due to differences in material properties is confounded by experiment factors and properties of adsorbed surface proteins. Beyond material properties, the number and strength of surface adhered cells will be determined by cell type, flow conditions, and properties of adsorbed proteins such as type, density, orientation, and conformation. Cell responses will then be influenced by altering biofilm formation for bacteria and potential immune responses in mammalian environments. Furthermore, biologically mediated material degradation may occur. Images of PDB IDs 1EI3 (Yang et al., 2000), 1BJ5 (Curry et al., 1998), 5WRA (Sugahara et al., 2017), and 5IEL (Kachalova et al., 2017) created with (PyMol, 2015). VdW, van der Waals force.

by protein adsorption followed by monocyte recruitment and differentiation into macrophages, formation of giant cells, and fibroblast recruitment for the formation of fibrotic capsules (Veiseh and Vegas, 2019). In blood-contacting materials, platelet and leukocyte adhesions are part of a complex cascade that leads to thrombosis with potentially fatal effects (Gorbet and Sefton, 2004). The *in vitro* evaluation of blood contacting materials has been well reviewed recently and is beyond the scope of this manuscript (Weber et al., 2018).

Following bacterial adhesion to a surface, some bacteria can form biofilms that may lead to serious infections. Biofilms are extracellular matrices of proteins and carbohydrates that contain bacteria colonies with distinct environments (Flemming et al., 2016). Bacteria in biofilms are less susceptible to antibiotics, making infections difficult to eliminate; antibiotics may be up to 1,000-fold less effective against sessile than planktonic bacterial states (Stewart, 2015). To initiate biofilm formation, sufficient bacterial load must be present at the surface; load requirements depend on biological conditions and species. Biofilm characteristics are predominantly determined by the environment; temperature and nutrient availability are primary drivers of growth; shear forces control biofilm thickness and density. In some cases, biofilms are induced by shear forces, and still conditions hinder biofilm formation (Weaver et al., 2012).

TYPICAL PROTEINS AND CELLS USED FOR FOULING EXPERIMENTS

Several types of proteins and cells are routinely used to characterize biomaterial fouling. For proteins, individual or mixtures are used to either reflect the most abundant proteins in human serum and extracellular environments (e.g., human serum albumin) or highlight important downstream processes such as cell adhesion (e.g., fibronectin) or thrombus formation (e.g., fibrinogen) (**Table 1**). Mixtures of proteins have been used to mimic abundant circulating proteins (Fabrizius-Homan and Cooper, 1991) or to study the Vroman effect (Goor et al., 2017).

Cell types for characterization should be selected to elucidate biomaterial responses relevant for the intended application or implant-related infections (**Table 1**).

METHODS FOR QUANTIFYING BULK PROTEIN FOULING ON PLANAR SURFACES

A number of quantitative methods are commonly employed to measure protein adsorption on low-fouling coatings using sensors, planar surfaces, or detection labels and reagents. Because of differences in detection, fouling results from different techniques and methods must be carefully examined before comparison. Each technique will introduce deviations in experimental parameters that influence fouling levels such as concentration, flow, temperature, and time. Furthermore, many techniques use sensors or surfaces that are coated with low-fouling materials; grafting efficiency will therefore further introduce variability. Additionally, it has recently been shown that minor deviations during sample preparation for characterization techniques can also impact fouling levels (Visova et al., 2020). To overcome these differences in sample preparation, as well as reduce variability between samples, several techniques for characterizing low-fouling coatings have been extended to high-throughput screening (HTS) (Hook et al., 2010, 2012; Magennis et al., 2016).

Several of these methods provide quantitative data without the need for fluorescent or radioactive labels, allowing for biofouling characterization with a wide variety of proteins and complex biofluids (**Table 2**), whereas techniques that require fluorescent or radioactive labels on proteins are generally limited to biofouling experiments with individual proteins.

SPR and QCM-D

Surface plasmon resonance (SPR) allows for the characterization of low-fouling surface coatings, usually polymeric films, with unmodified protein solutions and complex biofluids; SPR signal increases with protein adsorption allowing real-time measurements. SPR is limited to characterizing films that can be synthesized from or grafted to the sensor's gold surface; the immobilized coating must be compatible with flow conditions of the SPR microfluidics. Generally, SPR's limit of detection is reported around 0.3 ng cm^{-2}, which is above the fouling limit of several reported low-fouling surfaces, making comparisons difficult for very lower-fouling materials (Blaszykowski et al., 2012). Furthermore, the calculation of total protein non-specifically adsorbed relies on calibration standards that assume saturated monolayers of model proteins (Zhang et al., 2006).

Quartz crystal microbalance with dissipation monitoring (QCM-D) is less sensitive (1.8 ng cm^{-2}) (Edvardsson, 2009) than SPR but offers greater variety of sensor surface chemistry, with metallic and polymeric coatings commercially available for functionalization. The added complexity of QCM-D data compared to SPR affords additional capabilities providing insight into the adsorbed protein layer's mechanical properties (Tondaturo et al., 2018). Furthermore, the sensitivity of QCM-D sensors

TABLE 1 | Biological materials commonly used for biofouling characterization with respect to endpoint measurement.

	Biological material	Primary reason for choice	End-point measurement	References
Proteins	Albumin	Abundance in serum and blood	Non-specific adsorption	Brash et al., 2019
	Fibrinogen	Role in thrombosis	Non-specific adsorption, conformation bioactivity	Horbett, 2018
	Fibronectin	Role in cell adhesion		Parisi et al., 2020
	Vitronectin	Role in cell adhesion		Wilson et al., 2005; Franz et al., 2011
Biofluids	CSF	Biomaterials for central nervous system	Amount and profile of adsorbed proteins	Harris et al., 2011
	Serum	Typical protein source in cell culture and blood		Gunkel and Huck, 2013
	Whole blood	Required for testing compatibility of blood contacting materials	Adsorption, complement activation, thrombosis	Weber et al., 2018
Bacteria	*E. coli*	Biotechnology model organism, implicated in some implant associated infections	Adhesion	Francolini et al., 2017
	P. aeruginosa	Common bacteria implicated in hospital acquired infections, forms biofilms	Adhesion, biofilm formation	Wagner et al., 2016
	S. epidermidis/S. aureus	Responsible for over 50% of implant infections		Oliveira et al., 2018
Mammalian	Fibroblast	Lead to fibrosis following chronic inflammation	Adhesion	Witherel et al., 2019
	Macrophage	Implicated in immune responses to material	Adhesion, polarization	Huyer et al., 2020

CSF, cerebrospinal fluid; E. coli, Escherichia coli; P. aeruginosa, Pseudomonas aeruginosa; S. aureus/S. epidermidis, Staphylococcus aureus/Staphylococcus epidermidis.

TABLE 2 | Advantages and limitations of commonly employed techniques to characterize protein adsorption and cell adhesion.

	Technique	Advantages	Limitations	Label required	LOD	References
Protein adsorption	SPR	Good detection limit	Substrate must be planar, thin coatings, limited sensors options	–	0.3 ng cm^{-2}	Blaszykowski et al., 2012
	QCM-D	Good detection limit, sensitivity to viscoelasticity	Planar, thin materials, stringent substrate materials	–	1.8 nm cm^{-2}	Edvardsson, 2009
	Ellipsometry	Good detection limit	Specific material requirements	–	0.1 nm[a]/5 ng cm^{-2}	Richter and Brisson, 2005
	TIRF	Single molecule, time dynamic	Planar, label required, low concentration limit	+	—	Hedayati et al., 2020
	XPS	Elemental and bonding information	Qualitative, presence of high background signals in common polymeric materials (e.g., nitrogen)	–	10–200 ng cm^{-2}	Wagner et al., 2002
	ToF-SIMS	Good detection limit, high spatial resolution	Limited sampling depth	–	0.1–49 ng cm^{-2}	Wagner et al., 2002; Madiona et al., 2017
	Total protein assay (bicinchoninic acid)	Affordable	Requires detergents, large surface areas	–	0.5 ug mL^{-1}	Pierce Biotechnology, 2017
	ELISA	Protein type specific, orientation information	Expensive, time consuming	–/+	0.5–5 ng cm^{-2}	Ngo and Grunlan, 2017
	LC–MS	Protein specific information	High cost	–	1 pg mL^{-2}/2–4 pmol mm^{-2}	Rao et al., 2013; Maes et al., 2014
	Coated AFM	Quantitative adhesion force	Tip labeling/modification with proteins is required	–	10 pN	Medalsy et al., 2011
	Fluorescent labeling	Affordable, quantitative	Simple protein mixtures	+	1 ng cm^{-2}	Wei et al., 2014
	Radiolabeling	Quantitative, good detection limit, small label size	Handling, accessibility	+	0.05 ng cm^{-2}	Felgueiras et al., 2018
Cell adhesion	Visible light microscopy	Common instrumentation, cell geometry (e.g., spreading, elongation)	Rudimentary data provided	–/+	~0.3 μm	Ntziachristos, 2010
	SEM	Direct adhesion visualization	Low throughput, sample prep	–	10 nm	Santoro et al., 2017

Label required (+), label free (–). SPR, surface plasmon resonance; QCM-D, quartz crystal microbalance with dissipation monitoring; TIRF, total internal reflection fluorescence microscopy; XPS, x-ray photoelectron spectroscopy; ToF-SIMS, time of flight secondary ion mass spectrometry; ELISA, enzyme-linked immunosorbent assay; LC-MS, liquid chromatography-mass spectrometry; AFM, atomic force microscopy; SEM, scanning electron microscopy. [a]Thickness of overlayer.

to changes in the viscoelastic properties of overlayers can be used to characterize changes in cellular dynamics once adhered to a surface of interest (Kushiro et al., 2016). Similar to SPR, low-fouling coatings must be compatible with QCM-D's microfluidic system, and coating thickness may hinder protein adsorption within the detection volume of the sensor (Luan et al., 2017). Unique to QCM-D sensors, the viscosity and thickness of anti-fouling polymer brush layers on QCM-D sensors are known to influence fouling results.

Ellipsometry

Ellipsometry is a light-based method used to measure film thickness by variations in reflected polarized light and can detect protein adsorption down to 5 ng cm^{-2} with a large array of available surface chemistries for coatings (Welch et al., 2017). Unlike SPR and QCM-D, ellipsometry does not require flow conditions, but sensors must be made from reflective materials for sample characterization in liquid or air. The technique is routinely employed to characterize the modification of materials with polymer overlayers. Ellipsometry measurements can determine adsorbed protein film thickness and mass from refractive index and thickness values (Hook et al., 2001). Ellipsometry has also been combined with other methods, such as QCM-D to provide richer protein adsorption data. On a nanopillar surface, ellipsometry models in conjunction with QCM-D were used to distinguish between fibronectin adsorbed to the tops or in between nanopillars to elucidate how location of adsorbed protein impacts cell adhesion (Kasputis et al., 2015).

Atomic Force Microscopy

Atomic force microscopy (AFM) can image proteins adsorbed on surfaces, providing protein conformation information. On flat surfaces, cell adhesion and spreading have also been characterized by AFM. For example, AFM was used to determine the conformation of non-specifically adsorbed immunoglobulin G and its impact on *Staphylococcus epidermidis* adhesion (Hou et al., 2018). The conformation of bovine serum albumin (BSA) adsorbed onto surfaces with physiosorbed or covalently bound RGD peptide was also deduced by AFM to demonstrate that BSA conformation is maintained in "ECM-like environments" (Pinho and Piedade, 2013).

METHODS FOR MEASURING PROTEIN ADSORPTION ON COMPLEX MATERIALS

Not all low-fouling materials are amenable to characterization methods utilizing planar sensor surfaces, as described in *Methods for Quantifying Bulk Protein Fouling on Planar Surfaces*. For example, the material may not be amenable to surface grafting or important material properties; such stiffness and surface structures may not be recapitulated on the sensor surface. The following techniques are routinely employed to quantify protein adsorption without planar sensor surfaces. These techniques not only offer greater experimental flexibility and detection specificity but also require the careful selection of controls to ensure results can be accurately interpreted (**Tables 2**, **3**).

Methods for Characterizing Unlabeled Proteins

Extraction of Adsorbed Protein for Quantification

After materials are exposed to protein solutions or biological fluids, unlabeled proteins are removed from the surface of interest with a detergent compatible with total protein detection assay such as sodium dodecyl sulfate (Ju et al., 2009; Ma et al., 2015; Dong et al., 2016). For example, the bicinchoninic acid (BCA) assay detects protein peptide bonds and has been used for adsorbed protein quantification on a variety of biomaterials, with detection levels of $\sim 1\,\mu g\,cm^{-2}$. The absorbance signal produced by the BCA assay is amino acid dependent; calibration curves should therefore be prepared with proteins of interest (Walker, 1996).

Methods requiring extraction of adsorbed proteins are limited by the fact that most detergents do not quantitatively remove all proteins from surfaces (Riedel et al., 2016). Therefore, assays usually report values relative to positive controls; calibrations curves can estimate adsorbed protein amounts, assuming near quantitative removal (Jesmer et al., 2020). The use of detergents prevents the investigation of adsorbed protein conformation, or bioactivity.

Enzyme-Linked Immunosorbent Assay: Detecting Adsorbed Proteins

Enzyme-linked immunosorbent assays (ELISA) can be used to measure proteins non-specifically adsorbed to surfaces, blood complement activation, and proteins produced by adhered cells. ELISAs detect surface adsorbed proteins, which act as the capture layer. Generally, ELISAs are limited to detecting a single adsorbed protein; ELISAs are therefore suitable for fouling experiments using a simple protein solution (i.e., fibronectin solution) or a biofluid to detect a specific protein's adsorption from a complex mixture (i.e., fibrinogen adsorption from blood).

ELISA can provide adsorbed protein conformation and bioactivity information. ELISAs have been used to measure adsorbed fibronectin bioactivity, which is advantageous over total protein measurements that cannot assess bioactivity (Tziampazis et al., 2000; Seo et al., 2013). ELISAs can also be used to detect potential immune responses. To measure complement activation due to a hydrogel, an ELISA was used to measure C5b-9 complement activation in serum exposed to material surfaces (Li B. et al., 2019).

ELISA measurements are independent of the substrate material, eliminating the need for proxy surfaces like SPR's gold sensors. When measuring fibrinogen adsorption onto antifouling zwitterionic coatings on planar materials, ELISA and SPR were compared (Cheng et al., 2009). Upon quantifying fibrinogen adsorption, ELISA indicated greater adsorption than SPR due to differences in polymer grafting density between glass and the SPR gold sensor. Therefore, ELISAs may provide more relevant data for non-gold surfaces.

Liquid Chromatography With Mass Spectrometry: Determining Adsorbed Protein Content After Extraction

Understanding the types and ratios of adsorbed proteins may provide insight into potential downstream *in vivo* effects and immune responses upon implantation (Othman et al., 2018). To profile all adsorbed proteins, liquid chromatography with mass spectrometry (LC-MS) may be employed to provide more information than total protein methods such as BCA. For example, protein adsorption from serum onto surfaces of varying hydrophilicity (water contact angle of 49° to 92°) showed similar total protein levels on all surfaces, but LC-MS determined differences in the types of proteins adsorbed. The same surfaces also displayed different bioactivities, which was demonstrated by tracking cytokine release from macrophages seeded on the biomaterial surface; macrophages released more proinflammatory cytokines [tumor necrosis factor α (TNF-α), interleukin 6 (IL-6), IL-1b, interferon γ-induced protein 10] and less anti-inflammatory cytokines (arginase, IL-10) with increasing surface hydrophobicity (Visalakshan et al., 2019). Protein profiling provided key information that total protein characterization could not provide.

LC-MS protein identification has been used to relate adsorbed proteins on hydrogel implants to the potential FBR capsule formation and thickness. On hydrogels that varied in composition and stiffness, total adsorbed protein amounts did not correlate to FBR capsule thickness. LC-MS analysis of adsorbed proteins 30 min after implantation demonstrated that the presence of proteins associated with extracellular matrix construction and cell adhesion were strong predictors of FBR capsule thickness (Jansen et al., 2018).

Surface Sensitive Techniques: X-Ray Photoelectron Spectroscopy and Time of Flight Secondary Ion Mass Spectrometry

Surface sensitive techniques to determine material composition can characterize protein overlayers on biomaterials. Both x-ray photoelectron spectroscopy (XPS) and time of flight secondary ion mass spectrometry (ToF-SIMS) detect only the first ∼10 and 2 nm, respectively, of a material (Castner and Ratner,

TABLE 3 | Techniques for the characterization of biological responses to biomaterial surfaces.

Biological response	Technique	Advantages	Limitations	References
Thrombogenesis	ELISA, Optical density	Recapitulates blood response	Impacted by blood source, storage and test setup	Weber et al., 2018
Platelet activation	ELISA, microscopy	Recapitulates blood response	Impacted by blood source, storage and test set up. Expensive detection	Weber et al., 2018
Macrophage activation/polarization	ELISA, microscopy	Relevance to *in vivo* outcomes	M1–M2 classification may be too simplistic	Brown et al., 2012; Murray et al., 2015
Biofilm formation	Surface culture, microscopy	Relevant, challenging endpoint	Variable with strain and environment	Sjollema et al., 2018

2002), making them ideal techniques for quantification of adsorbed material without requiring extraction and collection. Although substrate composition (e.g., elemental composition overlap with protein) and film thickness impact the sensitivity of both techniques (Wagner et al., 2002). Film thickness impacts each technique differently as the sampling depth of XPS is deeper than ToF-SIMS, for example, on sodium styrenesulfonate-coated and bare gold surfaces exposed to various protein solutions, ToF-SIMS signals saturated before XPS signals of protein adsorption, due to the increased sampling depth of the XPS technique as adsorbed protein overlayers can be thicker than the ToF-SIMS sampling depth (Foster et al., 2016). XPS and ToF-SIMS have been used in conjunction to measure surface chemical composition and protein adsorption levels on gradient polyethylene glycol (PEG) surfaces. The high spatial resolution of the techniques and ability of both to detect protein *in situ* allowed for correlation between adsorbed protein and surface polymer density without requiring multiple sample surfaces (Menzies et al., 2012).

Methods for Quantifying Adsorbed Proteins Modified With Detection Labels

Quantification of fluorescent or radioactive protein is easily achieved using the corresponding instrumentation with standards for calibration; labeled proteins have improved limits of detection when compared to absorbance-based protein quantification methods (**Table 2**). Labels may limit fouling studies to individual proteins and alter protein properties such a hydrophobicity and bioactivity. Generally, *in vitro* fouling assays with labeled protein are carried out below physiological concentrations without competing proteins, which may poorly predict *in vivo* performance. Therefore, fluorescent and radioactive labels offer greater sensitivity, but current experimental design for fouling experiments may not always mimic *in vivo* conditions.

Fluorescent Labels

Because of their high sensitivity, fluorescently labeled proteins are commonly used to characterize non-specific protein adsorption to surfaces. Quantification of adsorbed fluorescent proteins is regularly performed by fluorescence microscopy or protein extraction for solution fluorescent measurements.

Fluorescent techniques can also provide information about protein folding, orientation, and reversibility of non-specific adsorption at single-molecule binding resolution. Using fibronectin with fluorescence resonance energy transfer (FRET) labels, residence time and folding state of adsorbed protein were determined on different polymeric PEG surfaces. Fibronectin's adsorption rate decreased with higher PEG density, but surface residence time increased because of more protein unfolding (Marruecos et al., 2016); greater residence time with higher PEG densities has not been observed with unlabeled proteins. Fluorescein, a commonly used fluorescent label, was shown to change the orientation of adsorbed lysozyme on surfaces in a modeling study (Romanowska et al., 2015). FRET pairs have also been used to confirm conformation of surface adsorbed protein (Marruecos et al., 2016). Single-molecule resolution TIRF for Alexa Fluor 647–labeled BSA and fibrinogen fouling on PEG surfaces determined that non-specific adsorption was reversible. Fouling was also inversely correlated to protein concentration on PEG surfaces, where $\sim$1 μg mL^{-1} BSA and fibrinogen solutions resulted in fouling, whereas the use 1 mg mL^{-1} solutions yielded surfaces with no detectable protein (Hedayati et al., 2020). The authors proposed that increased protein concentrations near the material surface could stabilize protein conformation and decrease the likelihood of proteins denaturing on the surface leading to lower fouling levels at the higher concentration.

Fluorescent labels can also alter protein properties that may influence adsorption degrees. For example, fluorescent labeling has been shown to influence the protein's isoelectric point (by $\sim$0.1), size, and charge (Bingaman et al., 2003). Characterization via single-labeled fluorescent proteins does not provide information on protein conformation or orientation and is limited to simple protein solutions; the use of biofluids is difficult because of labeling differences within the large protein population.

Radioactive Labels

In contrast to fluorescent tags, radioactive labels can be introduced during protein expression with a radioactive amino acid or by covalently grafting a small tag. Because of high sensitivity, radio-tagged protein assays have detection limits as low as 0.05 ng cm^{-2} (Felgueiras et al., 2018). While grafting small radiolabels has minor impacts on protein properties, oxidizing conditions used in many labeling reactions can result in

protein aggregation and degradation, resulting in greater protein adsorption over unlabeled proteins (Holmberg et al., 2007). Radiolabels are typically used to measure total adsorption of an individual protein and do not provide information about protein conformation or orientation.

Coated AFM: Modified Tips for Selective Protein Detection

Protein-coated AFM tips can quantify adhesive forces between individual adsorbed proteins and biomaterials, which can impact cell adhesion outcome. Fibronectin-coated AFM in concert with fluorescently labeled proteins can be used to correlate total protein adsorption (via fluorescence) and adhesive forces to surfaces; a strong linear relationship between single protein adhesive strength and total protein adsorption is usually observed (Taylor et al., 2008). In conjunction with ELISA, AFM can be used to measure protein adsorption force to multiple surface chemistries and protein conformation. Fibronectin-coated AFM also demonstrated that the strength of protein material interactions determines cell fate. Stronger interactions between fibronectin and materials led to decreased cell viability by hindering matrix remodeling (González-garcía et al., 2018).

CELLULAR ADHESION AND ACTIVATION

For biomaterials that will be exposed to cells, quantifying cell adhesion and activity is necessary as protein adsorption does not necessarily correlate with downstream cellular activities; even when protein adsorption is below detection limits, cells have been shown to interact with surfaces.

Low-fouling materials are generally designed to prevent or minimize cell adhesion, but cell adhesion can be advantageous for some medical implants. For example, adhesion of cells associated with anti-inflammatory pathways may improve biomaterial outcomes, and cell integration is necessary for dental and joint replacements, although cellular interactions with biomaterials should be studied to avoid deleterious immune responses for most medical implants.

Quantifying Mammalian Cell Fouling

Interactions between mammalian cells and biomaterials are routinely characterized by (1) detection of the adhered cells through microscopy or metabolic activity and (2) detection of signals produced by cells (i.e., adhesins or cytokines; **Tables 2**, **3**). These methods are complementary and together can provide detailed information regarding biomaterial fouling and potential immune outcomes. *In vitro* methods to recapitulate the full *in vivo* immune response remain an active area of research (Sharifi et al., 2019).

Adhered cells are commonly characterized by microscopy to determine cell number, morphology, elongation, and spreading, which can all be related to cell bioactivity. For example, cell morphology has been linked to macrophage phenotype, with elongated cells exhibiting anti-inflammatory properties (Luu et al., 2015). SEM and fluorescence microscopy have also been used to quantify cell elongation and spreading on grooved surface, which correlated with cytokine profiles (Luu et al., 2015). To study interactions between topographical surfaces with cells, a method combining focused ion beam and SEM (FIB-SEM) was developed to determine cell adhesion preferences and morphologies as a function of nanostructures. Cells were found to preferentially bind to protrusions over pores by visualizing adhesion points (Santoro et al., 2017).

Biochemical techniques used in concert with microscopy can find trends between bioactivity and cell number or morphology. ELISA assessment of IL-6 and TNF-α with fluorescent microscopy demonstrated that macrophage adhesion on fibronectin-coated surfaces correlated with a low inflammatory activation state; FRET experiments indicated that cells on surfaces with stabilized fibronectin had low inflammatory cytokine profiles (Faulón Marruecos et al., 2019). Interestingly, unfolded adsorbed fibronectin promoted a proinflammatory

TABLE 4 | Primary bacterial infections and conditions by implant site.

Implant site		Primary bacterial infection	Shear rate (s^{-1})	Fluid type	REF
Ocular surface		*P. aeruginosa*/*S. epidermidis*	0.35	Tears	Bakker et al., 2003; Dutot et al., 2009
Urinary tract		*P. aeruginosa*	15	Urine	Dohnt et al., 2011; Azevedo et al., 2017
Bone		*S. aureus*/CoNS	—	—	Li and Webster, 2017
Spinal column		Early *S. aureus,* late *P. acnes*	—	—	Lall et al., 2015
Peritoneal cavity		*S. epidermidis*/*S. aureus*	20–120	CSF	Bloomfield et al., 1998; Vinchon and Dhellemmes, 2006
Vascular	TIVAP	<30 d—*S. aureus* Total—CoNS	10–1,000Casa et al., 2015	Blood	Lebeaux et al., 2014
	Vascular graft	Early CoNS, Late *S. aureus*/*E. coli*			Saleem et al., 2010
	PICC/CVC	CoNS			Haddadin et al., 2020

CoNS, coagulase-negative staphylococci; CSF, cerebrospinal fluid; TIVAP, totally implantable venous access port; PICC, peripherally inserted central venous catheter; CVC, central venous catheter; early, <3 months after surgery; late, >3 months after surgery.

state, indicating the need to study protein stability and not only total amounts.

The treatment and preparation of materials before cell adhesion assays can impact cell adhesion outcomes; pre-exposing biomaterial surfaces to proteins prior to cell assay impacts cell density and spreading (Jansen et al., 2018). For example, protein choice during pre-exposure impacted the adhesion and spreading of human fibroblasts on polymer coated titanium surfaces; BSA did not significantly influence cell adhesion or spreading unlike fibrinogen, which promoted adhesion and spreading (Pei et al., 2011).

High-Throughput Methods to Measure Macrophage Adhesion and Activation

To minimize proinflammatory polarization of immune cells, implantable biomaterials are now being designed to promote anti-inflammatory polarizations. To this end, a high-throughput method for non-specific protein adsorption alongside macrophage adhesion and polarization, a component of inflammation (Brown et al., 2012), was developed using microprinted polymer spot arrays (Rostam et al., 2020). Polymer spot microarrays were assayed for cell attachment and macrophage polarization by microscopy and calprotectin/mannose receptor staining. HTS hits were then subjected to more rigorous screens for cytokine profile and phagocytic ability of macrophages as well as mass spectrometry of adsorbed proteins from fetal bovine serum.

Bacterial Fouling Related to Medical Implants

Resistance of material surfaces to bacterial colonization is commonly pursued through two main strategies of (1) adhesion resistance and (2) active killing. Adhesion resistance strategies prevent bacteria from adhering and eventually forming biofilms, usually through methods that repel protein and host cell adhesion. In active killing strategies, surfaces may kill settled bacteria on contact through chemical or physical means or the release antibacterial agents (Campoccia et al., 2013). Methods of testing *in vitro* bacterial fouling have been well reviewed recently (Azeredo et al., 2017; van de Lagemaat et al., 2017; Boudarel et al., 2018; Sjollema et al., 2018).

When measuring the resistance of a biomaterial to bacterial adhesion and biofilm formation, the environment of the intended implant location should be replicated. The implant site will also guide the selection of bacteria strain to investigate. Implant sites also vary in shear forces from fluid flow, immune environments, and host cell–bacteria interactions (Busscher et al., 2012) (**Table 4**). For example, two low fouling surfaces with similar resistance to fibrinogen adsorption showed drastically different biofilm formation when exposed to the *P. aeruginosa* due to differences in flow conditions; under static conditions, no biofilm was observed after 6 months (Wang et al., 2020), whereas biofilms formed after only 10 days under flow conditions (Cheng et al., 2009).

Tissue and Bacterial Cell Co-culture

Implanted materials that lead to infection will be in the presence not only of bacterial cells but also of the host tissue, both of which compete for the implant surface (Busscher et al., 2012). Co-cultures of bacterial and mammalian cells have therefore been used, especially with respect to bacterial effects on implant integration. Co-culture setup requires preliminary work with monoculture to determine optimal growth densities and conditions that will support both cell types (Zaatreh et al., 2016). In addition to live bacterial strains, co-culture setups including heat-killed bacteria have been used to study the influence of the presence of bacteria without requiring conditions that support both cell types. A study including heat-killed bacteria found that presence of low levels of bacterial signals could improve integration of biomaterials, although the authors highlight the limitations of their results to the specific experimental setup (Yue et al., 2015). Bacterial response to biomaterials are dictated by their environment leading to different outcomes when cultured alone or in the presence of eukaryotic cells; for example, surfaces exposed to mammalian cells may have antimicrobial activity by enhancing immune responses directed toward bacteria (Li J. et al., 2019; Yang et al., 2019).

Choosing Relevant Fouling Assays

The intended application will dictate the *in vitro* biofouling assay(s) required to assess biomaterials, with the site and length of implantation being prominent factors to select protein or biofluid sources, concentrations, cell types, flow rates and fluid-associated stress, and biological characterizations (e.g., cytokines related to immune responses). Immune responses are more important for long-term implants, and cell types should be chosen to investigate long-term biological responses such as the fibrotic response. Furthermore, some biomaterials require tissue integration (e.g., dental implant, joint replacement), whereas others benefit from the lack of tissue integration (e.g., catheters), which will also help identify requirements for *in vitro* biofouling experiments.

In combination with **Figures 1–3** was designed to help guide the selection of biofouling experiments, although each material in development will need to be carefully considered to select appropriate biofouling experiments and controls. **Figure 3** highlights the most common biofouling tests required for biomaterials as a function of duration of implantation (short vs. long term) and the site of biomaterial implantation (biomaterial site). Once the protein and cell fouling experiments are identified, experimental design must be carefully executed to establish *in vitro* conditions that mimic *in vivo* fouling, which is explained in **Figures 1**, **2**.

Despite being an affordable and accessible protein, BSA is not recommended for any specific implantation site in **Figure 3** as the protein is not physiologically relevant and differs in sequence and fouling profile, even compared to human serum albumin (Su et al., 2000). Blood serum is a commonly used and accessible biological material used for fouling experiments, but limitations in its applicability should be considered when planning fouling experiments. Blood serum is free of fibrinogen, which was found to adsorb to all tested

low-fouling PEG-based surfaces (Riedel et al., 2013), and the age of serum samples lead to different fouling profiles (Yang et al., 2009). Further, serum properties are not well-defined and vary by batch and supplier, and moreover, there are interspecies differences between the commonly used fetal bovine serum and human serum, which alter cell behavior *in vitro* (Heger et al., 2018).

Following the choice of appropriate biological material and conditions, techniques should be chosen that can measure the outcomes of biofouling in different ways to internally corroborate findings. More than one technique should be used to characterize biofouling in order to overcome the limitations of individual techniques (**Tables 2**, **3**), increase confidence in results, and improve ability to compare findings between papers. To further improve interstudy comparability, standard negative and positive controls such as glass and tissue culture plastic should be included in each *in vitro* assay; with consistent surface and experimental controls within the literature, it will improve our ability to compare published data to better interpret the antifouling properties of new materials. The same material should be used throughout characterization steps; for example, if a polymer coating is being characterized, the substrate material should be the same for all tests to control for differences in grafting density and stiffness. Finally, experimental details and the reasons for their choice should be clearly stated, and their impact on results discussed as outlined in the MIRIBEL standard (Faria et al., 2018).

CONCLUSIONS

The discovery and development of low-fouling or controlled fouling biomaterials remain an important active area of research. The current heterogeneity of *in vitro* biofouling experimental conditions and characterization methods hinders biomaterial discovery and translation. This review highlights how controls, experimental design, and characterization limitations must be considered for the interpretation of *in vitro* results. Ideally, *in vitro* conditions will mimic conditions for the biomaterial's intended application to accelerate translation into the real world and clinic. To this end, the review provides guidance for the selection and execution of *in vitro* fouling experiments, while stressing that the biomaterial under study will greatly influence the needed biofouling experimentation.

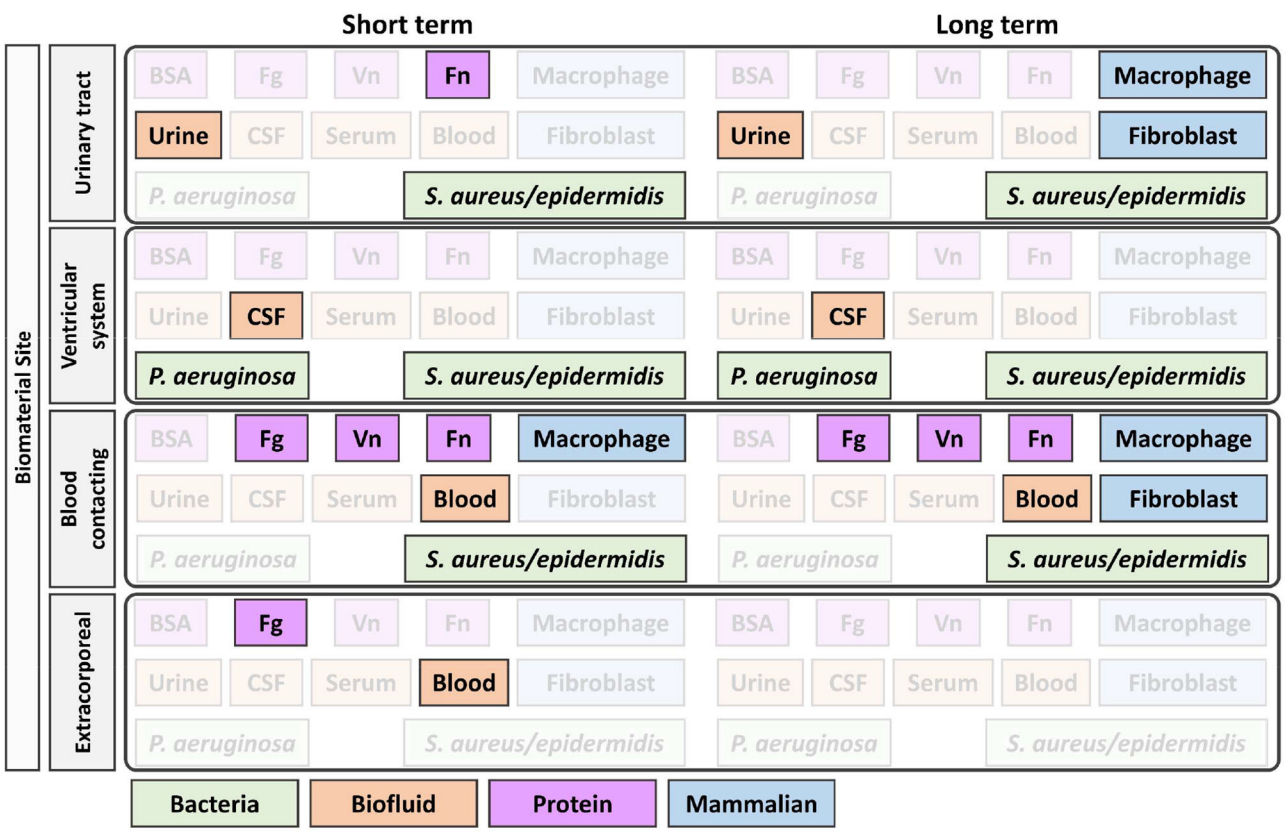

FIGURE 3 | Identification of appropriate *in vitro* biofouling experiments for low-fouling biomaterials. The site and length of implantation will determine the variety of biological components for screening. Above is an example of how the site and length of implantation can help guide the selection of biologic components for biofouling experiments. For experimental setup consideration of proteins and cells, refer to **Figures 1**, **2**, respectively. BSA, bovine serum albumin; Fg, fibrinogen; Vn, vitronectin; Fn, fibronectin; *P. aeruginosa*, *Pseudomonas aeruginosa*; *S. aureus/epidermidis*, *Staphylococcus aureus/Staphylococcus epidermidis*.

SUMMARY

Understanding the extent and nature of biomaterial fouling is crucial for the development of medical devices and antibacterial surfaces. In light of recent insights into protein–material interactions and heterogeneity of reported fouling values, we review common experimental conditions and detection methods for *in vitro* fouling measurements to establish guidelines for improved *in vitro* fouling experiments. The ultimate goal is to expedite the discovery of low-fouling biomaterials.

AUTHOR CONTRIBUTIONS

AJ and RW conceived, wrote, and prepared the manuscript. All authors contributed to the article and approved the submitted version.

FUNDING

This work was supported by the Natural Sciences and Engineering Research Council (NSERC; 2015-05429).

REFERENCES

Anderson, J. M., Rodriguez, A., and Chang, D. T. (2008). Foreign body reaction to biomaterials. *Semin. Immunol.* 20, 86–100. doi: 10.1016/j.smim.2007.11.004

Anselme, K., Ploux, L., and Ponche, A. (2010). Cell / material interfaces : influence of surface chemistry and surface topography on cell adhesion. *J. Adhes. Sci. Technol.* 24, 831–852. doi: 10.1163/016942409X12598231568186

Arciola, C. R., Campoccia, D., and Montanaro, L. (2018). Implant infections: adhesion, biofilm formation and immune evasion. *Nat. Rev. Microbiol.* 16, 397–409. doi: 10.1038/s41579-018-0019-y

Azeredo, J., Azevedo, N. F., Briandet, R., Cerca, N., Coenye, T., Costa, A. R., et al. (2017). Critical reviews in microbiology critical review on biofilm methods A. *Crit. Rev. Microbiol.* 43, 313–351. doi: 10.1080/1040841X.2016.1208146

Azevedo, A. S., Almeida, C., Gomes, L. C., Ferreira, C., Mergulhão, F. J., Melo, L. F., et al. (2017). An *in vitro* model of catheter-associated urinary tract infections to investigate the role of uncommon bacteria on the escherichia coli microbial consortium. *Biochem. Eng. J.* 118, 64–69. doi: 10.1016/j.bej.2016.11.013

Bakker, D. P., Plaats, A. Van Der Verkerke, G. *J., Busscher, H. J., and van der Mei, H. C.* (2003). Comparison of velocity profiles for different flow chamber designs used in studies of microbial adhesion to surfaces. *Appl. Environ. Microbiol.* 69, 6280–6287. doi: 10.1128/AEM.69.10.6280-6287.2003

Bell, T., and O'Grady, N. (2018). Prevention of central line-associated bloodstream infections. *Infect. Dis. Clin.* 31, 551–559. doi: 10.1016/j.idc.2017.05.007

Bingaman, S., Huxley, V. H., and Rumbaut, R. E. (2003). Fluorescent dyes modify properties of proteins used in microvascular research. *Microcirculation* 10, 221–231. doi: 10.1038/sj.mn.7800186

Blaszykowski, C., Sheikh, S., and Thompson, M. (2012). Surface chemistry to minimize fouling from blood-based fluids. *Chem. Soc. Rev.* 41, 5599–5612. doi: 10.1039/c2cs35170f

Bloomfield, I. G., Johnston, I. H., and Bilston, L. E. (1998). Effects of proteins, blood cells and glucose on the viscosity of cerebrospinal fluid. *Pediatr. Neurosurg.* 28, 246–251. doi: 10.1159/000028659

Boudarel, H., Mathias, J., Blaysat, B., and Grédiac, M. (2018). Towards standardized mechanical characterization of microbial bio films: analysis and critical review. *NPJ Biofilms Microbiomes* 4, 1–15. doi: 10.1038/s41522-018-0062-5

Brash, J. L., Horbett, T. A., Latour, R. A., and Tengvall, P. (2019). The blood compatibility challenge. part 2, protein adsorption phenomena governing blood reactivity. *Acta Biomater.* 94, 11–24. doi: 10.1016/j.actbio.2019.06.022

Brown, B. N., Ratner, B. D., Goodman, S. B., Amar, S., and Badylak, S. F. (2012). Macrophage polarization: an opportunity for improved outcomes in biomaterials and regenerative medicine. *Biomaterials* 33, 3792–3802. doi: 10.1016/j.biomaterials.2012.02.034

Busscher, H. J., van der Mei, H. C., Subbiahdoss, G., Jutte, P. C., van den Dungen, J. J., Zaat, A. M. (2012). Biomaterial-associated infection : locating the finish line in the race for the surface. *Sci. Transl. Med.* 4:153rv10. doi: 10.1126/scitranslmed.3004528

Campoccia, D., Montanaro, L., and Arciola, C. R. (2013). A review of the biomaterials technologies for infection-resistant surfaces. *Biomaterials* 34, 8533–8554. doi: 10.1016/j.biomaterials.2013.07.089

Casa, L. D. C., Deaton, D. H., and Ku, D. N. (2015). Role of high shear rate in thrombosis. *J. Vasc. Surg.* 61, 1068–1080. doi: 10.1016/j.jvs.2014.12.050

Castner, D. G., and Ratner, B. D. (2002). Biomedical surface science: foundations to frontiers. *Surf. Sci.* 500, 28–60. doi: 10.1016/S0039-6028(01)01587-4

Chandrasekaran, N., Dimartino, S., and Fee, C. J. (2013). Chemical engineering research and design study of the adsorption of proteins on stainless steel surfaces using QCM-D. *Chem. Eng. Res. Des.* 91, 1674–1683. doi: 10.1016/j.cherd.2013.07.017

Chen, S., Li, L., Zhao, C., and Zheng, J. (2010). Surface hydration: principles and applications toward low-fouling/nonfouling biomaterials. *Polymer* 51, 5283–5293. doi: 10.1016/j.polymer.2010.08.022

Cheng, G., Li, G., Xue, H., Chen, S., Bryers, J. D., and Jiang, S. (2009). Zwitterionic carboxybetaine polymer surfaces and their resistance to long-term biofilm formation. *Biomaterials* 30, 5234–5240. doi: 10.1016/j.biomaterials.2009.05.058

Curry, S., Mandelkow, H., Brick, P., and Franks, N. (1998). Crystal structure of human serum albumin complexed with fatty acid reveals an asymmetric distribution of binding sites. *Nat. Struct. Biol.* 5, 827–835. doi: 10.1038/1869

Dohnt, K., Sauer, M., Müller, M., Atallah, K., Weidemann, M., Gronemeyer, P., et al. (2011). An *in vitro* urinary tract catheter system to investigate bio fi lm development in catheter-associated urinary tract infections. *J. Microbiol. Methods* 87, 302–308. doi: 10.1016/j.mimet.2011.09.002

Dong, D., Li, J., Cui, M., Wang, J., Zhou, Y., Luo, L., et al. (2016). *In situ* "clickable" zwitterionic starch-based hydrogel for 3d cell encapsulation. *ACS Appl. Mater. Interfaces* 8, 4442–4455. doi: 10.1021/acsami.5b12141

Dutot, M., Paillet, H., Chaumeil, C., Warnet, J. -M., and Rat, P. (2009). Severe ocular infections with contact lens: role of multipurpose solutions. *Eye* 23, 470–476. doi: 10.1038/eye.2008.131

Edvardsson, M. (2009). *Q-Sense E4 Operator Manual.* Sweden: Q-Sense.

Fabrizius-Homan, D. J., and Cooper, S. L. (1991). Competitive adsorption of vitronectin with albumin, fibrinogen, and fibronectin on polymeric biomaterials. *J. Biomed. Mater. Res.* 25, 953–971. doi: 10.1002/jbm.820250804

Faria, M., Björnmalm, M., Thurecht, K. J., Kent, S. J., Parton, R. G., Kavallaris, M., et al. (2018). Minimum information reporting in bio-nano experimental literature. *Nat. Nanotechnol.* 13, 777–785. doi: 10.1038/s41565-018-0246-4

Faulón Marruecos, D., Saleh, L. S., Kim, H. H., Bryant, S. J., Schwartz, D. K., and Kaar, J. L. (2019). Stabilization of fibronectin by random copolymer brushes inhibits macrophage activation. *ACS Appl. Bio Mater.* 2, 4698–4702. doi: 10.1021/acsabm.9b00815

Felgueiras, H. P., Antunes, J. C., Martins, M. C. L., and Barbosa, M. A. (2018). Fundamentals of protein and cell interactions in biomaterials. Pept. Proteins Biomater. *Tissue Regen. Repair* 88, 956–970. doi: 10.1016/B978-0-08-100803-4.00001-2

Feng, T., Ji, W., Tang, Q., Wei, H., Zhang, S., Mao, J., et al. (2019). Low-fouling nanoporous conductive polymer-coated microelectrode for *in vivo* monitoring of dopamine in the rat brain. *Anal. Chem.* 91, 10786–10791. doi: 10.1021/acs.analchem.9b02386

Fernandez-yague, M. A., Abbah, S. A., Mcnamara, L., Zeugolis, D. I., Pandit, A., Biggs, M. J. (2015). Biomimetic approaches in bone tissue engineering : integrating biological and physicomechanical strategies. *Adv. Drug Deliv. Rev.* 84, 1–29. doi: 10.1016/j.addr.2014.09.005

Flemming, H., Wingender, J., Szewzyk, U., Steinberg, P., Rice, S. A., and Kjelleberg, S. (2016). Biofilms : an emergent form of bacterial life. *Nat. Publ. Gr.* 14, 563–575. doi: 10.1038/nrmicro.2016.94

Foggia, M. J., Quevedo, R. V., and Hansen, M. R. (2019). Intracochlear fibrosis and the foreign body response to cochlear implant biomaterials. *Laryngoscope Investig. Otolaryngol.* 4, 678–683. doi: 10.1002/lio2.329

Foster, R. N., Harrison, E. T., Castner, D. G. (2016). ToF-SIMS and XPS characterization of protein films adsorbed onto bare and sodium styrenesulfonate-grafted gold substrates. *Langmuir 32* (13), 3207–3216. doi: 10.1021/acs.langmuir.5b04743

Francolini, I., Vuotto, C., Piozzi, A., Donelli, G. (2017). antifouling and antimicrobial biomaterials: an overview. *APMIS* 125, 392–417. doi: 10.1111/apm.12675

Franz, S., Rammelt, S., Scharnweber, D., and Simon, J. C. (2011). Biomaterials immune responses to implants - a review of the implications for the design of immunomodulatory biomaterials. *Biomaterials* 32, 6692–6709. doi: 10.1016/j.biomaterials.2011.05.078

González-garcía, C., Cantini, M., Ballester-beltrán, J., Altankov, G., and Salmerón-sánchez, M. (2018). Acta biomaterialia the strength of the protein-material interaction determines cell fate. *Acta Biomater.* 77, 74–84. doi: 10.1016/j.actbio.2018.07.016

Goor, O. J. G. M., Brouns, J. E. P., and Dankers, P. Y. W. (2017). Introduction of anti-fouling coatings at the surface of supramolecular elastomeric materials: via post-modification of reactive supramolecular additives. *Polym. Chem.* 8, 5228–5238. doi: 10.1039/C7PY00801E

Gorbet, M. B., and Sefton, M. V. (2004). Biomaterial-associated thrombosis: roles of coagulation factors, complement, platelets and leukocytes. *Biomaterials* 25, 5681–5703.. doi: 10.1016/j.biomaterials.2004.01.023

Graham, M., and Cady, N. (2014). Nano and microscale topographies for the prevention of bacterial surface fouling. *Coatings* 4, 37–59. doi: 10.3390/coatings4010037

Gunkel, G., and Huck, W. T. S. (2013). S. cooperative adsorption of lipoprotein phospholipids, triglycerides, and cholesteryl esters are a key factor in nonspeci fi c adsorption from blood plasma to antifouling polymer surfaces. *J. Am. Chem. Soc.* 135, 7047–7052. doi: 10.1021/ja402126t

Haddadin, Y., Annamaraju, P., and Regunath, H. (2020). *Central Line Associated Blood Stream Infections (CLABSI). StatPearls,* 1–6.

Harris, C. A., Resau, J. H., Hudson, E. A., West, R. A., Moon, C., Black, A. D., et al. (2011). Reduction of protein adsorption and macrophage and astrocyte adhesion on ventricular catheters by polyethylene glycol and. *J. Biomed. Mater. Res. Part A* 98, 425–433. doi: 10.1002/jbm.a.33130

Hedayati, M., Marruecos, D. F., Krapf, D., Kaar, J. L., and Kipper, M. J. (2020). Protein adsorption measurements on low fouling and ultralow fouling surfaces: a critical comparison of surface characterization techniques. *Acta Biomater.* 102, 169–180. doi: 10.1016/j.actbio.2019.11.019

Heger, J. I., Froehlich, K., Pastuschek, J., Schmidt, A., Baer, C., Mrowka, R., et al. (2018). Human serum alters cell culture behavior and improves spheroid formation in comparison to fetal bovine serum. *Exp. Cell Res.* 365, 57–65. doi: 10.1016/j.yexcr.2018.02.017

Heggestad, J. T., Fontes, C. M., Joh, D. Y., Hucknall, A. M., and Chilkoti, A. (2019). In pursuit of zero 2.0, recent developments in nonfouling polymer brushes for immunoassays. *Adv. Mater.* 32:1903285. doi: 10.1002/adma.201903285

Holmberg, M., Stibius, K. B., Ndoni, S., Larsen, N. B., Kingshott, P., Hou, X. L., et al. (2007). Protein aggregation and degradation during iodine labeling and its consequences for protein adsorption to biomaterials. *Anal. Biochem.* 361, 120–125. doi: 10.1016/j.ab.2006.11.016

Hook, A. L., Anderson, D. G., Langer, R., Williams, P., Davies, M. C., and Alexander, M. R. (2010). High throughput methods applied in biomaterial development and discovery. *Biomaterials* 31, 187–198.. doi: 10.1016/j.biomaterials.2009.09.037

Hook, A. L., Chang, C. Y., Yang, J., Luckett, J., Cockayne, A., Atkinson, S., et al. (2012). Combinatorial discovery of polymers resistant to bacterial attachment. *Nat. Biotechnol.* 30, 868–875. doi: 10.1038/nbt.2316

Hook, F., Kasemo, B., Nylander, T., Fant, C., Sott, K., and Elwing, H. (2001). Variations in coupled water, viscoelastic properties, and film thickness of a mefp-1 protein film during adsorption and cross-linking: a quartz crystal microbalance with dissipation monitoring, ellipsometry, and surface plasmon resonnance study. *Anal. Chem.* 73, 5796–5804. doi: 10.1021/ac0106501

Horbett, T. A. (2018). Fibrinogen adsorption to biomaterials. *J. Mater. Res. Part A* 106, 2777–2788. doi: 10.1002/jbm.a.36460

Hou, W., Liu, Y., Zhang, B., He, X., and Li, H. G. (2018). Adsorption-associated orientational changes of immunoglobulin and regulated phagocytosis of staphylococcus epidermidis. *J. Biomed. Mater. Res. Part A* 106A, 2838–2849. doi: 10.1002/jbm.a.36472

Huyer, L. D., Pascual-gil, S., Wang, Y., Mandla, S., Yee, B., and Radisic, M. (2020). Advanced strategies for modulation of the material – macrophage interface. *Adv. Funct.* 1909331, 1–21. doi: 10.1002/adfm.201909331

Jansen, L. E., Amer, L. D., Chen, E. Y. T., Nguyen, T. V., Saleh, L. S., Emrick, T., et al. (2018). Zwitterionic PEG-PC hydrogels modulate the foreign body response in a modulus-dependent manner. *Biomacromolecules* 19, 2880–2888. doi: 10.1021/acs.biomac.8b00444

Jesmer, A. H., Huynh, V., and Wylie, R. G. (2020). Fabrication of low-fouling, high-loading polymeric surfaces through PH-controlled RAFT. *RSC Adv.* 10, 20302–20312. doi: 10.1039/D0RA02693J

Ju, H., McCloskey, B. D., Sagle, A. C., Kusuma, V. A., Freeman, B. D. (2009). Preparation, and Characterization of crosslinked poly(ethylene glycol) diacrylate hydrogels as fouling-resistant membrane coating materials. *J. Memb. Sci.* 330, 180–188. doi: 10.1016/j.memsci.2008.12.054

Kachalova, G. S., Vlaskina, A. V., Popov, A. P., Simanovskaia, A. A., Krukova, M. V., and Lipkin, A. V. (2017). *Structure of Lysozyme labeled with Fluorescein isothiocyanate (fitc) at 1.15 Angstroms Resolution*. PDB ID 5IEL 1–5. doi: 10.2210/pdb5iel/pdb

Kasputis, T., Pieper, A., Rodenhausen, K. B., Schmidt, D., Sekora, D., Rice, C., et al. (2015). Use of Precisely Sculptured Thin Film (STF) substrates with generalized ellipsometry to determine spatial distribution of adsorbed fibronectin to nanostructured columnar topographies and effect on cell adhesion. *Acta Biomater.* 18, 88–99. doi: 10.1016/j.actbio.2015.02.016

Kushiro, K., Lee, C., and Takai, M. (2016). Simultaneous characterization of protein - material and cell – protein interactions using dynamic QCM-D analysis on SAM surfaces. *Biomater. Sci.* 4, 989–997. doi: 10.1039/C5BM00613A

Lall, R. R., Wong, A. P., Lall, R. R., Lawton, C. D., Smith, Z. A., and Dahdaleh, N. S. (2015). Evidence-based management of deep wound infection after spinal instrumentation. *J. Clin. Neurosci.* 22, 238–242. doi: 10.1016/j.jocn.2014.07.010

Lebeaux, D., Fernández-hidalgo, N., Chauhan, A., Lee, S., Ghigo, J., Almirante, B., et al. (2014). Management of infections related to totally implantable venous-access ports : challenges and perspectives. *Lancet Infect. Dis.* 14, 146–159. doi: 10.1016/S1473-3099(13)70266-4

Li, B., Jain, P., Ma, J., Smith, J. K., Yuan, Z., Hung, H. C., et al. (2019). Trimethylamine N-oxide–derived zwitterionic polymers: a new class of ultralow fouling bioinspired materials. *Sci. Adv.* 5:eaaw9562. doi: 10.1126/sciadv.aaw9562

Li, B., and Webster, T. J. (2017). Bacteria antibiotic resistance : new challenges and opportunities for implant-associated orthopedic infections. *J. Orthop. Res.* 36, 22–32. doi: 10.1002/jor.23656

Li, J., Liu, W., Kilian, D., Zhang, X., Gelinsky, M., and Chu, P. K. (2019). Bioinspired interface design modulates pathogen and immunocyte responses in biomaterial-centered infection combination therapy. *Mater. Horizons* 6, 1271–1282. doi: 10.1039/C8MH01606B

Liu, Q., Singha, P., Handa, H., and Locklin, J. (2017). Covalent grafting of antifouling phosphorylcholine-based copolymers with antimicrobial nitric oxide releasing polymers to enhance infection-resistant properties of medical device coatings. *Langmuir* 33, 13105–13113. doi: 10.1021/acs.langmuir.7b02970

Luan, Y., Li, D., Wei, T., Wang, M., Tang, Z., Brash, J. L., et al. (2017). "Hearing Loss" in QCM measurement of protein adsorption to protein resistant polymer brush layers. *Anal. Chem. No.* 89, 4184–4191. doi: 10.1021/acs.analchem.7b00198

Luu, T. U., Gott, S. C., Woo, B. W. K., Rao, M. P., and Liu, W. F. (2015). Micro- and nanopatterned topographical cues for regulating macrophage cell shape and phenotype. *ACS Appl. Mater. Interfaces* 7, 28665–28672. doi: 10.1021/acsami.5b10589

Ma, Y., Bian, X., He, L., Cai, M., Xie, X., and Luo, X. (2015). Immobilization of poly(Acrylamide) brushes onto poly(Caprolactone) surface by combining atrp and "click" chemistry: synthesis, characterization and evaluation of protein adhesion. *Appl. Surf. Sci.* 329, 223–233. doi: 10.1016/j.apsusc.2014.12.149

Madiona, R. M. T., Welch, N. G., Scoble, J. A., Muir, B. W., and Pigram, P. J. (2017). Determining the limit of detection of surface bound antibody. *Biointerphases* 12:031007. doi: 10.1116/1.4986377

Maes, K., Smolders, I., Michotte, Y., and Van Eeckhaut, A. (2014). Strategies to reduce aspecific adsorption of peptides and proteins in liquid chromatography – mass spectrometry based bioanalyses: an overview. *J. Chromatogr. A* 1358, 1–13. doi: 10.1016/j.chroma.2014.06.072

Magennis, E. P., Hook, A. L., Davies, M. C., Alexander, C., Williams, P., and Alexander, M. R. (2016). Engineering serendipity: high-throughput discovery of materials that resist bacterial attachment. *Acta Biomater.* 34, 84–92. doi: 10.1016/j.actbio.2015.11.008

Marruecos, D. F., Kastantin, M., Schwartz, D. K., and Kaar, J. L. (2016). Dense poly(ethylene glycol) brushes reduce adsorption and stabilize the unfolded conformation of fibronectin. *Biomacromolecules* 17, 1017–1025. doi: 10.1021/acs.biomac.5b01657

Medalsy, I., Hensen, U., Muller, D. J. (2011). Imaging and quantifying chemical, and physical properties of native proteins at molecular resolution by force – Volume AFM. *Angew. Chem Int. Ed.* 50, 12103–12108. doi: 10.1002/anie.201103991

Menzies, D. J., Jasieniak, M., Griesser, H. J., Forsythe, J. S., Johnson, G., Mcfarland, G. et al. (2012). ToF-SIMS and XPS study of protein adsorption and cell attachment across, PEG-like plasma polymer films with lateral compositional gradients. *Surf. Sci.* 606, 1798–1807. doi: 10.1016/j.susc.2012.07.017

Miller, C. J., and Davidson, L. A. (2013). The interplay between cell signalling and mechanics in developmental processes. *Nat. Rev. Genet.* 14, 733–744. doi: 10.1038/nrg3513

Murray, P. J., Allen, J. E., Biswas, S. K., Fisher, E. A., Gilroy, D. W., Goerdt, S., et al. (2015). Macrophage activation and polarization: nomenclature and experimental guidelines. *Immunity* 41, 14–20. doi: 10.1016/j.immuni.2014.06.008

Ngo, B. K. D., and Grunlan, M. A. (2017). Protein resistant polymeric biomaterials. *ACS Macro Lett.* 6, 992–1000. doi: 10.1021/acsmacrolett.7b00448

Nguyen, A. T., Sathe, S. R., and Yim, E. K. (2016). From nano to micro : topographical scale and its impact on cell adhesion, morphology and contact guidance. *J. Phys. Condens. Matter No.* 28, 1–16. doi: 10.1088/0953-8984/28/18/183001

Norde, W. (1996). Driving forces for protein adsorption at solid surfaces. *Macromol. Symp.* 103, 5–18. doi: 10.1002/masy.19961030104

Ntziachristos, V. (2010). Going deeper than microscopy: the optical imaging frontier in biology. *Nat. Publ. Gr.* 7, 603–614. doi: 10.1038/nmeth.1483

Oliveira, W. F., Silva, P. M. S., Silva, R. C. S., Silva, G. M. M., Machado, G., Coelho, L. C. et al. (2018). *Staphylococcus aureus and staphylococcus epidermidis infections on implants. J. Hosp. Infect.* 98, 111–117. doi: 10.1016/j.jhin.2017.11.008

Othman, Z., Cillero, B., van Rijt, S., and Habibovic, S. P. (2018). Understanding Interactions between biomaterials and biological systems using proteomics. *Biomaterials* 167, 191–204. doi: 10.1016/j.biomaterials.2018.03.020

Parisi, L., Toffoli, A., Ghezzi, B., Mozzoni, B., Lumetti, S., and Macaluso, G. M. (2020). A Glance on the role of fibronectin in controlling cell response at biomaterial interface. *Jpn. Dent. Sci. Rev.* 56, 50–55. doi: 10.1016/j.jdsr.2019.11.002

Pei, J., Hall, H., and Spencer, N. D. (2011). The role of plasma proteins in cell adhesion to PEG surface-density-gradient- modified titanium oxide. *Biomaterials* 32, 8968–8978. doi: 10.1016/j.biomaterials.2011.08.034

Pereira, A. de los S., Rodriguez-Emmenegger, C., Surman, F., Riedel, T., Alles, A. *et al.* (2014). Use of pooled blood plasmas in the assessment of fouling resistance. *RSC Adv.* 4, 2318–2321. doi: 10.1039/C3RA43093F

Pierce Biotechnology (2017). *Instrution: Micro BCA Protein Assay Kit*. Rockford, IL: Thermo Sci, 1–6.

Pinho, A. C., and Piedade, A. P. (2013). Zeta potential, contact angles, and AFM imaging of protein conformation adsorbed on hybrid nanocomposite surfaces. *ACS Appl. Mater.* 5, 8187–8194. doi: 10.1021/am402302r

PyMol (2015) *The PyMol Molecular Graphics System Version 2. 3.4*. Schrodinger, LLC.

Rahmati, M., Silva, E. A., Reseland, J. E., Heyward, C. A., and Haugen, H. J. (2020). Biological responses to physicochemical properties of biomaterial surface. *Chem. Soc. Rev.* 49, 5178–5224. doi: 10.1039/D0CS00103A

Rao, W., Celiz, A. D., Scurr, D. J., Alexander, M. R., and Barrett, D. A. (2013). Ambient DESI and LESA-MS analysis of proteins adsorbed to a biometerial surface using in-situ surface tryptic Digestion. *J. Am. Soc. Mass Spectrom.* 24, 1927–1936. doi: 10.1007/s13361-013-0737-3

Ratner, B. D. (2019). Biomaterials: been there, done that, and evolving into the future. *Annu. Rev. Biomed. Eng.* 21, 171–191. doi: 10.1146/annurev-bioeng-062117-120940

Rennert, R. C., Rustad, K., Levi, K., Harwood, M., Sorkin, M., Wong, V. W., et al. (2014). Histological and mechanical analysis of the cardiac lead –tissue interface: implications for lead extraction. *Acta Biomater.* 10, 2200–2208. doi: 10.1016/j.actbio.2014.01.008

Richter, R. P., and Brisson, A. R. (2005). Following the formation of supported lipid bilayers on mica: a study combining, AFM, QCM-D, and ellipsometry. *Biophys. J.* 88, 3422–3433. doi: 10.1529/biophysj.104.053728

Riedel, T., Majek, P., Riedelova-Reicheltola, Z., Vorobii, M., Houska, M., and Rodriguez-Emmenegger, C. (2016). Total removal of intact blood plasma proteins deposited on surface-grafted polymer brushes. *Anal. Methods No.* 8, 6415–6419. doi: 10.1039/C6AY01833E

Riedel, T., Riedelova-Reicheltova, Z., Majek, P., Rodriguez-emmenegger, C., Houska, M., Dyr, J. E., et al. (2013). complete identification of proteins responsible for human blood plasma fouling on poly(ethylene glycol)-based surfaces. *Langmuir* 29, 3388–3397. doi: 10.1021/la304886r

Roach, P., Farrar, D., and Perry, C. C. (2005). Interpretation of protein adsorption : surface-induced conformational changes. *J. Am. Chem. Soc. No.* 127, 8168–8173. doi: 10.1021/ja042898o

Romanowska, J., Kokh, D. B., and Wade, R. C. (2015). when the label matters: adsorption of labeled and unlabeled proteins on charged surfaces. *Nano Lett.* 15, 7508–7513. doi: 10.1021/acs.nanolett.5b03168

Rostam, H. M., Fisher, L. E., Hook, A. L., Burroughs, L., Luckett, J. C., Figueredo, G. P., et al. (2020). Immune-instructive polymers control macrophage phenotype and modulate the foreign body response *in vivo*. *Matter* 2, 1–18. doi: 10.1016/j.matt.2020.03.018

Saint, S., Greene, T., Krein, S., Rogers, M., Ratz, D., Fowler, K., et al. (2016). A program to prevent catheter-associated urinary tract infection in acute care. *N. Engl. J. Med.* 374, 2111–2119. doi: 10.1056/NEJMoa1504906

Saleem, B. R., Meerwaldt, R., Tielliu, I. F. J., Verhoeven, E. L. G., *van den* Dungen, J. J. A. M., and Zeebregts, C. J. (2010). Conservative treatment of vascular prosthetic graft infection is associated with high mortality. *Am. J. Surg.* 200, 47–52. doi: 10.1016/j.amjsurg.2009.05.018

Santoro, F., Zhao, W., Joubert, L., Duan, L., Schnitker, J., van de Burgt, Y., et al. (2017). Revealing the cell – material interface with nanometer resolution by focused ion beam/ scanning electron microscopy. *ACS Nano* 11, 8320–8328. doi: 10.1021/acsnano.7b03494

Seo, J., Sakai, K., and Yui, N. (2013). Adsorption state of fibronectin on poly (dimethylsiloxane) surfaces with varied stiffness can dominate adhesion density of fibroblasts. *Acta Biomater.* 9, 5493–5501. doi: 10.1016/j.actbio.2012.10.015

Sharifi, F., Htwe, S. S., Righi, M., Liu, H., Pietralunga, A., Yesil-celiktas, O., et al. (2019). A foreign body response-on-a-chip platform. *Adv. Healthc. Mater.* 8:1801425. doi: 10.1002/adhm.201801425

Shen, M., Pan, Y. V., Wagner, M. S., Hauch, K. D., Castner, D. G., Ratner, B. D., et al. (2001). Inhibition of Monocyte Adhesion and Fibrinogen Adsorption on Glow Discharge Plasma Deposited Tetraethylene Glycol Dimethyl Ether. *J. Biomater. Sci. Polym. Ed.* 12, 961–978. doi: 10.1163/156856201753252507

Sjollema, J., Zaat, S. A. J., Fontaine, V., Ramstedt, M., Luginbuehl, R., Thevissen, K., et al. (2018). *In vitro* methods for the evaluation of antimicrobial surface designs. *Acta Biomater.* 70, 12–24. doi: 10.1016/j.actbio.2018.02.001

Stewart, P. S. (2015). Antimicrobial tolerance in biofilms. *Microb. Biofilms* 3, 269–285. doi: 10.1128/microbiolspec.MB-0010-2014.Antimicrobial

Su, T. J., Lu, J. R., Cui, Z. F., and Thomas, R. K. (2000). Fouling of ceramic membranes by albumins under dynamic filtration conditions. *J. Memb. Sci.* 173, 167–178. doi: 10.1016/S0376-7388(00)00370-7

Sugahara, M., Nakane, T., Masuda, T., Suzuki, M., Inoue, S., Song, C., et al. (2017). Hydroxyethyl cellulose matrix applied to serial crystallography. *Sci. Rep.* 7:703. doi: 10.1038/s41598-017-00761-0

Sundaram, H. S., Cho, Y., Dimitriou, M. D., Weinman, C. J., Finlay, J. A., Cone, G., et al. (2011). Fluorine-free mixed amphiphilic polymers based on pdms and peg side chains for fouling release applications. *Biofouling* 27, 589–602. doi: 10.1080/08927014.2011.587662

Swartzlander, M. D., Barnes, C. A., Blakney, A. K., Kaar, J. L., Kyriakides, T. R., and Bryant, S. J. (2015). Biomaterials linking the foreign body response and protein

adsorption to peg-based hydrogels using proteomics. *Biomaterials* 41, 26–36. doi: 10.1016/j.biomaterials.2014.11.026

Taylor, M., Urquhart, A. J., Anderson, D. G., Williams, P. M., Langer, R., Alexander, M. R., et al. (2008). A methodology for investigating protein adhesion and adsorption to microarrayed combinatorial polymers. *Macromol. Rapid Commun.* 29, 1298–1302. doi: 10.1002/marc.200800171

Tonda-turo, C., Carmagnola, I., and Ciardelli, G. (2018). Quartz crystal microbalance with dissipation monitoring: a powerful method to predict the *in vivo* behavior of bioengineered surfaces. *Front. Bioeng. Biotechnol.* 6:158. doi: 10.3389/fbioe.2018.00158

Trindade, R., Albrektsson, T., Tengvall, P., and Wennerberg, A. (2014). Foreign body reaction to biomaterials : on mechanisms for buildup and breakdown of osseointegration. *Clin. Implant Dent. Relat. Res.* 18, 192–203. doi: 10.1111/cid.12274

Tziampazis, E., Kohn, J., and Moghe, P. V. (2000). PEG-variant biomaterials as selectively adhesive protein templates: model surfaces for controlled cell adhesion and migration. *Biomaterials* 21, 511–520. doi: 10.1016/S0142-9612(99)00212-4

van de Lagemaat, M., Grotenhuis, A., van de Belt-Gritter, B., Roest, S., Loontjens, T. J. A., Busscher, H. J., et al. (2017). Comparison of methods to evaluate bacterial contact-killing materials. *Acta Biomater.* 59, 139–147. doi: 10.1016/j.actbio.2017.06.042

Veiseh, O., and Vegas, A. J. (2019). Domesticating the foreign body response: recent advances and applications. *Adv. Drug Deliv. Rev.* 144, 148–161. doi: 10.1016/j.addr.2019.08.010

Vinchon, M., and Dhellemmes, P. (2006). Cerebrospinal fluid shunt infection: risk factors and long-term follow-up. *Child's Nerv. Syst.* 22, 692–697. doi: 10.1007/s00381-005-0037-8

Visalakshan, R. M., Macgregor, M. N., Sasidharan, S., Ghazaryan, A., Landfester, K., Mierczynska-vasilev, A. M., et al. (2019). Biomaterial surface hydrophobicity-mediated serum protein adsorption and immune responses. *ACS Appl. Mater. Interfaces* 11, 27615–27623. doi: 10.1021/acsami.9b09900

Vishwakarma, A., Bhise, N. S., Evangelista, M. B., Rouwkema, J., Dokmeci, M. R., Ghaemmaghami, A. M., et al. (2016). Engineering immunomodulatory biomaterials to tune the inflammatory response. *Trends Biotechnol.* 34, 470–482. doi: 10.1016/j.tibtech.2016.03.009

Visova, I., Vrabcova, M., Forinova, M., Zhigunova, Y., Mironov, V., Houska, M., et al. (2020). Surface preconditioning influences the antifouling capabilities of zwitterionic and nonionic polymer brushes. *Langmuir* 36, 8485–8493. doi: 10.1021/acs.langmuir.0c00996

Vroman, L., Adams, A. L., Fischer, G. C., and Munoz, P. C. (1980). Interaction of high molecular weight kininogen, factor XIII, and fibrinogen in plasma at interfaces. *Blood* 55, 156–159. doi: 10.1182/blood.V55.1.156

Vu, V. P., Gifford, G. B., Chen, F., Benasutti, H., Wang, G., Groman, V., et al. (2019). Corona determines complement opsonization efficiency of preclinical and clinical nanoparticles. *Nat. Nanotechnol.* 14, 260–268. doi: 10.1038/s41565-018-0344-3

Wagner, M. S., Mcarthur, S. L., Shen, M., Horbett, T. A., Castner, D. G., Wagner, M. S., et al. (2002). Limits of detection for time of flight secondary ion mass spectrometry (tof-sims) and x-ray photoelectron spectroscopy (XPS): detection of low amounts of adsorbed protein. *J. Biomater. Sci. Polym. Ed.* 13, 407–428. doi: 10.1163/156856202320253938

Wagner, S., Sommer, R., Hinsberger, S., Lu, C., Hartmann, R. W., Empting, M., et al. (2016). Novel strategies for the treatment of pseudomonas aeruginosa infections. *J. Med. Chem. No*. 59, 5929–5969. doi: 10.1021/acs.jmedchem.5b01698

Walker, J. M. (1996). *The Protein Protocols Handbook*, *2nd* Edn, Totowa, NJ: Humana Press. doi: 10.1007/978-1-60327-259-9

Wang, H., Christiansen, D. E., Mehraeen, S., and Cheng, G. (2020). Winning the fight against biofilms: the first six-month study showing no biofilm formation on zwitterionic polyurethanes. *Chem. Sci.* 11, 4709–4721. doi: 10.1039/C9SC06155J

Weaver, W. M., Milisavljevic, V., Miller, J. F., and Di Carlo, D. (2012). Fluid flow induces biofilm formation in staphylococcus epidermidis polysaccharide intracellular adhesin-positive clinical isolates. *Appl. Environ. Microbiol.* 78, 5890–5896. doi: 10.1128/AEM.01139-12

Weber, M., Steinle, H., Golombek, S., Hann, L., Schlensak, C., Wendel, H. P., et al. (2018). Blood-contacting biomaterials : *in vitro* evaluation of the hemocompatibility. *Front. Bioeng. Biotechnol.* 6:99. doi: 10.3389/fbioe.2018.00099

Wei, Q., Becherer, T., Angioletti-uberti, S., Dzubiella, J., Wischke, C., Neffe, A. T., et al. (2014). Protein interactions with polymer coatings and biomaterials. *Angew. Chemie Int. Ed.* 53, 8004–8031. doi: 10.1002/anie.201400546

Welch, N. G., Scoble, J. A., Muir, B. W., and Pigram P. J. (2017). Orientation, and characterization of immobilized antibodies for improved immunoassays (review). *Biointerphases* 12:02D301-1. doi: 10.1116/1.4978435

Welch, N. G., Winkler, D. A., and Thissen, H. (2020). Antifibrotic strategies for medical devices. *Adv. Drug Deliv. Rev.* doi: 10.1016/j.addr.2020.06.008

Wilson, C. J., Clegg, R. E., Leavesley, D. I., and Pearcy, M. J. (2005). Mediation of biomaterial – cell interactions by adsorbed proteins: a review. *Tissue Eng.* 11, 1–18. doi: 10.1089/ten.2005.11.1

Witherel, C. E., Abebayehu, D., Barker, T. H., Spiller, K. L. (2019). Macrophage and fibroblast interactions in biomaterial- mediated fibrosis. *Adv. Healthc. Mater.* 1801451, 1–16. doi: 10.1002/adhm.201801451

Wu, Y., Zitelli, J. P., Tenhuisen, K. S., Yu, X., and Libera, M. R. (2011). Biomaterials differential response of staphylococci and osteoblasts to varying titanium surface roughness. *Biomaterials* 32, 951–960. doi: 10.1016/j.biomaterials.2010.10.001

Xie, X., Doloff, J. C., Yesilyurt, V., Sadraei, A., Mcgarrigle, J. J., Omami, M., et al. (2018). Glucose monitor by coating the sensor with a zwitterionic polymer. *Nat. Biomed. Eng.* 2, 894–906. doi: 10.1038/s41551-018-0273-3

Yang, C., Li, J., Zhu, C., Zhang, Q., Yu, J., Wang, J., et al. (2019). Advanced antibacterial activity of biocompatible tantalum nanofilm via enhanced local innate immunity. *Acta Biomater.* 89, 403–418. doi: 10.1016/j.actbio.2019.03.027

Yang, W., Xue, H., Li, W., And, J. Z., and Jiang, S. (2009). Pursuing "Zero" Protein Adsorption of Poly(Carboxybetaine) from Undiluted Blood Serum and plasma. *Langmuir* 25, 11911–11916. doi: 10.1021/la9015788

Yang, Y., Ramos, T. L., Heo, J., and Green, M. D. (2018). Zwitterionic poly (arylene ether sulfone) copolymer/poly (arylene ether sulfone) blends for fouling-resistant desalination membranes. *J. Mebrane Sci.* 561, 69–78. doi: 10.1016/j.memsci.2018.05.025

Yang, Z., Mochalkin, I., Veerapandian, L., Riley, M., and Doolittle, R. F. (2000). Crystal structure of native chicken fibrinogen at 5.5-å resolution. *Proc. Natl. Acad. Sci. U.S.A.* 97, 3907–3912. doi: 10.1073/pnas.080065697

Yeung, T., Georges, P. C., Flanagan, L. A., Marg, B., Ortiz, M., Funaki, M., et al. (2005). Effects of substrate stiffness on cell morphology, cytoskeletal structure, and adhesion. *Cell Motil. Cytoskeleton* 60, 24–34. doi: 10.1002/cm.20041

Yu, L., Hou, Y., Cheng, C., Schlaich, C., Noeske, P. -L. M., Wei, Q., (2017). High-antifouling polymer brush coatings on nonpolar surfaces via adsorption-cross-linking strategy. *ACS Appl. Bio Mater.* 9, 44281–44292. doi: 10.1021/acsami.7b13515

Yue, C., Mei, H. C. Van Der Kuijer, R., Busscher, H. J., and Rochford, E. T. J. (2015). Mechanism of cell integration on biomaterial implant surfaces in the presence of bacterial contamination. *J. Biomed. Mater. Res. Part A* 103, 3590–3598. doi: 10.1002/jbm.a.35502

Zaatreh, S., Wegner, K., Strau,ß, M., Pasold, J., Mittelmeier, W., Podbielski, A., et al. (2016). Co-Culture of S. epidermidis and human osteoblasts on implant surfaces: an advanced *in vitro* model for implant- associated infections. *PLoS ONE* 11, 1–16. doi: 10.1371/journal.pone.0151534

Zhang, Z., Chen, S., Chang, Y., and Jiang, S. (2006). Surface grafted sulfobetaine polymers via atom transfer radical polymerization as superlow fouling coatings. *J. Phys. Chem. B* 110, 10799–10804. doi: 10.1021/jp057266i

Conflict of Interest: The authors declare that the research was conducted in the absence of any commercial or financial relationships that could be construed as a potential conflict of interest.

Copyright © 2020 Jesmer and Wylie. This is an open-access article distributed under the terms of the Creative Commons Attribution License (CC BY). The use, distribution or reproduction in other forums is permitted, provided the original author(s) and the copyright owner(s) are credited and that the original publication in this journal is cited, in accordance with accepted academic practice. No use, distribution or reproduction is permitted which does not comply with these terms.

frontiers in Chemistry

MINI REVIEW
published: 21 December 2020
doi: 10.3389/fchem.2020.600317

Trends of Bead Counting-Based Technologies Toward the Detection of Disease-Related Biomarkers

Wenjiao Fan[1,2,3], *Dou Liu*[1,2,3], *Wei Ren*[1,2,3]* and *Chenghui Liu*[1,2,3]*

[1] Key Laboratory of Applied Surface and Colloid Chemistry Ministry of Education, Xi'an, China, [2] Key Laboratory of Analytical Chemistry for Life Science of Shaanxi Province, Xi'an, China, [3] School of Chemistry & Chemical Engineering, Shaanxi Normal University, Xi'an, China

Nowadays, the biomolecular assay platforms built-up based on bead counting technologies have emerged to be powerful tools for the sensitive and high-throughput detection of disease biomarkers. In this mini-review, we classified the bead counting technologies into statistical counting platforms and digital counting platforms. The design principles, the readout strategies, as well as the pros and cons of these platforms are introduced in detail. Finally, we point out that the digital bead counting technologies will lead the future trend for the absolute quantification of critical biomarkers, and the integration of new signal amplification approaches and routine optical/clinical instruments may provide new opportunities in building-up easily accessible digital assay platforms.

Keywords: bead counting strategy, statistical counting, planar array, suspension array, digital counting

OPEN ACCESS

Edited by:
Jie He,
University of Connecticut,
United States

Reviewed by:
Jafar Soleymani,
Tabriz University of Medical Sciences, Iran
Giovanni Valenti,
University of Bologna, Italy

****Correspondence:***
Chenghui Liu
liuch@snnu.edu.cn
Wei Ren
wei.ren@snnu.edu.cn

Specialty section:
This article was submitted to Analytical Chemistry, a section of the journal Frontiers in Chemistry

Received: *29 August 2020*
Accepted: *30 November 2020*
Published: *21 December 2020*

Citation:
Fan W, Liu D, Ren W and Liu C (2020) Trends of Bead Counting-Based Technologies Toward the Detection of Disease-Related Biomarkers. Front. Chem. 8:600317. doi: 10.3389/fchem.2020.600317

INTRODUCTION

Motivated by the growing demand for rapid and precise analysis of critical biomarkers (e.g., disease-associated nucleic acids and proteins), particle-based biomolecular assays and particle counting technologies have significantly enlarged the toolbox for bioanalysis (Rödiger et al., 2014). A lot of efforts have been devoted to the nanoparticle counting-based assays. For example, the nanoparticle counting strategies based on total internal reflection fluorescence microscopy (TIRFM) and dark field microscopy have been successfully applied for the sensitive detection of biomarkers (Ma et al., 2016, 2019; Qi et al., 2018). Compared with nanoparticles, micro-sized beads, especially magnetic beads have exhibited the potential to be adopted in broader application scenarios. In this review, we mainly focus on the particle-counting technologies which allow the precise readout of the target-induced fluorescence signals accumulated on microbeads. Generally, we classified this area into two categories (**Scheme 1**). One is the statistical counting, in which the target molecules are concentrated on the beads that act as the reaction carriers for fluorescent signal amplification and transduction, and the quantification of target molecules is achieved by counting/measuring the total fluorescent signals loaded on the beads. The other one is the digital counting strategy, in which each bead carries only one or none target molecule following Poisson distribution. Thus, after the single target-initiated fluorescence generation, the absolute number of the target biomolecules can be achieved by digitally counting the number of fluorescence carriers (e.g., beads). Regarding the precision and convenience of the biomolecular assays, bead counting strategies are superior to the homogeneous sensing strategies in two aspects.

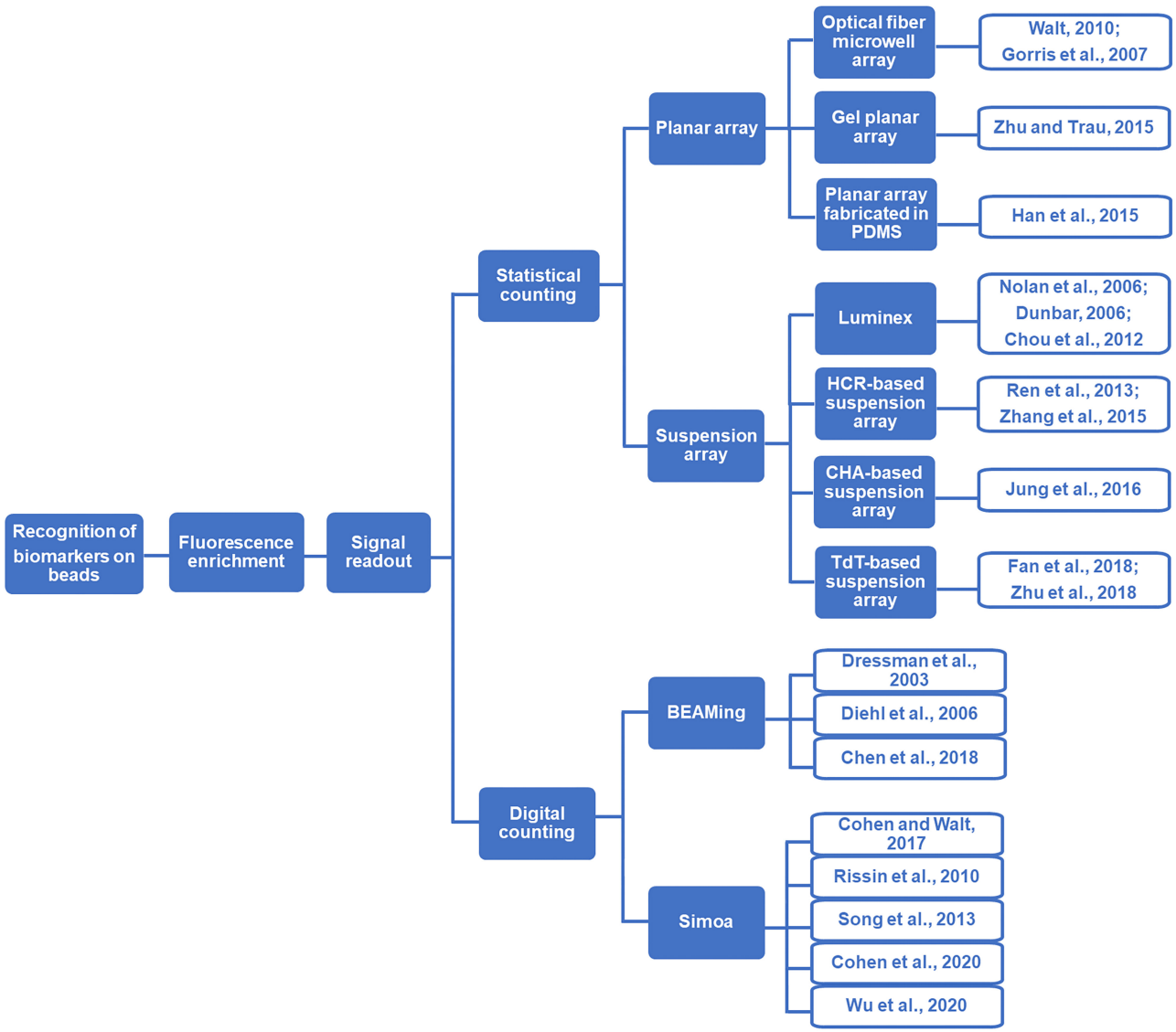

SCHEME 1 | Flow diagram illustration of bead counting-based technologies.

On the one hand, in the bead counting methods, the target biomolecule (such as nucleic acids, proteins, and antibodies/antigens)-induced response signals are anchored on the beads, which can get rid of the interference by separating the beads from the complex sample matrix. On the other hand, the commercially available and easily synthetic beads are solid and stable, which can be applied as satisfying microreactors for multi-step reactions. For example, compared with the emulsions used as microreactors in classical digital assays (e.g., droplet digital PCR, abbreviated as ddPCR), the bead-based digital assays are steady and facile due to the avoidance of using fragile emulsion droplets. Therefore, it is believed that the prosperity of the bead-counting technologies will lead to the more precise detection of critical biomarkers.

BEADS-BASED STRATEGIES FOR THE DETECTION OF BIOMOLECULES

Beads-Based Statistical Counting Strategies for the Detection of Biomolecules

In the statistical counting strategies, the fluorescence signals are accumulated on the beads via target-induced reactions. Therefore, the fluorescence intensity statistically collected from a large population of beads can reflect the concentration information of the target molecules. It should be noted that in such strategies, the concentration of target can only be obtained by substituting the experimental data into the standard curve established by a gradient of standard samples with known

concentrations. Basically, there are two representative types of statistical bead counting strategies: the solid-state planar arrays and the liquid-state suspension arrays, both of which have been applied widely in the detection of disease-related biomolecules (Parsa et al., 2018; Vafajoo et al., 2018). In the solid-state planar arrays, the beads are attached to a solid substrate after target capturing and fluorescence signal accumulation, and the fluorescence signals of the beads are monitored after the washing procedure (Sukhanova and Nabiev, 2008). As to the suspension arrays, after introducing the target-associate fluorescent tags onto the beads, the beads are monitored one by one when they pass through the laser beam without any separation procedure (Leng et al., 2015).

Solid-State Planar Bead Arrays

Generally, in the planar bead arrays, the target-specific fluorescence reporters are immobilized on the beads, which are then deposited onto a solid substrate or into microwells (Rödiger et al., 2014). Then, the beads carrying fluorescent signals are captured using an imaging system (e.g., a fluorescence microscope). In the following steps, the fluorescence images are processed and annotated by professional software for target quantification.

One of the most prominent planar bead strategies is the optical fiber microwell array described by Walt's group (Gorris et al., 2007; Walt, 2010). In this working principle, the target-specific beads are distributed into the microwells generated by hydrofluoric acid etching on an optical imaging fiber. After removing the extra beads and solutions, the fluorescence intensity of the beads is collected by an imaging system. Therefore, the amount of target can be reflected by the fluorescence signals specifically accumulated on the beads. Benefiting from the versatile design, not only nucleic acid but also protein can be sensitively analyzed with this array.

Zhu and Trau (2015) presented a gel planar array chip for high-throughput and multi-analyte bead-based immunoassays. The chip is fabricated on a glass slide by using polyacrylamide gel and polyethylene glycol (PEG) gel. The resulting chip consists of a number of polyacrylamide gel units for the immobilization of beads, and each gel unit is surrounded with a PEG ring to confine the sample within the microarrays. Consequently, the on-bead immunoreaction was confined in the microarrays. After the immunoreaction with the Alexa Flour labeled detection antibody, the target-specific fluorescent beads are monitored with a fluorescence microscope, and the target can be quantified by recording the total fluorescence signal loaded on the beads. In this method, the detection limits below the physiological threshold level for cancer diagnosis was achieved.

The Koh group developed a microhole planar array fabricated in PDMS (poly-dimethylsiloxane), where each microhole was designed to trap a single bead that functionalized with probe antibodies (Han et al., 2015). The beads were coded with quantum dots (QDs) of two different colors. After the specific immunoreactions on the surface of the QDs-encoded beads, multiple target proteins can be recognized by identifying the beads in the microholes with their precision x and y coordinates recorded, and then quantified by analyzing the fluorescence signals of QDs-embedded beads with photolithography. In this design, as low as 1 ng/mL target can be detected.

Liquid-State Suspension Bead Arrays

Although planar arrays play an important role in ultrasensitive bioanalysis, limitations on the quality of its results, binding rates, decoding speed, and overall flexibility still exist (Wilson et al., 2006; Leng et al., 2015). Fortunately, a series of liquid-state suspension bead assay strategies relying on monitoring free beads have been proposed for the efficient analysis of biomarkers, which may solve the challenges. Typically, the flow cytometric methods that count the suspending beads carrying varied fluorescence signals individually seems to be the most dominant. Flow cytometric is a versatile technology for the rapid interrogation of individual cells or beads in a one-by-one fashion (Adan et al., 2017). It can simultaneously measure the light scattering and the fluorescence intensity of individual beads in a fluid stream when they pass through the laser beam (Wilkerson, 2012). By statistically processing the fluorescence data collected from the suspension beads, the target biomarkers that induce the fluorescence accumulation on the beads can be quantified. This working scheme makes the flow cytometer (FCM) a powerful tool for the analysis of disease biomarkers in biomedical research and clinical diagnosis.

One of the most commonly used FCM systems is the Luminex family, a well-established platform using multiple kinds of fluorophores to encode a panel of beads ($\sim$5.5 μm polystyrene beads) (Nolan et al., 2006). In this system, each bead group corresponds to a specific target biomolecule. With more than one solid-state laser equipped on the FCM, the beads with different fluorescence colors and intensities are counted one by one in the liquid flow and decoded by the detectors. In this way, multiple targets can be analyzed simultaneously by using fluorescence-encoded beads (Dunbar, 2006; Chou et al., 2012).

Despite the high-throughput monitoring of disease biomarkers, higher detection sensitivity is always desired in the clinical diagnosis. In this regard, a series of on-bead signal amplification strategies have been reported to improve the sensitivity of the liquid-state suspension bead-based assays. For example, hybridization chain reaction (HCR) (Dirks and Pierce, 2004) is one of the most effective enzyme-free amplification strategies that have been integrated with the liquid-state bead-based sensitive detection of biomarkers (Ren et al., 2013). In these designs, the mute trigger of HCR is anchored on the beads. Only in the presence of target molecules, the trigger can be activated to initiate a cascade hybridization reaction of two metastable hairpin probes (Zhang et al., 2015). By labeling the fluorophore molecules on the hairpin probes, a lot of nicked double-stranded DNA (dsDNA) structures with fluorescent signals are enriched on the beads. With the help of the efficient HCR, even a low concentration of target molecule can induce an observable fluorescence signal that can be sensed and quantitively analyzed by FCM. Catalyzed hairpin assembly (CHA) is another mature nonenzymatic nucleic acid amplification strategy (Yin et al., 2008; Li et al., 2011). In CHA, a single-stranded DNA (ssDNA) is required as the catalyst to trigger the strand exchange reactions of two hairpin probes and initiate the cycling of CHA circuits.

In greater detail, the ssDNA catalyst can interact with a toehold on one of the hairpin probes (H1) and open the hairpin to expose a new ssDNA. And the newly exposed ssDNA can hybridize with a toehold on another hairpin probe (H2) and trigger the strand-exchange process. With the displacement, the free catalyst can participate in subsequent reaction cycles. In this way, lots of H1:H2 duplexes are formed even at the low level of target concentration without using the enzymes. As an enzyme-free strategy, the efficient CHA can be integrated with the bead-FCM system for the sensitive detection of biomarkers (Jung et al., 2016). And the system could be of use in analytical and diagnostic applications.

Compared with the enzyme-free amplification methods, the enzyme-involved amplification strategies are more effective. Terminal deoxynucleotidyl transferase (TdT) is a template-independent DNA polymerase that catalyzes the repetitive sequential addition of deoxynucleotides (dNTP) at the 3′-OH group of a DNA (Liu et al., 2014; Wang et al., 2017). Taking benefit of this intriguing property of TdT, effective signal amplification can be achieved without complicated probe design, which greatly simplifies the assay. Considering this, a set of high-sensitive strategies have been reported for both nucleic acid and protein sensing by conducting the target molecule-initiated TdT extension on the surface of beads (Fan et al., 2018; Zhu et al., 2018). After immobilizing fluorescent molecules on the product of target-initiated TdT extension, the beads with different fluorescence intensity are interrogated, and then statistically analyzed by FCM. In this way, as low as 5 fM nucleic acid and 0.5 pg/mL protein can be analyzed.

In conclusion, both the solid-state planar bead arrays and liquid-state suspension bead arrays can provide satisfying biomarker analyzing performance. To further improve the sensitivity of the bead-based statistical counting strategies, developing more efficient signal amplification methods and applying more sensitive fluorescence instruments are two most promising ways.

Beads-Based Digital Counting Strategies for the Detection of Disease Biomarkers

The statistical bead counting strategies have allowed the sensitive and multiplex detection of disease-related biomolecules, however, a standard curve is inevitable. In this consideration, the most precise and promising way of quantifying the biomolecules is to count their absolute number in a digital manner (Walt, 2013; Gooding and Gaus, 2016). In digital bioassays, the sample solution containing target molecules is divided into a great deal of separate microreactors. According to the Poisson distribution, the microreactors will be of one or none target biomolecules and ultimately show either positive or negative binary signal readout (Zhang and Noji, 2017). In this way, the target biomolecules can be digitally reflected by the number of positive microreactors. Compared with the statistical counting assays, the digital counting bioassays are able to provide the absolute number of target molecules without using a standard curve, expelling a series of interfering factors. Due to such advantages, the sensitivity of digital counting bioassay is reported to be much higher than that of the statistical counting assays.

BEAMing Platform

The ddPCR (e.g., Bio-Rad QX-100/QX-200) is the most mature digital counting bioassay, which has already been commercialized (Hindson et al., 2011; Pinheiro et al., 2012). It enables the absolute digital quantification of target molecules without the requirement of external/internal standard and is extremely suitable for precise quantification of low-abundance nucleic acids. Different from ddPCR which adopts pure emulsion droplets as the independent microreactors, BEAMing (Dressman et al., 2003) is developed depending on four principal components (beads, emulsion, amplification, magnetics, **Figure 1**). In BEAMing, a single target molecule and a single magnetic bead are simultaneously encapsulated in one drop of emulsion (Diehl et al., 2006; Chen et al., 2018). After the polymerase chain reaction (PCR) or loop-mediated isothermal amplification (LAMP) process on the beads inside the emulsions, the emulsions are broken and the beads are purified with the assistance of magnetic separation. After then, the number of variant DNA molecules in the population is analyzed by counting the fluorescence-positive beads using FCM. Nevertheless, in the principle of BEAMing, only the microemulsions containing both a target molecule and a bead can lead to the positive signal readout. Therefore, false negatives may occur when the nucleic acid target and bead are not encapsulated in one emulsion simultaneously. It should also be noted that the fragile emulsion reaction is prone to be affected by many factors to bring misleading results.

Single Molecule Arrays (Simoa)

Another prominent digital platform is the Simoa, which was firstly proposed by the Walt group (Rissin et al., 2010; Cohen and Walt, 2017). In the principle of Simoa, individual beads (∼2.7 μm paramagnetic beads) bound with either none or one target molecule are seeded into femtoliter-volume well arrays (**Figure 1**). Assisted by an enzyme-catalyzed fluorogenic reaction, the detection of the target is converted to counting the number of positive microwells that contain the beads with the target molecule (Song et al., 2013). As a result, the subfemtomolar level of target biomolecules can be detected by the Simoa system. However, the sensitivity of Simoa is impeded by the low loading efficiency of beads, in which just about 5% of the total beads can be sampled into the microwells and analyzed (Cohen et al., 2020). To overcome this barrier, recently, the dropcast Simoa (dSimoa) system for the ultrasensitive protein detection by single molecule counting with a higher sampling efficiency is proposed (Wu et al., 2020). In this approach, instead of loading the beads into the microwells, the beads are simply dropcast onto a microscope slide for single molecule counting. Therefore, the sampling efficiency is dramatically improved.

As a conclusion, the ultrahigh sensitive quantification of disease-biomolecules can be achieved by introducing bead-based digital counting strategies, which is with great promise to offer even the absolute number of target molecules in complex biological samples. Therefore, compared with the statistical counting strategies, the bead-based digital counting strategies are more precise and sensitive.

PERSPECTIVE

Although the digital assay strategies, including ddPCR, BEAMing, and Simoa have shown the future trend of biomarker analysis, we anticipate that the development of new bead-based digital platforms with commonly accessible equipment, simple operation, and wide applicability is of great significance for the prevalence of digital assays. Considering the advantages

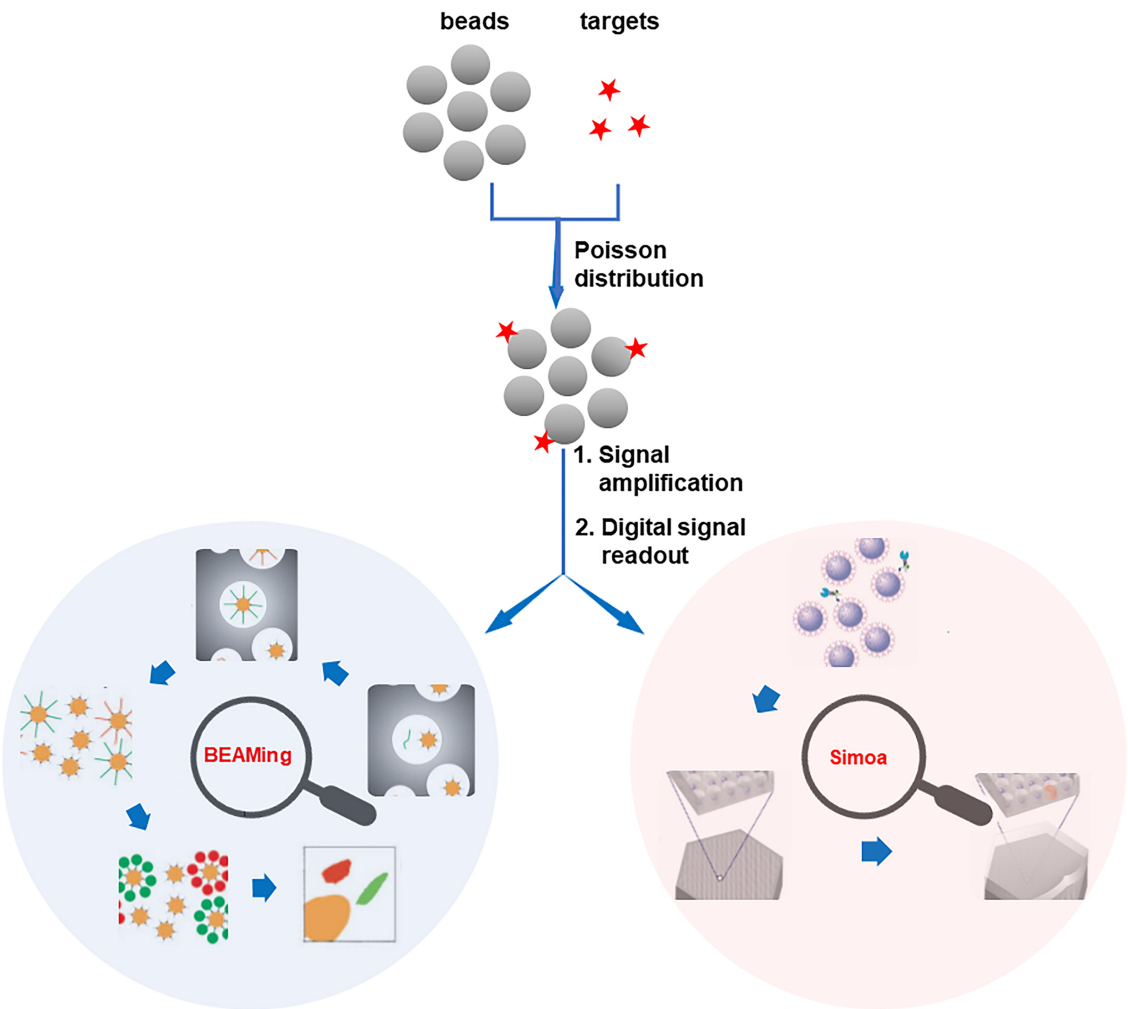

FIGURE 1 | Schematic illustration of 2-well-recognized digital bead counting bioassay technologies. Reproduced with permission from Dressman et al. (2003). Copyright 2003, National Academy of Sciences (BEAMing). Reproduced with permission from Rissin et al. (2010). Copyright 2010, Nature Publishing Group (Simoa).

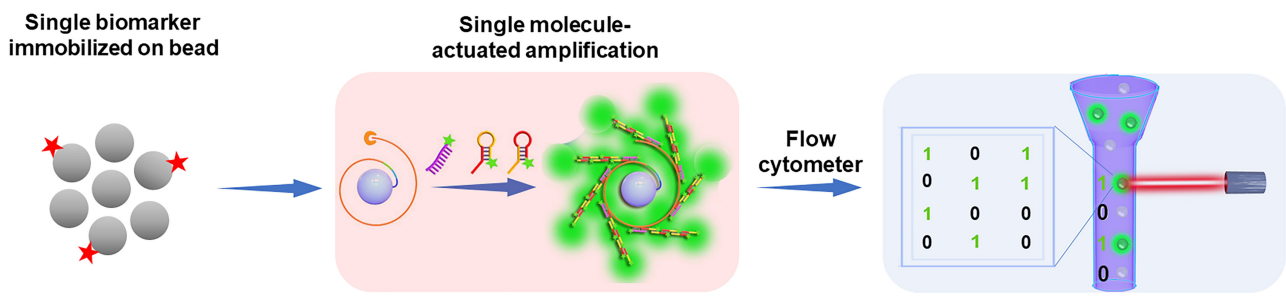

FIGURE 2 | Perspective on the digital counting platform: the integration of single molecule-initiated signal amplification strategies and conventional instruments (e.g., flow cytometer) may lead the future trend of digital assay technologies. Reproduced with permission from Fan et al. (2020). Copyright 2020, The Royal Society of Chemistry.

of bead-based approaches and the superior of digital counting assays, our group has developed a new digital platform based on the single molecule-initiated signal amplification that can illuminate a single bead for the ultrasensitive detection of biomolecules (dFlowSeim, Fan et al., 2020). In this scheme (**Figure 2**), according to the principle of the digital assay, one or none target molecule is immobilized on each bead (∼2.8 μm paramagnetic beads), and then an on-bead single molecule-actuated nucleic acid amplification is rationally designed to make sure that sufficient numbers of fluorescent molecules are gathered on the single bead to make it bright enough for FCM or fluorescence microscope sensing. As a result, the beads carrying one target will be identified as positive ones while the beads without capturing a target are identified as negative. Then the number of positive and negative beads can be facilely counted by the versatile FCM or fluorescence microscope to achieve the digital analysis of target biomolecules. The digital platform based on the single molecule-initiated signal amplification-illuminated beads has wide applicability. In the first place, FCM and fluorescence microscope are widely equipped and easily accessible in hospitals and ordinary biolabs. Then, this bead-based digital platform is emulsion-free, so unlike the BEAMing system, the digital analysis of target biomolecules can be achieved without the complicated emulsion-generation and emulsion-broken procedures. Additionally, it is a promising approach to achieve multiplexed biomolecule detection by encoding each kind of target molecules in a digital manner because the FCM is able to clearly discriminate the beads of varied sizes. As to the proposed digital platform, the efficiency of single molecule-initiated signal amplification is the key point for the enrichment of sufficient fluorescent molecules to illuminate the single bead. Therefore, it is predicted that with the development of high-efficient on-bead signal amplification strategies, the sensitivity, applicability, and flexibility of the bead-based digital platform will be significantly improved.

CONCLUSION

In this mini-review, a series of bead counting strategies, including statistical counting and digital counting for the analysis of disease-related biomolecules have been summarized. The design principles and advantages of the most popular bead counting-based assays have been described and discussed in detail. Finally, we point out that the digital assay will lead the future trend of the bead counting-based bioassays and the integration of routine instruments and emerging on-bead signal amplification technologies will broaden the way of digital assays.

AUTHOR CONTRIBUTIONS

WF and DL wrote and revised the manuscript. WR supervised and revised the manuscript. WR and CL were in charge of the whole manuscript. CL put forward the central idea of the manuscript and gives final modification. All authors contributed to the article and approved the submitted version.

FUNDING

This work was supported by the National Natural Science Foundation of China (21622507, 21904083) and the Fundamental Research Funds for the Central Universities (GK202003038, 2019TS030, GK201901003).

REFERENCES

Adan, A., Alizada, G., Kiraz,1, Y., Baran, Y., and Nalbant, A. (2017). Flow cytometry: basic principles and applications. *Crit. Rev. Biotechnol.* 37, 163–176. doi: 10.3109/07388551.2015.1128876

Chen, J., Xu, X., Huang, Z., Luo, Y., Tang, L., and Jiang, J.-H. (2018). BEAMing LAMP: single-molecule capture and on-bead isothermal amplification for digital detection of hepatitis C virus in plasma. *Chem. Commun.* 54, 291–294. doi: 10.1039/C7CC08403J

Chou, J., Wong, J., Christodoulides, N., Floriano, P. N., Sanchez, X., and McDevitt, J. (2012). Porous bead-based diagnostic platforms: bridging the gaps in healthcare. *Sensors* 12, 15467–15499. doi: 10.3390/s121115467

Cohen, L., Cui, N., Cai, Y., Garden, P. M., Li, X., Weitz, D. A., et al. (2020). Single molecule protein detection with attomolar sensitivity using droplet digital enzyme-linked immunosorbent assay. *ACS Nano* 14, 9491–9501. doi: 10.1021/acsnano.0c02378

Cohen, L., and Walt, D. R. (2017). Single-molecule arrays for protein and nucleic acid analysis. *Rev. Anal. Chem.* 10, 345–363. doi: 10.1146/annurev-anchem-061516-045340

Diehl, F., Li, M., He, Y., Kinzler, K. W., Vogelstein, B., and Dressman, D. (2006). BEAMing: single-molecule PCR on microparticles in water-in-oil emulsions. *Nat. Methods* 3, 551–559. doi: 10.1038/nmeth898

Dirks, R. M., and Pierce, N. A. (2004). Triggered amplification by hybridization chain reaction. *Proc. Natl. Acad. Sci. U. S. A.* 101, 15275–15278. doi: 10.1073/pnas.0407024101

Dressman, D., Yan, H., Traverso, G., Kinzler, K. W., and Vogelstein, B. (2003). Transforming single DNA molecules into fluorescent magnetic particles for detection and enumeration of genetic variations. *Proc. Natl. Acad. Sci. U. S.A.* 100, 8817–8822. doi: 10.1073/pnas.1133470100

Dunbar, S. A. (2006). Applications of LuminexR xMAPi technology for rapid, high-throughput multiplexed nucleic acid detection. *Clin. Chim. Acta* 363, 71–82. doi: 10.1016/j.cccn.2005.06.023

Fan, W., Qi, Y., Lu, X., Ren, W., Liu, C., and Li, Z. (2020). An emulsion-free digital flow cytometric platform for the precise quantification of microRNA based on single molecule extension-illuminated microbeads (dFlowSeim). *Chem. Commun.* 56, 7179–7182. doi: 10.1039/D0CC03059G

Fan, W., Qi, Y., Qiu, L., He, P., Liu, C., and Li, Z. (2018). Click chemical ligation-initiated on-bead DNA polymerization for the sensitive flow cytometric detection of 3′-terminal 2′-O-methylated plant MicroRNA. *Anal. Chem.* 90, 5390–5397. doi: 10.1021/acs.analchem.8b00589

Gooding, J. J., and Gaus, K. (2016). Single-molecule sensors: challenges and opportunities for quantitative analysis. *Angew. Chem. Int. Ed.* 55, 11354–11366. doi: 10.1002/anie.201600495

Gorris, H. H., Blicharz, T. M., and Walt, D. R. (2007). Optical-fiber bundles. *FEBS J.* 274, 5462–5470. doi: 10.1111/j.1742-4658.2007.06078.x

Han, S. W., Jang, E., and Koh, W.-G. (2015). Microfluidic-based multiplex immunoassay system integrated with an array of QD-encoded microbeads. *Sens. Actuat. B Chem.* 209, 242–251. doi: 10.1016/j.snb.2014.11.115

Hindson, B. J., Ness, K. D., Masquelier, D. A., Belgrader, P., Heredia, N. J., Makarewicz, A. J., et al. (2011). High-throughput droplet digital PCR system

for absolute quantitation of DNA copy number. *Anal. Chem.* 83, 8604–8610. doi: 10.1021/ac202028g

Jung, C., Allen, P. D., and Ellington, A. D. (2016). A stochastic DNA walker that traverses a microparticle surface. *Nat. Nanotechnol.* 11, 157–163. doi: 10.1038/nnano.2015.246

Leng, Y., Sun, K., Chen, X., and Li, W. (2015). Suspension arrays based on nanoparticle-encoded microspheres for high-throughput multiplexed detection. *Chem. Soc. Rev.* 44, 5552–5595. doi: 10.1039/C4CS00382A

Li, B., Ellington, A. D., and Chen, X. (2011). Rational, modular adaptation of enzyme-free DNA circuits to multiple detection methods. *Nucleic Acids Res.* 39:e110. doi: 10.1093/nar/gkr504

Liu, Z., Li, W., Nie, Z., Peng, F., Huang, Y., and Yao, S. (2014). Randomly arrayed G-quadruplexes for label-free and real-time assay of enzyme activity. *Chem. Commun.* 50, 6875–6878. doi: 10.1039/c4cc03103b

Ma, F., Li, Y., Tang, B., and Zhang, C. (2016). Fluorescent biosensors based on single-molecule counting. *Acc. Chem. Res.* 49, 1722–1730. doi: 10.1021/acs.accounts.6b00237

Ma, Y., Wang, X., Liu, H., Wei, L., and Xiao, L. (2019). Recent advances in optical microscopic methods for single-particle tracking in biological samples. *Anal. Bioanal. Chem.* 411, 4445–4463. doi: 10.1007/s00216-019-01638-z

Nolan, J. P., Yang, L., and van der Heyde, H. C. (2006). Reagents and instruments for multiplexed analysis using microparticles. *Curr. Protoc. Cytom.* 13, 13.8.1–13.8.10. doi: 10.1002/0471142956.cy1308s37

Parsa, S. F., Vafajoo, A., Rostami, A., Salarian, R., Rabiee, M., Rabiee, N., et al. (2018). Early diagnosis of disease using microbead array technology: a review. *Anal. Chim. Acta* 1032, 1–17. doi: 10.1016/j.aca.2018.05.011

Pinheiro, L. B., Coleman, V. A., Hindson, C. M., Herrmann, J., Hindson, B. J., Bhat, S., et al. (2012). Evaluation of a droplet digital polymerase chain reaction format for DNA copy number quantification. *Anal. Chem.* 84, 1003–1011. doi: 10.1021/ac202578x

Qi, Y., Lu, X., Feng, Q., Fan, W., Liu, C., and Li, Z. (2018). An enzyme-free MicroRNA assay based on fluorescence counting of click chemical ligation-illuminated magnetic nanoparticles with total internal reflection fluorescence microscopy. *ACS Sens.* 3, 2667–2674. doi: 10.1021/acssensors.8b01169

Ren, W., Liu, H., Yang, W., Fan, Y., Yang, L., Wang, Y., et al. (2013). A cytometric bead assay for sensitive DNA detection based on enzyme-free signal amplification of hybridization chain reaction. *Biosens. Bioelectron.* 49, 380–386. doi: 10.1016/j.bios.2013.05.055

Rissin, D. M., Kan, C. W., Campbell, T. G., Howes, S. C., Fournier, D. R., Song, L., et al. (2010). Single-molecule enzyme-linked immunosorbent assay detects serum proteins at subfemtomolar concentrations. *Nat. Nanotechnol.* 28, 595–599. doi: 10.1038/nbt.1641

Rödiger, S., Liebsch, C., Schmidt, C., Lehmann, W., Resch-Genger, U., Schedler, U., et al. (2014). Nucleic acid detection based on the use of microbeads: a review. *Microchim. Acta* 181, 1151–1168. doi: 10.1007/s00604-014-1243-4

Song, L., Shan, D., Zhao, M., Pink, B. A., Minnehan, K. A., York, L., et al. (2013). Direct detection of bacterial genomic DNA at sub-femtomolar concentrations using single molecule arrays. *Anal. Chem.* 85, 1932–1939. doi: 10.1021/ac303426b

Sukhanova, A., and Nabiev, I. (2008). Fluorescent nanocrystal-encoded microbeads for multiplexed cancer imaging and diagnosis. *Crit. Rev. Oncol. Hematol.* 68, 39–59. doi: 10.1016/j.critrevonc.2008.05.006

Vafajoo, A., Rostami, A., Parsa, S. F., Tahriri, M., Salarian, R., Rabiee, N., et al. (2018). Multiplexed microarrays based on optically encoded microbeads. *Biomed. Microdevices* 20:66. doi: 10.1007/s10544-018-0314-4

Walt, D. R. (2010). Fibre optic microarrays. *Chem. Soc. Rev.* 39, 38–50. doi: 10.1039/B809339N

Walt, D. R. (2013). Optical methods for single molecule detection and analysis. *Anal. Chem.* 85, 1258–1263. doi: 10.1021/ac3027178

Wang, L., Luo, M.-L., Zhang, Q., Tang, B., and Zhang, C.-Y. (2017). Single quantum dot-based nanosensor for rapid and sensitive detection of terminal deoxynucleotidyl transferase. *Chem. Commun.* 53, 11016–11019. doi: 10.1039/C7CC05485H

Wilkerson, M. J. (2012). Principles and applications of flow cytometry and cell sorting in companion animal medicine. *Vet. Clin. Small Anim.* 42, 53–71. doi: 10.1016/j.cvsm.2011.09.012

Wilson, R., Cossins, A. R., and Spiller, D. G. (2006). Encoded microcarriers for high-throughput multiplexed detection. *Angew. Chem. Int. Ed.* 45, 6104–6117.doi: 10.1002/anie.200600288

Wu, C., Garden, P. M., and Walt, D. R. (2020). Ultrasensitive detection of attomolar protein concentrations by dropcast single molecule assays. *J. Am. Chem. Soc.* 142, 12314–12323. doi: 10.1021/jacs.0c04331

Yin, P., Choi, H. M. P., Calvert, C. R., and Pierce, N. A. (2008). Programming biomolecular self-assembly pathways. *Nature* 451, 318–322. doi: 10.1038/nature06451

Zhang, Y., Liu, C., Sun, S., Tang, Y., and Li, Z. (2015). Phosphorylation-induced hybridization chain reaction on beads: an ultrasensitive flow cytometric assay for the detection of T4 polynucleotide kinase activity. *Chem. Commun.* 51, 5832–5835. doi: 10.1039/C5CC00572H

Zhang, Y., and Noji, H. (2017). Digital bioassays: theory, applications, and perspectives. *Anal. Chem.* 89, 92–101. doi: 10.1021/acs.analchem.6b04290

Zhu, L., Cheng, D., Lu, X., Qi, Y., He, P., Liu, C., et al. (2018). An ultrasensitive flow cytometric immunoassay based on bead surface-initiated template-free DNA extension. *Chem. Sci.* 9, 6605–6613. doi: 10.1039/C8SC02752H

Zhu, Q., and Trau, D. (2015). Gel pad array chip for high throughput and multi-analyte microbead-based immunoassays. *Biosens. Bioelectron.* 66, 370–378. doi: 10.1016/j.bios.2014.10.083

Conflict of Interest: The authors declare that the research was conducted in the absence of any commercial or financial relationships that could be construed as a potential conflict of interest.

Copyright © 2020 Fan, Liu, Ren and Liu. This is an open-access article distributed under the terms of the Creative Commons Attribution License (CC BY). The use, distribution or reproduction in other forums is permitted, provided the original author(s) and the copyright owner(s) are credited and that the original publication in this journal is cited, in accordance with accepted academic practice. No use, distribution or reproduction is permitted which does not comply with these terms.

frontiers in Chemistry

REVIEW
published: 11 January 2021
doi: 10.3389/fchem.2020.591311

Recent Progress in Quantitatively Monitoring Vesicular Neurotransmitter Release and Storage With Micro/Nanoelectrodes

Yuying Liu†, Jinchang Du†, Mengying Wang, Jing Zhang, Chunlan Liu and Xianchan Li**

Center for Imaging and Systems Biology, College of Life and Environmental Sciences, Minzu University of China, Beijing, China

Exocytosis is one of the essential steps for chemical signal transmission between neurons. In this process, vesicles dock and fuse with the plasma membrane and release the stored neurotransmitters through fusion pores into the extracellular space, and all of these steps are governed with various molecules, such as proteins, ions, and even lipids. Quantitatively monitoring vesicular neurotransmitter release in exocytosis and initial neurotransmitter storage in individual vesicles is significant for the study of chemical signal transmission of the central nervous system (CNS) and neurological diseases. Electrochemistry with micro/nanoelectrodes exhibits great spatial–temporal resolution and high sensitivity. It can be used to examine the exocytotic kinetics from the aspect of neurotransmitters and quantify the neurotransmitter storage in individual vesicles. In this review, we first introduce the recent advances of single-cell amperometry (SCA) and the nanoscale interface between two immiscible electrolyte solutions (nanoITIES), which can monitor the quantity and release the kinetics of electrochemically and non-electrochemically active neurotransmitters, respectively. Then, the development and application of the vesicle impact electrochemical cytometry (VIEC) and intracellular vesicle impact electrochemical cytometry (IVIEC) and their combination with other advanced techniques can further explain the mechanism of neurotransmitter storage in vesicles before exocytosis. It has been proved that these electrochemical techniques have great potential in the field of neuroscience.

Keywords: vesicle impact electrochemical cytometry (VIEC), amperometry, electrodes, neurotransmitter, exocytosis, vesicle

OPEN ACCESS

Edited by:
Chun Xu,
The University of Queensland, Australia

Reviewed by:
Andrew Ewing,
University of Gothenburg, Sweden
Ricardo Borges,
University of La Laguna, Spain

****Correspondence:***
Xianchan Li
xianchan.li@muc.edu.cn
Chunlan Liu
liuchunlan@muc.edu.cn

† These authors have contributed equally to this work

Specialty section:
This article was submitted to Electrochemistry, a section of the journal Frontiers in Chemistry

Received: *06 August 2020*
Accepted: *20 November 2020*
Published: *11 January 2021*

Citation:
Liu Y, Du J, Wang M, Zhang J, Liu C and Li X (2021) Recent Progress in Quantitatively Monitoring Vesicular Neurotransmitter Release and Storage With Micro/Nanoelectrodes. Front. Chem. 8:591311. doi: 10.3389/fchem.2020.591311

INTRODUCTION

The neuron is an important structural and functional unit of the central nervous system (CNS), which controls higher mental functions. Exocytosis is a fundamental process of chemical signal transmission between neurons and the key of intercellular communication (Meldolesi and Ceccarelli, 1981). Upon stimulation at the presynaptic membrane, depolarization of the cell membrane induces the Ca^{2+} channel to open and the Ca^{2+} influx triggers the exocytosis. The vesicles then fuse with the plasma membrane and release the loaded neurotransmitters, such as catecholamines, acetylcholine (ACh), and glutamate, into the synaptic space. When released

neurotransmitters bind to the specific receptors on the postsynaptic membrane, chemical signal transduction is completed. Hence, the vesicle is an essential cell organelle responsible for neuronal chemical communication. Understanding neurotransmitter storage in vesicles and the dynamic process of its exocytotic release from vesicles is of great significance in neuroscience.

Various analytical techniques, including fluorescence, electrochemistry, and mass spectrometry imaging (MSI), have been used to study the mechanism of exocytosis. Taking advantage of its great spatial resolution, fluorescence, especially total internal reflection fluorescence microscopy (TIRFM), has been successfully used to study the distribution of vesicles in a single cell and the mobility of vesicles during exocytosis (Yuan et al., 2015; Liu et al., 2017). MSI shows specific advantages in identifying the molecular information and visualizing the distribution of neurotransmitters in vesicles *in situ* (Lovric et al., 2017; Phan et al., 2017). Electrochemistry benefiting from its ultra-high temporal resolution and quantitative capability has been proven to be a powerful technique in the study of vesicle neurotransmitter release and storage.

Single-cell amperometry (SCA) is a long-standing method for studying exocytosis (Leszczyszyn et al., 1990; Wightman et al., 1991; Majdi et al., 2015; Li X. et al., 2016b,c; Ren et al., 2017). By using micro/nanoelectrodes, the electrochemically active neurotransmitters secreted from single vesicles during exocytosis, such as dopamine (DA), epinephrine, and norepinephrine, can be directly detected at a single-cell level. Through analyzing the recorded current transients caused by the oxidation of neurotransmitters under the constant potential applied on the electrode surface, one can quantify the amount of neurotransmitters released in a single exocytotic event and obtain detailed information about the exocytotic kinetics. To overcome the disadvantage of SCA that it can hardly monitor the non-electrochemically active neurotransmitters so far, nanoelectrodes equipped with the interface between two immiscible electrolyte solutions (nanoITIES) have been developed to monitor the concentration and kinetics of cholinergic transmitters released from single neurons (Shen et al., 2018; Welle et al., 2018).

With the aim to quantify the ratio of neurotransmitter release and infer whether the contents of vesicles are completely released during exocytosis, it is necessary to examine the storage of neurotransmitters in individual vesicles. Ewing's group developed vesicle impact electrochemical cytometry (VIEC) and intracellular vesicle impact electrochemical cytometry (IVIEC) which can detect the neurotransmitter content of isolated vesicles and vesicles in living cells, respectively. In VIEC, the microelectrode was placed directly into the vesicle suspension prepared from cells, and vesicles would be adsorbed on the electrode surface. Under a constant potential, the vesicles on the surface of the electrode rupture by electroporation and then their content are expelled and thus quantified on the electrode. The principle of IVIEC is similar to that of VIEC with its own advantage of monitoring vesicular content in living cells. The combination of SCA, VIEC/IVIEC, and other advanced analytical techniques provides efficient methodologies for studying exocytosis, vesicle properties, neuro-pharmacology, and neuro-toxicology.

This review aims to report new developed approaches, including SCA, ITIES, VIEC, and IVIEC, and their advanced progress in quantitatively monitoring vesicular neurotransmitter release in exocytosis and initial neurotransmitter storage in individual vesicles with electrochemistry. We have made an attempt to be comprehensive, but this review focuses on the last 5 years.

SINGLE-CELL AMPEROMETRY FOR MONITORING NEUROTRANSMITTER RELEASE DURING EXOCYTOSIS

Single-cell amperometry (SCA) originated from the pioneering studies by Wightman's group (Wightman et al., 1991). In this approach, a disk carbon fiber microelectrode is placed in proximity to the nerve cells to form a semi-synapse. Once stimulated, neurotransmitters released from cells are oxidized at the electrode thus producing a current transient. The dynamic information related to the fusion pore and release kinetics can be obtained by analyzing the current transients. The innovative development of SCA has initiated a new era in the neuroscience benefiting from its ultra-high temporal resolution (Majdi et al., 2015; Raghupathi et al., 2016; Moreira et al., 2017; Gu et al., 2020; He and Ewing, 2020). It has not only been widely used to monitor the exocytotic process of nerve cells but also been used to study the effects of various drugs on the exocytosis process (Machado et al., 2002; Manning et al., 2012; Trouillon and Ewing, 2013, 2014; Taleat et al., 2019; Ren et al., 2020).

Catecholamines

For the last three decades, improving the spatial resolution and readout speed of SCA are two of the most important areas for its application in neuroscience studies. One main strategy for this purpose is microelectrode arrays (MEAs), which decreases the spatial resolution down to $\sim$1 μm along with multiple readouts at different sites simultaneously on a single cell. Usually, cells are randomly attached on MEAs fabricated with lithography, leading to high chance that cells are not placed at the ideal site (Picollo et al., 2016; Huang et al., 2018; Tomagra et al., 2019). Recently, Wigstrom et al. developed a movable 16-platinum MEA, which is capable of being placed in close proximity to the membrane of single attached chromaffin cells (Wigstrom et al., 2016). As shown in **Figure 1**, this MEA could be placed on top of a cell by accurate placement with mechanical control, thus allowing multiple recordings at different cells cultured in the same batch with the same MEAs. Moreover, if coupled with the regular bottom MEAs, this on-top MEA can greatly enlarge the cell surface area imaged with electrochemistry with a comparable spatial resolution to optical methods, but with a much higher temporal resolution.

Another approach to improve the spatial resolution of SCA is decreasing the electrode size. In the last 5 years, the development of nanoelectrodes has opened a new window for

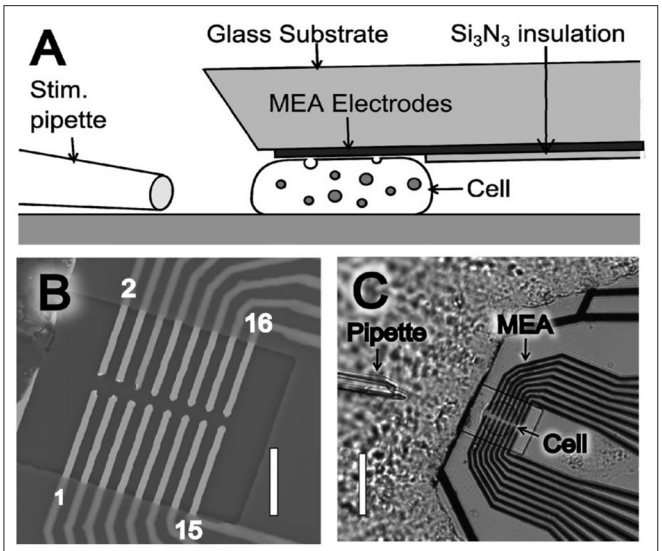

FIGURE 1 | (A) Illustration of the microelectrode array (MEA) device side view (not drawn to scale), where the thin film platinum electrodes are placed to touch and probe a cell. **(B)** Scanning electron microscope (SEM) image of a MEA showing the 16 exposed microelectrodes within an open window of the Si_3N_3 insulation layer. MEA electrodes are indicated by odd numbering (1–15) in the lower electrode row and even numbering (2–16) in the upper electrode row. Scale bar is 10 μm. **(C)** Light microscopy image of a MEA probe placed on top of a chromaffin. Scale bar is 30 μm. Reprinted from Wigstrom et al. (2016), with permission from American Chemical Society.

SCA to monitor the catecholamine release during exocytosis with a higher spatial resolution. For instance, a new kind of Au disk nanoelectrode with a radius down to 3 nm was developed and used for monitoring DA release from single rat pheochromocytoma (PC12) cells by using SCA (Liu et al., 2015). The results showed that the electrode could record eight current responses corresponding to DA release from eight vesicles in the active region, which proved its ability to identify characteristics of different release sites in the same region. Moreover, this nanoelectrode could define different release sites in the same active zone on a PC12 cell owing to its extremely high spatial resolution. The preparation method for this nanoelectrode is relatively practical and can be extended to other materials, leading to great potential for single-cell research.

One breakthrough of the application of SCA in neuroscience in the last 5 years is the real-time recording of catecholamine release from single exocytosis events *in vivo*. Ewing's group developed a novel method to record the neurotransmitter release from exocytosis at single varicosities in the *Drosophila* larval system with SCA (**Figure 2**) (Majdi et al., 2015). When they placed a regular carbon fiber microelectrode in close proximity to Type II varicosities which were stimulated with blue light, a train of current transients representing the oxidation of octopamine released were recorded at a potential of + 900 mV (vs. Ag/AgCl). Once analyzing each current transient in detail, various shapes of exocytotic events, including simple and complicated ones, reveal that partial release is prevalent in this condition.

In another elegant study, a brand new conical carbon fiber nanoelectrode (CFNE) fabricated by flame-etching the cylindrical carbon fiber microelectrode was placed into a single trained synapse formed between cultured superior cervical ganglion (SCG) and sympathetic neurons to monitor catecholamine release during exocytosis, as displayed in **Figure 3** (Li et al., 2014). When high K^+ was applied near the synapse, typical current transients were recorded in ca. 48% of cases. Approximately 42% of spikes exhibited a single rising phase followed by a single falling one (simple events), while 58% of events consisted in sequences of multiple sub-spikes (complexed events) with overall longer durations and more released norepinephrine than those of single events, respectively.

To elucidate the nature of the vesicular exocytosis in synapse, Li et al. reconstructed *in vivo*-like oriented neuronal networks in microfluidic channels between SCG neurons and their effector smooth muscle cells (SMC), which were placed in two separate microfluidic chambers initially (Li Y. et al., 2015). In consistency with the result in a Petri dish, they also recorded both single and complex spikes. However, the probability of successful detection increased from 61.0% in a Petri dish to 74.6% in this microfluidic chip, suggesting that the microfluidic strategy worked more effectively to form *in-vivo*-like neuronal synapses. Furthermore, the postsynaptic potential was successfully monitored with a glass nanopipette electrode, which again indicated that SCG-SMC synapses built in a microchip functioned effectively. This unique approach offers a platform to understand the true nature of neuronal exocytosis and the effect of drugs or chemicals, for example, harpagide, on it (Tang et al., 2020).

Dual Probes for DA

Fluorescence imaging, especially total internal reflection fluorescence microscopy (TIRFM), has aroused great interest in the neurotransmission study, such as exocytosis, benefiting from its great sensitivity for quantification and excellent spatial resolution capable of revealing the distribution of secretory vesicles and tracking their motility during exocytosis within a single cell (Park et al., 2012; Wilhelm et al., 2014; Kruss et al., 2017). However, its temporal resolution is not enough to determine the kinetic parameters of exocytotic events which could be obtained with SCA (Liu et al., 2017). To maximize the complementary advantages of TIRFM and SCA, a fluorescent false neurotransmitter 102 (FFN102) with both pH-dependent fluorescence and electroactivity was synthesized and used as a dual functional probe to track vesicular exocytosis with high spatial and temporal resolution using a coupled technique (TIRFM and SCA) (Liu et al., 2017). N13 cells, a stable clone of BON cells, were preincubated with FFN102 and then placed on a microdevice containing eight independent indium tin oxide (ITO) electrodes, one of which was set at +900 mV (vs. Ag/AgCl). Stimulation with 10 μM ionomycin, a calcium ionophore, resulted in extinctions of fluorescent vesicles in an individual cell with distinct spatial resolution showing the location of the releasing site and the movement of vesicles along the exocytotic period in TIRFM measurement. An independent SCA experiment recorded a series of current transients, representing the oxidation of FFN102 released on the

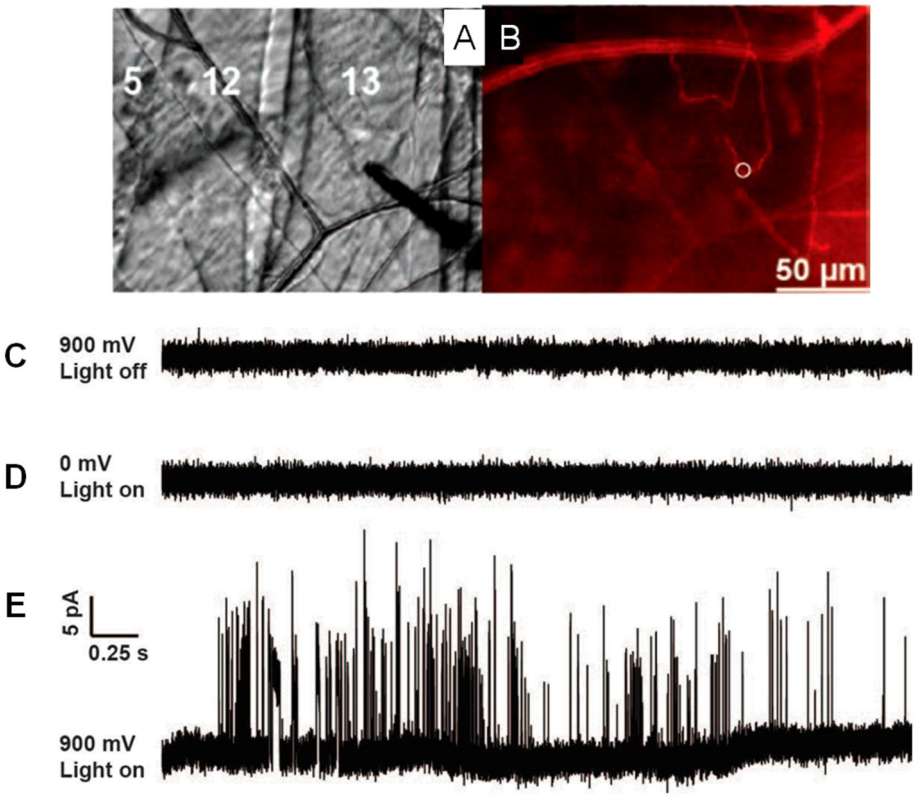

FIGURE 2 | (A) Microelectrode placement on the Type II varicosities in muscle 13 in *Drosophila* larvae. **(B)** Same view as 1C but with fluorescence, *m*Cherry-labeled octopaminergic terminals (Type II varicosities) presented as a red line and the white ring shows the placement of the microelectrode. **(C)** A potential of 900 mV (vs Ag/AgCl reference electrode) was applied, with no light stimulation. **(D)** A potential of 0 mV was applied, with blue light stimulation. **(E)** A 900-mV potential, stimulated with blue light. Same scale for all traces. Reprinted from Majdi et al. (2015), with permission from Wiley Online Library.

ITO electrode, at a single N13 cell after simulated with 10 µM ionomycin. Subsequently, TIRFM/SCA-coupled detection was monitored at the same cell successfully. As a typical example, **Figure 4** depicted the correlation of four fluorescence images recorded with a time interval of 25 ms and amperometric signal for a single vesicle which released the neurotransmitter at the active zone. With this well-defined correlation, one can localize the release vesicle in a living cell precisely with TIRFM while quantitating the release kinetics of the neurotransmitter from this vesicle with SCA with excellent temporal resolution.

Ascorbate

Ascorbate, the salt form of vitamin C in physiological conditions, acts as a neuromodulator of glutamatergic, cholinergic, dopaminergic, and GABAergic transmission (Xiao et al., 2018, 2019; Jin et al., 2020; Yu et al., 2020). It has been proposed that one pathway of cellular efflux of ascorbate is through co-secretion with catecholamine during exocytosis in chromaffin cells (Daniels et al., 1982). To investigate whether and how this happens, Wang et al. developed an elegant SCA method to selectively monitor endogenous ascorbate secretion from single chromaffin cells during exocytosis (Wang et al., 2017). To overcome the interference from the dominant neurotransmitters, such as norepinephrine, epinephrine, and DA in chromaffin vesicles, the carbon fiber microelectrodes (CFMEs) were pretreated in 10 mM sodium tetraborate (pH 9.5) at +1.3 V for 20 min. Cyclic voltammetry (CV) showed that after pretreatment, the oxidation potential of ascorbate was decreased to 0.0 V (vs. Ag/AgCl), at which the interference of catecholamines could be ignorable. As shown in **Figure 5**, high K^+ elicited many amperometric spikes representing ascorbate secretion from single vesicles during exocytosis in a Ca^{2+}-dependent manner.

Glutamate

Glutamate, the most dominant excitatory neurotransmitter in mammalian CNS, plays key roles in many life functions, such as memory formation, long-term potentiation, and synaptic plasticity (Herman and Jahr, 2007; Abramov et al., 2009; Brito-Moreira et al., 2011). Since the electrochemical activity of glutamate is poor at the regular electrode material, various enzymatic biosensors have been developed to monitor the glutamate concentration and the fluctuation of glutamate in the brain (Wu et al., 2018; Ganesana et al., 2019). Usually, the specific enzyme layer immobilized on the electrode with hydrogels is relatively thick for the purpose of loading enough enzyme for the substrate catalysis, so the diffusion of substrate to the electrode is

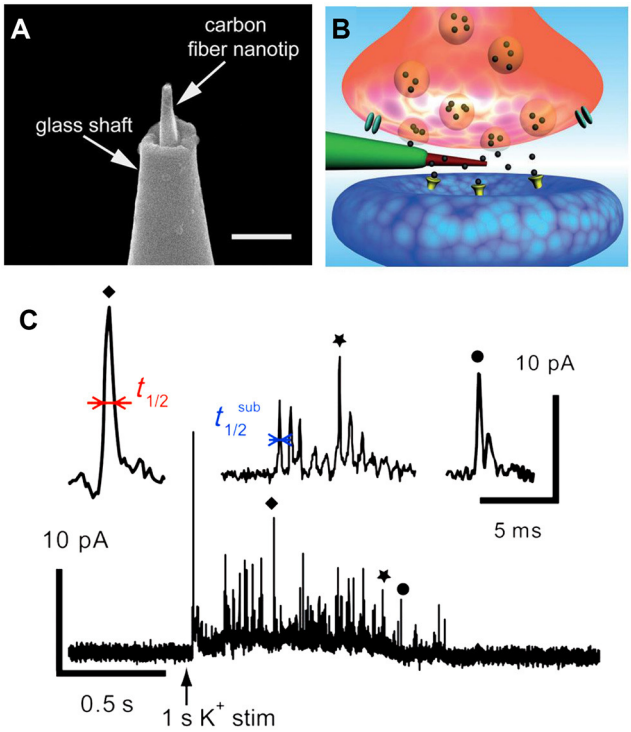

FIGURE 3 | (A) Amplified picture of the tip of the nanoelectrode; the scale bar is 1 μm. **(B)** Schematic representation of a nanosensor's tip inside an individual synapse. **(C)** High K^+-induced amperometric spike and two complex events were amplified above. Reprinted from Li et al. (2014), with permission from Wiley Online Library.

slow thus leading to slow response speed. This is the key factor that restricts enzymatic biosensors to be applied in monitoring neurotransmitter release in vesicular exocytosis that requires high temporal resolution.

To accelerate the response speed of glutamate enzymatic biosensor, Huang's group constructed a glutamate biosensor with the following brief steps: (1) platinization of CFME; (2) modification of polyetherimide (PEI) on the surface of platinized CFME; and (3) immobilization of glutamate oxidase (GluOx) through the covalent linking with poly(ethylene glycol) diglycidyl ether (PEDGE) (Qiu et al., 2018). Herein, GluOx catalyzes the oxidation of glutamate to α-ketoglutarate accompanied with the reduction of O_2 to H_2O_2 which could be monitored with platinized CFME effectively (**Figure 6A**). This assembled sensor exhibited excellent sensitivity and good selectivity, more importantly, fast response speed (response time, 70 ms) to glutamate, resulting in the capability of monitoring the dynamics of glutamate release in exocytosis. The following SCA experiments with this sensor at single hippocampal varicosity showed that many well-defined amperometric spikes were recorded specifically in the presence of GluOx on the electrode when high K^+ was applied. It was confirmed that this new glutamate sensor is efficient to measure the glutamate release during exocytosis. Using this approach, they further investigated the effect of $A\beta_{1-42}$ oligomer protein, which is proved highly related with Alzheimer's disease (AD), on the level of glutamate release in exocytosis in single hippocampal varicosity (Yang et al., 2019). The results showed that a short-duration (30 min) incubation with $A\beta_{1-42}$ increased vesicular glutamate release dramatically while a long-duration (300 min) treatment depleted vesicular glutamate release. It could provide valuable information on $A\beta_{1-42}$-induced abnormalities in neuron functions and the early pathogenesis of AD.

As another attempt, Wang et al. measured glutamate release during exocytosis through monitoring the reduction of H_2O_2 instead of its oxidation on the GluOx-modified microelectrode (**Figure 6B**) (Wang et al., 2019b). In this approach, gold nanoparticle hemispheres were deposited on CFME (33 μm in diameter) firstly to not only increase the electrode surface area but also provide a high surface curvature to keep the activity of GluOx. Then, an optimized amount of GluOx was adsorbed on the electrode by keeping the electrode in the GluOx solution for 2–3 h at room temperature, aiming to minimize the thickness of enzyme coating and improving the reaction speed of this glutamate sensor. Once the sensor was placed in the nucleus accumbens (NAc) region of the mouse brain, the authors recorded a train of amperometric spikes spontaneously (**Figure 6C**), which they ascribed to the spontaneous quantal release of vesicular glutamate in the synaptic cleft. However, more control experiments are desired for the purpose of convincing readers how the relatively huge electrode recorded single exocytotic release of a small amount of glutamate happening in the sub-micrometer synaptic cleft at an ultra-fast speed (milliseconds).

NanoITIES

The exocytotic dynamics of electrochemically active neurotransmitters and neuromodulators, such as DA, norepinephrine, epinephrine, and ascorbic acid, can be revealed by SCA, which provides a platform for studying related diseases. However, non-redox active neurotransmitters, such as acetylcholine (ACh), γ-aminobutyric acid (GABA), and glutamate, are equally important for brain functions. Elucidating the dynamic process of these neurotransmitters in exocytosis is extremely helpful for understanding the pathogenesis of related neurological diseases. While a specific enzyme nanosensor provides one strategy for monitoring non-redox active neurotransmitters, the nanoscale interface between two immiscible electrolyte solutions (nanoITIES) opens another wide window especially for the ionic neurotransmitters in physiological conditions. Technically, a glass pipette with a nanoscale pore at the tip is back-filled with selected organic reagents and then positioned into a biological environment for measurement. Quantitative current signals of neurotransmitters are obtained through recording the ionic current fluctuations caused by neurotransmitter transfer at the liquid–liquid interface (Wang et al., 2010; Amemiya et al., 2013). Hence, by carefully selecting the organic reagent, nanoITIES can specifically measure the concentration and release dynamics

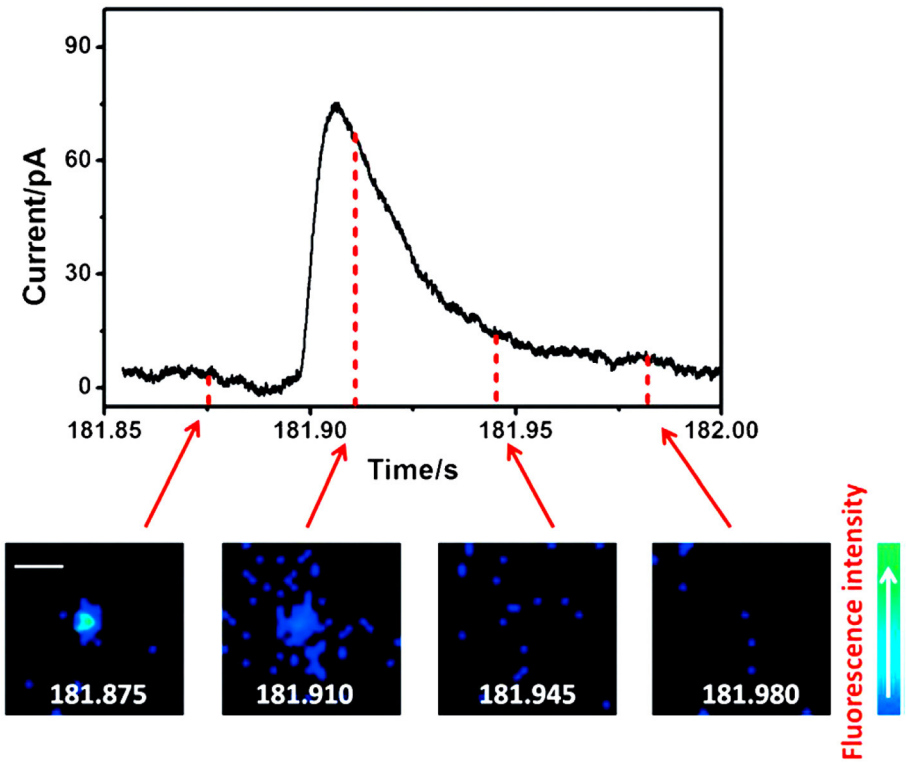

FIGURE 4 | Correlation of amperometric and fluorescence information for a single exocytotic event of fluorescent false neurotransmitter102 (FFN102)-stained BON N13 cells over an indium tin oxide (ITO) microdevice. Top: An exocytotic event appeared as the current spike in electrochemical detection. Bottom: Sequential pseudocolor total internal reflection fluorescence microscopy (TIRFM) images of a single exocytotic event viewed as a flash of fluorescence. Scale bar = 500 nm. Reprinted from Liu et al. (2017), with permission from Wiley Online Library.

of ionic neurotransmitters at the single-cell level with high spatial resolution.

The ion transfer of three functional chemicals, including ACh, serotonin (5-HT), and tryptamine, at the interface of 1,2-dichloroethane (DCE)/artificial seawater (ASW) was studied by using a nanoITIES pipette electrode with a radius of 7–35 nm (Colombo et al., 2015). The difference of the half wave transfer potentials for these three chemicals and the linear response to their concentration confirmed that the nanoITIES electrode could measure these chemicals quantitively and selectively.

GABA, an inhibitory neurotransmitter, was analyzed with nanoITIES (Iwai et al., 2018). Since GABA is electrically neutral in physiological conditions, organic acid was added to the original water/1,2-DCE interface to facilitate the production of a GABA ionic complex, which can be detected once it transfers through the nanopore of ITIES. This lays the foundation for the subsequent direct measurement of GABA at the single-cell level.

Recently, Shen's group monitored the concentration and release kinetics of ACh from an individual neuronal soma and at a real single synapse of *Aplysia nica* with a nanoITIES pipette electrode (Shen et al., 2018; Welle et al., 2018). As shown in **Figure 7**, the nanoITIES electrode can be accurately positioned near the synaptic cleft assisted by scanning electrochemical microscopy (SECM), an electrochemical technique that employs ultramicroelectrodes to record a faradaic current response while moving in proximity of a sample surface with extreme precision. The current response can reflect both the topography and the electrochemical activity of the surface/substrate (Page et al., 2017; Stephens et al., 2020) and a side optical microscope. Obvious amperometric spikes could be obtained at the nanoITIES pipette electrode for ACh release from the presynaptic membrane under the stimulation of a high concentration of K^+. They found that ACh release from the *Aplysia* neuron is Ca^{2+} dependent and its dynamic profiles are composed of singlet, doublet, and multiplet. This breakthrough for quantitative monitoring of ACh release in a real synapse opens up new opportunities to understanding neuronal communication and related diseases.

USING ELECTROCHEMICAL CYTOMETRY TO DETERMINE NEUROTRANSMITTER STORAGE OF SINGLE VESICLES

Quantitatively monitoring neurotransmitter release with high temporal resolution methods, such as SCA and ITIES, provides important information for chemical signaling between

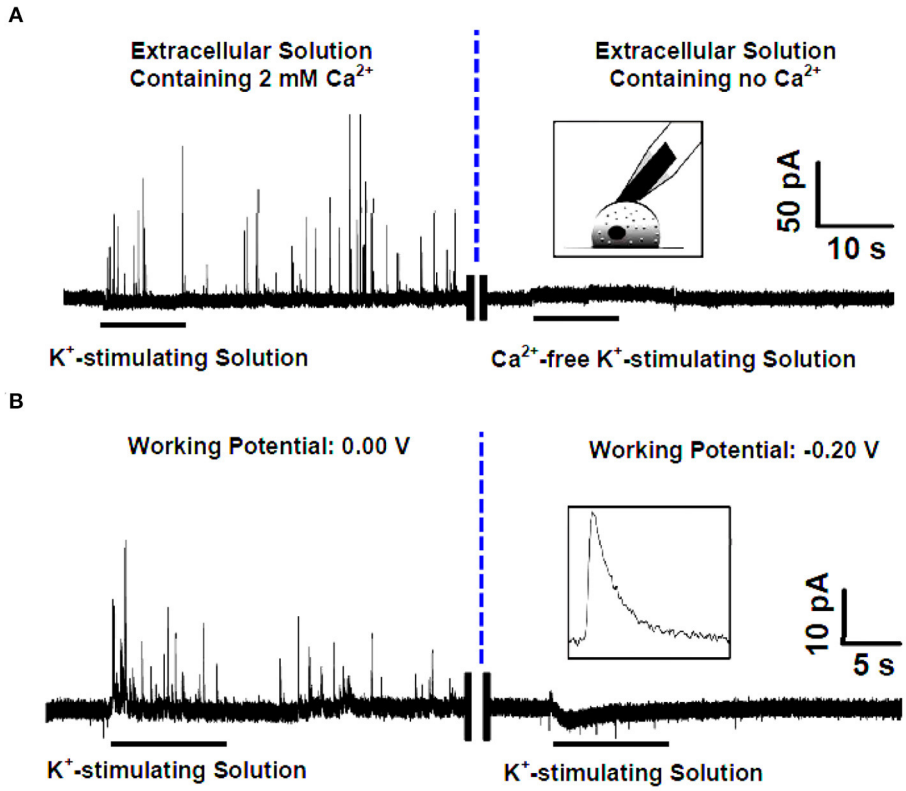

FIGURE 5 | (A) (Left) Amperometric spikes recorded with the pretreated carbon fiber microelectrode (CFE) closely attached to a single rat adrenal chromaffin cell that was cultured in the standard extracellular solution (i.e., containing 2 mM Ca^{2+}) and stimulated by K^+-stimulating solution. (Right) Current-time trace recorded with the pretreated CFE closely attached to a single rat adrenal chromaffin cell that was cultured in the Ca^{2+}-free extracellular solution and stimulated by Ca^{2+}-free K^+-stimulating solution. Inset, schematic illustration of the single-cell amperometry with the pretreated CFE. **(B)** High K^+ evoked amperometric spikes recorded with the pretreated CFE closely attached to a single rat adrenal chromaffin cell cultured in the standard extracellular solution (i.e., containing 2 mM Ca^{2+}) at different holding potentials of 0.0 V (left) and −0.20 V (right). Inset, a typical amperogram spike for ascorbate secretion. Reprinted from Wang et al. (2017), with permission from the American Chemical Society.

neurons. However, increasing evidence has indicated that neurotransmitter release during exocytosis is not the simple "all or none" (Elhamdani et al., 2001; Sombers et al., 2005; Camacho et al., 2006; Haynes et al., 2007; Omiatek et al., 2010, 2013; Dunevall et al., 2015; Calvo-Gallardo et al., 2016). For instance, Borges's group investigated catecholamine release in a single exocytotic event at single chromaffin cells with SCA and patch amperometry in which physical suction is applied at a small portion of the cell membrane to create sealing for capacitance measurements (Montesinos et al., 2008). Although not the main focus of their study, they found that the total charge released per exocytotic event stimulated with Ba^{2+} was 0.67 ± 0.08 pC measured with SCA, whereas the total charge stimulated with mechanical suction is 1.81 ± 0.09 pC measured with patch amperometry for the same cell line. To address whether and how the amount of neurotransmitter released in exocytosis is controlled, quantitation of neurotransmitter storage in single vesicles is essential. Therefore, a series of advanced electrochemical technologies, all termed as electrochemical cytometry, have been developed.

Vesicle Impact Electrochemical Cytometry (VIEC)

The first generation of electrochemical cytometry (EC) could be traced back to a decade ago. Omiatek et al. coupled capillary electrophoresis with electrochemical detection on a microfluidic device to achieve the quantitative determination of neurotransmitters stored in single mammalian vesicles (Omiatek et al., 2009, 2013). Since the complicated device limits its application, further attempts have been performed on liposomes [i.e., artificial vesicle, with the inspiration of single-entity electrochemistry to build a simpler system (Cheng and Compton, 2014; Kim et al., 2014)]. In 2015, the second generation of EC, termed as vesicle impact electrochemical cytometry (VIEC), was successfully developed (Dunevall et al., 2015). In this system, the CFME recorded bunches of oxidized current transients once it was put into a concentrated vesicle suspension isolated from adrenal chromaffin cells and a potential at + 0.7 V vs. Ag/AgCl applied (**Figure 8**). Quartz crystal microbalance experiments provided evidence for vesicle adsorption and rupture during VIEC. Through data processing, the estimated diameters of the

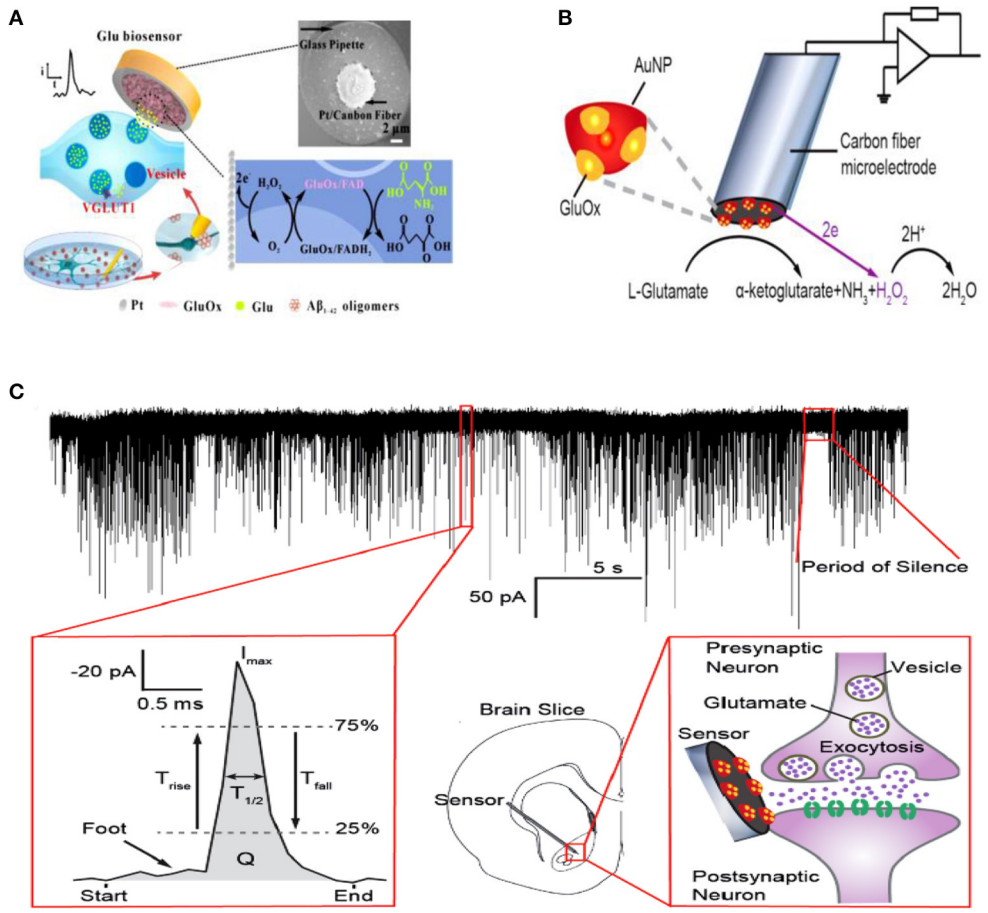

FIGURE 6 | (A) Schematic diagram showing the process of amperometric monitoring of glutamate exocytosis from single hippocampal varicosity; the top right shows the scanning electron microscope (SEM) images of a platinized carbon fiber microelectrode, and the bottom right shows the mechanism of Glu detection on the microsensor. **(B)** Schematic diagram of the amperometric glutamate sensor design consisting of a glutamate oxidase (GluOx)-coated gold nanoparticle-modified carbon fiber microelectrode. It displays the chemical enzyme catalysis reaction chain for glutamate with the subsequent detection scheme for electrochemical detection of the reporter molecule H_2O_2 produced. The red hemispheres represent gold nanoparticles, and GluOx that is immobilized at the surface is displayed in yellow (not drawn to scale). **(C)** Top: Amperometric current–time trace detecting spontaneous glutamate release during individual exocytotic events in mouse brain slice. Below: Definition of the current spike parameters used for exocytosis kinetic analysis after converting the amperometric recording to positive reduction current (left). Illustration of the placement of sensor in the nucleus accumbens of rodent brain slice for amperometric recording. Schemes are not drawn to scale (right). Reprinted from Yang et al. (2019) and Wang et al. (2019b), with permission from the American Chemical Society.

vesicles calculated with the number of molecules measured in VIEC matched very well with the direct measurement with nanosight tracking analysis. This suggested that the current transients recorded in VIEC were generated from the oxidation of catecholamine stored in single vesicles.

Further studies were performed to explore the mechanism of VIEC (Lovric et al., 2016; Li X. et al., 2017; Phan et al., 2017; Li et al., 2018). Mathematics simulation confirmed that the amount of neurotransmitters measured with VIEC was the total content in single vesicles, suggesting all the vesicular transmitters were expelled and oxidized on CFME (Li et al., 2018). Gradually increasing the applied potential on the working electrode increases the frequency of current transients gradually when other conditions were kept constant (Lovric et al., 2016). Analysis of the current transients indicates that a nanoscale pore was formed on the vesicle at the initial state (Li X. et al., 2017). Therefore, electroporation was proposed to be involved in VIEC. Moreover, the comparison of mammalian vesicles, lipidic liposomes decorated with a small amount of proteins, and pure lipidic liposomes in VIEC showed that the frequency of detected current transients was in an order $F_{mammalianvesicle} < F_{protein-decoratedliposome} < F_{pureliposome}$ (Lovric et al., 2016). Subsequent studies demonstrated that the increase of detection temperature could promote the occurrence of electroporation and increase the frequency of vesicular rupture events through increasing the diffusion rate of membrane proteins (Li X. et al., 2017). These two studies imply that vesicular membrane proteins affect the occurrence of electroporation, thus playing an important role in vesicle rupture on electrodes. Taking all together, a mechanism was proposed for quantification of

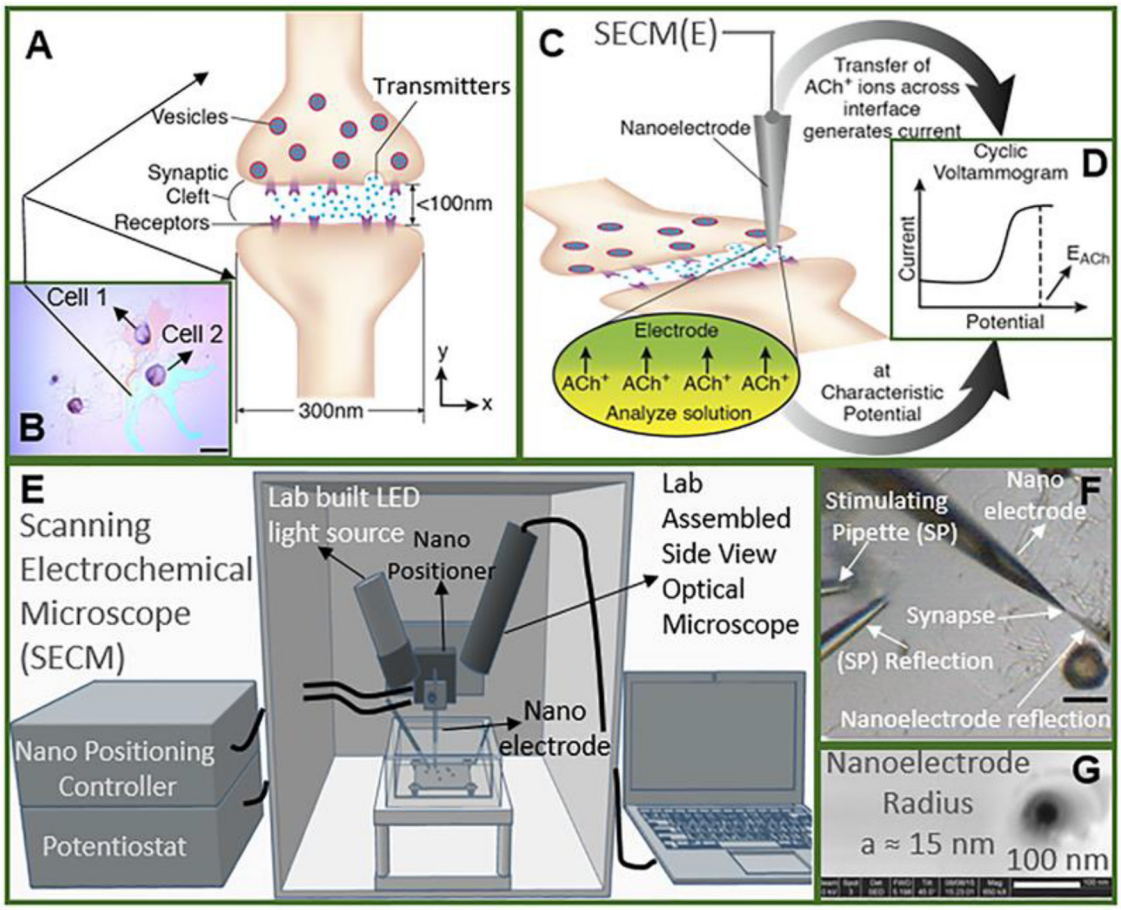

FIGURE 7 | Study of cholinergic neurotransmission at the single synaptic cleft with nanoelectrode and scanning electrochemical microscope (SECM). **(A)** Illustration of synaptic cleft dimensions. **(B)** Cultured living aplysia pedal ganglion neurons used for the experiment, where the axon from cell 1 (pink) formed a synaptic connection with the body of cell 2. Scale bar: 200 μm. **(C)** A nanoscale interface between two immiscible electrolyte solutions (nanoITIES) pipette electrode was positioned around the synaptic cleft to measure the concentration and release dynamics of acetylcholine (ACh^+) simultaneously using amperometry; the positioning of the nanoelectrode was achieved using the SECM with a spatial resolution of 5 nm. The zoom shows the nanoITIES formed at the tip of the nanoITIES pipette electrode, and ionic transmitter (ACh^+) transfers across the interface, generating a current and thus getting detected. **(D)** Cyclic voltammogram corresponding to ACh detection, where the detection potential follows the Nernstian equation, and a steady-state transfer potential, $E_{ACh} = -0.48$ V vs. $E_{1/2,\ TBA}$, selective for cholinergic neurotransmitter detection was used in amperometry to study its synaptic concentration dynamics. **(E)** A SECM and a lab-built side view optical microscope were used for the positioning of the nanoelectrode around synapses with a nm spatial resolution. The lab-built side-view optical microscope provided rough positioning before the fine positioning of 5 nm spatial resolution with SECM. After SECM positioning, the optical microscopic view of the nanoelectrode and the synapse are shown in **(F)**, where it can be seen that it is very hard to locate the synapse by visual observation alone. The combined use of the side-view optical microscope and nano-positioning platform, SECM, is critical. **(F)** A stimulating pipette was used to provide high-concentration K^+ stimulation. Reflection was used for the rough positioning of the nanoelectrode and stimulating pipette in the x, y, and z axes by an optical microscope, which was followed by the nanometer positioning of the nanoelectrode around the synapse achieved using nano-resolution SECM with details described in the supporting information. Scale bar: 150 μm. **(G)** High-resolution scanning electron microscope (SEM) picture of the nanopipette tip with the radius to be around 15 nm. Reprinted from Shen et al. (2018), with permission from the American Chemical Society.

vesicular catecholamine content with VIEC (Li X. et al., 2016a; Phan et al., 2017). As shown in **Figure 9**, vesicles were adsorbed on the working electrode firstly. Then the vesicular membrane protein in the proximity of the electrode migrates away, resulting in the gap between vesicle membrane and electrode close enough to facilitate electroporation. Through the nanosized pore formed, neurotransmitters fluxed to the electrode and were oxidized to produce a current transient on the electrode surface, making the quantification of neurotransmitter storage in single vesicles practical (Li X. et al., 2016a; Phan et al., 2017; Ranjbari et al., 2019).

In a recent report, the enzymatic glutamate sensor schemed in **Figure 6B** was applied to determine the glutamate storage in individual isolated synaptic vesicles (Wang et al., 2019a) with the same manner of VIEC. For reasons they did not state, a calibration curve obtained with large unilamellar vesicles (LUVs)

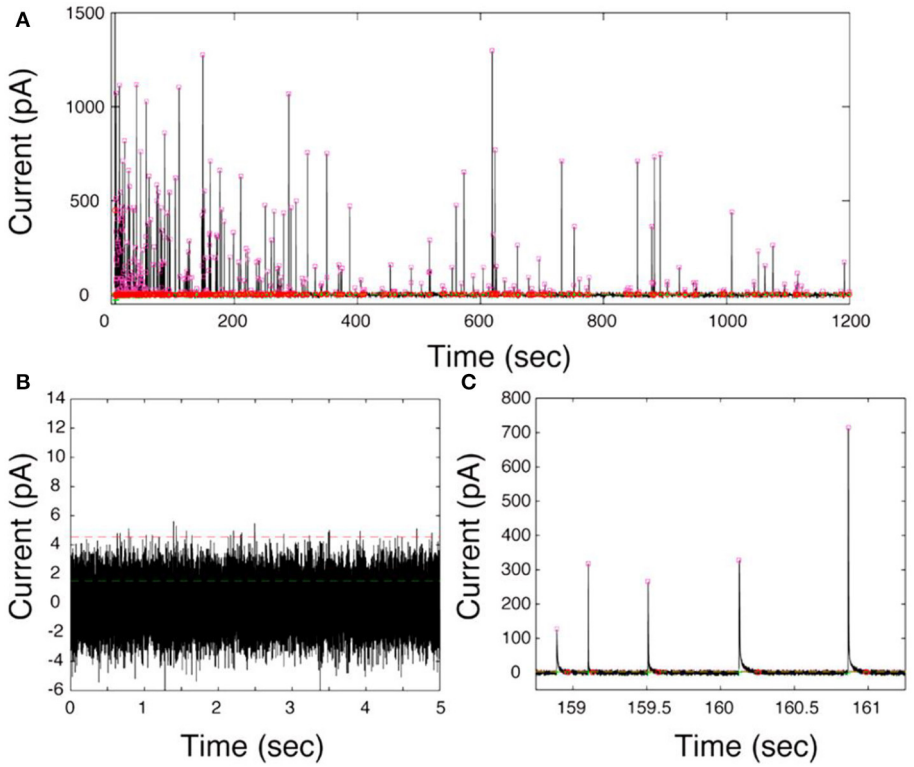

FIGURE 8 | (A) Representative current–time trace of VIEC in a suspension of chromaffin cell vesicles. **(B)** A 5-s baseline at 0 mV vs. Ag/AgCl in the presence of vesicles. **(C)** Expanded view of current transients. The pink squares represent the I_{max} of all peak candidates submitted for further analysis. The green lines represent the root mean square (RMS) and the red lines five times the RMS of the baseline noise. Reprinted from Dunevall et al. (2015), with permission from the American Chemical Society.

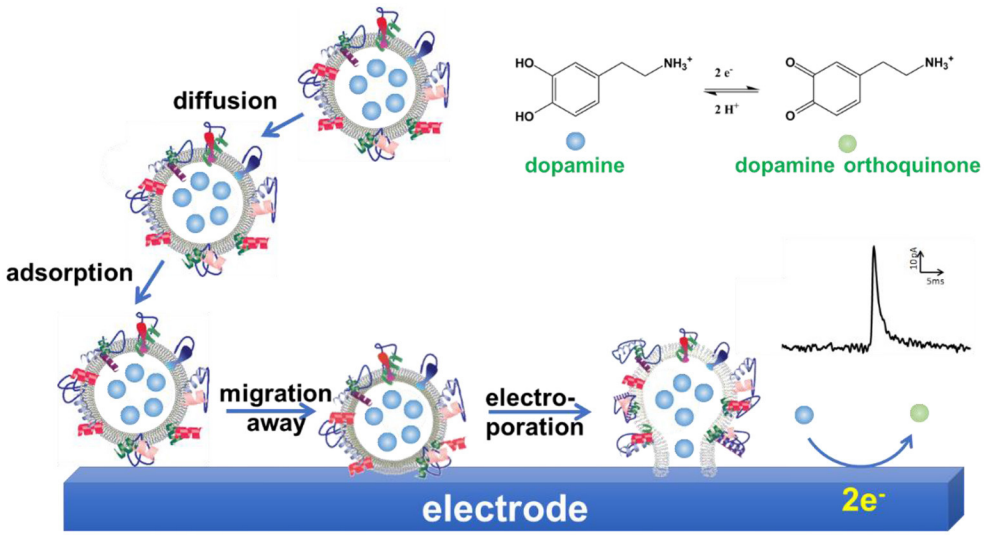

FIGURE 9 | Schematic illustration of a proposed mechanism of vesicle impact electrochemical cytometry (VIEC).

loaded with a known concentration of glutamate was used to precisely quantify the glutamate amount in individual vesicles instead of the absolute quantification with Faraday's equation. Nevertheless, each isolated synaptic vesicle from the mouse brain was found to contain 8,300 ± 600 glutamate molecules on average. This work provides a new methodology to determine

the quantity of glutamate in a single isolated synaptic vesicle, which is helpful to obtain intuitive information of glutamate in neurotransmission.

Intracellular Vesicle Impact Electrochemical Cytometry (IVIEC)

To minimize the effect of separation processes on vesicle properties, for example, the neurotransmitter leakage during sample preparation, quantification of vesicular content in the native cellular environment is preferred. To achieve this, an elegant and reliable technique, termed as intracellular vesicle impact electrochemical cytometry (IVIEC), was developed using nano-tip conical carbon fiber microelectrodes to quantify the neurotransmitter content of individual vesicles in living PC12 cells (Li X. et al., 2015, 2016a). In this approach, the nano-tip cone geometry readily facilitated the penetration through the cell membrane with little damage to cells and kept enough electrode surface area for the electrochemical reaction of the vesicular neurotransmitter. As displayed in **Figure 10**, obvious current transients were observed once the electrode was placed inside the cytoplasm of single living PC12 cells while none for the electrode kept outside of the cell. Early reports also observed similar current transients at the carbon fiber electrode when a small portion of the cell membrane was ruptured by suction in whole-cell patch amperometry, and vesicles could diffuse to the electrode, although the authors did not explore these current transients since they focused on quantifying free catecholamine in the cytosol and/or the release of catecholamine from chromaffin cells (Mosharov et al., 2003; Montesinos et al., 2008). Quantification of the single spikes with Faraday's equation revealed that the total amount of vesicular catecholamine storage measured by IVIEC was 114,500 ± 15,300 (mean ± SEM) molecules, which closely agreed with the value measured for freshly extracted vesicles in VIEC (Li et al., 2018). Furthermore, a 2-h treatment of PC12 cells with 100 μM L-3,4-dihydroxyphenylalanine (L-DOPA), a direct biochemical precursor to DA, increased the vesicular catecholamine content to 323,100 ± 29,000 (mean ± SEM) molecules as determined in IVIEC. Both results suggested that the current transients measured in IVIEC were from the oxidation of catecholamine stored in single vesicles, and the mechanism for VIEC is also applicable for IVIEC.

In addition to flame etching used for preparation of nano-tip conical carbon fiber microelectrodes in IVIEC, a wet-etching approach was used to prepare nanoscale sharp-tip nanoelectrodes for investigation of single vesicles in the intracellular environment recently (Roberts et al., 2020). Briefly, a regular cylindrical carbon fiber microelectrode was immersed in 4 M KOH solution and a potential of + 7 V applied (vs. a platinum wire) for 1–1.5 s to cleave a sharp tip. Then, an insulation layer was electropolymerized on the whole electrode except its tip (∼5 μm) which was hid in a silicone mask. Once the electrode tip penetrated through the cell membrane and gained access to the cytosol of an individual PC12 cell, a series of amperometric spikes were recorded when the potential was held at + 850 mV vs. Ag/AgCl. The researchers calculated the area of each peak and obtained an average of 140,000 ± 17,000 catecholamine molecules for 35 individual vesicles. Besides, this nanoscale electrode was further used to distinguish epinephrine-containing and norepinephrine-containing vesicles with fast-scan cyclic voltammetry.

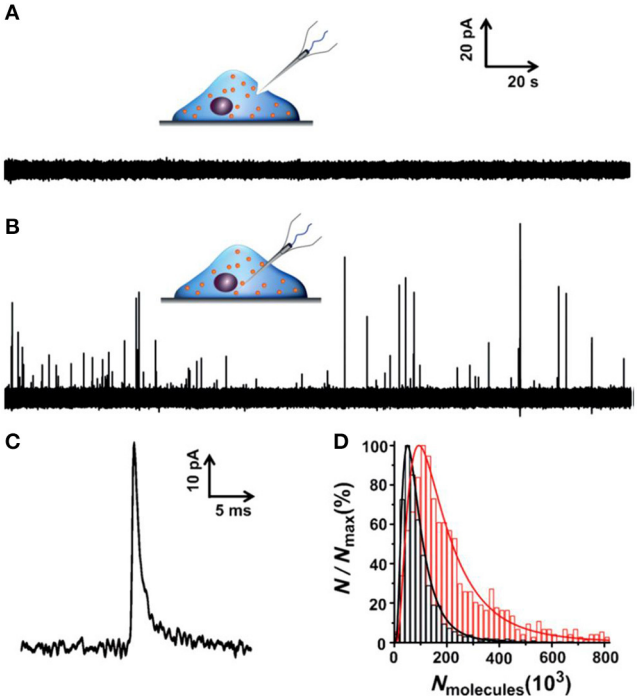

FIGURE 10 | (A,B) Amperometric traces for a nanotip conical carbon-fiber microelectrode pushed against a pheochromocytoma (PC12) cell without breaking into the cytoplasm **(A)** or placed inside a PC12 cell **(B)**. **(C)** Amplified amperometric current trace. **(D)** Normalized frequency histograms describing the distribution of the vesicular catecholamine amount as quantified from untreated PC12 cells by intracellular vesicle electrochemical cytometry (red, n = 1,017 events from 17 cells) and by K^+-stimulated exocytosis at the same electrode (black, n = 1,128 events from 17 cells). Bin size: 2×10^4 molecules. Fits were obtained from a log-normal distribution of the data. Reprinted from Li X. et al. (2015), with permission from Wiley Online Library.

Other Mimic-IVIEC Methods

A similar phenomenon was observed in other methodologies developed for monitoring intracellular reactive oxygen species (ROS) and reactive nitrogen species (RNS). While a platinized carbon nanoelectrode (i.d. 40 nm) was successfully used as SECM tip to measure the dynamic changes of ROS/RNS in the cytoplasm of a variety of human breast cells, a series of amperometric bursts, similar to amperometric events IVIEC, were observed 25 min after the MCF-10A cell was treated with diacylglycerol-lactone (DAG-lactone), a membrane-permeable analog of DAG that induces activation of some kinds of protein kinase C isoforms (Li Y. et al., 2017). Optical imaging confirmed that DAG-lactone treatment induced formation of numerous intracellular vacuoles, a nanoscale membrane compartment. The correlation of amperometric bursts and vacuole formation produced one possibility that vacuoles containing a high

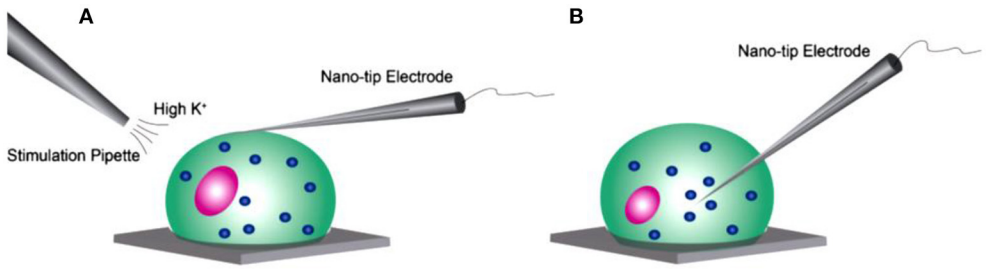

FIGURE 11 | Schematic representation of **(A)** single-cell amperometry (SCA) and **(B)** intracellular vesicle impact electrochemical cytometry (IVIEC). Reprinted from Ren et al. (2017), with permission from Wiley Online Library.

concentration of ROS/RNS burst on the electrode and the oxidation of ROS/RNS was detected as spikes, though other reasons could not be ruled out.

In another study, a new platinized nanowire SiC@C electrode (Pt-NWES) was developed to quantify ROS/RNS content in single phagolysosomes in living macrophages (Zhang et al., 2017). Similar to IVIEC, a constant potential (+ 0.85 V vs. Ag/AgCl reference) was applied on the electrode, resulting in large series of transient current spikes, each of which corresponds to the oxidation of ROS/RNS stored in single phagolysosomes on the electrode. In their subsequent report, further analysis of the single amperometric spikes showed that 75% events had a clear shoulder on the decay part. They proved that this shoulder was the oxidation of ROS/RNS newly produced inside phagolysosomes because of the stimulation by consumption of ROS/RNS on the electrode (Zhang et al., 2019). These new reports expand the application of IVIEC in cell biology.

Combining IVIEC With SCA

IVIEC can quantify the neurotransmitter storage precisely in individual vesicles in living cells while SCA is capable of quantitatively monitoring the dynamics of neurotransmitter release in exocytosis with very high temporal resolution (**Figure 11**). Combining these two elegant methods allows researchers to obtain more information on the nature of exocytosis and how related drugs affect its process (Li X. et al., 2015, 2016c; Lovric et al., 2016; Najafinobar et al., 2016; Fathali et al., 2017; Ren et al., 2017, 2019; Ye et al., 2018; Gu et al., 2019; Majdi et al., 2019; Taleat et al., 2019; Zhu et al., 2019; He and Ewing, 2020; Larsson et al., 2020).

Exocytotic Mode

The first attempt of combination of IVIEC and SCA was used to understand the exocytosis manner (Li X. et al., 2015). By comparing the catecholamine molecules released determined with SCA and those stored in single vesicles determined with IVIEC, researchers found that an average of ∼70% of vesicular neurotransmitters in storage were released during high K^+-stimulated exocytosis of PC12 cells, suggesting that partial or "subquantal" release is the dominant mode of exocytosis. Treatment of PC12 cells with L-DOPA resulted in the increase of neurotransmitter release and storage with almost equivalent levels, thus keeping the percentage released to be similar to that for control.

Recently, IVIEC was adapted to determine the neurotransmitter catecholamine in single vesicles in a living *Drosophila* larval neuromuscular neuron by inserting a sharp nanotip electrode into a varicosity with the assistance of fluorescence (Larsson et al., 2020). An average value of 441,000 octopamine molecules in storage was obtained for each vesicle. This is much higher than those released in exocytosis determined with SCA. By comparison, ∼4.5 and ∼10.7% of vesicular octopamine are released for single and complex exocytotic events, respectively. This might suggest that the presynaptic plasticity could be regulated in a huge range (Gu et al., 2019; Zhu et al., 2019).

Physical Treatment

The effect of physical treatment on chemical neurotransmission has been investigated with IVIEC and SCA. Gu et al. studied the effects of repetitive stimulation on plasticity of exocytosis and the related mechanism (Gu et al., 2019). The stimuli were performed with a 5-s delivery of 100 mM K^+ and repeated six times with a 2-min rest interval. In the aspect of exocytosis, the frequency of exocytotic events decreased gradually during short-interval repetitive stimuli, probably due to the decrease of the readily releasable pool (RRP) or fused vesicles. Further analysis of single exocytotic events showed that the molecule number of released neurotransmitters gradually increased during the repetitive stimuli, since a more stable fusion pore was formed during the later stimuli. Although vesicular neurotransmitter storage was slightly reduced after repetitive stimuli, the average release fraction/percentage of neurotransmitter was increased. This is an interesting finding which may provide a direct link between the fraction of neurotransmitter release and exocytotic plasticity.

Early studies have shown that external high osmotic pressure can decrease the quantity of neurotransmitters released during exocytosis (Borges et al., 1997; Troyer and Wightman, 2002). Consistent with these results, Fathali et al. found that the amount of catecholamine released from vesicles in hypertonic solution was greatly reduced compared to that in isotonic solution (Fathali et al., 2017). Moreover, to better understand whether osmotic stress affects the catecholamine content in single secretory vesicles, they measured the vesicular content with IVIEC and

found that extracellular hyperosmotic shock (730 mOsm/kg) reduced the vesicular catecholamine content to ∼ 60% of its original amount in the isotonic solution. Further characterization with transmission electron microscope (TEM) imaging revealed the vesicle size shrank, mainly in the halo, after cells were treated in the hypertonic environment. Taken together, the results showed vesicles could behave as an osmometer and maintain a relatively constant neurotransmitter concentration.

Endogenous Substances

Endogenous substances, such as ions, proteins, and lipids, have been shown to be involved in chemical neurotransmission directly or indirectly with fluorescence imaging or SCA measurement (He and Ewing, 2020; Xin and Wightman, 1998; Lovric et al., 2016; Najafinobar et al., 2016). The role of zinc, an important ion participating in various biological functions, for instance, learning and memory, on chemical neurotransmission was investigated by combining IVIEC and SCA systematically (Ren et al., 2017, 2019, 2020). It seemed that zinc treatment in the range of 0.1–100 μM reduced the vesicular neurotransmitter content, but the amount released during exocytosis was kept constant. The release fraction of neurotransmitters exhibited a clear increasing trend with the increase of zinc concentration, suggesting the function of zinc on the presynaptic strength which might be directly related to learning and memory.

As an essential energy source of organisms, adenosine triphosphate (ATP) is existing in almost all secretory vesicles with a high concentration (Borges, 2013). The study of extracellular ATP treatment using SCA and IVIEC indicated that it increased the release fraction of neurotransmitter during exocytosis, mainly through enhancing exocytotic release since the vesicular neurotransmitter storage was not statistically

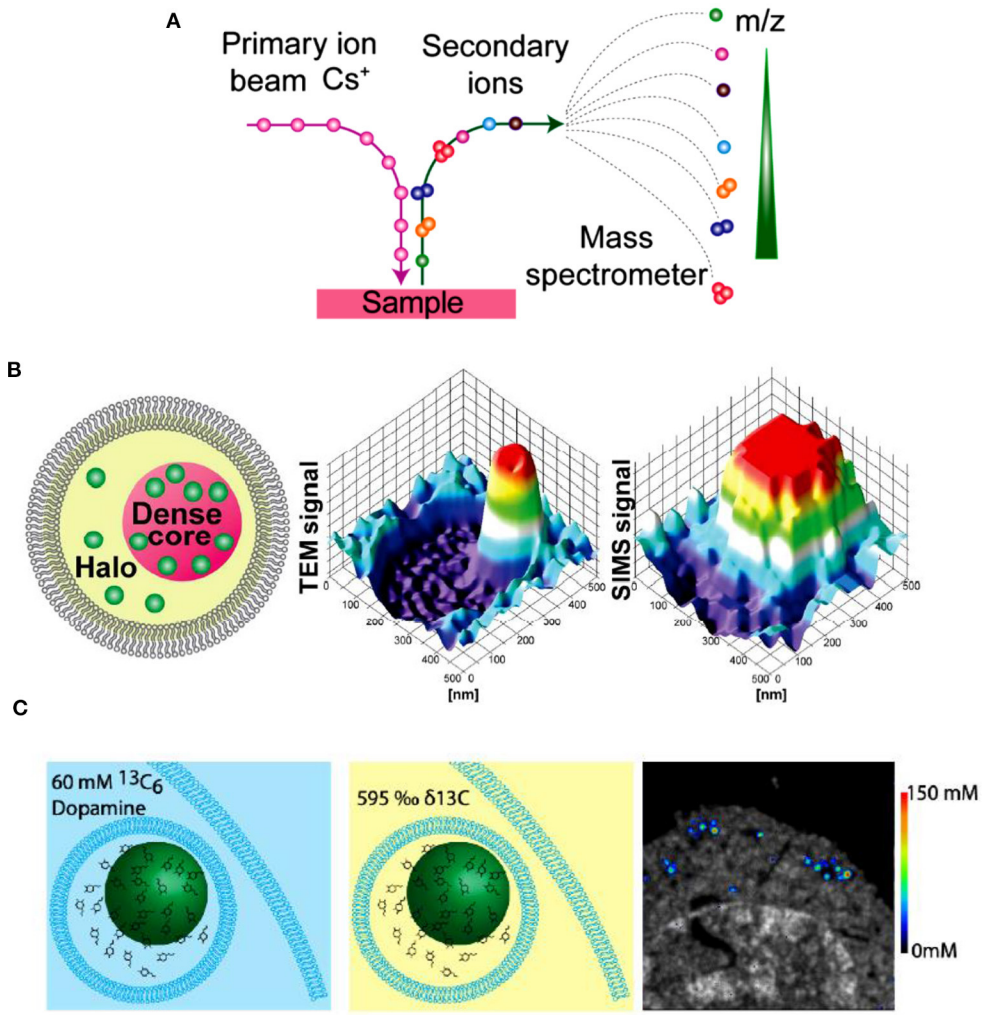

FIGURE 12 | (A) Principle of nano secondary ion mass spectrometry (NanoSIMS) measurement. **(B)** Correlation of transmission electron microscopy (TEM) and NanoSIMS imaging to study the distribution of dopamine loading inside single vesicles of PC12 by treatment with ^{13}C-L-DOPA and reserpine. From left to right: schematic of a dense core vesicle; 3D surface plots of TEM signals and NanoSIMS signal of $^{13}C^{14}N$. **(C)** The basic concept of a cell pellet embedded in epoxy resin and SIMS concentration imaging. Reprinted from Lovric et al. (2017), Thomen et al. (2020), with permission from the American Chemical Society.

influenced. Further pharmacological treatment suggested that purinergic autoreceptors might be involved in this process (Majdi et al., 2019).

Recently, the role of DJ-1 protein, an endogenous protein related to Parkinson's diseases (PD), on vesicular storage and release of neurotransmitter was studied with IVIEC and SCA (Yue et al., 2020). DJ-1 deficiency did not alter vesicular catecholamine storage significantly, but it extended the duration and decay time of exocytotic release, which might alter the postsynaptic signaling. This report provided a new insight in understanding the pathogenesis of DJ-1 deficiency-induced PD.

Drugs

Cocaine and methylphenidate (MPH) can both inhibit dopamine transporter (DAT), a presynaptic membrane-spanning protein pumping the released DA back into cells, and consequently they both block the reuptake of DA. However, the clearance of DA in the brain by MPH is slower than cocaine, so it is a potential pharmacotherapeutic candidate for treatment of cocaine abuse. Applying SCA and IVIEC at cocaine- and MPH-treated PC12 cells, the results showed that both drugs could reduce the amount of DA released during exocytosis and its storage in single vesicles. However, the fractions of DA released from vesicles went through opposite directions: treatment with cocaine decreased the fraction of neurotransmitter released to 65% when compared with the control (74%), while MPH increased it to 83%. This revealed that besides their inhibition on DAT, other mechanisms might be involved in their effect in chemical signaling (Zhu et al., 2019).

Two typical drugs, lidocaine and barbiturate, were used to demonstrate the effect of anesthetics on chemical signaling using PC12 cells as model cells (Ye and Ewing, 2018). Both drugs exhibit no change on vesicular neurotransmitter content. However, they regulate neurotransmitter release in different ways. Barbiturate selectively closes the larger fusion pores, thus reducing the quantity of catecholamine released during single exocytotic events. Lidocaine modulates the quantity of catecholamine released in a concentration-dependent manner (i.e., high concentration of lidocaine reduces it whereas low concentration enhances it).

The influences of cisplatin and tamoxifen, two anticancer drugs working through different mechanisms, on neuronal chemical transmission, were examined regarding their side effect on memory and cognition [i.e., "chemo-brain" (Li X. et al., 2016c; Taleat et al., 2019)]. Cisplatin affects exocytosis in a dose-dependent manner. Low concentrations of cisplatin stimulate catecholamine release whereas high concentrations inhibit it. Tamoxifen shows a similar function on exocytosis as cisplatin. However, tamoxifen alters the vesicular catecholamine content in a dose-dependent manner while cisplatin shows a subtle effect on vesicular catecholamine storage.

Combing IVIEC/VIEC With Nano Secondary Ion Mass Spectrometry

IVIEC has solved the difficulty of precise quantification of neurotransmitter storage in individual mammalian vesicles (ca. 70∼200 nm in diameter). Nevertheless, it cannot provide suborganellar neurotransmitter distribution in single vesicles since its spatial resolution can hardly meet this requirement to date. Nano secondary ion mass spectrometry (Nano-SIMS), one of MSI, exhibits elegant capacity to image elements and small chemical fragments at a super high spatial resolution, ∼ 50 nm. As schemed in **Figure 12A**, the impact of high-energy primary ion beam on the sample surface produces secondary ions, which enter the magnetic sector mass analyzer subsequently and are recorded as the m/z of the ions. Then, we can obtain the chemical composition of the sample surface. Moreover, the two-dimensional or three-dimensional chemical imaging of the sample can be obtained by scanning and sputtering the sample surface with Nano-SIMS.

In an effort to investigate the mechanism of neurotransmitter storage in single mammalian vesicles, Lovric et al. combined two imaging techniques (Nano-SIMS and TEM) with IVIEC to analyze the distribution of DA across single nanoscale vesicles in PC12 cells, as shown in **Figure 12B** (Lovric et al., 2017). Correlation between imaging and electrochemical data demonstrates that the transfer of DA between vesicular compartments, dense core and halo, is slow and kinetically limited. More recently, in order to achieve the absolute quantification of the concentrations of metabolites and drugs at the nanoscale level across organelles, Thomen et al. developed a Nano-SIMS method for absolute quantification of DA in single vesicles extracted from PC12 cells. In this work, VIEC was used to validate the vesicular DA content determined with Nano-SIMS. Both methods showed that the concentration of DA in PC12 vesicles is about 60 mM, crossly validating the reliability of these methods (Thomen et al., 2020).

Combing VIEC With Resistive-Pulse Sensing

Resistive-pulse sensing is a very sensitive electrochemical method which can study the properties of single entities, such as nanoparticle and macromolecule. The principle of this technique is to monitor the passage and translocation of the target by recording the ionic charge transfer at the tiny micro/nanopores when the target is passing through it (Holden et al., 2011, 2012; Li et al., 2016; McKelvey et al., 2016; Yu et al., 2019). Resistive pulse sensors have been developed and used to study the properties of individual artificial vesicles, such as size and surface charge (Chen et al., 2015; Darvish et al., 2016; Liu et al., 2018; Pan et al., 2019, 2020).

In a recent report, Zhang et al. combined the resistive pulse sensing with VIEC to simultaneously quantify the size and neurotransmitter content of individual nanoscale vesicles extracted from bovine adrenal glands (Zhang et al., 2020). As shown in **Figure 13**, single vesicles initially placed in the glass pipette passing through the nanopore powered by a periodic pressure produce a resistive pulse which could reflect the vesicle size quantitatively. Once the vesicle comes out of the pipette and reaches the disk microelectrode, the vesicle content is expelled which is powered with electroporation with extra assistance of surfactant and electrochemically oxidized on the electrode. Then, vesicle content could be evaluated by analyzing the produced current spike. They successfully quantized 278 vesicles with this combined technique and found out the vesicular catecholamine

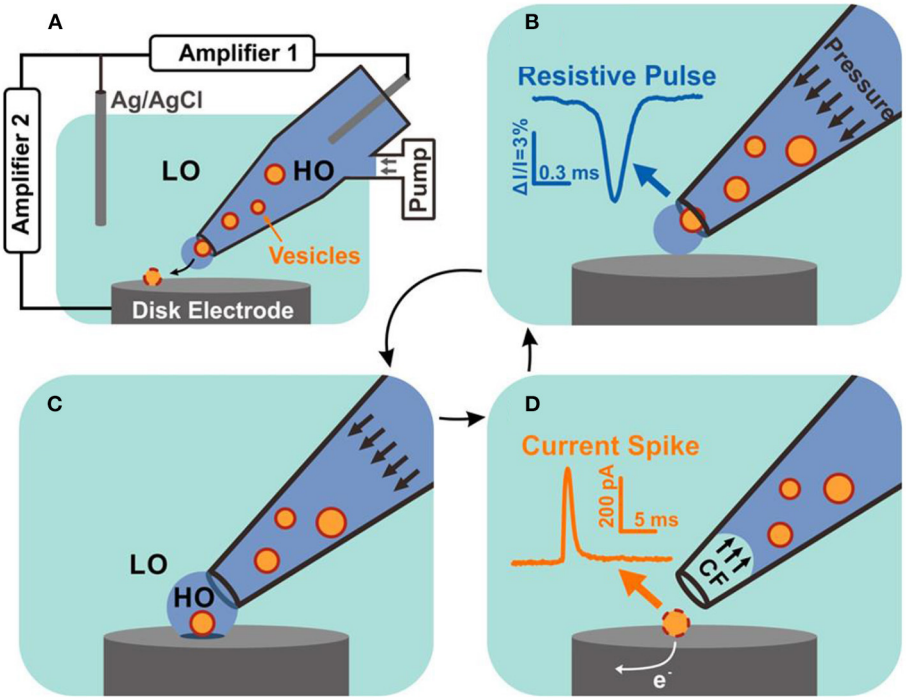

FIGURE 13 | Schematic diagram of resistive pulse-vesicle impact electrochemical cytometry (RP-VIEC). **(A)** Electrode configuration for RP-VIEC. Amplifier 1 records the RP at a potential of +13 mV vs. Ag/AgCl reference electrode. Amplifier 2 records the current spike for VIEC with electrode potential set to +700 mV vs. the same reference electrode. **(B–D)** Schematics showing a cycle induced by periodic pressure: **(B)** Pressure is applied to push a vesicle across the nanopore and generate an RP signal. **(C)** The vesicle attaches on the electrode surface and is surrounded by the outflowing buffer with relatively high osmolality (similar to vesicular lumen). LO, low osmolarity; HO, high osmolality. **(D)** Suspended pressure results in capillary force (CF) stopping solution outflow. The vesicle on the surface opens by electroporation aided by the relatively low osmolarity of the surrounding solution. Electroactive content of the vesicle is electrooxidized and generates a current spike. Reprinted from Zhang et al. (2020), with permission from the American Chemical Society.

concentration differed in dense core vesicles and non-dense core vesicle.

CONCLUSION AND PERSPECTIVES

Electrochemistry assembled with micro/nano electrodes provides a powerful tool for quantitative monitoring of neurotransmitter released from or stored in single vesicles. The exocytosis of several kinds of neurotransmitter or neuromodulator, such as catecholamines, ascorbate, glutamate, and Ach, has been successfully examined with electrochemical methods, including SCA and ITIES. The development of VIEC and IVIEC opens a new era for studying the vesicular content which may influence exocytosis. Combination of VIEC/IVIEC and SCA/Nano-SIMS/resistive-pulse sensing enables the quantitative investigation of single vesicles from multidimensions, including chemical contents storage, distribution, release, and physical properties.

Despite the elegant temporal resolution as well as its great spatial resolution and high sensitivity which promote the development of electrochemical approaches and their breakthrough application in neuroscience study, there are still unmet challenges. First, most amperometric studies are still limited for electrochemically active neurotransmitters, for example, catecholamines; the amperometric methodology of quantitatively examining the release of other kinds of neurotransmitters, such as ACh, neuropeptides, nucleotides, and nitric oxide is still highly desired though several attempts have been carried out. The enzyme-based electrochemical sensors and ITIES have great potential in this field although they have their own disadvantages to overcome. Secondly, improving the spatial resolution of electrochemical methods and imaging the neurotransmitter release during exocytosis at the nanoscale level is another direction to strive. In addition, distinguishing several kinds of neurotransmitters which exist in the same location brings another challenge for electrochemical methods. The interdisciplinary aspects which can bring new knowledge across fields may create new opportunities for meeting those challenges.

AUTHOR CONTRIBUTIONS

All authors listed have made a substantial, direct and intellectual contribution to the work, and approved it for publication.

FUNDING

The authors are grateful for the financial support from the Natural Science Foundation of China (No. 21974154) and Minzu University of China (Nos. 202000040255 and 2020000303).

REFERENCES

Abramov, E., Dolev, I., Fogel, H., Ciccotosto, G. D., Ruff, E., and Slutsky, I. (2009). Amyloid-beta as a positive endogenous regulator of release probability at hippocampal synapses. *Nat. Neurosci.* 12, 1567–1576. doi: 10.1038/nn.2433

Amemiya, S., Kim, J., Izadyar, A., Kabagambe, B., Shen, M., and Ishimatsu, R. (2013). Electrochemical sensing and imaging based on ion transfer at liquid/liquid interfaces. *Electrochim. Acta* 110, 836–845. doi: 10.1016/j.electacta.2013.03.098

Borges, R. (2013). The ATP or the natural history of neurotransmission. *Purinergic Signal* 9, 5–6. doi: 10.1007/s11302-012-9330-7

Borges, R., Travis, E. R., Hochstetler, S. E., and Wightman, R. M. (1997). Effects of external osmotic pressure on vesicular secretion from bovine adrenal medullary cells. *J. Biol. Chem.* 272, 8325–8331. doi: 10.1074/jbc.272.13.8325

Brito-Moreira, J., Paula-Lima, A. C., Bomfim, T. R., Oliveira, F. B., Sepulveda, F. J., De Mello, F. G., et al. (2011). Abeta oligomers induce glutamate release from hippocampal neurons. *Curr. Alzheimer Res.* 8, 552–562. doi: 10.2174/156720511796391917

Calvo-Gallardo, E., Lopez-Gil, A., Mendez-Lopez, I., Martinez-Ramirez, C., Padin, J. F., and Garcia, A. G. (2016). Faster kinetics of quantal catecholamine release in mouse chromaffin cells stimulated with acetylcholine, compared with other secretagogues. *J. Neurochem.* 139, 722–736. doi: 10.1111/jnc.13849

Camacho, M., Machado, J. D., Montesinos, M. S., Criado, M., and Borges, R. (2006). Intragranular pH rapidly modulates exocytosis in adrenal chromaffin cells. *J. Neurochem.* 96, 324–334. doi: 10.1111/j.1471-4159.2005.03526.x

Chen, L., He, H., and Jin, Y. (2015). Counting and dynamic studies of the small unilamellar phospholipid vesicle translocation with single conical glass nanopores. *Anal. Chem.* 87, 522–529. doi: 10.1021/ac5029243

Cheng, W., and Compton, R. G. (2014). Investigation of single-drug-encapsulating liposomes using the nano-impact method. *Angew. Chem. Int. Ed. Engl.* 53, 13928–13930. doi: 10.1002/anie.201408934

Colombo, M. L., Sweedler, J. V., and Shen, M. (2015). Nanopipet-based liquid-liquid interface probes for the electrochemical detection of acetylcholine, tryptamine, and serotonin via ionic transfer. *Anal. Chem.* 87, 5095–5100. doi: 10.1021/ac504151e

Daniels, A. J., Dean, G., Viveros, O. H., and Diliberto, E. J. Jr. (1982). Secretion of newly taken-up ascorbic acid by adrenomedullary chromaffin cells. *Science* 216, 737–739. doi: 10.1126/science.7079733

Darvish, A., Goyal, G., Aneja, R., Sundaram, R. V., Lee, K., Ahn, C. W., et al. (2016). Nanoparticle mechanics: deformation detection via nanopore resistive pulse sensing. *Nanoscale* 8, 14420–14431. doi: 10.1039/C6NR03371G

Dunevall, J., Fathali, H., Najafinobar, N., Lovric, J., Wigstrom, J., Cans, A. S., et al. (2015). Characterizing the catecholamine content of single mammalian vesicles by collision-adsorption events at an electrode. *J. Am. Chem. Soc.* 137, 4344–4346. doi: 10.1021/ja512972f

Elhamdani, A., Palfrey, H. C., and Artalejo, C. R. (2001). Quantal size is dependent on stimulation frequency and calcium entry in calf chromaffin cells. *Neuron* 31, 819–830. doi: 10.1016/S0896-6273(01)00418-4

Fathali, H., Dunevall, J., Majdi, S., and Cans, A. S. (2017). Extracellular osmotic stress reduces the vesicle size while keeping a constant neurotransmitter concentration. *ACS Chem. Neurosci.* 8, 368–375. doi: 10.1021/acschemneuro.6b00350

Ganesana, M., Trikantzopoulos, E., Maniar, Y., Lee, S. T., and Venton, B. J. (2019). Development of a novel micro biosensor for *in vivo* monitoring of glutamate release in the brain. *Biosens. Bioelectron.* 130, 103–109. doi: 10.1016/j.bios.2019.01.049

Gu, C., Larsson, A., and Ewing, A. G. (2019). Plasticity in exocytosis revealed through the effects of repetitive stimuli affect the content of nanometer vesicles and the fraction of transmitter released. *Proc. Natl. Acad. Sci. U. S. A.* 116, 21409–21415. doi: 10.1073/pnas.1910859116

Gu, C., Zhang, X., and Ewing, A. G. (2020). Comparison of disk and nanotip electrodes for measurement of single-cell amperometry during exocytotic release. *Anal. Chem.* 92, 10268–10273. doi: 10.1021/acs.analchem.0c02013

Haynes, C. L., Siff, L. N., and Wightman, R. M. (2007). Temperature-dependent differences between readily releasable and reserve pool vesicles in chromaffin cells. *Biochim. Biophys. Acta* 1773, 728–735. doi: 10.1016/j.bbamcr.2007.03.013

He, X., and Ewing, A. G. (2020). Counteranions in the stimulation solution alter the dynamics of exocytosis consistent with the hofmeister series. *J. Am. Chem. Soc.* 142, 12591–12595. doi: 10.1021/jacs.0c05319

Herman, M. A., and Jahr, C. E. (2007). Extracellular glutamate concentration in hippocampal slice. *J. Neurosci.* 27, 9736–9741. doi: 10.1523/JNEUROSCI.3009-07.2007

Holden, D. A., Hendrickson, G., Lyon, L. A., and White, H. S. (2011). Resistive pulse analysis of microgel deformation during nanopore translocation. *J. Phys. Chem. C Nanomater. Interfaces* 115, 2999–3004. doi: 10.1021/jp111244v

Holden, D. A., Watkins, J. J., and White, H. S. (2012). Resistive-pulse detection of multilamellar liposomes. *Langmuir* 28, 7572–7577. doi: 10.1021/la300993a

Huang, M., Delacruz, J. B., Ruelas, J. C., Rathore, S. S., and Lindau, M. (2018). Surface-modified CMOS IC electrochemical sensor array targeting single chromaffin cells for highly parallel amperometry measurements. *Pflugers Arch.* 470, 113–123. doi: 10.1007/s00424-017-2067-y

Iwai, N. T., Kramaric, M., Crabbe, D., Wei, Y., Chen, R., and Shen, M. (2018). GABA detection with nano-ITIES pipet electrode: a new mechanism, Water/DCE-octanoic acid interface. *Anal. Chem.* 90, 3067–3072. doi: 10.1021/acs.analchem.7b03099

Jin, J., Ji, W., Li, L., Zhao, G., Wu, W., Wei, H., et al. (2020). Electrochemically probing dynamics of ascorbate during cytotoxic edema in living rat brain. *J. Am. Chem. Soc.* 2020:45. doi: 10.1021/jacs.0c09011

Kim, B. K., Boika, A., Kim, J., Dick, J. E., and Bard, A. J. (2014). Characterizing emulsions by observation of single droplet collisions–attoliter electrochemical reactors. *J. Am. Chem. Soc.* 136, 4849–4852. doi: 10.1021/ja500713w

Kruss, S., Salem, D. P., Vukovic, L., Lima, B., Vander Ende, E., Boyden, E. S., et al. (2017). High-resolution imaging of cellular dopamine efflux using a fluorescent nanosensor array. *Proc. Natl. Acad. Sci. U. S. A.* 114, 1789–1794. doi: 10.1073/pnas.1613541114

Larsson, A., Majdi, S., Oleinick, A., Svir, I., Dunevall, J., Amatore, C., et al. (2020). Intracellular electrochemical nanomeasurements reveal that exocytosis of molecules at living neurons is subquantal and complex. *Angew. Chem. Int. Ed. Engl.* 59, 6711–6714. doi: 10.1002/anie.201914564

Leszczyszyn, D. J., Jankowski, J. A., Viveros, O. H., Diliberto, E. J. Jr., Near, J. A., and Wightman, R. M. (1990). Nicotinic receptor-mediated catecholamine secretion from individual chromaffin cells. Chemical evidence for exocytosis. *J. Biol. Chem.* 265, 14736–14737.

Li, T., He, X., Zhang, K., Wang, K., Yu, P., and Mao, L. (2016). Observing single nanoparticle events at the orifice of a nanopipet. *Chem. Sci.* 7, 6365–6368. doi: 10.1039/C6SC02241C

Li, X., Dunevall, J., and Ewing, A. G. (2016a). Quantitative chemical measurements of vesicular transmitters with electrochemical cytometry. *Acc. Chem. Res.* 49, 2347–2354. doi: 10.1021/acs.accounts.6b00331

Li, X., Dunevall, J., and Ewing, A. G. (2016c). Using single-cell amperometry to reveal how cisplatin treatment modulates the release of catecholamine transmitters during exocytosis. *Angew. Chem. Int. Ed. Engl.* 55, 9041–9044. doi: 10.1002/anie.201602977

Li, X., Dunevall, J., Ren, L., and Ewing, A. G. (2017). Mechanistic aspects of vesicle opening during analysis with vesicle impact electrochemical cytometry. *Anal. Chem.* 89, 9416–9423. doi: 10.1021/acs.analchem.7b02226

Li, X., Majdi, S., Dunevall, J., Fathali, H., and Ewing, A. G. (2015). Quantitative measurement of transmitters in individual vesicles in the cytoplasm of single cells with nanotip electrodes. *Angew. Chem. Int. Ed Engl.* 54, 11978–11982. doi: 10.1002/anie.201504839

Li, X., Mohammadi, A. S., and Ewing, A. G. (2016b). Single cell amperometry reveals curcuminoids modulate the release of neurotransmitters during exocytosis from PC12 cells. *J. Electroanal. Chem.* 781, 30–35. doi: 10.1016/j.jelechem.2016.10.025

Li, X., Ren, L., Dunevall, J., Ye, D., White, H. S., Edwards, M. A., et al. (2018). Nanopore opening at flat and nanotip conical electrodes during vesicle impact electrochemical cytometry. *ACS Nano* 12, 3010–3019. doi: 10.1021/acsnano.8b00781

Li, Y., Hu, K., Yu, Y., Rotenberg, S. A., Amatore, C., and Mirkin, M. V. (2017). Direct electrochemical measurements of reactive oxygen and nitrogen species in nontransformed and metastatic human breast cells. *J. Am. Chem. Soc.* 139, 13055–13062. doi: 10.1021/jacs.7b06476

Li, Y. T., Zhang, S. H., Wang, L., Xiao, R. R., Liu, W., Zhang, X. W., et al. (2014). Nanoelectrode for amperometric monitoring of individual vesicular

exocytosis inside single synapses. *Angew. Chem. Int. Ed. Engl.* 53, 12456–12460. doi: 10.1002/anie.201404744

Li, Y. T., Zhang, S. H., Wang, X. Y., Zhang, X. W., Oleinick, A. I., Svir, I., et al. (2015). Real-time monitoring of discrete synaptic release events and excitatory potentials within self-reconstructed neuromuscular junctions. *Angew. Chem. Int. Ed. Engl.* 54, 9313–9318. doi: 10.1002/anie.201503801

Liu, X., Savy, A., Maurin, S., Grimaud, L., Darchen, F., Quinton, D., et al. (2017). A dual functional electroactive and fluorescent probe for coupled measurements of vesicular exocytosis with high spatial and temporal resolution. *Angew. Chem. Int. Ed. Engl.* 56, 2366–2370. doi: 10.1002/anie.201611145

Liu, Y., Li, M., Zhang, F., Zhu, A., and Shi, G. (2015). Development of au disk nanoelectrode down to 3 nm in radius for detection of dopamine release from a single cell. *Anal. Chem.* 87, 5531–8. doi: 10.1021/ac5042999

Liu, Y., Xu, C., Chen, X., Wang, J., Yu, P., and Mao, L. (2018). Voltage-driven counting of phospholipid vesicles with nanopipettes by resistive-pulse principle. *Electrochem. Commun.* 89, 38–42. doi: 10.1016/j.elecom.2018.02.015

Lovric, J., Dunevall, J., Larsson, A., Ren, L., Andersson, S., Meibom, A., et al. (2017). Nano secondary ion mass spectrometry imaging of dopamine distribution across nanometer vesicles. *ACS Nano* 11, 3446–3455. doi: 10.1021/acsnano.6b07233

Lovric, J., Najafinobar, N., Dunevall, J., Majdi, S., Svir, I., Oleinick, A., et al. (2016). On the mechanism of electrochemical vesicle cytometry: chromaffin cell vesicles and liposomes. *Faraday Discuss* 193, 65–79. doi: 10.1039/C6FD00102E

Machado, J. D., Alonso, C., Morales, A., Gomez, J. F., and Borges, R. (2002). Nongenomic regulation of the kinetics of exocytosis by estrogens. *J. Pharmacol. Exp. Ther.* 301, 631–637. doi: 10.1124/jpet.301.2.631

Majdi, S., Berglund, E. C., Dunevall, J., Oleinick, A. I., Amatore, C., Krantz, D. E., et al. (2015). Electrochemical measurements of optogenetically stimulated quantal amine release from single nerve cell varicosities in drosophila larvae. *Angew. Chem. Int. Ed. Engl.* 54, 13609–13612. doi: 10.1002/anie.201506743

Majdi, S., Larsson, A., Najafinobar, N., Borges, R., and Ewing, A. G. (2019). Extracellular ATP regulates the vesicular pore opening in chromaffin cells and increases the fraction released during individual exocytosis events. *ACS Chem. Neurosci.* 10, 2459–2466. doi: 10.1021/acschemneuro.8b00722

Manning, B. M., Hebbel, R. P., Gupta, K., and Haynes, C. L. (2012). Carbon-fiber microelectrode amperometry reveals sickle-cell-induced inflammation and chronic morphine effects on single mast cells. *ACS Chem. Biol.* 7, 543–551. doi: 10.1021/cb200347q

McKelvey, K., Edwards, M. A., and White, H. S. (2016). resistive pulse delivery of single nanoparticles to electrochemical interfaces. *J. Phys. Chem. Lett.* 7, 3920–3924. doi: 10.1021/acs.jpclett.6b01873

Meldolesi, J., and Ceccarelli, B. (1981). Exocytosis and membrane recycling. *Philos. Trans. R. Soc. Lond. B. Biol. Sci.* 296, 55–65. doi: 10.1098/rstb.1981.0171

Montesinos, M. S., Machado, J. D., Camacho, M., Diaz, J., Morales, Y. G., Alvarez de la Rosa, D., et al. (2008). The crucial role of chromogranins in storage and exocytosis revealed using chromaffin cells from chromogranin a null mouse. *J. Neurosci.* 28, 3350–3358. doi: 10.1523/JNEUROSCI.5292-07.2008

Moreira, B., Tuoriniemi, J., Kouchak Pour, N., Mihalcikova, L., and Safina, G. (2017). Surface plasmon resonance for measuring exocytosis from populations of PC12 cells: mechanisms of signal formation and assessment of analytical capabilities. *Anal. Chem.* 89, 3069–3077. doi: 10.1021/acs.analchem.6b04811

Mosharov, E. V., Gong, L. W., Khanna, B., Sulzer, D., and Lindau, M. (2003). Intracellular patch electrochemistry: regulation of cytosolic catecholamines in chromaffin cells. *J. Neurosci.* 23, 5835–5845. doi: 10.1523/JNEUROSCI.23-13-05835.2003

Najafinobar, N., Lovric, J., Majdi, S., Dunevall, J., Cans, A. S., and Ewing, A. (2016). Excited fluorophores enhance the opening of vesicles at electrode surfaces in vesicle electrochemical cytometry. *Angew. Chem. Int. Ed. Engl.* 55, 15081–15085. doi: 10.1002/anie.201609178

Omiatek, D. M., Bressler, A. J., Cans, A. S., Andrews, A. M., Heien, M. L., and Ewing, A. G. (2013). The real catecholamine content of secretory vesicles in the CNS revealed by electrochemical cytometry. *Sci. Rep.* 3:1447. doi: 10.1038/srep01447

Omiatek, D. M., Dong, Y., Heien, M. L., and Ewing, A. G. (2010). Only a fraction of quantal content is released during exocytosis as revealed by electrochemical cytometry of secretory vesicles. *ACS Chem. Neurosci.* 1, 234–245. doi: 10.1021/cn900040e

Omiatek, D. M., Santillo, M. F., Heien, M. L., and Ewing, A. G. (2009). Hybrid capillary-microfluidic device for the separation, lysis, and electrochemical detection of vesicles. *Anal. Chem.* 81, 2294–2302. doi: 10.1021/ac802466g

Page, A., Kang, M., Armitstead, A., Perry, D., and Unwin, P. R. (2017). Quantitative visualization of molecular delivery and uptake at living cells with self-referencing scanning ion conductance microscopy-scanning electrochemical microscopy. *Anal. Chem.* 89, 3021–3028. doi: 10.1021/acs.analchem.6b04629

Pan, R., Hu, K., Jia, R., Rotenberg, S. A., Jiang, D., and Mirkin, M. V. (2020). Resistive-pulse sensing inside single living cells. *J. Am. Chem. Soc.* 142, 5778–5784. doi: 10.1021/jacs.9b13796

Pan, R., Hu, K., Jiang, D., Samuni, U., and Mirkin, M. V. (2019). Electrochemical resistive-pulse sensing. *J. Am. Chem. Soc.* 141, 19555–19559. doi: 10.1021/jacs.9b10329

Park, H., Li, Y., and Tsien, R. W. (2012). Influence of synaptic vesicle position on release probability and exocytotic fusion mode. *Science* 335, 1362–1366. doi: 10.1126/science.1216937

Phan, N. T. N., Li, X., and Ewing, A. G. (2017). Measuring synaptic vesicles using cellular electrochemistry and nanoscale molecular imaging. *Nat. Rev. Chem.* 1:0048. doi: 10.1038/s41570-017-0048

Picollo, F., Battiato, A., Bernardi, E., Marcantoni, A., Pasquarelli, A., Carbone, E., et al. (2016). Microelectrode arrays of diamond-insulated graphitic channels for real-time detection of exocytotic events from cultured chromaffin cells and slices of adrenal glands. *Anal. Chem.* 88, 7493–7499. doi: 10.1021/acs.analchem.5b04449

Qiu, Q.-F., Zhang, F.-L., Tang, Y., Zhang, X.-W., Jiang, H., Liu, Y.-L., et al. (2018). Real-time monitoring of exocytotic glutamate release from single neuron by amperometry at an enzymatic biosensor. *Electroanalysis* 30, 1054–1059. doi: 10.1002/elan.201700656

Raghupathi, R., Jessup, C. F., Lumsden, A. L., and Keating, D. J. (2016). Fusion pore size limits 5-ht release from single enterochromaffin cell vesicles. *J. Cell. Physiol.* 231, 1593–1600. doi: 10.1002/jcp.25256

Ranjbari, E., Majdi, S., and Ewing, A. (2019). Analytical techniques: shedding light upon nanometer-sized secretory vesicles. *Trends Chem.* 1, 440–451. doi: 10.1016/j.trechm.2019.02.014

Ren, L., Dowlatshahi Pour, M., Malmberg, P., and Ewing, A. G. (2019). altered lipid composition of secretory cells following exposure to zinc can be correlated to changes in exocytosis. *Chemistry* 25, 5406–5411. doi: 10.1002/chem.201900010

Ren, L., Oleinick, A., Svir, I., Amatore, C., and Ewing, A. G. (2020). Amperometric measurements and dynamic models reveal a mechanism for how zinc alters neurotransmitter release. *Angew. Chem. Int. Ed. Engl.* 59, 3083–3087. doi: 10.1002/anie.201913184

Ren, L., Pour, M. D., Majdi, S., Li, X., Malmberg, P., and Ewing, A. G. (2017). Zinc regulates chemical-transmitter storage in nanometer vesicles and exocytosis dynamics as measured by amperometry. *Angew. Chem. Int. Ed. Engl.* 56, 4970–4975. doi: 10.1002/anie.201700095

Roberts, J. G., Mitchell, E. C., Dunaway, L. E., McCarty, G. S., and Sombers, L. A. (2020). Carbon-fiber nanoelectrodes for real-time discrimination of vesicle cargo in the native cellular environment. *ACS Nano* 14, 2917–2926. doi: 10.1021/acsnano.9b07318

Shen, M., Qu, Z., DesLaurier, J., Welle, T. M., Sweedler, J. V., and Chen, R. (2018). Single synaptic observation of cholinergic neurotransmission on living neurons: concentration and dynamics. *J. Am. Chem. Soc.* 140, 7764–7768. doi: 10.1021/jacs.8b01989

Sombers, L. A., Maxson, M. M., and Ewing, A. G. (2005). Loaded dopamine is preferentially stored in the halo portion of PC12 cell dense core vesicles. *J. Neurochem.* 93, 1122–1131. doi: 10.1111/j.1471-4159.2005.03087.x

Stephens, L. I., Payne, N. A., and Mauzeroll, J. (2020). Super-resolution scanning electrochemical microscopy. *Anal. Chem.* 92, 3958–3963. doi: 10.1021/acs.analchem.9b05451

Taleat, Z., Larsson, A., and Ewing, A. G. (2019). Anticancer drug tamoxifen affects catecholamine transmitter release and storage from single cells. *ACS Chem. Neurosci.* 10, 2060–2069. doi: 10.1021/acschemneuro.8b00714

Tang, Y., Yang, X.-K., Zhang, X.-W., Wu, W.-T., Zhang, F.-L., Jiang, H., et al. (2020). Harpagide, a natural product, promotes synaptic vesicle release as measured by nanoelectrode amperometry. *Chem. Sci.* 11, 778–785. doi: 10.1039/C9SC05538J

Thomen, A., Najafinobar, N., Penen, F., Kay, E., Upadhyay, P. P., Li, X., et al. (2020). Subcellular mass spectrometry imaging and absolute quantitative analysis across organelles. *ACS Nano*. 14, 4316–4325. doi: 10.1021/acsnano.9b09804

Tomagra, G., Picollo, F., Battiato, A., Picconi, B., De Marchis, S., Pasquarelli, A., et al. (2019). Quantal release of dopamine and action potential firing detected in midbrain neurons by multifunctional diamond-based microarrays. *Front. Neurosci* 13:288. doi: 10.3389/fnins.2019.00288

Trouillon, R., and Ewing, A. G. (2013). Single cell amperometry reveals glycocalyx hinders the release of neurotransmitters during exocytosis. *Anal. Chem* 85, 4822–4828. doi: 10.1021/ac4008682

Trouillon, R., and Ewing, A. G. (2014). Actin controls the vesicular fraction of dopamine released during extended kiss and run exocytosis. *ACS Chem. Biol.* 9, 812–820. doi: 10.1021/cb400665f

Troyer, K. P., and Wightman, R. M. (2002). Temporal separation of vesicle release from vesicle fusion during exocytosis. *J. Biol. Chem*. 277, 29101–29107. doi: 10.1074/jbc.M202856200

Wang, K., Xiao, T., Yue, Q., Wu, F., Yu, P., and Mao, L. (2017). selective amperometric recording of endogenous ascorbate secretion from a single rat adrenal chromaffin cell with pretreated carbon fiber microelectrodes. *Anal. Chem.* 89, 9502–9507. doi: 10.1021/acs.analchem.7b02508

Wang, Y., Fathali, H., Mishra, D., Olsson, T., Keighron, J. D., Skibicka, K. P., et al. (2019a). Counting the number of glutamate molecules in single synaptic vesicles. *J. Am. Chem. Soc.* 141, 17507–17511. doi: 10.1021/jacs.9b09414

Wang, Y., Mishra, D., Bergman, J., Keighron, J. D., Skibicka, K. P., and Cans, A. S. (2019b). Ultrafast glutamate biosensor recordings in brain slices reveal complex single exocytosis transients. *ACS Chem. Neurosci.* 10, 1744–1752. doi: 10.1021/acschemneuro.8b00624

Wang, Y., Velmurugan, J., Mirkin, M. V., Rodgers, P. J., Kim, J., and Amemiya, S. (2010). Kinetic study of rapid transfer of tetraethylammonium at the 1,2-dichloroethane/water interface by nanopipet voltammetry of common ions. *Anal. Chem.* 82, 77–83. doi: 10.1021/ac902244s

Welle, T. M., Alanis, K., Colombo, M. L., Sweedler, J. V., and Shen, M. (2018). A high spatiotemporal study of somatic exocytosis with scanning electrochemical microscopy and nanoITIES electrodes. *Chem. Sci.* 9, 4937–4941. doi: 10.1039/C8SC01131A

Wightman, R. M., Jankowski, J. A., Kennedy, R. T., Kawagoe, K. T., Schroeder, T. J., Leszczyszyn, D. J., et al. (1991). Temporally resolved catecholamine spikes correspond to single vesicle release from individual chromaffin cells. *Proc. Natl. Acad. Sci. U. S. A.* 88, 10754–10758. doi: 10.1073/pnas.88.23.10754

Wigstrom, J., Dunevall, J., Najafinobar, N., Lovric, J., Wang, J., Ewing, A. G., et al. (2016). Lithographic microfabrication of a 16-electrode array on a probe tip for high spatial resolution electrochemical localization of exocytosis. *Anal. Chem.* 88, 2080–2087. doi: 10.1021/acs.analchem.5b03316

Wilhelm, B. G., Mandad, S., Truckenbrodt, S., Krohnert, K., Schafer, C., Rammner, B., et al. (2014). Composition of isolated synaptic boutons reveals the amounts of vesicle trafficking proteins. *Science* 344, 1023–1028. doi: 10.1126/science.1252884

Wu, F., Yu, P., Yang, X., Han, Z., Wang, M., and Mao, L. (2018). Exploring ferredoxin-dependent glutamate synthase as an enzymatic bioelectrocatalyst. *J. Am. Chem. Soc.* 140, 12700–12704. doi: 10.1021/jacs.8b08020

Xiao, T., Jiang, Y., Ji, W., and Mao, L. (2018). Controllable and reproducible sheath of carbon fibers with single-walled carbon nanotubes through electrophoretic deposition for *in vivo* electrochemical measurements. *Anal. Chem.* 90, 4840–4846. doi: 10.1021/acs.analchem.8b00303

Xiao, T., Wang, Y., Wei, H., Yu, P., Jiang, Y., and Mao, L. (2019). Electrochemical monitoring of propagative fluctuation of ascorbate in the live rat brain during spreading depolarization. *Angew. Chem. Int. Ed. Engl.* 58, 6616–6619. doi: 10.1002/anie.201901035

Xin, Q., and Wightman, R. M. (1998). Simultaneous detection of catecholamine exocytosis and Ca2+ release from single bovine chromaffin cells using a dual microsensor. *Anal. Chem.* 70, 1677–1681. doi: 10.1021/ac970746o

Yang, X. K., Tang, Y., Qiu, Q. F., Wu, W. T., Zhang, F. L., Liu, Y. L., et al. (2019). Abeta1-42 oligomers induced a short-term increase of glutamate release prior to its depletion as measured by amperometry on single varicosities. *Anal. Chem.* 91, 15123–15129. doi: 10.1021/acs.analchem.9b03826

Ye, D., and Ewing, A. (2018). On the action of general anesthetics on cellular function: barbiturate alters the exocytosis of catecholamines in a model cell system. *Chemphyschem* 19, 1173–1179. doi: 10.1002/cphc.201701255

Ye, D., Gu, C., and Ewing, A. (2018). Using single-cell amperometry and intracellular vesicle impact electrochemical cytometry to shed light on the biphasic effects of lidocaine on exocytosis. *ACS Chem. Neurosci.* 9, 2941–2947. doi: 10.1021/acschemneuro.8b00130

Yu, R. J., Ying, Y. L., Gao, R., and Long, Y. T. (2019). Confined nanopipette sensing: from single molecules, single nanoparticles, to single cells. *Angew. Chem. Int. Ed. Engl.* 58, 3706–3714. doi: 10.1002/anie.201803229

Yu, P., Wei, H., Zhong, P., Xue, Y., Wu, F., Liu, Y., et al. (2020). Single-carbon-fiber-powered microsensor for *in vivo* neurochemical sensing with high neuronal compatibility. *Angew. Chem. Int. Ed Engl.* 59, 22652–22658. doi: 10.1002/ange.202010195

Yuan, T., Lu, J., Zhang, J., Zhang, Y., and Chen, L. (2015). Spatiotemporal detection and analysis of exocytosis reveal fusion "hotspots" organized by the cytoskeleton in endocrine cells. *Biophys. J.* 108, 251–260. doi: 10.1016/j.bpj.2014.11.3462

Yue, Q., Li, X., Wu, F., Ji, W., Zhang, Y., Yu, P., et al. (2020). Unveiling the role of DJ-1 protein in vesicular storage and release of catecholamine with nano/micro-tip electrodes. *Angew. Chem. Int. Ed. Engl.* 59, 11061–11065. doi: 10.1002/anie.202002455

Zhang, X. W., Hatamie, A., and Ewing, A. G. (2020). Simultaneous quantification of vesicle size and catecholamine content by resistive pulses in nanopores and vesicle impact electrochemical cytometry. *J. Am. Chem. Soc.* 142, 4093–4097. doi: 10.1021/jacs.9b13221

Zhang, X. W., Oleinick, A., Jiang, H., Liao, Q. L., Qiu, Q. F., Svir, I., et al. (2019). Electrochemical monitoring of ROS/RNS homeostasis within individual phagolysosomes inside single macrophages. *Angew. Chem. Int. Ed. Engl.* 58, 7753–7756. doi: 10.1002/anie.201902734

Zhang, X. W., Qiu, Q. F., Jiang, H., Zhang, F. L., Liu, Y. L., Amatore, C., et al. (2017). Real-time intracellular measurements of ROS and RNS in living cells with single core-shell Nanowire electrodes. *Angew. Chem. Int. Ed. Engl.* 56, 12997–13000. doi: 10.1002/anie.201707187

Zhu, W., Gu, C., Dunevall, J., Ren, L., Zhou, X., and Ewing, A. G. (2019). Combined amperometry and electrochemical cytometry reveal differential effects of cocaine and methylphenidate on exocytosis and the fraction of chemical release. *Angew. Chem. Int. Ed. Engl.* 58, 4238–4242. doi: 10.1002/anie.201813717

Conflict of Interest: The authors declare that the research was conducted in the absence of any commercial or financial relationships that could be construed as a potential conflict of interest.

Copyright © 2021 Liu, Du, Wang, Zhang, Liu and Li. This is an open-access article distributed under the terms of the Creative Commons Attribution License (CC BY). The use, distribution or reproduction in other forums is permitted, provided the original author(s) and the copyright owner(s) are credited and that the original publication in this journal is cited, in accordance with accepted academic practice. No use, distribution or reproduction is permitted which does not comply with these terms.

frontiers in Chemistry

ORIGINAL RESEARCH
published: 15 January 2021
doi: 10.3389/fchem.2020.601649

Co-delivery of Salinomycin and Curcumin for Cancer Stem Cell Treatment by Inhibition of Cell Proliferation, Cell Cycle Arrest, and Epithelial–Mesenchymal Transition

Yongmei Zhao[1†], Kaikai Wang[1†], Yuanlin Zheng[1], Xiaobao Zeng[1], Yi Chieh Lim[2] and Tianqing Liu[3]*

[1] School of Pharmacy, Nantong University, Nantong, China, [2] Danish Cancer Society Research Center, Copenhagen, Denmark, [3] NICM Health Research Institute, Western Sydney University, Sydney, NSW, Australia

OPEN ACCESS

Edited by:
Jie He,
University of Connecticut,
United States

Reviewed by:
Ruibing Wang,
University of Macau, China
Seung Rim Hwang,
Chosun University, South Korea

***Correspondence:**
Tianqing Liu
michelle.tianqing.liu@gmail.com

[†] These authors have contributed equally to this work

Specialty section:
This article was submitted to Medicinal and Pharmaceutical Chemistry, a section of the journal Frontiers in Chemistry

Received: 02 September 2020
Accepted: 09 November 2020
Published: 15 January 2021

Citation:
Zhao Y, Wang K, Zheng Y, Zeng X, Lim YC and Liu T (2021) Co-delivery of Salinomycin and Curcumin for Cancer Stem Cell Treatment by Inhibition of Cell Proliferation, Cell Cycle Arrest, and Epithelial–Mesenchymal Transition. Front. Chem. 8:601649. doi: 10.3389/fchem.2020.601649

Malignant cancer is a devastating disease often associated with a poor clinical prognosis. For decades, modern drug discoveries have attempted to identify potential modulators that can impede tumor growth. Cancer stem cells however are more resistant to therapeutic intervention, which often leads to treatment failure and subsequent disease recurrence. Here in this study, we have developed a specific multi-target drug delivery nanoparticle system against breast cancer stem cells (BCSCs). Therapeutic agents curcumin and salinomycin have complementary functions of limiting therapeutic resistance and eliciting cellular death, respectively. By conjugation of CD44 cell-surface glycoprotein with poly(lactic-co-glycolic acid) (PLGA) nanoparticles that are loaded with curcumin and salinomycin, we investigated the cellular uptake of BCSCs, drug release, and therapeutic efficacy against BCSCs. We determined CD44-targeting co-delivery nanoparticles are highly efficacious against BCSCs by inducing G_1 cell cycle arrest and limiting epithelial–mesenchymal transition. This curcumin and salinomycin co-delivery system can be an efficient treatment approach to target malignant cancer without the repercussion of disease recurrence.

Keywords: nanomedicine, polymeric nanoparticles, curcumin, salinomycin, cancer stem cells

INTRODUCTION

Resistance to chemotherapy is the major cause of cancer relapse and mortality. Early indications of intrinsic resistance emphasized on the presence of cancer stem cells (CSCs), which are highly mesenchymal in nature and have the ability to self-renew, differentiate, and promote tumorigenesis. They play an important role in chemotherapy and radiotherapy resistance via enhanced anti-apoptotic, DNA repair, and reactive oxygen species (ROS)-protective mechanisms, often leading to tumor recurrence including metastasis. There is now overwhelming clinical evidence to support enriched CSCs as the dominant population in reviving tumor growth despite initial aggressive chemotherapeutic intervention. Therefore, effective elimination of CSCs is essential to impede tumor relapse and drug resistance to improve patients' survival. However, current treatments may harm the normal stem cell pool and result in severe side effects. Therefore, therapeutics to specifically remove CSCs remain a major challenge for anti-cancer treatment.

Salinomycin is a polyether ionophore antibiotic with efficacy as an anti-cancer drug (Naujokat and Steinhart, 2012). Pre-clinical data indicates salinomycin has the potential to reduce tumorigenicity by targeting CSCs and has been effective in several cancer types (Gupta et al., 2009; Lu et al., 2011; Ketola et al., 2012; Lim et al., 2020). The anti-cancer mechanism of salinomycin is associated with dysregulation of metal ions (Paulus et al., 1998), activation of autophagy-mediated cell death, and inhibition of stem cell maintenance (Lu et al., 2011; Yue et al., 2013; Mai et al., 2017). A recent study found that salinomycin and its derivative, ironomycin, exhibited a potent and selective activity against breast cancer stem cells (BCSCs) by accumulating and sequestering iron to induce ferroptosis, which is a recently described form of iron-dependent cell death marked by the oxidative modification of phospholipid membranes (Mai et al., 2017). However, it is challenging to efficiently deliver salinomycin (Sal) to tumor sites due to its hydrophobicity, unfavorable pharmacokinetic profile, and cytotoxicity during systemic drug administration (Naujokat and Steinhart, 2012). Curcumin (Cur) is a bioactive ingredient derived from the root of *Curcuma longa L*, which have been widely used in the prevention and treatment of a number of diseases, including cancer (Sharma et al., 2005; Zhou et al., 2011; Shanmugam et al., 2015; Gao et al., 2017; Motevalli et al., 2019). Curcumin is a potent tumor suppressor as it can inhibit tumor growth at cellular and *in vivo* level. Although the mechanism is not fully understood, studies have shown that curcumin can lead to inhibition of cancer cell invasion (Baek et al., 2003; Shao et al., 2017), cell cycle arrest, and induction of autophagic cell death. More recently, researchers have investigated the anti-metastasis potentials of curcumin (Basnet and Skalko-Basnet, 2011; Norris et al., 2013; Teiten et al., 2014; Kotcherlakota et al., 2016) and found it can inhibit CSCs' viability and their stemness via ROS and the signal transducer and activator of transcription 3 (STAT3) signaling pathway (Buhrmann et al., 2020). However, its therapeutic potential is limited due to its rapid metabolism and poor solubility and absorption (Tsai et al., 2011).

Nanomedicines provide new strategies in cancer targeting and treatment due to high drug loading capability, cancer-targeting ability, and even the potential to overcome the efflux pump-mediated drug resistance by delivering a high concentration of intracellular drugs (Cho et al., 2008). Our previous studies showed that conjugation of salinomycin with gold nanoparticles can efficiently induce ferroptotic cell death of BCSCs by increasing the generation of ROS, mitochondrial dysfunction, and lipid oxidation with higher iron accumulation and GPX-4 inactivation (Zhao et al., 2019). Here, the combination of salinomycin and curcumin was used to achieve synergetic effect in treating BCSCs. Salinomycin and curcumin were loaded onto poly(lactic-co-glycolic acid) (PLGA) polymeric nanoparticles via double emulsion method to form nanoparticles (Avgoustakis et al., 2002; Alam et al., 2017). Additionally, hyaluronic acid (HA) was also conjugated to nanoparticles as targeting moiety due to its specific interaction with the CD44 receptor, which is a cell surface glycoprotein and commonly overexpressed on BCSCs (Zöller, 2011; Ganesh et al., 2013; Sanfilippo et al., 2020). The CD44-targeting nanoparticles loaded with salinomycin and curcumin showed improved therapeutic efficiency against BCSCs by inducing G_1 cell cycle arrest and limiting epithelial–mesenchymal transition (EMT).

MATERIALS AND METHODS

Materials

Dulbecco's Modified Eagle Medium (DMEM), fetal bovine serum (FBS), penicillin–streptomycin, propidium iodide, Triton X-100, PageRuler Prestained Protein Ladder, and nitrocellulose membrane were purchased from Thermo Fisher. Curcumin, salinomycin, 1-ethyl-3-(3-dimethylaminopropyl)carbodiimide hydrochloride (EDC), and N-hydroxysuccinimide (NHS) were bought from Sigma-Aldrich and used directly without any purification. Mouse anti-vimentin, mouse anti-E-cadherin, and rabbit anti-β-actin primary antibodies purchased from Abcam. Odyssey blocking buffer, IRDye® 800CW goat anti-mouse secondary antibody, and IRDye® 680RD goat anti-rabbit secondary antibody were purchased from LI-COR.

Nanoparticle Synthesis and Surface Functionalization

NH2-PEG-NH2 (MW: 3.4 k), PLGA (MW: 10 k), and PLGA-PEG-NH2 (MW: 18.6 k) co-polymer were bought from Meiluo Tech Company. Curcumin and salinomycin were loaded into the PLGA-PEG-NH2 copolymer via the well-established double emulsion method (Avgoustakis et al., 2002). Briefly, curcumin (1 mg/ml) and salinomycin (molar ratio of Cur and Sal = 1:1) were dissolved in organic phase containing co-polymer (1.75%, *w*/*v*), and the mixture was mixed using an ultrasonic homogenizer (LABSONIC M, Sartorius, Germany). The primary particles were added into a PVA solution (10 ml, 2%, *w*/*v*), and the mixture was sonicated again. The free drugs were then removed by centrifugation at 20,000 rpm for 15 min and washed with water. The formed nanoparticles were labeled as PEG-PLGA-Cur-Sal.

After drug loading, targeting moiety HA was conjugated onto the polymeric nanoparticles via EDC coupling. Briefly, desalted HA (1 equivalent), EDC (3 equivalents), and NHS (3 equivalents) were dissolved in 2-(N-morpholino)ethanesulfonic acid (MES) buffer and stir in ice bath to activate carboxylic group for half an hour. PEG-PLGA-Cur-Sal was then added and the mixture was stirred for another 4 h at room temperature to form nanoparticles named HA-PEG-PLGA-Cur-Sal. They were purified by using centrifugation at 20,000 rpm for 15 min.

Characterization of the Nanoparticles

^{1}H NMR spectra were acquired on a Bruker AVANCE 400 MHz spectrometer. A gel permeation chromatography—multi-angle laser light scattering (GPC-MALLS) system consisting of a 1,515 isocratic pump (Waters), Styragel HT 6E and Styragel HT 3 columns (Waters), 2,414 differential refractive index detector (Waters), and a DAWN HELEOS laser light scattering detector (Wyatt) with THF as an eluent at a flow rate of 1 ml/min was used to measure the molecular weight and dispersity of the polymers. After drug loading, the size of the nanoparticles was measured via dynamic light scattering (DLS) to measure the

hydrodynamic diameter using a Malvern Zetasizer, and a Philips CM100 transmission electron microscope (TEM) was also used to observe their morphology.

Cancer Stem Cell Culture

MCF-7 cells were bought from ATCC (USA) and cultured in DMEM medium containing 10% (*v*/*v*) FBS and 1% (v/*v*) penicillin–streptomycin. They were kept in a humidified 37°C incubator with 5% CO_2. After serum-free treatment, BCSC subpopulations in the MCF-7 cells were isolated using MagCellect Human BCSC isolation kit (R&D Systems) according to protocols from the manufacturer. In brief, MCF-7 cells (1×10^7 cells/ml) were prepared in buffer and mixed with anti-human CD24 biotinylated antibody and then Streptavidin Ferrofluid for selection of $CD24^{low}$ cells. Those cells were subsequently incubated with a biotinylated anti-human CD44 antibody and Streptavidin Ferrofluid for selection of $CD44^{high}$ cells. After washing, magnetically tagged $CD24^{low}/CD44^{high}$ BCSCs were isolated through the magnet. The cells were directly treated with drug-loaded nanoparticles and control samples after isolation.

Drug Loading Efficiency and Drug Release Study

Salinomycin loading efficiency was analyzed by using a UV-Vis-NIR spectrophotometer following a published method (Wang et al., 2014). The drug concentration of curcumin was calculated using the linear portion of the calibration curve obtained by the UV spectrophotometer at 427 nm for serial drug concentrations.

Cellular Uptake Assay With Flow Cytometry

Flow cytometry was used to quantify cellular interaction following incubation of the cells with each treatment group. BCSCs were seeded in six-well culture plates (2×10^5 cells/well). Fluorescent dye Cy5.5 was encapsulated in the nanoparticles (NPs) to image cellular uptake. After pre-incubation for 24 h, cells were treated with HA-PEG-PLGA NPs and PEG-PLGA NPs, respectively. After 6 h, the cells were washed with PBS twice and cells of each well were collected and imaged using a FACSCanto A flow cytometer (BD Bioscience, USA). Fluorescent dye coumarin-6 was encapsulated in the NPs, and cellular uptake was monitored using a Leica TCS SP8 CARS confocal microscope (Leica, Germany) after 4-h incubation of untargeted PEG-PLGA NPs and targeted HA-PEG-PLGA NPs.

Proliferation Assay

Cells were seeded at 800 cells per well in 96-well plates and cultured until they reached ∼10% confluence. Cells were then treated overnight with various concentrations of drug-loaded nanoparticles or controls. Cell proliferation was monitored using the Incucyte Zoom (Essen, MI, USA). Images were taken at regular time intervals over 6 days, and cell growth curves were plotted with the Incucyte Zoom software.

Cell Cycle G1/S Assessment Using Flow Cytometry

Cells were seeded onto six-well plates and cultured overnight until they reached 80% confluence. After a subsequent 24-h treatment with drug-loaded nanoparticles or the relevant control, the cells were treated with 300 μl of 1 mg/ml propidium iodide, 0.1% (*v*/*v*) Triton X-100, and 0.8% (*v*/*v*) RNAse A solution for 30 min at room temperature. Cells were washed with PBS and harvested for cell cycle measurements while protected from light. Single cells were identified by measurement of forward and side scatter. Then, doublets were removed using pulse processing. Measurements took place using a B670LP-A filter on a FACSCanto A flow cytometer.

Wound Scratch Assays

Cell migration was assessed using an established wound scratch assay (Fan et al., 2011). Cells were seeded at 64,000 cells per well in 96-well plates and incubated until they reached more than 80% confluence. The plates were placed in an Incucyte wound maker (Essen, MI, USA) to ensure consistency in the wounds made on the cell monolayers in each well. The medium and cell debris were then removed and replaced with 200 μl of fresh medium containing drug-loaded nanoparticles or controls. The plates were placed in the Incucyte Zoom (Essen, MI, USA), and the wound width was monitored over 24 h for later analysis using Incucyte Zoom software.

Cell Attachment

Cells were seeded onto six-well plates and left to attach overnight until over 80% confluence and then treated with drug-loaded nanoparticles or controls for 24 h. The cells were washed with PBS and then detached using versene. They were then seeded 5×10^4 cells per well onto gelatin-precoated 96-well plates for 2 h. After washing with PBS and fixation using 4% PFA for 15 min, the cells were imaged using the Incucyte Zoom (Essen, MI, USA) and the number of cells attached was quantified using Incucyte Zoom software.

Western Blotting

The expression of EMT markers was assessed by western blotting. Cells were seeded onto six-well plates and cultured overnight until they reached over 80% confluence. They were then treated with drug-loaded nanoparticles or controls for 24 h, washed with PBS, and harvested with versene. Ice-cold lysis buffer was added to each cell pellet for 15 min, and protein supernatants were obtained after spinning at 16,000G for 15 min at 4°C. The total protein concentration in each extract was measured using the bicinchoninic acid protein assay.

Protein samples were diluted using Milli-Q water to give a concentration of 50 μg protein/20 μl. Loading buffer (5 μl) was added to each sample, and samples were heated at 75°C for 10 min. Samples were loaded into wells of 15% acrylamide gels with a protein ladder and run at 100 V. The proteins were subsequently transferred onto nitrocellulose membranes at 100 V for 1 h, then blocked with 5 ml of blocking buffer at 4°C overnight. Blots were treated with a mouse anti-vimentin monoclonal antibody (1:1,000) or a mouse anti-E-cadherin

monoclonal antibody (1:1,000) in blocking buffer for 1 h at room temperature on a shaker, while a rabbit anti-β-actin monoclonal antibody was used as a loading control (1:1,000). After washing with 1X TBST four times every 15 min for 1 h, the blots were incubated with goat anti-mouse polyclonal secondary antibodies (1:5,000) in the dark for 1 h. After washing for four times and drying, the membranes were scanned with the Odyssey CLx (LI-COR, NE, USA) imaging system and data were analyzed with Image Studio software.

Statistical Analysis

Multiple group comparisons were carried out using *T*-test, using GraphPad Prism version 7. This enabled significance against DMSO controls to be calculated. All results are shown as mean ± SEM of at least three replicates.

RESULT AND DISCUSSION

Nanoparticle Preparation and Drug Loading

PLGA-PEG-NH_2 co-polymer was validated via ^{1}H NMR spectrum (**Supplementary Figure 2**). PLGA-PEG-NH_2 co-polymer showed both the characteristic peak of PLGA (methyl group: 1.44–1.83 ppm and multiple peaks: 5.17–5.40 and 4.66–4.89 ppm) and the typical peak of PEG in which the methane proton is around 3.62 ppm (CH_2-CH_2-O) and validated the successful conjugation of PLGA-PEG-NH_2. PLGA-PEG nanoparticles loaded with salinomycin and curcumin were prepared using the well-established double emulsion solvent evaporation method (Avgoustakis et al., 2002; You et al., 2018). HA was conjugated onto nanoparticles via EDC coupling and confirmed by hexadecyltrimethylammonium bromide (CTAB) turbidimetric method (Chen and Wang, 2009; Song et al., 2009). The hydrodynamic size of the nanoparticles increased from 120.1 ± 5.5 to 153.4 ± 4.6 nm after conjugation with HA, which was measured by dynamic light scattering (**Table 1**). Nanoparticle morphology was confirmed by TEM (**Supplementary Figure 1**). The surface charge also exhibited a negative zeta potential value after HA conjugation because of the negative carboxylic moiety of HA, which confirmed the conjugation of HA onto the particles. Approximately 70% of salinomycin and 82% of curcumin were loaded in polymeric nanoparticles, characterized by measuring UV-Vis spectra. Free salinomycin and curcumin molecules were separated from the solution and subsequently removed by centrifugation.

Drug Release Study

The kinetics of the drug release was evaluated over time upon their *in vitro* incubation in PBS buffer at 37°C, and the results are summarized in **Figure 1**. The higher hydrophilic moiety of PEG amount in co-polymer contributed to greater drug release. During the initial hours, there was a rapid release that led to a higher loading of salinomycin and curcumin in the vicinity of the surface and faster drug diffusion (Panagi et al., 2001; Wang et al., 2013). After 12 h, levels of salinomycin and curcumin were observed as a sustained curve, possibly due to the slow release of drugs within the polymeric matrix. Post-24 h, ∼88% of salinomycin and 90% of curcumin were released from polymeric nanoparticles when pH was 7.4. When pH was reduced to 5.0, ∼96% of salinomycin and 94% of curcumin were released. This data suggests both salinomycin and curcumin can be released from the polymeric nanoparticles under a similar condition and is expected when coming in contact with tumor tissues.

In vitro CD44-Mediated Cellular Uptake

Flow cytometry analysis was used to determine the internalization of HA-PEG-PLGA NPs by cancer cells and if this correlation is associated with the over-expression of CD44

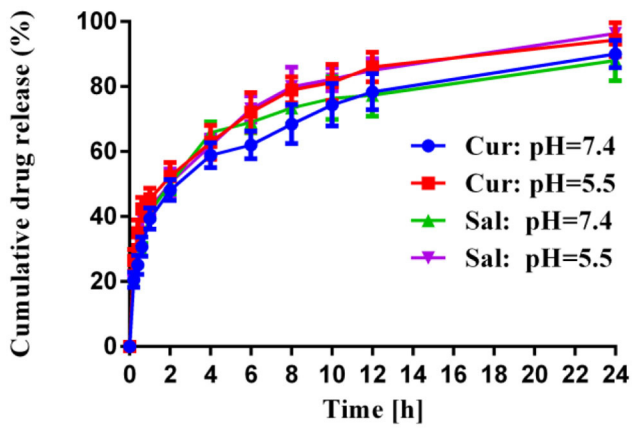

FIGURE 1 | *In vitro* release profiles of Cur and Sal from HA-PEG-PLGA-Cur-Sal nanoparticles in sodium phosphate buffer at pH 5.0 and pH 7.4 at 37°C, respectively. Error bars show mean ± standard deviation from experiments performed in triplicate.

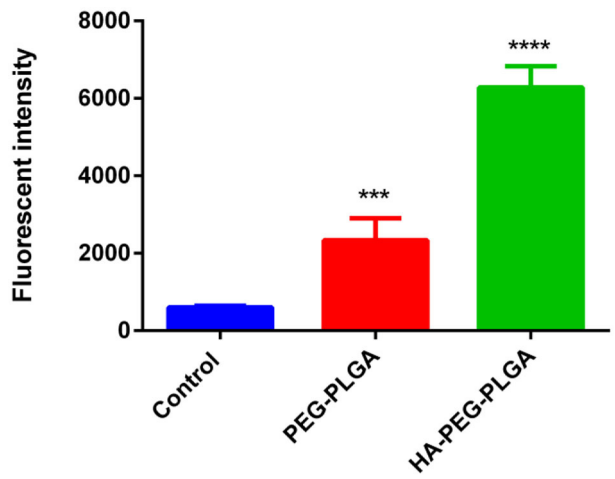

FIGURE 2 | Cell uptake of HA-PEG-PLGA NPs and PEG-PLGA NPs by flow cytometry. The BCSCs were incubated with different formulations for 6 h. Data are mean ± SD ($n = 3$) (***$p < 0.001$, ****$p < 0.0001$).

receptor. BCSCs treated with HA-PEG-PLGA NPs showed a higher fluorescence intensity than BCSCs incubated with PEG-PLGA NPs after 6 h. This is due to a HA receptor that leads to cellular internalization via HA receptor-mediated endocytosis. As shown in **Figure 2**, the cellular association of HA-PEG-PLGA NPs was approximately three times greater than non-specific PEG-PLGA NPs at 37°C. This suggests HA-PEG-PLGA NPs could enter into the cell membrane and efficiently target cells by binding with CD44 that is overexpressed in BCSCs. HA targeting ability was also confirmed by confocal fluorescence micrograph of MCF-7 cells after 4-h incubation of untargeted PEG-PLGA NPs and targeted HA-PEG-PLGA NPs at the same concentration of coumarin-6. Significant fluorescence signal of coumarin-6 was observed in HA-PEG-PLGA NPs (**Supplementary Figure 3**).

In vitro Cell Proliferation and Viability

The *in vitro* cytotoxicity analysis was grouped as follows: HA-PEG-PLGA-Cur-Sal, PEG-PLGA-Cur-Sal, PEG-PLGA-Cur, PEG-PLGA-Sal, PEG-PLGA, Cur, and Sal. These compounds were evaluated against BCSCs by using cell proliferation assay with an incubation period of 144 h. The cytotoxicity data of BCSCs summarized in **Figure 3A** show the different formulations using a series of eight different concentrations of Sal and each group received the same corresponding Sal concentration. Cur was kept at a constant concentration. From **Figure 3A**, HA-PEG-PLGA-Cur-Sal, which has a specific affinity with over-expressed CD44 receptor, showed the greatest cytotoxicity as compared to the remaining formulations at the same drug concentration. Additionally, PEG-PLGA-Cur-Sal showed increased cytotoxicity compared to formulations containing either Cur or Sal. ED50 values were derived as described by Tallarida (2011), and synergism was observed in both HA-PEG-PLGA-Cur-Sal and PEG-PLGA-Cur-Sal that exhibited a super-additive effect.

Cell Cycle Arrest Study

Chemotherapeutic drugs are highly toxic to the progression of cell cycle and thus can promote cellular death. To determine whether the drugs and their formulations cause cell cycle arrest, we investigate cell cycle progression by flow cytometry. The G1 phase of cell cycle is the initial cell cycle phase in which cells progress for subsequent duplication of itself. As shown in **Figure 3B**, both HA-PEG-PLGA-Cur-Sal and PEG-PLGA-Cur-Sal can significantly prolong the G_1/S phase of the cell cycle, while HA-PEG-PLGA-Cur-Sal promoted G_1/S arrest to a greater extent than the PEG-PLGA-Cur-Sal group. This suggests that HA-PEG-PLGA-Cur-Sal is the most effective in preventing BCSCs from subsequent progression into S-phase in which the genome duplication occurs. This indicates that co-delivery of salinomycin and curcumin causes extensive G_1/S arrest, leading to the subsequent activation of apoptosis.

Cell Migration and EMT

BCSCs play a pivotal role in migration, which is essential for the pathogenesis of cancer during invasion and metastasis. Conversely, lack of cellular migration can lead to a failure in regenerative therapies. To validate cell migration *in vitro*, we adopted wound-healing assay which is widely used as a model to determine cell migration *in vivo*. As shown in **Figures 4A,B**, BCSCs treated with HA-PEG-PLGA-Cur-Sal showed significant reduction of cell migration in both wound length and rate of wound closure when compared to other treated groups.

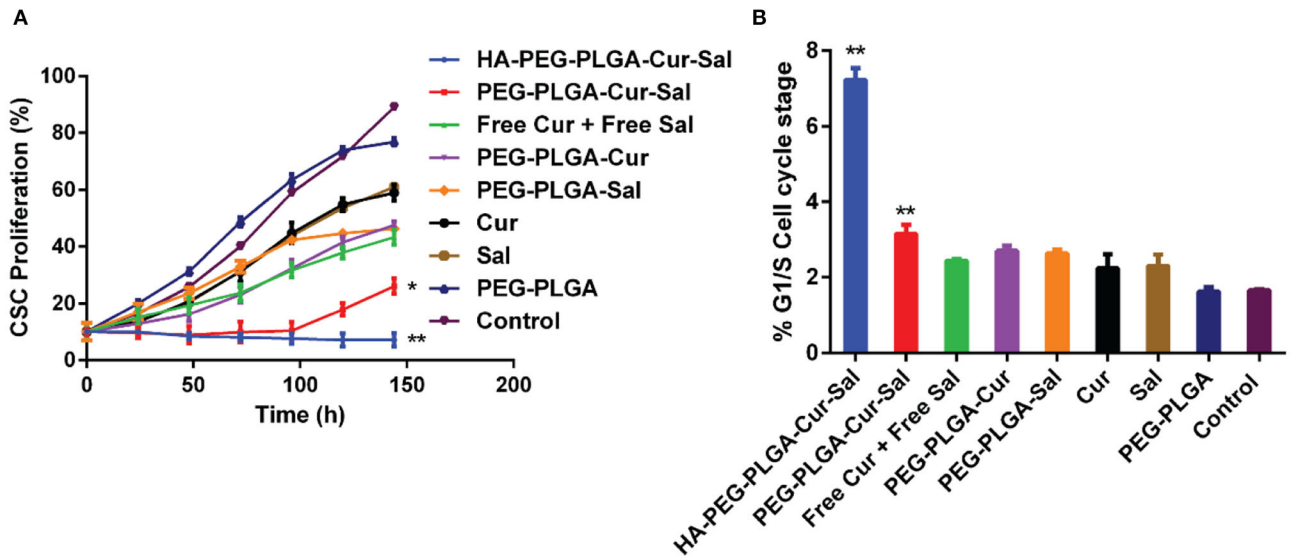

FIGURE 3 | (A) Cell proliferation study of HA-PEG-PLGA-Cur-Sal, PEG-PLGA-Cur-Sal, PEG-PLGA-Cur, PEG-PLGA-Sal, PEG-PLGA, Cur, and Sal against CSCs. **(B)** Cell cycle arrest study of HA-PEG-PLGA-Cur-Sal, PEG-PLGA-Cur-Sal, PEG-PLGA-Cur, PEG-PLGA-Sal, PEG-PLGA, Cur, and Sal against CSCs. Values are means ± standard deviations ($n = 5$, S.D.) (*$p < 0.05$, **$p < 0.01$).

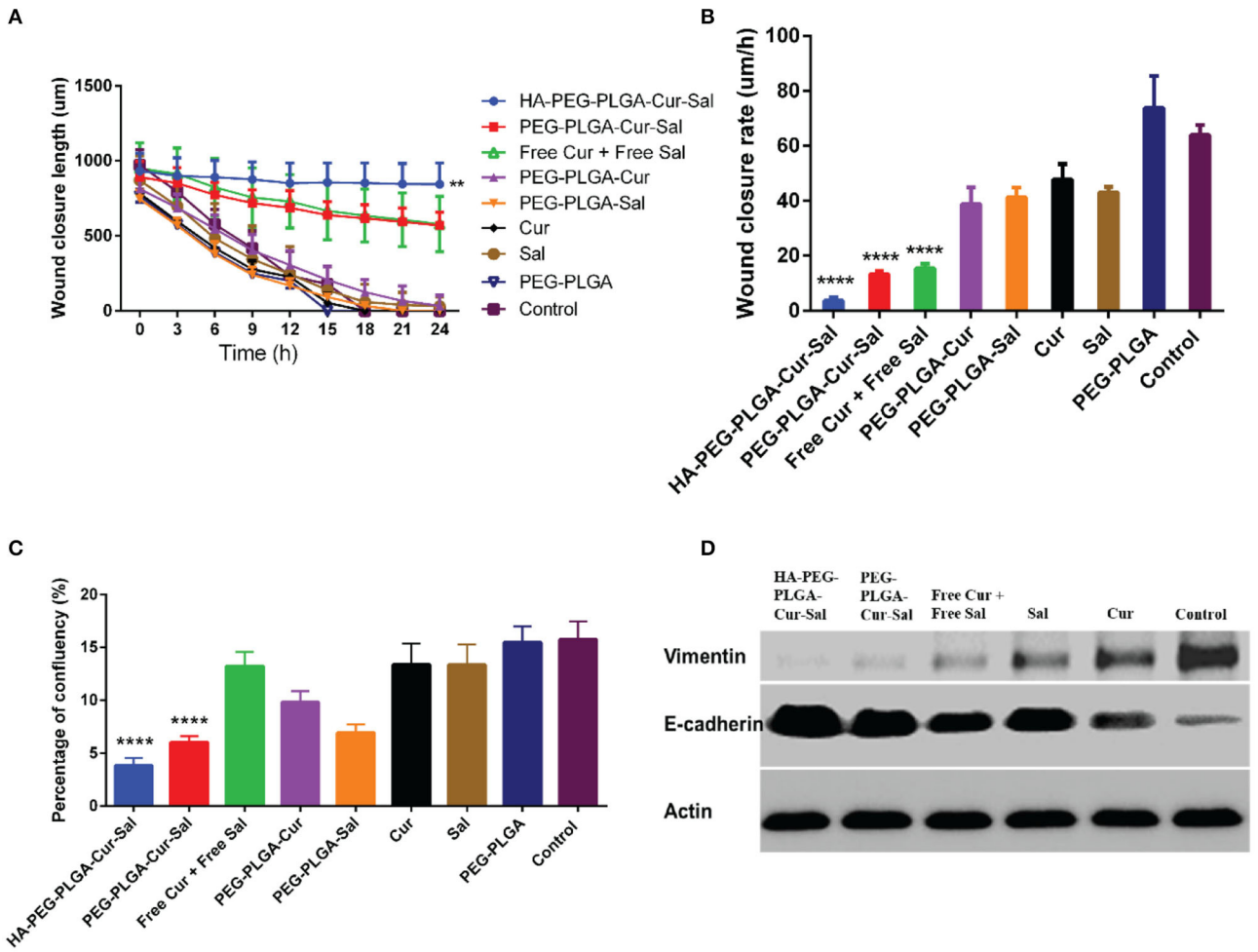

FIGURE 4 | Cell migration behavior after treatment of PEG-PLGA-Cur, PEG-PLGA-Sal, PEG-PLGA, Cur, and Sal against CSCs using wound healing assay: **(A)** wound closure length, **(B)** wound closure rate, and **(C)** percentage of confluency of wound healing assay. **(D)** Expression of epithelial–mesenchymal transition markers of HA-PEG-PLGA-Cur-Sal, PEG-PLGA-Cur-Sal, free Cur + free Sal, Cur, and Sal. Values are means ± standard deviations ($n = 5$, S.D.) (**$p < 0.01$, ****$p < 0.0001$).

The lack of migration has a direct impact on cancer cell invasion and tumor metastasis. In **Figure 4C**, data indicated BCSCs that received HA-PEG-PLGA-Cur-Sal treatment had the lowest cellular confluency during cell attachment assay due to its reduced adhesion ability of BCSCs. **Figure 4D** shows that the immunoblotting of vimentin (mesenchymal marker) and E-cadherin (epithelial maker) confirmed HA-PEG-PLGA-Cur-Sal could reverse the properties of EMT, thereby limiting BCSCs to migrate.

TABLE 1 | Hydrodynamic size and drug loading of the nanoparticles.

Sample	D_h (nm)[a]	Zeta potential (mV)	Sal loading (%)[b]	Cur loading (%)[b]
PEG-PLGA-Cur-Sal	120.1 ± 5.5	−3.1 ± 0.2	70	82
HA-PEG-PLGA-Cur-Sal	153.4 ± 4.6	−32.6 ± 2.5	–	–

[a] *Determined by DLS.*
[b] *Determined by UV-Vis spectroscopy.*

CONCLUSION

In summary, PLGA nanoparticle delivery system co-loaded with anticancer drug Sal and Cur was successfully synthesized and functionalized with HA as a targeting moiety. BCSCs showed higher sensitivity to this formulation with a combination of Sal and Cur by not only efficiently inducing cell death but also inhibiting cell migration and attachment. Our study revealed HA-PEG-PLGA-Cur-Sal could impede G1 phase cell cycle progression, leading to cell cycle arrest and subsequent induction of induced apoptosis of BCSCs. Collectively, our findings suggest that the combination HA-PEG-PLGA-Cur-Sal is an efficient therapeutic strategy against BCSCs and

has the potential of treating tumor metastasis and improve patient outcome.

DATA AVAILABILITY STATEMENT

The raw data supporting the conclusions of this article will be made available by the authors, without undue reservation.

AUTHOR CONTRIBUTIONS

YZha: methodology and data interpretation and writing—original draft preparation. KW: methodology and data interpretation. YZhe: experiments and data collection. YL: methodology validation and review. TL: conceptualization, supervision, and manuscript editing. XZ: revision of manuscript. All authors contributed to the article and approved the submitted version.

FUNDING

TL was supported by the National Health and Medical Research Council (NHMRC) Early Career Fellowship (Grant No. 1112258) and the WSU Vice-Chancellor's Research Fellowship. YZha was supported by the National Science Foundation of the Jiangsu Higher Education Institutions of China (Grant No. 19KJD350002) and the Jiangsu's Mass Entrepreneurship and Innovation Program. XZ was supported by the Natural Science Foundation of Nantong City (JC2018126).

SUPPLEMENTARY MATERIAL

The Supplementary Material for this article can be found online at: https://www.frontiersin.org/articles/10.3389/fchem.2020.601649/full#supplementary-material

REFERENCES

Alam, N., Koul, M., Mintoo, M. J., Khare, V., Gupta, R., Rawat, N., et al. (2017). Development and characterization of hyaluronic acid modified PLGA based nanoparticles for improved efficacy of cisplatin in solid tumor. *Biomed. Pharmacother.* 95, 856–864. doi: 10.1016/j.biopha.2017.08.108

Avgoustakis, K., Beletsi, A., Panagi, Z., Klepetsanis, P., Karydas, A. G., and Ithakissios, D. S. (2002). PLGA-mPEG nanoparticles of cisplatin: *in vitro* nanoparticle degradation, *in vitro* drug release and *in vivo* drug residence in blood properties. *J. Control. Release* 79, 123–135. doi: 10.1016/S0168-3659(01)00530-2

Baek, O.-S., Kang, O.-H., Choi, Y.-A., Choi, S.-C., Kim, T.-H., Nah, Y.-H., et al. (2003). Curcumin inhibits protease-activated receptor-2 and−4-mediated mast cell activation. *Clin. Chim. Acta* 338, 135–141. doi: 10.1016/j.cccn.2003.08.015

Basnet, P., and Skalko-Basnet, N. (2011). Curcumin: an anti-inflammatory molecule from a curry spice on the path to cancer treatment. *Molecules* 16, 4567–4598. doi: 10.3390/molecules16064567

Buhrmann, C., Yazdi, M., Dezfouli, A. B., Sahraneshin, F. S., and Shayan, P. (2020). Significant decrease in the viability and tumor stem cell marker expression in tumor cell lines treated with curcumin. *J. Herb. Med.* 22:100339. doi: 10.1016/j.hermed.2020.100339

Chen, Y.-H., and Wang, Q. (2009). Establishment of CTAB turbidimetric method to determine hyaluronic acid content in fermentation broth. *Carbohydr. Polym.* 78, 178–181. doi: 10.1016/j.carbpol.2009.04.037

Cho, K., Wang, X., Nie, S., Chen, Z., and Shin, D. M. (2008). Therapeutic nanoparticles for drug delivery in cancer. *Clin. Cancer Res.* 14, 1310–1316. doi: 10.1158/1078-0432.CCR-07-1441

Fan, F., Samuel, S., Gaur, P., Lu, J., Dallas, N. A., Xia, L., et al. (2011). Chronic exposure of colorectal cancer cells to bevacizumab promotes compensatory pathways that mediate tumour cell migration. *Br. J. Cancer* 104, 1270–1277. doi: 10.1038/bjc.2011.81

Ganesh, S., Iyer, A. K., Morrissey, D. V., and Amiji, M. M. (2013). Hyaluronic acid based self-assembling nanosystems for CD44 target mediated siRNA delivery to solid tumors. *Biomaterials* 34, 3489–3502. doi: 10.1016/j.biomaterials.2013.01.077

Gao, C., Tang, F., Gong, G., Zhang, J., and Wang, R. (2017). pH-Responsive prodrug nanoparticles based on a sodium alginate derivative for selective co-release of doxorubicin and curcumin into tumor cells. *Nanoscale* 9, 12533–12542. doi: 10.1039/C7NR03611F

Gupta, P. B., Onder, T. T., Jiang, G., Tao, K., Kuperwasser, C., Weinberg, R. A., et al. (2009). Identification of selective inhibitors of cancer stem cells by high-throughput screening. *Cell* 138, 645–659. doi: 10.1016/j.cell.2009.06.034

Ketola, K., Hilvo, M., Hyötyläinen, T., Vuoristo, A., Ruskeepää, A. L., Orešič, M., et al. (2012). Salinomycin inhibits prostate cancer growth and migration via induction of oxidative stress. *Br. J. Cancer* 106, 99–106. doi: 10.1038/bjc.2011.530

Kotcherlakota, R., Barui, A. K., Prashar, S., Fajardo, M., Briones, D., Rodríguez-Diéguez, A., et al. (2016). Curcumin loaded mesoporous silica: an effective drug delivery system for cancer treatment. *Biomater. Sci.* 4, 448–459. doi: 10.1039/C5BM00552C

Lim, Y. C., Ensbey, K. S., Offenhäuser, C., D'Souza, R., Cullen, J. K., Stringer, B. W., et al. (2020). Simultaneous targeting of DNA replication and homologous recombination in glioblastoma with a polyether ionophore. *Neuro Oncol.* 22, 216–228. doi: 10.1093/neuonc/noz159

Lu, D., Choi, M. Y., Yu, J., Castro, J. E., Kipps, T. J., and Carson, D. A. (2011). Salinomycin inhibits Wnt signaling and selectively induces apoptosis in chronic lymphocytic leukemia cells. *Proc. Natl. Acad. Sci. U.S.A.* 108, 13253–13257. doi: 10.1073/pnas.1110431108

Mai, T. T., Hamai, A., Hienzsch, A., Caneque, T., Muller, S., Wicinski, J., et al. (2017). Salinomycin kills cancer stem cells by sequestering iron in lysosomes. *Nat. Chem.* 9, 1025–1033. doi: 10.1038/nchem.2778

Motevalli, S. M., Eltahan, A. S., Liu, L., Magrini, A., Rosato, N., Guo, W., et al. (2019). Co-encapsulation of curcumin and doxorubicin in albumin nanoparticles blocks the adaptive treatment tolerance of cancer cells. *Biophys. Rep.* 5, 19–30. doi: 10.1007/s41048-018-0079-6

Naujokat, C., and Steinhart, R. (2012). Salinomycin as a drug for targeting human cancer stem cells. *J. Biomed. Biotechnol.* 2012:950658. doi: 10.1155/2012/950658

Norris, L., Karmokar, A., Howells, L., Steward, W. P., Gescher, A., and Brown, K. (2013). The role of cancer stem cells in the anti-carcinogenicity of curcumin. *Mol. Nutr. Food Res.* 57, 1630–1637. doi: 10.1002/mnfr.201300120

Panagi, Z., Beletsi, A., Evangelatos, G., Livaniou, E., Ithakissios, D. S., and Avgoustakis, K. (2001). Effect of dose on the biodistribution and pharmacokinetics of PLGA and PLGA–mPEG nanoparticles. *Int. J. Pharm.* 221, 143–152. doi: 10.1016/S0378-5173(01)00676-7

Paulus, E. F., Kurz, M., Matter, H., and Vértesy, L. (1998). Solid-state and solution structure of the salinomycin–sodium complex: stabilization of different conformers for an ionophore in different environments. *J. Am. Chem. Soc.* 120, 8209–8221. doi: 10.1021/ja973607x

Sanfilippo, V., Caruso, V. C. L., Cucci, L. M., Inturri, R., Vaccaro, S., and Satriano, C. (2020). Hyaluronan-metal gold nanoparticle hybrids for targeted tumor cell therapy. *Int. J. Mol. Sci.* 21:3085. doi: 10.3390/ijms21093085

Shanmugam, M. K., Rane, G., Kanchi, M. M., Arfuso, F., Chinnathambi, A., Zayed, M. E., et al. (2015). The multifaceted role of curcumin in cancer prevention and treatment. *Molecules* 20, 2728–2769. doi: 10.3390/molecules20022728

Shao, N., Jia, H., Li, Y., and Li, J. (2017). Curcumin improves treatment outcome of takayasu arteritis patients by reducing TNF-α: a randomized

placebo-controlled double-blind clinical trial. *Immunol. Res.* 65, 969–974. doi: 10.1007/s12026-017-8917-z

Sharma, R. A., Gescher, A. J., and Steward, W. P. (2005). Curcumin: the story so far. *Eur. J. Cancer* 41, 1955–1968. doi: 10.1016/j.ejca.2005.05.009

Song, J.-M., Im, J.-H., Kang, J.-H., and Kang, D.-J. (2009). A simple method for hyaluronic acid quantification in culture broth. *Carbohydr. Polym.* 78, 633–634. doi: 10.1016/j.carbpol.2009.04.033

Tallarida, R. J. (2011). Quantitative methods for assessing drug synergism. *Genes Cancer* 2, 1003–1008. doi: 10.1177/1947601912440575

Teiten, M. H., Dicato, M., and Diederich, M. (2014). Hybrid curcumin compounds: a new strategy for cancer treatment. *Molecules* 19, 20839–20863. doi: 10.3390/molecules191220839

Tsai, Y. M., Chien, C. F., Lin, L. C., and Tsai, T. H. (2011). Curcumin and its nano-formulation: the kinetics of tissue distribution and blood-brain barrier penetration. *Int. J. Pharm.* 416, 331–338. doi: 10.1016/j.ijpharm.2011.06.030

Wang, H., Jia, Y., Hu, W., Jiang, H., Zhang, J., and Zhang, L. (2013). Effect of preparation conditions on the size and encapsulation properties of mPEG-PLGA nanoparticles simultaneously loaded with vincristine sulfate and curcumin. *Pharm. Dev. Technol.* 18, 694–700. doi: 10.3109/10837450.2012.696267

Wang, Q., Wu, P., Ren, W., Xin, K., Yang, Y., Xie, C., et al. (2014). Comparative studies of salinomycin-loaded nanoparticles prepared by nanoprecipitation and single emulsion method. *Nanoscale Res. Lett.* 9:351. doi: 10.1186/1556-276X-9-351

You, L., Wang, J., Liu, T., Zhang, Y., Han, X., Wang, T., et al. (2018). Targeted brain delivery of rabies virus glycoprotein 29-modified deferoxamine-loaded nanoparticles reverses functional deficits in parkinsonian mice. *ACS Nano* 12, 4123–4139. doi: 10.1021/acsnano.7b08172

Yue, W., Hamai, A., Tonelli, G., Bauvy, C., Nicolas, V., Tharinger, H., et al. (2013). Inhibition of the autophagic flux by salinomycin in breast cancer stem-like/progenitor cells interferes with their maintenance. *Autophagy* 9, 714–729. doi: 10.4161/auto.23997

Zhao, Y., Zhao, W., Lim, Y. C., and Liu, T. (2019). Salinomycin-loaded gold nanoparticles for treating cancer stem cells by ferroptosis-induced cell death. *Mol. Pharm.* 16, 2532–2539. doi: 10.1021/acs.molpharmaceut.9b00132

Zhou, H., Beevers, C. S., and Huang, S. (2011). The targets of curcumin. *Curr. Drug Targets* 12, 332–347. doi: 10.2174/138945011794815356

Zöller, M. (2011). CD44: can a cancer-initiating cell profit from an abundantly expressed molecule? *Nat. Rev. Cancer* 11, 254–267. doi: 10.1038/nrc3023

Conflict of Interest: The authors declare that the research was conducted in the absence of any commercial or financial relationships that could be construed as a potential conflict of interest.

Copyright © 2021 Zhao, Wang, Zheng, Zeng, Lim and Liu. This is an open-access article distributed under the terms of the Creative Commons Attribution License (CC BY). The use, distribution or reproduction in other forums is permitted, provided the original author(s) and the copyright owner(s) are credited and that the original publication in this journal is cited, in accordance with accepted academic practice. No use, distribution or reproduction is permitted which does not comply with these terms.

frontiers in Chemistry

REVIEW
published: 10 March 2021
doi: 10.3389/fchem.2021.613209

Viral Mimicry as a Design Template for Nucleic Acid Nanocarriers

*Ina F. de la Fuente, Shraddha S. Sawant, Mark Q. Tolentino, Patrick M. Corrigan and Jessica L. Rouge**

Department of Chemistry, University of Connecticut, Storrs, CT, United States

Therapeutic nucleic acids hold immense potential in combating undruggable, gene-based diseases owing to their high programmability and relative ease of synthesis. While the delivery of this class of therapeutics has successfully entered the clinical setting, extrahepatic targeting, endosomal escape efficiency, and subcellular localization remain as major roadblocks. On the other hand, viruses serve as natural carriers of nucleic acids and have acquired a plethora of structures and mechanisms that confer remarkable transfection efficiency. Thus, understanding the structure and mechanism of viruses can guide the design of synthetic nucleic acid vectors. This review revisits relevant structural and mechanistic features of viruses as design considerations for efficient nucleic acid delivery systems. This article explores how viral ligand display and a metastable structure are central to the molecular mechanisms of attachment, entry, and viral genome release. For comparison, accounted for are details on the design and intracellular fate of existing nucleic acid carriers and nanostructures that share similar and essential features to viruses. The review, thus, highlights unifying themes of viruses and nucleic acid delivery systems such as genome protection, target specificity, and controlled release. Sophisticated viral mechanisms that are yet to be exploited in oligonucleotide delivery are also identified as they could further the development of next-generation nonviral nucleic acid vectors.

Keywords: nucleic acid delivery, viral mimicry, endosomal escape, nuclear targeting, nanoparticles

OPEN ACCESS

Edited by:
Chun Xu,
The University of Queensland,
Brisbane, Qld, Australia

Reviewed by:
Chad A. Mirkin,
Northwestern University, Evanston, IL, United States
Kai Ewert,
University of California, Santa Barbara, CA, United States

****Correspondence:***
Jessica L. Rouge
jessica.rouge@uconn.edu

Specialty section:
This article was submitted to Nanoscience, a section of the journal Frontiers in Chemistry

Received: *01 October 2020*
Accepted: *06 January 2021*
Published: *10 March 2021*

Citation:
de la Fuente IF, Sawant SS, Tolentino MQ, Corrigan PM and Rouge JL (2021) Viral Mimicry as a Design Template for Nucleic Acid Nanocarriers. Front. Chem. 9:613209. doi: 10.3389/fchem.2021.613209

INTRODUCTION

Undruggable targets are disease-implicated proteins that lack easy-to-bind pockets where conventional therapeutics like small molecules can bind (Crews, 2010; Duffy and Crown, 2021). However, around 80% of the human proteome is difficult to reach or target (Verdine and Walensky, 2007). The past decade has shown enormous progress in targeting the previously thought to be unreachable sites such as growth factors, enzymes, defective genes, or nuclear transcription factors (Lazo and Sharlow, 2016). In particular, therapeutic nucleic acids such as small interfering RNAs (siRNAs), microRNAs (miRNAs), antisense oligonucleotides (ASOs), synthetic messenger RNAs (mRNAs), and CRISPR-Cas9-guide RNAs are programmable, easy to synthesize, and thus have the potential to treat previously undruggable diseases such as cancer and viral diseases (Dowdy, 2017). They hold great promise in treating the root cause of the disease rather than just treating the symptoms by targeting the mutated genes, mRNA, or proteins with high specificity and selectivity (Keefe et al., 2010; Damha 2019). The challenge lies in delivery (Juliano, 2016; Dowdy, 2017; Dowdy and Levy, 2018; Johannes and Lucchino, 2018; Juliano, 2018).

For billions of years, cells have evolved to keep genomic material on one side of the membrane. Thus, transfection by bare nucleic acids across an anionic lipid barrier is fundamentally prevented by

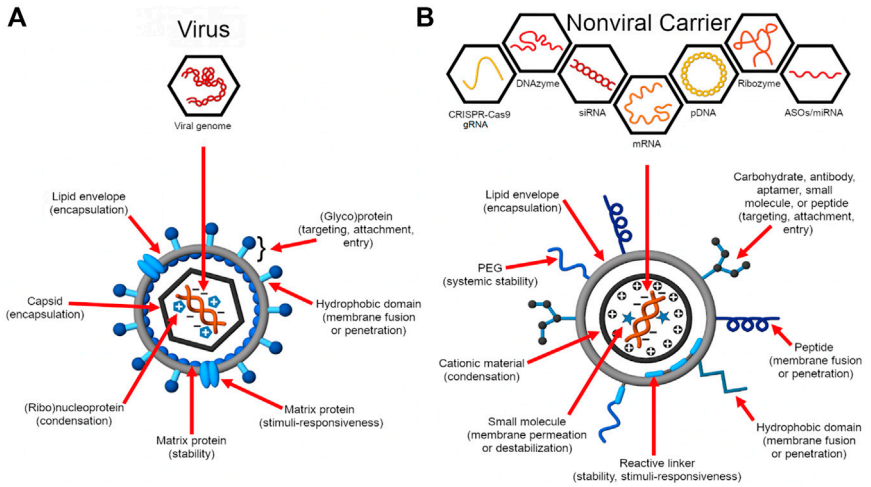

FIGURE 1 | Virus structure and function inform the design of nucleic acid delivery systems. **(A)** Viruses evolve to deliver their genome efficiently to the host cell for replication (Flint et al., 2015). As such, their genome encodes proteins essential for genome protection, tropism, intracellular trafficking, controlled genome release, and replication. **(B)** Synthetic carriers are designed to deliver a diversity of therapeutic nucleic acid cargo including pDNA, siRNA, ASOs, miRNA, mRNA, CRISPR-Cas9 guide RNAs (gRNAs), ribozymes, and DNAzymes (Ni et al., 2016; Ni et al., 2019). Analogous to viruses, functional domains are embedded on the construct that enable a balance between nucleic acid protection and programmed, stimulus-induced release.

the large size and density of negative charges (Dowdy, 2017; Dowdy and Levy, 2018; Johannes and Lucchino, 2018). Furthermore, medical translation necessitates a successful *in vivo* delivery. This is particularly challenging given the limited systemic stability of unmodified nucleic acids. Thus, an ideal delivery strategy should include nucleic acid protection from nuclease degradation and oxidation, prolonged systemic circulation, targeted delivery, efficient transfection across a membrane, facilitated access to the cytoplasm or nucleus, and little to no side effects (Zhu and Mahato, 2010). While progress has been made in designing and implementing safe, effective, and efficient nucleic acid delivery systems, realizing their therapeutic potential is, at present, challenged mainly by the lack of cellular target diversity and endosomal escape ability (Dowdy, 2017; Dowdy and Levy, 2018; Johannes and Lucchino, 2018; Juliano, 2018).

In contrast, viruses have evolved a diversity of enabling architectures for the infiltration of various host cells and controlled viral genome replication using the host cell machinery (Flint et al., 2015). While they have become longstanding models for engineering the transfection of therapeutic nucleic acids (**Figure 1**) (Ni et al., 2016), their delivery efficiency far outplays that of synthetic vectors (Ramamoorth and Narvekar, 2015). This underscores how our current molecular understanding of viral function and how this relates to nucleic acid transfection can be improved to achieve more effective translation to rational design.

This review, therefore, details the structure and intracellular fate of existing nucleic acid delivery strategies whose designs are either directly inspired by viruses or their resulting formulation exhibits many similarities to that of viruses. Hence, relevant structural and mechanistic features of viruses as design considerations for viable nucleic acid delivery systems are examined. This article also explores how a dynamic and stimulus-responsive structure can play an important role in designing an effective nucleic acid carrier. Importantly, it also highlights how sophisticated ligand display is central to the molecular mechanisms of carrier trafficking and nucleic acid release.

GENERAL STRUCTURE OF NUCLEIC ACID CARRIERS AND MECHANISM OF PROTECTION

An ideal carrier packs, stores, and protects nucleic acid cargo until it has reached the target site. In that regard, this section provides examples of select viruses and nonviral nucleic acid vectors and discusses their structural features relevant to the efficient packing and protection of nucleic acids. **Figure 2** presents examples of common viruses to show that despite differences in sizes and shapes, viruses collectively protect their genome through condensation and encapsulation. In addition to these two mechanisms of nucleic acid protection, nonviral carriers also use chemical modifications, self-generated sterics, or a combination of these strategies to achieve the same effect.

Structure of Viruses and Genome Protection

Viruses are obligate intracellular parasites (Gelderblom, 1996). They have evolved to transfect their DNA or RNA genome into the host cell for expression and subsequent production of more virus particles (Prasad and Schmid, 2011). At the core of virus structure are structural proteins that serve to protect the viral

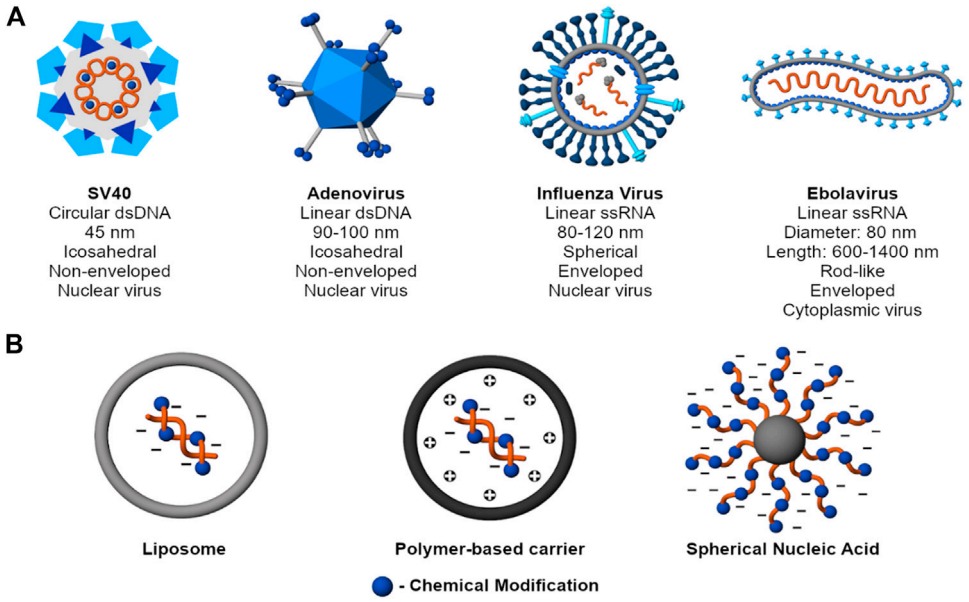

FIGURE 2 | Mechanisms to protect nucleic acid cargo. **(A)** Examples of common viruses (SV40 - Martini et al. 2007; Adenovirus - Greber et al., 1997; Russel, 2009; Influenza Virus - James and Whitley, 2017; Ebolavirus - Beniac et al., 2012; Falasca et al., 2015). Despite structural diversity, viruses collectively protect their genome through charge condensation and encapsulation by a capsid and, for an enveloped virus, an outer lipid membrane. **(B)** Examples of nonviral nucleic acid delivery systems. Beyond condensation and encapsulation, nonviral carriers also use chemical modifications, self-generated sterics, or a combination of strategies to achieve the same purpose.

genome until it is delivered to the target site. These structural proteins assemble to form the viral capsid, which is the protein coat that wraps around the genome. The high degree of folding and dense packing of capsid proteins protect them from proteolytic digestion, making them stable carriers of nucleic acid cargo (Flint et al., 2015). Moreover, the viral genome is typically condensed by viral proteins through charge neutralization (Gelderblom, 1996), allowing confinement within the interior of the capsid. Enveloped viruses possess an outer lipid envelope that provides additional encapsulation and can fuse with the host plasma membrane during uptake or endosomal escape. The protein components encoded by the viral genome display highly specific and often, multiple, roles essential for structural integrity, attachment, and replication in the host cell (Flint et al., 2015).

For example, the main components of the influenza virus are the lipid bilayer, glycoprotein spikes hemagglutinin (HA) and neuraminidase (NA), matrix proteins (M1 and M2), the heterotrimeric RNA-dependent RNA polymerase (RdRP), the viral RNA segments, a nucleoprotein (NP), and two nonstructural proteins (NS1 and NS2 a.k.a. nuclear export protein or NEP). The outermost layer of the virus is a lipid membrane decorated with glycoproteins that, in turn, may be recognized by antibodies to protect the host against infection (James and Whitley, 2017). Thus, these glycoproteins are critical in both immune response and the development of therapeutics. Hemagglutinin, specifically its subunit HA1, is responsible for the targeting of and uptake by the host cells. HA1 binds to sialic acid functionalized cell surface receptors, resulting in receptor-mediated endocytosis. The lipid bilayer is stabilized by M1 on its cytoplasmic periphery and is spanned by M2, a proton ionophore. The core of the virion contains the viral genome as well as proteins essential for viral gene replication (RdRP), gene encapsulation (NP), and nuclear translocation (NEP). Each protein-coding ssRNA segment is coated by NPs and associated with an RdRP, forming a ribonucleoprotein (RNP) complex that is anchored to M1. The viral envelope of influenza virus has been used as a carrier for nucleic acids such as siRNA (de Jonge et al., 2006) and miRNA (Li J. et al., 2013). Particularly, the reconstituted influenza virus membrane envelope, called "virosome," acts as an efficient carrier to target small nucleic acid such as siRNA *in vitro* as well as *in vivo* (de Jonge et al., 2006). As per this study, the functional integrity of HA viral protein helps in membrane fusion and efficient cytosolic delivery of siRNA.

Another example is the adenovirus (AdV), one of the largest (90–100 nm) non-enveloped double stranded linear DNA viruses. The icosahedral shaped capsid is made of many structural polypeptides. Most of the capsid coat (about 75%) is composed of a hexon protein, which is held together by protein IX. A unique feature of Adv capsid is that the vertices are made of a penton protein from which fiber knobs protrude out–both of which are essential for host cell entry. The viral genome is condensed by proteins V, VII and μ and is also covalently associated with the terminal protein. The cementing protein IIIa acts as capsid stabilizing protein by linking the facets of the icosahedron (Greber et al., 1997; Fay and Panté, 2015). Adenoviral vectors have been used for delivering shRNA, siRNA (Nayerossadat et al., 2012), and large sizes of DNA (up to 38 kb). However, unlike retroviruses, these cannot integrate the

carried DNA into the host genome. Thus, the desired gene expression is limited. Also, the immunogenic response caused by adenoviral infection and low cell specificity limits the use of such viral vector only to few tissues such as lungs and liver (Vorburger and Hunt, 2002).

Despite the structural and mechanistic differences among viruses, all viral capsids are metastable, which means they are stable enough to protect the genome until they reach the target site to uncoat it. Thus, the virus construct is spring-loaded in that potential energy is stored during its assembly. Upon reaching the target site, a chemical trigger such as low pH or proteolytic enzymes overcome the energetic barrier, resulting in virus disassembly and uncoating of the genome. Metastability is achieved by the inherent symmetrical arrangement of identical capsid protein subunits that is stabilized by nonspecific noncovalent interactions. In this regard, many capsid proteins self-assemble into virus-like particles (VLPs) (Flint et al., 2015).

VLPs are non-infectious, multiprotein complexes that mimic the viral capsid assembly but are devoid of the genome. Their utility as experimental tools and as therapeutic carriers has been thoroughly reviewed elsewhere (Rohovie et al., 2017; Roldão et al., 2017). Recombinant versions with attenuated or inactivated antigens can also be reconstructed from complementary DNA of a viral genome. While VLPs are historically produced and extracted from the natural hosts themselves, nowadays they are primarily produced through various cell cultures (Roldão et al., 2017). The use of mammalian and non-mammalian cells, baculoviruses, and bacteria has been reported, but VLPs are commonly expressed in yeast cells due to the relative ease of protein expression, scalability, and lower production cost compared to mammalian and insect cells (Kim and Kim, 2017; Roldão et al., 2017).

Like viruses, VLPs have been successfully used in developing vaccines and vaccine adjuvants, and their use in gene therapy and immunotherapy has also been explored (Rohovie et al., 2017; Roldão et al., 2017). Some of those that have shown potential for nucleic acid delivery include bacteriophage-based MS2 (Pan et al., 2012a; Pan et al., 2012b), bacteriophage-based M13 (Yata et al., 2014), animal virus-based hepatitis B virus core (Brandenburg et al., 2005), and plant-based cowpea chlorotic mottle virus (Lam and Steinmetz, 2019).

Target specificity can be tailored by chemical conjugation or directly expressing targeting ligands on the protein coat (Rohovie et al., 2017). For example, Yata et al. (2014) demonstrated the use of a hybrid VLP/cationic polymer-based system for efficient gene transfer. The construct specifically used bacteriophage M13 that was genetically modified to express the RGD peptide on its surface for tumor targeting and was complexed with a cationic polymer for enhanced cellular uptake. Similarly, Lam and Steinmetz (2019) recently delivered siRNA for the knockdown of GFP and FOXA1 target genes using cowpea chlorotic mottle VLPs. With an $SM(PEG)_4$ crosslinker, the VLPs were chemically labeled with m-lycotoxin, a cell-penetrating peptide, to enhance cellular uptake.

Strategies for Nucleic Acid Protection by Nonviral Carriers

While the ability of viruses and VLPs to efficiently encapsulate and transfect nucleic acids is remarkable, they are structurally more complex and, thus, typically require hosts for production and subsequent purification (Roldão et al., 2017), both of which may come at a high cost. Moreover, viruses and VLPs have a higher risk of triggering an immune response (Xue et al., 2015) and possess limited chemistry (Wagner, 2012). Therefore, tuning properties such as target specificity, particle stability, and subcellular localization is restricted, motivating the construction of non-viral vectors (Wagner, 2012). Beyond condensation and encapsulation, this section lists other strategies that have been employed for efficient protection of nucleic acid cargo such as chemical modifications and self-generated sterics. Furthermore, these strategies are often combined for enhanced protection.

Condensation by Cationic Materials

Viral assembly mainly involves electrostatic interactions between the capsid proteins and genomic cargo. Similarly, many first-generation designs of delivery agents relied on the electrostatic masking of the polyanionic backbone of nucleic acids for successful delivery into cells. Whereas viruses protect their nucleic acid cargo via capsid encapsulation, cationic materials such as natural and synthetic polymers, dendrimers, proteins, peptides, and cationic lipids as well as inorganic nanoparticles bearing a positive charge (to be discussed in Section *Utility of Inorganic Nanoparticles*) form an electrostatic interaction with the negative phosphate backbone of the nucleic acid cargo, providing protection from nuclease degradation (Ferrari et al., 1999; Moret et al., 2001; Thomas and Klibanov, 2003). This can be ascribed to the compaction of nucleic acids, which results in the blockage of enzymatic digestion sites, thereby conferring nuclease protection (Feng et al., 2015).

Electrostatic interactions also strengthen viral attachment to the surface of negatively—charged host cells. Thus, viruses such as the hepatitis C virus (Penin et al., 2001) and the influenza virus (Arinaminpathy and Grenfell, 2010) have conserved cationic regions in their glycoproteins that aid in membrane binding. In the same light, synthetic polycationic nucleic acid carriers not only allow compaction and protection from nuclease degradation but they also mediate cellular attachment and entry (Mislick and Baldeschwieler, 1996). However, this uptake mechanism is nonspecific, and polymeric materials tend to form aggregates with components of the blood such as serum proteins. For this reason, nonionic, hydrophilic polymers such as PEG are commonly added to confer stealth (Klibanov et al., 1990; Takemoto et al., 2014). Additionally, the structural flexibility of PEG makes its integration into different formulations very convenient. However, while PEG-ylation imparts blood compatibility and circulation longevity (Takemoto et al., 2014), it can compromise cellular uptake and/or endosomal escape (Fang et al., 2017).

To address this limitation, PEG-ylation typically involves responsive linkages that can be cleaved by cellular cues such as low pH or external stimuli such as temperature (Fang et al.,

2017). An alternative way of using cleavable PEG was demonstrated by Li and co-workers (2013) where they used MMP-7-cleavable peptides as linkers. Matrix Metalloproteinase-7 (MMP-7) belongs to a class of zinc-dependent, extracellular proteases that are overexpressed on the surface of breast tumor cells. In their construct, the outer surface of the polymer-based siRNA-delivery vector was decorated with PEG attached to the core of the particle using a peptide substrate of MMP-7. When the peptide substrate came to contact with MMP-7, the PEG outer layer was cleaved off, revealing a highly cationic dimethylaminoethyl methacrylate core that then engages the membrane, facilitating uptake. Thus, the selective attachment and entry of the resulting construct is afforded through proximity activation by MMP-7.

Peptide-based vectors tend to rely on positive charge character to condense nucleic acids for packaging and protection. In particular, these consist of cationic amphiphilic peptides that are composed of a hydrophobic and a hydrophilic domain that form a well-defined nanoparticle (Kang et al., 2019). The hydrophobic region consists of non-polar neutral amino acids whereas the hydrophilic region has polar aliphatic residues. These peptides self-assemble to form a micellular structure. Small molecule drugs and DNA can be co-delivered using these multifunctional micelle-plexes, where each peptide plays a different role. For example, displaying a cell penetrating peptide on the surface facilitates binding and entry. Histidine residues cause endosomal escape while lysine residues condense DNA. These types of complexes have been used to deliver siRNA and plasmid DNA. Recent studies have also shown that the addition of stearyl, an alkyl chain, or cholesterol to the hydrophobic domain of self-assembled peptides further enhances DNA condensation and transfection efficiency (Kang et al., 2019).

In addition, highly branched polypeptides are used as hybrid-peptide based gene delivery vehicles. This is achieved by covalently joining multi-functional peptide sequences. Functional peptides are separated by spacers such as repeats of glycine residues that confer flexibility. Nucleic acids are also packed by condensation. Redox-active disulfide bonds can be used to connect peptides in a branched fashion, delivering genes more efficiently than linear counterparts. These disulfide bonds are then reduced in the cytoplasm by glutathione to liberate the nucleic acid cargo as well as to reduce cytotoxicity. Highly branched arginine-rich polypeptides are multivalent and flexible—attributes beneficial for nucleic acid compaction and cellular entry. Many of these reducible multibranched cationic polypeptides have the potential to be non-toxic, degradable vectors for gene delivery (Kang et al., 2019).

Among various polycationic formulations, materials based on synthetic polymers such as polymeric nanoparticles, dendrimers, polymer micelles, polymersomes, polyplexes, and lipopolyplexes have benefited from their chemical diversity, relatively simple design, and potential for multi-functionality (Takemoto et al., 2014; Yuan and Li, 2017). The chemistry, molecular weight, weight relative to the nucleic acid, and overall topology of the polymer determine its stability and transfection efficiency. Intracellularly cleavable linkages are typically inserted within the polymeric chain, affording a dynamic structure that reveals the nucleic acid payload in response to a site-specific stimulus (Troiber and Wagner, 2011).

In a similar sense, multiblock copolymers impart modularity and enable multifunctionality. As an example, polymeric carriers are often based on the electrostatic condensation and shielding by a cationic polymer such as polydimethylaminoethyl methacrylate (pDMAEA). pDMAEA can then be copolymerized with a second block of p(N-(3-(1H-imidazol-1-yl)propyl)acrylamide (pImPAA) and poly(butyl acrylate) (pBA) that mediates an acid-triggered endosomal escape. PImPAA and PBA were designed based on viral membranolytic peptides, and they disrupt the endosomal membrane synergistically through electrostatic and hydrophobic interactions, respectively (Truong et al., 2013; Gillard et al., 2014). Such cationic polymer-based carriers serve as valuable tools for assessing the potency of nucleic acids under study. At this time, structural heterogeneity, imprecise surface conjugation, lack of structure-function insights, and cytotoxicity at therapeutically effective formulations currently hamper their clinical utility (Lv et al., 2006; Troiber and Wagner 2011).

Encapsulation by Lipid-Based Vectors

Nucleic acid protection through charge neutralization and condensation by cationic materials may only provide partial nuclease resistance (Moret et al., 2001). Moreover, additional encapsulation by lipid membranes to form lipopolyplexes has been shown to enhance protection from nucleases and the overall therapeutic efficacy of nucleic acids (Yen et al., 2018). For this reason, lipid-based vectors such as liposomes and solid lipid nanoparticles are commonly explored as nucleic acid carriers (Barba et al., 2019). Compared to other nucleic acid delivery systems, lipid-based carriers offer ease of manufacturing and scalability. Their lipid formulation mimics the lipid bilayer, imparting biocompatibility and conveniently facilitating cellular uptake (Ghasemiyeh and Mohammadi-Samani, 2018).

Among these, liposomes have shown the most promise (Barba et al., 2019). They are spherical vesicles made of a lipid bilayer with an aqueous core (Kulkarni et al., 2018; Barba et al., 2019) and can be designed to carry both hydrophilic and lipophilic cargo (Ghasemiyeh and Mohammadi-Samani, 2018; Barba et al., 2019). The earliest work demonstrating liposome-mediated gene delivery was in 1980 by Fraley et al. (1980) when SV40 DNA was encapsulated and delivered using large unilamellar vesicles. They found that using PS exhibited the highest delivery efficiency. Felgner et al. (1987) then showed that using synthetic cationic lipids such as DOTMA resulted in a higher transfection efficiency. Since then, cationic lipids bearing different structure modifications such as DOTAP, DOSPA, DMRIE, and DL-cholesterol have been incorporated in liposome-based gene delivery systems (Zhi et al., 2013; Yin et al., 2014). For anionic cargo such as nucleic acids, the cationic head group permits condensation of the large biomolecule (Zhi et al., 2013). Moreover, polycationic head groups such as polyamines can be used to form polycationic liposomes. These combine the ability of cationic liposomes to complex nucleic acids and that of polycations to mediate endosomal escape via the proton

sponge effect (Yamazaki et al., 2000; Sugiyama et al., 2004; Asai et al., 2011; Yonenaga et al., 2012). Nonionic lipids such as fusogenic DOPE and cholesterol can also be incorporated into the liposome to further enhance its stability and delivery efficiency (Wasungu and Hoekstra, 2006).

Modular release usually centers on the lipid formulation where the lipid envelope is destabilized either by an external stimulus such as temperature or an cellular stimulus such as low pH (Heidarli et al., 2017; Aghdam et al., 2019). As an example, Yatvin et al. (1978) introduced the idea that liposomes can preferentially release cargo at the diseased site in response to mild hyperthermic temperature (around 40°C). This was initially achieved using DPPC alone or with DSPC, which has a phase-transition temperature of 42–44°C, above which its membrane permeability increases (Kono et al., 2010; Aghdam et al., 2019). Among efforts that followed on the construction of heat-responsive liposomes (Matsumura and Maeda, 1986; Tomita et al., 1989; Maruyama et al., 1993; Gaber et al., 1995; Anyarambhatla and Needham, 1999; Needham et al., 2000), Anyarambhatla and Needham (1999) notably incorporated a lysolipid to DPPC to bring down the phase-transition temperature to a clinically achievable range (39–40°C) and initiate release within tens of seconds (Needham et al., 2000). As this design only achieved 50% cargo release within an hour at 42°C (Needham et al., 2000), succeeding studies focused on modulating the temperature-responsiveness of liposomes. One strategy is the incorporation of thermosensitive polymers that can impart a sharp and tunable phase transition temperature to the liposome. Upon heating, the polymeric components form hydrophobic domains that disrupt the lipid bilayer (Kono et al., 2010).

On the other hand, pH-sensitive liposomes exploit the differential acidification in the vicinity of malignant tumors or within endosomes for controlled release via membrane fusion or destabilization (Yatvin et al., 1980; Budker et al., 1996; Heidarli et al., 2017). Earlier anionic pH-responsive designs were constructed with a bilayer rich in PE that is stabilized by anionic lipids containing carboxylate head groups at physiological pH (Budker et al., 1996). PE typically forms an inverted hexagonal phase on its own (Chernomordik et al., 1995). Thus, when the anionic carboxylate head groups are protonated in a region of lower pH, the PE-rich bilayer is disrupted (Budker et al., 1996). While there were reports on using anionic liposomes for nucleic acid delivery (Wang and Huang 1989; Legendre and Szoka 1992), their negative charge limits both the efficient packing of polyanionic nucleic acids and interaction with the negatively charged cellular membrane. For this reason, cationic pH-sensitive liposomes were developed. These contain a weakly basic lipid component such as DOTAP and DODAP that have a pKa slightly below physiological pH (Budker et al., 1996; Sato et al., 2012).

Certain early formulations of lipid-based carriers were limited in part by toxicity and immunogenicity at high lipid concentrations, as well as by low bioavailability and low biodistribution (Zatsepin et al., 2016; Huggins et al., 2019). Overtime these formulations have been significantly improved. In addition, the ease of lipid synthesis and structural modifications permit thorough studies on structure-activity relationships and thus, enable a guided design of more efficient and safe delivery systems (Zhi et al., 2013). Furthermore, lipid-based carriers can be easily decorated with receptor ligands to target specific cell types such as tumor and angiogenic endothelial cells (Yonenaga et al., 2012). Such studies culminated in 2018 with the success of Patisiran (ONPATTRO®), a liposomal vector developed by Alnylam Pharmaceuticals, as the first US Food and Drug Administration approved synthetic carrier of siRNA into cells (Adams et al., 2018; Hoy, 2018; Wood, 2018).

Chemical Modifications

Chemical modifications may impart one or more of the following: *in vivo* stability, cellular delivery, reduced immunogenicity, and potency through enhanced target binding affinity (Judge et al., 2006; Corey, 2007; Whitehead et al., 2009). Such modifications may alter the phosphodiester backbone (phosphothiorates, boranophosphates, and locked nucleic acids), the ribose sugar (2′ modifications, 4′ thio), or the base (ribodifluorotoluyl nucleotide) (Corey 2007). In particular, 2′-O-modifications on siRNA impart nuclease resistance (Whitehead et al., 2009) and suppression of sequence-dependent immunostimulation by some sequences (Judge et al., 2005; Judge et al., 2006). Furthermore, Jackson et al. (Jackson et al., 2006) showed that by specifically modifying position two in the siRNA guide strand, off-target binding of other transcripts to the seed region is reduced. In addition, uncharged nucleic acid mimics such as peptide nucleic acids and morpholino oligomers present unique chemical properties and may improve biodistribution and efficacy. Details on the structure, properties, and applications of chemically modified nucleic acids and DNA/RNA mimics have been extensively reviewed elsewhere (Karkare and Bhatnagar, 2006; Summerton, 2006; Corey, 2007; Chery, 2016).

Utility of Inorganic Nanoparticles

Inorganic nanoparticles are emerging as appealing synthetic vectors for nucleic acid delivery owing to their unique properties such as tunable size and surface properties, multifunctional capabilities, chemical and thermal stability, and low inherent toxicity (Loh et al., 2015; Ding et al., 2014a). Incorporating nucleic acid cargo into inorganic nanoparticles can be accomplished using the following general strategies: complexation between negatively charged nucleic acid material and positively charged inorganic nanoparticle, direct conjugation of nucleic acid onto the inorganic particle with a stimuli-responsive linker, and addition of cationic amphiphilic polymer to facilitate the assembly formation between the inorganic nanoparticle and the nucleic acid (Loh et al., 2015).

Another approach to protect and deliver nucleic acid cargos is via encapsulation using metal-organic frameworks (MOFs) (Liang et al., 2015; Li Y. et al., 2019; Poddar et al., 2019; Tolentino et al., 2020). These are porous structures built from metal ions or metal clusters linked by organic ligands (Li G. et al., 2019). The nucleic acid can be accommodated in the MOF structure through electrostatic and coordination interactions. Such physical confinement and the characteristic positive

surface charge of MOFs offer effective protection of nucleic acid cargo against enzymatic degradation, which is, in many ways, analogous to viral capsids (Li Y. et al., 2019; Poddar et al., 2019).

While viruses deliver their nucleic acid cargo mostly through vesical fusion with the aid of some membrane fusion proteins (Harrison, 2008), inorganic nanoparticles do so with more complexity and hence present some formidable challenges. To achieve intracellular response, the nucleic acid cargo preferably needs to disassemble from the inorganic nanoparticle construct and escape the endosome. The mechanism by which these events (cell internalization and endosomal escape) occur depends on the identity and properties of the inorganic core, chemistry of the conjugation technique utilized, and response of other nanoparticle components to cellular or external stimuli (Sokolova and Epple, 2008). For example, magnetic iron oxide (Fe_3O_4) nanoparticle, when utilized as a delivery vehicle, can be stimulated to produce oscillating magnetic fields which could then promote more efficient endocytosis (Fouriki and Dobson, 2014). Furthermore, the inclusion of cell penetrating peptides and cationic amphiphilic polymers (e.g. polyethylenimine) as transfecting components assists in the endosomal escape via membrane destabilization and osmotic swelling, respectively (Thomas and Klibanov, 2003; Dowaidar et al., 2017). On the other hand, biocompatible MOFs like Zeolithic Imidazolate Framework-8 (ZIF-8) possess a hydrophobic and positively charged surface (Zhuang et al., 2014), which enable them to interact with the cell membrane and enable internalization through endocytosis.

A promising use of a metal nanoparticle for nucleic acid delivery is exemplified by spherical nucleic acids (SNAs). SNAs radially display a high density of nucleic acids around a spherical nanoparticle. The introduction of high concentrations of salt masks the polyanionic backbone of the nucleic acids, permitting clustering around a very small surface area (Mirkin et al., 1996; Cutler et al., 2011; Cutler et al., 2012). Moreover, the attachment of nucleic acids to a scaffold enhances their target binding affinity to complementary nucleic acids by restricting their conformational flexibility, reducing the entropic cost of binding (Lytton-Jean and Mirkin, 2005). SNAs have low immunogenicity (Massich et al., 2009) and are readily taken up by cells (Cutler et al., 2011) via caveolin-dependent endocytosis (Choi et al., 2013), eliminating the need for potentially toxic transfection agents (Cutler et al., 2011; Cutler et al., 2012). Unlike the abovementioned examples of inorganic nanoparticles, SNAs do not rely on complexation nor encapsulation to protect their nucleic acid cargo (Mirkin et al., 1996; Cutler et al., 2011; Cutler et al., 2012). The mechanism by which they protect nucleic acids is discussed more in Section *Self-Generated Sterics*.

Self-Generated Sterics

The overall 3D architecture of spherical nucleic acids (SNAs) imparts nuclease resistance through steric-shielding and enhanced local ionic strength (Seferos et al., 2009). This sterics-based mechanism of nucleic acid protection has defined an entire class of nucleic acid delivery systems. These nucleic acid displaying nanomaterials or NADNs, have recently been reviewed by Gudipati et al. (2019). While the metallic gold core provides a means of sensing and tracking the intracellular fate of the nanoconstructs (Mirkin et al., 1996; Cutler et al., 2012), it has limited therapeutic use. Thus, later generations of SNAs that have been developed contain biocompatible cores such as such proteins (Brodin et al., 2015; Samanta et al., 2020) and liposomes (Banga et al., 2014).

Designed to build upon the successful properties of SNAs, NADNs utilize densely packed oligonucleotides around a scaffold, enhancing oligonucleotide stability and permitting scavenger-mediated endocytosis but are built upon biodegradable core materials. The scaffolds of reported NADNs are chemically diverse (Rush et al., 2013; Banga et al., 2014, 2017; Awino et al., 2017; Ding et al., 2018; Roloff et al., 2018; Ruan et al., 2018) and can be programmed for responsiveness to biochemical stimuli (Awino et al., 2017; Santiana et al., 2017). For example, our lab developed nucleic acid nanocapsules (NANs) comprised of nucleic acids photochemically tethered to the surface of stimuli-responsive, crosslinked micelles (Awino et al., 2017; Santiana et al., 2017).

Overall, this section underscores that virus particles are metastable machines built to protect the viral genome and that its overall responsiveness to the environment enables it to carry out its function as an infectious particle. In a similar fashion, nonviral synthetic carriers are designed to protect nucleic acid cargo and facilitate controlled release. **Table 1** provides a summary of the structures and cellular trafficking of viral and nonviral carriers. Similar to viruses, functional components (as summarized in **Table 2**) are incorporated into the design of nonviral vectors that facilitate cellular entry (Section *Cellular Targeting, Attachment, and Entry*), endosomal escape (Section *Cytosolic Delivery*), and nuclear delivery (Section *Nuclear Delivery*).

CELLULAR TARGETING, ATTACHMENT, AND ENTRY

Tropism is the ability of viruses to target specific cell types by binding their surface protein or peptide ligands to specific host cell receptors. The elaborate means with which they make use of these ligands accounts for their cell target specificity and high uptake efficiency (Ni et al., 2016). Mechanisms governing the targeting and specific uptake of viruses and nonviral vectors alike rely on the use of electrostatic forces, multiple receptors for enhanced specificity, and multivalent interactions.

Receptor Ligands are Central to the Molecular Mechanisms of Targeting, Attachment, and Entry

Prior to entry, viruses often adhere to the cell surface via non-specific electrostatic interactions involving viral surface components (i.e. membrane glycoproteins) and negatively charged sugars (i.e. heparin sulfate) attached on the target cell surface (Grove and Marsh 2011; Mazzon and Marsh 2019).

TABLE 1 | Nucleic acid carriers: Properties and trafficking.

Vector	Core design	Mode of entry	Endosomal escape	Nuclear delivery	Nucleic acids delivered	Ref
Viruses and virus-like particles						
HIV	Enveloped, cone shaped capsid size: 100 nm	Sequential binding of spike protein GP120 to CD4 and a chemokine receptor promotes membrane fusion and direct cytosolic delivery.	N/A	Preinitiation complex is transported along the microtubule to the perinuclear region. NLS peptides on viral capsid promote karyopherin-mediated nuclear uptake.	DNA, siRNA, shRNA, miRNA	Bukrinsky (2004); Hamid, et al. (2015); Fanales-Belasio et al. (2010)
CCMV	Non-enveloped, icosahedral capsid size: 30 nm	Direct cytosolic delivery	N/A	N/A	siRNA, mRNA, dsDNA	Lam and Steinmetz (2019); Pretto and van Hest (2019); Villagrana-Escareño et al. (2019); Mukherjee et al. (2006)
MS2	Non-enveloped bacteriophage with complex structure and icosahedral head size: 27 nm	Receptor-mediated endocytosis (when targeting ligands are added)	Incorporation of penetrating or fusogenic peptides could facilitate endosomal escape.	N/A	shRNA, mRNA, miRNA, siRNA	Fu and Li (2016); Galaway and Stockley (2013); Ashley et al. (2011); Prel et al. (2015); Yao et al. (2015); Pan, et al. (2012a); Pan et al. (2012b); Lam and Steinmetz (2018)
M13	Non-enveloped filamentous bacteriophage composed of helically arranged coat proteins size: 880 nm length, 6.6 nm width	Receptor-mediated endocytosis (when targeting ligands are added)	Disruption of caveosomes and/or caveosome trafficking (need further studies)	N/A	Mammalian DNA transgene	Kim et al. (2012); Tian et al. (2015); Karimi et al. (201); Moon et al. (2015); Passaretti et al. (2020); Yata et al. (2014)
AAV	Nonenveloped, icosahedral capsid size: 20–25 nm	Clathrin-mediated endocytosis	Endosomal acidification exposes phospholipase domain that lyses endo-lysosomal membrane	Endosomal acidification exposes NLS domains that direct genes to nucleus	siRNA, DNA	Tomar et al. (2003); Xu et al. (2005)
AdV	Nonenveloped, icosahedral capsid with fiber knobs on vertices size: 90–100 nm	Binding to CAR and integrins facilitates integrin-dependent endocytosis	unknownCeramide-enhanced insertion to and membrane disruption of early endosomes by protein VI	Microtubule dynein/ dynactin motor complex	DNA transgene, therapeutic genes	Greber et al. (1997); Tatsis and Ertl (2004); Volpers and Kochanek (2004); Russell (2009); Fay and Panté (2015); Staring et al. (2018)
IV	Enveloped, spherical capsid with helical symmetry size: 80–120 nm shape: Spherical	Binding to sialic acid groups facilitates endocytosis.	pH drop in endosomes reveals hydrophobic HA2 subunit that mediates fusion	NLS sequences on nucleoprotein mediate karyopherin -dependent nuclear delivery	siRNA, miRNA	James and Whitley (2017); Couch (1996); Mammen et al. (1998); Pinto, et al. (1992); Neumann et al. (1997); Li et al. (2015); de Jonge et al. (2006); Li H. et al. (2013)
HBV	Enveloped, icosahedral capsid size: 42 nm	Binding of major surface antigens of HBV to cellular receptors NTCP and HSPG facilitate receptor mediated endocytosis.	Need further studies but shown to be insensitive to pH	Microtubule assisted perinuclear delivery; karyopherin-dependent nuclear entry	DNA	Li (2015); Venkatakrishnan and Zlotnick (2016); Tsukuda and Watashi (2020); Brandenburg et al. (2005)

(Continued on following page)

TABLE 1 | (*Continued*) Nucleic acid carriers: Properties and trafficking.

Vector	Core design	Mode of entry	Endosomal escape	Nuclear delivery	Nucleic acids delivered	Ref
EBOV	Enveloped, filamentous virus with helical symmetry Diameter: 80 nm, length: 600–1,400 nm	Macropinocytosis	Binding to NPC1 in late endosomes or lysosomes facilitates fusion and endosomal escape	N/A	none	Beniac et al. (2012); Falasca et al. (2015); Hunt, et al. (2012); Kondratowicz et al. (2011); Nanbo et al. (2010); Aleksandrowicz et al. (2011); Carette et al., 2011; Côté et al., 2011; Wang et al. (2016a)
SV40	Non-enveloped, icosahedral capsid size: 45 nm	SV40 VP1 protein binds to MHC-1 receptor and undergoes caveolin mediated internalization	Caveosomes undergo dynamic shape changes, and the virus is transported to the smooth endoplasmic reticulum.	Capsid disassembly occurs in smooth ER; exposed NLS peptide facilitates nuclear uptake via karyopherin -mediated pathway	none	Fay and Panté 2015, Norkin et al. (2002), Anderson et al. (1998), Martini et al. (2007), Pelkmans et al., 2001, Nakanishi et al. (2007)
Carbohydrate-based vector						
siRNA-GalNAc3 conjugates	Tris-GalNAc ligand of ASPGR is covalently attached to siRNA	Receptor-mediated endocytosis	Unknown	N/A	siRNA	Nair et al. (2014); Springer and Dowdy (2018)
Protein/Peptide-based vectors						
ARCs	Antibody is conjugated to alkyne-siRNA sense strand via a bifunctional azidoLys peptide linker	Receptor-mediated endocytosis	N/A	N/A	siRNA	Huggins et al. (2019)
REDV-Gm-TAT-Gm-NLS tandem peptide	Peptide sequences covalently linked with Gly repeats pack pDNA via electrostatic condensation size: 200 nm shape: Spherical	REDV selectively binds to integrin $\alpha 4\beta 1$ of endothelial cells, leading to endocytosis. TAT promotes membrane permeability.	NLS have buffering capacity	NLS facilitates karyopherin α/β mediated perinuclear delivery	pDNA	Hao et al. (2017)
T-Rp3	Modular His6-tagged protein composed of the recombinant DBP, a DBD, and TAT size: 100 nm shape: free from-toroidal; bound form-spherical	TAT facilitates endocytosis mostly via clathrin-dependent pathway	His6 tag induces "proton-sponge effect"	T-Rp3 interacts with microtubule and is transported to the perinuclear region nuclear entry is due to hydrophobic interaction of positively charged amino acid residues with NPC	pDNA, siRNA, dsRNA	Favaro et al. (2014); Favaro et al. (2018)
Polymer-based vectors						
A-C3	Cationic diblock copolymer pDMAEA-PImPAA-pBA condenses nucleic acids size: 200 nm shape: Spherical	Cationic pDMAEA facilitatesclathrin-mediated endocytosis	Ionizable PImPAA elicits proton sponge effect; hydrophobic PBA inserts into endosomal membrane	BA binds to NPC via hydrophobic interaction	pDNA, siRNA	Gillard et al. (2014), Truong et al. (2013)
PAT-SPN	Cationic diblock copolymer DMAEA-PAA-BA condenses nucleic acids; PEG shell is tethered to polyplex core through an MMP-7 peptide substrate size: 46 nm shape: Spherical	MMP-7 activated particle enter via endocytosis	pH-dependent membrane destabilization by endosomolytic PAA-BAA block	Not shown	DNA, siRNA	Li H. et al. (2013)

(Continued on following page)

TABLE 1 | (*Continued*) Nucleic acid carriers: Properties and trafficking.

Vector	Core design	Mode of entry	Endosomal escape	Nuclear delivery	Nucleic acids delivered	Ref
Lipid-based vectors						
Liposomes	Lipid combinations containing ionizable cationic lipids, fusogenic lipids, cholesterol, and PEG-lipids form spherical bilayers with an aqueous core size: <200 nm shape: Spherical	Direct fusion or endocytosis	Membrane fusion – can be made responsive to cellular (pH, enzymes, redox potential) or external (temperature, magnetic field, light) stimuli; may also be decorated with penetrating or fusogenic domains to facilitate escape	N/A	mRNA, siRNA, pDNA, ASOs	Semple et al. (2010); Akinc et al. (2010); Corbett et al. (2020); Callaway (2020); Jeffs et al. (2005); Wheeler et al. (1999); Lechardeur et al. (1999); Heidarli et al. (2017)
SLNPs	Nucleic acids combined with cationic lipids form neutral complexes that are encapsulated by solid lipids size: ~150 nm shape: Spherical	Phagocytosis or endocytosis (depends on cell type and surface modification)	Membrane destabilization	N/A	siRNA	Lobovkina et al. (2011); Arana et al. (2019)
Inorganic nanoparticles						
AuNPs	Covalent attachment of nucleic acid cargo or supramolecular assembly size: ~50 nm shape: Spherical, rod-like, star-like, triangular	Clathrin-mediated endocytosis	Polycationic functionalities on the surface disturb the pH balance leading to osmotic swelling and endosomal rupture - "proton sponge" mechanism	N/A	DNA, siRNA, miRNA	Burger et al. (2014); Ding et al. (2014a); Neshatian et al. (2014); Mendes et al. (2017); Xie et al. (2017)
Fe_3O_4 NPs	Covalent attachment of nucleic acid cargo or supramolecular assembly size: 50–100 nm shape: Spherical	Endocytosis that could be enhanced by the application of oscillating magnetic field	Osmotic swelling if polycationic polymers are used, membrane destabilization if coated with lipids or functionalized with cell penetrating peptides	N/A	DNA, siRNA	McBain et al. (2008); Cutler et al. (2010); Jiang et al. (2013); Urie and Rege (2015); Dowaidar et al. (2017); Cruz-Acuña et al. (2018)
NanoMOFs	Biomineralization, pore encapsulation,supramolecular assembly size: 30–300 nm shape: Spherical, ellipsoidal, cubic, hexagonal, octahedral	Endocytosis	Osmotic swelling induced by metal cations from degraded MOF	N/A	DNA, aptamers (DNA and RNA), miRNA, siRNA, pDNA	Liang et al. (2015); Peng et al. (2018); Sun et al. (2018); Li Y. et al. (2019); Teplensky et al. (2019); Sun et al. (2020)
NPSCs	Complexes of nucleic acid and Arg-rich inorganic nanoparticles are assembled on an oil drop size: 150–500 nm shape: Spherical	Direct fusion and cytosolic delivery	N/A	No data yet	siRNA, CRISPR-Cas9-gRNA	Jiang et al. (2015); Mout et al. (2017); Jiang et al. (2018)
usAuNP	Tiopronin-covered AuNPs conjugated to TFO size: 2–20 nm shape: Spherical	Caveolae-mediated endocytosis	Passive diffusion out of the endosome	2 and 6 nm gene carrying NP undergo passive diffusion whereas any size above 10 nm stays in cytoplasm.	c-myc promoter-binding TFO	Cai et al., 2011; Huang et al. (2012); Huo et al. (2014)
Nucleic acid displaying nanostructures (NADNs)						
SNAs	Outward display of densely packed nucleic acids physically adsorbed or covalently bonded to a nanoparticle core size: <100 nm shape: Spherical, rod-like, triangular prism	Caveolae-mediated endocytosis	N/A, most trapped in endosomes	N/A	siRNA, miRNA, DNAzymes, aptamers, ribozymes, immunostimulatory DNA	Mirkin et al. (1996); Elghanian et al. (1997); Jin et al. (2003); Rosi et al. (2006); Massich et al. (2009); Seferos et al. (2009); Cutler et al. (2011); Cutler et al. (2012); Young et al. (2012); Choi et al. (2013); Banga et al. (2014); Banga et al. (2017); Li et al. (2018); Rouge et al. (2015)

(Continued on following page)

TABLE 1 | (*Continued*) Nucleic acid carriers: Properties and trafficking.

Vector	Core design	Mode of entry	Endosomal escape	Nuclear delivery	Nucleic acids delivered	Ref
NANs	Nucleic acids are radially displayed on and photochemically tethered to the surface of crosslinked micelles. Hollow core permits co-delivery of small molecules and large biomolecules size: 20–180 nm shape: Spherical	Endocytosis	Micelle cross-linkages are enzymatically cleaved by endosomal esterases or proteases, revealing a hydrophobic surfactant tail that facilitates cytosolic access	N/A	DNA, siRNA, DNAzyme, pDNA	Awino et al. (2017); Santiana et al. (2017); Hartmann et al. (2018); Hartmann et al. (2020); Tolentino et al. (2020)
Nucleic acid Nanogel	Double stranded nucleic acid linkers with single stranded overhangs hybridize with multiple DNA strands clicked onto a polymeric backbone, serving as crosslinks that condense the construct into a nanogel size: 80–1,200 nm shape: Spherical	Endocytosis	Unknown	None	siRNA, Cas9/sgRNA	Ding et al. (2018); Ding et al. (2019); Ding et al. (2020)

Abbreviations: AAV, adeno-associated virus; siRNA, small interfering RNA; AdV, adenovirus; shRNA, small hairpin RNA; VLP, virus-like particle; NTPC, sodium taurocholate cotransporting polypeptide; HSPG, heparan sulfate glycoprotein; CCMV, cowpea chlorotic mottle virus; mRNA, messenger RNA; miRNA, microRNA; GalNAc, N-acetylgalactosamine; ASPGR, asioglycoprotein receptor; ARC, antibody-RNA conjugate; REDV, Arg-Glu-Asp-Val; G_m, Gly repeats; TAT, transactivator of transcription peptide; NLS, nuclear localization sequence; pDNA, plasmid DNA; DBD, DNA-binding domain; DBP, dynein-binding protein; pDMAEA, dimethylaminoethyl methacrylate; PImPAA, P(N-(3-(1H-imidazol-1-yl)propyl)acrylamide; pBA, poly (butyl acrylate); PAT-SPN, proximity-activated targeting smart polymeric nanoparticle; PEG, polyethylene glycol; MMP-7, matrix metalloproteinase-7; SLNP, solid lipid nanoparticle; AuNP, gold nanoparticles; Fe_3O_4 NP, iron oxide nanoparticle; NanoMOF, nano metal-organic framework; NPSC, nanoparticle stabilized nanocapsules; CRISPR-Cas9-gRNA, clustered regularly spaced palindromic sequences (CRISPR) CRISPR-associated (Cas9) guide RNA; usAuNP, ultrasmall gold nanoparticle; TFO, triplex forming oligonucleotides; SNA, spherical nucleic acids; NAN, nucleic acid nanocapsules.

Though such interactions may lack specificity, they provide the virus an initial foothold on the cell before recruiting specific cell receptors and facilitating entry (Grove and Marsh 2011). Most viruses, which include influenza virus, coronavirus, reovirus and polyomavirus, utilize the sialic acid receptors on the host cell surface for initial attachment (Maginnis 2018). Taking inspiration from this virus behavior, a number of delivery methods have either functionalized nucleic acid cargo with sialic acid (St-Pierre et al., 2016) or encapsulated them in nanocarriers decorated with sialic acids on the surface (Tang et al., 2019). A notable example of the latter strategy is demonstrated in the work of Tang et al. (2019). In their study, they have successfully delivered reporter (luciferase) and functional (antitumor p53) mRNAs to cancer cells using a liposomal nanoparticle containing surface sialic acids. Other than sialic acids, viruses utilize a plethora of receptor ligands which are proteoglycans (i.e. cell adhesion molecules) and lipids (i.e. PS) by nature, to mediate cellular attachment and entry (Maginnis, 2018). On the other hand, synthetic vectors make use of a more chemically diverse array of ligands but mostly for targeting purposes.

Targeted delivery is desired for synthetic vectors as it confers safety, efficacy, and efficiency. It limits the release of the therapeutic to diseased cells or tissues, minimizing adverse off-target effects that could outweigh therapeutic benefits. Secondly, it enhances efficacy by localizing a high concentration of the drug to a specific site. Third, efficiency is achieved by providing access to sites such as certain cells or subcellular locations (e.g. nucleus) that are normally inaccessible to the therapeutic (Rohovie et al., 2017). Many non-viral strategies have derived targeting domains from viral ligands for specific cell or tissue targeting. For example, the adenovirus-derived RGD peptide has been used to direct the nucleic acid delivery of lipoplexes, dendriplexes, and polyplexes to tumor cells overexpressing integrin $\alpha_v\beta_3$ on the cell surface (Danhier et al., 2012). The successful delivery of RGD-conjugated ASOs to melanoma cells has also been demonstrated (Alam et al., 2008; Juliano et al., 2008; Kang et al., 2008; Juliano et al., 2011). An RGD-based polycationic liposome was also developed to specifically target cancer cells and angiogenic endothelial cells (Yonenaga et al., 2012).

Other ligands of non-viral origin also offer targeting properties. For example, monoclonal antibodies have a been highly effective at targeting delivery of cytotoxic drugs to cancer cells (Sievers et al., 2001; Krop et al., 2010; Younes et al., 2010). Their ability to specifically and avidly bind to cell-specific receptors makes them equally viable targeting domains for biologics such as therapeutic nucleic acids. Their use in directing nucleic acid carriers has been demonstrated in several studies (Palanca-Wessels et al., 2011; Ngamcherdtrakul et al., 2015; Moffett et al., 2017; Huggins et al., 2019; Nanna et al., 2020). They can be either directly conjugated to the nucleic acid (Huggins et al., 2019; Nanna et al., 2020) or to the vector (Palanca-Wessels et al., 2011; Ngamcherdtrakul et al., 2015; Moffett et al., 2017). Antibody-RNA conjugates (ARCs) are promising in that they overcome possible limitations of nanoparticle-based formulations such as poor diffusivity, toxicity, and

TABLE 2 | Key components added to modulate trafficking.

Components	Examples	Mechanism of action	Nucleic acid carriers	Ref
Targeting, attachment, and entry				
Aptamers	Electrostatically adsorbed RNA-based CD30 aptamer	Binding to surface CD30 specifically overexpressed in ALK + ACLC promotes endocytosis	siRNA-loaded cationic polymer-based vector	Zhao et al. (2011)
	Surface-anchored RNA-based transferrin aptamer	Binding to cell surface transferrin receptor mediates endocytosis	siRNA-loaded liposomes	Wilner et al. (2012)
Peptides	Integrin-targeting peptides (e.g. RGD, REDV, AG86)	Binding to integrins facilitates clathrin- or receptor- mediated endocytosis	siRNA-peptide conjugates, pDNA-peptide complexes. siRNA-loaded liposomes	Yonenaga et al. (2012); Hao et al. (2017); Kang et al. (2019)
	GLP1	Binding to GLP1R on pancreatic islet beta cells facilitates endocytosis	ASO-GLP1 peptide conjugates	Ämmälä et al. (2018)
	TAT	Cationic naked or conjugated peptide can enter cells via macropinocytosis or receptor-mediated endocytosis	siRNA-TAT-EED conjugates	Lönn et al. (2016); Khan et al. (2020)
	R8	Acid-labile hydrazone linkages are cleaved around tumor cells, revealing cationic CPP that mediates endocytosis	siRNA-loaded, ACPP-decorated liposomes	Xiang et al. (2017)
	MPG	Hydrophobic domain of peptide facilitates direct cytosolic entry	Noncovalent MPG complexes peptide-siRNA and peptide-pDNA complexes	Simeoni (2003)
Carbohydrates	GalNAc	Multivalent binding to hepatocyte ASGPR mediates endocytosis	siRNA-GalNac conjugates	Nair et al. (2014)
Small molecules	Folate	Binding to folate-receptors overexpressed in cancer cells mediates endocytosis	pDNA loaded liposomes functionalized with folic acid as targeting ligand, miRNA-folate conjugates.	Sikorski et al. (2015); Cui et al. (2016); Orellana et al. (2017)
	Bivalent β-turn analogues	Mimic β-turn recognition motifs that facilitate protein-protein interactions; hydrophobic tail added to enhance membrane attachment	pDNA-loaded BIVs	Burgess (2001); Shi et al. (2010)
Antibodies	Surface-anchored Anti-CD3 and Anti-CD8 antibodies	Binding to surface CD3 and CD8 receptors on T-cells promotes endocytosis	mRNA-loaded polymer-based carrier	Moffett et al. (2017)
	Anti-CD22 mAb-SA	Binding to CD22 receptor in lymphoma cells promotes receptor-mediated endocytosis	siRNA-loaded polymer-based system	Palanca-Wessels et al. (2011)
	Surface-conjugated Anti-HER2 mAb	Binding to HER2 overexpressed in breast cancer cells facilitates endocytosis	siRNA-loaded inorganic- and polymer-based system	Ngamcherdtrakul et al. (2015)
	Anti-CD33 IgG4 mAb	Binding to CD33 $^{+}$ AML THP1 cells facilitates endocytosis	Antibody-siRNA conjugates (ARCs)	Huggins et al. (2019)
Endosomal escape				
Peptides	Fusogenic peptides (e.g. HA2-derived peptides, GALA, KALA)	Glu- or His-rich peptides undergo acid-driven conformational change to alpha-helical structure, leading to pore formation	pDNA entrapped in gelatin-silica nanoparticles modified with fusogenic peptides, or nanobiomimetic carrier composed of targeting and fusogenic peptides by which DNA is condensed.	Ye et al. (2012); Kusumoto et al. (2014); Alipour et al. (2017); Ni et al. (2019)
	Addition of 5–20 His to the targeting ligand	Proton sponge effect	pDNA-His modified peptide complexes	Lo and Wang (2008); Chang et al. (2010)
	Endosomal escape domains (EEDs)	Hydrophobic W- and F-containing peptides destabilize endo-lysosomal membranes	siRNA-TAT-EED conjugates	Lönn et al. (2016)
Small molecules	Oligonucleotide enhancing compounds (OECs)	Enhance membrane permeability	ASO/SSO/siRNA-OEC conjugates	Yang et al. (2015); Wang et al. (2017); Juliano et al. (2018); Seth et al. (2019)
	Cationic Amphilic drugs (CADs, e.g. chloroquine)	Weak bases that destabilize the endo-lysosomal membrane	Adjuvants for GalNAc-cholesterol-siRNA conjugates	Du Rietz et al. (2020)
	Nigericin	Ion exchange between endosomal H+ and cytosolic K+ results in endosomal swelling and rupture	miRNA-folate-nigericin conjugates	Orellana et al. (2019)
Polymer	PEI	Osmotic endosomal rupture	siRNA-loaded cationic polymer	Zhao et al. (2011)
	Multiblock (co)polymers (e.g. DMAEA-PAA-PBA, pDMAEA-PImPAA-PBA)	Endosomal rupture via ionic and hydrophobic interactions with membrane	DNA/RNA-polymer complexes	Li H. et al. (2013); Truong et al. (2013); Gillard et al. (2014)
Hydrophobic domains	Surfactant	Surfactant destabilizes endosomal membrane	Polymeric micelle, siRNA-DNA conjugates, DNAzyme-NANs	Zhang et al. (2015); Hartmann et al. (2018); Hartmann et al. (2020)
	Cationic or ionizable lipids (e.g. DOPE)	Lipid fusion destabilizes membrane	siRNA-loaded liposomes	Semple et al., 2010; Wilner et al. (2012)

(Continued on following page)

TABLE 2 | (*Continued*) Key components added to modulate trafficking.

Components	Examples	Mechanism of action	Nucleic acid carriers	Ref
Nuclear targeting and entry				
Aptamers	DTS (from SV40 enhancer region)	DTS binds to cytoplasmic NLS-tagged proteins bound for nuclear delivery	DTS sequence-containing plasmids	Miller and Dean (2009)
	NFκB-motif embedded on plasmid sequence	NFκB binds with motif on pDNA and shuttles construct to nucleus	pDNA/polymer complexes	Breuzard et al. (2008)
	Surface-displayed DNA-based nucleolin aptamer (AS411)	Active transport and binding to nucleolin localized in nuclear membrane	Polymeric micelle	Zhang et al. (2015)
Peptides	Dynein binding protein (DBP)	DBP binds to motor and is carried to centrosome through microtubules	Recombinant DBP-containing protein condensed with pDNA, siRNA and dsRNA	Favaro et al. (2018); Favaro et al. (2014); Dalmau-Mena et al. (2018)
	Nuclear localization signal (NLS)	Form weak, multiple interactions with cytoplasmic karyopherin bound for active nuclear transport via NPC	pDNA condensed with cationic NLS; AuNP conjugated complex of CRISPR/Cas9-gRNA, Cas9, and NLS; pDNA-NLS conjugates	Hao et al. (2017); Kim et al. (2017); Mout et al. (2017)
Small molecules	Dexamethasone (Dex)	Dex binds to nuclear membrane glucocorticoid receptor and dilates NPC; enhances affinity of polycations to nuclear membrane	HA/PEI1800-Dex/pDNA ternary complexes	Fan et al. (2013)

Abbreviations: CD, cluster of differentiation (receptor); ALK⁺, anaplastic lymphoma kinase; ACLC, anaplastic large cell lymphoma; siRNA, small interfering RNA; ASO, antisense oligonucleotide; GLP1, glucagon-like peptide 1; GLP1R, glucagon-like peptide 1 receptor; TAT, transactivator of transcription (peptide); EED, endosomal escape domain; CPP, cell-penetrating peptide; R8, Octa-Arg (peptide); GalNAc, N-acetylgalactosamine; ASGPR, asioglycoprotein receptor; BIV, bilamellar invaginated vesicle; miRNA, microRNA; mAb-SA, streptavidin-conjugated monoclonal antibody; HER2, human epidermal growth factor 2; IgG4, immunoglobin G4; AML, acute myeloid leukemia; HA2, hemagglutinin 2 (peptide); GALA, Glu-Ala-Leu-Ala (peptide); pDNA, plasmid DNA; SSO, splice-switching oligonucleotide; PEI, polyethylenimine; pDMAEA, dimethylaminoethyl methacrylate; PImPAA, P(N-(3-(1H-imidazol-1-yl)propyl)acrylamide; pBA, poly (butyl acrylate); PAA, propylacrylic acid; DOPE, dioleoylphosphatidylethanolamine; DTS, DNA nuclear targeting sequence; SV40, simian 40 virus; NFκB, nuclear factor kappa-light-chain-enhancer of activated B cells; dsRNA, double-stranded RNA; AuNP, gold nanoparticle; CRISPR-Cas9-gRNA, clustered regularly spaced palindromic sequences (CRISPR) CRISPR-associated (Cas9) guide RNA; NPC, nuclear pore complex; HA, hyaluronic acid.

immunogenicity while still significantly extending the half-life of the cargo (Nanna et al., 2020). Earlier conjugation methods for therapeutic attachment to antibodies involve nonselective conjugation to lysine or cysteine residues. Consequently, prior formulations suffer mainly from product heterogeneity (Huggins et al., 2019). Recently published works on ARC synthesis involved highly specific mechanisms for conjugation, giving a precise drug:antibody ratio of 2 (Huggins et al., 2019; Nanna et al., 2020).

Nucleic acid aptamers offer another promising approach in delivering nucleic acid cargos to specific cell-types (Dassie and Giangrande, 2013). Aptamers are short, chemically synthesized, single stranded oligonucleotides (DNA or RNA), which adopt a specific three-dimensional (3D) structure and bind to their ligands with high affinity (K_Ds in the pico-to nano-molar range) (Sun et al., 2014). Although aptamer-nucleic acid conjugates possess no innate mechanisms for endosomal escape on their own, aptamers can be conjugated on to nucleic acid carriers with endosomal escape activity as a way to improve cell specific targeting (Yan and Levy, 2018). For example, Zhao et al. (2011) designed a nanocomplex composed of a cationic PEI core endosomal escape component, CD30 RNA aptamer targeting lymphoma cells and siRNA that inhibits the expression of anaplastic lymphoma kinase (ALK). Such an assembly was proven to selectively bind lymphoma cells, deliver the siRNA intracellularly, silence ALK expression, and arrest the growth of lymphoma cells (Zhao et al., 2011).

Lastly, small molecules are commonly used as targeting ligands as they are easily synthesized at a modest cost. They are more stable than biological ligands such as aptamers and peptides, and their conjugation is often relatively simple. However, these molecules are often not the natural ligands of the target cell receptors and thus have lower affinity and specificity for a given receptor, the latter giving rise to off-target effects. Nevertheless, the relative structural simplicity and functional designability of small molecules make them attractive and viable targeting domains (Friedman et al., 2013).

For example, folate (Vitamin B9) is widely used for targeting folate receptor-positive cell lines, with a high affinity (K_D = 1 nM) and minimal toxicity. Folate-functionalized vectors are typically internalized via receptor-mediated endocytosis, but reduced folate carriers, though having lower affinity, directly enter the cytosol. Folate-expressing imaging agents are currently in Phase I and Phase II clinical trials, but they are not yet clinically approved for targeting therapeutic nanoparticles (Sikorski et al., 2015).

Likewise, benzamides (anisamide, in particular) target sigma receptors that are upregulated in cancer cell lines. Benzamide analogues can also target dopamine receptors selectively. So far, these have been used to deliver small molecule drugs such as doxorubicin encapsulated in liposomes but have not been explored in gene-delivery yet (Banerjee et al., 2004; Mach et al., 2004).

Multivalent Interactions Facilitate Cellular Uptake

Multivalent interactions between the viral ligands and host cell surface receptors not only amplify the strength of the interaction but also promote viral entry. This is exemplified by the influenza virus where the interaction of multiple capsid protein trimers (2-4 per 100 nm^2) with spatially concentrated sialic acid functionalities on the surface of the host cell (50–200 per 100 nm^2) is necessary for effective attachment and uptake (Mammen et al., 1998). Apart from high surface density, the spatial arrangement of the ligands is equally important. For example, the internalization of the simian virus 40 (SV40) necessitates the pentameric presentation of its viral capsid protein one to successfully bind to the cell-surface GM1 receptors and facilitate endocytosis (Ewers et al., 2010).

This parallels with carbohydrate-based delivery systems such as siRNAs and ASOs conjugated to N-acetylgalactosamine (GalNAc) for hepatic targeting. GalNAc involves multi-site interactions with asioglycoprotein receptors (ASPGR) of hepatocytes, facilitating endocytosis. (Nair et al., 2014; Debacker et al., 2020). In 2019, Alnylam's givosiran (GIVLAARI®) was the first US Food and Drug Administration approved GalNAc conjugate for acute hepatic porphyria, and other conjugates are underway (Debacker et al., 2020). ASPGR is a liver-specific receptor that has been targeted for hepatic-directed therapeutics. It is a heterooligomeric complex that is capable of interacting with multiple GalNAc molecules (Meier et al., 2000). The strong binding affinity of monomeric GalNAc with ASPGR is in the micromolar range, and the avidity of the interaction can be enhanced by 10^3 to 10^5, depending on the number and spacing of GalNAc units (Lee and Lee 2000). Specifically, the structure of ASPGR was found to optimally bind three divergent GalNAc residues (Lee and Lee 2000) spaced from a common branch point by 14–20 Å and separated from each other by 15–20 Å (Lee et al., 1983; Khorev et al., 2008).

Other synthetic vectors having multivalent interactions with cell receptors have been developed to mimic viral behavior and have shown an enhanced cellular uptake of the carriers or nucleic cargo. A prime example of this is the study of Nakagawa et al. (2010), wherein they delivered a splice switching antisense oligonucleotide (SSO) directly conjugated to anisamide, a sigma receptor present in plasma membranes, to tumor cells, and investigated their ability to modify the splicing of a reporter gene (luciferase). Mono-anisamide and tri-anisamide conjugates were synthesized, and it was demonstrated that the multivalent conjugate yielded a more enhanced receptor-specific cell uptake and biological effect (Nakagawa et al., 2010). Another study highlighting the beneficial effect of multivalency to nucleic acid cargo internalization is carried out by Kang et al. (2018). In their study, siRNA specific to Bcl2, an anti-apoptotic protein, was tethered to MUC-1- and nucleolin-targeting aptamers and delivered to cancer cells. Fluorescence microscopy revealed the positive correlation between aptamer valency (n = 1, 3, 9) and cellular internalization. Moreover, higher tumor accumulation was observed for multivalent aptamer conjugates compared to mono- and divalent conjugates. These studies underscore the critical need for multivalent interactions in designing delivery systems for nucleic acids.

Attachment to Multiple Receptors Confers Cell Target Specificity and Uptake Efficiency

Maginnis (2018) provides a comprehensive review of how virus interactions with host receptors govern pathogenicity. Worth noting are evolutionarily conserved mechanisms among viruses, redundancy in target primary receptors, and diversity of secondary receptors. One conserved mechanism is the conformational change involved in the sequential binding to multiple receptors that leads to fusion or endocytosis. For instance, the trimeric glycoprotein (GP) complex of the human immunodeficiency virus (HIV) is formed by the GP120/GP41 heterodimer and is necessary for cellular targeting and entry. GP120 binds CD4 on the surface of T-cells, T-cell precursors, macrophages, dendritic cells, and microglial cells. GP120 binding induces a conformational shift in the trimeric GP, revealing a GP120 binding domain specific for one of many chemokine coreceptors such as CXCR4 and CCR5. These coreceptors vary across different cells and thus mainly determine tropism (Fanales-Belasio et al., 2010; Wilen et al., 2012). The involvement of coreceptors form the basis of some anti-viral drugs such as Maraviroc, a US Food and Drug Administration and European Medicines Agency approved HIV/AIDS treatment. It acts by antagonizing CCR5, the secondary receptor of HIV in $CD4^+$ T cells. In particular, maraviroc binding induces a change to the inactive conformer of CCR5 (López-Huertas et al., 2017).

In terms of redundant receptors, integrins are of particular interest because they are commonly involved in the internalization of viruses. Integrins are heterodimeric cell surface receptors that mediate cell adhesion, migration, differentiation, and tumor growth. The binding of a virus to a host induces the clustering and/or structural changes of integrins, resulting in intracellular cues that enhance binding affinity, drive structural changes in the cytoskeleton, and/or facilitate uptake. This is demonstrated by certain viruses such as the adenovirus whose secondary attachment to integrins initiates intracellular signals that ultimately lead to viral uptake (Stewart and Nemerow, 2007). For the human cytomegalovirus, the binding of its glycoproteins to both the epidermal growth factor receptors (EGFR) and integrin on the host cell brings EGFR and integrins into close proximity, eliciting signaling responses that facilitate cellular uptake and nuclear trafficking (Wang et al., 2005).

For synthetic vectors, engaging multiple receptors presents an opportunity for programming more specific and efficient nucleic acid delivery systems. The use of multiple ligands for enhanced specificity and uptake is guided by knowing which receptors are overexpressed in the tissue or region of interest. Just as integrins are often implicated in virus entry, they have

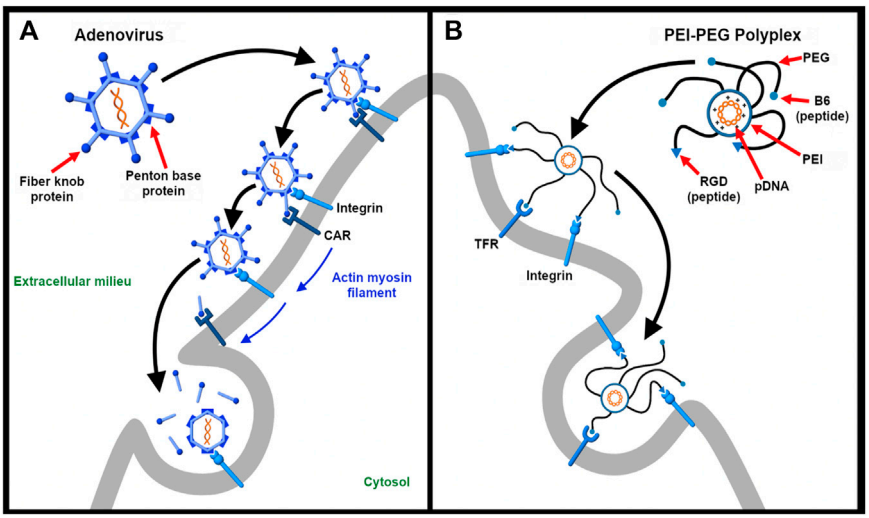

FIGURE 3 | Targeting multiple receptors enhances cellular specificity and transfection efficiency. **(A)**. The entry of adenovirus into the host cell occurs in a three-step process – binding, drifting, and shedding. First, the adenovirus binds to the Coxsackievirus and adenovirus receptor (CAR) of the host cell surface through fiber knobs jutting out the vertices of the icosahedral shaped viral capsid. Second, acto-myosin drifting of the virus-bound CAR receptor leads to internment of the penton base protein of the viral capsid by integrins expressed on the cell surface. Third, the slow drifting motion (0.1 μm/s) of the CAR receptor and the stable nature of binding causes mechanical stress onto the viral capsid, the first uncoating step in the capsid disassembling process. The protein VI of the inner capsid is exposed which makes lesions in the plasma membrane and undergoes integrin-dependent endocytosis (Burckhardt et al., 2011) **(B)**. As described by Nie et al. (Nie et al., 2011), a synthetic dual-ligand targeted vector system was constructed using a cationic polymer PEI to deliver pDNA. PEG moieties were used to shield the charge of the polyplex. Inspired from natural viruses, the polyplex was conjugated with Transferrin receptor (TFR)-binding B6 peptide and integrin-recognizing RGD sequence for dual targeting purpose. The receptor specificity of the dual targeted polyplex shows increased gene transfection as compared to the single targeting peptide. The integrin receptor binding helps in cellular association and the vector is internalized via TFR-mediated endocytosis.

become popular targets for drug and gene delivery for their natural abundance, efficient endocytosis, and differential expression on a number of tumor cells and angiogenic endothelial cells (Wang et al., 2010; Juliano et al., 2011). For instance, Nie et al. (2011) developed a synthetic dual-ligand targeted vector in which plasmid DNA is condensed by polyethylenimine (PEI). In this study, they conjugated PEG-ylated PEI-based polyplexes with peptides B6 and arginylglycylaspartic acid (RGD) that target transferrin and integrin, respectively. This strategy exploits the fact that tumor cells overexpress transferrin while vasculature that supply blood to these newly formed tumor cells overexpress integrins. Importantly, RGD-integrin binding stabilizes the B6-transferrin interaction. This design has shown to improve transfection efficiency and specificity. Thus, as illustrated in **Figure 3**, it demonstrates the power of mimicking the dual-receptor internalization of natural viruses such as the adenovirus, herpes simplex virus, and SV40 (Hussein et al., 2015).

In another study, Dong et al. (2018) depict the dual targeting ability of RGDK peptide sequence. In this particular example, they designed a siRNA/amphiphilic dendrimer complex decorated with a dual targeting peptide RGDK. The design of the targeting peptide is such that it protects and stabilizes the siRNA-dendrimer complex by electrostatic interaction. Similar to Nie et al.'s study, the RGD part binds to target integrin receptors on tumor vasculature while the full length RGDK interacts with neuropilin-1 (Nrp-1), which is expressed on tumor cells, thereby enhancing cellular uptake.

CYTOSOLIC DELIVERY

For a virus to deliver its genome to the cytosol or nucleus, it needs to penetrate either the cellular membrane or a subcellular membrane within the cytoplasm such as the endo-lysosomal membrane. This section talks about how viruses and synthetic carriers alike manage to bring their nucleic acid cargo into the host cell interior with mechanisms to overcome cellular barriers.

Direct Cytosolic Delivery

Some enveloped viruses such as HIV are able to directly translocate their genome into the cytosol via cell membrane fusion. As mentioned in Section *Attachment to Multiple Receptors Confers Cell Target Specificity and Uptake Efficiency*, the binding of the HIV glycoprotein to its primary receptor drives structural changes within the glycoprotein, facilitating a subsequent interaction with a coreceptor that then mediates viral entry (Wilen et al., 2012). Binding to two receptors enhances the strength of viral attachment (Grove and Marsh, 2011; Ni et al., 2016), and for HIV, this allows the N-terminal fusogenic peptide of GP41 to penetrate the membrane. The heptad repeats of GP41 interact to form a hairpin loop, facilitating the fusion of the viral and host cellular membranes (Chan et al., 1997; Fanales-Belasio et al., 2010).

For nonviral carriers, a particle can also be designed such that it directly transfects cargo to the cytosol. For instance, Motion

et al., (2012) reported a promising phosphatase-triggered liposome carrier that was directly inspired by HIV. It incorporates an inactive phosphorylated version of the GP41 peptide that, when dephosphorylated, shifts to its fusogenic alpha-helical conformer. The phosphorylated form, on the other hand, has an increased random coil structure that is unable to interact with a lipid membrane. Since phosphates are overexpressed and secreted by diseased tissues, the fusogenic peptide is activated in a diseased cell, facilitating fusion with the plasma membrane and targeted cytosolic delivery. Such system has great potential as a nucleic acid carrier. Additionally, studies have shown that exogenous miRNA (Vickers et al., 2011) and siRNA (Shahzad et al., 2011; Ding et al., 2014b) can be directly delivered to the cytosol of target cells using endogenous or reconstituted high density lipoprotein by targeting scavenger receptor B1 (Shahzad et al. 2011).

In addition, siRNA (Jiang et al., 2015; Jiang et al., 2018) and CRISPR-Cas9 ribonucleoprotein (CRISPR-Cas9-RNP) (Mout et al., 2017) can be directly transfected across the cell membrane using nanoparticle-stabilized nanocapsules (NPSCs). Previously shown to mediate the direct cytosolic delivery of small molecules (Yang et al., 2011) and proteins (Tang et al., 2013), NPSCs are formed by assembling a preformed complex of nucleic acids and arginine-coated nanoparticles on the surface of an oil droplet (Jiang et al., 2015). The inorganic- and lipid-based hybrid construct efficiently delivered nucleic acid cargo to the cytosol with an siRNA knockdown efficiency of 90% (Jiang et al., 2015; Jiang et al., 2018) and to the nucleus with a CRISPR-Cas9-RNP gene editing efficiency of 30% (Mout et al., 2017). *In vivo* assays of spleen-directed siRNA loaded NPSCs showed good selectivity and immunomodulatory activity, demonstrating the potential for targeted delivery (Jiang et al., 2018).

Endosomal Escape

Most viruses and synthetic nucleic acid carriers are internalized via endocytosis. While viruses manage to escape into the cytosol efficiently, synthetic carriers pale in contrast (Ramamoorth and Narvekar, 2015), only having around 1–2% endosomal release (Gilleron et al., 2013). Thus, endosomal escape is the bottleneck of nucleic acid delivery and ultimately determines therapeutic efficiency (Gilleron et al., 2013; Shete et al., 2014; Selby et al., 2017).

While direct fusion with the plasma membrane may seem simpler, endocytosis offers several advantages—one being evasion of molecular crowding in the cytosol and microtubule-assisted shuttling to the nucleus or other subcellular locations (Barrow et al., 2013). Furthermore, as endocytosis is often linked to signaling cascades, the invading particle can influence its intracellular fate by targeting the appropriate receptor (Nemerow and Stewart, 1999; Marsh and Helenius, 2006). For viruses, endocytosis can lower the risk of triggering an immune response because rapid endocytotic uptake minimizes the exposure of viral immunogenic epitopes to the extracellular milieu (Miyauchi et al., 2009). Importantly, the physical integrity of the viral capsid is responsive to both chemical and mechanical stimuli brought about by interactions with the host. This provides a basis for disassembly once the genome has reached its target site (Greber 2016; Yamauchi and Greber, 2016). Similarly, endocytosis enables opportunities to embed responsiveness of a nonviral carrier to endolysosomal cues. For these reasons and the overwhelming tendency for nonviral carriers to undergo endocytotic entry, research efforts are more directed toward enhancing endosomal escape efficiency.

Cellular Cues Drive Endosomal Escape via Membrane Fusion or Penetration

Staring et al. (2018) provides an excellent discussion of how viruses carry out endosomal escape to avoid degradation or recycling. For their remarkable endosomal escape efficiency, viruses have served as templates for engineering the endosomal escape mechanism of non-viral vectors. A unifying theme is a conformational change in viral structural proteins that drives viral and endo-lysosomal membrane fusion for enveloped viruses or membrane penetration by nonenveloped viruses. These structural rearrangements are triggered by cellular cues such as low pH or acid-dependent proteolytic activity. Such viral proteins or peptides contain ionizable groups such as critical histidine residues whose imidazole groups (pKa~6) are protonated as the pH drops in the endosome. These histidine residues act as pH sensors involved in pH-dependent structural changes of the protein or peptide as observed for the surface protein hemagglutinin (HA) glycoprotein (GP) of the influenza virus. Moreover, they also serve as internal buffers. This "proton sponge" effect leads to endosomal swelling and rupture. For this reason, histidine residues (5–20) are added to peptide domains (such as TAT) of nucleic acid carriers (Lo and Wang, 2008). A research study by Meng et al. (2016) has discussed a multifunctional peptide-based nanocarrier composed of different peptide fragments—a CPP segment (TAT) for cell penetration, an ELMD segment for endo-lysosomal membrane disruption, and stearyl moieties to improve hydrophobicity and cell membrane binding ability of the peptide-DNA complex. For the ELMD segment, six histidine resides were inserted to increase endosomal escape by "proton sponge" effect. All these amino acids were dextrorotatory to protect the DNA/peptide nanocarrier from proteolysis.

Membrane Fusion

For the endosomal escape of enveloped viruses, the influenza virus is a classic model (**Figure 4A**). The fusogenic HA has been used or mimicked as an endosomal escape domain. Following endocytosis, the acid-triggered proteolysis induces the conformational change of the viral GP spike. This exposes the hydrophobic subunit HA2 that facilitates the endosomal escape of the ribonucleoprotein contents into the cytosol (Pinto et al., 1992). Specifically, endosomal acidification induces a conformational change in HA that sequesters charged residues glutamate-15 and aspartate-19. This reveals a V-shaped HA conformer with a hydrophobic pocket that penetrates deeply into the endosomal membrane. The enhanced penetration increases the lateral pressure in the hydrophobic pocket and the surface tension at the interface of the viral and endosomal

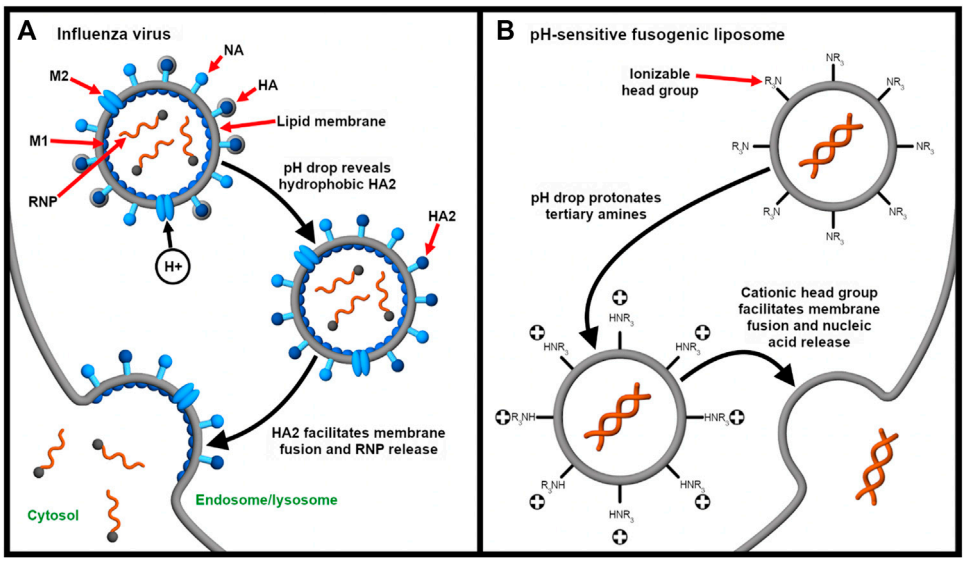

FIGURE 4 | Endocytosis provides an opportunity for integrating stimulus-responsive nucleic acid release. **(A)** The influenza virus releases its genome (complexed with nucleoproteins, gray spheres) into the cytosol in a pH-dependent manner. Endosomal acidification drives the influx of protons through the Matrix Protein 2 (M2) ionophore. This liberates the ribonucleoprotein (RNP) complex from Matrix Protein 1 (M1) and exposes the fusogenic subunit HA2, which, in turn, facilitates fusion of the viral and endosomal membranes (Pinto et al., 1992). Neuraminidase (NA) enables release of the influenza virus from the host cell after replication (James and Whitley 2017). **(B)** On the other hand, pH-responsive fusogenic liposomes are composed of ionizable lipids with weakly basic head groups that are rapidly protonated as the pH drops in the endosomes. This enables the protonated lipids to promote fusion and nucleic acid release before lysosomal degradation (Budker et al., 1996; Kogure et al., 2008; Sato et al., 2012).

membranes. Altogether, these drive the hemifusion of the two lipid membranes (Han et al., 2001).

Synthetic HA2 analogs have demonstrated improved endosomal escape ability (Ye et al., 2012). Ye et al. (2012) developed and studied different types of fusogenic peptides (HA2, R8, TAT, TAT-HA2, and TAT-R8) by conjugating them to gelatin-silica nanoparticles (GSNPs). These GSNPs were used to deliver plasmid DNA and their endosomal escape efficiency was measured and compared. They concluded that the endosomal escape efficiency of TAT-HA2 conjugate was superior as compared to others. Moreover, the concentration of the peptide dictates the extent of its interaction with the membrane. While the peptide domains only engage the membrane electrostatically at low concentrations, pore formation is observed at higher concentrations.

The endosomal escape of the influenza virus can be largely ascribed to the sequestering of the hydrophilic cap of HA to reveal a hydrophobic domain HA2 that then engages the endosomal membrane. This mechanism has inspired Lönn et al. (2016) to develop endosomal escape domains (EEDS), which are hydrophobic peptides containing tryptophan and phenylalanine residues. For EED-TAT-siRNA conjugates, the presence of indole and/or phenyl rings at an optimal distance of six PEG units from the TAT domain is able to significantly enhance the endosomal escape of siRNA. Additionally, the concept of hydrophobic unmasking has also been exhibited by nucleic acid nanocapsules. Amphiphilic surfactant-DNA conjugates were constructed to mimic the disassembly products of the nanocapsule. The membrane permeating ability of these conjugates (Hartmann et al., 2018) suggests that the hydrophobic group revealed only after disassembly could facilitate the endosomal escape of the degradation products.

Similarly, pH-sensitive fusogenic liposomes (**Figure 4B**) have been developed to mimic the acid-triggered endosomal escape of viruses (Budker et al., 1996). Sato et al. (2012) described the delivery of siRNA for gene silencing using low pH-activatable cationic liposomes. The responsiveness to low pH is enabled by using a lipid containing a tertiary amine head group that is almost neutral at physiological pH but is cationic at low endosomal pH (Moriguchi et al., 2005; Kogure et al., 2008; Sato et al., 2012). The lipid also consists of two long linoleyl fatty acid chains, forming cone-shaped molecules that further mediate endosomal escape through membrane fusion. Because the apparent pK of the ionizable lipid is 6.5, rapid membrane fusion and siRNA release is induced in the endosomes before lysosomal degradation occurs (Sato et al., 2012; Sakurai et al., 2014).

Membrane Penetration

Unlike enveloped viruses that possess a lipid envelope capable of fusing with the plasma or endo-lysosomal membrane, nonenveloped viruses make use of membranolytic peptides to escape the endosome. While membrane penetration is not completely understood, the exact mechanism can range from temporary membrane destabilization to pore formation to complete disruption (Staring et al., 2018). The elegance of viral endosomal escape using membranolytic peptides is exemplified by the adenovirus. The mechanical stress caused

by binding multiple receptors primes the shedding of the capsid coat (Burckhardt et al., 2011). This liberates membranolytic viral protein VI that then creates small lesions on the plasma membrane. As a response, the host secretes lipid hydrolase acid sphingomyelinase that catalyzes ceramide production for membrane repair. The increased level of ceramide enhances interaction of protein VI with the endosomal membrane, leading to endosomal rupture. This illustrates how the host cell's natural response to membrane damage is exploited by a virus for it to escape the limiting vesicle (Staring et al., 2018). Moreover, a study by Ortega-Esteban et al. (2015) showed that upon virus maturation, the expansion of the genome stiffens virions. As in the case of the adenovirus, the rise in internal pressure renders the capsid more susceptible to disruption and, thus, contributes to the overall endosomal escape mechanism and eventual uncoating of the virus at the nuclear pore complex (Ortega-Esteban et al., 2015; Greber 2016).

Similarly, the Glutamic acid-Alanine-Leucine-Alanine (GALA) peptide is a targeting and endosomal escape peptide that has been used in siRNA delivery (Subbarao et al., 1987; Kusumoto et al., 2013; Kusumoto et al., 2014). GALA was originally designed to undergo an acid-triggered change from a random coil to a membrane-disrupting alpha helical structure (Subbarao et al., 1987). Later on it was found to target the sialic acid residues on lung endothelium (Kusumoto et al., 2013), making it a promising multifunctional ligand. On the other hand, KALA is a modified version of GALA with alanine to lysine substitutions and reduced glutamic acid content. These features allow DNA condensation, endo-lysosomal disruption, and nucleic acid release (Wyman et al., 1997; Shaheen et al., 2011). Miura et al. (2017) performed a complete study of KALA as a fusogenic peptide. They modified the surface of a DNA-encapsulating liposome with KALA peptide sequences. In this study, they found that as compared to the full-length KALA sequence (27 residues), the short-KALA3 peptide (14 residues) was the shortest KALA peptide to form a α-helical structure at physiological pH. Thus, short-KALA3 can be used to elicit transgene expression (Miura et al., 2017). KALA peptide has also been used before for the delivery of siRNA-PEG conjugates (Mok and Park 2008).

Small Molecules for Enhancing Endosomal Escape Efficiency

The fact that fusogenic or membranolytic peptides are often required to gain cytosolic access underscores the necessity for an endosomal escape component in a drug delivery system. This idea has been extended to various small molecules that can be used as tools to cross the endo-lysosomal membrane either through direct conjugation to or co-delivery with the nucleic acid cargo (Gilleron et al., 2015; Osborn et al., 2015; Maxfield 1982; Juliano et al., 2018; Joris et al., 2018; Du Rietz et al., 2020; Yang et al., 2015; Wang et al., 2017). For example, cationic amphiphilic drugs (CADS) have been shown to enhance siRNA delivery due to their ability to increase the permeability of the endo-lysosomal membrane (Joris et al., 2018; Du Rietz et al., 2020). On the other hand, oligonucleotide enhancing compounds (OECs) are small molecules covalently linked to siRNAs, ASOs, and single stranded oligonucleotides and have been screened for improved cytosolic and nuclear delivery without an external carrier (Yang et al., 2015; Wang et al., 2017). Through a set of structure-activity experiments, hydrophobic phenyl rings, the presence and relative placement of a tertiary amine, and carbamate modifications were identified as essential and tunable features for enhancing the therapeutic availability of the oligonucleotides. How OECs influence the intracellular redistribution of oligonucleotides is not yet clear but, similar to CADs, involves an increase in endomembrane permeability rather than complete disruption. Though the potency imparted by OECs holds great promise, the challenge of enhancing efficacy while minimizing cytotoxicity remains (Juliano et al., 2018).

Additionally, Orellana et al. (2019) reported the use of nigericin, a novel, small molecule endosomal escape agent, to enhance the cytosolic delivery of folate-conjugated miRNA. Nigericin is a proton ionophore that exchanges osmotically inactive protons inside the endosomes with potassium ions in the cytosol. The combined high concentration of sodium and potassium ions raises the osmotic pressure inside the endosomes, resulting in endosomal rupture and release of the miRNA payload.

Intracellular Receptor Targeting as a Potential Endosomal Escape Strategy

For effective host cell infection, the Lassa virus (LASV, Jae et al., 2014) and ebolavirus (EBOV, Carette et al., 2011; Côté et al., 2011; Wang et al., 2016a) escape the endosome via a critical switch from their extracellular receptor (involved in cellular attachment and entry) to an intracellular endo-lysosomal receptor to mediate membrane fusion (Jae and Brummelkamp 2015). This is commonly due to the pH drop in the endosome that primes the viral glycoprotein (GP) for a receptor switch (Staring et al., 2018).

In particular, LASV was found to bind mainly to α-dystroglycan (Cao et al., 1998) as well as TAM receptor tyrosine kinases, DC-SIGN of dendritic cells, and C-type lectins of liver and lymph nodes (Shimojima et al., 2012) and is taken up mainly through macropinocytosis (Oppliger et al., 2016). The trimeric LASV spike protein is composed of a receptor-binding domain (GP1), a fusion protein subunit (GP2), and a unique stable signal peptide (SSP) (Burri et al., 2012) that directs the polypeptide to the endoplasmic reticulum and also interacts with GP2 during membrane fusion (Nunberg and York 2012). Structural studies support an entry model wherein endo-lysosomal pH (5.0–6.0) induces a conformational change in GP1 that facilitates an intracellular receptor switch to LAMP1, a late endosomal/lysosomal protein (Cohen-Dvashi et al., 2015; Li et al., 2016). Further acidification in the lysosomes (pH 4.0) sheds GP1, exposing GP2 that mediates membrane fusion (Li et al., 2016). The pH-dependence of the conformational change is attributed to the pH-sensing histidine triad on the surface of the spike protein (Cohen-Dvashi et al., 2015; Cohen-Dvashi et al., 2016). Mutation of these His residues reveals that LAMP1 binding is not necessary for membrane

fusion but greatly enhances viral infection efficiency (Cohen-Dvashi et al., 2016).

Similarly, attachment of EBOV to the host cell membrane facilitates internalization principally through macropinocytosis (Nanbo et al., 2010), with evidence that the virus is also taken up via clathrin-mediated endocytosis (Aleksandrowicz et al., 2011). Several cell membrane contact sites have been identified that seem to facilitate virus attachment such as β1-integrins and Tyro3 (TAM) family kinase receptors, but no sites for direct interaction with the EBOV GP have been identified yet. C-type lectins (L-SIGN, DC-SIGN, and hMGL) have also been shown to enhance adherence of the virus to the host cell membrane. Due to the broad tropism of EBOV across different cell types and different host organisms, it has been difficult to identify cell surface receptors that facilitate internalization (Hunt et al., 2012). So far, TIM-1 was determined to be the EBOV receptor for epithelial cells (Kondratowicz et al., 2011). Upon entry, endo-lysosomal acidification activates proteases cathepsin B and cathepsin L that cleave the EBOV GP. Proteolysis reveals the active conformer GP2, which then binds to Niemann-Pick C1 (NPC1), a cholesterol transporter embedded on the endo-lysosomal membrane. This interaction facilitates the fusion of the viral and lysosomal membranes, releasing the viral nucleocapsid into the cytosol (Carette et al., 2011).

Because NPC1 is involved in vesicular trafficking, it is even more interesting that it is responsible for limiting lipid nanoparticle-mediated siRNA delivery by shuttling the bulk of the lipid nanoparticles back to the outside of the cell after endocytosis (Sahay et al., 2013). Moreover, inhibition of NPC1 greatly increases the cytosolic delivery of the siRNA cargo (Wang et al., 2016b). A similar effect was observed when ESCRT-1, another endo-lysosomal protein involved in vesicular sorting, was knocked down to enhance the delivery of a therapeutic anti-miRNA (Wagenaar et al., 2015). Alternatively, the entrapment of oligonucleotides in the late endosomes can be exploited. Instead of inhibiting or knocking down endo-lysosomal-associated proteins such as NPC1, LAMP1, or ESCRT-1, a ligand that engages the intracellular receptor can be used to facilitate the cytosolic delivery of the cargo. This could potentially be applicable to lipid-based systems where membrane fusion precedes content release.

NUCLEAR DELIVERY

Unlike cytoplasmic viruses, nuclear viruses (such as SV40, adenovirus, influenza virus and HIV) need to travel further in order to replicate themselves in the nucleus of the host cell. They must cross a total of three cell barriers to reach the nucleus—the plasma membrane, cytosol and the nuclear membrane. Thus, they have evolved to use their structural features along with cellular transport machinery to hijack the well-protected nuclear import process. The size, structure, and composition of the viral proteins determines the mechanism by which it enters the nucleus. The structure and surface properties of nuclear viruses are also different from cytoplasmic viruses as the capsid of these viruses needs to be intact when they are traversing through the highly crowded cytosol but should breakdown in the perinuclear area (Cohen et al., 2011; Kobiler et al., 2012).

The nucleus is the main regulator of intracellular functions such as gene activation, cell division and proliferation, metabolism and protein production. As such, it is also considered as the most important target to deliver intact therapeutic exogenous oligonucleotides to treat diseases at the genetic level (Faustino et al., 2007; Pouton et al., 2007). However, cytosolic trafficking is a critical bottleneck for the efficient nuclear delivery of nucleic acids (Ni et al., 2019). Previous studies show that when a plasmid DNA is microinjected into the cytoplasm, the cellular enzymes degrade the DNA before it can reach the nucleus through Brownian motion (Cohen et al., 2009). Thus, it is necessary to protect as well as actively traffic the DNA to the perinuclear region.

To reach the nucleus, a number of different cytosolic trafficking strategies have been explored by nuclear viruses. Among these, the karyopherin-dependent and microtubule-assisted pathways have been extensively studied and mimicked for nucleic acid delivery (Bai et al., 2017). Thus, this section discusses these two common viral nuclear import mechanisms and how these pathways have inspired the development of nonviral vectors for therapeutic and diagnostic purposes (Cohen et al., 2011; Kobiler et al., 2012).

Karyopherin-Mediated Pathway

The nuclear trafficking of the viral ribonucleoproteins (vRNPs) is required for production and release of mature virions. To travel actively toward the nucleus, viruses use nuclear localization signals (NLSs) to mediate nucleus entry of the vRNPS. NLS sequences are short basic peptide motifs that are recognized by karyopherin proteins and are transported to the nucleus via karyopherin α/β-mediated pathway (Cros and Palese 2003). Detailed chemical and biophysical studies show that the influenza A virus, herpes simplex virus, and SV40 consist of these NLS sequences embedded in their viral proteins. These specific sequences interact with the α subunit of dimeric karyopherin α/β receptors with high specificity. The karyopherin α binding site classifies the type of NLS as either classical or nonclassical. The classical NLS (derived from SV40) binds to inner concave surface of the ARM domain of karyopherin α. On the other hand, nonclassical NLS are the viral peptides that bind specifically and exclusively to the minor groove of the karyopherin α (Xu et al., 2005). An example is the NLS obtained from influenza A virus Li G. et al. (2019). The trimeric karyopherin-NLS complex docks at the nuclear pore complex and is passaged across the nuclear envelope and released into the interior. This transport mechanism is based on nucleocytoplasmic gradient of the GTP bound form of Ran protein as the Ran-GTP/GDP ratio is high in the nucleus but low in the cytoplasm. This difference in concentration acts as the driving force to transport the trimeric complex inside the nucleus (Fay and Panté, 2015).

Miller and Dean (2009) summarized nuclear targeting ligands that can be used to deliver therapeutic nucleic acids. These ligands can be easily modified and conjugated to the surface of a

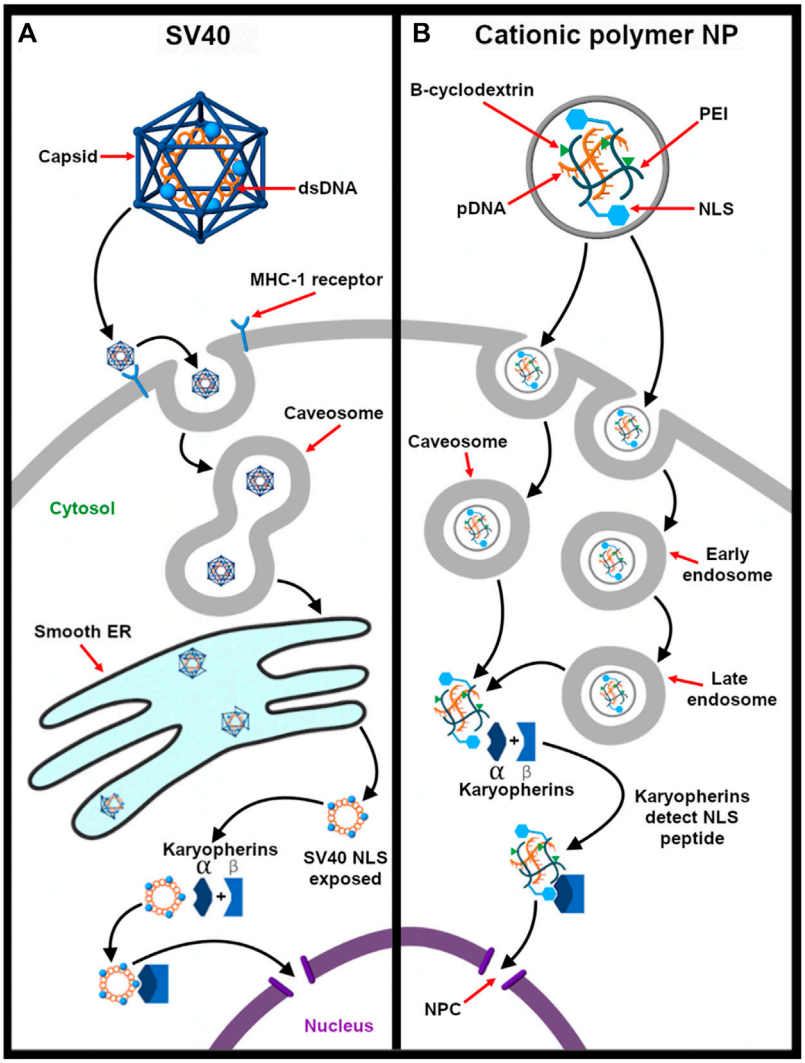

FIGURE 5 | Karyopherin-mediated nuclear delivery of SV40 and of a synthetic nanovector. **(A)** SV40 binds to MHC-1 class receptors present on the host cell surface. This mediates the recruitment of caveolin-1 positive vesicles, and the virus is eventually taken up into caveosomes. These caveosomes undergo dynamic structural changes to form long tubular membrane extensions, which are then released from caveosomes and are transported to the smooth ER (Pelkmans et al., 2001). Once inside the ER lumen, the disassembly of viral capsid begins, and the partially disassembled capsid undergoes structural changes in the cytosol to expose the NLS embedded in the minor capsid. The NLS moiety is recognized by the karyopherin family, and the viral genome is transported to the nucleus as karyopherin cargo (Nakanishi et al., 2007; Toscano and de Haan 2018). **(B)** In this study by Hu et al. (2012), PEI conjugated to β-cyclodextrin (PC) was used to transfect pDNA. Results shows that it is internalized by caveolae- and clathrin-dependent pathways. To enhance the nuclear delivery of DNA, the NLS peptide inspired from SV40 virus was combined and conjugated to the PC backbone. Compared to PC/pDNA, PC/NLS/pDNA shows higher gene transfection efficiency.

nanoparticle or directly to the gene of interest. Variants of virus-derived NLS peptides are most commonly used as nuclear targeting ligands (Kim et al., 2017). Thus, carriers decorated with or nucleic acid cargo associated with the NLS peptide sequence also undergo nuclear uptake via the karyopherin α/β pathway (Pan et al., 2012; Ray et al., 2015; Zanta et al., 1999; Cartier and Reszka, 2002). One such example by Hu et al., 2012 has been discussed in detail in **Figure 5** wherein the classical NLS peptide sequence derived from SV40 virus was used to deliver a plasmid DNA (pDNA) polyplex across the nuclear envelope via karyopherin-dependent pathway (Hu et al., 2012). Importantly, the unmasking of NLS peptide in case of SV40 and HIV virus only when it is needed reduces the off-target binding and increases the karyopherin-mediated uptake (Nakanishi et al., 2002; Fanales-Belasio et al., 2010). These kinds of smart techniques can be explored further as current synthetic carriers are designed to deliver the whole construct to the nucleus and not just the nucleic acid cargo (Hu et al., 2012; Favaro et al., 2018).

Alternatively, the DNA nuclear-targeting sequence (DTS) is a 72 bp aptamer derived from SV40 and has innate affinity for NLS-tagged cytoplasmic proteins such as transcription factors (TFs) (Gaal et al., 2011). DTS-containing plasmids bind to one or more TFs, and the complex is shuttled into the nucleus. If cells are undergoing proliferation due to injury, the addition of DTS/NLS

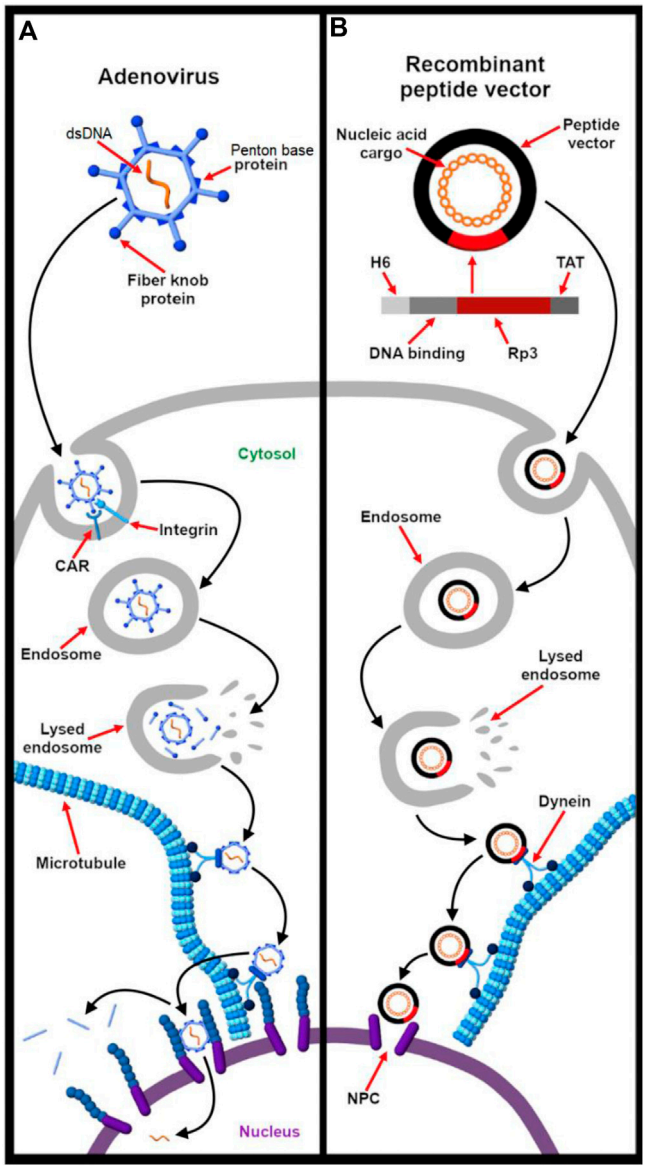

FIGURE 6 | Microtubule (MT)-assisted nuclear delivery of adenovirus mimicked by a recombinant peptide vector. **(A)** Adenovirus undergoes receptor-mediated endocytosis by targeting CAR and integrin receptors present on the cell surface. Once inside the endosome, protein VI contains an N-terminal amphipathic helix that fragments the endosomal membrane. An adjacent peptide motif is also exposed which helps to drive the viral capsid out of the endosome (Flatt and Butcher 2019). After endosomal escape, the hexon facet of the viral capsid interacts with the kinesin light chain and cytoplasmic dynein protein. Thus, the virion hijacks the host's dynein/dynactin motor proteins to hitchhike towards the nucleus. As the viral capsid docks onto the nuclear pore complex (NPC), the kinesin motor mediates a tug-of-war process for final uncoating of the viral capsid and release of the viral genome (Scherer and Vallee 2011). **(B)** To mimic this nuclear virus strategy, a peptide-based non-viral vector was synthesized by Favaro et al. (2018) wherein they used modular recombinant TRp3 protein (human dynein light chain) that interacts with dynein motor proteins and undergoes MT-assisted nuclear delivery. In addition to the MT-targeting protein, this peptide vector is composed of TAT for cell targeting, a DNA binding domain for electrostatic condensation of DNA and six histidine moieties for endosomal escape. Conclusively, this modular protein is able to efficiently deliver nucleic acid cargos including plasmid DNA, dsRNA and siRNA (Favaro et al., 2018).

sequence shows limited effect in gene expression as the guard of the nuclear envelope breaks down (Miller and Dean, 2009). So far, DTS expressing plasmids have been delivered by electroporation or direct injection. Thus, it is possible to use DTS as a targeting ligand for gene vectors but not *in vivo*. In addition, plasmids complexed with proteins like HMG-1, histone H2B proteins, karyopherin receptors, and nucleoplasmin show increased transgene expression due to nuclear uptake (Miller and Dean, 2009).

Microtubule-Assisted Transport

Many viruses use microtubule (MT) facilitated transport to traverse the cytoplasmic medium. Viral proteins induce rearrangement of microfilaments and recruit molecular motors

such as dynein and kinesin to traverse from the plus to the minus terminal of MTs (Döhner et al., 2005). The MT-organizing center nucleates the minus end of the MTs and is close to the nucleus. This is how the viral capsid is transported actively to reach nearby regions of the nucleus (Naghavi and Walsh, 2017). Viruses such as the adenovirus, adeno-associated virus (AAV), and influenza A virus are able to hijack the cellular microtubule transport system, intercepting traffic to the nucleus. Amongst these, the adenovirus and influenza A virus are released out of the endosome before traveling along the microtubule in a non-vesicle dependent manner. In contrast, AAV is transported while within the endosome and the endosomal vesicle ruptures near the nucleus. The ligands that attach the endosomal membrane to the MT system are still currently unknown (Cohen et al., 2011).

In an effort to mimic viruses, the dynein binding protein (DBP) is often used as a ligand for nuclear uptake as it can mediate the transport of cargo via the MT-assisted pathway (Favaro et al., 2014; Favaro et al., 2018). A review by Midoux et al., 2017 has listed the dynein binding viral proteins and selective peptide sequences that have been used for efficient nonviral gene delivery. These peptides help to actively deliver the nanovector to the centrosome wherein the dynein interacts dynamically with the nuclear envelope and rearranges the nuclear lamin protein filaments, thereby increasing the permeability of nucleus (Dalmau-Mena et al., 2018). Moreover, Cohen and Granek (2014) provided theoretical insights on the rational design of spherical nanocarriers that require active transport to the nucleus. One recent example using such pathway is a peptide vector synthesized by Favaro et al., 2018 (2018). In this study, a dynein binding protein (TRp3) was incorporated into the vector to enhance microtubule-assisted delivery of an encapsulated gene toward the nucleus of the cell (**Figure 6**).

CONCLUDING REMARKS

Evolution has honed viruses to be master hijackers of a broad range of host cells. They possess unique structural and mechanistic features wherein overarching themes such as capsid metastability, genome protection, stimuli-responsiveness, receptor duality, and synergistic ligand activity make them attractive templates for the design of non-viral nucleic acid carriers. Based on these outstanding characteristics of viruses, it is evident that an ideal carrier needs to find a balance between nucleic acid protection and release, two seemingly contradictory functions. A dynamic structure that responds to site-specific cues such as low pH or enzymatic activity help to control the release of nucleic acid cargo. These cues can vary with microenvironments within a cell, enabling biochemically controlled release mechanisms. Alternatively, the vector can be made sensitive to external stimuli such as light or temperature, which is more applicable to locally delivered formulations (Takemoto et al., 2014).

While therapeutic nucleic acids have made it to the clinical setting, extrahepatic targeting, endosomal escape, and controlled subcellular localization remain as major hurdles in their delivery (Juliano, 2016; Dowdy, 2017; Johannes and Lucchino, 2018; Juliano, 2018). Viruses commonly target multiple receptors for enhanced specificity and uptake, and this collective feature has been applied by synthetic carriers. Viral mimicry and the development of nucleic acid vectors iterate with our understanding of viral mechanism. Accordingly, advancements in techniques that identify viral ligands and corresponding host receptors, interrogate structure, and probe dynamics of ligand-receptor interactions may be translated to the design of more effective targeting domains for synthetic carriers.

In many ways, the outstanding difference in the transfection efficiency of viruses and synthetic vectors stems from the lack of a consensus of what drives endosomal escape. Escape from the endosome is influenced by a large range of factors such as nanoparticle properties (size, shape, and composition), mode of cellular uptake, and the type of cell (Selby et al., 2017). Moreover, mechanistic insights tend to be context-dependent as they are influenced by multiple factors such as the type of carrier, type of cell, and experimental conditions (LeCher et al., 2017). Structural studies on determinants of endosomal escape, while informative, often do not address the possible interplay of uptake route and intracellular trafficking. Moreover, uptake mechanisms are overlapping and poorly understood, making it difficult to determine the exact uptake mechanism of a particular construct (Nelemans and Gurevich, 2020). As uptake mechanisms typically involve signaling cascades, their relationship with intracellular trafficking are important considerations. Also, the implication of recycling pathways in viral and non-viral cytosolic access (Carette et al., 2011; Sahay et al., 2013; Wang et al., 2016a; Staring et al., 2018) suggests further studies on their exact role in therapeutic delivery. Filling such scientific gaps may help guide the design of more efficient nucleic acid delivery systems. Additionally, some viruses (such as the adenovirus) have been found to exploit cellular responses to membrane disruption concurrent with membrane fusion or penetration (Staring et al., 2018). In this light, future synthetic carriers may also be tailored to utilize host damage control to enhance therapeutic delivery. For this to be an effective strategy, it is imperative that the sensing of and response to invading particles by the host cell be exhaustively studied.

In summary, viruses can serve as a source of inspiration for chemists and materials scientists alike in the design considerations of non-viral vectors due to their efficient uptake and delivery of nucleic acid cargo. By designing nanoscale materials with stimuli-responsive properties and efficient targeting and internalization, therapeutic nucleic acids can be more rapidly brought forward for clinical application.

AUTHOR CONTRIBUTIONS

All authors listed have made a substantial, direct, and intellectual contribution to the work and approved it for publication.

REFERENCES

Adams, D., Gonzalez-Duarte, A., O'Riordan, W. D., Yang, C.-C., Ueda, M., Kristen, A. V., et al. (2018). Patisiran, an RNAi therapeutic, for hereditary transthyretin amyloidosis. *N. Engl. J. Med.* 379 (1), 11–21. doi:10.1056/NEJMoa1716153

Aghdam, A., Marjan, R. B., Mosafer, J., Baradaran, B., Hashemzaei, M., Baghbanzadeh, A., et al. (2019). Recent advances on thermosensitive and PH-sensitive liposomes employed in controlled release. *J. Control. Relea.* 315, 1–22. doi:10.1016/j.jconrel.2019.09.018

Akinc, A., Querbes, W., De, S., Qin, J., and Frank-Kamenetsky, M. (2010). Targeted delivery of RNAi therapeutics with endogenous and exogenous ligand-based mechanisms. *Mol. Ther.* 18 (7), 1357–1364. doi:10.1038/mt.2010.85

Alam, M. R., Dixit, V., Kang, H., Li, Z. B., Chen, X., Trejo, J., et al. (2008). Intracellular delivery of an anionic antisense oligonucleotide via receptor-mediated endocytosis. *Nuc. Acid. Res.* 36 (8), 2764–2776. doi:10.1093/nar/gkn115

Aleksandrowicz, P., Marzi, A., Biedenkopf, N., Beimforde, N., Becker, S., Hoenen, T., et al. (2011). Ebola virus enters host cells by macropinocytosis and clathrin-mediated endocytosis. *J. Infect. Dis.* 204 (3), S957–S967. doi:10.1093/infdis/jir326

Alipour, M., Hosseinkhani, S., Sheikhnejad, R., and Cheraghi, R. (2017). Nano-biomimetic carriers are implicated in mechanistic evaluation of intracellular gene delivery. *Sci. Rep.* 7 (1), 41507. doi:10.1038/srep41507

Ämmälä, C., Drury, W. J., Knerr, L., Ahlstedt, I., Stillemark-Billton, P., Wennberg-Huldt, C., et al. (2018). Targeted delivery of antisense oligonucleotides to pancreatic β-cells. *Sci. Adv.* 4 (10), eaat3386. doi:10.1126/sciadv.aat3386

Anyarambhatla, G. R., and Needham, D. (1999). Enhancement of the phase transition permeability of DPPC liposomes by incorporation of mppc: a new temperature-sensitive liposome for use with mild hyperthermia. *J. Liposome Res.* 9 (4), 491–506. doi:10.3109/08982109909035549

Arana, L., Bayón-Cordero, L., Sarasola, L., Berasategi, M., and Ruiz, S. (2019). Solid lipid nanoparticles surface modification modulates cell internalization and improves chemotoxic treatment in an oral carcinoma cell line. *Nanomaterials* 9 (3), 464. doi:10.3390/nano9030464

Arinaminpathy, N., and Grenfell, B. (2010). Dynamics of glycoprotein charge in the evolutionary history of human influenza. *PLoS One* 5 (12), e15674. doi:10.1371/journal.pone.0015674

Asai, T., Matsushita, S., Kenjo, E., Tsuzuku, T., Yonenaga, N., Koide, H., et al. (2011). Dicetyl phosphate-tetraethylenepentamine-based liposomes for systemic SiRNA delivery. *Bioconjug. Chem.* 22 (3), 429–435. doi:10.1021/bc1004697

Ashley, C. E., Carnes, E. C., Phillips, G. K., Durfee, P. N., Lino, C. A., Padilla, D. P., et al. (2011). Cell-specific delivery of diverse cargos by bacteriophage MS2 virus-like particles. *ACS Nano* 5 (7), 5729–5745. doi:10.1021/nn201397z

Awino, J. K., Gudipati, S., Hartmann, A. K., Santiana, J. J., and Cairns-Gibson, D. F. (2017). Nucleic acid nanocapsules for enzyme-triggered drug release. *J. Am. Chem. Soc.* 139 (18), 6278–6281. doi:10.1021/jacs.6b13087

Bai, H., Schiralli Lester, G. M., Petishnok, L. C., and Dean, D. A. (2017). Cytoplasmic transport and nuclear import of plasmid DNA. *Biosci. Rep.* 37, BSR20160616. doi:10.1042/BSR20160616

Banerjee, R., Tyagi, P., Li, S., and Huang, L. (2004). Anisamide-targeted stealth liposomes: a potent carrier for targeting doxorubicin to human prostate cancer cells. *Int. J. Cancer* 112 (4), 693–700. doi:10.1002/ijc.20452

Banga, R. J., Meckes, B., Narayan, S. P., Sprangers, A. J., Nguyen, S. T., and Mirkin, C. A. (2017). Cross-linked micellar spherical nucleic acids from thermoresponsive templates. *J. Am. Chem. Soc.* 139 (12), 4278–4281. doi:10.1021/jacs.6b13359

Banga, R. J., Chernyak, N., and Narayan, S. P. (2014). Liposomal spherical nucleic acids. *J. Am. Chem. Soc.* 136 (28), 9866–9869. doi:10.1021/ja504845f

Barba, A. A., Bochicchio, S., Dalmoro, A., and Lamberti, G. (2019). Lipid delivery systems for nucleic-acid-based-drugs: from production to clinical applications. *Pharmaceutics* 11 (8), 360. doi:10.3390/pharmaceutics11080360

Barrow, E., Nicola, A. V., and Liu, J. (2013). Multiscale perspectives of virus entry via endocytosis. *Virol. J.* 10, 177. doi:10.1186/1743-422X-10-177

Beniac, D. R., Melito, P. L., Devarennes, S. L., Hiebert, S. L., Rabb, M. J., and Lamboo, L. L. (2012). The organisation of ebola virus reveals a capacity for extensive, modular polyploidy. *PLOS One* 7 (1), e29608. doi:10.1371/journal.pone.0029608

Brandenburg, B., Stockl, L., Gutzeit, C., Roos, M., Lupberger, J., Schwartlander, R., et al. (2005). A novel system for efficient gene transfer into primary human hepatocytes via cell-permeable hepatitis B virus-like particle. *Hepatology* 42 (6), 1300–1309. doi:10.1002/hep.20950

Breuzard, G., Tertil, M., Gonçalves, C., Cheradame, H., Géguan, P., Pichon, C., et al. (2008). Nuclear delivery of NFkappaB-assisted DNA/polymer complexes: plasmid DNA quantitation by confocal laser scanning microscopy and evidence of nuclear polyplexes by FRET imaging. *Nucleic Acids Res.* 36 (12), e71. doi:10.1093/nar/gkn287

Brodin, J. D., Sprangers, A. J., McMillan, J. R., Mirkin, C. A., and Mirkin, C. A. (2015). DNA-mediated cellular delivery of functional enzymes. *J. Am. Chem. Soc.* 137 (47), 14838–14841. doi:10.1021/jacs.5b09711

Budker, V., Gurevich, V., Hagstrom, J. E., Bortzov, F., and Wolff, J. A. (1996). PH-sensitive, cationic liposomes: a new synthetic virus-like vector. *Nat. Biotechnol.* 14 (6), 760–764. doi:10.1038/nbt0696-760

Bukrinsky, M. (2004). A hard way to the nucleus. *Mol. Med.* 10 (1–6), 1–5. doi:10.1007/bf03401996

Burckhardt, C. J., Suomalainen, M., Schoenenberger, P., Boucke, K., Hemmi, S., and Greber, U. F. (2011). Drifting motions of the adenovirus receptor CAR and immobile integrins initiate virus uncoating and membrane lytic protein exposure. *Cell Host. Microbe.* 10 (2), 105–117. doi:10.1016/j.chom.2011.07.006

Burger, N., Biswas, A., Barzan, D., Kirchner, A., Hosser, H., Hausmann, M., et al.(2014). A method for the efficient cellular uptake and retention of small modified gold nanoparticles for the radiosensitization of cells. *Nanomedicine* 10 (6), 1365–1373. doi:10.1016/j.nano.2014.03.011

Burgess, K. (2001). Solid-phase syntheses of beta-turn analogues to mimic or disrupt protein-protein interactions. *Acc. Chem. Res.* 34 (10), 826–835. doi:10.1021/ar9901523

Burri, D. J., da Palma, J. R., Kunz, S., and Pasquato, A. (2012). Envelope glycoprotein of arenaviruses. *Viruses* 4 (10), 2162–2181. doi:10.3390/v4102162

Cai, X., Chen, H. H., Wang, C. L., Chen, S. T., Lai, S. F., Chien, C. C., et al. (2011). Imaging the cellular uptake of tiopronin-modified gold nanoparticles. *Anal. Bioanal. Chem.* 401 (3), 809–816. doi:10.1007/s00216-011-4986-3

Callaway, E. (2020). The race for coronavirus vaccines: a graphical guide. *Nature* 580 (7805), 576–577. doi:10.1038/d41586-020-01221-y

Cao, W., Henry, M. D., Borrow, P., Yamada, H., Elder, J. H., Ravkov, E. V., et al. (1998). Identification of alpha-dystroglycan as a receptor for lymphocytic choriomeningitis virus and Lassa fever virus. *Science* 282 (5396), 2079–2081. doi:10.1126/science.282.5396.2079

Carette, J. E., Raaben, M., Wong, A. C., Herbert, A. S., Obernosterer, G., et al. (2011). Ebola virus entry requires the cholesterol transporter niemann-pick C1. *Nature* 477 (7364), 340–343. doi:10.1038/nature10348

Cartier, R., and Reszka, R. (2002). Utilization of synthetic peptides containing nuclear localization signals for nonviral gene transfer systems. *Gene Ther.* 9 (3), 157–167. doi:10.1038/sj.gt.3301635

Chan, D. C., Fass, D., Berger, J. M., and Kim, P. S. (1997). Core structure of Gp41 from the HIV envelope glycoprotein. *Cell* 89 (2), 263–273. doi:10.1016/S0092-8674(00)80205-6

Chang, K. L., Higuchi, Y., Kawakami, S., Yamashita, F., and Hashida, M. (2010). Efficient gene transfection by histidine-modified chitosan through enhancement of endosomal escape. *Bioconjug. Chem.* 21 (6), 1087–1095. doi:10.1021/bc1000609

Chernomordik, L., Kozlov, M. M., and Zimmerberg, J. (1995). Lipids in biological membrane fusion. *J. Membr. Biol.* 146 (1), 1–14. doi:10.1007/BF00232676

Chery, J. (2016). RNA therapeutics: RNAi and antisense mechanisms and clinical applications. *Postdoc. J.: A J. Postdoc. Res. Postdoc. Aff.* 4 (7), 35–50. doi:10.14304/surya.jpr.v4n7.5

Choi, C. H. J., Hao, L., Narayan, S. P., Auyeung, E., and Mirkin, C. A. (2013). Mechanism for the endocytosis of spherical nucleic acid nanoparticle conjugates. *Proc. Natl. Acad. Sci.* 110 (19), 7625–7630. doi:10.1073/pnas.1305804110

Cohen, O., and Granek, R. (2014). Nucleus-targeted drug delivery: theoretical optimization of nanoparticles decoration for enhanced intracellular active transport. *Nano Lett.* 14 (5), 2515–2521. doi:10.1021/nl500248q

Cohen, R. N., van der Aavan der Aa, M. A., Macaraeg, N., Lee, A. P., and Szoka, F. C. (2009). Quantification of plasmid DNA copies in the nucleus after lipoplex and polyplex transfection. *J. Control. Relea.* 135 (2), 166–174. doi:10.1016/j.jconrel.2008.12.016

Cohen, S., Au, S., and Panté, N. (2011). How viruses access the nucleus. *Biochim. Biophys. Acta* 1813 (9), 1634–1645. doi:10.1016/j.bbamcr.2010.12.009

Cohen-Dvashi, H., Cohen, N., Israeli, H., and Diskin, R. (2015). Molecular mechanism for LAMP1 recognition by Lassa virus. *J. Virol.* 89 (15), 7584–7592. doi:10.1128/JVI.00651-15

Cohen-Dvashi, H., Israeli, H., Shani, O., Katz, A., and Diskin, R. (2016). Role of LAMP1 binding and PH sensing by the spike complex of Lassa virus. *J. Virol.* 90 (22), 10329–10338. doi:10.1128/JVI.01624-16

Corbett, K. S., Edwards, D., Leist, S. R., Abiona, O. M., Boyoglu-Barnum, S., Gillespie, R. A., et al. (2020). SARS-CoV-2 MRNA vaccine development enabled by prototype pathogen preparedness. *BioRxiv* [Epub ahead of print]. doi:10.1101/2020.06.11.145920

Côté, M., Misasi, J., Ren, T., Bruchez, A., Lee, K., Filone, C. M., et al. (2011). Small molecule inhibitors reveal Niemann-Pick C1 is essential for Ebola virus infection. *Nature* 477 (7364), 344–348. doi:10.1038/nature10380

Couch, R. B. (1996). "Orthomyxoviruses," in *Medical microbiology*. Editors S. Baron (Galveston, TX: University of Texas Medical Branch).

Crews, C. M. (2010). Targeting the undruggable proteome: the small molecules of my dreams. *Chem. Biol.* 17 (6), 551–555. doi:10.1016/j.chembiol.2010.05.011

Cros, J. F., and Palese, P. (2003). Trafficking of viral genomic RNA into and out of the nucleus: influenza, thogoto and borna disease viruses. *Virus. Res.* 95 (1), 3–12. doi:10.1016/S0168-1702(03)00159-X

Cruz-Acuña, M., Halman, J. R., Afonin, K. A., and Dobson, J. (2018). Magnetic nanoparticles loaded with functional RNA nanoparticles. *Nanoscale* 10 (37), 17761–17770. doi:10.1039/C8NR04254C

Cutler, J. I., Auyeung, E., and Mirkin, C. A. (2012). Spherical nucleic acids. *J. Am. Chem. Soc.* 134 (3), 1376–1391. doi:10.1021/ja209351u

Cutler, J. I., Zhang, K., Zheng, D., Auyeung, E., Prigodich, A. E., and Mirkin, C. A. (2011). Polyvalent nucleic acid nanostructures. *J. Am. Chem. Soc.* 133 (24), 9254–9257. doi:10.1021/ja203375n

Cutler, J. I., Zheng, D., Xu, X., Giljohann, D. A., and Mirkin, C. A. (2010). Polyvalent oligonucleotide iron oxide nanoparticle "click" conjugates. *Nano Lett.* 10 (4), 1477–1480. doi:10.1021/nl100477m

Dalmau-Mena, I., del Pino, P., Pelaz, B., Cuesta-Geijo, M. Á., Galindo, I., Moros, M., et al. (2018). Nanoparticles engineered to bind cellular motors for efficient delivery. *J. Nanobiotechnology* 16 (1), 33. doi:10.1186/s12951-018-0354-1

Damha, M. J. (2019). Exciting times in the field of nucleic acid therapeutics. *Trends Mol. Med.* 25 (12), 1051–1052. doi:10.1016/j.molmed.2019.10.005

Danhier, F., Le Breton, A., and Préat, V. (2012). RGD-based strategies to target alpha(v) beta(3) integrin in cancer therapy and diagnosis. *Mol. Pharm.* 9, 2961–2971. doi:10.1021/mp3002733

Dassie, J. P., and Giangrande, P. H. (2013). Current progress on aptamer-targeted oligonucleotide therapeutics. *Ther. Deliv.* 4 (12), 1527–1546. doi:10.4155/tde.13.118

de Jonge, J., Holtrop, M., Wilschut, J., and Huckriede, A. (2006). Reconstituted influenza virus envelopes as an efficient carrier system for cellular delivery of small-interfering RNAs. *Gene Ther.* 13 (5), 400–411. doi:10.1038/sj.gt.3302673

Debacker, A. J., Voutila, J., Catley, M., Blakey, D., and Habib, N. (2020). Delivery of oligonucleotides to the liver with GalNAc: from research to registered therapeutic drug. *Mol. Ther.* 28 (8), 1759–1771. doi:10.1016/j.ymthe.2020.06.015

Ding, F., Gao, X., Huang, X., Ge, H., Xie, M., Qian, J., et al. (2020). Polydopamine-coated nucleic acid nanogel for SiRNA-mediated low-temperature photothermal therapy. *Biomaterials* 245, 119976. doi:10.1016/j.biomaterials.2020.119976

Ding, F., Mou, Q., Ma, Y., Pan, G., Guo, Y., Tong, G., et al. (2018). A crosslinked nucleic acid nanogel for effective SiRNA delivery and antitumor therapy. *Angew. Chem. Int. Ed. Engl.* 57 (12), 3064–3068. doi:10.1002/anie.201711242

Ding, F., Huang, X., Gao, X., Xie, M., Pan, G., Li, Q., et al. (2019). A non-cationic nucleic acid nanogel for the delivery of the CRISPR/Cas9 gene editing tool. *Nanoscale* 11 (37), 17211–17215. doi:10.1039/C9NR05233J

Ding, Y., Jiang, Z., Saha, K., Kim, C. S., Kim, S. T., Landis, R. F., et al. (2014a). Gold nanoparticles for nucleic acid delivery. *Mol. Ther.* 22 (6), 1075–1083. doi:10.1038/mt.2014.30

Ding, Y., Wang, Y., Zhou, J., Gu, X., Wang, W., Liu, C., et al. (2014b). Direct cytosolic SiRNA delivery by reconstituted high density lipoprotein for target-specific therapy of tumor angiogenesis. *Biomaterials* 35 (25), 7214–7227. doi:10.1016/j.biomaterials.2014.05.009

Döhner, K., Nagel, C.-H., and Sodeik, B. (2005). Viral stop-and-go along microtubules: taking a ride with dynein and kinesins. *Trends Microbiol.* 13 (7), 320–327. doi:10.1016/j.tim.2005.05.010

Dong, Y., Yu, T., Ding, L., Laurini, E., Huang, Y., Zhang, M., et al. (2018). A dual targeting dendrimer-mediated SiRNA delivery system for effective gene silencing in cancer therapy. *J. Am. Chem. Soc.* 140 (47), 16264–16274. doi:10.1021/jacs.8b10021

Dowaidar, M., Hällbrink, M., Freimann, K., Kurrikoff, K., Zou, X., and Langel, Ü. (2017). Magnetic nanoparticle assisted self-assembly of cell penetrating peptides-oligonucleotides complexes for gene delivery. *Sci. Rep.* 7 (1), 9159. doi:10.1038/s41598-017-09803-z

Dowdy, S. F. (2017). Overcoming cellular barriers for RNA therapeutics. *Nat. Biotechnol.* 35 (3), 222–229. doi:10.1038/nbt.3802

Dowdy, S. F., and Levy, M. (2018). RNA therapeutics (almost) comes of age: targeting, delivery and endosomal escape. *Nucleic Acid Ther.* 28 (3), 107–108. doi:10.1089/nat.2018.29001.dow

Du Rietz, H., Hedlund, H., Wilhelmson, S., Nordenfelt, P., and Wittrup, A. (2020). Imaging small molecule-induced endosomal escape of SiRNA. *Nat. Commun.* 11 (1), 1809. doi:10.1038/s41467-020-15300-1

Duffy, M. J., and Crown, J. (2021). Drugging "undruggable" genes for cancer treatment: are we making progress?. *Int. J. Cancer* 148 (1), 8–17. doi:10.1002/ijc.33197

Elghanian, R., Storhoff, J. J., Mucic, R. C., Letsinger, R. L., and Mirkin, C. A. (1997). Selective colorimetric detection of polynucleotides based on the distance-dependent optical properties of gold nanoparticles. *Science* 277 (5329), 1078–1081. doi:10.1126/science.277.5329.1078

Ewers, H., Römer, W., Smith, A. E., Bacia, K., Dmitrieff, S., Chai, W., et al. (2010). GM1 structure determines SV40-induced membrane invagination and infection. *Nat. Cell Biol.* 12 (1), 11–12. doi:10.1038/ncb1999

Falasca, L., Agrati, C., Petrosillo, N., Di Caro, A., Capobianchi, M. R., Ippolito, G., et al. (2015). Molecular mechanisms of ebola virus pathogenesis: focus on cell death. *Cell Death Differ.* 22 (8), 1250–1259. doi:10.1038/cdd.2015.67

Fan, Y., Yao, J., Du, R., Hou, L., Zhou, J., Lu, Y., et al. (2013). Ternary complexes with core-shell bilayer for double level targeted gene delivery: *in vitro* and *in vivo* evaluation. *Pharm. Res.* 30 (5), 1215–1227. doi:10.1007/s11095-012-0960-9

Fanales-Belasio, E., Raimondo, M., Suligoi, B., and Buttò, S. (2010). HIV virology and pathogenetic mechanisms of infection: a brief overview. *Ann. Ist Super Sanita* 46 (1), 5–14. doi:10.4415/ANN_10_01_02

Fang, Y., Xue, J., Gao, S., Lu, A., Yang, D., Jiang, H., et al. (2017). Cleavable PEGylation: a strategy for overcoming the "PEG dilemma" in efficient drug delivery. *Drug Deliv.* 24 (2), 22–32. doi:10.1080/10717544.2017.1388451

Faustino, R. S., Nelson, T. J., Terzic, A., and Perez-Terzic, C. (2007). Nuclear transport: target for therapy. *Clin. Pharmacol. Ther.* 81 (6), 880–886. doi:10.1038/sj.clpt.6100141

Favaro, M. T., de Toledo, M. A., Alves, R. F., Santos, C. A., Beloti, L. L., Janissen, R., et al. (2014). Development of a non-viral gene delivery vector based on the dynein light chain Rp3 and the TAT peptide. *J. Biotechnol.* 173, 10–18. doi:10.1016/j.jbiotec.2014.01.001

Favaro, M. T. P., Unzueta, U., de Cabo, M., Villaverde, A., Ferrer-Miralles, N., and Azzoni, A. R. (2018). Intracellular trafficking of a dynein-based nanoparticle designed for gene delivery. *Eur. J. Pharm. Sci.* 112, 71–78. doi:10.1016/j.ejps.2017.11.002

Fay, N., and Panté, N. (2015). Nuclear entry of DNA viruses. *Front. Microbiol.* 6, 467. doi:10.3389/fmicb.2015.00467

Felgner, P. L., Gadek, T. R., Holm, M., Roman, R., Chan, H. W., Wenz, M., et al. (1987). Lipofection: a highly efficient, lipid-mediated DNA-transfection procedure. *Proc. Proc Natl Acad. Sci. U.S.A.* 84 (21), 7413–7417. doi:10.1073/pnas.84.21.7413

Feng, G., Chen, H., Li, J., Huang, Q., Gupte, M. J., Liu, H., et al. (2015). Gene therapy for nucleus pulposus regeneration by heme oxygenase-1 plasmid DNA carried by mixed polyplex micelles with thermo-responsive heterogeneous coronas. *Biomaterials* 52, 1–13. doi:10.1016/j.biomaterials.2015.02.024

Ferrari, S., Pettenazzo, A., Garbati, N., Zacchello, F., Behr, J. P., and Scarpa, M. (1999). Polyethylenimine shows properties of interest for cystic fibrosis gene therapy. *Biochim. Biophys. Acta* 1447 (2), 219–225. doi:10.1016/S0167-4781(99)00153-0

Flatt, J. W., and Butcher, S. J. (2019). Adenovirus flow in host cell networks. *Open Biol.* 9 (2), 190012. doi:10.1098/rsob.190012

Flint, J., Racaniello, V. R., Rall, G. F., Skalka, M., and Enquist, W. (2015). *Principles of virology*. 4th Edn. Hoboken, NJ: Wiley.

Fouriki, A., and Dobson, J. (2014). Oscillating magnet array-based nanomagnetic gene transfection of human mesenchymal stem cells. *Nanomedicine* 9 (7), 989–997. doi:10.2217/nnm.13.74

Fraley, R., Subramani, S., Berg, P., and Papahadjopoulos, D. (1980). Introduction of liposome-encapsulated SV40 DNA into cells. *J. Biol. Chem.* 255 (21), 10431–10435. doi:10.1016/s0021-9258(19)70482-7

Friedman, A. D., Claypool, S. E., and Liu, R. (2013). The smart targeting of nanoparticles. *Curr. Pharm. Des.* 19 (35), 6315–6329. doi:10.2174/13816128113199990375

Fu, Y., and Li, J. (2016). A novel delivery platform based on bacteriophage MS2 virus-like particles. *Virus. Res.* 211, 9–16. doi:10.1016/j.virusres.2015.08.022

Gaal, E. V. B., Roel van Eijk, R. S. O., Bakowska, M., Feyen, D., Jan Kok, R., Hennink, W. E., et al. (2011). DNA nuclear targeting sequences for non-viral gene delivery. *Pharm. Res.* 28 (7), 1707–1722. doi:10.1007/s11095-011-0407-8

Gaber, M. H., Hong, K., Huang, S. K., and Papahadjopoulos, D. (1995). Thermosensitive sterically stabilized liposomes: formulation and *in Vitro* studies on mechanism of doxorubicin release by bovine serum and human plasma. *Pharm. Res.* 12 (10), 1407–1416. doi:10.1023/a:1016206631006

Galaway, F. A., and Stockley, P. G. (2013). MS2 viruslike particles: a robust, semisynthetic targeted drug delivery platform. *Mol. Pharm.* 10 (1), 59–68. doi:10.1021/mp3003368

Gelderblom, H. R. (1996). "Structure and classification of viruses," in *Medical microbiology*. Editor S. Baron (Galveston, TX: University of Texas Medical Branch).

Ghasemiyeh, P., and Mohammadi-Samani, S. (2018). Solid lipid nanoparticles and nanostructured lipid carriers as novel drug delivery systems: applications, advantages and disadvantages. *Res. Pharm. Sci.* 13 (4), 288–303. doi:10.4103/1735-5362.235156

Gillard, M., Jia, Z., Hou, J. J., Song, M., Gray, P. P., Munro, T. P., et al. (2014). Intracellular trafficking pathways for nuclear delivery of plasmid DNA complexed with highly efficient endosome escape polymers. *Biomacromolecules* 15 (10), 3569–3576. doi:10.1021/bm5008376

Gilleron, J., Querbes, W., Zeigerer, A., Borodovsky, A., Marsico, G., Schubert, U., et al. (2013). Image-based analysis of lipid nanoparticle-mediated SiRNA delivery, intracellular trafficking and endosomal escape. *Nat. Biotechnol.* 31 (7), 638–646. doi:10.1038/nbt.2612

Gilleron, J., Paramasivam, P., Zeigerer, A., Querbes, W., Marsico, G., Andree, C., et al. (2015). Identification of SiRNA delivery enhancers by a chemical library screen. *Nucleic Acids Res.* 43 (16), 7984–8001. doi:10.1093/nar/gkv762

Greber, U. F. (2016). Virus and host mechanics support membrane penetration and cell entry. *J. Virol.* 90 (8), 3802–3805. doi:10.1128/JVI.02568-15

Greber, U. F., Suomalainen, M., Stidwill, R. P., Boucke, K., and Ebersold, M. W. (1997). The role of the nuclear pore complex in adenovirus DNA entry. *EMBO J.* 16 (19), 5998–6007. doi:10.1093/emboj/16.19.5998

Grove, J., and Marsh, M. (2011). The cell biology of receptor-mediated virus entry. *J. Cell Biol.* 195 (7), 1071–1082. doi:10.1083/jcb.201108131

Gudipati, S., Zhang, K., and Rouge, J. L. (2019). Towards self-transfecting nucleic acid nanostructures for gene regulation. *Trends Biotechnol.* 37 (9), 983–994. doi:10.1016/j.tibtech.2019.01.008

Hamid, F. B., Kim, J., and Shin, C.-G. (2015). Cellular and viral determinants of retroviral nuclear entry. *Can. J. Microbiol.* 62, 1. doi:10.1139/cjm-2015-0350

Han, X., Bushweller, J. H., Cafiso, D. S., and Tamm, L. K. (2001). Membrane structure and fusion-triggering conformational change of the fusion domain from influenza hemagglutinin. *Nat. Struct. Biol.* 8 (8), 715–720. doi:10.1038/90434

Hao, X., Li, Q., Guo, J., Ren, X., Feng, Y., Shi, C., et al. (2017). Multifunctional gene carriers with enhanced specific penetration and nucleus accumulation to promote neovascularization of HUVECs *in Vivo*. *ACS Appl. Mater. Inter.* 9 (41), 35613–35627. doi:10.1021/acsami.7b11615

Harrison, S. C. (2008). Viral membrane fusion. *Nat. Struct. Mol. Biol.* 15 (7), 690–698. doi:10.1038/nsmb.1456

Hartmann, A. K., Cairns-Gibson, D. F., Santiana, J. J., Tolentino, M. Q., and Barber, H. M. (2018). Enzymatically ligated DNA-surfactants: unmasking hydrophobically modified DNA for intracellular gene regulation. *ChemBioChem* 19 (16), 1734–1739. doi:10.1002/cbic.201800302

Hartmann, A. K., Gudipati, S., Pettenuzzo, A., Ronconi, L., and Rouge, J. L. (2020). Chimeric SiRNA-DNA surfactants for the enhanced delivery and sustained cytotoxicity of a gold(III) metallodrug. *Bioconjug. Chem.* 31 (4), 1063–1069. doi:10.1021/acs.bioconjchem.0c00047

Heidarli, E., Dadashzadeh, S., and Haeri, A. (2017). State of the art of stimuli-responsive liposomes for cancer therapy. *Iran J. Pharm. Res.* 16 (4), 1273–1304.

Corey, D. R. (2007). Chemical modification: the key to clinical application of RNA interference?. *J. Clin. Invest.* 117 (12), 3615–3622. doi:10.1172/JCI33483

Hoy, S. M. (2018). Patisiran: first global approval. *Drugs* 78 (15), 1625–1631. doi:10.1007/s40265-018-0983-6

Hu, Q., Wang, J., Shen, J., Liu, M., Jin, X., Tang, G., et al. (2012). Intracellular pathways and nuclear localization signal peptide-mediated gene transfection by cationic polymeric nanovectors. *Biomaterials* 33 (4), 1135–1145. doi:10.1016/j.biomaterials.2011.10.023

Huang, K., Ma, H., Liu, J., Huo, S., Kumar, A., Wei, T., et al. (2012). Size-dependent localization and penetration of ultrasmall gold nanoparticles in cancer cells, multicellular spheroids, and tumors *in Vivo*. *ACS Nano* 6 (5), 4483–4493. doi:10.1021/nn301282m

Huggins, I. J., Medina, C. A., van den Berg, A., and Jadhav, S. (2019). Site selective antibody-oligonucleotide conjugation via microbial transglutaminase. *Molecules* 24 (18), 3287. doi:10.3390/molecules24183287

Hunt, C. L., Lennemann, N. J., and Maury, W. (2012). Filovirus entry: a novelty in the viral fusion world. *Viruses* 4 (2), 258–275. doi:10.3390/v4020258

Huo, S., Jin, S., Ma, X., Xue, X., Yang, K., Kumar, A., et al. (2014). Ultrasmall gold nanoparticles as carriers for nucleus-based gene therapy due to size-dependent nuclear entry. *ACS Nano* 8 (6), 5852–5862. doi:10.1021/nn5008572

Hussein, H. A. M., Walker, L. R., Abdel-Raouf, U. M., Desouky, S. A., Montasser, A. K. M., Akula, S. A., et al. (2015). Beyond RGD: virus interactions with integrins. *Arch. Virol.* 160 (11), 2669–2681. doi:10.1007/s00705-015-2579-8

Jackson, A. L., Burchard, J., Leake, D., Reynolds, A., Schelter, J., Guo, J., et al. (2006). Position-specific chemical modification of siRNAs reduces "off-target" transcript silencing. *RNA* 12 (7), 1197–1205. doi:10.1261/rna.30706

Jae, L. T., Raaben, M., Herbert, A. S., Kuehne, A. I., Wirchnianski, A. S., Soh, T. K., et al. (2014). Lassa Virus Entry Requires a Virus entry. Lassa virus entry requires a trigger-induced receptor switch. *Science* 344 (6191), 1506–1510. doi:10.1126/science.1252480

Jae, L. T., and Brummelkamp, T. R. (2015). Emerging intracellular receptors for hemorrhagic fever viruses. *Trends Microbiol.* 23 (7), 392–400. doi:10.1016/j.tim.2015.04.006

James, S. H., and Whitley, R. J. (2017). "Influenza viruses," in *Infectious diseases* (Amsterdam, Netherlands: Elsevier), 1465–1471. doi:10.1016/B978-0-7020-6285-8.00172-6

Jeffs, L. B., Palmer, L. R., Ambegia, E. G., Giesbrecht, C., Ewanick, S., and MacLachlan, I. (2005). A scalable, extrusion-free method for efficient liposomal encapsulation of plasmid DNA. *Pharm. Res.* 22 (3), 362–372. doi:10.1007/s11095-004-1873-z

Jiang, S., Eltoukhy, A. A., Love, K. T., Langer, R., and Anderson, D. G. (2013). Lipidoid-coated iron oxide nanoparticles for efficient DNA and SiRNA delivery. *Nano Lett.* 13 (3), 1059–1064. doi:10.1021/nl304287a

Jiang, Y., Tang, R., Duncan, B., Jiang, Z., Yan, B., Mout, R., et al. (2015). Direct cytosolic delivery of SiRNA using nanoparticle-stabilized nanocapsules. *Angew. Chem. Int. Ed. Engl.* 54 (2), 506–510. doi:10.1002/anie.201409161

Jiang, Y., Hardie, J., Liu, Y., Ray, M., Luo, X., Das, R., et al. (2018). Nanocapsule-mediated cytosolic SiRNA delivery for anti-inflammatory treatment. *J. Control. Releas.* 283, 235–240. doi:10.1016/j.jconrel.2018.06.001

Jin, R., Wu, G., Li, Z., Mirkin, C. A., and Schatz, G. C. (2003). What controls the melting properties of DNA-linked gold nanoparticle assemblies?. *J. Am. Chem. Soc.* 125 (6), 1643–1654. doi:10.1021/ja021096v

Johannes, L., and Lucchino, M. (2018). Current challenges in delivery and cytosolic translocation of therapeutic RNAs. *Nucleic Acid Ther.* 28 (3), 178–193. doi:10.1089/nat.2017.0716

Joris, F., De Backer, L., Van de Vyver, T., Bastiancich, C., De Smedt, S. C., and Raemdonck, K. (2018). Repurposing cationic amphiphilic drugs as adjuvants to induce lysosomal SiRNA escape in nanogel transfected cells. *J. Control Releas.* 269, 266–276. doi:10.1016/j.jconrel.2017.11.019

Judge, A. D., Bola, G., and Lee, A. C. (2006). Design of noninflammatory synthetic SiRNA mediating potent gene silencing *in Vivo*. *Mol. Ther.* 13 (3), 494–505. doi:10.1016/j.ymthe.2005.11.002

Judge, A. D., Sood, V., Shaw, J. R., and Fang, D. (2005). Sequence-dependent stimulation of the mammalian innate immune response by synthetic SiRNA. *Nat. Biotechnol.* 23 (4), 457–462. doi:10.1038/nbt1081

Juliano, R. L. (2016). The delivery of therapeutic oligonucleotides. *Nucl. Acids Res.* 44 (14), 6518–6548. doi:10.1093/nar/gkw236

Juliano, R. L. (2018). Intracellular trafficking and endosomal release of oligonucleotides: what we know and what we don't. *Nucleic Acid Ther.* 28 (3), 166–177. doi:10.1089/nat.2018.0727

Juliano, R. L., Ming, X., Nakagawa, O., Xu, R., and Yoo, H. (2011). Integrin targeted delivery of gene therapeutics. *Theranostics* 1, 211–219. doi:10.7150/thno/v01p0211

Juliano, R. L., Wang, L., Tavares, F., Brown, E. G., James, L., Ariyarathna, Y., et al. (2018). Structure-activity relationships and cellular mechanism of action of small molecules that enhance the delivery of oligonucleotides. *Nucleic Acids Res.* 46 (4), 1601–1613. doi:10.1093/nar/gkx1320

Juliano, R., Alam, M. R., Dixit, V., and Kang, H. (2008). Mechanisms and strategies for effective delivery of antisense and SiRNA oligonucleotides. *Nucleic Acids Res.* 36 (12), 4158–4171. doi:10.1093/nar/gkn342

Kang, H., Alam, M. R., Dixit, V., Fisher, M., and Juliano, R. L. (2008). Cellular delivery and biological activity of antisense oligonucleotides conjugated to a targeted protein carrier. *Bioconjug. Chem.* 19 (11), 2182–2188. doi:10.1021/bc800270w

Kang, Y. Y., Song, J., Jung, H. S. G., Kwak, G., Yu, J.-H., Kim, S. H., et al. (2018). Implication of multivalent aptamers in DNA and DNA-RNA hybrid structures for efficient drug delivery *in vitro* and *in vivo*. *J. Ind. Eng. Chem.* 60, 250–258. doi:10.1016/j.jiec.2017.11.011

Kang, Z., Meng, Q., and Liu, K. (2019). Peptide-based gene delivery vectors. *J. Mater. Chem. B* 7 (11), 1824–1841. doi:10.1039/C8TB03124J

Karimi, M., Mirshekari, H., Moosavi Basri, S. M., Bahrami, S., Moghoofei, M., and Hamblin, M. R. (2016). Bacteriophages and phage-inspired nanocarriers for targeted delivery of therapeutic cargos. *Adv. Drug Deliv. Rev.* 106, 45–62. doi:10.1016/j.addr.2016.03.003

Karkare, S., and Bhatnagar, D. (2006). Promising nucleic acid analogs and mimics: characteristic features and applications of PNA, LNA, and morpholino. *Appl. Microbiol. Biotechnol.* 71 (5), 575–586. doi:10.1007/s00253-006-0434-2

Keefe, A. D., Pai, S., and Ellington, A. (2010). Aptamers as therapeutics. *Nat. Rev. Drug Discov.* 9 (7), 537–550. doi:10.1038/nrd3141

Khan, N., Halcrow, P. W., Lakpa, K. L., Afghah, Z., Miller, N. M., Dowdy, S. F., et al. (2020). Two-pore channels regulate Tat endolysosome escape and Tat-mediated HIV-1 LTR transactivation. *FASEB j.* 34 (3), 4147–4162. doi:10.1096/fj.201902534R

Khorev, O., Stokmaier, D., Schwardt, O., Cutting, B., and Ernst, B. (2008). Trivalent, gal/GalNAc-containing ligands designed for the asialoglycoprotein receptor. *Bioorg. Med. Chem.* 16 (9), 5216–5231. doi:10.1016/j.bmc.2008.03.017

Kim, A., Shin, T. H., Shin, S. M., Pham, C. D., Choi, D. K., Kwon, M. H., et al. (2012). Cellular internalization mechanism and intracellular trafficking of filamentous M13 phages displaying a cell-penetrating transbody and TAT peptide. *PLOS One* 7 (12), e51813. doi:10.1371/journal.pone.0051813

Kim, H. J., and Kim, H. J. (2017). Yeast as an expression system for producing virus-like particles: what factors do we need to consider?. *Lett. Appl. Microbiol.* 64 (2), 111–123. doi:10.1111/lam.12695

Kim, Y. H., Han, M.-E., and Oh, S.-O. (2017). The molecular mechanism for nuclear transport and its application. *Anat. Cell Biol.* 50 (2), 77. doi:10.5115/acb.2017.50.2.77

Klibanov, A. L., Maruyama, K., and Torchilin, V. P. (1990). Amphipathic polyethyleneglycols effectively prolong the circulation time of liposomes. *FEBS Lett.* 268 (1), 235–237. doi:10.1016/0014-5793(90)81016-H

Kobiler, O., Drayman, N., Butin-Israeli, V., and Oppenheim, A. (2012). Virus strategies for passing the nuclear envelope barrier. *Nucleus* 3 (6), 526–539. doi:10.4161/nucl.21979

Kogure, K., Akita, H., Yamada, Y., and Harashima, H. (2008). Multifunctional envelope-type nano device (MEND) as a non-viral gene delivery system. *Adv. Drug Deliv. Rev.* 60 (4), 559–571. doi:10.1016/j.addr.2007.10.007

Kondratowicz, A. S., Lennemann, N. J., Sinn, P. L., Davey, R. A., Hunt, C. L., Moller-Tank, S., et al. (2011). T-cell immunoglobulin and mucin domain 1 (TIM-1) is a receptor for zaire ebolavirus and lake victoria marburgvirus. *Proc. Natl. Acad. Sci. U.S.A.* 108 (20), 8426–8431. doi:10.1073/pnas.1019030108

Kono, K., Ozawa, T., Yoshida, T., Ozaki, F., Ishizaka, Y., Maruyama, K., et al. (2010). Highly temperature-sensitive liposomes based on a thermosensitive block copolymer for tumor-specific chemotherapy. *Biomaterials* 31 (27), 7096–7105. doi:10.1016/j.biomaterials.2010.05.045

Krop, I. E., Beeram, M., Modi, S., Jones, S. F., Holden, S. N., Yu, W., et al. (2010). Phase I study of trastuzumab-DM1, an HER2 antibody-drug conjugate, given every 3 Weeks to patients with HER2-positive metastatic breast cancer. *J. Clin. Oncol.* 28 (16), 2698–2704. doi:10.1200/JCO.2009.26.2071

Kulkarni, J. A., Cullis, P. R., and van der Meel, R. (2018). Lipid nanoparticles enabling gene therapies: from concepts to clinical utility. *Nucleic Acid Ther.* 28 (3), 146–157. doi:10.1089/nat.2018.0721

Kusumoto, K., Akita, H., Ishitsuka, T., Matsumoto, Y., Nomoto, T., Furukawa, R., et al. (2013). Lipid envelope-type nanoparticle incorporating a multifunctional peptide for systemic SiRNA delivery to the pulmonary endothelium. *ACS Nano* 7 (9), 7534–7541. doi:10.1021/nn401317t

Kusumoto, K., Akita, H., Santiwarangkool, S., and Harashima, H. (2014). Advantages of ethanol dilution method for preparing GALA-modified liposomal SiRNA carriers on the *in Vivo* gene knockdown efficiency in pulmonary endothelium. *Int. J. Pharm.* 473 (1–2), 144–147. doi:10.1016/j.ijpharm.2014.07.007

Lam, P., and Steinmetz, N. F. (2019). Delivery of SiRNA therapeutics using cowpea chlorotic mottle virus-like particles. *Biomater. Sci.* 7 (8), 3138–3142. doi:10.1039/C9BM00785G

Lam, P., and Steinmetz, N. F. (2018). Plant viral and bacteriophage delivery of nucleic acid therapeutics. *Wiley Interdiscip. Rev. Nanomed. Nanobiotech.* 10 (1), e1487. doi:10.1002/wnan.1487

Lazo, J. S., and Sharlow, E. R. (2016). Drugging undruggable molecular cancer targets. *Annu. Rev. Pharmacol. Toxicol.* 56 (1), 23–40. doi:10.1146/annurev-pharmtox-010715-103440

Lechardeur, D., Sohn, K. J., Haardt, M., Joshi, P. B., Monck, M., Graham, R. W., et al. (1999). Metabolic instability of plasmid DNA in the cytosol: a potential barrier to gene transfer. *Gene Ther.* 6 (4), 482–497. doi:10.1038/sj.gt.3300867

LeCher, J. C., Nowak, S. J., and McMurry, J. L. (2017). Breaking in and busting out: cell-penetrating peptides and the endosomal escape problem. *Biomol. Concepts* 8 (3–4), 131–141. doi:10.1515/bmc-2017-0023

Lee, Y. C., Townsend, R. R., Hardy, M. R., Lönngren, J., Arnarp, J., Haraldsson, M., et al. (1983). Binding of synthetic oligosaccharides to the hepatic gal/GalNAc lectin. Dependence on fine structural features. *J. Biol. Chem.* 258 (1), 199–202. doi:10.1016/s0021-9258(18)33240-x

Lee, Y. C., and Lee, R. T. (2000). "Interactions of oligosaccharides and glycopeptides with hepatic carbohydrate receptors," in *Carbohydrates in chemistry and biology* (New York, NY: John Wiley & Sons, Ltd), 549–561. doi:10.1002/9783527618255.ch72

Legendre, J. Y., and Szoka, F. C. (1992). Delivery of plasmid DNA into mammalian cell lines using PH-sensitive liposomes: comparison with cationic liposomes. *Pharm. Res.* 9 (10), 1235–1242. doi:10.1023/a:1015836829670

Li, G., Qi, X., Hu, Z., and Tang, Q. (2019). Mechanisms mediating nuclear trafficking involved in viral propagation by DNA viruses. *Viruses* 11 (11), 1035. doi:10.3390/v11111035

Li, Y., Zhang, K., Liu, P., Chen, M., Zhong, Y., Ye, Q., et al. (2019). Encapsulation of plasmid DNA by nanoscale metal-organic frameworks for efficient gene transportation and expression. *Adv. Mater.* 31 (29), e1901570. doi:10.1002/adma.201901570

Li, H., Yu, S. S., Miteva, M., Nelson, C. E., Werfel, T., Giorgio, T. D., et al. (2013). Matrix metalloproteinase responsive, proximity-activated polymeric nanoparticles for SiRNA delivery. *Adv. Funct. Mater.* 23 (24), 3040–3052. doi:10.1002/adfm.201202215

Li, J., Arévalo, M. T., and Zeng, M. (2013). Engineering influenza viral vectors. *Bioengineered* 4 (1), 9–14. doi:10.4161/bioe.21950

Li, H., Zhang, B., Lu, X., Tan, X., Jia, F., Xiao, Y., et al. (2018). Molecular spherical nucleic acids. *Proc. Natl. Acad. Sci. U.S.A.* 115 (17), 4340–4344. doi:10.1073/pnas.1801836115

Li, J., Yu, M., Zheng, W., and Liu, W. (2015). Nucleocytoplasmic shuttling of influenza A virus proteins. *Viruses* 7 (5), 2668–2682. doi:10.3390/v7052668

Li, S., Sun, Z., Pryce, R., Parsy, M. L., Fehling, S. K., Schlie, K., et al. (2016). Acidic PH-induced conformations and LAMP1 binding of the Lassa virus glycoprotein spike. *Plos Pathog.* 12 (2), e1005418. doi:10.1371/journal.ppat.1005418

Li, W. (2015). The hepatitis B virus receptor. *Annu. Rev. Cell Dev. Biol.* 31 (1), 125–147. doi:10.1146/annurev-cellbio-100814-125241

Liang, K., Ricco, R., Doherty, C. M., Styles, M. J., Bell, S., Kirby, N., et al. (2015). Biomimetic mineralization of metal-organic frameworks as protective coatings for biomacromolecules. *Nat. Commun.* 6 (1), 7240. doi:10.1038/ncomms8240

Lo, S. L., and Wang, S. (2008). An endosomolytic tat peptide produced by incorporation of histidine and cysteine residues as a nonviral vector for DNA transfection. *Biomaterials* 29 (15), 2408–2414. doi:10.1016/j.biomaterials.2008.01.031

Lobovkina, T., Jacobson, G. B., Gonzalez-Gonzalez, E., Hickerson, R. P., Leake, D., Kaspar, R. L., et al. (2011). *In Vivo* sustained release of SiRNA from solid lipid nanoparticles. *ACS Nano* 5 (12), 9977–9983. doi:10.1021/nn203745n

Loh, X. J., Lee, T. C., Dou, Q., and Deen, G. (2015). Utilising inorganic nanocarriers for gene delivery. *Biomater. Sci.* 4 (1), 70–86. doi:10.1039/C5BM00277J

Lönn, P., Kacsinta, A. D., Cui, X.-S., Hamil, A. S., Kaulich, M., Gogoi, K., et al. (2016). Enhancing endosomal escape for intracellular delivery of macromolecular biologic therapeutics. *Sci. Rep.* 6 (1), 32301. doi:10.1038/srep32301

López-Huertas, M. R., Jiménez-Tormo, L., Madrid-Elena, N., Gutiérrez, C., Rodríguez-Mora, S., Coiras, M., et al. (2017). The CCR5-antagonist maraviroc reverses HIV-1 latency *in Vitro* alone or in combination with the PKC-agonist bryostatin-1. *Sci. Rep.* 7, 2385. doi:10.1038/s41598-017-02634-y

Lv, H., Zhang, S., Wang, B., Cui, S., and Yan, J. (2006). Toxicity of cationic lipids and cationic polymers in gene delivery. *J. Control Release* 114 (1), 100–109. doi:10.1016/j.jconrel.2006.04.014

Lytton-Jean, A. K., and Mirkin, C. A. (2005). A thermodynamic investigation into the binding properties of DNA functionalized gold nanoparticle probes and molecular fluorophore probes. *J. Am. Chem. Soc.* 127 (37), 12754–12755. doi:10.1021/ja052255o

Mach, R. H., Huang, Y., Freeman, R. A., Wu, L., Vangveravong, S., and Luedtke, R. R. (2004). Conformationally-flexible benzamide analogues as dopamine D3 and sigma 2 receptor ligands. *Bioorg. Med. Chem. Lett.* 14 (1), 195–202. doi:10.1016/j.bmcl.2003.09.083

Maginnis, M. S. (2018). Virus-receptor interactions: the key to cellular invasion. *J. Mol. Biol.* 430 (17), 2590–2611. doi:10.1016/j.jmb.2018.06.024

Mammen, M., Choi, S. K., and Whitesides, G. M. (1998). Polyvalent interactions in biological systems: implications for design and use of multivalent ligands and inhibitors. *Angew. Chem. Int. Ed. Engl.* 37 (20), 2754–2794. doi:10.1002/(SICI)1521-3773(19981102)37:20<2754::AID-ANIE2754>3.0.CO;2-3

Marsh, M., and Helenius, A. (2006). Virus entry: open sesame. *Cell* 124 (4), 729–740. doi:10.1016/j.cell.2006.02.007

Maruyama, K., Unezaki, S., Takahashi, N., and Iwatsuru, M. (1993). Enhanced delivery of doxorubicin to tumor by long-circulating thermosensitive liposomes and local hyperthermia. *Biochim. Biophys. Acta* 1149 (2), 209–216. doi:10.1016/0005-2736(93)90203-C

Massich, M. D., Giljohann, D. A., Seferos, D. S., Ludlow, L. E., Horvath, C. M., and Mirkin, C. A. (2009). Regulating immune response using polyvalent nucleic acid-gold nanoparticle conjugates. *Mol. Pharm.* 6 (6), 1934–1940. doi:10.1021/mp900172m

Matsumura, Y., and Maeda, H. (1986). A new concept for macromolecular therapeutics in cancer chemotherapy: mechanism of tumoritropic accumulation of proteins and the antitumor agent smancs. *Cancer Res.* 46 (12), 6387–6392.

Maxfield, F. R. (1982). Weak bases and ionophores rapidly and reversibly raise the PH of endocytic vesicles in cultured mouse fibroblasts. *J. Cell Biol.* 95 (2), 676–681. doi:10.1083/jcb.95.2.676

Mazzon, M., and Marsh, M. (2019). Targeting viral entry as a strategy for broad-spectrum antivirals. *F1000Res* 8, 1628. doi:10.12688/f1000research.19694.1

McBain, S. C., Griesenbach, U., Xenariou, S., Keramane, A., Batich, C. D., Alton, E. W., et al. (2008). Magnetic nanoparticles as gene delivery agents: enhanced transfection in the presence of oscillating magnet arrays. *Nanotechnology* 19 (40), 405102. doi:10.1088/0957-4484/19/40/405102

Meier, M., Bider, M. D., Malashkevich, V. N., Spiess, M., and Burkhard, P. (2000). Crystal structure of the carbohydrate recognition domain of the H1 subunit of the asialoglycoprotein receptor. *J. Mol. Biol.* 300 (4), 857–865. doi:10.1006/jmbi.2000.3853

Mendes, R., Fernandes, A. R., and Baptista, P. V. (2017). Gold nanoparticle approach to the selective delivery of gene silencing in cancer-the case for combined delivery?. *Genes* 8 (3), 94. doi:10.3390/genes8030094

Meng, Z., Luan, L., Kang, Z., Feng, S., Meng, Q., and Liu, K. (2017). Histidine-enriched multifunctional peptide vectors with enhanced cellular uptake and endosomal escape for gene delivery. *J. Mater. Chem. B* 5 (1), 74–84. doi:10.1039/C6TB02862D

Midoux, P., Pigeon, L., Gonçalves, C., and Pichon, C. (2017). Peptides mediating DNA transport on microtubules and their impact on non-viral gene transfer efficiency. *Biosci. Rep.* 37 (5), BSR20170995. doi:10.1042/BSR20170995

Miller, A. M., and Dean, D. A. (2009). Tissue-specific and transcription factor-mediated nuclear entry of DNA. *Adv. Drug Deliv. Rev.* 61 (7–8), 603–613. doi:10.1016/j.addr.2009.02.008

Mirkin, C. A., Letsinger, R. L., Mucic, R. C., and Storhoff, J. J. (1996). A DNA-based method for rationally assembling nanoparticles into macroscopic materials. *Nature* 382 (6592), 607–609. doi:10.1038/382607a0

Mislick, K. A., and Baldeschwieler, J. D. (1996). Evidence for the role of proteoglycans in cation-mediated gene transfer. *Proc. Natl. Acad. Sci. U.S.A.* 93 (22), 12349–12354. doi:10.1073/pnas.93.22.12349

Miura, N., Tange, K., Nakai, Y., Yoshioka, H., Harashima, H., and Akita, H. (2017). Identification and evaluation of the minimum unit of a KALA peptide required for gene delivery and immune activation. *J. Pharm. Sci.* 106 (10), 3113–3119. doi:10.1016/j.xphs.2017.05.014

Miyauchi, K., Kim, Y., Latinovic, O., Morozov, V., and Melikyan, G. B. (2009). HIV enters cells via endocytosis and dynamin-dependent fusion with endosomes. *Cell* 137 (3), 433–444. doi:10.1016/j.cell.2009.02.046

Moffett, H. F., Coon, M. E., Radtke, S., Stephan, S. B., McKnight, L., Lambert, A., et al. (2017). Hit-and-Run programming of therapeutic cytoreagents using MRNA nanocarriers. *Nat. Commun.* 8 (1), 389. doi:10.1038/s41467-017-00505-8

Mok, H., and Park, T. G. (2008). Self-crosslinked and reducible fusogenic peptides for intracellular delivery of SiRNA. *Biopolymers* 89 (10), 881–888. doi:10.1002/bip.21032

Moon, J. S., Kim, W. G., Kim, C., Park, G. T., Heo, J., Yoo, S. Y., et al. (2015). M13 bacteriophage-based self-assembly structures and their functional capabilities. *Mini Rev. Org. Chem.* 12 (3), 271–281. doi:10.2174/1570193X1203150429105418

Moret, I., Esteban Peris, J., Guillem, V. M., Benet, M., Revert, F., Dasí, F., et al. (2001). Stability of PEI-DNA and DOTAP-DNA complexes: effect of alkaline PH, heparin and serum. *J. Control. Releas.* 76 (1–2), 169–181. doi:10.1016/s0168-3659(01)00415-1

Moriguchi, R., Kogure, K., Akita, H., Futaki, S., Miyagishi, M., Taira, K., et al. (2005). A multifunctional envelope-type nano device for novel gene delivery of SiRNA plasmids. *Int. J. Pharm.* 301 (1), 277–285. doi:10.1016/j.ijpharm.2005.05.021

Motion, J. P., Nguyen, J., and Szoka, F. C. (2012). Phosphatase-triggered fusogenic liposomes for cytoplasmic delivery of cell-impermeable compounds. *Angew. Chem. Int. Ed. Engl.* 51 (36), 9047–9051. doi:10.1002/anie.201204198

Mout, R., Ray, M., Yesilbag Tonga, G., Lee, Y. W., Tay, T., Sasaki, K., et al. (2017). Direct cytosolic delivery of CRISPR/Cas9-Ribonucleoprotein for efficient gene editing. *ACS Nano* 11 (3), 2452–2458. doi:10.1021/acsnano.6b07600

Mukherjee, S., Pfeifer, C. M., Johnson, J. M., Liu, J., and Zlotnick, A. (2006). Redirecting the coat protein of a spherical virus to assemble into tubular nanostructures. *J. Am. Chem. Soc.* 128 (8), 2538–2539. doi:10.1021/ja056656f

Naghavi, M. H., and Walsh., D. (2017). Microtubule regulation and function during virus infection. *J. Virol.* 91 (16), e00538-17. doi:10.1128/JVI.00538-17

Nair, J. K., Willoughby, J. L., Chan, A., Charisse, K., Alam, M. R., Wang, Q., et al. (2014). Multivalent N-Acetylgalactosamine-Conjugated SiRNA localizes in hepatocytes and elicits robust RNAi-mediated gene silencing. *J. Am. Chem. Soc.* 136 (49), 16958–16961. doi:10.1021/ja505986a

Nakagawa, O., Ming, X., Huang, L., and Juliano, R. L. (2010). Targeted intracellular delivery of antisense oligonucleotides via conjugation with small-molecule ligands. *J. Am. Chem. Soc.* 132 (26), 8848–8849. doi:10.1021/ja102635c

Nakanishi, A., Li, P. P., Qu, Q., Jafri, Q. H., and Kasamatsu, H. (2007). Molecular dissection of nuclear entry-competent SV40 during infection. *Virus. Res.* 124 (1–2), 226–230. doi:10.1016/j.virusres.2006.10.001

Nakanishi, A., Shum, D., Morioka, H., Otsuka, E., and Kasamatsu, H. (2002). Interaction of the Vp3 nuclear localization signal with the importin alpha 2/beta heterodimer directs nuclear entry of infecting simian virus 40. *J. VIROL.* 76, 9368. doi:10.1128/jvi.76.18.9368-9377.2002

Nanbo, A., Imai, M., Watanabe, S., Noda, T., Takahashi, K., Neumann, G., et al. (2010). Ebolavirus is internalized into host cells via macropinocytosis in a viral glycoprotein-dependent manner. *Plos Pathog.* 6 (9), e1001121. doi:10.1371/journal.ppat.1001121

Nanna, A. R., Kel'in, A. V., Theile, C., Zhi Xiang, V., Garg, A., Nair, J. K., Maier, M. A., et al. (2020). Generation and validation of structurally defined antibody-siRNA conjugates. *Nucleic Acids Res.* 48 (10), 5281–5293. doi:10.1093/nar/gkaa286

Nayerossadat, N., Maedeh, T., and Ali, P. A. (2012). Viral and nonviral delivery systems for gene delivery. *Adv. Biomed. Res.* 1, 27. doi:10.4103/2277-9175.98152

Needham, D., Anyarambhatla, G., Kong, G., and Dewhirst, M. W. (2000). A new temperature-sensitive liposome for use with mild hyperthermia: characterization and testing in a human tumor xenograft model. *Cancer Res.* 60 (5), 1197–1201. doi:10.1093/analys/60.1.13

Nelemans, L. C., and Gurevich, L. (2020). Drug delivery with polymeric nanocarriers-cellular uptake mechanisms. *Materials* 13 (2), 366. doi:10.3390/ma13020366

Nemerow, G. R., and Stewart, P. L. (1999). Role of αv integrins in adenovirus cell entry and gene delivery. *Microbiol. Mol. Biol. Rev.* 63 (3), 725–734. doi:10.1128/mmbr.63.3.725-734.1999

Neshatian, M., Chung, S., Yohan, D., Yang, C., and Chithrani, D. B. (2014). Determining the size dependence of colloidal gold nanoparticle uptake in a tumor-like interface (hypoxic). *Colloids Interf. Sci. Commun.* 1, 57–61. doi:10.1016/j.colcom.2014.07.004

Neumann, G., Castrucci, M. R., and Kawaoka, Y. (1997). Nuclear import and export of influenza virus nucleoprotein. *J. Virol.* 71 (12), 9690–9700. doi:10.1128/JVI.71.12.9690-9700.1997

Ngamcherdtrakul, W., Morry, J., Gu, S., Castro, D. J., Goodyear, S. M., Sangvanich, T., et al. (2015). Cationic polymer modified mesoporous silica nanoparticles for targeted SiRNA delivery to HER2+ breast cancer. *Adv. Funct. Mater.* 25 (18), 2646–2659. doi:10.1002/adfm.201404629

Ni, R., Zhou, J., Hossain, N., and Chau, Y. (2016). Virus-inspired nucleic acid delivery system: linking virus and viral mimicry. *Adv. Drug Deliv. Rev.* 106, 3–26. doi:10.1016/j.addr.2016.07.005

Ni, R., Feng, R., and Chau, Y. (2019). Synthetic approaches for nucleic acid delivery: choosing the right carriers. *Life* 9 (3), 59. doi:10.3390/life9030059

Nie, Y., Schaffert, D., Rödl, W., Ogris, M., Wagner, E., and Günther, M. (2011). Dual-targeted polyplexes: one step towards a synthetic virus for cancer gene therapy. *J. Control. Release* 152 (1), 127–134. doi:10.1016/j.jconrel.2011.02.028

Norkin, L. C., Anderson, H. A., Wolfrom, S. A., and Oppenheim, A. (2002). Caveolar endocytosis of Simian virus 40 is followed by Brefeldin A-sensitive transport to the endoplasmic reticulum, where the virus disassembles. *J. Virol.* 76 (10), 5156–5166. doi:10.1128/JVI.76.10.5156-5166.2002

Nunberg, J. H., and York, J. (2012). The curious case of arenavirus entry, and its inhibition. *Viruses* 4 (1), 83–101. doi:10.3390/v4010083

Oppliger, J., Torriani, G., Herrador, A., and Kunz, S. (2016). Lassa virus cell entry via dystroglycan involves an unusual pathway of macropinocytosis. *J. Virol.* 90 (14), 6412–6429. doi:10.1128/JVI.00257-16

Orellana, E. A., Abdelaal, A. M., Rangasamy, L., Tenneti, S., Myoung, S., Low, P. S., et al. (2019). Enhancing MicroRNA activity through increased endosomal release mediated by nigericin. *Mol. Ther. Nucleic Acids* 16, 505–518. doi:10.1016/j.omtn.2019.04.003

Orellana, E. A., Tenneti, S., Rangasamy, L., Lyle, L. T., Low, P. S., and Kasinski, A. L. (2017). FolamiRs: ligand-targeted, vehicle-free delivery of MicroRNAs for the treatment of cancer. *Sci. Transl. Med.* 9 (401). doi:10.1126/scitranslmed.aam9327

Ortega-Esteban, A., Condezo, G. N., Pérez-Berná, A. J., Chillón, M., Flint, S., Reguera, D., et al. (2015). Mechanics of viral chromatin reveals the pressurization of human adenovirus. *ACS Nano* 9 (11), 10826–10833. doi:10.1021/acsnano.5b03417

Osborn, M. F., Alterman, J. F., Nikan, M., Cao, H., Didiot, M. C., Hassler, M. R., et al. (2015). Guanabenz (Wytensin™) selectively enhances uptake and efficacy of hydrophobically modified siRNAs. *Nucleic Acids Res.* 43 (18), 8664–8672. doi:10.1093/nar/gkv942

Palanca-Wessels, M. C., Convertine, A. J., Richelle, C.-S., Booth, G. C., Lee, F., and Berguig, G. Y. (2011). Anti-CD22 antibody targeting of pH-responsive micelles enhances small interfering RNA delivery and gene silencing in lymphoma cells. *Mol. Ther.* 19 (8), 1529–1537. doi:10.1038/mt.2011.104

Pan, L., He, Q., Liu, J., Chen, Y., Ma, M., Zhang, L., et al. (2012). Nuclear-targeted drug delivery of TAT peptide-conjugated monodisperse mesoporous silica nanoparticles. *J. Am. Chem. Soc.* 134 (13), 5722–5725. doi:10.1021/ja211035w

Pan, Y., Jia, T., Zhang, Y., Zhang, K., Zhang, R., Li, J., et al. (2012a). MS2 VLP-based delivery of MicroRNA-146a inhibits autoantibody production in lupus-prone mice. *Int. J. Nanomedicine* 7, 5957–5967. doi:10.2147/IJN.S37990

Pan, Y., Zhang, Y., Jia, T., Zhang, K., Li, J., and Wang, L. (2012b). Development of a MicroRNA delivery system based on bacteriophage MS2 virus-like particles. *FEBS J.* 279 (7), 1198–1208. doi:10.1111/j.1742-4658.2012.08512.x

Passaretti, P., Sun, Y., Dafforn, T. R., and Oppenheimer, P. G. (2020). Determination and characterisation of the surface charge properties of the bacteriophage M13 to assist bio-nanoengineering. *RSC Adv.* 10 (42), 25385–25392. doi:10.1039/D0RA04086J

Pelkmans, L., Kartenbeck, J., and Helenius, A. (2001). Caveolar endocytosis of simian virus 40 reveals a new two-step vesicular-transport pathway to the ER. *Nat. Cell Biol.* 3 (5), 473–483. doi:10.1038/35074539

Peng, S., Bie, B., Sun, Y., Liu, M., Cong, H., Zhou, W., et al. (2018). Metal-organic frameworks for precise inclusion of single-stranded DNA and transfection in immune cells. *Nat. Commun.* 9 (1), 1293. doi:10.1038/s41467-018-03650-w

Penin, F., Combet, C., Germanidis, G., Frainais, P. O., Deléage, G., and Pawlotsky, J. M. (2001). Conservation of the conformation and positive charges of hepatitis C virus E2 envelope glycoprotein hypervariable region 1 points to a role in cell attachment. *J. Virol.* 75 (12), 5703–5710. doi:10.1128/JVI.75.12.5703-5710.2001

Pinto, L. H., Holsinger, L. J., and Lamb, R. A. (1992). Influenza virus M2 protein has ion channel activity. *Cell* 69 (3), 517–528. doi:10.1016/0092-8674(92)90452-I

Poddar, A., Conesa, J. J., Liang, K., Dhakal, S., Reineck, P., Bryant, G., et al. (2019). Encapsulation, visualization and expression of genes with biomimetically mineralized zeolitic imidazolate framework-8 (ZIF-8). *Small* 15 (36), e1902268. doi:10.1002/smll.201902268

Pouton, C., Wagstaff, K., Roth, D., Moseley, G., and Jans, D. (2007). "Targeted Targeted delivery to the nucleus. *Adv. Drug Deliv. Rev.* 59 (8), 698–717. doi:10.1016/j.addr.2007.06.010

Prasad, B. V. V., and Schmid, M. F. (2011). Principles of virus structural organization. *Adv. Exp. Med. Biol.* 726, 17–47. doi:10.1007/978-1-4614-0980-9_3

Prel, A., Caval, V., Gayon, R., Ravassard, P., Duthoit, C., Payen, E., et al. (2015). Highly efficient *in Vitro* and *in Vivo* delivery of functional RNAs using new versatile MS2-chimeric retrovirus-like particles. *Mol. Ther. Methods Clin. Dev.* 2, 15039. doi:10.1038/mtm.2015.39

Pretto, C., and van Hest, J. C. M. (2019). Versatile reversible cross-linking strategy to stabilize CCMV virus like particles for efficient SiRNA delivery. *Bioconjug. Chem.* 30 (12), 3069–3077. doi:10.1021/acs.bioconjchem.9b00731

Ramamoorth, M., and Narvekar, A. (2015). Non viral vectors in gene therapy- an overview. *J. Clin. Diagn. Res.* 9 (1), GE01–GE06. doi:10.7860/JCDR/2015/10443.5394

Ray, M., Tang, R., Jiang, Z., and Rotello, V. M. (2015). Quantitative tracking of protein trafficking to the nucleus using cytosolic protein delivery by nanoparticle-stabilized nanocapsules. *Bioconjug. Chem.* 26 (6), 1004–1007. doi:10.1021/acs.bioconjchem.5b00141

Rinaldi, S.-H., Zhi, D.-F., Zhao, Y.-N, Chen, H.-Y., Meng, Y., and Zhang, C.-M. (2016). Cationic lioposomes with folic acid as targeting ligand for gene delivery. *Bioorg. Med. Chem. Lett.* 26 (16), 4025–4029. doi:10.1016/j.bmcl.2016.06.085

Rohovie, M. J., Nagasawa, M., and Swartz, J. R. (2017). Virus-like particles: next-generation nanoparticles for targeted therapeutic delivery. *Bioeng. Translational Med.* 2 (1), 43–57. doi:10.1002/btm2.10049

Roldão, A., Silva, A. C., Mellado, M. C. M., Alves, P. M., and Carrondo, M. J. T. (2017). Viruses and virus-like particles in biotechnology: fundamentals and applications ☆. *Compr. Biotechnol.*, 633–656. doi:10.1016/B978-0-12-809633-8.09046-4

Roloff, A., Nelles, D. A., Thompson, M. P., Yeo, G. W., and Gianneschi, N. C. (2018). Self-transfecting micellar RNA: modulating nanoparticle cell interactions via high density display of small molecule ligands on micelle

coronas. *Bioconjug. Chem.* 29 (1), 126–135. doi:10.1021/acs.bioconjchem.7b00657

Rosi, N. L., Giljohann, D. A., Thaxton, C. S., Lytton-Jean, A. K. R., Han, M. S., and Mirkin, C. A. (2006). Oligonucleotide-modified gold nanoparticles for intracellular gene regulation. *Science* 312, 1027–1030. doi:10.1126/science.1125559

Rouge, J. L., Sita, T. L., Hao, L., Fotini, M. K., WilliamStegh, E. B., and Alexander, H. (2015). Ribozyme-spherical nucleic acids. *J. Am. Chem. Soc.* 137 (33), 10528–10531. doi:10.1021/jacs.5b07104

Ruan, W., Zheng, M., An, Y., Liu, Y., Lovejoy, D. B., Hao, M., et al. (2018). DNA nanoclew templated spherical nucleic acids for SiRNA delivery. *Chem. Commun.* 54 (29), 3609–3612. doi:10.1039/C7CC09257A

Rush, A. M., Thompson, M. P., Tatro, E. T., and Gianneschi, N. C. (2013). Nuclease-resistant DNA via high-density packing in polymeric micellar nanoparticle coronas. *ACS Nano* 7 (2), 1379–1387. doi:10.1021/nn305030g

Russell, W. C. (2009). Adenoviruses: update on structure and function. *J. Gen. Virol.* 90 (1), 1–20. doi:10.1099/vir.0.003087-0

Sahay, G., Querbes, W., Alabi, C., Eltoukhy, A., Sarkar, S., Zurenko, C., et al. (2013). Efficiency of SiRNA delivery by lipid nanoparticles is limited by endocytic recycling. *Nat. Biotechnol.* 31 (7), 653–658. doi:10.1038/nbt.2614

Sakurai, Y., Hatakeyama, H., Sato, Y., Hyodo, M., Akita, H., Ohga, N., et al. (2014). RNAi-mediated gene knockdown and anti-angiogenic therapy of RCCs using a cyclic RGD-modified liposomal-SiRNA system. *J. Control. Release* 173, 110–118. doi:10.1016/j.jconrel.2013.10.003

Samanta, D., Ebrahimi, S. B., Kusmierz, C. D., Cheng, H. F., and Mirkin, C. A. (2020). Protein spherical nucleic acids for live-cell chemical analysis. *J. Am. Chem. Soc.* 142 (31), 13350–13355. doi:10.1021/jacs.0c06866

Santiana, J. J., Sui, B., Gomez, N., and Rouge, J. L. (2017). Programmable peptide-cross-linked nucleic acid nanocapsules as a modular platform for enzyme specific cargo release. *Bioconjug. Chem.* 28 (12), 2910–2914. doi:10.1021/acs.bioconjchem.7b00629

Sato, Y., Hatakeyama, H., Sakurai, Y., Hyodo, M., Akita, H., and Harashima, H. (2012). A PH-sensitive cationic lipid facilitates the delivery of liposomal SiRNA and gene silencing activity *in Vitro* and *in Vivo*. *J. Controll. Release* 163 (3), 267–276. doi:10.1016/j.jconrel.2012.09.009

Scherer, J., and Vallee, R. B. (2011). Adenovirus recruits dynein by an evolutionary novel mechanism involving direct binding to PH-primed hexon. *Viruses* 3 (8), 1417–1431. doi:10.3390/v3081417

Seferos, D. S., Prigodich, A. E., Giljohann, D. A., Pinal, C., and Mirkin, C. A. (2009). Polyvalent DNA nanoparticle conjugates stabilize nucleic acids. *Nano Lett.* 9 (1), 308–311. doi:10.1021/nl802958f

Selby, L. I., Cortez-Jugo, C. M., Such, G. K., and Johnston, A. P. R. (2017). Nanoescapology: progress toward understanding the endosomal escape of polymeric nanoparticles. *Wiley Interdiscip. Rev. Nanomed. Nanobiotechnolnanomed. Nanobiotech.* 9 (5), e1452. doi:10.1002/wnan.1452

Semple, S. C., Akinc, A., Chen, J., Sandhu, A. P., Mui, B. L., Cho, C. K., et al. (2010). Rational design of cationic lipids for SiRNA delivery. *Nat. Biotechnol.* 28 (2), 172–176. doi:10.1038/nbt.1602

Seth, P. P., Tanowitz, M., and Bennett, C. (2019). Selective tissue targeting of synthetic nucleic acid drugs. *J. Clin. Invest.* 129 (3), 915–925. doi:10.1172/JCI125228

Shaheen, S. M., Akita, H., Nakamura, T., Takayama, S., Futaki, S., Yamashita, A., et al. (2011). KALA-modified multi-layered nanoparticles as gene carriers for MHC class-I mediated antigen presentation for a DNA vaccine. *Biomaterials* 32 (26), 6342–6350. doi:10.1016/j.biomaterials.2011.05.014

Shahzad, M. M., Mangala, L. S., Han, H. D., Lu, C., Bottsford-Miller, J., Nishimura, M., et al. (2011). Targeted delivery of small interfering RNA using reconstituted high-density lipoprotein nanoparticles. *Neoplasia* 13 (4), 309–319. doi:10.1593/neo.101372

Shete, H. K., Prabhu, R. H., and Patravale, V. B. (2014). Endosomal escape: a bottleneck in intracellular delivery. *J. Nanosci Nanotechnol* 14 (1), 460–474. doi:10.1166/jnn.2014.9082

Shi, Q., Nguyen, A. T., Angell, Y., Deng, D., Na, C. R., Burgess, K., et al. (2010). A combinatorial approach for targeted delivery using small molecules and reversible masking to bypass nonspecific uptake *in Vivo*. *Gene Ther.* 17 (9), 1085–1097. doi:10.1038/gt.2010.55

Shimojima, M., Ströher, U., Ebihara, H., Feldmann, H., and Kawaoka, Y. (2012). Identification of cell surface molecules involved in dystroglycan-independent Lassa virus cell entry. *J. Virol.* 86 (4), 2067–2078. doi:10.1128/JVI.06451-11

Sievers, E. L., Larson, R. A., Stadtmauer, E. A., Estey, E., Löwenberg, B., Dombret, H., et al. (2001). Efficacy and safety of gemtuzumab ozogamicin in patients with CD33-positive acute myeloid leukemia in first relapse. *J. Clin. Oncol.* 19 (13), 3244–3254. doi:10.1200/JCO.2001.19.13.3244

Sikorski, A. F., Toporkiewicz, M., Meissner, J., Matusewicz, L., and Czogalla, A. (2015). Toward a magic or imaginary bullet? Ligands for drug targeting to cancer cells: principles, hopes, and challenges, *Int. J. Nanomedicine* 10, 1399. doi:10.2147/IJN.S74514

Simeoni, F. (2003). Insight into the mechanism of the peptide-based gene delivery system MPG: implications for delivery of SiRNA into mammalian cells. *Nucleic Acids Res.* 31 (11), 2717–2724. doi:10.1093/nar/gkg385

Sokolova, V., and Epple, M. (2008). Inorganic nanoparticles as carriers of nucleic acids into cells. *Angew. Chem. Int. Ed.* 47 (8), 1382–1395. doi:10.1002/anie.200703039

Springer, A. D., and Dowdy, S. F. (2018). GalNAc-SiRNA conjugates: leading the way for delivery of RNAi therapeutics. *Nucleic Acid Ther.* 28 (3), 109–118. doi:10.1089/nat.2018.0736

St-Pierre, G., Pal, S., Østergaard, M. E., Zhou, T., Yu, J., Tanowitz, M., et al. (2016). Synthesis and biological evaluation of sialyl-oligonucleotide conjugates targeting leukocyte B trans-membranal receptor CD22 as delivery agents for nucleic acid drugs. *Bioorg. Med. Chem.* 24 (11), 2397–2409. doi:10.1016/j.bmc.2016.03.047

Staring, J., Raaben, M., and Brummelkamp, T. R. (2018). Viral escape from endosomes and host detection at a glance. *J. Cell Sci.* 131 (15), jcs.216259. doi:10.1242/jcs.216259

Stewart, P. L., and Nemerow, G. R. (2007). Cell integrins: commonly used receptors for diverse viral pathogens. *Trends Microbiol.* 15 (11), 500–507. doi:10.1016/j.tim.2007.10.001

Subbarao, N. K., Parente, R. A., Szoka, F. C., Nadasdi, L., and Pongracz, K. (1987). PH-dependent bilayer destabilization by an amphipathic peptide. *Biochemistry* 26 (11), 2964–2972. doi:10.1021/bi00385a002

Sugiyama, M., Matsuura, M., Takeuchi, Y., Kosaka, J., Nango, M., and Oku, N. (2004). Possible mechanism of polycation liposome (PCL)-Mediated gene transfer. *Biochim. Biophys. Acta* 1660 (1–2), 24–30. doi:10.1016/j.bbamem.2003.10.012

Summerton, J. E. (2006). "Morpholinos and PNAs compared," in *Peptide nucleic acids, morpholinos and related antisense biomolecules*. Editors C. G. Janson and M. J. During (Boston, MA: Medical Intelligence), 89–113. doi:10.1007/0-387-32956-0_6

Sun, H., Zhu, X., Lu, P. Y., Rosato, R. R., Tan, W., and Zu, Y. (2014). Oligonucleotide aptamers: new tools for targeted cancer therapy. *Mol. Ther. Nucleic Acids* 3, e182. doi:10.1038/mtna.2014.32

Sun, P., Li, Z., Wang, J., Gao, H., Yang, X., Wu, S., et al. (2018). Transcellular delivery of messenger RNA payloads by a cationic supramolecular MOF platform. *Chem. Commun.* 54 (80), 11304–11307. doi:10.1039/C8CC07047D

Sun, Y., Zheng, L., Yang, Y., Qian, X., Fu, T., Li, X., et al. (2020). Metal-organic framework nanocarriers for drug delivery in biomedical applications. *Nano-micro Lett.* 12 (1), 103. doi:10.1007/s40820-020-00423-3

Takemoto, H., Miyata, K., Nishiyama, N., and Kataoka, K. (2014). "Bioresponsive polymer-based nucleic acid carriers," in *Advances in genetics*. Editors L. Huang, D. Liu, and E. Wagner (Cambridge, MA: Academic Press), 88, 289–323. doi:10.1016/B978-0-12-800148-6.00010-9*Adv. Genet.*

Tang, Q., Liu, J., Jiang, Y., Zhang, M., Mao, L., and Wang, M. (2019). Cell-selective messenger RNA delivery and CRISPR/Cas9 genome editing by modulating the interface of phenylboronic acid-derived lipid nanoparticles and cellular surface sialic acid. *ACS Appl. Mater. Inter.* 11 (50), 46585–46590. doi:10.1021/acsami.9b17749

Tang, R., Kim, C. S., and Solfiell, D. J. (2013). Solfiell, Subinoy Rana, Rubul Mout, Elih M. Velázquez-Delgado, Apiwat Chompoosor, et al.Direct Delivery of Functional Proteins and Enzymes to the Cytosol Using Nanoparticle-Stabilized Nanocapsules. *ACS Nano* 7 (8), 6667–6673. doi:10.1021/nn402753y

Tatsis, N., and Ertl, H. C. (2004). Adenoviruses as vaccine vectors. *Mol. Ther.* 10 (4), 616–629. doi:10.1016/j.ymthe.2004.07.013

Teplensky, M. H., Fantham, M., Poudel, C., Hockings, C., Lu, M., Guna, A., et al. (2019). A highly porous metal-organic framework system to deliver payloads for gene knockdown. *Chem* 5 (11), 2926–2941. doi:10.1016/j.chempr.2019.08.015

Thomas, M., and Klibanov, A. M. (2003). Non-viral gene therapy: polycation-mediated DNA delivery. *Appl. Microbiol. Biotechnol.* 62 (1), 27–34. doi:10.1007/s00253-003-1321-8

Tian, Y., Wu, M., Liu, X., Liu, Z., Zhou, Q., Niu, Z., et al. (2015). Probing the endocytic pathways of the filamentous bacteriophage in live cells using ratiometric PH fluorescent indicator. *Adv. Healthc. Mater.* 4 (3), 413–419. doi:10.1002/adhm.201400508

Tolentino, M. Q., Hartmann, A. K., Loe, D. T., and Rouge, J. L. (2020). Controlled release of small molecules and proteins from DNA-surfactant stabilized metal organic frameworks. *J. Mater. Chem. B* 8, 5627. doi:10.1039/D0TB00767F

Tomar, R. S., Matta, H., and Chaudhary, P. M. (2003). Use of adeno-associated viral vector for delivery of small interfering RNA. *Oncogene* 22 (36), 5712–5715. doi:10.1038/sj.onc.1206733

Tomita, T., Watanabe, M., Takahashi, T, Kumai, K., Tadakuma, T., and Yasuda, T. (1989). Temperature-sensitive release of adriamycin, an amphiphilic antitumor agent, from dipalmitoylphosphatidylcholine-cholesterol liposomes. *Biochim. Biophys. Acta* 978 (2), 185–190. doi:10.1016/0005-2736(89)90113-2

Toscano, M. G., and de Haan, P. (2018). How simian virus 40 hijacks the intracellular protein trafficking pathway to its own benefit and ours and ours. *Front. Immunol.* 9, 1160. doi:10.3389/fimmu.2018.01160

Troiber, C., and Wagner, E. (2011). Nucleic acid carriers based on precise polymer conjugates. *Bioconjug. Chem.* 22 (9), 1737–1752. doi:10.1021/bc200251r

Truong, N. P., Gu, W., Prasadam, I., Jia, Z., Crawford, R., Xiao, Y., et al. (2013). An influenza virus-inspired polymer system for the timed release of SiRNA. *Nat. Commun.* 4 (1), 1902. doi:10.1038/ncomms2905

Tsukuda, S., and Watashi, K. (2020). Hepatitis B virus biology and life cycle. *Antivir. Res.* 182, 104925. doi:10.1016/j.antiviral.2020.104925

Urie, R., and Rege, K. (2015). Nanoscale inorganic scaffolds as therapeutics and delivery vehicles. *Curr. Opin. Chem. Eng.* 7, 120–128. doi:10.1016/j.coche.2014.12.004

Venkatakrishnan, B., and Zlotnick, A. (2016). The structural biology of hepatitis B virus: form and function. *Annu. Rev. Virol.* 3 (1), 429–451. doi:10.1146/annurev-virology-110615-042238

Verdine, G. L., and Walensky, L. D. (2007). The challenge of drugging undruggable targets in cancer: lessons learned from targeting BCL-2 family members. *Clin. Cancer Res.* 13 (24), 7264–7270. doi:10.1158/1078-0432.CCR-07-2184

Vickers, K. C., Palmisano, B. T., Shoucri, B. M., Shamburek, R. D., and Remaley, A. T. (2011). MicroRNAs are transported in plasma and delivered to recipient cells by high-density lipoproteins. *Nat. Cell. Biol.* 13 (4), 423–433. doi:10.1038/ncb2210

Villagrana-Escareño, M. V., Reynaga-Hernández, E., Galicia-Cruz, O. G., Durán-Meza, A. L., De la Cruz-González, V., Hernández-Carballo, C. Y., et al. (2019). VLPs derived from the CCMV plant virus can directly transfect and deliver heterologous genes for translation into mammalian cells. *Biomed. Res. Int.* 2019, 4630891. doi:10.1155/2019/4630891

Volpers, C., and Kochanek, S. (2004). Adenoviral vectors for gene transfer and therapy. *J. Gene Med.* 6 (S1), S164–S171. doi:10.1002/jgm.496

Vorburger, S. A., and Hunt, K. K. (2002). Adenoviral gene therapy. *Oncologist* 7, 46–59. doi:10.1634/theoncologist.7-1-46

Wagenaar, T. R., Tolstykh, T., Shi, C., Jiang, L., Zhang, J., Li, Z., et al. (2015). Identification of the endosomal sorting complex required for transport-I (ESCRT-I) as an important modulator of anti-MiR uptake by cancer cells. *Nucleic Acids Res.* 43 (2), 1204–1215. doi:10.1093/nar/gku1367

Wagner, E. (2012). Polymers for SiRNA delivery: inspired by viruses to Be targeted, dynamic, and precise. *Acc. Chem. Res.* 45 (7), 1005–1013. doi:10.1021/ar2002232

Wang, C. Y., and Huang, L. (1989). Highly efficient DNA delivery mediated by PH-sensitive immunoliposomes. *Biochemistry* 28 (24), 9508–9514. doi:10.1021/bi00450a039

Wang, H., Shi, Y., Song, J., Qi, J., Lu, G., Yan, J., et al. (2016a). Ebola viral glycoprotein bound to its endosomal receptor niemann-pick C1. *Cell* 164 (1), 258–268. doi:10.1016/j.cell.2015.12.044

Wang, H., Tam, Y. Y., Chen, S., Zaifman, J., van der Meel, R., Ciufolini, M. A., et al. (2016b). The niemann-pick C1 inhibitor NP3.47 enhances gene silencing potency of lipid nanoparticles containing SiRNA. *Mol. Ther.* 24 (12), 2100–2108. doi:10.1038/mt.2016.179

Wang, L., Ariyarathna, Y., Ming, X., Yang, B., James, L. I., Kreda, S. M., et al. (2017). A novel family of small molecules that enhance the intracellular delivery and pharmacological effectiveness of antisense and splice switching oligonucleotides. *ACS Chem. Biol.* 12 (8), 1999–2007. doi:10.1021/acschembio.7b00242

Wang, X., Huang, D. Y., Huong, S.-M., and Huang, E.-S. (2005). Integrin αvβ3 is a coreceptor for human cytomegalovirus. *Nat. Med.* 11 (5), 515–521. doi:10.1038/nm1236

Wang, Z., Chui, W. K., and Ho, P. C. (2010). Integrin targeted drug and gene delivery. *Expert Opin. Drug Deliv.* 7 (2), 159–171. doi:10.1517/17425240903468696

Wasungu, L., and Hoekstra, D. (2006). Cationic lipids, lipoplexes and intracellular delivery of genes. *J. Controlled Release* 116 (2), 255–264. doi:10.1016/j.jconrel.2006.06.024

Wheeler, J. J., Palmer, L., Ossanlou, M., MacLachlan, I., Graham, R. W., Zhang, Y. P., et al. (1999). Stabilized plasmid-lipid particles: construction and characterization. *Gene Ther.* 6 (2), 271–281. doi:10.1038/sj.gt.3300821

Whitehead, K. A., Langer, R., and Anderson, D. G. (2009). Knocking down barriers: advances in SiRNA delivery. *Nat. Rev. Drug Discov.* 8 (2), 129–138. doi:10.1038/nrd2742

Wilen, C. B., Tilton, J. C., and Doms, R. W. (2012). Molecular mechanisms of HIV entry. *Adv. Exp. Med. Biol.* 726, 223–242. doi:10.1007/978-1-4614-0980-9_10

Wilner, S. E., Wengerter, B., Maier, K., de Lourdes Borba MagalhãesDel Amo, D. S., Pai, S., et al. (2012). An RNA alternative to human transferrin: a new tool for targeting human cells. *Mol. Ther. Nucleic Acids* 1 (5), e21. doi:10.1038/mtna.2012.14

Wood, H. (2018). FDA approves patisiran to treat hereditary transthyretin amyloidosis. *Nat. Rev. Neurol.* 14 (10), 570. doi:10.1038/s41582-018-0065-0

Wyman, T. B., Nicol, F., Zelphati, O., Scaria, P. V., Plank, C., and Szoka, F. C. (1997). Design, synthesis, and characterization of a cationic peptide that binds to nucleic acids and permeabilizes bilayers. *Biochemistry* 36 (10), 3008–3017. doi:10.1021/bi9618474

Xiang, B., Jia, X. L., Qi, J. L., Yang, L. P., Sun, W. H., Yan, X., et al. (2017). Enhancing SiRNA-based cancer therapy using a new PH-responsive activatable cell-penetrating peptide-modified liposomal system. *Int. J. Nanomedicine* 12, 2385–2405. doi:10.2147/IJN.S129574

Xie, X., Liao, J., Shao, X., Li, Q., and Lin, Y. (2017). The effect of shape on cellular uptake of gold nanoparticles in the forms of stars, rods, and triangles. *Sci. Rep.* 7 (1), 3827. doi:10.1038/s41598-017-04229-z

Xu, D., McCarty, D., Fernandes, A., Fisher, M., Samulski, R. J., and Juliano, R. L. (2005). Delivery of MDR1 small interfering RNA by self-complementary recombinant adeno-associated virus vector. *Mol. Ther.* 11 (4), 523–530. doi:10.1016/j.ymthe.2004.12.019

Xue, H. Y., Guo, P., Wen, W. C., and Wong, H. L. (2015). Lipid-based nanocarriers for RNA delivery. *Curr. Pharm. Des.* 21 (22), 3140–3147. doi:10.2174/1381612821666150531164540

Yamauchi, Y., and Greber, U. F. (2016). Principles of virus uncoating: cues and the snooker ball. *Traffic* 17 (6), 569–592. doi:10.1111/tra.12387

Yamazaki, Y., Nango, M., Matsuura, M., Hasegawa, Y., Hasegawa, M., and Oku, N. (2000). Polycation liposomes, a novel nonviral gene transfer system, constructed from cetylated polyethylenimine. *Gene Ther.* 7 (13), 1148–1155. doi:10.1038/sj.gt.3301217

Yan, A. C., and Levy., M. (2018). Aptamer-mediated delivery and cell-targeting aptamers: room for improvement. *Nucleic Acid Ther.* 28 (3), 194–199. doi:10.1089/nat.2018.0732

Yang, B., Ming, X., Cao, C., Laing, B., Yuan, A., Porter, M. A., et al. (2015). High-throughput screening identifies small molecules that enhance the pharmacological effects of oligonucleotides. *Nucleic Acids Res.* 43 (4), 1987–1996. doi:10.1093/nar/gkv060

Yang, X. C., Samanta, B., Agasti, S. S., Jeong, Y., Zhu, Z. J., Rana, S., et al. (2011). Drug delivery using nanoparticle-stabilized nanocapsules. *Angew. Chem. Int. Ed. Engl.* 50 (2), 477–481. doi:10.1002/anie.201005662

Yao, Y., Jia, T., Pan, Y., Gou, H., Li, Y., Sun, Y., et al. (2015). Using a novel MicroRNA delivery system to inhibit osteoclastogenesis. *Int. J. Mol. Sci.* 16 (4), 8337–8350. doi:10.3390/ijms16048337

Yata, T., Lee, K. Y., Dharakul, T., Songsivilai, S., Bismarck, A., Mintz, P. J., et al. (2014). Hybrid nanomaterial complexes for advanced phage-guided gene delivery. *Mol. Ther. Nucleic Acids* 3, e185. doi:10.1038/mtna.2014.37

Yatvin, M. B., Kreutz, W., Horwitz, B. A., and Shinitzky, M. (1980). PH-sensitive liposomes: possible clinical implications. *Science* 210 (4475), 1253–1255. doi:10.1126/science.7434025

Yatvin, M. B., Weinstein, J. N., Dennis, W. H., and Blumenthal, R. (1978). Design of liposomes for enhanced local release of drugs by hyperthermia. *Science* 202 (4374), 1290–1293. doi:10.1126/science.364652

Ye, S.-f., Tian, M.-M., Wang, T.-X., Ren, L., Wang, D., Shen, L.-H., et al. (2012). Synergistic effects of cell-penetrating peptide tat and fusogenic peptide HA2-enhanced cellular internalization and gene transduction of organosilica nanoparticles. *Nanomed.: Nanotechno., Biol. Med.* 8 (6), 833–841. doi:10.1016/j.nano.2011.10.003

Yen, A., Cheng, Y., Sylvestre, M., Gustafson, H. H., Puri, S., and Pun, S. H. (2018). Serum nuclease susceptibility of MRNA cargo in condensed polyplexes. *Mol. Pharm.* 15 (6), 2268–2276. doi:10.1021/acs.molpharmaceut.8b00134

Yin, H., Kanasty, R. L., Eltoukhy, A. A., Vegas, A. J., Dorkin, J., and Anderson, D. G. (2014). Non-viral vectors for gene-based therapy. *Nat. Rev. Genet.* 15 (8), 541–555. doi:10.1038/nrg3763

Yonenaga, N., Kenjo, E., Asai, T., Tsuruta, A., Shimizu, K., Dewa, T., et al. (2012). RGD-based active targeting of novel polycation liposomes bearing SiRNA for cancer treatment. *J. Control Release* 160 (2), 177–181. doi:10.1016/j.jconrel.2011.10.004

Younes, A., Bartlett, N. L., Leonard, J. P., and Kennedy, D. A. (2010). Brentuximab vedotin (SGN-35) for relapsed CD30-positive lymphomas. *N. Engl. J. Med.* 363 (19), 1812–1821. doi:10.1056/NEJMoa1002965

Young, K. L., Scott, A. W., Hao, L., Sarah, E. M., Guoliang, L., and Mirkin, C. A. (2012). Hollow spherical nucleic acids for intracellular gene regulation based upon biocompatible silica shells. *Nano Lett.* 12 (7), 3867–3871. doi:10.1021/nl3020846

Yuan, W., and Li, H. (2017). "Polymer-based nanocarriers for therapeutic nucleic acids delivery," in *Nanostructures for drug delivery*. 445–460. doi:10.1016/B978-0-323-46143-6.00014-2

Zanta, M. A., Belguise-Valladier, P., and Behr, J. P. (1999). Gene delivery: a single nuclear localization signal peptide is sufficient to carry DNA to the cell nucleus. *Proc. Natl. Acad. Sci. U.S.A.* 96 (1), 91–96. doi:10.1073/pnas.96.1.91

Zatsepin, T. S., Kotelevtsev, Y. V., and Koteliansky, V. (2016). Lipid nanoparticles for targeted siRNA delivery - going from bench to bedside. *Int. J. Nanomedicine* 11, 3077–3086. doi:10.2147/IJN.S106625

Zhang, J., Chen, R., Fang, X., Chen, F., Wang, Y., and Chen, M. (2015). Nucleolin targeting AS1411 aptamer modified PH-sensitive micelles for enhanced delivery and antitumor efficacy of paclitaxel. *Nano Res.* 8 (1), 201–218. doi:10.1007/s12274-014-0619-4

Zhao, N., Bagaria, H. G., Wong, M. S., and Zu, Y. (2011). A nanocomplex that is both tumor cell-selective and cancer gene-specific for anaplastic large cell lymphoma. *J. Nanobiotechnology* 9, 2. doi:10.1186/1477-3155-9-2

Zhi, D., Zhang, S., Cui, S., Zhao, Y., Wang, Y., and Zhao, D. (2013). The headgroup evolution of cationic lipids for gene delivery. *Bioconjug. Chem.* 24 (4), 487–519. doi:10.1021/bc300381s

Zhu, L., and Mahato, R. I. (2010). Lipid and polymeric carrier-mediated nucleic acid delivery. *Expert Opin. Drug Deliv.* 7 (10), 1209–1226. doi:10.1517/17425247.2010.513969

Zhuang, J., Kuo, C. H., Chou, L. Y., Liu, D. Y., Weerapana, E., and Tsung, C. K. (2014). Optimized metal-organic-framework nanospheres for drug delivery: evaluation of small-molecule encapsulation. *ACS Nano* 8 (3), 2812–2819. doi:10.1021/nn406590q

Conflict of Interest: The authors declare that the research was conducted in the absence of any commercial or financial relationships that could be construed as a potential conflict of interest.

Copyright © 2021 de la Fuente, Sawant, Tolentino, Corrigan and Rouge. This is an open-access article distributed under the terms of the Creative Commons Attribution License (CC BY). The use, distribution or reproduction in other forums is permitted, provided the original author(s) and the copyright owner(s) are credited and that the original publication in this journal is cited, in accordance with accepted academic practice. No use, distribution or reproduction is permitted which does not comply with these terms.

frontiers in Chemistry

ORIGINAL RESEARCH
published: 11 March 2021
doi: 10.3389/fchem.2021.580025

Optical Devices Constructed From Responsive Microgels for Polyphenols Detection

Jingying Wang[1], *Xieli Zhang*[2,3], *Kaiyao Shi*[4]* and *Qiang Zhang*[2,3]*

[1]Department of Laboratory, 15189 Accredited Laboratory, Jilin Province Drug Resistance Monitoring Center, China-Japan Union Hospital of Jilin University, Changchun, China, [2]State Key Laboratory of Electroanalytical Chemistry, Changchun Institute of Applied Chemistry, Chinese Academy of Sciences, Changchun, China, [3]School of Applied Chemistry and Engineering University of Science and Technology of China, Hefei, China, [4]Provincial Key Laboratory for Gene Diagnosis of Cardiovascular Disease, Jilin Provincial Engineering Laboratory for Endothelial Function and Genetic Diagnosis, Department of Cardiology, China-Japan Union Hospital of Jilin University, Changchun, China

Polyphenols are used as antioxidants in various foods and beverages, which are considered to be a health benefit. The measurement of polyphenols contents is of great interest in food chemistry and health science. This work reported a microgels based photonic device (etalon) to detect polyphenols. Dopamine was used as a model compound of polyphenols. Herein, we proposed a "block" concept for dopamine detection. The dopamine was oxidized and formed dopamine films catalyzed by tyrosinase on the surface of etalon. As the etalon was immersed in $ZnCl_2$, the dopamine films blocked the $ZnCl_2$ diffusion into etalon that caused optical property changes. The film thickness is associated with the concentration of dopamine which can be readout via optical signals.

Keywords: microgels, optical devices, polyphenols detection, responsive polymer, photonic crystal (PC)

OPEN ACCESS

Edited by:
Ping Yu,
Institute of Chemistry (CAS), China

Reviewed by:
Wei-Lung Tseng,
National Sun Yat-sen University, Taiwan
Yanyan Huang,
Institute of Chemistry (CAS), China

****Correspondence:***
Qiang Zhang
qiang.zhang@ciac.ac.cn
Kaiyao Shi
shiky@jlu.edu.cn

Specialty section:
This article was submitted to Analytical Chemistry, a section of the journal Frontiers in Chemistry

Received: *04 July 2020*
Accepted: *01 February 2021*
Published: *11 March 2021*

Citation:
Wang J, Zhang X, Shi K and Zhang Q (2021) Optical Devices Constructed From Responsive Microgels for Polyphenols Detection. Front. Chem. 9:580025. doi: 10.3389/fchem.2021.580025

INTRODUCTION

Polyphenols are strong antioxidants existing in fruits and beverages like tea, red wine, and coffee, which play an important role in human health (Ponder and Hallmann, 2019; Zheng et al., 2020). The catechol structure allows polyphenols to scavenge free radicals and inhibit lipoprotein oxidation, reducing the incidence of cardiovascular diseases and some cancers (Ru et al., 2019; Gao et al., 2020; Zhang et al., 2020). Therefore, it is very important to detect such compounds in foods in the fields of food chemistry and healthy science. Up to now, some methods have been developed for polyphenols detection, such as chemiluminescence (Nalewaiko-Sieliwoniuk et al., 2015; Nalewajko-Sieliwoniuk et al., 2016; Zhao et al., 2017), mass spectra (Fayeulle et al., 2019), electrophoresis (Yasui and Ishii, 2014; Matei et al., 2016; Parveen et al., 2016), electroanalysis (Fu et al., 2012; Thangaraj et al., 2012; Alcalde et al., 2019) and chromatography (Hashim et al., 2020; Ovchinnikov et al., 2020; Yuan et al., 2020). However, these methods get involved with complicated sample purification, and the complex composition and the presence of interferences in the extracted samples often caused big experimental errors during polyphenols content measurement. Meanwhile, these detection are expensive and require professional technicians to complete, which significantly restricts their abroad applications.

Photonic materials are composed of close packed arrays of nanoparticles that self-assemble into crystal structures. As light illuminated the crystal structure, it will be constructed or deconstructed in a certain direction to generate an interference light. The color and optical properties (e.g., reflected light wavelength) of photonic materials depends on the distance between lattice planes. In recent

years, photonic materials have been explored as colorimetric sensors due to their attractive features such as visual readout, low cost, and easy handling (Hou et al., 2018; Zhang et al., 2018). For example, the Asher group developed a series of two-dimensional photonic crystals that were prepared by locking 3D ordered colloidal particles in hydrogels (Cai et al., 2015; Cai et al., 2016). Then, they utilized these materials to sense various chemical small molecules and biomacromolecules (Zhang et al., 2011; Zhang et al., 2013; Zhang et al., 2014b). Similarly, 3D photonic crystals have also been reported and used to sense various environmental factors, such as metal ions (Liu et al., 2020), RNA (Li et al., 2020), gas (Huang et al., 2019; Afsari and Sarraf, 2020; Huang et al., 2020), protein (Cai et al., 2016; Cai et al., 2017), and bacteria (Massad-Ivanir et al., 2014; Hou et al., 2018; Zhang et al., 2018). Our group prepared specific microgel-based optical devices (i.e., an etalon). We subsequently studied their optical properties and utilized the device to sense various environmental analytes, e.g., triglycerides (Zhang et al., 2015a), Tabun (Zhang et al., 2014b), Cu^{2+} (Zhang et al., 2015b), CO_2 (Zhang et al., 2015c) and H_2O_2 (Zhang et al., 2016). Briefly, etalons were prepared by depositing a single layer of microgels on an Au-coated glass substrate, and then another layer (15 nm) of Au was deposited on the microgels to form a sandwiching structure (Zhang et al., 2014a). The optical properties of etalon can be described using **Eq. 1**:

$$m\lambda = 2nd\cos\theta \tag{1}$$

where n is the refractive index of the microgels layer, d is the space between two Au layers, θ is the angle of incident light relative to the normal, and m is the order of reflected peaks that should be integers. Therefore, the reflection wavelength and etalon colors are dependent on the distance of Au-Au layers and the refractive index of microgels.

In the submission, we developed a "block" concept for polyphenols determination using etalons. First, the surfaces of etalons were modified using tyrosinase that could catalyze polyphenol oxidation generating polyphenol films on the etalon surface in presence of O_2. The thickness of polyphenol films depends on the concentration of polyphenols. When the device was soaked in $ZnCl_2$ solution, the polyphenol films blocked Zn^{2+} entering into etalon that caused optical property changes of etalons. Therefore, the concentration of polyphenols can be deduced according to optical property change of etalons. In this paper, dopamine was used as a mode compound of polyphenols for polyphenol detection research. In a comparison of electrochemical methods, mass spectroscopy-based methods, and fluorescent probes, this system does not get involved with bulk and expensive equipment, complicated sample pre-treatment, and complex operation.

EXPERIMENTAL SECTION

Synthesis of Microgels (MG-AAc)

N-isopropylacrylamide (11.9 mmol), acrylic acid (0.65 mmol), and N,N′-methylenebisacrylamide (0.65 mmol) were dissolved in 100 ml deionized (DI) water, and then the solution was filtered using a 0.45 μm filter. The solution was added into a 3-necked round bottom flask with a reflux condenser, nitrogen inlet, and temperature probe. The solution was heated to 70°C under N_2 atmosphere. The polymerization was then initiated using ammonium persulfate (0.2 mmol) in 1 ml of DI water. After 4 h reaction, the resulting suspension was cooled to room temperature and the filtered using Whatman #1 filter paper to remove any large aggregates formed during the polymerization. The microgel solution was purified for six times via centrifugation to remove unreacted monomers and supernatant. The purified microgels solution was kept in a brown glass jar before use.

Modification of Etalon Surfaces With Tyrosinase

The etalon was cleaned by rinsing with deionized (DI) water and ethanol separately. N-hydroxysuccinimide ester groups were attached on etalon surface by soaking into 3,3′-Dithiodipropionic acid di (N-hydroxysuccinimide ester) (DTSP) solution at a concentration of 0.1 mmol ml^{-1} for 2 h. Then, the etalon was taken out from solution, followed by washing with massive ethanol and stored in ethanol solution overnight to remove residual DTSP.

Tyrosinase was fixed on the etalon surface through covering the DTSP functionalized etalon with 100 μL tyrosinase aqueous solution (1 mg ml^{-1}) for 2 h. The residual tyrosinase was removed by rinsing the etalon surface with massive DI water.

Etalon Pre-Treatment Using Dopamine

100 μL dopamine aqueous solutions at a certain concentration were sprayed on the etalon surfaces. After 2 h, the dopamine aqueous solutions were removed from the etalon surfaces using micropipette, followed by washing with massive DI water to remove unreacted dopamine monomer from polydopamine film. The edge of these etalons was sealed using nail polish to prevent solvent and solute entering etalon from periphery.

Reflectance Spectroscopy

Reflectance measurements were completed in a home-made sample holder using a USB2000 + spectrophotometer, a HL-2000-FHSA tungsten light source, and a R400-7-VISNIR optical fiber reflectance probe, all from Ocean Optics (Dunedin, FL). The spectra were recorded using Ocean Optics Spectra Suite Spectroscopy Software over a wavelength range of 350–1025 nm. Measurements were performed in the sample holder that leads to careful sample positioning, test stability, and precise temperature control.

RESULTS AND DISCUSSIONS

First, microgels were synthesized by the precipitation polymerization of N-isopropylacrylamide, acrylic acid, N, N′-methylene bis (acrylamide) (crosslinker). The resultant microgels have been characterized using transmission electron microscope (TEM) and dynamic light scattering (DLS), as shown in **Figure 1**.

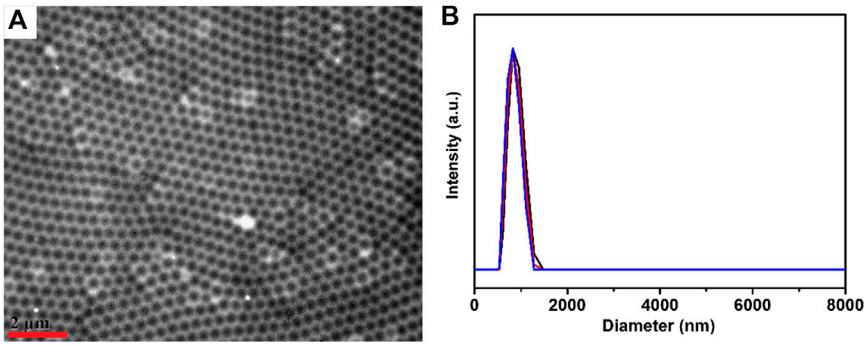

FIGURE 1 | (A) TEM image of microgels; the scale bar stands for 2 μm **(B)** microgel diameters at 30°C determined three times by DLS.

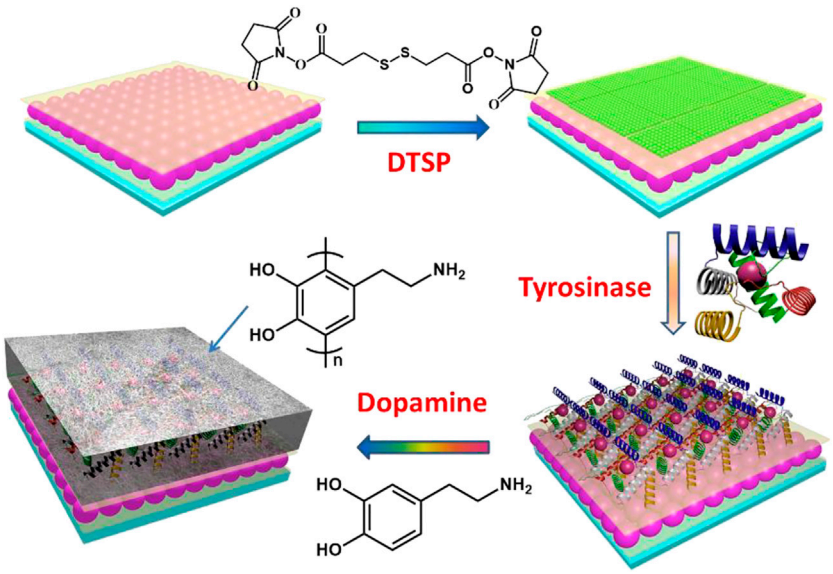

FIGURE 2 | Schematic process of etalons.

The microgels exhibited the diameters of ~340 nm (±10 nm) in dried state and diameters of 840 nm (±15 nm) in swelling state (polydispersity index: 1.03) at 30°C. The characterized microgels were then used to construct microgel-based etalons following previous reported protocol by our group (Xia et al., 2020). These etalons were comprised of single layer microgels sandwiched by two semi-transparent gold layers on glass substance, as shown in **Figure 2**. In order to deposit polyphenol films on the surfaces of etalons, we covalently fixed tyrosinase on etalon surfaces that can catalyze catechol oxidation generating benzoquinone and polyphenol films (Solem et al., 2016). Firstly, oxysuccinimide ester groups were attached on etalon surface via Au–S bonds by soaking etalons in DTSP solution (1 mg ml^{-1}). Tyrosinase was subsequently fixed on etalon surfaces through substitution reaction between amine groups of tyrosinase and oxysuccinimide ester groups on etalon surfaces. When catechols present in the system, tyrosinase catalyzes oxidation reactions of catechol into o-quinone (Desentis-Mendoza et al., 2006). Subsequently, a conjugate addition of diverse nucleophiles (catechols) with o-quinone takes place (Espín et al., 2001). These reactions repeatedly happened yielding polymers with high molecular weights and further forming polymeric films. The solute was prevented from entering into the etalon from edges by sealing fringes with nail polish. The schematic process of etalons was shown in **Figure 2**.

The process of surface modification was monitored using X-Ray photoelectron spectroscopy (XPS) surface analysis technique, and the results were shown in **Figure 3**. The N1s XP spectra showed there is trace amount of N atoms on the surface of etalons. It dramatically increased when the etalon surface was modified using DTSP, which was attributed to the imide groups of DTSP. The intensity change of N atoms was also observed when tyrosinase was attached on the surface of etalons. As the polydopamine films were deposited on the surfaces of etalons, enormous intensity increase of N atoms in XPS spectrum was observed due to the high content of N atoms in

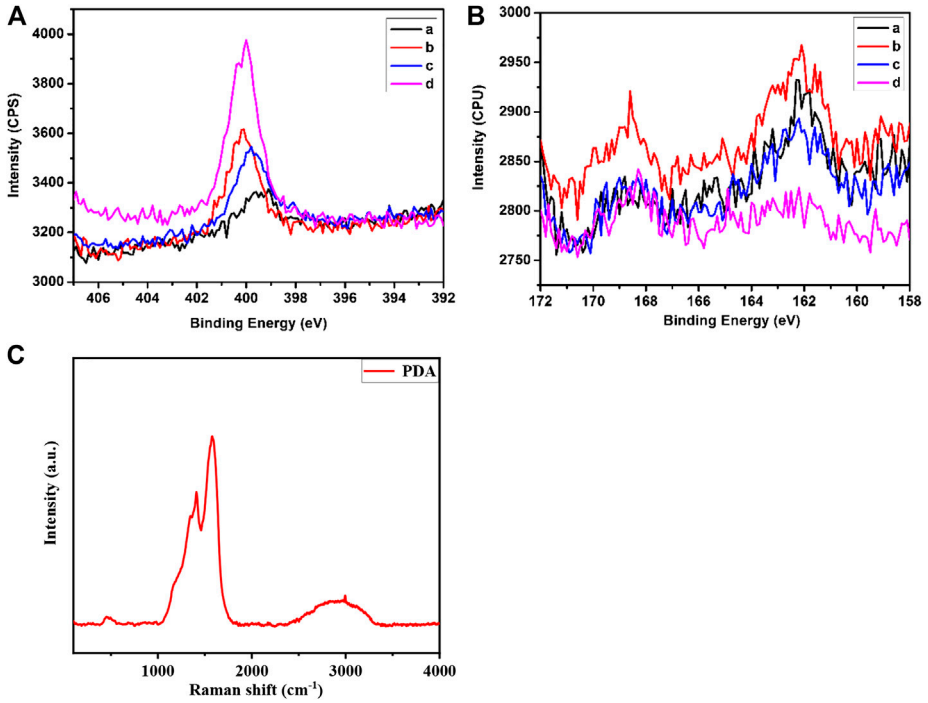

FIGURE 3 | Element-specific high-resolution XP spectra of N1s **(A)** and S2p **(B)** regions. Panels in the two pictures: a: etalon; b: etalon modified with DTSP; c: etalon modified with tyrosinase; d: etalon modified with polydopamine film **(C)** The Raman spectra of polydopamine film on the surface of the sensors.

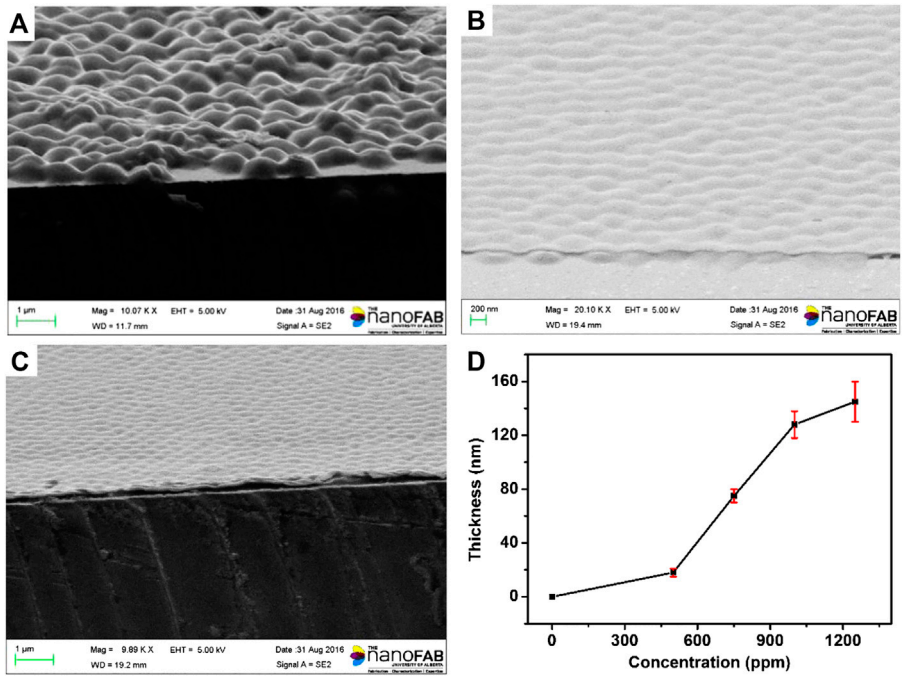

FIGURE 4 | SEM images of microgels: **(A)** etalon without surface modification **(B)** etalon modified using 500 ppm dopamine **(C)** etalon modified using 1000 ppm dopamine **(D)** The thickness of polydopamine film as a function of dopamine concentration. These values are averages of three repeat analyses using three etalon devices.

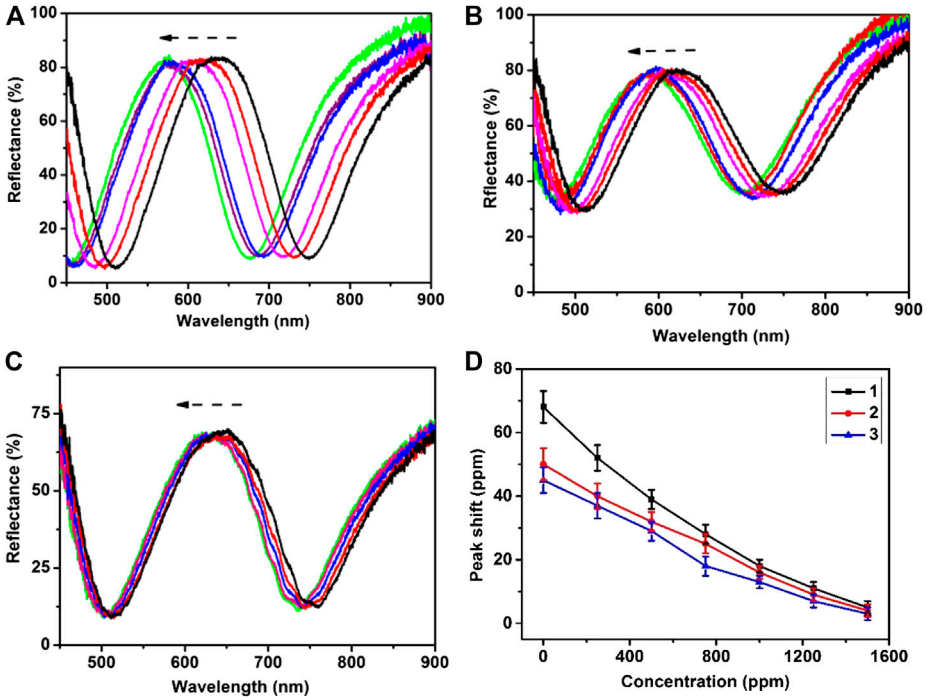

FIGURE 5 | Reflectance spectra of etalon upon exposure to the $ZnCl_2$ aqueous solution of 0.1 M recorded in 5 min: **(A)** etalon **(B)** etalon modified using 500 ppm dopamine **(C)** etalon modified using 1000 ppm dopamine **(D)** The peak shifts of reflectance spectra as a function of dopamine concentration: (1) in DI water, (2) in urine, (3) in serum. These values are averages of five repeat analyses using five etalon devices.

polydopamine films. The S2p XP spectra also confirm the modification process on etalon surfaces (**Figure 3B**). The surface modification of etalon with tyrosinase caused the intensity change of S2p (162 eV) in XPS spectra. The peak of S2p at 162 eV almost disappeared, when polydopamine film was deposited on etalon surfaces. The phenomenon was due to the fact that the etalon surfaces and S atoms were covered by polydopamine films. The structure of polydopamine film on the etalon surface also has been investigated by Raman spectra, which has been shown in **Figure 3C**. The strong adsorption peak at 1650 cm^{-1} was assigned to the C = C stretching vibration of benzene. The polydopamine films were also investigated using SEM through observing the cross-section of etalons. In comparison of pure etalons, obvious polymeric films were found on the top of polydopamine modified etalons (**Figure 4**). The thickness of polydopamine films depends on the concentration of dopamine solution. As shown in **Figure 4D**, the thickness of polydopamine film increases from 18 to 128 nm as concentration increasing of dopamine from 500 ppm to 1250 ppm.

The response of the etalons to $ZnCl_2$ was investigated at room temperature, and the reflectance spectra of etalons were shown in **Figure 5**. As can be seen, a characteristic peak at 630 nm was observed for pure etalon. When the etalon was exposed to 0.01M $ZnCl_2$, the reflectance spectrum of etalon exhibited a blue-shift of 65nm and got stable around 5min. The blue-shift of reflectance spectrum was attributed to deswelling of microgels caused by $ZnCl_2$. Our group has found in 2013 that the semi-transparent Au layer contains pores, which allow penetration of high molecular weight (Mw) polyelectrolytes (MW 100 000–200 000) from solution into etalons (Islam and Serpe, 2013). In the submission, $ZnCl_2$ penetrates the semi-transparent Au layer and enters microgels. Zn^{2+} could coordinate with carboxylate groups of microgels with a ratio of 1: 2. In this case, Zn^{2+} acts like crosslinkers which make microgels shrink. **Figure 5A** demonstrates reflectance spectra of etalons subjecting to 0.01 M $ZnCl_2$. When $ZnCl_2$ present in the system, the reflectance spectra exhibit fast a blue-shift of 66 nm. The reflectance spectra become stable at 5 min. Therefore, all of spectrum data in the following experiment were read out at 5 min. The amplitudes of peak shift of reflectance spectra are inversely proportional to the concentration of dopamine used to surface modification of etalons. The etalons modified using 500 ppm dopamine exhibit a blue shift of 52 nm in response to 0.01 M $ZnCl_2$, which is 14 nm less than that of pure etalon (66 nm). These values are averages of three repeat analyses using three different etalon devices. As the concentration of dopamine increases from 500 to 1250 ppm, the amplitude of spectra shift decreases from 52 to 10 nm. The similar trends of peak shifts were also observed when the detection was carried out in urine and serum. This phenomenon is attributed to thickness changes of dopamine films that block the diffusion of $ZnCl_2$ through the film into microgels. The calibration curvesof spectral shift as a function of dopamine concentration were shown in **Figure 5D**. The sensor exhibited a limit of detection of 11.5 ppm in DI water, 18.7 ppm in urine, and 21.4 ppm in serum. Five devices were used to measure dopamine

concentration at each point, which shows a maximum deviation of 8% between these devices. The result indicates a good device-to-device reproducibility for dopamine detection. Therefore, etalon can be used to quantitatively measure dopamine content in samples using the calibration curve. This method also can be used to detect other catecholamines with corresponding calibration curves.

CONCLUSION

A method of polyphenols detection was developed based on "block" concept using etalon devices. First, the etalon surfaces were modified using tyrosinase that could oxidize polyphenols into polymeric films. The polymeric films impede the diffusion of $ZnCl_2$ into etalons, which lead to different optical properties of etalons. The optical property of etalon is related to polyphenol concentration using surface modification of etalons. The concentration of polyphenol can be measured according to optical property change of etalons.

DATA AVAILABILITY STATEMENT

The raw data supporting the conclusions of this article will be made available by the authors, without undue reservation.

AUTHOR CONTRIBUTIONS

All authors listed have made a substantial, direct and intellectual contribution to the work, and approve it for publication.

FUNDING

This work was financially supported by the International Cooperation Project of Jilin Province Science and Technology Development Plan (20200801008GH), the National Natural Science Foundation of China (No: 21604091), the National Key Research and Development Program of China (2018YFD1100503), and the Department of Education of Jilin Province (JJKH20201031KJ).

REFERENCES

Afsari, A., and Sarraf, M. J. (2020). Design of a hydrogen sulfide gas sensor based on a photonic crystal cavity using graphene. *Superlattices Microstruct.* 138, 106362. doi:10.1016/j.spmi.2019.106362

Alcalde, B., Granados, M., and Saurina, J. (2019). Exploring the antioxidant features of polyphenols by spectroscopic and electrochemical methods. *Antioxidants* 8, 523. doi:10.3390/antiox8110523

Cai, Z., Kwak, D. H., Punihaole, D., Hong, Z., Velankar, S. S., Liu, X., et al. (2015). A photonic crystal protein hydrogel sensor for candida albicans. *Angew. Chem. Int. Ed.* 54, 13036–13040. doi:10.1002/anie.201506205

Cai, Z., Luck, L. A., Punihaole, D., Madura, J. D., and Asher, S. A. (2016). Photonic crystal protein hydrogel sensor materials enabled by conformationally induced volume phase transition. *Chem. Sci.* 7, 4557–4562. doi:10.1039/c6sc00682e

Cai, Z., Sasmal, A., Liu, X., and Asher, S. A. (2017). Responsive photonic crystal carbohydrate hydrogel sensor materials for selective and sensitive lectin protein detection. *ACS Sens.* 2, 1474–1481. doi:10.1021/acssensors.7b00426

Desentis-Mendoza, R. M., Hernández-Sánchez, H., Moreno, A., Rojas del C, E., Chel-Guerrero, L., and Tamariz, J. (2006). Enzymatic polymerization of phenolic compounds using laccase and tyrosinase from ustilago maydis. *Biomacromolecules* 7, 1845–1854. doi:10.1021/bm060159p

Espín, J. C., Soler-Rivas, C., Cantos, E., Tomás-Barberán, F. A., and Wichers, H. J. (2001). Synthesis of the antioxidant hydroxytyrosol using tyrosinase as biocatalyst. *J. Agric. Food Chem.* 49, 1187–1193. doi:10.1021/jf001258b

Fayeulle, N., Meudec, E., Boulet, J. C., Vallverdu-Queralt, A., Hue, C., and Boulanger, R. (2019). Fast discrimination of chocolate quality based on average-mass-spectra fingerprints of cocoa polyphenols. *J. Agric. Food Chem.* 67, 2723–2731. doi:10.1021/acs.jafc.8b06456

Fu, Y., Lin, Y., Chen, T., and Wang, L. (2012). Study on the polyfurfural film modified glassy carbon electrode and its application in polyphenols determination. *J. Electroanal. Chem.* 687, 25–29. doi:10.1016/j.jelechem.2012.09.040

Gao, H., Yuan, X., Wang, Z., Gao, Q., and Yang, J. (2020). Profiles and neuroprotective effects of Lycium ruthenicum polyphenols against oxidative stress-induced cytotoxicity in PC12 cells. *J. Food Biochem.* 44, e13112. doi:10.1111/jfbc.13112

Hashim, S. N. N. S., Boysen, R. I., Yang, Y., Schwarz, L. J., Danylec, B., and Hearn, M. T. W. (2020). Parallel enrichment of polyphenols and phytosterols from Pinot noir grape seeds with molecularly imprinted polymers and analysis by capillary high-performance liquid chromatography electrospray ionisation tandem mass spectrometry. *Talanta* 208, 120397. doi:10.1016/j.talanta.2019.120397

Hou, J., Li, M., and Song, Y. (2018). Recent advances in colloidal photonic crystal sensors: materials, structures and analysis methods. *Nano Today* 22, 132–144. doi:10.1016/j.nantod.2018.08.008

Huang, B., Wang, Y., and Mao, C. (2019). Temperature-independent gas pressure sensor with high birefringence photonic crystal fiber-based reflective lyot filter. *Sensors* 19, 5312. doi:10.3390/s19235312

Huang, G., Li, Y., Chen, C., Yue, Z., Zhai, W., Li, M., et al. (2020). Hydrogen sulfide gas sensor based on titanium dioxide/amino-functionalized graphene quantum dots coated photonic crystal fiber. *J. Phys. D: Appl. Phys.* 53, 325102. doi:10.1088/1361-6463/ab89cc

Islam, M. R., and Serpe, M. J. (2013). Penetration of polyelectrolytes into charged poly (N-isopropylacrylamide) microgel layers confined between two surfaces. *Macromolecules* 46, 1599–1606. doi:10.1021/ma302637n

Li, Q., Zhou, S., Zhang, T., Zheng, B., and Tang, H. (2020). Bioinspired sensor chip for detection of miRNA-21 based on photonic crystals assisted cyclic enzymatic amplification method. *Biosens. Bioelectron.* 150, 111866. doi:10.1016/j.bios.2019.111866

Liu, R., Duan, S., Bao, L., Wu, Z., Zhou, J., and Yu, R. (2020). Photonic crystal enhanced gold-silver nanoclusters fluorescent sensor for Hg^{2+} ion. *Analytica Chim. Acta* 1114, 50–57. doi:10.1016/j.aca.2020.04.011

Massad-Ivanir, N., Mirsky, Y., Nahor, A., Edrei, E., Bonanno-Young, L. M., and Ben Dov, N. (2014). Trap and track: designing self-reporting porous Si photonic crystals for rapid bacteria detection. *Analyst* 139, 3885–3894. doi:10.1039/c4an00364k

Matei, A. O., Gatea, F., Teodor, E. D., and Radu, G. L. (2016). Polyphenols analysis from different medicinal plants extracts using capillary zone electrophoresis (CZE). *Revista De Chim.* 67, 1051–1055.

Nalewajko-Sieliwoniuk, E., Malejko, J., Pawlukiewicz, A., and Kojło, A. (2016). A novel multicommuted flow method with nanocolloidal manganese (IV)-based chemiluminescence detection for the determination of the total polyphenol index. *Food Anal. Methods* 9, 991–1001. doi:10.1007/s12161-015-0274-8

Nalewajko-Sieliwoniuk, E., Malejko, J., Święczkowska, M., and Kowalewska, A. (2015). A study on the selection of chemiluminescence system for the flow injection determination of the total polyphenol index of plant-derived foods. *Food Chem.* 176, 175–183. doi:10.1016/j.foodchem.2014.12.053

Ovchinnikov, D. V., Bogolitsyn, K. G., Druzhinina, A. S., Kaplitsin, P. A., Parshina, A. E., and Pikovskoi, I. I. (2020). Study of polyphenol components in extracts of arctic brown algae of fucus vesiculosus type by liquid chromatography and mass-spectrometry. *J. Anal. Chem.* 75, 633–639. doi:10.1134/S1061934820050147

Parveen, S., Memon, S. Q., Siyal, A. N., Memon, N., and Khuhawar, M. Y. (2016). Large-volume sample staking of rice polyphenols prior to their determination by non-aqueous capillary electrophoresis. *Food Anal. Methods* 9, 2152–2160. doi:10.1007/s12161-015-0394-1

Ponder, A., and Hallmann, E. (2019). The effects of organic and conventional farm management and harvest time on the polyphenol content in different raspberry cultivars. *Food Chem.* 301, 125295. doi:10.1016/j.foodchem.2019.125295

Ru, Q., Xiong, Q., Tian, X., Chen, L., Zhou, M., Li, Y., et al. (2019). Tea polyphenols attenuate methamphetamine-induced neuronal damage in PC12 Cells by alleviating oxidative stress and promoting DNA repair. *Front. Physiol.* 10, 1450. doi:10.3389/fphys.2019.01450

Solem, E., Tuczek, F., and Decker, H. (2016). Tyrosinase versus catechol oxidase: one asparagine makes the difference. *Angew. Chem. Int. Ed.* 55, 2884–2888. doi:10.1002/anie.201508534

Thangaraj, R., Manjula, N., and Kumar, A. S. (2012). Rapid simultaneous electrochemical sensing of tea polyphenols. *Anal. Methods* 4, 2922–2928. doi:10.1039/c2ay25563d

Xia, X., Zhang, X., Serpe, M. J., and Zhang, Q. (2020). Microgel-based devices as wearable capacitive electronic skins for monitoring cardiovascular risks. *Adv. Mater. Technol.* 5, 2070011. doi:10.1002/admt.201900818

Yasui, M., and Ishii, T. (2014). A new method for detection of self-associated tea polyphenols using native-polyacrylamide gel electrophoresis. *Bunseki Kagaku* 63, 687–692. doi:10.2116/bunsekikagaku.63.687

Yuan, B., Dinssa, F. F., Simon, J. E., and Wu, Q. (2020). Simultaneous quantification of polyphenols, glycoalkaloids and saponins in African nightshade leaves using ultra-high performance liquid chromatography tandem mass spectrometry with acid assisted hydrolysis and multivariate analysis. *Food Chem.* 312, 126030. doi:10.1016/j.foodchem.2019.126030

Zhang, J.-T., Cai, Z., Kwak, D. H., Liu, X., and Asher, S. A. (2014a). Two-dimensional photonic crystal sensors for visual detection of lectin concanavalin a. *Anal. Chem.* 86, 9036–9041. doi:10.1021/ac5015854

Zhang, J.-T., Chao, X., Liu, X., and Asher, S. A. (2013). Two-dimensional array Debye ring diffraction protein recognition sensing. *Chem. Commun.* 49, 6337–6339. doi:10.1039/c3cc43396j

Zhang, J.-T., Wang, L., Luo, J., Tikhonov, A., Kornienko, N., and Asher, S. A. (2011). 2-D array photonic crystal sensing motif. *J. Am. Chem. Soc.* 133, 9152–9155. doi:10.1021/ja201015c

Zhang, Q.-M., Berg, D., Mugo, S. M., and Serpe, M. J. (2015b). Lipase-modified pH-responsive microgel-based optical device for triglyceride sensing. *Chem. Commun.* 51, 9726–9728. doi:10.1039/c5cc02853a

Zhang, Q. M., Ahiabu, A., Gao, Y., and Serpe, M. J. (2015a). CO_2-switchable poly (N-isopropylacrylamide) microgel-based etalons. *J. Mater. Chem. C* 3, 495–498. doi:10.1039/c4tc02600d

Zhang, Q. M., Berg, D., Duan, J., Mugo, S. M., and Serpe, M. J. (2016). Optical devices constructed from ferrocene-modified microgels for H_2O_2 sensing. *ACS Appl. Mater. Inter.* 8, 27264–27269. doi:10.1021/acsami.6b11462

Zhang, Q. M., Wang, W., Su, Y.-Q., Hensen, E. J. M., and Serpe, M. J. (2015c). Biological imaging and sensing with multiresponsive microgels. *Chem. Mater.* 28, 259–265. doi:10.1021/acs.chemmater.5b04028

Zhang, Q. M., Xu, W., and Serpe, M. J. (2014b). Optical devices constructed from multiresponsive microgels. *Angew. Chem. Int. Ed.* 53, 4827–4831. doi:10.1002/anie.201402641

Zhang, R., Wang, Q., and Zheng, X. (2018). Flexible mechanochromic photonic crystals: routes to visual sensors and their mechanical properties. *J. Mater. Chem. C* 6, 3182–3199. doi:10.1039/c8tc00202a

Zhang, Y., Lan, M., Lü, J. P., Li, J. F., Zhang, K. Y., Zhi, H., et al. (2020). Antioxidant, anti-inflammatory and cytotoxic activities of polyphenols extracted from chroogomphus rutilus. *Chem. Biodivers.* 17, e1900479. doi:10.1002/cbdv.201900479

Zhao, S., Chen, C., Li, Z., Yuan, Z., and Lu, C. (2017). Hydroxyl radical induced chemiluminescence of hyperbranched polyethyleneimine protected silver nanoclusters and its application in tea polyphenols detection. *Anal. Methods* 9, 3114–3120. doi:10.1039/c7ay00903h

Zheng, Q., Li, W., Zhang, H., Gao, X., and Tan, S. (2020). Optimizing synchronous extraction and antioxidant activity evaluation of polyphenols and polysaccharides from Ya'an Tibetan tea (Camellia sinensis). *Food Sci. Nutr.* 8, 489–499. doi:10.1002/fsn3.1331

Conflict of Interest: The authors declare that the research was conducted in the absence of any commercial or financial relationships that could be construed as a potential conflict of interest.

Copyright © 2021 Wang, Zhang, Shi and Zhang. This is an open-access article distributed under the terms of the Creative Commons Attribution License (CC BY). The use, distribution or reproduction in other forums is permitted, provided the original author(s) and the copyright owner(s) are credited and that the original publication in this journal is cited, in accordance with accepted academic practice. No use, distribution or reproduction is permitted which does not comply with these terms.

frontiers in Chemistry

REVIEW
published: 11 March 2021
doi: 10.3389/fchem.2021.603639

Structural Proteomics Methods to Interrogate the Conformations and Dynamics of Intrinsically Disordered Proteins

Rebecca Beveridge[1]* *and Antonio N. Calabrese*[2]*

[1]Department of Pure and Applied Chemistry, University of Strathclyde, Glasgow, United Kingdom, [2]Astbury Centre for Structural Molecular Biology, School of Molecular and Cellular Biology, Faculty of Biological Sciences, University of Leeds, Leeds, United Kingdom

Intrinsically disordered proteins (IDPs) and regions of intrinsic disorder (IDRs) are abundant in proteomes and are essential for many biological processes. Thus, they are often implicated in disease mechanisms, including neurodegeneration and cancer. The flexible nature of IDPs and IDRs provides many advantages, including (but not limited to) overcoming steric restrictions in binding, facilitating posttranslational modifications, and achieving high binding specificity with low affinity. IDPs adopt a heterogeneous structural ensemble, in contrast to typical folded proteins, making it challenging to interrogate their structure using conventional tools. Structural mass spectrometry (MS) methods are playing an increasingly important role in characterizing the structure and function of IDPs and IDRs, enabled by advances in the design of instrumentation and the development of new workflows, including in native MS, ion mobility MS, top-down MS, hydrogen-deuterium exchange MS, crosslinking MS, and covalent labeling. Here, we describe the advantages of these methods that make them ideal to study IDPs and highlight recent applications where these tools have underpinned new insights into IDP structure and function that would be difficult to elucidate using other methods.

Keywords: mass spectrometry, ion mobility, intrinsically disordered protein, hydrogen-deuterium exchange, crosslinking mass spectrometry

OPEN ACCESS

Edited by:
Ping Yu,
Institute of Chemistry (CAS), China

Reviewed by:
Xia Guan,
Louisiana State University,
United States
Zhirong Liu,
Peking University, China

Correspondence:
Rebecca Beveridge
rebecca.beveridge@strath.ac.uk
Antonio N. Calabrese
A.Calabrese@leeds.ac.uk

Specialty section:
This article was submitted to Analytical Chemistry, a section of the journal Frontiers in Chemistry

Received: *07 September 2020*
Accepted: *19 January 2021*
Published: *11 March 2021*

Citation:
Beveridge R and Calabrese AN (2021) Structural Proteomics Methods to Interrogate the Conformations and Dynamics of Intrinsically Disordered Proteins. Front. Chem. 9:603639. doi: 10.3389/fchem.2021.603639

INTRODUCTION

Interrogating the structure–function relationship of proteins and protein complexes has long been a productive area of scientific research, contributing to our understanding of biological processes and disease mechanisms and hence to the development of therapies. It was previously accepted that each protein has a specific three-dimensional conformation, composed of an intricate arrangement of secondary structure elements such as α-helices and β-sheets that dictates its function. More recently, however, it has emerged that not all proteins have a single specific conformation in their native state, and instead, they interconvert between multiple transient conformations, ranging from compact to extended, unhindered by energetic constraints (Wright and Dyson 2015). Such proteins, termed intrinsically disordered proteins (IDPs), are highly prevalent in biology, with bioinformatics studies indicating that the eukaryotic proteome is ~20% disordered, with 36% of eukaryotic proteins containing >20% disorder and 12% carrying >50% disorder (Oldfield et al., 2005; Peng et al., 2015).

All proteins are dynamic to some extent, lying on a continuum between being mainly structured with minimum dynamics and mainly disordered with minimum structure. In proteins that are considered as "structured", minimal dynamic behavior is an important feature that facilitates functions such as catalysis and macromolecular associations (Boehr et al., 2009), while spatial flexibility between structured domains can be afforded by disordered regions, such as those found in antibodies (Thielges et al., 2008). Disordered regulatory domains make excellent switches as they can be readily altered by posttranslational modifications, such as phosphorylation, for example, during different stages of the cell cycle or upon cell stress (Suryadinata et al., 2010). IDPs or proteins that contain intrinsically disordered regions (IDRs) are also players in liquid-liquid phase separation mechanisms, scaffolding the formation of intracellular biomolecular condensates that play key roles in cellular homeostasis, stress, and disease (Banani et al., 2017). IDPs exhibit binding plasticity, which means that they are often involved in cell signaling networks as they can bind to many protein partners transiently, but with high specificity (Wright and Dyson 2015). There are several ways in which IDPs can interact with other proteins. They may fold upon binding to their structured partners, also known as a "disorder-to-order" transition (Wright and Dyson 2009) or form a so-called "fuzzy complex," in which the IDP samples various conformations on the surface of its binding partner (Sharma et al., 2015). A further advantage of disorder is that it economizes genome and protein resources, as the interface of an IDP in a protein–protein complex is similar to that formed between ordered proteins but consists of fewer residues from the disordered partner (Liu and Huang 2014). Overall, the flexible nature of IDPs and IDRs enables them to perform important functions in the cell that are complementary to the roles of ordered proteins.

IDPs often play an important role in signaling networks, thereby controlling cellular behavior, and their high propensity to aggregate means that they are often implicated in diseases such as cancer and neurodegenerative diseases (Uversky et al., 2008). For example, mutations in the protein p53, which binds other proteins mainly via disordered interactions, are found in many types of cancer including cancers of the colon, lung, breast, and brain (Hollstein et al., 1991), while mutations in the IDP breast cancer type 1 susceptibility protein (BRCA1) are, as the name suggests, often implicated in breast cancer (Semmler et al., 2019). Protein aggregation in the brain is often associated with neurodegenerative diseases, with α-synuclein (aSyn) aggregation being a pathogenic hallmark of Parkinson's disease (Baba et al., 1998), and amyloid-beta (Aβ) and tau playing a role in the development of Alzheimer's disease (Irvine et al., 2008).

Despite their biological and medical significance, a lack of suitable methods to interrogate IDPs means that they have remained underrepresented in the scientific literature. Resistance of IDPs and IDRs to crystallization renders them unsuitable for analysis by X-ray crystallography (XRC). Cryoelectron microscopy (cryo-EM) can effectively elucidate structures of mobile protein domains, although it remains challenging to elucidate copopulated states that differ with respect to the orientation of these domains, and IDRs are still missing from the structures (Murata and Wolf 2018). NMR is the most often used method to study IDPs as it can provide a signature for intrinsic disorder (low ^{1}H and ^{15}N amide chemical shift dispersion due to high solvent exposure) and provide information on transient secondary structure elements (usually alpha-helices) adopted in the overall conformational ensemble (Jensen et al., 2013). However, NMR cannot distinguish between multiple coexisting conformations, especially because rapid interconversions (on the NMR timescale) result in signal averaging. Other methods that are often used to study IDPs include small angle X-ray scattering (SAXS) (Kikhney and Svergun 2015), single molecule Förster resonance energy transfer (smFRET) (Kikhney and Svergun 2015), and computational methods such as Monte Carlo (MC) and molecular dynamics (MD) simulations (Baker and Best 2014; Mittal et al., 2014).

Structural mass spectrometry (MS) methods (**Figure 1**), also known as structural proteomics methods, are undergoing an explosion in their application to study proteins and protein complexes, in part due to their wide applicability to many different protein types including structured, disordered, monomeric, and multimeric proteins (Politis and Schmidt 2018). Structural MS methods are able to capture transient interactions, can be used to study proteins and complexes up to the megadalton range, and can discern interactions in complex mixtures such as whole cell lysates and even intact cells (Liu et al., 2017). A key advantage of using MS-based methods to study IDPs is that they do not have any preference for the folded form of a protein that is displayed by XRC and cryo-EM, and they overcome size limitations afforded by NMR. They are often used in conjunction with other methods, providing complementary data that can be combined in order to predict structural preferences of proteins and complexes (Rout and Sali 2019).

Each method will be described more fully in the relevant sections, but in brief, native MS (nMS) reports on the binding stoichiometry of protein–protein and protein–ligand complexes on the basis of their mass (Beveridge et al., 2016). A key advantage of nMS over other techniques is that multiple binding stoichiometries can be simultaneously detected in complex mixtures, including those that are populated to a low extent, allowing detection of transient interactions (Leney and Heck 2017; Beveridge et al., 2020). nMS also provides information on the position of the protein on the structure-disorder continuum as the number of charges carried by a protein upon ionization is related to its fold (Beveridge et al., 2014). The shape of the charge state distribution (CSD) for an IDP can also reveal more detailed conformational preferences (Natalello et al., 2017; Santambrogio et al., 2019). nMS is often combined with ion mobility (IMMS) measurements or fragmentation methods for "top-down" mass spectrometry measurements (Stuchfield and Barran 2018; Donnelly et al., 2019). IMMS allows the size distribution of a protein or protein complex to be measured, in terms of its rotationally averaged collision cross section (CCS) (Sharon and Robinson 2007; Jurneczko and Barran 2011; Eyers et al., 2018). In top-down experiments, nonergodic fragmentation methods such as electron capture dissociation

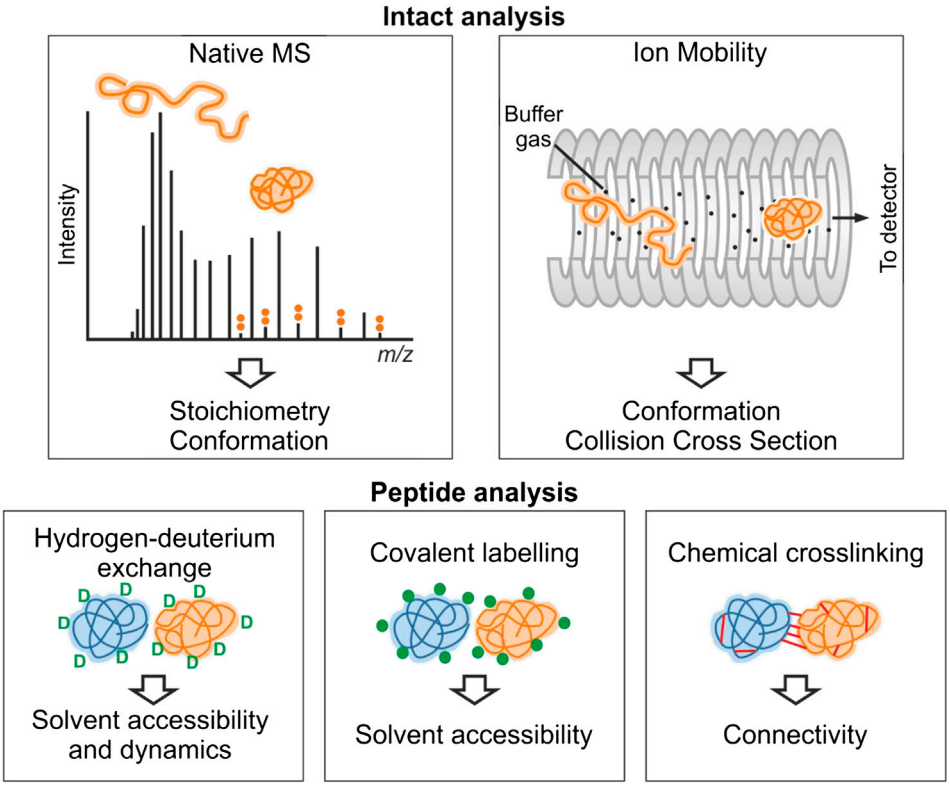

FIGURE 1 | Overview of structural mass spectrometry methods. The information obtained from each experimental method is shown. Native MS and ion mobility analyses require the protein to be analyzed by MS intact under gentle ionization conditions that preserve noncovalent interactions. For an IDP, the CSD observed by native MS typically is multimodal consistent with multiple conformational states. These conformations (e.g., collapsed and extended) can be further separated by ion mobility. In hydrogen-deuterium exchange experiments, backbone amide hydrogen atoms undergo exchange with deuterium. Covalent-labeling methods involve modification of solvent accessible side-chains with a suitable probe, and in chemical crosslinking experiments, residue pairs in close spatial proximity are joined covalently. For these three methods, the protein(s) involved are typically proteolysed, and the labels are detected by analysis of the resultant peptide fragments.

(ECD) or electron transfer dissociation (ETD) are implemented to break backbone peptide bonds, without disrupting any other structural elements. This can be used to locate binding sites of small molecules on proteins (Xie et al., 2006; Breuker and McLafferty 2008). With respect to IDPs, top-down MS has often been used to localize the binding of metal ions to a specific domain (Wongkongkathep et al., 2018). Conformational changes and binding events can also be localized using HDX-MS, which is a solution-phase technique that provides complementary information to nMS methods (Trabjerg et al., 2018). Differences in the uptake of deuterium are measured, which reflect changes in solvent accessibility of different regions of the protein upon ligand binding. Protein footprinting methods are additional solution phase approaches that label surface/solvent exposed residues to inform on protein structure and interactions. Crosslinking-MS (XL-MS) can be used to reveal sites of interactions, either within proteins or between proteins, informing on protein–protein interactions, and providing distance restraints to predict and validate protein models (Sinz et al., 2015; Leitner et al., 2016; Orbán-Németh et al., 2018).

As an update to the review published in 2013 (Beveridge et al., 2013), we will here provide an overview of the new advances in structural proteomics methods and their applications to the study of IDP behavior over the last 5 years.

NATIVE MASS SPECTROMETRY

nMS is a widely applicable technique that informs on the stoichiometry and structural preferences of proteins and protein complexes. Upon "soft" transfer from solution into the gas phase by nanoelectrospray ionization (nESI), proteins can retain aspects of their conformation inside the mass spectrometer and the mass to charge (m/z) ratio of protein ions can be measured. The "mass" informs on the stoichiometry of a protein complex, and the number of charges that it carries informs on its structural preferences (Santambrogio et al., 2019). Structured proteins typically carry a low number of charges per unit mass and present over a narrow range of charge states, as their compact nature means that there is low solvent accessible surface area (SASA) upon which protons can be accommodated. In contrast, proteins that are unfolded have a larger SASA and can hence carry a higher number of charges (Kaltashov and Mohimen 2005; Testa et al., 2011; Beveridge et al., 2014). A protein that is completely denatured will have a

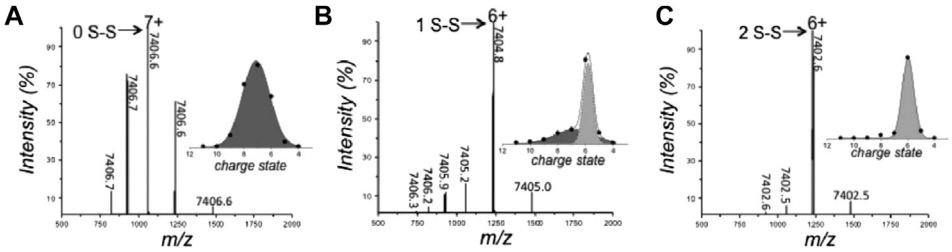

FIGURE 2 | Analysis of the conformation and oxidative state of hCox17 species by native MS. nMS spectra of the hCox17 (10 μM) refolding reaction at pH 6.7. hCox17 species are labeled according to their charge state and number of disulfide bridges. Insets show the Gaussian fits to the observed CSDs. **(A)** Fully reduced hCox17 in the presence of 50 mM DTT. **(B)** Partially oxidized hCox17, 8 h after the removal of DTT. **(C)** Completely oxidized hCox17, 17 h after the removal of DTT. Figure adapted from (Fraga et al., 2017).

Gaussian-like CSD with a high number of charges. IDPs, however, often exhibit residual structure which means that wide CSDs are typically observed, ranging from low to high charge states, which correspond to compact and extended conformations, respectively (**Figure 1**). Gaussian curves can be fitted to the deconvoluted CSDs of IDPs, which is postulated to inform on the number of conformational families adopted. In addition, the SASA can be estimated from the CSD of IDPs, which can be used as a constraint during modeling and IDP classification (Testa et al., 2011).

The rise in popularity of nMS is evidenced by the fact that it is now often used as part of a multimethod approach to study the biophysical characteristics of IDPs (Hagiwara et al., 2016; Fraga et al., 2017; Hamdi et al., 2017). Recently, Fraga et al. (2017) implemented nMS and other tools to interrogate the disorder-to-order transition of the human small copper chaperone, hCox17, that occurs upon the formation of disulfide bonds. Fully reduced hCox17 was desalted to remove DTT from the reaction mixture, and refolding was analyzed over a series of timepoints by combining information obtained from nMS with chromatography, fluorescence, circular dichroism (CD), Fourier transform infrared spectroscopy (FTIR), SAXS, and NMR. Of these methods, nMS affords the unique advantage of simultaneously determining the oxidation state of the protein and its conformational preferences. In its fully reduced form, hCox17 presents in a Gaussian-shaped CSD with charge states ranging from $[M+5H]^{5+}$ to $[M+9H]^{9+}$, with the highest intensity corresponding to $[M+7H]^{7+}$ (**Figure 2A**). After 8 h of refolding, the protein is a mixture of fully reduced protein and a species which contains one disulfide bond. Fitting Gaussian curves to this deconvoluted spectrum reveals a compact conformation with high intensity centered around $[M+6H]^{6+}$ (containing one disulfide bond) and an extended one at much lower intensity centered around $[M+7H]^{7+}$ (reduced) (**Figure 2B**). This change in CSD suggests that a significant compaction occurs upon formation of the first disulfide bond. After 17 h refolding, the native form, which contains two disulfide bonds, accumulates, but the main charge state remains at $[M+6H]^{6+}$ (**Figure 2C**), indicating that no significant further compaction occurs. In agreement with this assertion from nMS, SAXS experiments discerned that fully reduced Cox17 has a radius of gyration (R_g) of 24.2 ± 0.3 Å which compacts to 21 Å that is stable for the following 4 h. After 6 h, there is a small decrease of 1 Å. Differences in the refolding times are likely a result of differential solution conditions employed (i.e., pH was 8.4 and 6.7 for SAXS and nMS, respectively). This study demonstrates the suitability of studying preferred protein conformations with nMS, the agreement of nMS with solution phase SAXS measurements, and the complementarity of nMS with other methods such as NMR and CD, which reveal secondary structure elements. A similar study was undertaken by Snijder et al. (2015), in which nMS and IMMS was used to delineate the conformational preferences of different oxidation states of human alpha-defensin.

Structural properties of the flexible dimer formed between the intrinsically disordered N^{TAIL} domain and the phosphoprotein X domain (P^{XD}) from measles virus (MeV) were revealed by CSD analysis (D'Urzo et al., 2015). Each component was analyzed with nMS, which reported a wide CSD for each protein. Fitting of Gaussian curves to the deconvoluted spectra revealed a mixture of three conformational families for N^{TAIL} and two for P^{XD}. Upon mixing the two proteins at equimolar concentrations, the dominant peaks in the spectrum corresponded to the unbound proteins, with lower-intensity peaks corresponding to a 1:1 dimer, reflecting the transient nature of the interaction. Interestingly, the dimer also exhibits a wide CSD ranging from $[D+9H]^{9+}$ to $[D+21H]^{21+}$, indicating that the significant disorder is retained upon complex formation. The CSD corresponds to approximately two conformations, an open and a closed, with estimated SASA values of 16.1 nm^2 and 9.5 nm^2, respectively. These values, along with the CCSs measured by IMMS, were used as distance restraints in computational modeling, resulting in the first structural model of this fuzzy complex.

CSD analysis formed an important part of the study into the conformational preferences of the disordered C-terminal domain of p27 ($p27^C$) and two of its permutants (Beveridge et al., 2019a): one in which oppositely charged residues were more evenly spaced along the protein sequence ($p27^C$-κ14) and the other in which oppositely charged residues are linearly segregated ($p27^C$-κ56) (Das and Pappu 2013; Das et al., 2016). nMS provided a clearer distinction between the conformational preferences of the permutants than could be achieved with other biophysical techniques, revealing the more disordered nature of $p27^C$-κ14 with respect to the wildtype and the

compaction of p27^{C}-κ56. While these systems were further interrogated by IMMS (see below), the CSDs alone were sufficient to inform on the conformational preferences of these disordered proteins and their response to differential ionic strengths of the solutions from which they were ionized (lower ionic strength had a negligible effect on p27^{C}-κ14, promoted extended conformations of p27^{C}-WT and caused further compaction of p27^{C}-κ56).

CSD analysis also provided important information during the study of MAGE-A4 which is a key target for cancer therapy (Hagiwara et al., 2016). In this study, nMS was used alongside structure-based homology modeling, circular dichroism, and NMR to discern the conformational effects of nine mutations that have been implicated in cancer. nMS reported a reduction in charge state range of all mutants compared to the wildtype, centered around lower charge states, suggestive of a more compact form being dominant in solution. NMR analysis indicated that MAGE-A4 contains both structured and disordered regions and reported small alterations to its hydrophobic core in the mutants studied. As in the p27^{C} study described above, differences identified with nMS were more apparent than with any other methods. Understanding the behavior of MAGE-A4 at the molecular level is the first step required for its exploitation in translational research toward cancer therapies.

nMS is also useful in discerning the stoichiometry of protein complexes and can be particularly beneficial in the study of IDP-containing complexes, as their flexibility and transient binding nature often precludes analysis by alternative techniques. Recently, Stephani et al. (2020) used nMS to study the protein C53, which consists of two globular domains that are joined by a disordered linker region that contains ATG8 interacting motifs. The stoichiometry of the complex formed between ATG8 and C53 remained elusive, until nMS revealed that complexes comprising 1:1 and 1:2 ratios of C53 to ATG8 were both detected.

Ion Mobility Mass Spectrometry

nMS is frequently coupled with ion mobility spectrometry, which separates protein conformations according to their size. Three types of ion mobility will be described in this section: drift tube ion mobility-MS (^{DT}IMMS), traveling wave IMMS (TWIMMS), and trapped ion mobility mass spectrometry (TIMS).

Drift Tube Ion Mobility Mass Spectrometry

^{DT}IMMS requires the simplest instrumentation of all IMMS types. Protein ions are pulsed into a drift tube, across which is applied a weak electric field that pulls the ions through the cell (Gabelica and Marklund 2018). The ions are hindered by collisions with an inert buffer gas such as helium, and since larger ions experience a higher number of collisions, extended protein conformations are slowed down to a greater extent than compact conformations. The arrival time distribution (ATD) of the ions exiting the cell is recorded, and when combined with m/z measurement, their sizes can be directly converted to a rotationally averaged collision cross-section (CCS) that reveals low-resolution information on the conformational distribution of an IDP (Stuchfield and Barran 2018).

^{DT}IMMS was used to thoroughly interrogate the structural preferences of p27^{C}-WT and the permutants p27^{C}-κ14 and p27^{C}-κ56, described above (Beveridge et al., 2019a). Analysis of CCS distributions allowed quantitation of conformational alterations in the charge pattern variants and their response to salt concentrations (Beveridge et al., 2019a). p27^{C}-κ14 is highly dynamic when sprayed from a low salt solution (10 mM ammonium acetate), displaying a wide CCS distribution that has little preference for any particular shape (**Figure 3A**). Upon increased salt concentrations (100 mM and 200 mM ammonium acetate for middle and high salt concentration solutions, respectively), p27^{C}-κ14 is stabilized in extended conformations with CCSs centered around 2000 Å^2, with just a small proportion of molecules in compact conformations (750–1,500 Å^2) (**Figures 3B,C**). p27^{C}-WT is also highly dynamic when sprayed from the low salt solution (**Figure 3D**) and is stabilized in an extended conformation above 2000 Å^2 in the middle salt solution (**Figure 3E**), with the smaller conformations below 1,500 Å^2 representing a slightly higher relative abundance than for p27^{C}-κ14. When sprayed from a high salt solution, a compact conformation centered around 1,000 Å^2 becomes the most abundant for p27^{C}-WT, with extended conformations above 1,500 Å^2 in much lower signal intensity (**Figure 3F**). p27^{C}-κ56 adopts compact conformations (highest intensity around 1,000 Å^2) when sprayed from a low salt solution (**Figure 3G**). The middle salt solution causes an increase in size of the protein, with highest intensity increasing to 1600 Å^2 and both the minima and maxima of the CCS distribution increasing by 250 Å^2 (**Figure 3H**). The high salt concentration leads to even further expansion (**Figure 3I**). This work demonstrates the strength of ^{DT}IMMS in discerning the behavior of IDPs and their response to differential solution conditions from which they are sprayed. In an additional work on p27, the interaction mechanisms of p27 constructs with the cellular binding partner Cdk2/cyclin A were interrogated. It was found that the KID domain of p27 (p27^{KID}), which folds upon binding to Cdk2/cyclin A, causes the rigid dimer to become more dynamic. As expected, full-length p27 (p27^{FL}) is tamed upon binding, with the most extended conformations no longer being accessible upon complex formation (Beveridge et al., 2019b). In this work, the strength of IMMS is its ability to visualize both the bound and unbound form of an IDP, without the preference for the bound form that is displayed by many techniques.

Bowers and coworkers have developed ^{DT}IMMS methods to study the conformations and aggregation of Aβ, a protein fragment that is the main component of amyloid plaques found in Alzheimer's disease patients (Murphy and LeVine 2010). In 2011, the conversion of Aβ-derived peptides from disordered monomers to structured beta-sheet amyloid fibrils was traced (Bleiholder et al., 2011), revealing differential assembly pathways for the different peptides. In the last five years, ^{DT}IMMS has provided extensive characterization of Aβ including delineating mechanisms of aggregation inhibition (Zheng et al., 2016; Downey et al., 2019) and detecting prominent oligomers (Economou et al., 2016). Work by the same group provided the first experimental evidence of an interaction between two IDPs whose aggregation is associated with

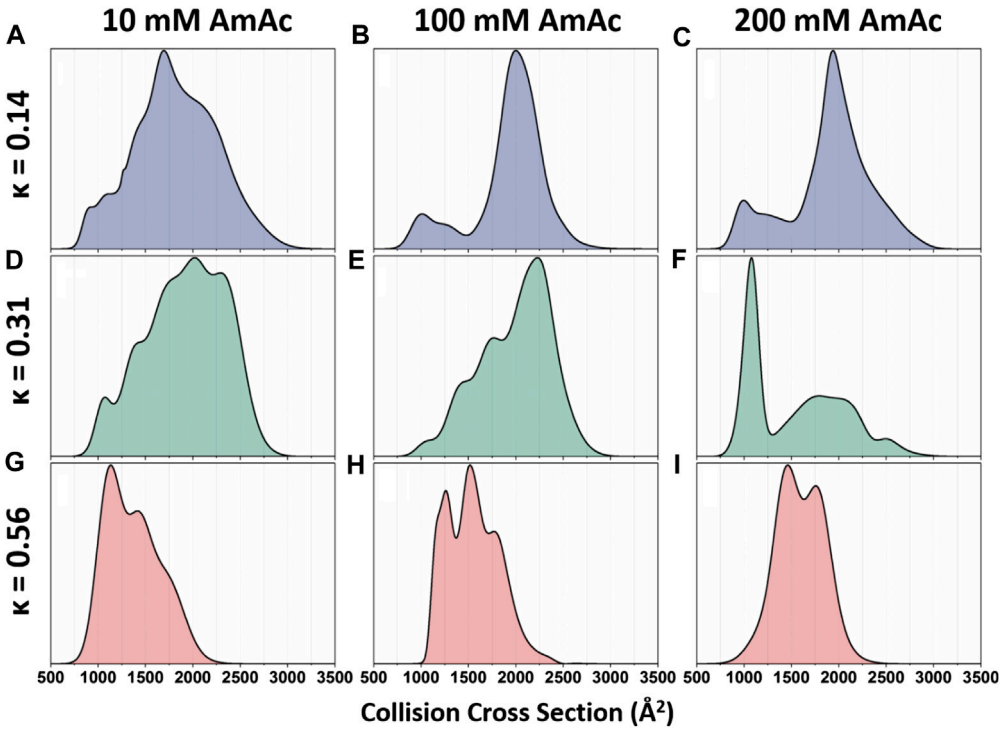

FIGURE 3 | Global collision cross-section distributions of all three p27 permutants sprayed from 10 mM, 100 mM, or 200 mM ammonium acetate. Global collision cross-section distributions are shown for the **(A–C)** $p27^{C}$-κ14 (blue), **(D–F)** $p27^{C}$-WT (green), and **(G–I)** $p27^{C}$-κ56 (red) permutants. Global CCSDs are obtained by combining CCSDs of individual charge states into single feature-rich distributions. Oppositely charged residues are well mixed in sequences with low κ values, whereas oppositely charged residues are segregated in sequences with high κ values (Das and Pappu 2013). Figure adapted from (Beveridge et al., 2019a).

diseases in different tissues, namely, islet amyloid polypeptide (IAPP), implicated in type 2 diabetes, and a fragment of tau, implicated in Alzheimer's (Arya et al., 2019). They also shed further light on the coaggregation of nonhomologous peptides derived from PrP and IAPP, determining that the PrP peptide promotes the transition of IAPP into its aggregation-prone β-hairpin conformation (Ilitchev et al., 2018).

Travelling Wave Ion Mobility Mass Spectrometry

Due to TWIMMS being implemented into the first commercially available integrated IMMS device (Synapt, Waters, United Kingdom), this has become the most widely used type of IMMS separation for protein structural studies (Illes-Toth et al., 2015; Konijnenberg et al., 2016; Van der Rest et al., 2017). The Synapt G1 was released in 2006, and more recent versions have provided users with enhanced resolution and sensitivity. During ion separation via TWIMMS, traveling waves propel ions through the ion mobility device at different speeds according to their charge and size (Lanucara et al., 2014). Unlike ^{DT}IMMS, the direct calculation of CCS from TWIMMS data is not possible, and CCSs can only be calculated by careful calibration with known standards (Ruotolo et al., 2008; Bush et al., 2012). TWIMMS has provided important insights into the metal-induced conformational changes of human metallothionein-2A (Chen et al., 2014; Dong et al., 2018) and into the conformational variability of the NAC complex which helped to describe its nature of substrate recognition during chaperone activity (Martin et al., 2018). Additionally, TWIMMS effectively demonstrated that the disordered tails of histone proteins play an important role in stabilizing the core regions of the functionally important histone dimers (Saikusa et al., 2015).

TWIMMS was recently used to discern how the small EDRK-rich factor 1 (SERF) protein increases the fibrillation rate of $A\beta_{1-40}$ and aSyn. SERF and its homologues have been shown to accelerate amyloid formation of many amyloidogenic proteins in vitro, but the mechanism behind this had remained elusive. SERF was analyzed alone and in complex with $A\beta_{1-40}$ or aSyn by IMMS to investigate protein–protein interactions that could affect the critical early steps of amyloid formation, leading to altered aggregation rates (Meinen et al., 2019). Monomeric SERF displays a wide CSD (charge states $[M+5H]^{5+}$ to $[M+15H]^{15+}$) and a wide CCS distribution (900–2,200 $Å^2$), reflective of its highly disordered nature. In a 1:1 mixture of SERF with $A\beta_{1-40}$, complexes were identified with 1:1, 1:2, and 2:1 stoichiometries, while in an equimolar mixture with aSyn, 1:1, 1:2, 2:1, and 2:2 complexes were detected. IMMS reported that all these complexes exhibit extreme heterogeneity, with much wider CCS distributions than expected from complexes of similar sizes. For example, the 2:2 SERF:aSyn complexes have conformations that are as large as antibodies (up to 7,000 $Å^2$), despite being approximately one-third of the mass. Overall, this IMMS data provided the first evidence that SERF forms dynamic complexes

with $A\beta_{1-40}$ and aSyn, in which the authors used to propose a model in which SERF provides a binding surface that increases the pool of conformations that these proteins can explore to accelerate primary nucleation. It has been tentatively postulated that accelerating amyloid formation with SERF may reduce the time that the proteins spend as neurotoxic intermediates.

An exciting recent development is the commercialization of cyclic IMMS instrumentation (Waters, United Kingdom), in which the ions are separated by passing them around a circular ion mobility cell. The number of passes around the cell can be controlled by the user to increase the effective distance over which the ions are separated, hence, increasing the resolution of the IM measurement, before the ions are ejected into the mass analyzer (Eldrid et al., 2019; Giles et al., 2019; Ujma et al., 2019). This was used by Thalassinos and coworkers (Eldrid et al., 2020) to compare the gas phase behavior of a structured protein (cytochrome c) and an IDP (human islet amyloid polypeptide hIAPP, also referred to as amylin), discovering differences in the gas-phase unfolding of the distinct protein types.

Trapped Ion Mobility Spectrometry

During TIMS separation, ions are propelled through the IMS cell with a gas flow and hindered by an electronic gradient in the opposite direction. This means that increased charge slows the ions down, and larger surface area speeds them up, in contrast to how separation is achieved in ^{DT}IMMS (Ridgeway et al., 2018). Garabedian et al. (2018) used TIMS to study the conformational preferences of the intrinsically disordered AT-HOOK peptide, which is the DNA binding region of the mammalian high mobility group protein (HMGA2). This disordered protein influences the remodeling of chromatin structure, thereby regulating the expression of certain genes, and is a target in several cancer therapies. The structural effects of seven separate point mutations and their influence on complex formation of the peptide with AT-rich regions of DNA hairpins were elucidated. Specifically, the RGRP core (residues 4–7) was found to be essential for stabilizing peptide-DNA interactions, with the weakest complex being formed with the R6A mutant, suggesting that this basic residue is important in binding DNA.

Ion Mobility Mass Spectrometry Studies of Tau

A protein that has come under particular scrutiny by IMMS in recent years is tau (Eschmann et al., 2015; Ganguly et al., 2015; Jebarupa et al., 2018; Ahmadi et al., 2019), a 441 residue protein comprising disordered N-terminal (~200 residues) and C-terminal (~80 residues) regions (Cleveland et al., 1977). The central region of the protein is thought to have residual structure and form the core of amyloid fibrils (Fitzpatrick et al., 2017). Deposition of tau aggregates in the neurons and glia of the brain is a hallmark of neurodegenerative disease (Ferrer et al., 2014). Eschmann et al. (2015) used ^{DT}IMMS in combination with transmission electron microscopy (TEM), thioflavin T (ThT) fluorescence, electron paramagnetic resonance (EPR), and Overhauser dynamic nuclear polarization (ODNP) to study a peptide fragment of tau called R2 (residues 273–284) that contains a nucleating six-residue segment and forms cross beta-sheet fibrils, similar to those found in pathological aggregation. They discovered differences in the relative abundances of monomer, dimer, and conformational populations that dictate the propensity for fibril formation. In a separate study, Ganguly et al. (2015) compared this same peptide with a second peptide that contains a similar nucleating six-residue segment (R3 306–317), as well as a mutant of the first peptide (R2 delta-K280) that is associated with a neurodegenerative tauopathy. IMMS determined that R3 homodimers are the most stable, followed by heterodimers containing R3, and the least stable dimers are homodimers of R2wt and R2-dK280. ThT assays showed that R3 has a higher propensity to aggregate than wtR2 or R2-dK280. R2-dK280 binds more strongly to R3 than R2wt does, suggesting a possible mechanism for the tauopathy. In a study by Jebarupa et al. (2018), the largest human tau isoform was analyzed with TWIMMS, which uncovered the extreme plasticity of the protein, with conformations ranging from compact to extended. Compact conformations were removed upon acidification of the starting solution, whereas alkaline pH caused compaction due to charge neutralization. Changes in structure at both high and low pH can be linked to the higher propensity to aggregate under both conditions. The interaction of tau with a molecular tweezer assembly modulator has been investigated by TWIMMS combined with top-down MS (Nshanian et al., 2019).

Native Top-Down Mass Spectrometry

As described above, protein–ligand interactions can be maintained in the gas phase upon careful ionization from their starting solution, allowing determination of binding stoichiometry. Moreover, during top-down experiments, electron capture dissociation (ECD) or electron transfer dissociation (ETD) is used to cleave covalent backbone bonds of proteins without disturbing noncovalent interactions, including those between protein and ligand. This has allowed site localization of ligand and metal binding to proteins (Xie et al., 2006). Early work investigating the potential of top-down MS to localize protein–ligand interactions focused on the complex formed between aSyn and spermine (Xie et al., 2006). Upon fragmentation of aSyn via ECD, product ions were identified that retained the bound spermine, allowing localization of the spermine binding site to residues 106–138, consistent with NMR studies. More recently, top-down MS was used to characterize cobalt and manganese binding to aSyn (Wongkongkathep et al., 2018), as these metals have been implicated in accelerated aSyn aggregation. nMS revealed that at a 1:5 protein to metal concentration, aSyn is present in the unbound form and with one or two bound metal ions, with the same binding patterns observed for both manganese and cobalt. Upon ECD fragmentation of the 1:1 aSyn-cobalt species, the majority of the C-terminal fragments have cobalt bound, while the majority of N-terminal fragments up to residue 118 do not, suggesting that the cobalt binding site is located in the C-terminal tail. The binding of manganese occurred via similar interactions. Interestingly, due to the binding of cobalt and manganese to aSyn being governed by electrostatic interactions, their complexes were

highly stable in the gas phase and even survived high energy dissociation via collisional activation dissociation (CAD). CAD revealed the same site localization as ECD, but differences in the fragmentation of the cobalt-aSyn complex with respect to the apo form suggested a structural rearrangement upon cobalt binding, a hypothesis that was confirmed with IMMS experiments. To test the assertions in site localization made by ECD analysis, three truncated aSyn variants (1–60, 61–140, and 96–140) were also characterized. As expected, cobalt and manganese bind to both the 61–140 and 96–140 fragments, but not to the N-terminal 1–60 fragments.

Top-down MS was also used to interrogate the binding of the "molecular tweezer" CLR01 to tau (Nshanian et al., 2019). CLR01 has been found to inhibit aggregation of amyloidogenic proteins without toxic side effects (Sinha et al., 2011; Acharya et al., 2014; Vöpel et al., 2017). It binds specifically to lysine residues in disordered proteins and remodels their assembly into nontoxic, nonamyloidogenic structures. nMS shows that CLR01 binds to tau in a 1:1 stoichiometry. A 4R-repeat domain fragment (residues 257–239, 11 kDa) also binds with 1:1 stoichiometry. Top-down ECD-MS of the 10+ charge state of the CLR01-bound 4R-fragment revealed c- and z-product ions that imply that the core of the tau fragment is the likely region of ligand binding, between K294 and K331, that includes lysine residues at positions 294, 298, 311, 317, 321, and 331. This corresponds to the microtubule-binding domain, which spans the two nucleating peptides, as described above, which are essential for seeding. Sequence coverage drops from 61% to 46% for the 4R-repeat domain fragment, suggesting compaction of the protein, which is consistent with IMMS data showing compaction of the 9+, 8+, and 7+ charge states. Interestingly, IMMS studies also indicate that CLR01 causes compaction of Aβ-dimers and tetramers (Zheng et al., 2015).

HYDROGEN-DEUTERIUM EXCHANGE-MASS SPECTROMETRY

HDX-MS is a sensitive and versatile method that locates changes in solvent accessibility of proteins and protein complexes, thereby reporting on structural differences and alterations in flexibility (Trabjerg et al., 2018). In an HDX-MS experiment, the protein of interest is diluted into a deuterated buffer, and the deuterium from the solvent is allowed to exchange with the backbone amide hydrogens for a given amount of time. The reaction is quenched by the addition of a low-pH buffer, and the protein is then digested with an acid-stable protease (usually pepsin). Finally, the deuterium uptake of each peptide is measured via liquid chromatography- (LC-) MS. This allows identification of regions of protein sequence that are more or less exposed upon structural perturbation, for example, upon ligand/cofactor binding (Beveridge et al., 2016). Given that the analysis is performed on the digested peptides, there are no limitations on the maximum size of the system that can be studied, and HDX-MS can be applied to study IDRs and IDPs.

In recent years, huge improvements have been made to HDX methodologies that have increased its applicability to study residual structure in IDPs. Efforts toward this have included reducing the temperature and pH of the experiments to slow exchange (Goswami et al., 2013) and specialist apparatus to allow fast mixing on the msec timescale. Fast mixing apparatus includes microfluidic chip-based technologies (Liuni et al., 2010; Yamamoto et al., 2011; Rob et al., 2012; Svejdal et al., 2019) and quench-flow systems (Rist et al., 2005; Keppel et al., 2011; Keppel and Weis 2013; Walters et al., 2013). One such quench-flow apparatus was designed and constructed by Keppel and Weis using solely off-the-shelf components and allows HDX measurements on the 50–5000 msec timescale (Keppel and Weis 2013). Briefly, three syringes are used to deliver the sample (in H_2O buffer, syringe 1), label (D_2O buffer, syringe 2), and quench (syringe 3). Deuteration is initiated in the first mixing "T" where the sample in H_2O buffer is combined with D_2O buffer. The two flows are mixed at an angle of 180° and the resulting reaction mixture exits the tee through a short delay line before it is combined with quench at the second "T" mixer. A key advantage of this approach is that the exchange time can be simply adjusted by altering the flow rate. The quenched sample can be immediately frozen in liquid nitrogen or the system can be connected directly to an LC, ESI-MS, or a pepsin column for online sample labeling and analysis. The authors tested this msec HDX setup by comparing the deuterium uptakes of the CREB binding protein $CBP^{2059-2117}$ alone and in complex with the activator of retinoid and thyroid receptor, $ACTR^{1018-1088}$. Unbound CBP is known to be a molten globule that populates two folded states, but in a previous work using a conventional HDX approach, unstructured regions of CBP could not be distinguished from the structured core since exchange was almost complete along the full length of the protein within 10 s (Keppel et al., 2011). Shifting to an msec exchange timescale provided a distinction between the N- and C-terminal domains, where the exchange is at the near-intrinsic rate, and the helical core of the protein, where the exchange is significantly slower. Upon binding ACTR, HDX of many peptides in the core region of CBP became too slow for detection in the 3500 ms time course. The C- and N-terminal domains also incurred increased protection, suggesting that the fraying ends of helices one and three were stabilized upon binding of ACTR. Such details could not be uncovered with conventional HDX; hence, shifting the experiment to an msec timescale is highly advantageous in the analysis of IDPs. In subsequent research, Keppel and Weis used the quench-flow apparatus to study a similar construct of ACTR (residues 1,023–1,093) to probe its residual helicity (Keppel and Weis 2015). They quantified the rate of HDX in terms of midpoint values for each peptide, which represent the time required to reach 50% deuteration, relative to a fully deuterated control ($t_{50\%}$) (Al-Naqshabandi and Weis 2017). The fastest exchanging peptide is from the N-terminus of the protein, which is 50% deuterated at 0.2 s and is almost fully exchanged by 3.5 s. In contrast, a peptide corresponding to a portion of the protein that has been shown to form a residual helix by NMR takes 1.6 s to reach 50% and is only 65% deuterated after 3.5 s. After residue-averaging the data from overlapping peptides, there is a good correlation between residues with $t_{50\%}$ values greater than 0.5 s and the regions of ACTR that

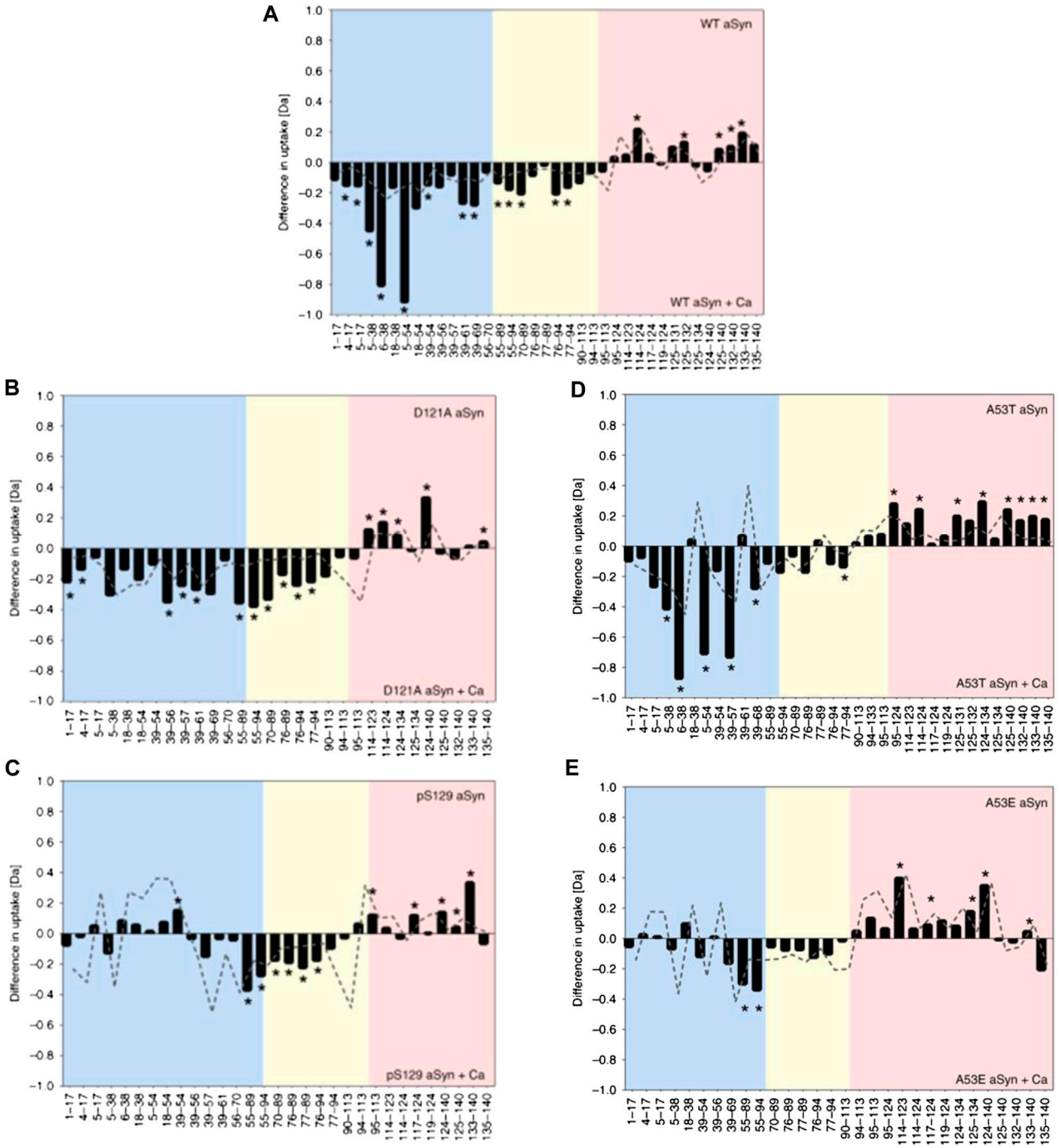

FIGURE 4 | HDX-MS reveals differential responses of aSyn variants to calcium binding. Differential deuterium uptake between aSyn in the absence and presence of added calcium for WT aSyn **(A)**, variants D121A **(B)**, and pS129 **(C)** and familial mutations A53T **(D)** and A53E **(E)**. The N-terminus is colored blue, the NAC yellow, and C-terminus red. Negative values represent increased deuterium uptake in the calcium-bound state, correlating to increased solvent exposure and lower hydrogen bonding. Positive values represent decreased deuterium uptake in the presence of calcium. The start and end of each peptide is marked on the *x*-axis. Figure adapted from (Stephens et al., 2020).

become helical in complex with CBP (Demarest et al., 2002). There is also a good agreement between the regions that display protection in HDX and the regions of transient helices that have been measured by NMR of the protein in isolation (Kjaergaard et al., 2011), but with lower spatial resolution. Nevertheless, HDX has the advantage of being applicable to nonisotopically labeled protein and to much larger proteins than NMR. Additional applications of HDX by the Weis group include investigating

the influence of crowding on the structure of IDPs (Rusinga and Weis 2017a; Rusinga and Weis 2017b), which requires extensive clean-up of the protein to remove artificial crowders prior to MS.

Kish et al. developed a fully automated online flow mixing and quenching system, allowing reproducible HDX measurements between 50 ms and 5 min, with a 1 ms timescale resolution and temperature control (0–25°C) (Kish et al., 2019). The authors used the setup to uncover novel mechanistic details regarding the structural dynamics involved in the allosteric regulation of GlyP. They correlated structural changes in the activated (pSer14) and inhibited (glucose-6-phosphate bound) forms of the enzyme to functional regulation, determining that the 250s' loop transitions from a disordered state to a more ordered conformation upon activation of the enzyme. A change in stability of the 280 s loop was also identified that provided the first direct evidence of allosteric regulation of substrate access to the active site.

Whilst proving to be highly beneficial, specialized msec fast HDX setups are not always required for analysis of IDPs. Stephens et al. (2020) used a commercially available HDX manager (Waters, USA) equipped with a sample handling robot (LEAP technologies, USA) to delineate how changes in the structural preferences of monomeric aSyn correlate with its propensity to aggregate. Solvent exposure of WT aSyn was compared with a phosphorylated version at residue S129 (pS129) and a mutant version (D121A). pS129 has an increased C-terminus negative charge and is commonly found in Lewy bodies but rarely in its soluble state, indicating increased aggregation propensity. D121A has a reduced C-terminal negative charge and a reduced aggregation propensity compared to the wildtype. The response of the constructs to calcium binding was compared, as calcium binds at the C-terminus, neutralizes negative charges, skews conformational preferences, and enhances the rate of aggregation. Upon calcium binding by WT aSyn, the rate of HDX becomes lower in the C-terminus (residues 95–140) and higher in the NAC (residues 61–95) and N-terminus (residue 1–61), indicating more compact and extended orientations, respectively (**Figure 4A**). The mutant D121A undergoes a similar change (**Figure 4B**), but for pS129 (**Figure 4C**), the N-terminus is much less solvent exposed, indicating a correlation between the solvent exposure of the N-terminal region with reduced aggregation propensity in the calcium-bound state. To further investigate the correlation between monomeric structure and aggregation propensity, the aggregation rates of familial aSyn mutants A30P, E46K, H50Q, G51D, A53T, and A53E were studied with ThT-based kinetic assays. It was determined that A53T, E46K, and H50Q aggregate faster than the WT protein, and the aggregation rate can be further enhanced by the addition of calcium. A30P, A53E, and G51D aggregate slower than WT aSyn and are insensitive to calcium or aggregate slower in its presence. A53T and A53E conformations were therefore probed via HDX, as the T and E mutations at position 53 have opposite effects on aggregation rates (increased rate and decreased rate, respectively). In the absence of calcium, no conformational differences could be identified between the mutants or between mutant and WT. In the presence of calcium, protection is observed at the C-terminus (as is identified with all other variants). A53T, like WT, has significant deprotection of N-terminus upon calcium binding (**Figure 4D**), indicating a localized unfolding event; whereas for A53E, there are very few significant differences at the NAC or N-terminus (**Figure 4E**). Therefore, perturbation in the N-terminal region upon calcium binding correlates with higher aggregation propensity. Despite much research into the aggregation behavior of aSyn, this method represents an important development in the ability to correlate IDP conformation with aggregation propensity.

CHEMICAL CROSSLINKING MASS SPECTROMETRY

Chemical crosslinking mass spectrometry (XL-MS) informs on the structure of proteins and protein complexes, by identifying residue pairs that are within close spatial proximity (Calabrese and Radford 2018; Schneider et al., 2018; Chavez and Bruce 2019; Iacobucci et al., 2020). These residue-level distance restraints are particularly useful in integrative structural studies, wherein information from a range of techniques is utilized to make structural predictions (Calabrese and Pukala 2013; Kahraman et al., 2013; Schmidt et al., 2013; Schmidt and Robinson 2014; Sinz 2014; Faini et al., 2016; Joseph et al., 2017). A typical XL-MS workflow involves incubation of the protein assembly of interest with a suitable crosslinking reagent that covalently links proximal residues targeted by the reactive groups of the crosslinker. The most common commercially available crosslinkers comprise two N-hydroxysuccinimide- (NHS-) ester functional groups, connected by a spacer arm, that primarily react with Lys side-chains and to a lesser extent of those of Ser, Thr, and Tyr (Kalkhof and Sinz 2008; Madler et al., 2009). Recent developments to increase the applicability of XL-MS to proteins with more diverse primary structures include crosslinking reagents that target carboxylic acids (hydrazides) (Leitner et al., 2014) and radical based methods (e.g., photoreactive diazirine and benzophenone) (Preston et al., 2014; Horne et al., 2018) that react nonspecifically with any sidechain. The spacer arm can also be decorated with functionalities to assist in identification of crosslinked peptides by semiautomated spectral assignment methods (by incorporating MS-cleavable groups) or facilitate enrichment (e.g., biotin, alkyne, or phosphonic acid) (Leitner et al., 2012; Gotze et al., 2015; Schmidt and Sinz 2017; Iacobucci et al., 2018; Yu and Huang 2018; Steigenberger et al., 2019). Enrichment is the key to XL-MS workflows when studying large, complex systems due to the inherent low abundance of XL peptides.

One of the challenges when using XL-MS reagents to study dynamic proteins/assemblies with multiple copopulated states is that the experimentally derived distance restraints constitute a snapshot of interresidue distances spanning the ensemble (Rappsilber 2011; Bonomi et al., 2017; Filella-Merce et al., 2020). In such cases, computational methods can be used to derive structural ensembles consistent with the data (Ding et al., 2017; Webb et al., 2018; Calabrese et al., 2020). Alternatively, the distance restraints from XL-MS can be mapped onto previously determined ensembles (Degiacomi et al., 2017; Bullock et al., 2018; Calabrese et al., 2020). For IDPs, untangling and modeling

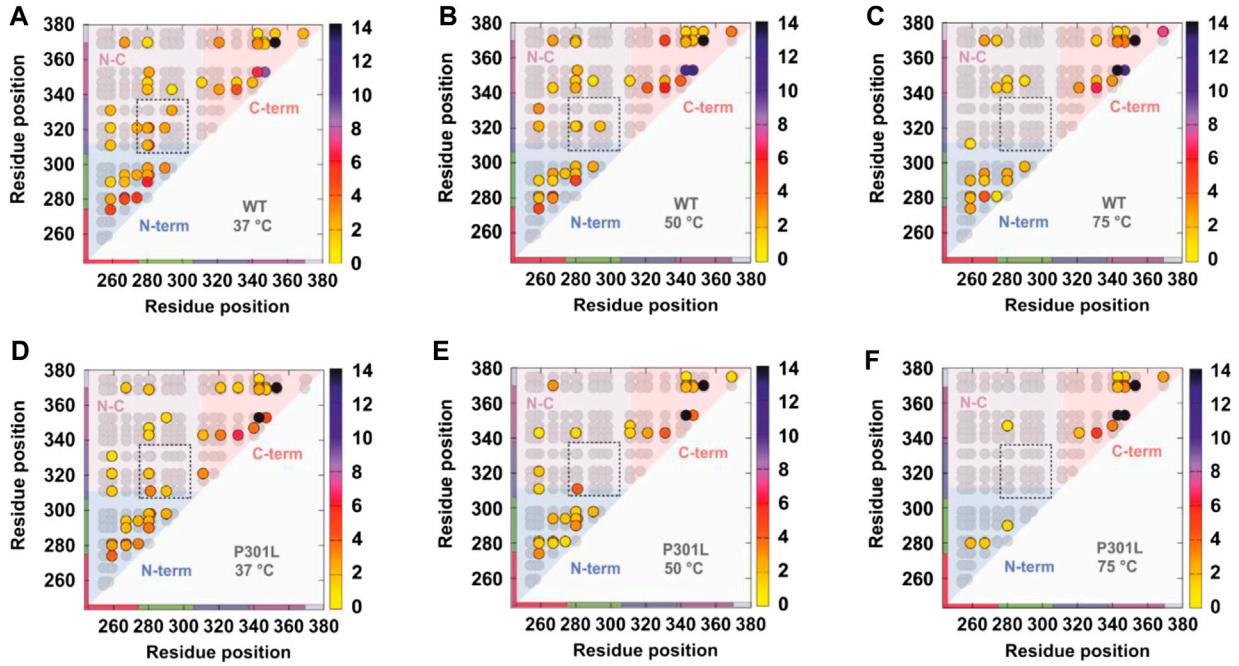

FIGURE 5 | Comparative crosslinking of the tau repeat domain. Contact maps showing all theoretical crosslinks (Lys-Lys pairs) in the tau repeat domain (gray circles) and the detected crosslinks (colored circles). **(A–C)** Detected crosslinks in the wild type tau repeat domain at **(A)** 37°C, **(B)** 50°C, and **(C)** 75°C. **(D–F)** Detected crosslinks in the P301L tau repeat domain at **(A)** 37°C, **(B)** 50°C, and **(C)** 75°C. The detected crosslinks are colored according to the frequency by which they were observed—the scale is shown on the right hand side of each panel. The contact maps are shaded to denote crosslinks within the N-terminus (blue), C-terminus (red), and between the N- and C-termini (pink). Note that fewer long range contacts are observed with increasing temperature and that the P301L mutation promotes extended states (fewer long range crosslinks). Figure reproduced from (Chen et al., 2019).

these conformational families using restraints from XL-MS, and indeed using data from any technique, remains challenging.

Several studies have used XL-MS as a tool to interrogate the architectures of IDPs that undergo pathogenic self-assembly in order to elucidate the structural/molecular determinants of amyloid formation. In one recent study, restraints derived from XL experiments were used in molecular dynamics simulations to derive model structures of monomeric tau (Popov et al., 2019). The models derived were globular in nature, whereas other evidence suggests that tau populates an ensemble of structures, including more elongated states (Mylonas et al., 2008; Narayanan et al., 2010; Elbaum-Garfinkle and Rhoades 2012; Mirbaha et al., 2018). This suggests that XL-MS may be overrepresenting the abundance of globular states in solution as has been observed for other flexible systems (Calabrese et al., 2020). A similar approach has also been used to derive a conformational ensemble for the protein aSyn. Again, compact conformations were visualized (Brodie et al., 2016; Brodie et al., 2019), which does not capture the breadth of the conformational ensemble, as demonstrated using other techniques (Nath et al., 2012; Schwalbe et al., 2014). These studies show that challenges remain in using XL-MS restraints to derive structural models that represent the overall ensembles of IDPs, especially in capturing the more elongated states adopted. Nevertheless, the study of these monomeric aggregation-prone proteins can be used as a starting point to understand their assembly mechanism and associated conformational conversions in more detail.

Comparative XL has also been used to decode interregion contacts in tau and elucidate how mutations that are associated with enhanced aggregation kinetics alter the structure of the monomer (Chen et al., 2019). Disease-associated mutations known to influence tau aggregation have been shown to occur near the amyloid motif that drives self-assembly and is involved in key contacts in patient-derived tau amyloid fibrils (Chen et al., 2019). The authors studied the effect of the mutation P301L, a known familial mutation that is associated with increased neurodegeneration in model systems (Rizzu et al., 1999; Ramsden et al., 2005). Crosslinking experiments were performed using the tau repeat domain at three temperatures (37°, 50°, and 75°) to probe the relative thermostabilities of the wild type and P301L variant (**Figure 5**) (Chen et al., 2019). Contacts within the C-terminal and N-terminal domains were detected, as were crosslinks between the N and C termini (**Figure 5**) (Chen et al., 2019). Notably, P301L increased the susceptibility of tau to heat denaturation, as measured by fewer short and long-range XLs (**Figure 5**), suggesting that the mutation modulates the propensity of tau to adopt aggregation prone conformations that expose the key amyloid forming motif (Chen et al., 2019). These data combined with structural modeling and biophysical experiments suggested that P301L promotes the formation of extended tau conformations and

implies that flanking regions surrounding key amyloid-forming motifs are keys to regulating tau aggregation propensity.

A similar comparative approach has been used to elucidate interresidue contacts between the N and C terminal domains of the cellular isoform of the prion protein (PrP^C) (McDonald et al., 2019). When PrP^C undergoes conformational conversion to an infectious isoform (PrP^{Sc}), it undergoes aggregation leading to toxic deposits associated with prion diseases (Ambadi Thody et al., 2018). PrP^C comprises a disordered N-terminal domain and a folded C-terminal domain whose structure has been solved (Riek et al., 1996; Zahn et al., 2000), but the determinants of the interaction between the two domains remained unknown (Spevacek et al., 2013; Evans et al., 2016; Wu et al., 2017). The function of PrP^C in healthy individuals also remains mysterious; however, it is known to bind divalent metal ions (Spevacek et al., 2013; Evans et al., 2016; Wu et al., 2017). XL-MS was used to elucidate interdomain contacts in murine PrP^C, as well as two variants, one in which the central region of the protein was deleted (known to result in a neonatal lethal phenotype in mice (Li et al., 2007)) and the other which contained a single point mutation in the C-terminal domain (E199K) (the homologous murine mutation of the E200K mutation associated with familial Creutzfeldt–Jakob disease in humans) (Mead 2006). Crosslinks between the N- and C-terminal domains were detected in the wild type protein, and using quantitative methods, it was shown that Cu^{2+} binding triggers a conformational change in the protein, as the abundance of some crosslinked peptides pairs varied in the presence of Cu^{2+} (McDonald et al., 2019). Similarly, structural changes were detected between the wild type and two variants. These data were corroborated with those from paramagnetic relaxation enhancement (PRE) NMR experiments (Karamanos et al., 2015), and the combined data were used in MD simulations to generate models of PrP^C.

Whilst XL-MS can provide residue level distance restraints, native MS can inform on the global properties of a protein/assembly without ensemble averaging. Thus, combining these two methods is becoming increasingly a commonplace for structural studies (Sinz et al., 2015). Such an approach was used to study the architecture of the p53 monomer and tetramer (Arlt et al., 2017). p53 is ca. 40% intrinsically disordered DNA binding protein that functions as a transcription factor (Laptenko et al., 2016), playing a crucial role in cancer prevention as a tumor suppressor (Hafner et al., 2019). Native MS using a mixture of heavy and light p53 suggested that the tetramer assembles as a dimer of dimers. Inter and intramolecular crosslinks in p53 were detected (Arlt et al., 2017) and compared with a model of p53 from a previous integrative study (Tidow et al., 2007). Many detected crosslinks were inconsistent with this structure, which led to the authors proposing that a structural reassignment of the assembly was necessary (Arlt et al., 2017). Native MS and XL-MS has also been used to study oligomerization of synaptobrevin-2 (Wittig et al., 2019), a membrane protein that is a constituent of the SNARE complex, which is involved in signal transmission in neurons (Takamori et al., 2006). The authors showed using crosslinking that in proteoliposomes, full-length synaptobrevin-2 was monomeric, while in detergent, low abundance oligomers could be captured by crosslinking (Wittig et al., 2019). A truncated version of synaptobrevin-2 had a higher oligomerization propensity than the wild type protein, but similar interaction interfaces were detected to the full length protein by XL-MS (Wittig et al., 2019). Native ion mobility-MS showed that the synaptobrevin-2 oligomers grew isotropically, consistent with them remaining dynamically disordered (Bleiholder et al., 2011).

FOOTPRINTING MASS SPECTROMETRY

Chemical footprinting methods rely on treating a protein assembly with a chemical probe. The mass addition from the probe can be detected and quantified by MS to inform on the solvent accessibility of residues and how this changes with time or upon a binding event that is thought to perturb the structure (Wang and Chance 2017; Liu et al., 2020). Such methods have shown great promise to inform on the architecture of proteins and their assemblies and are now emerging as powerful tools to interrogate IDP structure, assembly, and interactions.

Hydroxyl radicals have been extensively used to study IDP structure. A number of methods have been developed to produce hydroxyl radicals ($\dot{O}H$) to label surface-exposed residues, including using fast photochemical oxidation of proteins (FPOP) (Hambly and Gross 2005), synchrotron radiolysis of water (Wang and Chance 2011; Wang and Chance 2017), and atmospheric plasma jets (De Backer et al., 2018). The reactivity of residue sidechains toward hydroxyl radicals is a function of both its solvent accessibility (Huang et al., 2015), local environment (Cornwell et al., 2018), and intrinsic reactivity (Takamoto and Chance 2006; Xu and Chance 2007). The intrinsic reaction rates of different amino acids have been measured and span four orders of magnitude, with sulfur-containing (Cys and Met) and aromatic (Trp, Tyr, Phe, and His) residues being the most reactive (Takamoto and Chance 2006; Xu and Chance 2007). In such experiments, mass additions of 16 Da (addition of OH) are typically detected, but other modifications can also occur (Xu and Chance 2007) such as +14 Da modifications as a result of aldehyde/ketone formation. Quantification of the abundance of these modifications at either the peptide or residue level is typically achieved using LC-MS and bottom up proteomics methods.

In one recent example, Gross and coworkers used FPOP to pulse-label $A\beta_{1-42}$ throughout its aggregation cycle (Li et al., 2016). During an FPOP experiment, low concentrations of H_2O_2 are added to a protein solution immediately prior to its irradiation at 248 nm with a pulsed laser (Hambly and Gross 2005). This generates $\dot{O}H$ that can react with solvent accessible sidechains (Hambly and Gross 2005). Scavengers (glutamine or histidine) are also added to the solution at concentrations that limit the lifetime of $\dot{O}H$ to less than ~1 μs (i.e., the labeling pulse is faster than protein folding/unfolding) (Hambly and Gross 2005; Gau et al., 2013; Yan et al., 2014), although recent evidence

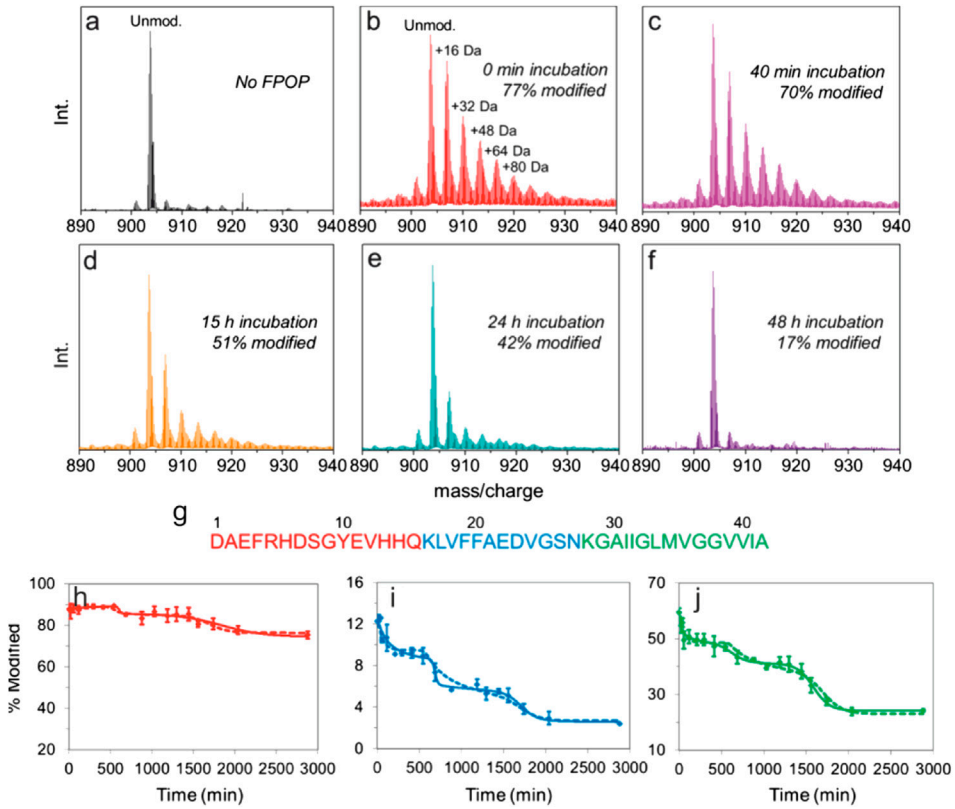

FIGURE 6 | FPOP analysis to probe amyloid-β (1–42) amyloid assembly. **(A–F)** Intact mass spectra of amyloid-β (1–42) (5+ charge state) **(A)** not subjected to FPOP and after FPOP labeling at **(B)** 0 min, **(C)** 40 min, **(D)** 15 h, **(E)** 24 h, and **(F)** 48 h aggregation timepoints. **(G)** Sequence of amyloid-β (1–42) colored according to the three peptides produced after Lys-N digestion. **(H–J)** Extent of modification of the three Lys-N peptides of amyloid-β (1–42) as a function of aggregation time for the **(H)** N-terminal peptides, **(I)** central peptide, and **(J)** C-terminal peptide. The solid and dashed lines are simulated data derived using a simple kinetic model as outlined in (Li et al., 2016). Figure adapted with permission from (Li et al., 2016). Copyright: 2016 American Chemical Society.

suggests that radicals may be longer-lived (Vahidi and Konermann 2016). Dose-response experiments can also be performed by increasing/decreasing the scavenger concentration to alter the length of the labeling pulse (Niu et al., 2017). In this example, samples were taken at periodic intervals over a 48 h time course of $A\beta_{1-42}$ aggregation. Analysis at the intact level revealed that, as expected, the extent of FPOP modifications decreased over time, as the protein formed higher order species (**Figure 6**). Remarkably, the data revealed several stepwise transitions in the extent of FPOP modification over time, consistent with a simplified kinetic model; wherein, monomeric species initially predominate that progressively oligomerize. Critical thresholds are reached throughout the aggregation time course that favor the formation of progressively larger oligomers, aggregates/protofibrils, and mature fibrils (**Figure 6**) (Li et al., 2016). The oxidative modifications on $A\beta_{1-42}$ could be localized to the peptide and amino acid level to reveal key regions that are involved in structural transitions associated with aggregation (**Figure 6**). Pulsed HDX-MS has also been used to study $A\beta_{1-42}$ aggregation under similar conditions, but this FPOP data revealed an additional conformational transition in the aggregation process that was not detected by HDX-MS (Zhang et al., 2013). Combined, this study demonstrates the power of FPOP to interrogate multistep self-assembly processes of IDPs, which will undoubtedly be a key tool going forward to temporally characterize, in residue-level detail, other assembly/aggregation mechanisms.

Data from oxidative footprinting by synchrotron radiolysis of water have also been used in integrative studies, combined with SAXS data to generate model IDP structures. To oxidatively label proteins by synchrotron radiolysis, a high energy synchrotron X-ray beam is used to generate $^{\cdot}OH$ by water photolysis (Takamoto and Chance 2006). This method has the advantage of being able to perform dose-response experiments by measuring the extent of oxidation as a function of X-ray exposure time (Takamoto and Chance 2006). From such data, a rate of footprinting can be measured on a per residue basis for comparison with the known intrinsic reactivity to derive a protection factor (Huang et al., 2015). There is a good correlation between protection factors derived from these experiments and the solvent accessibility of the residues in the protein structure (Huang et al., 2015). Specialized software called iSPOT (Huang et al., 2016) has been specifically developed to integrate SAXS and footprinting data in one modeling pipeline.

This strategy was validated using protein assemblies with known structures (Popov et al., 2019), and has been recently used to study the intrinsically disordered N-terminal transactivation domain (NTD) of estrogen receptor-alpha (Peng et al., 2019). The iSPOT-derived structural models from SAXS and footprinting data revealed metastable long-range contacts in the IDP that may be essential for receptor function (Peng et al., 2019).

Ligand-directed footprinting strategies have also been developed to study the interactions of intrinsically disordered or unfolded proteins with folded protein counterparts. These protocols, described as ligand-footprint MS (LiF-MS) (Parker et al., 2019) and tag-transfer XL-MS (Horne et al., 2018), rely on installing a reactive diazirine moiety on the disordered/unfolded binding partner. After assembling the protein complex, UV irradiation produces a carbene that rapidly inserts into any nearby covalent bond (including with solvent), forming a crosslink at the interaction interface (Horne et al., 2018; Parker et al., 2019). Following cleavage of the crosslinker, a mass tag or fingerprint is left at the interaction site which can be identified by MS. The LiF-MS method has been validated by studying the interaction between SLiMs (short linear motifs) and mitogen-activated protein kinase (MAPK) (Parker et al., 2019). SLiMs are present in disordered regions of proteins that are involved in interactions with folded protein domains (Davey et al., 2015). Upon binding, the SLiM remains dynamically disordered, making structural characterization of these assemblies by crystallography challenging. The LiF-MS approach was validated using assemblies with available crystal structures and then applied to complexes with no high-resolution structures. Use of the data in computational docking revealed that the binding mode differs between MAPKs and that the complexes are malleable (Parker et al., 2019). A similar tag-transfer XL approach to study the interaction of dynamic proteins with folded proteins has also been developed. This method also exploits diazirine chemistry and uses MS to detect a mass tag left on the partner protein at the interaction site (Horne et al., 2018; Calabrese et al., 2020). This approach was validated using a high-affinity regulatory peptide-protein complex MCL1 with BID, with the detected crosslinks mapping to the binding cleft of MCL1 (Horne et al., 2018). This approach has been used to map interaction interfaces of unfolded outer membrane proteins with periplasmic chaperones Skp and SurA, revealing the primary sites on these chaperones which contact the unfolded clients (Horne et al., 2018; Calabrese et al., 2020).

One of the main challenges in using footprinting approaches to inform on protein structure is translating the detected chemical labeling intensity to a structural model (Schmidt et al., 2017; Aprahamian et al., 2018; Aprahamian and Lindert 2019), with recent evidence suggesting that rather than "solvent accessibility," such experiments may report on a more nuanced parameter termed "chemical accessibility" (Ziemianowicz et al., 2020). Moreover, such methods also inherently report a snapshot of the conformational ensemble, which presents a significant methodological challenge for data interpretation that is exacerbated for IDPs which populate broad conformational landscapes.

CONCLUSIONS AND OUTLOOK

Our understanding of the role of intrinsic disorder in biological mechanisms has dramatically expanded in recent years. Such advances could only be progressed by new approaches to interrogate protein structure and function, including developments in experimental methodologies, integrative methods, and computer simulations. Mass spectrometry, too, has seen a vast array of new tools developed that are specifically tailored, or ideally suited, to study IDPs. The power of subsecond HDX experiments is only now being realized (Rist et al., 2005; Liuni et al., 2010; Keppel et al., 2011; Yamamoto et al., 2011; Rob et al., 2012; Keppel and Weis 2013; Walters et al., 2013; Svejdal et al., 2019), and future developments in this area are essential to characterize IDP dynamics as they undergo motions on shorter timescales than folded proteins, for which experiments were first designed to interrogate. Similarly, rapid XL and covalent labeling chemistries are key to capturing structural information about dynamic ensembles over short timescales. Diazirines may be able to fulfill this role, as they react within nanoseconds (Admasu et al., 1998), but irradiation times of seconds to hours are still used (Horne et al., 2018).

It is now emerging that it is possible to generate drug-like small molecules that can target IDPs and/or their interactions with binding partners (Vassilev et al., 2004; Hammoudeh et al., 2009; Iconaru et al., 2015). In many cases, these small molecules do not function by high affinity binding, but rather by transient interactions that modulate the conformation ensemble. However, detecting structural perturbations by small molecules, and how this influences IDP/IDR function, remains challenging. In many cases, an integrative approach must be taken, which presents an ideal opportunity to apply MS techniques.

One exciting, growing area of MS capability lies in the ability to deduce structural information pertaining to proteins and their assemblies in situ, including in lysates, live cells, tissues, and organisms. The suite of structural MS methods spanning native MS, limited proteolysis, XL-MS, FPOP, and other covalent labeling techniques are all well suited to inform on IDP structure and assembly in situ. FPOP labeling can be performed in cell or in *C. elegans* (Espino et al., 2015; Espino and Jones 2019), and XL-MS pipelines have been developed to probe the architecture of protein assemblies directly in cells and tissues (Chavez et al., 2018; Götze et al., 2019; Mendes et al., 2019; O'Reilly et al., 2020). Rapid advances in experimental workflows and MS instrumentation have facilitated the use of structural MS to tackle this increased sample complexity.

Intriguingly, it has been shown using experiments to probe the thermal stability of proteins by limited proteolysis on a proteome-wide scale that only half of proteins had unfolding profiles consistent with them being intrinsically disordered (Leuenberger et al., 2017). This suggests that many predicted IDPs may be more rigid in situ, possibly as a result of ligand binding. Such an observation demonstrates the urgent unmet need for new tools to study IDP structure in-cell, with MS poized to play a leading role in this endeavor. Exciting opportunities include biotin labeling and biotin proximity tagging experiments that have been shown to selectively label IDPs/IDRs (Minde et al.,

2020). One could envisage applications for such methods to probe disorder both in and out of cells, thereby validating assertions made about IDPs in situ. In addition, it is possible to generate native mass spectra of complexes directly from lysates, where proteins have been overexpressed (Vimer et al., 2020) or are present at endogenous levels (Skinner et al., 2017). New instrumentation and so-called native Omics workflows (Gault et al., 2020) have also been developed to facilitate multistage tandem mass spectrometry to enable ligand identification. One could envisage a role for these methods, in combination with top-down sequencing, to identify otherwise unknown modulators of IDP structure/function.

In recent years, developments in structural MS methods have been instrumental in advancing our understanding of protein behavior, shedding light on protein conformations and interactions. Now that the importance of IDPs in health and disease is becoming increasingly apparent and MS based methods tailored to study IDPs are being realized, structural MS is set to remain integral in the quest to decipher IDP structure and function, both *in vitro* and in cell, uncovering new insights into the role of IDPs in biological mechanisms.

AUTHOR CONTRIBUTIONS

Both authors contributed equally to this manuscript.

FUNDING

RB acknowledges support of a UKRI Future Leaders Fellowship (Grant Reference MR/T020970/1) and a Chancellor's Fellowship from the University of Strathclyde. ANC acknowledges support of a Sir Henry Dale Fellowship jointly funded by the Wellcome Trust and the Royal Society (Grant Number 220628/Z/20/Z) and a University Academic Fellowship from the University of Leeds.

REFERENCES

Acharya, S., Safaie, B. M., Wongkongkathep, P., Ivanova, M. I., Attar, A., Klärner, F. G., et al. (2014). Molecular basis for preventing α-synuclein aggregation by a molecular tweezer. *J. Biol. Chem.* 289 (15), 10727–10737. doi:10.1074/jbc.M113.524520

Admasu, A., Gudmundsdóttir, A. D., Platz, M. S., Watt, D. S., Kwiatkowski, S., and Crocker, P. J. (1998). A laser flash photolysis study of p-tolyl(trifluoromethyl) carbene. *J. Chem. Soc. Perkin Trans.* 2 (5), 1093–1100. doi:10.1039/a707586c

Ahmadi, S., Zhu, S., Sharma, R., Wilson, D. J., and Kraatz, H. B. (2019). Interaction of metal ions with tau protein. The case for a metal-mediated tau aggregation. *J. Inorg. Biochem.* 194, 44–51. doi:10.1016/j.jinorgbio.2019.02.007

Al-Naqshabandi, M. A., and Weis, D. D. (2017). Quantifying protection in disordered proteins using millisecond hydrogen exchange-mass spectrometry and peptic reference peptides. *Biochemistry* 56 (31), 4064–4072. doi:10.1021/acs.biochem.6b01312

Ambadi Thody, S., Mathew, M. K., and Udgaonkar, J. B. (2018). Mechanism of aggregation and membrane interactions of mammalian prion protein. *Biochim. Biophys. Acta - Biomembranes* 1860 (9), 1927–1935. doi:10.1016/j.bbamem.2018.02.031

Aprahamian, M. L., Chea, E. E., Jones, L. M., and Lindert, S. (2018). Rosetta protein structure prediction from hydroxyl radical protein footprinting mass spectrometry data. *Anal. Chem.* 90 (12), 7721–7729. doi:10.1021/acs.analchem.8b01624

Aprahamian, M. L., and Lindert, S. (2019). Utility of covalent labeling mass spectrometry data in protein structure prediction with rosetta. *J. Chem. Theor. Comput* 15 (5), 3410–3424. doi:10.1021/acs.jctc.9b00101

Arlt, C., Flegler, V., Ihling, C. H., Schäfer, M., Thondorf, I., and Sinz, A. (2017). An integrated mass spectrometry based approach to probe the structure of the full-length wild-type tetrameric p53 tumor suppressor. *Angew. Chem. Int. Ed. Engl.* 56 (1), 275–279. doi:10.1002/anie.201609826

Arya, S., Claud, S. L., Cantrell, K. L., and Bowers, M. T. (2019). Catalytic prion-like cross-talk between a key alzheimer's disease tau-fragment R3 and the type 2 diabetes peptide IAPP. *ACS Chem. Neurosci.* 10 (11), 4757–4765. doi:10.1021/acschemneuro.9b00516

Baba, M., Nakajo, S., Tu, P. H., Tomita, T., Nakaya, K., Lee, V. M., et al. (1998). Aggregation of alpha-synuclein in Lewy bodies of sporadic Parkinson's disease and dementia with Lewy bodies. *Am. J. Pathol.* 152 (4), 879–884.

Baker, C. M., and Best, R. B. (2014). Insights into the binding of intrinsically disordered proteins from molecular dynamics simulation. *Wires Comput. Mol. Sci.* 4 (3), 182–198. doi:10.1002/wcms.1167

Banani, S. F., Lee, H. O., Hyman, A. A., and Rosen, M. K. (2017). Biomolecular condensates: organizers of cellular biochemistry. *Nat. Rev. Mol. Cell Biol* 18 (5), 285–298. doi:10.1038/nrm.2017.7

Beveridge, R., Chappuis, Q., Macphee, C., and Barran, P. (2013). Mass spectrometry methods for intrinsically disordered proteins. *Analyst* 138 (1), 32–42. doi:10.1039/c2an35665a

Beveridge, R., Covill, S., Pacholarz, K. J., Kalapothakis, J. M., MacPhee, C. E., and Barran, P. E. (2014). A mass-spectrometry-based framework to define the extent of disorder in proteins. *Anal. Chem.* 86 (22), 10979–10991. doi:10.1021/ac5027435

Beveridge, R., Kessler, D., Rumpel, K., Ettmayer, P., Meinhart, A., and Clausen, T. (2020). Native mass spectrometry can effectively predict PROTAC efficacy. *ACS Cent. Sci.* 6 (7), 1223–1230. doi:10.1021/acscentsci.0c00049

Beveridge, R., Migas, L. G., Das, R. K., Pappu, R. V., Kriwacki, R. W., and Barran, P. E. (2019a). Ion mobility mass spectrometry uncovers the impact of the patterning of oppositely charged residues on the conformational distributions of intrinsically disordered proteins. *J. Am. Chem. Soc.* 141 (12), 4908–4918. doi:10.1021/jacs.8b13483

Beveridge, R., Migas, L. G., Kriwacki, R. W., and Barran, P. E. (2019b). Ion mobility mass spectrometry measures the conformational landscape of p27 and its domains and how this is modulated upon interaction with Cdk2/cyclin A. *Angew. Chem. Int. Ed. Engl.* 58 (10), 3114–3118. doi:10.1002/anie.201812697

Beveridge, R., Migas, L. G., Payne, K. A., Scrutton, N. S., Leys, D., and Barran, P. E. (2016). Mass spectrometry locates local and allosteric conformational changes that occur on cofactor binding. *Nat. Commun.* 7, 12163. doi:10.1038/ncomms12163

Bleiholder, C., Dupuis, N. F., Wyttenbach, T., and Bowers, M. T. (2011). Ion mobility-mass spectrometry reveals a conformational conversion from random assembly to β-sheet in amyloid fibril formation. *Nat. Chem.* 3 (2), 172–177. doi:10.1038/nchem.945

Boehr, D. D., Nussinov, R., and Wright, P. E. (2009). The role of dynamic conformational ensembles in biomolecular recognition. *Nat. Chem. Biol.* 5 (11), 789–796. doi:10.1038/nchembio.232

Bonomi, M., Heller, G. T., Camilloni, C., and Vendruscolo, M. (2017). Principles of protein structural ensemble determination. *Curr. Opin. Struct. Biol.* 42, 106–116. doi:10.1016/j.sbi.2016.12.004

Breuker, K., and McLafferty, F. W. (2008). Stepwise evolution of protein native structure with electrospray into the gas phase, 10^{-12} to 10^{2} s. *Proc. Natl. Acad. Sci. USA* 105 (47), 18145–18152. doi:10.1073/pnas.0807005105

Brodie, N. I., Petrotchenko, E. V., and Borchers, C. H. (2016). The novel isotopically coded short-range photo-reactive crosslinker 2,4,6-triazido-1,3,5-triazine (TATA) for studying protein structures. *J. Proteomics* 149, 69–76. doi:10.1016/j.jprot.2016.02.024

Brodie, N. I., Popov, K. I., Petrotchenko, E. V., Dokholyan, N. V., and Borchers, C. H. (2019). Conformational ensemble of native α-synuclein in solution as determined by short-distance crosslinking constraint-guided discrete molecular dynamics simulations. *PLoS Comput. Biol.* 15 (3), e1006859. doi:10.1371/journal.pcbi.1006859

Bullock, J. M. A., Thalassinos, K., and Topf, M. (2018). Jwalk and MNXL web server: model validation using restraints from crosslinking mass spectrometry. *Bioinformatics* 34 (20), 3584–3585. doi:10.1093/bioinformatics/bty366

Bush, M. F., Campuzano, I. D., and Robinson, C. V. (2012). Ion mobility mass spectrometry of peptide ions: effects of drift gas and calibration strategies. *Anal. Chem.* 84 (16), 7124–7130. doi:10.1021/ac3014498

Calabrese, A. N., and Radford, S. E. (2018). Mass spectrometry-enabled structural biology of membrane proteins. *Methods* 147, 187–205. doi:10.1016/j.ymeth.2018.02.020

Calabrese, A. N., and Pukala, T. L. (2013). Chemical cross-linking and mass spectrometry for the structural analysis of protein assemblies. *Aust. J. Chem.* 66 (7), 749–759. doi:10.1071/ch13164

Calabrese, A. N., Schiffrin, B., Watson, M., Karamanos, T. K., Walko, M., Humes, J. R., et al. (2020). Inter-domain dynamics in the chaperone SurA and multi-site binding to its unfolded outer membrane protein clients. *Nat. Comm.* 11, 2155. doi:10.1038/s41467-020-15702-1

Chavez, J. D., and Bruce, J. E. (2019). Chemical cross-linking with mass spectrometry: a tool for systems structural biology. *Curr. Opin. Chem. Biol.* 48, 8–18. doi:10.1016/j.cbpa.2018.08.006

Chavez, J. D., Lee, C. F., Caudal, A., Keller, A., Tian, R., and Bruce, J. E. (2018). Chemical crosslinking mass spectrometry analysis of protein conformations and supercomplexes in heart tissue. *Cell Syst* 6 (1), 136–141. doi:10.1016/j.cels.2017.10.017

Chen, D., Drombosky, K. W., Hou, Z., Sari, L., Kashmer, O. M., Ryder, B. D., et al. (2019). Tau local structure shields an amyloid-forming motif and controls aggregation propensity. *Nat. Commun.* 10 (1), 2493. doi:10.1038/s41467-019-10355-1

Chen, S. H., Chen, L., and Russell, D. H. (2014). Metal-induced conformational changes of human metallothionein-2A: a combined theoretical and experimental study of metal-free and partially metalated intermediates. *J. Am. Chem. Soc.* 136 (26), 9499–9508. doi:10.1021/ja5047878

Cleveland, D. W., Hwo, S. Y., and Kirschner, M. W. (1977). Physical and chemical properties of purified tau factor and the role of tau in microtubule assembly. *J. Mol. Biol.* 116 (2), 227–247. doi:10.1016/0022-2836(77)90214-5

Cornwell, O., Radford, S. E., Ashcroft, A. E., and Ault, J. R. (2018). Comparing hydrogen deuterium exchange and fast photochemical oxidation of proteins: a structural characterisation of wild-type and dn6 β2-microglobulin. *J. Am. Soc. Mass Spectrom.* 29 (12), 2413–2426. doi:10.1007/s13361-018-2067-y

D'Urzo, A., Konijnenberg, A., Rossetti, G., Habchi, J., Li, J., Carloni, P., et al. (2015). Molecular basis for structural heterogeneity of an intrinsically disordered protein bound to a partner by combined ESI-IM-MS and modeling. *J. Am. Soc. Mass Spectrom.* 26 (3), 472–481. doi:10.1007/s13361-014-1048-z

Das, R. K., Huang, Y., Phillips, A. H., Kriwacki, R. W., and Pappu, R. V. (2016). Cryptic sequence features within the disordered protein $p27^{Kip1}$ regulate cell cycle signaling. *Proc. Natl. Acad. Sci. USA* 113 (20), 5616–5621. doi:10.1073/pnas.1516277113

Das, R. K., and Pappu, R. V. (2013). Conformations of intrinsically disordered proteins are influenced by linear sequence distributions of oppositely charged residues. *Proc. Natl. Acad. Sci. USA* 110 (33), 13392–13397. doi:10.1073/pnas.1304749110

Davey, N. E., Cyert, M. S., and Moses, A. M. (2015). Short linear motifs - ex nihilo evolution of protein regulation. *Cell Commun Signal* 13 (1), 43. doi:10.1186/s12964-015-0120-z

De Backer, J., Razzokov, J., Hammerschmid, D., Mensch, C., Hafideddine, Z., Kumar, N., et al. (2018). The effect of reactive oxygen and nitrogen species on the structure of cytoglobin: a potential tumor suppressor. *Redox Biol.* 19, 1–10. doi:10.1016/j.redox.2018.07.019

Degiacomi, M. T., Schmidt, C., Baldwin, A. J., and Benesch, J. L. P. (2017). Accommodating protein dynamics in the modeling of chemical crosslinks. *Structure* 25 (11), 1751–e5. doi:10.1016/j.str.2017.08.015

Demarest, S. J., Martinez-Yamout, M., Chung, J., Chen, H., Xu, W., Dyson, H. J., et al. (2002). Mutual synergistic folding in recruitment of CBP/p300 by p160 nuclear receptor coactivators. *Nature* 415 (6871), 549–553. doi:10.1038/415549a

Ding, Y. H., Gong, Z., Dong, X., Liu, K., Liu, Z., Liu, C., et al. (2017). Modeling protein excited-state structures from "Over-length" chemical cross-links. *J. Biol. Chem.* 292 (4), 1187–1196. doi:10.1074/jbc.M116.761841

Dong, S., Wagner, N. D., and Russell, D. H. (2018). Collision-induced unfolding of partially metalated metallothionein-2A: tracking unfolding reactions of gas-phase ions. *Anal. Chem.* 90 (20), 11856–11862. doi:10.1021/acs.analchem.8b01622

Donnelly, D. P., Rawlins, C. M., DeHart, C. J., Fornelli, L., Schachner, L. F., Lin, Z., et al. (2019). Best practices and benchmarks for intact protein analysis for top-down mass spectrometry. *Nat. Methods* 16 (7), 587–594. doi:10.1038/s41592-019-0457-0

Downey, M. A., Giammona, M. J., Lang, C. A., Buratto, S. K., Singh, A., and Bowers, M. T. (2019). Inhibiting and remodeling toxic amyloid-beta oligomer formation using a computationally designed drug molecule that targets alzheimer's disease. *J. Am. Soc. Mass Spectrom.* 30 (1), 85–93. doi:10.1007/s13361-018-1975-1

Economou, N. J., Giammona, M. J., Do, T. D., Zheng, X., Teplow, D. B., Buratto, S. K., et al. (2016). Amyloid β-protein assembly and alzheimer's disease: dodecamers of Aβ42, but not of Aβ40, seed fibril formation. *J. Am. Chem. Soc.* 138 (6), 1772–1775. doi:10.1021/jacs.5b11913

Elbaum-Garfinkle, S., and Rhoades, E. (2012). Identification of an aggregation-prone structure of tau. *J. Am. Chem. Soc.* 134 (40), 16607–16613. doi:10.1021/ja305206m

Eldrid, C., Ujma, J., Kalfas, S., Tomczyk, N., Giles, K., Morris, M., et al. (2019). Gas phase stability of protein ions in a cyclic ion mobility spectrometry traveling wave device. *Anal. Chem.* 91 (12), 7554–7561. doi:10.1021/acs.analchem.8b05641

Eldrid, C., Ujma, J., Britt, H., Cragnolini, T., Kalfas, S., Cooper-Shepherd, D., et al. (2020). Cyclic ion mobility – collision activation experiments elucidate protein behaviour in the gas-phase. doi:10.26434/chemrxiv.11687100

Eschmann, N. A., Do, T. D., LaPointe, N. E., Shea, J. E., Feinstein, S. C., Bowers, M. T., et al. (2015). Tau aggregation propensity engrained in its solution state. *J. Phys. Chem. B* 119 (45), 14421–14432. doi:10.1021/acs.jpcb.5b08092

Espino, J. A., and Jones, L. M. (2019). Illuminating biological interactions with *in Vivo* protein footprinting. *Anal. Chem.* 91 (10), 6577–6584. doi:10.1021/acs.analchem.9b00244

Espino, J. A., Mali, V. S., and Jones, L. M. (2015). In cell footprinting coupled with mass spectrometry for the structural analysis of proteins in live cells. *Anal. Chem.* 87 (15), 7971–7978. doi:10.1021/acs.analchem.5b01888

Evans, E. G., Pushie, M. J., Markham, K. A., Lee, H. W., and Millhauser, G. L. (2016). Interaction between prion protein's copper-bound octarepeat domain and a charged C-terminal pocket suggests a mechanism for N-terminal regulation. *Structure* 24 (7), 1057–1067. doi:10.1016/j.str.2016.04.017

Eyers, C. E., Vonderach, M., Ferries, S., Jeacock, K., and Eyers, P. A. (2018). Understanding protein-drug interactions using ion mobility-mass spectrometry. *Curr. Opin. Chem. Biol.* 42, 167–176. doi:10.1016/j.cbpa.2017.12.013

Faini, M., Stengel, F., and Aebersold, R. (2016). The evolving contribution of mass spectrometry to integrative structural biology. *J. Am. Soc. Mass Spectrom.* 27 (6), 966–974. doi:10.1007/s13361-016-1382-4

Ferrer, I., López-González, I., Carmona, M., Arregui, L., Dalfó, E., Torrejón-Escribano, B., et al. (2014). Glial and neuronal tau pathology in tauopathies: characterization of disease-specific phenotypes and tau pathology progression. *J. Neuropathol. Exp. Neurol.* 73 (1), 81–97. doi:10.1097/NEN.0000000000000030

Filella-Merce, I., Bardiaux, B., Nilges, M., and Bouvier, G. (2020). Quantitative structural interpretation of protein crosslinks. *Structure* 28 (1), 75–e4. doi:10.1016/j.str.2019.10.018

Fitzpatrick, A. W. P., Falcon, B., He, S., Murzin, A. G., Murshudov, G., Garringer, H. J., et al. (2017). Cryo-EM structures of tau filaments from Alzheimer's disease. *Nature* 547 (7662), 185–190. doi:10.1038/nature23002

Fraga, H., Pujols, J., Gil-Garcia, M., Roque, A., Bernardo-Seisdedos, G., Santambrogio, C., et al. (2017). Disulfide driven folding for a conditionally disordered protein. *Sci. Rep.* 7 (1), 16994. doi:10.1038/s41598-017-17259-4

Gabelica, V., and Marklund, E. (2018). Fundamentals of ion mobility spectrometry. *Curr. Opin. Chem. Biol.* 42, 51–59. doi:10.1016/j.cbpa.2017.10.022

Ganguly, P., Do, T. D., Larini, L., LaPointe, N. E., Sercel, A. J., Shade, M. F., et al. (2015). Tau assembly: the dominant role of PHF6 (VQIVYK) in microtubule binding region repeat R3. *J. Phys. Chem. B* 119 (13), 4582–4593. doi:10.1021/acs.jpcb.5b00175

Garabedian, A., Bolufer, A., Leng, F., and Fernandez-Lima, F. (2018). Peptide sequence influence on the conformational dynamics and DNA binding of the intrinsically disordered AT-hook 3 peptide. *Sci. Rep.* 8 (1), 10783. doi:10.1038/s41598-018-28956-z

Gau, B. C., Chen, J., and Gross, M. L. (2013). Fast photochemical oxidation of proteins for comparing solvent-accessibility changes accompanying protein folding: data processing and application to barstar. *Biochim. Biophys. Acta* 1834, 1230–1238. doi:10.1016/j.bbapap.2013.02.023

Gault, J., Liko, I., Landreh, M., Shutin, D., Bolla, J. R., Jefferies, D., et al. (2020). Combining native and 'omics' mass spectrometry to identify endogenous ligands bound to membrane proteins. *Nat. Methods* 17 (5), 505–508. doi:10.1038/s41592-020-0821-0

Giles, K., Ujma, J., Wildgoose, J., Pringle, S., Richardson, K., Langridge, D., et al. (2019). A cyclic ion mobility-mass spectrometry system. *Anal. Chem.* 91 (13), 8564–8573. doi:10.1021/acs.analchem.9b01838

Goswami, D., Devarakonda, S., Chalmers, M. J., Pascal, B. D., Spiegelman, B. M., and Griffin, P. R. (2013). Time window expansion for HDX analysis of an intrinsically disordered protein. *J. Am. Soc. Mass Spectrom.* 24 (10), 1584–1592. doi:10.1007/s13361-013-0669-y

Götze, M., Pettelkau, J., Fritzsche, R., Ihling, C. H., Schäfer, M. A., and Sinz, A. (2015). Automated assignment of MS/MS cleavable cross-links in protein 3D-structure analysis. *J. Am. Soc. Mass Spectrom.* 26 (1), 83–97. doi:10.1007/s13361-014-1001-1

Götze, M., Iacobucci, C., Ihling, C. H., and Sinz, A. (2019). A simple cross-linking/mass spectrometry workflow for studying system-wide protein interactions. *Anal. Chem.* 91 (15), 10236–10244. doi:10.1021/acs.analchem.9b02372

Hafner, A., Bulyk, M. L., Jambhekar, A., and Lahav, G. (2019). The multiple mechanisms that regulate p53 activity and cell fate. *Nat. Rev. Mol. Cell Biol* 20 (4), 199–210. doi:10.1038/s41580-019-0110-x

Hagiwara, Y., Sieverling, L., Hanif, F., Anton, J., Dickinson, E. R., Bui, T. T., et al. (2016). Consequences of point mutations in melanoma-associated antigen 4 (MAGE-A4) protein: insights from structural and biophysical studies. *Sci. Rep.* 6 (1), 25182. doi:10.1038/srep25182

Hambly, D. M., and Gross, M. L. (2005). Laser flash photolysis of hydrogen peroxide to oxidize protein solvent-accessible residues on the microsecond timescale. *J. Am. Soc. Mass Spectrom.* 16 (12), 2057–2063. doi:10.1016/j.jasms.2005.09.008

Hamdi, K., Salladini, E., O'Brien, D. P., Brier, S., Chenal, A., Yacoubi, I., et al. (2017). Structural disorder and induced folding within two cereal, ABA stress and ripening (ASR) proteins. *Sci. Rep.* 7 (1), 15544. doi:10.1038/s41598-017-15299-4

Hammoudeh, D. I., Follis, A. V., Prochownik, E. V., and Metallo, S. J. (2009). Multiple independent binding sites for small-molecule inhibitors on the oncoprotein c-myc. *J. Am. Chem. Soc.* 131 (21), 7390–7401. doi:10.1021/ja900616b

Hollstein, M., Sidransky, D., Vogelstein, B., and Harris, C. (1991). p53 mutations in human cancers. *Science* 253 (5015), 49–53. doi:10.1126/science.1905840

Horne, J. E., Walko, M., Calabrese, A. N., Levenstein, M. A., Brockwell, D. J., Kapur, N., et al. (2018). Rapid mapping of protein interactions using tag-transfer photocrosslinkers. *Angew. Chem. Int. Ed. Engl.* 57 (51), 16688–16692. doi:10.1002/anie.201809149

Huang, W., Ravikumar, K. M., Chance, M. R., and Yang, M. R. S. (2015). Quantitative mapping of protein structure by hydroxyl radical footprinting-mediated structural mass spectrometry: a protection factor Analysis. *Biophys. J.* 108 (1), 107–115. doi:10.1016/j.bpj.2014.11.013

Huang, W., Ravikumar, K. M., Parisien, M., and Yang, S. (2016). Theoretical modeling of multiprotein complexes by iSPOT: integration of small-angle X-ray scattering, hydroxyl radical footprinting, and computational docking. *J. Struct. Biol.* 196 (3), 340–349. doi:10.1016/j.jsb.2016.08.001

Iacobucci, C., Götze, M., Ihling, C. H., Piotrowski, C., Arlt, C., Schäfer, M., et al. (2018). A cross-linking/mass spectrometry workflow based on MS-cleavable cross-linkers and the MeroX software for studying protein structures and protein-protein interactions. *Nat. Protoc.* 13 (12), 2864–2889. doi:10.1038/s41596-018-0068-8

Iacobucci, C., Götze, M., and Sinz, A. (2020). Cross-linking/mass spectrometry to get a closer view on protein interaction networks. *Curr. Opin. Biotechnol.* 63, 48–53. doi:10.1016/j.copbio.2019.12.009

Iconaru, L. I., Ban, D., Bharatham, K., Ramanathan, A., Zhang, W., Shelat, A. A., et al. (2015). Discovery of small molecules that inhibit the disordered protein, p27(Kip1). *Sci. Rep.* 5 (1), 15686. doi:10.1038/srep15686

Ilitchev, A. I., Giammona, M. J., Olivas, C., Claud, S. L., Lazar Cantrell, K. L., Wu, C., et al. (2018). Hetero-oligomeric amyloid assembly and mechanism: prion fragment PrP(106-126) Catalyzes the islet amyloid polypeptide β-hairpin. *J. Am. Chem. Soc.* 140 (30), 9685–9695. doi:10.1021/jacs.8b05925

Illes-Toth, E., Ramos, M. R., Cappai, R., Dalton, C., and David, P. (2015). Distinct higher-order α-synuclein oligomers induce intracellular aggregation. *Biochem. J.* 468 (3), 485–493. doi:10.1042/BJ20150159

Irvine, G. B., El-Agnaf, O. M., Shankar, G. M., and Walsh, D. M. (2008). Protein aggregation in the brain: the molecular basis for Alzheimer's and Parkinson's diseases. *Mol. Med.* 14 (7), 451–464. doi:10.2119/2007-00100.Irvine

Jebarupa, B., Muralidharan, M., Srinivasu, B. Y., Mandal, A. K., and Mitra, G. (2018). Effect of altered solution conditions on tau conformational dynamics: plausible implication on order propensity and aggregation. *Biochim. Biophys. Acta - Proteins Proteomics* 1866 (5), 668–679. doi:10.1016/j.bbapap.2018.04.004

Jensen, M. R., Ruigrok, R. W., and Blackledge, M. (2013). Describing intrinsically disordered proteins at atomic resolution by NMR. *Curr. Opin. Struct. Biol.* 23 (3), 426–435. doi:10.1016/j.sbi.2013.02.007

Joseph, A. P., Polles, G., Alber, F., and Topf, M. (2017). Integrative modelling of cellular assemblies. *Curr. Opin. Struct. Biol.* 46, 102–109. doi:10.1016/j.sbi.2017.07.001

Jurneczko, E., and Barran, P. E. (2011). How useful is ion mobility mass spectrometry for structural biology? The relationship between protein crystal structures and their collision cross sections in the gas phase. *Analyst* 136 (1), 20–28. doi:10.1039/c0an00373e

Kahraman, A., Herzog, F., Leitner, A., Rosenberger, G., Aebersold, R., and Malmström, L. (2013). Cross-link guided molecular modeling with ROSETTA. *PLoS One* 8 (9), e73411. doi:10.1371/journal.pone.0073411

Kalkhof, S., and Sinz, A. (2008). Chances and pitfalls of chemical cross-linking with amine-reactive N-hydroxysuccinimide esters. *Anal. Bioanal. Chem.* 392 (1–2), 305–312. doi:10.1007/s00216-008-2231-5

Kaltashov, I. A., and Mohimen, A. (2005). Estimates of protein surface areas in solution by electrospray ionization mass spectrometry. *Anal. Chem.* 77 (16), 5370–5379. doi:10.1021/ac050511+

Karamanos, T. K., Kalverda, A. P., Thompson, G. S., and Radford, S. E. (2015). Mechanisms of amyloid formation revealed by solution NMR. *Prog. Nucl. Magn. Reson. Spectrosc.* 88–89, 86–104. doi:10.1016/j.pnmrs.2015.05.002

Keppel, T. R., Howard, B. A., and Weis, D. D. (2011). Mapping unstructured regions and synergistic folding in intrinsically disordered proteins with amide H/D exchange mass spectrometry. *Biochemistry* 50 (40), 8722–8732. doi:10.1021/bi200875p

Keppel, T. R., and Weis, D. D. (2013). Analysis of disordered proteins using a simple apparatus for millisecond quench-flow H/D exchange. *Anal. Chem.* 85 (10), 5161–5168. doi:10.1021/ac4004979

Keppel, T. R., and Weis, D. D. (2015). Mapping residual structure in intrinsically disordered proteins at residue resolution using millisecond hydrogen/deuterium exchange and residue averaging. *J. Am. Soc. Mass Spectrom.* 26 (4), 547–554. doi:10.1007/s13361-014-1033-6

Kikhney, A. G., and Svergun, D. I. (2015). A practical guide to small angle X-ray scattering (SAXS) of flexible and intrinsically disordered proteins. *FEBS Lett.* 589 (19), 2570–2577. doi:10.1016/j.febslet.2015.08.027

Kish, M., Smith, V., Subramanian, S., Vollmer, F., Lethbridge, N., Cole, L., et al. (2019). Allosteric regulation of glycogen phosphorylase solution phase structural dynamics at high spatial resolution. doi:10.1101/654665

Kjaergaard, M., Brander, S., and Poulsen, F. M. (2011). Random coil chemical shift for intrinsically disordered proteins: effects of temperature and pH. *J. Biomol. NMR* 49 (2), 139–149. doi:10.1007/s10858-011-9472-x

Konijnenberg, A., Ranica, S., Narkiewicz, J., Legname, G., Grandori, R., Sobott, F., et al. (2016). Opposite structural effects of epigallocatechin-3-gallate and dopamine binding to α-synuclein. *Anal. Chem.* 88 (17), 8468–8475. doi:10.1021/acs.analchem.6b00731

Lanucara, F., Holman, S. W., Gray, C. J., and Eyers, C. E. (2014). The power of ion mobility-mass spectrometry for structural characterization and the study of conformational dynamics. *Nat. Chem.* 6 (4), 281–294. doi:10.1038/nchem.1889

Laptenko, O., Tong, D. R., Manfredi, J., and Prives, C. (2016). The tail that wags the dog: how the disordered C-terminal domain controls the transcriptional

activities of the p53 tumor-suppressor protein. *Trends Biochem. Sci.* 41 (12), 1022–1034. doi:10.1016/j.tibs.2016.08.011

Leitner, A., Faini, M., Stengel, F., and Aebersold, R. (2016). Crosslinking and mass spectrometry: an integrated technology to understand the structure and function of molecular machines. *Trends Biochem. Sci.* 41 (1), 20–32. doi:10.1016/j.tibs.2015.10.008

Leitner, A., Joachimiak, L. A., Unverdorben, P., Walzthoeni, T., Frydman, J., Förster, F., et al. (2014). Chemical cross-linking/mass spectrometry targeting acidic residues in proteins and protein complexes. *Proc. Natl. Acad. Sci. USA* 111 (26), 9455–9460. doi:10.1073/pnas.1320298111

Leitner, A., Reischl, R., Walzthoeni, T., Herzog, F., Bohn, S., Förster, F., et al. (2012). Expanding the chemical cross-linking toolbox by the use of multiple proteases and enrichment by size exclusion chromatography. *Mol. Cell Proteomics* 11 (3), 014126. doi:10.1074/mcp.M111.014126

Leney, A. C., and Heck, A. J. (2017). Native mass spectrometry: what is in the name?. *J. Am. Soc. Mass Spectrom.* 28 (1), 5–13. doi:10.1007/s13361-016-1545-3

Leuenberger, P., Ganscha, S., Kahraman, A., Cappelletti, V., Boersema, P. J., von Mering, C., et al. (2017). Cell-wide analysis of protein thermal unfolding reveals determinants of thermostability. *Science* 355 (6327), eaai7825. doi:10.1126/science.aai7825

Li, A., Christensen, H. M., Stewart, L. R., Roth, K. A., Chiesa, R., and Harris, D. A. (2007). Neonatal lethality in transgenic mice expressing prion protein with a deletion of residues 105–125. *EMBO J.* 26 (2), 548–558. doi:10.1038/sj.emboj.7601507

Li, K. S., Rempel, D. L., and Gross, M. L. (2016). Conformational-sensitive fast photochemical oxidation of proteins and mass spectrometry characterize amyloid beta 1–42 aggregation. *J. Am. Chem. Soc.* 138 (37), 12090–12098. doi:10.1021/jacs.6b07543

Liu, F., Lössl, P., Scheltema, R., Viner, R., and Heck, A. J. R. (2017). Optimized fragmentation schemes and data analysis strategies for proteome-wide cross-link identification. *Nat. Commun.* 8, 15473. doi:10.1038/ncomms15473

Liu, X. R., Zhang, M. M., and Gross, M. L. (2020). Mass spectrometry-based protein footprinting for higher-order structure analysis: fundamentals and applications. *Chem. Rev.* 120 (10), 4355–4454. doi:10.1021/acs.chemrev.9b00815

Liu, Z., and Huang, Y. (2014). Advantages of proteins being disordered. *Protein Sci.* 23 (5), 539–550. doi:10.1002/pro.2443

Liuni, P., Rob, T., and Wilson, D. J. (2010). A microfluidic reactor for rapid, low-pressure proteolysis with on-chip electrospray ionization. *Rapid Commun. Mass Spectrom.* 24 (3), 315–320. doi:10.1002/rcm.4391

Mädler, S., Bich, C., Touboul, D., and Zenobi, R. (2009). Chemical cross-linking with NHS esters: a systematic study on amino acid reactivities. *J. Mass Spectrom.* 44 (5), 694–706. doi:10.1002/jms.1544

Martin, E. M., Jackson, M. P., Gamerdinger, M., Gense, K., Karamonos, T. K., Humes, J. R., et al. (2018). Conformational flexibility within the nascent polypeptide-associated complex enables its interactions with structurally diverse client proteins. *J. Biol. Chem.* 293 (22), 8554–8568. doi:10.1074/jbc.RA117.001568

McDonald, A. J., Leon, D. R., Markham, K. A., Wu, B., Heckendorf, C. F., Schilling, K., et al. (2019). Altered domain structure of the prion protein caused by Cu2+ binding and functionally relevant mutations: analysis by cross-linking, MS/MS, and NMR. *Structure* 27 (6), 907–e5. doi:10.1016/j.str.2019.03.008

Mead, S. (2006). Prion disease genetics. *Eur. J. Hum. Genet.* 14 (3), 273–281. doi:10.1038/sj.ejhg.5201544

Meinen, B. A., Gadkari, V. V., Stull, F., Ruotolo, B. T., and Bardwell, J. C. A. (2019). SERF engages in a fuzzy complex that accelerates primary nucleation of amyloid proteins. *Proc. Natl. Acad. Sci. USA* 116 (46), 23040–23049. doi:10.1073/pnas.1913316116

Mendes, M. L., Fischer, L., Chen, Z. A., Barbon, M., O'Reilly, F. J., Giese, S. H., et al. (2019). An integrated workflow for crosslinking mass spectrometry. *Mol. Syst. Biol.* 15 (9), e8994. doi:10.15252/msb.20198994

Minde, D. P., Ramakrishna, M., and Lilley, K. S. (2020). Biotin proximity tagging favours unfolded proteins and enables the study of intrinsically disordered regions. *Commun. Biol.* 3 (1), 38. doi:10.1038/s42003-020-0758-y

Mirbaha, H., Chen, D., Morazova, O. A., Ruff, K. M., Sharma, A. M., Liu, X., et al. (2018). Inert and seed-competent tau monomers suggest structural origins of aggregation. *eLife* 7, e36584. doi:10.7554/eLife.36584

Mittal, A., Lyle, N., Harmon, T. S., and Pappu, R. V. (2014). Hamiltonian switch metropolis Monte Carlo simulations for improved conformational sampling of intrinsically disordered regions tethered to ordered domains of proteins. *J. Chem. Theor. Comput* 10 (8), 3550–3562. doi:10.1021/ct5002297

Murata, K., and Wolf, M. (2018). Cryo-electron microscopy for structural analysis of dynamic biological macromolecules. *Biochim. Biophys. Acta (BBA) - Gen. Subjects* 1862 (2), 324–334. doi:10.1016/j.bbagen.2017.07.020

Murphy, M. P., and LeVine, H., III (2010). Alzheimer's disease and the amyloid-beta peptide. *J. Alzheimers Dis.* 19 (1), 311–323. doi:10.3233/JAD-2010-1221

Mylonas, E., Hascher, A., Bernadó, P., Blackledge, M., Mandelkow, E., and Svergun, D. I. (2008). Domain conformation of tau protein studied by solution small-angle X-ray scattering. *Biochemistry* 47 (39), 10345–10353. doi:10.1021/bi800900d

Narayanan, R. L., Dürr, U. H., Bibow, S., Biernat, J., Mandelkow, E., and Zweckstetter, M. (2010). Automatic assignment of the intrinsically disordered protein tau with 441-residues. *J. Am. Chem. Soc.* 132 (34), 11906–11907. doi:10.1021/ja105657f

Natalello, A., Santambrogio, C., and Grandori, R. (2017). Are charge-state distributions a reliable tool describing molecular ensembles of intrinsically disordered proteins by native MS?. *J. Am. Soc. Mass Spectrom.* 28 (1), 21–28. doi:10.1007/s13361-016-1490-1

Nath, A., Sammalkorpi, M., DeWitt, D. C., Trexler, A. J., Elbaum-Garfinkle, S., O'Hern, C. S., et al. (2012). The conformational ensembles of α-synuclein and tau: combining single-molecule FRET and simulations. *Biophys. J.* 103 (9), 1940–1949. doi:10.1016/j.bpj.2012.09.032

Niu, B., Mackness, B. C., Rempel, D. L., Zhang, H., Cui, W., Matthews, C. R., et al. (2017). Incorporation of a reporter peptide in FPOP Compensates for adventitious scavengers and permits time-dependent measurements. *J. Am. Soc. Mass Spectrom.* 28 (2), 389–392. doi:10.1007/s13361-016-1552-4

Nshanian, M., Lantz, C., Wongkongkathep, P., Schrader, T., Klärner, F. G., Blümke, A., et al. (2019). Native top-down mass spectrometry and ion mobility spectrometry of the interaction of tau protein with a molecular tweezer assembly modulator. *J. Am. Soc. Mass Spectrom.* 30 (1), 16–23. doi:10.1007/s13361-018-2027-6

Oldfield, C. J., Cheng, Y., Cortese, M. S., Brown, C. J., Uversky, V. N., and Dunker, A. K. (2005). Comparing and combining predictors of mostly disordered proteins. *Biochemistry* 44 (6), 1989–2000. doi:10.1021/bi047993o

Orbán-Németh, Z., Beveridge, R., Hollenstein, D. M., Rampler, E., Stranzl, T., Hudecz, O., et al. (2018). Structural prediction of protein models using distance restraints derived from cross-linking mass spectrometry data. *Nat. Protoc.* 13 (3), 478–494. doi:10.1038/nprot.2017.146

O'Reilly, F. J., Xue, L., Graziadei, A., Sinn, L., Lenz, S., Tegunov, D., et al. (2020). In-cell architecture of an actively transcribing-translating expressome. *Science* 369 (6503), 554–557.

Parker, B. W., Goncz, E. J., Krist, D. T., Statsyuk, A. V., Nesvizhskii, A. I., and Weiss, E. L. (2019). Mapping low-affinity/high-specificity peptide-protein interactions using ligand-footprinting mass spectrometry. *Proc. Natl. Acad. Sci. USA* 116 (42), 21001–21011. doi:10.1073/pnas.1819533116

Peng, Y., Cao, S., Kiselar, J., Xiao, X., Du, Z., Hsieh, A., et al. (2019). A metastable contact and structural disorder in the estrogen receptor transactivation domain. *Structure* 27 (2), 229–e224. doi:10.1016/j.str.2018.10.026

Peng, Z., Yan, J., Fan, X., Mizianty, M. J., Xue, B., Wang, K., et al. (2015). Exceptionally abundant exceptions: comprehensive characterization of intrinsic disorder in all domains of life. *Cell Mol Life Sci* 72 (1), 137–151. doi:10.1007/s00018-014-1661-9

Politis, A., and Schmidt, C. (2018). Structural characterisation of medically relevant protein assemblies by integrating mass spectrometry with computational modelling. *J. Proteomics* 175, 34–41. doi:10.1016/j.jprot.2017.04.019

Popov, K. I., Makepeace, K. A. T., Petrotchenko, E. V., Dokholyan, N. V., and Borchers, C. H. (2019). Insight into the structure of the "unstructured" tau protein. *Structure* 27 (11), 1710–e1714. doi:10.1016/j.str.2019.09.003

Preston, G. W., Radford, S. E., Ashcroft, A. E., and Wilson, A. J. (2014). Analysis of amyloid nanostructures using photo-cross-linking: *in situ* comparison of three widely used photo-cross-linkers. *ACS Chem. Biol.* 9 (3), 761–768. doi:10.1021/cb400731s

Ramsden, M., Kotilinek, L., Forster, C., Paulson, J., McGowan, E., SantaCruz, K., et al. (2005). Age-Dependent neurofibrillary tangle formation, neuron loss, and memory impairment in a mouse model of human tauopathy (P301L). *J. Neurosci.* 25 (46), 10637–10647. doi:10.1523/JNEUROSCI.3279-05.2005

Rappsilber, J. (2011). The beginning of a beautiful friendship: cross-linking/mass spectrometry and modelling of proteins and multi-protein complexes. *J. Struct. Biol.* 173 (3), 530–540. doi:10.1016/j.jsb.2010.10.014

Ridgeway, M. E., Lubeck, M., Jordens, J., Mann, M., and Park, M. A. (2018). Trapped ion mobility spectrometry: a short review. *Int. J. Mass Spectrom.* 425, 22–35. doi:10.1016/j.ijms.2018.01.006

Riek, R., Hornemann, S., Wider, G., Billeter, M., Glockshuber, R., and Wüthrich, K. (1996). NMR structure of the mouse prion protein domain PrP(121–231). *Nature* 382 (6587), 180–182. doi:10.1038/382180a0

Rist, W., Rodriguez, F., Jørgensen, T. J., and Mayer, M. P. (2005). Analysis of subsecond protein dynamics by amide hydrogen exchange and mass spectrometry using a quenched-flow setup. *Protein Sci.* 14 (3), 626–632. doi:10.1110/ps.041098305

Rizzu, P., Van Swieten, J. C., Joosse, M., Hasegawa, M., Stevens, M., Tibben, A., et al. (1999). High prevalence of mutations in the microtubule-associated protein tau in a population study of frontotemporal dementia in Netherlands. *Am. J. Hum. Genet.* 64 (2), 414–421. doi:10.1086/302256

Rob, T., Liuni, P., Gill, P. K., Zhu, S., Balachandran, N., Berti, P. J., et al. (2012). Measuring dynamics in weakly structured regions of proteins using microfluidics-enabled subsecond H/D exchange mass spectrometry. *Anal. Chem.* 84 (8), 3771–3779. doi:10.1021/ac300365u

Rout, M. P., and Sali, A. (2019). Principles for integrative structural biology studies. *Cell* 177 (6), 1384–1403. doi:10.1016/j.cell.2019.05.016

Ruotolo, B. T., Benesch, J. L., Sandercock, A. M., Hyung, S. J., and Robinson, C. V. (2008). Ion mobility-mass spectrometry analysis of large protein complexes. *Nat. Protoc.* 3 (7), 1139–1152. doi:10.1038/nprot.2008.78

Rusinga, F. I., and Weis, D. D. (2017a). Automated strong Cation-exchange Cleanup to remove macromolecular crowding agents for protein hydrogen exchange mass spectrometry. *Anal. Chem.* 89 (2), 1275–1282. doi:10.1021/acs.analchem.6b04057

Rusinga, F. I., and Weis, D. D. (2017b). Soft interactions and volume exclusion by polymeric crowders can stabilize or destabilize transient structure in disordered proteins depending on polymer concentration. *Proteins* 85 (8), 1468–1479. doi:10.1002/prot.25307

Saikusa, K., Nagadoi, A., Hara, K., Fuchigami, S., Kurumizaka, H., Nishimura, Y., et al. (2015). Mass spectrometric approach for Characterizing the disordered tail regions of the histone H2A/H2B dimer. *Anal. Chem.* 87 (4), 2220–2227. doi:10.1021/ac503689w

Santambrogio, C., Natalello, A., Brocca, S., Ponzini, E., and Grandori, R. (2019). Conformational characterization and classification of intrinsically disordered proteins by native mass spectrometry and charge-state distribution analysis. *Proteomics* 19 (6), 1800060. doi:10.1002/pmic.201800060

Schmidt, C., Macpherson, J. A., Lau, A. M., Tan, K. W., Fraternali, F., and Politis, A. (2017). Surface accessibility and dynamics of macromolecular assemblies probed by covalent labeling mass spectrometry and integrative modeling. *Anal. Chem.* 89 (3), 1459–1468. doi:10.1021/acs.analchem.6b02875

Schmidt, C., and Robinson, C. V. (2014). A comparative cross-linking strategy to probe conformational changes in protein complexes. *Nat. Protoc.* 9 (9), 2224–2236. doi:10.1038/nprot.2014.144

Schmidt, C., Zhou, M., Marriott, H., Morgner, N., Politis, A., and Robinson, C. V. (2013). Comparative cross-linking and mass spectrometry of an intact F-type ATPase suggest a role for phosphorylation. *Nat. Commun.* 4, 1985. doi:10.1038/ncomms2985

Schmidt, R., and Sinz, A. (2017). Improved single-step enrichment methods of cross-linked products for protein structure analysis and protein interaction mapping. *Anal. Bioanal. Chem.* 409 (9), 2393–2400. doi:10.1007/s00216-017-0185-1

Schneider, M., Belsom, A., and Rappsilber, J. (2018). Protein tertiary structure by crosslinking/mass spectrometry. *Trends Biochem. Sci.* 43 (3), 157–169. doi:10.1016/j.tibs.2017.12.006

Schwalbe, M., Ozenne, V., Bibow, S., Jaremko, M., Jaremko, L., Gajda, M., et al. (2014). Predictive atomic resolution descriptions of intrinsically disordered hTau40 and α-synuclein in solution from NMR and small angle scattering. *Structure* 22 (2), 238–249. doi:10.1016/j.str.2013.10.020

Semmler, L., Reiter-Brennan, C., and Klein, A. (2019). BRCA1 and breast cancer: a review of the underlying mechanisms resulting in the tissue-specific tumorigenesis in mutation Carriers. *J. Breast Cancer* 22 (1), 1–14. doi:10.4048/jbc.2019.22.e6

Sharma, R., Raduly, Z., Miskei, M., and Fuxreiter, M. (2015). Fuzzy complexes: specific binding without complete folding. *FEBS Lett.* 589 (19), 2533–2542. doi:10.1016/j.febslet.2015.07.022

Sharon, M., and Robinson, C. V. (2007). The role of mass spectrometry in structure elucidation of dynamic protein complexes. *Annu. Rev. Biochem.* 76 (1), 167–193. doi:10.1146/annurev.biochem.76.061005.090816

Sinha, S., Lopes, D. H., Du, Z., Pang, E. S., Shanmugam, A., Lomakin, A., et al. (2011). Lysine-specific molecular tweezers are broad-spectrum inhibitors of assembly and toxicity of amyloid proteins. *J. Am. Chem. Soc.* 133 (42), 16958–16969. doi:10.1021/ja206279b

Sinz, A., Arlt, C., Chorev, D., and Sharon, M. (2015). Chemical cross-linking and native mass spectrometry: a fruitful combination for structural biology. *Protein Sci.* 24 (8), 1193–1209. doi:10.1002/pro.2696

Sinz, A. (2014). The advancement of chemical cross-linking and mass spectrometry for structural proteomics: from single proteins to protein interaction networks. *Expert Rev. Proteomics* 11 (6), 733–743. doi:10.1586/14789450.2014.960852

Skinner, O. S., Haverland, N. A., Fornelli, L., Melani, R. D., Do Vale, L. H. F., Seckler, H. S., et al. (2017). Top-down characterization of endogenous protein complexes with native proteomics. *Nat. Chem. Biol.* 14, 36. doi:10.1038/nchembio.2515

Snijder, J., van de Waterbeemd, M., Glover, M. S., Shi, L., Clemmer, D. E., and Heck, A. J. (2015). Conformational landscape and pathway of disulfide bond reduction of human alpha defensin. *Protein Sci.* 24 (8), 1264–1271. doi:10.1002/pro.2694

Spevacek, A. R., Evans, E. G., Miller, J. L., Meyer, H. C., Pelton, J. G., and GlennMillhauser, L. M. G. L. (2013). Zinc drives a tertiary fold in the prion protein with familial disease mutation sites at the interface. *Structure* 21 (2), 236–246. doi:10.1016/j.str.2012.12.002

Steigenberger, B., Pieters, R. J., Heck, A. J. R., and Scheltema, R. A. (2019). PhoX: an IMAC-enrichable cross-linking reagent. *ACS Cent. Sci.* 5 (9), 1514–1522. doi:10.1021/acscentsci.9b00416

Stephani, M., Picchianti, L., Gajic, A., Beveridge, R., Skarwan, E., Sanchez de Medina Hernandez, V., et al. (2020). A cross-kingdom conserved ER-phagy receptor maintains endoplasmic reticulum homeostasis during stress. *Elife* 9. doi:10.7554/eLife.58396

Stephens, A. D., Zacharopoulou, M., Moons, R., Fusco, G., Chiki, N., et al. (2020). Extent of N-terminus exposure of monomeric alpha-synuclein determines its aggregation propensity. *Nat. Commun.* 11 (1), 2820. doi:10.1038/s41467-020-16564-3

Stuchfield, D., and Barran, P. (2018). Unique insights to intrinsically disordered proteins provided by ion mobility mass spectrometry. *Curr. Opin. Chem. Biol.* 42, 177–185. doi:10.1016/j.cbpa.2018.01.007

Suryadinata, R., Sadowski, M., and Sarcevic, B. (2010). Control of cell cycle progression by phosphorylation of cyclin-dependent kinase (CDK) substrates. *Biosci. Rep.* 30 (4), 243–255. doi:10.1042/BSR20090171

Svejdal, R. R., Dickinson, E. R., Sticker, D., Kutter, J. P., and Rand, K. D. (2019). Thiol-ene microfluidic chip for performing hydrogen/deuterium exchange of proteins at subsecond time scales. *Anal. Chem.* 91 (2), 1309–1317. doi:10.1021/acs.analchem.8b03050

Takamori, S., Holt, M., Stenius, K., Lemke, E. A., Grønborg, M., Riedel, D., et al. (2006). Molecular anatomy of a trafficking organelle. *Cell* 127 (4), 831–846. doi:10.1016/j.cell.2006.10.030

Takamoto, K., and Chance, M. R. (2006). Radiolytic protein footprinting with mass spectrometry to probe the structure of macromolecular complexes. *Annu. Rev. Biophys. Biomol. Struct.* 35, 251–276. doi:10.1146/annurev.biophys.35.040405.102050

Testa, L., Brocca, S., and Grandori, R. (2011). Charge-surface correlation in electrospray ionization of folded and unfolded proteins. *Anal. Chem.* 83 (17), 6459–6463. doi:10.1021/ac201740z

Thielges, M. C., Zimmermann, J., Yu, W., Oda, M., and Romesberg, F. E. (2008). Exploring the energy landscape of antibody-antigen complexes: protein dynamics, flexibility, and molecular recognition. *Biochemistry* 47 (27), 7237–7247. doi:10.1021/bi800374q

Tidow, H., Melero, R., Mylonas, E., Freund, S. M., Grossmann, J. G., Carazo, J. M., et al. (2007). Quaternary structures of tumor suppressor p53 and a specific p53 DNA complex. *Proc. Natl. Acad. Sci. USA* 104 (30), 12324–12329. doi:10.1073/pnas.0705069104

Trabjerg, E., Nazari, Z. E., and Rand, K. D. (2018). Conformational analysis of complex protein states by hydrogen/deuterium exchange mass spectrometry (HDX-MS): challenges and emerging solutions. *Trac Trends Anal. Chem.* 106, 125–138. doi:10.1016/j.trac.2018.06.008

Ujma, J., Ropartz, D., Giles, K., Richardson, K., Langridge, D., Wildgoose, J., et al. (2019). Cyclic ion mobility mass spectrometry distinguishes anomers and open-ring forms of pentasaccharides. *J. Am. Soc. Mass Spectrom.* 30 (6), 1028–1037. doi:10.1007/s13361-019-02168-9

Uversky, V. N., Oldfield, C. J., and Dunker, A. K. (2008). Intrinsically disordered proteins in human diseases: introducing the D2 Concept. *Annu. Rev. Biophys.* 37 (1), 215–246. doi:10.1146/annurev.biophys.37.032807.125924

Vahidi, S., and Konermann, L. (2016). Probing the time scale of FPOP (fast photochemical oxidation of proteins): radical reactions extend over tens of milliseconds. *J. Am. Soc. Mass Spectrom.* 27 (7), 1156–1164. doi:10.1007/s13361-016-1389-x

Van der Rest, G., Rezaei, H., and Halgand, F. (2017). Monitoring conformational landscape of ovine prion protein monomer using ion mobility coupled to mass spectrometry. *J. Am. Soc. Mass Spectrom.* 28 (2), 303–314. doi:10.1007/s13361-016-1522-x

Vassilev, L. T., Vu, B. T., Graves, B., Carvajal, D., Podlaski, F., Filipovic, Z., et al. (2004). *In Vivo* activation of the p53 pathway by small-molecule antagonists of MDM2. *Science* 303 (5659), 844–848. doi:10.1126/science.1092472

Vimer, S., Ben-Nissan, G., and Sharon, M. (2020). Direct characterization of overproduced proteins by native mass spectrometry. *Nat. Protoc.* 15 (2), 236–265. doi:10.1038/s41596-019-0233-8

Vöpel, T., Bravo-Rodriguez, K., Mittal, S., Vachharajani, S., Gnutt, D., Sharma, A., et al. (2017). Inhibition of huntingtin exon-1 aggregation by the molecular tweezer CLR01. *J. Am. Chem. Soc.* 139 (16), 5640–5643. doi:10.1021/jacs.6b11039

Walters, B. T., Mayne, L., Hinshaw, J. R., Sosnick, T. R., and Englander, S. W. (2013). Folding of a large protein at high structural resolution. *Proc. Natl. Acad. Sci. USA* 110 (47), 18898–18903. doi:10.1073/pnas.1319482110

Wang, L., and Chance, M. R. (2017). Protein footprinting comes of age: mass spectrometry for biophysical structure assessment. *Mol. Cell Proteomics* 16 (5), 706–716. doi:10.1074/mcp.O116.064386

Wang, L., and Chance, M. R. (2011). Structural mass spectrometry of proteins using hydroxyl radical based protein footprinting. *Anal. Chem.* 83 (19), 7234–7241. doi:10.1021/ac200567u

Webb, B., Viswanath, S., Bonomi, M., Pellarin, R., Greenberg, C. H., Saltzberg, D., et al. (2018). Integrative structure modeling with the integrative modeling platform. *Protein Sci.* 27 (1), 245–258. doi:10.1002/pro.3311

Wittig, S., Haupt, C., Hoffmann, W., Kostmann, S., Pagel, K., and Schmidt, C. (2019). Oligomerisation of synaptobrevin-2 studied by native mass spectrometry and chemical cross-linking. *J. Am. Soc. Mass Spectrom.* 30 (1), 149–160. doi:10.1007/s13361-018-2000-4

Wongkongkathep, P., Han, J. Y., Choi, T. S., Yin, S., Kim, H. I., and Loo, J. A. (2018). Native top-down mass spectrometry and ion mobility MS for Characterizing the cobalt and manganese metal binding of α-synuclein protein. *J. Am. Soc. Mass Spectrom.* 29 (9), 1870–1880. doi:10.1007/s13361-018-2002-2

Wright, P. E., and Dyson, H. J. (2015). Intrinsically disordered proteins in cellular signalling and regulation. *Nat. Rev. Mol. Cell Biol* 16 (1), 18–29. doi:10.1038/nrm3920

Wright, P. E., and Dyson, H. J. (2009). Linking folding and binding. *Curr. Opin. Struct. Biol.* 19 (1), 31–38. doi:10.1016/j.sbi.2008.12.003

Wu, B., McDonald, A. J., Markham, K., Rich, C. B., McHugh, K. P., Tatzelt, J., et al. (2017). The N-terminus of the prion protein is a toxic effector regulated by the C-terminus. *eLife* 6, e23473. doi:10.7554/eLife.23473

Xie, Y., Zhang, J., Yin, S., and Loo, J. A. (2006). Top-down ESI-ECD-FT-ICR mass spectrometry localizes noncovalent protein-ligand binding sites. *J. Am. Chem. Soc.* 128 (45), 14432–14433. doi:10.1021/ja063197p

Xu, G., and Chance, M. R. (2007). Hydroxyl radical-mediated modification of proteins as probes for structural proteomics. *Chem. Rev.* 107 (8), 3514–3543. doi:10.1021/cr0682047

Yamamoto, T., Shimizu, Y., Ueda, T., Shiro, Y., and Suematsu, M. (2011). Application of micro-reactor chip technique for millisecond quenching of deuterium incorporation into 70S ribosomal protein complex. *Int. J. Mass Spectrom.* 302 (1), 132–138. doi:10.1016/j.ijms.2010.08.029

Yan, Y., Chen, G., Wei, H., Huang, R. Y., Mo, J., Rempel, D. L., et al. (2014). Fast photochemical oxidation of proteins (FPOP) maps the epitope of EGFR binding to adnectin. *J. Am. Soc. Mass Spectrom.* 25 (12), 2084–2092. doi:10.1007/s13361-014-0993-x

Yu, C., and Huang, L. (2018). Cross-Linking mass spectrometry: an emerging technology for interactomics and structural biology. *Anal. Chem.* 90, 144–165. doi:10.1021/acs.analchem.7b04431

Zahn, R., Liu, A., Lührs, T., Riek, R., von Schroetter, C., López García, F., et al. (2000). NMR solution structure of the human prion protein. *Proc. Natl. Acad. Sci. USA* 97 (1), 145–150. doi:10.1073/pnas.97.1.145

Zhang, Y., Rempel, D. L., Zhang, J., Sharma, A. K., Mirica, L. M., and Gross, M. L. (2013). Pulsed hydrogen-deuterium exchange mass spectrometry probes conformational changes in amyloid beta (Aβ) peptide aggregation. *Proc. Natl. Acad. Sci. USA* 110 (36), 14604–14609. doi:10.1073/pnas.1309175110

Zheng, X., Liu, D., Klärner, F. G., Schrader, T., Bitan, G., and Bowers, M. T. (2015). Amyloid β-protein assembly: the effect of molecular tweezers CLR01 and CLR03. *J. Phys. Chem. B* 119 (14), 4831–4841. doi:10.1021/acs.jpcb.5b00692

Zheng, X., Wu, C., Liu, D., Li, H., Bitan, G., Shea, J. E., et al. (2016). Mechanism of C-terminal fragments of amyloid β-protein as Aβ inhibitors: do C-terminal interactions play a key role in their inhibitory activity?. *J. Phys. Chem. B* 120 (8), 1615–1623. doi:10.1021/acs.jpcb.5b08177

Ziemianowicz, D. S., MacCallum, J. L., and Schriemer, D. C. (2020). Correlation between labeling yield and surface accessibility in covalent labeling mass spectrometry. *J. Am. Soc. Mass Spectrom.* 31 (2), 207–216. doi:10.1021/jasms.9b00083

Conflict of Interest: The authors declare that the research was conducted in the absence of any commercial or financial relationships that could be construed as a potential conflict of interest.

Copyright © 2021 Beveridge and Calabrese. This is an open-access article distributed under the terms of the Creative Commons Attribution License (CC BY). The use, distribution or reproduction in other forums is permitted, provided the original author(s) and the copyright owner(s) are credited and that the original publication in this journal is cited, in accordance with accepted academic practice. No use, distribution or reproduction is permitted which does not comply with these terms.

frontiers in Chemistry

MINI REVIEW
published: 26 March 2021
doi: 10.3389/fchem.2021.632021

Wide-Bandgap Halide Perovskites for Indoor Photovoltaics

Lethy Krishnan Jagadamma and Shaoyang Wang*

Energy Harvesting Research Group, SUPA, School of Physics and Astronomy, St. Andrews, Scotland, United Kingdom

Indoor photovoltaics (IPVs) are receiving great research attention recently due to their projected application in the huge technology field of Internet of Things (IoT). Among the various existing photovoltaic technologies such as silicon, Cadmium Telluride (CdTe), Copper Indium Gallium Selenide (CIGS), organic photovoltaics, and halide perovskites, the latter are identified as the most promising for indoor light harvesting. This suitability is mainly due to its composition tuning adaptability to engineer the bandgap to match the indoor light spectrum and exceptional optoelectronic properties. Here, in this review, we are summarizing the state-of-the-art research efforts on halide perovskite-based indoor photovoltaics, the effect of composition tuning, and the selection of various functional layer and device architecture onto their power conversion efficiency. We also highlight some of the challenges to be addressed before these halide perovskite IPVs are commercialized.

Keywords: composition tuning, triple cation, triple anion, $CH_3NH_3PbI_3$, internet of things, power conversion efficiency, indoor light spectra

OPEN ACCESS

Edited by:
Ping Yu,
Institute of Chemistry (CAS), China

Reviewed by:
Dillip K. Panda,
Clemson University, United States
Fang Hao,
General Motors (United States), United States

****Correspondence:***
Lethy Krishnan Jagadamma
lkj2@st-andrews.ac.uk

Specialty section:
This article was submitted to Electrochemistry, a section of the journal Frontiers in Chemistry

Received: *23 November 2020*
Accepted: *27 January 2021*
Published: *26 March 2021*

Citation:
Jagadamma LK and Wang S (2021) Wide-Bandgap Halide Perovskites for Indoor Photovoltaics. Front. Chem. 9:632021. doi: 10.3389/fchem.2021.632021

INTRODUCTION

Photovoltaic devices convert light to electricity. The term has already become synonymous with solar cells, which are a type of photovoltaic device in which the incident light is sunlight. There are indoor photovoltaic (IPV) devices that convert light from artificial light sources such as white light-emitting diode (LED) and fluorescent lamps inside the buildings to electrical energy (Chen, 2019; Li et al., 2020). The history of indoor photovoltaics dates back to the 1970s when the amorphous silicon solar cells were used to power watches and calculators (Minnaert and Veelaert, 2014). For over 40 years, silicon solar cells were the ones mainly used for harvesting indoor light, and IPV research field was almost stagnant until 2010. However, over the last five years, IPVs are gaining much research attention and this is reflected in the increasing number of research publications on this topic published every year (**Figure 1A**). This increasing interest can be attributed to the combined effect of four main factors: 1) emergence of efficient third-generation thin-film solar cells such as organic and hybrid perovskites; 2) replacement of incandescent lights inside the buildings by solid-state white LEDs and fluorescent lamps (FLs); 3) the boom of disruptive technology such as the Internet of Things (IoT) and the associated unprecedented commercial opportunities; and 4) the continued decrease of power requirement for wireless sensors.

The concept of the IoT, initially coined by Kevin Ashton in 1999, has now projected to be a 1.6 trillion market in 2025 (Kramp et al., 2013). IoT is a smart network of connected physical objects with embedded sensors and actuators. IoT industry is projected to make an economic impact of $11 trillion by 2025 and as many as 75 billion connected IoT devices. Furthermore, it is noticeable that half of those components to be installed will be located inside buildings (Mathews et al., 2019). Wireless sensors are the most fundamental components in these smart devices (**Figure 1B**) (Davies, 2015). Sustainably, powering these sensors is a huge challenge. At present, these sensors are powered by batteries which limit the IoT potential by service interruptions due to battery replacement and

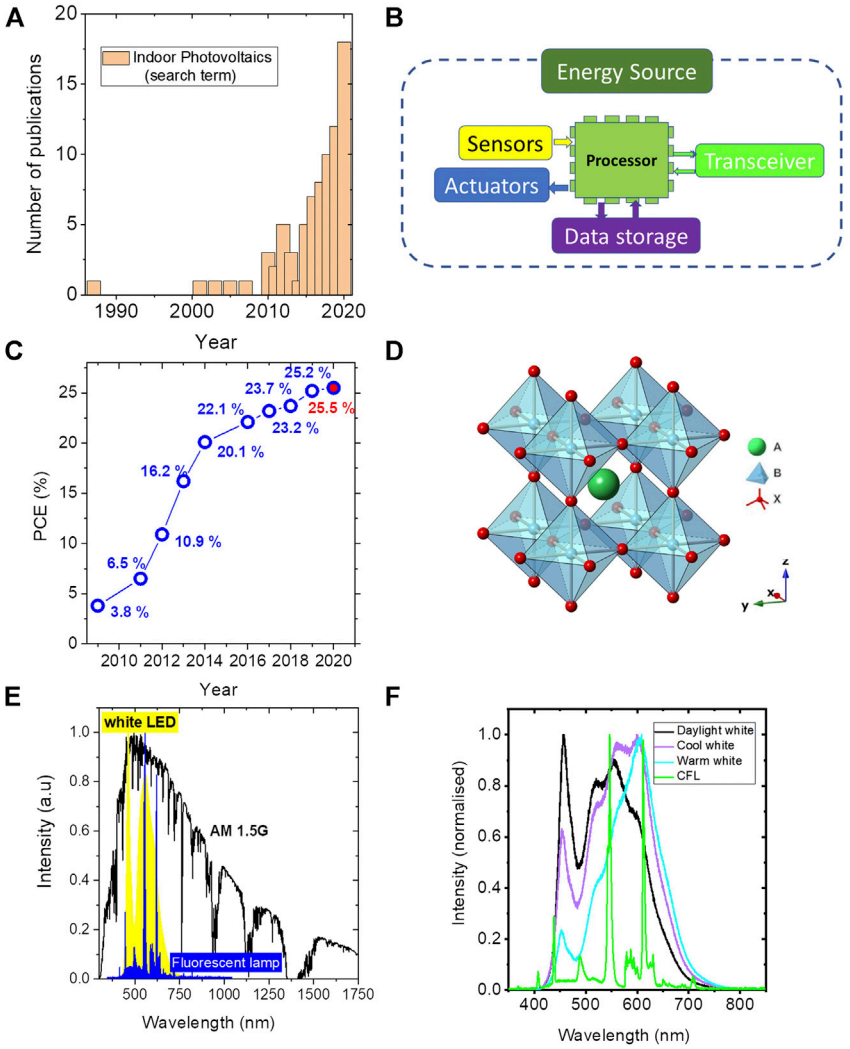

FIGURE 1 | (A) The graph showing the number of IPV related publications as a function of year. **(B)** The main components in an IoT system. **(C)** The advancement of PCE for hybrid perovskite solar cells over the last decade. **(D)** Perovskite crystal structure with cubic symmetry. Organic or inorganic cations occupy position A (green) whereas metal cations and halogens occupy the B (bluish-grey) and X (red) positions, respectively. **(E)** Comparison of 1 Sun spectrum to indoor artificial light spectra. **(F)** Spectra of different types of white LEDs and CFL lamp used inside the buildings.

TABLE 1 | Different photovoltaic materials and their bandgap.

Photovoltaic material	Bandgap (eV)	Tunable (bandgap)
Crystalline silicon (c-si)	1.1	X
Amorphous silicon (a-Si)	1.7	X
CdTe	1.45	X
CIGS	1.01–1.68	✓
Organic photovoltaics	1.0–2	✓
Halide perovskites	1.1–3.3	✓

eventually cause an environmental problem (due to battery disposal). These sensors only require μW-mW of power for their efficient functioning. Light energy is available in the ambient environment and can be accessed easily via photovoltaic devices without requesting additional devices or multiple energy transfer, thus becoming the most promising candidate to power IoT sensor system.

Different types of PV materials including III-IV, CIGS, organic, dye-sensitized, and perovskite are taken into consideration for efficient indoor light harvesting. **Table 1** shows the main photovoltaic materials available and their bandgap. In contrast to conventional solar cell technologies such as silicon, the emerging PV technologies based on organic and halide perovskite semiconductors have tunable bandgap. In the history of photovoltaics, no other light harvesting material has ever triggered research attention and promising avenues to harness solar energy similar to

organometal halide perovskites (Jena et al., 2019; Miyasaka et al., 2020; Mhaisalkar et al., 2020). Within a decade, the power conversion efficiency (PCE) of these perovskite solar cells has made an amazing advancement from 3.81% in 2009 to 25.5% today (**Figure 1C**). Represented by a general chemical formula of ABX_3, this family of materials provide a framework to bind organic and inorganic component to a molecular composite, where A is an organic or inorganic cation, B is a divalent cation, such as Pb^{2+} and Sn^{2+}, and X is halogen, I^-, Br^-, or Cl^-. Organic cations, A, can be methylammonium (MA) $CH_3NH_3^+$, ethylammonium (EA) $C_2H_5NH_3^+$, formamidinium (FA) $HC(NH_2)_2^+$, and even inorganic Cs (**Figure 1D**). These materials possess exceptional optoelectronic properties needed for a photovoltaic material such as direct bandgap which is tunable (1.17–3.3 eV), high absorption (absorption length of 200–300 nm) in the visible range, low exciton binding energy ~30 meV (comparable to RT thermal energy), high electron and hole bulk mobility (~2000 $cm^2/(V.s)$ and ~300 $cm^2/(V.s)$, respectively), large diffusion length (>1 μm), and ability to form high-quality crystals at relatively low processing temperatures (RT to 150°C) via vacuum or wet synthesis methods (Grätzel, 2014; Stoumpos and Kanatzidis, 2015; Green et al., 2015; Park, 2015).

The distributed nature of the IoT sensors requires that the indoor light energy harvesters also be distributed in nature. Thus, IPVs, which are suitable for powering the sensors, need to have high PCE, ease of processability, low cost, earth abundance of constituting materials, flexibility, conformability, and lightweight. Halide perovskite photovoltaic devices integrate all these requirements. Along with the extraordinary power conversion efficiency under one sun, halide perovskites have shown remarkable efficiency under indoor lighting as well. Even though recently Li et al. (2020), Chen (2019), and Lee et al. (2019b) have reviewed thin-film indoor photovoltaics, the growing potential and increasing number of publications related to halide perovskite IPVs demand a review focusing on the halide perovskite IPV itself.

Factors Affecting Indoor Light Harvesting

The common perception is that high-performance Si solar cells can perform the same under indoor lighting condition. This is not true and is especially pertinent with the phasing out of the incandescent light bulbs which have a similar broad emission spectrum to that of the solar spectrum. Identifying which photovoltaic technology is suitable for IPV depends mainly on the 1) indoor light spectrum and 2) factors determining the power conversion efficiency.

Indoor Light Spectrum and Maximum Theoretical Efficiency of IPVs

Indoor lighting in residential buildings and offices is now dominated by fluorescent lamps and white light-emitting diodes which are entirely different in intensity (1,000 times lower) and spectral content (narrow spectrum vs. broad) from the solar spectrum (**Figure 1E**). The intensity of standard sunlight spectrum (AM 1.5G) is 100 mW/cm^2 and the typical indoor artificial light intensity is 0.05–1 mW/cm^2 (~200–2000 lux). The low available light intensity inside the building was one reason why indoor photovoltaic technology was not receiving much attention for many years. However, when the IoT gained popularity since 2010, indoor photovoltaics also started receiving its attention. This is because the IoT sensors only require μW-mW of power to operate. Depending on the correlated color temperature, three main types of white LED lighting used inside buildings are warm white, cool white, and daylight white. The typical spectra of these light sources are shown in (**Figure 1F**). As shown in the spectra, a warm white LED has a higher orange spectral range compared to blue; cool white LED has higher blue spectral content compared to warm white. Inside buildings, warm white LEDs are usually used in living rooms, bedrooms, and hallways. Cool white LEDs are usually used in kitchens, study areas, bathrooms, offices, and retail stores; daylight LEDs are used in commercial, retail, and art studios (integral-led.com).

Different spectral content and wavelength range of indoor light sources mean that the optimum bandgap and thermodynamically limited maximum power conversion efficiency (Shockley-Queisser limit) are different for indoor photovoltaics compared to outdoor solar cells. Under the solar spectrum (100 mW/cm^2), the maximum theoretical efficiency is 33% and the optimum bandgap is 1.4 eV (Shockley and Queisser, 1961). In the case of indoor lighting conditions, the optimum material bandgap is ~1.9 eV and the maximum theoretical efficiency can reach as high as ~60% for LEDs and 50% for fluorescent lamps (Müller et al., 2013; Ho et al., 2020) (**Figure 2A**). This implies that the active layer composition of the perovskite indoor photovoltaics needs to be modified for higher photon energy indoor lightings compared to that of 1 Sun. This aspect is further detailed in *Band Structure of Halide Perovskite Semiconductors*.

Indoor Photovoltaic Performance Parameters

The photovoltaic power conversion efficiency (η) is determined by three performance parameters open-circuit voltage (Voc), short circuit current density (Jsc), and fill factor (FF) as

$$\eta(\%) = \frac{J_{sc} \times V_{oc} \times FF \times 100\,\%}{P_{\text{in}}},$$

where P_{in} is the input light intensity. The dependence of these performance parameters on the incident light intensity is shown as follows (Goo et al., 2018; Koster et al., 2005):

$$J_{sc} \propto I^{\alpha}, \tag{1}$$

$$V_{oc} = \frac{nk_BT}{q}\ln\left(\frac{J_{sc}}{J_o} + 1\right), \tag{2}$$

where I is the incident light intensity, α is the recombination factor n is the ideality factor, k_B is the Boltzmann factor, and J_o is the diode saturation current/leakage current.

FF depends indirectly on the light intensity through the following relation (Green, 1981):

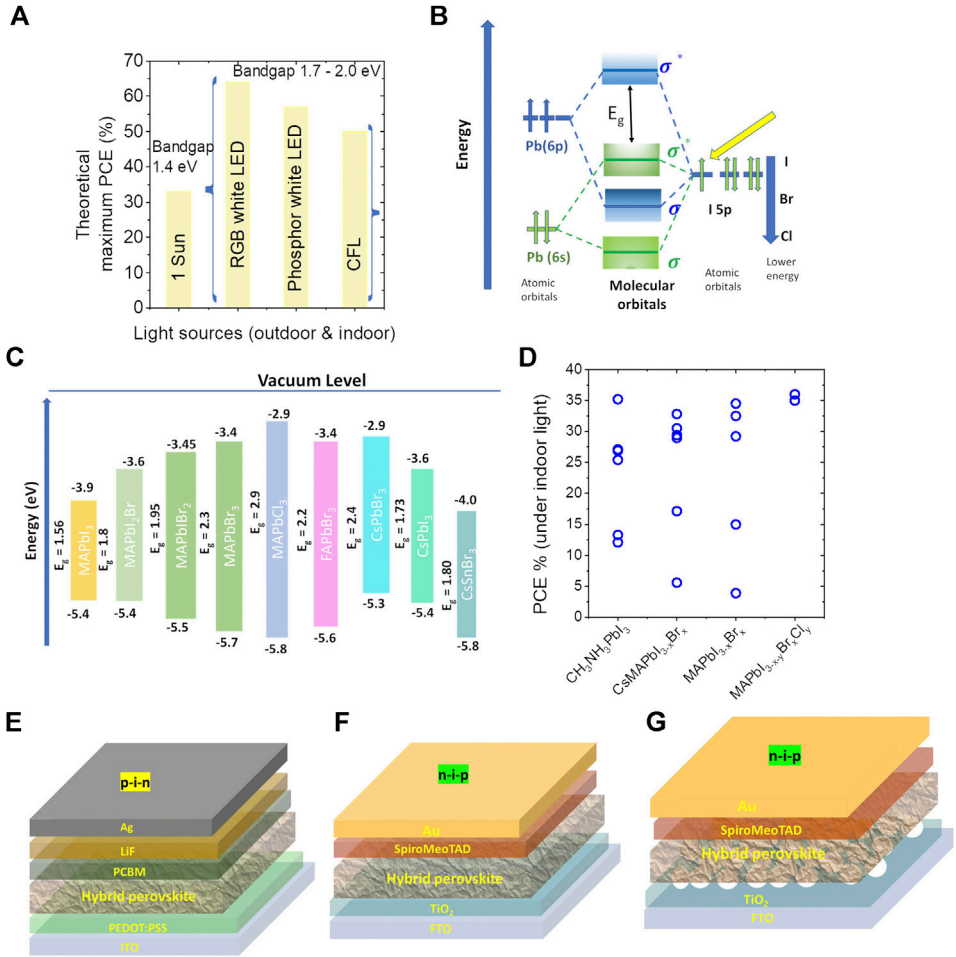

FIGURE 2 | (A) Maximum theoretical efficiency of IPVs as a function of bandgap, **(B)** electronic band structure of halide perovskites, **(C)** some typical wide-bandgap halide perovskites, and **(D)** power conversion efficiency of halide perovskite indoor photovoltaic devices as a function of different composition. Different photovoltaic device architectures, **(E)** planar *p-i-n*, **(F)** planar *n-i-p*, and **(G)** mesoporous *n-i-p* architectures.

$$FF_{s+sh} = FF_s\left[1 - \frac{(v_{oc}+0.7)}{v_{oc}}\frac{FF_s}{r_{sh}}\right], \quad (3)$$

$$FF_s = FF_0\,(1 - r_s), \quad (4)$$

where FF_{s+sh} is the FF taking into account both series and shunt resistance, FF_s is the FF considering only the series resistance, (R_s) and FF_0 is the ideal FF without taking into consideration either series or shunt resistance (R_{SH}).

v_{oc} is the normalized open-circuit voltage given by

$$v_{oc} = \frac{V_{oc}}{V_T}, \quad (5)$$

where V_T is the thermal voltage,

$$V_T = \frac{k_B\,T}{q}, \quad (6)$$

where r_s and r_{SH} are the normalized series and shunt resistance given by

$$r_s = \frac{R_s}{R_{CH}}, \quad (7)$$

$$r_{SH} = \frac{R_{SH}}{R_{CH}}, \quad (8)$$

where R_{CH} is the characteristic resistance, expressed as

$$R_{CH} = \frac{V_{OC}}{(J_{SC} \times A)}, \quad (9)$$

where A is the area of the photovoltaic device. Under the low light intensity, J_{sc} falls faster than V_{oc} due to its power-law dependence. Also, the influence of shunt resistance on FF becomes high (**Eq. 3**) and the dependence on Rs is relaxed, which is in direct contrast with the FF dependence of R_{SH} and R_s under 1 Sun (Steim et al., 2011). This requires stringent interface

engineering to minimize the recombination losses of the photogenerated carriers.

In this review, we will be mainly focusing on the wide-bandgap halide perovskite semiconductors suitable for indoor light harvesting. Halide perovskite bandgap can be tuned from 1.1 to 3.7 eV by interchanging/mixing B cation (Ge, Sn, and Pb) or halogens (X = Cl, Br and I) (Hu et al., 2019; Jena et al., 2019; Mhaisalkar et al., 2020). This is highly advantageous considering the different spectral features of the indoor light sources. Since the bandgap modification is required for maximizing indoor light harvesting, understanding the band structure of halide perovskite is highly important and constitutes the focus of discussion for the next section.

Band Structure of Halide Perovskite Semiconductors

Electronic band structure determines the optoelectronic properties such as optical absorption of the incoming photons, charge transfer from the active layer to the charge-transporting layers, and opportunity for bandgap engineering. Halide perovskites are direct bandgap semiconductors with sharp absorption edges. In halide perovskites, both the valence band maximum (VBM) and conduction band minimum (CBM) are constituted by antibonding sigma orbitals but with different degree of contribution from B cation and X anion *s* and *p* orbitals (Walsh, 2015; He et al., 2017). The A cation has no direct contribution to the electronic band structure but has a strong indirect influence via the octahedral tilting and hence the B-X-B bond angles (Kang and Wang, 2017; Elumalai et al., 2016; Stoumpos and Kanatzidis, 2015). Through steric and Coulombic interactions, A cations deform the BX_6 octahedral unit, and this tilting changes the absorption edges and electronic bandgap. The valence band is formed by mixing of halide np^6 orbitals (where *n* is the principal quantum number) and metal (B cation) ns^2 orbitals with a major contribution from halide np^6 orbitals (and a minor contribution from the ns^2). The conduction band is constituted by mixing of B cation's *np* orbital with halide's np^6 orbital with a major contribution from metal *p* orbital (and a minor contribution from halide *p* orbital).

As the halide ions are moved from I ($5p^6$) to Br ($4p^6$) to Cl ($3p^6$), the energies of the halide np^6 orbitals downshift the VBM by 0.8 eV and shift the CBM by 0.19 eV, thus widening the bandgap (Stoumpos and Kanatzidis, 2015; Ravi et al., 2016; Walsh, 2015; Olthof, 2016; He et al., 2017). However, replacing the Pb with Sn, the conduction band is downshifted with Sn 5*p* and reduces the bandgap. It is worth noting that the wide-bandgap perovskites are important for Si/perovskite (1.7 eV) and perovskite/perovskite (1.8 eV) tandem solar cells (Tong et al., 2020). When selecting the suitable wide-bandgap perovskites for indoor solar cells, the bandgap of the bottom cell perovskite composition can be used as a good starting point for optimizing the bandgap required for indoor photovoltaics. Taking $CH_3NH_3PbI_3$ as a typical example, the band structure of halide perovskite is shown in **Figure 2B** (He et al., 2017; Huang et al., 2017). **Figure 2C** shows the energy level structure of some wide-bandgap halide perovskites (Tao et al., 2019; Wu et al., 2018; Huang et al., 2019).

With this background understanding of band structure of halide perovskites, in the next section, the indoor photovoltaic properties of halide perovskites would be reviewed with special emphasis on the selection of the active layer materials and the device architecture.

Halide Perovskite-Based Indoor Photovoltaics

Most of the initial reports on the indoor photovoltaic performance of hybrid perovskites were focused on the most widely investigated hybrid perovskite composition of $CH_3NH_3PbI_3$. $CH_3NH_3PbI_3$ has a bandgap of 1.56 eV, lower than the theoretically predicted optimum bandgap reported for indoor photovoltaics. By interface engineering and controlling the traps at the interfaces and carrier dynamics, $CH_3NH_3PbI_3$-based indoor photovoltaic devices have demonstrated a power conversion efficiency ranging from 20% to 34% under indoor lighting conditions (Chen et al., 2015; Dagar et al., 2018; Lucarelli et al., 2017; Di Giacomo et al., 2016). Raifuku et al. (2016) have previously shown that hybrid perovskite solar cells perform better under low-intensity illumination such as 0.1 mW/cm^2, compared to crystalline silicon. They demonstrated that, at low-intensity levels, perovskite solar cells can retain 70% of their open-circuit voltage at 1 Sun. Concerning interface engineering in indoor photovoltaics, the study reported by Li et al. is highly significant as they demonstrated that the ionic liquid of 1-butyl-3-methylimidazolium tetrafluoroborate ([BMIM]BF4) can passivate the surface traps on the electron transport layer of PCBM and prevent moisture and oxygen erosion to the perovskite active layer. These indoor photovoltaic devices based on $CH_3NH_3PbI_3$ showed a power conversion efficiency of 35.2% under indoor lighting conditions (Li et al., 2018).

We have previously reported that, compared to $CH_3NH_3PbI_3$, the mixed halides of iodide-bromide and iodide-chloride can have a higher power conversion efficiency of 23% under indoor white LED and CFL lighting (Jagadamma et al., 2019). In 2018, Guo et al. showed that $CH_3NH_3PbI_3$ doped with Cl and citric acid can convert indoor white LED light to electricity with 26% power conversion efficiency. They attribute this enhanced efficiency to the perovskite crystal modulation effects and their improved quality (Guo et al., 2017). Very recently, Sun et al. reported bandgap engineered $Cs_{0.05}MA_{0.95}PbBr_xI_{3-x}$ perovskites with a systematic variation of its bandgap from 1.6 to 1.75 eV by increasing the bromide to iodide ratio. These solar cells demonstrated a record efficiency of 36% under white light-emitting diode and 33.2% under CFL lamp (Sun et al., 2020). Using the similar approach of composition engineering to tune the bandgap of $CH_3NH_3PbI_3$, that is by increasing the bromide to iodide ratio (1.56 eV–1.76 eV), very recently Lim et al. have also reported a power conversion efficiency of 34% under white LED illumination (Lim et al., 2020). Triple cation and triple anion-based perovskite solar cells have also been tested for their efficiency under indoor lighting conditions. Under white LED illumination, CsFAMA triple cation-based devices demonstrated a PCE of 21% (Mica et al., 2020). By adjusting the anion I/Br/Cl content in the $MAPbI_{3-x-y}Br_yCl_x$ composition, the bandgap was tuned from 1.6 to 1.8 eV and record indoor PCE of 36% was demonstrated (Cheng et al., 2019).

TABLE 2 | PCE and V_{oc} of some typical halide perovskite-based indoor photovoltaics with different functional layers and device architecture.

Device configuration	Architecture and functional layers	Voc (V) (indoor)	PCE (indoor)
p-i-n	ITO/PEDOT:PSS/CA- $MAPbI_3$/PCBM/PEIE/Ag Guo et al. (2017)	0.81	28.1
p-i-n	ITO/NiOx/$MAPbI_3$/PCBM/BMIMBF4/PCBM/Ag Li et al. (2018)	0.87	35.2
p-i-n	ITO/NiOx/$MAPbCl_{0.1}I_{2.9}$/PCBM/LiF/Ag Jagadamma et al. (2019)	0.90	23
n-i-p planar	ITO/NbO_x-TiO_2/CsMAPbIBr/Spiro/Au Sun et al. (2020) higher incident input power (0.8 mW/cm^2)	0.999	36.3
p-i-n	ITO/NiO/$MAPbI_{2-x}BrCl_x$/PCBM/BCP/Ag Cheng et al. (2019)	1.03	36.2
n-i-p planar	ITO/TiO_2/$MAPb_{3-x}Br_x$/Spiro/Au Lim et al. (2020)	0.82	34.5
n-i-p (meso)	FTO/TiO_2/m-TiO2/MAPI/Spiro/Au Di Giacomo et al. (2016)	0.350	4.8 (10.6 under one sun)

It should be noted that, among the various perovskite-based IPVs reported so far, this bandgap-tuned composition of 1.8 eV has resulted in the highest Voc (>1 V) under 1,000 lux white LED indoor illumination. Pb-free perovskites are also gaining attention in indoor PV application and a very recent report showed a PCE of 4.5% under white LED illumination (Peng et al., 2020). In **Figure 2D**, the power conversion efficiency of halide perovskite indoor photovoltaics as a function of their composition is provided. **Figure 2D** shows that the $CH_3NH_3PbI_3$ solar cells with interface engineering are giving a comparable performance to bandgap engineered wide-bandgap semiconductors. This implies that there is enough room to improve the PCE of wide-bandgap halide perovskites by interface engineering and modifying the device architecture. To understand the role of device architecture on the Voc loss (and hence on power conversion efficiency), indoor photovoltaic efficiency as a function of different architecture is reviewed in the next section.

This is partly motivated by the report by Raifuku et al., where they showed that, under low light intensity, planar, structure outperforms mesoporous architecture and retains better Voc under low-intensity illumination (Raifuku et al., 2016). The two common device architectures in perovskite solar cells are *n-i-p* and *p-i-n* as shown in **Figures 2E and 2F**. In *n-i-p* configuration, there is mesoporous and planar device configuration. **Table 2** lists a summary of PCE (and Voc) of halide perovskite indoor photovoltaics as a function of device architecture. Both *n-i-p* and *p-i-n* PV device architectures are found to be showing good power conversion efficiencies under indoor lighting. Previously, Lee et al. have reported the significance of selecting different device architectures and the functional layers in maximizing the power output of indoor photovoltaics devices (Lee et al., 2019a). They have noticed that in mesoporous *n-i-p* architecture replacing the Spiro-MeOTAD hole transporting layer with PTAA reduces the output power dramatically and in inverted *p-i-n* architecture, replacing the PEDOT:PSS HTL by Poly-TPD enhances the maximum output power.

CHALLENGES AND FUTURE OUTLOOK

Halide perovskite semiconductors have thus already demonstrated their remarkable potential in realizing highly efficient IPVs. However, along with further efforts toward achieving the theoretically predicted PCE and accelerating their real-life application in IoT systems, the following challenges need to be addressed.

Photo-Induced Phase Segregation

Normally, wide-bandgap halide perovskites are obtained by replacing iodide (I-) ions with bromide (Br-), to form mixed halides. However, when the Br content is more than 20%, halide phase segregation (iodide rich and bromide rich phases) occurs upon photoexcitation of mixed halide perovskites (Hoke et al., 2015). The iodide-rich regions act as traps for photogenerated carriers and limit the open-circuit voltage in the corresponding solar cells. So, the advantage of the wide bandgap is not reflected in the open-circuit voltage of the IPV as expected (Yang et al., 2018). The voltage deficit can be expressed as $V_{deficit} = \frac{E_g}{q} - V_{oc}$. The additive strategy and 3D/2D heterostructure are found to be promising to suppress the phase segregation effects and hence to overcome the V_{oc} loss (Tong et al., 2020).

Stability and Pb Toxicity

Like outdoor perovskite solar cells, the indoor perovskite solar cells should also demonstrate high stability and robust encapsulation to prevent any Pb leakage to the indoor ambient. Compared to outdoor conditions, inside the buildings, these devices are exposed to mild weather conditions in terms of temperature and humidity. Even though extensive stability characterization standards are available for outdoor solar cells, no standard stability test conditions exist for indoor photovoltaics and a new stability standard has to be developed for indoor photovoltaics (Khenkin et al., 2020).

S-Shape Challenge

In indoor photovoltaic devices using metal oxide transport layers such as SnO_2, TiO_2, ZnO, there is a possibility that these devices suffer s-shape challenge (light soaking effect) limiting the power conversion efficiency (Jiang et al., 2018; Yan et al., 2017). These metal oxide layers have defects which are filled during the 1 Sun measurement due to the UV-spectral component and high incident light intensity. However, since indoor light has no UV-spectral component and low intensity, the s-shape challenge is more critical for indoor photovoltaics. More research efforts would need to develop metal oxide charge-transporting layers suitable for indoor applications and need no UV excitation to fill the trap states.

V_{oc} Loss

Voltage loss of the indoor perovskite photovoltaic devices is much higher compared to the outdoor 1 Sun solar cell devices. Comparing the optimum bandgap differences (1.4 eV vs. 1.9 eV), presently, the Voc loss is more than 1 V for the indoor PVs even if the intensity differences are accounted. One main reason is that wide-bandgap perovskite solar cells usually suffer from high Voc losses with respect

to their theoretical limit (Mahesh et al., 2020). There should be more research efforts to enhance the Voc improvement of indoor perovskite solar cells to achieve the theoretically predicted maximum power conversion efficiency of 50%–60%.

AUTHOR CONTRIBUTIONS

LJ designed the manuscript and wrote the substantial part of the manuscript, and SW also contributed to writing. Both authors agree with the content of the work.

FUNDING

LJ acknowledges the funding through the UKRI-Future Leaders Fellowship (MR/T022094/1).

ACKNOWLEDGMENTS

LJ acknowledges Julia Payne, School of Chemistry, University of St Andrews, for providing the crystal structure of halide perovskites.

REFERENCES

Chen, C.-Y., Chang, J.-H., Chiang, K.-M., Lin, H.-L., Hsiao, S.-Y., and Lin, H.-W. (2015). Perovskite photovoltaics for dim-light applications. *Adv. Funct. Mater.* 25, 7064–7070. doi:10.1002/adfm.201503448

Chen, F.-C. (2019). Emerging organic and organic/inorganic hybrid photovoltaic devices for specialty applications: low-level-lighting energy conversion and biomedical treatment. *Adv. Opt. Mater.* 7, 1800662. doi:10.1002/adom.201800662

Cheng, R., Chung, C. C., Zhang, H., Liu, F., Wang, W. T., Zhou, Z., et al. (2019). Tailoring triple-anion perovskite material for indoor light harvesting with restrained halide segregation and record high efficiency beyond 36%. *Adv. Energy Mater.* 9, 1901980. doi:10.1002/aenm.201901980

Dagar, J., Castro-Hermosa, S., Lucarelli, G., Cacialli, F., and Brown, T. M. (2018). Highly efficient perovskite solar cells for light harvesting under indoor illumination via solution processed SnO2/MgO composite electron transport layers. *Nano Energy* 49, 290–299. doi:10.1016/j.nanoen.2018.04.027

Davies, R. (2015). The internet of things opportunities and challenges. Available at: https://www.europarl.europa.eu/RegData/etudes/BRIE/2015/557012/EPRS_BRI(2015)557012_EN.pdf.

Di Giacomo, F., Zardetto, V., Lucarelli, G., Cinà, L., Di Carlo, A., Creatore, M., et al. (2016). Mesoporous perovskite solar cells and the role of nanoscale compact layers for remarkable all-round high efficiency under both indoor and outdoor illumination. *Nano Energy* 30, 460–469. doi:10.1016/j.nanoen.2016.10.030

Elumalai, N., Mahmud, M., Wang, D., and Uddin, A. (2016). Perovskite solar cells: progress and advancements. *Energies* 9, 861. doi:10.3390/en9110861

Goo, J. S., Shin, S.-C., You, Y.-J., and Shim, J. W. (2018). Polymer surface modification to optimize inverted organic photovoltaic devices under indoor light conditions. *Solar Energ. Mater. Solar Cell* 184, 31–37. doi:10.1016/j.solmat.2018.04.023

Grätzel, M. (2014). The light and shade of perovskite solar cells. *Nat. Mater.* 13, 838–842. doi:10.1038/nmat4065

Green, M. A., Jiang, Y., Soufiani, A. M., and Ho-Baillie, A. (2015). Optical properties of photovoltaic organic-inorganic lead halide perovskites. *J. Phys. Chem. Lett.* 6, 4774–4785. doi:10.1021/acs.jpclett.5b01865

Green, M. A. (1981). Solar cell fill factors: general graph and empirical expressions. *Solid-State Electron.* 24, 788–789. doi:10.1016/0038-1101(81)90062-9

Guo, Y., Sato, W., Shoyama, K., Halim, H., Itabashi, Y., Shang, R., et al. (2017). Citric Acid modulated growth of oriented lead perovskite crystals for efficient solar cells. *J. Am. Chem. Soc.* 139, 9598–9604. doi:10.1021/jacs.7b03856

He, X., Qiu, Y., and Yang, S. (2017). Fully-inorganic trihalide perovskite nanocrystals: a new research frontier of optoelectronic materials. *Adv. Mater.* 29, 1700775. doi:10.1002/adma.201700775

Ho, J. K. W., Yin, H., and So, S. K. (2020). From 33% to 57%-An elevated potential of efficiency limit for indoor photovoltaics. *J. Mater. Chem. A* 8, 1717–1723. doi:10.1039/c9ta11894b

Hoke, E. T., Slotcavage, D. J., Dohner, E. R., Bowring, A. R., Karunadasa, H. I., and McGehee, M. D. (2015). Reversible photo-induced trap formation in mixed-halide hybrid perovskites for photovoltaics. *Chem. Sci.* 6, 613–617. doi:10.1039/c4sc03141e

Hu, Z., Lin, Z., Su, J., Zhang, J., Chang, J., and Hao, Y. (2019). A review on energy band-gap engineering for perovskite photovoltaics. *Sol. RRL* 3, 1900304–1900309. doi:10.1002/solr.201900304

Huang, H., Bodnarchuk, M. I., Kershaw, S. V., Kovalenko, M. V., and Rogach, A. L. (2017). Lead halide perovskite nanocrystals in the research spotlight: stability and defect tolerance. *ACS Energy Lett.* 2, 2071–2083. doi:10.1021/acsenergylett.7b00547

Huang, J., Xiang, S., Yu, J., and Li, C.-Z. (2019). Highly efficient prismatic perovskite solar cells. *Energy Environ. Sci.* 12, 929–937. doi:10.1039/c8ee02575d

integral-led.com. Available at: https://integral-led.com/education/warm-white-or-c.

Jagadamma, L. K., Blaszczyk, O., Sajjad, M. T., Ruseckas, A., and Samuel, I. D. W. (2019). Efficient indoor p-i-n hybrid perovskite solar cells using low temperature solution processed NiO as hole extraction layers. *Solar Energ. Mater. Solar Cell* 201, 110071. doi:10.1016/j.solmat.2019.110071

Jena, A. K., Kulkarni, A., and Miyasaka, T. (2019). Halide perovskite photovoltaics: background, status, and future prospects. *Chem. Rev.* 119, 3036–3103. doi:10.1021/acs.chemrev.8b00539

Jiang, Z., Soltanian, S., Gholamkhass, B., Aljaafari, A., and Servati, P. (2018). Light-soaking free organic photovoltaic devices with sol-gel deposited ZnO and AZO electron transport layers. *RSC Adv.* 8, 36542–36548. doi:10.1039/C8RA07071G

Kang, J., and Wang, L. W. (2017). High defect tolerance in lead halide perovskite CsPbBr3. *J. Phys. Chem. Lett.* 8, 489–493. doi:10.1021/acs.jpclett.6b02800

Khenkin, M. V., Katz, E. A., Abate, A., Bardizza, G., Berry, J. J., Brabec, C., et al. (2020). Consensus statement for stability assessment and reporting for perovskite photovoltaics based on ISOS procedures. *Nat. Energ.* 5, 35–49. doi:10.1038/s41560-019-0529-5

Koster, L. J. A., Mihailetchi, V. D., Ramaker, R., and Blom, P. W. M. (2005). Light intensity dependence of open-circuit voltage of polymer:fullerene solar cells. *Appl. Phys. Lett.* 86, 123509–123513. doi:10.1063/1.1889240

Kramp, T., van Kranenburg, R., and Lange, S. (2013). Introduction to the internet of things. Berlin, Germany: Springer.

Lee, H. K. H., Barbé, J., Meroni, S. M. P., Du, T., Lin, C.-T., Pockett, A., et al. (2019a). Outstanding indoor performance of perovskite photovoltaic cells - effect of device architectures and interlayers. *Sol. RRL* 3, 1800207. doi:10.1002/solr.201800207

Lee, H. K. H., Barbé, J., and Tsoi, W. C. (2019b). *Organic and perovskite photovoltaics for indoor applications*. Amsterdam, The Netherlands: Elsevier.

Li, M., Igbari, F., Wang, Z. K., and Liao, L. S. (2020). Indoor thin-film photovoltaics: progress and challenges. *Adv. Energ. Mater.* 10, 2000641. doi:10.1002/aenm.202000641

Li, M., Zhao, C., Wang, Z. K., Zhang, C. C., Lee, H. K. H., Pockett, A., et al. (2018). Interface modification by ionic liquid: a promising candidate for indoor light harvesting and stability improvement of planar perovskite solar cells. *Adv. Energ. Mater.* 8, 1801509. doi:10.1002/aenm.201801509

Lim, J. W., Kwon, H., Kim, S. H., You, Y. J., Goo, J. S., Ko, D. H., et al. (2020). Unprecedentedly high indoor performance (efficiency > 34 %) of perovskite photovoltaics with controlled bromine doping. *Nano Energy* 75, 104984. doi:10.1016/j.nanoen.2020.104984

Lucarelli, G., Di Giacomo, F., Zardetto, V., Creatore, M., and Brown, T. M. (2017). Efficient light harvesting from flexible perovskite solar cells under indoor white light-emitting diode illumination. *Nano Res.* 10, 2130–2145. doi:10.1007/s12274-016-1402-5

Mahesh, S., Ball, J. M., Oliver, R. D. J., McMeekin, D. P., Nayak, P. K., Johnston, M. B., et al. (2020). Revealing the origin of voltage loss in mixed-halide perovskite solar cells. *Energ. Environ. Sci.* 13, 258–267. doi:10.1039/c9ee02162k

Mathews, I., Kantareddy, S. N., Buonassisi, T., and Peters, I. M. (2019). Technology and market perspective for indoor photovoltaic cells. *Joule* 3, 1415–1426. doi:10.1016/j.joule.2019.03.026

Mhaisalkar, S. G., Mathews, N., Bolink, H. J., and Bahulayan, D. (2020). Advances in perovskite optoelectronics: bridging the gap between laboratory and fabrication. *Adv. Energ. Mater.* 10, 2000393. doi:10.1002/aenm.202000393

Mica, N. A., Bian, R., Manousiadis, P., Jagadamma, L. K., Tavakkolnia, I., Haas, H., et al. (2020). Triple-cation perovskite solar cells for visible light communications. *Photon. Res.* 8, A16–A24. doi:10.1364/prj.393647

Minnaert, B., and Veelaert, P. (2014). A proposal for typical artificial light sources for the characterization of indoor photovoltaic applications. *Energies* 7, 1500–1516. doi:10.3390/en7031500

Miyasaka, T., Kulkarni, A., Kim, G. M., Öz, S., and Jena, A. K. (2020). Perovskite solar cells: can we go organic-free, lead-free, and dopant-free? *Adv. Energ. Mater.* 10, 1902500. doi:10.1002/aenm.201902500

Müller, M. F., Freunek, M., and Reindl, L. M. (2013). Maximum efficiencies of indoor photovoltaic devices. *IEEE J. Photovoltaics* 3, 59–64. doi:10.1109/JPHOTOV.2012.2225023

Olthof, S. (2016). Research Update: the electronic structure of hybrid perovskite layers and their energetic alignment in devices. *APL Mater.* 4, 091502. doi:10.1063/1.4960112

Park, N.-G. (2015). Perovskite solar cells: an emerging photovoltaic technology. *Mater. Today* 18, 65–72. doi:10.1016/j.mattod.2014.07.007

Peng, Y., Huq, T. N., Mei, J., Portilla, L., Jagt, R. A., Occhipinti, L. G., et al. (2020). Lead-free perovskite-inspired absorbers for indoor photovoltaics. *Adv. Energ. Mater.* 11, 2002761. doi:10.1002/aenm.202002761

Raifuku, I., Ishikawa, Y., Ito, S., and Uraoka, Y. (2016). Characteristics of perovskite solar cells under low-illuminance conditions. *J. Phys. Chem. C* 120, 18986–18990. doi:10.1021/acs.jpcc.6b05298

Ravi, V. K., Markad, G. B., and Nag, A. (2016). Band edge energies and excitonic transition probabilities of colloidal CsPbX3 (X = Cl, Br, I) perovskite nanocrystals. *ACS Energ. Lett.* 1, 665–671. doi:10.1021/acsenergylett.6b00337

Shockley, W., and Queisser, H. J. (1961). Detailed balance limit of efficiency of p-n junction solar cells. *J. Appl. Phys.* 32, 510–519. doi:10.1063/1.1736034

Steim, R., Ameri, T., Schilinsky, P., Waldauf, C., Dennler, G., Scharber, M., et al. (2011). Organic photovoltaics for low light applications. *Solar Energ. Mater. Solar Cell* 95, 3256–3261. doi:10.1016/j.solmat.2011.07.011

Stoumpos, C. C., and Kanatzidis, M. G. (2015). The renaissance of halide perovskites and their evolution as emerging semiconductors. *Acc. Chem. Res.* 48, 2791–2802. doi:10.1021/acs.accounts.5b00229

Sun, H., Deng, K., Jiang, Y., Ni, J., Xiong, J., and Li, L. (2020). Realizing stable Artificial photon energy harvesting based on perovskite solar cells for diverse applications. *Small* 16, 1906681. doi:10.1002/smll.201906681

Tao, S., Schmidt, I., Brocks, G., Jiang, J., Tranca, I., Meerholz, K., et al. (2019). Absolute energy level positions in tin- and lead-based halide perovskites. *Nat. Commun.* 10, 2560. doi:10.1038/s41467-019-10468-7

Tong, J., Jiang, Q., Zhang, F., Kang, S. B., Kim, D. H., and Zhu, K. (2020). Wide-bandgap metal halide perovskites for tandem solar cells. *ACS Energ. Lett.* 6, 232–248. doi:10.1021/acsenergylett.0c02105

Walsh, A. (2015). Principles of chemical bonding and band gap engineering in hybrid organic-inorganic halide perovskites. *J. Phys. Chem. C* 119, 5755–5760. doi:10.1021/jp512420b

Wu, Y., Chen, W., Chen, G., Liu, L., He, Z., and Liu, R. (2018). The impact of hybrid compositional film/structure on organic-inorganic perovskite solar cells. *Nanomaterials* 8, 356–427. doi:10.3390/nano8060356

Yan, Y., Cai, F., Yang, L., Li, J., Zhang, Y., Qin, F., et al. (2017). Light-soaking-free inverted polymer solar cells with an efficiency of 10.5% by compositional and surface modifications to a low-temperature-processed TiO2electron-transport layer. *Adv. Mater.* 29. doi:10.1002/adma.201604044

Yang, T. C.-J., Fiala, P., Jeangros, Q., and Ballif, C. (2018). High-bandgap perovskite materials for multijunction solar cells. *Joule* 2, 1421–1436. doi:10.1016/j.joule.2018.05.008

Conflict of Interest: The authors declare that the research was conducted in the absence of any commercial or financial relationships that could be construed as a potential conflict of interest.

Copyright © 2021 Jagadamma and Wang. This is an open-access article distributed under the terms of the Creative Commons Attribution License (CC BY). The use, distribution or reproduction in other forums is permitted, provided the original author(s) and the copyright owner(s) are credited and that the original publication in this journal is cited, in accordance with accepted academic practice. No use, distribution or reproduction is permitted which does not comply with these terms.

frontiers in Chemistry

REVIEW
published: 15 April 2021
doi: 10.3389/fchem.2021.637501

Recent Advances in TiO_2-Based Heterojunctions for Photocatalytic CO_2 Reduction With Water Oxidation: A Review

Kai Li[1,2], *Chao Teng*[1]*, *Shuang Wang*[1,3] *and Qianhao Min*[2]*

[1]Institute of Marine Biomedicine, Shenzhen Polytechnic, Shenzhen, China, [2]State Key Laboratory of Analytical Chemistry for Life Science, School of Chemistry and Chemical Engineering, Nanjing University, Nanjing, China, [3]College of Engineering and Applied Sciences, Nanjing University, Nanjing, China

OPEN ACCESS

Edited by:
Ping Yu,
Institute of Chemistry, China

Reviewed by:
Chang-Yong Nam,
Brookhaven National Laboratory,
United States
Yuqing Lin,
Capital Normal University, China
Limin Zhang,
East China Normal University, China

***Correspondence:**
Chao Teng
tengchao@szpt.edu.cn
Qianhao Min
minqianhao@nju.edu.cn

Specialty section:
This article was submitted to Green and Sustainable Chemistry, a section of the journal Frontiers in Chemistry

Received: 03 December 2020
Accepted: 01 February 2021
Published: 15 April 2021

Citation:
Li K, Teng C, Wang S and Min Q (2021) Recent Advances in TiO_2-Based Heterojunctions for Photocatalytic CO_2 Reduction With Water Oxidation: A Review. Front. Chem. 9:637501. doi: 10.3389/fchem.2021.637501

Photocatalytic conversion of CO_2 into solar fuels has gained increasing attention due to its great potential for alleviating the energy and environmental crisis at the same time. The low-cost TiO_2 with suitable band structure and high resistibility to light corrosion has proven to be very promising for photoreduction of CO_2 using water as the source of electrons and protons. However, the narrow spectral response range (ultraviolet region only) as well as the rapid recombination of photo-induced electron-hole pairs within pristine TiO_2 results in the low utilization of solar energy and limited photocatalytic efficiency. Besides, its low selectivity toward photoreduction products of CO_2 should also be improved. Combination of TiO_2 with other photoelectric active materials, such as metal oxide/sulfide semiconductors, metal nanoparticles and carbon-based nanostructures, for the construction of well-defined heterostructures can enhance the quantum efficiency significantly by promoting visible light adsorption, facilitating charge transfer and suppressing the recombination of charge carriers, resulting in the enhanced photocatalytic performance of the composite photocatalytic system. In addition, the adsorption and activation of CO_2 on these heterojunctions are also promoted, therefore enhancing the turnover frequency (TOF) of CO_2 molecules, so as to the improved selectivity of photoreduction products. This review focus on the recent advances of photocatalytic CO_2 reduction via TiO_2-based heterojunctions with water oxidation. The rational design, fabrication, photocatalytic performance and CO_2 photoreduction mechanisms of typical TiO_2-based heterojunctions, including semiconductor-semiconductor (S-S), semiconductor-metal (S-M), semiconductor-carbon group (S-C) and multicomponent heterojunction are reviewed and discussed. Moreover, the TiO_2-based phase heterojunction and facet heterojunction are also summarized and analyzed. In the end, the current challenges and future prospects of the TiO_2-based heterostructures for photoreduction of CO_2 with high efficiency, even for practical application are discussed.

Keywords: TIO_2-based photocatalysts, heterostructures, CO_2 photoreduction, water oxidation, high efficiency

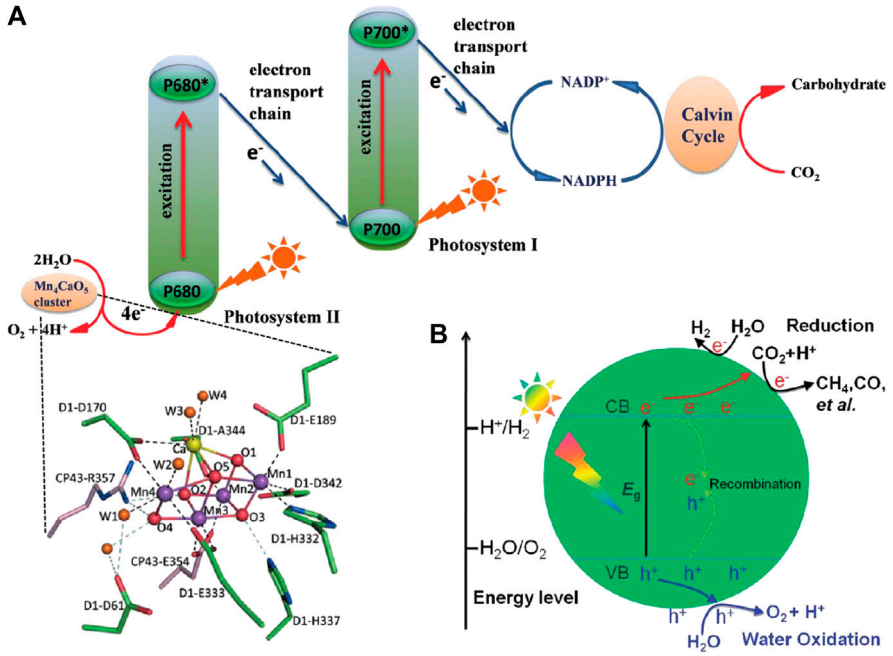

FIGURE 1 | Schematic diagrams of **(A)** natural photosynthesis and **(B)** semiconductor photocatalytic reduction of CO_2. Reproduced from Liu et al. (2016) with permission from Wiley-VCH and Wei et al. (2018) with permission from the Royal Society of Chemistry.

INTRODUCTION

Energy and environmental crizes are two major bottlenecks restricting the sustainable development of human society. For a long time, the excessive consumption of fossil fuels has caused severe energy shortages, and the CO_2 released during the combustion process has become the main factor leading to global warming (Stott et al., 2000; Meinshausen et al., 2009; Solomon et al., 2009; Höök and Tang, 2013). It is urgent to develop and utilize renewable clean energy while reducing the concentration of CO_2 in the atmosphere (Brockway et al., 2019; Shindell and Smith, 2019). Notably, as a simple form of carbon storage, the rich carbon resources contained in CO_2 have huge development potential. Using CO_2 as a carbon feedstock to prepare carbon-based fuels can help alleviate the energy crisis and global warming at the same time, and has become a current research hotspot in the fields of both energy and environment (Olah et al., 2011; Kondratenko et al., 2013; Aresta et al., 2014; Ganesh, 2014; Li et al., 2019). However, the liner molecule with high thermodynamic stability and kinetic inertness makes it a great challenge for the activation and conversion of CO_2 (Ola and Maroto-Valer, 2015; Wei L. et al., 2018; Li et al., 2019; Nguyen et al., 2020). A lot of energy needs to be injected to break the C=O bond (dissociation energy about 750 kJ mol^{-1}) in CO_2 (Kim et al., 2017). Moreover, the extremely low water solubility of CO_2 (about 30 mM under 25°C at 1 atm) results in the low conversion efficiency of CO_2 in the aqueous reaction system (Xie et al., 2014). Therefore, a highly efficient reaction mode is also in great demand.

TABLE 1 | The possible reactions during the photocatalytic CO_2 reduction process.

	Reactions	ΔG^0 (kJ·mol^{-1})
1	$H_2O\ (l) \rightarrow H_2\ (g) + 1/2O_2\ (g)$	237
2	$CO_2\ (g) \rightarrow CO\ (g) + 1/2O_2\ (g)$	257
3	$CO_2\ (g) + H_2O\ (l) \rightarrow HCOOH\ (l) + 1/2O_2\ (g)$	286
4	$CO_2\ (g) + H_2O\ (l) \rightarrow HCHO\ (l) + O_2\ (g)$	522
5	$CO_2\ (g) + 2H_2O\ (l) \rightarrow CH_3OH\ (l) + 3/2O_2\ (g)$	703
6	$CO_2\ (g) + 2H_2O\ (l) \rightarrow CH_4\ (g) + 2O_2\ (g)$	818

Fortunately, the natural photosynthesis motivated by solar energy to covert CO_2 into carbonhydrates as well as the release of O_2 by water oxidation provides a very promising solution to reduce the CO_2 level in atmosphere, which inspires the development of artificial photosynthesis systems (Barber, 2009; Dogutan and Nocera, 2019; Zhang and Sun, 2019). As shown in **Figure 1A**, the water oxidation process takes place in the photosystem II (PSII) of green plants to provide electrons and protons for the CO_2 fixation and conversion in the photosystem I (PSI). Since a series of pioneering works devoted by Fujishima and Honda on semiconductor photocatalysis in the 1970s (Fujishima and Honda, 1972; Inoue et al., 1979), substantial efforts have been made for the combination of the two individual processes within a single artificial architecture to mimic the natural photosynthesis (shown in **Figure 1B**) during the past decades (Ma et al., 2014; Tu et al., 2014; White et al., 2015; Liu X. et al., 2016; Li et al., 2019; Xu and Carter, 2019).

TABLE 2 | Electrochemical potentials of H_2O oxidation and CO_2 reduction into various products.

	Reactions	E^0 (V) *vs.* NHE at pH 7
1	$2H_2O + 4h^+ \rightarrow O_2 + 4H^+$	1.23
2	$CO_2 + e^- \rightarrow CO_2^-$	−1.9
3	$CO_2 + 2H^+ + 2e^- \rightarrow CO + H_2O$	−0.53
4	$CO_2 + 2H^+ + 2e^- \rightarrow HCOOH$	−0.61
5	$CO_2 + 4H^+ + 4e^- \rightarrow HCHO + H_2O$	−0.48
6	$CO_2 + 6H^+ + 6e^- \rightarrow CH_3OH + H_2O$	−0.38
7	$CO_2 + 8H^+ + 8e^- \rightarrow CH_4 + 2H_2O$	−0.24
8	$2H^+ + 2e^- \rightarrow H_2$	−0.41

In a typical semiconductor photocatalytic process, the semiconductor photocatalyst is excited by the incident photons with energy greater than or equal to its bandgap energy (E_g), where electrons (e^-) are excited to the conduction band (CB) to participate in the reduction reactions, remaining holes (h^+) in the valence band (VB) for the oxidation reactions. Considering that CO_2 molecule is very stable and the photocatalytic CO_2 reduction is a series of uphill reactions ($\Delta G^0>0$, see in **Table 1**) (Wei L. et al., 2018), a large energy input is necessary to covert CO_2 into solar fuels, corresponding to the photons in the ultraviolet or shortwave visible regions. In addition, the band structure of ideal semiconductors needs to meet the redox potentials of CO_2 reduction and water oxidation reactions at the same time, as listed in **Table 2** (Habisreutinger et al., 2013; White et al., 2015). Generally, the CB edge position (E_{CB}) should be more negative than the potential for reducing CO_2, whereas the VB edge position (E_{VB}) should be more positive than the potential for oxidizing H_2O to O_2. So far, the photocatalytic activity of numerous photocatalysts, etc. TiO_2 (Habisreutinger et al., 2013; Ma et al., 2014; Ola and Maroto-Valer, 2015), ZnO (Lee K. M. et al., 2016; Nie et al., 2018; Kegel et al., 2018), WO_3 (Chen et al., 2012; Shi et al., 2019; Wang H. et al., 2019), SnO_2 (He et al., 2015; You et al., 2020), Cu_2O (An et al., 2014; Shi et al., 2019), CdS (Kuai et al., 2015; Kuehnel et al., 2017; Wei Z. H. et al., 2018; Bie et al., 2019; Low et al., 2019), Bi_2WO_6 (Cao et al., 2018; Liu et al., 2021), $BiVO_4$ (Mao et al., 2012; Wei Z. H. et al., 2018), BiOBr (Ye et al., 2016; Wu et al., 2018), g-C_3N_4 (He et al., 2015; Nie et al., 2018; Thi Thanh Truc et al., 2019; Wang et al., 2020a) and graphene (An et al., 2014; Xiong et al., 2016; Shehzad et al., 2018a; Zhao H. et al., 2018; Bie et al., 2019), have been investigated intensively, in which few of them can realize the synergism of photocatalytic CO_2 reduction and water oxidation. In particular, the low-cost TiO_2 with suitable band structure and high resistibility to light corrosion is a very promising candidate, which has become the benchmark in this field (Habisreutinger et al., 2013; Ma et al., 2014; Ola and Maroto-Valer, 2015). However, the wide band gap of TiO_2 (3.2 eV for anatase) responses to UV light only, which accounts for only 3–5% of the incoming solar spectrum, thus restricting the conversion efficiency of solar energy. Besides, the fast recombination of photo-induced e^-/h^+ pairs within TiO_2 results in the low charge separation efficiency, therefore reducing its photocatalytic performance further. Moreover, the low selectivity toward photoreduction products of CO_2 based on aqueous TiO_2 suspension photocatalytic system should also be improved.

In the past few decades, various of strategies have been developed to enhance the photocatalytic performance of TiO_2. Among them, the nanostructured TiO_2 with single crystalline phase exhibited the decreased recombination rate of charge carriers, comparing to the polycrystalline samples that possess large amount of grain boundaries and defects acting as recombination centers (Tu et al., 2014; Xu et al., 2015). Moreover, crystal facet engineering has been adopted to tune the surface energy and active sites of TiO_2, contributing to the adsorption and activation of CO_2 (Liu L. et al., 2016; Xiong et al., 2018; Tu et al., 2020). Obviously, the preference adsorption of CO_2 molecules at the surface oxygen vacancy sites of TiO_2 can reduce the reactive barrier of CO_2 photoreduction reactions, in which one oxygen atom of CO_2 is trapped by a bridging oxygen vacancy defect to induce affinity interactions (Lee et al., 2011; Liu L. et al., 2016; Tan et al., 2017). Moreover, the localized electrons of oxygen vacancies can form adventitious energy levels, extending the photoresponsive range of semiconductor photocatalyst. Besides, surface oxygen vacancies with typical defect states can trap electrons or holes to inhibit their recombination (Wang et al., 2018). To sum up, the significance of surface oxygen vacancies on defected TiO_2 has been ascertained in the enhancement of CO_2 adsorption, activation, dissolution, and stabilization of reaction intermediates (Nguyen et al., 2020). In addition, metal/nonmetal ion doping is used to introduce additional energy level between the band gap of TiO_2, resulting in the reduced band width and enhanced visible light adsorption (Tu et al., 2014; Ola and Maroto-Valer, 2015; Shehzad et al., 2018b; Patil et al., 2019). Dye sensitized TiO_2 displays enhanced photoreduction efficiency of CO_2 due to the injection of photosensitized electrons from the energy level of dye molecule to the CB of TiO_2 with more negative potential, while the superior visible light responsibility of dye molecules can also improve the utilization of incident light (Ma et al., 2014; Ola and Maroto-Valer, 2015; Lee J. S. et al., 2016; Woo et al., 2019). Although these strategies have proven to be effective, the charge separation efficiency, light energy utilization and product selectivity still need to be further improved to fulfill the demand of more efficient photoreduction of CO_2, even for the practical application in the future.

As is known, construction of heterojunction between TiO_2 and cocatalyst with matching electronic band structures can significantly promote the separation of photogenerated e^- and h^+, enlarge the spectra response range, while the physicochemical properties of some special cocatalyst can promote the photocatalytic CO_2 reduction or water oxidation to a certain extent, thereby resulting in high photoreduction efficiency of CO_2 over the heterostructured phocatalytic system with enhanced reduction products selectivity (Ma et al., 2014; Wang et al., 2014; Wei L. et al., 2018; Nguyen et al., 2020).

In addition to photocatalysts, photoreactors as well as reaction modes also play vital roles in affecting the photoreduction efficiency of CO_2. Generally, the two key parameters which determine the types of photoreactors

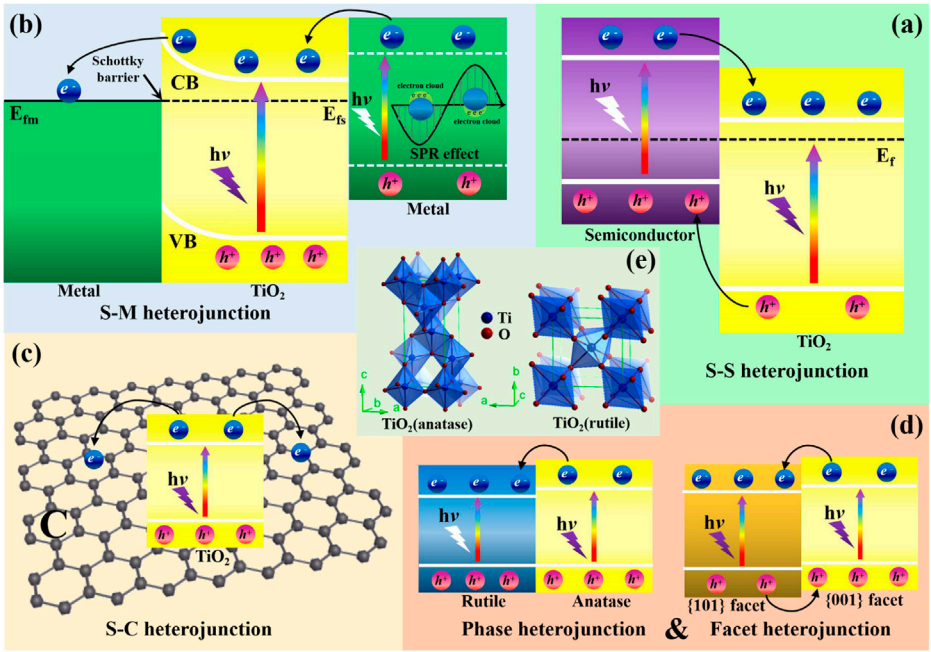

FIGURE 2 | Separation and transfer of photogenerated charge carriers in the TiO_2-based **(A)** S-S heterojunction, **(B)** S-M heterojunction, **(C)** S-C heterojunction and **(D)** phase and facet heterojunction; **(E)** Crystalline structures of TiO_2 (anatase) and TiO_2 (rutile).

utilized in CO_2 photoreduction are the phases involved (i.e., gas-solid, liquid-solid) and the mode of operation (i.e., batch, semi-batch or continuous). In the solid-liquid cases, photocatalysts are usually dispersed in alkaline mediums (aqueous solution) which can realize higher CO_2 solubility, resulting in the formation of CO_3^{2-} and HCO_3^-. However, these species are difficult to be reduced in comparison with CO_2 (Corma and Garcia, 2013). In order to overcome the above drawbacks, the solid-vapor mode has been widely applied where the generation rate of the products for CO_2 photoreduction can be improved significantly (Xie et al., 2014; Xie et al., 2016; Xiong et al., 2017b). In addition, the exposure of photocatalysts in a CO_2 atmosphere can reduce the generation of H_2, thus enhancing the selectivity for CO_2 reduction. Obviously, the solid-vapor mode is more suitable for CO_2 photoreduction in the presence of H_2O.

In this review, we will mainly focus on the recent advances of photocatatytic CO_2 reduction processes with water oxidation using TiO_2-based heterojunction as photocatalysts. Different categories of heterojunctions, including S-S heterojunction (**Figure 2A**), S-M heterojunction (**Figure 2B**), S-C heterojunction (**Figure 2C**), multicomponent heterojunction, phase heterojunction and facet heterojunction (**Figure 2D**) are reviewed individually. In addition, the unique functions of cocatalysts among different heterostructured photocatalytic systems (etc. photosensitizer, CO_2 reduction promoter, water oxidation promoter and surface plasmon resonance (SPR) source) as well as the photoreduction mechanisms of CO_2 are discussed in detail. In the end, we will look forward to the prospects, opportunities and challenges of photocatalytic CO_2 reduction, predict the research directions of this field in the future, and put forward our opinions on the construction of efficient multifunctional integrated photocatalytic CO_2 reduction systems. We believe that this review will provide some useful guidelines for the construction of heterostructured photocatalysts for photoreduction of CO_2 with high performance in the future.

PHOTOREDUCTION OF CO_2 TO SOLAR FUELS ON TIO_2-BASED HETEROJUNCTIONS

From the perspective of semiconductor photocatalysis, the premise of high photocatalytic efficiency is the efficient separation and rapid transfer of photogenerated e^-/h^+ pairs, thereby prolonging their lifetimes and inhibiting their recombination. The strategy for the construction of heterojunction by coupling semiconductor (TiO_2) with a secondary substance including other semiconductors (Aguirre et al., 2017; Yang et al., 2017; She et al., 2018; Xu et al., 2018a; Jin et al., 2019; Low et al., 2019; Thi Thanh Truc et al., 2019; Wu et al., 2019), metal nanoparticles (Xie et al., 2013; Neațu et al., 2014; Jiao et al., 2015; Xiong et al., 2015; Lee K. Y. et al., 2016; Yu et al., 2016; Cheng et al., 2017; Tahir et al., 2017; Xiong et al., 2017C; Chong et al., 2018; Low et al., 2018; Tan et al., 2018; Tasbihi et al., 2018a; Wei Y. et al., 2018; Zhao Y. et al., 2018; Khatun et al., 2019; Wang R. et al., 2019; Zeng et al., 2020; Ziarati et al., 2020; Wang et al., 2021) and carbon-

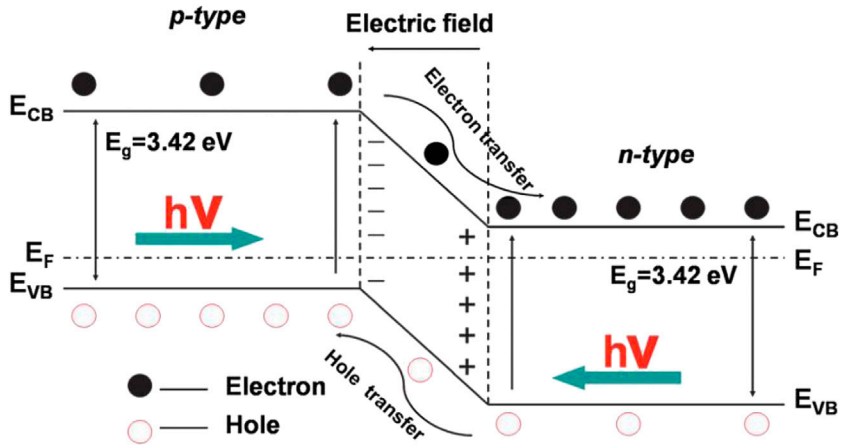

FIGURE 3 | Schematic diagram showing the energy band structure and electron-hole pair separation in the p-n heterojunction. Reproduced from Wang et al. (2014) with permission from the Royal Society of Chemistry.

based nanostructures (Xia et al., 2007; Tu et al., 2013; Gui et al., 2014; Chowdhury et al., 2015; Xiong et al., 2016; Lin et al., 2017; Tan et al., 2017; Wang et al., 2017; Li et al., 2018; Olowoyo et al., 2018; Shehzad et al., 2018a; Zhang J. et al., 2018; Zubair et al., 2018; Bie et al., 2019; Olowoyo et al., 2019; Wang R. et al., 2019; Rodríguez et al., 2020) has been generally applied. Since different phases (etc. anatase, brookite, or rutile) and exposed facets (etc. (001) or (101)) of TiO_2 exhibit various of band structure and reactivity, TiO_2-based phase heterojunction (Reñones et al., 2016; Hwang et al., 2019; Jin et al., 2019; Chen et al., 2020; Lee J. S. et al., 2016; Xiong et al., 2020) or facet heterojunction (Yu et al., 2014; Cao et al., 2016; Liu L. et al., 2016; Xiong et al., 2016; Xiong et al., 2017a; Di Liberto et al., 2019) are also fabricated for photocatalytic CO_2 reduction, which exhibits enhanced photocatalytic efficiency in comparison with pristine TiO_2. On the one hand, the heterostructure facilitates the separation of photoinduced charge carriers which then transfer across the heterointerface to restrain recombination. On the other hand, the additional active sites introduced by the cocatalysts favor for the adsorption and activation of CO_2, thus enhancing the photoreduction efficiency of CO_2. Besides, the promoted quantum efficiency and product selectivity can also be expected by the constructed heterojunctions, since light-excitation attributes, band structure, and separation efficiency of photogenerated charge carriers of heterojunctions play vital roles in the selectivity of CO_2 photoreduction products. Moreover, various cocatalysts with different reactive active sites can also affect the product selectivity greatly, where the adsorption/activation of CO_2 as well as the adsorption/desorption of the intermediates are tuned (Fu et al., 2019).

In this section, the rational design, fabrication, photocatalytic performance and photoreduction mechanism of CO_2 over the TiO_2-based typical categories of heterojunctions (S-S, S-M, S-C, multicomponent, phase and facet heterojunction) will be reviewed and discussed in detail. In addition, the selectivity toward photoreduction products is another focus. The relative mechanism was concluded and analyzed in the certain case.

TiO_2 Based Z-scheme S-S Heterojunction for CO_2 Photoreduction

Coupling n-type TiO_2 with a p-type semiconductor possessing matching energy band structure to form a p-n heterojunction is one of the most classic S-S heterojunction (Zeng et al., 2014; Aguirre et al., 2017; Lee et al., 2017; Zhang L. et al., 2018; Iqbal et al., 2020; Zhang et al., 2020). As shown in **Figure 3**, the contacting of the two semiconductors leads to the diffusion of e^- and h^+, then forms a space-charge region at the interface of the p-n heterojunction (Wang et al., 2014). As a result, a strong built-in electrical field is created which can drive the photoinduced e^- and h^+ to transfer in the opposite directions, therefore enhancing the separation efficiency of charge carriers. In addition to p-n heterojunction, TiO_2-based non-p-n heterojunctions are also common (Yang et al., 2017; She et al., 2018; Jin et al., 2019; Low et al., 2019; Thi Thanh Truc et al., 2019; Wu et al., 2019). Typically, two closely integrated semiconductors with staggered band configurations can form a type II-1 heterojunction (shown in **Figure 4A**) (Zhang and Jaroniec, 2018), in which the band bending facilitates the charge transfer at the heterointerface. Specifically, e^- and h^+ are separated individually in both semiconductor 1 (SC-1) and semiconductor 2 (SC-2) under the irradiation of incident light. The difference in energy level leads to the transfer of e^- from the CB of SC-1 with more negative potential to the CB of SC-2. Meanwhile, h^+ can transfer from the VB of SC-2 to the VB of SC-1 with more positive potential. Similar to the p-n heterojunction, the reverse migration of e^- and h^+ in the type II-1 heterojunction improves the separation efficiency of charge carriers, thus endowing the enhanced photocatalytic performance of the heterostructured system. However, the way of carrier transfer in the above

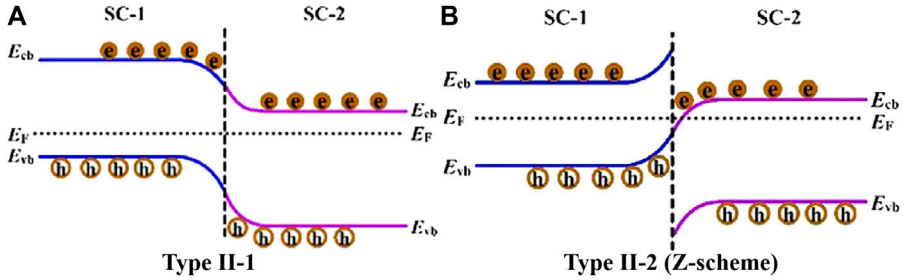

FIGURE 4 | Photogenerated charge carrier transfer process for two types of non p-n heterojunctions: **(A)** type II-1, and **(B)** type II-2 (direct Z-scheme). Reproduced from Zhang and Jaroniec (2018) with permission from Elsevier and Copyright Clearance Center.

heterojunctions will lead to a decrease in their redox ability, making it difficult to ensure the optimal photocatalytic activity.

Recently, study on the construction of all-solid-state Z-scheme heterojunction has gained great attention of researchers (Kuai et al., 2015; Aguirre et al., 2017; Takayama et al., 2017; Yang et al., 2017; She et al., 2018; Low et al., 2019; Thi Thanh Truc et al., 2019; Wang et al., 2019; Raza et al., 2020; Wang et al., 2020). Comparing to the p-n and type II-1 heterojunctions, the carrier transfer mode in the Z-scheme heterojunction is more favorable for photocatalytic application. In general, the band bending at the interface of direct Z-scheme heterojunction (type II-2) is conducive to the recombination of photoinduced e^- and h^+ with weaker reduction and oxidation ability, so that e^- in the more negative CB of SC-1 and h^+ in the more positive VB of SC-2 can be remained (shown in **Figure 4B**). As a result, both high separation efficiency and optimal redox ability of photoinduced charge carriers can be realized, thus endowing the high photocatalytic performance of the Z-scheme system. In this section, recent advances for the construction of TiO_2-based all-solid-state indirect and direct Z-scheme heterojunctions as well as their application for photocatalytic CO_2 reduction with water oxidation will be reviewed and discussed in detail. Photocatalytic CO_2 reduction performance of the typical TiO_2-based all-solid-state Z-scheme heterojunctions are listed in **Table 3**.

Construction of indirect Z-scheme system between TiO_2 and another semiconductor using noble metals such as Pt (Wang et al., 2020a), Au (Wang et al., 2020b) and Ag (Tahir, 2020) as electron mediators has gained increased attention due its enhanced separation efficiency of photogenerated e^-/h^+ pairs with the recombination of inefficient charge carriers, thereby improving the photoreduction efficiency of CO_2. As reported by Tahir, $ZnFe_2O_4/Ag/TiO_2$ nanocomposite was fabricated by physical mixing Ag/TiO_2 nanorods and $ZnFe_2O_4$ nanospheres in methanol solution under continuous stirring (Tahir, 2020). Compared to the point contact between 0D TiO_2 nanoarticles and 0D $ZnFe_2O_4$ nanospheres, the stronger interaction between 0D $ZnFe_2O_4$ nanospheres and 1D TiO_2 nanorods is beneficial to the transfer of photogenerated electrons and holes at the interface. At the same time, the migration of these charge carriers along the 1D nanostructure is more efficient, which significantly inhibits their recombination. Moreover, the UV irradiation induced Z-scheme carrier transfer pathway ensures the high redox capability of the remaining carriers with the recombination of inefficient species within Ag nanoparticles, resulting in the superior CO generation rate of 1025 μmol g_{cat}^{-1} h^{-1}. Compared to $ZnFe_2O_4$, graphic-C_3N_4 (g-C_3N_4) is more preferred for the construction of TiO_2-based Z-scheme heterojunction due to its fully visible light utilization, improved CO_2 adsorption capacity (derived from its surface π bond) and proper band structure for CO_2 photoreduction with H_2O oxidation (Wu et al., 2019; Wang et al., 2020a). Moreover, it can also trap photogenerated electrons to enhance charge separation efficiency within the heterojunction. On this basis, g-C_3N_4 was coated on the surface of Au/TiO_2 hybrid to form a Z-scheme photocatalyst (**Figure 5A,B**) for visible-light-driven (VLD) photocatalytic CO_2 reduction (Wang et al., 2020a). In particular, the efficient separation of photogenerated e^-/h^+ pairs within anatase TiO_2 is attributed to the formation of {001}/{101} facet heterojunction. Then, photogenerated electrons in the CB of TiO_2 are directionally transferred through Au and recombine with photogenerated holes in the VB of g-C_3N_4, thereby boosting the photoreduction of CO_2 by photogenerated electrons in the CB of g-C_3N_4 (shown in **Figure 5C**). Notably, the high selectivity toward CO_2 photoreduction (>99%) was realized with few H_2 generation, while the selectivity for CH_4 generation (63.3%) was also enhanced compared to pure g-C_3N_4 (1.4%). The following work of this group (Wang et al., 2020a) devoted to further improving the selectivity for CH_4 generation with high apparent quantum efficiency (AQE) under visible light irradiation, in which 3D ordered macroporous (3DOM) TiO_2@C was coupled with g-C_3N_4 using Pt as electron mediator (3DOM-CNPTC) (shown in **Figure 5D,E**). The DFT calculation revealed the enrichment of photogenerated electorns by abundant N-sites on the interface between Pt and g-C_3N_4, which can reduce the adsorbed CO_2 to CH_4 directly in the presence of H_2O, thereby improving the selectivity for CH_4 generation (81.7%). In addition, the strong visible light adsorption by g-C_3N_4 and Pt as well as the multiple scattering of incident light within the 3DOM structure (**Figure 5F**) result in the high AQE of the Z-scheme heterojunction (5.67%), which is 140 folds than that of P25 (0.04%). Interestingly, the interaction between TiO_2 and g-C_3N_4 could also be strengthened by Al-O links which was introduced into the Z-scheme through impregnation (Wu et al., 2019). Specifically, TiO_2 nanotubes (TNTs) fabricated *via* anodization of Ti foils are dipped

TABLE 3 | Photocatalytic CO_2 reduction performance on typical TiO_2-based S-S (Z-scheme), S-M, S-C, multicomponent, phase and facet heterojunctions.

Photocatalyst	Reductant	Light source	Generation rate of main products ($\mu mol \cdot g_{cat}^{-1} \cdot h^{-1}$)	Quantum efficiency (%)	References
Indirect Z-scheme heterojunction					
$CdS/rGO/TiO_2$	H_2O vapor	300 W Xe lamp	CH_4: 0.12 ($\mu mol \cdot h^{-1}$)	-	Kuai et al. (2015)
$CuGaS_2$-RGO-TiO_2	Na_2S aqueous solution	300 W Xe lamp (λ > 330 nm)	CO: 0.15 H_2: 28.8 ($\mu mol \cdot h^{-1}$)	-	Takayama et al. (2017)
Al–O Linked porous-g-C_3N_4/TiO_2-nanotube (PCN/TNT)	Na_2SO_4 aqueous solution	150 W Xe lamp	CH_3COOH HCOOH CH_3OH	-	Wu et al. (2019)
$ZnFe_2O_4$/Ag/TiO_2 nanorods	H_2O vapor	200 W Hg lamp	CO: 1025 CH_4: 132 CH_3OH: 30.8 C_2H_6: 19.1 ($\mu mol \cdot h^{-1}$)	-	Tahir (2020)
g-C_3N_4/Pt/3DOM-TiO_2@C	H_2O vapor	300 W Xe lamp ($\lambda \geq$ 420 nm)	CO: 1.47 CH_4: 6.56 H_2: 0.82	5.67	Wang et al. (2020a)
(Au/A-TiO_2)@g-C_3N_4	H_2O vapor	300 W Xe lamp ($\lambda \geq$ 420 nm)	CH_4: 37.4 CO: 21.7	1.91	Wang et al. (2020b)
Direct Z-scheme heterojunction					
Cu_2O/TiO_2	H_2O vapor	1 kW high-pressure Hg (Xe) arc lamp ($\lambda \geq$ 305 nm)	CO: 2.11	-	Aguirre et al. (2017)
$ZnIn_2S_4/TiO_2$	H_2O vapor	300 W Xe lamp	CH_4: 1.135	-	Yang et al. (2017)
$TiO_2/CuInS_2$	H_2O vapor	350 W Xe lamp	CH_4: 2.5	-	Xu et al. (2018b)
TiO_2/CdS	H_2O vapor	300 W Xe lamp	CH_4: 11.9 $\mu mol \cdot h^{-1} \cdot m^{-2}$	-	Low et al. (2019)
$Zn_3In_2S_6/TiO_2$	H_2O vapor	300 W Xe lamp	CH_4: 6.19 CO: 23.35	-	She et al. (2018)
Nb-TiO_2/g-C_3N_4	H_2O vapor	Two 30 W white bulbs	CH_4: 562 CO: 420 HCOOH: 698	-	Thi Thanh Truc et al. (2019)
Copper (II)-porphyrin zirconium metal-organic framework (PCN-224(Cu))/TiO_2	Na_2SO_4 aqueous solution	300 W Xe lamp	CO: 37.21	-	Wang L. et al. (2019)
WO_3-TiO_2/Cu_2ZnSnS_4	H_2O vapor	400 W Xe lamp (λ > 420 nm)	CH_4: 1.69 CO: 15.37	0.52	Raza et al. (2020)
Au-TiO_2	H_2O vapor	AM1.5 G simulated sunlight	CH_4: 302	-	Zeng et al. (2020)
		50 W white cold LED light (λ > 400 nm)	HCHO: 420 CO: 323	-	
Single metal					
3DOM Au/TiO_2	H_2O vapor	300 W Xe lamp	CH_4: 2.89	-	Jiao et al. (2015)
Pt^{2+}-Pt^0/TiO_2	H_2O vapor	300 W Xe lamp	H_2: 394.7 CH_4: 37.78 CO: 8.03	0.36	Xiong et al. (2015)
Ag/TiO_2	H_2O vapor	300 W Xe lamp	CH_4: 1.40	0.16 (400 nm); 0.013 (520 nm)	Yu et al. (2016)
Ag/TiO_2 nanorod arrays	H_2O vapor	300 W Xe lamp (λ > 420 nm)	CH_4: 1.13 CO: 12	-	Cheng et al. (2017)
Pt/TiO_2 Pt/TiO_2-COK-12	H_2O vapor	Four 6 W lamps ($\lambda \leq$ 365 nm)	CH_4 CO	-	Tasbihi et al. (2018a)
Ag/TiO_2 nanotube arrays (TNTAs)	H_2O vapor	300 W Xe lamp	CH_4	-	Low et al. (2018)
Pt/TiO_2-Al_2O_3 foam	H_2O vapor	UV 8 W Hg lamp	H_2: 22.5 CH_4: 1.21 CO: 0.54	-	Tasbihi et al. (2018b)
Au-TiO_2 Nanotubes (TNTs)	H_2O vapor	300 W Xe lamp	CH_4: 14.67%	-	Khatun et al. (2019)
Au/TiO_2	H_2O vapor	300 W Xe lamp	CH_4: 70.34 CO: 19.75	-	Wang R. et al. (2019)
Au/TiO_2	H_2O vapor	300 W Xe lamp	CH_4: 0.2 CO: 1.2	-	Wang et al. (2021)
Metal alloy					
(Au, Cu)/TiO_2	H_2O vapor	AM1.5 G simulated sunlight	H_2: 286 CH_4: 2200 ± 300	-	Neaţu et al. (2014)

(Continued on following page)

TABLE 3 | (*Continued*) Photocatalytic CO_2 reduction performance on typical TiO_2-based S-S (Z-scheme), S-M, S-C, multicomponent, phase and facet heterojunctions.

Photocatalyst	Reductant	Light source	Generation rate of main products ($\mu mol \cdot g_{cat}^{-1} \cdot h^{-1}$)	Quantum efficiency (%)	References
AgPd/TiO_2	Triethylamine (TEA) aqueous solution	300 W Xe lamp	H_2: 144.5 CH_4: 79.0	-	Tan et al. (2018)
PtRu/TiO_2	H_2O vapor	300 W Xe lamp	H_2: 16.5 CH_4: 38.7 CO: 2.6	0.98	Wei Y. et al. (2018)
Hierarchical urchin-like yolk@shell $TiO_{2-x}H_x$ (HUY@S-TOH)/AuPd	H_2O (liquid)	300 W Xe lamp	CH_4: 47.0	-	Ziarati et al. (2020)
Graphene and its derivatives					
Graphene-TiO_2	H_2O vapor	300 W Xe lamp	CH_4: 8 C_2H_6: 16.8	-	Tu et al. (2013)
RGO/Pt-TiO_2 nanotubes (TNTs)	H_2O vapor	500 W tungsten-halog--en lamp	CH_4: 10.96 ($\mu mol \cdot m^{-2}$)	-	Sim et al. (2015)
TiO_2/Nitrogen doped rGO (NrGO)	H_2O vapor	400 W Xe lamp	CO: 50	0.0072	Lin et al. (2017)
GO/oxygen rich TiO_2 ($OTiO_2$)	H_2O vapor	300 W Xe lamp	CH_4: 0.43	0.0103	Tan et al. (2017)
rGO/TiO_2	H_2O vapor	500 W Hg lamp	CH_4: 12.75 CO: 11.93	-	Shehzad et al. (2018a)
((Pt/TiO_2)@rGO)	H_2O vapor	300 W Xe lamp	H_2: 5.6 CH_4: 41.3 CO: 0.4	1.93	Zhao Y. et al. (2018)
Graphene quantum dots (GQDs)/TiO_2	H_2O vapor	100 W Xe solar simulator	CH_4: 1.98 ($ppm \cdot cm^{-2} \cdot h^{-1}$)	-	Zubair et al. (2018)
rGO/TiO_2	Triethanolamine (TEOA) aqueous solution	8 W UV-A lamp	CH_3OH: 2330	-	Olowoyo et al. (2019)
CNT					
MWCNT/TiO_2	H_2O vapor	15 W UV lamp	CH_4: 11.74 HCOOH: 18.67 C_2H_5OH: 29.87	-	Xia et al. (2007)
MWCNT/TiO_2	H_2O (liquid)	15 W energy saving light bulb	CH_4: 0.17	-	Gui et al. (2014)
Ag-MWCNT@TiO_2	H_2O vapor	15 W energy saving light bulb	CH_4: 0.91 C_2H_6: 0.048	-	Gui et al. (2015)
MWCNT/TiO_2	TEOA aqueous solution	8 W UV-A lamp	H_2: 2360.0 CH_3OH: 3246.1 HCOOH: 68.5	-	Olowoyo et al. (2019)
CNT/TiO_2/Cu	H_2O vapor	300 W Xe lamp	CH_4: 1.1 CO: 8.1	-	Rodríguez et al. (2020)
Other carbon forms					
Carbon@TiO_2 hollow spheres	H_2O vapor	300 W Xe lamp	CH_4: 4.2 CH_3OH: 9.1	-	Wang et al. (2017)
N, S-containing carbon quantum dots (NCQDs)/TiO_2	H_2O vapor	300 W Xe lamp	CH_4: 0.13 CO: 0.19	-	Li et al. (2018)
Carbon nanofibers@TiO_2	H_2O vapor	350 W Xe lamp	CH_4: 13.52	-	Zhang J. et al. (2018)
MgO-Pt-TiO_2	H_2O vapor	100 W Xe lamp	H_2: 14 CH_4: 1.2 CO: 1.8	-	Xie et al. (2014)
Pt-rGO-TiO_2 Pd-rGO-TiO_2 Ag-rGO-TiO_2 Au-rGO-TiO_2	H_2O vapor	15 W energy saving light bulb	CH_4: 0.28 CH_4: 0.20 CH_4: 0.17 CH_4: 0.13	-	Tan et al. (2015)
Pt-Cu_2O/TiO_2	H_2O vapor	300 W Xe lamp	CH_4: 1.42 CO: 0.05	-	Xiong et al. (2017c)
WSe_2-Graphene-TiO_2	Na_2SO_3 aqueous solution	300 W Xe lamp	CH_3OH: 6.33	-	Biswas et al. (2018)
Pt/MgAl layered double oxides (MgAl-LDO)/TiO_2	H_2O (liquid)	300 W Xe lamp	CH_4: 1.42 CO: 2.3	-	Chong et al. (2018)
TiO_2-Graphene few-layered MoS_2	H_2O vapor	300 W Xe lamp	CO: 92.33	-	Jung et al. (2018)
Au/Al_2O_3/TiO_2	H_2O vapor	450 W Xe lamp	CO: 11.8	-	Zhao H. et al. (2018)
TiO_2-MnO_x-Pt	H_2O vapor	350 W Xe lamp	CH_4: 34.67 CH_3OH: 30.33 ($\mu mol \cdot m^{-2} \cdot h^{-1}$)	-	Meng et al. (2019)
Ag-MgO-TiO_2	H_2O vapor	300 W Xe lamp	CH_4: 0.86 CH_3OH: 0.06	0.091	Xu et al. (2018a)
Au@TiO_2 hollow spheres (THS)@CoO	H_2O vapor	300 W Xe lamp	CH_4: 13.3	-	Zhu et al. (2019)

(Continued on following page)

TABLE 3 | (*Continued*) Photocatalytic CO_2 reduction performance on typical TiO_2-based S-S (Z-scheme), S-M, S-C, multicomponent, phase and facet heterojunctions.

Photocatalyst	Reductant	Light source	Generation rate of main products ($\mu mol \cdot g_{cat}^{-1} \cdot h^{-1}$)	Quantum efficiency (%)	References
Phase heterojunction					
Anatase-rutile TiO_2 fibers	H_2O vapor	Four 6 W UV lamps	CO: 10.19 CH_4: 1.34 H_2: 19.94	0.036	Reñones et al. (2016)
Anatase-rutile TiO_2 nanoparticles with oxygen vacancy	H_2O vapor	300 W Xe lamp	CH_4: 43.2	-	Xiong et al. (2020)
Disordered Anatase/ordered rutile (A_d/R_o) TiO_2 nanoparticles	H_2O vapor	Solar simulator 1 Sun	CH_4: 3.98 CO: 3.02	0.273	Hwang et al. (2019)
Pt-loaded anatase-rutile TiO_2 nanoparticles	H_2O vapor	200 W Hg–Xe light	CH_4 CO	-	Lee et al. (2016)
N-doped carbon coating paragenetic anatase/rutile heterojunction	TEOA and MeCN	300 W Xe lamp	CO: 24.31	-	Chen et al. (2020)
$SrCO_3$-Modified brookite/anatase TiO_2 heterojunction	H_2O vapor	300 W Xe lamp	CH_4: 19.66 CO: 2.64	-	Jin et al. (2019)
Facet heterojunction					
{101}/{001} TiO_2	H_2O vapor	300 W Xe lamp	CH_4: 1.35	-	Yu et al. (2014)
Oxygen-deficient {101}/{001} TiO_2	H_2O vapor	100 W Hg lamp/450 W Xe lamp	CO: ~10.91 (UV-vis) CO: ~5.36 (visible)	0.31 (UV-vis) 0.134 (visible)	Liu L. et al. (2016)
Pt-loaded {101}/{001} TiO_2	0.1 M $KHCO_3$ solution	250 W Hg lamp	CH_4: 4.0	-	Cao et al. (2016)
Pt-loaded {101}/{001} TiO_2	H_2O vapor	300 W Xe lamp	CH_4: 4.6 H_2: 9.9	-	Xiong et al. (2017a)
Graphene supported {101}/{001} TiO_2	H_2O vapor	300 W Xe lamp	CO: 70.8 CH_4: 27.4	CO: 0.0557 CH_4: 0.0864	Xiong et al. (2016)

in $AlCl_3$ solution followed by calcination to obtain Al-O-modified TNTs, which is then combined with porous g-C_3N_4 (PCN) *via* solid sublimation and transition of urea/$NaHCO_3$ hybrid to from Al-O linked PCN/TNT composites. Results show that the low charge transfer efficiency at the interface between TiO_2 and g-C_3N_4 caused by lattice mismatch of the two components can be significantly improved by introducing Al-O links to replace surface hydroxyl groups, thereby enhancing the separation efficiency of photogenerated charge carriers and benefiting for photoreduction of CO_2 with increased yields of acetic acid, formic acid and methanol. According to Kuai's research, rGO could also serve as electron mediator for the construction of Z-scheme heterojunction between TiO_2 and CdS (Kuai et al., 2015). The remarkably prolonged photoluminasence (PL) decay time of CdS/rGO/TiO_2 (2.4 ns) reveals the different electron migration mechanism compared to CdS/TiO_2 (0.38 ns), which follows the carrier transfer mode in type II heterojunction. Obviously, the presence of rGO leads to the establishment of Z-scheme system, in which photogenerated electrons in the CB of TiO_2 are extracted by rGO and then transferred to the VB of CdS to recombine with photogenerated holes there, resulting in the enrichment of photogenerated electrons and holes in the CB of CdS and the VB of TiO_2, respectively. Although the photoreduction efficiency of CO_2 is still low on CdS/rGO/TiO_2, the attempt to construct Z-scheme heterojunction with low-cost carbon material instead of noble metal as electron mediator is successful, while the high selectivity for CH_4 generation is also promising.

Recently, construction of direct Z-scheme system by coupling two different semiconductors with matching geometric and band structure has become research hotspot in the field of photocatalytic CO_2 reduction, which is more facile to synthesis and more convenient for charge transfer at the interface. In particular, semiconductors with narrow band gap are more preferred in the TiO_2-based direct Z-scheme heterojunction to improve the utilization of visible light. Typically, $ZnInS_2$ nanosheets were decorated onto the surface of 1D TiO_2 nanobelts *via* hydrothermal process (Yang et al., 2017). The authors claimed the Z-scheme electron transfer mechanism between $ZnInS_2$ and TiO_2 based on the experimental results of CH_4 generation. Since the CB potential of TiO_2 is lower than the redox potential of CO_2/CH_4, it is reasonable to believe that photogenerated electrons in the CB of $ZnInS_2$ are retained due to the Z-scheme electron transfer mechanism and take in charge for photocatalytic CO_2 reduction to produce CH_4. However, stronger evidence is needed to prove this conjecture. In another work, a similar 3D hierarchical nanostructure was constructed by depositing $CuInS_2$ nanoplates on TiO_2 nanofibers (Xu et al., 2018b). DFT calculations revealed the higher Fermi level (E_F) of $CuInS_2$ than that of TiO_2, which forces electrons transfer from $CuInS_2$ to TiO_2 after their contact and creates a build in internal electric filed at the

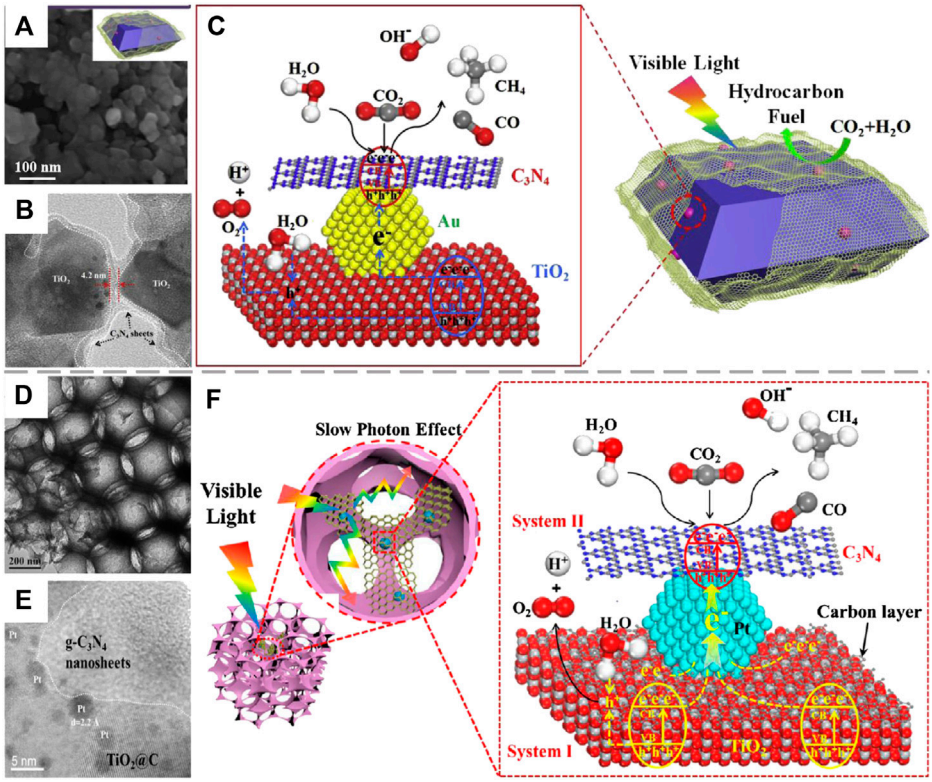

FIGURE 5 | (A) SEM and **(B)** HRTEM images of (Au/A-TiO_2)@g-C_3N_4 catalyst; **(C)** Schematic for photorecatalytic CO_2 reduction with H_2O to produce CH_4 and CO over (Au/A-TiO_2)@g-C_3N_4. Reproduced from Wang et al., 2020a with permission from Elsevier and Copyright Clearance Center. **(D)** TEM and **(E)** HRTEM images of 3DOM-CNPTC photocatalyst; **(F)** The mechanism of 3DOM-CNPTC catalyst for photocatalytic CO_2 reduction with H_2O to CH_4. Reproduced from Wang et al. (2020) with permission from Elsevier and Copyright Clearance Center.

interface. The recombination of photogenerated electrons in the CB of TiO_2 and photogenerated holes in the VB of $CuInS_2$ under the guidance of the internal electric filed leads to the accomplishment of high efficient Z-scheme charge transfer pathway. As a result, photogenerated electrons enriched in the CB of $CuInS_2$ facilitate the photocatalytic reduction of CO_2 to produce CH_4 and CH_3OH in the presence of protons provided by water oxidation. *In situ* irradiated X-ray photoelectron spectroscopy (ISI-XPS) was also applied to provide direct evidence of Z-scheme electron transfer mechanism (Low et al., 2019). The binding energy shifts of Ti 2p (by 0.3 eV) and Cd 3 days (by -0.2 eV) under light irradiation indicate the decreased electron density of TiO_2 as well as the increased electron density of CdS, suggesting that photogenerated electrons migrates from TiO_2 to CdS, which agrees well with Z-scheme mechanism. The ternary semiconductor of $Zn_3In_2S_6$ was also used by She et al. for the construction of direct Z-scheme heterojunction with TiO_2 (She et al., 2018). Higher CO and CH_4 yields were realized on $Zn_3In_2S_6/TiO_2$ in comparison with $ZnInS_2/TiO_2$ and $CuInS_2/TiO_2$, which could be attributed to the higher crystallinity of the two constituents that favored for charge separation (shown in **Figure 6**). In addition, modification on TiO_2 to narrow its band gap for the improved visible light adsorption is also an efficient strategy to further enhance the photocatalytic performance of the TiO_2-based Z-scheme heterojunction. As reported by Truc et al., E_g of TiO_2 (3.2 eV) was reduced to 2.91 eV after Nb doping (Thi Thanh Truc et al., 2019). The as-obtained Nb-TiO_2 was grinded with melamine followed by calcination at 550 °C to form Nb-TiO_2/g-C_3N_4 heterojunction with a clear boundary at the interface. The well matched lattice spacing of the TiO_2 {101} (0.353 nm) and g-C_3N_4 {002} (0.320 nm) facets benefits to the electron transfer at the interface following Z-scheme mechanism, resulting in high efficiency for photocatalytic CO_2 reduction. The advantages of low cost, full visible light spectrum responsibility (400–700 nm) and superior generation rate of CH_4 (562 μmol g_{cat}^{-1} h^{-1}), CO (420 μmol g_{cat}^{-1} h^{-1}) and HCOOH (698 μmol g_{cat}^{-1} h^{-1}), make Nb-TiO_2/g-C_3N_4 a promising VLD photocatalyst for practical application in the future to reduce the CO_2 level in the atmosphere. Moreover, the high O_2 yield of Nb-TiO_2/g-C_3N_4 (1702 μmol g_{cat}^{-1} h^{-1}) indicates that the artificial Z-scheme system can mimic the nature photosynthesis by green plants well.

For a long time, stability is one of the main defects facing the photocatalysts that restricts their long-term performance. The photocatalytic activity decreased continuously in the process of illumination due to photocorrosion. Construction of Z-scheme heterojunction can also protect the narrow band gap semiconductor coupled with TiO_2 from photo-oxidation. As

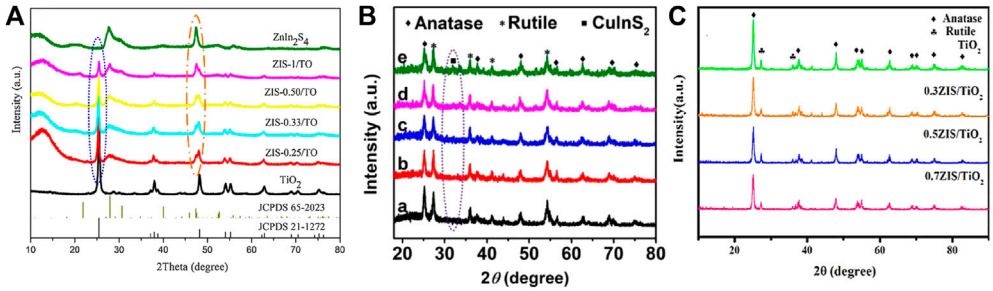

FIGURE 6 | XRD patterns of **(A)** $ZnInS_2/TiO_2$ series, **(B)** $CuInS_2/TiO_2$ series and **(C)** $Zn_3In_2S_6/TiO_2$ series. Reproduced from Yang et al. (2017) and Xu et al. (2018) with permission from Elsevier and Copyright Clearance Center, and She et al. (2018) with permission from Wiley-VCH, respectively.

reported by Aguirre et al., XPS spectra of Cu_2O exhibited an increased Cu(II) content with the extension of illumination time, indicating that Cu(I) was partially oxidized by photogenerated holes (Aguirre et al., 2017). On the contrary, Cu(I) in the Cu_2O/TiO_2 heterojunction showed no obvious change in valence state, revealing the protection of TiO_2 toward Cu_2O by injecting photogenerated electrons into the VB of Cu_2O to recombine with photogenerated holes there, which also demonstrated the Z-scheme electron transfer mechanism between TiO_2 and Cu_2O. Interestingly, a stable direct Z-scheme heterojunction can also be formed between TiO_2 and metal organic frameworks (MOFs) as PCN-224(Cu) (Wang L. et al., 2019). It is worth nothing that the high specific surface area as well as porous structure of MOFs benefits for CO_2 adsorption, while the alternative ligands endow MOFs with adjustable band structure and spectra response range, thus providing a series of promising candidates for the design and construction of direct Z-scheme systems for efficient photocatalytic CO_2 reduction. With deepening of the research on the Z-scheme photocatalytic system and the recognition of its photocatalytic performance, more and more different types of Z-scheme photocatalysts have been developed (Raza et al., 2020; Zeng et al., 2020), accelerating the process of photocatalytic CO_2 reduction from basic research to practical application.

TiO_2 Based S-M Heterojunction for CO_2 Photoreduction

As reported by previous literatures, TiO_2 modified by metal nanoparticles exhibits enhanced photocatalytic performance due to the promoted charge carrier separation efficiency, expanded light adsorption range as well as high selectivity toward reduction products. In general, Schottky barrier at the interface of semiconductor and metal prevents recombination of photogenerated e^-/h^+ pairs (Ma et al., 2014; Wang et al., 2014; Ola and Maroto-Valer, 2015; Li et al., 2019). Specifically, the higher work function of metal (W_m) than that of semiconductor (W_s) results in the higher Fermi level of semiconductor (E_{Fs}) than that of metal (E_{Fm}) (shown in **Figure 7A**). Contacting semiconductor with metal leads to charge transfer at the interface until the alignment of their Fermi levels. During the process, migration of electrons from semiconductor to metal results in band bending of the semiconductor and creates a space charge region at the interface (Schottky barrier), which could prevent backflow of photogenerated electrons to inhibit their recombination with photogenerated holes (shown in **Figure 7B**). The promoted charge separation efficiency benefits for photocatalytic CO_2 reduction as well as the enhanced water oxidation efficiency. In addition, metals can enrich electrons to create high electron density regions on their surfaces, which are favoring for photoreducing CO_2 to hydrocarbons in the presence of water due to their lower redox potential than CO. Besides, local surface plasmon resonance (LSPR) effect of certain metals can enhance visible light adsorption of the Schottky heterojunction and inject hot electrons into the CB of semiconductor, thereby facilitating the photoreduction of CO_2 (shown in **Figure 7C**). In this section, strategies for coupling TiO_2 with different metal nanoparticles as well as their different enhancement mechanisms of photocatalytic performance will be reviewed and discussed in detail. Photocatalytic CO_2 reduction performance of the typical TiO_2-based S-M heterojunctions are listed in **Table 3**.

As a classic noble metal cocatalyst, Pt has been widely used in the photocatalysis field for both water splitting and CO_2 reduction. In particular, TiO_2 loaded with Pt nanoparticles has been demonstrated to be efficient for photoreduction CO_2 to CH_4. As reported by Fresno et al., a series of Pt/TiO_2 photocatalysts with different Pt loading amount were fabricated by treating P25 in the Pt precursor-contained aqueous solution *via* the deposition-precipitation procedure (Tasbihi et al., 2018a). The as-obtained sample (**Figure 8A**) displays ca. 100% selectivity toward CH_4 generation at the optimum Pt content (>0.58 wt% of TiO_2), which can be ascribed to the strong chemisorption of CO on Pt nanoparticles (proved by the FTIR spectra in ATR mode (shown in **Figure 8B**) along with *in-situ* NAP-XPS analysis) and the further reduction of CO to CH_4 (shown in **Figure 8C**). However, the adsorption features of CO can not be observed on bare TiO_2, which yields CO as the main product under the same condition. The correspondingly net selectivities and quantum yield indices (QYI) are shown in **Figure 8D**. In another work, Pt/TiO_2 was synthesized by the hydrolysis of Titanium (IV) butoxide (TEOT) in the presence of $H_2PtCl_6{\cdot}6H_2O$, resulting in the doping of Pt^{2+} into the lattice of TiO_2 and loading of Pt nanoparicles (Pt^0) on the surface of TiO_2 (Xiong et al., 2015). The low

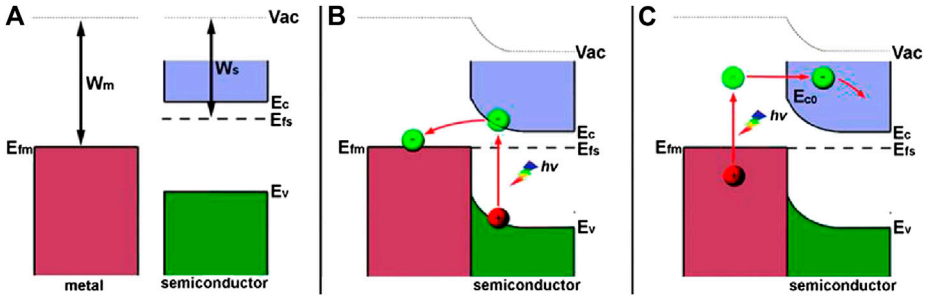

FIGURE 7 | Band structure of semiconductor **(A)** before contact and **(B)** after contact with metal to form the Schottky barrier; **(C)** the SPR effect induced hot electron transfer. Reproduced from Bai et al. (2015) with permission from the Royal Society of Chemistry.

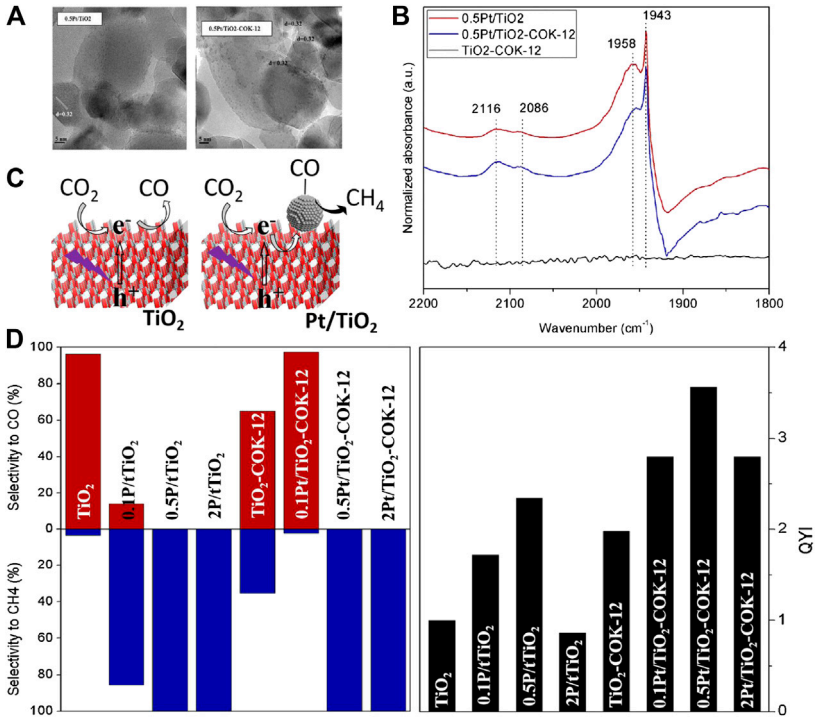

FIGURE 8 | (A) TEM images of 0.5 Pt/TiO_2 and 0.5 Pt/TiO_2-COK-12, **(B)** FTIR spectra of the TiO_2, 0.5 Pt/TiO_2 and 0.5 Pt/TiO_2-COK-12 catalysts after reaction, in the CO stretching region, **(C)** Schematic representation of the proposed reaction pathway over TiO_2 and Pt/TiO_2 catalysts, and **(D)** Net selectivities and quantum yield indices (QYI) obtained with the different catalysts. The QYI with TiO_2 is 1 by definition. Reproduced from Tasbihi et al. (2018a) with permission from Elsevier and Copyright Clearance Center.

recombination efficiency of photogenetated e^-/h^+ pairs due to the deposition of Pt^0 as well as strong visible light adsorption attributed to Pt^{2+} doping significantly enhance photocatalytic performance of Pt^{2+}-Pt^0/TiO_2 with higher quantum yield (1.42%) for CO_2 conversion than that of bare TiO_2 (0.36%). Moreover, plenty of electrons enriched by Pt^0 and protons supplied by water oxidation benefit for the high selectivity toward CH_4 formation (E_{red}/SCE = −0.48 V). Compared with the formation of CO (E_{red}/SCE = -0.77 V), this reaction is more feasible in thermodynamics. In summary, the kinetic feasibility (strong chemisorption of CO on Pt) and thermodynamic convenience contribute to photoreduction of CO_2 to CH_4. On this basis, Pt/TiO_2 were deposited on porous supports with large surface area (etc. COK-12 (Tasbihi et al., 2018a) and Al_2O_3 foam (Tasbihi et al., 2018b)) to promote active sites exposure and achieve higher CH_4 yield.

Coupling TiO_2 with noble metals that can induce the LSPR effect has also been adapted by researchers for efficient photocatalytic CO_2 reduction. As reported by Wang et al., 0D/2D Au/TiO_2 was synthesized by *in situ* growth of Au nanoparticles on the surface of TiO_2 nanosheets *via* chemically reduction (Wang R. et al., 2019). The hot electrons induced by the LSPR effect of Au under visible light irradiation (550 nm) could

inject into the CB of TiO_2 and reduce CO_2 to CO. However, as the only electron source (TiO_2 can not be excited by visible light), the limited hot electrons cannot further reduce CO to CH_4. Interestingly, the Au/TiO_2 hybrid yielded CH_4 as the main product under 300 W Xe lamp irradiation that contained a certain amount of UV light. Specifically, recombination of photogenerated electrons and holes was suppressed owing to the Schottky barrier that facilitated transfer of e^- from the CB of TiO_2 to Au. Moreover, h^+ remained in the VB of TiO_2 could oxidize water to provided plenty of protons for CH_4 generation. On this basis, facet engineering was introduced by Wang et al. for the rational design of interface between Au and exposed facet of TiO_2 to realize higher charge separation efficiency (Wang et al., 2021). Results showed that the lower height of Schottky barrier on the Au/TiO_2{101} interface resulted in more smooth migration of photogenerated electrons from the CB of TiO_2 to Au compared to the Au/TiO_2{001} interface, thereby exhibiting better performance for photocatalytic CO_2 reduction. Notably, the architecture of TiO_2 among Au/TiO_2 heterojunction also plays an important role for efficient photoreduction of CO_2 (Jiao et al., 2015; Khatun et al., 2019). Jiao et al. (Jiao et al., 2015) prepared 3D ordered macroporous (3DOM) TiO_2 to support Au nanopaticles, which were uniformly dispersed in the inner wall of the 3DOM structure. The multiple scattering of incident light within the 3DOM structure enhanced light utilization efficiency of the heterojunction, while the ordered macroporous also improved the mass transfer efficiency of the reactants. In addition, the SPR effect of Au induced by visible light irradiation provided extra electrons for photocatalytic CO_2 reduction, which was benefited for CH_4 generation. In another work, electrochemical anodization was used to fabricate TiO_2 nanotubes (TNTs) with light adsorption edge in the visible region, indicating its weak photocatalytic activity illuminated by visible light (Khatun et al., 2019). Coupling with Au by electronchemical deposition significantly improved visible light adsorption of TNTs and promoted charge separation efficiency due to the LSPR effect of Au nanoparticles. The excellent CH_4 yield (14.67% of CO_2 was converted to CH_4) under visible light irradiation made Au-TNTs a very promising solar-driven photocatalyst to convert CO_2 into hydrocarbon fuels. Similarly, plasmonic Ag were electronchemical deposited into the inner space of TiO_2 nanotube arrays (**Figure 9A**) to investigate the enhancement of SPR effect on photocatalytic performance, while the morphology and structure of as-obtained Ag-TNTAs-E are shown in **Figures 9B,C** (Low et al., 2018). The direct evidences of the existence of Schottky barrier between Ag and TiO_2 as well as migration of hot electrons induced by the SPR effect of Ag nanoparticles can be found in the synchronous-illumination X-ray photoelectron spectroscopy (SIXPS) spectra based on the shift of Ti $2p_{3/2}$ peak before and after illumination (**Figures 9D,E**). Moreover, the SPR effect of Ag nanoparticles was strengthened by the multiple scatted light in TNTAs (**Figure 9F**), while the derived near field effect accelerated charge transfer at the heterointerface to promote separation efficiency of photogenerated e^-/h^+ pairs, thereby endowing enhanced VLD activity of Ag-TNTAs for CO_2 photoreduction. Although promoting photoreduction efficiency of CO_2 and clarifying the involved mechanisms are the focus of current research, the improvement of photocatalyst synthesis methods also deserves attention. The silver mirror reaction was adopted by Yu et al. to deposited Ag on TiO_2 nanoparticles (Yu et al., 2016). CH_3OH generated in CO_2-saturated 1 M $NaHCO_3$ solution is the main product of photocatalytic CO_2 reduction, which is more valuable than the primary products such as CO and CH_4. In another work, Ag(I) adsorbed by TiO_2 nanorod arrays were completely reduced by cold plasma within 30 s to form uniformly distributed Ag nanoparticles (Cheng et al., 2017). This fast and efficient strategy is very promising for the fabrication of metal nanoparticles decorated semiconductor photocatalysts on a large scale.

Bimetallic nanoalloys that combined advantages of the two metal components are efficient cocatalysts for photocatalytic CO_2 reduction and have been introduced in the TiO_2-based photocatalytic systems. As reported by Neaţu et al., Au and Cu species were deposited on TiO_2 nanopartcles stepwisely followed by calcining in H_2 atmosphere to form Au-Cu alloy (Neaţu et al., 2014). In this case, Au is served as visible light harvester due to its LSPR effect while Cu can covalently bind with CO reduced from CO_2 and direct the generation of CH_4. Therefore, high VLD photocatalytic activity with outstanding CH_4 selectivity (97%) was achieved. Other bimetallic nanoalloys, such as Au-Ag (Tahir et al., 2017), Au-Pd (Ziarati et al., 2020), Ag-Pd (Tan et al., 2018) and Pt-Ru (Wei Y. et al., 2018) nanoparticles are also been used to enhance photocatalytic performance of TiO_2 for selective reduction of CO_2. Among them, the combination of bimetallic nanoalloys and modified TiO_2 (etc. hydrogenated black TiO_2 ($TiO_{2-x}H_x$) (Ziarati et al., 2020) and N-doped TiO_2 (Tan et al., 2018)) exhibited considerably enhanced visible light utilization and charge separation efficiency, which could become the future development trend of TiO_2-based S-M heterojunction for solar-driven CO_2 photoreduction. Moreover, construction of S-M heterojunction with hierachical architecture is also in great demand (Ziarati et al., 2020).

TiO_2 Based S-C Heterojunction for CO_2 Photoreduction

Recently, coupling TiO_2 with carbon-based nanomaterials including graphene and its derivatives (etc. graphene (GR) (Tu et al., 2013; Xiong et al., 2016; Biswas et al., 2018; Jung et al., 2018; Shehzad et al., 2018; Zhao et al., 2018; Zubair et al., 2018; Bie et al., 2019), graphene oxide (GO) (Chowdhury et al., 2015; Tan et al., 2017) and reduced graphene oxide (rGO) (An et al., 2014; Kuai et al., 2015; Sim et al., 2015; Tan et al., 2015; Lin et al., 2017; Olowoyo et al., 2019)), carbon nanotubes (CNTs) (Xia et al., 2007; Gui et al., 2014; Gui et al., 2015; Olowoyo et al., 2018; Rodríguez et al., 2020) and carbon quantum dots (CQDs) (Li et al., 2018; Wang K. et al., 2019) to construct TiO_2-carbon heterojunction for photocatalytic reduction of CO_2 has been widely concerned. The unique physicochemical properties of nanocarbon that responsible for the enhanced photocatalytic performance of the S-C heterojunction can be concluded as follows: 1) the large surface area and high mechanical stability of nanocarbon could provide a stable support for the uniformly distributed TiO_2

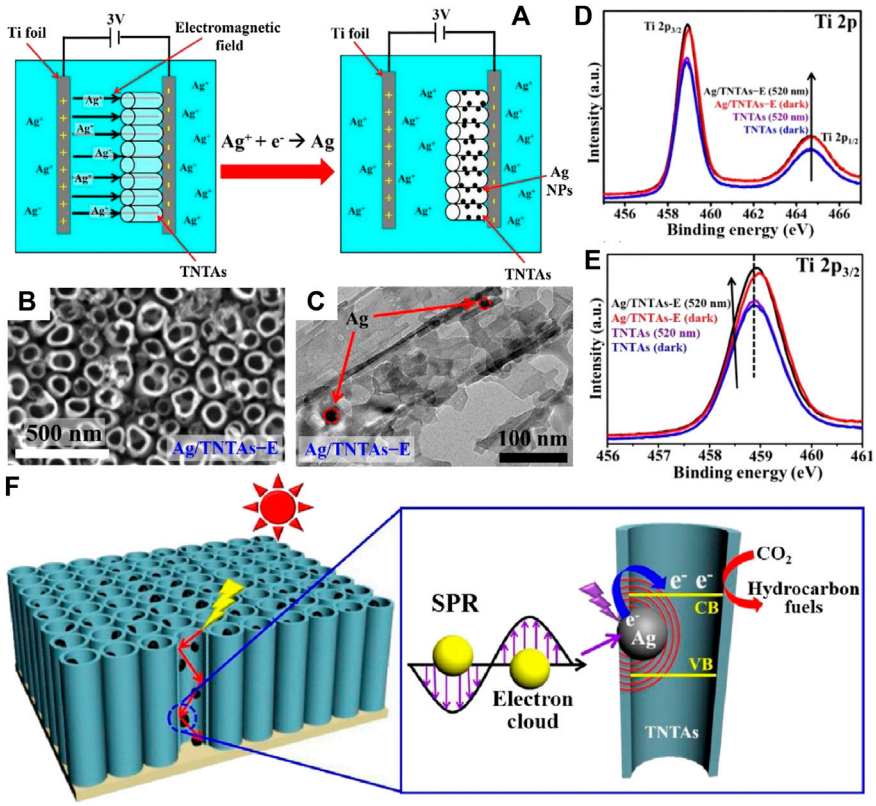

FIGURE 9 | (A) Schematic illustration of electrochemical deposition methods for loading Ag NPs into the TNTAs, **(B)** SEM image (top view) and **(C)** TEM image (side view) of Ag/TNTAs-E, Comparison of high-resolution SIXPS spectra of **(D)** Ti 2p and **(E)** Ti $2p_{3/2}$ for TNTAs and Ag/TNTAs-E in the dark and under 520 nm LED light irradiation, and **(F)** Schematic illustration of the enhanced SPR effect of Ag NPs in the TNTAs structure. Reproduced from Low et al. (2018) with permission from Elsevier and Copyright Clearance Center.

nanoparticles with increased exposure of active sites and enhanced CO_2 adsorption capacity; 2) the high charge carrier mobility, large capacitance of nanocarbon as well as the formation of Ti-O-C bond at the highly dispersed S-C interface facilitates the migration of electrons from TiO_2 to carbon materials, thereby enhancing the separation efficiency of photogenerated e^- and h^+ and inhibiting their recombination; 3) the optical properties of carbon materials, such as good optical transparency and wide spectrum adsorption range (especially for CQDs, expands to near IR region), contribute to the utilization of visible light of the TiO_2-based S-C heterojunction and result in the improved quantum efficiency. In this section, S-C heterojunctions including TiO_2-GR series, TiO_2-CNT and TiO_2-CQDs are reviewed and discussed in detail, respectively. Photocatalytic CO_2 reduction performance of the typical TiO_2-based S-C heterojunctions are listed in **Table 3**.

Coupling TiO_2 With Graphene and Its Derivatives

Construction of TiO_2-carbon heterojunction using graphene or its derivatives as the guest/host component derives improved photocatalytic performance due to its excellent electrical properties and chemical stability. It is worth nothing that the path of graphite-GO-rGO has been generally adopted by researchers to obtain graphene, whereas various of strategies have been developed for the fabrication of TiO_2-graphene nanocomposites. As reported by Tu et al., *in situ* simultaneous reduction-hydrolysis technique was developed for the fabrication of TiO_2-graphene 2D sandwich-like hybrid nanosheets (Tu et al., 2013). During the process, GO was reduced to graphene (rGO) by ethylenediamine (En) while Ti (IV) was hydrolyzed to TiO_2 nanoparticles and loaded on rGO through Ti-O-C bonds. The abundant surface Ti^{3+} sites generated from En reduction could trap photogenerated electrons efficiently, thereby decreasing the recombination efficiency of charge carriers. Moreover, the synergism of Ti^{3+} sites and garphene favors for the generation of C_2H_6, which is inspiring for C-C coupling during the photoreduction process of CO_2. In another work, the suspension of GO and TiO_2 in ethanol was ultrasonicated and refluxed to form Ti-O-C bonds, while GO was partially reduced to rGO during the process (Shehzad et al., 2018a). The tightly connected two phases improve charge separation at the heterointerface, while the enlarged light absorption coefficient is attributed to the reduced bandgap energy by the formation the Ti-O-C bonds. As a result, the rGO/TiO_2 nanocomposites exhibited greater yields of CH_4 (12.75 μmol g_{cat}^{-1} h^{-1}) and CO (11.93 μmol g_{cat}^{-1} h^{-1}) than anatase for 4 folds. Theoretical calculation was applied by Olowoyo et al. to investigate the enhanced photocatalytic performance of rGO/TiO_2 in reducing

CO_2 (Olowoyo et al., 2019). Results reveal that the high electron density of rGO has significant influence on the TiO_2 bands and endows visible light responsibility of the composite. Moreover, the different electron migration paths within rGO/TiO_2 under different light sources were observed. Compared to the electron transfer from TiO_2 to rGO under UVA, irradiation by visible light leads to the direct generation of electorns and holes in rGO or TiO_2, respectively. Both of the two pathways are efficient for photogenerated charge separation and favor for methanol production. In addition, the large adsorption capacity of CO_2 is another feature of TiO_2/graphene that contribute to photocatalytic CO_2 reduction (Chowdhury et al., 2015). As reported by Chowdhury et al., TiO_2/GO nanocomposites was obtained from the aqueous suspension of GO and TiO_2 under ultrasonication flowed by continuous stirring. The synergism of physisorption (intermolecular electrostatic interactions as van der Waals forces or London dispersion forces) and chemisorption (coordination of O atoms with surface Lewis acid center (Ti sites), or coordination of C atom with surface Lewis acid center (oxygen functionalities of GO or TiO_2)) led to the high adsorption amount of CO_2 (1.88 mmol g^{-1}), which facilitated its activation and photocatalytic reduction. Considering that photoreduction of CO_2 requires the participation of electrons and protons produced by photooxidation of H_2O, the adsorption capability of H_2O molecule by photocatalyst is also critical. In view of the compete adsorption of H_2O and CO_2 on the active sites, proper partial pressures of CO_2 and H_2O are in great demand that determines the CH_4 yield on GO-doped oxygen-rich TiO_2 (Tan et al., 2017). Notably, the CO_2 adsorption capacity and charge separation efficiency can be further improved by introducing nitrogen dopants into rGO to form NrGO/TiO_2 system (Lin et al., 2017). On the one hand, the positive electrostatic potential regions created by nitrogen dopants on the surface of NrGO benefit for CO_2 adsorption and activation. On the other hand, the injection of electrons from quaternary-N species existed in NrGO matrix to the delocalized π-system facilitates the transfer of electrons and inhibits the recombination of photogenerated e^-/h^+ pairs. These findings are very helpful for the design of photocatalytic system based on heteroatom-doped graphene for CO_2 conversion with high efficiency. Furthermore, construction of well-defined nanostructure offers another thought to improve photocatalytic performance of TiO_2/graphene heterojunction (Zubair et al., 2018). Typically, TiO_2 nanotube arrays (TNT) with attractive 1D vectorial charge transfer can suppress recombination of photogenerated charge carriers efficiently. Graphene quantum dots (GQDs) decorated on TiO_2 nanotube (G-TNT) promotes charge transfer at the heterointerface, which could also enhance the light utilization of the heterojunction due to its superior visible light responsibility. Besides, the high surface area of the heterojunction contributes to the exposure of active sites that favor for CO_2 adsorption and activation. Consequently, a 5.6 fold CH_4 yield was obtained on G-TNT in comparison with pure TNT. On this basis, Pt nanoparticles were employed for the construction of rGO/Pt-TNT ternary composite with promoted visible light responsibility and photoreduction selectivity of CO_2 to produce CH_4 (Sim et al., 2015). In particular, the LSPR effect of Pt expands light adsorption range of the heterojunction to 450 nm that can be activated by visible light. Similarly, the high selectivity for CH_4 generation (99.1%, compared to CO yield) was also proved by Zhao et al. on (Pt/TiO_2)@rGO system (Zhao H. et al., 2018), in which vectorial electron transfer from TiO_2 to rGO through Pt was also demonstrated.

Coupling TiO_2 With CNT

Generally, charge transfer along the 1D CNT leads to high separation efficiency of photogenerated e^-/h^+ pairs and endows superior photocatalytic performance of TiO_2/CNT heterojunction. Moreover, CNT can also serve as support to reduce the aggregation of TiO_2 nanoparticles, thus resulting in the formation of highly dispersed heterointerface and large exposure of active sites. As reported by Xia et al., the multi-walled CNT (MWCNT)/TiO_2 hybrid fabricated *via* sol-gel method yielded C_2H_5OH as the main photoreduction product of CO_2 under UV light irradiation (Xia et al., 2007). In a further study, MWCNT/TiO_2 with core-shell nanostructure was demonstrated to be visible light active (due to the excellent visible light adsorption ability of CNT) that can convert CO_2 to CH_4 (Gui et al., 2014). A following work carried out by this group introduced Ag nanoparticles to MWCNT/TiO_2 system (Ag-MWCNT@TiO_2) for the further enhanced photocatalytic performance (Gui et al., 2015). In particular, the Schottky barrier between Ag and TiO_2 prevents backflow of photogenerated electrons that transferred from TiO_2 to Ag. The synergism of MWCNT and Ag nanoparticles greatly enhances separation efficiency of photogenerated charge carriers and restricts their recombination, thereby resulting in higher CH_4 formation rate (0.91 μmol g_{cat}^{-1} h^{-1}) in comparison with the binary system (MWCNT@TiO_2, 0.17 μmol g_{cat}^{-1} h^{-1}). Further studies revealed the mechanism of electron transfer between TiO_2 and CNT (Olowoyo et al., 2019). Specifically, strong attachment between MWCNT and the {101} facet of anatase TiO_2 introduces common orbitals within the band gap of TiO_2, which is the fundamental of charge transfer between the two phases and enables visible light responsibility of the composites. Electron transfer from TiO_2 with higher density of initial states to MWCNT under irradiation of both UVA and visible light is more probable basing on the computation results. In addition, the tight contact between MWCNT and TiO_2 due to the combination of sonothermal and hydrothermal methods results in extremely high photocatalytic activity with CH_3OH generation rate of 2360 μmol g_{cat}^{-1} h^{-1}, much higher than that of the similar photocatalytic systems. A recent study reported the fabrication of TiO_2/CNT composite in the medium of supercritical CO_2 (Rodríguez et al., 2020). Although photocatalytic activity of the product is relatively weak (CO, 8.1 μmol g_{cat}^{-1} h^{-1}; CH_4, 1.1 μmol g_{cat}^{-1} h^{-1}), it can also provide a novel strategy for the synthesis of TiO_2-based photocatalyst and leave a large space for performance improvement.

Coupling TiO_2 With CQDs

As a new class of 0D carbon-based nanomaterial, the excellent photoelectric properties of CQDs, such as wide spectral response range, photo-induced charge transfer ability, up-conversion

function and anti-photocorrosion property, make it a promising cocatalyst to enhance photocatalytic performance of traditional semiconductor photocatalyst as TiO_2 (Li et al., 2018; Wang K. et al., 2019). As reported by Li et al., N, S-containing CQDs (NCQDs) was synthesized *via* a microwave-assisted method using thiourea and citric acid as precursors, which then assembled with P25 under continuous stirring at 80°C to form NCQDs-TiO_2 nanocomposites. Particularly, TiO_2 sensitized by NCQDs can be activated by visible light, while electrons transferred from rutile TiO_2 in P25 to NCQDs prevented recombination of photogenerated e^-/h^+ pairs, thus enhancing photoreduction efficiency of CO_2. Although the photoelectric properties of CQDs are attractive, relative research about coupling CQDs with TiO_2 or other semiconductors to construct heterostructured photocatalyst for photocatalytic CO_2 reduction is still few. In our opinion, as an important characteristic distinguished from other carbon-based materials, up-conversion function of CQDs is worth developing to improve the light energy utilization of heterostructured photocatalysts, especially for the wide band gap semiconductor-contained systems.

In addition to carbon-based nanomaterials analyzed above, other carbon forms can also combine with TiO_2 to obtain heterojunction for photocatalytic CO_2 reduction with high efficiency. For instance, Zhang et al. coated TiO_2 on electrospun carbon nanofibers to promote active sites exposure as well as charge separation and transfer of the nanocomposites (Zhang J. et al., 2018). Besides, the heat produced by carbon nanofibers due to its photothermal conversion function accelerates the diffusion kinetics of reactants and products during photocatalytic process, thus further enhancing the photoreduction efficiency of CO_2. The local photothermal effect induced by carbon species is also highlighted by Wang et al. among the hybrid carbon@TiO_2 hollow spheres (Wang et al., 2017). Moreover, the multiple scattering of incident light within the hollow structure improves light utilization of the hybrid (shown in **Figure 10**) and contributes to improve the quantum efficiency of photocatalytic CO_2 reduction. This result indicates that not only component, but also architecture of the heterojunction photocatalysts plays important role in improving photocatalytic performance.

TiO_2 Based Multicomponent Heterojunction for CO_2 Photoreductions

Construction of TiO_2-based multicomponent heterojunction to introduce two different functional co-catalysts for efficient VLD photocatalytic CO_2 reduction has been widely adopted, in which TiO_2 combined with any two of another semiconductor (AS), metal nanoparticles (MNPs) and nanocarbon (C) to form ternary composites is currently the most studied system. Previous research revealed the highest selectivity of Pt for CH_4 generation compared to other noble metal cocatalysts (Pt > Pd > Au > Rh > Ag) due to its excellent electron extraction ability that derives high electron density around it and facilitates CO_2 photoreduction (Xie et al., 2014). However, the consequent increase in H_2 production is unfavorable and should be suppressed to realize further enhanced photoreduction efficiency of CO_2. Xie et al. coated MgO amorphous layers on Pt/TiO_2 hybrid to improve chemisorption of CO_2, which was then reduced to CH_4 directly by photogenerated electrons enriched on adjacent Pt nanoparticles with high efficiency, thus benefiting for the selective formation of CH_4. The similar function of Cu_2O was demonstrated by Xiong et al. from the Pt-Cu_2O/TiO_2 nanocomposite (Xiong et al., 2017c). Notably, the charge separation efficiency of the ternary system decreased with the increasing amount of MgO, indicating that excess MgO may restrict electrons transfer from TiO_2 to Pt. Therefore, TiO_2/MNPs/AS ternary heterojunctions with rational designed architecture and efficient carrier migration path are necessary. According to Meng's research, MnO_x and Pt were selectively deposited on the {001} and {101} facet of TiO_2 (**Figure 11A,B,C**), respectively (Meng et al., 2019). The series connection of S-M (Pt and TiO_2{101}), facet (TiO_2{101} and {001}) and p-n (TiO_2{101} and MnO_x) heterojunction accelerated migration of photogenerated electrons along the path of MnOx→TiO_2 {001}→TiO_2{101}→Pt while photogenerated holes in the opposite direction (shown in **Figure 11D,F**). As a result, the separation efficiency of photogenerated charge carriers is greatly improved, so as to the enhanced photocatalytic performance with CH_4 and CH_3OH as the main products. In another work, Z-scheme heterojunction that is favoring for the recombination of inefficient charge carriers was constructed by coupling TiO_2 and $ZnFe_2O_4$ using Ag as electron mediator (Tahir, 2020). Superior CO yield (1025 μmol g_{cat}^{-1} h^{-1}) accompanied with the generation of CH_4 (132 μmol g_{cat}^{-1} h^{-1}) and CH_3OH (31 μmol g_{cat}^{-1} h^{-1}) should be attributed to the enhanced charge separation efficiency under UV light irradiation. It is worth nothing that the magnetic properties of $ZnFe_2O_4$ should not be ignored which facilitate the recovery of photocatalyst from solid-liquid suspension, although the solid-gas mode is undertaken in this study. Moreover, Ag could also promote visible light adsorption of the ternary system due to its strong LSPR effect, which had been demonstrated by Xu et al. using MgO-Ag-TiO_2 as photocatalyst (Xu and Carter, 2019). In order to further investigate the synergism of the LSPR effect and chemisorption of CO_2 on the improvement of photoreduction efficiency of CO_2, TiO_2/MNPs/AS heterojunctions as Au/Al_2O_3/TiO_2 (Zhao Y. et al., 2018) and Au@TiO_2 hollow spheres (THS) @CoO (Zhu et al., 2019) were synthesized. On this basis, MgAl layered double oxides (MgAl-LDO) were developed to provide both Lewis basic sites (MgO) and Lewis acid sites (Al_2O_3) for CO_2 chemisorption and H_2O dissociation among the Pt/MgAl-LDO/TiO_2 nanocomposite, respectively (Chong et al., 2018). Benefiting from the generation of monodentate carbonate (m-CO_3^{2-}) on the surface of MgO accompanied with the supply of H^+ from H_2O dissociation by Al_2O_3, the activation of CO_2 became easier and led to the increased CH_4 yield by 11 folds compared to Pt/TiO_2.

In a typical TiO_2/C/AS system, nanocarbon is served as electron channel to guide photogenerated electrons flow from TiO_2 to the AS while photogenerated holes left in the VB of TiO_2, thereby resulting in the spatial separation of photoinduced redox reactions with enhanced CO_2 photoreduction efficiency. As reported by Jung et al., mesoporous TiO_2 and a few layers of

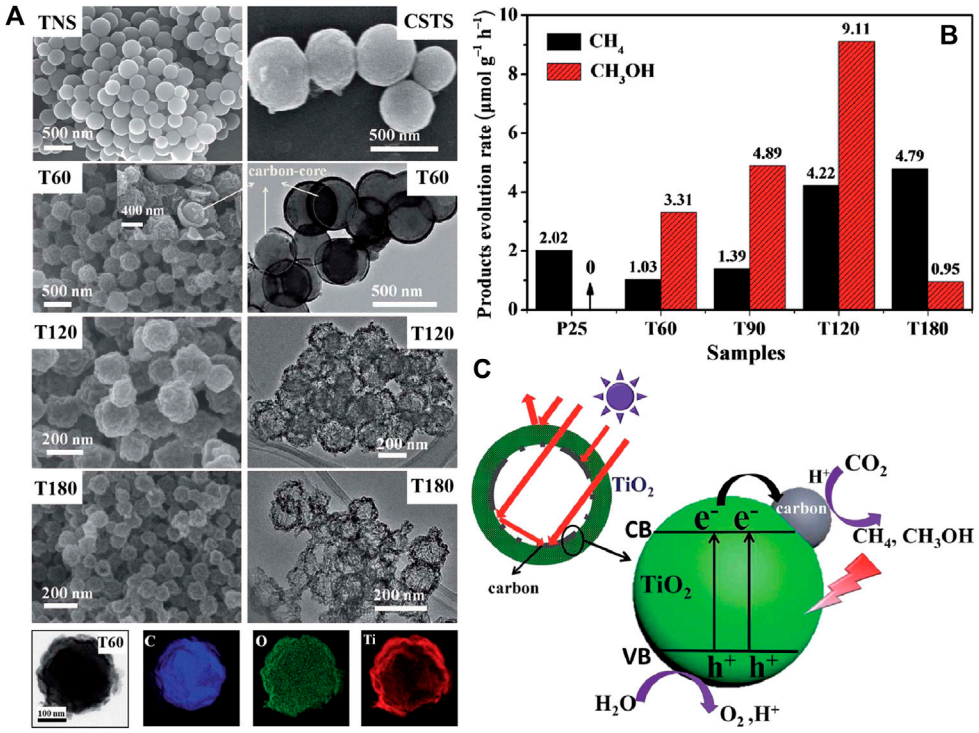

FIGURE 10 | (A) FESEM images of TNS, CSTS, T60, T120 and T180, and TEM images of T60, T120 and T180, and STEM image of T60 and the corresponding elemental mapping images of C, O and Ti; **(B)** Comparison of the photocatalytic CH_4 or CH_3OH evolution rate of carbon@TiO_2 composite samples and P25 (under simulated solar light); and **(C)** Photoexcitation process of the carbon@TiO_2 composite photocatalyst with hollow structure. Reproduced from Wang et al. (2017) with permission from the Royal Society of Chemistry.

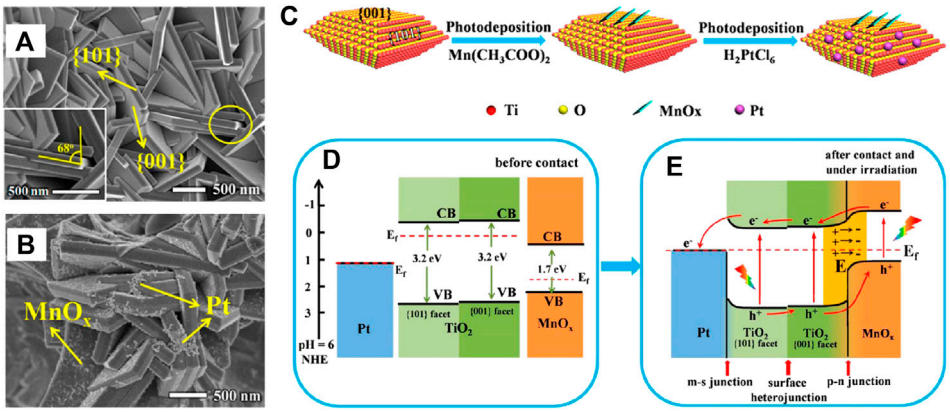

FIGURE 11 | SEM images of as-prepared **(A)** TiO_2 and **(B)** TiO_2-MnO_x-Pt (TMP); **(C)** Schematic diagram of selective photodeposition process of MnO_x nanoflakes and Pt nanoparticles on anatase TiO_2 {001} and {101} facets; Schematic diagram of proposed photocatalytic CO_2 reduction mechanism of sample TMP. The relative band energy positions of TiO_2, Pt, and MnO_x **(A)** before contact and **(B)** after contact and under irradiation. Reproduced from Meng et al. (2019) with permission from the American Chemical Society.

MoS_2 were assembled with graphene aerogel *via* one-pot hydrothermal method to construct a 3D hierarchical structure (Jung et al., 2018). In addition to high separation efficiency of photogenerated e^-/h^+ pairs, the improvement of light utilization and mass transfer efficiency based on the 3D structure of graphene with efficient visible light adsorption (Biswas et al., 2018) is also important factor that contribute to photocatalytic CO_2 reduction. Compared to semiconductors as MoS_2 (Jung et al., 2018), $CuGaS_2$ (Takayama et al., 2017) or WSe_2 (Biswas et al., 2018), noble metal nanoparticles are more efficient for the accumulation of photogenerated electrons transferred through electron channel (graphene) and favoring for the generation of

more valuable products as CH_4 and CH_3OH (Tan et al., 2015; Meng et al., 2019; Tahir, 2020). However, the high cost as well as relative low resistance toward photocorrosion restricts their application on a large scale. Photocatalytic CO_2 reduction performance of the typical TiO_2-based multicomponent heterojunctions above are listed in **Table 3**. In the future, the development of noble metal-free multicomponent heterojunction based on TiO_2 for efficient solar-driven photocatalytic CO_2 reduction will become one of the main directions in this field.

TiO_2 Based Phase and Facet Heterojunctions for CO_2 Photoreduction

TiO_2 Based Phase Heterojunction

Phase heterojunction composed of different crystal phases of the same semiconductor exhibits greater photocatalytic activity than the single-phased photocatalyst (Ma et al., 2014; Wei L. et al., 2018; Nguyen et al., 2020). This is because the contact of crystal phases with different energy band structure leads to an increase in carrier separation efficiency at the interface. Moreover, the unique interfacial trapping sites may become new photocatalytic active sites. As is known, there are four main crystal phases of TiO_2 (including anatase, rutile, brookite, and TiO_2 (B)) existed in nature, in which rutile is the most thermodynamically stable phase and can be obtained by calcining the other three polymorphs (Ma et al., 2014). Among them, as the two most widely studied TiO_2 crystal phases with photocatalytic activity, the difference in the lattice structure of anatase and rutile leads to different electronic band structures, and ultimately results in a difference in band gap width. Compared to rutile (E_g = 3.02 eV for bulk material), anatase tends to show higher photocatalytic activity due to its wider band gap (E_g = 3.20 eV for bulk material) that gives stronger redox ability to the photogenerated carriers. In addition, the higher concentration of oxygen vacancies in anatase leads to more efficient charge separation, whereas the larger specific surface area leads to more active sites exposure, which are also important factors for its better photocatalytic performance than rutile. However, the narrower band gap enables rutile to respond to photons close to the visible region. Besides, the higher crystallinity results in the better charge carrier mobility within rutile. At present, the integration of the advantages of anatase and rutile to construct a phase heterojunction for photocatalytic CO_2 reduction has attracted increasing attention of researchers. As a classic anatase-rutile phase heterojunction, the commercial Degussa P25 has been regarded as a benchmark for both photocatalytic oxidation and reduction reactions. As reported by Reñones et al., hierarchical TiO_2 nanofibres composed of anatase and rutile nanoparticles were synthesized by the calcination of electrospun TiO_2 fibers under Ar atmosphere (Reñones et al., 2016). The phase composition of the fibers depend on the calcination conditions, in which higher rutile amount (81:19) was obtained under static Ar atmosphere (Fibers B) than the dynamic sample (Fibers A, 93:7). Notably, the faster charge transport along the grain boundaries in fibers is attributed to the improved nanocrystals connection, whereas the fibers with higher anatase content exhibits lower recombination efficiency of e^-/h^+ pairs, thus endowing greater photocatalytic efficiency for reducing CO_2 to CO (10.19 μmol g_{cat}^{-1} h^{-1}). In addtion, the overall apparent quantum yields (AQY) of Fibers B (0.036%) is also higher than P25 (0.030%), indicating the enhanced utilization of incident light. However, the large amount of hydrogen evolution (19.94 μmol g_{cat}^{-1} h^{-1}) during the photocatalytic process needs to be suppressed to further improve the photoreduction efficiency of CO_2. A hydrothermal method was developed by Xiong et al. for the fabrication of anatase-rutile heterophase TiO_2 nanoparticles using $K_2TiO(C_2O_4)_2{\cdot}2H_2O$ as Ti source, which simplifies the synthesis process and makes the reaction conditions more mild (Xiong et al., 2020). Ethylene glycol (EG) was added to the hydrothermal system in order to introduce oxygen vacancy into TiO_2 (TiO_{2-x}), which could trap photogenerated e^- to restrain the recombination of e^-/h^+ pairs, thereby enhancing the photocatalytic performance of the catalysts. Electron paramagnetic resonance (EPR) spectra revealed that the concentration of oxygen vacancy increased with the increasing amount of EG during the formation process of TiO_{2-x}. However, the excess oxygen vacancies, especially the bulk oxygen vacancies, will act as the recombination center of carriers, resulting in the lower photocatalytic efficiency of as-obtained anatase-rutile heterojunction. Thus, the concentration and distribution of oxygen vacancies should be reasonably designed and constructed to promote the performance of the semiconductor photocatalysts. As reported by Xiong et al. (Xiong et al., 2020), the TiO_2-EG10 sample synthesized using 30 ml H_2O and 10 ml EG as solvent exhibits the optimized photocatalytic activity in reducing CO_2 to CH_4 (43.2 μmol g_{cat}^{-1} h^{-1}), which is 54 times higher than that of P25 (0.8 μmol g_{cat}^{-1} h^{-1}). Usually, the optimization of oxygen vacancy concentration in photocatalyst is based on the feedback of experimental results rather than theoretical design. Therefore, the critical oxygen vacancy concentration in different photocatalytic systems is various, which is difficult to give a definite value. Considering the poor visible light responsibility of anatase/rutile phase heterojunction, it is necessary to reduce its band gap width to improve the utilization of incoming solar spectrum. In addition, the combination of disordered anatase (A_d) with more active sites and ordered rutile (R_o) for fast transport of e^- and h^+ to suppress charge recombination can further enhance the photoreduction efficiency of CO_2 by TiO_2. On this basis, a phase-selective A_d/R_o TiO_2 was prepared by treating P25 in the sodium alkyl amine solutions at room temperature and ambient atmosphere, in which anatase among P25 was selective reduced to produce more Ti^{3+} defects (Hwang et al., 2019). The existence of multi-internal energy bands of Ti^{3+} defect sites in A_d reduces the band gap of A_d/R_o TiO_2 to 2.62 eV, while the newly conduction band (-0.27 eV) is well match the redox potential of CO_2/CH_4 (-0.24 V vs. NHE). As a result, the VLD A_d/R_o TiO_2 exhibits enhanced reactivity to convert CO_2 into CH_4 (3.98 μmol g_{cat}^{-1} h^{-1}), which is higher than metal (W, Ru, Ag, and Pt)-doped P25. To further improve the CH_4 generation selectivity, 0.1% mass Pt was loaded on the H_2O_2 modified TiO_2 (M-TiO_2, containing two phases of anatase and rutile) through photoelectrodeposition (Pt/M-TiO_2) (Lee J. S. et al., 2016). As electron sinks, photogenerated electrons

are enriched by Pt nanoparticles and form high charge density areas near their surface, which is favoring for the photoreduction of CO_2 to CH_4 in cooperation with sufficient protons generated by water oxidation. Notably, the yield of CH_4 on Pt/M-TiO_2 is about 60 times that of bare M-TiO_2, whereas no CO formation can be observed, indicating its high selectivity toward photoreduction products of CO_2. Compared with the common method that fabricates phase heterojunction by calcining TiO_2 gel, the MOFs (NH_2-MIL-125) derived method was adopted by Chen et al. (Chen et al., 2020) to fabricate anatase-rutile junction with large surface area and porous structure that favored for CO_2 adsorption. Besides, the *in situ* phase transformation from anatase (211) plane to rutile (211) plane results in the highly dispersed anatase/rutile interface for efficient interfacial charge separation, inhibiting the recombination of photogenerated e^-/h^+ pairs significantly. Moreover, the N-doped carbon layer (generated by the pyrolysis of organic ligands) coating on the anatase/rutile heterostructure promotes the electric conductivity of the photocatalytic system, and expandes its light absorption range to 700 nm. The synergism of N-doped carbon and paragenetic anatase/rutile heterostructure derives the enhanced photoreduction efficiency of CO_2 to CO, which is 7.6 folds compared with P25. Although the added value of the product (CO) is limited, this method has guiding significance for the design and synthesis of other MOFs derived heterostructured photocatalytic systems. In addition to rutile, anatase can also form a phase heterojunction with brookite for photocatalytic CO_2 reduction (Jin et al., 2019). Generally, Sr^{2+} ions were introduced to the $TiCl_4$-involed hydrothermal system for the fabrication of $SrCO_3$-modified brookite/anatase TiO_2 heterophase junctions (HPJs). Similar to the anatase-rutile system, the interfacial electron transfer from brookite to anatase promotes the photogenerated charge separation. Moreover, the surface modification of HPJs by $SrCO_3$ can improve the adsorption of CO_2/H_2O, which can also serve as an efficient cocatalyst for the selective reduction of CO_2 to CH_4. Especially, 1.0 w/w% $SrCO_3$/HPJs composite shows the selectivity of ca. 7.45 for CH_4/CO (19.66/2.64 μmol g_{cat}^{-1} h^{-1}), which is ca. 32.4 folds compared with pristine brookite TiO_2 (0.79/3.46 μmol g_{cat}^{-1} h^{-1}). This work can also provide guidance for the development of heterojunctions composed of TiO_2 HPJs and alkaline earth metal carbonates *via* a facile one pot hydrothermal route.

TiO_2 Based Facet Heterojunction

The difference of geometrical and electronic structures between different crystal facets of the same semiconductor results in the distinctness of their photocatalytic activity. Facet engineering has been applied to control the exposed crystal facet of semiconductors, in order to increase the exposure of active sites and promote the adsorption and activation of substrates, so as to achieve enhanced photocatalytic performance. In terms of anatase TiO_2, the {101} has the lowest surface energy (0.44 J m^{-2}) among the low-index facets (including {001}, {010} and {101}) and dominant for CO_2 adsorption basing on first-principles calculations (Yu et al., 2014). The photogenerated electrons transferred from the {101} of TiO_2 to CO_2 facilitates its activation and reduction. Moreover, the enriched photogenerated holes on the {001} of TiO_2 can accelerate the oxidation reactions. Photocatalytic CO_2 reduction over anatase TiO_2 with coexposed {001} and {101} facets was reported by Yu et al. for the first time with the propose of "facet heterojunction" concept (Yu et al., 2014). The facet ratio of {001} and {101} can be tuned by adjusting the amount of HF during the fabrication process, as see in **Figures 12A,B**, while the correspondingly schematic illustration is displayed in **Figure 12C**. In particular, the formation of facet heterojunction between {001} and {101} contributes to the transfer and separation of photogenerated carriers, which is beneficial to the enrichment of e^- and h^+ on {101} and {001}, respectively (shown in **Figure 12D**). As a result, photocatalytic CO_2 reduction occurs selectively on the {101} facet, while the optimized photocatalytic performance is realized when the facet ratio of {101} to {001} is 45–55, in which CO_2 is reduced to CH_4 with a generation rate of 1.35 μmol g_{cat}^{-1} h^{-1} (**Figure 12E**). On this basis, oxygen vacancies were introduced to the {101} and {001} facets coexposed anatase TiO_2 for the further enhancement of photocatalytic performance, where TiO_2 fabricated *via* hydrothermal route in the presence of HF was reduced by $NaBH_4$ to generate surface oxygen defects (Liu L. et al., 2016). In addition to the high charge separation efficiency at the interface of {001} and {101} facets, the visible light responsibility attributed to the newly generated Ti^{3+} energy state as well as the improved CO_2 adsorption and activation derived from the synergism of Ti^{3+} and oxygen vacancies resulted in the enhanced photoreduction efficiency of CO_2. An explicit atomistic model of the interface was applied for further investigation of charge transfer between coexposed {101} and {001} facets of anatase TiO_2 (Di Liberto et al., 2019). The first principles calculations revealed that the localization of h^+ on oxygen ion of the {001} side and the migration of e^- to Ti ion of the {101} side promoted the charge separation and suppressed their recombination, hence responsible for the enhanced photocatalytic activity of the facet junction. In another work, HF was also used by Cao et al. (Cao et al., 2016) for tuning the ratio of coexposed {101} and {001} facets of anatase TiO_2 in a hydrothermal system where nanotube titanic acid (NTA) was used as precursor to facilitate the mass transfer of HF, thereby simplifying the generation of {001} facet. Notably, the anatase TiO_2 nanocrystals with coexposed 51% {001} and 49% {101} facets exhibit the highest photocatalytic activity for reducing CO_2 to CH_4 (1.58 μmol g_{cat}^{-1} h^{-1}) among pure TiO_2 series, which can be further improved to 4.0 μmol g_{cat}^{-1} h^{-1} by decorating 1wt% Pt^0 nanoparticles on their surfaces. The effect of Pt loading for the enhanced photocatalytic performance of anatase TiO_2 facet heterojunction ({101}/{001}) was further investigated by Xiong et al. (Xiong et al., 2017a). Pt precursors (H_2PtCl_6 or Pt $(NH_3)_4Cl_2$) and deposition methods (photodeposition or chemical reduction) had significant influence on size, distribution, and valence states of Pt nanoparticles, hence led to the difference of photocatatic performance. In particular, the well dispersed Pt nanoparticles fabricated by chemical reducing H_2PtCl_6 (HC) possessed suitable particle size and high Pt^0/Pt^{II} ratio (1.15), which led to efficient separation of photogenerated carriers and high efficiency for photoreduction CO_2. Coupling

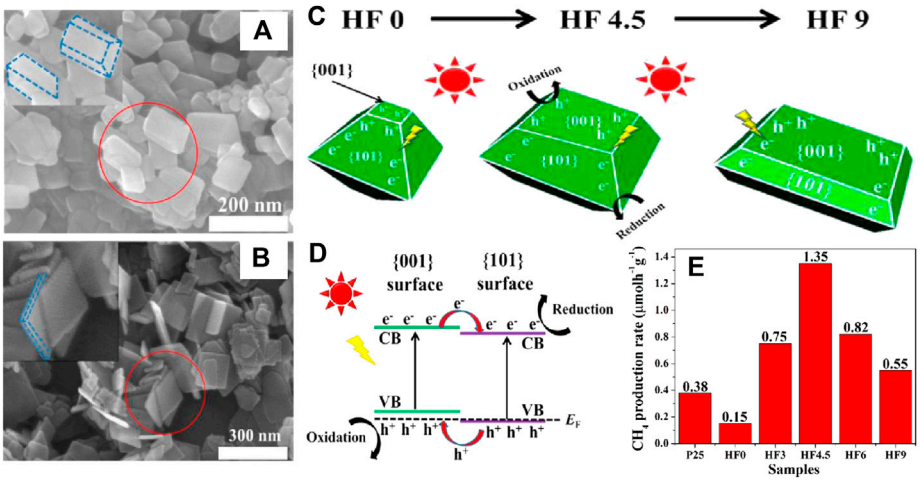

FIGURE 12 | FESEM images of **(A)** HF4.5 and **(B)** HF9; Schematic illustration of **(C)** tuning the ratio of {101} to {001} facets of anatase TiO_2 by adjusting the amount of HF, and **(D)** charge transfer at the interface of {101}-{001} facet heterojunction of anatase TiO_2; **(E)** Comparison of the photocatalytic CH_4-production activity of P25 and the TiO_2 samples prepared by varying HF amount. Reproduced from Yu et al. (2014) with permission from the American Chemical Society.

with graphene is also an efficient strategy to enhance the activity of anatase TiO_2 facet heterojunction ({101}/{001}) for the photoreduction of CO_2 (Xiong et al., 2016). Charge transfer between {101} and {001} facets along with the migration of electrons from TiO_2 to graphene greatly improved the separation efficiency of photogenerated carriers, thus increasing the yield of CO by photoreducing CO_2. Photocatalytic CO_2 reduction performance of the typical TiO_2-based phase or facet heterojunctions above are listed in **Table 3**.

CONCLUSIONS AND PROSPECTS

This review summarizes the recent advances in the rational design, fabrication and photocatalytic performance of TiO_2-based heterojunctions for converting CO_2 into solar fuels with water oxidation. Generally, photocatalytic CO_2 reduction that mimic the nature photosynthesis of green plants exhibits great potential for the reduction of CO_2 level in the atmosphere and storage of solar energy in hydrocarbon fuels, so as to alleviate the impact of energy crisis and climate change on the development of human society. However, some obstacles, such as low solar energy conversion efficiency, slow generation rate and poor selectivity toward reduction products of CO_2, and common photocorrosion phenomenon facing the current photocatalytic systems, restricts the practical application of this very promising technology. In recent years, tremendous efforts have been devoted to fabricate TiO_2-based heterojunctions, in order to realize enhanced photocatalytic performance for CO_2 conversion, thus giving new life to this traditional and systematically studied photocatalyst. Although the composition, morphology, architecture and photocatalytic mechanism of TiO_2-based heterojunctions are various, they have much in common that favors for photoreduction of CO_2 as follows: 1) the efficient electron transfer at the heterointerface that promotes spatial separation of photogenerated e^-/h^+ pairs and prolongs their lifetime to participate in the photoinduced redox reactions; 2) the expanded light adsorption range and enhanced visible light responsibility, making it possible for solar-driven photocatalytic CO_2 reduction; 3) the enlarged CO_2 adsorption capacity due to the high specific surface area with highly exposed active sites that combine CO_2 by chemical action, which could also activate the adsorbed CO_2 molecules and facilitate hydrocarbon generation; 4) the increase in selectivity toward specific photoreduction products of CO_2 is attributed to the contribution of the cocatalysts.

Although considerable progress has been made on TiO_2-based heterojunction for photocatalytic CO_2 reduction, it is still far from practical application. On the one hand, the formation of multi-carbon products has always been a bottleneck in this field. The study of CO_2 photoreduction intermediates combined with *in-situ* analysis technology and theoretical calculations needs to be more in-depth in order to clarify the formation mechanisms of different hydrocarbons and guide for the rational design of photocatalysts for the generation of multi-carbon product with high selectivity. On the other hand, pre-defined design of the components and their spatial arrangement in the heterojunction for the optimized phtotcatalytic performance is still a great challenge. It is worth nothing that the difference in synthesis conditions limits the flexibility of component selection, which also complicates the synthesis procedure and reduces the yield of expected heterojunction photocatalyst. At the same time, the randomness arrangement of different components in many cases and the variability of the catalyst morphology and structure affect the photocatalytic performance significantly, which also makes it difficult to clarify the contribution of each component and the synergism mechanism. How to overcome the above limitations to select components of the heterojunction based on photocatalytic performance only, and achieve precise control at the structural unit level, thus realizing efficient synergy of each component for

photocatalytic CO_2 reduction is one of the main directions of future development in this field. To our knowledge, recent advances in DNA origami superlattice structure (Tian et al., 2016; Tian et al., 2020) may provide a possible solution and guide the design and construction of well-ordered heterojunction photocatalysts in the future. Specifically, the precisely control of the topological structure, arrangement sequence, and assembly quantity of each building block (polyhedral DNA frame) during the self-assembly process makes it possible for heterojunction photocatalysts with controllable structure and adjustable performance, which is expected to become the future research hotspot in the field of photocatalytic CO_2 reduction. In addition, efficient solar harvesting systems are in great demand to replace artificial light sources with high energy consumption, since efficient photoreduction of CO_2 is based on high light intensity. On the one hand, upconversion quantum dots can be introduced into the heterostructured photocatalyst, in which some of the long-waved visible light in the incident light can be converted into short-waved partial that can excite the photocatalyst to generate e^- and h^+ pairs. On the other hand, focusing lens system can be added to the photoreactor to enhance the concentration of sunlight, then the photocatalyst can operate under higher light intensity and exhibit optimized activity. Although the efficiency of photocatalytic CO_2 reduction is far less than that of electrocatalysis, relying entirely on solar energy will become its irreplaceable advantage. Furthermore, the enrichment of CO_2 in air will become an important consideration in the design of heterojunction photocatalysts, which meet the needs of practical applications. Fortunately, the research on CO_2 storage and controlled release provides the possible solution while the visible light-triggered capture and release of CO_2 from stable MOFs become the most promising candidate (Park et al., 2011; Li et al., 2016; Lyndon et al., 2015). Obviously, combination of photocatalyst and the above MOFs can realize the efficient recycling of CO_2 and improve the efficiency of its conversion into solar fuel, which is expected to become a research hot spot in the future.

In summary, the heterojunction photocatalysts with well-organized structure, optimized solar energy conversion efficiency, ideal turnover frequency of CO_2, and high reduction product selectivity are still the direction of efforts in the future. We hope that this review can inspire new ideas to guide the design and synthesis of high-performance photocatalysts for photoreduction of CO_2 into solar fuels, thus accelerating the industrialization process of this very promising technology and providing practical help to alleviate energy and environmental crises.

AUTHOR CONTRIBUTIONS

KL designed and wrote the review with input from CT, YT, SW, and QM for conceiving, writing, and editing the manuscript.

FUNDING

This study was supported by Shenzhen Science and Technology Innovation Program (Grand No. GJHZ20190819151807167), Post-doctoral Foundation Project of Shenzhen Polytechnic (Grand No. 6020330008K0), the Fundamental Research Funds for the Central Universities (Grand No. 020514380141), and China Postdoctoral Science Foundation (Grand No. 2020M671437).

REFERENCES

Aguirre, M. E., Zhou, R., Eugene, A. J., Guzman, M. I., and Grela, M. A. (2017). Cu_2O/TiO_2 heterostructures for CO_2 reduction through a direct Z-scheme: protecting Cu_2O from photocorrosion. *Appl. Catal. B* 217, 485–493. doi:10.1016/j.apcatb.2017.05.058

An, X., Li, K., and Tang, J. (2014). Cu_2O/reduced graphene oxide composites for the photocatalytic conversion of CO_2. *ChemSusChem* 7 (4), 1086–1093. doi:10.1002/cssc.201301194

Aresta, M., Dibenedetto, A., and Angelini, A. (2014). Catalysis for the valorization of exhaust carbon: from CO_2 to chemicals, materials, and fuels. Technological use of CO_2. *Chem. Rev.* 114 (3), 1709–1742. doi:10.1021/cr4002758

Bai, S., Jiang, J., Zhang, Q., and Xiong, Y. (2015). Steering charge kinetics in photocatalysis: intersection of materials syntheses, characterization techniques and theoretical simulations. *Chem. Soc. Rev.* 44, 2893–2939. doi:10.1039/c5cs00064e

Barber, J. (2009). Photosynthetic energy conversion: natural and artificial. *Chem. Soc. Rev.* 38 (1), 185–196. doi:10.1039/b802262n

Bie, C., Zhu, B., Xu, F., Zhang, L., and Yu, J. (2019). *In situ* grown monolayer N-doped graphene on CdS hollow spheres with seamless contact for photocatalytic CO_2 reduction. *Adv. Mater.* 31 (42), 1902868. doi:10.1002/adma.201902868

Biswas, M. R. U. D., Ali, A., Cho, K. Y., and amd Oh, W. C. (2018). Novel synthesis of WSe_2 -graphene-TiO_2 ternary nanocomposite *via* ultrasonic technics for high photocatalytic reduction of CO_2 into CH_3OH. *Ultrason. Sonochem.* 42, 738–746. doi:10.1016/j.ultsonch.2017.12.030

Brockway, P. E., Owen, A., Brand-Correa, L. I., and Hardt, L. (2019). Estimation of global final-stage energy-return-on-investment for fossil fuels with comparison to renewable energy sources. *Nat. Energ.* 4 (7), 612–621. doi:10.1038/s41560-019-0425-z

Cao, S., Shen, B., Tong, T., Fu, J., and Yu, J. (2018). 2D/2D heterojunction of ultrathin MXene/Bi_2WO_6 nanosheets for improved photocatalytic CO_2 reduction. *Adv. Funct. Mater.* 28 (21), 1800136. doi:10.1002/adfm.201800136

Cao, Y., Li, Q., Li, C., Li, J., and Yang, J. (2016). Surface heterojunction between (001) and (101) facets of ultrafine anatase TiO_2 nanocrystals for highly efficient photoreduction CO_2 to CH_4. *Appl. Catal. B* 198, 378–388. doi:10.1016/j.apcatb.2016.05.071

Chen, S., Gao, H., Han, M., Chen, X., Zhang, X., Dong, W., et al. (2020). *In situ* self-transformation synthesis of N-doped carbon coating paragenetic anatase/rutile heterostructure with enhanced photocatalytic CO_2 reduction activity. *ChemCatChem* 12, 3274–3284. doi:10.1002/cctc.202000137

Chen, X., Zhou, Y., Liu, Q., Li, Z., Liu, J., and Zou, Z. (2012). Ultrathin, single-crystal WO_3 nanosheets by two-dimensional oriented attachment toward enhanced photocatalystic reduction of CO_2 into hydrocarbon fuels under visible light. *ACS Appl. Mater. Inter.* 4 (7), 3372–3377. doi:10.1021/am300661s

Cheng, X., Dong, P., Huang, Z., Zhang, Y., Chen, Y., Nie, X., et al. (2017). Green synthesis of plasmonic Ag nanoparticles anchored TiO_2 nanorod arrays using cold plasma for visible-light-driven photocatalytic reduction of CO_2. *J. Co$_2$* Util. 20, 200–207. doi:10.1016/j.jcou.2017.04.009

Chong, R., Su, C., Du, Y., Fan, Y., Ling, Z., Chang, Z., et al. (2018). Insights into the role of MgAl layered double oxides interlayer in Pt/TiO_2 toward photocatalytic CO_2 reduction. *J. Catal.* 363, 92–101. doi:10.1016/j.jcat.2018.04.020

Chowdhury, S., Parshetti, G. K., and Balasubramanian, R. (2015). Post-combustion CO_2 capture using mesoporous TiO_2/graphene oxide nanocomposites. *Chem. Eng. J.* 263, 374–384. doi:10.1016/j.cej.2014.11.037

Corma, A., and Garcia, H. (2013). Photocatalytic reduction of CO_2 for fuel production: possibilities and challenges. *J. Catal.* 308, 168–175. doi:10.1016/j.jcat.2013.06.008

Di Liberto, G., Tosoni, S., and Pacchioni, G. (2019). Role of heterojunction in charge carriers separation in coexposed anatase (001)-(101) surfaces. *J. Phys. Chem. Lett.* 10, 2372–2377. doi:10.1021/acs.jpclett.9b00504

Dogutan, D. K., and Nocera, D. G. (2019). Artificial photosynthesis at efficiencies greatly exceeding that of natural photosynthesis. *Acc. Chem. Res.* 52 (11), 3143–3148. doi:10.1021/acs.accounts.9b00380

Fu, J., Jiang, K., Qiu, X., Yu, J., and Liu, M. (2019). Product selectivity of photocatalytic CO2 reduction reactions. *Mater. Today* 32, 222–243. doi:10.1016/j.mattod.2019.06.009

Fujishima, A., and Honda, K. (1972). Electrochemical photolysis of water at a semiconductor electrode. *Nature* 238 (5358), 37–38. doi:10.1038/238037a0

Ganesh, I. (2014). Conversion of carbon dioxide into methanol-a potential liquid fuel: fundamental challenges and opportunities (a review). *Renew. Sustain. Energ. Rev* 31, 221–257. doi:10.1016/j.rser.2013.11.045

Gui, M. M., Chai, S. P., Xu, B. Q., and Mohamed, A. R. (2014). Enhanced visible light responsive MWCNT/TiO_2 core–shell nanocomposites as the potential photocatalyst for reduction of CO_2 into methane. *Sol. Energ. Mater. Sol. Cell* 122, 183–189. doi:10.1016/j.solmat.2013.11.034

Gui, M. M., Wong, W. M. P., Chai, S. P., and Mohamed, A. R. (2015). One-pot synthesis of Ag-MWCNT@TiO_2 core-shell nanocomposites for photocatalytic reduction of CO_2 with water under visible light irradiation. *Chem. Eng. J.* 278, 272–278. doi:10.1016/j.cej.2014.09.022

Habisreutinger, S. N., Schmidt-Mende, L., and Stolarczyk, J. K. (2013). Photocatalytic reduction of CO_2 on TiO_2 and other semiconductors. *Angew. Chem. Int. Ed.* 52 (29), 7372–7408. doi:10.1002/anie.201207199

He, Y., Zhang, L., Fan, M., Wang, X., Walbridge, M. L., Nong, Q., et al. (2015). Z-scheme SnO_{2-x}/g-C_3N_4 composite as an efficient photocatalyst for dye degradation and photocatalytic CO_2 reduction. *Sol. Energ. Mater. Sol. Cell* 137, 175–184. doi:10.1016/j.solmat.2015.01.037

Höök, M., and Tang, X. (2013). Depletion of fossil fuels and anthropogenic climate change-A review. *Energy Policy* 52, 797–809. doi:10.1016/j.enpol.2012.10.046

Hwang, H. M., Oh, S., Shim, J. H., Kim, Y. M., Kim, A., Kim, D., et al. (2019). Phase-selective disordered anatase/ordered rutile interface system for visible-light-driven, metal-free CO_2 reduction. *ACS Appl. Mater. Inter.* 11, 35693–35701. doi:10.1021/acsami.9b10837

Inoue, T., Fujishima, A., Konishi, S., and Honda, K. (1979). Photoelectrocatalytic reduction of carbon dioxide in aqueous suspensions of semiconductor powders. *Nature* 277 (5698), 637–638. doi:10.1038/277637a0

Iqbal, F., Mumtaz, A., Shahabuddin, S., Abd Mutalib, M. I., Shaharun, M. S., Nguyen, T. D., et al. (2020). Photocatalytic reduction of CO_2 to methanol over $ZnFe_2O_4$/TiO_2 (p-n) heterojunctions under visible light irradiation. *J. Chem. Technol. Biot.* 95 (8), 2208–2221. doi:10.1002/jctb.6408

Jiao, J., Wei, Y., Zhao, Z., Zhong, W., Liu, J., Li, J., et al. (2015). Synthesis of 3D ordered macroporous TiO_2-supported Au nanoparticle photocatalysts and their photocatalytic performances for the reduction of CO_2 to methane. *Catal. Today* 258, 319–326. doi:10.1016/j.cattod.2015.01.030

Jin, J., Chen, S., Wang, J., Chen, C., and Peng, T. (2019). $SrCO_3$-modified brookite/anatase TiO_2 heterophase junctions with enhanced activity and selectivity of CO_2 photoreduction to CH_4. *Appl. Surf. Sci.* 476, 937–947. doi:10.1016/j.apsusc.2019.01.176

Jung, H., Cho, K. M., Kim, K. H., Yoo, H. W., Al-Saggaf, A., Gereige, I., et al. (2018). Highly efficient and stable CO_2 reduction photocatalyst with a hierarchical structure of mesoporous TiO_2 on 3D graphene with few-layered MoS_2. *ACS Sustain. Chem. Eng.* 6 (5), 5718–5724. doi:10.1021/acssuschemeng.8b00002

Kegel, J., Povey, I. M., and Pemble, M. E. (2018). Zinc oxide for solar water splitting: a brief review of the material's challenges and associated opportunities. *Nano Energy* 54, 409–428. doi:10.1016/j.nanoen.2018.10.043

Khatun, F., Abd Aziz, A., Sim, L. C., and Monir, M. U. (2019). Plasmonic enhanced Au decorated TiO_2 nanotube arrays as a visible light active catalyst towards photocatalytic CO_2 conversion to CH_4. *J. Environ. Chem. Eng.* 7, 103233. doi:10.1016/j.jece.2019.103233

Kim, K. H., Kim, S., Moon, B. C., Choi, J. W., Jeong, H. M., Kwon, Y., et al. (2017). Quadruple metal-based layered structure as the photocatalyst for conversion of carbon dioxide into a value added carbon monoxide with high selectivity and efficiency. *J. Mater. Chem. A.* 5 (18), 8274–8279. doi:10.1039/c7ta01623a

Kondratenko, E. V., Mul, G., Baltrusaitis, J., Larrazabal, G. O., and Perez-Ramirez, J. (2013). Status and perspectives of CO_2 conversion into fuels and chemicals by catalytic, photocatalytic and electrocatalytic processes. *Energy Environ. Sci.* 6 (11), 3112–3135. doi:10.1039/c3ee41272e

Kuai, L., Zhou, Y., Tu, W., Li, P., Li, H., Xu, Q., et al. (2015). Rational construction of a CdS/reduced graphene oxide/TiO_2 core-shell nanostructure as an all-solid-state Z-scheme system for CO_2 photoreduction into solar fuels. *RSC Adv.* 5 (107), 88409–88413. doi:10.1039/c5ra14374h

Kuehnel, M. F., Orchard, K. L., Dalle, K. E., and Reisner, E. (2017). Selective photocatalytic CO_2 reduction in water through anchoring of a molecular Ni catalyst on CdS nanocrystals. *J. Am. Chem. Soc.* 139 (21), 7217–7223. doi:10.1021/jacs.7b00369

Lee, J. D., Sorescu, C., and Deng, X. Y. (2011). Electron-induced dissociation of CO_2 on TiO_2(110). *J. Am. Chem. Soc.* 133 (26), 10066–10069. doi:10.1021/ja204077e

Lee, J. S., Won, D. I., Jung, W. J., Son, H. J., Pac, C., and Kang, S. O. (2016). Widely controllable syngas production by a dye-sensitized TiO_2 hybrid system with Re^{I} and Co^{III} catalysts under visible-light irradiation. *Angew. Chem. Int. Ed.* 56 (4), 976–980. doi:10.1002/anie.201608593

Lee, K. M., Lai, C. W., Ngai, K. S., and Juan, J. C. (2016). Recent developments of zinc oxide based photocatalyst in water treatment technology: a review. *Water Res.* 88, 428–448. doi:10.1016/j.watres.2015.09.045

Lee, K. Y., Sato, K., and Mohamed, A. R. (2016). Facile synthesis of anatase-rutile TiO_2 composites with enhanced CO_2 photoreduction activity and the effect of Pt loading on product selectivity. *Mater. Lett.* 163, 240–243. doi:10.1016/j.matlet.2015.10.094

Lee, J. H., Kim, S. I., Park, S. M., and Kang, M. (2017). A p-n heterojunction NiS-sensitized TiO_2 photocatalytic system for efficient photoreduction of carbon dioxide to methane. *Ceram. Int.* 43 (2), 1768–1774. doi:10.1016/j.ceramint.2016.10.122

Li, H., Sadiq, M. M., Suzuki, K., Ricco, R., Doblin, C., Hill, A. J., et al. (2016). Magnetic metal-organic frameworks for efficient carbon dioxide capture and remote trigger release. *Adv. Mater.* 28 (9), 1839–1844. doi:10.1002/adma.201505320

Li, M., Wang, M., Zhu, L., Li, Y., Yan, Z., Shen, Z., et al. (2018). Facile microwave assisted synthesis of N-rich carbon quantum dots/dual-phase TiO_2 heterostructured nanocomposites with high activity in CO_2 photoreduction. *Appl. Catal. B* 231, 269–276. doi:10.1016/j.apcatb.2018.03.027

Li, X., Yu, J., Jaroniec, M., and Chen, X. (2019). Cocatalysts for selective photoreduction of CO_2 into solar fuels. *Chem. Rev.* 119, 3962–4179. doi:10.1021/acs.chemrev.8b00400

Lin, L. Y., Nie, Y., Kavadiya, S., Soundappan, T., and Biswas, P. (2017). N-doped reduced graphene oxide promoted nano TiO_2 as a bifunctional adsorbent/photocatalyst for CO_2 photoreduction: effect of N species. *Chem. Eng. J.* 316, 449–460. doi:10.1016/j.cej.2017.01.125

Liu, L., Jiang, Y., Zhao, H., Chen, J., Cheng, J., Yang, K., et al. (2016). Engineering coexposed {001} and {101} facets in oxygen-deficient TiO_2 nanocrystals for enhanced CO_2 photoreduction under visible light. *ACS Catal.* 6 (2), 1097–1108. doi:10.1021/acscatal.5b02098

Liu, X., Inagaki, S., and Gong, J. (2016). Heterogeneous molecular systems for photocatalytic CO_2 reduction with water oxidation. *Angew. Chem. Int. Ed.* 55 (48), 14924–14950. doi:10.1002/anie.201600395

Liu, Y., Shen, D., Zhang, Q., Lin, Y., and Peng, F. (2021). Enhanced photocatalytic CO_2 reduction in H_2O vapor by atomically thin Bi_2WO_6 nanosheets with hydrophobic and nonpolar surface. *Appl. Catal. B* 283, 119630. doi:10.1016/j.apcatb.2020.119630

Low, J., Qiu, S., Xu, D., Jiang, C., and Cheng, B. (2018). Direct evidence and enhancement of surface plasmon resonance effect on Ag-loaded TiO_2 nanotube arrays for photocatalytic CO_2 reduction. *Appl. Surf. Sci.* 434, 423–432. doi:10.1016/j.apsusc.2017.10.194

Low, J., Dai, B., Tong, T., Jiang, C., and Yu, J. (2019). *In situ* irradiated X-ray photoelectron spectroscopy investigation on a direct Z-scheme TiO_2/CdS composite film photocatalyst. *Adv. Mater.* 31, 1802981. doi:10.1002/adma.201802981

Lyndon, R., Konstas, K., Thornton, A. W., Seeber, A. J., Ladewig, B. P., and Hill, M. R. (2015). Visible light-triggered capture and release of CO2 from stable metal

organic frameworks. *Chem. Mater.* 27 (23), 7882–7888. doi:10.1021/acs.chemmater.5b02211

Ma, Y., Wang, X., Jia, Y., Chen, X., Han, H., and Li, C. (2014). Titanium dioxide-based nanomaterials for photocatalytic fuel generations. *Chem. Rev.* 114 (19), 9987–10043. doi:10.1021/cr500008u

Mao, J., Peng, T., Zhang, X., Li, K., and Zan, L. (2012). Selective methanol production from photocatalytic reduction of CO_2 on $BiVO_4$ under visible light irradiation. *Catal. Commun.* 28, 38–41. doi:10.1016/j.catcom.2012.08.008

Meinshausen, M., Meinshausen, N., Hare, W., Raper, S. C. B., Frieler, K., Knutti, R., et al. (2009). Greenhouse-gas emission targets for limiting global warming to 2 °C. *Nature* 458 (7242), 1158–1162. doi:10.1038/nature08017

Meng, A., Zhang, L., Cheng, B., and Yu, J. (2019). TiO_2-MnO_x-Pt hybrid multiheterojunction film photocatalyst with enhanced photocatalytic CO_2-reduction activity. *ACS Appl. Mater. Inter.* 11, 5581–5589. doi:10.1021/acsami.8b02552

Neațu, Ș., Maciá-Agulló, J. A., Concepción, P., and Garcia, H. (2014). Gold-copper nanoalloys supported on TiO_2 as photocatalysts for CO_2 reduction by water. *J. Am. Chem. Soc.* 136 (45), 15969–15976. doi:10.1021/ja506433k

Nguyen, T. P., Nguyen, D. L. T., Nguyen, V. H., Le, T. H., Vo, D. V. N., Trinh, Q. T., et al. (2020). Recent advances in TiO_2-based photocatalysts for reduction of CO_2 to fuels. *Nanomaterials* 10 (2), 337. doi:10.3390/nano10020337

Nie, N., Zhang, L., Fu, J., Cheng, B., and Yu, J. (2018). Self-assembled hierarchical direct Z-scheme g-C_3N_4/ZnO microspheres with enhanced photocatalytic CO_2 reduction performance. *Appl. Surf. Sci.* 441, 12–22. doi:10.1016/j.apsusc.2018.01.193

Ola, O., and Maroto-Valer, M. M. (2015). Review of material design and reactor engineering on TiO_2 photocatalysis for CO_2 reduction. *J. Photochem. Photobiol. C* 24, 16–42. doi:10.1016/j.jphotochemrev.2015.06.001

Olah, G. A., Prakash, G. K. S., and Goeppert, A. (2011). Anthropogenic chemical carbon cycle for a sustainable future. *J. Am. Chem. Soc.* 133 (33), 12881–12898. doi:10.1021/ja202642y

Olowoyo, J. O., Kumar, M., Jain, S. L., Babalola, J. O., Vorontsov, A. V., and Kumar, U. (2018). Insight into reinforced photocatalytic activity of CNT-TiO_2 nanocomposite for CO_2 reduction and water splitting. *J. Phys. Chem. C* 123, 367–378. doi:10.1021/acs.jpcc.8b07894

Olowoyo, J. O., Kumar, M., Singh, B., Oninla, V. O., Babalola, J. O., Valdés, H., et al. (2019). Self-assembled reduced graphene oxide-TiO_2 nanocomposites: synthesis, DFTB+ calculations, and enhanced photocatalytic reduction of CO_2 to methanol. *Carbon* 147, 385–397. doi:10.1016/j.carbon.2019.03.019

Park, J., Yuan, D., Pham, K. T., Li, J. R., Yakovenko, A., and Zhou, H. C. (2011). Reversible alteration of CO2 adsorption upon photochemical or thermal treatment in a metal-organic framework. *J. Am. Chem. Soc.* 134 (1), 99–102. doi:10.1021/ja209197f

Patil, S. B., Basavarajappa, P. S., Ganganagappa, N., Jyothi, M. S., Raghu, A. V., and Reddy, K. R. (2019). Recent advances in non-metals-doped TiO_2 nanostructured photocatalysts for visible-light driven hydrogen production, CO_2 reduction and air purification. *Inter. J. Hydrogen Energ.* doi:10.1016/j.ijhydene.2019.03.164

Raza, A., Shen, H., Haidry, A. A., Sun, L., Liu, R., and Cui, S. (2020). Studies of Z-scheme WO_3-TiO_2/Cu_2ZnSnS_4 ternary nanocomposite with enhanced CO_2 photoreduction under visible light irradiation. *J. Co₂* Util. 37, 260–271. doi:10.1016/j.jcou.2019.12.020

Reñones, P., Moya, A., Fresno, F., Collado, L., Vilatela, J. J., and de la Peña O'Shea, V. A. (2016). Hierarchical TiO_2 nanofibres as photocatalyst for CO_2 reduction: influence of morphology and phase composition on catalytic activity. *J. Co₂* Util. 15, 24–31. doi:10.1016/j.jcou.2016.04.002

Rodríguez, V., Camarillo, R., Martínez, F., Jiménez, C., and Rincón, J. (2020). CO_2 photocatalytic reduction with CNT/TiO_2 based nanocomposites prepared by high-pressure technology. *J. Supercrit. Fluids* 163, 104876. doi:10.1016/j.supflu.2020.104876

She, H., Wang, Y., Zhou, H., Li, Y., Wang, L., Huang, J., et al. (2018). Preparation of $Zn_3In_2S_6$/TiO_2 for enhanced CO_2 photocatalytic reduction activity *via* Z-scheme electron transfer. *ChemCatChem* 11, 753–759. doi:10.1002/cctc.201801745

Shehzad, N., Tahir, M., Johari, K., Murugesan, T., and Hussain, M. (2018a). Improved interfacial bonding of graphene-TiO_2 with enhanced photocatalytic reduction of CO_2 into solar fuel. *J. Environ. Chem. Eng.* 6, 6947–6957. doi:10.1016/j.jece.2018.10.065

Shehzad, N., Tahir, M., Johari, K., Murugesan, T., and Hussain, M. (2018b). A critical review on TiO_2 based photocatalytic CO_2 reduction system: strategies to improve efficiency. *J. Co₂ Util.* 26, 98–122. doi:10.1016/j.jcou.2018.04.026

Shi, W., Guo, X., Cui, C., Jiang, K., Li, Z., Qu, L., et al. (2019). Controllable synthesis of Cu_2O decorated WO_3 nanosheets with dominant (001) facets for photocatalytic CO_2 reduction under visible-light irradiation. *Appl. Catal. B* 243, 236–242. doi:10.1016/j.apcatb.2018.09.076

Shindell, D., and Smith, C. J. (2019). Climate and air-quality benefits of a realistic phase-out of fossil fuels. *Nature* 573 (7774), 408–411. doi:10.1038/s41586-019-1554-z

Sim, L. C., Leong, K. H., Saravanan, P., and Ibrahim, S. (2015). Rapid thermal reduced graphene oxide/Pt-TiO_2 nanotube arrays for enhanced visible-light-driven photocatalytic reduction of CO_2. *Appl. Surf. Sci.* 358, 122–129. doi:10.1016/j.apsusc.2015.08.065

Solomon, S., Plattner, G. K., Knutti, R., and Friedlingstein, P. (2009). Irreversible climate change due to carbon dioxide emissions. *Proc. Natl. Acad. Sci. U. S. A.* 106, 1704–1709. doi:10.1073/pnas.0812721106

Stott, P. A., Tett, S., Jones, G., Allen, M., Mitchell, J., and Jenkins, G. (2000). External control of 20th century temperature by natural and anthropogenic forcings. *Science* 290 (5499), 2133–2137. doi:10.1126/science.290.5499.2133

Tahir, M., Tahir, B., and Amin, N. A. S. (2017). Synergistic effect in plasmonic Au/Ag alloy NPs co-coated TiO_2 NWs toward visible-light enhanced CO_2 photoreduction to fuels. *Appl. Catal. B* 204, 548–560. doi:10.1016/j.apcatb.2016.11.062

Tahir, M. (2020). Well-designed $ZnFe_2O_4$/Ag/TiO_2 nanorods heterojunction with Ag as electron mediator for photocatalytic CO_2 reduction to fuels under UV/visible light. *J. Co₂* Util. 37, 134–146. doi:10.1016/j.jcou.2019.12.004

Takayama, T., Sato, K., Fujimura, T., Kojima, Y., Iwase, A., and Kudo, A. (2017). Photocatalytic CO_2 reduction using water as an electron donor by a powdered Z-scheme system consisting of metal sulfide and an RGO-TiO_2 composite. *Faraday Discuss.* 198, 397–407. doi:10.1039/c6fd00215c

Tan, L. L., Ong, W. J., Chai, S. P., and Mohamed, A. R. (2015). Noble metal modified reduced graphene oxide/TiO_2 ternary nanostructures for efficient visible-light-driven photoreduction of carbon dioxide into methane. *Appl. Catal. B* 166-167, 251–259. doi:10.1016/j.apcatb.2014.11.035

Tan, L. L., Ong, W. J., Chai, S. P., and Mohamed, A. R. (2017). Photocatalytic reduction of CO_2 with H_2O over graphene oxide-supported oxygen-rich TiO_2 hybrid photocatalyst under visible light irradiation: process and kinetic studies. *Chem. Eng. J.* 308, 248–255. doi:10.1016/j.cej.2016.09.050

Tan, D., Zhang, J., Shi, J., Li, S., Zhang, B., Tan, X., et al. (2018). Photocatalytic CO_2 transformation to CH_4 by Ag/Pd bimetals supported on N-doped TiO_2 nanosheet. *ACS Appl. Mater. Inter.* 10 (29), 24516–24522. doi:10.1021/acsami.8b06320

Tasbihi, M., Fresno, F., Simon, U., Villar-García, I. J., Pérez-Dieste, V., Escudero, C., et al. (2018a). On the selectivity of CO_2 photoreduction towards CH_4 using Pt/TiO_2 catalysts supported on mesoporous silica. *Appl. Catal. B* 239, 68–76. doi:10.1016/j.apcatb.2018.08.003

Tasbihi, M., Kočí, K., Edelmannová, M., Troppová, I., Reli, M., and Schomäcker, R. (2018b). Pt/TiO_2 photocatalysts deposited on commercial support for photocatalytic reduction of CO_2. *J. Photochem. Photobiol. A.* 366, 72–80. doi:10.1016/j.jphotochem.2018.04.012

Thi Thanh Truc, N., Giang Bach, L., Thi Hanh, N., Pham, T. D., Thi Phuong Le Chi, N., Trinh Tran, D., et al. (2019). The superior photocatalytic activity of Nb doped TiO_2/g-C_3N_4 direct Z-scheme system for efficient conversion of CO_2 into valuable fuels. *J. Colloid Interf. Sci.* 540, 1–8. doi:10.1016/j.jcis.2019.01.005

Tian, Y., Lhermitte, J. R., Bai, L., Vo, T., Xin, H. L., Li, H., et al. (2020). Ordered three-dimensional nanomaterials using DNA-prescribed and valence-controlled material voxels. *Nat. Mater.* doi:10.1038/s41563-019-0550-x

Tian, Y., Zhang, Y., Wang, T., Xin, H. L., Li, H., and Gang, O. (2016). Lattice engineering through nanoparticle-DNA frameworks. *Nat. Mater.* 15, 654–661. doi:10.1038/NMAT4571

Tu, W., Zhou, Y., Liu, Q., Yan, S., Bao, S., Wang, X., et al. (2013). An *in situ* simultaneous reduction-hydrolysis technique for fabrication of TiO_2-graphene 2D sandwich-like hybrid nanosheets: graphene-promoted selectivity of photocatalytic-driven hydrogenation and coupling of CO_2 into methane and ethane. *Adv. Funct. Mater.* 23 (14), 1743–1749. doi:10.1002/adfm.201202349

Tu, W., Zhou, Y., and Zou, Z. (2014). Photocatalytic conversion of CO_2 into renewable hydrocarbon fuels: state-of-the-art accomplishment, challenges, and prospects. *Adv. Mater.* 26 (27), 4607–4626. doi:10.1002/adma.201400087

Tu, W., Guo, W., Hu, J., He, H., Li, H., Li, Z., et al. (2020). State-of-the-art advancements of crystal facet-exposed photocatalysts beyond TiO_2: design and dependent performance for solar energy conversion and environment applications. *Mater. Today* 33, 75–86. doi:10.1016/j.mattod.2019.09.003

Wang, H., Zhang, L., Chen, Z., Hu, J., Li, S., Wang, Z., et al. (2014). Semiconductor heterojunction photocatalysts: design, construction, and photocatalytic performances. *Chem. Soc. Rev.* 43 (15), 5234. doi:10.1039/c4cs00126e

Wang, W., Xu, D., Cheng, B., Yu, J., and Jiang, C. (2017). Hybrid carbon@TiO_2 hollow spheres with enhanced photocatalytic CO_2 reduction activity. *J. Mater. Chem. A.* 5 (10), 5020–5029. doi:10.1039/c6ta11121a

Wang, H., Yong, D., Chen, S., Jiang, S., Zhang, X., Shao, W., et al. (2018). Oxygen-vacancy-mediated exciton dissociation in BiOBr for boosting charge-carrier-involved molecular oxygen activation. *J. Am. Chem. Soc.* 140 (5), 1760–1766. doi:10.1021/jacs.7b10997

Wang, H., Zhang, L., Wang, K., Sun, X., and Wang, W. (2019). Enhanced photocatalytic CO_2 reduction to methane over $WO_3{\cdot}0.33H_2O$ *via* Mo doping. *Appl. Catal. B* 243, 771–779. doi:10.1016/j.apcatb.2018.11.021

Wang, K., Jiang, R., Peng, T., Chen, X., Dai, W., and Fu, X. (2019). Modeling the effect of Cu doped TiO_2 with carbon dots on CO_2 methanation by H_2O in a photo-thermal system. *Appl. Catal. B* 256, 117780. doi:10.1016/j.apcatb.2019.117780

Wang, L., Jin, P., Huang, J., She, H., and Wang, Q. (2019). Integration of copper(II)-porphyrin zirconium metal-organic framework and titanium dioxide to construct Z-scheme system for highly improved photocatalytic CO_2 reduction. *ACS Sustain. Chem. Eng.* 7, 15660–15670. doi:10.1021/acssuschemeng.9b03773

Wang, R., Shen, J., Sun, K., Tang, H., and Liu, Q. (2019). Enhancement in photocatalytic activity of CO_2 reduction to CH_4 by 0D/2D Au/TiO_2 plasmon heterojunction. *Appl. Surf. Sci.* 493, 1142–1149. doi:10.1016/j.apsusc.2019.07.121

Wang, C., Liu, X., He, W., Zhao, Y., Wei, Y., Xiong, J., et al. (2020a). All-solid-state Z-scheme photocatalysts of g-C_3N_4/Pt/macroporous-(TiO_2@carbon) for selective boosting visible-light-driven conversion of CO_2 to CH_4. *J. Catal.* 389, 440–449. doi:10.1016/j.jcat.2020.06.026

Wang, C., Zhao, Y., Xu, H., Li, Y., Wei, Y., Liu, J., et al. (2020b). Efficient Z-scheme photocatalysts of ultrathin g-C_3N_4-wrapped Au/TiO_2-nanocrystals for enhanced visible-light-driven conversion of CO_2 with H_2O. *Appl. Catal. B* 263, 118314. doi:10.1016/j.apcatb.2019.118314

Wang, A., Wu, S., Dong, J., Wang, R., Wang, J., Zhang, J., et al. (2021). Interfacial facet engineering on the Schottky barrier between plasmonic Au and TiO_2 in boosting the photocatalytic CO_2 reduction under ultraviolet and visible light irradiation. *Chem. Eng. J.* 404, 127145. doi:10.1016/j.cej.2020.127145

Wei, L., Yu, C., Zhang, Q., Liu, H., and Wang, Y. (2018). TiO_2-based heterojunction photocatalysts for photocatalytic reduction of CO_2 to solar fuels. *J. Mater. Chem. A.* 6, 22411–22436. doi:10.1039/c8ta08879a

Wei, Y., Wu, X., Zhao, Y., Wang, L., Zhao, Z., Huang, X., et al. (2018). Efficient photocatalysts of TiO_2 nanocrystals-supported PtRu alloy nanoparticles for CO_2 reduction with H_2O: synergistic effect of Pt-Ru. *Appl. Catal. B* 236, 445–457. doi:10.1016/j.apcatb.2018.05.043

Wei, Z. H., Wang, Y. F., Li, Y. Y., Zhang, L., Yao, H. C., and Li, Z. J. (2018). Enhanced photocatalytic CO_2 reduction activity of Z-scheme CdS/$BiVO_4$ nanocomposite with thinner $BiVO_4$ nanosheets. *J. Co₂ Util.* 28, 15–25. doi:10.1016/j.jcou.2018.09.008

White, J. L., Baruch, M. F., Pander, J. E., Hu, Y., Fortmeyer, I. C., Park, J. E., et al. (2015). Light-driven heterogeneous reduction of carbon dioxide: photocatalysts and photoelectrodes. *Chem. Rev.* 115 (23), 12888–12935. doi:10.1021/acs.chemrev.5b00370

Woo, S. J., Choi, S., Kim, S. Y., Kim, P. S., Jo, J. H., Kim, C. H., et al. (2019). Highly selective and durable photochemical CO_2 reduction by molecular Mn(I) catalyst fixed on particular dye-sensitized TiO_2 platform. *ACS Catal.* 9 (3), 2580–2593. doi:10.1021/acscatal.8b03816

Wu, J., Li, X., Shi, W., Ling, P., Sun, Y., Jiao, X., et al. (2018). Efficient visible-light-driven CO_2 reduction mediated by defect-engineered BiOBr atomic layers. *Angew. Chem. Int. Ed.* 130 (28), 8855–8859. doi:10.1002/ange.201803514

Wu, J., Feng, Y., Logan, B. E., Dai, C., Han, X., Li, D., et al. (2019). Preparation of Al–O-Linked porous-g-C_3N_4/TiO_2-nanotube Z-scheme composites for efficient photocatalytic CO_2 conversion and 2,4-dichlorophenol decomposition and mechanism. *ACS Sustain. Chem. Eng.* 7, 15289–15296. doi:10.1021/acssuschemeng.9b02489

Xia, X. H., Jia, Z. J., Yu, Y., Liang, Y., Wang, Z., and Ma, L. L. (2007). Preparation of multi-walled carbon nanotube supported TiO_2 and its photocatalytic activity in the reduction of CO_2 with H_2O. *Carbon* 45 (4), 717–721. doi:10.1016/j.carbon.2006.11.028

Xie, S., Wang, Y., Zhang, Q., Fan, W., Deng, W., and Wang, Y. (2013). Photocatalytic reduction of CO_2 with H_2O: significant enhancement of the activity of Pt-TiO_2 in CH_4 formation by addition of MgO. *Chem. Commun.* 49 (24), 2451–2453. doi:10.1039/c3cc00107e

Xie, S., Wang, Y., Zhang, Q., Deng, W., and Wang, Y. (2014). MgO-and Pt-promoted TiO_2 as an efficient photocatalyst for the preferential reduction of carbon dioxide in the presence of water. *ACS Catal.* 4, 3644–3653. doi:10.1021/cs500648p

Xie, S., Zhang, Q., Liu, G., and Wang, Y. (2016). Photocatalytic and photoelectrocatalytic reduction of CO_2 using heterogeneous catalysts with controlled nanostructures. *Chem. Commun.* 52 (1), 35–59. doi:10.1039/c5cc07613g

Xiong, Z., Wang, H., Xu, N., Li, H., Fang, B., Zhao, Y., et al. (2015). Photocatalytic reduction of CO_2 on Pt^{2+}-Pt^0/TiO_2 nanoparticles under UV/Vis light irradiation: a combination of Pt^{2+} doping and Pt nanoparticles deposition. *Inter. J. Hydrogen Energ.* 40 (32), 10049–10062. doi:10.1016/j.ijhydene.2015.06.075

Xiong, Z., Luo, Y., Zhao, Y., Zhang, J., Zheng, C., and Wu, J. C. S. (2016). Synthesis, characterization and enhanced photocatalytic CO_2 reduction activity of graphene supported TiO_2 nanocrystals with coexposed {001} and {101} facets. *Phys. Chem. Chem. Phys.* 18 (19), 13186–13195. doi:10.1039/c5cp07854g

Xiong, Z., Lei, Z., Chen, X., Gong, B., Zhao, Y., Zhang, J., et al. (2017a). CO_2 photocatalytic reduction over Pt deposited TiO_2 nanocrystals with coexposed {101} and {001} facets: effect of deposition method and Pt precursors. *Catal. Commu.* 96, 1–5. doi:10.1016/j.catcom.2017.03.013

Xiong, Z., Lei, Z., Gong, B., Chen, X., Zhao, Y., Zhang, J., et al. (2017b). A novel reaction mode using H_2 produced from solid-liquid reaction to promote CO_2 reduction through solid-gas reaction. *Catal. Commun.* 89, 4–8. doi:10.1016/j.catcom.2016.10.010

Xiong, Z., Lei, Z., Kuang, C. C., Chen, X., Gong, B., Zhao, Y., et al. (2017c). Selective photocatalytic reduction of CO_2 into CH_4 over Pt-Cu_2O TiO_2 nanocrystals: the interaction between Pt and Cu_2O cocatalysts. *Appl. Catal. B* 202, 695–703. doi:10.1016/j.apcatb.2016.10.001

Xiong, Z., Lei, Z., Li, Y., Dong, L., Zhao, Y., and Zhang, J. (2018). A review on modification of facet-engineered TiO_2 for photocatalytic CO_2 reduction. *J. Photochem. Photobiol. C* 36, 24–47. doi:10.1016/j.jphotochemrev.2018.07.002

Xiong, J., Zhang, M., and Cheng, G. (2020). Facile polyol-triggered anatase-rutile heterophase TiO_{2-x} nanoparticles for enhancing photocatalytic CO_2 reduction. *J. Colloid Interf. Sci.* 579, 872–877. doi:10.1016/j.jcis.2020.06.103

Xu, Q., Yu, J., Zhang, J., Zhang, J., and Liu, G. (2015). Cubic anatase TiO_2 nanocrystals with enhanced photocatalytic CO_2 reduction activity. *Chem. Commun.* 51 (37), 7950–7953. doi:10.1039/c5cc01087j

Xu, F., Meng, K., Cheng, B., Yu, J., and Ho, W. (2018a). Enhanced photocatalytic activity and selectivity for CO_2 reduction over a TiO_2 nanofibre mat using Ag and MgO as bi-cocatalyst. *ChemCatChem* 11, 465–472. doi:10.1002/cctc.201801282

Xu, F., Zhang, J., Zhu, B., Yu, J., and Xu, J. (2018b). $CuInS_2$ sensitized TiO_2 hybrid nanofibers for improved photocatalytic CO_2 reduction. *Appl. Catal. B* 230, 194–202. doi:10.1016/j.apcatb.2018.02.042

Xu, S., and Carter, E. A. (2019). Theoretical insights into heterogeneous (photo) electrochemical CO_2 reduction. *Chem. Rev.* 119, 6631–6669. doi:10.1021/acs.chemrev.8b00481

Yang, G., Chen, D., Ding, H., Feng, J., Zhang, J. Z., Zhu, Y., et al. (2017). Well-designed 3D $ZnIn_2S_4$ nanosheets/TiO_2 nanobelts as direct Z-scheme photocatalysts for CO_2 photoreduction into renewable hydrocarbon fuel with high efficiency. *Appl. Catal. B* 219, 611–618. doi:10.1016/j.apcatb.2017.08.016

Ye, L., Jin, X., Liu, C., Ding, C., Xie, H., Chu, K. H., et al. (2016). Thickness-ultrathin and bismuth-rich strategies for BiOBr to enhance photoreduction of CO_2 into solar fuels. *Appl. Catal. B* 187, 281–290. doi:10.1016/j.apcatb.2016.01.044

You, F., Wan, J., Qi, J., Mao, D., Yang, N., Zhang, Q., et al. (2020). Lattice distortion in hollow multi-shelled structures for efficient visible light CO_2 reduction with

SnS_2/SnO_2 junction. *Angew. Chem. Int. Ed.* 132 (2), 731–734. doi:10.1002/ange.201912069

Yu, J., Low, J., Xiao, W., Zhou, P., and Jaroniec, M. (2014). Enhanced photocatalytic CO_2-reduction activity of anatase TiO_2 by coexposed {001} and {101} facets. *J. Am. Chem. Soc.* 136 (25), 8839–8842. doi:10.1021/ja5044787

Yu, B., Zhou, Y., Li, P., Tu, W., Li, P., Tang, L., et al. (2016). Photocatalytic reduction of CO_2 over Ag/TiO_2 nanocomposites prepared with a simple and rapid silver mirror method. *Nanoscale* 8 (23), 11870–11874. doi:10.1039/c6nr02547a

Zeng, G., Qiu, J., Li, Z., Pavaskar, P., and Cronin, S. B. (2014). CO_2 reduction to methanol on TiO_2-passivated GaP photocatalysts. *ACS Cataly* 4 (10), 3512–3516. doi:10.1021/cs500697w

Zeng, S., Vahidzadeh, E., VanEssen, C. G., Kar, P., Kisslinger, R., Goswami, A., et al. (2020). Optical control of selectivity of high rate CO_2 photoreduction *via* interband- or hot electron Z-scheme reaction pathways in Au-TiO_2 plasmonic photonic crystal photocatalyst. *Appl. Catal. B* 267, 118644. doi:10.1016/j.apcatb.2020.118644

Zhang, B., and Sun, L. (2019). Artificial photosynthesis: opportunities and challenges of molecular catalysts. *Chem. Soc. Rev.* 48, 2216–2264. doi:10.1039/c8cs00897c

Zhang, J., Fu, J., Chen, S., Lv, J., and Dai, K. (2018). 1D carbon nanofibers@TiO_2 core-shell nanocomposites with enhanced photocatalytic activity toward CO_2 reduction. *J. Alloys Compd.* 746, 168–176. doi:10.1016/j.jallcom.2018.02.265

Zhang, L., Cao, H., Pen, Q., Wu, L., Hou, G., Tang, Y., et al. (2018). Embedded CuO nanoparticles@TiO_2-nanotube arrays for photoelectrocatalytic reduction of CO_2 to methanol. *Electrochim. Acta* 283, 1507–1513. doi:10.1016/j.electacta.2018.07.072

Zhang, L., and Jaroniec, M. (2018). Toward designing semiconductor-semiconductor heterojunctions for photocatalytic applications. *Appl. Surf. Sci.* 430, 2–17. doi:10.1016/j.apsusc.2017.07.192

Zhang, L., Cao, H., Lu, Y., Zhang, H., Hou, G., Tang, Y., et al. (2020). Effective combination of $CuFeO_2$ with high temperature resistant Nb-doped TiO_2 nanotube arrays for CO_2 photoelectric reduction. *J. Colloid Interf. Sci.* 568, 198–206. doi:10.1016/j.jcis.2020.01.082

Zhao, H., Zheng, X., Feng, X., and Li, Y. (2018). CO_2 reduction by plasmonic Au nanoparticle-decorated TiO_2 photocatalyst with an ultrathin Al_2O_3 interlayer. *J. Phys. Chem. C* 122, 18949–18956. doi:10.1021/acs.jpcc.8b04239

Zhao, Y., Wei, Y., Wu, X., Zheng, H., Zhao, Z., Liu, J., et al. (2018). Graphene-wrapped Pt/TiO_2 photocatalysts with enhanced photogenerated charges separation and reactant adsorption for high selective photoreduction of CO_2 to CH_4. *Appl. Catal. B* 226, 360–372. doi:10.1016/j.apcatb.2017.12.071

Zhu, S., Liao, W., Zhang, M., and Liang, S. (2019). Design of spatially separated Au and CoO Ziaratidual cocatalysts on hollow TiO_2 for enhanced photocatalytic activity towards the reduction of CO_2 to CH_4. *Chem. Eng. J.* 361, 461–469. doi:10.1016/j.cej.2018.12.095

Ziarati, A., Badiei, A., Luque, R., Dadras, M., and Burgi, T. (2020). Visible light CO_2 reduction to CH_4 using hierarchical yolk@shell $TiO_{2-x}H_x$ modified with plasmonic Au-Pd nanoparticles. *ACS Sustain. Chem. Eng.* 8, 3689–3696. doi:10.1021/acssuschemeng.9b06751

Zubair, M., Kim, H., Razzaq, A., Grimes, C. A., and In, S. I. (2018). Solar spectrum photocatalytic conversion of CO_2 to CH_4 utilizing TiO_2 nanotube arrays embedded with graphene quantum dots. *J. Co_2 Util.* 26, 70–79. doi:10.1016/j.jcou.2018.04.004

Conflict of Interest: The authors declare that the research was conducted in the absence of any commercial or financial relationships that could be construed as a potential conflict of interest.

Copyright © 2021 Li, Teng, Wang and Min. This is an open-access article distributed under the terms of the Creative Commons Attribution License (CC BY). The use, distribution or reproduction in other forums is permitted, provided the original author(s) and the copyright owner(s) are credited and that the original publication in this journal is cited, in accordance with accepted academic practice. No use, distribution or reproduction is permitted which does not comply with these terms.

frontiers in Chemistry

ORIGINAL RESEARCH
published: 28 April 2021
doi: 10.3389/fchem.2021.620017

Iterative Exponential Growth of Oxygen-Linked Aromatic Polymers Driven by Nucleophilic Aromatic Substitution Reactions

*Tyler J. Jaynes[1†], Mona Sharafi[1†], Joseph P. Campbell[1†], Jessica Bocanegra[1], Kyle T. McKay[1], Kassondra Little[1], Reilly Osadchey Brown[1], Danielle L. Gray[2], Toby J. Woods[2], Jianing Li[1] and Severin T. Schneebeli[1]**

[1]Department of Chemistry, University of Vermont, Burlington, VT, United States, [2]George L. Clark X-Ray Facility and 3M Materials Laboratory, University of Illinois at Urbana-Champaign, Urbana, IL, United States

This work presents the first transition metal-free synthesis of oxygen-linked aromatic polymers by integrating iterative exponential polymer growth (IEG) with nucleophilic aromatic substitution (S_NAr) reactions. Our approach applies methyl sulfones as the leaving groups, which eliminate the need for a transition metal catalyst, while also providing flexibility in functionality and configuration of the building blocks used. As indicated by 1) ^{1}H-^{1}H NOESY NMR spectroscopy, 2) single-crystal X-ray crystallography, and 3) density functional theory (DFT) calculations, the unimolecular polymers obtained are folded by nonclassical hydrogen bonds formed between the oxygens of the electron-rich aromatic rings and the positively polarized C–H bonds of the electron-poor pyrimidine functions. Our results not only introduce a transition metal-free synthetic methodology to access precision polymers but also demonstrate how interactions between relatively small, neutral aromatic units in the polymers can be utilized as new supramolecular interaction pairs to control the folding of precision macromolecules.

Keywords: iterative convergent/divergent polymer synthesis, SNAr reactions, nonclassical hydrogen bonding, nuclear magnetic resonance spectroscopy, polymer folding, iterative exponential polymer growth, transition metal-free coupling

OPEN ACCESS

Edited by:
Jie He,
University of Connecticut,
United States

Reviewed by:
Mina Mazzeo,
University of Salerno, Italy
Lingyao Meng,
University of New Mexico,
United States

***Correspondence:**
Severin T. Schneebeli
severin.schneebeli@uvm.edu

†These authors have contributed equally to this work

Specialty section:
This article was submitted to Polymer Chemistry, a section of the journal Frontiers in Chemistry

Received: *21 October 2020*
Accepted: *11 February 2021*
Published: *28 April 2021*

Citation:
Jaynes TJ, Sharafi M, Campbell JP, Bocanegra J, McKay KT, Little K, Osadchey Brown R, Gray DL, Woods TJ, Li J and Schneebeli ST (2021) Iterative Exponential Growth of Oxygen-Linked Aromatic Polymers Driven by Nucleophilic Aromatic Substitution Reactions. Front. Chem. 9:620017. doi: 10.3389/fchem.2021.620017

INTRODUCTION

The backbones of conjugated and heteroatom-linked aromatic polymers tend to possess fewer conformational degrees of freedom than polymers with more flexible aliphatic or partially aliphatic backbones. This reduced amount of conformational freedom can help enhance the folding of aromatic polymers, to advance a variety of useful properties such as selective supramolecular recognition (Goodman et al., 2007; Liu et al., 2015; Otte, 2016; Schneebeli et al., 2016; Adhikari et al., 2017; Xie et al., 2020), selective catalysis (Rajappan et al., 2020; Sharafi et al., 2020), and self-assembly (Cole et al., 2017; Greene et al., 2017; Bonduelle, 2018; Ong and Swager, 2018; Delawder et al., 2019; Zhao et al., 2019). However, while the precise chemical structures, lengths, and sequences of such macromolecules (Dobscha et al., 2019; Gerthoffer et al., 2020; Zhao et al., 2020) dictate their folding, and with it their functionalities and physical properties (Chen et al., 2015; Hanlon et al., 2017), it remains challenging to synthesize polyaromatic structures with precise lengths and/or sequences as

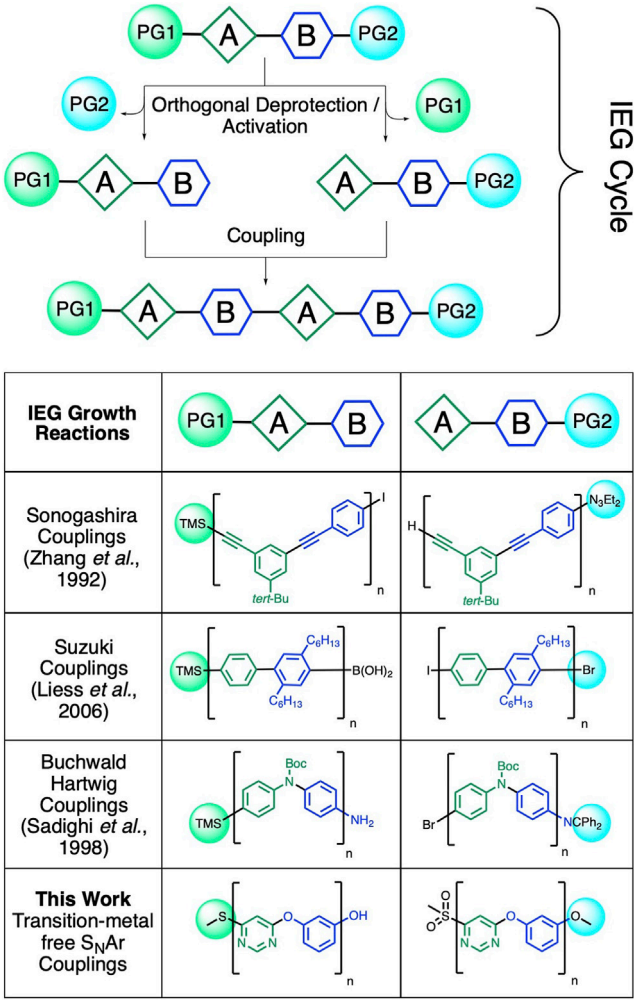

FIGURE 1 | Comparison of previously reported transition metal (TM)-catalyzed IEG methods to our TM-free strategy for the construction of well-defined polyaromatic precision macromolecules. Our approach eliminates the need for transition metal catalysts by introducing methyl sulfones as efficient leaving groups for S_NAr-based IEG processes.

unimolecular entities. One of the most efficient ways to precisely control the length and sequence of synthetic polymers is by iteratively coupling (Jones et al., 1997) polymer strands together in a convergent/divergent fashion (Hawker et al., 1997; Read et al., 2000; Grayson and Frechet, 2001; Li et al., 2005; Liess et al., 2006; Binauld et al., 2011). This methodology (**Figure 1**) is generally referred to as iterative exponential growth (IEG) (Barnes et al., 2015; Leibfarth et al., 2015).

IEG requires a dormant monomer that includes two distinct functionalities, which are orthogonally deprotected/activated for coupling, to afford two reactive species that can be coupled together selectively. These two reactive species are then combined in a chemo-selective manner, resulting in a dormant dimer, which contains, again, protected/masked functionalities identical to the original dormant monomer (**Figure 1**). Repeating this simple protocol results in the creation of architecturally defined structures with an exponential gain in polymer length. The IEG method has been applied extensively to synthesize flexible linear polymers (Barnes et al., 2015; Huang et al., 2017)—for example, *via* copper-catalyzed azide–alkyne click (CuAAC) reactions. However, it still remains a challenge to efficiently utilize arylation chemistry with an IEG-reaction framework, as is required in order to access conjugated or heteroatom-linked polyaromatic polymers with IEG methodology. In particular, while transition metal–catalyzed arylation reactions have been utilized previously to synthesize conjugated and/or heteroatom-linked polyaromatic macromolecules (**Figure 1**), (Zhang et al., 1992; Louie and Hartwig, 1998; Sadighi et al., 1998; Liess et al., 2006), there are (to the best of our knowledge) currently no transition metal-free reactions available to achieve exponential polymer growth for conjugated or heteroatom-linked polyaromatic structures. We are now able to meet this synthetic challenge by marrying iterative exponential polymer growth with nucleophilic aromatic substitution (S_NAr) reactions (Beugelmans et al., 1994; Blaziak et al., 2016; Landovsky et al., 2019) with a unique masking/unmasking technique. Unmasking was achieved by simply oxidizing aromatic sulfides to sulfones—a mild, simple, and scalable reaction well suited for IEG applications. At the same time, the IEG coupling reactions also proceeded under mild conditions (mild heating to ~50°C), which represents an advantage over transition metal–catalyzed alternatives [which tend to require stronger heating (Sadighi et al., 1998)].

Our new synthetic technology for precision polymer growth helps resolve a number of concerns, which exist with traditional, transition metal–catalyzed cross-coupling methodology (Sun and Shi, 2014; Li et al., 2020). These issues include, but are not limited to 1) the inherent toxicity of many transition metal catalysts, which goes hand in hand with the need to accomplish/demonstrate complete removal of any residual transition metal, especially for healthcare-related applications (which can be difficult to achieve with polymers containing many Lewis basic groups like the ones presented in this article), 2) the relatively high cost of the required transition metal catalysts and complex ligands, which are often needed for high-yielding cross-coupling reactions suitable for polymer growth. Transition metal-free cross-coupling protocols like the one presented in this article have the potential to overcome these fundamental challenges associated with transition metal–catalyzed polymer growth.

RESULTS AND DISCUSSION

To implement our sulfide oxidation–driven IEG coupling strategy, we first tested a variety of sulfone leaving groups for their ability to couple with phenolate anions in our IEG scheme (for related work, see: Guan et al., 2015). We discovered that simple methyl sulfones (**Figure 1**) are best suited for this purpose; as with sulfone substituents larger than methyl (e.g., phenyl), we tended to get lower IEG coupling yields. For our synthetic scheme, we decided to protect the phenols with methyl groups (which can readily be removed in high yield with BBr_3). However, it is very likely that instead of just methyl groups, alternative

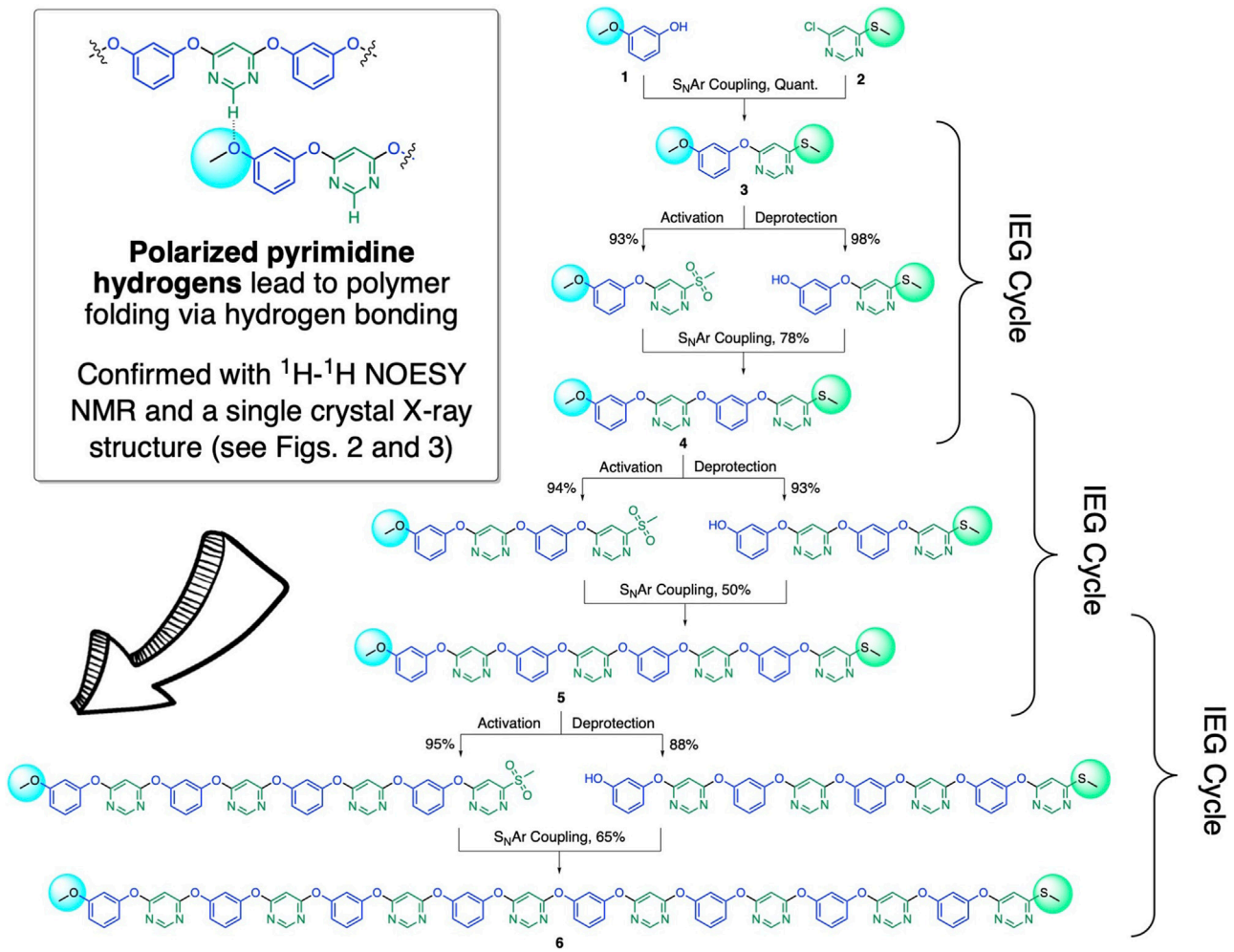

SCHEME 1 | Synthesis of unimolecular polymers with alternating resorcinol and pyrimidine units with S_NAr-based IEG couplings, based on masking/unmasking *via* methyl sulfide to methyl sulfone oxidation. The general reaction conditions for deprotection/activation and IEG coupling are the following: **(i)** Coupling: K_2CO_3, DMF, 60°C, 12 h, room temperature. **(ii)** Deprotection of terminal methoxyl groups to generate nucleophilic phenols: BBr_3, CH_2Cl_2, −78°C to room temperature, 12 h. **(iii)** Activation of methyl sulfides to generate electrophilic methyl sulfones: *m*CPBA, EtOAc, room temperature, 24 h.

phenol protection groups (e.g., benzyl) can also be also be utilized in the future to further enhance the functional group tolerance of our IEG coupling scheme. To start the IEG couplings, we first condensed 3-methoxyphenol (**1**) with 4-chloro-6-(methylthio) pyrimidine (**2**) in quantitative yield under standard S_NAr conditions with K_2CO_3 as the base (Van Rossom et al., 2012). The resulting dimeric product 4-(3-methoxyphenoxy)-6-(methylthio)pyrimidine (**3**) was then split in half for the next IEG deprotection/activation/coupling cycle. The first aliquot was subjected to BBr_3 for methoxyl deprotection, while the second aliquot was activated via oxidization to the methyl sulfone with *m*CPBA. Following these deprotection/activation steps, we were able to perform an S_NAr-based IEG coupling, again in the presence of K_2CO_3 as the base. Ultimately, by iteratively implementing (**Scheme 1**) our new, transition metal-free IEG methodology, we were able to access macromolecules with up to 16 perfectly alternating AB units—where A and B represent resorcinol and pyrimidine rings—for the first time in a fully unimolecular fashion.

We hypothesized that the electron-deficient pyrimidine units in our unimolecular oligomers might be able to promote folding (**Scheme 1**, inset) *via* hydrogen bonding of and/or π-stacking with the electron-rich resorcinol units. To investigate this hypothesis, we grew single crystals suitable for single-crystal X-ray diffraction analysis of compound **3** by slow vapor diffusion of hexanes into ethyl acetate solutions of **3**. The packing observed (**Figures 2A,B**) upon analysis of the diffraction pattern of a single crystal of compound **3** clearly demonstrates the ability of the positively polarized -N=CH-N= hydrogens in the pyrimidine rings to form intermolecular hydrogen bonds with the methoxyl group of another molecule of **3** in the solid state. There are other hydrogen bonding interactions that are weaker, but still significant, that also contribute (**Supplementary Table S1**) to the supramolecular packing of this structure. To estimate the

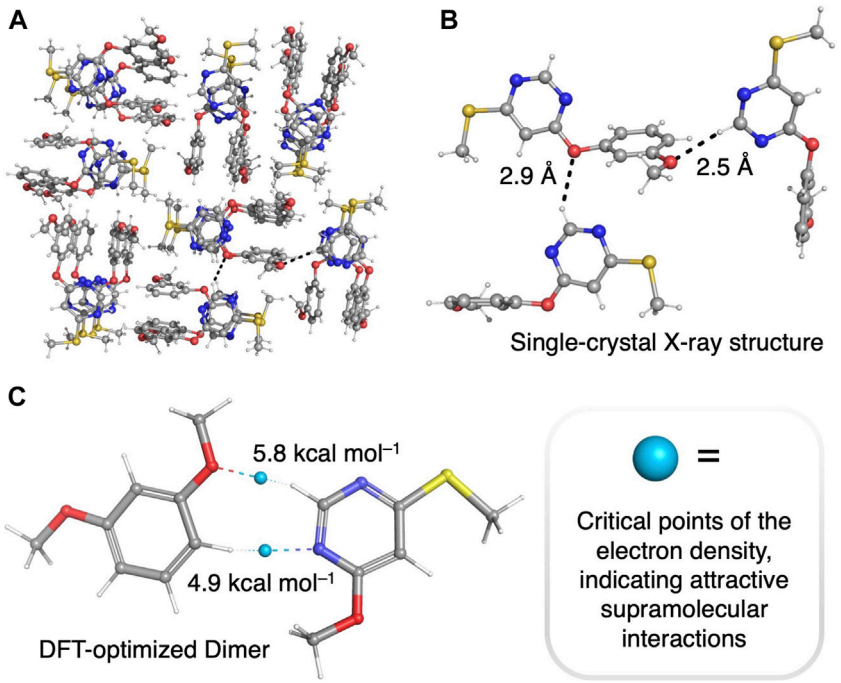

FIGURE 2 | (A, B) Single-crystal X-ray structure of 4-(3-methoxyphenoxy)-6-(methylthio)pyrimidine **(3)**. **(C)** DFT-optimized structure (B3LYP/6-31G** level) of a model hydrogen-bonded dimer, 1,3-dimethoxyphenol in complex with 4-methoxy-6-(methylthio)pyrimidine. NCI critical points of the electron density (calculated at the B3LYP/6-31G** level of theory) are illustrated with blue spheres. Color code: C: gray; H: white; N: blue; O: red; S: yellow.

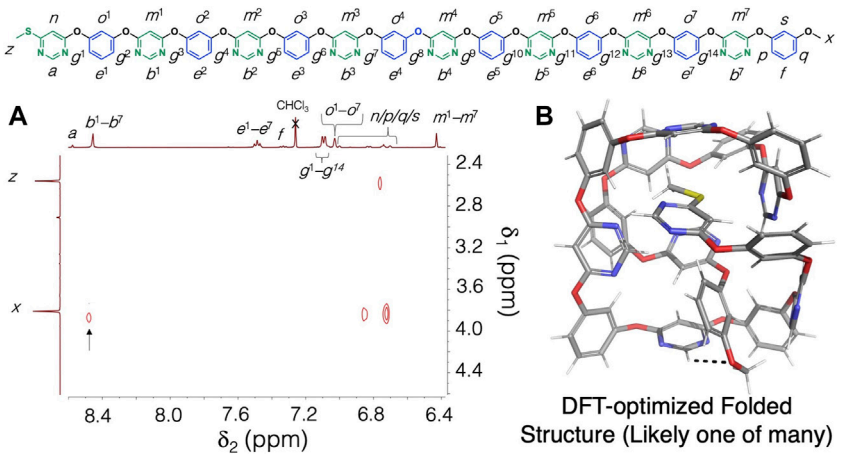

FIGURE 3 | (A) Partial ^{1}H-^{1}H NOESY NMR (500 MHz, $CDCl_3$, 298 K) of the hexadecamer **6**. The key NOE cross peak, which is consistent with polymer folding, is highlighted with an arrow. **(B)** The corresponding model of a potential folded structure of compound **6**. The structure shown represents the lowest energy conformation found with a MacroModel conformational search (OPLS3e force field), which was then refined with a DFT optimization at the B3LYP-D3/6-31G** level of theory.

strength of the [pyrimidine–CH···OCH_3] hydrogen bonds observed in the crystal structure of **3**, we optimized a model dimer—1,3-dimethoxyphenol in complex with 4-methoxy-6-(methylthio)pyrimidine—with density functional theory at the B3LYP (Lee et al., 1988; Becke, 1993)/6-31G** level of theory. Next, we used the noncovalent interactions (NCI) code (Johnson et al., 2010) implemented in the Jaguar (Bochevarov et al., 2013) software package to find all major attractive supramolecular interactions present in our model dimer, characterized as critical points of the electron density. The NCI critical points of the DFT-optimized structure of the model dimer (**Figure 2C**) clearly show the presence of a [pyrimidine–CH···OCH_3] hydrogen bond, with a strength of ~5.8 kcal/mol.

Having established that the pyrimidine rings are attracted to the resorcinol units in the solid state via [CH···O] hydrogen bonding, we next embarked on investigating the ability of the polymer **6**—the longest unimolecular, alternating pyrimidine/resorcinol polymer synthesized to date—to fold, driven by [CH···O] hydrogen bonding interactions. To demonstrate folding, we recorded a ^{1}H-^{1}H NOESY NMR spectrum of the hexadecamer **6** in $CDCl_3$ at 298 K. The ^{1}H-^{1}H NOESY NMR spectrum displays (**Figure 3A**) a NOE cross peak between the proton resonance *x* of the terminal methoxyl group and the -NCHN- proton resonances (b^1–b^7, which all overlap at the same resonance frequency at 8.48 ppm). Notably, this NOE cross peak is absent in the ^{1}H-^{1}H NOESY NMR spectrum of the dimer **3** (**Supplementary Figure S1**), which demonstrates that folding and/or supramolecular aggregation (and not just simply the fact that the proton corresponding to resonance b^7 is present in a pyrimidine ring next to the terminal methoxyl group) is responsible for the observed NOE cross peak. Furthermore, a ^{1}H DOSY NMR spectrum of **6** (**Supplementary Figure S10**) confirmed that the compound does not aggregate significantly in solution, and thus the NOE cross peak observed must be stemming from intramolecular folding of the polymer chains. A folded model of the hexadecamer **6** (optimized with DFT at the B3LYP-D3/6-31G** level) is shown in **Figure 3B**. The structure shown represents the lowest energy conformation obtained from a MacroModel conformational search (carried out without constraints and the OPLS3e force field (Harder et al., 2016) of the hexadecamer **6**. While other potential, folded structures exist, the observed NOE cross peak is consistent with the DFT-optimized structure shown in **Figure 2B**, which shows a [CH···O] hydrogen bonding contact between a pyrimidine CH functionality and the terminal methoxyl group in **6**. For property characterization, we also performed differential scanning calorimetry (DSC) of **6** (see **Supplementary Figure S11** for the DSC thermogram). As **6** is still a relatively low molecular weight compound and fully unimolecular, we did not observe any phase transitions in the temperature range investigated (30–335°C).

Overall, our results demonstrate that methyl sulfones can be effective leaving groups for transition metal-free, iterative exponential growth processes. Furthermore, the electrophilic pyrimidine cores present in our polymers not only help further enhance the yields for the S_NAr-based IEG coupling reactions but also provide polarized C–H bonds, capable of directing the folding of the unimolecular alternating pyrimidine–resorcinol polymers presented in this work.

MATERIALS AND METHODS

General Methods and Materials of Synthesis

All commercially available starting materials were purchased from Sigma-Aldrich, Fisher Scientific, or Oakwood Chemical. Unless noted otherwise, all reagents were used as received without further purification. When needed, dichloromethane (CH_2Cl_2) and dimethylformamide (DMF) were dried using a Glass Contour solvent purification system by SG Water United States, LLC. Removal of solvents was accomplished on a Büchi R-210 rotary evaporator and further concentration was attained under a Fisher Scientific Maxima C-Plus vacuum line. Column chromatography was performed manually with Sorbent grade 60 silica with a mesh size between 230 and 400 using a forced flow of indicated solvents or automatically with a *Teledyne* CombiFlash® Rf+ chromatography system.

All ^{1}H NMR spectra (see: **Supplementary Figures S2, S4, S6, S8**) and ^{13}C (^{1}H) NMR spectra (see: **Supplementary Figures S3, S5, S7, S9**) were recorded on a Bruker ARX 500 (125 MHz) spectrometer, and all ^{1}H-^{1}H NOESY NMR were recorded at 298 K on a Varian Unity Inova 500 (500 MHz) spectrometer. Samples for NMR spectroscopy were dissolved in $CDCl_3$, and the spectra were referenced to the residual solvent peak ($CDCl_3$: 7.26 ppm for ^{1}H and 77.16 ppm for ^{13}C (^{1}H) NMR; or to tetramethylsilane [TMS, 0.00 ppm for ^{1}H and ^{13}C (^{1}H) NMR]) as the internal standard. Chemical shift values were recorded in parts per million (ppm). Data are reported as follows: chemical shift, multiplicity (s = singlet, d = doublet, t = triplet, q = quartet, m = multiplet, and dd = doublet of doublets), coupling constants (Hz), and number of protons. ^{1}H-^{1}H NOESY NMR spectra were acquired with a NOE mixing time of 600 ms. The datasets were processed with MestReNova v10.0.2-15,465 using Bernstein polynomial fits (with a polynomial order of 3) for baseline corrections. The ^{1}H DOSY NMR spectra were acquired on a Varian Unity Inova 500 (500 MHz) spectrometer, equipped with a HCN probe with *Z*-axis gradients, and a Highland Technologies L700 gradient amplifier. The standard DOSY Varian pulse program "Dbppste" was used, with a stimulated echo sequence and bipolar gradient pulse pairs. All experiments were acquired at 25°C, and DOSY spectra were processed/analyzed using Agilent's VnmrJ (version 4.2) software, employing the discrete approach for the inverse Laplace transform in the diffusion dimension. High resolution mass spectra were obtained on a Waters XEVO G2-XS QTof in positive ESI mode. Differential scanning calorimetry (DSC) was performed on a PerkinElmer Pyris 1 differential scanning calorimeter on aluminum plates.

General Synthetic Procedure for the IEG Deprotection/Activation and Coupling Steps

Methoxyl Deprotection: For deprotection of the terminal methoxyl groups, dormant oligomers **3, 4,** and **5** (0.224 mmol) were dissolved in anhydrous CH_2Cl_2 (4 ml) under an atmosphere of dry nitrogen. The reaction mixtures were then cooled to –78°C, and a 1.0 M solution of BBr_3 in CH_2Cl_2 (0.896 mmol of BBr_3) was added dropwise *via* syringe into the stirring solution. Next, the reaction mixtures were allowed to warm to room temperature over the course of ~1 h, stirred at room temperature for an additional 12 h, cooled to 0°C, and finally quenched by adding MeOH (1 ml) and ice chips until fuming ceased. The mixtures were then added to a separatory funnel, and the organic layers were removed. The aqueous layers were extracted with CH_2Cl_2 (3 × 5 ml), and the combined organic layers were dried over anhydrous Na_2SO_4, filtered, and concentrated under reduced pressure to afford the deprotected phenols in 88–98% yield

(see also **Scheme 1**). The free phenols were carried forward for the IEG coupling steps without further purification.

Activation of the Electrophilic Coupling Sites *via* Sulfide Oxidation: Dormant oligomers **3, 4,** and **5** (0.23 mmol) were dissolved in anhydrous EtOAc (4 ml), and a solution of 70% *meta*-chloroperoxybenzoic acid in water (0.92 mmol of *m*CPBA) was added. After stirring for 16 h at room temperature, the reaction mixtures were added to a separatory funnel, the organic layers were washed with a 0.5 N aqueous NaOH solution (5 × 4 ml) and brine (2 × 3 ml). Finally, the organic layers were dried over anhydrous Na_2SO_4, filtered, and concentrated under reduced pressure to afford the electrophilic methyl sulfones in 93–95% yield (see also **Scheme 1**). The activated sulfones were carried forward for the IEG coupling steps without further purification.

Coupling of Active IEG Units: The methyl sulfone oligomers (0.26 mmol) and K_2CO_3 (0.55 mmol) were added to a flame-dried, 5 ml round-bottomed flask under a nitrogen atmosphere, and anhydrous DMF (4 ml) was added. Next, the oligomers with the free phenolic ends (0.18 mmol) were added to the reaction mixtures at room temperature. Afterward, the reaction mixtures were warmed to 40°C and stirred at 40°C for 12 h. Next, the reaction mixtures were diluted with a 0.5 N aqueous HCl solution (5 ml), transferred to a separatory funnel, and extracted with EtOAc (3 × 5 ml). The combined organic phases were washed with brine (3 × 3 ml) and with a 0.5 N aqueous NaOH solution (2 × 3 ml) to ensure that any potentially remaining phenol was removed. Finally, the combined organic layers were dried over anhydrous Na_2SO_4, filtered, and concentrated under reduced pressure. The crude products were purified via flash column chromatography over silica gel (eluent: 0–15% ethyl acetate in hexanes) to afford the coupled IEG products **4, 5,** and **6** in a 48–98% yield (see also **Scheme 1**). For the hexadecameric product **6**, the yield was determined from a quantitative ^{1}H NMR spectrum obtained from the crude reaction mixture (in the presence of dimethyl sulfone as the internal standard for ^{1}H NMR integration) since a significant amount of material was lost during silica column chromatography purification as a result of the reduced solubility of this relatively large oligomer in the purification solvent. In general, we found that reduced solubility in hexanes of the IEG polymers with increasing lengths presented a challenge for purification of the compounds via chromatographic methods, which resulted in variable yields for the purified products.

Single-Crystal X-Ray Crystallography

Single crystals of **3** were grown by slow vapor diffusion of hexanes into ethyl acetate solutions of **3**. Intensity data were collected on a Bruker D8 Venture kappa diffractometer equipped with a Photon II detector. An Iμs microfocus source provided the Mo Kα radiation (λ = 0.71073 A) that was monochromated with multilayer mirrors. The collection, cell refinement, and integration of intensity data were carried out with the APEX3 software (Bruker, 2018). A multi-scan absorption correction was performed with SADABS (Krause et al., 2015). The initial structure solution was solved with the intrinsic phasing methods SHELXT (Sheldrick, 2015b) and refined with the full-matrix least-squares SHELXL (Sheldrick, 2015a) program. The 1 3 5 and -2 5 4 reflections were omitted from the final refinement due to being partially obscured by the beam stop in some orientations.

Crystal data for 3: $C_{12}H_{12}N_2O_2S$, M_r = 248.30, crystal size 0.374 × 0.363 × 0.254 mm^3, monoclinic, space group $P2_1$/n, a = 7.9829(5), b = 14.2529(8), c = 20.6830(11) Å, α = 90°, β = 91.442(2)°, γ = 90°, V = 2352.6(2) Å^3, Z = 8, ρ_{calcd} = 1.402 mg m^{-3}, T = 100 (2) K, $R_1[F^2 > 2\sigma(F^2)]$ = 0.0288, and wR_2 = 0.0790.

Density Functional Theory

All structures were optimized with the Jaguar software package at the B3LYP-D3/6-31G** and B3LYP-D3/6-31G** levels (for the NCI critical point calculations) of theory. NCI critical points of the electron density were calculated with the Jaguar software package at the B3LYP-D3/6-31G** level.

CONCLUSION

This work demonstrates a unique IEG technique, which employs nucleophilic aromatic substitution (S_NAr) reactions as a tool to fabricate architecturally defined oxygen-linked ABAB polymers with a metal-free coupling strategy. The monomers are designed to exhibit both nucleophilic and electrophilic character, either of which can be accessed selectively *via* deprotection of methoxyl groups and *via* oxidation of aromatic sulfides. Integrating S_NAr reactions with iterative exponential growth eliminates the need for expensive transition metal catalysts, which have been required so far in order to carry out iterative exponential growth of conjugated and/or unimolecular, heteroatom-linked aromatic polymers. Our transition metal-free IEG methodology allowed us to access heteroatom-linked, unimolecular aromatic polymers with up to 16 alternating resorcinol and pyrimidine units, enabling us to investigate, for the first time, the [CH···O] hydrogen bond–driven folding of such polymers with single-crystal X-ray crystallography, ^{1}H-^{1}H NOESY NMR spectroscopy, and density functional theory (DFT). Overall, our new IEG methodology advances fundamental capacity to access new unimolecular polymers needed to investigate the diverse physical and electronic properties of heteroatom-linked polyaromatic systems. We are currently applying our new transition metal-free IEG methodology to longer precision polymers with extended solubilizing chains.

DATA AVAILABILITY STATEMENT

The crystal data for the single crystal X-ray structure reported in this paper have been deposited in the Cambridge Crystallographic Data Centre (CCDC: 2036161).

AUTHOR CONTRIBUTIONS

TJ, MS, JC, and SS wrote the article. SS obtained funding for the project. TJ, MS, JC, JB, KM, KL, and RB conducted the experiments. DG and TW solved the crystal structure reported in the article. All authors helped analyze the data and revise the article.

FUNDING

The IEG synthesis of the polymers was supported by the National Science Foundation (Grants CHE-1609137 and CHE-1848444 awarded to SS) as well as by UVM Chemistry, SURF, and Biochemistry undergraduate research fellowship grants awarded to TJ, KL, and ROB. JL was supported by an NSF grant (CHE-1945394) and KM was partially supported by an NIH R01 award (R01GM129431 to JL). The folding studies of the sequence-defined IEG polymers were supported by the Army Research Office (Grant 71015-CH-YIP awarded to SS). The UVM Mass Spectrometry facilities were supported by the National Institutes of Health (Grants S10-OD018126 and P30-GM118228).

ACKNOWLEDGMENTS

We thank B. O'Rourke for high-resolution mass spectrometry and M. DiPinto for help with DSC.

SUPPLEMENTARY MATERIAL

The Supplementary Material for this article can be found online at: https://www.frontiersin.org/articles/10.3389/fchem.2021.620017/full#supplementary-material.

REFERENCES

Adhikari, B., Yamada, Y., Yamauchi, M., Wakita, K., Lin, X., Aratsu, K., et al. (2017). Light-induced unfolding and refolding of supramolecular polymer nanofibres. *Nat. Commun.* 8, 15254. doi:10.1038/ncomms15254

Barnes, J. C., Ehrlich, D. J., Gao, A. X., Leibfarth, F. A., Jiang, Y., Zhou, E., et al. (2015). Iterative exponential growth of stereo- and sequence-controlled polymers. *Nat. Chem.* 7, 810–815. doi:10.1038/nchem.2346

Becke, A. D. (1993). Density-functional thermochemistry. III. The role of exact exchange. *J. Chem. Phys.* 98, 5648–5652. doi:10.1063/1.464913

Beugelmans, R., Singh, G. P., Bois-Choussy, M., Chastanet, J., and Zhu, J. (1994). SNAr-based macrocyclization: an application to the synthesis of vancomycin family models. *J. Org. Chem.* 59, 5535–5542. doi:10.1021/jo00098a010

Binauld, S., Damiron, D., Connal, L. A., Hawker, C. J., and Drockenmuller, E. (2011). Precise synthesis of molecularly defined oligomers and polymers by orthogonal iterative divergent/convergent approaches. *Macromol. Rapid Commun.* 32, 147–168. doi:10.1002/marc.201000548

Blaziak, K., Danikiewicz, W., and Makosza, M. (2016). How does nucleophilic aromatic substitution really proceed in nitroarenes? computational prediction and experimental verification. *J. Am. Chem. Soc.* 138, 7276–7281. doi:10.1021/jacs.5b13365

Bochevarov, A. D., Harder, E., Hughes, T. F., Greenwood, J. R., Braden, D. A., Philipp, D. M., et al. (2013). Jaguar: a high-performance quantum chemistry software program with strengths in life and materials sciences. *Int. J. Quantum Chem.* 113, 2110–2142. doi:10.1002/qua.24481

Bonduelle, C. (2018). Secondary structures of synthetic polypeptide polymers. *Polym. Chem.* 9, 1517–1529. doi:10.1039/c7py01725a

Bruker (2018). *APEX3*. Madison, WI: Bruker AXS, Inc..

Chen, L., Wang, H., Zhang, D. W., Zhou, Y., and Li, Z. T. (2015). Quadruple switching of pleated foldamers of tetrathiafulvalene-bipyridinium alternating dynamic covalent polymers. *Angew. Chem. Int. Ed. Engl.* 54, 4028–4031. doi:10.1002/anie.201410757

Cole, J. P., Hanlon, A. M., Rodriguez, K. J., and Berda, E. B. (2017). Protein-like structure and activity in synthetic polymers. *J. Polym. Sci. Part A: Polym. Chem.* 55, 191–206. doi:10.1002/pola.28378

Delawder, A. O., Natraj, A., Colley, N. D., Saak, T., Greene, A. F., and Barnes, J. C. (2019). Synthesis, self-assembly, and photomechanical actuator performance of a sequence-defined polyviologen crosslinker. *Supramol. Chem.* 31, 523–531. doi:10.1080/10610278.2019.1632453

Dobscha, J. R., Castillo, H. D., Li, Y., Fadler, R. E., Taylor, R. D., Brown, A. A., et al. (2019). Sequence-defined macrocycles for understanding and controlling the build-up of hierarchical order in self-assembled 2D arrays. *J. Am. Chem. Soc.* 141, 17588–17600. doi:10.1021/jacs.9b06410

Gerthoffer, M. C., Wu, S., Chen, B., Wang, T., Huss, S., Oburn, S. M., et al. (2020). 'Sacrificial' supramolecular assembly and pressure-induced polymerization: toward sequence-defined functionalized nanothreads. *Chem. Sci.* 11, 11419–11424. doi:10.1039/D0SC03904G

Goodman, C. M., Choi, S., Shandler, S., and Degrado, W. F. (2007). Foldamers as versatile frameworks for the design and evolution of function. *Nat. Chem. Biol.* 3, 252–262. doi:10.1038/nchembio876

Grayson, S. M., and Fréchet, J. M. (2001). Convergent dendrons and dendrimers: from synthesis to applications. *Chem. Rev.* 101, 3819–3868. doi:10.1021/cr990116h

Greene, A. F., Danielson, M. K., Delawder, A. O., Liles, K. P., Li, X., Natraj, A., et al. (2017). Redox-responsive artificial molecular muscles: reversible radical-based self-assembly for actuating hydrogels. *Chem. Mater.* 29, 9498–9508. doi:10.1021/acs.chemmater.7b03635

Guan, Y., Wang, C., Wang, D., Dang, G., Chen, C., Zhou, H., et al. (2015). Methylsulfone as a leaving group for synthesis of hyperbranched poly(arylene pyrimidine ether)s by nucleophilic aromatic substitution. *RSC Adv.* 5, 12821–12823. doi:10.1039/c5ra00634a

Hanlon, A. M., Martin, I., Bright, E. R., Chouinard, J., Rodriguez, K. J., Patenotte, G. E., et al. (2017). Exploring structural effects in single-chain "folding" mediated by intramolecular thermal Diels-Alder chemistry. *Polym. Chem.* 8, 5120–5128. doi:10.1039/c7py00320j

Harder, E., Damm, W., Maple, J., Wu, C., Reboul, M., Xiang, J. Y., et al. (2016). OPLS3: a force field providing broad coverage of drug-like small molecules and proteins. *J. Chem. Theory Comput.* 12, 281–296. doi:10.1021/acs.jctc.5b00864

Hawker, C. J., Malmström, E. E., Frank, C. W., and Kampf, J. P. (1997). Exact linear analogs of dendritic polyether macromolecules: design, synthesis, and unique properties. *J. Am. Chem. Soc.* 119, 9903–9904. doi:10.1021/ja972027x

Huang, Z., Zhao, J., Wang, Z., Meng, F., Ding, K., Pan, X., et al. (2017). Combining orthogonal chain-end deprotections and thiol-maleimide Michael coupling: engineering discrete oligomers by an iterative growth strategy. *Angew. Chem. Int. Ed. Engl.* 56, 13612–13617. doi:10.1002/anie.201706522

Johnson, E. R., Keinan, S., Mori-Sánchez, P., Contreras-García, J., Cohen, A. J., and Yang, W. (2010). Revealing noncovalent interactions. *J. Am. Chem. Soc.* 132, 6498–6506. doi:10.1021/ja100936w

Jones, L., Schumm, J. S., and Tour, J. M. (1997). Rapid solution and solid phase syntheses of oligo(1,4-phenylene ethynylene)s with thioester termini: molecular scale wires with alligator clips. derivation of iterative reaction efficiencies on a polymer support. *J. Org. Chem.* 62, 1388–1410. doi:10.1021/jo962336q

Krause, L., Herbst-Irmer, R., Sheldrick, G. M., and Stalke, D. (2015). Comparison of silver and molybdenum microfocus X-ray sources for single-crystal structure determination. *J. Appl. Crystallogr.* 48, 3–10. doi:10.1107/S1600576714022985

Landovský, T., Eigner, V., Babor, M., Tichotová, M., Dvořáková, H., and Lhoták, P. (2019). Regioselective S_NAr reaction of the phenoxathiin-based thiacalixarene as a route to a novel macrocyclic skeleton. *Chem. Commun. (Camb)* 56, 78–81. doi:10.1039/c9cc08335a

Lee, C., Yang, W., and Parr, R. G. (1988). Development of the Colle-Salvetti correlation-energy formula into a functional of the electron density. *Phys. Rev. B Condens. Matter* 37, 785–789. doi:10.1103/physrevb.37.785

Leibfarth, F. A., Johnson, J. A., and Jamison, T. F. (2015). Scalable synthesis of sequence-defined, unimolecular macromolecules by Flow-IEG. *Proc. Natl. Acad. Sci. U.S.A.* 112, 10617–10622. doi:10.1073/pnas.1508599112

Li, G., Nieves-Quinones, Y., Zhang, H., Liang, Q., Su, S., Liu, Q., et al. (2020). Transition-metal-free formal cross-coupling of aryl methyl sulfoxides and alcohols via nucleophilic activation of C-S bond. *Nat. Commun.* 11, 2890. doi:10.1038/s41467-020-16713-8

Li, G., Wang, X., and Wang, F. (2005). A novel *in situ* deprotection/coupling and iterative divergent/convergent strategy for the synthesis of oligo(1,4-phenyleneethynylene)s. *Tetrahedron Lett.* 46, 8971–8973. doi:10.1016/j.tetlet.2005.10.113

Liess, P., Hensel, V., and Schlüter, A.-D. (2006). Oligophenylene rods: a repetitive approach. *Eur. J. Org. Chem.* 1996, 1037–1040. doi:10.1002/jlac.199619960703

Liu, X., Weinert, Z. J., Sharafi, M., Liao, C., Li, J., and Schneebeli, S. T. (2015). Regulating molecular recognition with C-shaped strips attained by chirality-assisted synthesis. *Angew. Chem. Int. Ed. Engl.* 54, 12772–12776. doi:10.1002/anie.201506793

Louie, J., and Hartwig, J. F. (1998). The largest discrete oligo(*m*-aniline). An Exponential growth strategy using palladium-catalyzed amination of aryl sulfonates. *Macromolecules* 31, 6737–6739. doi:10.1021/ma981073u

Ong, W. J., and Swager, T. M. (2018). Dynamic self-correcting nucleophilic aromatic substitution. *Nat. Chem.* 10, 1023–1030. doi:10.1038/s41557-018-0122-8

Otte, M. (2016). Size-selective molecular flasks. *ACS Catal.* 6, 6491–6510. doi:10.1021/acscatal.6b01776

Rajappan, S. C., Mccarthy, D. R., Campbell, J. P., Ferrell, J. B., Sharafi, M., Ambrozaite, O., et al. (2020). Selective monofunctionalization enabled by reaction-history-dependent communication in catalytic rotaxanes. *Angew. Chem. Int. Ed. Engl.* 59, 16668. doi:10.1002/anie.202006305

Read, M. W., Escobedo, J. O., Willis, D. M., Beck, P. A., and Strongin, R. M. (2000). Convenient iterative synthesis of an octameric tetracarboxylate-functionalized oligophenylene rod with divergent end groups. *Org. Lett.* 2, 3201–3204. doi:10.1021/ol000204k

Sadighi, J. P., Singer, R. A., and Buchwald, S. L. (1998). Palladium-catalyzed synthesis of monodisperse, controlled-length, and functionalized oligoanilines. *J. Am. Chem. Soc.* 120, 4960–4976. doi:10.1021/ja980052c

Schneebeli, S., Li, J., Sharafi, M., Weinert, Z., Cohen, I., Liao, C., et al. (2016). Controlled self-assembly inside C-shaped polyaromatic strips. *Synlett* 27, 2145–2149. doi:10.1055/s-0035-1561479

Sharafi, M., Mckay, K. T., Ivancic, M., Mccarthy, D. R., Dudkina, N., Murphy, K. E., et al. (2020). Size-selective catalytic polymer acylation with a molecular tetrahedron. *Chem* 6, 1469–1494. doi:10.1016/j.chempr.2020.05.011

Sheldrick, G. M. (2015a). Crystal structure refinement with SHELXL. *Acta Crystallogr. C Struct. Chem.* 71, 3–8. doi:10.1107/S2053229614024218

Sheldrick, G. M. (2015b). SHELXT-integrated space-group and crystal-structure determination. *Acta Crystallogr. A. Found Adv.* 71, 3–8. doi:10.1107/S2053273314026370

Sun, C. L., and Shi, Z. J. (2014). Transition-metal-free coupling reactions. *Chem. Rev.* 114, 9219–9280. doi:10.1021/cr400274j

Van Rossom, W., Caers, J., Robeyns, K., Van Meervelt, L., Maes, W., and Dehaen, W. (2012). (Thio)ureido anion receptors based on a 1,3-alternate oxacalix[2]arene[2]pyrimidine scaffold. *J. Org. Chem.* 77, 2791–2797. doi:10.1021/jo300004p

Xie, J., Li, X., Wang, S., Li, A., Jiang, L., and Zhu, K. (2020). Heteroatom-bridged molecular belts as containers. *Nat. Commun.* 11, 3348. doi:10.1038/s41467-020-17134-3

Zhang, J., Moore, J. S., Xu, Z., and Aguirre, R. A. (1992). Nanoarchitectures. 1. Controlled synthesis of phenylacetylene sequences. *J. Am. Chem. Soc.* 114, 2273–2274. doi:10.1021/ja00032a060

Zhao, W., Qiao, B., Tropp, J., Pink, M., Azoulay, J. D., and Flood, A. H. (2019). Linear supramolecular polymers driven by anion-anion dimerization of difunctional phosphonate monomers inside cyanostar macrocycles. *J. Am. Chem. Soc.* 141, 4980–4989. doi:10.1021/jacs.9b00248

Zhao, W., Tropp, J., Qiao, B., Pink, M., Azoulay, J. D., and Flood, A. H. (2020). Tunable adhesion from stoichiometry-controlled and sequence-defined supramolecular polymers emerges hierarchically from cyanostar-stabilized anion-anion linkages. *J. Am. Chem. Soc.* 142, 2579–2591. doi:10.1021/jacs.9b12645

Conflict of Interest: The authors declare that the research was conducted in the absence of any commercial or financial relationships that could be construed as a potential conflict of interest.

Copyright © 2021 Jaynes, Sharafi, Campbell, Bocanegra, McKay, Little, Osadchey Brown, Gray, Woods, Li and Schneebeli. This is an open-access article distributed under the terms of the Creative Commons Attribution License (CC BY). The use, distribution or reproduction in other forums is permitted, provided the original author(s) and the copyright owner(s) are credited and that the original publication in this journal is cited, in accordance with accepted academic practice. No use, distribution or reproduction is permitted which does not comply with these terms.

frontiers in Chemistry

ORIGINAL RESEARCH
published: 20 July 2021
doi: 10.3389/fchem.2021.593637

Investigation of Nucleation and Growth at a Liquid–Liquid Interface by Solvent Exchange and Synchrotron Small-Angle X-Ray Scattering

*Elyse A. Schriber[1], Daniel J. Rosenberg[2,3], Ryan P. Kelly[1], Anita Ghodsi[1] and J. Nathan Hohman[1]**

[1]Institute of Materials Science and Department of Chemistry, University of Connecticut, Storrs, CT, United States, [2]Molecular Biophysics and Integrated Bioimaging Division, Lawrence Berkeley National Laboratory, Berkeley, CA, United States, [3]Biophysics Group, University of California, Berkeley, Berkeley, CA, United States

Hybrid nanomaterials possess complex architectures that are driven by a self-assembly process between an inorganic element and an organic ligand. The properties of these materials can often be tuned by organic ligand variation, or by swapping the inorganic element. This enables the flexible fabrication of tailored hybrid materials with a rich variety of properties for technological applications. Liquid-liquid interfaces are useful for synthesizing these compounds as precursors can be segregated and allowed to interact only at the interface. Although procedurally straightforward, this is a complex reaction in an environment that is not easy to probe. Here, we explore the interfacial crystallization of mithrene, a supramolecular multi-quantum well. This material sandwiches a well-defined silver-chalcogenide layer between layers of organic ligands. Controlling mithrene crystal size and morphology to be useful for applications requires understanding details of its crystal growth, but the specific mechanism for this reaction remain only lightly investigated. We performed a study of mithrene crystallization at an oil-water interfaces to elucidate how the interfacial free energy affects nucleation and growth. We exchanged the oil solvent on the basis of solvent viscosity and surface tension, modifying the dynamic contact angle and interfacial free energy. We isolated and characterized the reaction byproducts via scanning electron microscopy (SEM). We also developed a high-throughput small angle X-ray scattering (SAXS) technique to measure crystallization at short reaction timescales (minutes). Our results showed that modifying interfacial surface energy affects both the reaction kinetics and product size homogeneity and yield. Our SAXS measurements reveal the onset of crystallinity after only 15 min. These results provide a template for exploring directed synthesis of complex materials via experimental methods.

Keywords: mocha, metal-organic chalcogenolate, self-asssembly, hybrid material, mithrene

OPEN ACCESS

Edited by:
Cristina Leonelli, University of Modena and Reggio Emilia, Italy

Reviewed by:
Dennis Douroumis, University of Greenwich, United Kingdom
Stephan E. Wolf, University of Erlangen-Nuremberg, Germany

***Correspondence:**
J. Nathan Hohman
james.hohman@uconn.edu

Specialty section:
This article was submitted to Solid State Chemistry, a section of the journal Frontiers in Chemistry

Received: *12 August 2020*
Accepted: *27 May 2021*
Published: *20 July 2021*

Citation:
Schriber EA, Rosenberg DJ, Kelly RP, Ghodsi A and Hohman J N (2021) Investigation of Nucleation and Growth at a Liquid–Liquid Interface by Solvent Exchange and Synchrotron Small-Angle X-Ray Scattering. Front. Chem. 9:593637. doi: 10.3389/fchem.2021.593637

INTRODUCTION

The metal-organic chalcogenolates (MOCHas) of coinage metals (Cu, Ag, Au) and simple organic ligands have attracted interest as a class of hybrid nanostructured materials (Dance et al., 1984; Dance and Fisher, 1994; Yeung et al., 2020; Hu et al., 2009; Laibinis et al., 1991; Lavenn et al., 2016) with interesting optoelectronic properties (Veselska et al., 2019; Yan et al., 2017; Mak et al., 2010), mechanochemistry (Jodlowski et al., 2016; Yan et al., 2018), and intrinsic chemical tunability (Cheng

et al., 2014; Kumar et al., 2013). These compounds have properties reminiscent of monolayer materials but express them in their bulk state. Mithrene, silver (I) benzeneselenolate, is a well understood example of this material class. It is a direct gap semiconductor with a large exciton binding energy, that exhibits optical properties similar to transition metal dichalcogenide monolayers like MoS_2 (Chen et al., 2017; Trang et al., 2018; Maserati et al., 2020; Yao et al., 2020). A classic synthetic method for mithrene is nucleation and growth occurring at an oil-water interface, in **Figure 1A** an image of the toluene-water interface and a schematic in **Figure 1B** help illustrate this synthetic environment.

The liquid-liquid interface offers a unique phase boundary for the formation of solid materials, including crystalline materials (Gautam et al., 2004) and low-dimensional organic materials like graphene (Biswas and Drzal, 2009). Biphasic synthesis can be used to grow large (>3 μm) rhombic single crystals, providing a useful way to access complex materials via a straightforward synthetic approach. In our earlier studies, we examined the role of reagent concentration and temperature on its interfacial crystallization (Schriber et al., 2018; Forster et al., 2002) and their role in the assembly of both the target crystals and an amorphous byproduct (Schriber et al., 2018; Popple et al., 2018). These studies focused on modifying external components to the interfacial synthesis, as opposed to affecting the interface itself.

Here, we took inspiration from heterogeneous nucleation studies of aerosol and cloud drop formation at fluid interfaces in the atmosphere (Hienola et al., 2007) and focused our studies on modifying the liquid-liquid interface of this synthesis through solvent exchange. By switching out the organic solvent based on solvent viscosity and surface tension, we were able to establish that changes to the interfacial free energy and even inversion of the organic and aqueous component changes the reaction kinetics and the nucleation and growth process of mithrene. Using temperature reduction, we were able to isolate and identify the amorphous biproduct as the kinetic product, and mithrene as the thermodynamic product of this synthesis. In **Figure 1C**, the trend between temperature increase and decrease can be seen in a graphical image, with temperature on the *y*-axis and incubation time no the *x*-axis. Furthermore, using synchrotron small-angle X-ray scattering, we were able to observe the presence of crystalline mithrene 15 min into the synthesis, which far surpasses the time-resolution of methods like SEM.

METHODS AND MATERIALS

Materials

Silver nitrate (>99%) and diphenyl diselenide (98%) were used as received by Sigma-Aldrich (St. Louis, MO) and TCI America (Portland, OR). Toluene was used as received by EMD Millipore (Hayward, CA). 18.2 MΩ deionized water was supplied by Millipore (Billerica, MA). Glass scintillation vials and Thermo-Fast™ 96-Well Full-Skirted Plates were purchased from Thomas

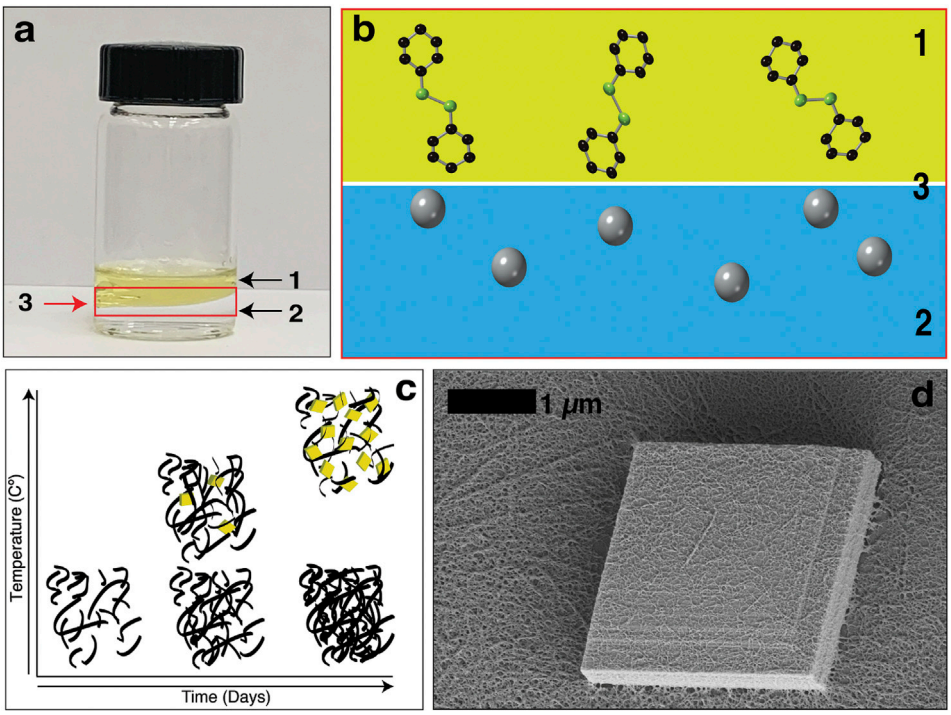

FIGURE 1 | (A) An image of the interfacial synthesis of mithrene. Where (1) is the diphenyl diselenide in toluene layer, (2) is the aqueous silver nitrate layer, and (3) is the oil-water interface. **(B)** Diphenyl diselenide molecules and the silver ions in the aqueous solution at the interface. **(C)** A graph showing that temperature control during the interfacial synthesis can be used to isolate the kinetic and thermodynamic products. **(D)** Scanning electron micrograph of a single mithrene microcrystal, where the layered structure is evident, and the amorphous polymer presence is on the surface of the microcrystal.

Scientific (24-400). Plastic conical 1.5 ml tubes were purchased from Thomas Scientific. Dichloromethane (99.6%) was used as received by Acros Organics. DMSO (99.7%) was used as received by Cambridge Isotope Labs Incorporated. Ethyl acetate (<99.5%) was used as received by Fisher Scientific. Cyclohexane (≥99%) was used as received by Avantor.

Preparation of Silver Benzeneselenolate (Mithrene)

Mithrene is prepared via crystallization at an immiscible liquid-liquid interface, as previously reported (Schriber et al., 2018). Volumetric 3.0 mM solutions of diphenyl diselenide (DPSe) and silver nitrate were prepared in toluene and water, respectively. Immiscible interfaces were obtained by first pipetting 3.0 ml of the aqueous silver nitrate into a 20 ml glass vial. 3 ml of the DPSe solution is gently pipetted onto the aqueous solution. Solutions were capped and allowed to rest on the benchtop for timed intervals. Samples were exposed to normal room lighting.

For the solvent exchange experiments, diphenyl diselenide was suspended in dichloromethane, DMSO, cyclohexane, ethyl acetate, and methyl ethyl ketone to make 3 mM stock solutions. These were pipetted into a 4-dram vial, along with 3 mM aqueous silver nitrate, with the less dense solvent layered on top. Each sample was allowed to incubate at room temperature for 3 days prior to imaging of the interface and harvesting of the product. Harvest was completed using two methods. The interface scooping method, angling the vial and scooping the interface with glass substrate that was rinsed in ethanol and allowed to dry and the dropcast method as detailed below for the time-interval SAXS.

To study crystallization at various time intervals, interfaces were prepared in triplicate and the reaction was quenched at each time interval. Reaction quenching was performed by removal of the aqueous silver nitrate layer via careful pipetting using 10 μL pipette and a 1 ml pipette to prevent breakage of the interface into the silver nitrate layer and product loss. The remaining DPSe solutions were swirled in the glass vial. The crystalline product adheres strongly to the glass, and the remaining DPSe solution was removed by decanting. Glass vials were then placed in a vacuum desiccator for 12 h to ensure that all toluene was removed from the reaction products. The reaction products were then suspended by sonicating for 15 s in 50/50 (v/v) D.I. water/ethanol solvent for SAXS measurements. This suspension was then deposited in a plastic 1.5 ml microtubes, selected as the product has poor adhesion to the plastic. Additional brief sonication was sufficient to keep particles in suspension. For growths under 1 h, suspensions were combined from the products of three reactions (Schriber et al., 2018). While we cannot quantify if there is additional reaction between any residual precursors in the samples after preparation for SAXS measurements, SAXS is a contrast technique and each time point profile will overwhelmingly represent scattering contributions from the most prevalent species. Only in the case of ordered crystal growth will Bragg peaks be observed, allowing us to qualitatively analyze the profiles for presence of crystalline mithrene.

For the cold synthesis, 3 mM of aqueous silver nitrate was added to a 4-dram vial prior to the gentle layering of 3 mM diphenyl diselenide in toluene. The sample was place in a refrigerator at 5°C and allowed to incubate for 3 days. After the allotted time, the product was harvested using the scooping method (Schriber et al., 2018) using silicon substrate.

Scanning Electron Microscopy

Samples were imaged on a Nanoscience instruments Phenom ProX scanning electron microscope at accelerating voltages between 5 and 15 kV. Samples were prepared on a glass substrate unless otherwise indicated.

Transmission Electron Microscopy

Transmission electron microscopy was performed on a ZEISS ULTRA-55 field emission scanning electron microscope in scanning transmission electron microscopy mode at accelerating voltages ranging between 15 and 30 kV. Suspended samples of mithrene prepared via the interfacial method for three days were deposited on a Ted Pella lacey carbon grid.

SAXS Sample Preparation and Data Collection

SAXS data was collected at the SIBYLS beamline (BL12.3.1), at the Advanced Light Source at Lawrence Berkeley National Laboratory, Berkeley, California (Classen et al., 2010). X-ray wavelength was set at $\lambda = 0.127$ nm and the sample-to-detector distance was 2010 mm, resulting in scattering vector q, ranging from 0.1 nm^{-1} to 5 nm^{-1}. The scattering vector is defined as $q = 4\pi\sin\theta/\lambda$, where 2θ is the scattering angle. Data was collected using a Dectris PILATUS3X 2M detector at 20°C and processed as previously described (Dyer et al., 2014). Immediately prior to data collection, samples were deposited into 96-well plates, where three 30 μL samples at each time measurement was bracketed with two 30 μL blank 1:1 v/v D.I. water/ethanol samples. Samples are transferred from the 96-well plate to the X-ray beam by a TECAN liquid handling robot as previously reported(Hura et al., 2009; Dyer et al., 2014). Samples were exposed to the X-ray beam for a total of 30 s and scattering images were collected at a frame rate of 0.5 s for a total of 60 images. Two background samples were collected for each sample to reduce error in subtraction and to ensure that the process was not subject to instrument variations. Each collected image was circularly integrated and normalized for beam intensity to generate a 1-dimensional scattering profile by beamline specific software.

SAXS Data Analysis

The 1-dimensional scattering profile of each sample was background subtracted by each of the two corresponding solvents, producing two sets of background subtracted sample profiles and a third which averaged the two. Profiles were examined for radiation damage. Scattering profiles over the

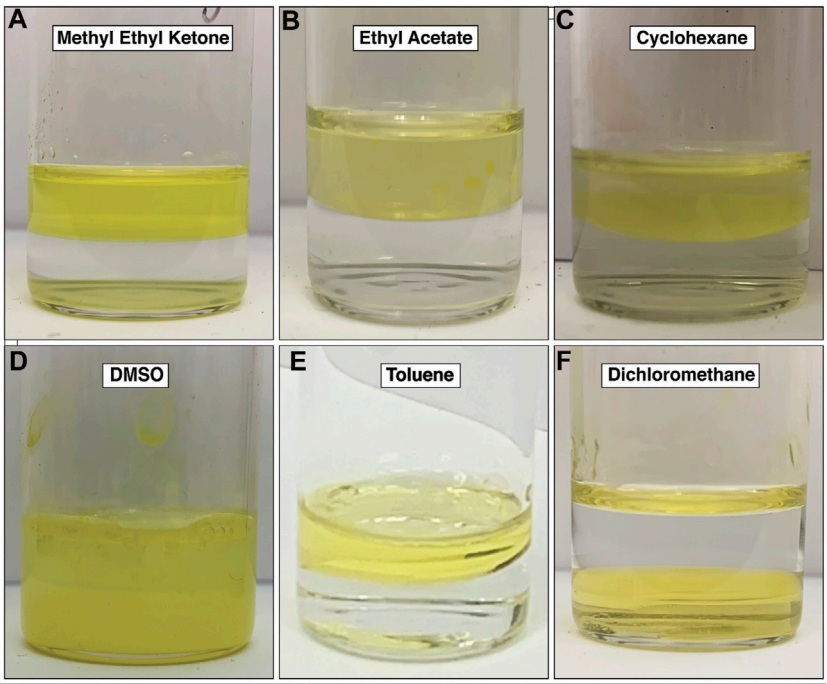

Solvent	Viscosity (cP)	Surface Tension (mN/m)
Methyl Ethyl Ketone	0.40	24.60
Cyclohexane	0.997	24.95
Ethyl Acetate	0.426	23.9
Toluene	0.56	28.53
Dichloromethane	0.43	28.12
DMSO	2.0	43.53

FIGURE 2 | (A)–(F) Images of each interface using different organic solvents. The dichloromethane interface inverted **(F)** and the DMSO interface broke, with product sinking to the bottom of the vial. The toluene interface is also imaged as a frame of reference. Table 1. Each solvent is listed with its literature viscosity in centipoise (cP), and its literature air-liquid surface tension in millinewtons-per-meter (mN/m).

30 s exposure were sequentially averaged together until radiation damage affects were seen to begin changing the scattering curve. Averaging was performed with web-based software FrameSlice (sibyls.als.lbl.gov/ran). Experimental SAXS profiles were analyzed from averaged 1-D data using SCÅTTER (Hura et al., 2009; Rambo and Tainer, 2013) and the Irena (Ilavsky and Jemian, 2009) SAS macros for Igor Pro (Wavemetrics Inc.).

RESULTS AND DISCUSSION

Solvent Exchange and Cold Synthesis

Under standard interfacial environment conditions, 3 days of incubation yields ~1 mg of product total, including both the crystalline mithrene product and the amorphous polymer byproduct. Scanning electron microscopy (SEM) imaging of harvested crystals show significant presence of mithrene crystallites with well-defined edges and standard rhomboidal morphology with the presence of the filamentous polymer. In **Figure 1C**, a high-resolution TEM image shows the polymer coating the surface of a ~2 μm mithrene crystallite, where the step edges are well resolved, and the individual strands of the byproduct can be distinguished. Exchanging out the organic solvent resulted in shifting reaction kinetics, mithrene edge morphology, and overall product yield and size as compared to the toluene synthesis.

The density of dichloromethane is higher than that of water. Using this organic solvent required adding the organic solvent first and then layering the aqueous phase. After three days of

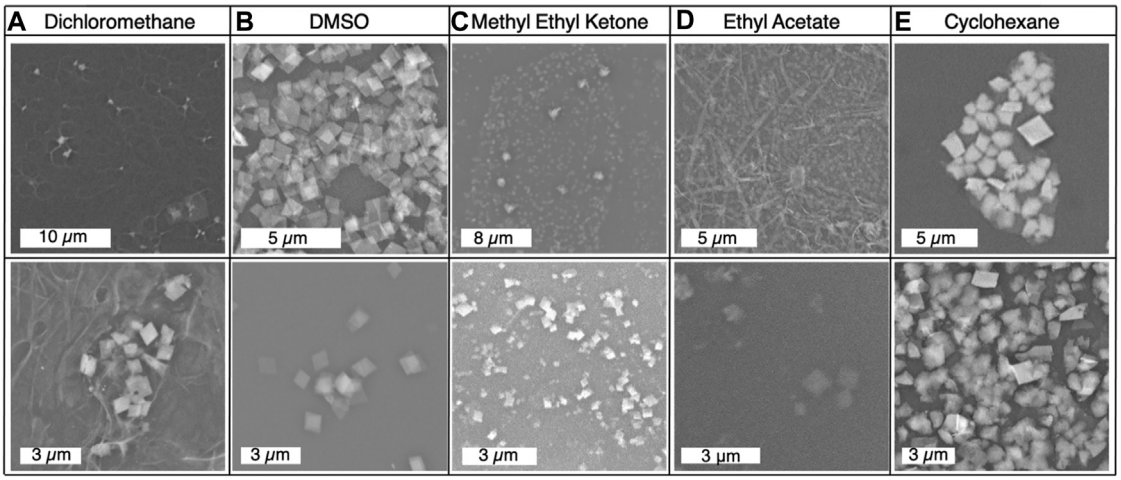

FIGURE 3 | (A)–(E) Scanning electron micrographs of each product from the solvent exchange syntheses, with products imaged from both dropcasted sample and interface harvested sample using the scooping method.

incubation, some of the aqueous phase had become sandwiched in between a thin layer of organic phase on the surface and the majority of the organic phase still on the bottom. In **Figure 2F**, this inversion of the interface can be seen after 3 days of incubation. The resultant product was neither rich in the amorphous byproduct or mithrene crystallites, a "pocket" of byproduct and very thin crystallites was observed under the SEM. **Figure 3A** depicts this pocket of mithrene crystallites with the standard rhomboidal morphology, but very little presence of the polymer byproduct. We attribute this significant loss of product to the fact that only a thin organic phase was present above the aqueous phase, so the lack of diphenyl diselenide precursor to silver nitrate became the limiting factor when harvesting product using the interface scooping method. Using the drop-casting method, where product from the inverted interface was also harvested, also showed minimal presence of crystallites as well, suggesting that inverting the interface changes the interfacial environment enough to reduce product yield and there is synthetic reliance on the organic solvent and precursor being layered on the aqueous phase. DMSO is somewhat miscible in water, therefore, after three days of incubation, diffusion into the aqueous solvent had produced no visible interface, and the majority of the product had aggregated at the bottom of the glass vial. In **Figure 2D**, the broken interface and aggregation at the bottom can be seen. Even with the broken interface, the DMSO synthesis had the highest yield of mithrene crystallites with the classic rhomboidal shape and sharp edges. These crystals were smaller and more homogenous in size, (~1 μm) see **Figure 3B**. This is reminiscent of the mithrene crystals produced using a different solvothermal synthesis with benzeneselenol as the selenium precursor. There was very little presence of the amorphous polymer byproduct. We believe that the slow diffusion of the DMSO into the aqueous layer overtime still allowed for mithrene crystals to form at an interface, but the reducing interfacial surface tension caused the polymer raft to break and the products then sunk to the bottom of the vial.

Methyl ethyl ketone produced an interface with the aqueous layer that had the flattest meniscus, comparative to the other solvents that produced an interface, see **Figure 2A**. This synthesis yielded very small mithrene crystallites (>500 nm), compared to the toluene synthesis, embedded in the amorphous polymer product. The interface between the ethyl acetate and the aqueous layer had a more curved meniscus, and an exceptionally small quantity of mithrene was recovered, see **Figures 2B**, **3D** for reference. The amorphous polymer was favored, and its diameter was thicker and more rod-like than prior syntheses. Some exceptionally thin mithrene crystals were observed after dropcasting, shown in figure **Figure 3D** (bottom). The meniscus between cyclohexane and the aqueous layer has the most curvature, shown in **Figure 2C**. At the interface, there was less mithrene present than DMSO, and these crystals, while stoichiometrically the same as mithrene, had different morphologies. In **Figure 3E**, there are some thick classic mithrene crystals, surrounded by small immature or misshapen mithrene crystals, the smaller crystals do not have sharp edges and have heterogenous morphologies with both thin and thick areas on individual crystals.

The cold synthesis was performed to identify whether the amorphous polymer or the mithrene crystallites were the thermodynamic or kinetic product of the reaction. Under room temperature conditions, after 3 days, there is presence of both mithrene and the amorphous polymer, so differentiating between the two requires removal of energy. After three days of incubation in a 4°C environment, there is no presence of mithrene crystallites, and instead a heavy coating of the amorphous polymer, that adopts a more rigid rod-like morphology. In

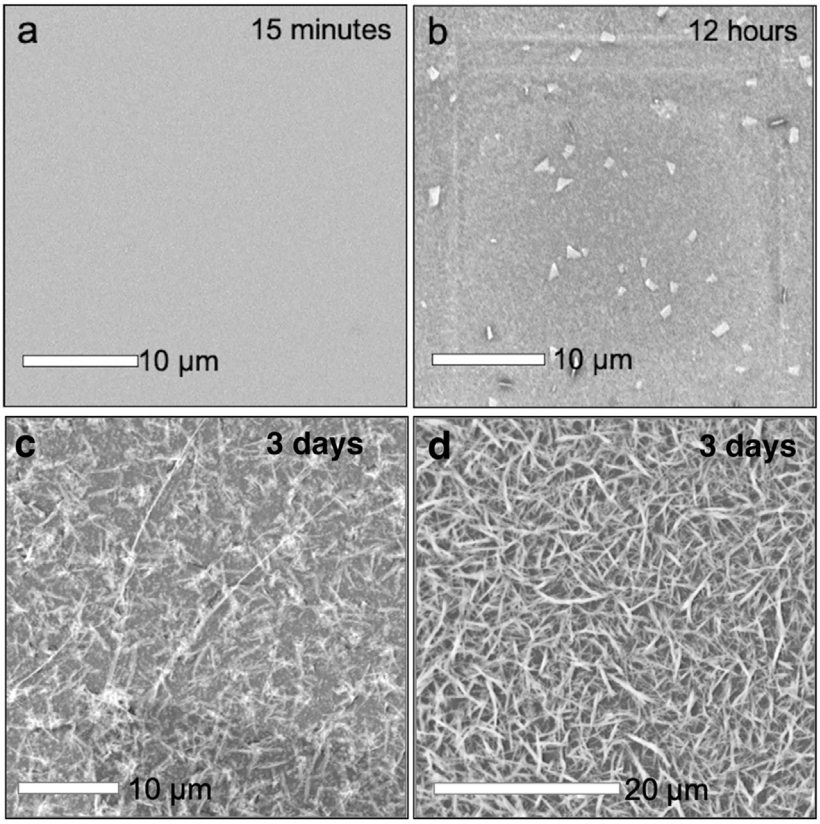

FIGURE 4 | (A)–(D) Scanning electron micrographs of early stage mithrene synthesis, where at 15 min of growth, samples that were dropcasted onto substrate show no presence of mithrene or polymer product. At 12 h of growth, there are immature crystals present, a result of the quenching the reaction and subsequent dropcasting. In comparison is the cold synthesis, where at three days of incubation at 5°C, there is no mithrene presence and a thick coating of the amorphous polymer product.

Figures 4A–D comparison of 12 h of incubation time at room temperature vs. 3 days in 4°C shows that mithrene crystals do not grow in cold temperatures, but the polymer product grows in abundance. This is significant evidence that points toward the mithrene product being the thermodynamic product and the polymer, the kinetic product. It also provides a method for isolating the polymer byproduct.

Small-Angle X-Ray Scattering of Mithrene

In order to detect the presence of early time-stage synthetic products, a synchrotron-based SAXS source was used (Classen et al., 2013) which minimizes background and produces high intensity scattering. This instrument provided the resolution to detect the presence of the highest intensity (002) diffraction peak of mithrene in the SAXS profiles at extremely low concentrations and early synthetic time points. Unlike diffraction techniques, where interatomic distances between atoms in a crystal lattice are derived from light scattering by using the Bragg equation, scattering from amorphous or semi-crystalline polymers is described in terms of electron density at a point in reciprocal space. The information in a SAXS profile can include d-spacing from larger spaces between lattices, but also includes scattering from any electron density seen by the X-ray beam and is described by the magnitude of the scattering wavevector.

Mithrene has a diffraction peak corresponding to the (002) crystallographic plane that appears at 4.4 nm^{-1} or at a d-spacing of 1.46 nm. This lattice spacing is observed in the SAXS regime of reciprocal space. Despite the random orientation of suspended crystallites, they will diffract to high intensity. Solution methods allow for concentrating of the early phase products, therefore the possibility of crystallites being seen via solution SAXS is much higher than that of GIWAXS, where only one reaction can be probed per thin film.

Using the quenching method as described in the experimental section, the reaction was stopped at different time points starting with 5 min, 15 min, 1 h, and then hourly until 24 h into the synthesis. Taking advantage of the high-throughput SAXS endstation (Hura et al., 2009), that allowed for rapid data collection from a large number of samples, we were able to collect data on all time points within an hour. After 15 min, a broad diffraction peak was present at 4.4 nm^{-1} in all sample SAXS profiles with sufficient sample concentration to produce adequate scattering profiles.

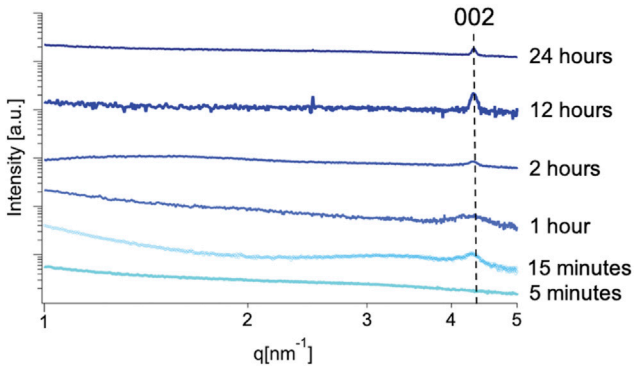

FIGURE 5 | Solution SAXS profiles of early stage mithrene samples from 5 min to 24 h. Each profile has been normalized to intensity. Qualitatively, the profiles in the lower q regime differ significantly. This could be attributed to aggregation of sample in solution, as non-ideal solution was used and samples from early time scales will have less product presence. This difference could also be attributed to the size heterogeneity of the polymer product in solution.

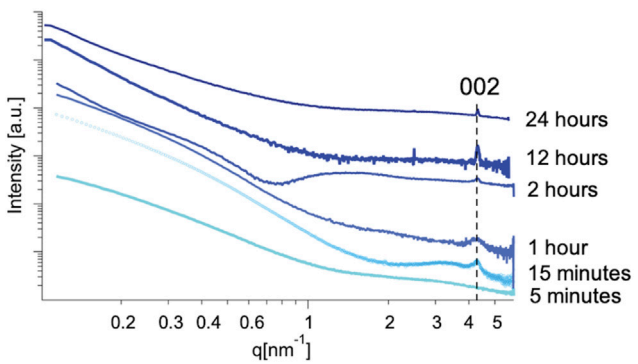

FIGURE 6 | Cropped SAXS profiles of mithrene grown for 5 min, 15 min, 12-h, and 24 h. The 15-min profile shows a broad Bragg peak at 4.4 nm^{-1} which corresponds well with the known interlayer spacing of mithrene crystallites and the (002) crystallographic plane, the 24-h profile shows a sharper peak also corresponding with the (002) crystallographic plane, as well as the 12-h profile and the 5-min profile shows a complete absence of the peak.

In the case of our experiment, we were able to trace the emergence of crystalline order to <15 min using this method, where a broad peak at 4.4 nm^{-1} corresponding with the (002) crystallographic plane of the mithrene unit cell (Cuthbert et al., 2002; Schriber et al., 2018) appears in solutions from reactions quenched after 15 min of growth, but is not present in profiles from 5 min of growth, see **Figures 5**, **6**. In each SAXS profile, we have contributions from both the amorphous polymer and the crystalline mithrene phase, thus producing a distribution of experimental intensities throughout each scattering profile. In earlier time points (**Figure 5**), where the mithrene (002) peak is either not present or is very broad and low intensity, the scattering profile is dominated by the amorphous polymer that can form clusters with significant size polydispersity and different spatial configurations. In order to obtain structural information from these SAXS profiles, determination of the scattering origins and developing a method for interpreting the scattering is essential. While past efforts by Vonk and Kortleve (1967), Vonk (1973) and recently, Li et al. (2019) have been successful at developing SAXS models for similar polymer systems, deconvoluting and modeling scattering contributions from both the mithrene system and the amorphous polymer is challenging and beyond the scope of this manuscript. Otherwise, overall intensity is dependent on concentration, which was not quantified during this experiment, but does not alter the location of a diffraction peak.

CONCLUSION

Biphasic conditions present a difficult environment for performing *in-situ* experiments, where recreating conditions can often be plagued with environmental variables that are incompatible with standard methods. The reaction involves the organization of components into structurally well-defined aggregates (Huie, 2003). In many systems, it is both impractical and impossible to change the parameters that determine the behavior of the system and this makes studying each component's role in the formation of the aggregates difficult (Whitesides and Grzybowski, 2002). While modeling provides the best analysis at the interface, it is also time-consuming and computationally expensive, especially when multiple phases are present. Altering solvent viscosity and the interfacial surface tension provides a tool for studying some aspects of the interfacial environment without having to resort to such methods. We determined that mithrene interfacial synthesis itself is robust but that changes to the interfacial environment will change the product yield, the reaction kinetics and the ratio between the polymer product and mithrene crystallites. The cold synthesis allowed us to identify the kinetic and thermodynamic products in the reaction and provided a useful synthetic method for isolating the two products of this reaction for individual analysis, something that had not been possible prior. The SAXS analysis provided a useful tool for observing the early-stage crystal product of the mithrene synthesis using the standard toluene-water interface. While it is difficult to quantify whether or not additional reorganization of the samples occurred between reaction quenching and placement in the X-ray beam, this was deemed unnecessary as a contrast technique like SAXS produces scattering from the most prevalent phase in the sample, and the location of the Bragg peak observed matches literature values for mithrene. The *ex-situ* approach presented that utilizes the high-throughput SAXS pipeline allows for analysis of large numbers of samples at multiple time points to be characterized. *In-situ* observation of crystal growth at the liquid-liquid interface is feasible using synchrotron sources and will be a future area of study for these systems.

DATA AVAILABILITY STATEMENT

Publicly available datasets were analyzed in this study. This data can be found here: https://www.ccdc.cam.ac.uk/structures Cambridge Crystallographic Data Centre 186570.

AUTHOR CONTRIBUTIONS

The experiments were conceived and designed by ES and JH and were executed and analyzed by ES., DR., RK., AG, and JH. Experiments at the synchrotron were performed by DR and ES and the data analyzed by ES. Imaging was performed by JH, RK, and AG. The manuscript was written through contributions from all authors.

FUNDING

Work at Beamline 12.3.1 of the ALS was supported through the Integrated Diffraction Analysis Technologies (IDAT) program, supported by DOE Office of Biological and Environmental Research. Additional support comes from a High-End Instrumentation Grant S10OD018483.

ACKNOWLEDGMENTS

Work at the Molecular Foundry was supported by the Office of Science, Office of Basic Energy Sciences, of the U.S. Department of Energy under Contract DE-AC02-05CH11231. Work at Beamline 12.3.1 of the Advanced Light Source, a U.S. DOE Office of Science User Facility under Contract No. DE-AC02-05CH11231 is supported in part by the ALS-ENABLE program funded by the National Institutes of Health, National Institute of General Medical Sciences, grant P30 GM124169-01. The authors would like to thank Derek Popple for experimental support.

SUPPLEMENTARY MATERIAL

The Supplementary Material for this article can be found online at: https://www.frontiersin.org/articles/10.3389/fchem.2021.593637/full#supplementary-material.

REFERENCES

Biswas, S., and Drzal, L. T. (2009). A Novel Approach to Create a Highly Ordered Monolayer Film of Graphene Nanosheets at the Liquid–Liquid Interface. *Nano Lett.* 9, 167–172. doi:10.1021/nl802724f

Chen, Y.-C., Lu, A.-Y., Lu, P., Yang, X., Jiang, C.-M., and Mariano, M. (2017). Structurally Deformed MoS2 for Electrochemically Stable, Thermally Resistant, and Highly Efficient Hydrogen Evolution Reaction. *Adv. Mater.* 29, 1703863. doi:10.1002/adma.201703863

Cheng, R., Jiang, S., Chen, Y., Liu, Y., Weiss, N., and Cheng, H.-C. (2014). Few-layer Molybdenum Disulfide Transistors and Circuits for High-Speed Flexible Electronics. *Nat. Commun.* 5, 5143. doi:10.1038/ncomms6143

Classen, S., Hura, G. L., Holton, J. M., Rambo, R. P., Rodic, I., and McGuire, P. J. (2013). Implementation and Performance of SIBYLS: a Dual Endstation Small-Angle X-ray Scattering and Macromolecular Crystallography Beamline at the Advanced Light Source. *J. Appl. Crystallogr.* 46, 1–13. doi:10.1107/S0021889812048698

Classen, S., Rodic, I., Holton, J., Hura, G. L., Hammel, M., and Tainer, J. A. (2010). Software for the High-Throughput Collection of SAXS Data Using an Enhanced Blu-Ice/DCS Control System. *J. Synchrotron Radiat.* 17, 774–781. doi:10.1107/S0909049510028566

Cuthbert, H. L., Wallbank, A. I., Taylor, N. J., and Corrigan, J. F. (2002). Synthesis and Structural Characterization of $[Cu_{20}Se_4(\mu_3\text{-SePh})(PPh_3)_6]$ and $[Ag(SePh)]\infty$. *Z. Für Anorg. Allg. Chem.* 628, 2483–2488. doi:10.1002/1521-3749(200211)628:11<2483::AID-ZAAC2483>3.0.CO;2-U

Dance, I., and Fisher, K. (1994). Metal Chalcogenide Cluster Chemistry. *Met. Chalcogenide Clust. Chem.* 41, 637–803.

Dance, I. G., Choy, A., and Scudder, M. L. (1984). Syntheses, Properties, and Molecular and crystal Structures of $(Me_4N)_{44}[E_4M_{10}(SPh)_{16}]$ (E=S, Se; M=Zn, Cd): Molecular Supertetrahedral Fragments of the Cubic Metal Chalcogenide Lattice. *J. Am. Chem. Soc.* 106, 6285–6295. doi:10.1021/ja00333a030

Dyer, K. N., Hammel, M., Rambo, R. P., Tsutakawa, S. E., Rodic, I., and Classen, S. (2014). "High-Throughput SAXS for the Characterization of Biomolecules in Solution: A Practical Approach," in *In* Structural Genomics: General Applications *Methods in Molecular Biology*. Editor Y. W. Chen (Totowa, NJ: Humana Press), 245–258. doi:10.1007/978-1-62703-691-7_18

Forster, P. M., Thomas, P. M., and Cheetham, A. K. (2002). Biphasic Solvothermal Synthesis: A New Approach for Hybrid Inorganic–Organic Materials. *Chem. Mater.* 14, 17–20. doi:10.1021/cm010820q

Gautam, U. K., Ghosh, M., and Rao, C. N. R. (2004). Template-Free Chemical Route to Ultrathin Single-Crystalline Films of CuS and CuO Employing the Liquid–Liquid Interface. *Langmuir* 20, 10775–10778. doi:10.1021/la048040u

Hienola, A. I., Winkler, P. M., Wagner, P. E., Vehkamäki, H., Lauri, A., and Napari, I. (2007). Estimation of Line Tension and Contact Angle from Heterogeneous Nucleation Experimental Data. *J. Chem. Phys.* 126, 094705. doi:10.1063/1.2565769

Hu, L., Zhang, Z., Zhang, M., Efremov, M. Y., Olson, E. A., and de la Rama, L. P. (2009). Self-Assembly and Ripening of Polymeric Silver–Alkanethiolate Crystals on Inert Surfaces. *Langmuir* 25, 9585–9595. doi:10.1021/la900898r

Huie, J. C. (2003). Guided Molecular Self-Assembly: a Review of Recent Efforts. *Smart Mater. Struct.* 12, 264–271. doi:10.1088/0964-1726/12/2/315

Hura, G. L., Menon, A. L., Hammel, M., Rambo, R. P., Poole, F. L., II, and Tsutakawa, S. E. (2009). Robust, High-Throughput Solution Structural Analyses by Small Angle X-ray Scattering (SAXS). *Nat. Methods* 6, 606–612. doi:10.1038/nmeth.1353

Ilavsky, J., and Jemian, P. R. (2009). Irena: Tool Suite for Modeling and Analysis of Small-Angle Scattering. *J. Appl. Crystallogr.* 42, 347–353. doi:10.1107/S0021889809002222

Jodlowski, A. D., Yépez, A., Luque, R., Camacho, L., and de Miguel, G. (2016). Benign-by-Design Solventless Mechanochemical Synthesis of Three-, Two-, and One-Dimensional Hybrid Perovskites. *Angew. Chem. Int. Ed.* 55, 14972–14977. doi:10.1002/anie.201607397

Kumar, R., Jayaramulu, K., Kumar Maji, T., and Rao, C. N. R. (2013). Hybrid Nanocomposites of ZIF-8 with Graphene Oxide Exhibiting Tunable Morphology, Significant CO 2 Uptake and Other Novel Properties. *Chem. Commun.* 49, 4947–4949. doi:10.1039/C3CC00136A

Laibinis, P. E., Whitesides, G. M., Allara, D. L., Tao, Y. T., Parikh, A. N., and Nuzzo, R. G. (1991). Comparison of the Structures and Wetting Properties of Self-Assembled Monolayers of N-Alkanethiols on the Coinage Metal Surfaces, Copper, Silver, and Gold. *J. Am. Chem. Soc.* 113, 7152–7167. doi:10.1021/ja00019a011

Lavenn, C., Guillou, N., Monge, M., Podbevšek, D., Ledoux, G., and Fateeva, A. (2016). Shedding Light on an Ultra-bright Photoluminescent Lamellar Gold Thiolate Coordination Polymer [Au(p-SPhCO2Me)]n. *Chem. Commun.* 52, 9063–9066. doi:10.1039/C5CC10448C

Li, X.-Y., Ding, J.-J., Liu, Y.-P., and Tian, X.-Y. (2019). A New Small-Angle X-ray Scattering Model for Polymer Spherulites with a Limited Lateral Size of the Lamellar Crystals. *IUCrJ* 6, 968–983. doi:10.1107/S2052252519011035

Mak, K. F., Lee, C., Hone, J., Shan, J., and Heinz, T. F. (2010). Atomically Thin MoS_2: A New Direct-Gap Semiconductor. *Phys. Rev. Lett.* 105, 136805. doi:10.1103/PhysRevLett.105.136805

Maserati, L., Refaely-Abramson, S., Kastl, C., Chen, T., Borys, C., J., and Eisler, C. N. (2020). Anisotropic 2D Excitons Unveiled in Organic–Inorganic Quantum wells. *Mater. Horiz.* 8 (1), 197–208. doi:10.1039/C9MH01917K

Popple, D. C., Schriber, E. A., Yeung, M., and Hohman, J. N. (2018). Competing Roles of Crystallization and Degradation of a Metal-Organic Chalcogenolate Assembly under Biphasic Solvothermal Conditions. *Langmuir* 34 (47), 14265–14273. doi:10.1021/acs.langmuir.8b03282

Rambo, R. P., and Tainer, J. A. (2013). Accurate Assessment of Mass, Models and Resolution by Small-Angle Scattering. *Nature* 496, 477–481. doi:10.1038/nature12070

Schriber, E. A., Popple, D. C., Yeung, M., Brady, M. A., Corlett, S. A., and Hohman, J. N. (2018). Mithrene Is a Self-Assembling Robustly Blue Luminescent Metal–Organic Chalcogenolate Assembly for 2D Optoelectronic Applications. *ACS Appl. Nano Mater.* 1, 3498–3508. doi:10.1021/acsanm.8b00662

Trang, B., Yeung, M., Popple, D. C., Schriber, E. A., Brady, M. A., and Kuykendall, T. R. (2018). Tarnishing Silver Metal into Mithrene. *J. Am. Chem. Soc.* 140 (42), 13892–13903. doi:10.1021/jacs.8b08878

Veselska, O., Dessal, C., Melizi, S., Guillou, N., Podbevšek, D., and Ledoux, G. (2019). New Lamellar Silver Thiolate Coordination Polymers with Tunable Photoluminescence Energies by Metal Substitution. *Inorg. Chem.* 58, 99–105. doi:10.1021/acs.inorgchem.8b01257

Vonk, C. G. (1973). Investigation of Non-ideal Two-phase Polymer Structures by Small-Angle X-ray Scattering. *J. Appl. Crystallogr.* 6, 81–86. doi:10.1107/S0021889873008204

Vonk, C. G., and Kortleve, G. (1967). X-ray Small-Angle Scattering of Bulk Polyethylene. *Kolloid-z. Z. Für Polym.* 220, 19–24. doi:10.1007/BF02086052

Whitesides, G. M., and Grzybowski, B. (2002). Self-Assembly at All Scales. *Science* 295, 2418–2421. doi:10.1126/science.1070821

Yan, H., Hohman, J. N., Li, F. H., Jia, C., Solis-Ibarra, D., and Wu, B. (2017). Hybrid Metal–Organic Chalcogenide Nanowires with Electrically Conductive Inorganic Core through Diamondoid-Directed Assembly. *Nat. Mater.* 16, 349–355. doi:10.1038/nmat4823

Yan, H., Yang, F., Pan, D., Lin, Y., Hohman, J. N., and Solis-Ibarra, D. (2018). Sterically Controlled Mechanochemistry under Hydrostatic Pressure. *Nature* 554, 505–510. doi:10.1038/nature25765

Yao, K., Collins, M. S., Nell, K. M., Barnard, E. S., Borys, N. J., and Kuykendall, T. (2020). Strongly Quantum-Confined Blue-Emitting Excitons in Chemically Configurable Multiquantum Wells. *ACS Nano* 15 (3), 4085–4092. doi:10.1021/acsnano.0c08096

Yeung, M., Popple, D. C., Schriber, E. A., Teat, S. J., Beavers, C. M., and Demessence, A. (2020). Corrosion of Late- and Post-Transition Metals into Metal–Organic Chalcogenolates and Implications for Nanodevice Architectures. *ACS Appl. Nano Mater.* 3, 3568–3577. doi:10.1021/acsanm.0c00057

Conflict of Interest: The authors declare that the research was conducted in the absence of any commercial or financial relationships that could be construed as a potential conflict of interest.

Copyright © 2021 Schriber, Rosenberg, Kelly, Ghodsi and Hohman. This is an open-access article distributed under the terms of the Creative Commons Attribution License (CC BY). The use, distribution or reproduction in other forums is permitted, provided the original author(s) and the copyright owner(s) are credited and that the original publication in this journal is cited, in accordance with accepted academic practice. No use, distribution or reproduction is permitted which does not comply with these terms.

Frontiers in Chemistry

Explores all fields of chemical science across the periodic table

Advances our understanding of how atoms, ions, and molecules come together and come apart. It explores the role of chemistry in our everyday lives - from electronic devices to health and wellbeing.

Discover the latest Research Topics

See more →

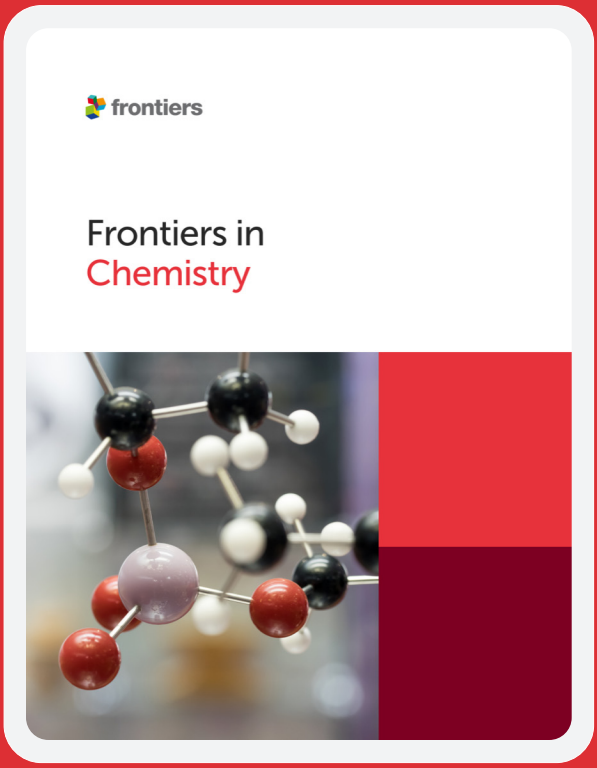

Frontiers

Avenue du Tribunal-Fédéral 34
1005 Lausanne, Switzerland
frontiersin.org

Contact us

+41 (0)21 510 17 00
frontiersin.org/about/contact